

# Axiomatic Design and Fabrication of Composite Structures

*Applications in Robots,  
Machine Tools, and  
Automobiles*

**Dai Gil Lee  
Nam Pyo Suh**

**OXFORD**  
UNIVERSITY PRESS

2006



Oxford University Press, Inc., publishes works that further  
Oxford University's objective of excellence  
in research, scholarship, and education.

Auckland Cape Town Dar es Salaam Hong Kong Karachi  
Kuala Lumpur Madrid Melbourne Mexico City Nairobi  
New Delhi Shanghai Taipei Toronto

With offices in  
Argentina Austria Brazil Chile Czech Republic France Greece  
Guatemala Hungary Italy Japan Poland Portugal Singapore  
South Korea Switzerland Thailand Turkey Ukraine Vietnam

Copyright © 2006 by Oxford University Press, Inc.

Published by Oxford University Press, Inc.  
198 Madison Avenue, New York, New York 10016

[www.oup.com](http://www.oup.com)

Oxford is a registered trademark of Oxford University Press

All rights reserved. No part of this publication may be reproduced,  
stored in a retrieval system, or transmitted, in any form or by any means,  
electronic, mechanical, photocopying, recording, or otherwise,  
without the prior permission of Oxford University Press.

Library of Congress Cataloging-in-Publication Data

Lee, Dai Gil.

Axiomatic design and fabrication of composite structures: applications in robots,  
machine tools and automobiles/Dai Gil Lee, Nam Pyo Suh.

p. cm. — (Oxford series on advanced manufacturing)

Includes bibliographical references and index.

ISBN-13 978-0-19-517877-7

ISBN 0-19-517877-7

1. Composite construction. 2. Structural optimization. I. Suh, Nam P.,  
1936— II. Title. III. Series.

TA664.L44 2005

624.1'8—dc22 2004065453

9 8 7 6 5 4 3 2 1

Printed in the United States of America  
on acid-free paper

## Preface

Advanced high-performance composites are unique in several respects. With these composites, the entire process of designing and manufacturing a part can be done *a priori* before the part has actually been manufactured. We design the desired composite by selecting the right material components to satisfy the specific requirements of the product and predict the part performance in the anticipated service environment through analytical means. We can also design the fabrication process after the part is designed. This process of design and manufacturing minimizes the probability of failure and reduces the need for testing, in addition to satisfying the functional requirements of the part. For this reason, advanced composites are widely used in constructing airplanes. However, their use in other applications, such as in machine tools, has been limited because the parts have not been properly designed to maximize their *functional advantages*. Instead, the high cost of composite parts has been cited as the reason for not using advanced composites.

The purpose of this book is to present an integrated approach to the design and manufacturing of products from advanced composites. It shows how the basic behavior of composites and their constitutive relationships can be incorporated during the design stage, which minimizes the complexity associated with manufacturing composite parts and reduces the repetitive “design-build-test” cycle. “Designing it right the first time” is going to determine the competitiveness of a company, the reliability of the part, the robustness of fabrication processes, and ultimately, the cost and development time of composite parts. Most of all, it should expand the use of advanced composite parts in fields that use composites only to a limited extent at this time. To achieve these goals, this book presents the design and fabrication of novel composite parts made for machine tools and other applications.

Although there are books that cover various individual subjects treated in this book—composite materials, composite structures, mechanics, fabrication of composites, and axiomatic design—it is difficult for those not yet initiated into the field to learn about the design and fabrication of advanced composite parts for machine components and other applications, because they do not provide an integrated treatment of this multidisciplinary subject. This may be one of the reasons why composite parts are not extensively used in many fields that can benefit by using advanced composites. In traditional design and engineering practice, the designers of the part use the published data on material properties and the structure–property relationships to design parts. The idea that the structure itself can be designed from the beginning for each individual application and fabricated is not part of the common engineering culture. Furthermore, the idea that design and

fabrication of these parts must begin with functional requirements rather than physical parts is not commonly put into practice.

The advanced composite materials have “three highs”: high specific stiffness, high specific strength, and high damping, which are desirable properties in machines and structures. To use composites in these applications, they must be designed rationally, considering their desired performance, basic properties together with governing conservation laws, and fabrication methods. Notwithstanding the importance of the tripartite relationship among design, fabrication, and materials properties, many books and papers exclusively treat mechanics, characterization, and manufacturing of composites—but not the design of composite parts. In the early development phase of composite materials, the need to characterize material properties and develop manufacturing methods naturally dominated the composites field. Now, after four decades of using composites, significant advances have been made in manufacturing and in understanding structure–property relationships. This knowledge base needs to be combined with rational design methodologies to capture the immense potential of advanced composites as illustrated in this book. The design method adopted in this book is axiomatic design theory.

This book consists of two parts. The first part (chapters 1–10) covers the fundamental materials of axiomatic design, which become the foundation for later chapters. The second part (chapters 11–15) covers the advanced topics in composite mechanics, dealing with fabrication based on axiomatic design and the materials presented in the first part. In every chapter, easy and background topics are presented first. Sometimes, isotropic materials are discussed first to emphasize the differences between composites and isotropic materials.

This book is designed for a two-semester sequence in design and manufacture of composite structures. In the second semester, lecturers may use their own design examples or give term projects to their students to design composite structures. After a brief introduction to axiomatic design in chapter 1, the subsequent chapters treat fundamentals of composite structures—mechanics, fabrication, and performance of continuous fiber-reinforced composites. Continuum mechanics of composites are treated first, and then the micromechanics of composites are presented in later chapters. This approach to the mechanics of composites has been found to be useful in dealing with engineering issues in designing and manufacturing composites. In these chapters, many design examples are given in order to illustrate how the basic knowledge can be utilized in designing composite structures. One unique aspect of composite fabrication is the joining of composite parts. This topic is treated in detail in chapters 9 and 12. A systematic design of composite parts based on axiomatic design makes up the rest of the book. Chapter 11 presents a more comprehensive introduction to axiomatic design. The design of various composite and polymeric parts based on axiomatic design is discussed in chapters 12 to 15, using the design and fabrication of plastic parts for robots, machine tools, and automotive structures.

The materials presented in chapters 12 to 15 are based on papers published in international journals, many of which received “best paper awards.” Also many of these products and processes have been commercially adopted in industry. The first named author also received a national medal from the government of Korea for the work.

Homework problems are given in many chapters. Since the calculation of mechanical characteristics of composite structures is time consuming, a software

program has been developed, which should aid readers. The program file is provided on a CD-ROM, included with the book.

This book has been used to teach design and fabrication of composites to graduate students at the Korea Advanced Institute of Science and Technology in a one-semester course. Axiomatic design has been taught throughout the world, both to students and industrial engineers, at KAIST, MIT, and industrial sites. The goal of the composites course was to teach the fundamentals of mechanics and properties of anisotropic solids, and eliminate the development of composite parts by trial-and-error processes and by the application of axiomatic design theory. The axiomatic design course dealt with the design and manufacture of many artifacts, including composites.

This book is a comprehensive treatise on advanced composites, but leaves out several important topics related to composites. It does not cover the composites made of polymers reinforced with chopped fibers, which are used in many automotive applications. It also does not cover composites with metal matrix and ceramic fibers. Other topics that are not covered include nanocomposites and the use of woven fabric as a reinforcing element in thin parts. These topics should be covered in another book.

As the cost of composites continues to decrease with further expansion in volume, and as fabrication techniques improve, the field of composites will continue to expand. We hope that this book will be of value to those who will lead the effort to advance the field of composite engineering in the decades to come.

Dai Gil Lee  
Nam Pyo Suh

# Contents

## Part I: Basics

1	Introduction to Design of Composite Materials	3
2	Introduction to Composite Materials	14
3	Macromechanical Behavior of Unidirectional Composites	64
4	Composite Lamination Theory	110
5	Failure Criteria for Composite Materials	152
6	Behavior of Composite Laminated Plates and Beams	202
7	Micromechanics for Composite Materials	256
8	Transport Phenomena in Composite Materials	289
9	Machining and Joining of Composite Materials	335
10	Dynamic and Fatigue Performances of Composite Materials	400

## Part II: Applications

11	Fundamentals of Axiomatic Design	449
12	Axiomatic Design of Materials and Materials-Processing Techniques	486
13	Axiomatic Design of Composite Robot Structures	513
14	Axiomatic Design of Composite Machine Tool Structures	565
15	Axiomatic Design of Composite Automotive Parts and Infrastructures	621
	Glossary	675
	Index	695

## Part I

# BASICS

# 1

## Introduction to Design of Composite Materials

### 1.1 Introduction

The idea that materials can be *designed* to satisfy specific performance requirements is relatively new (Suh, 1990; Olson, 2000; Suh, 2001). The old paradigm<sup>1</sup> for materials development was similar to the way a chef cooks. He uses his imagination to mix various ingredients, tastes the resulting food, and then modifies it until it appeals to his taste. Similarly, materials were first produced by adding various alloying elements to a pool of molten materials based on phase diagrams, which were then cast and cooled at varying solidification rates to obtain desired microstructures. The material was then hot- and cold-worked to refine the microstructure. It was then tested to determine its properties. After the properties were determined, it was made available to customers whose needs matched the properties of the material. With the accumulation of materials data and advances in materials science and engineering, the process of developing new materials has become more sophisticated. However, the old paradigm of repetitive trial and error that has coupled the material properties is still used in the field of materials development. As a result, it takes a long time—more than a decade—to develop new materials and have them adopted by industry. It is a difficult area for new venture firms to survive and prosper in.

The use of high-performance composites is a departure from the old paradigm of material development. Composites can be designed first to satisfy the performance requirements of a structure and then manufactured. This is possible because the desired property can be achieved by choosing the right set of design parameters without coupling it with or affecting other properties, unlike old metallurgical processes that couple the properties so that each desired property cannot be changed independently of other properties. This field has developed rapidly during the past three decades thanks to the convergence of available materials and the need for new lightweight materials. Many new polymeric resins and high-performance reinforcing fibers have been developed to produce lightweight high-performance materials for the transportation and defense industries. In many ways, composites mimic natural materials.

The use of high-performance composites has been limited to a few fields, primarily aeronautics and astronautics, because of two reasons: high cost and the lack of design knowledge. Engineers and designers regarded high performance of composites in the same way they have viewed aluminum alloys or steel alloys—materials with certain bulk properties. In this book, we show how we can design

composites and a composite of composites to make parts for machine tools and other applications. Some of these products are beginning to make significant inroads to replacing traditional products.

This book is divided into three parts: mechanics of anisotropic solids, basic properties of composite materials, and the design and fabrication of composites. This book is unique in that these three topics are presented in an integrated fashion, so the reader does not have to read several books to be able to design and fabricate composite parts. Furthermore, no other book treats the axiomatic design and fabrication of composites. The basic research papers on these topics have received many international awards. Many of the products that form the case studies given in later chapters are being produced commercially. These products provide better performance, often at a lower cost, than the products they have replaced.

## 1.2 Historical Perspective of the Materials World

Human history began with the use of naturally produced materials: stones, wood, animal hides, and vegetable fibers. These materials were found to have certain properties, which were appropriate for various applications, ranging from hunting implements to primitive clothing. Many natural materials are composites of two or more different constituents. Wood is a fibrous composite composed of high tensile strength cellulose and lignin matrix. Bamboo is another natural composite that grows very tall due to its reinforcing fibers, in spite of its slender shape. Bone is also a natural composite that consists of short and soft collagen fibers embedded in a mineral apatite matrix. These natural materials have stood the long test of time because they possess the right properties.

This practice of using naturally found materials was followed by a long period of developing new materials by trial-and-error processes. Perhaps one of the oldest examples is the use of the straw-reinforced bricks to construct dwellings. Even many modern metal alloys, polymers, and ceramics have been developed by trial-and-error processes. Since the properties of these empirically produced materials could not be predicted *a priori*, they were tested for their properties after they were made. When promising new materials were found, applications for the materials were sought. This approach of developing materials—starting from the “invention” of processes to finding applications for the synthesized material—has been the paradigm used in the materials field until fairly recently.

Such an empirical approach to materials development may be depicted using a tetrahedron as shown in figure 1.1. The vertices represent performance, properties, morphology (microstructure or nanostructure), and processes. According to this traditional view, the relationships among these four elements define the materials world. Many materials scientists and engineers have studied these various relationships. In recent years, the major emphasis of research has been on the microstructure–property relationship of various materials rather than the structure–process relationship.

While it is true that these four elements are related to each other and that it is important to know their relationships, this way of viewing the materials world does not provide the most logical means of designing and developing new materials that can satisfy specific customer needs. The idea that we should attempt to design materials logically so that the desired materials properties can be “designed-in” *a priori* is not given sufficient emphasis by this traditional view.

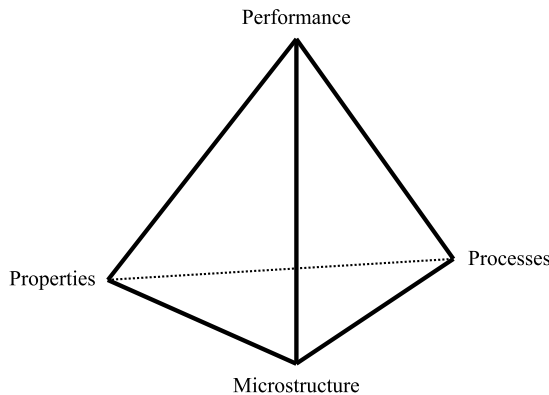


**Figure 1.1** The traditional tetragonal view of the materials world.

An alternate means of representing the materials world is shown in figure 1.2, which shows the four domains of the materials world and a “mapping process” between them to design and process materials. The four domains are: the customer domain, the functional domain, the physical domain, and the process domain. In the customer domain, the desired *performance* of the materials is specified. Then, in the functional domain, the *properties* of the materials—that is, functional requirements (FRs) of materials—that can provide the desired performance are defined. These FRs are then satisfied by designing a material with a specific *microstructure*, characterized by design parameters (DPs) in the physical domain. Finally, we design processing techniques—specified by the *process variables* (PVs) in the process domain—to create the microstructure specified by DPs in the physical domain.<sup>2</sup>

In the field of composites, the development of new composites generally follows the modern paradigm of the materials world represented in figure 1.2, which starts out specifying the customer needs for a composite structure. Based on the specified needs, the desired properties (FRs) of the composite are specified in the functional domain. To create the composite with the specified properties, we design the morphology of the composite in the physical domain in terms of DPs. Then, we design a means of manufacturing the composite, which is characterized by PVs.

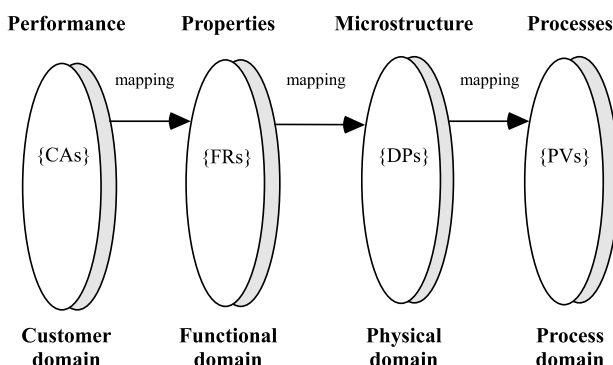


**Figure 1.2** Four domains of the materials world: *Performance* of materials characterizes the customer domain (customer attributes—CAs), *properties* characterize the functional domain (functional requirements—FRs), *microstructure* characterizes the physical domain (design parameters—DPs), and *process variables* (PVs) characterize the process domain.

### 1.3 Introduction to Axiomatic Design of Composites

The design of materials and processes described in the preceding section and depicted in figure 1.2 follows the basic principles of axiomatic design. Axiomatic design theory has been used to develop new materials that the customer requires by mapping between these domains (Suh, 1990, 2001). To develop new materials based on the axiomatic design theory, customer needs, properties, microstructure, and processes, which constitute characteristic vectors in each domain, are mapped from domain to domain. The sequence of mapping is from the customer domain (where the desired performance of the materials is specified) to the functional domain (where the properties of materials are defined), then to the physical domain (where the microstructure of the material is designed to satisfy the FRs), and finally to the process domain (where the processing variables of the process chosen to produce the desired microstructure are specified).

Since later chapters describe the construction of composite parts based on axiomatic design, the theory will be briefly introduced here, which will be followed by a more full exposition of axiomatic design in chapter 11. There are several key concepts that are fundamental to axiomatic design. They are the existence of domains, mapping, axioms, and decomposition, obtained by zigzagging between the domains, theorems, and corollaries.

#### 1.3.1. Key Concepts of Axiomatic Design Theory

As shown in figure 1.2, the world of design is made up of four domains: the *customer domain*, the *functional domain*, the *physical domain*, and the *process domain*. The domain on the left relative to the domain on the right represents “what we want to achieve,” whereas the domain on the right represents the design solution, “how we propose to satisfy the requirements specified in the left domain.”

The *customer domain* is characterized by the needs (or attributes) that the customer is looking for in a product or process or system or material. In the *functional domain*, the customer needs are specified in terms of FRs and constraints. In order to satisfy the specified FRs, we conceive DPs in the *physical domain*. Finally, to produce the product specified in terms of DPs, we develop a process that is characterized by PVs in the *process domain*.

Once we identify and define the perceived customer needs (or the attributes the customer is looking for in a product), these needs must be translated to FRs. This must be done within a “solution-neutral environment.” That means that the FRs must be defined without ever thinking about existing products or what has been already designed or what the design solution should be. Often designers and engineers identify solutions first by looking at existing materials or products before they define FRs, which leads to a description of what exists rather than what is needed.

After the FRs are chosen, we map them into the physical domain to conceive a design with specific DPs that can satisfy the FRs. The mapping process is typically a one-to-many process, that is, for a given FR, there can be many possible DPs. We must choose the right DP by making sure that other FRs are not affected by the chosen DP and that the FR can be satisfied within its design range.

During the mapping process that involves a set of FRs going from the functional domain to the physical domain, we must make the right design decisions using the independence axiom. When several designs that satisfy the independence axiom are available, the information axiom can be used to select the best design. When only

one FR is to be satisfied by having an acceptable DP, the independence axiom is always satisfied and the information axiom is the only axiom the one-FR design must satisfy.

The basic postulate of the axiomatic approach to design is that there are fundamental axioms that govern the design process. The first axiom is called the *independence axiom*. It states that the independence of FRs must always be maintained, where FRs are defined as *the minimum set of independent requirements* that characterize the design goals. The second axiom is called the *information axiom*, and it states that among those designs that satisfy the independence axiom, the design that has the smallest information content is the best design. Because the information content is defined in terms of probability, the second axiom also states that the design that has the highest probability of success is the best design. In an ideal design, the information content should be zero to satisfy the FR every time and all the time.

The axioms are formally stated as:

Axiom 1: The independence axiom

*Maintain the independence of the FRs.*

Axiom 2: The information axiom

*Minimize the information content of the design.*

To design, we have to go from “what” in the functional domain to “how” in the physical domain, which requires *mapping*. The mapping process between the domains can be expressed mathematically in terms of the characteristic vectors that define the design goals and design solutions. At a given level of the design hierarchy, the set of functional requirements that defines the specific design goals constitutes the {FR} vector in the functional domain. Similarly, the set of design parameters in the physical domain that has been chosen to satisfy the FRs constitutes the {DP} vector. The relationship between these two vectors can be written as

$$\{\text{FR}\} = [A]\{\text{DP}\} \quad (1.1)$$

where  $[A]$  is called the *design matrix* that relates FRs to DPs and characterizes the product design. Equation (1.1) is a design equation for the design of a product. The design matrix is of the following form for a design that has three FRs and three DPs:

$$[A] = \begin{bmatrix} A_{11} & A_{12} & A_{13} \\ A_{21} & A_{22} & A_{23} \\ A_{31} & A_{32} & A_{33} \end{bmatrix} \quad (1.2)$$

When equation (1.1) is written in a differential form as

$$\{d\text{FR}\} = [A]\{d\text{DP}\}$$

The elements of the design matrix are given by

$$A_{ij} = \frac{\partial \text{FR}_i}{\partial \text{DP}_j}$$

There are two special cases of the design matrix: the diagonal matrix and the triangular matrix. In the diagonal matrix, all  $A_{ij}=0$  except those where  $i=j$ :

$$[A] = \begin{bmatrix} A_{11} & 0 & 0 \\ 0 & A_{22} & 0 \\ 0 & 0 & A_{33} \end{bmatrix} \quad (1.3)$$

In the lower triangular (LT) matrix, all upper triangular elements are equal to zero:

$$[A] = \begin{bmatrix} A_{11} & 0 & 0 \\ A_{21} & A_{22} & 0 \\ A_{31} & A_{32} & A_{33} \end{bmatrix} \quad (1.4)$$

For the design of processes involving mapping from the {DP} vector in the physical domain to the {PV} vector in the process domain, the design equation may be written as

$$\{\text{DP}\} = [B]\{\text{PV}\} \quad (1.5)$$

where  $[B]$  is the design matrix that defines the characteristics of the process design and is similar in form to  $[A]$ .

To satisfy the independence axiom, the design matrix must be either diagonal or triangular. When the design matrix  $[A]$  is diagonal, each of the FRs can be satisfied independently by means of one DP. Such a design is called an *uncoupled* design. When the matrix is triangular, the independence of FRs can be guaranteed if and only if the DPs are determined in a proper sequence. Such a design is called a *decoupled* design. Any other form of the design matrix is called a full matrix and results in a *coupled* design. Therefore, when several FRs must be satisfied, we must develop designs that will enable us to create either a diagonal or a triangular design matrix.

The design goals are often subject to constraints. Constraints provide bounds on the acceptable design solutions and differ from the FRs in that they do not have to be independent.

Functional requirements and DPs (as well as PVs) must be decomposed to the final (“leaf”) level until we create a hierarchy. To decompose FR and DP characteristic vectors, we must zigzag between the domains. That is, we start out in the “what” domain and go to the “how” domain. This is illustrated in figure 1.3. From an FR in the functional domain, we go to the physical domain to conceptualize a design and determine its corresponding DP. Then, we come back to the functional domain to create  $\text{FR}_1$  and  $\text{FR}_2$  at the next level that collectively satisfies the highest level FR.  $\text{FR}_1$  and  $\text{FR}_2$  are the FRs for the highest level DP. Then we go to the physical domain to find  $\text{DP}_1$  and  $\text{DP}_2$  by conceptualizing a design at this level, which satisfies  $\text{FR}_1$  and  $\text{FR}_2$ , respectively. This process of decomposition is continued until the FR can be satisfied without further decomposition when all of the branches reach the final, or “leaf” state. The final state is indicated by thick boxes in figure 1.3.

The information axiom provides a quantitative measure of the merits of a given design, and thus is useful in selecting the best among those designs that are acceptable. Among the designs that are equally acceptable from the functional point of view, one of these designs may be superior to others in terms of the probability of achieving the design goals as expressed by the FRs. The information axiom states that the design with the highest probability of success is the best design.

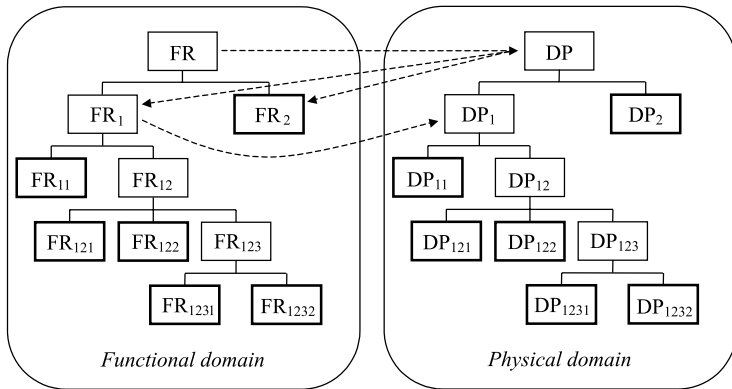


**Figure 1.3** Zigzagging to decompose FRs and DPs in the functional and the physical domains and to create the FR and DP hierarchies. Boxes with thick lines represent “leaves,” which do not require further decomposition.

Information content  $I_i$  for a given  $\text{FR}_i$  is defined in terms of the probability  $P_i$  of satisfying  $\text{FR}_i$ .

$$I_i = \log_2 \frac{1}{P_i} = -\log_2 P_i \quad (1.6)$$

The probability is determined by the overlap between the design range and the system range shown in figure 1.4. The information axiom states that the design that has the smallest  $I$  is the best design, since it requires the least amount of information to achieve the design goals. When all probabilities are equal to 1.0, the information content is zero, and conversely, the information required is infinite when one or more probabilities are equal to zero. That is, if the probability is small, we must supply more information to satisfy the FR.

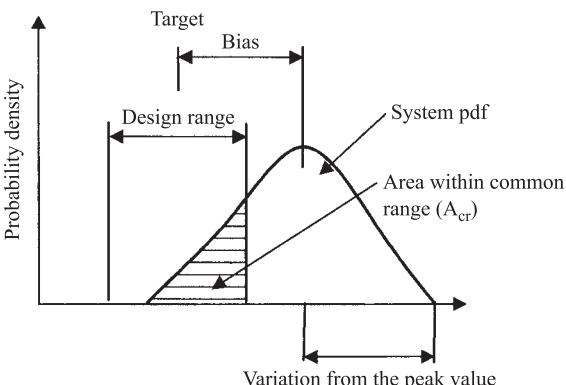


**Figure 1.4** Design range, system range, common range, and system probability density function for a functional requirement. The vertical axis (the ordinate) represents the probability density and the horizontal axis (the abscissa) represents either the FR or DP, depending on the mapping domains involved. When the mapping is between the functional domain and the physical domain, as in product design, the abscissa is for the FR. When the mapping is between the physical domain and the process domain as in process design, the abscissa is for the DP.

The overlap between the design range, which is specified by the designer, and the system range, which is the actual performance of the designed system, determines the information content. When the system range is completely inside the design range, the information content is zero. When it is completely outside of the design range, it is impossible to satisfy the FR, and the information content is infinite.

### 1.3.2 Examples of Design of Composites

#### **EXAMPLE 1.1 DESIGN OF A CUTTING TOOL MATERIAL**

We need a material for a cutting tool, which must have the following properties: good wear resistance to abrasion, high stiffness, and high toughness. These three properties are difficult to obtain with a single material. Most materials that are very hard and have good abrasion resistance typically have low toughness, fracturing into pieces, especially under dynamic loads, very much like glass.

Design the material and the processing technique for a cutting tool.

#### **Solution**

The FRs of the material to be designed may be stated as follows:

FR1 = Provide wear resistance<sup>3</sup>

FR2 = Provide high stiffness

FR3 = Impart toughness

Having defined the FRs, we have to conceptualize a solution and specify the solution in terms of DPs.<sup>3</sup> One way of making such a cutting tool material is to bond densely packed powders made of hard materials (such as tungsten carbide) with a tough material (such as cobalt) so that a crack cannot readily propagate through the “composite” as shown in figure 1.5. The wear resistance of the material is controlled by the hard particles and the toughness is provided by the thin layer of the binding material that constitutes the matrix phase. The stiffness of the material is provided by the highly compacted powder, which is hard and has high modulus.

It should be noted that in this example, we had to satisfy three FRs (i.e., wear resistance, stiffness, and toughness) and we achieved them by selecting three DPs (i.e., hardness of the powder, thickness of the tool, and the binding of the power by the matrix phase). We have three FRs and three DPs. In an ideal design, this is

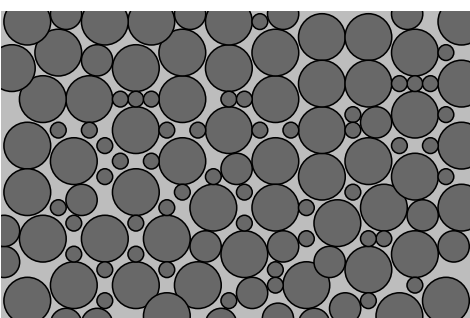


**Figure 1.5** A composite of hard particles (gray) and tough matrix materials (white) to create a material with wear resistance and toughness.

always the case. The relationship between the FRs and DPs may be represented by the following design equation for the composite:

$$\left\{ \begin{array}{l} \text{FR}_1 \\ \text{FR}_2 \\ \text{FR}_3 \end{array} \right\} = \left\{ \begin{array}{l} \text{Wear resistance} \\ \text{Stiffness} \\ \text{Toughness} \end{array} \right\} = \left[ \begin{array}{ccc} X & 0 & 0 \\ 0 & X & X \\ 0 & 0 & X \end{array} \right] \left\{ \begin{array}{l} \text{DP}_1 = \text{Hardness of WC} \\ \text{DP}_2 = \text{Thickness of tool} \\ \text{DP}_3 = \text{binder (Co)} \end{array} \right\} \quad (1.7)$$

In equation (1.7),  $X$  and 0 imply a strong relationship and no relationship, respectively, between the FR and the DP. When the matrix is either a diagonal or a triangular matrix, the design is called uncoupled or decoupled, respectively. Such designs are sound designs in that the FRs can be achieved. These designs satisfy the independence axiom of axiomatic design. This is further discussed in chapter 11. The design of the composite that is schematically illustrated in figure 1.5 is a decoupled design according to equation (1.7).

Having designed the microstructure of the composite, the next step in the composite material development is to design the manufacturing process to produce materials with the structure shown in figure 1.5. There are several ways the composite can be manufactured. One is to ball mill the hard powder (such as tungsten carbide) together with a ductile metal (such as cobalt) that can wet the powder surface and then compact the powder into a desired shape before sintering them to consolidate and bond the powder. Another means of creating the structure shown in figure 1.5 is to compact the powder first and then infiltrate the compacted powder, which has porosity, with a molten metal. A design equation that relates the DPs to PVs can be written to determine if the process is going to work.

For the first process, the process variables may be stated as follows:

$\text{PV}_1$  = Volume fraction of WC

$\text{PV}_2$  = Die dimension

$\text{PV}_3$  = Ball milling and sintering process

The design equation may be written as

$$\left\{ \begin{array}{l} \text{DP}_1 = \text{Hardness of WC} \\ \text{DP}_2 = \text{Thickness of tool} \\ \text{DP}_3 = \text{Binder (Co)} \end{array} \right\} = \left[ \begin{array}{ccc} X & 0 & 0 \\ 0 & X & X \\ 0 & 0 & X \end{array} \right] \left\{ \begin{array}{l} \text{PV}_1 = \text{Vol.\% of WC} \\ \text{PV}_2 = \text{Dimension of die} \\ \text{PV}_3 = \text{Ball milling/sintering} \end{array} \right\} \quad (1.8)$$

This process is also a decoupled design.

#### EXAMPLE 1.2 UNIAXIAL COMPOSITE WITH TRANSVERSE TOUGHNESS

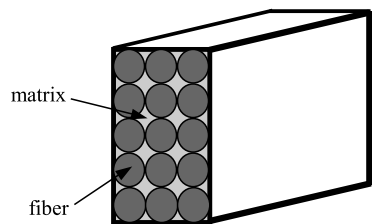
Suppose we need to make a material that has the following three FRs:

FR1 = Provide high specific strength along the axial direction to decrease the weight

FR2 = Provide the required load capability along the axial direction

FR3 = Resist fracture along the transverse direction

**Figure 1.6** A composite with uniaxially aligned fibers bonded by a matrix phase.



### Solution

To create a composite with these properties, we need to design a suitable microstructure. There may be several different solutions. One way is to use aramid fibers bonded together with a polymeric matrix phase, as shown in figure 1.6. Because the fibers are axially aligned, cracks will not easily propagate across the fiber, making the composite tough along the transverse direction. By selecting a fiber material with a desired high specific strength, the specific strength along its axial direction may be determined. Then the total cross-sectional area of the composite can be determined to provide the required axial load capability of the composite. It should again be noted that for the three different properties of the composites—high specific strength, high load capability, and high toughness—we have chosen three different design parameters.

The DPs may be stated as:

$$\text{DP1} = \text{Specific strength of the fiber}$$

$$\text{DP2} = \text{Total cross-sectional area of the composite}$$

$$\text{DP3} = \text{Axial alignment of the fibers/ductile matrix phase}$$

The design equation for the FR/DP relationship may be written as:

$$\left\{ \begin{array}{l} \text{FR}_1 = \text{Specific strength} \\ \text{FR}_2 = \text{Load capability} \\ \text{FR}_3 = \text{Toughness} \end{array} \right\} = \begin{bmatrix} X & x & 0 \\ 0 & X & 0 \\ 0 & 0 & X \end{bmatrix} \times \left\{ \begin{array}{l} \text{DP}_1 = \text{Specific strength of fiber} \\ \text{DP}_2 = \text{Cross-sectional area} \\ \text{DP}_3 = \text{Fibers/ductile matrix phase} \end{array} \right\}$$

The composite shown in figure 1.6 can be made by laying down fibers that have been coated with a bonding material such as epoxy and molding them under compression in a die. It can also be made by using a “pultrusion” machine that pulls a bundle of fibers with the resin through a die to make the uniaxial material with the desired cross-sectional shape, or by compressing layers of “prepreg” tapes in autoclave molding.

In both of these examples, the properties (i.e., FRs) that can satisfy customer needs were identified first. Then a new material with the desired properties (defined in terms of the microstructure, i.e., DPs) was designed, followed by the design of a new manufacturing process (specified in terms of PVs). This sequential way of going from the customer needs for a material that can provide desired performance to properties, microstructure, and processes in a logical

progression can create new materials quickly and reliably at low development cost. Many modern composite materials have been developed following the mapping sequence given in figure 1.2.

## 1.4 Conclusions

1. Composite materials must be designed to satisfy customer needs and the functional requirements.
2. Axiomatic design theory provides the theoretical framework for the design of composites.
3. Composites can be designed to be uncoupled or decoupled designs that satisfy the independence of FRs.
4. To be able to design and fabricate composite structures, the mechanics and the properties of composites must be understood, followed by design theory and methodology.

### Notes

1. There were exceptions to the traditional paradigm described in the following section: the field of powder metallurgy and the field of ceramics. In powder metallurgy, the idea that the material can be designed (or selected) first to satisfy a given set of performance requirements is well accepted. However, it is limited to making relatively small parts. In ceramics, various powders were mixed and fired to obtain desired properties and colors. However, traditional ceramic parts were brittle.
2. Historically, materials were developed through an inverse mapping—from processing techniques to microstructure and properties, and finally to applications. Even in the case of plastics, various processing techniques, such as the polymerization process and the incorporation of fibers in polymers, were developed first, followed by characterization of the properties and the microstructure of resulting polymers.
3. In axiomatic design, FRs are stated starting out with a verb. DPs and PVs are stated starting out with a noun for convenience.

### References

- Olson, G. 2000. "Designing a New Material World," *Science* 288 (5468), pp. 993–998.  
Suh, N. P. 1990. *The Principles of Design*, Oxford University Press, New York.  
Suh, N. P. 2001. *Axiomatic Design: Advances and Applications*, Oxford University Press, New York.

**2**

## ■ Introduction to Composite Materials

### 2.1 Introduction to Modern Composites

Composite materials are composed of two or more distinct constituents combined on a macroscopic scale to form a useful material. Composite materials are different from normal alloys. In the case of alloys, different materials can be combined on a microscopic scale, but the resulting material is macroscopically homogeneous. Composite materials are typically macroscopically inhomogeneous. Figure 2.1 shows the schematic drawing of phases of a composite material.

The continuous phase, which is less stiff or strong, is termed “matrix.” Normally, the properties of the matrix are improved on incorporating another constituent (reinforcement) to produce a composite. The examples of matrices are ceramic, metallic, or polymeric materials. Generally, polymers have low strengths and low Young’s moduli, ceramics are strong, stiff, and brittle, and metals have intermediate strengths and moduli, together with good ductility.

Another major constituent in a composite is a reinforcing phase or reinforcement, which is in most cases discontinuous, but harder, stronger, and stiffer than the matrix. There are some exceptions: ductile metal reinforcement in a ceramic matrix and rubber-like reinforcement in a brittle polymer matrix. Particulate reinforcements have dimensions that are approximately equal in all directions (i.e., equiaxial), whose shapes may be spherical, cubic, platelet, or any regular or irregular geometry. The arrangement of the particulate reinforcement may be random or with a preferred orientation. In most particulate-reinforced composites, the orientation of the particles is considered to be random. A fibrous reinforcement is characterized by the high aspect ratio of length to the cross-sectional dimension.

The need for fiber placement in a different manner according to the functional requirements has led to various types of composites, as shown in figure 2.2. Long fibers with very high aspect ratios are called continuous-fiber-reinforced composites, whereas discontinuous-fiber composites are fabricated using short fibers with an aspect ratio of several hundreds to several thousands. The orientation of the discontinuous fibers may be random or preferred. The continuous-fibers can be all parallel (unidirectional continuous-fiber composite), can be oriented at right angles to each other (crossply or woven fabric continuous-fiber composite), or can be oriented along several directions (multidirectional continuous-fiber composite). Multilayered composites or laminates are another category of fiber-reinforced composites that are made by stacking laminae (also called plies) in a specified stacking sequence.

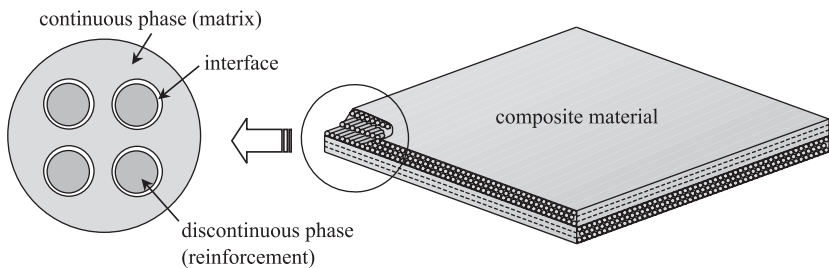


**Figure 2.1** Schematic drawing of phases of a composite material.

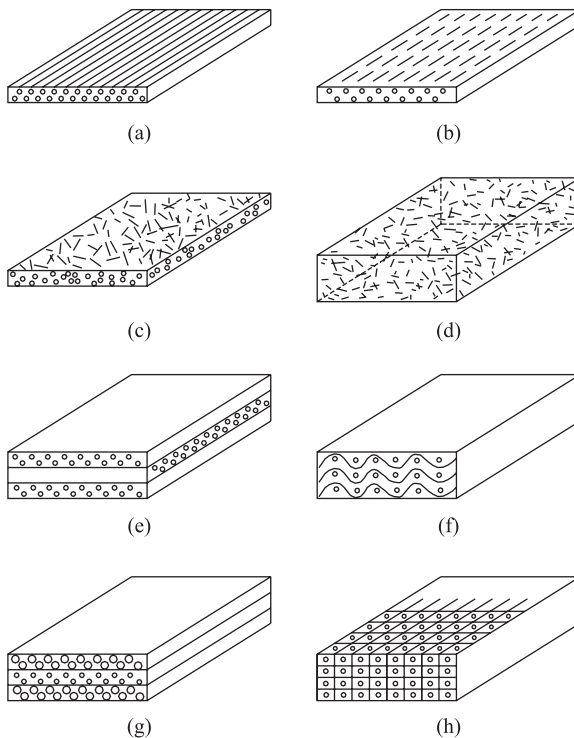
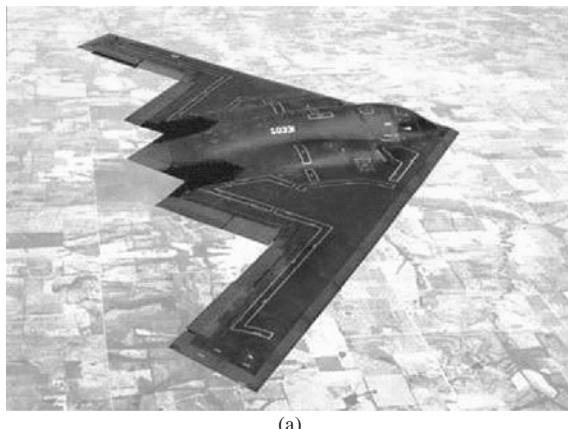


**Figure 2.2** Types of composites:  
 (a) Unidirectional lamina (ply) with continuous fiber;  
 (b) unidirectional lamina with discontinuous fiber; (c) random orientation in a plane; (d) 3-D random orientation short fibers/whisker; (e) laminate; (f) woven fabric composite; (g) hybrid-fiber composite; (h) 3-D woven/stitched/braided composites.

Hybrid composites may consist of mixed chopped and continuous fibers or mixed fiber types such as glass/carbon to benefit from the different properties of the fibers employed. For example, a mixture of glass and carbon fibers incorporated into a polymer matrix gives a relatively inexpensive composite, owing to the low cost of glass fibers, but with enhanced mechanical properties provided by the high stiffness of carbon fiber and toughness of glass fiber (example: one-piece automotive propeller shaft discussed in chapter 15). Sandwich structures composed of high-stiffness or high-strength faces and low-stiffness or low-strength but lighter core material have extremely high flexural stiffness-to-weight and high flexural strength-to-weight ratios and are widely used in aerospace, high-speed trains, and infrastructures such as buildings and bridges, as shown in figure 2.42.

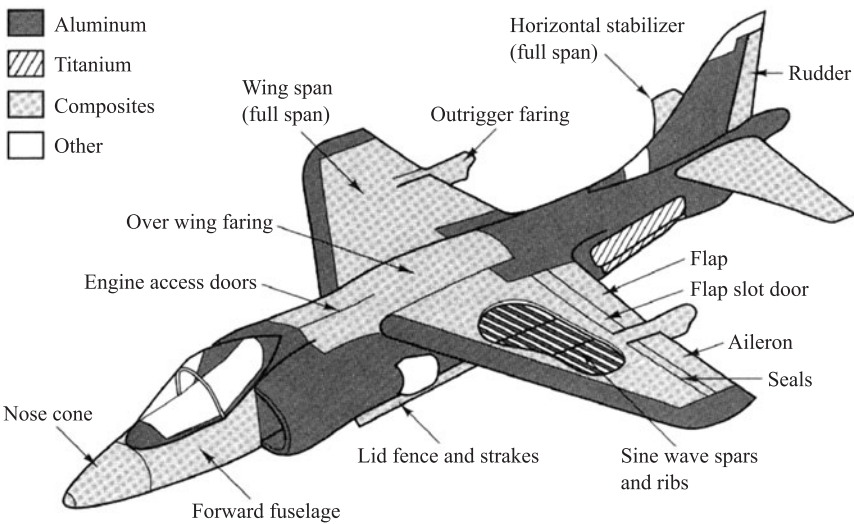
Since the 1960s, there has been a rapid increase in the production of synthetic composites or advanced composites, those incorporating fine fibers in various

polymers and metals. The rapid expansion of composites has been due to the development of carbon fibers, which have significantly higher specific stiffness (stiffness/density) and specific strength (strength/density) than glass fibers. These properties of the carbon fiber composites are utilized in aerospace (figure 2.3), sporting goods (figure 2.4), machine tool structures (Lee et al., 1985; Lee and Choi, 2000) (figure 2.5), and robot structures (Lee et al., 1991, 1993; Oh et al., 1999) (figure 2.6). Glass-fiber composites are used extensively in automotive (figure 2.7) and chemical industries (figure 2.8) and in marine applications (figure 2.9) because of their resistance to environmental or chemical attacks and because they are inexpensive.



(a)

AV-8B  
Composite applications



(b)

**Figure 2.3** Usages of composites in aerospace: (a) B-2 stealth bomber made almost entirely of composite materials (courtesy of Northrop Co.); (b) AV-8B Harrier II fighter plane (built by McDonnel Douglas Co.) depicting the extensive use of composite materials; composites account for 26% of the plane's weight and are primarily carbon-fiber-reinforced epoxy.

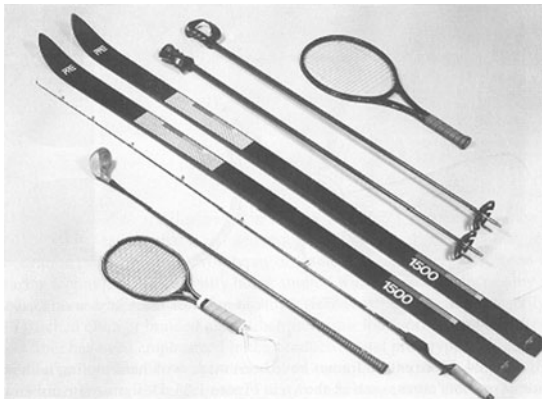


**Figure 2.4** Various sporting goods.



(a)



(b)

**Figure 2.5** Usage of composites in machine tool structures: (a) Carbon epoxy composite spindle shaft bonded with steel sleeves (first attempt in machine tool history) (from Lee et al., 1985); (b) high-speed aerostatic spindle whose rotor and housing are made of carbon-fiber composite shaft (rotating speed: 100,000 rpm, power: 1.0 kW) (from Lee and Choi, 2000). The designs of these machine tool structures are discussed in chapter 14.

These days, both glass- and carbon-fiber composites are used for infrastructure constructions and repairs, such as for bridges and concrete reinforcement (figure 2.10), because of their high strength and environmental resistance.

The relative importance of the four basic materials in a historical context has been presented by Ashby (1987); this is depicted schematically in figure 2.11, which shows the steadily increasing importance of polymers, composites, and ceramics and the decreasing role of metals.

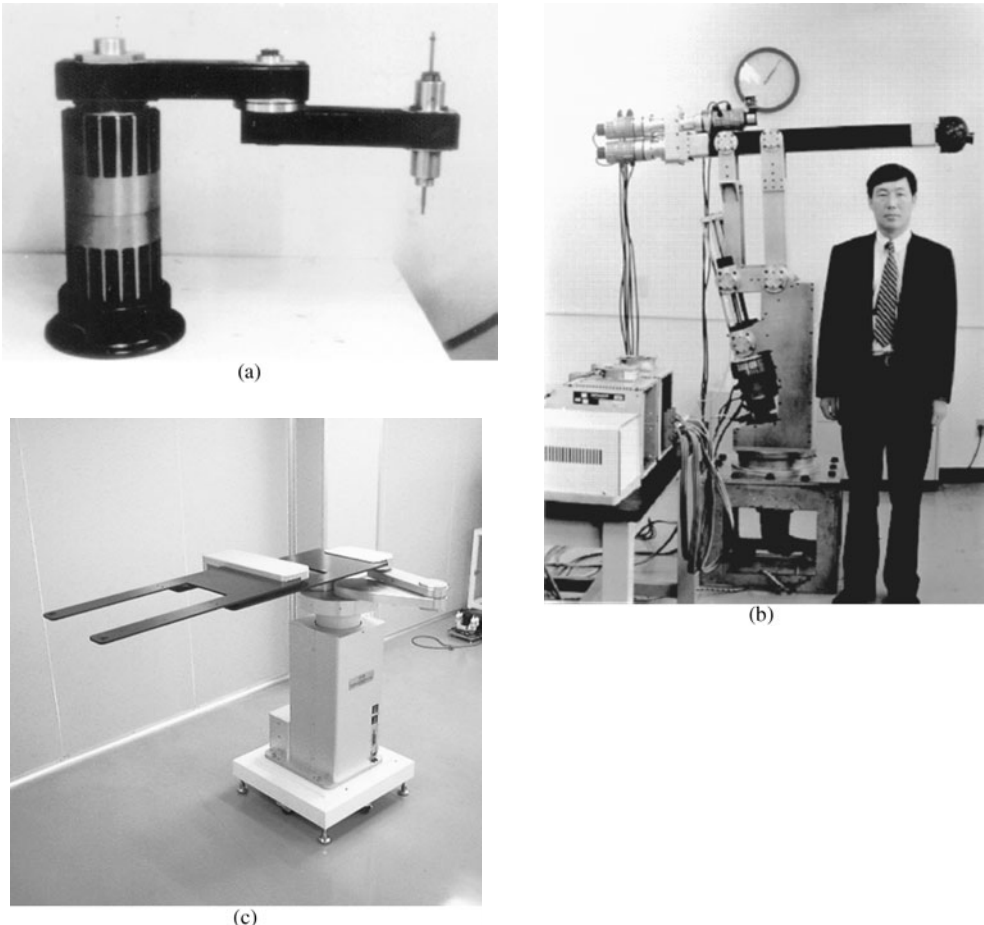


**Figure 2.6** Carbon epoxy composite robot structures: (a) SCARA robot (from Lee et al., 1991); (b) Anthropomorphic robot (from Lee et al., 1993); (c) LCD (liquid crystal display) glass panel handling robot (from Oh et al., 1999). The designs of these robots are discussed in chapter 13.

Along with this structural performance, there is a freedom to select the orientation of the fibers for optimum performance, which is important from the axiomatic design point of view because we have more design parameters to satisfy the functional requirements.

## 2.2 Reinforcements for Composites

Reinforcements are in the form of particles, flakes, whiskers (monocrystalline fibers with diameters of a few micrometers and lengths a few millimeters), short fibers, continuous fibers, or sheets. Most reinforcements used in composites have a fibrous form because materials possess the greatest strength and stiffness in this form. Griffith (1920) measured the tensile strengths of glass rods and glass fibers of different diameters and found that as the rods and fibers got thinner, they got



(a)



(b)

**Figure 2.7** Examples of composite automotive structure: (a) Chrysler's Plymouth Prowler made of seven sheet molding compound (SMC) body panels and windshield frame; (b) body panels of Chrysler Dodge Viper made of glass-fiber composite by resin transfer molding (RTM) (courtesy of Chrysler Co.).



**Figure 2.8** Internal view of 23 m × 12 m glass-fiber composite enclosure for Strathclyde Water Services.

stronger (1500 MPa at  $d=2\text{ }\mu\text{m}$ , 170 MPa at  $d=20\text{ }\mu\text{m}$ ), apparently because the smaller the diameter, the smaller the likelihood that failure-inducing surface cracks would be generated during fabrication and handling. Griffith found that for very small diameters the fiber strength approached the theoretical cohesive strength between adjacent layers of atoms, whereas for large diameters the fiber strength dropped to near the strength of bulk glass. Results similar to those published by Griffith have been reported for a wide variety of other materials; however, there are other reasons for the differences between fiber and bulk behavior. For example, polymeric fibers are stronger and stiffer than bulk polymers because of the highly aligned and extended polymer chains in the fibers and the randomly oriented polymer chains in the bulk polymer.

**Figure 2.9** Norwegian minehunter made of water-resistant polyester glass-fiber composite.



(a)



(b)



(c)

**Figure 2.10** Infrastructural usages of composites: (a) Composite electrical poles; (b) bridge repairing (courtesy of Xsys Technologies, Inc.); (c) 112 m (371 ft) long composite bridge for expanding golf course with low maintenance cost in Scotland.

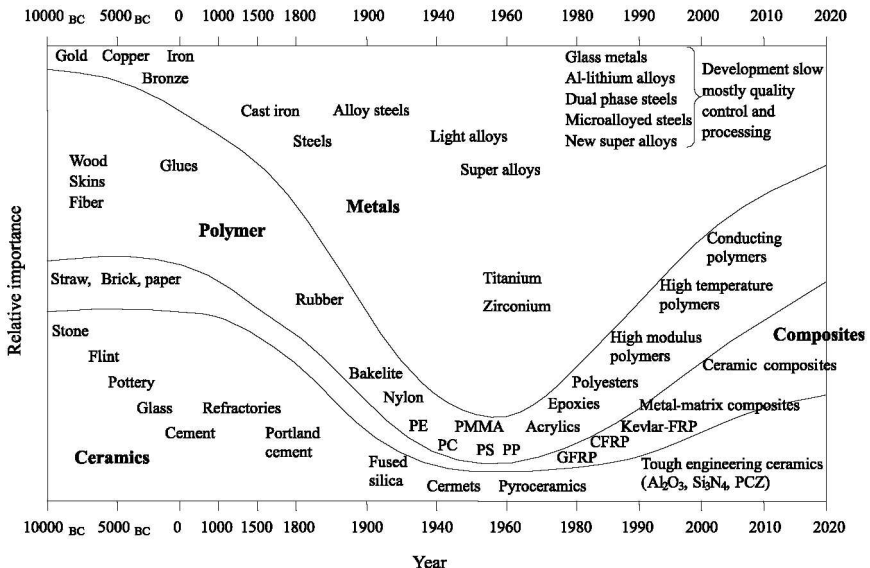


**Figure 2.11** Schematic diagram showing the relative importance of the four classes of materials (ceramics, composites, polymers, metals) in mechanical and civil engineering as a function of time; the time scale is nonlinear (redrawn from Ashby, 1987).

There is another particular necessity that the diameter of the fiber should be small. During processing and fabrication or stacking, fibers should have enough flexibility, that is, the inverse of stiffness  $EI$  ( $E$ : elastic modulus,  $I$ : moment inertia of its cross-section). The elastic modulus of a material is normally independent of its form or size for a given composition and density. Therefore, the flexibility of a material is determined by the shape and size of the cross-section. From simple bending theory, the *flexibility* and moment of inertia  $I$  for bending of a cylindrical body of diameter  $d$  under a bending moment are expressed as

$$\text{Flexibility} = \frac{1}{EI} = \frac{64}{\pi d^4 E} \quad (2.1)$$

$$I = \frac{1}{64} \pi d^4 \quad (2.2)$$

Equation (2.1) indicates that flexibility becomes very large as the fiber diameter becomes small.

### 2.2.1 Glass Fibers

Glass is a noncrystalline material with a short-range network structure and used most widely due to its low material price. It has no distinctive microstructure and the mechanical properties are isotropic. A variety of different chemical compositions is commercially available. Common glass fibers are silica based (55–65%  $\text{SiO}_2$ ) and contain several other oxides of calcium, boron, sodium, aluminum, and iron. Table 2.1 gives compositions of some commonly used glass fibers (Chawla, 1998). The designation E stands for electrical because E-glass

**Table 2.1 Approximate Chemical Compositions of Glass Fibers, from Chawla (1998)**

<i>Composition (%)</i>	<i>E-glass</i>	<i>C-glass</i>	<i>S-glass</i>
SiO <sub>2</sub>	55.2	65.0	65.0
Al <sub>2</sub> O <sub>3</sub>	8.0	4.0	25.0
CaO	18.7	14.0	—
MgO	4.6	3.0	10.0
Na <sub>2</sub> O	0.3	8.5	0.3
K <sub>2</sub> O	0.2	—	—
B <sub>2</sub> O <sub>3</sub>	7.3	5.0	—

is a good electrical insulator in addition to having good strength and a moderate Young's modulus.

Most of the continuous glass fiber produced is E-glass type but, notwithstanding the designation E, electrical uses of E-glass fiber are only a small fraction of the total market. This glass is based on the eutectic ternary system CaO–Al<sub>2</sub>O<sub>3</sub>–SiO<sub>2</sub>, with some B<sub>2</sub>O<sub>3</sub> substituting for SiO<sub>2</sub> and some MgO for CaO. The B<sub>2</sub>O<sub>3</sub> lowers the liquidus temperature substantially, giving a wider working temperature range and consequently making fiber manufacture by drawing easier. Molten glass is exuded under gravity from a melting tank through a platinum orifice and rapidly pulled to draw it down to a 10 µm-diameter fiber. Normally, about 200 orifices are used on the same melting tank, giving fibers that are gathered into a strand, sized with starch–oil emulsion to minimize surface damage, and wound on to a drum at speeds up to 50 m/s. These strands can be chopped into 25–50 mm lengths to make chopped strand mat (CSM), wound parallel to give roving or ribbon, or twisted to form yarn for weaving into glass-fiber cloth or woven roving (WR). Freshly drawn and carefully handled fibers have tensile strengths of approximately *E*/20 but a typical value may be nearer to *E*/50, where *E* is the Young's modulus of glass. A size is used to minimize surface damage, but other active coatings may be applied. Active coatings which enhance the wetting and bonding between fibers and matrix are known as coupling agents. They are usually complex organosilanes, the exact chemistry of which is adjusted to suit the type of matrix.

C stands for corrosion because C-glass has a better resistance to chemical corrosion.

S-glass is based on the SiO<sub>2</sub>–Al<sub>2</sub>O<sub>3</sub>–MgO system. S stands for the high silica content (sometimes stands for strength) that makes S-glass withstand higher temperatures than other glasses. This fiber has also higher stiffness and higher strength than E-glass. However, it is more difficult to draw into fibers due to its limited working range and is therefore much more expensive. S-glass fibers are still used for some specialist applications such as military armor due to its high temperature and impact resistances but their commercial uses have been largely superseded by fibers such as carbon and aramid with superior mechanical properties.

## 2.2.2 Carbon and Graphite Fibers

Carbon is a very light element with a density of  $2.27 \times 10^3 \text{ kg/m}^3$ . Carbon can exist in a variety of crystalline forms. The graphite structure, wherein the carbon atoms are

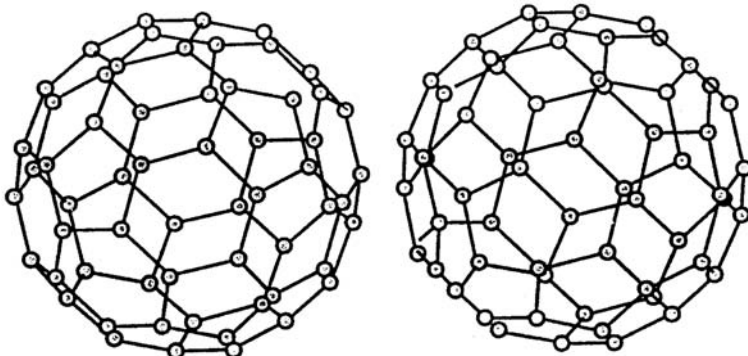


Figure 2.12 Stereographic projection of  $C_{60}$ .

arranged in the form of hexagonal layers, is most important in the performance of the fiber. The other well-known form of carbon is the covalent diamond structure, wherein the carbon atoms are arranged in a three-dimensional configuration with little structural flexibility.

Another polymorphic form of carbon was discovered in 1985 (figure 2.12). Each molecule is composed of groups of carbon atoms that are bonded to one another to form both hexagon (six-carbon atom) and pentagon (five-carbon atom) geometrical configurations (Callister, 2000). Figure 2.12 depicts of 20 hexagons and 12 pentagons, which are arrayed such that no two pentagons share a common side. The molecular surface exhibits the symmetry of a soccer ball. The material composed of  $C_{60}$  is known as Buckminsterfullerene, or “buckyball” named in honor of R. Buckminster Fuller, who invented the geodesic dome, from which a host of novel carbon structures and morphologies have been obtained. Among these are bucky tubes, which are nanotubes with closed ends and fullerene onions (Dresselhaus et al., 1996).

Carbon in the graphite form, as shown in figure 2.13, is highly anisotropic, with a theoretical Young's modulus in a layer being equal to about 1000 GPa, while that along the *c*-axis is equal to about 35 GPa. The graphite structure has very dense packing in the layer planes. The high-strength bond between carbon atoms in the layer plane results in an extremely high modulus, while a weak van der Waals type bond between the neighboring layers results in a lower modulus in that direction. Consequently, the very high degree of preferred orientation of hexagonal planes should be the fiber direction.

Previously, the term “graphite fiber” was used to describe fibers that had a carbon content in excess of 99% (high stiffness, low strength), whereas the term “carbon fiber” described fibers that had a carbon content of 80–95% (low stiffness, high strength). These fibers are usually produced by subjecting organic precursor fibers such as polyacrylonitrile (PAN) or rayon to a sequence of heat treatments, so that the precursor is converted to carbon by pyrolysis. They are also produced from petroleum and coal tar pitch containing a complex mixture of high-molecular-weight aliphatic and aromatic hydrocarbons. The pitch is heated to above 350°C to polymerize it to molecular weights of about 1000. The structure of the molecules is such that an ordered liquid crystal or mesophase is formed. The polymer is extruded through holes in a hot-walled metal cylinder while the cylinder rotates. This process, which is known as melt spinning, orients the hot mesophase pitch.

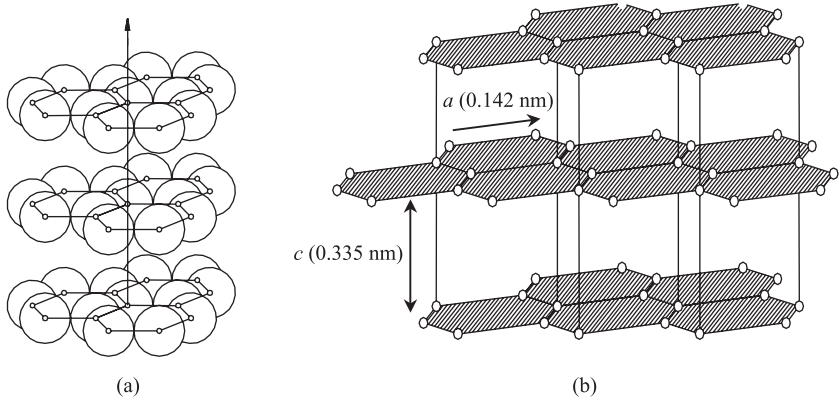
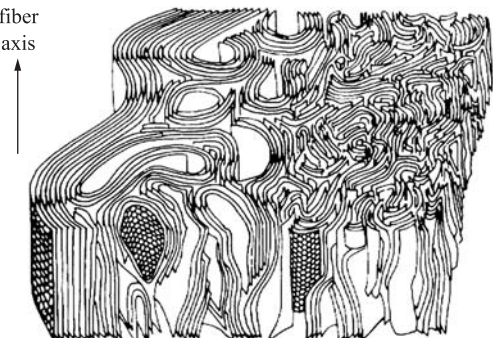


**Figure 2.13** Graphite structure: (a) Densely packed graphitic layer structure; (b) hexagonal lattice structure.

**Figure 2.14** Schematic representation of the three-dimensional structure of the orientation of the basal planes of the graphite in a carbon fiber (redrawn from Bennett and Johnson, 1978).



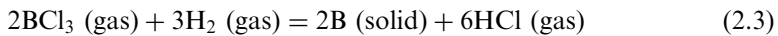
After oxidation to induce cross-linking, and prevent the fibers remelting and sticking together, the fibers are carbonized at temperatures up to 2000°C, giving low-modulus carbon fibers. The degree of graphitization is controlled by heat treatment at temperatures up to 2900°C. A high degree of perfection of the graphite may be obtained, together with good axial alignment of the basal planes, which leads to high-density, very high modulus fibers. Figure 2.14 shows a three-dimensional representation of the arrangement of the basal planes in PAN-based carbon fiber (Bennett and Johnson, 1978).

The major difference between graphite fibers and carbon fibers is that graphite fibers are subjected to higher temperature pyrolysis than carbon fibers. The result is that carbon fibers are typically less than 95% carbon, whereas graphite fibers are at least 99% carbon. Carbon fibers have high strength with moderate stiffness, whereas graphite fibers have high stiffness with moderate strength. However, the names “carbon” and “graphite” are now often used interchangeably to describe fibers based on the element of carbon because these two fibers possess both high strength and stiffness these days. Therefore, the term “carbon fiber” rather than “graphite fiber” is used in this book.

### 2.2.3 Boron Fibers

Boron fiber is produced by chemical vapor deposition from boron trichloride on to a heated substrate such as 10 µm diameter tungsten wire to yield a coating of boron

approximately 50  $\mu\text{m}$  thick with an extremely small grain size of only 2–3 nm. The chemical deposition of boron is expressed as



During the process, the tungsten wire is pulled into a reaction chamber at one end through a mercury seal and out at the other end through another mercury seal.

The boron fiber has a high cost, compared with other fibers, due to the tungsten substrate, which limits its widespread use.

#### 2.2.4 Ceramic Fibers

Ceramic fibers, such as silicon carbide fiber and aluminum oxide fiber, are fabricated by one of the three methods: chemical vapor deposition, polymer pyrolysis, and sol–gel technique. For example, SCS-6 is a thick silicon carbide fiber (diameter = 142  $\mu\text{m}$ ) that is produced by chemical vapor deposition of silicon- and carbon-containing compounds onto a pyrolytic graphite-coated carbon-fiber core. Ceramic fibers have high stiffness and moderate strength and are used in metal-matrix and ceramic-matrix composites for high-temperature applications.

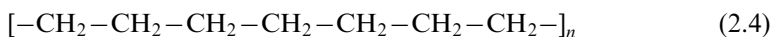
#### 2.2.5 Organic Fibers

In general, polymeric chains have a random coil configuration such as the cooked-spaghetti structure, in which the macromolecular chains are attracted by weak van der Waals interactions rather than strong covalent interactions, resulting in a low strength and stiffness. Because the covalent carbon–carbon bond is very strong, linear chain polymers such as polyethylene are potentially very strong and stiff. Although conventional polymers show a Young's modulus,  $E$ , of about 10 GPa, highly drawn polymers with a Young's modulus of about 70 GPa can be obtained easily. In order to obtain high-stiffness and high-strength polymers, the polymer chains should be extended and packed in parallel arrays.

There are two important organic fibers: polyethylene, known under the commercial names *Spectra®* and *Dyneema®* of AlliedSignal (USA) and DSM (Dutch State Mines), respectively, and aramid, known under the commercial name *Kevlar®* of DuPont.

##### *Oriented Polyethylene Fibers*

Polyethylene (PE) is a particularly simple, linear macromolecule (figure 2.15), with the following chemical formula:



It is easier to obtain an extended and oriented chain structure in polyethylene than in other polymers. Drawing of melt-crystallized polyethylene (molecular mass between  $10^4$  and  $10^5$ ) to very high draw ratios can result in moduli of up to 70 GPa. Tensile drawing, die drawing, or hydrostatic extrusion can be used to obtain a high modulus. The density of polyethylene fiber is 0.97, which is lower than that of water. Its strength and modulus are slightly lower than those of aramid fibers but the specific property values based on a unit weight are about 30% to 40% higher than those of aramid. However, polyethylene fibers have only low-temperature (lower than

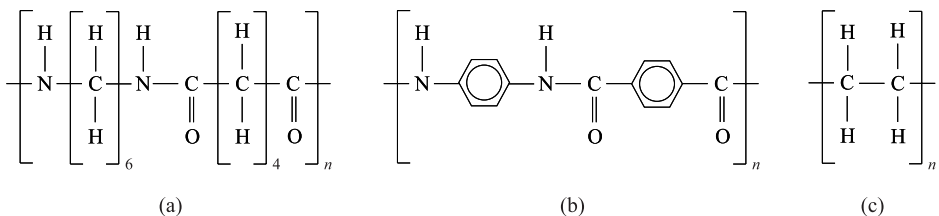


**Figure 2.15** Molecular structures of several polymers: (a) Nylon; (b) aramid; (c) polyethylene.

150°C) applications. High-modulus polyethylene fibers, such as Spectra® or Dyneema®, are hard to bond with any polymeric matrix. Some kind of surface treatment such as cold gas (argon or ammonia) plasma must be given to the polyethylene fiber to bond with polymeric resins. Plasma consists of gas molecules in an excited state of dissociation. When polymers are treated with plasma, surface modification occurs by removal of any surface contaminants and highly oriented surface layers, or addition of polar and functional groups on the surface, and the introduction of surface roughness, which contribute to an enhanced fiber/matrix interfacial strength.

Aramid Fibers

Aramid can be viewed as nylon with extra benzene rings in the polymer chain to increase stiffness, as shown in figure 2.15. Aramid fibers have a glass transition temperature of about 360°C, burn with difficulty, and do not melt like nylon. The carbonization of aramid fibers occurs around 425°C, but the fibers can be used at 300°C for a limited time. The dimensional stability of aramid fibers is good because the coefficient of thermal expansion (CTE) is low ( $-4.0 \times 10^{-6}/\text{K}$ , slightly negative). However, they have low electrical and thermal conductivity and high thermal capacity, which can be advantageous or disadvantageous.

## 2.3 Matrices

The matrix in a fiber-reinforced composite transfers stresses between the fibers and protects the surface of the fibers from mechanical abrasion and adverse environments. The matrix transmits the tensile load little, but has a major role on the interlaminar shear strength and in-plane shear strength. The interlaminar shear strength and stiffness are important design considerations under bending loads and bending vibrations, whereas the in-plane shear strength is important under torsional loads.

As shown in figure 2.11, polymers are increasingly used due to their advantageous properties such as low density, chemical resistance, easy manufacturing automation, and low energy requirement (low pressure or low temperature) for product manufacturing. However, their strength and stiffness are low compared with metals and ceramics, and considerable benefit can be obtained by reinforcing polymers. Therefore, the most common matrix materials for composites are polymeric materials.

Structurally, polymers are giant chain-like molecules (macromolecules) with covalently bonded carbon atoms forming the backbone of chain. The process of

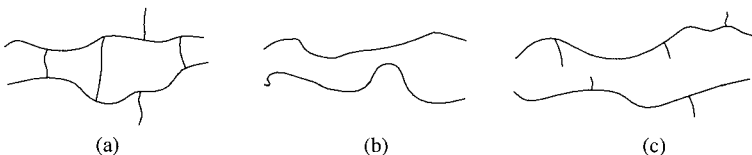


**Figure 2.16** Schematic representation of polymers: (a) Cross-linked; (b) linear; (c) branched.

forming large molecules from small ones is called polymerization. There are two important classes of polymerization (McCrumb et al., 1997):

1. Condensation polymerization: In this process, a stepwise reaction of molecules occurs and in each step a molecule of a simple compound, generally water, forms as a by-product.
2. Addition polymerization: In this process, monomers join to form a polymer without producing any by-product. Addition polymerization is generally carried out in the presence of catalysts. The linear addition of ethylene molecules ( $\text{CH}_2$ ) results in polyethylene with the final mass of polymer being the sum of monomer masses ( $\text{CH}_2)_n$ .

Based on their behavior, there are two major classes of polymers, produced either by condensation or addition polymerization, namely, thermosetting and thermoplastic polymers. It has been estimated that over three-quarters of all matrices of polymeric matrix composites (PMCs) are thermosetting polymers. Thermosetting polymers, or thermosets, are resins that readily cross-link during curing. Curing involves the application of heat and pressure, ultraviolet ray, or the addition of a catalyst known as a curing agent or hardener.

The type of chain structure of polymers is schematically illustrated in figure 2.16. The bonds of the link in the polymer chain are strong covalent chain. These strong bonds of the cross-links pull the chains together, which restricts the movement of the polymer chains and so increases the glass transition temperature. Near the glass transition temperature, the polymeric material changes from a hard, sometimes brittle (glass-like) solid with low fracture toughness values,  $K_{IC}$ , of typically 0.5 to  $1.0 \text{ MPa m}^{1/2}$  to a soft, tough (leather-like) solid. Over a temperature range around glass transition temperature, the modulus of the polymeric material is reduced by as much as five orders of magnitude, and the material is also highly viscoelastic. When an external load is applied, it exhibits an instantaneous (elastic) deformation followed by a slow viscous deformation. Thermosets are brittle at room temperature and cannot be reshaped by reheating because of the cross-links. Thermosets just degrade on reheating, and in some cases may burn, but do not soften sufficiently for reshaping. However, the stiffness is increased as the weak van der Waals bonding between polymer chains is replaced by the strong cross-links (Matthew and Rawlings, 1994). Also, thermosets may be used at higher temperatures as they have higher softening temperatures and better creep properties than thermoplastics. They are more resistant to chemical attack than most thermoplastics.

### 2.3.1 Thermosets

Thermosetting resins are the most common type of matrix system for composite materials because they have low melt viscosity, good fiber impregnation, and fairly

low processing temperatures. They are also lower in cost than thermoplastic resins. Consequently, over three-quarters of all matrices of polymeric matrix composites are thermosetting polymers, even though they are difficult to recycle.

### *Unsaturated Polyester*

This is most widely used in the matrix for composite materials because it is relatively inexpensive, has low viscosity, and can be cured at room temperature; however, it undergoes large shrinkage (4–8%) on curing, causing sink marks on the product surface. The starting material for a thermoset polyester matrix is an unsaturated polyester resin that contains a number of C=C double bonds. It is prepared by the reaction of maleic anhydride and ethylene or propylene glycol, as shown in figure 2.17.

Saturated acids, such as isophthalic or orthophthalic, are also added to modify the chemical structure between the cross-linking sites. However, they do not contain any C=C double bond but modify the properties of final products. The resulting polymeric liquid is dissolved in a reactive (polymerizable) diluent, such as styrene, which reduces its viscosity and makes it easier to handle. The diluent also contains C=C double bonds and acts as a cross-linking agent by bridging adjacent polyester molecules. Small amounts of an inhibitor, such as hydroquinone or benzoquinone, are added to the liquid mix to prevent premature polymerization during storage. The curing reaction for polyester resins is initiated by adding small quantities of organic peroxide ( $-O-O-$ ), such as benzoyl peroxide or methyl ethyl ketone peroxide) or an aliphatic azo ( $-N=N-$ ) compound to the liquid mix. Figure 2.18 shows examples of initiation of free radicals of benzoyl peroxide and 2,2'-azobisisobutyronitrile (AIBN) (Fried, 1995). The liable bond of the initiator can be broken by heat or irradiation, such as ultraviolet or gamma irradiation.

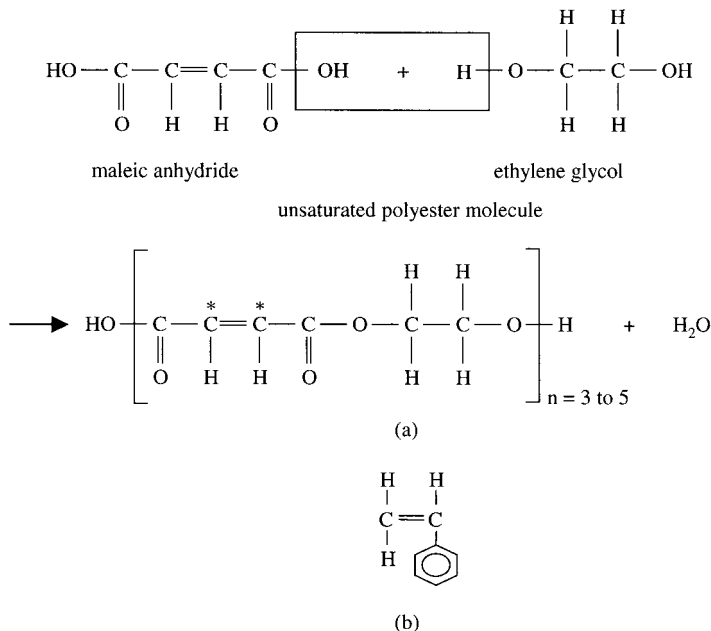
In figure 2.18,  $k_d$  represents the dissociation rate-constant and it follows an Arrhenius dependence on temperature  $T$ ,  $k_d = \exp[-E_a/(RT)]$ , where  $E_a$  is the activation energy and  $R$  is the ideal gas constant.

With the application of heat (in the temperature range 110–160°C), the catalyst decomposes rapidly into free radicals, which react mostly with the styrene molecules and break their C=C bonds. Styrene radicals, in turn, join with the polyester molecules at their unsaturation points and eventually form cross-links between them (figure 2.19). The resulting material is a solid polyester resin. The organic peroxide is very flammable and should be treated carefully.

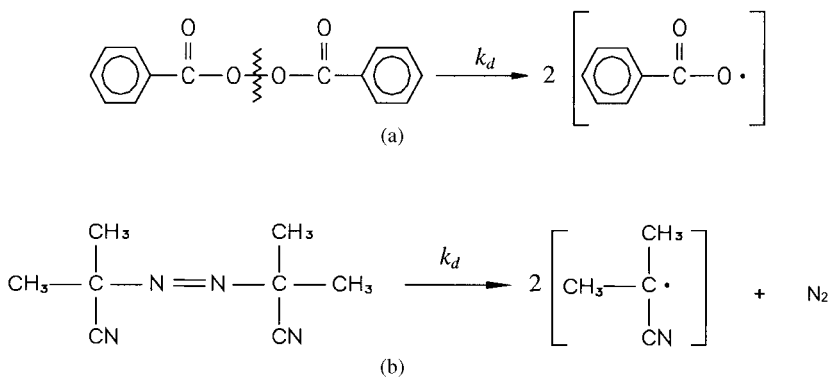
### *Epoxy*

Epoxy resins are low-molecular-weight organics that contain a number of epoxide groups, which are three-membered rings with one oxygen and two carbon atoms, as shown in figure 2.20 (Mallick, 1988). A common starting material is diglycidyl ether of bisphenol A (DGEBA) that contains two epoxide groups, one at each end of the molecule as shown in figure 2.20.

Other ingredients that may be mixed with the starting liquid are diluents, to reduce its viscosity, and flexibilizers (rubber toughening), to improve the impact strength of the cured epoxy matrix. Each epoxy molecule is end-capped with the epoxy group. A curing agent is mixed into the liquid epoxy to polymerize and form a



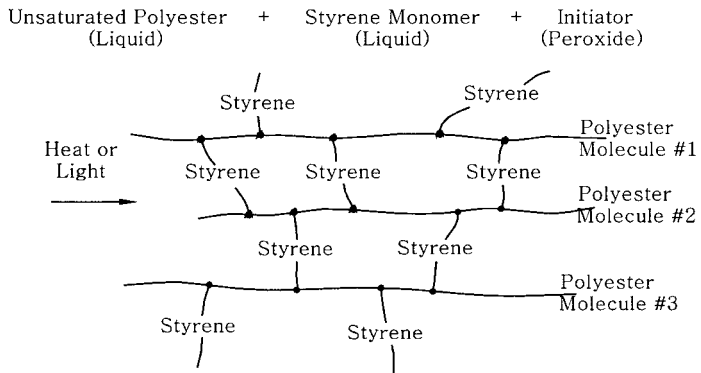
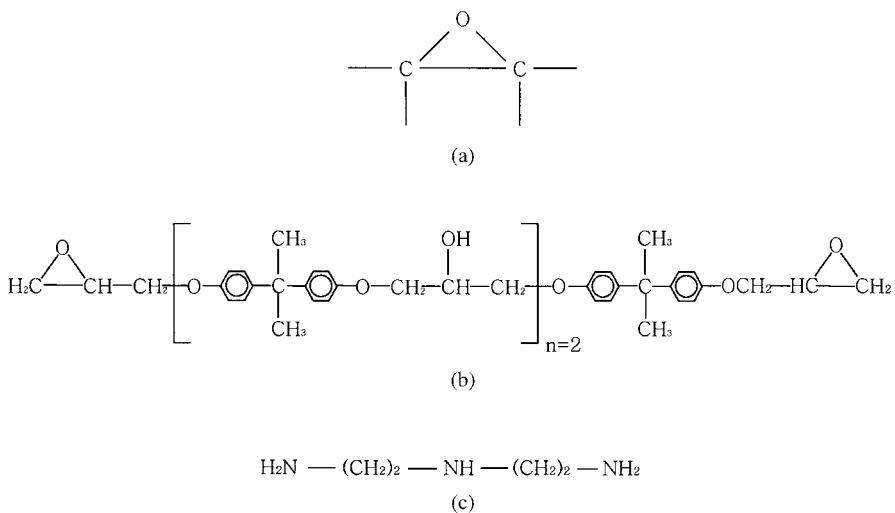
**Figure 2.17** Principal ingredients in the preparation of a thermosetting polyester matrix:  
 (a) Unsaturated polyester molecule; asterisk (\*) denotes unsaturation points (reactive sites) in  
 the unsaturated polyester molecule; (b) Styrene molecule.



**Figure 2.18** Examples of free-radical initiation: (a) Benzoyl peroxide; (b) 2,2'-azobis(isobutyronitrile) (AIBN).

solid network cross-linked polymer. One such curing agent is diethylene triamine (DETA) as shown in figure 2.20. Hydrogen atoms in the amine ( $\text{NH}_2$ ) groups of DETA molecules form cross-links with each other (figure 2.21) and a three-dimensional network structure is slowly formed. The resulting material is a solid epoxy resin.

Epoxy resins are more expensive and more viscous than polyester resins, making impregnation of fibers more difficult. They are cured at 180°C for aerospace purposes and at between room temperature and 120°C for commercial uses. If the

**Figure 2.19** Schematic representation of a cross-linked polyester resin.**Figure 2.20** Epoxy group and principal ingredients in the preparation of an epoxy matrix: (a) Epoxy group; (b) molecule of diglycidyl ether of bisphenol A (DGEBA), epoxy resin; (c) molecule of diethylene triamine (DETA), curing agent.

curing reaction is slowed by lowering the reaction temperature or other means before all the molecules are cross-linked, the resin would exist in a partially cross-linked stage (also called B-stage). At this stage, cross-links have formed at widely spaced points in the reactive mass, which enables them to be preimpregnated in fibers at a partially cured state to make “prepreg”. The prepreg may be stored, often at subzero temperatures, for a reasonable length of time (sometimes for longer than 1 year at  $-30^{\circ}\text{C}$ ) before being molded into the final shape and then cured. The shrinkage on curing is smaller than for polyesters, being typically 1–5%. The continuous-use temperature for DGEBA-based epoxies is  $150^{\circ}\text{C}$  ( $300^{\circ}\text{F}$ ) or less. Higher heat resistance can be obtained with epoxies based on novolacs and cycloaliphatics, which have a continuous-use temperature that extends to  $250^{\circ}\text{C}$  ( $480^{\circ}\text{F}$ ). In general, the heat resistance of an epoxy is improved if it contains more aromatic rings in its basic chain.

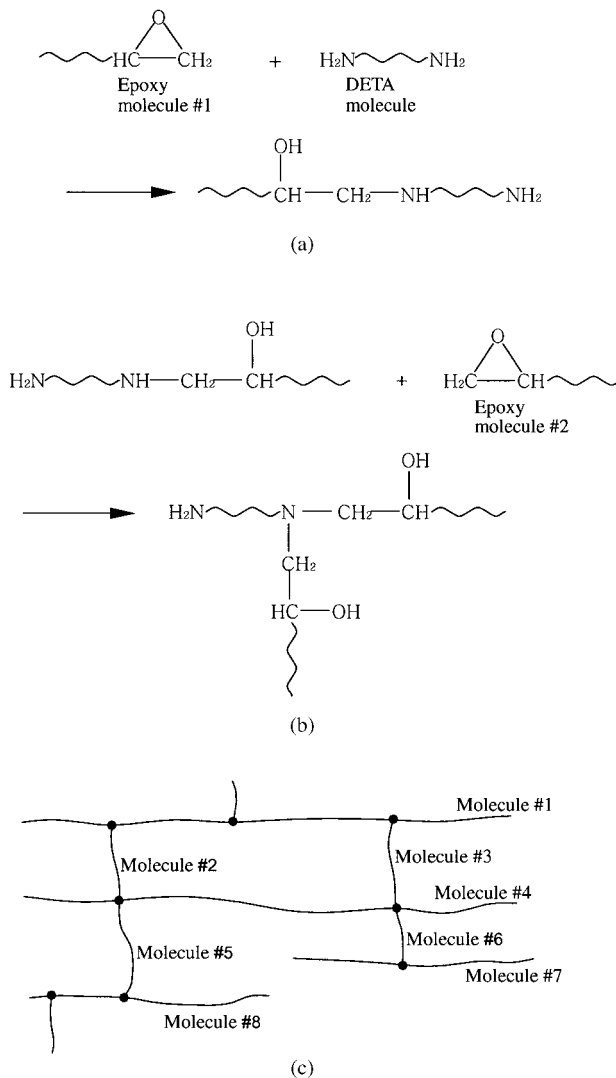


**Figure 2.21** Schematic representation of a cross-linked epoxy resin: (a) Reaction of epoxide group with DETA (diethylene triamine) molecule; (b) formation of cross-links; (c) three-dimensional network structure of solid epoxy (from Mallick, 1988).

### Phenolic Resins

Because of low cost and good fire resistance with minimum smoke levels, their usage has been increased lately due to more stringent fire, smoke, and toxicity regulations. They are inherently brittle but have an excellent dimensional stability and chemical and thermal strength with a heat deflection temperature (HDT) typically of 180°C. They are applied as filled molding materials in many areas such as electrical insulators or under-the-hood automotive components. They are also utilized as friction-resistant materials in brake linings or transmission bands, and as binders for plywood, wood-particle board, or fiber-based acoustical and thermal padding. Aramid paper honeycomb Nomex® produced by DuPont is made of aramid paper followed by dip-coating with phenolic resin. Airplane interiors are generally made of aramid–phenolic composites. They are also extensively found in adhesives and coatings. Phenolic resins are the second most used thermoset resins after polyurethanes.

Phenolic resins are products of the condensation reaction of phenol and formaldehyde, and water is the by-product of the reaction. A variety of phenolic resins can be produced by adjusting the phenol-to-formaldehyde ratio, and the characteristics of the resin product depend on the proportions of the reactants and the catalyst employed.

Single-stage (resole) resins are produced with an alkaline catalyst and a molar excess of formaldehyde. The reaction is carefully controlled to allow the production of low-molecular-weight, non-cross-linked resins. Single-stage resins complete the curing reaction in a heated mold with no additional catalyst to form a three-dimensionally cross-linked polymer. The resole resins have a limited shelf-life of typically 2 months to 1 year. They are used for odor-free applications such as casting, bonding, and laminating applications.

Two-stage (novolac) resins are produced by the acid-catalyzed reaction of phenol and formaldehyde with excess of phenol. The resin product is brittle thermoplastic at room temperature. It can be melted, but it does not cross-link. Novolacs can only be cured by the addition of a hardener, which is almost always formaldehyde supplied as hexamethylenetetramine. Upon heating above 160°C, hexamethylenetetramine in the presence of moisture (a by-product of the condensation reaction) decomposes to yield ammonia and the formaldehyde necessary to complete the cross-linking reaction. Phenolic compounds formulated with novolac resins are the most widely used and offer wide molding latitude and improved dimensional stability, compared with resole-based materials, as well as an infinitely long shelf-life prior to heating. Resole materials, which do not liberate ammonia during or after molding, are preferred for applications in which metal corrosion or odor may be concern.

An undesirable feature of phenolic resins is that volatile by-products, such as water and ammonia, are evolved during curing, hence high pressures are necessary in composite production.

### *Vinyl Esters*

The C=C double bonds (unsaturated points) occur only at the ends of a vinyl ester molecule, and therefore, cross-linking can take place only at the ends. Because of fewer cross-links, a cured vinyl ester resin is more flexible and has higher fracture toughness than a cured polyester resin. Another unique characteristic of a vinyl ester molecule is that it contains a number of OH (hydroxyl) groups along its length. These OH groups can form hydrogen bonds with similar groups on a glass-fiber surface, resulting in good wet-out and adhesion with glass fibers. Vinyl ester resins, like unsaturated polyester resins, are dissolved in styrene monomer, which reduces its viscosity (Mallick, 1988). Vinyl esters possess the good mechanical properties and chemical resistance of epoxy, and the benefits of unsaturated polyester resins, such as low viscosity and fast curing. However, the volumetric shrinkage of vinyl ester resins is high (5–10%) and only moderate adhesive strengths are achieved, compared with epoxy resins.

### *Polyimides*

They are more expensive and less widely used than polyesters or epoxies but can withstand relatively high service temperatures. The polyimide chain, which is rigid

and heat resistant owing to the presence of aromatic ring structures, results in a high stiffness, a low coefficient of thermal expansion, and a service temperature as high as 400°C for several hours. However, like other thermosets, they are brittle. Polyimide resin systems are used for electrical and low-friction products in the aerospace industry, as well as in office equipment. It is a good bearing material, exhibiting low friction, high wear resistant, low creep, and dimensional stability. Thus, it is used for self-lubricated parts, such as bearings, bushings, thrust washers, wear rings, and seals.

The most common polyimide resin system is PMR-15, developed and licensed for production by the NASA (National Aeronautics and Space Administration) Lewis Research Center. PMR-15 exhibits good chemical resistance, except when exposed to strong alkalies. It is self-extinguishing when the ignition source is removed, with low smoke generation and a high char yield (70%) that forms an insulating barrier against further flame spread (Laramee, 1988).

### *Bismaleimides*

Bismaleimides (BMI) are formed by the reaction of a diamine with maleic anhydride. They have service temperatures between 180° and 200°C with an upper limit of 230°C. They have good resistance to hygrothermal effects; however, they are quite brittle, with reduced damage resistance and toughness, and may undergo cure-shrinkage. They must be cured at higher temperatures than conventional epoxies. Bismaleimide systems with improved toughness are available at the sacrifice of mechanical properties.

### 2.3.2 Thermoplastics

They soften or melt on heating and become solid when cooled-down, which is a suitable property for liquid-flow forming. When the structure is amorphous, there is no apparent order among the molecules and the chains are arranged randomly, as shown in figure 2.22 (Chawla, 1998). Small plate-like single crystalline regions called lamellae or crystallites can be obtained by precipitation of the polymer from a dilute solution. In the lamellae, long molecular chains are folded in a regular manner.

The degree of crystallinity of the thermoplastic is dependent on the cool-down time. This is because the polymer needs time to become organized into the orderly pattern of the crystalline state; too quick a cooling rate will not allow crystallization to occur.

Generally, short fibers are used as the reinforcements with thermoplastics due to the high viscosity of thermoplastics, although some continuous-fiber-reinforced thermoplastics are also produced. Well-known thermoplastics for composites include acrylic, nylon (polyamide), shown in figure 2.15, polystyrene, polypropylene, thermoplastic polyesters (polyethylene terephthalate: PET, polybutylene terephthalate: PBT), and polycarbonates. Some of the new high-temperature matrix materials include polyamideimide, polyphenylene sulfide (PPS), polyarylsulfone, and polyetherether ketone (PEEK). The last is an attractive matrix material because of its toughness and impact properties, which are functions of its crystalline content and morphology. However, PEEK should be heated above the melting point of its crystalline compound (343°C), which may induce high thermal residual stresses

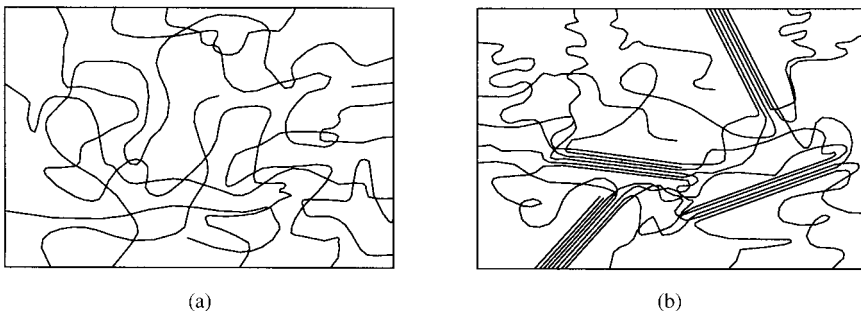


**Figure 2.22** Possible arrangements of polymer molecules: (a) Amorphous; (b) semicrystalline (from Chawla, 1998).

between the fibers and the matrix. PEEK has a long-term use temperature of 250°C and a short-term use temperature of 300°C.

### 2.3.3 Metals

The most commonly used metal matrices are based on aluminum and titanium. Both of these metals have low densities (aluminum:  $2.7 \times 10^3 \text{ kg/m}^3$ , titanium:  $4.5 \times 10^3 \text{ kg/m}^3$ ) and are available as alloys. Magnesium, although lighter (density:  $1.74 \times 10^3 \text{ kg/m}^3$ ), is unsuitable because of its great affinity to oxygen, which promotes corrosion.

### 2.3.4 Ceramic Matrix Materials

Ceramic materials are very hard and brittle, but have high temperature resistance. Generally, they consist of one or more metals combined with a nonmetal, such as oxygen, carbon, or nitrogen. They have strong covalent and ionic bonds and have low failure strains with low toughness or fracture energies. Thus, one of the main objectives in producing ceramic matrix composites is to increase the toughness. Ceramic matrix composite (CMC) development has lagged behind other composites because most of the processing routes for CMCs involve high temperatures and can only be employed with high-temperature reinforcements. Common matrix materials are alumina, glass,  $\text{Si}_3\text{N}_4$ , and  $\text{SiC}$ .

## 2.4 Reinforcement–Matrix Interactions

The bonding between reinforcement and matrix is critical to the performance of the composite material. Usually, a strong bond between reinforcement and matrix is desired so that the loads can be transferred efficiently between the reinforcements via the matrix. The fracture behavior is dependent on the strength of the interface. A weak interface results in a low stiffness and strength but high resistance to fracture, and sometimes high impact energy absorption, whereas a strong interface produces high stiffness and strength but often a low resistance to fracture (i.e., brittle behavior). The interface shown in figure 2.1 is a distinct phase in some cases, produced by a reaction between the matrix and the reinforcement; in other

instances the interface is developed in a few atomic thicknesses around the reinforcement, across which there is a change in properties from those of the matrix to those of the reinforcement. Thus, at the interface there is usually a discontinuity in chemical nature, crystal and molecular structures, and mechanical and other properties. The surface roughness of the reinforcement also has an influence on the reinforcement–matrix interaction characteristics.

#### 2.4.1 Wetting of Matrix into Fibers

Interfacial bonding is due to adhesion between the reinforcement and the matrix, in addition to mechanical interlocking or keying. For adhesion to occur during the manufacture of a composite, the reinforcement and the matrix must be brought into intimate contact. If the surfaces of two bodies come into intimate contact, where one of the bodies is commonly in liquid form, wetting is said to have taken place. Good wettability means that the liquid (matrix) will flow over the reinforcement, covering every valley of the rough surfaces of the reinforcement with displacement of all air and other contaminants. Wetting will only occur if the viscosity of the matrix is not too high and if wetting results in a decrease in the surface free energy of the system. The surface free energy of an interface is measured in  $J/m^2$  and can be shown to be equal to the surface tension, which has units of force per unit length ( $N/m$ ).

If we denote by  $\gamma_{SG}$ ,  $\gamma_{LG}$ , and  $\gamma_{SL}$  the free energy per unit area of the solid–gas, liquid–gas and solid–liquid interfaces, respectively, the force balance at equilibrium of the spreading film of figure 2.23 gives Young's equation:

$$\gamma_{SG} = \gamma_{SL} + \gamma_{LG} \cos \theta \quad (2.5)$$

Rearranging the above equation gives

$$\cos \theta = \frac{\gamma_{SG} - \gamma_{SL}}{\gamma_{LG}} \quad (2.6)$$

where  $\theta$  is called the contact angle. For a contact angle  $\theta = 180^\circ$ , the drop is spherical with only point contact with the solid, and no wetting takes place. At  $\theta = 0^\circ$ , perfect wetting occurs. For intermediate values ( $0^\circ < \theta < 180^\circ$ ), the degree of wetting increases as  $\theta$  decreases, and to make a liquid spread across a solid surface, a force (pressure) should be applied to the liquid. Often it is considered that the liquid does not wet the solid if  $\theta > 90^\circ$ . From figure 2.23, the wetting will not occur if  $\gamma_{SG}$  is similar to or less than  $\gamma_{LG}$ . Thus, thermoplastic matrices will generally wet thermosetting polymer reinforcements, but the reverse will not occur because thermosetting polymers have higher surface free energy than thermoplastic resins (Kinloch, 1987). Both thermosetting and thermoplastic matrices will wet metallic reinforcements readily because metals generally have higher surface free energies.

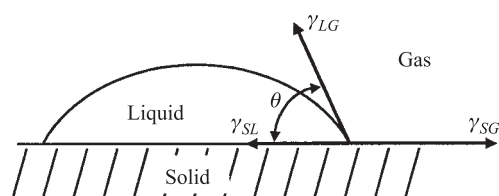


**Figure 2.23** Liquid in equilibrium with a solid with contact angle  $\theta$ .

More details on surface free energy are given in chapter 9 (see “Plasma Surface Treatment”).

Once the matrix has wet the reinforcement, and is in intimate contact with it, different types of bond may be formed, depending on the surface free energy, surface contaminants, or added surface active agents (coupling agents). Therefore, for a given system more than one bonding mechanism may be operative at the same time such as mechanical, electrostatic, and chemical bondings.

In many composites a good bond is only achieved by coating the fibers with a thin layer of a primer, or “size,” which is chemically compatible with both the fiber and the polymer matrix. For example, a vinylsilane size is applied to the surface of glass fibers to reinforce unsaturated polyester resin (Powell, 1994). The vinyl groups promote adhesion to the resin, and the silane groups are compatible with the glass. A vinylsilane size is not suitable for epoxy resin and glass fibers, but an aminosilane will do because the amino groups are compatible with the epoxy resin. Another example is the reinforcement of rubber with a nylon woven cloth. Normally, rubber and nylon will not bond at all, but coating the nylon with a toluene di-isocyanate in a solution of methylene chloride permits a strong bond.

#### *Chemical Reaction and Interdiffusion*

The diffusion process involves the diffusion of free chain ends at the interface between two polymers, which leads to chain entanglements and an increase in the adhesive strength. This effect is employed in some coupling agents, such as silane coupling. Interdiffusion can also take place in nonpolymeric systems, if it is accompanied by a chemical reaction.

#### *Mechanical Bonding*

The mechanical interlocking, or keying, of two surfaces is effective as the area of interface between the matrix and the reinforcement increases. The area of the interface of the reinforcement increases first as the surface roughness of the reinforcement increases, but decreases beyond a certain roughness value. Also, the fracture energy between the reinforcement and the matrix is dependent on the surface profile of the surface. Therefore, the optimum surface roughness of the reinforcement depends on the matrix property, coupling agent, and surface free energy relations. The mechanical bond is most effective when the force is applied parallel to the interface because the peel stress in the interface does not contribute much for this type of loading.

#### *Electrostatic Bonding*

This type of bonding occurs when the surfaces of the matrix and the reinforcement are oppositely charged. Electrostatic interactions are short range and are only effective over small distances of atomic order.

## 2.5 Wetting of Polymeric Matrix into Reinforcing Fibers

Processes for wetting polymeric matrix into fibers can be divided into two methods. In one method, fibers and matrix are processed directly into the finished structure.

Examples of such processes are filament winding and pultrusion. In the second method, the matrix is impregnated into the fiber to prepare ready-to-mold sheets that can be stored and later processed to form laminated structures by autoclave molding or compression molding.

Ready-to-mold fiber-reinforced polymer sheets are available in two basic forms, prepgres and sheet molding compounds.

### 2.5.1 Prepgres

This is the short terminology for preimpregnated fiber-reinforced plastics. Prepgres consist of roving, woven fabric, continuous unidirectional fiber reinforcement sheets, or random chopped fiber sheets impregnated with partially cured resin system. These differ from sheet molding compounds in that thickening agents, fillers, pigments, and additives are rarely, if ever, present. Most prepgres are based on epoxy resin systems (rarely polyester systems) and reinforcements usually include glass, carbon, and aramid fibers. The width of prepreg sheets varies from less than 25 mm (1 inch) for tape winding to over 1 m (40 inches) for commercial products, such as golf shafts and fishing rods. The thickness of a ply cured from prepreg sheets is normally in the range 0.125–0.250 mm (0.005–0.01 inch). Resin content in commercially available prepgres is between 40% and 50% by volume. Unidirectional fiber-reinforced prepgres are manufactured by pulling a row of uniformly spaced (collimated) fibers through a resin bath containing catalyzed epoxy resin dissolved in an appropriate solvent (figure 2.24). The solvent is used to control the viscosity of the liquid resin. Fibers preimpregnated with liquid resin are then passed through a chamber in which heat is applied in a controlled manner to advance the curing reaction to the B stage. At the end of the B stage, the prepreg sheet is backed up with a release film or waxed paper and wound around a take-up roll. The backup material is separated from the prepreg sheet just before it is placed in the mold. The normal shelf life (storage time before molding) for epoxy prepgres is about 1 month at 25°C; however, it can be stored for more than 1 year at –30°C.

### 2.5.2 Sheet Molding Compound (SMC)

This is a continuous sheet of ready-to-mold composite material containing fibers and mineral fillers dispersed in a thermosetting resin. The resin is in an uncured, but highly viscous (thickened) state. It is cured (cross-linked), and transformed into a finished product by the compression molding operation.

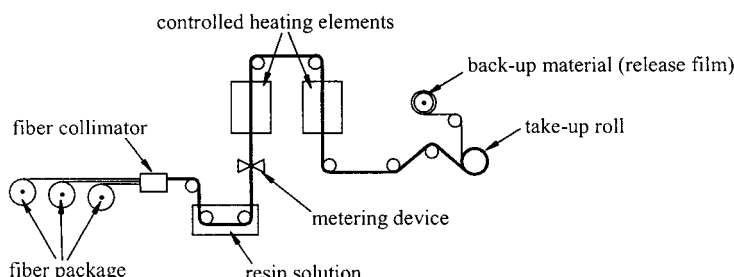


**Figure 2.24** Schematic of prepreg manufacturing.

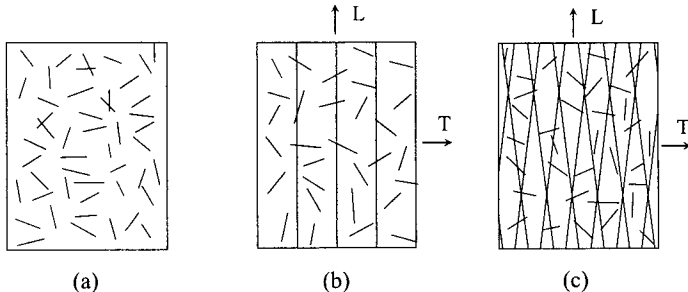


**Figure 2.25** Various forms of sheet molding compounds: (a) SMC-R; (b) SMC-CR; (c) XMC; L and T refer to longitudinal and transverse directions, respectively.

The development of SMC started in the early 1950s after the finding that the viscosity of unsaturated polyester resins increases with the addition of Group IIA metallic oxides, hydroxides, or carbonates (Meyer, 1987). The compound can be used to produce economically many structural composite parts of complex shapes and designs in a relatively short molding time. Many structural automotive components, such as bumper beams, grille opening panels, side panels, tailgates, and hoods are produced with high-strength SMC materials. Other applications of SMC composites are found in appliances (washing machine doors, refrigerator housings), furniture (chairs, tabletops), business machines (computer housings), and construction (door panels, bathtubs) (Mallick and Newman, 1990).

Sheet molding compounds are designated according to the form of fibers used in them (figure 2.25). These designations are:

1. SMC-R, in which R represents randomly oriented short fibers in the sheet.
2. SMC-CR, in which C represents continuous parallel fibers on one side of the sheet and R represents randomly oriented short fibers on the other side of the same sheet.
3. XMC, in which X represents criss-crossed continuous fibers in the sheet.

In both SMC-R and SMC-CR, the fiber content is shown by the weight percent at the end of each letter designation. For example, SMC-R40 contains 40 wt% of randomly oriented short fibers; SMC-C30R10 contains 30 wt% of continuous parallel fibers and 10 wt% of randomly oriented short fibers. The fiber content in XMC is in the region of 70 wt%, with the majority of the fibers in the continuous form. It may also contain small amounts of randomly oriented short fibers for improving the transverse properties. The angle between the criss-crossed fibers in XMC is usually in the range 5–7°.

#### *Fillers*

Fillers in SMC reduce the volumetric shrinkage of the resin, improve the moldability by promoting better flow, and enhance the surface quality of the molded part. They also reduce material cost, since they are generally much less expensive than the resin they replace in the resin paste. Calcium carbonate ( $\text{CaCO}_3$ ) is the most commonly used filler in SMC. Kaolin clay, talc, glass spheres (both solid and hollow), and alumina trihydrate ( $\text{Al}_2\text{O}_3 \cdot 3\text{H}_2\text{O}$ ) are also used as fillers. Among these fillers, hollow glass spheres have the lowest specific gravity; however, they tend to crush at the high

pressures used during molding operations. Alumina trihydrate acts as a filler as well as a fire retardant, since the water of hydration in its molecule is released at elevated temperatures (about 220°C).

The filler-to-resin ratio in SMC influences the resin paste viscosity, which controls the fiber surface wet out and resin flow in the mold. In general, the higher the fiber content, the lower the filler-to-resin ratio. For example, typical filler-to-resin ratios for SMC-R30, SMC-R50, and SMC-R65 are 1.5, 0.5, and 0, respectively.

Electrically conductive fillers are sometimes used in glass-fiber-reinforced sheet molding compounds to reduce the accumulation of static charge, which may otherwise interfere with electromagnetic or radio frequencies. Examples of these fillers are carbon black, carbon fibers, short aluminum or copper fibers, powders or flakes, and aluminized chopped glass fibers.

Catalysts in SMC are used to initiate the curing reaction at elevated temperatures, as stated in section 2.3.1.

#### *Inhibitors*

Inhibitors in SMC are added in very small amounts to prevent or reduce any curing reaction that may occur during mixing, maturation, and storage. This also improves the shelf life of SMC rolls prior to molding. When the SMC sheet is placed in a heated mold, the curing reaction is first slowed by the inhibitor, but its effect is overcome as a result of rapid generation of free radicals from the catalyst. As the inhibitor concentration decreases, the reaction rate accelerates in the mold. Hydroquinone and parabenoquinone are two common inhibitors used in SMC formulations.

#### *Internal Mold Release Agent*

Internal mold release agent in SMC prevents the resin from adhering to the mold surface, thus facilitating part ejection from the mold. Mold release agents are selected on the basis of their melting points (m.p.), which must be lower than the mold temperature. Commonly used mold release agents are zinc stearate (m.p. 133°C) and calcium stearate (m.p. 150°C). They can be used at mold temperatures up to 155°C and 165°C, respectively. Both are in powder form at room temperature but dissolve easily in the resin formulation. They are added in small concentrations, usually less than 2 wt% of the total compound. In addition to these internal mold release agents, smoother part ejection from the mold may require periodic spraying of the mold surface with a mold release agent.

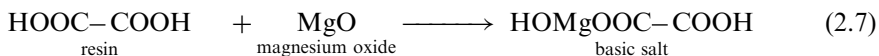
#### *Thickener*

This increases the viscosity of the resin by physical reaction rather than chemical reaction so that the SMC sheet can be handled, cut, stacked, and draped on the mold surface. In the thickened state, the resin is uncured, but its viscosity is in the range 30–100 kPa·s. In this condition, the SMC sheet is dry and feels nontacky, but it is still pliable.

Common thickeners used for polyester and vinylester SMCs are alkaline Group IIA metal oxides and hydroxides, such as MgO, CaO, and Mg(OH)<sub>2</sub>.

Addition of these oxides or hydroxides sets off a two-step reaction with the resin. An example is shown below.

Step 1 :



Step 2 :



The neutral salt formed in this reaction has a higher molecular weight than the resin. It can, in turn, react with other basic salts, creating large increases in the molecular weight. The metal oxide/hydroxide thickeners react with the resin immediately upon mixing with the resin formulation. The viscosity of the mixture increases rapidly in the beginning and tends to level off after a period of time (typically several days) called the maturation time.

When an SMC sheet is placed in a heated mold, the resin viscosity is reduced in a few seconds, since the high-molecular-weight neutral salt molecules in the thickened SMC dissociate into resin molecules at the molding temperature.

#### *Low-Profile Additives*

Low-profile additives are thermoplastic powders that are mixed with polyester and vinylester resins to control the shrinkage of SMC composites. Both resins exhibit 4–10% reduction in linear dimensions due to both the polymerization (curing) shrinkage in the mold and the thermal shrinkage while cooling outside the mold. Besides causing dimensional changes of the molded part, shrinkage may create a number of surface defects, such as waviness, sink marks (figure 8.13), and voids.

Shrinkage in SMC composites is reduced significantly by the addition of 10–20 wt% of a thermoplastic material, such as polyvinylacetate, polycaprolactone, and polyacrylate copolymers. At the onset of curing, thermoplastic additives separate and form a dispersed second phase in the resin. The thermoplastic phase absorbs small quantities of unpolymerized resin and styrene. The higher thermal expansion of the thermoplastic phase and the vapor pressure of the absorbed styrene resists the curing shrinkage of the resin. Microvoids are formed in the thermoplastic phase as the residual resin and styrene polymerize. When the molded part begins to cool outside the mold, both the matrix and the dispersed thermoplastic phase shrink. However, since the glass transition temperature of the cured polyester resin is higher than that of the thermoplastic additive, the thermal contraction rate of the cured matrix is much less than that of the thermoplastic phase. The difference between the two shrinkage rates causes void and microcrack formation at the interface of the two phases, which, in turn, compensates for the thermal shrinkage of the cured matrix.

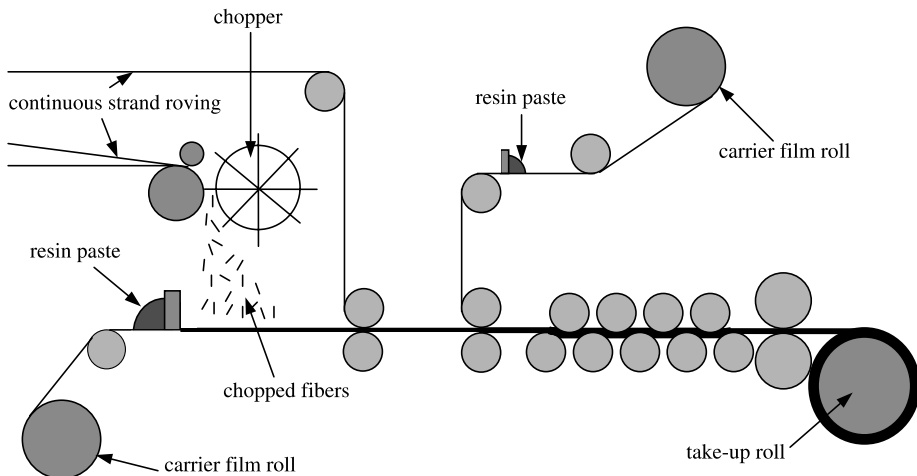


**Figure 2.26** Schematic drawing of SMC production.

#### *Pigments and Other Additives*

Organic or inorganic pigments, either in powder form or in a carrier resin, are added to a sheet molding compound to produce color in the molded part. Also other additives such as flame retardants, ultraviolet (UV) absorbers, and impact modifiers may be added. If a small amount of an impact modifier, such as acrylonitrile–butadiene copolymer or styrene–butadiene copolymer, is added to the SMC, the impact energy absorption, fracture toughness, and damage resistance of the SMC composite are increased dramatically.

#### *Production of SMC Sheet*

To manufacture SMC, a continuous polyethylene or cellophane film is coated with a suitably formulated polyester resin system into which is deposited a layer of either a chopped strand mat or chopped rovings with or without continuous fibers (SMC-R and SMC-CR). A second layer of polyethylene film, similarly coated with resin system, is placed over the reinforcement, and the sandwich thus formed is passed through a series of rollers to press the glass fibers into the resin and ensure thorough wetting. For XMC, these processes are carried out on a filament winding machine. The XMC sheet is removed by slitting the filament-wound roll along its length. The sandwich is then wound into a roll and left while the resin thickens. Figure 2.26 shows a schematic drawing of SMC production.

## 2.6 Properties of Typical Composite Materials

### 2.6.1 Fiber and Void Fractions

Theoretical calculations for strength, modulus, and other properties of a fiber-reinforced composite are based on the fiber volume fraction in the material. Experimentally, it is easier to determine the fiber weight fraction  $W_f$  from which the fiber volume fraction  $V_f$  and composite density  $\rho_c$  can be calculated when

there is *no void*:

$$V_f = \frac{W_f/\rho_f}{W_f/\rho_f + (1 - W_f)/\rho_m} \quad (2.9)$$

$$\rho_c = \frac{1}{W_f/\rho_f + (1 - W_f)/\rho_m} \quad (2.10)$$

where  $W_f$  = fiber weight fraction

$1 - W_f$  = matrix weight fraction

$\rho_f$  = fiber density

$\rho_m$  = matrix density

There are two methods to determine the fiber weight fraction experimentally: the ignition loss method (ASTM D2854-68) and the matrix digestion method (ASTM D3171-76). The ignition loss method is used for polymeric matrix composites that contain fibers that do not lose weight at high temperatures, such as glass fibers. In this method, cured resin is burnt off from a small test sample at 565°C (1050°F) in a muffle furnace. In the matrix digestion method, the matrix (either polymeric or metal) is dissolved away in a suitable liquid medium, such as concentrated nitric acid.

During the impregnation of matrix into fibers or during the curing process of laminates, air or other volatiles may be trapped in the material. The trapped air or volatiles exist in the cured laminate as microvoids, which may significantly affect some of its mechanical properties. A high void content over 2% by volume usually leads to lower fatigue resistance, greater susceptibility to water diffusion, and increased variation in mechanical properties. The void content in a composite laminate can be estimated by comparing the actual density with the density without voids:

$$V_v = \frac{\rho_c - \rho}{\rho_c} \quad (2.11)$$

where  $V_v$  = volume fraction of voids

$\rho_c$  = density without void from equation (2.10)

$\rho$  = actual density measured experimentally

## 2.6.2 Approximate Composite Material Properties

### Axial Modulus

There are several sets of approximate equations for obtaining the composite elastic and strength properties from those of the fiber and matrix materials (Hahn, 1980; Stellbrink, 1996). These equations should not be used when the experimental data are available because they only show the trends of properties. If we assume that the axial strain in the unidirectional fiber is uniform, as shown in figure 2.27, such that the axial strains in the fibers and the matrix are identical, that is,

$$\bar{\varepsilon}_1 = \varepsilon_f = \varepsilon_m \quad (2.12)$$

where  $\bar{\varepsilon}_1$  = axial strain in the composite

$\varepsilon_f$  = axial strain in the fiber

$\varepsilon_m$  = axial strain in the matrix

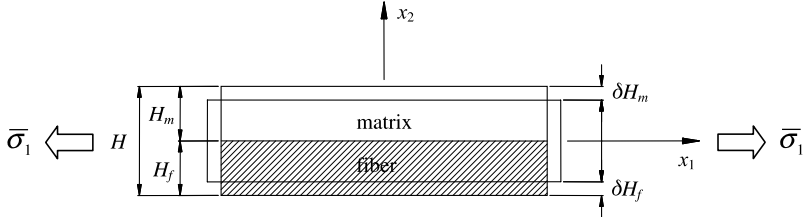


**Figure 2.27** Axial and transverse displacements of the unidirectional composite under axial load.

Let  $E_{f1}$  be the fiber axial modulus,  $E_m$  the matrix modulus,  $V_f$  the fiber volume fraction, and  $V_m$  matrix volume fraction. Axial force equilibrium of the composite requires that the average axial composite stress  $\bar{\sigma}_1$  be related to the axial stress in the fiber and matrix through the respective area quantities ( $A = A_f + A_m$ ), that is,

$$\bar{\sigma}_1 A = \sigma_f A_f + \sigma_m A_m \quad (2.13)$$

where  $\sigma_f$  = axial stress in the fiber

$\sigma_m$  = axial stress in the matrix

$A$  = cross-sectional area of the composite

$A_f$  = cross-sectional area of the fiber

$A_m$  = cross-sectional area of the matrix

Using equation (2.12), the effective axial composite modulus  $E_1$  is

$$E_1 = \frac{\bar{\sigma}_1}{\bar{\varepsilon}_1} = \frac{\sigma_f A_f}{\varepsilon_f A} + \frac{\sigma_m A_m}{\varepsilon_m A} \quad (2.14)$$

Using Hooke's law for the fiber and matrix ( $E = \sigma/\varepsilon$ ) and recognizing that the area and volume relationships are equivalent, we have

$$E_1 = E_{f1} V_f + E_m V_m \quad (2.15)$$

This type of equation is known as a rule of mixtures (ROM). It expresses the effective axial modulus of a unidirectional fibrous composite in terms of the modulus and the volume fraction of each constituent. Experimental evidence indicates that the rule of mixtures provides accurate prediction of the effective unidirectional axial modulus of composite over a wide range of fiber volume fraction. It may be shown theoretically by means of more advanced treatments that the predicted discrepancies are extremely small under all circumstances. The equal strain treatment is often described as a "Voigt model" (Hull and Clyne, 1996).

#### Axial Poisson's Ratio

The effective composite axial (major) Poisson's ratio  $\nu_{12}$  is defined as the negative ratio of lateral average strain  $\bar{\varepsilon}_2$  to the strain  $\bar{\varepsilon}_1$  produced by applying stress  $\bar{\sigma}_1$  only. For the dimensions shown in figure 2.27, the transverse strain  $\bar{\varepsilon}_2$  under uniform axial

stress,  $\bar{\sigma}_1$ , can be expressed as the transverse deformation  $\delta H$ , per height,  $H$ , in terms of fiber height  $H_f$ , matrix height  $H_m$ , and the respective Poisson's ratios,  $v_f$  and  $v_m$ , as

$$\bar{\varepsilon}_2 = \frac{\delta H}{H} = \frac{\delta H_f + \delta H_m}{H} = -\frac{v_f \bar{\varepsilon}_1 (V_f H) + v_m \bar{\varepsilon}_1 (V_m H)}{H} \quad (2.16)$$

where  $\delta H_f$  = transverse deformation of fiber height  $H_f$

$\delta H_m$  = transverse deformation of matrix height  $H_m$

The effective composite axial (or major) Poisson's ratio,  $v_{12}$ , is then

$$v_{12} = -\frac{\bar{\varepsilon}_2}{\bar{\varepsilon}_1} = v_f V_f + v_m V_m \quad (2.17)$$

Thus, the composite major Poisson's ratio is also approximated by a rule of mixtures expression.

#### Transverse Modulus

An approximate effective transverse modulus,  $E_2$ , can be estimated through consideration of a unidirectional composite subjected to the uniform average transverse stress,  $\bar{\sigma}_2$ , as depicted in figure 2.28. In this case we assume that the transverse stress is constant throughout the composite. Then the total transverse deformation  $\delta_2$  of the composite for a total thickness  $H$  is

$$\delta_2 = \bar{\varepsilon}_2 H = \varepsilon_f (V_f H) + \varepsilon_m (V_m H) \quad (2.18)$$

Therefore, the average transverse strain in the composite is

$$\bar{\varepsilon}_2 = \varepsilon_f V_f + \varepsilon_m V_m = \frac{\bar{\sigma}_2}{E_{f2}} V_f + \frac{\bar{\sigma}_2}{E_m} V_m \quad (2.19)$$

where  $E_{f2}$  is the transverse modulus of the fiber.

The effective transverse composite modulus is

$$\frac{1}{E_2} = \frac{\bar{\varepsilon}_2}{\bar{\sigma}_2} = \frac{V_f}{E_{f2}} + \frac{V_m}{E_m} \quad (2.20)$$

The equal stress treatment is often described as a “Reuss model.” Although this treatment is simple and convenient, it gives a poor approximation for  $E_2$  (Hull and Clyne, 1996).

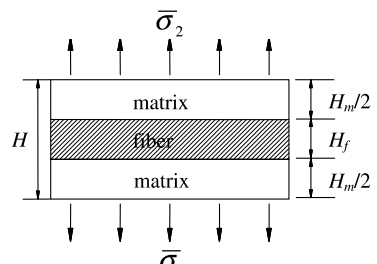


Figure 2.28 Axial and transverse displacements of the unidirectional composite under transverse load.

### Axial Shear Modulus

The effective composite axial shear modulus,  $G_{12}$ , is defined as

$$G_{12} = \frac{\bar{\tau}_{12}}{\bar{\gamma}_{12}} \quad (2.21)$$

under pure shear loading  $\bar{\tau}_{12}$ , as shown in figure 2.29. Assuming that the stress state is uniform throughout both the fiber and matrix, the shear strains in the fiber and matrix,  $\gamma_f$  and  $\gamma_m$ , are

$$\gamma_m = \frac{\bar{\tau}_{12}}{G_m} \quad (2.22)$$

$$\gamma_f = \frac{\bar{\tau}_{12}}{G_{f12}} \quad (2.23)$$

where  $G_{f12}$  is the axial shear modulus of the fiber and  $G_m$  is the shear modulus of the matrix.

The distorted length  $\bar{\delta}$  of the composite is the sum of distorted lengths of fiber  $\delta_f$  and matrix  $\delta_m$ , or

$$\bar{\delta} = \delta_f + \delta_m = \bar{\gamma}_f H_f + \bar{\gamma}_m H_m = \frac{\bar{\tau}_{12}}{G_{f12}} (V_f H) + \frac{\bar{\tau}_{12}}{G_m} (V_m H) \quad (2.24)$$

Then the average shear strain  $\bar{\gamma}_{12}$  for small deformation is calculated as

$$\bar{\gamma}_{12} = \frac{\bar{\delta}}{H} = \frac{(\bar{\tau}_{12}/G_{f12}) (V_f H) + (\bar{\tau}_{12}/G_m) (V_m H)}{H} = \frac{\bar{\tau}_{12}}{G_{f12}} V_f + \frac{\bar{\tau}_{12}}{G_m} V_m \quad (2.25)$$

Combining equations (2.21) and (2.25) gives the result

$$\frac{1}{G_{12}} = \frac{V_f}{G_{f12}} + \frac{V_m}{G_m} \quad (2.26)$$

Equation (2.26) has the same form of the transverse modulus in equation (2.20), and it also gives a poor prediction for  $G_{12}$ .

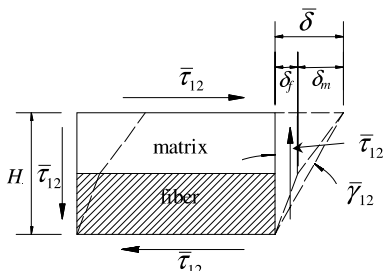


**Figure 2.29** Shear deformation of the unidirectional composite under shear load.

### 2.6.3 Composite Properties

Composite properties vary over a wide range according to the choice of fiber and matrix and the direction of loading. The designation of the different composites consists of the name of the fiber followed by the name of the matrix. The labels longitudinal ( $L$  or 1-direction) and transverse ( $T$  or 2-direction) represent the properties in the direction of the fiber (axial) and the properties perpendicular to the fiber (transverse). Since the properties of composites are functions of volume fraction, the fiber volume fractions should be specified. If the fiber volume fraction is not specified, it may have the typical value of 60% or should be read from the context. Figure 2.30 shows the fiber strength divided by the specific gravity ( $S/\rho_g$ ) of several fibers and the stiffness divided by the specific gravity ( $E/\rho_g$ ). Figure 2.31 shows the composite strength divided by the specific gravity ( $S/\rho_g$ ) of several composite materials and the stiffness divided by the specific gravity ( $E/\rho_g$ ). Tables 2.2 and 2.3 list the properties of constituent materials for composite materials, and typical composite materials and conventional materials.

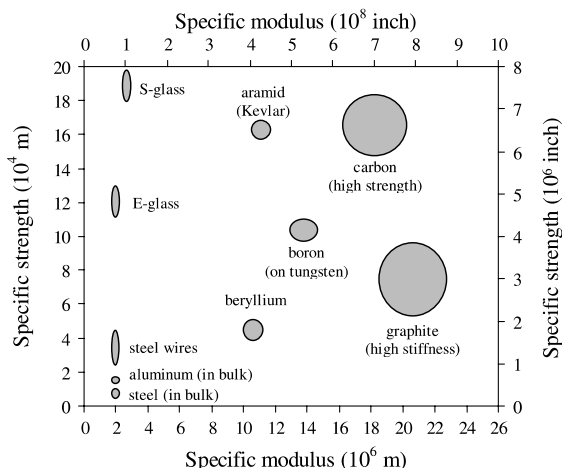


**Figure 2.30** Specific strength ( $S/\rho_g$ ) versus specific modulus ( $E/\rho_g$ ) for a variety of fibers used in structural composite materials (from Daniel and Ishai, 1994).

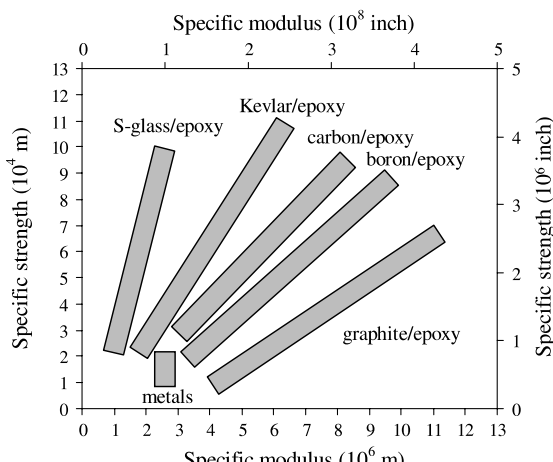


**Figure 2.31** Specific strength ( $S/\rho_g$ ) versus specific modulus ( $E/\rho_g$ ) for a variety of composites (from Daniel and Ishai, 1994).

**Table 2.2 Properties of Metals and Commonly Used Reinforcing Fibers and Matrix for Composites**

Material	Density $\rho$ [ $10^3 \text{ kg/m}^3$ ( $\text{lb/in}^3$ )]	Modulus $E_I$ [GPa ( $\text{Msi}$ )]	Specific stiffness $E_I/\rho g$ [ $10^6 \text{ m}$ ]	Tensile strength $X^t$ [MPa ( $\text{ksi}$ )]	Specific strength $X^t/\rho g$ [ $10^3 \text{ m}$ ]
Metals					
Steel (SAE 1010)	7.8 (0.284)	207 (30)	2.68	365 (53)	4.68
Steel (AISI 4340)	7.8 (0.284)	207 (30)	2.68	1515 (220)	19.4
Al (6061-T6)	2.7 (0.097)	69 (10)	2.60	310 (45)	11.5
Al (7178-T6)	2.7 (0.097)	69 (10)	2.60	537 (78)	19.9
Stainless (AISI 440 H&T)	7.8 (0.284)	196 (28.5)	2.54	1790 (260)	22.9
Titanium alloy (Ti-6Al-4O)	4.5 (0.163)	110 (16)	2.53	1068 (155)	23.7
Fibers (axial properties)					
AS4	1.80 (0.065)	235 (34)	13.1	3600 (522)	200
T300	1.76 (0.064)	231 (33)	13.1	3650 (530)	208
P100S	2.15 (0.078)	724 (105)	33.7	2250 (319)	102
IM8	1.8 (0.065)	310 (45)	17.2	5170 (750)	287
Boron	2.6 (0.094)	385 (55.8)	14.8	3800 (551)	146
Kevlar 49	1.44 (0.052)	124 (18)	8.61	3620 (525)	251
SCS-6	3.3 (0.119)	400 (58.0)	12.1	3500 (507)	106
Nicalon	2.55 (0.092)	180 (28)	7.06	2000 (290)	78.4
Alumina	3.95 (0.143)	379 (55)	9.60	1590 (230)	40.1
S-2 Glass	2.46 (0.090)	86.8 (12.6)	3.53	4590 (665)	186
E-Glass	2.58 (0.093)	69 (10.0)	2.69	3790 (550)	134
Sapphire	3.97 (0.143)	435 (63)	11.0	3600 (522)	90.7
Matrix materials					
Epoxy	1.38 (0.050)	4.6 (0.67)	0.33	58.6 (8.5)	4.25
Polyimide	1.46 (0.053)	3.5 (0.5)	0.24	103 (15)	7.05
Copper	8.9 (0.32)	117 (17)	1.31	400 (58)	4.50
Silicon carbide	3.2 (0.116)	400 (58)	12.5	310 (45)	9.69

## 2.7 Advantages and Disadvantages of Composite Materials

Fiber-reinforced composite materials offer a combination of strength and modulus that is either comparable to or better than many traditional metallic materials. Because of their low specific gravities, the strength-weight ratios and modulus-weight ratios of these composite materials are much superior to those metallic materials (figures 2.30, 2.31). Composite materials can be tailored to meet the specific demands of each particular application. Available design parameters are the choice of materials (fiber, matrix), the volume fraction of fiber and matrix, fabrication method, number of layers in a given direction, thickness of individual layers, type of layer (unidirectional or fabric), and the layer stacking sequence. Structures made of polymeric matrix fiber-reinforced composite materials usually have higher natural

**Table 2.3 Properties of Commonly Used Composite Materials**

<i>Material</i>	<i>Density</i> $[10^3 \text{ kg/m}^3]$ (lb/in $^3$ )	<i>Longitudinal</i> <i>modulus</i> $E_1$ [GPa (Msi)]	<i>Transverse</i> <i>modulus</i> $E_2$ [GPa (Msi)]	<i>Poisson's</i> <i>ratio</i> $\nu_{12}$	<i>Poisson's</i> <i>ratio</i> $\nu_{23}$	<i>Shear</i> <i>modulus</i> $G_{12}$ [GPa (Msi)]	<i>Shear</i> <i>modulus</i> $G_{23}$ [GPa (Msi)]	<i>Specific</i> <i>stiffness</i> $E_1/\rho g [10^6 \text{ m}]$
AS4/3501-6	1.52 (0.055)	148 (21.5)	10.5 (1.46)	0.30	0.59	5.61 (0.81)	3.17 (0.46)	9.74
T300/5208	1.54 (0.056)	132 (19.2)	10.8 (1.56)	0.24	0.59	5.65 (0.82)	3.38 (0.49)	8.73
USN150 (High-strength carbon epoxy)	1.54 (0.056)	131 (19.0)	10.8 (1.56)	0.28	0.59	5.65 (0.82)	3.38 (0.49)	8.73
Kevlar 49/epoxy	1.38 (0.05)	76.8 (11.0)	5.5 (0.8)	0.34	0.37	2.07 (0.3)	1.4 (0.20)	5.57
Boron/Al	2.65 (0.096)	227 (32.9)	139 (20.2)	0.24	0.36	57.6 (8.35)	49.1 (7.12)	8.73
E glass/epoxy	2.10 (0.076)	39.0 (5.7)	8.6 (1.24)	0.28	0.40	3.8 (0.54)	4.12 (0.60)	1.86

48

<i>Material</i>	<i>Longitudinal</i> <i>tensile strength</i> $X' [\text{MPa (ksi)}]$	<i>Transverse</i> <i>tensile strength</i> $Y' [\text{MPa (ksi)}]$	<i>In-plane</i> <i>shear strength</i> $S [\text{MPa (ksi)}]$	<i>Specific</i> <i>strength</i> $X'/\rho g [10^3 \text{ m}]$	<i>Longitudinal</i> <i>CTE</i> $\alpha_1 [\mu/\text{ }^\circ\text{C}]$ ( $\mu/\text{ }^\circ\text{F}$ )	<i>Transverse</i> <i>CTE</i> $\alpha_2 [\mu/\text{ }^\circ\text{C}]$ ( $\mu/\text{ }^\circ\text{F}$ )	<i>Fiber</i> <i>volume</i> <i>fraction</i> $V_f$
AS4/3501-6	2137 (310)	53.4 (7.75)	89 (12.9)	141	-0.8 (-0.44)	29 (16)	0.62
T300/5208	1513 (219.5)	43.4 (6.3)	62 (9.0)	98.2	-0.77 (-0.43)	25 (13.6)	0.62
USN150 (High-strength carbon epoxy)	2000 (290)	61.0 (6.9)	70 (10.2)	128	-0.9 (-0.5)	27 (15)	0.62
Kevlar 49/epoxy	1380 (200)	27.6 (4.0)	49 (7.1)	100	-4 (-2.2)	57 (32)	0.55
Boron/Al	1290 (187)	117 (17)	128 (18.5)	48.7	5.94 (3.3)	16.6 (9.2)	0.46
E glass/epoxy	1080 (157)	39.0 (5.7)	89 (12.9)	51.4	7.0 (3.9)	21 (11.7)	0.55

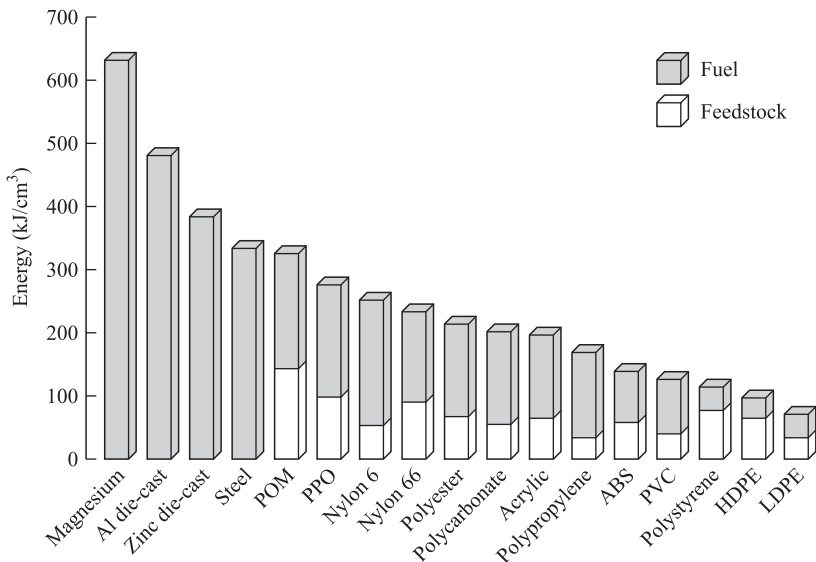


**Figure 2.32** Energy requirements to produce metal alloys and plastics; for plastics the energy required to manufacture the plastic is shown separately from the fuel equivalent of the raw material (from McCrum et al., 1997).

frequencies and higher material damping capacity than those made of conventional materials, such as aluminum and steel (Jeong et al., 1995). Also, composite materials in the fiber direction have higher fatigue endurance limit than steel or aluminum. Toughened composites can give higher impact energies than aluminum alloys (Cheon and Lee, 2001). The potential for corrosion of composite materials is significantly lower than metallic materials. Nearly all structures are exposed to temperature change during their lifetimes. The strains associated with temperature change can result in changes in size or shape, and thermal stresses. In some applications these thermal effects can be critical (e.g., machine tool spindles and space shuttle doors). Thus, there are many applications where a material with a zero or near-zero coefficient of thermal expansion (CTE) can result in significant benefits. Through proper design, it is possible to have zero-CTE composites or to design the CTE of the composite to match that of other components to minimize thermal mismatch and the resulting thermal stresses.

The greatest disadvantages of composite materials are the costs of the materials, the lack of well-defined design rules, and currently, difficulty in recycling of materials. The cost problem of composite structures can be solved partly by the use of automated methods such as filament winding, pultrusion, and tape laying. Also, composite structures can be fabricated exactly to the required size with little or no material waste.

Plastics and fiber-reinforced plastics are increasingly employed in automotive parts, due to the thrust toward replacing heavier metal parts with lighter material parts to lower emissions and to save fuel. The energy consumed in propelling a car, in an average life of 160,000 km, is 10–15 times the energy used to manufacture it (McCrumb et al., 1997). Therefore, a light vehicle is very important, even if the energy input for the production of a lighter plastic or plastic composite exceeds that of the heavier metal part it replaces.

Plastics are usually considered that they have higher energy content than that of competitive metals; however, the energy content of plastics is less than that of competitive metals on a volume basis, as shown in figure 2.32. For example, a typical steel car hood requires as much as 27 kg of crude oil equivalent, taking into account the significant stamping waste that has to be recycled. The same hood in polymer composite requires 16 kg of crude oil equivalent because of its lower mass, negligible trimming waste, energy-conserving forming process, and large proportion of mineral fillers and glass-fiber reinforcement, which have a low crude oil equivalent. Thus, the switch from steel to polymeric materials leads to energy saving during the fabrication, as well as the operation period, of vehicles.

## 2.8 Overview of Composite Fabrication Methods

The choice of a composite fabrication process is strongly influenced by the chemical and physical natures of the matrix (i.e., thermoset or thermoplastic, metal, ceramic) and the temperature required to form, melt, or cure the matrix. However, the process that ultimately is chosen for an industrial application must permit the user to take full advantage of the unique attributes or capabilities it possesses. Otherwise, alternative technologies may offer a more cost-effective manufacturing process.

### 2.8.1 Compression Molding

Although compression molding is one of the oldest manufacturing techniques in the plastics industry for molding thermosetting materials, such as phenolic and alkyd powders and rubber compounds, it is widely used with the recent development of high-strength sheet molding compounds (SMC) and a greater emphasis on the mass production of composite materials (Mallick and Newman, 1990).

The process of compression molding shown in figure 2.33 can be described as follows. First, a stack of SMC plies, called a *charge*, is placed in the preheated mold. The plies are die-cut to the desired shape and size from a properly matured SMC roll. The ply dimensions are selected to cover 60–70% of the mold area with the charge.

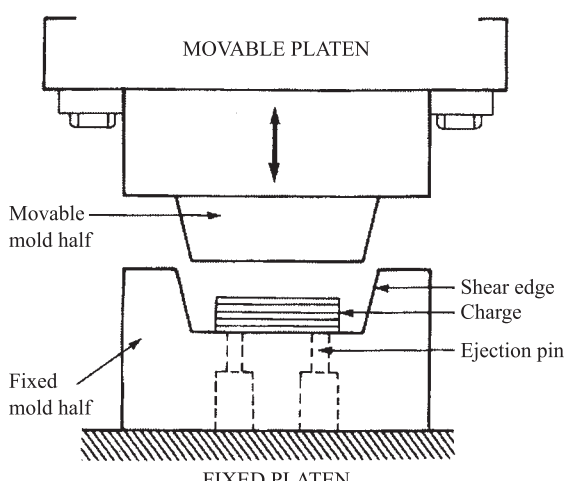


**Figure 2.33** Schematic of a compression molding (from Mallick and Newman, 1990).

Since the charge weight should be kept constant for each part, any variation in SMC sheet weight per unit area is made up by adding small strips cut from the SMC roll.

After the charge has been placed in the bottom mold half, the top mold is quickly moved to contact the top surface of the charge. Then the top mold is closed at a slower rate, usually at 5–10 mm/s. As the molding pressure increases with the continued mold closure, the SMC flows toward the cavity extremities, forcing the air in the cavity to escape through the shear edges or other vents. The molding pressure based on the projected area ranges from 1 to 40 MPa depending on the part complexity, flow length, and SMC viscosity at the mold temperature. The common mold surface temperature is approximately 149°C.

After the cavity has been filled, the mold remains closed for a predetermined period of time to assure a reasonable level of curing and ply consolidation throughout the part. The curing time, which may vary from one to several minutes, depends on several factors, including the resin–catalyst–inhibitor reactivity, part thickness, and mold temperature. At the end of the curing time, the top mold is opened and the part is removed from the bottom mold with the aid of ejection pins. The part is then allowed to cool outside the mold, while the mold surfaces are cleaned of any remaining debris and sprayed with an external mold release agent in preparation for the molding of the next part.

Compression molding is discussed in more detail in section 8.6.

### 2.8.2 Autoclave Vacuum Bag Degassing Method

The vacuum bagging process is used predominantly in the aerospace industry where composite part performance rather than high production rate is a major consideration. The starting material is normally a prepreg, although the wet lay-up laminates may be also vacuum bag molded.

Figure 2.34 shows the schematic drawing of an autoclave vacuum bag molding process. The mold surface is covered with a nonporous Teflon sheet or a Teflon-coated glass fabric separator (used for preventing sticking in the mold) or pasted with mold release for high-surface-quality products. Then the prepreg plies are laid up on the mold in the desired fiber orientation angle as well as in the desired stacking sequence. Plies are trimmed from the prepreg roll into the desired shape, size, and orientation by means of a cutting device, which may be simply a mat knife. Laser

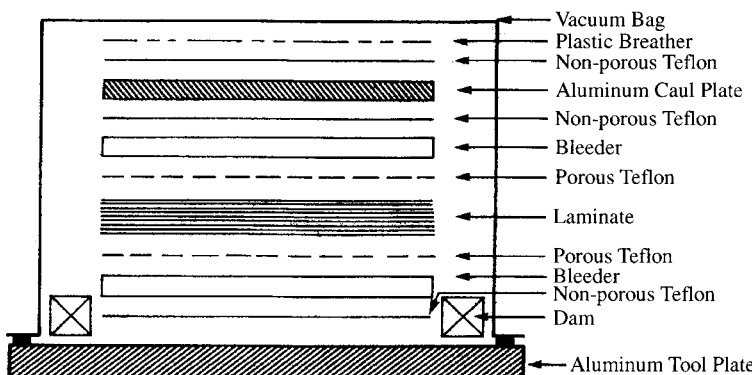


**Figure 2.34** Schematic of a vacuum bag molding process.

beams, high-speed water jets, and trimming dies are also used. The layer-by-layer stacking operation can be performed either manually or by numerically controlled automatic tape-laying machines.

After the lay-up operation is completed, a porous release cloth (or porous Teflon film) and a few layers of bleeder papers are placed on top of the prepreg stack. Sometimes the release cloth and/or the bleeder papers are placed also on bottom of the prepreg stack when the number of preps stacked is large or to have higher fiber volume content. The bleeder papers are used to absorb the excess resin in the prepreg as it flows out during the molding process. The complete lay-up is covered with another sheet of Teflon-coated glass-fabric separator (or nonporous Teflon film), a caul plate, and then a thin heat-resistant vacuum bag. The entire assembly is placed inside a preheated autoclave, where a combination of external pressure and vacuum is applied to consolidate and densify separate plies into a solid laminate. An autoclave is a closed vessel for controlling temperature and pressure for curing polymeric matrix composites.

Typically, a prepreg contains 34 wt% of resin to allow 1–2 wt% resin loss during molding. Then the actual fiber content in the cured laminate is 60 vol%, which is considered an industry standard for aerospace applications.

Figure 2.35 shows a typical two-stage cure cycle for a B-staged carbon-fiber epoxy prepreg. The first stage involves increasing the temperature up to 130°C for aerospace purpose structures (80°C for commercial purpose structure) and dwelling at this temperature about 1 hour for consolidation and bleeding out excess resin in prepreg. During the heat-up process the resin viscosity in the prepreg first decreases, attains a minimum during the period of temperature dwell and an external pressure of about 0.7 MPa (100 psi) and internal vacuum are applied on the preps to bleed out the excess resin, as well as to remove any entrapped air and volatiles from the prepreg. At the second stage, the autoclave temperature is increased to initiate the cross-linking of resin. The cure temperature and pressure are maintained for 2 hours or more until a predetermined degree of cure has been achieved. The temperature is then gradually decreased while the part is still under pressure. At the end of the cure cycle, the part is removed from the vacuum bag and, if necessary, postcured at an elevated temperature in an oven.

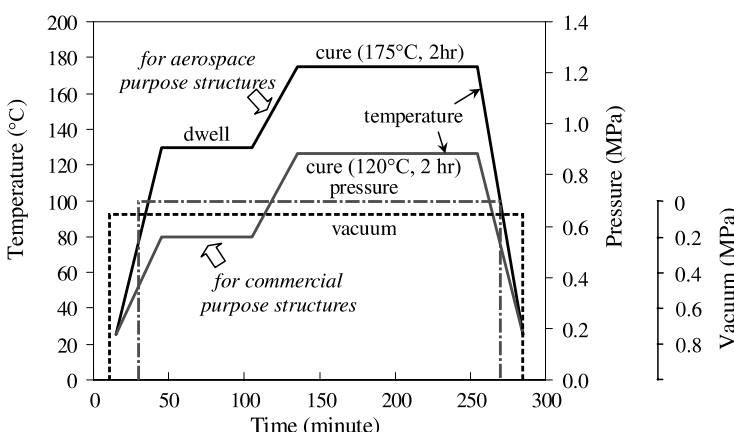
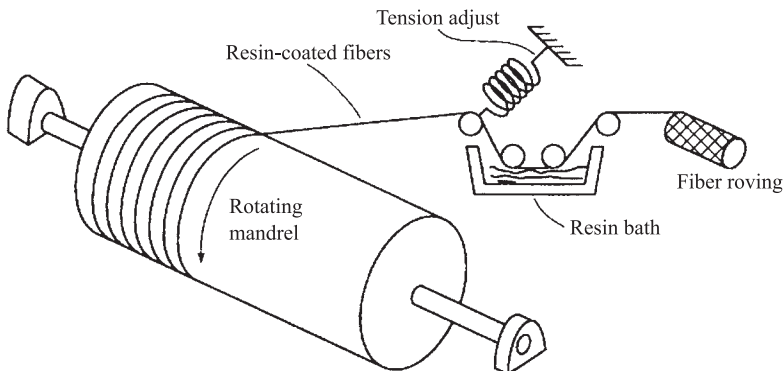


Figure 2.35 Typical two-stage cure cycle for an epoxy matrix composite material.



**Figure 2.36** Schematic drawing of filament winding operation.

More details on the autoclave vacuum bag degassing process are presented in section 8.8.

### 2.8.3 Filament Winding

Figure 2.36 shows a schematic drawing of a filament winding process. Filament winding is a technique used for the manufacture of surfaces of revolution such as pipes, tubes, cylinders, and spheres. A continuous band composed of yarn (an assemblage of twisted filaments), tow (an untwisted bundle of continuous filaments), or roving (a number of yarns, strands, tows, or ends collected into a parallel bundle with little or no twist) goes from the creels to a resin bath and may be gathered into a band of given width and wound over a rotating male mandrel (wet winding).

The winding angles and the placement of the reinforcements are controlled through specially designed machines, traversing at speeds synchronized with the mandrel rotation.

The reinforcements may be wrapped in adjacent bands with the step of width of a band, which eventually cover the entire mandrel surface. The resin content can be controlled by varying the winding tension with a specially designed tensioner.

In addition to the wet winding, a prepreg tape of resin-impregnated fibers is wrapped over a mandrel to produce a hollow part. This method reduces fiber damage during the winding operation and the resin content of the laminate can be controlled more accurately with prepgres.

The winding angle used for construction of hollow structures depends on the strength or stiffness requirements and may vary from longitudinal through helical to circumferential (or hoop), as shown in figure 2.37.

For open-ended structures such as cylinders or conical shapes, mandrel design is simple; however, careful consideration is required to design the mandrel for end-closed structures. Concepts frequently used for the construction of mandrels include collapsible metal or glass, low-melting alloys, eutectic salts, soluble plasters, fragile or break-out plasters, and inflatables.

The filament winding process is discussed in more detail in section 8.7.1.

### 2.8.4 Pultrusion

Pultrusion is a continuous manufacturing process used to produce high-fiber-content reinforced plastic structural parts. The name pultrusion originates from “pull” and

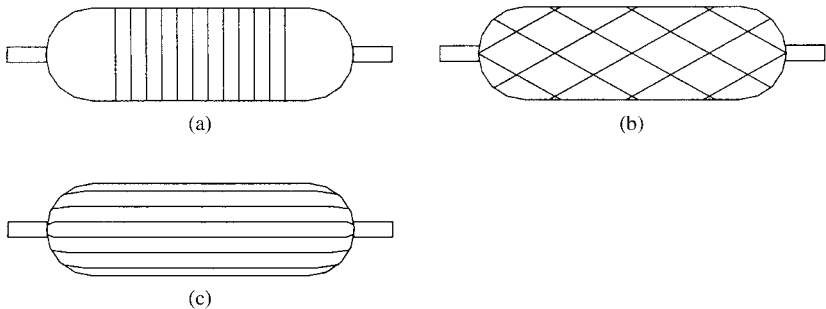


**Figure 2.37** Filament winding patterns: (a) Hoop or circumferential; (b) helical; (c) longitudinal.

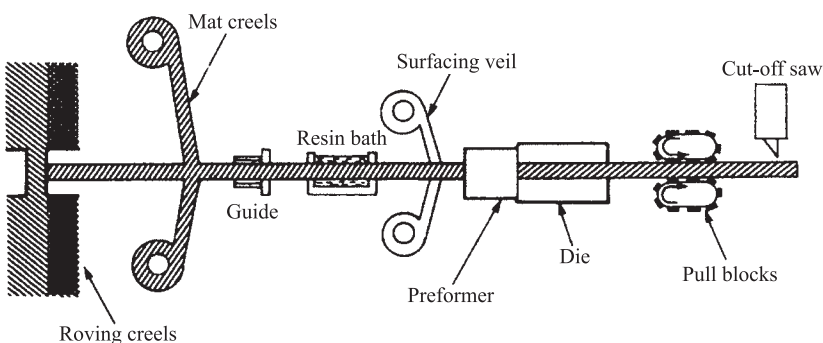


**Figure 2.38** Schematic diagram of pultrusion process.

“extrusion.” Figure 2.38 shows a schematic drawing of the process. Guide plates are used to position the longitudinal reinforcements, frequently combined with mat or biaxial fabric in their designed locations in the shape being pultruded. Then the reinforcements are passed through a resin bath containing a catalyst. After this process, the resin-impregnated fibers pass through a preformer that gradually bends the resin-impregnated fibers to form the shape being pultruded and to reduce the amount of excess resin. The heated die has the shape of the finished component to be produced. The resin is cured in the die and the composite is pulled out by either a reciprocating pulling or a caterpillar system. The reciprocating pulling system has two pull blocks that move forward in the pulling direction and backward alternately. These pull blocks have mechanically operated clamps that open and close to maintain a steady pulling force on the part. The caterpillar-type pulling system has a set of lower tracks and a set of upper tracks. A set of chains having a clamping system travels on each of these tracks.

Pultrusion differs from filament winding in that filament winding places the primary reinforcement in the hoop direction, while pultrusion has the primary reinforcement in the longitudinal direction. Pultrusion can produce a variety of reinforced solid, tubular, or structural profiles, as shown in figure 2.39. The pultrusion process can produce 2–200 m of product per hour depending on the shape and the resin used.

Most of the commonly used continuous reinforcements such as glass, carbon, and aramid fibers work with pultrusion. A variety of reinforcement forms can be used, including roving, mat, and fabric. All resins can be chosen to work with pultrusion

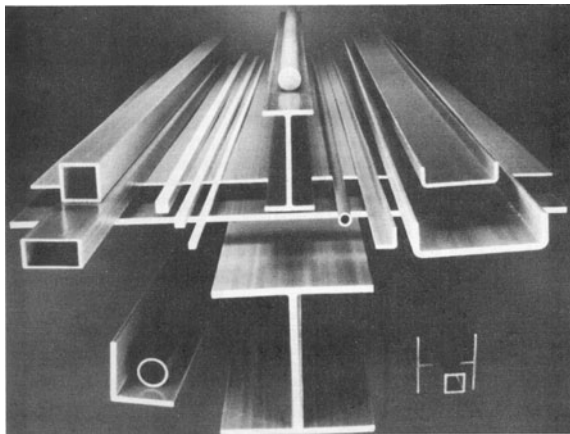


**Figure 2.39** Pultruded structural shapes.

provided they meet certain requirements. The resin needs to cure quickly because of the high-speed continuous nature of the process. Viscosity values around 500 mPa·s are typical for pultruded resin. Polyester is a popular resin for pultrusion because it shrinks slightly on curing and thus easily releases from the die. In contrast, epoxy resins tend to stick to the die and other parts of the pultrusion equipment. Release agents, viscosity modifiers, and nonsticking cloth represent possible means to prevent sticking.

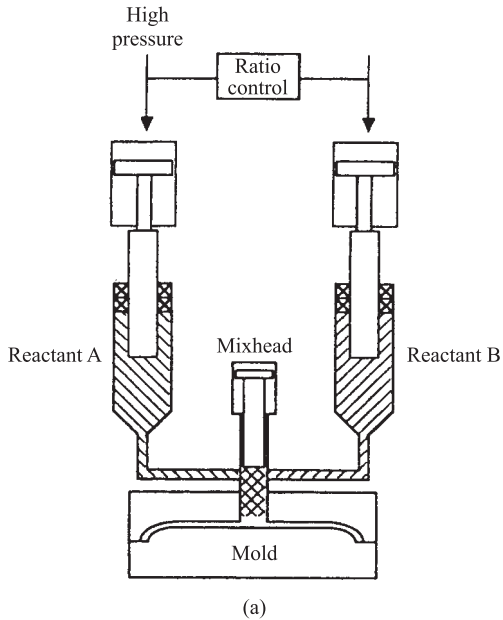
In order to improve the properties in the hoop direction of pultruded products, the pull winding process has been developed. The process combines the standard continuous unidirectional fibers of the pultrusion process with hoop-wound continuous fibers. The longitudinal fibers are used for axial and bending resistance, while the hoop fibers are used for hoop tension and compression resistance.

Further discussion of the pultrusion process is found in section 8.7.2.

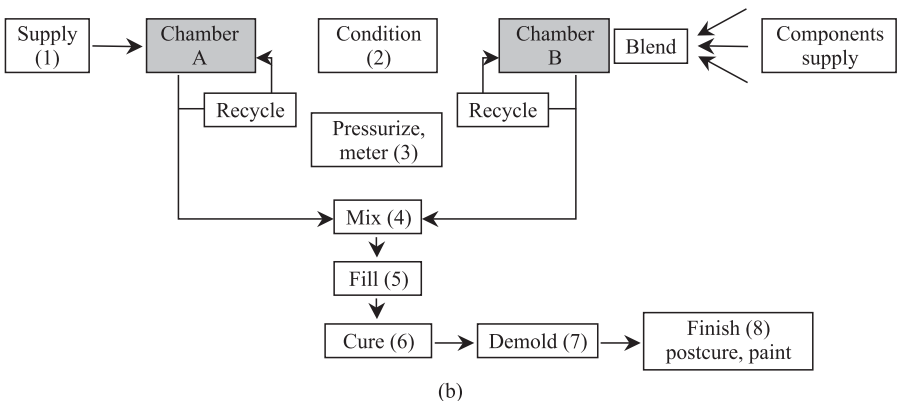
### 2.8.5 Liquid Composite Molding

Among various polymeric matrix composite manufacturing techniques, liquid composite molding processes, such as resin transfer molding (RTM) and structural reaction injection molding (SRIM), have been recognized as relatively new but very high potential processes. A schematic of the SRIM process is shown in figure 2.40(c). The process combines the high production rate of the reaction injection molding (RIM) process, as shown in figure 2.40(a), with preplaced reinforcements to produce high-strength structural composites.

The RIM process is quite different from conventional thermoplastic injection molding (TIM) because it uses polymerization in the mold rather than cooling to form a solid polymer. Other reaction molding processes, like monomer casting or thermoset injection molding, also use polymerization to set the part shape; however, they employ hot mold walls to activate the reaction. In RIM, monomer and mold temperature are not so different and the reaction is activated by impingement mixing, as shown in figure 2.40(a). Two or more liquid reactants flow at high pressure, typically 10–20 MPa, into a mixing chamber. Usually the flow rate ratio between the two streams must be carefully metered to give the correct stoichiometry of the reactants. In the mixhead the streams impinge at high velocity, mix, and begin to polymerize as they flow out into the mold cavity. Because the mixture is initially at a low viscosity, low pressure, less than 1 MPa, is needed to fill the mold.



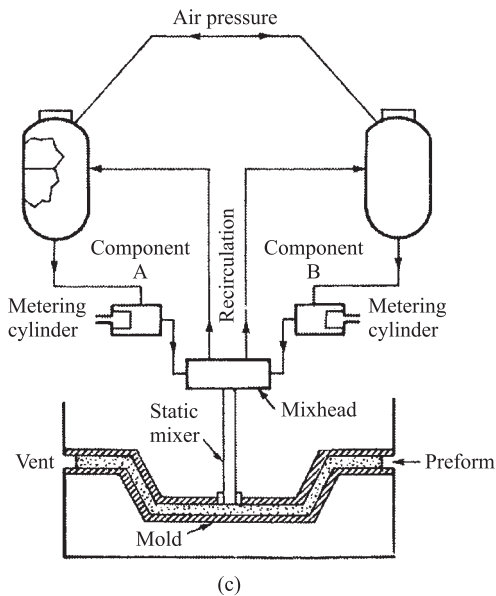
(a)



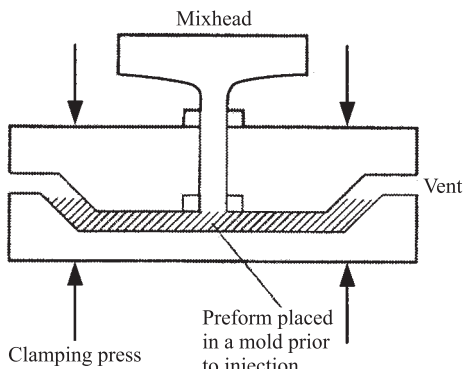
(b)

**Figure 2.40** Schematic drawing of reaction injection molding (RIM) and structural reaction injection molding (SRIM): (a) Reaction injection molding (RIM); when the mixhead ram moves back, two or more liquid reactants flow at high pressure (10–20 MPa) into the mixhead chamber. There they impinge and begin to polymerize as they flow into the mold. (b) Eight unit operations for the reaction injection molding (RIM) (from Macosko, 1989). (c) Structural reaction injection molding (SRIM).

Reaction injection molding can be broken down into eight unit operations, which are illustrated in figure 2.40(b) (Macosko, 1989). Supply tanks are used to store and blend components. They maintain the level in conditioning tanks at the machine. The conditioning tanks control temperature and degree of dispersion of the reactants by low-pressure recirculation. The recirculation loop is also used to inject inert gas (a process called “nucleation” in the industry), which serves to compensate for shrinkage during the mold curing step. The third step in RIM is high-pressure metering of the reactants to the mixhead at sufficient flow rate for good mixing and at the proper ratio for complete polymerization. From the impingement chamber



(c)

**Figure 2.40** Continued.**Figure 2.41** Schematic drawing of resin transfer molding (RTM).

the reacting mixture flows into the mold, filling it in typically less than five seconds. There it cures, polymerizes, and solidifies sufficiently to take the stresses of demolding. The final operation consists of various finishing, including trimming of flash, postcuring, cleaning, and painting. The RIM process was developed from polyurethane rigid-foam technology.

A very similar process is called structural reaction injection molding (SRIM). The schematic drawing in figure 2.40(c) shows the basic SRIM process. In the process, preform reinforcements are placed in a closed mold and the SRIM resin is rapidly introduced into the mold; it reacts quickly to cure fully with a few seconds. This reaction is in progress as the resin flows through the reinforcement. Therefore wetout and displacement of the air in the mold must occur rapidly.

Resin transfer molding, as shown in figure 2.41, like SRIM in figure 2.40(c), is a reactive polymer processing method in which liquid reactants cure in a mold containing fiber reinforcements to produce a composite part. In RTM, resins are mixed by a static mixer at low pressure and pumped into the mold at a rate much slower than that of SRIM resins (minutes vs. seconds). Mold filling pressure is often

less than 0.7 MPa for RTM, and the force needed to clamp the mold is also low. This allows reinforced epoxy molds to be used, which are much cheaper than the conventional steel molds. The mold filling pressure of SRIM is often several times higher than that of RTM because of the much higher filling rate.

Resins used in RTM are typically low-viscosity liquids (100–1000 mPa · s, or 100–1000 cP). Normally, resin systems have two components and require a mixing ratio around 100:1 for polyester resin.

Resins for SRIM are similarly two-part, low-viscosity liquids (10–100 mPa · s, or 10–100 cP) at room temperature. They are highly reactive in comparison with RTM resins and require very fast, high-pressure impingement mixing to achieve thorough mixing before entering the mold. Mix ratios of typical systems are near 1:1, which is desirable for rapid impingement mixing.

Liquid composite molding is discussed in more detail in section 8.5.

### EXAMPLE 2.1

Compare the flexural stiffnesses between the isotropic sandwich construction and the monocoque (thin-walled) construction, as shown in figure 2.42, when  $h_c/t_f = 10$ . The sandwich construction employs two identical faces of thickness  $t_f$ , and a core depth of  $h_c$ . The monocoque construction is a flat sheet construction of thickness  $2t_f$ , hence approximately the same weight as the sandwich construction using the same face material.

#### Solution

(a) For the sandwich construction, the flexural stiffness per unit width is

$$\begin{aligned} E_s I_s &= E_f \frac{1}{12} \left[ (h_c + 2t_f)^3 - h_c^3 \right] + E_c \frac{1}{12} h_c^3 \\ &= \frac{E_f}{12} \left[ 3(h_c)^2 (2t_f) + 3h_c (2t_f)^2 + (2t_f)^3 \right] + E_c \frac{h_c^3}{12} \quad (2.27) \\ &= \frac{E_f t_f h_c^2}{2} \left[ 1 + 2 \frac{t_f}{h_c} + \frac{4}{3} \left( \frac{t_f}{h_c} \right)^2 + \frac{1}{6} \frac{E_c h_c}{E_f t_f} \right] \end{aligned}$$

when  $t_f/h_c \ll 1$ , and  $E_f/E_c \gg 1$ , such that  $E_f t_f \gg E_c h_c$ , equation (2.27) reduces to

$$E_s I_s = \frac{E_f t_f h_c^2}{2} \quad (2.28)$$

(b) For the monocoque construction:

$$E_m I_m = E_f \frac{(2t_f)^3}{12} = \frac{2E_f t_f^3}{3} \quad (2.29)$$

Hence, we have

$$\frac{E_s I_s}{E_m I_m} = \frac{3}{4} \left( \frac{h_c}{t_f} \right)^2 \quad (2.30)$$

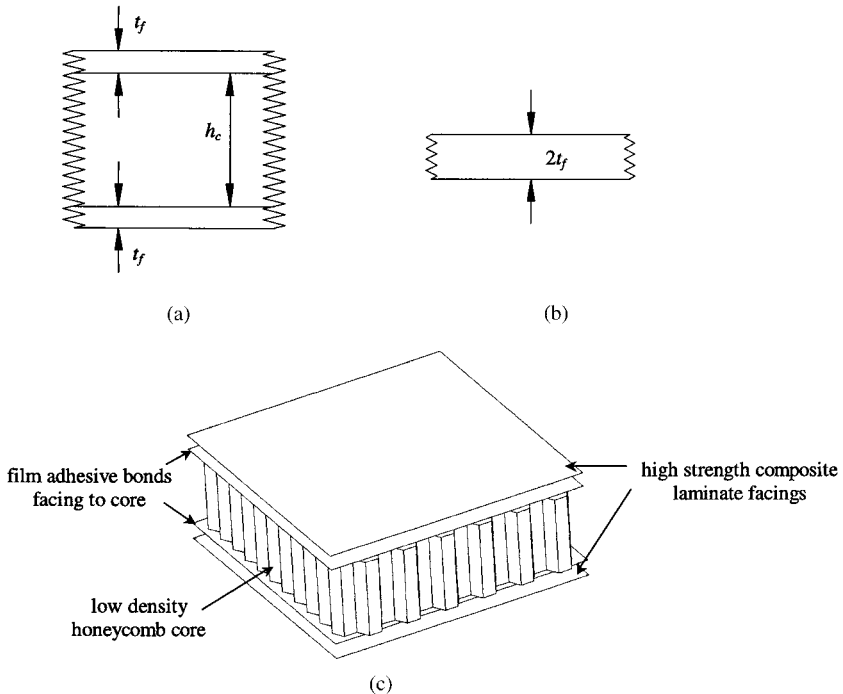


**Figure 2.42** Schematic of sandwich structure: (a) Sandwich construction; (b) monocoque construction; (c) schematic drawing.

When  $hc/t_f = 10$ ,

$$\frac{E_s I_s}{E_m I_m} = \frac{3}{4} \times 100 = 75$$

The above solutions did not consider the Poisson effect in calculating the stiffness  $E$ , which is valid only for narrow-beam analysis. More details on this problem are presented in chapter 6.

### EXAMPLE 2.2

Compare the ratio of the maximum bending stress in a sandwich face with that in a monocoque structure of approximately the same weight as in example 2.1.

#### Solution

For the sandwich construction:

$$\sigma_s = \frac{M}{I_s} \cdot \left( t_f + \frac{h_c}{2} \right) \approx \frac{2M}{t_f h_c^2} \cdot \frac{h_c}{2} = \frac{M}{t_f h_c}$$

$$\sigma_m = \frac{M}{I_m} (t_f) = \frac{3}{2} \frac{M}{t_f^2}$$

where  $M$  represents bending moment per unit width. Hence

$$\frac{\sigma_s}{\sigma_m} = \frac{2t_f}{3h_c} = \frac{1}{15}$$

### EXAMPLE 2.3

In order to reduce the material cost, a hybrid beam instead of an all carbon-fiber beam is recommended because the material price of carbon-fiber epoxy composite material is about 10 times higher than that of glass-fiber epoxy composite material (\$3.0/kg) and the material price of Kevlar-49-fiber epoxy composite is about five times higher than that of glass-fiber epoxy composite material. Both beams have the same overall dimensions. The hybrid beam contains carbon-fiber epoxy composites (T300/5208) in the outer layers and either E-glass or Kevlar 49 fibers in the core. The total carbon-fiber thickness in the hybrid beam is equal to the core thickness ( $h_c/t_f=2$ ). Compare the percentage of stiffness ( $EI$ ) penalty against cost savings for each hybrid beam over an all carbon-fiber epoxy beam.

#### Solution

We refer to table 2.3 for material properties.

(a) *All carbon-fiber epoxy beam:*

$$EI = \frac{E_{\text{carbon}}}{12} (h_c + 2t_f)^3 = \frac{E_{\text{carbon}}}{12} 8h_c^3 = \frac{2}{3} E_{\text{carbon}} h_c^3 = 2.26 E_{\text{glass}} h_c^3$$

$$\frac{EI}{Cost} = \frac{2.26 E_{\text{glass}} h_c^3}{10 C_{\text{glass}} \times 1540 \text{ kg/m}^3 \times 2h_c} = 7.33 \times 10^{-5} \frac{E_{\text{glass}} h_c^2}{C_{\text{glass}}} (\text{m}^3/\text{kg})$$

(b) *Carbon epoxy + glass epoxy beam:*

$$EI = E_{\text{carbon}} \frac{1}{12} [(2h_c)^3 - h_c^3] + E_{\text{glass}} \frac{1}{12} h_c^3 = 1.97 E_{\text{glass}} h_c^3 + E_{\text{glass}} \frac{1}{12} h_c^3 \\ = 2.06 E_{\text{glass}} h_c^3$$

$$\frac{EI}{Cost} = \frac{2.06 E_{\text{glass}} h_c^3}{10 C_{\text{glass}} \times 1540 \text{ kg/m}^3 \times h_c + C_{\text{glass}} \times 2100 \text{ kg/m}^3 \times h_c} \\ = 11.8 \times 10^{-5} \frac{E_{\text{glass}} h_c^2}{C_{\text{glass}}} (\text{m}^3/\text{kg})$$

(c) *Carbon epoxy + Kevlar 49 epoxy:*

$$EI = 1.97 E_{\text{glass}} h_c^3 + E_{\text{kevlar}} \frac{1}{12} h_c^3 \\ = 1.97 E_{\text{glass}} h_c^3 + 0.164 E_{\text{glass}} h_c^3 = 2.13 E_{\text{glass}} h_c^3$$

$$\frac{EI}{Cost} = \frac{2.13E_{\text{glass}}h_c^3}{10C_{\text{glass}} \times 1540 \text{ kg/m}^3 \times h_c + 5C_{\text{glass}} \times 1380 \text{ kg/m}^3 \times h_c}$$

$$= 9.55 \times 10^{-5} \frac{E_{\text{glass}}h_c^2}{C_{\text{glass}}} (\text{m}^3/\text{kg})$$

where  $C_{\text{glass}}$  represents the cost of glass fiber per unit mass.

Therefore, the carbon epoxy + glass epoxy hybrid beam has the best figure of merit.

	All carbon epoxy	Carbon epoxy + glass epoxy	Carbon epoxy + Kevlar 49 epoxy
Cost	1	0.55	0.75
$EI$	1	0.912	0.947
$EI/\text{Cost}$	1	1.61	1.26

## 2.9 Concluding Remarks

1. Composite materials are modern materials that can be tailor-made to satisfy customer needs, based on use of appropriate materials in the right place. Many composite materials have been developed for various applications such as transportation, machinery, and sports equipment.
2. Most composite materials have anisotropic properties, which makes the design complicated, but provides the freedom to produce the desired properties and performance. These anisotropic properties can be designed to satisfy specific customer needs.

## Problems

- 2.1. Explain the difference between condensation polymerization and addition polymerization by presenting polymerization equations for polyamide (nylon 6.6) and polypropylene.
- 2.2. Explain why over three-quarters of all matrices of polymeric matrix composites are thermosetting polymers, even though they are difficult to recycle.
- 2.3. An architectural student moved into a new dormitory. Since the dormitory was not furnished, he collected wooden planks (thickness  $t$ , width  $b$ , and length  $l$ ) to make book shelves supported by two bricks. He used two planks stacked together to increase the bending stiffness of the planks. A mechanical engineering student made similar shelves, but used one plank of thickness  $1.3 t$  rather than two planks of thickness  $t$ . Which is the better design when there is no friction between the two planks?
- 2.4. In Problem 2.3, the architectural student pasted an adhesive between the two planks. When the weight of a book including the shelf per unit length is  $w$ , what interlaminar shear strength should the adhesive possess to avoid the

interlaminar delamination of the two planks? Assume that the two planks are simply supported by two bricks between the plank length  $l$ . In this case, is the design improved?

- 2.5. Why does a thread become stiffer when it is wetted with glue and consolidated?
- 2.6. A continuous and aligned glass-fiber-reinforced polyester composite consists of 40%  $V_f$  of glass fibers having a modulus of elasticity of 69 GPa and 60% polyester having modulus of 3.4 GPa.
  - (a) Compute the longitudinal modulus of the composite.
  - (b) If the cross-sectional area is  $250 \text{ mm}^2$  and a stress of 50 MPa is applied in the longitudinal direction, compute the magnitude of the load carried by each of the fiber and matrix phases.
  - (c) Determine the strain that is sustained by each phase when the stress in part (b) is applied.
- 2.7. Why are small-diameter fibers beneficial for composite reinforcements?
- 2.8. Two-stage (novolac) resins are produced by the acid-catalyzed reaction of phenol and formaldehyde with excess of phenol. Novolacs can be cured by the addition of hexamethylenetetramine, which decomposes upon heating above  $160^\circ\text{C}$  in the presence of moisture to yield ammonia and the formaldehyde necessary to complete the cross-linking reaction. Write down the chemical equation for the formation of ammonia and the formaldehyde from the hexamethylenetetramine in the presence of moisture (a by-product of the condensation reaction).
- 2.9. PEEK has a melting temperature of  $343^\circ\text{C}$  with a Young's modulus of 3.8 GPa and tensile strength of 100 MPa at  $20^\circ\text{C}$ . When carbon fibers of 60% volume fraction are reinforced with PEEK at the temperature higher than the melting temperature and cooled down to  $20^\circ\text{C}$ , estimate the thermal residual stress produced in the PEEK matrix. Is the matrix safe in terms of the thermal residual stress? The coefficient of thermal expansion (CTE) of the carbon fiber in the longitudinal direction is almost zero and its longitudinal Young's modulus is 240 GPa. The CTE of PEEK at  $20^\circ\text{C}$  is  $55 \times 10^{-6}/^\circ\text{C}$ . Assume that the carbon fibers and the PEEK matrix are perfectly bonded at  $343^\circ\text{C}$ . Use the matrix properties at  $20^\circ\text{C}$  throughout the cooling process with linear elastic characteristics.
- 2.10. What material commercially available has the lowest energy content on a volume basis (energy required to produce the material plus fuel equivalent of the raw material)? What material commercially available has the highest energy content?
- 2.11. Become familiar with any computer language (C, Pascal, Fortran, Basic) for later chapter use.

### References

- Ashby, M. F. 1987. "Technology of the 1990s: Advanced Materials and Predictive Design," *Philosophical Transactions of the Royal Society of London*, Vol. 322A, pp. 393–407.
- Bennett, S. C., and Johnson, D. J. 1978. "Structural Heterogeneity in Carbon Fibers," *Proceedings of the 5th London Carbon and Graphite Conference*, Vol. 1, Society for Chemical Industry, London, pp. 377–386.
- Callister, W. D., Jr. 2000. *Materials Science and Engineering, An Introduction*, 5th ed., John Wiley & Sons, New York.
- Chawla, K. K. 1998. *Composite Materials: Science and Engineering*, 2nd ed., Springer, New York, chapters 2 and 3.

- Cheon, S. S., and Lee, D. G. 2001. "Impact Characteristics of Glass Fiber Composites with respect to Fiber Volume Fraction," *Journal of Composite Materials*, Vol. 35, No. 1, pp. 27–56.
- Daniel, I. M., and Ishai, O. 1994. *Engineering Mechanics of Composite Materials*, Oxford University Press, Oxford, pp. 28–36.
- Dresselhaus, M. S., Dresselhaus, G., and Eklund, P. C. 1996. *Science of Fullerenes and Carbon Nanotubes*, Academic Press, San Diego.
- Fried, J. R. *Polymer Science and Technology*, Prentice-Hall, Englewood Cliffs N. J., pp. 29–30.
- Griffith, A. A. 1920. "The Phenomena of Rupture and Flow in Solids." *Philosophical Transactions of the Royal Society of London*, Vol. 221A, pp. 163–198.
- Hahn, H. T. 1980. "Simplified Formulas for Elastic Moduli of Unidirectional Continuous Fiber Composites," *Composites Technology Review*, Vol. 2, No. 3, pp. 5–7.
- Hull, D., and Clyne, T. W. 1996. *An Introduction to Composite Materials*, 2nd ed., Cambridge University Press, Cambridge, Chapter 6.
- Jeong, K. S., Lee, D. G., and Kwak, Y. K. 1995. "Experimental Investigation of the Dynamic Characteristics of the Carbon Fiber Epoxy Composite Thin Beams," *Composite Structures*, Vol. 49, pp. 37–56.
- Kinloch, A. J. 1987. *Adhesion and Adhesives Science and Technology*, Chapman & Hall, London.
- Laramée, R. E. 1988. "Thermal and Related Properties of Engineering Thermosets," in *Engineering Materials Handbook*, Vol. 2, *Engineering Plastics*, ASM International, Metals Park, Ohio, pp. 434–444.
- Lee, D. G., and Choi, J. K. 2000. "Design and Manufacture of an Aerostatic Spindle Bearing System with Carbon Fiber-Epoxy Composites," *Journal of Composite Materials*, Vol. 34, No. 14, pp. 1150–1175.
- Lee, D. G., Sin, H. C., and Suh, N. P. 1985. "Manufacturing of a Graphite Epoxy Composite Spindle for a Machine Tool," *Annals of the CIRP*, pp. 365–368.
- Lee, D. G., Kim, K. S., and Kwak, Y. K. 1991. "Manufacturing of a SCARA Type Direct-Drive Robot with Graphite Fiber Epoxy Composite Materials," *Robotica*, Vol. 9, pp. 219–229.
- Lee, D. G., Jeong, K. S., Kim, K. S., and Kwak, Y. K. 1993. "Development of the Anthropomorphic Robot with Carbon Fiber Epoxy Composite Materials," *Composite Structures*, Vol. 25, pp. 405–416.
- Macosko, C. W. 1989. *RIM Fundamentals of Reaction Injection Molding*, Hanser Publishers, Munich.
- Mallick, P. K. 1988. *Fiber Reinforced Composites*, Marcel Dekker, New York, Chapter 2.
- Mallick, P. K., and Newman, S. 1990. *Composite Materials Technology*, Hanser Publishers, Munich.
- Matthew, F. L., and Rawlings, R. D. 1994. *Composite Materials: Engineering and Science*, Chapman & Hall, London, Chapter 5.
- McCrum, N. G., Buckley, C. P., and Bucknall, C. B. 1997. *Principles of Polymer Engineering*, 2nd ed., Oxford University Press, Oxford.
- Meyer, R. W. 1987. *Handbook of Polyester Molding Compounds and Molding Technology*, Chapman & Hall, New York.
- Oh, J. H., Lee, D. G., and Kim, H. S. 1999. "Composite Robot End Effector for Manipulating Large LCD Glass Panels," *Composite Structures*, Vol. 47, pp. 497–506.
- Powell, P. C. 1994. *Engineering with Fiber Polymer Laminates*, Chapman & Hall, London.
- Stellbrink, K. K. U. 1996. *Micromechanics of Composites*, Hanser Publishers, Munich.

**3**

# Macromechanical Behavior of Unidirectional Composites

## 3.1 Introduction

Composite materials can be viewed and analyzed at different levels and on different scales, depending on the particular characteristics and behavior under consideration. The discipline that investigates the behavior and interactions of materials at the atomic or molecular scale is called nanomechanics. If the scale of observation is on the order of the fiber diameter, particle size, or matrix interstices between reinforcements, we call the discipline micromechanics. It deals with the state of deformation and stress in the constituents and local failures, such as fiber and matrix failures and interface failure (debonding).

Macromechanics treats the material behavior at the level of laminae—use the average anisotropic, homogeneous properties of reinforcement and matrix are used in the analysis. A lamina, or ply, is a plane (or curved) layer of unidirectional fibers or woven fabric in a matrix. In the case of unidirectional fibers, it is called the unidirectional lamina (UD). Hybrid laminates can be made, consisting of layers having different fibers and/or matrix material. Thus, the directional properties of the individual layers may be quite different from each other.

This chapter presents the basic macromechanics of anisotropic materials. It presents the equilibrium conditions and the geometric compatibility conditions in a most general form. It then introduces the constitutive relationship to relate the stress state to the strain state. It finally reduces these equations for unidirectional orthotropic elastic materials, relating the proportionality constants to material properties of composites.

Since composite structures are usually made of several laminates consolidated or bonded together with different ply angles (i.e., stacking angles) and the coordinate system used in the solution of a problem, in general, does not always coincide with the material coordinate systems for each lamina, it is necessary that stresses and strains in the principal material coordinates should be transformed into the global coordinate system (i.e., laminate coordinates). The transformations of stresses and strains also require the transformation of stiffness.

The stress and strain are second-order tensors, whereas the stiffness and compliance are fourth-order tensors. Therefore, these quantities obey the tensor transformation laws, which relate the components in one coordinate system to those in another coordinate system, which is rotated with respect to the reference coordinate system.

In this chapter, we will also develop the equations for the transformation of stress, strain, and stiffness in Cartesian coordinates.

For the application of anisotropic macromechanics to the design problem, let us consider the following example.

### EXAMPLE 3.1

Consider the problem of repairing a worn-out garment by patching a new piece of cloth on the worn-out area. The new piece of cloth was cut to the size shown in figure 3.1. The warp direction is  $45^\circ$  from the direction of applied stresses. If the modulus  $E_1$  of the cloth in the warp direction is 200 MPa, and  $E_2$  in the weft direction 100 MPa, shear modulus  $G_{12}$  50 MPa and the Poisson's ratio 0.3, respectively, what shape will the patched cloth have under 1.0 MPa stresses in the  $x$ - and  $y$ -directions of figure 3.1?

#### Solution

The resulting deformed shape of figure 3.1 is a parallelogram rather than a rectangle, although only tensile stresses were applied. The answers to this problem are  $\varepsilon_x = \varepsilon_y = 6.0 \times 10^{-3}$  m/m,  $\gamma_{xy} = -5.0 \times 10^{-3}$  m/m, and can be calculated after we learn anisotropic macromechanics in this chapter or by using the Axiomatic CLPT program attached to this book. This kind of behavior is typical of anisotropic materials. In fact, every material has essentially anisotropic properties. If many particles of anisotropic properties in a structure are randomly distributed, the resulting properties of aggregates will show more or less isotropic properties that are not dependent on the direction.

Therefore, the isotropic properties of materials are exceptions rather than the rule. The best way to learn macromechanics might be to start with anisotropic macromechanics, moving to isotropic macromechanics as an exceptional case. However, the anisotropic macromechanics is much more complicated than isotropic macromechanics; consequently, we usually start with the latter in undergraduate courses. Since this method is only for convenience, not for the rule of nature, we should be very careful that the anisotropic behavior of a material is totally different from the isotropic behavior, as we have already seen in this example. We may have to abandon any experience and intuition gained from the study of isotropic materials for success in the study of anisotropic macromechanics.

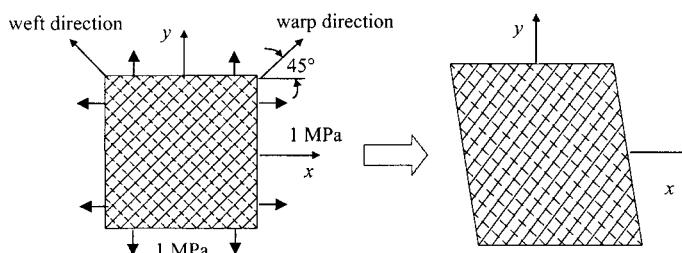


**Figure 3.1** A piece of cloth under tensile stress in example 3.1 (the deformation shape is exaggerated for clarity).

As shown in example 3.1, macromechanical analysis and design of composite structures would require a complete knowledge of the properties of individual layers. A single layer or ply composite, therefore, represents a basic building block for laminate constructions. Thus, the macroscopic properties and behavior of unidirectional composites are presented in this chapter and the microscopic behavior is treated in chapter 7.

### 3.2 Nomenclature

The lamina or ply is an anisotropic (usually orthotropic) material with principal axes in the direction of the fibers (longitudinal), normal to the fibers in the plane of the lamina (in-plane transverse), and normal to the plane of the lamina, as shown in figure 3.2(a). These principal axes (sometimes called material or ply axes) are designated  $x_1$ ,  $x_2$ , and  $x_3$ , respectively.

A laminate is made up of two or more laminae or plies stacked together at various orientations, as shown in figure 3.2(b). Since the principal axes differ from ply to ply, it is more convenient to analyze laminates using a common fixed system or global system of coordinates ( $x-y-z$ ). The global system of coordinates is sometimes called the *laminate coordinates*. By convention, the orientation of a ply (or ply angle) is measured counterclockwise by the angle between the reference  $x$ -axis and the fiber orientation ( $x_1$ -axis) on the  $x-y$  plane.

Laminate stacking sequences can be easily described for composites composed of layers of the same material with equal ply thickness by simply listing the ply orientations  $\theta$  ( $-90 < \theta \leq 90$ ) from the bottom of the laminate to the top using brackets. Some other textbooks use the convention in which that the ply number is counted from the top to the bottom of a laminate. Thus, the notation  $[0/90/0]$  uniquely defines a three-layer laminate. If a ply is repeated, a subscript is utilized to denote the number of repeating plies. Thus,  $[0/90_3/0]$  indicates that the  $90^\circ$  ply is repeated three times. Any laminate in which the ply stacking sequence below the midplane is a mirror image of the stacking sequence above the midplane is referred to as a symmetric laminate. For a symmetric laminate, such as a  $[0/90_2/0]$  plate, the notation can be abbreviated by using  $[0/90]_S$ , where the subscript “ $S$ ” denotes that the stacking sequence is repeated symmetrically. Angle ply laminates are denoted

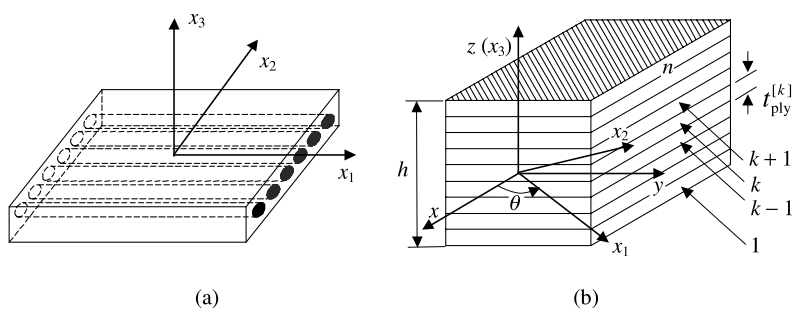


**Figure 3.2** Schematic of composite material: (a) Unidirectional lamina with principal coordinate axes ( $x_1, x_2, x_3$  coordinate system); (b) laminate composed of  $n$  plies with global  $x, y, z$  coordinate system with  $z$ -axis perpendicular to the plane of the laminate and positive upward.

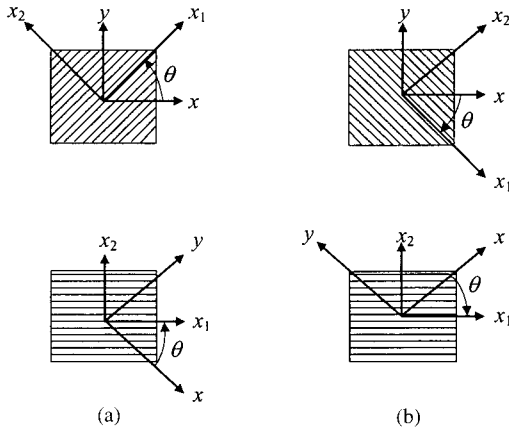


**Figure 3.3** Ply angle notation: (a) Positive angle; (b) negative angle.

by  $[0/30/-30]_S$ , which can be abbreviated to  $[0/\pm 30]_S$ . For laminates with repeating sets of plies, such as  $[0/\pm 30/0/\pm 30]_S$ , an abbreviated notation is of the form  $[0/\pm 30]_{2S}$ . If a symmetric laminate contains a layer that is split at the centerline, then a bar is utilized to denote the split. Thus, the laminate  $[0/90/0]$  can be abbreviated to  $[0/\overline{90}]_S$ . The sandwich structure made of composite faces and a honeycomb core may be represented by  $[(0_3/90_2/45/-45_3)_2/C_3]_S$ , where  $C_3$  represents a honeycomb core that has three times thickness of the lamina. This sandwich structure has the equivalent thickness of 42 laminae. The ply angle  $\theta$  is measured counterclockwise in the range  $-90 \leq \theta \leq 90$ , where positive and negative ply angles are shown in figure 3.3.

### 3.3 Cartesian Tensors and Generalized Hooke's Law

Stress is defined as force per unit area of a body. We can represent the stress components acting on the surfaces of an elemental cube at a point as shown in figure 3.4.

There are nine stress components,  $\sigma_{ij}$  (three normal and six shear), acting on the six faces of an elemental cube. The components  $\sigma_{ij}$  represent the force per unit area in the  $j$ -direction on a face whose normal is in the  $i$ -direction. Rotational equilibrium requires that  $\sigma_{ij} = \sigma_{ji}$ . Thus, there are only six independent stress components;  $i=j$  gives three normal stresses, while  $i \neq j$  gives three shear stresses. For a stress component on a face whose outward normal is in the direction of

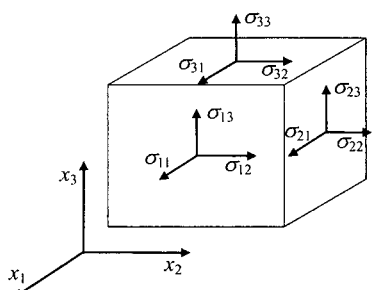


**Figure 3.4** Stress state at a point in a continuum.

a positive axis, the stress component is positive when it is in the direction of a positive axis. Also, when a stress component is on a face whose outward normal is in the direction of a negative axis, the stress component is positive when it is in the direction of a negative axis.

The displacement of a point in a deformed body with respect to its original position in the undeformed state can be represented by a vector  $\mathbf{u}$  with components  $u_1$ ,  $u_2$ , and  $u_3$ , which are the projections of  $\mathbf{u}$  on the  $x_1$ ,  $x_2$ , and  $x_3$  axes.

The strain of a point in a deformed body with respect to its original position in the undeformed state is defined as the ratio of change in length to original length. The strain components  $\varepsilon_{ij}$  are defined as

$$\varepsilon_{ij} = \frac{1}{2} \left( \frac{\partial u_i}{\partial x_j} + \frac{\partial u_j}{\partial x_i} \right) \quad (3.1)$$

Similar to the stress components,  $\varepsilon_{ij}$  with  $i=j$  are the normal strains, while  $i \neq j$  gives the shear strains.

The engineering shear strains,  $\gamma_{ij}$ , are defined as the angle change from  $90^\circ$  of the rectangular volume element into a parallelogram due to the shear stresses,  $\sigma_{ij}$  (or  $\tau_{ij}$ ) when  $i \neq j$ . For example, for the  $x_1$ - $x_2$ -plane shown in figure 3.5, shear stresses  $\sigma_{12}$  and  $\sigma_{21}$  cause the square element with  $90^\circ$  corner angles to become a parallelogram with the corner angle  $\phi$ , as shown. Then, the change in angle  $\gamma_{12}$  is

$$\gamma_{12} = \frac{\pi}{2} - \phi = 2\varepsilon_{12} \quad (3.2)$$

The engineering shear strain  $\gamma_{ij}$  is defined as twice the value of the tensor shear strain.

Both the stress  $\sigma_{ij}$  and strain  $\varepsilon_{ij}$  are second-order tensor quantities, where in three-dimensional space they have  $3^2 = 9$  components, while the engineering shear strains  $\gamma_{ij}$  are not tensors.

The tensors expressed in the rectangular Cartesian coordinates are called Cartesian tensors. The second-order Cartesian tensor components satisfy the following tensor transformation rule:

$$\sigma_{i'j'} = l_{i'k} l_{j'l} \sigma_{kl} \quad (3.3)$$

where  $\sigma_{i'j'}$  is the tensor expressed in the primed axes  $x'_i, x'_j, x'_k$  rotated arbitrarily with respect to the  $x_i, x_j, x_k$  coordinates, and  $l_{i'k}$  is the direction cosine between the primed axis  $x'_i$  and the unprimed axis  $x_k$ , as shown in figure 3.6.

Having defined several notations and terminology that will be used in future analysis, we can now proceed to develop the macromechanical characteristics of composite laminae.

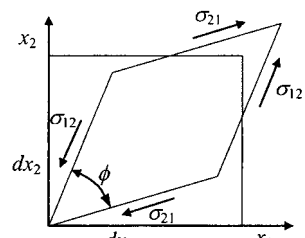
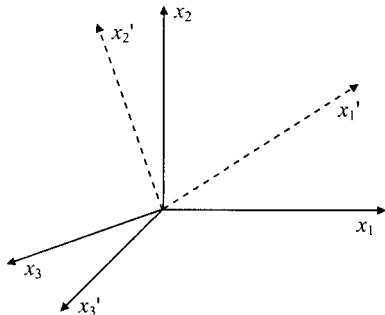


Figure 3.5 Shearing of a square element.



**Figure 3.6** Transformation of Cartesian coordinate.

Every analysis of a mechanical system involves three steps (Crandall et al., 1978):

1. Study of forces (force and moment equilibriums)
2. Study of motion and deformation (geometric compatibility)
3. Application of laws relating the forces to the motion and deformation (constitutive equation).

### 3.3.1 Equilibrium Equation

A force balance at a material point of a composite material can be made in the  $x_1$ ,  $x_2$ , and  $x_3$  directions, resulting in three equations of equilibrium. If the material point is assumed to be infinitely smaller than any dimension of the structure containing it, but infinitely larger than the size of the molecular lattice spacing of the material (a continuum assumption), a small cube of dimensions  $dx_1$ ,  $dx_2$ , and  $dx_3$ , as shown in figure 3.7, can be constructed. Without the above assumption of larger elements than atoms or molecules, a quantum mechanics approach rather than the continuum

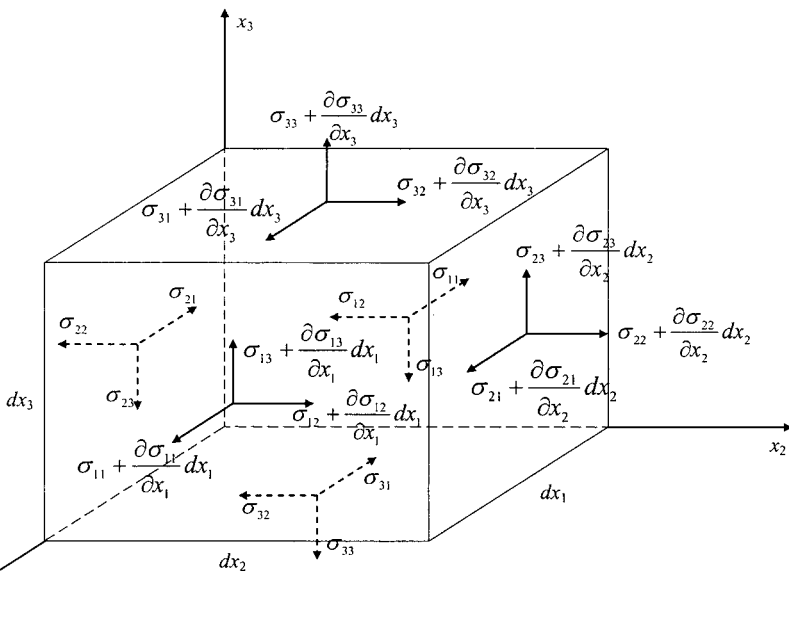


**Figure 3.7** Variation of stresses in a small cubic element.

mechanics approach should be adopted. The positive values of all stresses acting on each surface of the element are shown in figure 3.7.

In addition to the surface stresses acting on the element, body force components  $F_1$ ,  $F_2$ , and  $F_3$  (force per unit volume), such as gravitational, magnetic, or centrifugal forces, can also act on the body.

A force balance in the  $x_1$ -direction yields

$$\begin{aligned} & \left( \sigma_{11} + \frac{\partial \sigma_{11}}{\partial x_1} dx_1 \right) dx_2 dx_3 + \left( \sigma_{21} + \frac{\partial \sigma_{21}}{\partial x_2} dx_2 \right) dx_1 dx_3 + \left( \sigma_{31} + \frac{\partial \sigma_{31}}{\partial x_3} dx_3 \right) dx_1 dx_2 \\ & - \sigma_{11} dx_2 dx_3 - \sigma_{21} dx_1 dx_3 - \sigma_{31} dx_1 dx_2 + F_1 dx_1 dx_2 dx_3 \\ & = \rho \frac{\partial^2 u_1}{\partial t^2} dx_1 dx_2 dx_3 \end{aligned} \quad (3.4)$$

Cancelling terms and dividing the remaining terms by the volume ( $dV = dx_1 dx_2 dx_3$ ) results in the following:

$$\frac{\partial \sigma_{11}}{\partial x_1} + \frac{\partial \sigma_{21}}{\partial x_2} + \frac{\partial \sigma_{31}}{\partial x_3} + F_1 = \rho \frac{\partial^2 u_1}{\partial t^2} \quad (3.5a)$$

where  $\rho$  and  $t$  represent the density of the material and the time, respectively, and  $u_1$  represents the displacement of a particle in the  $x_1$ -direction. Similarly, equilibrium in the  $x_2$  and  $x_3$  directions yields

$$\frac{\partial \sigma_{12}}{\partial x_1} + \frac{\partial \sigma_{22}}{\partial x_2} + \frac{\partial \sigma_{32}}{\partial x_3} + F_2 = \rho \frac{\partial^2 u_2}{\partial t^2} \quad (3.5b)$$

$$\frac{\partial \sigma_{13}}{\partial x_1} + \frac{\partial \sigma_{23}}{\partial x_2} + \frac{\partial \sigma_{33}}{\partial x_3} + F_3 = \rho \frac{\partial^2 u_3}{\partial t^2} \quad (3.5c)$$

These equations can be expressed in one equation using the indicial notation in which, if two indices are repeated in an expression, these indices take on successively the values  $x_1$ ,  $x_2$ , and  $x_3$  and the resulting expressions are added.

$$\sigma_{ji,j} + F_i = \rho \frac{\partial^2 u_i}{\partial t^2} \quad (3.6a)$$

or, since  $\sigma_{ij} = \sigma_{ji}$

$$\sigma_{ij,j} + F_i = \rho \frac{\partial^2 u_i}{\partial t^2} \quad (3.6b)$$

where a comma between indices denotes differentiation. Since the identity of the repeated indices is inconsequential to the final result, the pair used in adding is called *dummy* indices.

### 3.3.2 Geometric Compatibility

When the displacement field is given, we can readily compute the strain tensor field by substituting  $u_i$  into equation (3.1). The inverse problem of finding the

displacement field from a strain field is not so simple. The displacement field, composed of three functions  $u_i$ , must be determined by integration of the six partial differential equations given by equation (3.1). To ensure single-valued, continuous solutions  $u_i$ , we must impose certain restrictions on the  $\varepsilon_{ij}$ . That is, we cannot give an arbitrary strain field  $\varepsilon_{ij}$  and expect it automatically to be associated with a single-valued continuous displacement field, which is an analogy of the continuity equation in fluid mechanics (White, 1999). The actual deformations must have single-valued continuous displacement fields (Shames and Cozzarelli, 1992). Hence  $u_i$  is a single-valued and continuous function that satisfies the compatibility equations.

Using equation (3.1), we can form the following derivatives:

$$\begin{aligned}\varepsilon_{ij,kl} &= \frac{1}{2}(u_{i,jkl} + u_{j,ikl}) \\ \varepsilon_{kl,ij} &= \frac{1}{2}(u_{k,lkj} + u_{l,kij}) \\ \varepsilon_{lj,ki} &= \frac{1}{2}(u_{l,jki} + u_{j,lki}) = \frac{1}{2}(u_{l,kij} + u_{j,ikl}) \\ \varepsilon_{ki,lj} &= \frac{1}{2}(u_{k,ilj} + u_{i,klj}) = \frac{1}{2}(u_{k,lkj} + u_{i,jkl})\end{aligned}\quad (3.7)$$

where a comma between indices denotes differentiation. The rearrangement of the order of differentiation in the last two equations is valid because of the continuity of  $u_i$ . By adding the first two equations and then subtracting the last two equations, we obtain the compatibility equations, which may be expressed as

$$\varepsilon_{ij,kl} + \varepsilon_{kl,ij} - \varepsilon_{lj,ki} - \varepsilon_{ki,lj} = 0 \quad (3.8)$$

These form a set of 81 compatibility equations that a strain field must satisfy in order for  $u_i$  to be a single-valued and continuous. The above 81 equations become in fact only six different equations, which are expressed in  $x,y,z$ -coordinates as follows (Timoshenko and Goodier, 1970):

$$\begin{aligned}\frac{\partial^2 \varepsilon_x}{\partial y^2} + \frac{\partial^2 \varepsilon_y}{\partial x^2} &= \frac{\partial^2 \gamma_{xy}}{\partial x \partial y}, \quad 2 \frac{\partial^2 \varepsilon_x}{\partial y \partial z} = \frac{\partial}{\partial x} \left( -\frac{\partial \gamma_{yz}}{\partial x} + \frac{\partial \gamma_{xz}}{\partial y} + \frac{\partial \gamma_{xy}}{\partial z} \right) \\ \frac{\partial^2 \varepsilon_y}{\partial z^2} + \frac{\partial^2 \varepsilon_z}{\partial y^2} &= \frac{\partial^2 \gamma_{yz}}{\partial y \partial z}, \quad 2 \frac{\partial^2 \varepsilon_y}{\partial x \partial z} = \frac{\partial}{\partial y} \left( \frac{\partial \gamma_{yz}}{\partial x} - \frac{\partial \gamma_{xz}}{\partial y} + \frac{\partial \gamma_{xy}}{\partial z} \right) \\ \frac{\partial^2 \varepsilon_z}{\partial x^2} + \frac{\partial^2 \varepsilon_x}{\partial z^2} &= \frac{\partial^2 \gamma_{xz}}{\partial x \partial z}, \quad 2 \frac{\partial^2 \varepsilon_z}{\partial x \partial y} = \frac{\partial}{\partial z} \left( \frac{\partial \gamma_{yz}}{\partial x} + \frac{\partial \gamma_{xz}}{\partial y} - \frac{\partial \gamma_{xy}}{\partial z} \right)\end{aligned}\quad (3.9)$$

### 3.3.3 Constitutive Equations—Generalized Hooke's Law

We saw in the preceding sections that the state of stress in continuous material is completely determined by the stress tensor  $\sigma_{ij}$ , and the state of deformation by the strain tensor  $\varepsilon_{ij}$ . We must relate these tensors, using a constitutive relationship.

Let us assume that when an elastic material is maintained at a fixed temperature there is a one-to-one analytic relation

$$\sigma_{ij} = F_{ij}(\varepsilon_{11}, \varepsilon_{22}, \dots, \varepsilon_{12}) \quad (i, j = 1, 2, 3) \quad (3.10)$$

between the  $\sigma_{ij}$  and  $\varepsilon_{ij}$  such that the  $\varepsilon_{ij}$  vanish when the strains are all zero (Sokolnikoff, 1956). This last assumption implies that in the initial unstrained state the body is unstressed. Now, if the functions  $F_{ij}$  are expanded in the power series in  $\varepsilon_{ij}$  and only the linear terms retained in the expansions, we get

$$\sigma_{ij} = C_{ijkl}\varepsilon_{kl} \quad (i, j, k, l = 1, 2, 3) \quad (3.11)$$

The coefficients  $C_{ijkl}$ , in the linear forms of equation (3.11), in general will vary from point to point of the material. If the  $C_{ijkl}$  are independent of the position of the point, the material is called elastically *homogeneous*. From now on we will confine our attention to those material in which the  $C_{ijkl}$  do not vary throughout the region under consideration. Equation (3.11) is a natural generalization of Hooke's law, and it is used in all developments of the linear theory of elasticity. The  $C_{ijkl}$  are the fourth-order elasticity tensor, which has  $3^4 = 81$  components. However, there is no actual material that has 81 independent elastic constants.

Since  $\sigma_{ij} = \sigma_{ji}$ ,

$$\sigma_{ij} = C_{ijkl}\varepsilon_{kl} = C_{jikl}\varepsilon_{kl} = \sigma_{ji} \quad (3.12)$$

or

$$C_{ijkl} = C_{jikl} \quad (3.13)$$

Since  $\varepsilon_{ij} = \varepsilon_{ji}$ ,

$$\sigma_{ij} = C_{ijkl}\varepsilon_{kl} = C_{ijlk}\varepsilon_{lk} = C_{ijlk}\varepsilon_{kl} \quad (3.14)$$

or

$$C_{ijkl} = C_{ijlk} \quad (3.15)$$

In addition, if a strain energy density function,  $W$ , exists (Shames and Cozzarelli, 1992),

$$W = \frac{1}{2}\sigma_{ij}\varepsilon_{ij} = \frac{1}{2}C_{ijkl}\varepsilon_{ij}\varepsilon_{kl} = \frac{1}{2}C_{klji}\varepsilon_{kl}\varepsilon_{ij} = \frac{1}{2}C_{klij}\varepsilon_{ij}\varepsilon_{kl} \quad (3.16)$$

in such a way that

$$\frac{\partial W}{\partial \varepsilon_{ij}} = C_{ijkl}\varepsilon_{kl} = \sigma_{ij} \quad (3.17)$$

from equation (3.16), we have

$$C_{ijkl} = C_{klij} \quad (3.18)$$

From equations (3.13), (3.15), and (3.18), we have 21 independent elastic constants of  $C_{ijkl}$  (Table 3.1).

**Table 3.1 Independent Elastic Constants in the Generalized Hooke's law**

<i>Relation</i>	<i>C<sub>mnpq</sub></i>		
Normal stress–normal strain	<i>C<sub>1111</sub></i>	<i>C<sub>1122</sub></i>	
	<i>C<sub>2222</sub></i>	<i>C<sub>1133</sub></i>	
	<i>C<sub>3333</sub></i>	<i>C<sub>2233</sub></i>	
Shear stress–shear strain	<i>C<sub>1212</sub></i>	<i>C<sub>1213</sub></i>	
	<i>C<sub>1313</sub></i>	<i>C<sub>1323</sub></i>	
	<i>C<sub>2323</sub></i>	<i>C<sub>2312</sub></i>	
Normal stress–shear strain	<i>C<sub>1112</sub></i>	<i>C<sub>2212</sub></i>	<i>C<sub>3312</sub></i>
	<i>C<sub>1113</sub></i>	<i>C<sub>2213</sub></i>	<i>C<sub>3313</sub></i>
	<i>C<sub>1123</sub></i>	<i>C<sub>2223</sub></i>	<i>C<sub>3323</sub></i>

**Table 3.2 Index Difference between the Tensor and the Engineering Notations**

<i>Tensor notation</i>	<i>Engineering notation</i>
11	1
22	2
33	3
23	4
13	5
12	6

**Table 3.3 Shear Strains in the Tensor and the Engineering Notations**

<i>Tensor notation</i>	<i>Engineering notation</i>		
$\varepsilon_{12}$	$\frac{1}{2}\varepsilon_6$	or	$\frac{1}{2}\gamma_{12}$
$\varepsilon_{13}$	$\frac{1}{2}\varepsilon_5$	or	$\frac{1}{2}\gamma_{13}$
$\varepsilon_{23}$	$\frac{1}{2}\varepsilon_4$	or	$\frac{1}{2}\gamma_{23}$

Since  $\sigma_{ij} = \sigma_{ji}$  and  $\varepsilon_{ij} = \varepsilon_{ji}$ , the following engineering notation (or contracted notation) is widely used:

$$\sigma_{11} = \sigma_1, \sigma_{22} = \sigma_2, \sigma_{33} = \sigma_3, \sigma_{23} = \sigma_4, \sigma_{31} = \sigma_5, \sigma_{12} = \sigma_6 \quad (3.19)$$

$$\varepsilon_{11} = \varepsilon_1, \varepsilon_{22} = \varepsilon_2, \varepsilon_{33} = \varepsilon_3, 2\varepsilon_{23} = \varepsilon_4 = \gamma_{23},$$

$$2\varepsilon_{31} = \varepsilon_5 = \gamma_{31}, 2\varepsilon_{12} = \varepsilon_6 = \gamma_{12} \quad (3.20)$$

Table 3.2 lists the difference between indices of the tensor notation and the engineering notation and Table 3.3 lists the difference between shear strains of the two notations.

Using the relationship of equations (3.19) and (3.20), equation (3.11) can be written in a contracted form:

$$\sigma_i = C_{ij}\varepsilon_j \quad (i, j = 1, \dots, 6) \quad (3.21)$$

The contracted equation (3.21) is not a tensor relationship.

As already mentioned, there are 21 independent elastic constants, which is obvious from equation (3.21):  $6 \times 6 - 6C_2 = 36 - 6 \times 5/2 = 21$ .

The fully expanded forms of equation (3.11) in matrix form are as follows:

$$\{\sigma\} = [C]\{\varepsilon\} \quad (3.22)$$

$$\left\{ \begin{array}{l} \sigma_{11} \\ \sigma_{22} \\ \sigma_{33} \\ \sigma_{23} \\ \sigma_{31} \\ \sigma_{12} \\ \sigma_{32} \\ \sigma_{13} \\ \sigma_{21} \end{array} \right\} = \left[ \begin{array}{cccccccccc} C_{1111} & C_{1122} & C_{1133} & C_{1123} & C_{1131} & C_{1112} & C_{1132} & C_{1113} & C_{1121} \\ C_{2211} & C_{2222} & C_{2233} & C_{2223} & C_{2231} & C_{2212} & C_{2232} & C_{2213} & C_{2221} \\ C_{3311} & C_{3322} & C_{3333} & C_{3323} & C_{3331} & C_{3312} & C_{3332} & C_{3313} & C_{3321} \\ C_{2311} & C_{2322} & C_{2333} & C_{2323} & C_{2331} & C_{2312} & C_{2332} & C_{2313} & C_{2321} \\ C_{3111} & C_{3122} & C_{3133} & C_{3123} & C_{3131} & C_{3112} & C_{3132} & C_{3113} & C_{3121} \\ C_{1211} & C_{1222} & C_{1233} & C_{1223} & C_{1231} & C_{1212} & C_{1232} & C_{1213} & C_{1221} \\ C_{3211} & C_{3222} & C_{3233} & C_{3223} & C_{3231} & C_{3212} & C_{3232} & C_{3213} & C_{3221} \\ C_{1311} & C_{1322} & C_{1333} & C_{1323} & C_{1331} & C_{1312} & C_{1332} & C_{1313} & C_{1321} \\ C_{2111} & C_{2122} & C_{2133} & C_{2123} & C_{2131} & C_{2112} & C_{2132} & C_{2113} & C_{2121} \end{array} \right] \left\{ \begin{array}{l} \varepsilon_{11} \\ \varepsilon_{22} \\ \varepsilon_{33} \\ \varepsilon_{23} \\ \varepsilon_{31} \\ \varepsilon_{12} \\ \varepsilon_{32} \\ \varepsilon_{13} \\ \varepsilon_{21} \end{array} \right\} \quad (3.23)$$

or

$$\left\{ \begin{array}{l} \sigma_{11} \\ \sigma_{22} \\ \sigma_{33} \\ \sigma_{23} \\ \sigma_{13} \\ \sigma_{12} \end{array} \right\} = \left[ \begin{array}{ccccccc} C_{1111} & C_{1122} & C_{1133} & 2C_{1123} & 2C_{1113} & 2C_{1112} \\ C_{2211} & C_{2222} & C_{2233} & 2C_{2223} & 2C_{2213} & 2C_{2212} \\ C_{3311} & C_{3322} & C_{3333} & 2C_{3323} & 2C_{3313} & 2C_{3312} \\ C_{2311} & C_{2322} & C_{2333} & 2C_{2323} & 2C_{2313} & 2C_{2312} \\ C_{1311} & C_{1322} & C_{1333} & 2C_{1323} & 2C_{1313} & 2C_{1312} \\ C_{1211} & C_{1222} & C_{1233} & 2C_{1223} & 2C_{1213} & 2C_{1212} \end{array} \right] \left\{ \begin{array}{l} \varepsilon_{11} \\ \varepsilon_{22} \\ \varepsilon_{33} \\ \varepsilon_{23} \\ \varepsilon_{13} \\ \varepsilon_{12} \end{array} \right\} \quad (3.24)$$

and the fully expanded forms of equation (3.21) in matrix form are as follows:

$$\{\sigma\}' = [C]' \{\varepsilon\}' \quad (3.25)$$

$$\left\{ \begin{array}{l} \sigma_1 \\ \sigma_2 \\ \sigma_3 \\ \sigma_4 = \tau_{23} \\ \sigma_5 = \tau_{31} \\ \sigma_6 = \tau_{12} \end{array} \right\} = \left[ \begin{array}{cccccc} C_{11} & C_{12} & C_{13} & C_{14} & C_{15} & C_{16} \\ C_{21} & C_{22} & C_{23} & C_{24} & C_{25} & C_{26} \\ C_{31} & C_{32} & C_{33} & C_{34} & C_{35} & C_{36} \\ C_{41} & C_{42} & C_{43} & C_{44} & C_{45} & C_{46} \\ C_{51} & C_{52} & C_{53} & C_{54} & C_{55} & C_{56} \\ C_{61} & C_{62} & C_{63} & C_{64} & C_{65} & C_{66} \end{array} \right] \left\{ \begin{array}{l} \varepsilon_1 \\ \varepsilon_2 \\ \varepsilon_3 \\ \varepsilon_4 = 2\varepsilon_{23} \\ \varepsilon_5 = 2\varepsilon_{13} \\ \varepsilon_6 = 2\varepsilon_{12} \end{array} \right\} \quad (3.26)$$

**Table 3.4 Relationship between the Elastic Tensor Stiffness  $C_{mnpq}$  ( $m, n, p, q = 1, 2, 3$ ) and the Engineering Stiffness  $C_{ij}$  ( $i, j = 1-6$ )**

j	i					
	1	2	3	4	5	6
1						
2		$C_{ij} = C_{mnpq}$			$C_{ij} = C_{mnpq}$	
3						
4						
5		$C_{ij} = C_{mnpq}$			$C_{ij} = C_{mnpq}$	
6						

**Table 3.5 Relationship between the Tensor Compliance  $S_{mnpq}$  ( $m, n, p, q = 1, 2, 3$ ) and the Engineering Compliance  $S_{ij}$  ( $i, j = 1-6$ )**

j	i					
	1	2	3	4	5	6
1						
2		$S_{ij} = S_{mnpq}$			$S_{ij} = 2S_{mnpq}$	
3						
4						
5		$S_{ij} = 2S_{mnpq}$			$S_{ij} = 4S_{mnpq}$	
6						

Table 3.4 shows the relationship between  $C_{ijkl}$  and  $C_{ij}$ . Although they have the same values, they are listed for comparison with the relationship of the compliance matrix that is introduced in Table 3.5.

If equation (3.11) is inverted, through matrix transformation, we obtain

$$\varepsilon_{ij} = S_{ijkl}\sigma_{kl} \quad (3.27)$$

The  $S_{ijkl}$  matrix is the *compliance matrix*, which is the inverse matrix of the stiffness matrix of  $C_{ijkl}$ . The compliance matrix has similar relationships to equations (3.13), (3.15), and (3.18):

$$\begin{aligned} S_{ijkl} &= S_{jikl} \\ S_{ijkl} &= S_{ijlk} \\ S_{ijkl} &= S_{klij} \end{aligned} \quad (3.28)$$

If equation (3.27) is expanded, for example, when  $i = 1$  and  $j = 1$ :

$$\begin{aligned} \varepsilon_{11} = \varepsilon_1 = S_{1111}\sigma_{11} + S_{1122}\sigma_{22} + S_{1133}\sigma_{33} + S_{1123}\sigma_{23} + S_{1132}\sigma_{32} \\ + S_{1131}\sigma_{31} + S_{1113}\sigma_{13} + S_{1112}\sigma_{12} + S_{1121}\sigma_{21} \end{aligned} \quad (3.29)$$

or,

$$\begin{aligned}\varepsilon_1 = & S_{1111}\sigma_{11} + S_{1122}\sigma_{22} + S_{1133}\sigma_{33} + 2S_{1123}\sigma_{23} \\ & + 2S_{1131}\sigma_{31} + 2S_{1112}\sigma_{12}\end{aligned}\quad (3.30)$$

If equation (3.27) is expanded, for example, when  $i=1$  and  $j=2$ :

$$\begin{aligned}\varepsilon_{12} = \frac{1}{2}\varepsilon_6 = & S_{1211}\sigma_{11} + S_{1222}\sigma_{22} + S_{1233}\sigma_{33} + S_{1223}\sigma_{23} + S_{1232}\sigma_{32} \\ & + S_{1231}\sigma_{31} + S_{1213}\sigma_{13} + S_{1212}\sigma_{12} + S_{1221}\sigma_{21}\end{aligned}\quad (3.31)$$

or,

$$\begin{aligned}\varepsilon_6 = & 2S_{1211}\sigma_{11} + 2S_{1222}\sigma_{22} + 2S_{1233}\sigma_{33} + 4S_{1223}\sigma_{23} \\ & + 4S_{1231}\sigma_{31} + 4S_{1212}\sigma_{12}\end{aligned}\quad (3.32)$$

When equation (3.27) is expressed using the engineering (contracted) notation, that is,

$$\varepsilon_i = S_{ij}\sigma_j \quad (3.33)$$

and then expanded, for example, when  $i=1$  and 6, we get

$$\varepsilon_1 = S_{11}\sigma_1 + S_{12}\sigma_2 + S_{13}\sigma_3 + S_{14}\sigma_4 + S_{15}\sigma_5 + S_{16}\sigma_6 \quad (3.34)$$

$$\varepsilon_6 = S_{61}\sigma_1 + S_{62}\sigma_2 + S_{63}\sigma_3 + S_{64}\sigma_4 + S_{65}\sigma_5 + S_{66}\sigma_6 \quad (3.35)$$

Comparing equations (3.30) and (3.32) with equations (3.34) and (3.35), we find that

$$S_{11} = S_{1111}, \quad S_{14} = 2S_{1123}, \quad S_{66} = 4S_{1212}, \dots \quad (3.36)$$

The results of equation (3.36) are summarized in table 3.5.

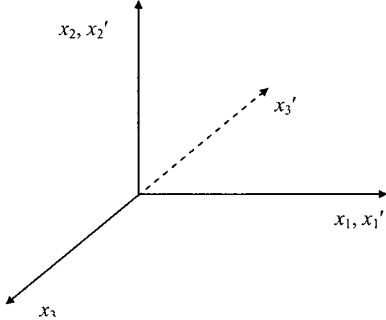
### 3.3.4 Monoclinic Material

When an elastic material is fully anisotropic without any symmetric plane, it is called a *triclinic* material, while, if it has symmetric properties with respect to one plane, it is called a *monoclinic* material. When an elastic body has symmetric properties with respect to the  $x_1-x_2$ -plane, the resulting symmetry can be expressed by the fact that the  $C'_{ij}$ 's discussed above must be invariant under the transformations  $x_1 = x'_1$ ,  $x_2 = x'_2$ , and  $x_3 = -x'_3$ , as shown in figure 3.8.

The stresses and strains of the primed coordinate system are related to those of the unprimed coordinate system by equation (3.3).

$$\sigma_{i'j'} = l_{ik}l_{j'l}\sigma_{kl} \quad (3.37)$$

$$\varepsilon_{i'j'} = l_{ik}l_{j'l}\varepsilon_{kl} \quad (3.38)$$

**Figure 3.8** Symmetry about  $x_1$ - $x_2$ -plane.

For example,

$$\begin{aligned}\sigma_{1'1'} &= \sigma_{1'} = l_{1'1}l_{1'1}\sigma_{11} + l_{1'2}l_{1'2}\sigma_{22} + 2l_{1'1}l_{1'2}\sigma_{12} + 2l_{1'1}l_{1'3}\sigma_{13} + 2l_{1'2}l_{1'3}\sigma_{23} + l_{1'3}l_{1'3}\sigma_{33} \\ &= \sigma_{11} = \sigma_1\end{aligned}\quad (3.39)$$

$$2\varepsilon_{2'3'} = \varepsilon_{4'} = 2l_{2'k}l_{3'l}\varepsilon_{kl} = 2l_{2'2}l_{3'3}\varepsilon_{23} = -2\varepsilon_{23} = -\varepsilon_4 \quad (3.40)$$

Repeating the above calculations for different indices and summarizing, we have

$$\sigma_i' = \sigma_i \quad \text{for } i = 1, 2, 3, 6 \quad (3.41)$$

$$\varepsilon_i' = \varepsilon_i \quad \text{for } i = 1, 2, 3, 6 \quad (3.42)$$

$$\varepsilon_{4'} = -\varepsilon_4 \quad (3.43)$$

$$\varepsilon_{5'} = -\varepsilon_5 \quad (3.44)$$

$$\sigma_{4'} = -\sigma_4 \quad (3.45)$$

$$\sigma_{5'} = -\sigma_5 \quad (3.46)$$

When equation (3.21) is expressed in the two coordinate systems when  $i=4$  and recognizing that  $C'_{ij}$ s are not dependent on the coordinate system:

$$\begin{aligned}\sigma_{4'} &= C_{41}\varepsilon_{1'} + C_{42}\varepsilon_{2'} + C_{43}\varepsilon_{3'} + C_{44}\varepsilon_{4'} + C_{45}\varepsilon_{5'} + C_{46}\varepsilon_{6'} \\ &= C_{41}\varepsilon_1 + C_{42}\varepsilon_2 + C_{43}\varepsilon_3 - C_{44}\varepsilon_4 - C_{45}\varepsilon_5 + C_{46}\varepsilon_6\end{aligned}\quad (3.47)$$

and

$$-\sigma_4 = -C_{41}\varepsilon_1 - C_{42}\varepsilon_2 - C_{43}\varepsilon_3 - C_{44}\varepsilon_4 - C_{45}\varepsilon_5 - C_{46}\varepsilon_6 = \sigma_{4'} \quad (3.48)$$

Comparing equation (3.47) with (3.48), we find that  $C_{41} = C_{42} = C_{43} = C_{46} = 0$ . From similar examinations of  $\sigma_{1'}$ ,  $\sigma_{2'}$ ,  $\sigma_{3'}$ ,  $\sigma_{5'}$ , and  $\sigma_{6'}$ , we have 13 independent stiffness constants, as shown in table 3.6.

**Table 3.6 Stiffness Constant of a Monoclinic Material  
(Symmetric with Respect to  $x_3=0$  Plane)**

$$[C_{ij}] = \begin{bmatrix} C_{11} & C_{12} & C_{13} & 0 & 0 & C_{16} \\ C_{12} & C_{22} & C_{23} & 0 & 0 & C_{26} \\ C_{13} & C_{23} & C_{33} & 0 & 0 & C_{36} \\ 0 & 0 & 0 & C_{44} & C_{45} & 0 \\ 0 & 0 & 0 & C_{45} & C_{55} & 0 \\ C_{16} & C_{26} & C_{36} & 0 & 0 & C_{66} \end{bmatrix}$$

### 3.3.5 Orthotropic Material

If the material under consideration has a second plane of material symmetry, say the  $x_2-x_3$ -plane of figure 3.8, the  $\sigma_1$ ,  $\sigma_2$ ,  $\sigma_3$ , and  $\sigma_4$  stress components must be equal to the corresponding stresses in the primed coordinate systems. Also, we have  $\sigma_6' = -\sigma_6$  and  $\varepsilon_6' = -\varepsilon_6$ . Following the same procedures as in the previous section gives  $C_{16} = C_{26} = C_{36} = C_{45} = 0$ . Then the stiffness matrix has the form of an *orthotropic* (orthogonally anisotropic) material with nine independent constants (table 3.7). A material with two perpendicular planes of material symmetry also exhibits symmetry about the third, mutually perpendicular one, whose verification is left as problem 3.2.

For the stiffness constant of table 3.7, the constitutive equation for orthotropic material can be written in matrix form as

$$\left\{ \begin{array}{l} \sigma_1 \\ \sigma_2 \\ \sigma_3 \\ \sigma_4 = \tau_{23} \\ \sigma_5 = \tau_{31} \\ \sigma_6 = \tau_{12} \end{array} \right\} = \begin{bmatrix} C_{11} & C_{12} & C_{13} & 0 & 0 & 0 \\ C_{12} & C_{22} & C_{23} & 0 & 0 & 0 \\ C_{13} & C_{23} & C_{33} & 0 & 0 & 0 \\ 0 & 0 & 0 & C_{44} & 0 & 0 \\ 0 & 0 & 0 & 0 & C_{55} & 0 \\ 0 & 0 & 0 & 0 & 0 & C_{66} \end{bmatrix} \left\{ \begin{array}{l} \varepsilon_1 \\ \varepsilon_2 \\ \varepsilon_3 \\ \varepsilon_4 = \gamma_{23} \\ \varepsilon_5 = \gamma_{31} \\ \varepsilon_6 = \gamma_{12} \end{array} \right\} \quad (3.49)$$

**Table 3.7 Stiffness Constant of an Orthotropic Material  
(Symmetric with Respect to Three Orthogonal Planes)**

$$[C_{ij}] = \begin{bmatrix} C_{11} & C_{12} & C_{13} & 0 & 0 & 0 \\ C_{12} & C_{22} & C_{23} & 0 & 0 & 0 \\ C_{13} & C_{23} & C_{33} & 0 & 0 & 0 \\ 0 & 0 & 0 & C_{44} & 0 & 0 \\ 0 & 0 & 0 & 0 & C_{55} & 0 \\ 0 & 0 & 0 & 0 & 0 & C_{66} \end{bmatrix}$$

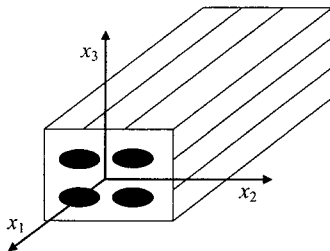


**Figure 3.9** Orthotropic composite with oval fibers.

Three important observations can be made with respect to the stress-strain relations of orthotropic materials in equation (3.49) (Daniel and Ishai, 1994):

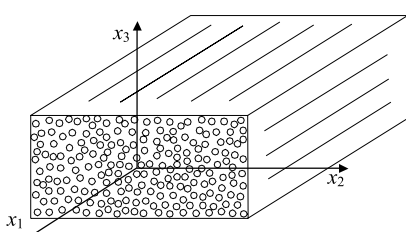
1. No interaction exists between normal stresses  $\sigma_1, \sigma_2, \sigma_3$  and shear strains  $\varepsilon_4, \varepsilon_5, \varepsilon_6$ ; that is, normal stresses acting along principal material directions produce only normal strains.
2. No interaction exists between shear stresses  $\sigma_4, \sigma_5, \sigma_6$  and normal strains  $\varepsilon_1, \varepsilon_2, \varepsilon_3$ ; that is, shear stresses acting on principal material planes produce only shear strains.
3. No interaction exists between shear stresses and shear strains on different planes; that is, a shear stress acting on a principal plane produces a shear strain only on that plane.

Figure 3.9 shows an orthotropic fibrous material whose fibers have an oval shape with attached principal coordinates (Herakovich, 1998). When fibers have a circular shape, the composite usually exhibits transversely isotropic properties in the  $x_2-x_3$ -plane, which is the topic of the next section.

### 3.3.6 Transversely Isotropic Material

An orthotropic material is called transversely isotropic when one of its principal planes is a plane of isotropy, that is, at every point there is a plane on which the mechanical properties are the same in all directions. Many unidirectional composites with fibers packed in a hexagonal array, or close to it, can be considered transversely isotropic, with the  $x_2-x_3$ -plane (normal to the fibers) as the plane of isotropy (figure 3.10).

The stress-strain relations for a transversely isotropic material are simplified by noting that subscripts 2 and 3 (for an  $x_2-x_3$  plane of isotropy) in the material constants are interchangeable in table 3.7, that is,  $C_{12} (C_{1122})=C_{13} (C_{1133}), C_{22} (C_{2222})=C_{33} (C_{3333}),$  and  $C_{55} (C_{1313})=C_{66} (C_{1212}).$  Rotating 45° around the  $x_1$ -axis and imposing the invariance of the constitutive equation, we obtain the relation:  $C_{44}=(C_{22}-C_{33})/2.$  The stiffness matrix for a transversely isotropic material then has the form of table 3.8.



**Figure 3.10** Transversely isotropic material.

**Table 3.8 Stiffness Constant of a Transversely Isotropic Material (Isotropic in  $x_2$ - $x_3$ -Plane)**

$$[C_{ij}] = \begin{bmatrix} C_{11} & C_{12} & C_{12} & 0 & 0 & 0 \\ C_{12} & C_{22} & C_{23} & 0 & 0 & 0 \\ C_{12} & C_{23} & C_{22} & 0 & 0 & 0 \\ 0 & 0 & 0 & \frac{C_{22} - C_{23}}{2} & 0 & 0 \\ 0 & 0 & 0 & 0 & C_{66} & 0 \\ 0 & 0 & 0 & 0 & 0 & C_{66} \end{bmatrix}$$

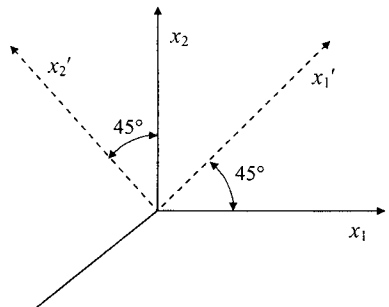


**Figure 3.11**  $x_1'$ ,  $x_2'$ ,  $x_3'$ , coordinates obtained by rotating counterclockwise  $x_1$ - and  $x_2$ -axes  $45^\circ$  around the  $x_3$ -axis.

### 3.3.7 Isotropic Material

An isotropic material is one whose properties are independent of direction and whose planes are all planes of symmetry. In this case we have the following additional relations between stiffness coefficients:  $C_{11} = C_{22}$ ,  $C_{12} = C_{23}$ . Also, rotating the  $x_1$ -and  $x_2$ -axes  $45^\circ$  counterclockwise around the  $x_3$ -axis, as shown in figure 3.11, for example, we have the following relations:

$$\sigma_{1'2'} = \sigma_{6'} = l_{1'k}l_{2'l}\sigma_{kl} = \frac{1}{2}(-\sigma_{11} + \sigma_{22}) = \frac{1}{2}(-\sigma_1 + \sigma_2) \quad (3.50)$$

Also,

$$\varepsilon_{1'2'} = \frac{1}{2}\varepsilon_{6'} = l_{1'k}l_{2'l}\varepsilon_{kl} = \frac{1}{2}(-\varepsilon_{11} + \varepsilon_{22}) = \frac{1}{2}(-\varepsilon_1 + \varepsilon_2) \quad (3.51)$$

From the results of table 3.8,

$$\sigma_{6'} = C_{66}\varepsilon_{6'} \quad (3.52)$$

or, using the results of equations (3.50), (3.51), and (3.52):

$$\frac{1}{2}(-\sigma_1 + \sigma_2) = C_{66}(-\varepsilon_1 + \varepsilon_2) \quad (3.53)$$

From the results of table 3.8,

$$\begin{aligned} \sigma_1 &= C_{11}\varepsilon_1 + C_{12}\varepsilon_2 + C_{12}\varepsilon_3 \\ \sigma_2 &= C_{12}\varepsilon_1 + C_{22}\varepsilon_2 + C_{23}\varepsilon_3 \end{aligned} \quad (3.54)$$

**Table 3.9 Stiffness Constant of an Isotropic Material**

$$[C_{ij}] = \begin{bmatrix} C_{11} & C_{12} & C_{12} & 0 & 0 & 0 \\ C_{12} & C_{11} & C_{12} & 0 & 0 & 0 \\ C_{12} & C_{12} & C_{11} & 0 & 0 & 0 \\ 0 & 0 & 0 & \frac{C_{11} - C_{12}}{2} & 0 & 0 \\ 0 & 0 & 0 & 0 & \frac{C_{11} - C_{12}}{2} & 0 \\ 0 & 0 & 0 & 0 & 0 & \frac{C_{11} - C_{12}}{2} \end{bmatrix}$$

Substituting equation (3.54) into equation (3.53) yields

$$(C_{12} - C_{11} + 2C_{66})\varepsilon_1 + (C_{22} - C_{12} - 2C_{66})\varepsilon_2 + (C_{23} - C_{12})\varepsilon_3 = 0$$

Finally, we have the following additional relations:

$$C_{66} = \frac{1}{2}(C_{11} - C_{12}) \quad (3.55)$$

Thus, an isotropic material has only two independent elastic constants, and the stiffness matrix is listed in table 3.9.

### 3.3.8 Summary of Material Symmetries

Table 3.10 summarizes results for the different combinations of materials and coordinate systems used in this book. In using the results of table 3.10,

**Table 3.10 Elastic Coefficients in the Stress–Strain Relationships for Different Materials**

<i>Class of material</i>	<i>Number of nonzero coefficients</i>	<i>Number of independent coefficients</i>
<i>Three-dimensional case</i>		
Generally anisotropic	36	21
One plane of symmetry	20	13
Two planes of symmetry	12	9
Transversely isotropic	12	5
Isotropic	12	2
<i>Two-dimensional case (lamina)</i>		
General anisotropic	9	6
One plane of symmetry	9	6
Two planes of symmetry	5	4
Transversely isotropic	5	4
Isotropic	5	2

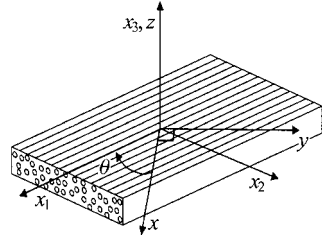


**Figure 3.12** Orthotropic lamina with principal coordinate system ( $x_1, x_2, x_3$ ) and nonprincipal coordinate system ( $x, y, z$ ).

we should always remember that the stress-strain relationships have the same form of anisotropic material if a nonprincipal coordinate system  $x,y,z$ , as shown in figure 3.12, is employed (monoclinic characteristics in this case) (Gibson, 1994).

### 3.4 Engineering Constants of Composite Materials

So far, we obtained the constitutive equations in terms of stiffness coefficients  $C_{ij}$  and compliance coefficients  $S_{ij}$ . However, these coefficients are not measured directly in the laboratory. The constants that are measured in the laboratory are called engineering constants. In order to establish the relationship between the engineering constants and the compliance coefficients, we consider an orthotropic material in the principal material coordinates, that is, for a unidirectional fibrous composite, the axes aligned parallel and perpendicular to the fiber direction ( $x_1, x_2, x_3$ ), as shown in figure 3.12. For this orthotropic material, the constitutive equation (3.33) can be written in matrix form as

$$\begin{Bmatrix} \varepsilon_1 \\ \varepsilon_2 \\ \varepsilon_3 \\ \varepsilon_4 \\ \varepsilon_5 \\ \varepsilon_6 \end{Bmatrix} = \begin{bmatrix} S_{11} & S_{12} & S_{13} & 0 & 0 & 0 \\ S_{21} & S_{22} & S_{23} & 0 & 0 & 0 \\ S_{31} & S_{32} & S_{33} & 0 & 0 & 0 \\ 0 & 0 & 0 & S_{44} & 0 & 0 \\ 0 & 0 & 0 & 0 & S_{55} & 0 \\ 0 & 0 & 0 & 0 & 0 & S_{66} \end{bmatrix} \begin{Bmatrix} \sigma_1 \\ \sigma_2 \\ \sigma_3 \\ \sigma_4 \\ \sigma_5 \\ \sigma_6 \end{Bmatrix} \quad (3.56)$$

Let us make a rule that for the Poisson's ratios,  $\nu_{ij}$ , the first subscript,  $i$ , refers to the direction of the applied stress, and the second subscript  $j$  corresponds to the direction of associated lateral strain. Thus, for  $\sigma_i \neq 0$ ,  $i \neq j$ ,

$$\nu_{ij} = -\frac{\varepsilon_j}{\varepsilon_i} \quad (i, j = 1, 2, 3) \quad (3.57)$$

For an orthotropic material subjected to a three-dimensional state of stress, the equations for strains in terms of stresses and engineering constants take the

following form in the principal material coordinates:

$$\varepsilon_1 = \frac{\sigma_1}{E_1} - \frac{\nu_{21}}{E_2} \sigma_2 - \frac{\nu_{31}}{E_3} \sigma_3 \quad (3.58)$$

$$\varepsilon_2 = -\frac{\nu_{12}}{E_1} \sigma_1 + \frac{\sigma_2}{E_2} - \frac{\nu_{32}}{E_3} \sigma_3 \quad (3.59)$$

$$\varepsilon_3 = -\frac{\nu_{13}}{E_1} \sigma_1 - \frac{\nu_{23}}{E_2} \sigma_2 + \frac{\sigma_3}{E_3} \quad (3.60)$$

$$\varepsilon_4 = \frac{\sigma_4}{G_{23}} \quad (3.61)$$

$$\varepsilon_5 = \frac{\sigma_5}{G_{13}} \quad (3.62)$$

$$\varepsilon_6 = \frac{\sigma_6}{G_{12}} \quad (3.63)$$

The above equations can be rewritten in matrix form for an orthotropic material:

$$\begin{Bmatrix} \varepsilon_1 \\ \varepsilon_2 \\ \varepsilon_3 \\ \varepsilon_4 \\ \varepsilon_5 \\ \varepsilon_6 \end{Bmatrix} = \begin{bmatrix} \frac{1}{E_1} & \frac{-\nu_{21}}{E_2} & \frac{-\nu_{31}}{E_3} & 0 & 0 & 0 \\ \frac{-\nu_{12}}{E_1} & \frac{1}{E_2} & \frac{-\nu_{32}}{E_3} & 0 & 0 & 0 \\ \frac{-\nu_{13}}{E_1} & \frac{-\nu_{23}}{E_2} & \frac{1}{E_3} & 0 & 0 & 0 \\ 0 & 0 & 0 & \frac{1}{G_{23}} & 0 & 0 \\ 0 & 0 & 0 & 0 & \frac{1}{G_{13}} & 0 \\ 0 & 0 & 0 & 0 & 0 & \frac{1}{G_{12}} \end{bmatrix} \begin{Bmatrix} \sigma_1 \\ \sigma_2 \\ \sigma_3 \\ \sigma_4 \\ \sigma_5 \\ \sigma_6 \end{Bmatrix} \quad (3.64)$$

Equating equivalent terms in equation (3.56) with those in equation (3.64) gives the individual compliance coefficients explicitly in terms of the engineering constants:

$$\begin{aligned} S_{11} &= \frac{1}{E_1}, & S_{12} &= -\frac{\nu_{21}}{E_2}, & S_{13} &= -\frac{\nu_{31}}{E_3}, \\ S_{21} &= -\frac{\nu_{12}}{E_1}, & S_{22} &= \frac{1}{E_2}, & S_{23} &= -\frac{\nu_{32}}{E_3}, \\ S_{31} &= -\frac{\nu_{13}}{E_1}, & S_{32} &= -\frac{\nu_{23}}{E_2}, & S_{33} &= \frac{1}{E_3}, \\ S_{44} &= \frac{1}{G_{23}}, & S_{55} &= \frac{1}{G_{13}}, & S_{66} &= \frac{1}{G_{12}} \end{aligned} \quad (3.65)$$

Using the symmetry of the compliance matrix (i.e.,  $S_{ij}=S_{ji}$ ) gives

$$\frac{v_{12}}{E_1} = \frac{v_{21}}{E_2}, \quad \frac{v_{13}}{E_1} = \frac{v_{31}}{E_3}, \quad \frac{v_{23}}{E_2} = \frac{v_{32}}{E_3} \quad (3.66)$$

For a transversely isotropic material with  $E_1 \gg E_2$  and  $E_2 = E_3$ ,  $v_{21}$  is much smaller than  $v_{12}$ , but  $v_{23} = v_{32}$ . Therefore,  $v_{12}$  is called the major Poisson's ratio, while  $v_{21}$  is called the minor Poisson's ratio.

Inversion of equation (3.64) gives the stiffness form of the constitutive equations in terms of engineering constants for an orthotropic material:

$$\begin{Bmatrix} \sigma_1 \\ \sigma_2 \\ \sigma_3 \\ \sigma_4 \\ \sigma_5 \\ \sigma_6 \end{Bmatrix} = \begin{bmatrix} C_{11} & C_{12} & C_{13} & 0 & 0 & 0 \\ C_{21} & C_{22} & C_{23} & 0 & 0 & 0 \\ C_{31} & C_{32} & C_{33} & 0 & 0 & 0 \\ 0 & 0 & 0 & C_{44} & 0 & 0 \\ 0 & 0 & 0 & 0 & C_{55} & 0 \\ 0 & 0 & 0 & 0 & 0 & C_{66} \end{bmatrix} \begin{Bmatrix} \varepsilon_1 \\ \varepsilon_2 \\ \varepsilon_3 \\ \varepsilon_4 \\ \varepsilon_5 \\ \varepsilon_6 \end{Bmatrix} \quad (3.67)$$

Or, in terms of engineering constants of an orthotropic material:

$$\begin{Bmatrix} \sigma_1 \\ \sigma_2 \\ \sigma_3 \\ \sigma_4 \\ \sigma_5 \\ \sigma_6 \end{Bmatrix} = \begin{bmatrix} \frac{1 - v_{23}v_{32}}{E_2E_3\Delta} & \frac{v_{21} + v_{23}v_{31}}{E_2E_3\Delta} & \frac{v_{31} + v_{21}v_{32}}{E_2E_3\Delta} & 0 & 0 & 0 \\ \frac{v_{21} + v_{23}v_{31}}{E_2E_3\Delta} & \frac{1 - v_{13}v_{31}}{E_1E_3\Delta} & \frac{v_{32} + v_{12}v_{31}}{E_1E_3\Delta} & 0 & 0 & 0 \\ \frac{v_{31} + v_{21}v_{32}}{E_2E_3\Delta} & \frac{v_{32} + v_{12}v_{31}}{E_1E_3\Delta} & \frac{1 - v_{12}v_{21}}{E_1E_2\Delta} & 0 & 0 & 0 \\ 0 & 0 & 0 & G_{23} & 0 & 0 \\ 0 & 0 & 0 & 0 & G_{13} & 0 \\ 0 & 0 & 0 & 0 & 0 & G_{12} \end{bmatrix} \begin{Bmatrix} \varepsilon_1 \\ \varepsilon_2 \\ \varepsilon_3 \\ \varepsilon_4 \\ \varepsilon_5 \\ \varepsilon_6 \end{Bmatrix} \quad (3.68)$$

where

$$\Delta = \frac{1 - v_{12}v_{21} - v_{23}v_{32} - v_{13}v_{31} - 2v_{21}v_{32}v_{13}}{E_1E_2E_3} \quad (3.69)$$

is the determinant of the upper left submatrix ( $3 \times 3$ ) in equation (3.64).

For a transversely isotropic material (isotropic plane:  $x_2-x_3$ -plane) with  $E_2 = E_3$ ,  $\nu_{12} = \nu_{13}$ ,  $G_{12} = G_{13}$ , and  $G_{23} = E_2/2(1 + \nu_{23})$ , equation (3.64) reduces to

$$\left\{ \begin{array}{c} \varepsilon_1 \\ \varepsilon_2 \\ \varepsilon_3 \\ \varepsilon_4 \\ \varepsilon_5 \\ \varepsilon_6 \end{array} \right\} = \left[ \begin{array}{cccccc} \frac{1}{E_1} & \frac{-\nu_{12}}{E_1} & \frac{-\nu_{12}}{E_1} & 0 & 0 & 0 \\ \frac{-\nu_{12}}{E_1} & \frac{1}{E_2} & \frac{-\nu_{23}}{E_2} & 0 & 0 & 0 \\ \frac{-\nu_{12}}{E_1} & \frac{-\nu_{23}}{E_2} & \frac{1}{E_2} & 0 & 0 & 0 \\ 0 & 0 & 0 & \frac{2(1 + \nu_{23})}{E_2} & 0 & 0 \\ 0 & 0 & 0 & 0 & \frac{1}{G_{12}} & 0 \\ 0 & 0 & 0 & 0 & 0 & \frac{1}{G_{12}} \end{array} \right] \left\{ \begin{array}{c} \sigma_1 \\ \sigma_2 \\ \sigma_3 \\ \sigma_4 \\ \sigma_5 \\ \sigma_6 \end{array} \right\} \quad (3.70)$$

### EXAMPLE 3.2

Determine the stiffness and compliance coefficients for a T300/5208 carbon epoxy composite material when the  $x_2-x_3$ -plane is a transversely isotropic plane ( $E_1 = 132$  GPa,  $E_2 = E_3 = 10.8$  GPa,  $\nu_{12} = \nu_{13} = 0.24$ ,  $\nu_{23} = 0.59$ ,  $G_{12} = G_{13} = 5.65$  GPa,  $G_{23} = 3.38$  GPa).

#### Solution

From equation (3.64) or (3.70) with  $\nu_{23} = \nu_{32}$ , the compliance coefficients are (in 1/GPa):

$$S_{11} = \frac{1}{E_1} = 7.576 \times 10^{-3}, \quad S_{12} = -\frac{\nu_{21}}{E_2} = -1.964 \times 10^{-2}/10.8 = -1.818 \times 10^{-3}$$

$$S_{22} = S_{33} = \frac{1}{E_2} = 92.59 \times 10^{-3}, \quad S_{23} = \frac{-\nu_{32}}{E_3} = -0.59/10.8 = -54.63 \times 10^{-3}$$

$$S_{44} = \frac{1}{G_{23}} = 295.9 \times 10^{-3}, \quad S_{55} = S_{66} = \frac{1}{G_{13}} = 177.0 \times 10^{-3}$$

and  $\Delta = 4.137 \times 10^{-5}$ /GPa<sup>3</sup>, therefore, the corresponding stiffness coefficients are (in GPa) from equation (3.68),

$$\begin{aligned} C_{11} &= 135.0, & C_{12} = C_{13} &= 6.47, & C_{22} = C_{33} &= 16.9, \\ C_{23} &= 10.1, & C_{44} &= 3.41, & C_{55} = C_{66} &= 5.65 \end{aligned}$$

### EXAMPLE 3.3

Determine the strains when the material in example 3.2 is subjected  $\sigma_1 = 100$  MPa and  $\sigma_2 = 20$  MPa.

**Solution**

From the results of example 3.2 and using equation (3.56),

$$\begin{aligned}\varepsilon_1 &= S_{11}\sigma_1 + S_{12}\sigma_2 \\&= (7.576 \times 10^{-12}) \times (100 \times 10^6) - (1.818 \times 10^{-12}) \times (20 \times 10^6) \\&= 721.0 \times 10^{-6}(\text{m/m}) \\ \varepsilon_2 &= S_{12}\sigma_1 + S_{22}\sigma_2 \\&= (-1.818 \times 10^{-12}) \times (100 \times 10^6) + (92.59 \times 10^{-12}) \times (20 \times 10^6) \\&= 1670 \times 10^{-6}(\text{m/m}) \\ \varepsilon_3 &= S_{13}\sigma_1 + S_{23}\sigma_2 \\&= (-1.818 \times 10^{-12}) \times (100 \times 10^6) + (-54.63 \times 10^{-12}) \times (20 \times 10^6) \\&= -1274 \times 10^{-6}(\text{m/m}) \\ \varepsilon_6 &= S_{16}\sigma_1 + S_{26}\sigma_2 = 0 \quad (\text{since } S_{16} = S_{26} = 0)\end{aligned}$$

### 3.5 Restrictions on Elastic Constants

#### 3.5.1 Isotropic Materials

For isotropic materials, the shear modulus is determined in terms of the elastic modulus,  $E$ , and Poisson's ratio,  $\nu$ , as

$$G = \frac{E}{2(1 + \nu)} \quad (3.71)$$

In order that  $E$  and  $G$  always be positive, that is, that a positive normal stress or shear stress times the respective normal strain or shear strain yields positive work (Jones, 1975),

$$\nu > -1 \quad (3.72)$$

If an isotropic body is subjected to uniform tensile stresses,  $\sigma_1 = \sigma_2 = \sigma_3 = \sigma$ , then the volumetric strain, the sum of the three normal or extensional strains, is defined by

$$\frac{\Delta V}{V} = \varepsilon_1 + \varepsilon_2 + \varepsilon_3 = \frac{\sigma}{E/3(1 - 2\nu)} = \frac{\sigma}{K} \quad (3.73)$$

Then the bulk modulus  $K$ ,

$$K = \frac{E}{3(1 - 2\nu)} \quad (3.74)$$

is positive only if

$$\nu < \frac{1}{2} \quad (3.75)$$

Thus, in isotropic materials, Poisson's ratio is restricted to the range

$$-1 < \nu < \frac{1}{2} \quad (3.76)$$

### 3.5.2 Orthotropic Materials

For orthotropic materials, the relations between elastic constants must be investigated with rigor in order to avoid the pitfalls of an intuition built up on the basis of working with isotropic materials. The sum of the work done by all stress components must be positive in order to avoid creation of energy, which requires that the matrices relating stress to strain be positive definite. Thus, both the stiffness and compliance matrices must be positive definite.

If only one normal stress is applied at a time, the corresponding strain is determined by the diagonal elements of the compliance matrix. Thus, the diagonal elements of the compliance elements in equation (3.64) must be positive, or, in terms of the engineering constants,

$$E_1, E_2, E_3, G_{23}, G_{31}, G_{12} > 0 \quad (3.77)$$

Similarly, under suitable constraints, deformation is possible in which only one extensional strain arises. Again, work is produced by the corresponding stress alone. Thus, since the work done is determined by the diagonal elements of the stiffness matrix, those elements must be positive, that is,

$$C_{11}, C_{22}, C_{33}, C_{44}, C_{55}, C_{66} > 0 \quad (3.78)$$

or, from equation (3.68)

$$(1 - \nu_{23}\nu_{32}), (1 - \nu_{13}\nu_{31}), (1 - \nu_{12}\nu_{21}) > 0 \quad (3.79)$$

and, from equation (3.69)

$$\Delta \times (E_1 E_2 E_3) = (1 - \nu_{12}\nu_{21} - \nu_{23}\nu_{32} - \nu_{13}\nu_{31} - 2\nu_{21}\nu_{32}\nu_{13}) > 0 \quad (3.80)$$

since the determinant of a positive definite matrix must be positive.

By the condition of symmetry of the compliances in equation (3.66), the conditions of equation (3.79) can be written as

$$\begin{aligned} -\sqrt{\frac{E_2}{E_1}} &< \nu_{21} < \sqrt{\frac{E_2}{E_1}}, & -\sqrt{\frac{E_1}{E_2}} &< \nu_{12} < \sqrt{\frac{E_1}{E_2}} \\ -\sqrt{\frac{E_3}{E_2}} &< \nu_{32} < \sqrt{\frac{E_3}{E_2}}, & -\sqrt{\frac{E_2}{E_3}} &< \nu_{23} < \sqrt{\frac{E_2}{E_3}} \\ -\sqrt{\frac{E_1}{E_3}} &< \nu_{13} < \sqrt{\frac{E_1}{E_3}}, & -\sqrt{\frac{E_3}{E_1}} &< \nu_{31} < \sqrt{\frac{E_3}{E_1}} \end{aligned} \quad (3.81)$$

Equation (3.80) can be rearranged as

$$\nu_{21}\nu_{32}\nu_{13} < \frac{1 - \nu_{21}^2(E_1/E_2) - \nu_{32}^2(E_2/E_3) - \nu_{13}^2(E_3/E_1)}{2} < \frac{1}{2} \quad (3.82)$$

The above equation can be regrouped as

$$\begin{aligned}
 & 1 - v_{21}^2 \left( \frac{E_1}{E_2} \right) - v_{32}^2 \left( \frac{E_2}{E_3} \right) - v_{13}^2 \left( \frac{E_3}{E_1} \right) - 2v_{21}v_{32}v_{13} \\
 &= 1 - v_{32}^2 \frac{E_2}{E_3} - v_{13}^2 \frac{E_3}{E_1} + v_{32}^2 \frac{E_2}{E_3} v_{13}^2 \frac{E_3}{E_1} \\
 &\quad - \left( v_{21}^2 \frac{E_1}{E_2} + 2v_{21}v_{32}v_{13} \sqrt{\frac{E_1}{E_2} \cdot \frac{E_2}{E_1}} + v_{32}^2 v_{13}^2 \frac{E_2}{E_1} \right) \\
 &= \left( 1 - v_{32}^2 \frac{E_2}{E_3} \right) \left( 1 - v_{13}^2 \frac{E_3}{E_1} \right) - \left( v_{21} \sqrt{\frac{E_1}{E_2}} + v_{32}v_{13} \sqrt{\frac{E_2}{E_1}} \right)^2 > 0 \quad (3.83)
 \end{aligned}$$

or

$$- \left( 1 - v_{32}^2 \frac{E_2}{E_3} \right)^{\frac{1}{2}} \left( 1 - v_{13}^2 \frac{E_3}{E_1} \right)^{\frac{1}{2}} < v_{21} \sqrt{\frac{E_1}{E_2}} + v_{32}v_{13} \sqrt{\frac{E_2}{E_1}} < \left( 1 - v_{32}^2 \frac{E_2}{E_3} \right)^{\frac{1}{2}} \left( 1 - v_{13}^2 \frac{E_3}{E_1} \right)^{\frac{1}{2}} \quad (3.84)$$

Therefore,

$$\begin{aligned}
 & -v_{32}v_{13} \frac{E_2}{E_1} - \left( 1 - v_{32}^2 \frac{E_2}{E_3} \right)^{\frac{1}{2}} \left( 1 - v_{13}^2 \frac{E_3}{E_1} \right)^{\frac{1}{2}} \left( \frac{E_2}{E_1} \right)^{\frac{1}{2}} < v_{21} < -v_{32}v_{13} \frac{E_2}{E_1} \\
 & \quad + \left( 1 - v_{32}^2 \frac{E_2}{E_3} \right)^{\frac{1}{2}} \left( 1 - v_{13}^2 \frac{E_3}{E_1} \right)^{\frac{1}{2}} \left( \frac{E_2}{E_1} \right)^{\frac{1}{2}} \quad (3.85)
 \end{aligned}$$

The preceding restrictions on engineering constants for orthotropic materials are used to examine experimental data to see if they are physically consistent within the framework of the mathematical elasticity model. For a composite material, for example, we have the measured values of  $E_1$ ,  $E_2$ , and  $v_{12}$  are 81 GPa, 9.0 GPa, and 2.0, respectively.

Since  $\sqrt{E_1/E_2} = 3.0$ , and the condition  $-\sqrt{E_1/E_2} < v_{12} < \sqrt{E_1/E_2}$  in equation (3.81) is satisfied,  $v_{12} = 2.0$  is a reasonable value even though our intuition based on isotropic materials rejects such a large number.

#### EXAMPLE 3.4

For an example of a macromechanics application, consider the problem of repairing a worn-out garment by patching a new piece of cloth on the worn-out area of example 3.1. The warp direction is  $45^\circ$  from the direction of applied stress. If the modulus  $E_1$  of the cloth in the warp direction is 200 MPa, and  $E_2$  in the weft direction 100 MPa, shear modulus  $G_{12}$  50 MPa, and the Poisson's ratio 0.3, respectively, what shape will the patched cloth have under 1.0 MPa stress in the  $x$ - and  $y$ -directions of figure 3.1?

Since the stresses and the coordinate system adopted in figure 3.1 are not expressed in the principal coordinates (or material coordinates), we are not able to solve the problem right now because all the formulas derived in the previous

sections are expressed in the principal coordinate system. Therefore, the transformations of stresses and strains, as well as stiffnesses with respect to the coordinate system, which is rotated from the principal material coordinates, are necessary to solve the problem in general coordinates (or global coordinates), which the designer wishes to use.

### 3.6 Stress, Strain, Stiffness, and Compliance Transformation about z-Axis

#### 3.6.1 Stress and Strain Transformation

Let us consider a rotation through an angle  $\theta$  about a common  $z$ - (or  $x_3$ -) axis, as shown in figure 3.13. Stress and strain matrices in the principal material coordinate system ( $x_1, x_2, x_3$ ) are denoted  $\{\sigma_{ij}\}$  or  $\{\sigma_i\}$  and quantities in the global coordinate system ( $x, y, z$ ) are denoted  $\{\sigma_{xy}\}$  or  $\{\sigma_x\}$ . The principal material coordinate system has the positive ply angle  $\theta$  measured counterclockwise from the  $x$ -axis to the  $x_1$ -axis.

The stress and strain have the following tensor transformation rules.

$$\sigma_{ij} = l_{ip}l_{jq}\sigma_{pq} \quad (i,j = 1, 2, 3 \text{ and } p, q = x, y, z) \quad (3.86)$$

$$\varepsilon_{ij} = l_{ip}l_{jq}\varepsilon_{pq} \quad (i,j = 1, 2, 3 \text{ and } p, q = x, y, z) \quad (3.87)$$

where  $l_{ip}$  are direction cosines of angles between the  $x_i$ -axis and  $x_p$ -axis. The direction cosines have the following values ( $\cos\theta = m$ ,  $\sin\theta = n$ ):

$$\begin{aligned} l_{1x} &= m, & l_{1y} &= n, & l_{1z} &= 0, & l_{2x} &= -n, \\ l_{2y} &= m, & l_{2z} &= 0, & l_{3x} &= 0, & l_{3y} &= 0, & l_{3z} &= 1 \end{aligned}$$

Using engineering notation, we have

$$\{\sigma_i\} = [T_1]\{\sigma_x\} \quad (3.88)$$

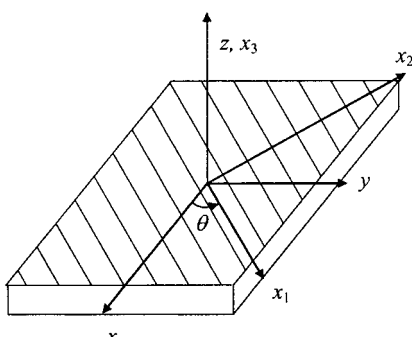


**Figure 3.13** Transformation of the coordinates  $x_1, x_2, x_3$  with respect to the global coordinates  $x, y, z$  about a common axis  $z$  ( $x_3$ ) of the coordinate systems.

Expanding equation (3.88), we have

$$cpt \begin{Bmatrix} \sigma_1 \\ \sigma_2 \\ \sigma_3 \\ \sigma_4 \\ \sigma_5 \\ \sigma_6 \end{Bmatrix} = \begin{bmatrix} m^2 & n^2 & 0 & 0 & 0 & 2mn \\ n^2 & m^2 & 0 & 0 & 0 & -2mn \\ 0 & 0 & 1 & 0 & 0 & 0 \\ 0 & 0 & 0 & m & -n & 0 \\ 0 & 0 & 0 & n & m & 0 \\ -mn & mn & 0 & 0 & 0 & m^2 - n^2 \end{bmatrix} \begin{Bmatrix} \sigma_x \\ \sigma_y \\ \sigma_z \\ \tau_{yz} \\ \tau_{zx} \\ \tau_{xy} \end{Bmatrix} \quad (3.89)$$

or in equation form:

$$\begin{aligned} \sigma_1 &= m^2\sigma_x + n^2\sigma_y + 2mn\tau_{xy} \\ \sigma_2 &= n^2\sigma_x + m^2\sigma_y - 2mn\tau_{xy} \\ \sigma_3 &= \sigma_z \\ \sigma_4 &= m\tau_{yz} - n\tau_{zx} \\ \sigma_5 &= n\tau_{yz} + m\tau_{zx} \\ \sigma_6 &= -mn(\sigma_x - \sigma_y) + (m^2 - n^2)\tau_{xy} \end{aligned} \quad (3.90)$$

In equation (3.88), the stress transformation matrix  $[T_1]$  is defined as

$$[T_1] = \begin{bmatrix} m^2 & n^2 & 0 & 0 & 0 & 2mn \\ n^2 & m^2 & 0 & 0 & 0 & -2mn \\ 0 & 0 & 1 & 0 & 0 & 0 \\ 0 & 0 & 0 & m & -n & 0 \\ 0 & 0 & 0 & n & m & 0 \\ -mn & mn & 0 & 0 & 0 & m^2 - n^2 \end{bmatrix} \quad (3.91)$$

Inverting Equation (3.88) yields:

$$\{\sigma_x\} = [T_1]^{-1}\{\sigma_i\} \quad (3.92)$$

Expanding Equation (3.92), we have

$$\begin{Bmatrix} \sigma_x \\ \sigma_y \\ \sigma_z \\ \tau_{yz} \\ \tau_{zx} \\ \sigma_{xy} \end{Bmatrix} = \begin{bmatrix} m^2 & n^2 & 0 & 0 & 0 & -2mn \\ n^2 & m^2 & 0 & 0 & 0 & 2mn \\ 0 & 0 & 1 & 0 & 0 & 0 \\ 0 & 0 & 0 & m & n & 0 \\ 0 & 0 & 0 & -n & m & 0 \\ mn & -mn & 0 & 0 & 0 & m^2 - n^2 \end{bmatrix} \begin{Bmatrix} \sigma_1 \\ \sigma_2 \\ \sigma_3 \\ \sigma_4 \\ \sigma_5 \\ \sigma_6 \end{Bmatrix} \quad (3.93)$$

or in equation form:

$$\begin{aligned}
 \sigma_x &= m^2\sigma_1 + n^2\sigma_2 - 2mn\sigma_6 \\
 \sigma_y &= n^2\sigma_1 + m^2\sigma_2 + 2mn\sigma_6 \\
 cpt \quad \sigma_z &= \sigma_3 \\
 \tau_{yz} &= m\sigma_4 + n\sigma_5 \\
 \tau_{zx} &= -n\sigma_4 + m\sigma_5 \\
 \tau_{xy} &= mn(\sigma_1 - \sigma_2) + (m^2 - n^2)\sigma_6
 \end{aligned} \tag{3.94}$$

and

$$[T_1]^{-1} = \begin{bmatrix} m^2 & n^2 & 0 & 0 & 0 & -2mn \\ n^2 & m^2 & 0 & 0 & 0 & 2mn \\ 0 & 0 & 1 & 0 & 0 & 0 \\ 0 & 0 & 0 & m & n & 0 \\ 0 & 0 & 0 & -n & m & 0 \\ mn & -mn & 0 & 0 & 0 & m^2 - n^2 \end{bmatrix} \tag{3.95}$$

Likewise,

$$\{\varepsilon_i\} = [T_2]\{\varepsilon_x\} \tag{3.96}$$

Expanding equation (3.96) yields:

$$\left\{ \begin{array}{c} \varepsilon_1 \\ \varepsilon_2 \\ \varepsilon_3 \\ \varepsilon_4 \\ \varepsilon_5 \\ \varepsilon_6 \end{array} \right\} = \begin{bmatrix} m^2 & n^2 & 0 & 0 & 0 & mn \\ n^2 & m^2 & 0 & 0 & 0 & -mn \\ 0 & 0 & 1 & 0 & 0 & 0 \\ 0 & 0 & 0 & m & -n & 0 \\ 0 & 0 & 0 & n & m & 0 \\ -2mn & 2mn & 0 & 0 & 0 & m^2 - n^2 \end{bmatrix} \left\{ \begin{array}{c} \varepsilon_x \\ \varepsilon_y \\ \varepsilon_z \\ \gamma_{yz} \\ \gamma_{zx} \\ \gamma_{xy} \end{array} \right\} \tag{3.97}$$

or in equation form:

$$\begin{aligned}
 \varepsilon_1 &= m^2\varepsilon_x + n^2\varepsilon_y + mn\gamma_{xy} \\
 \varepsilon_2 &= n^2\varepsilon_x + m^2\varepsilon_y - mn\gamma_{xy} \\
 \varepsilon_3 &= \varepsilon_z \\
 \varepsilon_4 &= m\gamma_{yz} - n\gamma_{zx} \\
 \varepsilon_5 &= n\gamma_{yz} + m\gamma_{zx} \\
 \varepsilon_6 &= -2mn(\varepsilon_x - \varepsilon_y) + (m^2 - n^2)\gamma_{xy}
 \end{aligned} \tag{3.98}$$

From equation (3.97), the strain transformation matrix  $[T_2]$  is defined as

$$[T_2] = \begin{bmatrix} m^2 & n^2 & 0 & 0 & 0 & mn \\ n^2 & m^2 & 0 & 0 & 0 & -mn \\ 0 & 0 & 1 & 0 & 0 & 0 \\ 0 & 0 & 0 & m & -n & 0 \\ 0 & 0 & 0 & n & m & 0 \\ -2mn & 2mn & 0 & 0 & 0 & m^2 - n^2 \end{bmatrix} \quad (3.99)$$

Inverting equation (3.96) yields

$$\{\varepsilon_x\} = [T_2]^{-1}\{\varepsilon_i\} \quad (3.100)$$

Expanding equation (3.100) yields

$$\begin{Bmatrix} \varepsilon_x \\ \varepsilon_y \\ \varepsilon_z \\ \gamma_{yz} \\ \gamma_{zx} \\ \gamma_{xy} \end{Bmatrix} = \begin{bmatrix} m^2 & n^2 & 0 & 0 & 0 & -mn \\ n^2 & m^2 & 0 & 0 & 0 & mn \\ 0 & 0 & 1 & 0 & 0 & 0 \\ 0 & 0 & 0 & m & n & 0 \\ 0 & 0 & 0 & -n & m & 0 \\ 2mn & -2mn & 0 & 0 & 0 & m^2 - n^2 \end{bmatrix} \begin{Bmatrix} \varepsilon_1 \\ \varepsilon_2 \\ \varepsilon_3 \\ \varepsilon_4 \\ \varepsilon_5 \\ \varepsilon_6 \end{Bmatrix} \quad (3.101)$$

Or in equation form

$$\begin{aligned} \varepsilon_x &= m^2\varepsilon_1 + n^2\varepsilon_2 - mn\varepsilon_6 \\ \varepsilon_y &= n^2\varepsilon_1 + m^2\varepsilon_2 + mn\varepsilon_6 \\ \varepsilon_z &= \varepsilon_3 \\ \gamma_{yz} &= m\varepsilon_4 + n\varepsilon_5 \\ \gamma_{zx} &= -n\varepsilon_4 + m\varepsilon_5 \\ \gamma_{xy} &= 2mn(\varepsilon_1 - \varepsilon_2) + (m^2 - n^2)\varepsilon_6 \end{aligned} \quad (3.102)$$

and

$$[T_2]^{-1} = \begin{bmatrix} m^2 & n^2 & 0 & 0 & 0 & -mn \\ n^2 & m^2 & 0 & 0 & 0 & mn \\ 0 & 0 & 1 & 0 & 0 & 0 \\ 0 & 0 & 0 & m & n & 0 \\ 0 & 0 & 0 & -n & m & 0 \\ 2mn & -2mn & 0 & 0 & 0 & m^2 - n^2 \end{bmatrix} \quad (3.103)$$

### 3.6.2 Stiffness Transformation

Since the stiffness  $C_{ijkl}$  is the fourth-order tensor, the stiffness transformation equation follows the tensor transformation rule:

$$C_{ijkl} = l_ip l_jq l_kr l_ls C_{pqrs} \quad (i,j,k,l = 1, 2, 3 \text{ and } p,q,r,s = x,y,z) \quad (3.104)$$

For the transformation of figure 3.13, however, we can obtain the transformation matrix using the results of equations (3.88) and (3.96).

Since

$$\{\sigma_i\} = [C_{ij}]\{\varepsilon_j\} \quad (3.105)$$

$$[T_1]\{\sigma_x\} = [C_{ij}][T_2]\{\varepsilon_x\}$$

or

$$\{\sigma_x\} = [T_1]^{-1}[C_{ij}][T_2]\{\varepsilon_x\} \quad (3.106)$$

Equation (3.106) can be simplified as

$$\{\sigma_x\} = [\bar{C}_{ij}]\{\varepsilon_x\} \quad (3.107)$$

using the transformed stiffness matrix  $[\bar{C}_{ij}]$ , which is defined as

$$[\bar{C}_{ij}] = [T_1]^{-1}[C_{ij}][T_2] \quad (3.108)$$

Using  $[T_i(-\theta)] = [T_i(\theta)]^{-1}$  ( $i = 1, 2$ ), and starting from the stiffness  $[C_{ij}]$  of the *orthotropic material* in table 3.7, which is expressed in the principal material axes, we have the following transformed stiffness matrix, which has the same stiffness shape as the *monoclinic material* in table 3.6 ( $z = 0$ , symmetry plane).

$$[\bar{C}_{ij}] = \begin{bmatrix} \bar{C}_{11} & \bar{C}_{12} & \bar{C}_{13} & 0 & 0 & \bar{C}_{16} \\ \bar{C}_{12} & \bar{C}_{22} & \bar{C}_{23} & 0 & 0 & \bar{C}_{26} \\ \bar{C}_{13} & \bar{C}_{23} & \bar{C}_{33} & 0 & 0 & \bar{C}_{36} \\ 0 & 0 & 0 & \bar{C}_{44} & \bar{C}_{45} & 0 \\ 0 & 0 & 0 & \bar{C}_{45} & \bar{C}_{55} & 0 \\ \bar{C}_{16} & \bar{C}_{26} & \bar{C}_{36} & 0 & 0 & \bar{C}_{66} \end{bmatrix} \quad (3.109)$$

The elements of  $\bar{C}_{ij}$  are expressed as follows:

$$\bar{C}_{11} = m^4 C_{11} + 2m^2 n^2 (C_{12} + 2C_{66}) + n^4 C_{22} \quad (3.110a)$$

$$\bar{C}_{12} = m^2 n^2 (C_{11} + C_{22} - 4C_{66}) + (m^4 + n^4) C_{12} \quad (3.110b)$$

$$\bar{C}_{13} = m^2 C_{13} + n^2 C_{23} \quad (3.110c)$$

$$\bar{C}_{16} = m^3 n (C_{11} - C_{12} - 2C_{66}) + mn^3 (C_{12} - C_{22} + 2C_{66}) \quad (3.110d)$$

$$\bar{C}_{22} = n^4 C_{11} + 2m^2 n^2 (C_{12} + 2C_{66}) + m^4 C_{22} \quad (3.110e)$$

$$\bar{C}_{23} = n^2 C_{13} + m^2 C_{23} \quad (3.110f)$$

$$\bar{C}_{26} = mn^3 (C_{11} - C_{12} - 2C_{66}) + m^3 n (C_{12} - C_{22} + 2C_{66}) \quad (3.110g)$$

$$\bar{C}_{33} = C_{33} \quad (3.110h)$$

$$\bar{C}_{36} = mn (C_{13} - C_{23}) \quad (3.110i)$$

$$\bar{C}_{44} = m^2 C_{44} + n^2 C_{55} \quad (3.110j)$$

$$\bar{C}_{45} = mn (C_{55} - C_{44}) \quad (3.110k)$$

$$\bar{C}_{55} = n^2 C_{44} + m^2 C_{55} \quad (3.110l)$$

$$\bar{C}_{66} = m^2 n^2 (C_{11} - 2C_{12} + C_{22}) + (m^2 - n^2)^2 C_{66} \quad (3.110m)$$

Equation (3.110) is valid only for the transformation from an orthotropic material. For a general anisotropic material with a fully populated  $[C_{ij}]$  matrix, other references should be consulted (Reddy, 1997). The number of independent stiffness coefficients of monoclinic materials in table 3.6 is 13; however, the number of independent stiffness coefficients in equations (3.110) is still 9, although the number of nonzero stiffness coefficients is the same as the monoclinic material.

### 3.6.3 Compliance Transformation

The transformed compliance matrix has the same symmetric form as the transformed stiffness matrix,

$$[\bar{S}_{ij}] = \begin{bmatrix} \bar{S}_{11} & \bar{S}_{12} & \bar{S}_{13} & 0 & 0 & \bar{S}_{16} \\ \bar{S}_{12} & \bar{S}_{22} & \bar{S}_{23} & 0 & 0 & \bar{S}_{26} \\ \bar{S}_{13} & \bar{S}_{23} & \bar{S}_{33} & 0 & 0 & \bar{S}_{36} \\ 0 & 0 & 0 & \bar{S}_{44} & \bar{S}_{45} & 0 \\ 0 & 0 & 0 & \bar{S}_{45} & \bar{S}_{55} & 0 \\ \bar{S}_{16} & \bar{S}_{26} & \bar{S}_{36} & 0 & 0 & \bar{S}_{66} \end{bmatrix} \quad (3.111)$$

However, the individual elements of the compliance matrix exhibit differences in coefficients because of the differences between the engineering and tensor shear strains, and consequently in compliances, as listed in table 3.5. In expanded form, the equations are

$$\bar{S}_{11} = m^4 S_{11} + m^2 n^2 (2S_{12} + S_{66}) + n^4 S_{22} \quad (3.112a)$$

$$\bar{S}_{12} = m^2 n^2 (S_{11} + S_{22} - S_{66}) + (m^4 + n^4) S_{12} \quad (3.112b)$$

$$\bar{S}_{13} = m^2 S_{13} + n^2 S_{23} \quad (3.112c)$$

$$\bar{S}_{16} = m^3 n (2S_{11} - 2S_{12} - S_{66}) + mn^3 (2S_{12} - 2S_{22} + S_{66}) \quad (3.112d)$$

$$\bar{S}_{22} = n^4 S_{11} + m^2 n^2 (2S_{12} + S_{66}) + m^4 S_{22} \quad (3.112e)$$

$$\bar{S}_{23} = n^2 S_{13} + m^2 S_{23} \quad (3.112f)$$

$$\bar{S}_{26} = mn^3 (2S_{11} - 2S_{12} - S_{66}) + m^3 n (2S_{12} - 2S_{22} + S_{66}) \quad (3.112g)$$

$$\bar{S}_{33} = S_{33} \quad (3.112h)$$

$$\bar{S}_{36} = 2mn(S_{13} - S_{23}) \quad (3.112i)$$

$$\bar{S}_{44} = m^2 S_{44} + n^2 S_{55} \quad (3.112j)$$

$$\bar{S}_{45} = mn(S_{55} - S_{44}) \quad (3.112k)$$

$$\bar{S}_{55} = n^2 S_{44} + m^2 S_{55} \quad (3.112l)$$

$$\bar{S}_{66} = 4m^2 n^2 (S_{11} - 2S_{12} + S_{22}) + (m^2 - n^2)^2 S_{66} \quad (3.112m)$$

### 3.7 Plane Stress Constitutive Relations

A plane stress state is defined to be one in which all transverse stresses are negligible. It is often the case in the analysis of composites that a condition of plane stress actually exists or is a very good approximation, because most laminates are typically thin and experience a plane state of stress (Herakovich, 1998). For a lamina in the  $x_1-x_2$ -plane, as shown in figure 3.14, the transverse stress components are  $\sigma_{33}$ ,  $\sigma_{13}$ , and  $\sigma_{23}$  (Reddy, 1997). Although these stress components are small in

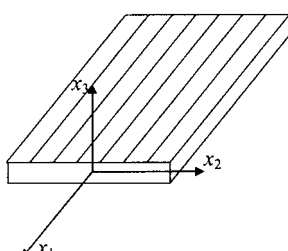


**Figure 3.14** One lamina in a plane state of stress with the principal material coordinates  $x_1$ ,  $x_2$ ,  $x_3$ .

comparison with  $\sigma_{11}$ ,  $\sigma_{22}$ , and  $\sigma_{12}$ , sometimes they can induce interlaminar failures, because fiber reinforced composite laminates are weak (see chapter 5) in the transverse direction (because fibers exist only in the  $x_1-x_2$ -plane). When the interlaminar delamination failure is not important, the transverse interlaminar stresses ( $\sigma_{33}=\sigma_3$ ,  $\sigma_{23}=\sigma_4$ ,  $\sigma_{13}=\sigma_5$ ) may be neglected for thin plates or shells, and the constitutive equations (3.58)–(3.63) for orthotropic material become simpler:

$$\varepsilon_1 = \frac{\sigma_1}{E_1} - \frac{\nu_{21}}{E_2} \sigma_2 \quad (3.113a)$$

$$\varepsilon_2 = -\frac{\nu_{12}}{E_1} \sigma_1 + \frac{\sigma_2}{E_2} \quad (3.113b)$$

$$\varepsilon_3 = -\frac{\nu_{13}}{E_1} \sigma_1 - \frac{\nu_{23}}{E_2} \sigma_2 \quad (3.113c)$$

$$\varepsilon_4 = 0 \quad (3.113d)$$

$$\varepsilon_5 = 0 \quad (3.113e)$$

$$\varepsilon_6 = \frac{\sigma_6}{G_{12}} \quad (3.113f)$$

Equations (3.113a), (3.113b), and (3.113f), can be rewritten by inverting

$$\{\sigma_i\} = [Q_{ij}] \{\varepsilon_j\} \quad (i, j = 1, 2, 6)$$

where

$$[Q_{ij}] = \begin{bmatrix} Q_{11} & Q_{12} & 0 \\ Q_{12} & Q_{22} & 0 \\ 0 & 0 & Q_{66} \end{bmatrix} \quad (3.114)$$

or expanding

$$\begin{Bmatrix} \sigma_1 \\ \sigma_2 \\ \sigma_6 \end{Bmatrix} = \begin{bmatrix} Q_{11} & Q_{12} & 0 \\ Q_{12} & Q_{22} & 0 \\ 0 & 0 & Q_{66} \end{bmatrix} \begin{Bmatrix} \varepsilon_1 \\ \varepsilon_2 \\ \varepsilon_6 \end{Bmatrix} \quad (3.115)$$

The matrix  $Q_{ij}$  is called the plane-stress *reduced stiffness*, whose elements are given by

$$Q_{11} = \frac{E_1}{1 - \nu_{12}\nu_{21}} \quad (3.116a)$$

$$Q_{12} = \frac{\nu_{12}E_2}{1 - \nu_{12}\nu_{21}} = \frac{\nu_{21}E_1}{1 - \nu_{12}\nu_{21}} = Q_{21} \quad (3.116b)$$

$$Q_{22} = \frac{E_2}{1 - \nu_{12}\nu_{21}} \quad (3.116c)$$

$$Q_{66} = G_{12} \quad (3.116d)$$

From equation (3.116b), we can see that the reciprocal relationship holds:

$$\frac{\nu_{12}}{E_1} = \frac{\nu_{21}}{E_2} \quad (3.117)$$

As shown in equations (3.116) and (3.117), for plane stress problems, *the four engineering constants*  $E_1$ ,  $E_2$ ,  $\nu_{12}$ , and  $G_{12}$  are required to specify the elastic stiffness constants completely.

### EXAMPLE 3.5

Determine the reduced stiffness coefficients  $Q_{ij}$  and compliance coefficients  $S_{ij}$  for plane stress of T300/5208 carbon epoxy composite material ( $E_1 = 132$  GPa,  $E_2 = 10.8$  GPa,  $\nu_{12} = 0.24$ ,  $G_{12} = 5.65$  GPa). Compare the reduced values with the values of example 3.2.

#### Solution

$$\nu_{21} = \left( \frac{E_2}{E_1} \right) \times \nu_{12} = \left( \frac{10.8}{132} \right) \times 0.24 = 1.964 \times 10^{-2}$$

$$Q_{11} = \frac{E_1}{(1 - \nu_{12}\nu_{21})} = \frac{132}{(1 - 0.24 \times 0.0196)} = 132.6 \text{ GPa}, \quad Q_{12} = 2.60 \text{ GPa},$$

$$Q_{22} = 10.9 \text{ GPa}, \quad Q_{66} = 5.65 \text{ GPa}, \quad Q_{16} = Q_{26} = 0$$

$$S_{11} = \frac{1}{E_1} = 7.576 \times 10^{-3} \text{ 1/GPa}, \quad S_{12} = -1.818 \times 10^{-3} \text{ /GPa},$$

$$S_{22} = 92.59 \times 10^{-3} \text{ 1/GPa},$$

$$S_{66} = 177.0 \times 10^{-3} \text{ 1/GPa}, \quad S_{16} = S_{26} = 0$$

The values of  $Q_{ij}$  are much different from those of  $C_{mnpq}$  of example 3.2 except that the magnitude  $Q_{11}$  is similar to that of  $C_{11}$  ( $= C_{1111}$ ).

When we want to express the plane stresses in the global coordinates  $x$ ,  $y$ ,  $z$  rather than principal material coordinates  $x_1$ ,  $x_2$ ,  $x_3$ , as shown in figure 3.13, the 2-D transformations for rotation about the  $x_3$ - (or  $z$ -) axis are straightforward simplifications of the 3-D equation (3.107). For the plane stress problem, we have the reduced stiffness matrix  $[Q_{ij}]$ , as shown in equation (3.114), rather than  $[C_{ij}]$ . Then the stress transformation equations have the following simplified forms:

$$\begin{Bmatrix} \sigma_1 \\ \sigma_2 \\ \sigma_6 \end{Bmatrix} = [T_1]' \begin{Bmatrix} \sigma_x \\ \sigma_y \\ \tau_{xy} \end{Bmatrix} \quad (3.118)$$

Expanding equation (3.118) yields

$$\begin{aligned}\sigma_1 &= \cos^2 \theta \sigma_x + \sin^2 \theta \sigma_y + 2 \cos \theta \sin \theta \tau_{xy} \\ \sigma_2 &= \sin^2 \theta \sigma_x + \cos^2 \theta \sigma_y - 2 \cos \theta \sin \theta \tau_{xy} \\ \sigma_6 &= -\cos \theta \sin \theta \sigma_x + \cos \theta \sin \theta \sigma_y + (\cos^2 \theta - \sin^2 \theta) \tau_{xy}\end{aligned}\quad (3.119)$$

The inverse transformation of equation (3.118) has the form

$$\left\{ \begin{array}{l} \sigma_x \\ \sigma_y \\ \tau_{xy} \end{array} \right\} = [T_1]'^{-1} \left\{ \begin{array}{l} \sigma_1 \\ \sigma_2 \\ \sigma_6 \end{array} \right\} \quad (3.120)$$

Expanding equation (3.120) yields

$$\begin{aligned}\sigma_x &= \cos^2 \theta \sigma_1 + \sin^2 \theta \sigma_2 - 2 \cos \theta \sin \theta \sigma_6 \\ \sigma_y &= \sin^2 \theta \sigma_1 + \cos^2 \theta \sigma_2 + 2 \cos \theta \sin \theta \sigma_6 \\ \tau_{xy} &= \cos \theta \sin \theta \sigma_1 - \cos \theta \sin \theta \sigma_2 + (\cos^2 \theta - \sin^2 \theta) \sigma_6\end{aligned}\quad (3.121)$$

where

$$[T_1]' = \begin{bmatrix} m^2 & n^2 & 2mn \\ n^2 & m^2 & -2mn \\ -mn & mn & m^2 - n^2 \end{bmatrix} \quad (3.122)$$

in which  $m = \cos \theta$  and  $n = \sin \theta$ .

The engineering strain transformation equations have the following simplified forms:

$$\left\{ \begin{array}{l} \varepsilon_1 \\ \varepsilon_2 \\ \varepsilon_6 \end{array} \right\} = [T_2]' \left\{ \begin{array}{l} \varepsilon_x \\ \varepsilon_y \\ \gamma_{xy} \end{array} \right\} \quad (3.123)$$

Expanding equation (3.123) yields

$$\begin{aligned}\varepsilon_1 &= \cos^2 \theta \varepsilon_x + \sin^2 \theta \varepsilon_y + \cos \theta \sin \theta \gamma_{xy} \\ \varepsilon_2 &= \sin^2 \theta \varepsilon_x + \cos^2 \theta \varepsilon_y - \cos \theta \sin \theta \gamma_{xy} \\ \varepsilon_6 &= -2 \cos \theta \sin \theta \varepsilon_x + 2 \cos \theta \sin \theta \varepsilon_y + (\cos^2 \theta - \sin^2 \theta) \gamma_{xy}\end{aligned}\quad (3.124)$$

The inverse transformation of equation (3.123) has the form

$$\left\{ \begin{array}{l} \varepsilon_x \\ \varepsilon_y \\ \gamma_{xy} \end{array} \right\} = [T_2]'^{-1} \left\{ \begin{array}{l} \varepsilon_1 \\ \varepsilon_2 \\ \varepsilon_6 \end{array} \right\} \quad (3.125)$$

Expanding equation (3.125) yields

$$\begin{aligned}\varepsilon_x &= \cos^2 \theta \varepsilon_1 + \sin^2 \theta \varepsilon_2 - \cos \theta \sin \theta \varepsilon_6 \\ \varepsilon_y &= \sin^2 \theta \varepsilon_1 + \cos^2 \theta \varepsilon_2 + \cos \theta \sin \theta \varepsilon_6 \\ \gamma_{xy} &= 2 \cos \theta \sin \theta \varepsilon_1 - 2 \cos \theta \sin \theta \varepsilon_2 + (\cos^2 \theta - \sin^2 \theta) \varepsilon_6\end{aligned}\quad (3.126)$$

where

$$[T_2]' = \begin{bmatrix} m^2 & n^2 & mn \\ n^2 & m^2 & -mn \\ -2mn & 2mn & m^2 - n^2 \end{bmatrix} \quad (3.127)$$

The transformed reduced stiffness matrix  $[\bar{Q}_{ij}]$  ( $i, j = 1, 2, 6$ ) for the plane stress becomes

$$[\bar{Q}_{ij}] = \{[T_1]'\}^{-1} [Q_{ij}] [T_2]' \quad (3.128)$$

As in the 3-D case, using  $\{[T_1(\theta)]'\}^{-1} = [T_1(-\theta)]'$  and  $\{[T_2(\theta)]'\}^{-1} = [T_2(-\theta)]'$ , the elements of  $[\bar{Q}_{ij}]$  are

$$\bar{Q}_{11} = m^4 Q_{11} + 2m^2 n^2 (Q_{12} + 2Q_{66}) + n^4 Q_{22} \quad (3.129a)$$

$$\bar{Q}_{12} = m^2 n^2 (Q_{11} + Q_{22} - 4Q_{66}) + (m^4 + n^4) Q_{12} \quad (3.129b)$$

$$\bar{Q}_{22} = n^4 Q_{11} + 2m^2 n^2 (Q_{12} + 2Q_{66}) + m^4 Q_{22} \quad (3.129c)$$

$$\bar{Q}_{66} = m^2 n^2 (Q_{11} - 2Q_{12} + Q_{22}) + (m^2 - n^2)^2 Q_{66} \quad (3.129d)$$

$$\bar{Q}_{16} = m^3 n (Q_{11} - Q_{12} - 2Q_{66}) + mn^3 (Q_{12} - Q_{22} + 2Q_{66}) \quad (3.129e)$$

$$\bar{Q}_{26} = mn^3 (Q_{11} - Q_{12} - 2Q_{66}) + m^3 n (Q_{12} - Q_{22} + 2Q_{66}) \quad (3.129f)$$

where  $m = \cos \theta$ ,  $n = \sin \theta$ .

By the use of a trigonometric double or triple angle identity, the transformed reduced stiffnesses can be rewritten (Jones, 1975; Tsai and Hahn, 1980) using  $U_i$  ( $i = 1, \dots, 5$ ), which are invariants with respect to  $\theta$ :

$$\bar{Q}_{11} = U_1 + U_2 \cos 2\theta + U_3 \cos 4\theta \quad (3.130a)$$

$$\bar{Q}_{12} = U_4 - U_3 \cos 4\theta \quad (3.130b)$$

$$\bar{Q}_{22} = U_1 - U_2 \cos 2\theta + U_3 \cos 4\theta \quad (3.130c)$$

$$\bar{Q}_{66} = U_5 - U_3 \cos 4\theta \quad (3.130d)$$

$$\bar{Q}_{16} = \frac{1}{2} U_2 \sin 2\theta + U_3 \sin 4\theta \quad (3.130e)$$

$$\bar{Q}_{26} = \frac{1}{2} U_2 \sin 2\theta - U_3 \sin 4\theta \quad (3.130f)$$

in which

$$U_1 = \frac{1}{8}(3Q_{11} + 3Q_{22} + 2Q_{12} + 4Q_{66}) \quad (3.131a)$$

$$U_2 = \frac{1}{2}(Q_{11} - Q_{22}) \quad (3.131b)$$

$$U_3 = \frac{1}{8}(Q_{11} + Q_{22} - 2Q_{12} - 4Q_{66}) \quad (3.131c)$$

$$U_4 = \frac{1}{8}(Q_{11} + Q_{22} + 6Q_{12} - 4Q_{66}) \quad (3.131d)$$

$$U_5 = \frac{1}{8}(Q_{11} + Q_{22} - 2Q_{12} + 4Q_{66}) \quad (3.131e)$$

Another form of equations of  $Q_{ij}$  can be derived using a different form of invariants  $I_1$ ,  $I_2$ ,  $R_1$ , and  $R_2$ :

$$\bar{Q}_{11} = I_1 + I_2 + R_1 \cos 2\theta + R_2 \cos 4\theta \quad (3.132a)$$

$$\bar{Q}_{12} = I_1 - I_2 - R_2 \cos 4\theta \quad (3.132b)$$

$$\bar{Q}_{22} = I_1 + I_2 - R_1 \cos 2\theta + R_2 \cos 4\theta \quad (3.132c)$$

$$\bar{Q}_{66} = I_2 - R_2 \cos 4\theta \quad (3.132d)$$

$$\bar{Q}_{16} = \frac{1}{2}R_1 \sin 2\theta + R_2 \sin 4\theta \quad (3.132e)$$

$$\bar{Q}_{26} = \frac{1}{2}R_1 \sin 2\theta - R_2 \sin 4\theta \quad (3.132f)$$

in which

$$I_1 = \frac{1}{4}(Q_{11} + Q_{22} + 2Q_{12}) \quad (3.133a)$$

$$I_2 = \frac{1}{8}(Q_{11} + Q_{22} - 2Q_{12} + 4Q_{66}) \quad (3.133b)$$

$$R_1 = \frac{1}{2}(Q_{11} - Q_{22}) \quad (3.133c)$$

$$R_2 = \frac{1}{8}(Q_{11} + Q_{22} - 2Q_{12} - 4Q_{66}) \quad (3.133d)$$

The transformed compliance  $[\bar{S}]$  is the inverse of the transformed reduced stiffness, i.e.,

$$[\bar{S}] = [\bar{Q}]^{-1} \quad (3.134)$$

Using (3.128), it can be written that

$$[\bar{S}] = [T_2]'^{-1}[Q]^{-1}[T_1]' = [T_2]'^{-1}[S][T_1]' \quad (3.135)$$

The explicit expressions for the  $\bar{S}_{ij}$  terms as function of  $S_{ij}$  and the fiber orientation  $\theta$  are the same as those given in equation (3.112) for  $i, j = 1, 2$ , and 6. They are rewritten here for convenience:

$$\bar{S}_{11} = m^4 S_{11} + m^2 n^2 (2S_{12} + S_{66}) + n^4 S_{22} \quad (3.136a)$$

$$\bar{S}_{12} = m^2 n^2 (S_{11} + S_{22} - S_{66}) + (m^4 + n^4) S_{12} \quad (3.136b)$$

$$\bar{S}_{22} = n^4 S_{11} + m^2 n^2 (2S_{12} + S_{66}) + m^4 S_{22} \quad (3.136c)$$

$$\bar{S}_{66} = 4m^2 n^2 (S_{11} - 2S_{12} + S_{22}) + (m^2 - n^2)^2 S_{66} \quad (3.136d)$$

$$\bar{S}_{16} = m^3 n (2S_{11} - 2S_{12} - S_{66}) + mn^3 (2S_{12} - 2S_{22} + S_{66}) \quad (3.136e)$$

$$\bar{S}_{26} = mn^3 (2S_{11} - 2S_{12} - S_{66}) + m^3 n (2S_{12} - 2S_{22} + S_{66}) \quad (3.136f)$$

These equations can also be expressed in terms of engineering material constants from

$$S_{11} = \frac{1}{E_1}, \quad S_{12} = -\frac{\nu_{12}}{E_1} = -\frac{\nu_{21}}{E_2} = S_{21}, \quad S_{22} = \frac{1}{E_2}, \quad S_{66} = \frac{1}{G_{12}} \quad (3.137)$$

$$\bar{S}_{11} = \frac{1}{E_1} \left[ m^4 + m^2 n^2 \left( -2\nu_{12} + \frac{E_1}{G_{12}} \right) + n^4 \frac{E_1}{E_2} \right] \quad (3.138a)$$

$$\bar{S}_{12} = \frac{1}{E_1} \left[ m^2 n^2 \left( 1 + \frac{E_1}{E_2} - \frac{E_1}{G_{12}} \right) - (m^4 + n^4) \nu_{12} \right] \quad (3.138b)$$

$$\bar{S}_{22} = \frac{1}{E_1} \left[ n^4 + m^2 n^2 \left( -2\nu_{12} + \frac{E_1}{G_{12}} \right) + m^4 \frac{E_1}{E_2} \right] \quad (3.138c)$$

$$\bar{S}_{66} = \frac{1}{E_1} \left[ 4m^2 n^2 \left( 1 + 2\nu_{12} + \frac{E_1}{E_2} \right) + (m^2 - n^2)^2 \frac{E_1}{G_{12}} \right] \quad (3.138d)$$

$$\bar{S}_{16} = \frac{1}{E_1} \left[ m^3 n \left( 2 + 2\nu_{12} - \frac{E_1}{G_{12}} \right) + mn^3 \left( -2\nu_{12} - 2 \frac{E_1}{E_2} + \frac{E_1}{G_{12}} \right) \right] \quad (3.138e)$$

$$\bar{S}_{26} = \frac{1}{E_1} \left[ mn^3 \left( 2 + 2\nu_{12} - \frac{E_1}{G_{12}} \right) + m^3 n \left( -2\nu_{12} - 2 \frac{E_1}{E_2} + \frac{E_1}{G_{12}} \right) \right] \quad (3.138f)$$

### 3.8 Lamina Engineering Constants

The engineering constants of an off-axis lamina in terms of the known material properties ( $E_1$ ,  $E_2$ ,  $v_{12}$ ,  $G_{12}$ ) can be expressed (with respect to the global coordinates) by the transformed constitutive equation:

$$\begin{Bmatrix} \varepsilon_x \\ \varepsilon_y \\ \gamma_{xy} \end{Bmatrix} = \begin{bmatrix} \bar{S}_{11} & \bar{S}_{12} & \bar{S}_{16} \\ \bar{S}_{12} & \bar{S}_{22} & \bar{S}_{26} \\ \bar{S}_{16} & \bar{S}_{26} & \bar{S}_{66} \end{bmatrix} \begin{Bmatrix} \sigma_x \\ \sigma_y \\ \tau_{xy} \end{Bmatrix} \quad (3.139)$$

$$\begin{Bmatrix} \sigma_x \\ \sigma_y \\ \tau_{xy} \end{Bmatrix} = \begin{bmatrix} \bar{Q}_{11} & \bar{Q}_{12} & \bar{Q}_{16} \\ \bar{Q}_{12} & \bar{Q}_{22} & \bar{Q}_{26} \\ \bar{Q}_{16} & \bar{Q}_{26} & \bar{Q}_{66} \end{bmatrix} \begin{Bmatrix} \varepsilon_x \\ \varepsilon_y \\ \gamma_{xy} \end{Bmatrix} \quad (3.140)$$

#### EXAMPLE 3.4 (CONTINUED)

Now we can calculate the strains of the patch. Since the warp direction is  $45^\circ$  from the  $x$ -axis, which is the direction of applied stress, the compliances in equations (3.138) can be calculated. From the values of  $E_1$  of 200 MPa,  $E_2$  of 100 MPa,  $G_{12}$  of 50 MPa, and the Poisson's ratio 0.3,

$$\begin{aligned} \bar{S}_{11} &= \frac{1}{E_1} \left[ m^4 + m^2 n^2 \left( -2v_{12} + \frac{E_1}{G_{12}} \right) + n^4 \frac{E_1}{E_2} \right] \\ &= \frac{1}{200} \left[ \frac{1}{4} + \frac{1}{4} \left( -2 \times 0.3 + \frac{200}{50} \right) + \frac{1}{4} \frac{200}{100} \right] = 8.0 \times 10^{-3} (1/\text{MPa}) \end{aligned}$$

By the same method,  $\bar{S}_{12} = -2.0 \times 10^{-3} (1/\text{MPa})$ ,  $\bar{S}_{22} = 8.0 \times 10^{-3} (1/\text{MPa})$ ,  $\bar{S}_{66} = 18.0 \times 10^{-3} (1/\text{MPa})$ ,  $\bar{S}_{16} = -2.5 \times 10^{-3} (1/\text{MPa})$ , and  $\bar{S}_{26} = -2.5 \times 10^{-3} (1/\text{MPa})$ .

Then, from equation (3.139),

$$\varepsilon_x = \bar{S}_{11}\sigma_x + \bar{S}_{12}\sigma_y + \bar{S}_{16}\tau_{xy} = 6.0 \times 10^{-3} (\text{m/m})$$

$$\varepsilon_y = \bar{S}_{12}\sigma_x + \bar{S}_{22}\sigma_y + \bar{S}_{26}\tau_{xy} = 6.0 \times 10^{-3} (\text{m/m})$$

$$\gamma_{xy} = \bar{S}_{16}\sigma_x + \bar{S}_{26}\sigma_y + \bar{S}_{66}\tau_{xy} = -5.0 \times 10^{-3} (\text{m/m})$$

The deformation corresponding to the strains is shown in figure 3.1, which shows the occurrence of negative shear strain. Since the stresses are not applied to the principal axes, the shear strain occurs, even though only normal stresses were applied.

Now we can calculate the deformation of an orthotropic lamina subjected to stresses in the nonprincipal directions. Therefore, we are in the position to calculate the stiffness of a lamina in the nonprincipal directions, that is, in the laminate axes.

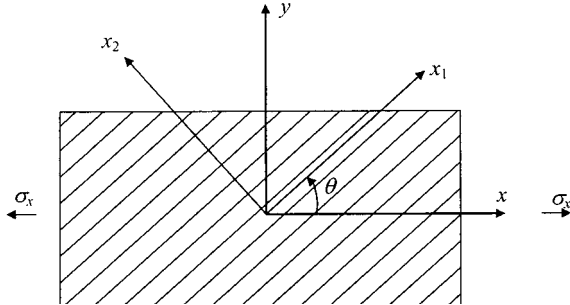


**Figure 3.15** Off-axis lamina under the tensile stress  $\sigma_x$ .

When the unidirectional lamina is under the loading  $\sigma_x \neq 0$  with  $\sigma_y = \tau_{xy} = 0$ , as shown in figure 3.15, the first equation (3.139) becomes

$$\varepsilon_x = \bar{S}_{11}\sigma_x \quad (3.141)$$

Since the definition of Young's modulus  $E_x$  of any material is the ratio of the applied stress to the strain produced by the applied stress, we have

$$E_x = \frac{\sigma_x}{\varepsilon_x} = \frac{1}{\bar{S}_{11}} \quad (3.142)$$

From the result of equation (3.138a), we have

$$E_x = \frac{1}{\bar{S}_{11}} = \frac{E_1}{m^4 + m^2n^2[-2\nu_{12} + (E_1/G_{12})] + n^4(E_1/E_2)} \quad (3.143)$$

By similar methods, we have

$$E_y = \frac{1}{\bar{S}_{22}} = \frac{E_1}{n^4 + m^2n^2[-2\nu_{12} + (E_1/G_{12})] + m^4(E_1/E_2)} \quad (3.144)$$

$$G_{xy} = \frac{1}{\bar{S}_{66}} = \frac{E_1}{4m^2n^2[1 + 2\nu_{12} + (E_1/E_2)] + (m^2 - n^2)^2(E_1/G_{12})} \quad (3.145)$$

Poisson's ratio,  $\nu_{xy}$ , is defined as the ratio of the negative of the lateral strain  $\varepsilon_y$  to the axial strain  $\varepsilon_x$ , under the applied stress  $\sigma_x$ , only. Using equations (3.138), we have

$$\nu_{xy} = -\frac{\varepsilon_y}{\varepsilon_x} = -\frac{\bar{S}_{12}}{\bar{S}_{11}} = -\frac{m^2n^2[1 + (E_1/E_2) - (E_1/G_{12})] - (m^4 + n^4)\nu_{12}}{m^4 + m^2n^2[-2\nu_{12} + (E_1/G_{12})] + n^4(E_1/E_2)} \quad (3.146)$$

As shown in equations (3.129), the coefficients  $\bar{Q}_{16}$  and  $\bar{Q}_{26}$  are not zero unless  $\theta = 0^\circ$  or  $90^\circ$ , which means that the response of orthotropic materials exhibits the normal-shear coupling when the material is loaded in other than principal material coordinates. Therefore, shear strain is produced by normal stress, or vice versa, as shown in example 3.4. To measure the tendency of the normal-shear coupling, the coefficients of mutual influence have been defined (Lekhnitskii, 1963).

The coefficient of mutual influence of the first kind,  $\eta_{x,xy}$ , is defined as the ratio of the normal strain  $\varepsilon_x$  to the shear strain  $\gamma_{xy}$  for an applied shear stress  $\tau_{xy}$

$$\eta_{x,xy} = \frac{\varepsilon_x}{\gamma_{xy}} \quad (3.147)$$

The definition of the mutual influence  $\eta$  is opposite to the convention used for Poisson's ratio  $\nu$ . The coefficient of mutual influence of the second kind,  $\eta_{xy,x}$ , is defined as the ratio of the shear strain  $\gamma_{xy}$  to the normal strain  $\varepsilon_x$  for an applied normal stress  $\sigma_x$ ,

$$\eta_{xy,x} = \frac{\gamma_{xy}}{\varepsilon_x} \quad (3.148)$$

For example, when  $\sigma_x \neq 0$  with  $\sigma_y = \tau_{xy} = 0$ , the coefficient of mutual influence of the second kind,  $\eta_{xy,x}$ , is obtained using equations (3.138) and (3.139):

$$\eta_{xy,x} = \frac{\gamma_{xy}}{\varepsilon_x} = \frac{\bar{S}_{16}}{\bar{S}_{11}} = \frac{m^3 n [2 + 2\nu_{12} - (E_1/G_{12})] + mn^3 [-2\nu_{12} - (2E_1/E_2) + (E_1/G_{12})]}{m^4 + m^2 n^2 [-2\nu_{12} + (E_1/G_{12})] + n^4 (E_1/E_2)} \quad (3.149)$$

Figures 3.16 and 3.17 show the elastic constants of a glass epoxy composite and a boron epoxy composite (Jones, 1975), in which,  $E_x$  is divided by  $E_2$  and  $G_{xy}$  is divided by  $G_{12}$ . In both Figures,  $G_{xy}$  is largest at  $\theta = 45^\circ$ . The coefficient of mutual influence  $\eta_{xy,x}$  is zero at  $\theta = 0^\circ$  and  $90^\circ$ , which corresponds to the principal material coordinates, but achieves values of magnitude that are large with compared with  $\nu_{xy}$  for intermediate angles.  $E_y$  behaves like  $E_x$ , except that  $E_y$  is small for  $\theta$  near  $0^\circ$  and large for  $\theta$  near  $90^\circ$ .

Other anisotropic elastic coefficients are Chentsov coefficients, which relate shear stresses in one plane to the other shear strains. The Chentsov coefficients do not affect the in-plane lamina behavior because the coefficients are related to  $\bar{S}_{44}$ ,  $\bar{S}_{45}$ ,  $\bar{S}_{55}$  in equation (3.111), but not listed in equation (3.138). The Chentsov coefficient,

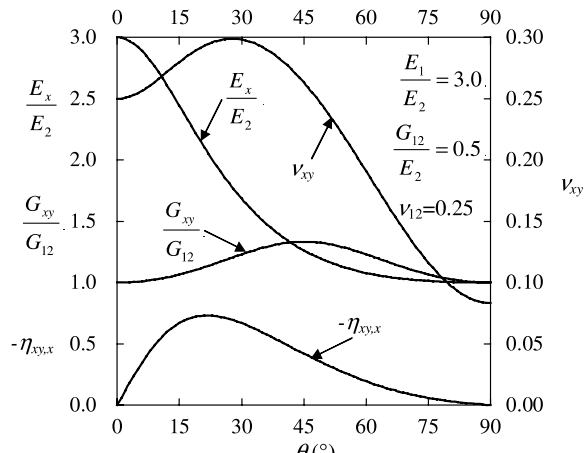


**Figure 3.16** Normalized moduli for a glass epoxy composite with respect to ply angle  $\theta$ .

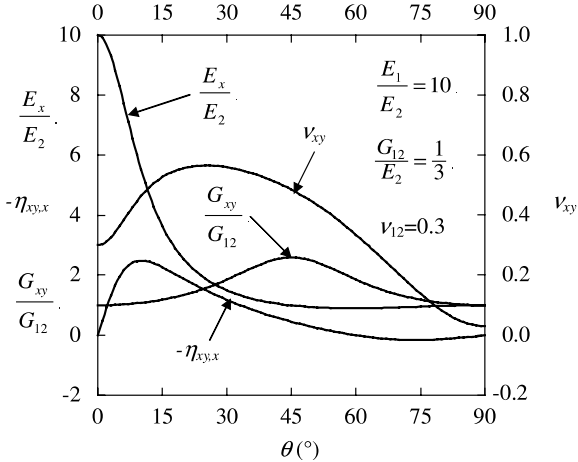


**Figure 3.17** Normalized moduli for a boron epoxy composite with respect to ply angle  $\theta$ .

$\mu_{xy,kl}$ , is defined as the coefficient that characterizes the shear strain in the  $xy$ -plane due to the shear stress in the  $kl$ -plane  $\tau_{kl}$ , and all other stresses zero, that is,

$$\mu_{xy,kl} = \frac{\gamma_{xy}}{\gamma_{kl}} \quad (3.150)$$

The definition of the Chentsov coefficient  $\mu$  is opposite to the convention used for Poisson's ratio  $\nu$ .

The Chentsov coefficients also satisfy the reciprocal relation:

$$\frac{\mu_{xy,kl}}{G_{kl}} = \frac{\mu_{kl,xy}}{G_{xy}} \quad (3.151)$$

The generalized Hooke's law can be expressed using the mutual coefficients as

$$\varepsilon_x = \frac{1}{E_x} (\sigma_x - \nu_{xy}\sigma_y - \nu_{xz}\sigma_z + \eta_{yz,x}\tau_{yz} + \eta_{zx,x}\tau_{zx} + \eta_{xy,x}\tau_{xy}) \quad (3.152a)$$

$$\varepsilon_y = \frac{1}{E_y} (-\nu_{yx}\sigma_x + \sigma_y - \nu_{yz}\sigma_z + \eta_{yz,y}\tau_{yz} + \eta_{zx,y}\tau_{zx} + \eta_{xy,y}\tau_{xy}) \quad (3.152b)$$

$$\varepsilon_z = \frac{1}{E_z} (-\nu_{zx}\sigma_x - \nu_{zy}\sigma_y + \sigma_z + \eta_{yz,z}\tau_{yz} + \eta_{zx,z}\tau_{zx} + \eta_{xy,z}\tau_{xy}) \quad (3.152c)$$

$$\gamma_{yz} = \frac{1}{G_{yz}} (\eta_{x,yz}\sigma_x + \eta_{y,yz}\sigma_y + \eta_{z,yz}\sigma_z + \tau_{yz} + \mu_{zx,yz}\tau_{zx} + \mu_{xy,yz}\tau_{xy}) \quad (3.152d)$$

$$\gamma_{zx} = \frac{1}{G_{zx}} (\eta_{x,zx}\sigma_x + \eta_{y,zx}\sigma_y + \eta_{z,zx}\sigma_z + \mu_{yz,zx}\tau_{yz} + \tau_{zx} + \mu_{xy,zx}\tau_{xy}) \quad (3.152e)$$

$$\gamma_{xy} = \frac{1}{G_{xy}} (\eta_{x,xy}\sigma_x + \eta_{y,xy}\sigma_y + \eta_{z,xy}\sigma_z + \mu_{yz,xy}\tau_{yz} + \mu_{zx,xy}\tau_{zx} + \tau_{xy}) \quad (3.152f)$$

Equations (3.152) have some mixed characteristics because the definitions  $\nu$ ,  $\eta$ , and  $\mu$  are not same as already noted. All the equations from (3.142) to (3.152) are

valid only for a single *lamina*, but *not for a laminate* composed of several laminae with different ply angles. For example, we cannot calculate  $E_x$  of a plate of composed of two laminae with  $+30^\circ$  and  $-30^\circ$  stacking angles by averaging  $E_x$  ( $+30^\circ$ ) and  $E_x$  ( $-30^\circ$ ) (see problem 3.12). Therefore, we should not try to obtain the laminate engineering constants by averaging the properties of constituent laminas. The equations valid for the laminate are derived in the next chapter.

### 3.9 Concluding Remarks

This chapter presented the basic governing equations for unidirectional composites. It emphasized the fact that all materials must satisfy the three governing conditions of continuum mechanics: equilibrium condition, geometric compatibility, and the constitutive relationship (i.e., the stress-strain relationship). The important material properties that govern anisotropic materials are also derived and related to material constants we measure through testing. It was shown that the number of independent material constants can be as many as 21, which reduces down to two independent constants for a homogeneous isotropic elastic material. For orthotropic materials the number of independent materials constants reduces down to nine.

Anisotropic properties of composites are often obtained by laminating several layers of thin composite sheets with different ply angles. To obtain the desired properties of these laminated composites, the stiffness and compliance of each layer must be related to the overall stress, strain, and stiffness constants of the composite. This chapter derived the transformation rules of stress, strain, and stiffness of a lamina from the principal coordinate system to the global coordinate system.

### Problems

- 3.1. Verify that a monoclinic material has 13 independent elastic constants by completely deriving the result of table 3.6.
- 3.2. Show that a material with two mutually perpendicular planes of symmetry also has symmetry about the third mutually perpendicular plane.
- 3.3. For a transversely isotropic material (isotropic in the  $x_2-x_3$ -plane), determine  $G_{23}$  in terms of  $E_1$ ,  $E_2$ ,  $E_3$ ,  $\nu_{12}$ ,  $\nu_{23}$ , and  $\nu_{13}$  using the orthotropic material properties (generalized Hooke's law).
- 3.4. For isotropic materials, derive equations (3.71) and (3.74).
- 3.5. For a cantilever beam subjected to an end load of  $P$  (per unit width) in the negative  $x_3$ -direction, verify that the stresses calculated using the elementary bending theory from strength of materials have the following forms:

$$\begin{aligned}\sigma_{11} &= \frac{P}{I}(l - x_1)x_3 \\ \sigma_{13} &= -\frac{Ph^2}{8I} \left[ 1 - \left( \frac{2x_3}{h} \right)^2 \right] \\ \sigma_{33} &= 0\end{aligned}$$

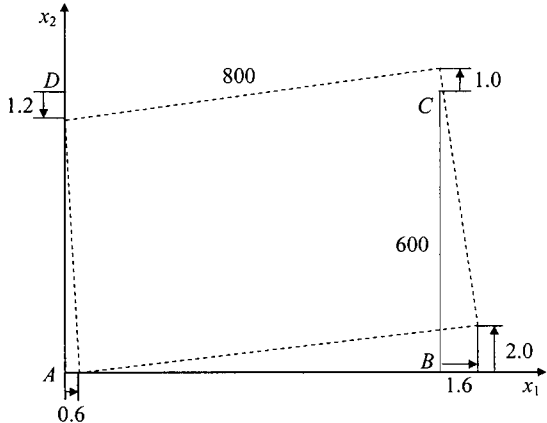


**Figure 3.18** Rectangle before and after deformation in problem 3.7.

where  $I$  and  $h$  are the sectional moment of inertia and thickness of the beam, and  $l$  is the length of the beam in the  $x_1$ -direction, where  $x_1$  is measured from the clamped end of the beam. Determine the conditions for compliance  $S_{ij}$  to satisfy the strain compatibility due to above stresses.

- 3.6. Rework example 3.3 to find strains using equation (3.68) rather than equation (3.64).
- 3.7. An 800 mm by 600 mm rectangle  $ABCD$  is deformed due to loading as shown in figure 3.18. The deformed geometry is shown by the dashed lines in figure 3.18. Determine the components of plane strain at point  $A$ .
- 3.8. The displacement field in a member has the form

$$u_1 = a_0 x_1^2 x_2^2 + a_1 x_1 x_2^2 + a_2 x_1^2 x_2$$

$$u_2 = b_0 x_1^2 x_2 + b_1 x_1 x_2$$

$$\gamma_{12} = c_0 x_1^2 x_2 + c_1 x_1 x_2 + c_2 x_1^2 + c_3 x_2^2$$

Find the strains for the displacement field. What relationships connecting the constants ( $a_i$ ,  $b_i$ , and  $c_i$ ) make the foregoing expressions possible?

- 3.9. Using the fully-populated plane constitutive equation (3.139), prove that

$$\frac{\eta_{xy,x}}{E_x} = \frac{\eta_{x,xy}}{G_{xy}}$$

- 3.10. A unidirectional carbon-fiber epoxy composite material, T300/5208, has the following properties:

$$E_1 = 132 \text{ GPa}, \quad E_2 = 10.8 \text{ GPa}, \quad \nu_{12} = 0.24, \quad G_{12} = 5.65 \text{ GPa}$$

- (a) Determine the values of the invariants of  $U_i$  ( $i = 1, \dots, 5$ ).
- (b) Plot  $\bar{Q}_{11}$  and  $\bar{Q}_{66}$  with respect to ply angle  $\theta$ .
- 3.11. Consider a unidirectional lamina with the fibers at an angle  $\theta = 45^\circ$  to the loading axis with the material properties of problem 3.10.
  - (a) What is the state of strain in the lamina when this lamina is subjected to a tensile stress  $\sigma_x$ ? (Express this in terms of  $\sigma_x$ .)
  - (b) How does this change if the ply angle is  $-45^\circ$ ?

- 3.12.** A composite plate is composed of two plies with stacking sequence of  $[\pm 30]_T$ , where subscript “T” represents “Total.” Is it reasonable to calculate the stiffness  $E_x$  by averaging  $E_x(+30^\circ)$  and  $E_x(-30^\circ)$ ?
- 3.13.** A student derived the constitutive equation for an orthotropic material under the plane stress condition by reducing the stiffness results of table 3.7 rather than using equation (3.115) as follows:

$$\begin{Bmatrix} \sigma_1 \\ \sigma_2 \\ \sigma_6 \end{Bmatrix} = \begin{bmatrix} C_{11} & C_{12} & 0 \\ C_{12} & C_{22} & 0 \\ 0 & 0 & C_{66} \end{bmatrix} \begin{Bmatrix} \varepsilon_1 \\ \varepsilon_2 \\ \varepsilon_6 \end{Bmatrix}$$

Do you think that the constitutive equation is correct?

- 3.14.** Starting from equation (3.49) with tensor shear strains of an orthotropic material, such as equation (3.24), show that the transformed stiffness matrix  $[\bar{C}]$  for rotation about the  $x_3$ -( $z$ -axis) can be written as

$$[C] = [T_1]^{-1} \begin{bmatrix} C_{11} & C_{12} & C_{13} & 0 & 0 & 0 \\ C_{21} & C_{22} & C_{23} & 0 & 0 & 0 \\ C_{13} & C_{23} & C_{33} & 0 & 0 & 0 \\ 0 & 0 & 0 & 2C_{44} & 0 & 0 \\ 0 & 0 & 0 & 0 & 2C_{55} & 0 \\ 0 & 0 & 0 & 0 & 0 & 2C_{66} \end{bmatrix} [T_1]$$

$$= \begin{bmatrix} \bar{C}_{11} & \bar{C}_{12} & \bar{C}_{13} & 0 & 0 & 2\bar{C}_{16} \\ \bar{C}_{12} & \bar{C}_{22} & \bar{C}_{23} & 0 & 0 & 2\bar{C}_{26} \\ \bar{C}_{13} & \bar{C}_{23} & \bar{C}_{33} & 0 & 0 & 2\bar{C}_{36} \\ 0 & 0 & 0 & 2\bar{C}_{44} & 2\bar{C}_{45} & 0 \\ 0 & 0 & 0 & 2\bar{C}_{45} & 2\bar{C}_{55} & 0 \\ \bar{C}_{16} & \bar{C}_{26} & \bar{C}_{36} & 0 & 0 & 2\bar{C}_{66} \end{bmatrix}$$

- 3.15.** Show that  $\{[T_1(\theta)]'\}^{-1} = [T_1(-\theta)]'$  and  $\{[T_2(\theta)]'\}^{-1} = [T_2(-\theta)]'$  in equation (3.128).
- 3.16.** To specify the characteristics of a unidirectional composite ply, normally we should know  $E_1$ ,  $E_2$ ,  $G_{12}$ , and  $\nu_{12}$  in the principal material direction. However, an engineer measured the properties of a ply in the  $0^\circ$ ,  $45^\circ$ , and  $90^\circ$ , directions using a strain rosette. From the experimental results, is it possible to obtain  $G_{12}$  in terms of  $E_{0^\circ}$ ,  $E_{45^\circ}$ ,  $E_{90^\circ}$ , and  $\nu_{12}$ ? If it is, write down the equation for  $G_{12}$ .
- 3.17.** A filament-wound thin cylindrical pressure vessel (diameter 500 mm, thickness 10 mm) shown in figure 8.17(a), is pressurized to 1.0 MPa. When the fiber winding angle of the pressure vessel is  $54.74^\circ$  only (not  $\pm 54.74^\circ$ ) from the longitudinal axis, calculate the normal stresses in the longitudinal and transverse-to-fiber directions, and the shear stress.

- 3.18.** Calculate the normal strains in the longitudinal and transverse to fiber direction, and the shear strain of problem 3.17 using the composite material properties of T300/5208 in problem 3.10.
- 3.19.** Develop a computer program, which calculates  $[C_{ij}]$  and  $[S_{ij}]$  when the nine engineering constants  $E_1$ ,  $E_2$ ,  $E_3$ ,  $\nu_{12}$ ,  $\nu_{23}$ ,  $\nu_{31}$ ,  $G_{12}$ ,  $G_{23}$ , and  $G_{31}$  are given. Then modify your computer program to calculate the elements of  $\{\sigma_x\}$ ,  $\{\varepsilon_x\}$ ,  $[\bar{C}_{ij}]$ ,  $[\bar{Q}_{ij}]$  and  $[\bar{S}_{ij}]$  from  $\{\sigma_i\}$ ,  $\{\varepsilon_i\}$ ,  $[C_{ij}]$ ,  $[Q_{ij}]$ , and  $[S_{ij}]$  with the input  $\theta$ .

### References

- Crandall, S. H., Dahl, N. C., and Lardner, T. J. 1978. *An Introduction to the Mechanics of Solids*, McGraw-Hill, New York.
- Daniel, I. M., and Ishai, O. 1994. *Engineering Mechanics of Composite Materials*, Oxford University Press, Oxford.
- Gibson, R. F. 1994. *Principles of Composite Material Mechanics*, McGraw-Hill, New York.
- Herakovich, C. T. 1998. *Mechanics of Fibrous Composites*, John Wiley & Sons, New York.
- Jones, R. M. 1975. *Mechanics of Composite Materials*, McGraw-Hill, New York.
- Lekhnitskii, S. G. 1963. *Theory of Elasticity of an Anisotropic Body*, Holden-Day, San Francisco.
- Reddy, J. N. 1997. *Mechanics of Laminate Composite Plates*, CRC Press, Boca Raton.
- Shames, I. H., and Cozzarelli, F. A. 1992. *Elastic and Inelastic Stress Analysis*, Prentice-Hall, Englewood Cliffs, N. J.
- Sokolnikoff, I. S. 1956. *Mathematical Theory of Elasticity*, 2nd ed., McGraw-Hill, New York.
- Timoshenko, S. P., and Goodier, J. N. 1970. *Theory of Elasticity*, 3rd ed., McGraw-Hill, New York.
- Tsai, S. W., and Hahn, H. T. 1980. *Introduction to Composite Materials*, Technomic Publishing, New York.
- White, F. M. 1999. *Fluid Mechanics*, 4th ed., McGraw-Hill, New York.

**4**

# Composite Lamination Theory

## 4.1 Introduction

### How Do We Design a Composite?

Suppose we want to design and manufacture a composite with certain desired properties (i.e., functional requirements). The first thing we have to do is to design the composite that can satisfy the functional requirements (FRs), which are specified to satisfy customer needs. After the product is designed, we then determine the manufacturing process that can make the product. To design the composite, we need a basic mechanical understanding of multilayer composites that are manufactured by consolidating continuous fiber composite prepgs, which is the topic of this book. There are other kinds of composites, but they are not included in this chapter.

In chapter 3, we learned about the stiffness properties of a lamina, but not of a laminate composed of several laminae (or plies). Since the laminate properties of composite cannot be calculated by averaging the properties of constituent laminae (see problem 4.5), in this chapter, the methods for laminate design and analysis are presented.

### How Do We Make the Composite?

There are several different kinds of composites, which are typically classified by manufacturing processes used to make the composite. One way of making a composite is to use continuous carbon or glass fibers with certain binders such as epoxy or polyester, as discussed in chapter 2. A cheaper process is to blend chopped glass fibers or carbon fibers in an epoxy or polyester matrix and mold them into the desired shape by using compression molding or injection molding. Although these processes are cheaper than the lamination process for continuous carbon-fiber epoxy composites, the stiffness, strength, and toughness are less than for continuous fiber composites. Many automobile parts are manufactured this way. Still another way is to put the reinforcing fibers in a mold and then infiltrate the fibers with a resin by injecting the resin into the mold, which is known as resin transfer molding. There are other ways of making composites. From the axiomatic design point of view, we must design the composite first to satisfy its FR before adopting a manufacturing process. In this book, we will only consider the composites with long continuous fibers.

Composite structures are usually made by stacking several laminae with different ply angles because fibers in a composite structure must be placed in more than one direction, and the composite lamina is weak or flexible in directions transverse to the fibers. Sometimes, the thermal expansion or vibration and damping properties of

composite structures require stacking several laminae with different ply angles and stacking sequences. The proper selection and stacking (or tailoring) of different plies are key features of composite structures.

### What Is the Goal of This Chapter?

In this chapter, the linear elastic response of a laminated composite subjected to in-plane loads as well as bending moments is analyzed to provide the basis for designing composite structures.

## 4.2 Classical Lamination Theory

The classical lamination theory (CLT) is an extension of the classical plate theory to composite laminates. Because of the stress and deformation hypotheses that are an inseparable part of classical lamination theory, a more correct name would be classical thin lamination theory, or even classical laminated plate theory (CLPT) (Jones, 1975, Daniel and Ishai, 1994).

In classical lamination theory, individual laminae are assumed to be homogeneous and orthotropic. A typical laminate with local ply coordinate or principal material coordinate ( $x_1, x_2, x_3$ ) and global laminate coordinate ( $x, y, z$ ) is depicted in figure 4.1.

The following important assumptions are made concerning the classical lamination theory:

1. The laminate consists of perfectly bonded layers (or plies).
2. The normals to the midplane of the laminate remain straight and normal to the deformed midplane after deformation (Kirchhoff hypothesis for plates and Kirchhoff–Love hypothesis for shells).
3. The normals to the midplane of the laminate do not change length (constant thickness).

The classical lamination theory applies only to plates that are infinitely long and wide (Matthews and Rawlings, 1994). In other words, it ignores edges. In many real situations, laminates will have edges, for example, a plate containing a hole or a plate of finite width. At such edges the through-thickness normal stress  $\sigma_z$

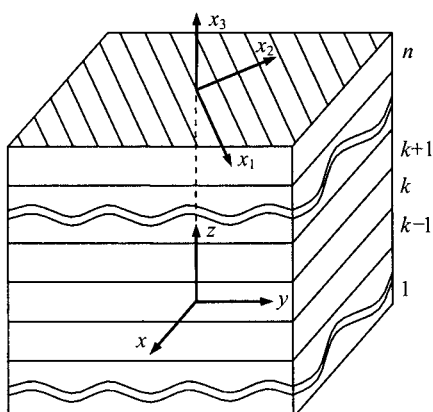


**Figure 4.1** Composite laminate with local ply coordinates ( $x_1, x_2, x_3$ ) and global laminate coordinates ( $x, y, z$ ).

and shear stresses ( $\tau_{xz}$ ,  $\tau_{yz}$ ) have comparable magnitude to the in-plane stresses ( $\sigma_x$ ,  $\sigma_y$ ,  $\tau_{xy}$ ). It is found that the stresses in the area within one plate thickness from the edge can be high enough to exceed the low through-thickness (interlaminar) strengths. The interlaminar stress and strength problems will be treated in chapter 5.

The assumption that normals remain straight and normal to the deformed midplane requires that the shear strains  $\gamma_{zx}$  and  $\gamma_{zy}$  be zero. The assumption of constant thickness requires that

$$\varepsilon_z = \frac{\partial w}{\partial z} = \varepsilon_3 = 0 \quad (4.1)$$

Then the displacement,  $w$ , in the  $z$ -direction is a function of  $x$  and  $y$  only:

$$w = w(x, y) \quad (4.2)$$

Consider the deformation of a section of a laminate in the  $x-z$ -plane as shown in figure 4.2, and assume that the point  $C$  at the geometric midplane undergoes displacements  $u_0(x, y)$ ,  $v_0(x, y)$ , and  $w_0(x, y)$  along the  $x$ -,  $y$ - and  $z$ -directions, respectively. Since the line  $ABCD$ , originally straight and perpendicular to the midplane of the laminate, is assumed to remain straight and perpendicular, the displacement  $u$  in the  $x$ -direction of a point  $B$  that is located on the normal  $ABCD$  at a distance  $z$  from the midplane is given by (Agarwal and Broutman, 1990)

$$u = u_0 - z \frac{\partial w_0}{\partial x} \quad (4.3)$$

By similar reasoning, the displacement  $v$  in the  $y$  direction of a point  $B$  at a distance  $z$  from the geometric midplane is

$$v = v_0 - z \frac{\partial w_0}{\partial y} \quad (4.4)$$

The laminate strains can be obtained from the derived displacements,  $u$  and  $v$ , as follows:

$$\varepsilon_x = \frac{\partial u}{\partial x} = \frac{\partial u_0}{\partial x} - z \frac{\partial^2 w_0}{\partial x^2} \quad (4.5a)$$

$$\varepsilon_y = \frac{\partial v}{\partial y} = \frac{\partial v_0}{\partial y} - z \frac{\partial^2 w_0}{\partial y^2} \quad (4.5b)$$

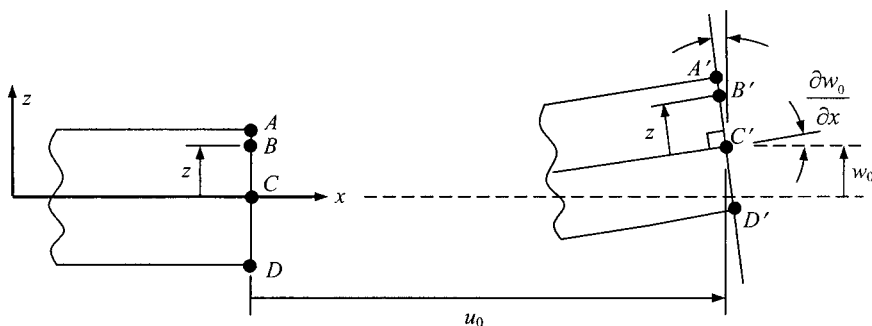


Figure 4.2 Bending and extension of the line  $ABCD$  in the  $x-z$ -plane.

$$\gamma_{xy} = \frac{\partial u}{\partial y} + \frac{\partial v}{\partial x} = \frac{\partial u_0}{\partial y} + \frac{\partial v_0}{\partial x} - 2z \frac{\partial^2 w_0}{\partial x \partial y} \quad (4.5c)$$

Equations (4.5) can be rewritten in terms of the midplane strains and the plate curvatures as follows:

$$\begin{Bmatrix} \varepsilon_x \\ \varepsilon_y \\ \gamma_{xy} \end{Bmatrix} = \begin{Bmatrix} \varepsilon_x^0 \\ \varepsilon_y^0 \\ \gamma_{xy}^0 \end{Bmatrix} + z \begin{Bmatrix} \kappa_x \\ \kappa_y \\ \kappa_{xy} \end{Bmatrix} \quad (4.6)$$

where the midplane strains are

$$\begin{Bmatrix} \varepsilon_x^0 \\ \varepsilon_y^0 \\ \gamma_{xy}^0 \end{Bmatrix} = \begin{Bmatrix} \frac{\partial u_0}{\partial x} \\ \frac{\partial v_0}{\partial y} \\ \frac{\partial u_0}{\partial y} + \frac{\partial v_0}{\partial x} \end{Bmatrix} \quad (4.7)$$

and the plate curvatures are

$$\begin{Bmatrix} \kappa_x \\ \kappa_y \\ \kappa_{xy} \end{Bmatrix} = - \begin{Bmatrix} \frac{\partial^2 w_0}{\partial x^2} \\ \frac{\partial^2 w_0}{\partial y^2} \\ 2 \frac{\partial^2 w_0}{\partial x \partial y} \end{Bmatrix} \quad (4.8)$$

where the curvature  $\kappa_{xy}$  defined in equation (4.8) is not a tensor, but has the same engineering shear strain characteristics as  $\gamma_{xy}$ .

Composite structures deform according to a change in temperature or moisture content, especially polymeric composite structures, because the moisture absorption by polymeric matrices can induce swelling of the structure. Thus, thermal and hygroscopic strains develop in the body as a result of temperature and hygroscopic changes. The constitutive equation for an orthotropic lamina with temperature change  $\Delta T$  and specific moisture concentration change  $\Delta C$  can be written in the principal material coordinates as

$$\begin{Bmatrix} \varepsilon_1 \\ \varepsilon_2 \\ \varepsilon_6 \end{Bmatrix} = [S_{ij}] \begin{Bmatrix} \sigma_1 \\ \sigma_2 \\ \sigma_6 \end{Bmatrix} + \begin{Bmatrix} \alpha_1 \Delta T \\ \alpha_2 \Delta T \\ 0 \end{Bmatrix} + \begin{Bmatrix} \beta_1 \Delta C \\ \beta_2 \Delta C \\ 0 \end{Bmatrix} \quad (4.9)$$

where  $\alpha_1$  and  $\alpha_2$  are the coefficients of thermal expansion (CTE) and  $\beta_1$  and  $\beta_2$  are the coefficients of hygroscopic expansion (CHE) (called also swelling) in the axial and transverse directions to the fiber, respectively. The shear terms,  $\alpha_6 (= 2\alpha_{12})$  and  $\beta_6 (= 2\beta_{12})$ , are zero because an orthotropic material does not exhibit shear strains in the principal material coordinates, but  $\alpha_{xy}$  and  $\beta_{xy}$  in the global coordinates may not be zero. The specific moisture concentration  $C$  represents the amount of moisture in a fixed volume of composite as a fraction of the dry mass of composite, which is defined in equation (8.80). The coefficients of thermal expansion and hygroscopic

expansion are second-order tensors similar to the strain in equation (3.87) if expressed using tensor notations and transform like second-order tensors (Vinson and Sierakowski, 1986):

$$\alpha_{ij} = l_{ip}l_{jq}\alpha_{pq} \quad (i,j = 1,2 \text{ and } p,q = x,y) \quad (4.10)$$

$$\beta_{ij} = l_{ip}l_{jq}\beta_{pq} \quad (i,j = 1,2 \text{ and } p,q = x,y) \quad (4.11)$$

Equation (4.9) can be inverted to give

$$\begin{Bmatrix} \sigma_1 \\ \sigma_2 \\ \sigma_6 \end{Bmatrix} = [Q_{ij}] \begin{Bmatrix} \varepsilon_1 \\ \varepsilon_2 \\ \varepsilon_6 \end{Bmatrix} - [Q_{ij}] \begin{Bmatrix} \alpha_1 \Delta T \\ \alpha_2 \Delta T \\ 0 \end{Bmatrix} - [Q_{ij}] \begin{Bmatrix} \beta_1 \Delta C \\ \beta_2 \Delta C \\ 0 \end{Bmatrix} \quad (4.12)$$

Equation (4.12) must be converted from the principal material coordinates ( $x_1, x_2, x_3$ ) to the global coordinates ( $x, y, z$ ) for the analysis of laminate structures. Using the results of equations (3.118), (3.123), (4.10), and (4.11), we have

$$[T_1]' \begin{Bmatrix} \sigma_x \\ \sigma_y \\ \tau_{xy} \end{Bmatrix} = [Q_{ij}] [T_2]' \begin{Bmatrix} \varepsilon_x \\ \varepsilon_y \\ \gamma_{xy} \end{Bmatrix} - [Q_{ij}] [T_2]' \begin{Bmatrix} \alpha_x \Delta T \\ \alpha_y \Delta T \\ \alpha_{xy} \Delta T \end{Bmatrix} - [Q_{ij}] [T_2]' \begin{Bmatrix} \beta_x \Delta C \\ \beta_y \Delta C \\ \beta_{xy} \Delta C \end{Bmatrix} \quad (4.13)$$

where the shear component  $\alpha_{xy}$  of the coefficients of thermal expansion and the shear component  $\beta_{xy}$  of the coefficients of hygroscopic expansion are not tensor quantities, but engineering values similar to  $\gamma_{xy}$  in equation (3.123). Then equation (4.13) becomes, with the definition of equation (3.128),

$$\begin{Bmatrix} \sigma_x \\ \sigma_y \\ \tau_{xy} \end{Bmatrix} = [\bar{Q}_{ij}] \begin{Bmatrix} \varepsilon_x - \alpha_x \Delta T - \beta_x \Delta C \\ \varepsilon_y - \alpha_y \Delta T - \beta_y \Delta C \\ \gamma_{xy} - \alpha_{xy} \Delta T - \beta_{xy} \Delta C \end{Bmatrix} \quad (4.14)$$

Using equation (4.6), equation (4.14) becomes for the  $k$ th layer

$$\begin{Bmatrix} \sigma_x \\ \sigma_y \\ \tau_{xy} \end{Bmatrix}^{[k]} = [\bar{Q}_{ij}]^{[k]} \begin{Bmatrix} \varepsilon_x^0 \\ \varepsilon_y^0 \\ \gamma_{xy}^0 \end{Bmatrix} + [\bar{Q}_{ij}]^{[k]} z \begin{Bmatrix} \kappa_x \\ \kappa_y \\ \kappa_{xy} \end{Bmatrix} - [\bar{Q}_{ij}]^{[k]} \begin{Bmatrix} \alpha_x \Delta T + \beta_x \Delta C \\ \alpha_y \Delta T + \beta_y \Delta C \\ \alpha_{xy} \Delta T + \beta_{xy} \Delta C \end{Bmatrix} \quad (4.15)$$

Thus, the variation of stress through the laminate thickness is obtained by calculating the stress variations in all the plies. In general, the variation of stress through the laminate thickness is not linear. Stresses are discontinuous at the interface of two plies in the classical lamination theory, and the stress gradient in two adjoining plies is also different, unlike the actual stresses, because such discontinuities do not exist in the real world. Therefore, the classical lamination theory has some

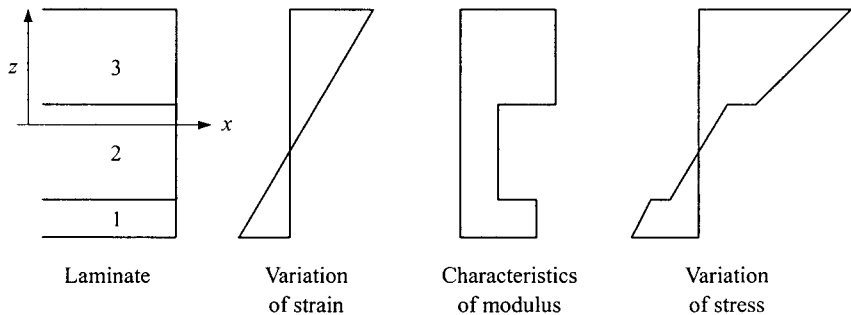


**Figure 4.3** Variation of strain and stress in a three-ply laminate.

limitations in calculating stresses and consequently the failure criterion using the calculated stresses. However, the stiffness calculated using the classical lamination theory conforms well to the actual stiffness. Typical strain and stress variations in a three-ply laminate are shown in figure 4.3.

### 4.3 Forces per Unit Length

For the laminate in figure 4.1, global coordinates  $(x, y, z)$ , with  $z$  perpendicular to the plane of the laminate and *positive upward*, was employed. The origin of the coordinate system is located on the laminar midplane, centered between the top and bottom surfaces. The laminate has  $n$  layers numbered *from bottom to top*. Each ply has a fiber ply angle  $\theta_k$ , as depicted in figure 4.4, and the  $z$ -coordinate of the bottom of the  $k$ th ply is designated  $z_{k-1}$  with the top of the layer being  $z_k$ . The thickness of the  $k$ th ply is then  $t_{\text{ply}}^{[k]} = z_k - z_{k-1}$ . The top surface of the laminate is denoted  $z_n$  and the total thickness is  $h$ .

The in-plane forces per unit length  $\{N\}$  depicted in figure 4.5 are defined as the through-thickness integrals of the planar stresses in the laminate:

$$N_x = \int_{-(h/2)}^{(h/2)} \sigma_x dz \quad (4.16a)$$

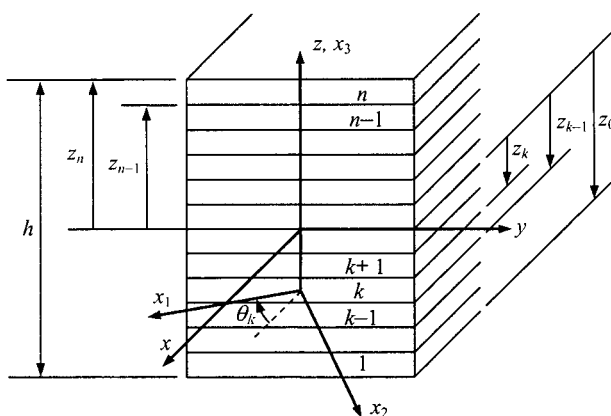


**Figure 4.4** Notation of laminate coordinate.

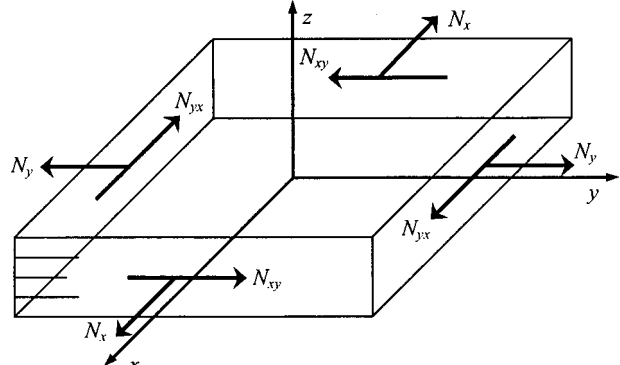


**Figure 4.5** In-plane forces per unit length of a laminate.

$$N_y = \int_{-(h/2)}^{(h/2)} \sigma_y dz \quad (4.16b)$$

$$N_{xy} = \int_{-(h/2)}^{(h/2)} \tau_{xy} dz \quad (4.16c)$$

Combining equations (4.15) and (4.16) gives

$$\begin{Bmatrix} N_x \\ N_y \\ N_{xy} \end{Bmatrix} = \int_{-(h/2)}^{(h/2)} [\bar{Q}_{ij}] dz \begin{Bmatrix} \varepsilon_x^0 \\ \varepsilon_y^0 \\ \gamma_{xy}^0 \end{Bmatrix} + \int_{-(h/2)}^{(h/2)} [\bar{Q}_{ij}] z dz \begin{Bmatrix} \kappa_x \\ \kappa_y \\ \kappa_{xy} \end{Bmatrix} - \int_{-(h/2)}^{(h/2)} [\bar{Q}_{ij}] \begin{Bmatrix} \alpha_x \Delta T + \beta_x \Delta C \\ \alpha_y \Delta T + \beta_y \Delta C \\ \alpha_{xy} \Delta T + \beta_{xy} \Delta C \end{Bmatrix} dz \quad (4.17)$$

When  $\Delta T$  and  $\Delta C$  are uniform through the thickness of the laminate, equation (4.17) becomes

$$\begin{Bmatrix} N_x \\ N_y \\ N_{xy} \end{Bmatrix} = \int_{-(h/2)}^{(h/2)} [\bar{Q}_{ij}] dz \begin{Bmatrix} \varepsilon_x^0 \\ \varepsilon_y^0 \\ \gamma_{xy}^0 \end{Bmatrix} + \int_{-(h/2)}^{(h/2)} [\bar{Q}_{ij}] z dz \begin{Bmatrix} \kappa_x \\ \kappa_y \\ \kappa_{xy} \end{Bmatrix} - \Delta T \int_{-(h/2)}^{(h/2)} [\bar{Q}_{ij}] \begin{Bmatrix} \alpha_x \\ \alpha_y \\ \alpha_{xy} \end{Bmatrix} dz - \Delta C \int_{-(h/2)}^{(h/2)} [\bar{Q}_{ij}] \begin{Bmatrix} \beta_x \\ \beta_y \\ \beta_{xy} \end{Bmatrix} dz \quad (4.18)$$

Let us define  $[A]$ , the in-plane stiffness,  $[B]$ , the bending–stretching coupling,  $\{\Gamma^T\}$ , the laminate thermal in-plane influence coefficient, and  $\{\Gamma^H\}$ , the laminate

hygroscopic in-plane influence coefficient matrices as follows:

$$[A] = \int_{-(h/2)}^{(h/2)} [\bar{Q}_{ij}] dz = \sum_{k=1}^n [\bar{Q}_{ij}]^{[k]} (z_k - z_{k-1}) = \sum_{k=1}^n [\bar{Q}_{ij}]^{[k]} t_{\text{ply}}^{[k]} \quad (4.19a)$$

$$[B] = \int_{-(h/2)}^{(h/2)} [\bar{Q}_{ij}] z dz = \frac{1}{2} \sum_{k=1}^n [\bar{Q}_{ij}]^{[k]} (z_k^2 - z_{k-1}^2) \quad (4.19b)$$

$$\{\Gamma^T\} = \begin{Bmatrix} \Gamma_x^T \\ \Gamma_y^T \\ \Gamma_{xy}^T \end{Bmatrix} = \int_{-(h/2)}^{(h/2)} [\bar{Q}_{ij}] \begin{Bmatrix} \alpha_x \\ \alpha_y \\ \alpha_{xy} \end{Bmatrix} dz = \sum_{k=1}^n [\bar{Q}_{ij}]^{[k]} \begin{Bmatrix} \alpha_x \\ \alpha_y \\ \alpha_{xy} \end{Bmatrix}^{[k]} (z_k - z_{k-1}) = \sum_{k=1}^n \{\xi^T\}^{[k]} t_{\text{ply}}^{[k]} \quad (4.19c)$$

$$\{\Gamma^H\} = \begin{Bmatrix} \Gamma_x^H \\ \Gamma_y^H \\ \Gamma_{xy}^H \end{Bmatrix} = \int_{-(h/2)}^{(h/2)} [\bar{Q}_{ij}] \begin{Bmatrix} \beta_x \\ \beta_y \\ \beta_{xy} \end{Bmatrix} dz = \sum_{k=1}^n [\bar{Q}_{ij}]^{[k]} \begin{Bmatrix} \beta_x \\ \beta_y \\ \beta_{xy} \end{Bmatrix}^{[k]} (z_k - z_{k-1}) = \sum_{k=1}^n \{\xi^H\}^{[k]} t_{\text{ply}}^{[k]} \quad (4.19d)$$

where  $[\bar{Q}_{ij}]^{[k]}$  represents the stiffness matrix of the  $k$ th ply. The ply (or lamina) thermal influence coefficient  $\{\xi^T\}^{[k]}$  and hygroscopic influence coefficient  $\{\xi^H\}^{[k]}$  are defined as

$$\{\xi^T\}^{[k]} = \begin{Bmatrix} \xi_x^T \\ \xi_y^T \\ \xi_{xy}^T \end{Bmatrix}^{[k]} = [\bar{Q}_{ij}]^{[k]} \begin{Bmatrix} \alpha_x \\ \alpha_y \\ \alpha_{xy} \end{Bmatrix}^{[k]} \quad (4.20a)$$

$$\{\xi^H\}^{[k]} = \begin{Bmatrix} \xi_x^H \\ \xi_y^H \\ \xi_{xy}^H \end{Bmatrix}^{[k]} = [\bar{Q}_{ij}]^{[k]} \begin{Bmatrix} \beta_x \\ \beta_y \\ \beta_{xy} \end{Bmatrix}^{[k]} \quad (4.20b)$$

Then the equation for the in-plane forces *per unit length* can be written as

$$\begin{Bmatrix} N_x \\ N_y \\ N_{xy} \end{Bmatrix} = [A] \begin{Bmatrix} \varepsilon_x^0 \\ \varepsilon_y^0 \\ \gamma_{xy}^0 \end{Bmatrix} + [B] \begin{Bmatrix} \kappa_x \\ \kappa_y \\ \kappa_{xy} \end{Bmatrix} - \begin{Bmatrix} \Gamma_x^T \\ \Gamma_y^T \\ \Gamma_{xy}^T \end{Bmatrix} \Delta T - \begin{Bmatrix} \Gamma_x^H \\ \Gamma_y^H \\ \Gamma_{xy}^H \end{Bmatrix} \Delta C \quad (4.21)$$

or can be rewritten

$$\{N\} + \{N^T\} + \{N^H\} = [A]\{\varepsilon^0\} + [B]\{\kappa\} \quad (4.22)$$

where

$$\{N^T\} = \begin{Bmatrix} N_x^T \\ N_y^T \\ N_{xy}^T \end{Bmatrix} = \begin{Bmatrix} \Gamma_x^T \\ \Gamma_y^T \\ \Gamma_{xy}^T \end{Bmatrix} \Delta T \quad (4.23)$$

$$\{N^H\} = \begin{Bmatrix} N_x^H \\ N_y^H \\ N_{xy}^H \end{Bmatrix} = \begin{Bmatrix} \Gamma_x^H \\ \Gamma_y^H \\ \Gamma_{xy}^H \end{Bmatrix} \Delta C \quad (4.24)$$

$\{N^T\}$  and  $\{N^H\}$  are called the equivalent thermal force and the equivalent hydroscopic force, respectively, expressed in  $x,y,z$ -coordinates.

#### 4.4 Moments per Unit Length

The moments per unit length  $\{M\}$  depicted in figure 4.6 are defined as the through-thickness integrals of the planar moments in the laminate:

$$M_x = \int_{-(h/2)}^{(h/2)} \sigma_x z dz \quad (4.25a)$$

$$M_y = \int_{-(h/2)}^{(h/2)} \sigma_y z dz \quad (4.25b)$$

$$M_{xy} = \int_{-(h/2)}^{(h/2)} \tau_{xy} z dz \quad (4.25c)$$

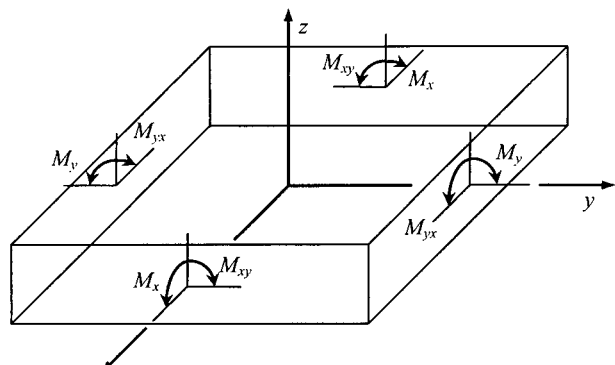


Figure 4.6 Moments per unit length of a laminate.

Substituting equation (4.15) into equation (4.25) yields

$$\begin{Bmatrix} M_x \\ M_y \\ M_{xy} \end{Bmatrix} = \int_{-(h/2)}^{(h/2)} [\bar{Q}_{ij}] z dz \begin{Bmatrix} \varepsilon_x^0 \\ \varepsilon_y^0 \\ \gamma_{xy}^0 \end{Bmatrix} + \int_{-(h/2)}^{(h/2)} [\bar{Q}_{ij}] z^2 dz \begin{Bmatrix} \kappa_x \\ \kappa_y \\ \kappa_{xy} \end{Bmatrix} - \int_{-(h/2)}^{(h/2)} [\bar{Q}_{ij}] \begin{Bmatrix} \alpha_x \Delta T + \beta_x \Delta C \\ \alpha_y \Delta T + \beta_y \Delta C \\ \alpha_{xy} \Delta T + \beta_{xy} \Delta C \end{Bmatrix} dz \quad (4.26)$$

When  $\Delta T$  and  $\Delta C$  are uniform through the thickness of the laminate, equation (4.26) becomes

$$\begin{Bmatrix} M_x \\ M_y \\ M_{xy} \end{Bmatrix} = \int_{-(h/2)}^{(h/2)} [\bar{Q}_{ij}] z dz \begin{Bmatrix} \varepsilon_x^0 \\ \varepsilon_y^0 \\ \gamma_{xy}^0 \end{Bmatrix} + \int_{-(h/2)}^{(h/2)} [\bar{Q}_{ij}] z^2 dz \begin{Bmatrix} \kappa_x \\ \kappa_y \\ \kappa_{xy} \end{Bmatrix} - \Delta T \int_{-(h/2)}^{(h/2)} [\bar{Q}_{ij}] \begin{Bmatrix} \alpha_x \\ \alpha_y \\ \alpha_{xy} \end{Bmatrix} z dz - \Delta C \int_{-(h/2)}^{(h/2)} [\bar{Q}_{ij}] \begin{Bmatrix} \beta_x \\ \beta_y \\ \beta_{xy} \end{Bmatrix} z dz \quad (4.27)$$

Let us define the bending stiffness matrix  $[D]$ , the laminate thermal bending influence coefficient matrix  $\{\Lambda^T\}$ , and the laminate hygroscopic bending influence coefficient matrix  $\{\Lambda^H\}$  as follows:

$$[D] = \int_{-(h/2)}^{(h/2)} [\bar{Q}_{ij}] z^2 dz = \frac{1}{3} \sum_{k=1}^n [\bar{Q}_{ij}]^{[k]} (z_k^3 - z_{k-1}^3) \quad (4.28a)$$

$$\begin{aligned} \{\Lambda^T\} &= \begin{Bmatrix} \Lambda_x^T \\ \Lambda_y^T \\ \Lambda_{xy}^T \end{Bmatrix} = \int_{-(h/2)}^{(h/2)} [\bar{Q}_{ij}] \begin{Bmatrix} \alpha_x \\ \alpha_y \\ \alpha_{xy} \end{Bmatrix} z dz = \frac{1}{2} \sum_{k=1}^n [\bar{Q}_{ij}]^{[k]} \begin{Bmatrix} \alpha_x \\ \alpha_y \\ \alpha_{xy} \end{Bmatrix} (z_k^2 - z_{k-1}^2) \\ &= \frac{1}{2} \sum_{k=1}^n \{\xi^T\}^{[k]} (z_k^2 - z_{k-1}^2) \end{aligned} \quad (4.28b)$$

$$\begin{aligned} \{\Lambda^H\} &= \begin{Bmatrix} \Lambda_x^H \\ \Lambda_y^H \\ \Lambda_{xy}^H \end{Bmatrix} = \int_{-(h/2)}^{(h/2)} [\bar{Q}_{ij}] \begin{Bmatrix} \beta_x \\ \beta_y \\ \beta_{xy} \end{Bmatrix} z dz = \frac{1}{2} \sum_{k=1}^n [\bar{Q}_{ij}]^{[k]} \begin{Bmatrix} \beta_x \\ \beta_y \\ \beta_{xy} \end{Bmatrix} (z_k^2 - z_{k-1}^2) \\ &= \frac{1}{2} \sum_{k=1}^n \{\xi^H\}^{[k]} (z_k^2 - z_{k-1}^2) \end{aligned} \quad (4.28c)$$

Then the equation for the moments per unit length can be written as

$$\begin{Bmatrix} M_x \\ M_y \\ M_{xy} \end{Bmatrix} = [B] \begin{Bmatrix} \varepsilon_x^0 \\ \varepsilon_y^0 \\ \gamma_{xy}^0 \end{Bmatrix} + [D] \begin{Bmatrix} \kappa_x \\ \kappa_y \\ \kappa_{xy} \end{Bmatrix} - \begin{Bmatrix} \Lambda_x^T \\ \Lambda_y^T \\ \Lambda_{xy}^T \end{Bmatrix} \Delta T - \begin{Bmatrix} \Lambda_x^H \\ \Lambda_y^H \\ \Lambda_{xy}^H \end{Bmatrix} \Delta C \quad (4.29)$$

or can be rewritten as

$$\{M\} + \{M^T\} + \{M^H\} = [B]\{\varepsilon^0\} + [D]\{\kappa\} \quad (4.30)$$

where

$$\{M^T\} = \begin{Bmatrix} M_x^T \\ M_y^T \\ M_{xy}^T \end{Bmatrix} = \begin{Bmatrix} \Lambda_x^T \\ \Lambda_y^T \\ \Lambda_{xy}^T \end{Bmatrix} \Delta T \quad (4.31a)$$

$$\{M^H\} = \begin{Bmatrix} M_x^H \\ M_y^H \\ M_{xy}^H \end{Bmatrix} = \begin{Bmatrix} \Lambda_x^H \\ \Lambda_y^H \\ \Lambda_{xy}^H \end{Bmatrix} \Delta C \quad (4.31b)$$

$\{M^T\}$  and  $\{M^H\}$  are called the equivalent thermal bending moment and the equivalent hygroscopic bending moment, respectively, expressed in  $x,y,z$ -coordinates.

Equation (4.22) can be inverted to get

$$\begin{aligned} \{\varepsilon^0\} &= [A]^{-1}\{N\} - [A]^{-1}[B]\{\kappa\} + [A]^{-1}\{\Gamma^T\}\Delta T + [A]^{-1}\{\Gamma^H\}\Delta C \\ &= [A^*]\{N\} + [B^*]\{\kappa\} + \{\Gamma^{*T}\}\Delta T + \{\Gamma^{*H}\}\Delta C \end{aligned} \quad (4.32)$$

where

$$[A^*] = [A]^{-1} \quad (4.33a)$$

$$[B^*] = -[A]^{-1}[B] \quad (4.33b)$$

$$\{\Gamma^{*T}\} = [A]^{-1}\{\Gamma^T\} \quad (4.33c)$$

$$\{\Gamma^{*H}\} = [A]^{-1}\{\Gamma^H\} \quad (4.33d)$$

Substituting equation (4.32) into equation (4.30), we have

$$\{M\} = [C^*]\{N\} + [D^*]\{\kappa\} + \{[B]\{\Gamma^{*T}\} - \{\Lambda^T\}\}\Delta T + \{[B]\{\Gamma^{*H}\} - \{\Lambda^H\}\}\Delta C \quad (4.34)$$

where

$$[C^*] = [B][A]^{-1} \quad (4.35a)$$

$$[D^*] = [D] - [B][A]^{-1}[B] \quad (4.35b)$$

Then the curvature matrix  $\{\kappa\}$  can be calculated from equation (4.34):

$$\begin{aligned}\{\kappa\} &= [D^*]^{-1} \{ \{M\} - [C^*]\{N\} \} \\ &\quad - [D^*]^{-1} \{ [B]\{\Gamma^{*T}\} - \{\Lambda^T\} \} \Delta T - [D^*]^{-1} \{ [B]\{\Gamma^{*H}\} - \{\Lambda^H\} \} \Delta C\end{aligned}\quad (4.36)$$

Substituting equation (4.36) into equation (4.32), we have

$$\begin{aligned}\{\varepsilon^0\} &= \left\{ [A^*] - [B^*][D^*]^{-1}[C^*] \right\} \{N\} + [B^*][D^*]^{-1}\{M\} \\ &\quad - [B^*][D^*]^{-1} \{ [B]\{\Gamma^{*T}\} - \{\Lambda^T\} \} \Delta T \\ &\quad - [B^*][D^*]^{-1} \{ [B]\{\Gamma^{*H}\} - \{\Lambda^H\} \} \Delta C + \{\Gamma^{*T}\} \Delta T + \{\Gamma^{*H}\} \Delta C\end{aligned}\quad (4.37)$$

For symmetric laminates,  $[B]$  and  $[\Lambda]$  matrices are identically zero (see problems 4.1 and 4.3), which makes the above equations much simpler and analytic solutions possible. For the general cases, the analytic solutions are not easy to obtain because several  $[6 \times 6]$  matrix inversions are required.

In principle, however, using computers we can calculate the strain  $\{\varepsilon^0\}$  on the midplane from equation (4.37) and the curvature  $\{\kappa\}$  of the laminate from equation (4.36) when the in-plane force per unit length  $\{N\}$  and moment per unit length  $\{M\}$ , as well as the temperature difference  $\Delta T$  and specific moisture concentration  $\Delta C$ , are given. When there are no hygrothermal effects, the equations become simpler to be calculated analytically. The following sections will concentrate on these simpler cases.

#### 4.5 Laminate Equations when $\Delta T = \Delta C = 0$

When  $\Delta T$  and  $\Delta C$  are equal to zero, equations (4.22) and (4.30) can be combined to give

$$\begin{Bmatrix} N \\ M \end{Bmatrix} = \begin{bmatrix} A & B \\ B & D \end{bmatrix} \begin{Bmatrix} \varepsilon^0 \\ \kappa \end{Bmatrix} \quad (4.38)$$

Equation (4.38) can be expanded as

$$\begin{Bmatrix} N_x \\ N_y \\ N_{xy} \\ M_x \\ M_y \\ M_{xy} \end{Bmatrix} = \begin{bmatrix} A_{11} & A_{12} & A_{16} & B_{11} & B_{12} & B_{16} \\ A_{12} & A_{22} & A_{26} & B_{12} & B_{22} & B_{26} \\ A_{16} & A_{26} & A_{66} & B_{16} & B_{26} & B_{66} \\ B_{11} & B_{12} & B_{16} & D_{11} & D_{12} & D_{16} \\ B_{12} & B_{22} & B_{26} & D_{12} & D_{22} & D_{26} \\ B_{16} & B_{26} & B_{66} & D_{16} & D_{26} & D_{66} \end{bmatrix} \begin{Bmatrix} \varepsilon_x^0 \\ \varepsilon_y^0 \\ \gamma_{xy}^0 \\ \kappa_x \\ \kappa_y \\ \kappa_{xy} \end{Bmatrix} \quad (4.39)$$

From equation (4.39), we can see the coupling between the bending and stretching response of a laminate due to the  $[B]$  matrix. When  $[B]$  is equal to zero such as a symmetric laminate about its midplane (see problem 4.1), the in-plane response is

decoupled from the bending response. Equation (4.38) can be inverted using the results of equations (4.37) and (4.36)

$$\left\{ \begin{array}{c} \varepsilon^0 \\ \kappa \end{array} \right\} = \begin{bmatrix} A' & B' \\ C' & D' \end{bmatrix} \left\{ \begin{array}{c} N \\ M \end{array} \right\} \quad (4.40)$$

where

$$[A'] = [A^*] - [B^*][D^*]^{-1}[C^*] \quad (4.41a)$$

$$[B'] = [B^*][D^*]^{-1} \quad (4.41b)$$

$$[C'] = -[D^*]^{-1}[C^*] \quad (4.41c)$$

$$[D'] = [D^*]^{-1} \quad (4.41d)$$

From equations (4.33) and (4.35), we can prove easily that

$$[C'] = [B']^T = [B'] \quad (4.42)$$

Therefore, equation (4.40) can be written as

$$\left\{ \begin{array}{c} \varepsilon^0 \\ \kappa \end{array} \right\} = \begin{bmatrix} A' & B' \\ B' & D' \end{bmatrix} \left\{ \begin{array}{c} N \\ M \end{array} \right\} \quad (4.43)$$

Equation (4.43) can be expanded as

$$\left\{ \begin{array}{c} \varepsilon_x^0 \\ \varepsilon_y^0 \\ \gamma_{xy}^0 \\ \kappa_x \\ \kappa_y \\ \kappa_{xy} \end{array} \right\} = \begin{bmatrix} A'_{11} & A'_{12} & A'_{16} & B'_{11} & B'_{12} & B'_{16} \\ A'_{12} & A'_{22} & A'_{26} & B'_{12} & B'_{22} & B'_{26} \\ A'_{16} & A'_{26} & A'_{66} & B'_{16} & B'_{26} & B'_{66} \\ B'_{11} & B'_{12} & B'_{16} & D'_{11} & D'_{12} & D'_{16} \\ B'_{12} & B'_{22} & B'_{26} & D'_{12} & D'_{22} & D'_{26} \\ B'_{16} & B'_{26} & B'_{66} & D'_{16} & D'_{26} & D'_{66} \end{bmatrix} \left\{ \begin{array}{c} N_x \\ N_y \\ N_{xy} \\ M_x \\ M_y \\ M_{xy} \end{array} \right\} \quad (4.44)$$

## 4.6 Symmetric Laminate under $N$ when $M = \Delta T = \Delta C = 0$

When the stacking sequence of a laminate is symmetric about its midplane, the bending-stretching coupling matrix  $[B]$  is identically zero (see problem 4.1). When this laminate is subjected to in-plane force  $\{N\}$  only, the curvature  $\{\kappa\}$  reduces to zero from equations (4.43), (4.41b), and (4.33b) because

$$[B'] = [B^*][D^*]^{-1} = -[A]^{-1}[B][D^*]^{-1} = 0 \quad (4.45)$$

Then equations (4.39) and (4.44) become

$$\begin{Bmatrix} N_x \\ N_y \\ N_{xy} \end{Bmatrix} = \begin{bmatrix} A_{11} & A_{12} & A_{16} \\ A_{12} & A_{22} & A_{26} \\ A_{16} & A_{26} & A_{66} \end{bmatrix} \begin{Bmatrix} \varepsilon_x^0 \\ \varepsilon_y^0 \\ \gamma_{xy}^0 \end{Bmatrix} \quad (4.46)$$

$$\begin{Bmatrix} \varepsilon_x^0 \\ \varepsilon_y^0 \\ \gamma_{xy}^0 \end{Bmatrix} = \begin{bmatrix} a_{11} & a_{12} & a_{16} \\ a_{12} & a_{22} & a_{26} \\ a_{16} & a_{26} & a_{66} \end{bmatrix} \begin{Bmatrix} N_x \\ N_y \\ N_{xy} \end{Bmatrix} \quad (4.47)$$

where

$$[a] = [A'] = [A^*] = [A]^{-1} \quad (4.48)$$

The elements of matrix  $[a]$  have the following forms because it is the inverse of  $[A]$ :

$$a_{11} = \frac{1}{|A|} (A_{22}A_{66} - A_{26}^2) \quad (4.49a)$$

$$a_{22} = \frac{1}{|A|} (A_{11}A_{66} - A_{16}^2) \quad (4.49b)$$

$$a_{12} = \frac{1}{|A|} (A_{16}A_{26} - A_{12}A_{66}) \quad (4.49c)$$

$$a_{66} = \frac{1}{|A|} (A_{11}A_{22} - A_{12}^2) \quad (4.49d)$$

$$a_{16} = \frac{1}{|A|} (A_{12}A_{26} - A_{22}A_{16}) \quad (4.49e)$$

$$a_{26} = \frac{1}{|A|} (A_{12}A_{16} - A_{11}A_{26}) \quad (4.49f)$$

where  $|A|$  is the determinant of matrix  $[A]$ , which is expanded as

$$|A| = (A_{11}A_{22} - A_{12}^2)A_{66} + 2A_{12}A_{26}A_{16} - A_{11}A_{26}^2 - A_{22}A_{16}^2 \quad (4.50)$$

In order to obtain the engineering constants of a composite laminate, let us define the laminate average stress  $\{\bar{\sigma}\}$  as follows:

$$\{\bar{\sigma}\} = \frac{1}{h} \{N\} = \frac{1}{h} [A] \{\varepsilon^0\} \quad (4.51)$$

Inverting equation (4.51) gives the midplane strains  $\{\varepsilon^0\}$ , which are the laminate strains of a flat laminate plate without curvature:

$$\{\varepsilon^0\} = h[a]\{\bar{\sigma}\} \quad (4.52)$$

Equation (4.52) can be expanded as

$$\begin{Bmatrix} \varepsilon_x^0 \\ \varepsilon_y^0 \\ \gamma_{xy}^0 \end{Bmatrix} = h \begin{bmatrix} a_{11} & a_{12} & a_{16} \\ a_{12} & a_{22} & a_{26} \\ a_{16} & a_{26} & a_{66} \end{bmatrix} \begin{Bmatrix} \bar{\sigma}_x \\ \bar{\sigma}_y \\ \bar{\tau}_{xy} \end{Bmatrix} \quad (4.53)$$

If we apply  $\bar{\sigma}_x$  only ( $\bar{\sigma}_y = \bar{\tau}_{xy} = 0$ ), we obtain the following engineering constants:

*Axial Modulus of the Laminate:*

$$E_x = \frac{\bar{\sigma}_x}{\varepsilon_x^0} = \frac{1}{ha_{11}} = \frac{|A|}{h(A_{22}A_{66} - A_{26}^2)} \quad (4.54)$$

*Major Poisson's Ratio of the Laminate:*

$$\nu_{xy} = -\frac{\varepsilon_y^0}{\varepsilon_x^0} = -\frac{a_{12}}{a_{11}} = -\frac{A_{16}A_{26} - A_{12}A_{66}}{A_{22}A_{66} - A_{26}^2} \quad (4.55)$$

*Coefficient Of Mutual Influence of the Laminate:*

$$\eta_{xy,x} = \frac{\gamma_{xy}^0}{\varepsilon_x^0} = \frac{a_{16}}{a_{11}} = \frac{A_{12}A_{26} - A_{22}A_{16}}{A_{22}A_{66} - A_{26}^2} \quad (4.56)$$

If we apply  $\bar{\sigma}_y$  only ( $\bar{\sigma}_x = \bar{\tau}_{xy} = 0$ ), we obtain the following engineering constants:

*Transverse Modulus of the Laminate:*

$$E_y = \frac{\bar{\sigma}_y}{\varepsilon_y^0} = \frac{1}{ha_{22}} = \frac{|A|}{h(A_{11}A_{66} - A_{16}^2)} \quad (4.57)$$

*Minor Poisson's Ratio of the Laminate:*

$$\nu_{yx} = -\frac{\varepsilon_x^0}{\varepsilon_y^0} = -\frac{a_{12}}{a_{22}} = -\frac{A_{16}A_{26} - A_{12}A_{66}}{A_{11}A_{66} - A_{16}^2} \quad (4.58)$$

*Coefficient of Mutual Influence of the Laminate:*

$$\eta_{xy,y} = \frac{\gamma_{xy}^0}{\varepsilon_y^0} = \frac{a_{26}}{a_{22}} = \frac{A_{12}A_{16} - A_{11}A_{26}}{A_{11}A_{66} - A_{16}^2} \quad (4.59)$$

If we apply  $\bar{\tau}_{xy}$  only ( $\bar{\sigma}_x = \bar{\sigma}_y = 0$ ), we obtain the following engineering constants:

*Shear Modulus of the Laminate:*

$$G_{xy} = \frac{\bar{\tau}_{xy}}{\gamma_{xy}^0} = \frac{1}{ha_{66}} = \frac{|A|}{h(A_{11}A_{22} - A_{12}^2)} \quad (4.60)$$

*Coefficients of Mutual Influence of the Laminate:*

$$\eta_{x,xy} = \frac{\varepsilon_x^0}{\gamma_{xy}^0} = \frac{a_{16}}{a_{66}} = \frac{A_{12}A_{26} - A_{22}A_{16}}{A_{11}A_{22} - A_{12}^2} \quad (4.61a)$$

and

$$\eta_{y,xy} = \frac{\varepsilon_y^0}{\gamma_{xy}^0} = \frac{a_{26}}{a_{66}} = \frac{A_{12}A_{16} - A_{11}A_{26}}{A_{11}A_{22} - A_{12}^2} \quad (4.61b)$$

#### 4.6.1 Balanced Symmetric Laminate under $N$

when  $M = \Delta T = \Delta C = 0$

A laminate is balanced when it consists of pairs of plies with equal thickness  $t_{\text{ply}}^{[k]}$  and elastic properties with ply angles  $+\theta_k$  and  $-\theta_k$  with respect to global (laminate) reference axes. Balanced laminates can include  $0^\circ$  and  $90^\circ$  plies in addition to the off-axis fiber orientations with  $+\theta_k$  and  $-\theta_k$ . For the balanced laminates, the components  $A_{16}$  and  $A_{26}$  of stiffness matrix  $[A]$  are equal to zero from the results of equations (3.130e) and (3.130f). When the laminate is balanced and symmetric, the engineering constants become much simpler. For example, the elements of matrix  $[a]$  have the simpler form

$$a_{11} = \frac{A_{22}}{A_{11}A_{22} - A_{12}^2} \quad (4.62a)$$

$$a_{22} = \frac{A_{11}}{A_{11}A_{22} - A_{12}^2} \quad (4.62b)$$

$$a_{12} = -\frac{A_{12}}{A_{11}A_{22} - A_{12}^2} \quad (4.62c)$$

$$a_{66} = \frac{1}{A_{66}} \quad (4.62d)$$

$$a_{16} = a_{26} = 0 \quad (4.62e)$$

For this case, we have the following simple engineering constants:

*Axial Modulus of the Laminate:*

$$E_x = \frac{\bar{\sigma}_x}{\varepsilon_x^0} = \frac{1}{ha_{11}} = \frac{1}{h} \left( A_{11} - \frac{A_{12}^2}{A_{22}} \right) \quad (4.63)$$

*Transverse Modulus of the Laminate:*

$$E_y = \frac{\bar{\sigma}_y}{\varepsilon_y^0} = \frac{1}{ha_{22}} = \frac{1}{h} \left( A_{22} - \frac{A_{12}^2}{A_{11}} \right) \quad (4.64)$$

*Major Poisson's Ratio of the Laminate:*

$$\nu_{xy} = -\frac{\varepsilon_y^0}{\varepsilon_x^0} = -\frac{a_{12}}{a_{11}} = \frac{A_{12}}{A_{22}} \quad (4.65)$$

*Minor Poisson's Ratio of the Laminate:*

$$\nu_{yx} = -\frac{\varepsilon_x^0}{\varepsilon_y^0} = -\frac{a_{12}}{a_{22}} = \frac{A_{12}}{A_{11}} \quad (4.66)$$

*Shear Modulus of the Laminate:*

$$G_{xy} = \frac{\bar{\tau}_{xy}}{\gamma_{xy}^0} = \frac{1}{ha_{66}} = \frac{1}{h} A_{66} \quad (4.67)$$

*Coefficients of Mutual Influence of the Laminate:*

$$\eta_{xy,x} = \frac{\gamma_{xy}^0}{\varepsilon_x^0} = \frac{a_{16}}{a_{11}} = 0 \quad (4.68)$$

$$\eta_{xy,y} = \frac{\gamma_{xy}^0}{\varepsilon_y^0} = \frac{a_{26}}{a_{22}} = 0 \quad (4.69)$$

$$\eta_{x,xy} = \frac{\varepsilon_x^0}{\gamma_{xy}^0} = \frac{a_{16}}{a_{66}} = 0 \quad (4.70)$$

$$\eta_{y,xy} = \frac{\varepsilon_y^0}{\gamma_{xy}^0} = \frac{a_{26}}{a_{66}} = 0 \quad (4.71)$$

We also have simpler constitutive equations:

$$\varepsilon_x^0 = a_{11}N_x + a_{12}N_y \quad (4.72a)$$

$$\varepsilon_y^0 = a_{12}N_x + a_{22}N_y \quad (4.72b)$$

$$\gamma_{xy}^0 = a_{66}N_{xy} \quad (4.72c)$$

#### EXAMPLE 4.1

A carbon-fiber epoxy composite laminate with stacking sequence [0/ $\pm 45$ ]S is subjected to  $N_x = 10^4$  N/m, ( $N_y = N_{xy} = 0$ ). Find the engineering constants and

resulting strains. The engineering properties of the unidirectional carbon-fiber epoxy composite are

$$E_1 = 130 \text{ GPa}$$

$$E_2 = 10.5 \text{ GPa}$$

$$\nu_{12} = 0.28$$

$$G_{12} = 6.0 \text{ GPa}$$

$$t_{\text{ply}} = 0.135 \text{ mm}$$

### Solution

From equation (3.116),

$$Q_{11} = 130.8 \text{ GPa}$$

$$Q_{22} = 10.6 \text{ GPa}$$

$$Q_{66} = 6.0 \text{ GPa}$$

$$Q_{12} = 2.96 \text{ GPa}$$

From equation (3.131),

$$U_1 = 56.77 \text{ GPa}$$

$$U_2 = 60.10 \text{ GPa}$$

$$U_3 = 13.94 \text{ GPa}$$

$$U_4 = 16.89 \text{ GPa}$$

$$U_5 = 19.94 \text{ GPa}$$

From equation (3.130),

$$\bar{Q}_{11} = U_1 + U_2 \cos 2\theta + U_3 \cos 4\theta$$

$$\bar{Q}_{22} = U_1 - U_2 \cos 2\theta + U_3 \cos 4\theta$$

$$\bar{Q}_{12} = U_4 - U_3 \cos 4\theta$$

$$\bar{Q}_{66} = U_5 - U_3 \cos 4\theta$$

$$\bar{Q}_{16} = \frac{1}{2} U_2 \sin 2\theta + U_3 \sin 4\theta$$

$$\bar{Q}_{26} = \frac{1}{2} U_2 \sin 2\theta - U_3 \sin 4\theta$$

Table 4.1 lists the numerical values of the reduced stiffness  $\bar{Q}_{ij}$  in the laminate coordinates.

Then,

$$[A] = \int_{-(h/2)}^{(h/2)} [\bar{Q}_{ij}] dz = \sum_{k=1}^n [\bar{Q}_{ij}]^{[k]} (z_k - z_{k-1}) = \sum_{k=1}^n [\bar{Q}_{ij}]^{[k]} t_{\text{ply}}^{[k]}$$

**Table 4.1 Numerical Values of  $\bar{Q}_{ij}$  (GPa)**

	$\bar{Q}_{11}$	$\bar{Q}_{22}$	$\bar{Q}_{12}$	$\bar{Q}_{66}$	$\bar{Q}_{16}$	$\bar{Q}_{26}$
$0^\circ$	130.8	10.6	2.96	6.0	0	0
$+45^\circ$	42.83	42.83	30.83	33.87	30.07	30.07
$-45^\circ$	42.83	42.83	30.83	33.87	-30.07	-30.07

can be calculated:

$$A_{11} = 58.45 \text{ MN/m}$$

$$A_{22} = 25.98 \text{ MN/m}$$

$$A_{66} = 19.91 \text{ MN/m}$$

$$A_{12} = 17.45 \text{ MN/m}$$

$$A_{16} = A_{26} = 0$$

From equation (4.62),

$$a_{11} = 21.40 \times 10^{-9} \text{ m/N}$$

$$a_{22} = 48.15 \times 10^{-9} \text{ m/N}$$

$$a_{66} = 50.23 \times 10^{-9} \text{ m/N}$$

$$a_{12} = -14.37 \times 10^{-9} \text{ m/N}$$

$$a_{16} = a_{26} = 0$$

Thus,

$$\begin{aligned}\varepsilon_x^0 &= a_{11}N_x + a_{12}N_y \\ &= 21.40 \times 10^{-9}(\text{m/N}) \times 10^4(\text{N/m}) - 14.37 \times 10^{-9}(\text{m/N}) \times 0 \\ &= 214 \times 10^{-6} (\text{m/m}) \\ &= 214 \mu\text{S} (\text{microstrain})\end{aligned}$$

$$\begin{aligned}\varepsilon_y^0 &= a_{12}N_x + a_{22}N_y \\ &= -14.37 \times 10^{-9}(\text{m/N}) \times 10^4(\text{N/m}) + 48.15 \times 10^{-9}(\text{m/N}) \times 0 \\ &= -144 \mu\text{S} (\text{microstrain})\end{aligned}$$

$$\gamma_{xy}^0 = a_{66}N_{xy} = 0$$

#### EXAMPLE 4.2

We have already calculated the strains of example 4.1 when the carbon-fiber epoxy composite laminate of example 4.1 is subjected to the in-plane force  $N_x = 10^4 \text{ N/m}$ , ( $N_y = N_{xy} = 0$ ):

$$\varepsilon_x^0 = 214 \mu\text{S}$$

$$\varepsilon_y^0 = -144 \mu\text{S}$$

$$\gamma_{xy}^0 = 0$$

**Table 4.2 Stresses of Each Ply in the Global Coordinate (MPa)**

	$\sigma_x^{[k]}$	$\sigma_y^{[k]}$	$\tau_{xy}^{[k]}$
0°	27.6	-0.89	0
45°	4.73	0.43	2.10
-45°	4.73	0.43	-2.10

Now calculate the required in-plane force  $N$  to yield the above strains, that is, verify that  $N_x = 10^4(\text{N/m})$ ,  $N_y = N_{xy} = 0$ .

### Solution

With the results of table 4.1, the stresses in the  $k$ th ply  $\sigma_x^{[k]}$ ,  $\sigma_y^{[k]}$ , and  $\tau_{xy}^{[k]}$  in the laminate coordinates (global coordinates) using equation (4.15) can be calculated as follows:

$$\sigma_x^{[k]} = \bar{Q}_{11}^{[k]} \varepsilon_x^0 + \bar{Q}_{12}^{[k]} \varepsilon_y^0 + \bar{Q}_{16}^{[k]} \gamma_{xy}^0$$

For the 0° ply, we have

$$\begin{aligned} \sigma_x^{[0]} &= \bar{Q}_{11}^{[0]} \varepsilon_x^0 + \bar{Q}_{12}^{[0]} \varepsilon_y^0 + \bar{Q}_{16}^{[0]} \gamma_{xy}^0 \\ &= 130.8 \times 10^9 (\text{N/m}^2) \times 214 \times 10^{-6} + 2.96 \times 10^9 (\text{N/m}^2) \times (-144 \times 10^{-6}) + 0 \\ &= 27.6 \text{ MPa} \end{aligned}$$

where the superscript “0” of  $\sigma_x^{[0]}$  represents the tensile stress of the 0° ply in the  $x$ -direction. Similarly, other stress components can be obtained. Table 4.2 lists the stress components.

Then the elements of  $\{N\}$  can be calculated from the definition of equation (4.16),

$$\begin{aligned} N_x &= 2t_{\text{ply}} (\sigma_x^{[0]} + \sigma_x^{[45]} + \sigma_x^{[-45]}) \\ &= 2 \times (0.135 \times 10^{-3} \text{ m}) \times [(27.6 + 4.73 + 4.73) \times 10^6] \text{ N/m}^2 \\ &= 10^4 \text{ N/m} \\ N_y &= 2t_{\text{ply}} (\sigma_y^{[0]} + \sigma_y^{[45]} + \sigma_y^{[-45]}) \\ &= 2 \times (0.135 \times 10^{-3} \text{ m}) \times [(-0.89 + 0.43 + 0.43) \times 10^6] \text{ N/m}^2 \\ &= -8.1 \text{ N/m} \approx 0 \\ N_{xy} &= 2t_{\text{ply}} (\tau_{xy}^{[0]} + \tau_{xy}^{[45]} + \tau_{xy}^{[-45]}) \\ &= 2 \times (0.135 \times 10^{-3} \text{ m}) \times [(0 + 2.10 - 2.10) \times 10^6] \text{ N/m}^2 \\ &= 0 \text{ N/m} \end{aligned}$$

which proves that the calculation of example 4.1 was correct. Figure 4.7 shows the stress distributions of table 4.2.

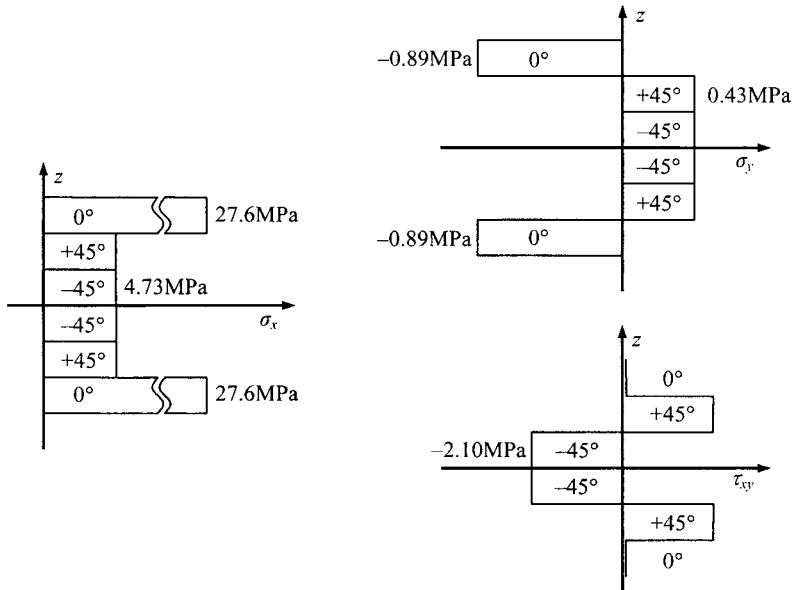


**Figure 4.7** Stress distributions of table 4.2 (stresses not scaled).

### EXAMPLE 4.3

Determine an optimum wrap angle  $\phi$  for a filament-wound composite pressure vessel that is fabricated by winding S-glass-fiber epoxy with a helical wrap angle  $\pm\phi$  from the vessel axis. The diameter and thickness of the pressure vessel are 500 mm and 10 mm, respectively. The stiffness properties of S-glass-fiber epoxy are as follows:

$$E_1 = 43.5 \text{ GPa}$$

$$E_2 = 11.5 \text{ GPa}$$

$$\nu_{12} = 0.27$$

$$G_{12} = 3.45 \text{ GPa}$$

### Solution

A simple analysis may give  $\phi = 54.74^\circ$  (see problem 3.18) because the hoop stress  $\sigma_h$  is twice that of the axial stress  $\sigma_a$ , such that

$$\frac{\sigma_h}{\sigma_a} = \frac{\sigma_f \sin^2 \phi}{\sigma_f \cos^2 \phi} = \tan^2 \phi = \tan^2 54.74^\circ = 2.0$$

The above analysis does not consider the transverse modulus of composite material and the interaction between the laminae, therefore, it is called a *netting analysis*.

When the vessel of radius  $r$  is pressurized with pressure  $p$ , the in-plane load  $N_h$  (N/m) ( $= pr$ ) in the hoop direction per unit hoop width is twice the in-plane

load  $N_a$  (N/m) ( $=pr/2$ ) in the axial direction. Then the overall strains of the pressure vessel with the stacking sequence of  $[\pm 54.74]_S$  can be calculated using equation (4.72) with the balanced symmetric stacking assumption:

$$\begin{aligned}\varepsilon_a &= 0.012 \times 10^{-6}pr \\ \varepsilon_h &= 0.068 \times 10^{-6}pr\end{aligned}$$

where the dimensions of  $p$  and  $r$  are Pa and m, respectively.

Since the two strains are much different, the above solution may not be an optimum.

Alternatively, when the stacking sequence is  $[\pm 64.81]_S$ , the two strains become:

$$\begin{aligned}\varepsilon_a &= 0.045 \times 10^{-6}pr \\ \varepsilon_h &= 0.045 \times 10^{-6}pr\end{aligned}$$

Therefore, if the functional requirement is to have equal strains in the hoop and axial directions, the optimum stacking angle should be  $[\pm 64.81]_S$ . The detailed calculation for the above strains is left to problem 4.9.

The functional requirement for pressure vessels is frequently the maximum internal pressure that can be sustained, which will be treated in chapter 5.

Although the above problem is simple, the netting analysis does not give satisfactory results that the designer requires. Therefore, the netting analysis should not be used whenever possible.

#### 4.6.2 Quasi-Isotropic Laminate under $N$ when $M = \Delta T = \Delta C = 0$

A quasi-isotropic laminate is the laminate whose in-plane elastic stiffness response is isotropic. However, it has anisotropic strength properties. All symmetric laminates with  $2n$  equal thickness plies ( $n \geq 3$ ) and  $n$  equal angles between fiber orientations are quasi-isotropic. For  $n$  equal angles of  $\Delta\theta$  between fiber orientations, we can get

$$\Delta\theta = \frac{\pi}{n} \quad (4.73)$$

The simplest type of quasi-isotropic laminate is the one with the stacking sequence of  $[0/\pm 60]_S$ . Another type is the  $\pi/4$  quasi-isotropic laminate, or  $[0/\pm 45/90]_S$ . Other examples are  $[0/\pm 36/\pm 72]_S$  and  $[0/\pm 30/\pm 60/90]_S$ . All shear coupling coefficients of the quasi-isotropic laminates are zero because they are balanced. For the  $[0/\pm 60]_S$  laminate, we have from equation (3.130)

$$\bar{Q}_{11}^{[0]} = U_1 + U_2 + U_3$$

$$\bar{Q}_{22}^{[0]} = U_1 - U_2 + U_3$$

$$\bar{Q}_{12}^{[0]} = U_4 - U_3$$

$$\bar{Q}_{66}^{[0]} = U_5 - U_3$$

$$\bar{Q}_{16}^{[0]} = \bar{Q}_{26}^{[0]} = 0$$

$$\bar{Q}_{11}^{[60]} = \bar{Q}_{11}^{[-60]} = U_1 - \frac{1}{2}U_2 - \frac{1}{2}U_3$$

$$\bar{Q}_{22}^{[60]} = \bar{Q}_{22}^{[-60]} = U_1 + \frac{1}{2}U_2 - \frac{1}{2}U_3$$

$$\bar{Q}_{12}^{[60]} = \bar{Q}_{12}^{[-60]} = U_4 + \frac{1}{2}U_3$$

$$\bar{Q}_{66}^{[60]} = \bar{Q}_{66}^{[-60]} = U_5 + \frac{1}{2}U_3$$

$$\bar{Q}_{16}^{[60]} = -\bar{Q}_{16}^{[-60]}$$

$$\bar{Q}_{26}^{[60]} = -\bar{Q}_{26}^{[-60]}$$

Thus,

$$A_{11} = 2t_{\text{ply}} \left[ (U_1 + U_2 + U_3) + 2 \left( U_1 - \frac{1}{2}U_2 - \frac{1}{2}U_3 \right) \right] = 6t_{\text{ply}} \times U_1$$

$$A_{22} = 2t_{\text{ply}} \left[ (U_1 - U_2 + U_3) + 2 \left( U_1 + \frac{1}{2}U_2 - \frac{1}{2}U_3 \right) \right] = 6t_{\text{ply}} \times U_1$$

$$A_{12} = 2t_{\text{ply}} \left[ (U_4 - U_3) + 2 \left( U_4 + \frac{1}{2}U_3 \right) \right] = 6t_{\text{ply}} \times U_4$$

$$A_{66} = 2t_{\text{ply}} \left[ (U_5 - U_3) + 2 \left( U_5 + \frac{1}{2}U_3 \right) \right] = 6t_{\text{ply}} \times U_5$$

Using equations (4.63) to (4.66), we have

$$E_x = E_y$$

$$\nu_{xy} = \nu_{yx}$$

Table 4.3 shows the four-point bending test results of the quasi-isotropic laminates. From the test results of table 4.3, we may derive several conclusions:

1. All tensile moduli of quasi-isotropic laminates are the same.
2. Poisson's ratios are approximately 0.3 ( $= U_4/U_1$ ).
3. All compressive moduli of quasi-isotropic laminates are the same, but slightly less than the tensile ones.
4. Strengths are dependent on the direction (i.e., anisotropic).

**Table 4.3 An Example of Elastic and Strength Properties of the Quasi-isotropic Composite Laminates (Data from TELAC Laboratory of MIT)**

Stacking sequence	$E_x$ (GPa) [tension]	$E_x$ (GPa) [compression]	Strength (MPa)
[±60/0]s	54.4	49.6	536
[−15/45/−75]s	54.9	50.9	333
[90/−30/30]s	55.2	52.7	322
[45/−15/−75]s	53.7	51.6	340
[−60/0/60]s	55.2	52.9	580
[−45/15/75]s	55.2	53.9	327
[−30/30/90]s	53.9	53.8	324

#### 4.7 Pure Bending of Symmetric Laminates under $M$ when $N = \Delta T = \Delta C = 0$

When the stacking sequence of a laminate is symmetric about its midplane, the bending–stretching coupling matrix  $[B]$  is identically zero, as already mentioned for the in-plane problem (see problem 4.1). Then from equations (4.41b) and (4.33b),

$$[B'] = [B^*][D^*]^{-1} = -[A]^{-1}[B][D^*]^{-1} \quad (4.74)$$

is identically zero. When only bending moment  $\{M\}$  is applied to this laminate, the mid-plane strain  $\{\varepsilon^0\}$  for this case becomes zero from equation (4.43). Then equations (4.39) and (4.44) become

$$\begin{Bmatrix} M_x \\ M_y \\ M_{xy} \end{Bmatrix} = \begin{bmatrix} D_{11} & D_{12} & D_{16} \\ D_{12} & D_{22} & D_{26} \\ D_{16} & D_{26} & D_{66} \end{bmatrix} \begin{Bmatrix} \kappa_x \\ \kappa_y \\ \kappa_{xy} \end{Bmatrix} \quad (4.75)$$

$$\begin{Bmatrix} \kappa_x \\ \kappa_y \\ \kappa_{xy} \end{Bmatrix} = \begin{bmatrix} d_{11} & d_{12} & d_{16} \\ d_{12} & d_{22} & d_{26} \\ d_{16} & d_{26} & d_{66} \end{bmatrix} \begin{Bmatrix} M_x \\ M_y \\ M_{xy} \end{Bmatrix} \quad (4.76)$$

where

$$[d] = [D'] = [D^*]^{-1} = [D]^{-1} \quad (4.77)$$

The elements of matrix  $[d]$  have the following expressions, because it is the inverse of  $[D]$ :

$$d_{11} = \frac{1}{|D|} (D_{22}D_{66} - D_{26}^2) \quad (4.78a)$$

$$d_{22} = \frac{1}{|D|} (D_{11}D_{66} - D_{16}^2) \quad (4.78b)$$

$$d_{12} = \frac{1}{|D|} (D_{16}D_{26} - D_{12}D_{66}) \quad (4.78c)$$

$$d_{66} = \frac{1}{|D|} (D_{11}D_{22} - D_{12}^2) \quad (4.78d)$$

$$d_{16} = \frac{1}{|D|} (D_{12}D_{26} - D_{22}D_{16}) \quad (4.78e)$$

$$d_{26} = \frac{1}{|D|} (D_{12}D_{16} - D_{11}D_{26}) \quad (4.78f)$$

where  $|D|$  is the determinant of matrix  $[D]$ , which is expanded as

$$|D| = (D_{11}D_{22} - D_{12}^2)D_{66} + 2D_{12}D_{26}D_{16} - D_{11}D_{26}^2 - D_{22}D_{16}^2 \quad (4.79)$$

#### EXAMPLE 4.4

A carbon-fiber epoxy composite laminate with stacking sequence  $[0/\pm 45]_S$  is subjected to pure bending  $M_x = 100$  (Nm/m), ( $M_y = M_{xy} = 0$ ). Find the resulting radius of curvature  $R_x$ . The engineering properties of the unidirectional carbon-fiber epoxy composite are

$$E_1 = 130 \text{ GPa}$$

$$E_2 = 10.5 \text{ GPa}$$

$$\nu_{12} = 0.28$$

$$G_{12} = 6.0 \text{ GPa}$$

$$t_{\text{ply}} = 0.135 \text{ mm}$$

#### Solution

From equation (3.116),

$$Q_{11} = 130.8 \text{ GPa}$$

$$Q_{22} = 10.6 \text{ GPa}$$

$$Q_{66} = 6.0 \text{ GPa}$$

$$Q_{12} = 2.96 \text{ GPa}$$

From equation (3.131),

$$U_1 = 56.77 \text{ GPa}$$

$$U_2 = 60.10 \text{ GPa}$$

$$U_3 = 13.94 \text{ GPa}$$

$$U_4 = 16.89 \text{ GPa}$$

$$U_5 = 19.94 \text{ GPa}$$

From equation (3.130),

$$\bar{Q}_{11} = U_1 + U_2 \cos 2\theta + U_3 \cos 4\theta$$

$$\bar{Q}_{22} = U_1 - U_2 \cos 2\theta + U_3 \cos 4\theta$$

$$\begin{aligned}\overline{Q}_{12} &= U_4 - U_3 \cos 4\theta \\ \overline{Q}_{66} &= U_5 - U_3 \cos 4\theta \\ \overline{Q}_{16} &= \frac{1}{2} U_2 \sin 2\theta + U_3 \sin 4\theta \\ \overline{Q}_{26} &= \frac{1}{2} U_2 \sin 2\theta - U_3 \sin 4\theta\end{aligned}$$

From the results of table 4.1, we can calculate bending stiffness  $[D]$ :

$$[D] = \int_{-(h/2)}^{(h/2)} [\overline{Q}_{ij}] z^2 dz = \sum_{k=1}^n [\overline{Q}_{ij}]^{[k]} \frac{1}{3} (z_k^3 - z_{k-1}^3)$$

Since the values of  $(1/3)(z_k^3 - z_{k-1}^3)$  are

$$0.0156 \times 10^{-9} (\text{m}^3) \quad \text{for the } 0^\circ \text{ply}$$

$$0.0057 \times 10^{-9} (\text{m}^3) \quad \text{for the } 45^\circ \text{ply}$$

$$0.0008 \times 10^{-9} (\text{m}^3) \quad \text{for the } -45^\circ \text{ply}$$

$$\begin{aligned}D_{11} &= 2 \times (130.8 \times 10^9 \text{ N/m}^2 \times 0.0156 \times 10^{-9} \text{ m}^3 + 42.83 \times 10^9 \text{ N/m}^2 \\ &\quad \times 0.0057 \times 10^{-9} \text{ m}^3 + 42.83 \times 10^9 \text{ N/m}^2 \times 0.0008 \times 10^{-9} \text{ m}^3) \\ &= 5.25 \text{ Nm}\end{aligned}$$

Similarly,

$$D_{22} = 0.891 \text{ Nm}$$

$$D_{66} = 0.631 \text{ Nm}$$

$$D_{12} = 0.497 \text{ Nm}$$

$$D_{16} = 0.295 \text{ Nm}$$

$$D_{26} = 0.295 \text{ Nm}$$

From equation (4.78),

$$d_{11} = 0.230 \text{ (1/Nm)}$$

$$d_{22} = 1.38 \text{ (1/Nm)}$$

$$d_{66} = 1.89 \text{ (1/Nm)}$$

$$d_{12} = -0.109 \text{ (1/Nm)}$$

$$d_{16} = -0.0567 \text{ (1/Nm)}$$

$$d_{26} = -0.596 \text{ (1/Nm)}$$

Thus, when  $M_x = 100 \text{ (Nm/m)}$  is applied, we have

$$\begin{aligned}\kappa_x &= d_{11} M_x + d_{12} M_y + d_{16} M_{xy} \\ &= 0.230 \text{ (1/Nm)} \times 100 \text{ (Nm/m)} \\ &= 23.0 \text{ (1/m)}\end{aligned}$$

$$\begin{aligned}\kappa_y &= d_{12}M_x = -10.9 \text{ (1/m)} \\ \kappa_{xy} &= d_{16}M_x = -5.67 \text{ (1/m)}\end{aligned}$$

Therefore, the radius of curvature  $R_x = 1/\kappa_x = (1/23.0) \text{ m} = 4.35 \times 10^{-2} \text{ m}$ .

#### EXAMPLE 4.5

When the carbon-fiber epoxy composite laminate of example 4.4 under the pure bending moment  $M_x = 100 \text{ (Nm/m)}$ , ( $M_y = M_{xy} = 0$ ) has the curvatures  $\{\kappa\}$

$$\kappa_x = 23.0 \text{ (1/m)}$$

$$\kappa_y = -10.9 \text{ (1/m)}$$

$$\kappa_{xy} = -5.67 \text{ (1/m)}$$

verify that  $M_x = 100 \text{ (Nm/m)}$ , and  $M_y = M_{xy} = 0$ . Also calculate the stresses in the laminate with respect to the global axis.

#### Solution

With the results of table 4.1, the stresses in the  $k$ th ply in the laminate coordinate (global coordinate) using equation (4.15) can be calculated as follows:

$$\begin{aligned}\left\{ \begin{array}{l} \sigma_x \\ \sigma_y \\ \tau_{xy} \end{array} \right\}^{[k]} &= [\bar{Q}_{ij}]^{[k]} \left\{ \begin{array}{l} \varepsilon_x^0 \\ \varepsilon_y^0 \\ \gamma_{xy}^0 \end{array} \right\} + [\bar{Q}_{ij}]^{[k]} z \left\{ \begin{array}{l} \kappa_x \\ \kappa_y \\ \kappa_{xy} \end{array} \right\} - [\bar{Q}_{ij}]^{[k]} \left\{ \begin{array}{l} \alpha_x \Delta T + \beta_x \Delta C \\ \alpha_y \Delta T + \beta_y \Delta C \\ \alpha_{xy} \Delta T + \beta_{xy} \Delta C \end{array} \right\} \\ \sigma_x^{[0]} &= \bar{Q}_{11}^{[0]} z \kappa_x + \bar{Q}_{12}^{[0]} z \kappa_y + \bar{Q}_{16}^{[0]} z \kappa_{xy} \\ &= z \left[ (130.8 \times 10^9 \text{ N/m}^2) \times \left( 23.0 \frac{1}{\text{m}} \right) + (2.96 \times 10^9 \text{ N/m}^2) \times \left( -10.9 \frac{1}{\text{m}} \right) + 0 \right] \\ &= 2976 \times 10^9 z \text{ (N/m}^3\text{)} \\ \sigma_y^{[0]} &= \bar{Q}_{12}^{[0]} z \kappa_x + \bar{Q}_{22}^{[0]} z \kappa_y + \bar{Q}_{26}^{[0]} z \kappa_{xy} \\ &= z \left[ (2.96 \times 10^9 \text{ N/m}^2) \times \left( 23.0 \frac{1}{\text{m}} \right) + (10.6 \times 10^9 \text{ N/m}^2) \times \left( -10.9 \frac{1}{\text{m}} \right) + 0 \right] \\ &= -47.5 \times 10^9 z \text{ (N/m}^3\text{)} \\ \tau_{xy}^{[0]} &= \bar{Q}_{16}^{[0]} z \kappa_x + \bar{Q}_{26}^{[0]} z \kappa_y + \bar{Q}_{66}^{[0]} z \kappa_{xy} \\ &= z \left( 6.0 \times 10^9 \text{ N/m}^2 \right) \times \left( -5.67 \frac{1}{\text{m}} \right) \\ &= -34.0 \times 10^9 z \text{ (N/m}^3\text{)}\end{aligned}$$

**Table 4.4 Numerical Values of Stress Components (N/m<sup>3</sup>)**

	$\sigma_x^{[k]} 10^9$	$\sigma_y^{[k]} 10^9$	$\tau_{xy}^{[k]} 10^9$
0°	2976 $z$	-47.5 $z$	-34.0 $z$
+45°	479 $z$	71.7 $z$	193 $z$
-45°	820 $z$	413 $z$	-556 $z$

Similarly, other stress components can be obtained. Table 4.4 lists the stress components.

Since the values of  $\int_{-(h/2)}^{(h/2)} z^2 dz$  are

$$0.0156 \times 10^{-9} (\text{m}^3) \text{ for the } 0^\circ \text{ ply}$$

$$0.0057 \times 10^{-9} (\text{m}^3) \text{ for the } 45^\circ \text{ ply}$$

$$0.0008 \times 10^{-9} (\text{m}^3) \text{ for the } -45^\circ \text{ ply}$$

{M} can be calculated from the definition of equation (4.25),

$$\begin{aligned} M_x &= \int_{-(h/2)}^{(h/2)} \sigma_x z dz \\ &= 2 \times (2976 \times 0.0156 + 479 \times 0.0057 + 820 \times 0.0008) \text{ Nm/m} \\ &= 99.6 \text{ Nm/m} \approx 100 \text{ Nm/m} \end{aligned}$$

$$\begin{aligned} M_y &= \int_{-(h/2)}^{(h/2)} \sigma_y z dz \\ &= 2 \times (-47.5 \times 0.0156 + 71.7 \times 0.0057 + 413 \times 0.0008) \text{ Nm/m} \\ &= -3.82 \times 10^{-3} \text{ Nm/m} \approx 0 \text{ Nm/m} \end{aligned}$$

$$\begin{aligned} M_{xy} &= \int_{-(h/2)}^{(h/2)} \tau_{xy} z dz \\ &= 2 \times (-34.0 \times 0.0156 + 193 \times 0.0057 - 556 \times 0.0008) \text{ Nm/m} \\ &= 0.25 \text{ Nm/m} \approx 0 \text{ Nm/m} \end{aligned}$$

which proves that the calculation of example 4.4 was correct. Figure 4.8 shows the stress distributions of table 4.4.

#### 4.8 Bending and Stretching of Laminates under $N$ and $M$ when $\Delta T = \Delta C = 0$

The relations between the applied forces and moments and the midplane strains and laminate curvatures are provided by equation (4.38). The matrix equation represents six simultaneous algebraic equations, involving six unknowns that are three midplane strains and three laminate curvatures. For a general laminate in

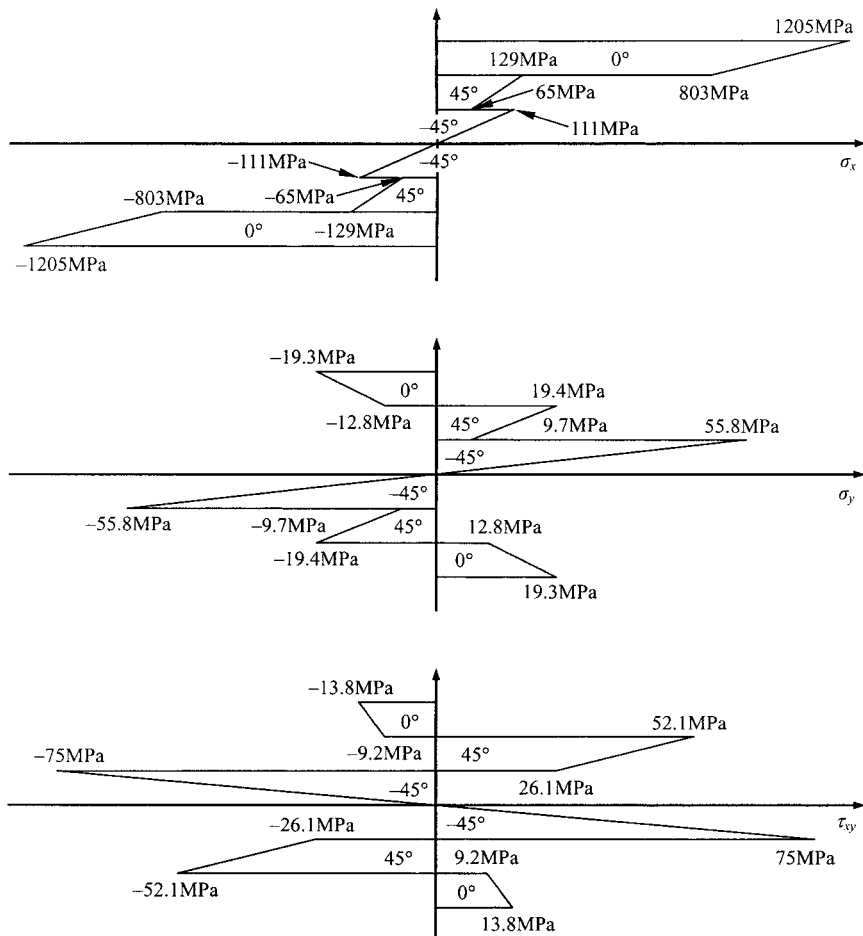


Figure 4.8 Stress distributions of table 4.4 (stresses not to scale).

which the coupling matrix  $[B]$  is not zero, the solution of these equations requires inverting the  $[6 \times 6]$  matrix of equation (4.38), which can be done easily using computers. In this section, we will demonstrate the calculation procedure using a simple example rather than using the computer program such as *Axiomatic CLPT* provided with this book.

#### EXAMPLE 4.6

Calculate the necessary in-plane forces and moments to maintain  $\varepsilon_x^0 = 1000 (\mu\text{S})$  for the same material of example 4.1 with the stacking sequence of  $[90/0]_{2T}$ . The engineering material properties of the unidirectional carbon-fiber epoxy composite are:

$$E_1 = 130 \text{ GPa}$$

$$E_2 = 10.5 \text{ GPa}$$

$$\nu_{12} = 0.28$$

$$G_{12} = 6.0 \text{ GPa}$$

$$t_{\text{ply}} = 0.135 \text{ mm}$$

**Table 4.5 Numerical Values of  $\bar{Q}_{ij}$  (GPa)**

	$\bar{Q}_{11}$	$\bar{Q}_{22}$	$\bar{Q}_{12}$	$\bar{Q}_{66}$	$\bar{Q}_{16}$	$\bar{Q}_{26}$
0°	130.8	10.6	2.96	6.0	0	0
90°	10.6	130.8	2.96	6.0	0	0

**Table 4.6 Geometrical Relations of Example 4.5**

Ply no.	$\theta$	$t_{\text{ply}}$ (mm)	$\int_{-(h/2)}^{(h/2)} z dz$ (mm <sup>2</sup> )	$\int_{-(h/2)}^{(h/2)} z^2 dz$ (mm <sup>3</sup> )
1	90°	0.135	-0.0273	0.0057
2	0°	0.135	-0.0091	0.0008
3	90°	0.135	0.0091	0.0008
4	0°	0.135	0.0273	0.0057

**Solution**

We have the stiffness  $\bar{Q}_{ij}$  in table 4.5 and geometrical relations in table 4.6. For example,  $B_{11}$  can be calculated as follows:

$$\begin{aligned} B_{11} &= 10.6 \times 10^9 \text{ N/m}^2 \times (-0.0273 \times 10^{-6} \text{ m}^2) + 130.8 \times 10^9 \text{ N/m}^2 \\ &\quad \times (-0.0091 \times 10^{-6} \text{ m}^2) + 10.6 \times 10^9 \text{ N/m}^2 \times (0.0091 \times 10^{-6} \text{ m}^2) \\ &\quad + 130.8 \times 10^9 \text{ N/m}^2 \times (0.0273 \times 10^{-6} \text{ m}^2) \\ &= 2.188 \times 10^3 \text{ N} \end{aligned}$$

Similarly, we can calculate the other stiffness constants of  $[A]$ ,  $[B]$ , and  $[D]$  as shown in table 4.7.

Then

$$\begin{aligned} N_x &= A_{11}\varepsilon_x^0 + A_{12}\varepsilon_y^0 + A_{16}\gamma_{xy}^0 + B_{11}\kappa_x + B_{12}\kappa_y + B_{16}\kappa_{xy} \\ &= A_{11}\varepsilon_x^0 = 3.82 \times 10^4 \text{ N/m} \\ N_y &= A_{12}\varepsilon_x^0 = 1.60 \times 10^3 \text{ N/m} \\ N_{xy} &= 0 \\ M_x &= B_{11}\varepsilon_x^0 + B_{12}\varepsilon_y^0 + B_{16}\gamma_{xy}^0 + D_{11}\kappa_x + D_{12}\kappa_y + D_{16}\kappa_{xy} = B_{11}\varepsilon_x^0 \\ &= 2.188 \text{ N} \cdot \text{m/m} \\ M_y &= M_{xy} = 0 \end{aligned}$$

#### 4.9 Bending and Stretching of Laminates under $\Delta T$ when $M = N = \Delta C = 0$

The coefficients of thermal expansion (CTE) are obtained by measuring strains as a function of temperature and determining the slopes of the thermal strain versus

**Table 4.7 Stiffness Constants of Example 4.7**

$ij$	$A_{ij}$ (MN/m)	$B_{ij}$ (N)	$D_{ij}$ (Nm)
11	38.18	2188	0.919
22	38.18	-2188	0.919
12	1.598	0	0.038
66	3.24	0	0.078
16	0	0	0
26	0	0	0

temperature curves. Since the CTEs are in general not constant but vary with temperature, we frequently use average values within some limited temperature range.

Once the CTEs are obtained in the principal material coordinate, the CTEs can be transformed to the global coordinate using the tensor transformation relations of equation (4.10) or equation (3.96) for the engineering strains. If we only consider the orthotropic material, the engineering shear component ( $\alpha_{12}$ ) of CTE is zero in the principal material coordinate. Then the engineering CTEs ( $\alpha_x$ ,  $\alpha_y$ ,  $\alpha_{xy}$ ) of the  $k$ th ply in the global coordinate are expressed in terms of longitudinal ( $\alpha_1$ ) and transverse principal ( $\alpha_2$ ) CTEs as follows:

$$\alpha_x^{[k]} = m^2\alpha_1 + n^2\alpha_2 \quad (4.80a)$$

$$\alpha_y^{[k]} = n^2\alpha_1 + m^2\alpha_2 \quad (4.80b)$$

$$\alpha_{xy}^{[k]} = 2mn(\alpha_1 - \alpha_2) \quad (4.80c)$$

where  $m$  and  $n$  represent  $\cos \theta^{[k]}$  and  $\sin \theta^{[k]}$ , respectively.

Again, the relations of equation (4.80) are only valid for a *lamina*, not for a laminate, as already explained in chapter 3, because the plies in the laminate interact; consequently, the CTEs for the laminate should be derived in the same manner for the laminate strains.

The average engineering CTEs of the *laminate* are calculated from equation (4.32) when  $\{N\} = \{\kappa\} = \Delta C = 0$ :

$$\begin{aligned} \{\alpha\} &= \frac{1}{\Delta T} \{\varepsilon^0\} = \{\Gamma^{*T}\} = [A]^{-1} \{\Gamma^T\} = [a] \{\Gamma^T\} \\ &= [a] \int_{-(h/2)}^{(h/2)} [\bar{Q}_{ij}] \begin{Bmatrix} \alpha_x \\ \alpha_y \\ \alpha_{xy} \end{Bmatrix} dz = [a] \sum_{k=1}^n [\bar{Q}_{ij}]^{[k]} \begin{Bmatrix} \alpha_x \\ \alpha_y \\ \alpha_{xy} \end{Bmatrix}^{[k]} (z_k - z_{k-1}) \end{aligned} \quad (4.81)$$

or

$$\{\alpha\} = [a] \sum_{k=1}^n \{\xi^T\}^{[k]} t_{\text{ply}}^{[k]} \quad (4.82)$$

where  $\{\xi^T\}^{[k]}$  is defined as

$$\{\xi^T\}^{[k]} = [\bar{Q}_{ij}]^{[k]} \begin{Bmatrix} \alpha_x \\ \alpha_y \\ \alpha_{xy} \end{Bmatrix}^{[k]} \quad (4.83)$$

are ply thermal influence coefficients.

The hygrothermal residual stresses in the plies with respect to the global axis can be calculated using

$$\begin{Bmatrix} \sigma_x \\ \sigma_y \\ \tau_{xy} \end{Bmatrix}^{[k]} = [\bar{Q}_{ij}]^{[k]} \begin{Bmatrix} \varepsilon_x^0 \\ \varepsilon_y^0 \\ \gamma_{xy}^0 \end{Bmatrix} + [\bar{Q}_{ij}]^{[k]} z \begin{Bmatrix} \kappa_x \\ \kappa_y \\ \kappa_{xy} \end{Bmatrix} - [\bar{Q}_{ij}]^{[k]} \begin{Bmatrix} \alpha_x \Delta T + \beta_x \Delta C \\ \alpha_y \Delta T + \beta_y \Delta C \\ \alpha_{xy} \Delta T + \beta_{xy} \Delta C \end{Bmatrix} \quad (4.15)$$

When  $\varepsilon_x^0$ ,  $\varepsilon_y^0$ ,  $\gamma_{xy}^0$ ,  $\kappa_x$ ,  $\kappa_y$ , and  $\kappa_{xy}$  are all zero, the above stresses, or  $\{N^T\}$  and  $\{N^H\}$  in equation (4.22) represent the mechanical reaction stresses or forces necessary to hold the laminate without deformation; consequently, they are called hygrothermal residual stresses or forces. When only a temperature difference exists with no curvature, the above equation is simplified as follows:

$$\begin{aligned} \begin{Bmatrix} \sigma_x \\ \sigma_y \\ \tau_{xy} \end{Bmatrix}^{[k]} &= [\bar{Q}_{ij}]^{[k]} \begin{Bmatrix} \varepsilon_x^0 \\ \varepsilon_y^0 \\ \gamma_{xy}^0 \end{Bmatrix} - [\bar{Q}_{ij}]^{[k]} \begin{Bmatrix} \alpha_x \\ \alpha_y \\ \alpha_{xy} \end{Bmatrix}^{[k]} \Delta T \\ &= [\bar{Q}_{ij}]^{[k]} \begin{Bmatrix} \varepsilon_x^0 \\ \varepsilon_y^0 \\ \gamma_{xy}^0 \end{Bmatrix} - \{\xi^T\}^{[k]} \Delta T \end{aligned} \quad (4.84)$$

For the symmetric laminate without bending moment, we have  $[B] = \{\kappa\} = 0$ . When there is no applied force and hygroscopic swelling ( $\Delta C = \{N\} = 0$ ), equation (4.22) reduces

$$[A]\{\varepsilon^0\} = \{N^T\} = \{\Gamma^T\}\Delta T$$

or,

$$\{\varepsilon^0\} = [a]\{\Gamma^T\}\Delta T = \{\alpha\}\Delta T \quad (4.85)$$

The laminate strain  $\{\varepsilon^0\}$  is simply the product of the laminate CTE,  $\{\alpha\}$ , and the temperature difference  $\Delta T$  when there is *only a temperature difference* without any applied force, moment, or hygroscopic swelling.

#### EXAMPLE 4.7

Determine the stresses, strains, and laminate engineering coefficients of thermal expansion when the laminate of example 4.1 is subjected to the temperature

change of  $\Delta T = 155.6^\circ\text{C}$  ( $= -280^\circ\text{F}$ ) without any mechanical forces or moments. The principal CTEs of the material are

$$\begin{aligned}\alpha_1 &= -0.36 \times 10^{-6}(1/\text{ }^\circ\text{C}) (= -0.20 \times 10^{-6}(1/\text{ }^\circ\text{F})) \\ \alpha_2 &= 28.80 \times 10^{-6}(1/\text{ }^\circ\text{C}) (= 16.0 \times 10^{-6}(1/\text{ }^\circ\text{F})) \\ \alpha_{12} &= 0\end{aligned}$$

### Solution

From the results of example 4.1, we have  $\bar{Q}_{ij}$  in table 4.1.

The CTEs in the global coordinates are listed in table 4.8.

Then the values of

$$\{\xi\}^{[k]} = [\bar{Q}_{ij}]^{[k]} \begin{Bmatrix} \alpha_x \\ \alpha_y \\ \alpha_{xy} \end{Bmatrix}^{[k]} \quad (\text{ply thermal influence coefficients})$$

can be calculated. For example,

$$\begin{aligned}\xi_x^{[0]} &= \bar{Q}_{11}^{[0]}\alpha_x^{[0]} + \bar{Q}_{12}^{[0]}\alpha_y^{[0]} + \bar{Q}_{16}^{[0]}\alpha_{xy}^{[0]} = (130.8 \times 10^9 \text{ N/m}^2) \times (-0.36 \times 10^{-6}/\text{ }^\circ\text{C}) \\ &\quad + (2.96 \times 10^9 \text{ N/m}^2) \times (28.80 \times 10^{-6}/\text{ }^\circ\text{C}) + 0 = 38.16 \times 10^3(\text{N/m}^2 \text{ }^\circ\text{C})\end{aligned}$$

Similarly, other components of the ply thermal influence coefficients can be obtained as shown in table 4.9.

Then the laminate thermal influence coefficients are calculated by equation (4.19c),

$$\{\Gamma^T\} = \int_{-(h/2)}^{(h/2)} [\bar{Q}_{ij}] \begin{Bmatrix} \alpha_x \\ \alpha_y \\ \alpha_{xy} \end{Bmatrix} dz = \sum_{k=1}^n [\bar{Q}_{ij}]^{[k]} \begin{Bmatrix} \alpha_x \\ \alpha_y \\ \alpha_{xy} \end{Bmatrix}^{[k]} (z_k - z_{k-1}) = \sum_{k=1}^n \{\xi\}^{[k]} t_{\text{ply}}^{[k]}$$

**Table 4.8 CTEs in the Global Coordinates of Example 4.8 ( $10^{-6}/\text{ }^\circ\text{C}$ )**

	$\alpha_x^{[k]}$	$\alpha_y^{[k]}$	$\alpha_{xy}^{[k]}$
$0^\circ$	-0.36	28.80	0
$+45^\circ$	14.22	14.22	-29.16
$-45^\circ$	14.22	14.22	29.16

**Table 4.9 Ply Thermal Influence Coefficients  $\{\xi\}^{[k]}$  ( $10^3 \text{ N/m}^2 \text{ }^\circ\text{C}$ )**

	$\xi_x^{[k]}$	$\xi_y^{[k]}$	$\xi_{xy}^{[k]}$
$0^\circ$	38.16	304.2	0
$+45^\circ$	170.6	170.6	-132.5
$-45^\circ$	170.6	170.6	132.5

For example,

$$\begin{aligned}\Gamma_x^T &= 2 \times (38.16 \times 10^3 + 170.6 \times 10^3 + 170.6 \times 10^3) \text{N/m}^2 \text{ } ^\circ\text{C} \times 0.135 \times 10^{-3} \text{ m} \\ &= 102.4 \text{ N/m } ^\circ\text{C}\end{aligned}$$

Similarly, we can calculate

$$\begin{aligned}\Gamma_y^T &= 174.2 \text{ N/m } ^\circ\text{C} \\ \Gamma_{xy}^T &= 0\end{aligned}$$

Since we have matrix  $[a]$  from the results of example 4.1,

$$\begin{aligned}a_{11} &= 21.40 \times 10^{-9} \text{ m/N} \\ a_{22} &= 48.15 \times 10^{-9} \text{ m/N} \\ a_{66} &= 50.23 \times 10^{-9} \text{ m/N} \\ a_{12} &= -14.37 \times 10^{-9} \text{ m/N} \\ a_{16} = a_{26} &= 0\end{aligned}$$

we can calculate the coefficients of laminate thermal expansion using equation (4.81) or (4.82):

$$\{\alpha\} = [a] \int_{-(h/2)}^{(h/2)} [\bar{Q}_{ij}] \left\{ \begin{array}{c} \alpha_x \\ \alpha_y \\ \alpha_{xy} \end{array} \right\} dz = [a] \sum_{k=1}^n \xi_x^{[k]} t_{\text{ply}}^{[k]} = [a]\{\Gamma^T\}$$

$$\begin{aligned}\alpha_x &= a_{11}\Gamma_x^T + a_{12}\Gamma_y^T + a_{16}\Gamma_{xy}^T \\ &= 21.40 \times 10^{-9} \text{ m/N} \times 102.4 \text{ N/m } ^\circ\text{C} - 14.37 \times 10^{-9} \text{ m/N} \times 174.2 \text{ N/m } ^\circ\text{C} \\ &= -0.312 \times 10^{-6} (1/^\circ\text{C})\end{aligned}$$

Similarly, we have

$$\begin{aligned}\alpha_y &= 6.921 \times 10^{-6} (1/^\circ\text{C}) \\ \alpha_{xy} &= 0 \\ \varepsilon_x^0 &= (-0.312 \times 10^{-6}/^\circ\text{C}) \times (-155.6^\circ\text{C}) = 48.6 \times 10^{-6} \text{ m/m} = 48.6 \mu\text{S} \\ \varepsilon_y^0 &= (6.921 \times 10^{-6}/^\circ\text{C}) \times (-155.6^\circ\text{C}) = -1077 \times 10^{-6} \text{ m/m} = -1077 \mu\text{S} \\ \gamma_{xy}^0 &= 0\end{aligned}$$

The stresses in the plies with respect to the global axis can be calculated using equation (4.84). For example, the stress of the  $0^\circ$  ply in the  $x$ -direction is

$$\begin{aligned}\sigma_x^{[0]} &= 130.8 \times 10^9 \text{ N/m}^2 \times 48.6 \times 10^{-6} + 2.96 \times 10^9 \text{ N/m}^2 \times (-1077 \times 10^{-6}) \\ &\quad - 38.16 \times 10^3 \text{ N/m}^2 \text{ } ^\circ\text{C} \times (-155.6^\circ\text{C}) = 9.12 \times 10^6 \text{ N/m}^2 = 9.12 \text{ MPa}\end{aligned}$$

where the superscript  $[0]$  of  $\sigma_x^{[0]}$  represents the tensile stress of the  $0^\circ$  ply in the  $x$ -direction. Similarly, we can calculate the other components of the thermal stresses in the laminate with respect to the global axis, as listed in table 4.10.

**Table 4.10 Thermal Stresses in the Laminate Example 4.7 (MPa)**

	$\sigma_x^{[k]}$	$\sigma_y^{[k]}$	$\tau_{xy}^{[k]}$
0°	9.12	36.0	0.0
+45°	-4.56	-18.0	-51.5
-45°	-4.56	-18.0	51.5

**EXAMPLE 4.8**

Determine the curvatures of a two-layer asymmetric [0/90]<sub>T</sub> laminate after it is cooled down from the curing temperature, 176.7°C (350°F), to room temperature, 21.1°C (70°F). The principal CTEs of the material are

$$\alpha_1 = -0.36 \times 10^{-6}(1/\text{°C})$$

$$\alpha_2 = 28.8 \times 10^{-6}(1/\text{°C})$$

$$\alpha_{12} = 0$$

The material properties of the unidirectional carbon-fiber epoxy composite are

$$E_1 = 130 \text{ GPa}$$

$$E_2 = 10.5 \text{ GPa}$$

$$\nu_{12} = 0.28$$

$$G_{12} = 6.0 \text{ GPa}$$

$$t_{\text{ply}} = 0.135 \text{ mm}$$

**Solution**

Using the results of example 4.7, we can calculate the stiffness values of table 4.11. Then we can calculate the ply and laminate thermal influence coefficients  $\{\xi\}$ , as listed in table 4.12.

Then the laminate thermal influence coefficients are calculated as follows:

$$\Gamma_x^T = 46.26 \text{ N/m } \text{°C}$$

$$\Gamma_y^T = 46.26 \text{ N/m } \text{°C}$$

$$\Gamma_{xy}^T = 0$$

**Table 4.11 Stiffness Constants of Example 4.8**

$ij$	$A_{ij}$ (MN/m)	$B_{ij}$ (N)	$D_{ij}$ (Nm)
11	19.09	-1094	0.1131
22	19.09	+1094	0.1131
12	0.799	0	0.0047
66	1.62	0	0.0096
16	0	0	0
26	0	0	0

**Table 4.12 Ply Thermal Influence Coefficients  $\{\xi\}^{[k]}$  of Example 4.8 ( $10^3 \text{N/m}^2 \cdot {}^\circ\text{C}$ )**

	$\xi_x^{[k]}$	$\xi_y^{[k]}$	$\xi_{xy}^{[k]}$
0°	38.16	304.2	0
90°	304.2	38.16	0

From equation (4.28b), we have

$$\{\Lambda^T\} = \int_{-(h/2)}^{(h/2)} [\bar{Q}_{ij}] \begin{Bmatrix} \alpha_x \\ \alpha_y \\ \alpha_{xy} \end{Bmatrix} z dz = \frac{1}{2} \sum_{k=1}^n \{\xi\}^{[k]} (z_k^2 - z_{k-1}^2)$$

$$\begin{aligned} \Lambda_x &= (38.16 \times 10^3) \times (-0.0091 \times 10^{-6}) + (304.2 \times 10^3) \times (0.0091 \times 10^{-6}) \\ &= 2.421 \times 10^{-3} \text{ N/}{}^\circ\text{C} \end{aligned}$$

$$\Lambda_y = -2.421 \times 10^{-3} \text{ N/}{}^\circ\text{C}$$

$$\Lambda_{xy} = 0$$

From equations (4.22) and (4.30), we have

$$\{N\} = [A]\{\varepsilon^0\} + [B]\{\kappa\} - \{\Gamma^T\}\Delta T = 0$$

$$\{M\} = [B]\{\varepsilon^0\} + [D]\{\kappa\} - \{\Lambda^T\}\Delta T = 0$$

To solve the above equations simultaneously, we can use equations (4.33c), (4.35b), and (4.36):

$$\{\kappa\} = -[D^*]^{-1} ([B]\{\Gamma^{*T}\} - \{\Lambda^T\})\Delta T$$

where

$$\begin{aligned} [D^*] &= [D] - [B][A]^{-1}[B] \\ \{\Gamma^{*T}\} &= [A]^{-1}\{\Gamma^T\} \end{aligned}$$

After numerical (but tedious) calculation, we can obtain

$$\begin{aligned} \kappa_x &= -15.2 \text{ (1/m)} \\ \kappa_y &= 15.2 \text{ (1/m)} \\ \kappa_{xy} &= 0 \\ \varepsilon_x^0 &= -1200 \mu\text{S} \\ \varepsilon_y^0 &= -1200 \mu\text{S} \\ \gamma_{xy}^0 &= 0 \end{aligned}$$

This problem can be solved also directly from equations (4.22) and (4.30),

$$A_{11}\varepsilon_x^0 + A_{12}\varepsilon_y^0 + A_{16}\gamma_{xy}^0 + B_{11}\kappa_x + B_{12}\kappa_y + B_{16}\kappa_{xy} = N_x^T$$

$$A_{12}\varepsilon_x^0 + A_{22}\varepsilon_y^0 + A_{26}\gamma_{xy}^0 + B_{12}\kappa_x + B_{22}\kappa_y + B_{26}\kappa_{xy} = N_y^T$$

$$A_{16}\varepsilon_x^0 + A_{26}\varepsilon_y^0 + A_{66}\gamma_{xy}^0 + B_{16}\kappa_x + B_{26}\kappa_y + B_{66}\kappa_{xy} = N_{xy}^T$$

$$B_{11}\varepsilon_x^0 + B_{12}\varepsilon_y^0 + B_{16}\gamma_{xy}^0 + D_{11}\kappa_x + D_{12}\kappa_y + D_{16}\kappa_{xy} = M_x^T$$

$$B_{12}\varepsilon_x^0 + B_{22}\varepsilon_y^0 + B_{26}\gamma_{xy}^0 + D_{12}\kappa_x + D_{22}\kappa_y + D_{26}\kappa_{xy} = M_y^T$$

$$B_{16}\varepsilon_x^0 + B_{26}\varepsilon_y^0 + B_{66}\gamma_{xy}^0 + D_{16}\kappa_x + D_{26}\kappa_y + D_{66}\kappa_{xy} = M_{xy}^T$$

or

$$19.09 \times 10^6 \varepsilon_x^0 + 0.799 \times 10^6 \varepsilon_y^0 - 1.094 \times 10^3 \kappa_x = -25.7 \times 280 \quad (\text{A})$$

$$0.799 \times 10^6 \varepsilon_x^0 + 19.09 \times 10^6 \varepsilon_y^0 + 1.094 \times 10^3 \kappa_y = -25.7 \times 280 \quad (\text{B})$$

$$1.62 \times 10^6 \gamma_{xy} = 0 \quad (\text{C})$$

$$-1.094 \times 10^3 \varepsilon_x^0 + 0.1131 \kappa_x + 0.0047 \kappa_y = -1.345 \times 10^{-3} \times 280 \quad (\text{D})$$

$$1.094 \times 10^3 \varepsilon_y^0 + 0.0047 \kappa_x + 0.1131 \kappa_y = 1.345 \times 10^{-3} \times 280 \quad (\text{E})$$

$$0.0096 \kappa_{xy} = 0 \quad (\text{F})$$

Although solving equations (A)–(F) seems to be tedious, we have  $\varepsilon_x^0 = \varepsilon_y^0$  and  $\kappa_x = -\kappa_y$  from the stacking sequence of  $[0/90]_T$ . Then the above equations are easily solved to give the previous results. For more complicated problems, the program *Axiomatic CLPT* attached to this book may be used.

## 4.10 Properties of Laminates through Thickness Direction

Up to now, we have developed the composite lamination theory based on the assumption that the interlaminar shear strains  $\gamma_{xz}$  and  $\gamma_{yz}$  are zero, and the displacement  $w$  is a function of  $x$  and  $y$  only (Kirchhoff's hypothesis for plates),

$$w = w(x, y) \quad (4.2)$$

For the effective properties of laminates through their thickness, we may combine lamination theory with the three-dimensional Hooke's law, which relieves the Kirchhoff's hypothesis (Herakovich, 1998):

$$w = w(x, y, z) \quad (4.86)$$

When the symmetric laminate is subjected to only  $N_x$ , with all other applied forces and moments being zero, the through-thickness strain  $\varepsilon_z^{[k]}$  is constant in any  $k$ th layer, which can be calculated from the three-dimensional generalized Hooke's law and the compliance matrix of equation (3.111):

$$\varepsilon_z^{[k]} = \bar{S}_{31}^{[k]} \sigma_x^{[k]} + \bar{S}_{32}^{[k]} \sigma_y^{[k]} + \bar{S}_{36}^{[k]} \tau_{xy}^{[k]} \quad (4.87)$$

where  $\bar{S}_{ij}^{[k]}$  are the elements of compliance matrix of the  $k$ th layer in equation (3.111), which is the inverse of  $[\bar{C}_{ij}]^{[k]}$  in equation (3.110). The laminate strains  $\{\varepsilon_x^0\}$  are

calculated from equation (4.47) as

$$\begin{Bmatrix} \varepsilon_x^0 \\ \varepsilon_y^0 \\ \gamma_{xy}^0 \end{Bmatrix} = \begin{Bmatrix} a_{11} \\ a_{12} \\ a_{16} \end{Bmatrix} N_x \quad (4.88)$$

Then the plane stresses appearing in equation (4.87) can be calculated from equation (3.140) as

$$\begin{Bmatrix} \sigma_x \\ \sigma_y \\ \tau_{xy} \end{Bmatrix}^{[k]} = \begin{bmatrix} \bar{Q}_{11} & \bar{Q}_{12} & \bar{Q}_{16} \\ \bar{Q}_{12} & \bar{Q}_{22} & \bar{Q}_{26} \\ \bar{Q}_{16} & \bar{Q}_{26} & \bar{Q}_{66} \end{bmatrix}^{[k]} \begin{Bmatrix} a_{11} \\ a_{12} \\ a_{16} \end{Bmatrix} N_x \quad (4.89)$$

Substituting equation (4.89) into (4.87) yields

$$\varepsilon_z^{[k]} = \{\bar{S}_{31} \bar{S}_{32} \bar{S}_{36}\}^{[k]} \begin{bmatrix} \bar{Q}_{11} & \bar{Q}_{12} & \bar{Q}_{16} \\ \bar{Q}_{12} & \bar{Q}_{22} & \bar{Q}_{26} \\ \bar{Q}_{16} & \bar{Q}_{26} & \bar{Q}_{66} \end{bmatrix}^{[k]} \begin{Bmatrix} a_{11} \\ a_{12} \\ a_{16} \end{Bmatrix} N_x \quad (4.90)$$

The average through-thickness strain,  $\bar{\varepsilon}_z$ , can be calculated as follows:

$$\bar{\varepsilon}_z = \frac{1}{h} \int_{-h/2}^{h/2} \varepsilon_z^{[k]} dz = \sum_{k=1}^n \frac{t_{\text{ply}}^{[k]}}{h} \{\bar{S}_{31} \bar{S}_{32} \bar{S}_{36}\}^{[k]} \begin{bmatrix} \bar{Q}_{11} & \bar{Q}_{12} & \bar{Q}_{16} \\ \bar{Q}_{12} & \bar{Q}_{22} & \bar{Q}_{26} \\ \bar{Q}_{16} & \bar{Q}_{26} & \bar{Q}_{66} \end{bmatrix}^{[k]} \begin{Bmatrix} a_{11} \\ a_{12} \\ a_{16} \end{Bmatrix} N_x \quad (4.91)$$

where  $t_{\text{ply}}^{[k]}$  is the ply thickness.

For the symmetric laminate subjected to  $N_x$  only, with all other applied forces and moments being zero, we have the in-plane strains in the  $k$ th layer from equation (4.88). Now the through-thickness Poisson's ratio,  $\nu_{xz}$ , can be calculated:

$$\nu_{xz} = -\frac{\bar{\varepsilon}_z}{\varepsilon_x} \quad \text{when } N_x \neq 0 \quad (4.92)$$

or

$$\nu_{xz} = -\sum_{k=1}^n \frac{t_{\text{ply}}^{[k]}}{h a_{11}} \{\bar{S}_{31} \bar{S}_{32} \bar{S}_{36}\}^{[k]} \begin{bmatrix} \bar{Q}_{11} & \bar{Q}_{12} & \bar{Q}_{16} \\ \bar{Q}_{12} & \bar{Q}_{22} & \bar{Q}_{26} \\ \bar{Q}_{16} & \bar{Q}_{26} & \bar{Q}_{66} \end{bmatrix}^{[k]} \begin{Bmatrix} a_{11} \\ a_{12} \\ a_{16} \end{Bmatrix} \quad (4.93)$$

Similarly,  $\nu_{yz}$  can be calculated as follows:

$$\nu_{yz} = -\sum_{k=1}^n \frac{t_{\text{ply}}^{[k]}}{h a_{22}} \{\bar{S}_{31} \bar{S}_{32} \bar{S}_{36}\}^{[k]} \begin{bmatrix} \bar{Q}_{11} & \bar{Q}_{12} & \bar{Q}_{16} \\ \bar{Q}_{12} & \bar{Q}_{22} & \bar{Q}_{26} \\ \bar{Q}_{16} & \bar{Q}_{26} & \bar{Q}_{66} \end{bmatrix}^{[k]} \begin{Bmatrix} a_{21} \\ a_{22} \\ a_{26} \end{Bmatrix} \quad (4.94)$$

The approximate coefficient of thermal expansion (CTE) of a symmetric laminate with uniform temperature throughout the laminate can be derived similarly. The through-thickness CTE,  $\alpha_z$ , is defined as

$$\alpha_z = \frac{\Delta w}{h\Delta T} = \frac{1}{h\Delta T} \int_{-h/2}^{h/2} \varepsilon_z dz \quad (4.95)$$

The total strain  $\varepsilon_z$  is the sum of the mechanical and thermal strains. For the plane stress condition

$$\varepsilon_z^{[k]} = \bar{S}_{13}^{[k]} \sigma_x^{[k]} + \bar{S}_{23}^{[k]} \sigma_y^{[k]} + \bar{S}_{36}^{[k]} \tau_{xy}^{[k]} + \alpha_z^{[k]} \Delta T \quad (4.96)$$

Combining equations (4.95) and (4.96), we have

$$\alpha_z = \frac{1}{h\Delta T} \sum_{k=1}^n \left( \bar{S}_{13}^{[k]} \sigma_x^{[k]} + \bar{S}_{23}^{[k]} \sigma_y^{[k]} + \bar{S}_{36}^{[k]} \tau_{xy}^{[k]} + \alpha_z^{[k]} \Delta T \right) t_{\text{ply}}^{[k]} \quad (4.97)$$

Using the result of equations (4.84) and (4.85), the stresses in equation (4.97) are expressed as

$$\begin{aligned} \begin{Bmatrix} \sigma_x \\ \sigma_y \\ \tau_{xy} \end{Bmatrix}^{[k]} &= [\bar{Q}_{ij}]^{[k]} \begin{Bmatrix} \varepsilon_x^0 \\ \varepsilon_y^0 \\ \gamma_{xy}^0 \end{Bmatrix} - [\bar{Q}_{ij}]^{[k]} \begin{Bmatrix} \alpha_x \\ \alpha_y \\ \alpha_{xy} \end{Bmatrix} \Delta T \\ &= \begin{bmatrix} \bar{Q}_{11} & \bar{Q}_{12} & \bar{Q}_{16} \\ \bar{Q}_{12} & \bar{Q}_{22} & \bar{Q}_{26} \\ \bar{Q}_{16} & \bar{Q}_{26} & \bar{Q}_{66} \end{bmatrix}^{[k]} \left( \begin{Bmatrix} \alpha_x \\ \alpha_y \\ \alpha_{xy} \end{Bmatrix} - \begin{Bmatrix} \alpha_x \\ \alpha_y \\ \alpha_{xy} \end{Bmatrix} \right)^{[k]} \Delta T \end{aligned} \quad (4.98)$$

Finally, the warpage,  $w_0$ , which is the out-of-plane deformation, can be calculated by integrating equation (4.8) (curvature-deflection relations):

$$w_0 = -\frac{1}{2} (\kappa_x x^2 + \kappa_y y^2 + \kappa_{xy} xy) + \text{rigid body motion} \quad (4.99)$$

## 4.11 Concluding Remarks

The classical lamination theory (CLT) or classical lamination plate theory (CLPT) of multilayer composites is presented as the basis for stress and deformation analysis. It includes the effect of temperature change and moisture absorption. This classical theory assumes that the thickness of the each layer remain constant and does not consider the edge effect. Many examples are given to illustrate the application of the theory in analysis and design.

## Problems

- 4.1. Prove that the matrix  $[B]$  is identically zero, while matrices  $[A]$  and  $[D]$  are not zero when the stacking sequence of the plies is symmetric about the midplane of the laminate.

- 4.2.** Prove that the  $A_{11}$  of the quasi-isotropic laminate with  $2n$  equal-thickness plies and  $n$  equal angles between fiber orientations ( $n \geq 3$ ) is a constant independent of the arbitrary direction  $\phi$  from the global  $x$ -axis in the plane of the laminate.
- 4.3.** For symmetric laminates, prove that matrices  $[\Lambda]$  are identically zero.
- 4.4.** Prove equation (4.42).
- 4.5. (a)** Find the engineering constants  $E_x$ ,  $E_y$ ,  $\nu_{xy}$ ,  $G_{xy}$ ,  $\alpha_x$ ,  $\alpha_y$ ,  $\alpha_{xy}$  of  $[45]_T$ ,  $[\pm 45]_T$ , and  $[\pm 45]_S$ . Explain why the characteristics of the three laminates are different. The material properties of the unidirectional carbon-fiber epoxy composite are

$$\begin{aligned} E_1 &= 130 \text{ GPa}, & E_2 &= 10.5 \text{ GPa}, & \nu_{12} &= 0.28, & G_{12} &= 6.0 \text{ GPa}, \\ \alpha_1 &= -0.36 \times 10^{-6}/^\circ\text{C}, & \alpha_2 &= 28.8 \times 10^{-6}/^\circ\text{C}, & \alpha_{12} &= 0, \\ \beta_1 &\cong 0, & \beta_2 &= 0.44, & \beta_{12} &= 0, & t_{\text{ply}} &= 0.135 \text{ mm} \end{aligned}$$

- (b)** Express  $\alpha_x$  and  $\alpha_y$  of  $[\pm 45]_S$  in terms of the unidirectional material properties of  $E_1$ ,  $E_2$ ,  $\nu_{12}$ , and  $\alpha_2$  and show that they are much smaller than  $\alpha_2$ .
- 4.6.** A carbon-fiber epoxy composite laminate with stacking sequence  $[\pm 15]_T$  is subjected to biaxial forces  $N_x = N_y = 10^4 \text{ N/m}$  ( $N_{xy} = 0$ ). Find the resulting laminate curvatures and midplane strains. Also plot the resulting stresses with respect to the global coordinate. Use the material properties of problem 4.5.
- 4.7.** A company has hired you as a consultant in preparation for their next scientific expedition. They had a plate of carbon-fiber epoxy composite manufactured by another company. Unfortunately, the company that built the plate went bankrupt after a fire and cannot be contacted. The company that has hired you does not know what the lay-up of the plate is. You have been hired to figure out what the lay-up is. They have obtained the following information which you can use to figure out the lay-up:

1. The material was the same as problem 4.5.
2. The laminate was cured flat at  $176.7^\circ\text{C}$  and it remained flat as it cooled down to room temperature.
3. The measured laminate thickness is 0.81 mm.
4. All ply angles are in increments of  $5^\circ$ .
5. Several longitudinal tension tests (not to failure) were run on the plate.

The average results were:

$$\begin{aligned} E_x &= 71.5 \text{ GPa} \\ \nu_{xy} &= 0.203 \\ \eta_{xy,x} &= 0 \end{aligned}$$

A special bonding fixture was used to apply the following curvatures:

$$\begin{aligned} \kappa_x &= 10 \frac{1}{\text{m}} \\ \kappa_y &= 0 \\ \kappa_{xy} &= 0 \end{aligned}$$

and it was found that the following moments were applied to cause those curvatures:

$$M_x = 35.7 \text{ Nm/m}$$

$$M_y = 5.09 \text{ Nm/m}$$

$$M_{xy} = 9.76 \text{ Nm/m}$$

Use this information to determine the lay-up of the plate. Be explicit in explaining why you make certain assumptions and arrive at certain conclusions, and base these on provided facts. (The second part of the problem is continued in problem 5.7 of chapter 5.)

- 4.8.** Calculate the midplane strains and curvatures of the laminate with stacking sequence of  $[\pm 45]_T$  when the laminate was cured at  $121.1^\circ\text{C}$  and cooled to  $21.1^\circ\text{C}$ . The unidirectional ply properties (T300/5208) of the laminate are:

$$t_{\text{ply}} = 0.127 \text{ mm}, \quad E_1 = 132 \text{ GPa}, \quad E_2 = 10.8 \text{ GPa},$$

$$\nu_{12} = 0.24, \quad \nu_{23} = 0.59, \quad G_{12} = 5.65 \text{ GPa},$$

$$\alpha_1 = -0.77 \times 10^{-6}/^\circ\text{C}, \quad \alpha_2 = 25 \times 10^{-6}/^\circ\text{C},$$

$$\beta_1 = 0, \quad \beta_2 = 0.2$$

- 4.9.** Calculate the stresses and strains of the pressure vessel of example 4.3 when the stacking sequence of plies is  $[\pm 54.74]_S$  and the applied pressure is 1.0 MPa. Also repeat for the stacking sequence of  $[\pm 64.81]_S$ . Make a table that shows the axial and hoop strains with respect to the stacking angle  $\theta$  for the stacking sequence type of  $[\pm \theta]_S$ . Is there any stacking angle that gives zero strain both in the axial and hoop directions?
- 4.10.** A sandwich beam is composed of an upper carbon epoxy face ( $E_{c1} = 100 \text{ GPa}$ ,  $t_{f1} = 1 \text{ mm}$ ), a bottom glass epoxy face ( $E_{g1} = 50 \text{ GPa}$ ,  $t_{f2} = 1 \text{ mm}$ ), and center polyurethane foam core ( $E_c = 1.0 \text{ GPa}$ ,  $t_c = 50 \text{ mm}$ ).
- (a) Calculate the flexural rigidity  $D$  of the beam based on perfect bonding between the faces and the core.
  - (b) Calculate the flexural rigidity  $D$  of the beam without bonding between the faces and the core.
- 4.11.** Integrating the equilibrium equation in the  $z$ -direction, calculate the interlaminar shear stress  $\tau_{zx}$  in the core of a sandwich beam with respect to the  $z$ -axis measured from the midplane. The beam is composed of two faces of identical material (Young's modulus =  $E_f$ , thickness =  $t_f$ ) and a core (Young's modulus =  $E_c$ , thickness =  $t_c$ ) with respect to the distance  $z$  from the midplane when subjected to a bending moment  $M_x = Px$  ( $P$  = constant applied load,  $x$  = axis of the beam in the longitudinal direction).
- 4.12.** Express the elements of matrices  $[A]$ ,  $[B]$ , and  $[D]$  of  $[0/90]_T$  and  $[0/90]_S$  laminates in terms of the material stiffness  $Q_{ij}$  if all the plies have equal thickness  $t$ . Compare the differences of stiffness of the two stacking sequences.
- 4.13.** Show that the Poisson's ratio of the quasi-isotropic material is approximately 0.3.
- 4.14.** Derive equation (4.94).
- 4.15.** Draw  $\nu_{xz}$  for the two stacking sequences  $[\theta]_T$  and  $[\pm \theta]_S$  with respect to  $\theta$ . Use the material properties of T300/5208 in problem 4.8 with  $E_2 = E_3$ .

- 4.16.** Calculate  $\alpha_z$  for the stacking sequence  $[\pm 30]_S$ . Assume that the plate is heated from  $21.1^\circ\text{C}$  to  $121.1^\circ\text{C}$ . Use the material properties of T300/5208 in problem 4.8 with  $E_2 = E_3$ .
- 4.17.** A  $[\pm 45]_T$  antisymmetric carbon-fiber epoxy laminate was cooled down from the curing temperature of  $120^\circ\text{C}$  to the room temperature of  $20^\circ\text{C}$  and the following deformations were measured:

$$\begin{aligned}\varepsilon_x^0 &= \varepsilon_y^0 = -1.0 \times 10^{-3}, & \gamma_{xy} &= 0, \\ \kappa_x &= \kappa_y = 0, & \kappa_{xy} &= 2.5 \text{ m}^{-1}\end{aligned}$$

Compute the thermal residual stresses due to the temperature decrease. Use the material properties of problem 4.5.

- 4.18.** A  $[\pm 30]_S$  laminate of the same material as in problem 4.5 was cured at  $180^\circ\text{C}$  and cooled down to  $20^\circ\text{C}$  where it absorbed 0.5% moisture. Determine the hygrothermal residual stresses.
- 4.19.** A  $[\pm 30]_S$  laminate of the same material as in problem 4.8 is clamped on all sides to a rigid frame and undergoes a temperature change  $\Delta T = -100^\circ\text{C}$ . Determine the forces  $\{N\}$  developed.
- 4.20.** Find the thermal residual stresses and warpage  $w_0$  in example 4.8.
- 4.21.** Show that for a  $[\pm 45]_S$  angle-ply laminate, the in-plane lamina shear modulus  $G_{12}$  is related to the laminate modulus and Poisson's ratio as follows:

$$G_{12} = \frac{E_x}{2(1 + \nu_{xy})}$$

- 4.22.** Calculate the thermal residual stresses in the laminates of  $[0/90]_S$  and  $[\pm 45]_S$  in terms of the temperature difference  $\Delta T$  and the lamina mechanical and thermal properties.
- 4.23.** Modify your computer program to compute the midplane strains and curvature of the laminate under  $\{N\}$ ,  $\{M\}$ ,  $\Delta T$ , and  $\Delta C$ , as well as the stresses in the laminate axes.

## References

- Agarwal, B. D., and Broutman, L. J. 1990. *Analysis and Performance of Fiber Composites*, 2nd Ed., John Wiley & Sons, New York.
- Daniel, I. M., and Ishai, O. 1994. *Engineering Mechanics of Composite Materials*, Oxford University Press, Oxford.
- Herakovich, C. T. 1998. *Mechanics of Fibrous Composites*, John Wiley & Sons, New York.
- Jones, R. M. 1975. *Mechanics of Composite Materials*, McGraw-Hill, New York.
- Matthews, F. L., and Rawlings, R. D. 1994. *Composite Materials: Engineering and Science*, Chapman & Hall, New York.
- Vinson, J. R., and Sierakowski, R. L. 1986. *The Behavior of Structures Composed of Composite Materials*, Martinus Nijhoff Publishers, Dordrecht, The Netherlands.

## 5

# Failure Criteria for Composite Materials

### 5.1 Introduction

Products should be designed and manufactured to function as intended, safely and reliably, for the prescribed design lifetime and, at the same time, to compete successfully in the marketplace. Any change in the size, shape, or material properties of a machine or machine part that renders it incapable of performing its intended functional requirements must be regarded as a mechanical failure. Failure of a machine or machine part to function properly might be brought about by any one, or a combination, of many different responses to loads and environments while in service. For example, too much deformation (robot arms) or too little elastic deformation (archery bow) might produce failure. Progression of a crack due to fluctuating loads might lead to failure after a period of time if resulting excessive deflection or fracture of the part interferes with proper function.

There are many failure modes in composite structures such as force- and temperature-induced elastic deformation, yielding, brittle failure, fatigue, wear, corrosion, impact, and creep. Designers should be acquainted with the failure modes actually observed in the field and with the conditions leading to those failures because the strict liability concept of products generally prevails nowadays.

Since advanced composite structures have been used in aircraft and spacecraft, leisure goods, and accurate, fast machines, the design of composite structures may be generally divided into two categories: stiffness and strength designs. For the stiffness design, which is generally employed for the design of machinery, such as machine tools and robots, the accuracy and deformation or speed of operation are primary concerns, therefore, the stresses induced are usually far less than the strength of materials used. However, in the strength design employed for the design of, for example, aircraft, automobiles, and trains, the primary concern is to reduce the weight of the structure, therefore, the stresses in structures may be the same order of magnitude of material strength. Consequently, the appropriate selection of failure criteria for composite structures in the strength design is most important. This is a complicated task because the failure mechanism of composite structures is not fully understood yet. Moreover, composite structures with edges and holes may induce three-dimensional stress states.

In this chapter, failure criteria such as yielding, brittle failure, and crack propagation, which might lead to ultimate failure for composite structures,

as well as stress concentration around holes, are presented. Also the interlaminar stresses that lead to delamination at the edges of composite structures are discussed.

The impact and fatigue failures of composite structures are treated in chapter 10.

## 5.2 Ply Stresses

Since it is not possible to obtain strengths in all possible lamina orientations or for all combinations of laminae, the failure criterion should be obtained as the basic layer data, that is, ply data in the principal material coordinates. Therefore, the stresses obtained in the global coordinates should be transformed into the values in the principal material coordinates to check whether it is safe or not by the failure criterion.

The 2-D transformation equations for rotation about the  $x_3$ - (z-) axis of figure 3.13 are simplifications of equations (3.91) and (3.99), and we already have equations (3.122) and (3.127) for the transformation. Thus, the relationships between the stresses  $\sigma_x$ ,  $\sigma_y$ , and  $\tau_{xy}$  expressed in the global coordinates  $x$ ,  $y$ ,  $z$  (or laminate coordinates) and the stresses  $\sigma_1$ ,  $\sigma_2$ , and  $\sigma_6$  expressed in the principal material coordinates (or ply coordinates)  $x_1$ ,  $x_2$ ,  $x_3$  are as follows (the prime ('') in  $[T_1]'$  and  $[T_2]'$  is dropped for convenience from now on):

$$\begin{Bmatrix} \sigma_1 \\ \sigma_2 \\ \sigma_6 \end{Bmatrix} = [T_1] \begin{Bmatrix} \sigma_x \\ \sigma_y \\ \tau_{xy} \end{Bmatrix} \quad (5.1)$$

$$\begin{Bmatrix} \varepsilon_1 \\ \varepsilon_2 \\ \varepsilon_6 \end{Bmatrix} = [T_2] \begin{Bmatrix} \varepsilon_x \\ \varepsilon_y \\ \gamma_{xy} \end{Bmatrix} \quad (5.2)$$

$$[T_1] = \begin{bmatrix} m^2 & n^2 & 2mn \\ n^2 & m^2 & -2mn \\ -mn & mn & m^2 - n^2 \end{bmatrix} \quad (5.3)$$

$$[T_2] = \begin{bmatrix} m^2 & n^2 & mn \\ n^2 & m^2 & -mn \\ -2mn & 2mn & m^2 - n^2 \end{bmatrix} \quad (5.4)$$

where  $m = \cos \theta$  and  $n = \sin \theta$ .

We sometimes call the stresses  $\sigma_x$ ,  $\sigma_y$ , and  $\tau_{xy}$  the laminate stresses, and  $\sigma_1$ ,  $\sigma_2$ , and  $\sigma_6$  the ply stresses, because they are expressed in the laminate coordinates and in the ply coordinates, respectively.

### EXAMPLE 5.1

Calculate the ply stresses (stresses expressed in the principal material axes  $x_1$ ,  $x_2$ ,  $x_3$ , or simply ply axes) of the composite laminate with stacking sequence  $[0/\pm 45]_S$  of example 4.1 when the laminate is subjected to  $N_x = 10^4 \text{ N/m}$  ( $N_y = N_{xy} = 0$ ).

**Table 5.1 Ply Stresses Expressed in the Principal Material (or Ply) Axes of Example 5.1 (MPa)**

	$\sigma_1^{[k]}$	$\sigma_2^{[k]}$	$\tau_{12}^{[k]}$
0°	27.6	-0.89	0.00
45°	4.68	0.47	2.14
-45°	4.68	0.47	2.14

**Solution**

Using the results of stresses of each ply expressed in the global (or laminate) axes in table 4.2 of example 4.2, we can calculate the ply stresses expressed in the principal material (or global) axes.

For example, the ply stresses of a +45° ply in the fiber direction  $\sigma_1^{[45]}$  is calculated as follows:

$$\begin{aligned}\sigma_1^{[45]} &= (\cos 45^\circ)^2 \sigma_x^{[45]} + (\sin 45^\circ)^2 \sigma_y^{[45]} + 2(\cos 45^\circ)(\sin 45^\circ) \tau_{xy}^{[45]} \\ &= \left(\frac{\sqrt{2}}{2}\right)^2 \times 4.73 \text{ MPa} + \left(\frac{\sqrt{2}}{2}\right)^2 \times 0.43 \text{ MPa} + 2\left(\frac{\sqrt{2}}{2}\right)\left(\frac{\sqrt{2}}{2}\right) \times 2.10 \text{ MPa} \\ &= 4.68 \text{ MPa}\end{aligned}$$

By the same method, we can calculate other components of the ply stresses:

$$\sigma_2^{[45]} = 0.47 \text{ MPa}$$

$$\sigma_6^{[45]} = -2.14 \text{ MPa}$$

Table 5.1 shows the ply stresses expressed in the principal material (or ply) axes.

**EXAMPLE 5.2**

Calculate the ply strain of  $\varepsilon_1^{[45]}$  in the principal material axes  $x_1, x_2, x_3$  under the load  $N_x = 10^4 \text{ N/m}$  ( $N_y = N_{xy} = 0$ ) when the composite laminate has the stacking sequence [0/+45]S, as in example 5.1.

**Solution**

Since we have the laminate strains expressed in the global coordinates (or laminate axes  $x, y, z$ ) from example 4.1, we can transform the laminate strains to obtain the ply strains using equation (5.2). Since the midplane strains from example 4.1 are

$$\varepsilon_x^0 = 214 \mu\text{s}$$

$$\varepsilon_y^0 = -144 \mu\text{s}$$

$$\gamma_{xy}^0 = 0 \mu\text{s}$$

For example, the strain of a 45° ply in the fiber direction  $\varepsilon_1^{[45]}$  is

$$\begin{aligned}\varepsilon_1^{[45]} &= (\cos 45^\circ)^2 \varepsilon_x^{[45]} + (\sin 45^\circ)^2 \varepsilon_y^{[45]} + (\cos 45^\circ)(\sin 45^\circ) \gamma_{xy}^{[45]} \\ &= (\cos 45^\circ)^2 (\varepsilon_x^0) + (\sin 45^\circ)^2 (\varepsilon_y^0) + (\cos 45^\circ)(\sin 45^\circ) (\gamma_{xy}^0) \\ &= \left(\frac{\sqrt{2}}{2}\right)^2 \times 214 \mu\text{S} + \left(\frac{\sqrt{2}}{2}\right)^2 \times (-144) \mu\text{S} + \left(\frac{\sqrt{2}}{2}\right) \left(\frac{\sqrt{2}}{2}\right) \times 0 \mu\text{S} \\ &= 35 \mu\text{S}\end{aligned}$$

The other method to calculate the ply strains is to utilize the results of example 5.1.

Since we have the reduced stiffness in the principal material axes from the results of example 4.1, the ply strains in the principal material axes can be calculated directly:

$$Q_{11} = 130.8 \text{ GPa}$$

$$Q_{22} = 10.6 \text{ GPa}$$

$$Q_{12} = 2.96 \text{ GPa}$$

$$Q_{66} = 6.0 \text{ GPa}$$

From  $[S_{ij}] = [Q_{ij}]^{-1}$

$$S_{11} = \frac{Q_{22}}{Q_{11}Q_{22} - Q_{12}^2} = 7.69 \times 10^{-12} \text{ m}^2/\text{N}$$

$$S_{22} = \frac{Q_{11}}{Q_{11}Q_{22} - Q_{12}^2} = 94.9 \times 10^{-12} \text{ m}^2/\text{N}$$

$$S_{12} = -\frac{Q_{12}}{Q_{11}Q_{22} - Q_{12}^2} = -2.15 \times 10^{-12} \text{ m}^2/\text{N}$$

$$S_{66} = \frac{1}{Q_{66}} = 166.7 \times 10^{-12} \text{ m}^2/\text{N}$$

$$S_{16} = S_{26} = 0$$

Therefore, the strain in the fiber direction of a 45° ply, for example, is

$$\begin{aligned}\varepsilon_1^{[45]} &= S_{11}\sigma_1^{[45]} + S_{12}\sigma_2^{[45]} + S_{16}\sigma_6^{[45]} \\ &= (7.69 \times 10^{-12} \text{ m}^2/\text{N}) \times (4.68 \times 10^6 \text{ N/m}^2) \\ &\quad + (-2.15 \times 10^{-12} \text{ m}^2/\text{N}) \times (0.47 \times 10^6 \text{ N/m}^2) + 0 = 35 \mu\text{S}\end{aligned}$$

### 5.3 Composite Laminate Stresses around a Hole

The presence of a notch in a stressed member creates highly localized stresses at the root of the notch. The ratio of the maximum stress at the notch root to the nominal stress is called the theoretical stress concentration factor  $K_t$ . We call it theoretical because the yielding for ductile material or notch sensitivity for material under a dynamic load is not considered.

When a composite structure is constructed by joining separately fabricated parts by a mechanical joining method, several holes for bolting or riveting should be drilled or bored. Therefore, stress estimation for the plate with holes is very important. Although few analytic solutions are possible for the stress calculation of a composite plate with holes, the analytical solutions are seldom possible due to the three-dimensional nature of the stress. When a uniaxial tensile stress  $\sigma$  is applied to the plate far from the hole of radius  $a$ , as shown in figure 5.1, the tangential stress  $\sigma_x$  at the horizontal radius ( $\theta = 90^\circ$ ) of the hole is much higher than the nominal stress  $\sigma$ . In this case, the hole stress concentration factor  $K_t$  at  $\theta = 90^\circ$  and  $r = a$  is defined as

$$K_t(a, 90^\circ) = \frac{\sigma_x(a, 90^\circ)}{\sigma} \quad (5.5)$$

The stress concentration factor  $K_t(a, \theta)$  for an infinite wide isotropic plate with a hole at the hole radius is expressed as (Timoshenko and Goodier, 1970)

$$K_t(a, \theta) = \frac{\sigma_\theta}{\sigma} = 1 - 2 \cos 2\theta \quad (5.6)$$

Therefore, the stress concentration factor  $K_t(a, \theta)$  is 3 at the horizontal radius ( $\theta = 90^\circ$ ). The stress concentration factor for other geometry, such as finite width, compared with the hole size, can be found in design books (e.g., Shigley et al., 2004).

For a symmetric laminated plate with orthotropic properties, the stress concentration factor  $K_t(a, \theta)$  at a hole radius that is small compared with the plate width is expressed as (Lekhnitskii, 1963)

$$K_t(a, \theta) = \frac{\bar{\sigma}_\theta}{\sigma} = \frac{-K \cos^2 \theta + (1+n) \sin^2 \theta}{\sin^4 \theta - m \sin^2 \theta \cos^2 \theta + K^2 \cos^4 \theta} \quad (5.7)$$

where  $\bar{\sigma}_\theta$  = average laminate tangential stress through thickness along the circumference of hole, and

$$K = \sqrt{\frac{E_x}{E_y}}$$

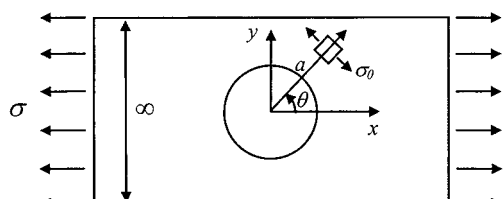


**Figure 5.1** Plate with a circular hole subjected to a uniform stress  $\sigma$ .

$$m = 2\nu_{xy} - \frac{E_x}{G_{xy}}$$

$$n = \sqrt{2K - m}$$

For isotropic materials, we have from equation (3.71)

$$\frac{E}{G} = 2(1 + \nu)$$

Therefore,  $m = -2$ ,  $K = 1$ , and  $n = 2$ , which simplifies equation (5.7) as

$$\frac{\bar{\sigma}_\theta}{\sigma} = 1 - 2 \cos 2\theta$$

Since this is of the same form as equation (5.6), we have proved that equation (5.7) is also valid for the isotropic case.

The stress concentration factor  $K_t$  at  $\theta = 90^\circ$  of a symmetric laminate plate with orthotropic in-plane stiffness properties is simplified as

$$K_t(a, 90^\circ) = \frac{\bar{\sigma}_\theta}{\sigma} = 1 + n = 1 + \sqrt{2K - m} = 1 + \sqrt{2 \sqrt{\frac{E_x}{E_y}} - 2\nu_{xy} + \frac{E_x}{G_{xy}}} \quad (5.8)$$

Using the results of equations (4.63), (4.64), (4.65), and (4.67), equation (5.8) can be expressed in terms of the in-plane stiffness  $A_{ij}$ :

$$K_t(a, 90^\circ) = 1 + \sqrt{\frac{2}{A_{22}}} \sqrt{\sqrt{A_{11}A_{22}} - A_{12} + \frac{A_{11}A_{22} - A_{12}^2}{2A_{66}}} \quad (5.9)$$

For example, the stress concentration factor  $K_t(a, 90^\circ)$  of a laminate composed of six plies, whose stacking sequence is  $[0/\pm 45]_S$ , can be calculated from the results of example 4.1 when the ply properties are

$$E_1 = 130 \text{ GPa}$$

$$E_2 = 10.5 \text{ GPa}$$

$$\nu_{12} = 0.28$$

$$G_{12} = 6.0 \text{ GPa}$$

$$t_{\text{ply}} = 0.135 \text{ mm}$$

From example 4.1, we have

$$a_{11} = 21.40 \times 10^{-9} \text{ m/N}$$

$$a_{22} = 48.15 \times 10^{-9} \text{ m/N}$$

$$a_{12} = -14.37 \times 10^{-9} \text{ m/N}$$

$$a_{66} = 50.23 \times 10^{-9} \text{ m/N}$$

$$a_{16} = a_{26} = 0$$

Therefore, from equations (4.63), (4.64), (4.65), and (4.67), we have

$$E_x = \frac{\bar{\sigma}_x}{\varepsilon_x^0} = \frac{1}{ha_{11}} = \frac{1}{6 \times 0.135 \times 10^{-3} \times 21.40 \times 10^{-9}} = 57.7 \text{ GPa}$$

$$E_y = \frac{\bar{\sigma}_y}{\varepsilon_y^0} = \frac{1}{ha_{22}} = \frac{1}{6 \times 0.135 \times 10^{-3} \times 48.15 \times 10^{-9}} = 25.6 \text{ GPa}$$

$$\nu_{xy} = -\frac{a_{12}}{a_{11}} = \frac{14.37 \times 10^{-9}}{21.40 \times 10^{-9}} = 0.672$$

$$G_{xy} = \frac{\bar{\tau}_{xy}}{\gamma_{xy}^0} = \frac{1}{ha_{66}} = \frac{1}{6 \times 0.135 \times 10^{-3} \times 50.23 \times 10^{-9}} = 24.6 \text{ GPa}$$

Substituting the above results into equation (5.8), we have the stress concentration factor  $K_t(a, 90^\circ)$  of 3.0. The stress concentration factor for the plate with stacking sequence  $[0/\pm 60]_S$  is also 3.0. The latter laminate is called quasi-isotropic, as explained in section 4.6.2. The stress concentration factor  $K_t(a, 90^\circ)$  with respect to stacking angles  $\theta$  for the stacking sequence type  $[0/\pm\theta]_S$  is listed in table 5.2.

Figure 5.2 shows the hole stress concentration factor  $K_t(a, 90^\circ)$  of composite laminate plates with stacking sequence  $[0/\pm\theta]_S$  versus the angle  $\theta$ . The value of  $K_t(a, 90^\circ)$  has the smallest value of 2.94 when  $\theta = 52^\circ$  in figure 5.2.

When an infinite-width composite laminate plate has a hole and is subjected to a load in the fiber direction and in the transverse direction, the average tangential stress  $\bar{\sigma}_\theta$  can be determined by separately calculating the stresses due to the axial and transverse loads and adding them (see problem 5.2). When the average laminate stress  $\bar{\sigma}_\theta$  is obtained from equation (5.7) in terms of the applied nominal stress  $\sigma$ , the ply stresses in the principal material coordinates are calculated by the following procedure:

1. Obtain the average laminate stresses in the global axes  $x, y, z$  shown in figure 5.1 using equation (3.121):

$$\begin{aligned}\bar{\sigma}_x &= \sin^2 \theta \times \bar{\sigma}_\theta \\ \bar{\sigma}_y &= \cos^2 \theta \times \bar{\sigma}_\theta \\ \bar{\tau}_{xy} &= -\sin \theta \cos \theta \times \bar{\sigma}_\theta\end{aligned}\tag{5.10}$$

**Table 5.2 Stress Concentration Factor  $K_t(a, 90^\circ)$  of Laminate with Stacking Sequence  $[0/\pm\theta]_S$**

$\theta$	$E_x$ (GPa)	$\nu_{xy}$	$E_y$ (GPa)	$G_{xy}$ (GPa)	$K$	$m$	$n$	$K_t$
$0^\circ$	130.0	0.28	10.5	6.0	3.52	-21.11	5.31	6.31
$15^\circ$	116.0	0.67	10.8	10.6	3.28	-9.60	4.02	5.02
$30^\circ$	79.7	1.01	13.7	19.9	2.41	-1.99	2.61	3.61
$45^\circ$	57.7	0.672	25.6	24.6	1.50	-1.00	2.00	3.00
$60^\circ$	51.7	0.298	51.7	19.9	1.00	-2.00	2.00	3.00
$75^\circ$	50.7	0.094	79.6	10.6	0.798	-4.60	2.49	3.49
$90^\circ$	50.6	0.036	90.6	6.0	0.747	-8.37	3.14	4.14

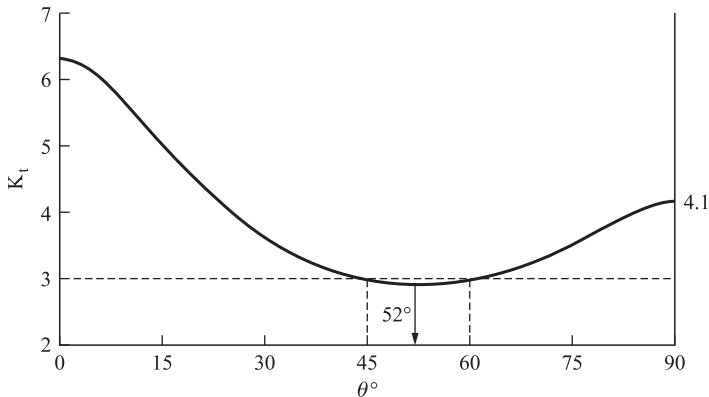


**Figure 5.2** Stress concentration factor  $K_t(a, 90^\circ)$  of composite laminate plates with a hole of radius  $a$  versus  $\theta$  of stacking sequence  $[0/\pm\theta]_s$ .

2. Obtain the average laminate strains in the global axes  $x, y, z$  using equation (4.52):

$$\varepsilon_\alpha^0 = h a_{\alpha\beta} \bar{\sigma}_\beta \quad (5.11)$$

3. Obtain the ply stresses in the global (or laminate) axes  $x, y, z$  using equation (4.15):

$$\sigma_\alpha^{[k]} = \bar{Q}_{\alpha\beta}^{[k]} \varepsilon_\beta^0 \quad (5.12)$$

4. Obtain the ply stresses and strains in the  $k$ th ply axes using equations (5.1) and (5.2):

$$\begin{Bmatrix} \sigma_1 \\ \sigma_2 \\ \sigma_6 \end{Bmatrix}^{[k]} = [T_1]^{[k]} \begin{Bmatrix} \sigma_x \\ \sigma_y \\ \tau_{xy} \end{Bmatrix}^{[k]} \quad (5.1)$$

$$\begin{Bmatrix} \varepsilon_1 \\ \varepsilon_2 \\ \varepsilon_6 \end{Bmatrix}^{[k]} = [T_2]^{[k]} \begin{Bmatrix} \varepsilon_x \\ \varepsilon_y \\ \gamma_{xy} \end{Bmatrix}^{[k]} \quad (5.2)$$

## 5.4 Failure Criteria of Composite Materials

Since the composite laminate may introduce coupling between normal stresses and shear stresses and/or normal strains and shear strains, even though its laminae have orthotropic properties, the failure criteria should be developed on the ply stress or strain basis because they are represented in the principal material coordinates. However, the failure criteria developed using the ply stress or strain in the principal material coordinates will be far from exact because the composite failure occurs in several different modes, such as fiber breakage, matrix cracking, and

ply delamination. The situation becomes more involved when the composite laminate is subjected to multiaxial loading.

Failure prediction of a structure is generally performed by comparing stresses (or strains) due to applied loads with the allowable strength (or strain) of the material. When biaxial or multiaxial stress fields are involved, an appropriate failure theory is used for this comparison. For isotropic materials that exhibit yielding, such as low-carbon steel or an aluminum alloy, either the Tresca theory (maximum shear stress theory) or the von Mises theory (distortional energy theory) is commonly used for design against yielding. For isotropic materials that do not exhibit yielding, such as cast iron, either the maximum normal stress theory (Rankine theory) or the modified Mohr theory is used for design against brittle failure (Shigley et al., 2004).

Since fiber-reinforced composite materials are not isotropic and do not show gross yielding, the failure theories developed for ductile isotropic metals are not directly applicable, but theories developed for brittle materials may have more relevance. Several failure theories have been proposed for composite materials, some of which are summarized in this section.

#### 5.4.1 Maximum Stress Criterion

The maximum stress criterion for unidirectional orthotropic materials is an extension of the maximum normal stress theory (Rankine theory) for isotropic brittle materials. The maximum stress failure criterion states that failure occurs whenever any one component of stress attains its maximum allowable value, independent of the values of all other components of stress. The allowable values must be determined from a series of tests in which the specimen is under a uniform, uniaxial state of stress. The notation used for the strength values includes superscripts *t* and *c* for tension and compression, respectively. The notation *X* indicates the ultimate normal stress magnitude in the fiber direction, while *Y* and *Z* indicate the ultimate normal stress magnitudes in the two transverse directions. The notation *S* indicates the ultimate shear stress in the plane of the lamina, while *Q* and *R* indicate the ultimate interlaminar shear stresses in the plane perpendicular to the lamina plane.

The design condition for the maximum stress failure criterion for each ply can be expressed as

$$\begin{aligned} X^c &< \sigma_1^{[k]} < X^t \\ Y^c &< \sigma_2^{[k]} < Y^t \\ Z^c &< \sigma_3^{[k]} < Z^t \\ |\sigma_4^{[k]} = \tau_{23}^{[k]}| &< Q \\ |\sigma_5^{[k]} = \tau_{13}^{[k]}| &< R \\ |\sigma_6^{[k]} = \tau_{12}^{[k]}| &< S \end{aligned} \quad (5.13)$$

The absolute sign is used for ultimate shear stress criteria because the shear strength in the principal material coordinate direction is independent of the sign of the shear stress (see problem 5.3).

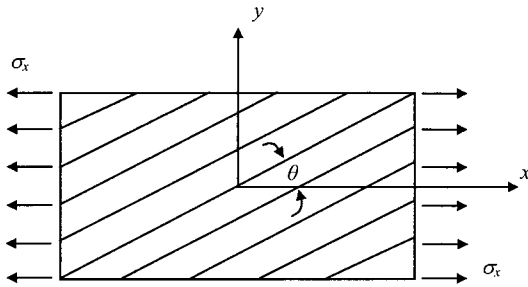


**Figure 5.3** Off-axis tensile coupon subjected to tensile stress  $\sigma_x$ .

When an off-axis unidirectional tensile coupon, shown in figure 5.3, is used to characterize the material properties, the maximum allowable normal stress  $\sigma_x$  can be expressed as a function of the in-plane strength parameters with respect to stacking angle  $\theta$ . Since the ply stresses in the principal material coordinates are expressed from equation (3.119) as

$$\begin{aligned}\sigma_1^{[\theta]} &= \sigma_x \cos^2 \theta \\ \sigma_2^{[\theta]} &= \sigma_x \sin^2 \theta \\ \sigma_6^{[\theta]} &= \tau_{12}^{[\theta]} = -\sigma_x \sin \theta \cos \theta\end{aligned}\quad (5.14)$$

substituting equation (5.14) into equation (5.13) yields

$$\begin{aligned}\frac{X^c}{\cos^2 \theta} < \sigma_x &< \frac{X^t}{\cos^2 \theta} \\ \frac{Y^c}{\sin^2 \theta} < \sigma_x &< \frac{Y^t}{\sin^2 \theta} \\ -\frac{S}{\sin \theta \cos \theta} < \sigma_x &< \frac{S}{\sin \theta \cos \theta}\end{aligned}\quad (5.15)$$

The conditions of equation (5.15) can be plotted on a graph of ultimate  $\sigma_x$  versus fiber stacking angle  $\theta$ , as shown in figure 5.4, when the material is unidirectional glass-fiber epoxy, whose strength values are listed as follows:

$$X^t = 1030 \text{ MPa}$$

$$X^c = -1030 \text{ MPa}$$

$$Y^t = 27.6 \text{ MPa}$$

$$Y^c = -138 \text{ MPa}$$

$$S = 41.3 \text{ MPa}$$

When the stacking angle  $\theta$  is very small, the coupon will fail in the fiber failure mode ( $X^t$ ). The coupon will fail in the transverse tension mode ( $Y^t$ ) when  $\theta$  is large, approaching  $90^\circ$ , while the coupon will fail in the shear failure mode ( $S$ ) when  $\theta$  is in the intermediate range.

The maximum stress failure criterion has limitations for predicting the failure stress in multiaxial stress states because of its lack of coupling or interaction effects

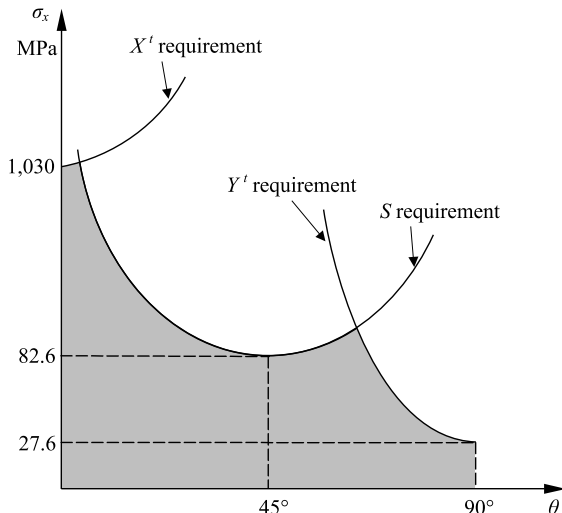


**Figure 5.4** Maximum axial stress  $\sigma_x$  versus fiber stacking angle  $\theta$  for the uniaxial glass-fiber epoxy coupon based on the maximum stress failure criterion (not to scale in  $\sigma_x$ -axis).

between the various components of stress. A multiaxial, far-field average stress state will result in considerably different local microlevel stresses (Herakovich, 1998).

One thing to remember about the test of figure 5.3 is that the measured stiffness is  $\bar{Q}_{11}$  rather than  $E_x$  when the specimen length is short because the end grip condition is  $\varepsilon_y = \gamma_{xy} = 0$  (see problem 5.4). The value of  $E_x$  is properly calculated from equation (4.54) only when the specimen length is long and slender (Jones, 1975).

### EXAMPLE 5.3

We obtained the ply stresses of a plate with stacking sequence  $[0/\pm 45]_S$  subjected to  $N_x = 10^4$  N/m, ( $N_y = N_{xy} = 0$ ) in example 5.1. Determine whether the laminate is safe by the maximum stress criterion when the strength properties of the materials are:

$$X^t = 1661 \text{ MPa}$$

$$X^c = -1698 \text{ MPa}$$

$$Y^t = 53.9 \text{ MPa}$$

$$Y^c = -221 \text{ MPa}$$

$$S = 105 \text{ MPa}$$

#### Solution

From the results of table 5.1, the ply stresses satisfy the following safety conditions:

$$-1698 < \sigma_1^{[k]} < 1661$$

$$-221 < \sigma_2^{[k]} < 53.9$$

$$-105 < \sigma_6^{[k]} < 105$$

Therefore, the laminate is safe under the applied load based on the maximum stress criterion.

#### EXAMPLE 5.4

Calculate the maximum in-plane load  $N_x$  that will cause the failure of the laminate with stacking sequence  $[0/\pm 45]_S$ . The stiffness properties of the unidirectional ply are

$$E_1 = 130 \text{ GPa}$$

$$E_2 = 10.5 \text{ GPa}$$

$$\nu_{12} = 0.28$$

$$G_{12} = 6.0 \text{ GPa}$$

$$t_{\text{ply}} = 0.135 \text{ mm}$$

#### Solution

From example 4.1, we have

$$a_{11} = 21.40 \times 10^{-9} \text{ m/N}$$

$$a_{22} = 48.15 \times 10^{-9} \text{ m/N}$$

$$a_{12} = -14.37 \times 10^{-9} \text{ m/N}$$

$$a_{66} = 50.23 \times 10^{-9} \text{ m/N}$$

$$a_{16} = a_{26} = 0$$

From equation (4.47)

$$\varepsilon_x^0 = a_{11}N_x = a_{11}(h\bar{\sigma}_x) = 0.81 \text{ mm} \times 21.40 \times 10^{-9} \text{ m/N} \times \bar{\sigma}_x$$

$$= 17.33 \times 10^{-6} \times \bar{\sigma}_x / \text{MPa}$$

$$\varepsilon_y^0 = a_{12}N_x = a_{11}(h\bar{\sigma}_x) = 0.81 \text{ mm} \times (-14.37) \times 10^{-9} \text{ m/N} \times \bar{\sigma}_x$$

$$= -11.64 \times 10^{-6} \times \bar{\sigma}_x / \text{MPa}$$

$$\gamma_{xy}^0 = a_{16}N_x = a_{16}(h\bar{\sigma}_x) = 0.81 \text{ mm} \times 0 \text{ m/N} \times \bar{\sigma}_x = 0$$

Table 4.1 shows numerical values for stiffness.

For example, the laminate stresses of the  $0^\circ$  ply are calculated from equation (4.15) when there is no curvature and hygrothermal effect:

$$\begin{aligned} \sigma_x^{[0]} &= [\bar{Q}_{ij}]^{[0]} \begin{Bmatrix} \varepsilon_x^0 \\ \varepsilon_y^0 \\ \gamma_{xy}^0 \end{Bmatrix} = \bar{Q}_{11}^{[0]} \varepsilon_x^0 + \bar{Q}_{12}^{[0]} \varepsilon_y^0 + \bar{Q}_{16}^{[0]} \gamma_{xy}^0 \\ &= [130.8 \times 17.33 + 2.96 \times (-11.64)] \times 10^3 \times \bar{\sigma}_x = 2.23 \times 10^6 \bar{\sigma}_x \end{aligned}$$

**Table 5.3 Ply Stresses in the Global Axes of Example 5.4 (MPa)**

	$0^\circ$	$45^\circ$	$-45^\circ$
$\sigma_x^{[k]}$	$2.23\bar{\sigma}_x$	$0.383\bar{\sigma}_x$	$0.383\bar{\sigma}_x$
$\sigma_y^{[k]}$	$-0.072\bar{\sigma}_x$	$0.036\bar{\sigma}_x$	$0.036\bar{\sigma}_x$
$\tau_{xy}^{[k]}$	0	$0.171\bar{\sigma}_x$	$-0.171\bar{\sigma}_x$

**Table 5.4 Ply Stresses in the Principal Material Coordinate of Example 5.4 (MPa)**

	$0^\circ$	$45^\circ$	$-45^\circ$
$\sigma_1^{[k]}$	$2.23\bar{\sigma}_x$	$0.381\bar{\sigma}_x$	$0.381\bar{\sigma}_x$
$\sigma_2^{[k]}$	$-0.072\bar{\sigma}_x$	$0.039\bar{\sigma}_x$	$0.039\bar{\sigma}_x$
$\sigma_6^{[k]}$	0	$0.174\bar{\sigma}_x$	$-0.174\bar{\sigma}_x$

**Table 5.5 Critical Stresses that will Induce Failure According to the Maximum Stress Criterion**

Failure condition	$\bar{\sigma}_x$ (MPa)		
	$0^\circ$	$45^\circ$	$-45^\circ$
$X^t$	745	4360	4360
$X^c$	-761	-4457	-4457
$Y^t$	-749	1382	1382
$Y^c$	3069	-5667	-5667
$S$	$\infty$	$\pm 603$	$\pm 603$

Other stress components of each ply listed in table 5.3 are calculated by the same routine.

The stresses of table 5.3 are transformed into the principal material coordinates using equation (5.1), as listed in table 5.4.

The failure (or critical) conditions using the maximum stress criterion are

$$X^t \text{criterion : } \sigma_1^{[k]} = 1661 \text{ MPa}$$

$$X^c \text{criterion : } \sigma_1^{[k]} = -1698 \text{ MPa}$$

$$Y^t \text{criterion : } \sigma_2^{[k]} = 53.9 \text{ MPa}$$

$$Y^c \text{criterion : } \sigma_2^{[k]} = -221 \text{ MPa}$$

$$S \text{ criterion : } |\tau_{12}^{[k]}| = 105 \text{ MPa}$$

The critical stresses  $\bar{\sigma}_x$  that satisfy the above equality conditions are listed in table 5.5.

The smallest value of  $\bar{\sigma}_x$  in table 5.5 is 603 MPa when the  $\pm 45^\circ$  plies fail by the shear failure mode according to the maximum stress criterion.

The in-plane load  $N_x$  per unit width of plate at the shear failure is

$$N_x = h\bar{\sigma}_x = 603 \text{ MPa} \times 0.81 \text{ mm} = 4.88 \times 10^5 \text{ N/m}$$

When the value of  $N_x$  reaches  $4.88 \times 10^5 \text{ N/m}$ , the  $\pm 45^\circ$  plies will fail first (first ply failure) in the shear failure mode, but the  $0^\circ$  plies may not fail by the maximum stress criterion. Whether the  $0^\circ$  plies fail may be determined by calculating the ply stresses again after setting  $\bar{Q}_{ij}^{[45^\circ]} = 0$ , and comparing the calculated ply stresses with the strengths of material.

### EXAMPLE 5.5

Determine a wrap angle  $\theta$  that gives the maximum sustainable pressure for a filament-wound composite pressure vessel that is fabricated by winding S-glass-fiber epoxy with a helical wrap angle  $\pm\theta$  from the vessel axis. Use the maximum stress criterion. The properties of S-glass-fiber epoxy are as follows:

$$E_1 = 43.5 \text{ GPa}, \quad E_2 = 11.5 \text{ GPa}, \quad v_{12} = 0.27, \quad G_{12} = 3.45 \text{ GPa}$$

$$X^t = 1540 \text{ MPa}, \quad X^c = 900 \text{ MPa}, \quad Y^t = 49 \text{ MPa}, \quad Y^c = 200 \text{ MPa}, \quad S = 69 \text{ MPa}$$

### Solution

For the maximum sustainable pressure, we have the stacking sequence  $[\pm 53.25]_S$ , which is almost the same as  $[\pm 54.74]_S$ , obtained from netting analysis in example 4.3. The detailed calculation for the above strains is left to problem 5.6.

#### 5.4.2 Maximum Strain Criterion

The maximum strain criterion states that failure occurs whenever any one component of strain reaches its maximum allowable value, independent of values of all other components of strain, which is the strain equivalent of the maximum stress theory. Using the superscripts  $t$  and  $c$  to denote tension and compression, respectively, the criterion is expressed as

$$\begin{aligned} \varepsilon_1^c &< \varepsilon_1^{[k]} < \varepsilon_1^t \\ \varepsilon_2^c &< \varepsilon_2^{[k]} < \varepsilon_2^t \\ \varepsilon_3^c &< \varepsilon_3^{[k]} < \varepsilon_3^t \\ -\Gamma_{23} &< \gamma_{23}^{[k]} < \Gamma_{23} \\ -\Gamma_{31} &< \gamma_{31}^{[k]} < \Gamma_{31} \\ -\Gamma_{12} &< \gamma_{12}^{[k]} < \Gamma_{12} \end{aligned} \tag{5.16}$$

where  $\varepsilon_i^c$  and  $\varepsilon_i^t$  represent the allowable compressive and tensile strains of the unidirectional composite lamina, and  $\Gamma_{ij}$  represent the allowable shear strains of the unidirectional composite lamina.

For a unidirectional lamina subjected to a uniaxial load at angle  $\theta$  to the fibers as shown in figure 5.3, the allowable stresses can be found from the maximum strain theory assuming the material properties are linearly elastic. Since the lamina is in the plane stress condition, the constitutive equation is, from equations (3.58), (3.59), and (3.63):

$$\begin{aligned}\varepsilon_1^{[k]} &= \frac{1}{E_1} \sigma_1^{[k]} - \frac{\nu_{21}}{E_2} \sigma_2^{[k]} = \frac{1}{E_1} (\sigma_1^{[k]} - \nu_{12} \sigma_2^{[k]}) \\ \varepsilon_2^{[k]} &= -\frac{\nu_{12}}{E_1} \sigma_1^{[k]} + \frac{1}{E_2} \sigma_2^{[k]} = \frac{1}{E_2} (-\nu_{21} \sigma_1^{[k]} + \sigma_2^{[k]}) \\ \varepsilon_6^{[k]} &= \gamma_{12}^{[k]} = \frac{1}{G_{12}} \sigma_6^{[k]} = \frac{1}{G_{12}} \tau_{12}^{[k]}\end{aligned}\quad (5.17)$$

Substituting equation (5.14) into equation (5.17),

$$\begin{aligned}\varepsilon_1^{[\theta]} &= \frac{1}{E_1} (\cos^2 \theta - \nu_{12} \sin^2 \theta) \sigma_x \\ \varepsilon_2^{[\theta]} &= \frac{1}{E_2} (-\nu_{21} \cos^2 \theta + \sin^2 \theta) \sigma_x \\ \varepsilon_6^{[\theta]} &= -\frac{1}{G_{12}} (\sin \theta \cos \theta) \sigma_x\end{aligned}\quad (5.18)$$

Substituting equation (5.18) into the first equation of equation (5.16), for example, gives

$$\frac{E_1 \varepsilon_1^c}{\cos^2 \theta - \nu_{12} \sin^2 \theta} < \sigma_x < \frac{E_1 \varepsilon_1^t}{\cos^2 \theta - \nu_{12} \sin^2 \theta} \quad (5.19)$$

Since we have assumed that the composite is linear elastic up to failure, we can put

$$\begin{aligned}E_1 \varepsilon_1^c &= X^c \\ E_1 \varepsilon_1^t &= X^t\end{aligned}\quad (5.20)$$

then equation (5.19) becomes

$$\frac{X^c}{\cos^2 \theta - \nu_{12} \sin^2 \theta} < \sigma_x < \frac{X^t}{\cos^2 \theta - \nu_{12} \sin^2 \theta} \quad (5.21a)$$

From the second and third relationships, we can derive

$$\frac{Y^c}{\sin^2 \theta - \nu_{21} \cos^2 \theta} < \sigma_x < \frac{Y^t}{\sin^2 \theta - \nu_{21} \cos^2 \theta} \quad (5.21b)$$

$$-\frac{S}{\sin \theta \cos \theta} < \sigma_x < \frac{S}{\sin \theta \cos \theta} \quad (5.21c)$$

The maximum strain failure criterion (i.e., equations (5.21a), (5.21b), and (5.21c)) gives similar predictions to the maximum stress failure criterion. As seen in equation (5.21), the maximum strain failure criterion allows for some interactions of stress components due to Poisson's effect. Since fiber-reinforced composite materials are usually brittle, the maximum strain failure criterion may predict better the failure of composite materials than the maximum stress failure criterion thanks to the inclusion of Poisson's effect. In fact, the maximum strain failure criterion is known to predict better than other failure criteria for the failure of brittle composite materials (Swanson, 1997), and major aircraft manufacturers employ this criterion for the design of their composite aircraft components.

#### 5.4.3 Tsai–Hill Criterion

The Tsai–Hill criterion is an extension of Hill's deviatoric or distortional energy criterion, and Hill's deviatoric criterion is also an extension of the yield criterion of von Mises.

For a three-dimensional state of stress in the principal material directions, the von Mises yield criterion for ductile materials has the form (Shigley et al., 2004)

$$(\sigma_1 - \sigma_2)^2 + (\sigma_2 - \sigma_3)^2 + (\sigma_3 - \sigma_1)^2 = 2S_y^2 \quad (5.22)$$

where  $S_y$  is the yield stress of materials.

Hill modified this criterion and proposed the following form for ductile materials with anisotropy (Hill, 1950):

$$F(\sigma_2 - \sigma_3)^2 + G(\sigma_3 - \sigma_1)^2 + H(\sigma_1 - \sigma_2)^2 + 2L\tau_{23}^2 + 2M\tau_{31}^2 + 2N\tau_{12}^2 = 1 \quad (5.23)$$

Equation (5.23) is no longer the distortional energy criterion, because distortion cannot be separated from dilatation in anisotropic materials.

Tsai adapted this criterion to a unidirectional lamina with transverse isotropy (figure 3.10). The material parameters in equation (5.23) can be calculated by conducting brain experiments (Gibson, 1994).

For pure shear loadings along the 23-, 31-, and 12-planes, equation (5.23) gives

$$\begin{aligned} 2L &= \frac{1}{Q^2} \\ 2M &= \frac{1}{R^2} \\ 2N &= \frac{1}{S^2} \end{aligned} \quad (5.24)$$

For a uniaxial loading along the 1-direction with  $\sigma_1 = X'$  and all other stresses equal to zero, equation (5.23) reduces to

$$G + H = \frac{1}{(X')^2} \quad (5.25)$$

Similarly, uniaxial loadings along the 2- and 3-directions give the equations

$$F + H = \frac{1}{(Y')^2} \quad (5.26)$$

$$F + G = \frac{1}{(Z^t)^2} \quad (5.27)$$

During the above derivations, the yield strengths in tension and compression cannot be differentiated because we use the square of strengths in the equation. Therefore, we can remove the superscript  $t$  in equation (5.25). Solving equations (5.25) through (5.27) simultaneously, we find that

$$\begin{aligned} 2F &= \frac{1}{Y^2} + \frac{1}{Z^2} - \frac{1}{X^2} \\ 2G &= \frac{1}{X^2} + \frac{1}{Z^2} - \frac{1}{Y^2} \\ 2H &= \frac{1}{X^2} + \frac{1}{Y^2} - \frac{1}{Z^2} \end{aligned} \quad (5.28)$$

If plane stress is assumed ( $\sigma_3 = \tau_{31} = \tau_{32} = 0$ ), then this criterion for a unidirectional lamina with transverse isotropy of the 2–3-plane (figure 3.10), equation (5.23) combined with equations (5.24) and (5.28), reduces to

$$\frac{\sigma_1^2}{X^2} - \frac{\sigma_1\sigma_2}{X^2} + \frac{\sigma_2^2}{Y^2} + \frac{\tau_{12}^2}{S^2} = 1 \quad (5.29)$$

because  $Y = Z$ .

As with the Hill's equation, failure is avoided if the left-hand side of equation (5.29) is less than 1, while failure is predicted if the left-hand side is equal to or larger than 1.

In using the Tsai–Hill criterion, we should acknowledge the problem of this criterion: The von Mises and Hill criteria are developed based on principal stress differences and the corresponding shear stresses and strains drive slip and dislocation movement in metallic crystals. Hill's criterion predicts that failure will never occur under a hydrostatic state of stress  $\sigma_1 = \sigma_2 = \sigma_3$ ,  $\tau_{23} = \tau_{31} = \tau_{12} = 0$ , which is the experimental evidence. However, a hydrostatic state of stress in an anisotropic material can produce shear strains and consequently, failure.

Another limitation of the Tsai–Hill criterion is that all strength parameters appear as second-order terms with no distinction between positive and negative strengths, which are generally different in magnitude. While this causes no difficulty for shear stress in the principal material coordinates, it represents a severe limitation for normal stresses in that the sign of the normal stress must be known *a priori* and the appropriate strength value is used in the failure criterion (Herakovich, 1998).

The second term in equation (5.29) has the strength coefficient  $1/X^2$  rather than  $1/(XY)$ , although the related stresses are  $\sigma_1\sigma_2$ , which is another limitation because  $X$  and  $Y$  normally are much different in magnitude.

For the off-axis lamina of figure 5.3, the Tsai–Hill failure criterion takes the form

$$\frac{\cos^4 \theta}{X^2} + \left( \frac{1}{S^2} - \frac{1}{X^2} \right) \sin^2 \theta \cos^2 \theta + \frac{\sin^4 \theta}{Y^2} = \frac{1}{\sigma_x^2} \quad (5.30)$$

For the special case  $X^t = X^c$  and  $Y^t = Y^c$ , equation (5.29) represents a continuous surface in  $\sigma_1$ ,  $\sigma_2$ ,  $\tau_{12}$  stress space or a curve in any two-dimensional stress space.

#### 5.4.4 Tsai–Wu Tensor Failure Criterion

Tsai and Wu proposed a complete quadratic tensor polynomial with the linear terms included. The criterion assumes that there exists a scalar function  $f(\sigma_i)$  of the form

$$f(\sigma_i) = F_i \sigma_i + F_{ij} \sigma_i \sigma_j \quad (5.31)$$

Failure corresponds to the condition

$$f(\sigma_i) \geq 1 \quad (5.32)$$

Thus, states of stress inside the surface are “safe” and those on or outside the surface correspond to failure. The value of  $f(\sigma_i)$  is sometimes called as *failure index*.

Although equation (5.31) is very complicated, some simplification is possible. We assume that  $F_i$  and  $F_{ij}$  have strength tensor characteristics of the second and fourth rank, respectively, and the usual contracted stress notation is used with the convention that  $\sigma_4 = \tau_{23}$ ,  $\sigma_5 = \tau_{31}$ , and  $\sigma_6 = \tau_{12}$ . Since there is no difference in the positive and negative shear stresses,  $F_4 = F_5 = F_6 = 0$ . For orthotropic materials in the principal material axes, the normal/shear coupling terms and shear/shear coupling terms in the different planes disappear, which renders  $F_{14} = F_{15} = F_{16} = F_{24} = F_{25} = F_{26} = F_{34} = F_{35} = F_{36} = F_{45} = F_{56} = F_{64} = 0$ . Thus, the reduced form of the scalar function  $f(\sigma_i)$  for an orthotropic material is

$$\begin{aligned} f(\sigma_i) = & F_1 \sigma_1 + F_2 \sigma_2 + F_3 \sigma_3 + F_{11} \sigma_1^2 + F_{22} \sigma_2^2 + F_{33} \sigma_3^2 + F_{44} \sigma_4^2 + F_{55} \sigma_5^2 + F_{66} \sigma_6^2 \\ & + 2F_{12} \sigma_1 \sigma_2 + 2F_{13} \sigma_1 \sigma_3 + 2F_{23} \sigma_2 \sigma_3 \end{aligned} \quad (5.33)$$

The strength tensors  $F_i$  and  $F_{ij}$  can be expressed in terms of the engineering strengths. For example, under tensile load only,  $\sigma_1 = X'$ , the failure criterion (5.33) reduces to

$$F_1 X' + F_{11} (X')^2 = 1 \quad (5.34)$$

for compressive failure at the stress  $\sigma_1 = X^c$ , the failure criterion (5.33) reduces to

$$F_1 X^c + F_{11} (X^c)^2 = 1 \quad (5.35)$$

Solving equations (5.34) and (5.35) gives  $F_1$  and  $F_{11}$  as

$$F_1 = \frac{1}{X'} + \frac{1}{X^c} \quad (5.36)$$

$$F_{11} = -\frac{1}{X' X^c} \quad (5.37)$$

By the same method, other strength tensors can be found:

$$F_2 = \frac{1}{Y^t} + \frac{1}{Y^c} \quad (5.38)$$

$$F_3 = \frac{1}{Z^t} + \frac{1}{Z^c} \quad (5.39)$$

$$F_{22} = -\frac{1}{Y^t Y^c} \quad (5.40)$$

$$F_{33} = -\frac{1}{Z^t Z^c} \quad (5.41)$$

$$F_{44} = \frac{1}{Q^2} \quad (5.42)$$

$$F_{55} = \frac{1}{R^2} \quad (5.43)$$

$$F_{66} = \frac{1}{S^2} \quad (5.44)$$

The remaining strength tensors are  $F_{12}$ ,  $F_{13}$ , and  $F_{23}$ , corresponding to interaction terms involving normal components of stress. These tensors should be determined from three independent tests in which  $\sigma_1 = \sigma_2$ ,  $\sigma_1 = \sigma_3$ , or  $\sigma_2 = \sigma_3$ , with all other  $\sigma_i = 0$ .

For example, if  $\sigma_1 = \sigma_2 = \sigma$ , equation (5.33) reduces to

$$f(\sigma) = F_1\sigma + F_2\sigma + F_{11}\sigma^2 + F_{22}\sigma^2 + 2F_{12}\sigma^2 = 1 \quad (5.45)$$

Using the already determined strength tensors,  $F_{12}$  in equation (5.45) can be solved as

$$F_{12} = \frac{1}{2\sigma^2} - \frac{1}{2\sigma} \left( \frac{1}{X^t} + \frac{1}{X^c} + \frac{1}{Y^t} + \frac{1}{Y^c} \right) + \frac{1}{2} \left( \frac{1}{X^t X^c} + \frac{1}{Y^t Y^c} \right) \quad (5.46)$$

To conduct a test in which a specimen fails under a biaxial state of stress (e.g.,  $\sigma_1 = \sigma_2$ ) is not easy. In an actual test to obtain  $F_{12}$ , however, there is no *a priori* reason that  $\sigma_1$  must equal to  $\sigma_2$ . Wu has suggested that in order to determine  $F_{12}$  accurately, the biaxial ratio  $B = \sigma_1/\sigma_2$  must be optimized to account for the sensitivity of  $F_{12}$  to experimental scatter in applied stresses.

Tsai and Hahn (1980) have proposed the equation

$$F_{12} = -0.5\sqrt{F_{11}F_{22}} \quad (5.47)$$

There are some indications that interaction coefficients  $F_{12}$ ,  $F_{13}$ , and  $F_{23}$  are small, and they are often taken to be zero (Narayanaswami and Adelman, 1977).

For a planar state of stress with  $F_{12}=0$ , the tensor failure criterion (5.33) reduces to

$$f(\sigma_i) = F_1\sigma_1 + F_2\sigma_2 + F_{11}\sigma_1^2 + F_{22}\sigma_2^2 + F_{66}\sigma_6^2 = 1 \quad (5.48)$$

For the special case of an off-axis lamina of figure 5.3 with the applied stress  $\sigma_x$ , the tensor failure criterion (5.48) takes the form

$$\begin{aligned} & \left( -\frac{1}{X'X^c} \cos^4 \theta - \frac{1}{Y'Y^c} \sin^4 \theta + \frac{1}{S^2} \cos^2 \theta \sin^2 \theta \right) \sigma_x^2 \\ & + \left[ \left( \frac{1}{X'} + \frac{1}{X^c} \right) \cos^2 \theta + \left( \frac{1}{Y'} + \frac{1}{Y^c} \right) \sin^2 \theta \right] \sigma_x - 1 = 0 \end{aligned} \quad (5.49)$$

The tensor failure criterion can be used directly to predict the first ply failure, which may correspond to ultimate laminate failure if the major load is in compression, which will be discussed in section 7.4.2, and will usually correspond to matrix cracking if the major load is in tension, which will be discussed in section 7.4.1. This criterion does not directly differentiate between matrix and fiber failure, but can be interpreted indirectly by assuming that the first ply failure corresponds to matrix failure and last ply failure corresponds to ultimate failure of the laminate (Swanson, 1997).

Two additional criteria for the ply-failure prediction are based on separating the matrix failure and the fiber failure. Hahn et al. (1982) recommend the following:

*Fiber Failure:*

$$F_1\sigma_1 + F_{11}\sigma_1^2 = 1 \quad (5.50)$$

*Matrix Failure:*

$$F_2\sigma_2 + F_{22}\sigma_2^2 + F_{66}\sigma_6^2 = 1 \quad (5.51)$$

A similar criterion has been made by Hashin (1980):

*Fiber Failure:*

$$F_1\sigma_1 + F_{11}\sigma_1^2 + F_{66}\sigma_6^2 = 1 \quad (5.52)$$

*Matrix Failure:*

$$F_2\sigma_2 + F_{22}\sigma_2^2 + F_{66}\sigma_6^2 = 1 \quad (5.53)$$

#### 5.4.5 Applicability of Failure Theories

The validity of the failure theories presented until now depends on the failure modes which are related to the types of material and loading. The maximum stress and strain failure theories are more applicable when brittle behavior is predominant, typically in the first quadrant of the failure envelope ( $\sigma_1 > 0$ ,  $\sigma_2 > 0$ ). The interactive failure theories, such as the Tsai–Hill and Tsai–Wu theories, are more applicable when ductile behavior under shear or compression loading is predominant.

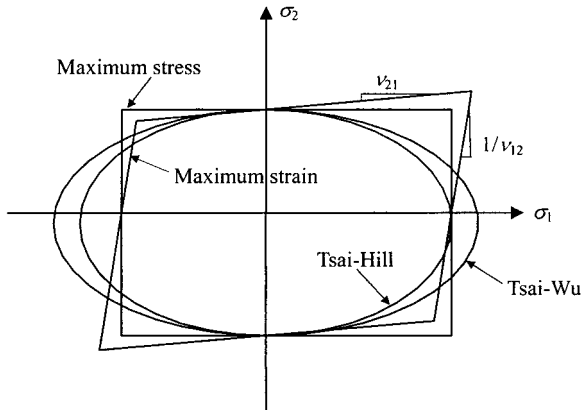


**Figure 5.5** Failure envelopes due to different failure criteria.

Composite materials that exhibit transitions between brittle and ductile behavior with the type of loading are best described by the combined failure theory that is composed of the maximum strain theory in the first quadrant and the interactive theory in the remaining quadrants.

When material behavior and failure modes are not known and when a conservative approach is required, several criteria should be evaluated and the most conservative envelope in each quadrant may be used. Figure 5.5 shows the four criteria applied to plane stress cases.

On the macroscopic scale, there are three possible in-plane failure mechanisms: fiber, matrix, and shear failures. After the first ply failure (FPF) in a laminate, in which failure is caused by any of the three failure modes, the applied load gets redistributed in the remaining intact plies. There is a redistribution of the loads due to the overall laminate stiffness reduction as a result of stiffness loss due to the FPF. As the laminate stiffness is reduced, the load gets redistributed according to the relative stiffnesses of the intact plies. As the load gets increased, a second ply failure occurs associated with a failure mode. The laminate stiffness is further reduced, and the load is further redistributed according to the relative stiffnesses of the remaining intact plies. The load is further increased to assess the load capability of the laminate until a last ply failure (LPF) of the laminate occurs.

The failed ply in a laminate may be modeled by having the failed ply remain in the same position in the laminate configuration, but reducing the values of some of its elastic properties. This will reflect the practical case in which the failed ply is physically still there in the laminate configuration, but unable to carry any more load. However, it is not easy to quantify this reduction for a general case of laminate configuration, in that the reduction will depend on the type of loading, material used, and the orientation of the plies. A simple conservative design for initial estimation is to make the elastic constants of failed plies zero values. However, it should be noted during the LPF analysis that by numerically setting the failed ply elastic constant values to zero, the stresses are set to zero not the strains, because in the laminate analysis the strains in the global axes are common to all plies with their elastic values set to zero.

## 5.5 Delamination Failure Due to Interlaminar Stresses

### 5.5.1 Interlaminar Stress

In the classical lamination theory so far developed, only the stresses in the plane of the laminate,  $\sigma_x$ ,  $\sigma_y$ , and  $\tau_{xy}$  are considered. However, the state of stress in the vicinity of free edges becomes three-dimensional, with nonzero through-thickness or interlaminar stresses. The interlaminar stresses include the normal stress,  $\sigma_z$ , and two interlaminar shear stresses,  $\tau_{yz}$  and  $\tau_{zx}$ , as shown in figure 5.6.

Delamination due to interlaminar stresses can reduce the failure stress of the laminate below that predicted by the in-plane failure criteria discussed in the previous section, which necessitates a separate treatment of interlaminar stresses.

If we consider a balanced symmetric laminate composed of orthotropic plies, there is no coupling between bending and extension because  $[B]=0$ . When the laminate is subjected to an in-plane load  $N_x$ , as shown in figure 5.6, it will only extend in the  $x$ -direction and contract in the  $y$ - and  $z$ -directions, but will not bend.

The strains in the midplane of the laminate are expressed from equations (4.47) and (4.62) as

$$\varepsilon_x^0 = \frac{A_{22}}{A_{11}A_{22} - A_{12}^2} N_x \quad (5.54a)$$

$$\varepsilon_y^0 = -\frac{A_{12}}{A_{11}A_{22} - A_{12}^2} N_x \quad (5.54b)$$

$$\gamma_{xy}^0 = 0 \quad (5.54c)$$

The stresses in the laminate axes are expressed from equation (4.15)

$$\begin{Bmatrix} \sigma_x \\ \sigma_y \\ \tau_{xy} \end{Bmatrix}^{[k]} = \begin{bmatrix} \bar{Q}_{11} & \bar{Q}_{12} & \bar{Q}_{16} \\ \bar{Q}_{12} & \bar{Q}_{22} & \bar{Q}_{26} \\ \bar{Q}_{16} & \bar{Q}_{26} & \bar{Q}_{66} \end{bmatrix}^{[k]} \begin{Bmatrix} \varepsilon_x^0 \\ \varepsilon_y^0 \\ 0 \end{Bmatrix} \quad (5.55)$$

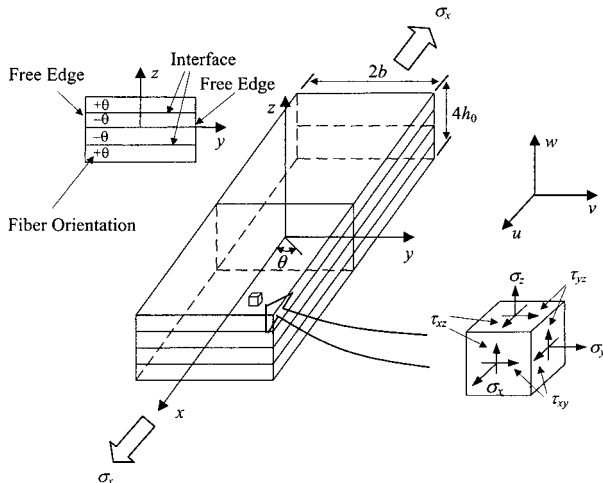


Figure 5.6 Finite-width laminate geometry and stresses under axial load.

Although there is no  $\gamma_{xy}^0$  in the laminate axes, the shear stress  $\tau_{xy}$  is not zero, because  $\bar{Q}_{16}$  and  $\bar{Q}_{26}$  are not, in general, zero, from equation (3.129). Actually, the shear stress  $\tau_{xy}$  is not possible at the edge ( $y = \pm b$ ) of laminate of figure 5.6. This contradictory phenomenon occurred because the classical lamination theory neglected the interlaminar shear stresses.

The free body diagram of each ply of the laminate in figure 5.7 can be used to explain the physical mechanism of shear transfer between plies. Since  $\tau_{xy}$  must be zero on a free edge, a couple caused by  $\tau_{xy}$  acting along the other edges of the free body must be reacted against. The only possible reacting couple to satisfy moment equilibrium is caused by  $\tau_{xz}$  acting on part of the lower face of the ply at the interface with the next ply.

There is an elasticity approach to considering a three-dimensional stress state (Pipes and Pagano, 1970). The stress-strain relations for each orthotropic ply are expressed in laminate axes from equation (3.109):

$$\left\{ \begin{array}{c} \sigma_x \\ \sigma_y \\ \sigma_z \\ \tau_{yz} \\ \tau_{zx} \\ \tau_{xy} \end{array} \right\}^{[k]} = \left[ \begin{array}{cccccc} \bar{C}_{11} & \bar{C}_{12} & \bar{C}_{13} & 0 & 0 & \bar{C}_{16} \\ \bar{C}_{12} & \bar{C}_{22} & \bar{C}_{23} & 0 & 0 & \bar{C}_{26} \\ \bar{C}_{13} & \bar{C}_{23} & \bar{C}_{33} & 0 & 0 & \bar{C}_{36} \\ 0 & 0 & 0 & \bar{C}_{44} & \bar{C}_{45} & 0 \\ 0 & 0 & 0 & \bar{C}_{45} & \bar{C}_{55} & 0 \\ \bar{C}_{16} & \bar{C}_{26} & \bar{C}_{36} & 0 & 0 & \bar{C}_{66} \end{array} \right] \left\{ \begin{array}{c} \varepsilon_x \\ \varepsilon_y \\ \varepsilon_z \\ \gamma_{yz} \\ \gamma_{zx} \\ \gamma_{xy} \end{array} \right\}^{[k]} \quad (5.56)$$

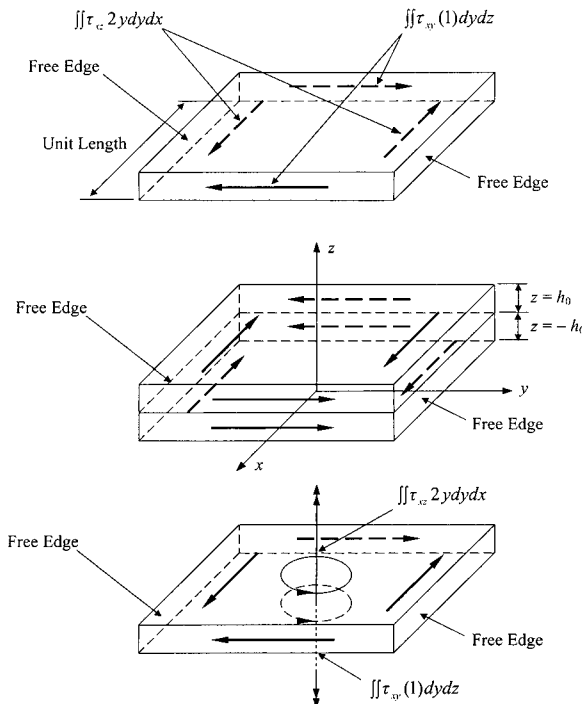


**Figure 5.7** Interlaminar shear stress mechanism (from Pipes and Pagano, 1970).

The strain-displacement relations are

$$\begin{aligned}\varepsilon_x &= \frac{\partial u}{\partial x}, \quad \varepsilon_y = \frac{\partial v}{\partial y}, \quad \varepsilon_z = \frac{\partial w}{\partial z} \\ \gamma_{yz} &= \frac{\partial v}{\partial z} + \frac{\partial w}{\partial y}, \quad \gamma_{zx} = \frac{\partial w}{\partial x} + \frac{\partial u}{\partial z}, \quad \gamma_{xy} = \frac{\partial u}{\partial y} + \frac{\partial v}{\partial x}\end{aligned}\quad (5.57)$$

Consider a laminate loaded by tractions applied on its ends  $x = \text{constant}$ , such that the stress components are independent of  $x$ . In such a body, the stress equilibrium equations reduce to

$$\begin{aligned}\frac{\partial \tau_{xy}}{\partial y} + \frac{\partial \tau_{zx}}{\partial z} &= 0 \\ \frac{\partial \sigma_y}{\partial y} + \frac{\partial \tau_{yz}}{\partial z} &= 0 \\ \frac{\partial \tau_{yz}}{\partial y} + \frac{\partial \sigma_z}{\partial z} &= 0\end{aligned}\quad (5.58)$$

Integration of the stress-displacement relations, where all stress components are taken to be independent of the axial coordinate  $x$ , results in displacements of the following functional form within each ply (Timoshenko and Goodier, 1970):

$$\begin{aligned}u &= -(C_1z + C_2)y + (C_3y + C_4z + C_5)x + U(y, z) \\ v &= (C_1z + C_2)x - \frac{1}{2}C_3x^2 + V(y, z) \\ w &= -C_1xy + C_6x - \frac{1}{2}C_4x^2 + C_7 + W(y, z)\end{aligned}\quad (5.59)$$

Since symmetric laminates under extensional loading only are concerned, symmetry conditions for the displacements with respect to the  $x-y$ - and  $x-z$ -planes can be imposed:

(a) *Symmetry Conditions with Respect to  $x-y$ -Plane:*

$$\begin{aligned}u(x, y, z) &= u(x, y, -z) \\ v(x, y, z) &= v(x, y, -z) \\ w(x, y, z) &= -w(x, y, -z)\end{aligned}\quad (5.60)$$

(b) *Symmetry Conditions with Respect to  $x-z$ -Plane:*

$$\begin{aligned}v(x, y, z) &= -v(x, -y, z) \\ w(x, y, z) &= w(x, -y, z)\end{aligned}\quad (5.61)$$

Using equations (5.60) and (5.61), in conjunction with the displacement continuity conditions at the interfaces, we have

$$C_1 = C_2 = C_3 = C_4 = C_6 = C_7 = 0 \quad (5.62)$$

for each layer, while  $C_5$  is the same for each layer. Hence, the general form of the displacement field is given by

$$\begin{aligned} u &= C_5x + U(y, z) \\ v &= V(y, z) \\ w &= W(y, z) \end{aligned} \quad (5.63)$$

The class of problems defined by displacements of this form is a uniform axial extension, since the strain component  $\varepsilon_x = C_5$  is a constant.

Substituting the displacement relations in equation (5.63) into equation (5.57) and subsequently into equations (5.56) and (5.58) successively, yields the governing displacement equilibrium equations within each ply:

$$\begin{aligned} \bar{C}_{66} \frac{\partial^2 U}{\partial y^2} + \bar{C}_{55} \frac{\partial^2 U}{\partial z^2} + \bar{C}_{26} \frac{\partial^2 V}{\partial y^2} + \bar{C}_{45} \frac{\partial^2 V}{\partial z^2} + (\bar{C}_{36} + \bar{C}_{45}) \frac{\partial^2 W}{\partial y \partial z} &= 0 \\ \bar{C}_{26} \frac{\partial^2 U}{\partial y^2} + \bar{C}_{45} \frac{\partial^2 U}{\partial z^2} + \bar{C}_{22} \frac{\partial^2 V}{\partial y^2} + \bar{C}_{44} \frac{\partial^2 V}{\partial z^2} + (\bar{C}_{23} + \bar{C}_{44}) \frac{\partial^2 W}{\partial y \partial z} &= 0 \\ (\bar{C}_{36} + \bar{C}_{45}) \frac{\partial^2 U}{\partial y \partial z} + (\bar{C}_{23} + \bar{C}_{44}) \frac{\partial^2 V}{\partial y \partial z} + \bar{C}_{44} \frac{\partial^2 W}{\partial y^2} + \bar{C}_{33} \frac{\partial^2 W}{\partial z^2} &= 0 \end{aligned} \quad (5.64)$$

Equation (5.64) was solved by the finite difference method (Pipes and Pagano, 1970). Due to symmetry of the laminate about several planes, a quarter of the laminate cross-section in the  $y-z$ -plane at any value of  $x$  may be solved, as shown in figure 5.8.

The boundary conditions along the upper surface are

$$\tau_{yz} = \sigma_z = \tau_{xz} = 0 \quad (5.65)$$

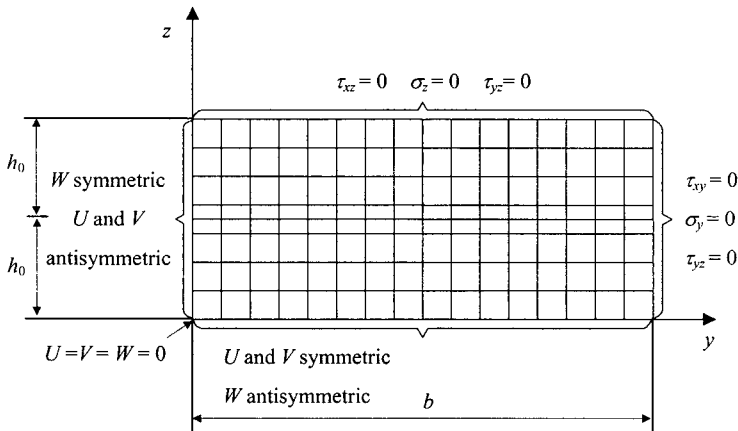


**Figure 5.8** A quarter of the laminate cross-section in the  $y-z$ -plane at any value of  $x$  for finite difference representation and related boundary conditions (from Pipes and Pagano, 1970).

The boundary conditions along the outer edge are

$$\tau_{xy} = \sigma_y = \tau_{yz} = 0 \quad (5.66)$$

Since  $U$  and  $V$  are symmetric, and  $W$  is antisymmetric along  $z=0$ , the boundary conditions are

$$\begin{aligned} \frac{\partial U(y, 0)}{\partial z} &= 0 \\ \frac{\partial V(y, 0)}{\partial z} &= 0 \\ W(y, 0) &= 0 \end{aligned} \quad (5.67)$$

Since  $U$  and  $V$  are antisymmetric and  $W$  is symmetric, the boundary conditions along the line  $y=0$

$$\begin{aligned} U(0, z) &= 0 \\ V(0, z) &= 0 \\ \frac{\partial W(0, z)}{\partial y} &= 0 \end{aligned} \quad (5.68)$$

Finally, special conditions at the corner  $(b, 2h_0)$  require discussion. Although five traction-free conditions are available ( $\sigma_y = \sigma_z = \tau_{xy} = \tau_{xz} = \tau_{yz} = 0$ ), only three of the five can be employed without over-specification of the solution. Numerical results indicated that the solution was insensitive to the particular three traction-free conditions specified at the corner and the remaining two are always satisfied.

For a carbon-fiber epoxy composite material with stacking sequence  $[\pm 45]_S$ , figure 5.9 shows the stresses  $\sigma_x$ ,  $\tau_{xy}$ , and  $\tau_{xz}$  at the ply interface ( $z = h_0$ ) when  $b = 8h_0$ .

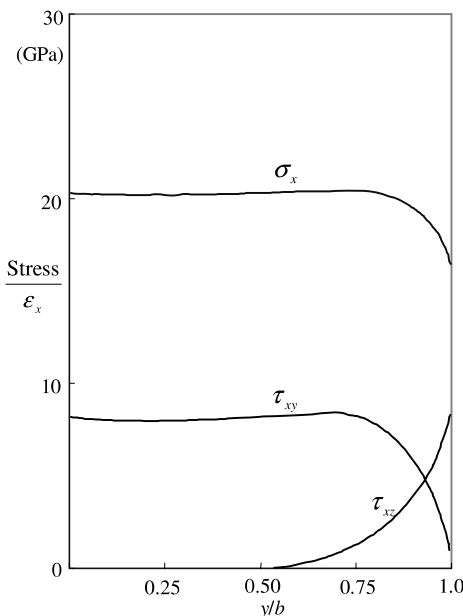


**Figure 5.9** Stresses at the ply interface of the laminate with stacking sequence  $[\pm 45]_S$  (from Pipes and Pagano, 1970).

The material properties of the composite are

$$\begin{aligned} E_1 &= 138 \text{ GPa}, & G_{12} = G_{23} = G_{31} &= 5.86 \text{ GPa}, \\ E_2 = E_3 &= 14.5 \text{ GPa}, & \nu_{12} = \nu_{13} = \nu_{23} &= 0.21 \end{aligned} \quad (5.69)$$

In figure 5.9, the stresses obtained by classical lamination theory represent those in the center portion of the cross-section. However, as the free edge is approached,  $\sigma_x$  decreases,  $\tau_{xy}$  goes to zero, and  $\tau_{xz}$  increases from zero to infinity with singularity at  $y = \pm b$ . The planar stress distribution predicted by classical lamination theory is distorted by the presence of  $\tau_{xz}$ ,  $\sigma_z$ , and  $\tau_{yz}$  in regions near the laminate free edge. However, these interlaminar stress components decay rapidly with the distance from the edge. In fact, numerical results for laminate geometries  $b/h_0 = 4.8$  and 12.0 indicate that the region of disturbance is restricted to a width equal to the laminate thickness,  $4h_0$  (Pagano and Soni, 1989).

Therefore, the presence of the interlaminar stress near the free edge may be considered to be a boundary-layer or edge effect that is restricted to a region near the free edge, while the stress distribution in interior regions of the laminate is adequately described by classical lamination theory.

The interlaminar shear stress,  $\tau_{xz}$ , has a distribution over the cross-section thickness, as shown by several profiles at various distances from the middle of the laminate in figure 5.10.

Stress values that have been extrapolated from the numerical data are shown by dashed lines. The value of  $\tau_{xz}$  is zero at the upper surface of the laminate and at the middle surface. The maximum value for any profile always occurs at the interface between plies. The largest value of  $\tau_{xz}$  occurs at the intersection of the free edge with the interface between plies and appears to be a singularity, although it cannot be proved by use of a numerical technique.

The existence of interlaminar stresses can make laminates delaminate near free edges whether they are at the free edge of a plate, around a hole, or at the ends of a tubular shaft used for propeller shafts.

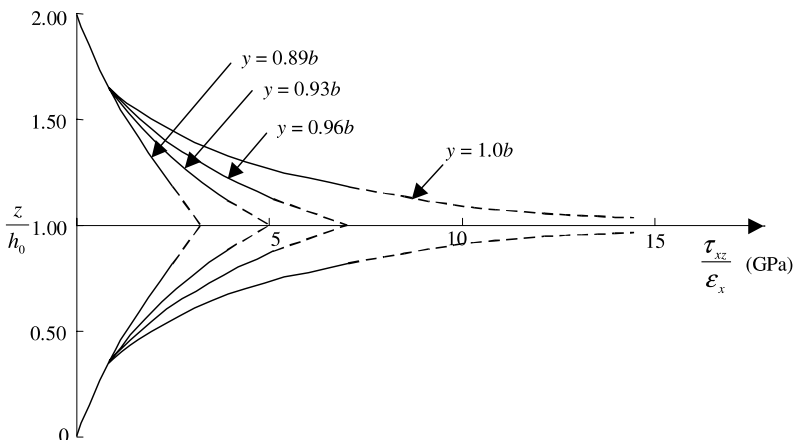


**Figure 5.10** Interlaminar shear stress distribution through the laminate thickness (from Pipes and Pagano, 1970).

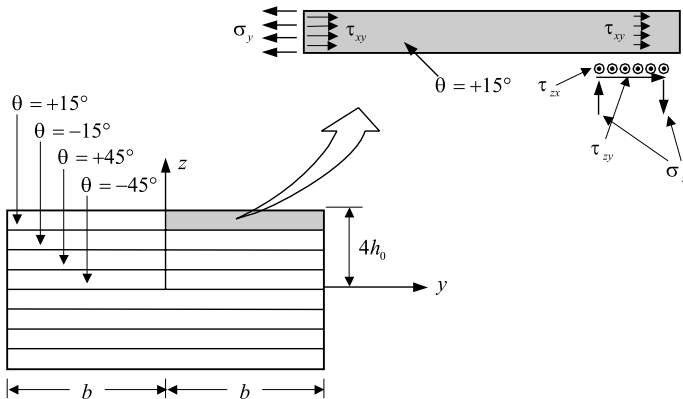


**Figure 5.11** Interlaminar stress distribution in the top ply of  $[\pm 15/\pm 45]_s$  laminate.

Pipes and Pagano (1970) investigated the interlaminar stresses in laminates of stacking sequence  $[\pm 45/\pm 15]_s$ . They hypothesized that the interlaminar normal stress,  $\sigma_z$ , can be changed from tension to compression by changing the stacking sequence. In fact, it was reported that fatigue strengths changed 170 MPa when the positions of the  $\pm 15^\circ$  plies and  $\pm 45^\circ$  plies were reversed. However, classical lamination theory predicts that tensile stresses are unaffected by stacking sequence for balanced symmetric laminates.

When the balanced symmetric  $[\pm 15/\pm 45]_s$  laminate in figure 5.11 is subjected to a load in the  $x$ -direction, as in figure 5.6, the interlaminar stress transfer involves a balance of moments of stresses. Since  $\tau_{xy}$  is zero on a free edge, but finite elsewhere, its moment must be balanced by the moment of interlaminar shear stresses,  $\tau_{zx}$ . Also, the moment due to  $\sigma_z$  must balance the moment due to  $\sigma_y$ .

In figure 5.11, a tensile stress  $\sigma_y$  in the  $15^\circ$  ply induces a tensile stress  $\sigma_z$  at the free edge, or conversely, a compressive stress  $\sigma_y$  induces a compressive stress  $\sigma_z$ . Pipes and Pagano (1970) hypothesized that the interlaminar normal stress  $\sigma_z$  goes to zero in the region where classical lamination theory applies and perhaps to infinity at the free edge. The interlaminar normal stress  $\sigma_z$  is self-equilibrating.

If the  $45^\circ$  plies were placed on the outside of the laminate, a compressive  $\sigma_y$  would be predicted with classical lamination theory, which would induce compressive  $\sigma_z$  and not cause the laminate to delaminate (see problem 5.11).

They reasoned that  $\sigma_z$  is distributed through the thickness as shown in figure 5.12 for two stacking sequences,  $[15/-15/45/-45]_s$  and  $[15/45/-45/-15]_s$ . The latter stacking sequence will provide a greater strength than the former because of fewer tendencies to delaminate (Jones, 1975).

By similar reasoning, the stacking sequence  $[\pm 45/\pm 15]_s$  will lead to interlaminar compressive stresses that are the mirror images of the tensile stresses of the stacking sequence  $[\pm 15/\pm 45]_s$  and will be much stronger dynamically.

### 5.5.2 Delamination Failure

The initiation of delamination is generally followed by stable delamination growth, which eventually leads to unstable growth and ultimate failure. The onset of delamination can be predicted by using either mechanics of materials approaches or fracture mechanics approaches (Gibson, 1994).

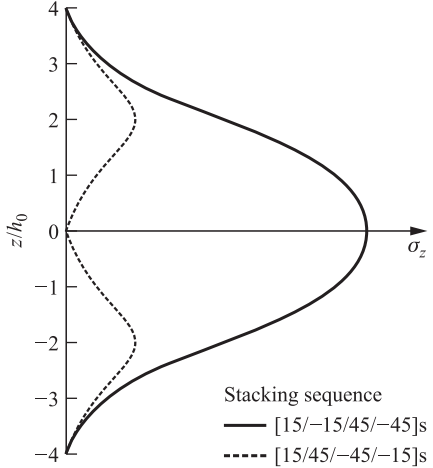


**Figure 5.12** Distribution of interlaminar normal stress  $\sigma_z$  in the boundary layer region with respect to  $z$ .

In this section, the mechanics of materials approaches will be discussed and the fracture mechanics approaches will be discussed in later sections.

One of the first mechanics of materials approaches to the prediction is based on the premise that delamination will begin when the average value of the interlaminar tensile normal stress,  $\bar{\sigma}_z$ , near the free edge reaches the interlaminar tensile strength,  $Z'$ ; Kim and Soni (1984) averaged the interlaminar tensile stress,  $\sigma_z$ , over a critical length,  $b_0$  as shown in figure 5.13.

$$\bar{\sigma}_z = \frac{1}{b_0} \int_{b-b_0}^b \sigma_z(y, 0) dy = Z' \quad (5.70)$$

The distance  $b$  was the half-width of the laminate and the critical length  $b_0$  was assumed to be equal to one ply thickness. Due to the difficulty of measuring the interlaminar tensile strength, which is a laminate property, they assumed that the interlaminar tensile strength is equal to the transverse tensile strength,  $Y'$ , of the unidirectional ply.

Since a more general criterion is required for cases where delamination may be affected by interlaminar shear stresses,  $\tau_{yz}$ ,  $\tau_{zx}$ , Brewer and Lagace (1988) proposed the *quadratic delamination criterion*:

$$\left(\frac{\bar{\tau}_{yz}}{Q}\right)^2 + \left(\frac{\bar{\tau}_{zx}}{R}\right)^2 + \left(\frac{\bar{\sigma}_z'}{Z'}\right)^2 + \left(\frac{\bar{\sigma}_z^c}{Z^c}\right)^2 = 1 \quad (5.71)$$

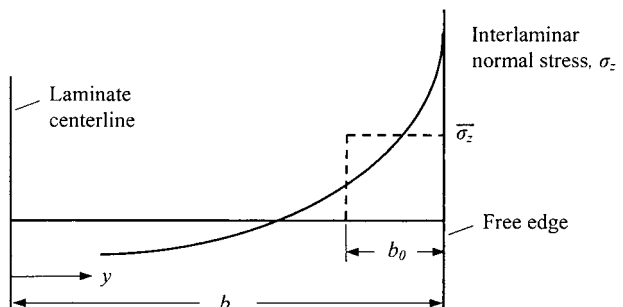


**Figure 5.13** Graphical representation of average interlaminar normal stress near free edge.

where  $\bar{\tau}_{yz}, \bar{\tau}_{zx}$  = average interlaminar shear stresses  
 $\bar{\sigma}_z^t, \bar{\sigma}_z^c$  = average interlaminar tensile and compressive normal stresses,  
respectively  
 $Q, R$  = interlaminar shear strengths  
 $Z^t, Z^c$  = interlaminar tensile and compressive strengths, respectively.

Again, they assumed that the interlaminar strengths are equal to their respective strength of the unidirectional ply.

The average stress components  $\bar{\sigma}_{ij}$  are defined as

$$\bar{\sigma}_{ij} = \frac{1}{\lambda_{avg}} \int_0^{\lambda_{avg}} \sigma_{ij} d\lambda \quad (5.72)$$

where  $\lambda$  = distance from the free edge

$\lambda_{avg}$  = averaging dimension

Brewer and Lagace (1988) found that for the AS1/3501-6 carbon-fiber epoxy composite with the stacking sequences  $[\pm 15]_{ns}$ ,  $[\pm 15/0]_{ns}$ , and  $[0/\pm 15]_{ns}$ , the first and fourth terms in equation (5.71) were negligible, so that the quadratic delamination criterion became the simplified form

$$\left(\frac{\bar{\tau}_{xz}}{R}\right)^2 + \left(\frac{\bar{\sigma}_z^t}{Z^t}\right)^2 = 1 \quad (5.73)$$

With the assumption of transverse isotropy, the interlaminar tensile strength  $Z'$  was assumed to be equal to the tensile strength of the unidirectional ply in the  $y$ -direction ( $Z' = Y' = 53.9$  MPa). The parameters  $\lambda_{avg}$  and  $R$  were used as curve-fitting parameters to obtain the best agreement with experimental data.

In the corresponding experiments, laminate specimens were tested under displacement control and the instantaneous drop in the tensile load at delamination onset was observed. The best-fit parameters for all the laminate configurations tested were  $\lambda_{avg} = 0.178$  mm and  $R = 105$  MPa. The validity of the quadratic delamination criterion and the assumption of transverse isotropy were discovered with the observation that the best-fit value of  $R$  was the same as the in-plane shear strength of thin material.

The delamination of a laminate results in the reduction of stiffness of the laminate because the stiffness of a laminate is not the simple average of stiffnesses of constituent plies (see problem 4.5). Conversely, the stiffness loss or reduction of natural frequency can be used to characterize the growth of delamination.

From the classical lamination theory, the axial modulus of a balanced symmetric laminate under axial force only is expressed by equation (4.63):

$$E_x = \frac{\bar{\sigma}_x}{\varepsilon_x^0} = \frac{1}{ha_{11}} = \frac{1}{h} \left( A_{11} - \frac{A_{12}^2}{A_{22}} \right) \quad (5.74)$$

The corresponding stiffness of a laminate that has been totally delaminated along one or more interfaces, as shown in figure 5.14(b), is given by the rule of mixture

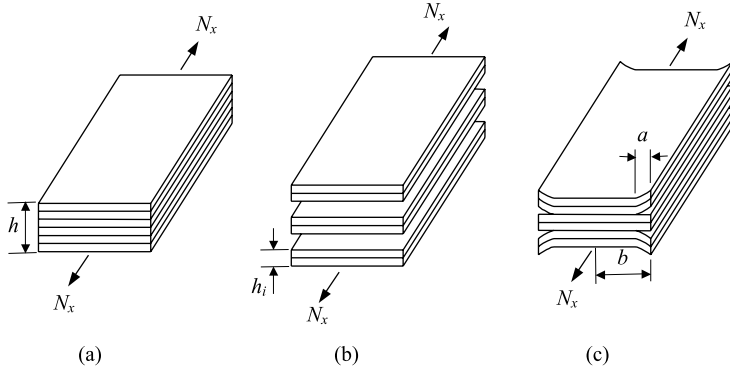


**Figure 5.14** Stiffness reduction of a laminate due to delamination: (a) Without delamination; (b) total delamination; (c) partial delamination (from O'Brien, 1982).

formula (O'Brien, 1982):

$$E_{td} = \frac{1}{h} \sum_{i=1}^m E_{xi} h_i \quad (5.75)$$

where  $E_{td}$  = longitudinal Young's modulus of a laminate totally delaminated along one or more interfaces

$E_{xi}$  = longitudinal Young's modulus of  $i$ th sublamine formed by the delamination

$h_i$  = thickness of the  $i$ th sublamine

$m$  = number of sublaminates formed by the delamination

The longitudinal Young's modulus of a laminate that has been partially delaminated along the same interface of figure 5.14(c) is given by the rule of mixture formula

$$E_{pd} = (E_{td} - E_x) \frac{a}{b} + E_x \quad (5.76)$$

where  $E_{pd}$  = longitudinal Young's modulus of a laminate partially delaminated along one or more interfaces

$a$  = distance that delamination extends in from free edge

$b$  = half-width of laminate

## 5.6 Failure Due to Fracture

The classical failure criteria so far described in the previous sections implicitly assume that failure occurs by separation of the atomic lattice across the entire plane of fracture as a single event. However, from theoretical consideration, the forces required to accomplish this behavior are usually much larger than the measured tensile strength of brittle materials. More realistically, the measured forces are more closely related to the force required to separate a few lines of atoms at a time.

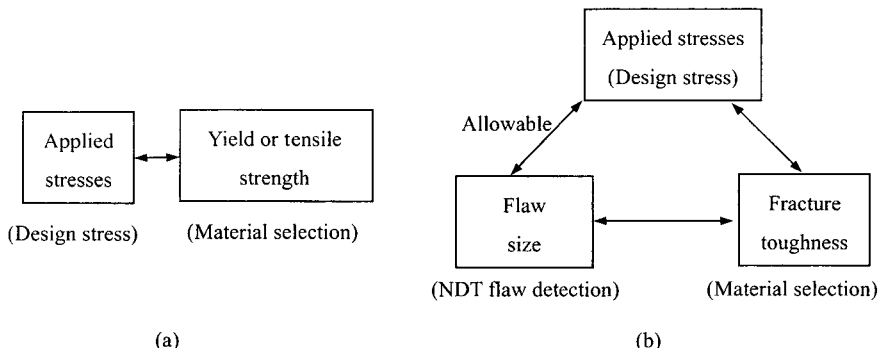


**Figure 5.15** Comparison of the fracture mechanics approach to design with the traditional strength of materials approach: (a) Strength of materials approach; (b) fracture mechanics approach (from Anderson, 1995).

This perspective of fracture by progressive separation of the fracture plane is fundamental to the development of a modern fracture theory (Sanford, 2003).

Since defects, such as notches, cracks, delamination, or other discontinuities, exist in composites even before service begins, and that cracks can grow during service, the criterion for the crack growth until it becomes critical, and the part removal time from service—"the damage-tolerant design"—should be clarified (Shigley et al., 2004).

In traditional structural design, the anticipated design stress is compared with the yield or failure properties of candidate materials; a material is assumed to be adequate if its strength is greater than the expected applied stress. When there exist a crack, flaw, inclusion, or defect of unknown small radius in a part, the elastic stress-concentration factor approach is used. In this approach, the stress-concentration factor becomes infinity as the root radius approaches zero, thus rendering the stress-concentration factor approaches useless. Furthermore, even if the radius of curvature of the flaw tip is known, the high local stresses there will lead to local plastic deformation surrounded by a region of elastic deformation. Elastic stress-concentration factors are no longer valid for this situation, so analysis from the point of view of stress-concentration factors does not lead to criteria useful for design when very sharp cracks are present.

The fracture mechanics approach has three important variables, rather than two in traditional approach as shown in figure 5.15 (Anderson, 1995). The additional structural variable is flaw size, and fracture toughness replaces strength as the relevant material property. Fracture mechanics quantifies the combinations of these three variables.

There are two alternative approaches to fracture analysis: the stress intensity approach and the energy criterion approach.

### 5.6.1 Stress Intensity Approach

There are three types of loading that a crack can experience, as shown in figure 5.16. Mode I loading, where the principal load is applied normal to the crack plane, tends to open the crack. Mode II corresponds to in-plane shear loading and tends to slide one crack face with respect to the other. Mode III refers to out-of-plane shear.

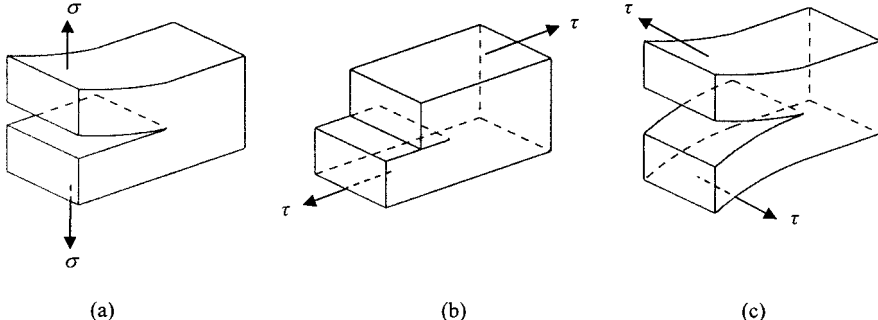


**Figure 5.16** Modes of crack propagation: (a)  $K_I$ , opening mode; (b)  $K_{II}$ , in-plane shear mode; (c)  $K_{III}$ , out-of-plane shear mode.

A cracked body can be loaded in any one of three modes, or a combination of two or three modes.

For the mode I singular field on the crack plane, the stress fields ahead of a crack tip in an infinite isotropic linear elastic material can be written using a polar coordinate system (Anderson, 1995):

$$\begin{aligned}\sigma_x &= \frac{K_I}{\sqrt{2\pi r}} \cos\left(\frac{\theta}{2}\right) \left[ 1 - \sin\left(\frac{\theta}{2}\right) \sin\left(\frac{3\theta}{2}\right) \right] \\ \sigma_y &= \frac{K_I}{\sqrt{2\pi r}} \cos\left(\frac{\theta}{2}\right) \left[ 1 + \sin\left(\frac{\theta}{2}\right) \sin\left(\frac{3\theta}{2}\right) \right] \\ \tau_{xy} &= \frac{K_I}{\sqrt{2\pi r}} \cos\left(\frac{\theta}{2}\right) \sin\left(\frac{\theta}{2}\right) \cos\left(\frac{3\theta}{2}\right)\end{aligned}\quad (5.77)$$

$\sigma_z = 0$  for plane stress,  $\sigma_z = v(\sigma_x + \sigma_y)$  for plane strain

$$\tau_{xz} = \tau_{yz} = 0$$

where

$$K_I = \sigma \sqrt{\pi a} \quad (5.78)$$

$K_I$  is called the stress intensity factor of mode I.

The polar coordinate axes  $r$  and  $\theta$  for the crack tip problem are defined in figure 5.17. When  $\theta = 0$ , the shear stress  $\tau_{xy}$  is zero, which means that the crack plane is a principal plane for pure mode I loading, and the stresses in the  $x$ - and  $y$ -directions are equal:

$$\sigma_x = \sigma_y = \frac{K_I}{\sqrt{2\pi r}} \quad (5.79)$$

As shown in equation (5.77), the stress intensity factor  $K_I$  defines the amplitude of the crack tip singularity. That is, stresses near the crack tip increase in proportion to  $K_I$ . If  $K_I$  is known, it is possible to solve for all components of stress, strain, and displacement as a function of  $r$  and  $\theta$ . This simple parameter description of crack tip conditions turns out to be one of the most important concepts in fracture

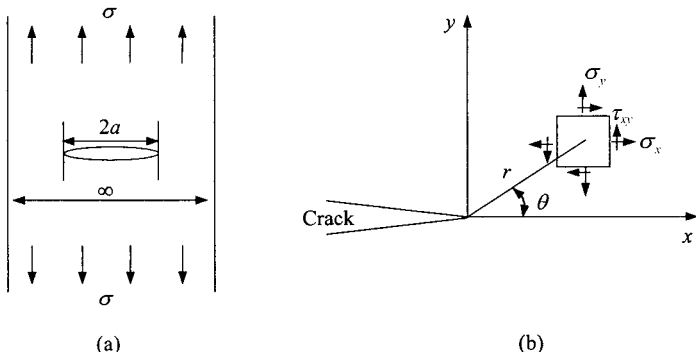


**Figure 5.17** Definition of the coordinate axis ahead of a crack tip. The  $z$  direction is normal to the page: (a) Global view; (b) local view at the crack tip.

mechanics. Therefore, closed-form solutions for  $K_I$  have been derived for a number of simple configurations (Sanford, 2003). For more complex situations the stress intensity factor can be estimated by experiment or numerical analysis. Once  $K_I$  is evaluated, the limiting value of  $K_I$  that is necessary for crack propagation in that material is measured. This limiting value is a characteristic of the stress intensity factor  $K_C$ , which is determined from standard tests. Failure is defined as whenever the stress intensity factor,  $K_I$ , exceeds the critical stress intensity factor,  $K_C$ . The crack propagation condition is

$$K_C = \sigma_C \sqrt{\pi a} \quad (5.80)$$

Most currently available values of  $K$  and  $K_C$  are for tensile loading, which is called mode I. Accordingly, these values are designated  $K_I$  and  $K_{IC}$ . Modes II and III pertain to shear loading as shown in figure 5.16, whose  $K_{II}$  and  $K_{III}$  are expressed as

$$\begin{aligned} K_{II} &= \tau \sqrt{\pi a} \\ K_{III} &= \tau \sqrt{\pi a} \end{aligned} \quad (5.81)$$

where the shear stress,  $\tau$ , is different for modes II and III.

Most available values of  $K_{IC}$  (such as those in table 5.6) are for relatively thick members, such that the material at the crack root is approximately in a state of plane strain, that is, the material at the crack root is under the enforcing condition of  $\varepsilon_z \approx 0$  in the thickness direction. Crack root material in sufficiently thin members is free to contract in the thickness direction, giving  $\sigma_z \approx 0$  or a condition of plane stress. The plane strain tensile loading, with  $\sigma_z$  being tensile, offers less opportunity for redistributing high crack root stresses by shear yielding (see problem 5.12).

Because of this, values of  $K_{IC}$  for plane strain are sufficiently lower than those for plane stress. Thus, the more readily available plane strain values of  $K_{IC}$  are often used for conservative calculations when the value of  $K_{IC}$  for the actual thickness is not known (Felbeck and Atkins, 1996).

The fracture toughness and allowable flaw size in figure 5.15, which are design parameters of a given material, usually decrease, often rapidly for metallic materials, when the yield strength is elevated (Hertzberg, 1996).

**Table 5.6 Experimental Fracture Toughness Values of Some Composites and Structural Metals (from Agarwal and Broutman, 1990)**

Material	Tensile strength (MPa)	$K_{IC}$ (MPa $\sqrt{m}$ )
Carbon-fiber epoxy:		
[0/ $\pm 45$ ]s	540–660	32–37
Quasi-isotropic	450–610	22–56
Crossply	640–760	43–54
Carbon-fiber polyimide, [0/45/90/ $-45$ ]s	420	37–41
Boron-fiber aluminum:		
Unidirectional	1010–2010	56–107
Quasi-isotropic	350–410	28–35
Crossply	680–760	34–42
Glass-fiber epoxy,		
Random short fibers	80–560	19–30
2024-T6 aluminum	440	44
7075-T6 aluminum	500	24
Ti-6Al-4V	900	180
4340 steel	1500	170

The stress analyses for the anisotropic material are more complicated. However, the stress intensity factors for certain loading conditions and crack geometries are the same as those for the isotropic material. For example, Lekhnitskii (1963), showed that if the crack shown in figure 5.17 lies in an anisotropic material for which the  $x-y$ -plane is a plane of material property symmetry, then the stresses are given by

$$\sigma_{ij} = \frac{K_I}{\sqrt{2\pi r}} F_{ij}(\theta, s_1, s_2) \quad (5.82)$$

where the functions  $F_{ij}(\theta, s_1, s_2)$  include not only trigonometric functions of angle  $\theta$ , but also  $s_1$  and  $s_2$ , which are complex roots of the characteristic equation that correspond to a differential equation in the stress function (Lekhnitskii, 1963).

The magnitudes of the stresses at point  $(r, \theta)$  in an isotropic material are completely determined by the stress intensity factors as in equation (5.77), but in the anisotropic material case, these magnitudes also depend on  $s_1$  and  $s_2$  (Gibson, 1994).

Several experimental investigations have shown that the concept of a critical stress intensity factor can be used to describe the fracture behavior of through-thickness cracked unidirectional composites and other angle ply composites (Konish et al., 1972; Parhizgar et al., 1982), because the fracture toughness,  $K_{IC}$ , has been found to be an essentially constant material property for a variety of randomly oriented short fiber composites (Sun and Sierakowski, 1980).

**EXAMPLE 5.6**

A large sheet is to be fabricated from 2024-T6 aluminum. It is required that the critical flaw size be greater than 3 mm, the resolution limit of available flaw detection procedures. To save weight, the material of the sheet is changed from 2024-T6 aluminum to 7075-T6 aluminum. Is such a strength increment allowable? Assume plane-strain conditions and use the material data of table 5.6.

**Solution**

For the 2024-T6 aluminum, the crack propagation condition from equation (5.80) is

$$44 \text{ MPa}\sqrt{m} = 440 \text{ MPa}\sqrt{\pi a}$$

$$2a = 6.4 \text{ mm}$$

which exceeds the minimum flaw size requirement ( $2a = 3.0 \text{ mm}$ ).

For the 7075-T6 aluminum, the crack propagation condition is

$$24 \text{ MPa}\sqrt{m} = 500 \text{ MPa}\sqrt{\pi a}$$

$$2a = 1.5 \text{ mm}$$

which is the half of minimum flaw size requirement. Therefore, it is not possible to use the 7075-T6 aluminum to raise the strength of the material.

**EXAMPLE 5.7**

A quasi-isotropic carbon-fiber epoxy composite laminate is in a state of single edge notched tension (SENT) as shown in figure 5.18 (Anderson, 1995).

The stress intensity factor  $K_I$  of SENT specimen is represented by

$$K_I = \frac{P}{B\sqrt{W}} f\left(\frac{a}{W}\right) \quad (5.83)$$

where  $P$  is the applied force,  $B$  is plate thickness,  $W$  is plate width, and  $f(a/W)$  is a dimensionless function. For the SENT specimen,  $f(a/W)$  has the following form (Anderson, 1995):

$$f\left(\frac{a}{W}\right) = \frac{\sqrt{2 \tan(\pi a/2W)}}{\cos(\pi a/2W)} \left[ 0.752 + 2.02\left(\frac{a}{W}\right) + 0.37\left(1 - \sin\frac{\pi a}{2W}\right)^3 \right] \quad (5.84)$$

- (a) When the fracture toughness  $K_{IC}$  and tensile strength  $X^t$  of the composite material are  $30 \text{ MPa} \cdot \sqrt{m}$  and  $500 \text{ MPa}$ , respectively, determine the critical value

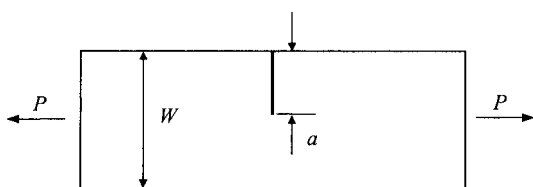


**Figure 5.18** Shape of single edge notched tension (SENT) specimen.

of the stress that would cause unstable propagation of the crack. The width  $W$  and crack length  $a$  are 25 mm and 3 mm, respectively. Compare this stress with the tensile strength of the material, which does not take cracks into account.

(b) When  $a/W$  becomes zero, find the stress intensity factor  $K_I$  for the SENT specimen.

### Solution

From

$$\begin{aligned} K_I &= \frac{P}{B\sqrt{W}} f\left(\frac{a}{W}\right) \\ &= \frac{P}{BW} \sqrt{\pi a} \sqrt{\frac{W}{\pi a}} f\left(\frac{a}{W}\right) \\ &= \sigma \sqrt{\pi a} \sqrt{\frac{W}{\pi a}} f\left(\frac{a}{W}\right) \end{aligned}$$

(a) When  $\frac{a}{W} = \frac{3}{25} = 0.12$

$$\sqrt{\frac{W}{\pi a}} f\left(\frac{a}{W}\right) = 1.22$$

The critical stress is then

$$\sigma_C = \frac{K_{IC}}{1.22\sqrt{\pi a}} = \frac{30}{1.22\sqrt{\pi \times 0.003}} = 253 \text{ MPa}$$

The cracked laminate can sustain less than 50% of the strength (500 MPa) that an uncracked element could withstand.

(b) When  $\frac{a}{W} \rightarrow 0$ , since  $\lim_{\theta \rightarrow 0} \frac{\tan \theta}{\theta} = 1$ ,

$$\sqrt{\frac{W}{\pi a}} f\left(\frac{a}{W}\right) = \lim_{\frac{a}{W} \rightarrow 0} \sqrt{\frac{2W}{\pi a}} \tan \frac{\pi a}{2W} (0.752 + 0.37) = 1.12$$

or  $K_I = 1.12\sigma\sqrt{\pi a}$ .

### 5.6.2 Whitney–Nuismer Failure Criteria for Notched Composites

Whitney and Nuismer developed a simpler approach that can be used as a design guide of composite laminates (Whitney and Nuismer, 1974; Nuismer and Whitney, 1975). They developed two criteria for the strength of notched composite materials. The first criterion is based on the stress at a point a fixed distance away from the notch and may be referred to as the point stress criterion. They developed the first criterion because larger holes, in tension specimens cause greater strength reduction than do smaller holes, although the stress concentration factor is independent of hole size. They thought that the local high stress near the small circular hole boundary might have greater opportunity to redistribute high stress because the normal stress near the hole boundary in the case of a smaller hole is more concentrated, as shown in figure 5.19.

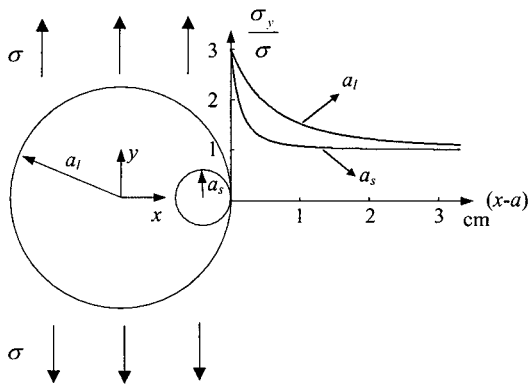


**Figure 5.19** Normal stress distributions near the boundary of circular holes in an infinite isotropic plate ( $a_l=2$  cm,  $a_s=0.5$  cm).

For an infinite orthotropic plate with a hole of radius  $a$  in figure 5.19, the normal stress,  $\sigma_y(x, 0)$ , along the  $x$ -axis near the hole is expressed approximately under uniform stress,  $\sigma$ , at infinity (Lekhnitskii, 1968):

$$\sigma_y(x, 0) = \frac{\sigma}{2} \left\{ 2 + \left(\frac{a}{x}\right)^2 + 3\left(\frac{a}{x}\right)^4 - (K_t - 3) \left[ 5\left(\frac{a}{x}\right)^6 - 7\left(\frac{a}{x}\right)^8 \right] \right\} \quad (5.85)$$

where  $K_t$  is the orthotropic stress concentration factor for an infinite-width plate derived in equation (5.9):

$$K_t = K_t(a, 90^\circ) = 1 + \sqrt{\frac{2}{A_{22}}} \sqrt{\sqrt{A_{11}A_{22}} - A_{12} + \frac{A_{11}A_{22} - A_{12}^2}{2A_{66}}} \quad (5.86)$$

The point stress criterion assumes that failure would occur when  $\sigma_y$  at some fixed distance,  $d_0$ , ahead of the hole first reaches the unnotched tensile strength of the material,  $\sigma_0$ , that is, when

$$\sigma_y(a + d_0, 0) = \sigma_0 \quad (5.87)$$

By combining equations (5.85) and (5.87), we find the ratio of notched strength,  $\sigma_n$ , to unnotched strength,  $\sigma_0$ :

$$\frac{\sigma_n}{\sigma_0} = \frac{2}{2 + \xi_1^2 + 3\xi_1^4 - (K_t - 3)(5\xi_1^6 - 7\xi_1^8)} \quad (5.88)$$

where

$$\xi_1 = \frac{a}{a + d_0} \quad (5.89)$$

For a very large hole,  $\xi_1 \rightarrow 1$ , and from equation (5.88),  $\sigma_n/\sigma_0 \rightarrow 1/K_t$ , which is the conventional theoretical stress concentration factor. For a very small hole,  $\xi_1 \rightarrow 0$ , then  $\sigma_n/\sigma_0 \rightarrow 1$ , as expected.

The second criterion, the average stress criterion, assumes that failure would occur when the average value of  $\sigma_y$  over some fixed distance,  $a_0$ , ahead of the hole

first reaches the unnotched tensile strength of the material, that is, when

$$\frac{1}{a_0} \int_a^{a+a_0} \sigma_y(x, 0) dx = \sigma_0 \quad (5.90)$$

By combining equations (5.85) and (5.90), the ratio of notched strength,  $\sigma_n$ , to unnotched strength,  $\sigma_0$  is found:

$$\frac{\sigma_n}{\sigma_0} = \frac{2(1 - \xi_2)}{2 - \xi_2^2 - \xi_2^4 + (K_t - 3)(\xi_2^6 - \xi_2^8)} \quad (5.91)$$

where

$$\xi_2 = \frac{a}{a + a_0} \quad (5.92)$$

As in the point stress criterion, the expected limits are recovered for the cases when  $\xi_2 \rightarrow 1$  and  $\xi_2 \rightarrow 0$ . The two failure criteria, equation (5.87) and (5.90), may be applied to crack problems. For an infinite plate with a crack length  $2a$  subjected to a uniform stress,  $\sigma$ , parallel to the  $y$ -axis at infinity, as shown in figure 5.17, the exact elasticity solution for the normal stress,  $\sigma_y$ , along the  $x$ -axis near the edge of the crack is given by Lekhnitskii (1968):

$$\sigma_y(x, 0) = \frac{\sigma x}{\sqrt{x^2 - a^2}} = \frac{K_I x}{\sqrt{\pi a(x^2 - a^2)}} \quad (5.93)$$

where  $x > a$  and  $K_I = \sigma \sqrt{\pi a}$  is the stress intensity factor of mode I.

By combining equations (5.87) and (5.93), we find the ratio of notched strength,  $\sigma_n$ , to unnotched strength,  $\sigma_0$ :

$$\frac{\sigma_n}{\sigma_0} = \sqrt{1 - \xi_1^2} \quad (5.94)$$

Here,  $\xi_1$  is the same form as in equation (5.89), but  $a$  represents the half crack length rather than the radius of the hole in this case.

Similarly, combining equations (5.90) and (5.93), we find the ratio of notched strength,  $\sigma_n$ , to unnotched strength,  $\sigma_0$ :

$$\frac{\sigma_n}{\sigma_0} = \sqrt{\frac{1 - \xi_2}{1 + \xi_2}} \quad (5.95)$$

Here, again  $\xi_2$  is the same form as in equation (5.92), but  $a$  represents the half crack length rather than the radius of the hole in this case.

The crack size effect can be better visualized by writing equations (5.94) and (5.95) in terms of the measured values of the fracture toughness,  $K_Q$ ,

$$K_Q = \sigma_n \sqrt{\pi a} = \sigma_0 \sqrt{\pi a(1 - \xi_1^2)}, \text{ for the point stress} \quad (5.96)$$

$$K_Q = \sigma_n \sqrt{\pi a} = \sigma_0 \sqrt{\pi a \frac{1 - \xi_2}{1 + \xi_2}}, \text{ for the average stress} \quad (5.97)$$

For large crack lengths, the value of  $K_Q$  asymptotically approaches a constant value. For *the point stress* and *the average stress criteria*, these asymptotic values are, respectively,

$$K_{Q'} = \sigma_0 \sqrt{2\pi d_0} \quad \text{for the point stress} \quad (5.98)$$

$$K_{Q'} = \sigma_0 \sqrt{0.5\pi a_0} \quad \text{for the average stress} \quad (5.99)$$

The two failure criteria are based on the assumption that the characteristic distance,  $d_0$  or  $a_0$ , remains constant for all hole or crack sizes in at least a laminate of a particular material system. Whitney and Nuismer (1974) carried out experiments to examine the effect of changes in the material system, the laminate stacking sequences, and the notch shape and size on the models. From the experimental data on two material systems, glass-fiber epoxy and carbon-fiber epoxy, with stacking sequences  $[0/\pm 45/90]_{2s}$  and  $[0/90]_{4s}$ , containing through-thickness circular holes and sharp-tipped cracks of several sizes, they found that  $d_0 = 1.0$  mm and  $a_0 = 3.8$  mm. They also found that the experimental results and predictions from both the criteria were quite good, but the experimental data showed a large scatter. Even though it may not be concluded that  $d_0$  and  $a_0$  are universal constants, the equations can be used for a particular material system under uniaxial loading. These criteria may be used for any through-thickness discontinuity for which the theoretical stress distribution can be found, not just for circular holes or straight cracks.

### EXAMPLE 5.8

The plate in example 5.7 has a center crack of length  $2a = 6$  mm, rather than an edge crack, and is subjected to a uniform uniaxial stress. Find fracture strengths of the laminate according to the fracture mechanics criterion, the point stress criterion, and average stress criterion.

#### Solution

From the fracture mechanics criterion:

$$\sigma_C = \frac{K_{IC}}{\sqrt{\pi a}} = \frac{30 \text{ MPa}\sqrt{\text{m}}}{\sqrt{\pi(0.003 \text{ m})}} = 309 \text{ MPa}$$

From the point stress criterion with  $d_0 = 1.0$  mm:

$$\sigma_n = \sigma_0 \sqrt{1 - \xi_1^2} = 500 \text{ MPa} \sqrt{1 - \left(\frac{3}{3+1}\right)^2} = 330 \text{ MPa}$$

From the average stress criterion with  $a_0 = 3.8$  mm:

Since,  $\xi_2 = a/(a + a_0) = 3.0/(3.0 + 3.8) = 0.441$

$$\sigma_n = \sigma_0 \sqrt{\frac{1 - \xi_2}{1 + \xi_2}} = 500 \text{ MPa} \sqrt{\frac{1 - 0.441}{1 + 0.441}} = 311 \text{ MPa}$$

The results from all three calculations are close and the fracture mechanics criterion is slightly more conservative.

### 5.6.3 Energy Criterion Approach

Since stress analysis of the crack tip region for anisotropic materials is not always possible, another useful approach is to apply the “energy release rate” approach to crack propagation. The strain energy release rate approach has proved to be a powerful tool in both experimental and computational studies of crack growth.

Griffith (1920) noted that when a crack is introduced to a stressed plate of elastic brittle material, a balance must be met between the decrease in potential energy related to the release of stored elastic energy and work done by movement of the external loads and the increase in surface energy resulting from the presence of the crack. Likewise, an existing crack would grow by some increment if the necessary additional surface energy were supplied by the system. For a crack with length  $2a$  of figure 5.17, the surface energy is the product of the total crack surface area ( $2 \times 2aB$ ) ( $B$ : plate thickness), and the specific surface energy,  $\gamma_s$ . The surface energy has units of energy/unit area. Griffith used the stress analysis of Inglis (1913) for the case of an infinitely large plate containing an elliptical crack subjected to a fixed displacement sufficient to cause a crack under tensile stress,  $\sigma$ , and computed the decrease in potential energy of the cracked plate to be  $(\pi\sigma^2a^2B)/E$ . Therefore, the change in potential energy of the plate associated with the introduction of a crack may be given by

$$U - U_0 = -\frac{\pi\sigma^2a^2B}{E} + 4aB\gamma_s \quad (5.100)$$

The condition of equilibrium is obtained by differentiating the potential energy  $U$  with respect to the crack length and setting equal to zero:

$$\frac{\partial U}{\partial a} = 4B\gamma_s - \frac{2\pi\sigma^2aB}{E} = 0$$

or, the critical stress  $\sigma_C$  for the fracture initiation is

$$\sigma_C = \sqrt{\frac{2E\gamma_s}{\pi a}} \quad (5.101)$$

which represents the equilibrium condition.

The condition of equilibrium represented by equation (5.101) was based on the plane stress condition. For the plane strain condition (triaxial stress conditions associated with the suppression of strains in one direction), the equilibrium equation is expressed as

$$\sigma_C = \sqrt{\frac{2E\gamma_s}{\pi a(1 - \nu^2)}} \quad (5.102)$$

where  $\nu$  is Poisson's ratio.

The Griffith theory of brittle fracture is subject to two severe restrictions (Sanford, 2003). First, since the change in strain energy was computed for the case of an infinite body containing an isolated crack of length  $2a$ , the theory is valid only for real problems that approximate this condition. Second, the theory applies only to truly brittle materials for which there is no mechanism of energy dissipation (e.g., plastic deformation) other than the formation of surface energy as the crack extends. These restrictions are of little concern to the glass and ceramic industries,

and Griffith's theory in its original form is still widely used within these communities. On the other hand, these restrictions become significant when the size of critical flaws is larger than microscopic or plastic deformation at the crack tip (even highly localized) is involved. Orowan (1955) demonstrated that even highly brittle fractures of low-carbon steels exhibited significant plastic deformation along the fracture surface. As a result the plastic work of fracture exceeded the surface energy by many orders of magnitude. To account for materials that are capable of plastic work, equations (5.101) and (5.102) are revised for plane stress and plane strain cases, respectively, as follows:

$$\sigma_C = \left\{ \frac{2E(\gamma_S + \gamma_P)}{\pi a} \right\}^{1/2} \quad \text{for plane stress} \quad (5.103)$$

where  $\gamma_P$  represents the plastic work per unit area of surface created, and is typically much larger than  $\gamma_S$ , and

$$\sigma_C = \left\{ \frac{2E(\gamma_S + \gamma_P)}{\pi a(1 - \nu^2)} \right\}^{1/2} \quad \text{for plane strain} \quad (5.104)$$

Orowan's extension of the Griffith theory was generalized by Irwin (1957). He used the strain energy release rate,  $G_C$ , that includes all sources of resistance to crack extension. Then the critical stresses  $\sigma_C$  of crack propagation are expressed as

$$\sigma_C = \sqrt{\frac{EG_C}{\pi a}} \quad \text{for plane stress} \quad (5.105)$$

and

$$\sigma_C = \sqrt{\frac{EG_C}{\pi a(1 - \nu^2)}} \quad \text{for plane strain} \quad (5.106)$$

where  $G_C$  is a new bulk material property that can be determined only from fracture measurements on the specific material being considered. Since the Orowan–Irwin fracture criterion, equations (5.105) and (5.106), were developed as extensions of the Griffith condition, it can be applied only to the same condition of an isolated crack of length  $2a$  in an infinite sheet under remote tension in either plane stress or plane strain. For this case, we already have equation (5.80):

$$K_C = \sigma_C \sqrt{\pi a} \quad (5.107)$$

Comparing equation (5.107) and equations (5.105) and (5.106) for the same failure event reveals that

$$K_C^2 = EG_C \quad \text{for plane stress} \quad (5.108)$$

$$K_C^2 = \frac{EG_C}{1 - \nu^2} \quad \text{for plane strain} \quad (5.109)$$

Therefore, at least for this problem, the critical energy release rate  $G_C$  based on global energy concepts, and the critical stress intensity factor based on the local stress field, are equivalent and can be used interchangeably.

The results of equations (5.105) and (5.106) can be generalized by defining the strain energy release rate  $G$  as the rate of change of potential energy  $U$  with respect to the crack area  $A$  (Anderson, 1995):

$$G = -\frac{\partial U}{\partial A} \quad (5.110)$$

$$U = \Phi - W \quad (5.111)$$

where  $\Phi$  is the strain energy stored in the body, and  $W$  is the work done by external forces.

Consider a cracked plate subjected to a constant load  $P$ , which is said to be load controlled. For this case,

$$W = P\Delta \quad (5.112)$$

where  $\Delta$  is the displacement of the plate at the load applied.

If the behavior of the plate is linearly elastic,

$$\Phi = \frac{1}{2}P\Delta \quad (5.113)$$

then,

$$U = \frac{1}{2}P\Delta - P\Delta = -\frac{1}{2}P\Delta = -\Phi \quad (5.114)$$

Using equation (5.114), the strain energy release rate  $G$  is calculated as

$$G = -\frac{1}{b}\left(\frac{dU}{da}\right)_P = \frac{P}{2b}\left(\frac{d\Delta}{da}\right)_P \quad (5.115)$$

where  $b$  is the width of the plate.

When the displacement  $\Delta$  is fixed, which is said to be displacement controlled, the work done  $W$  by external force  $P$  is zero. For this case,  $W=0$  and  $U=\Phi$ . Thus,

$$G = -\frac{1}{b}\left(\frac{dU}{da}\right)_\Delta = -\frac{\Delta}{2b}\left(\frac{dP}{da}\right)_\Delta \quad (5.116)$$

Let us define the compliance  $C$ , which is the inverse of the plate stiffness, as

$$C = \frac{\Delta}{P} \quad (5.117)$$

Substituting equation (5.117) into equations (5.115) and (5.116) results in

$$G = \frac{P^2}{2b} \frac{dC}{da} \quad (5.118)$$

for both load control and displacement control.

### 5.6.4 Interlaminar Fracture

Delamination, or interlaminar fracture, is a very important failure mode in composite laminates. Delamination provides one of the few examples of self-similar crack growth in composite laminates (e.g., crack growth by a simple enlargement of the initial crack without branching or direction changes). A delamination is a crack separating adjacent plies, and the plane of the crack lies in the plane of the interface between plies. Like a crack in a metallic material, a delamination grows in a stable manner until it reaches a critical size, whereupon further growth occurs in an unstable manner. However, interlaminar stresses have a complicated three-dimensional nature, which inhibits the effective use of the stress intensity factor approach, but makes the problem ideally suited for the strain energy release rate approach.

The most important modes of delamination are modes I and II, and the corresponding fracture toughnesses are usually characterized by the strain energy release rates  $G_{IC}$  and  $G_{IIC}$ , respectively.

Among the many test methods developed so far, the most widely used methods are the double cantilever beam (DCB) test for  $G_{IC}$  and the end-notched flexure (ENF) test for  $G_{IIC}$  (figure 5.20).

The compliance  $C$  is calculated by considering the DCB specimen as two cantilever beams of length  $a$  joined at the crack tip. For a unidirectional composite DCB specimen with the fiber direction along the longitudinal axis,

$$C = \frac{\delta}{P} = \frac{8}{E_1 b} \left( \frac{a}{h} \right)^3 \quad (5.119)$$

The strain energy release rate,  $G_I$ , is then found by substituting equation (5.119) into equation (5.118):

$$G_I = \frac{12P^2 a^2}{E_1 b^2 h^3} \quad (5.120)$$

For the end-notched flexure specimen of figure 5.20(b), the deflection  $\delta$  can be calculated by Castigliano's energy method (Shigley et al., 2004):

$$\delta = \frac{2L^3 + 3a^3}{12E_1 I} P \quad (5.121)$$

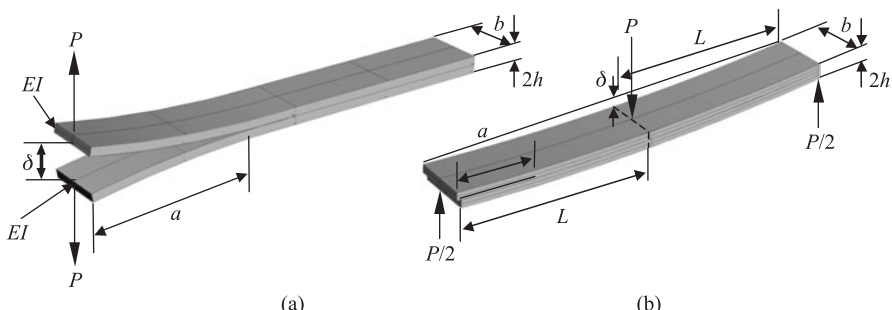


**Figure 5.20** Double cantilever beam (DCB) and end-notched flexure (ENF) specimens: (a) DCB specimen; (b) ENF specimen.

then,

$$C = \frac{\delta}{P} = \frac{2L^3 + 3a^3}{12E_1 I} = \frac{2L^3 + 3a^3}{8E_1 bh^3} \quad (5.122)$$

where  $I$  is the area moment of inertia of the intact beam (height:  $2h$ ). Substituting equation (5.122) into equation (5.118) yields

$$G_{II} = \frac{9P^2 a^2}{16E_1 b^2 h^3} = \frac{9P^2 a^2 C}{2b(2L^3 + 3a^3)} \quad (5.123)$$

When  $G_{IC}$  and  $G_{IIC}$  are measured separately, various interactive criteria for mixed mode delamination growth may be developed. One of the simplest and most widely used of these criteria is given by the equation

$$\frac{G_I}{G_{IC}} + \frac{G_{II}}{G_{IIC}} = 1 \quad (5.124)$$

where  $G_I$ ,  $G_{II}$  = strain energy release rates for delamination growth in modes I and II, respectively.

$G_{IC}$ ,  $G_{IIC}$  = critical strain energy release rates for delamination growth in modes I and II, respectively.

Good agreement between the predictions by equation (5.124) and experimental data has been reported (O'Brien et al., 1987; Johnson et al., 1987).

When the effects of shear deformation are included in deriving equations (5.119) and (5.122), that is, Timoshenko beam theory, the strain energy release rates  $G_I$  and  $G_{II}$  (Carlsson et al., 1986) are modified as follows:

$$G_I = \frac{12P^2}{E_1 b^2 h} \left[ \left( \frac{a}{n} \right)^2 + 0.1 \frac{E_1}{G_{31}} \right] \quad (5.125)$$

$$G_{II} = \frac{9P^2 a^2}{16E_1 b^2 h^3} \left[ 1 + 0.2 \frac{E_1}{G_{31}} \left( \frac{h}{a} \right)^2 \right] \quad (5.126)$$

where  $G_{31}$  is the transverse shear modulus of the specimen.

## 5.7 Concluding Remarks

The failure criteria for composite materials are presented for the strength design of composite structures. The transformation of the ply stresses from the global axes to the principal material axes is presented for the failure criteria on the ply basis. The stress concentration factors around a hole or a crack in a composite structure and the interlaminar stresses at the plate boundaries are discussed. The stress intensity factor and strain energy release rate of composite structures are presented for the design of composite structures using fracture mechanics approach. Several criteria

for the crack and delamination problems are presented to be used in the design of composite structures.

## Problems

- 5.1.** A composite laminate plate with stacking sequence of  $[\pm 35/0]_S$ , is subjected to the following load.

$$N_x = 15000 \text{ N/m}$$

$$N_y = 10000 \text{ N/m}$$

$$N_{xy} = 5000 \text{ N/m}$$

The material properties of the unidirectional carbon-fiber epoxy composite are

$$E_1 = 130 \text{ GPa}$$

$$E_2 = 10.5 \text{ GPa}$$

$$\nu_{12} = 0.28$$

$$G_{12} = 6.0 \text{ GPa}$$

$$t_{\text{ply}} = 0.135 \text{ mm}$$

- (a) Find the laminate strains for this multiaxial loading.
- (b) Calculate the laminate stresses of each ply in the global axes.
- (c) Sketch out these laminate stresses in the global axes. Show that they sum to the proper loadings.
- (d) Calculate the ply stresses in ply axes.
- (e) Calculate the ply strains in ply axes using transformation.
- (f) Using the compliances show that  $\varepsilon_\alpha^{[45]} (\alpha = 1, 2, 6)$  has been properly calculated in (e).

- 5.2.** A composite laminate is made up of two different carbon-fiber epoxy: unidirectional tape and fabric prepreg. The lay-up is shown in figure 5.21.

The basic ply values for the two materials are given in table 5.7.

+40°	tape
-40°	tape
0°	fabric
----- symmetric -----	

**Figure 5.21** The lay-up of the composite laminate for problem 5.2.

**Table 5.7 Elastic Constants for Basic Ply of Problem 5.2**

	Unidirectional	Fabric
$E_1$	130 GPa	72.5 GPa
$E_2$	10.5 GPa	72.6 GPa
$\nu_{12}$	0.28	0.059
$G_{12}$	6.0 GPa	4.5 GPa
$t_{\text{ply}}$	0.135 mm	0.35 mm

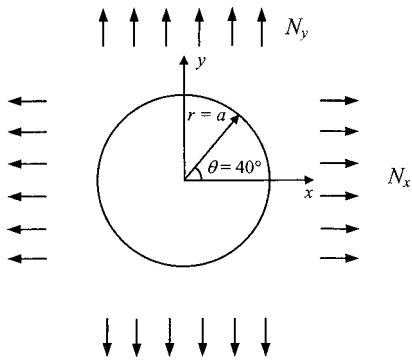


**Figure 5.22** Schematic diagram of the hole in the composite laminate.

Note that the  $0^\circ$  fabric designation implies that the warp fibers are along the laminate longitudinal axis and the weft fibers are along the laminate transverse axis.

The laminate is loaded by  $N_x = 2.5 \times 10^4 \text{ N/m}$  and  $N_y = 1.5 \times 10^4 \text{ N/m}$ . The laminate has a hole drilled in it and we are interested in the point on the hole where  $\theta = 40^\circ$  and  $r = a$ , as in figure 5.22.

At this point, find:

- (a) laminate strains
- (b) ply stresses in laminate axes
- (c) ply stresses in ply axes
- (d) ply strains in ply axes

- 5.3. (a) Prove that the shear strength in the principal material coordinate direction is independent of the sign of the shear stress.
- (b) However, prove that the positive and negative shear stresses applied to a lamina with stacking angle of  $45^\circ$  will produce different stress states viewed on the material coordinate.
- 5.4. Prove that the measured stiffness of the test of figure 5.3 is  $\bar{Q}_{11}$  rather than  $E_x$  when the specimen length is short.
- 5.5. Calculate the theoretical stress concentration factor  $K_t$  of the  $[0/\pm 52]_S$  laminate of figure 5.2.
- 5.6. For the maximum sustainable pressure of the pressure vessel of example 5.5, find that  $\theta = 53.25$  is the optimum wrap angle from the stacking sequence type of  $[\pm\theta]_S$ , which is a little different from the value obtained from netting analysis.
- 5.7. The laminate in problem 4.7 will be used in an expedition to Antarctica. The company is concerned that the cold may cause problems. The plate is unloaded and unrestrained (no mechanical load is applied) in its use. First-ply failure is considered unacceptable and is considered to be failure of the part. Using the maximum stress criteria, determine if there is a temperature that causes part failure. Use the strength data below:

$$X' = 1661 \text{ MPa}, \quad X^c = -1698 \text{ MPa}, \quad Y' = 53.9 \text{ MPa},$$

$$Y^c = -221 \text{ MPa}, \quad S = 105 \text{ MPa}$$

- 5.8. A boron epoxy composite material has the following properties:

$$E_1 = 207 \text{ GPa}, \quad E_2 = 19 \text{ GPa}, \quad G_{12} = 6.4 \text{ GPa}, \quad \nu_{12} = 0.21, \quad X_t = 1.585 \text{ GPa},$$

$$X_c = 1.6 \text{ GPa}, \quad Y_t = 62.7 \text{ MPa}, \quad Y_c = 125 \text{ MPa}, \quad S = 62 \text{ MPa}, \quad t_{\text{ply}} = 0.25 \text{ mm}$$

The laminate stacking sequence is [0/90]<sub>S</sub> under the load of  $N_x$ .

- (a) What percentage of the load is carried by the 0 degree plies?
- (b) Which ply will fail first? Use the maximum stress criterion.
- (c) What is the maximum load,  $N_{\max 1}$ , that the laminate can carry at incipient failure?
- What stress exists in the remaining two plies, at the failure load of the two others?
- (d) If the structure can tolerate failure of two plies, what is the maximum load,  $N_{\max 2}$ , that the other two plies can withstand to failure?

**5.9.** Derive equation (5.49).

**5.10.** Derive equation (5.64).

**5.11.** Prove that  $[\pm 15/\pm 45]_S$  produces a tensile stress of  $\sigma_y$  in the  $15^\circ$  ply under the uniform tensile stress  $\sigma_x$ , while  $[\pm 45/\pm 15]_S$  produces a compressive stress  $\sigma_y$  under the uniform tensile stress  $\sigma_x$ . Also calculate the stress  $\sigma_y$  in the stacking sequence of  $[15/45/-45/-15]_S$ . Use the material properties of problem 5.1.

**5.12.** Demonstrate that the plane strain tensile loading offers less opportunity for redistributing high crack root stresses by shear yielding when  $\sigma_z$  is tensile by considering three dimensional Mohr stress circles for  $\sigma_z=0$  and  $\sigma_z=a$  positive value.

**5.13.** For the cross-ply laminate with stacking sequence  $[0/90]_S$ , draw the interlaminar stresses  $\sigma_z$  and  $\tau_{yz}$  similar to figure 5.11.

**5.14.** Derive equations (5.91), (5.95), (5.98), and (5.99).

**5.15.** Derive equations (5.120) and (5.123).

**5.16.** Derive equation (5.125).

**5.17.** Modify your computer program to compute the ply stresses in the laminate axes as well as in the ply axes. Include the several failure criteria into the program to evaluate the failure index (FI) of composite plates.

## References

- Agarwal, B. D., and Broutman, L. J. 1990. *Analysis and Performance of Fiber Composite*, 2nd ed., John Wiley & Sons, New York.
- Anderson, T. L. 1995. *Fracture Mechanics, Fundamentals and Applications*, 2nd ed., CRC Press, Boca Raton, Fl.
- Brewer, J. C., and Lagace, P. A. 1988. "Quadratic Stress Criterion for Initiation of Delamination," *Journal of Composite Materials*, Vol. 22, pp. 1141–1155.
- Carlsson, L. A., Gillespie, J. W., Jr., and Pipes, R. B. 1986. "On the Analysis and Design of End Notch Flexure (ENF) Specimen for Mode II Testing," *Journal of Composite Materials*, Vol. 20, pp. 594–604.
- Felbeck, D. K., and Atkins, A. G. 1996. *Strength and Fracture of Engineering Solid*, Prentice-Hall, Upper Saddle River, N.J.
- Gibson, R. F. 1994. *Principles of Composite Materials Mechanics*, McGraw-Hill, New York.
- Griffith, A. A. 1920. "The Phenomena of Rupture and Flaw in Solids," *Philosophical Transactions of the Royal Society*, Vol. 221A, pp. 163–198.
- Hahn, H. T., Erikson, J. B., and Tsai, S. W. 1982. "Characterization of Matrix/Interface-Controlled Strength of Unidirectional Composite," in *Fracture of Composite Materials*, Edited by Shi, G., and Tamuzs, V. P., Martinus Nijhoff Publishers, New York, pp. 197–214.
- Hashin, Z. 1980. "Failure Criteria for Unidirectional Fiber Composites," *Journal of Applied Mechanics*, Vol. 102, pp. 329–334.
- Herakovich, C. T. 1998. *Mechanics of Fibrous Composites*, John Wiley & Sons, New York.

- Hertzberg, R. W. 1996. *Deformation and Fracture Mechanics of Engineering Materials*, 4th ed., John Wiley & Sons, New York.
- Hill, R. 1950. *The Mathematical Theory of Plasticity*, Oxford University Press, Oxford.
- Inglis, C. E. 1913. "Stresses in a Plate due to the Presence of Cracks and Sharp Corners," *Transaction of the Institute of Naval Architects*, Vol. 55, pp. 219–230.
- Irwin, G. R. 1957. "Analysis of Stress and Strains near the End of a Crack Traversing a Plate," *Journal of Applied Mechanics*, Vol. 79, pp. 361–364.
- Johnson, W. S., and Wangalgiri, P. D. 1987. "Influence of the Resin on Interlaminar Mixed-Mode Fracture," in *Toughened Composites*, Edited by Johnston, N. J., ASTM STP 937, Philadelphia, pp. 295–315.
- Jones, R. M. 1975. *Mechanics of Composite Materials*, McGraw-Hill, New York.
- Kim, R. Y., and Soni, S. R. 1984. "Experimental and Analytical Studies on the Onset of Delamination in Laminated Composites," *Journal of Composite Materials*, Vol. 18, pp. 70–80.
- Konish, H. J., Swedlow, J. L., and Cruse, T. A. 1972. "Experimental Investigation of Fracture in an Advanced Composites," *Journal of Composite Materials*, Vol. 6, pp. 114–124.
- Lekhnitskii, S. G. 1963. *Theory of Elasticity of an Anisotropic Elastic Body*, Holden-Day, San Francisco.
- Lekhnitskii, S. G. 1968. *Anisotropic Plates*, Gordon and Breach Science Publishers, New York.
- Narayanaswami, R., and Adelman, H. M. 1977. "Evaluation of the Tensor Polynomial and Hoffman Strength Theories for Composite Materials," *Journal of Composite Materials*, Vol. 11, pp. 366–377.
- Nuismer, R. J., and Whitney, J. M. 1975. "Uniaxial Failure of Composite Laminates Containing Stress Concentration," in *Fracture Mechanics of Composites*, ASTM STP 593, Philadelphia, pp. 117–142.
- O'Brien, T. K. 1982. "Characterization of Delamination Onset and Growth in a Composite Laminate," in *Damage in Composite Materials*, Edited by Reifsnider, K. L., ASTM STP 775, Philadelphia, pp. 140–167.
- O'Brien, T. K., Johnston, N. J., Raju, I. S., Morris, D. H., and Simonds, R. A. 1987. "Comparisons of Various Configurations of the Edge Delamination Test for Interlaminar Fracture Toughness," in *Toughened Composites*, Edited by Johnston, N. J., ASTM STP 937, Philadelphia, pp. 199–221.
- Orowan, E. 1955. "Energy of Fracture," *Welding Journal, Research Supplement*, Vol. 34, No. 3, pp. 157–160.
- Pagano, N. J., and Soni, S. R. 1989. "Models for Studying Free-Edge Effects," in *Interlaminar Response of Composite Materials*, Edited by Pagano, N. J., Elsevier, Amsterdam, Chapter 1, pp. 1–68.
- Parhizgar, S., Zachary, L. W., and Sun, C. T. 1982. "Application of the Principles of Linear Fracture Mechanics to the Composite Materials," *International Journal of Fracture*, Vol. 20, pp. 3–15.
- Pipes, R. B., and Pagano, N. J. 1970. "Interlaminar Stresses in Composite Laminates Under Uniform Axial Extension," *Journal of Composite Materials*, Vol. 4, pp. 538–548.
- Sanford, R. J. 2003. *Principles of Fracture Mechanics*, Prentice-Hall, Upper Saddle River, N.J.
- Shigley, J. E., Mischke, C. R., and Budynas, R. G. 2004. *Mechanical Engineering Design*, 7th ed., McGraw-Hill, New York.
- Sun, C. T., and Sierakowski, R. L. 1980. "Fracture Characterization of Composites with Chopped Fiberglass Reinforcement," *SAMPE Quarterly*, Vol. 11, No. 4, pp. 15–21.
- Swanson, R. S. 1997. *Introduction to Design and Analysis with Advanced Composite Materials*, Prentice-Hall, Upper Saddle River, N.J.
- Timoshenko, S. P., and Goodier, J. N. 1970. *Theory of Elasticity*, 3rd ed., McGraw-Hill, New York.

- Tsai, S. W., and Hahn, H. T. 1980. *Introduction to Composite Materials*, Technomic Publishing Company, Lancaster, PA.
- Whitney, J. M., and Nuismer, R. J. 1974. "Stress Fracture Criteria for Laminated Composites Containing Stress Concentration," *Journal of Composite Materials*, Vol. 8, pp. 253-265.

**6**

# Behavior of Composite Laminated Plates and Beams

## 6.1 Introduction

The drastic increase in the use of composite materials in all types of engineering structures such as aircraft, spacecraft, automobiles, robots, machine tools, sports goods, underwater structures, medical prosthetic devices, electronic circuit boards, and infrastructures makes it necessary to design and analyze composite structures or structural components made from composite materials. Since many machine structures are composed of plates and beams, a clear foundation for the theory of laminated anisotropic plates and beams, including the problems of bending under transverse load, stability or buckling, and vibration is indispensable for the application of composite structures to these machines. Therefore, in this chapter, the governing differential equations of composite laminate plates are derived using the definitions of chapters 3 and 4 for a variety of loadings and boundary conditions. Plates and beams are treated under static and dynamic loads including bending, buckling, vibration, and impact loads. Shear deformation effects for the bending and buckling of composite plates are briefly discussed, which is necessary to assess the natural frequency and damping of composite structures. The vibration of beams is solved both by the analytic method and superposition method.

Composite sandwich structures are also discussed because they give the highest specific stiffness in bending and their use is increasing nowadays due to their energy-saving merit.

Since the box-type beams are widely employed in machine tools and robot structures due to both their high bending and torsional stiffnesses, they are treated in detail, which should provide basic tools in chapters 13 and 14.

## 6.2 Equilibrium Equation

In chapter 3, we derived the equilibrium equations for a material point, which is rewritten here for the  $k$ th layers of the plate in the global coordinates  $x, y, z$ :

$$\frac{\partial \sigma_x^{[k]}}{\partial x} + \frac{\partial \tau_{yx}^{[k]}}{\partial y} + \frac{\partial \tau_{zx}^{[k]}}{\partial z} + F_x^{[k]} = \rho^{[k]} \frac{\partial^2 u}{\partial t^2} \quad (6.1)$$

$$\frac{\partial \tau_{xy}^{[k]}}{\partial x} + \frac{\partial \sigma_y^{[k]}}{\partial y} + \frac{\partial \tau_{zy}^{[k]}}{\partial z} + F_y^{[k]} = \rho^{[k]} \frac{\partial^2 v}{\partial t^2} \quad (6.2)$$

$$\frac{\partial \tau_{xz}^{[k]}}{\partial x} + \frac{\partial \tau_{yz}^{[k]}}{\partial y} + \frac{\partial \sigma_z^{[k]}}{\partial z} + F_z^{[k]} = \rho^{[k]} \frac{\partial^2 w}{\partial t^2} \quad (6.3)$$

where  $F_x^{[k]}$ ,  $F_y^{[k]}$ , and  $F_z^{[k]}$  represent body forces (force/volume of material) of the  $k$ th layer in the  $x$ ,  $y$ , and  $z$ -directions, respectively.  $\rho^{[k]}$  and  $t$  represent the density of the  $k$ th layer and the time, and  $u$ ,  $v$ , and  $w$  represent the displacements of a particle in the  $x$ ,  $y$ , and  $z$ -directions, respectively.

Neglecting the body force  $F_x^{[k]}$  for simplicity of derivation, we can integrate equation (6.1) in the thickness direction to obtain the governing equation of composite plates in the  $x$ -direction. Integrating term by term across each ply, and summing across the plates, we have

$$\sum_{k=1}^n \int_{z_{k-1}}^{z_k} \frac{\partial \sigma_x^{[k]}}{\partial x} dz + \sum_{k=1}^n \int_{z_{k-1}}^{z_k} \frac{\partial \tau_{yx}^{[k]}}{\partial y} dz + \sum_{k=1}^n \int_{z_{k-1}}^{z_k} \frac{\partial \tau_{zx}^{[k]}}{\partial z} dz = \sum_{k=1}^n \int_{z_{k-1}}^{z_k} \rho^{[k]} \frac{\partial^2 u}{\partial t^2} dz \quad (6.4)$$

Interchanging the integration and differentiation of the first two terms, we have

$$\frac{\partial}{\partial x} \left( \sum_{k=1}^n \int_{z_{k-1}}^{z_k} \sigma_x^{[k]} dz \right) + \frac{\partial}{\partial y} \left( \sum_{k=1}^n \int_{z_{k-1}}^{z_k} \tau_{yx}^{[k]} dz \right) + \sum_{k=1}^n \tau_{zx} \Big|_{z_{k-1}}^{z_k} = \rho h \frac{\partial^2 u}{\partial t^2} \quad (6.5)$$

where

$$\rho = \frac{1}{h} \int_{-\frac{h}{2}}^{\frac{h}{2}} \rho^{[k]} dz = \frac{1}{h} \sum_{k=1}^n \rho^{[k]} (z_k - z_{k-1}) \quad (6.6)$$

The first two terms in the parentheses are  $N_x$  and  $N_{yx}$  defined in equation (4.16). Since the interlaminar shear stresses cancel each other between the laminate plies, the third term of equation (6.5) vanishes; only externally applied shear stresses remain on the top ( $\tau_{nx}$ , at  $z=z_n=h/2$ ) and bottom ( $\tau_{1x}$ , at  $z=z_0=-h/2$ ) surfaces. Then equation (6.5) can be written as

$$\frac{\partial N_x}{\partial x} + \frac{\partial N_{yx}}{\partial y} + \tau_{nx} - \tau_{1x} = \rho h \frac{\partial^2 u}{\partial t^2} \quad (6.7a)$$

By the same method, the equations in the  $y$ - and  $z$ -directions can be derived as follows:

$$\frac{\partial N_{yx}}{\partial x} + \frac{\partial N_y}{\partial y} + \tau_{ny} - \tau_{1y} = \rho h \frac{\partial^2 v}{\partial t^2} \quad (6.7b)$$

$$\frac{\partial Q_x}{\partial x} + \frac{\partial Q_y}{\partial y} + \sigma_{nz} - \sigma_{1z} = \rho h \frac{\partial^2 w}{\partial t^2} \quad (6.7c)$$

where

$$\begin{aligned}\sigma_{nz} &= \sigma_z & \text{at } z = h/2 \\ \sigma_{1z} &= \sigma_z & \text{at } z = -h/2\end{aligned}$$

The transverse shear force resultants  $Q_x$  and  $Q_y$  are defined as

$$Q_x = \int_{-\frac{h}{2}}^{\frac{h}{2}} \tau_{xz} dz \quad (6.8)$$

$$Q_y = \int_{-\frac{h}{2}}^{\frac{h}{2}} \tau_{yz} dz \quad (6.9)$$

The moment equilibrium equation of the composite plate in the  $x$ -direction can be derived by multiplying the equilibrium equation (6.1) by  $z$  and then integrating in the ply thickness direction:

$$\sum_{k=1}^n \int_{z_{k-1}}^{z_k} \frac{\partial \sigma_x^{[k]}}{\partial x} z dz + \sum_{k=1}^n \int_{z_{k-1}}^{z_k} \frac{\partial \tau_{yx}^{[k]}}{\partial y} z dz + \sum_{k=1}^n \int_{z_{k-1}}^{z_k} \frac{\partial \tau_{zx}^{[k]}}{\partial z} z dz = \sum_{k=1}^n \int_{z_{k-1}}^{z_k} \rho^{[k]} \frac{\partial^2 u}{\partial t^2} z dz \quad (6.10)$$

By interchanging integration and differentiation, the first two terms of equation (6.10) become the differentiations of the moment resultants in the  $x$ - and  $y$ -directions and the third term of equation (6.10) can be integrated by parts as follows:

$$\frac{\partial M_x}{\partial x} + \frac{\partial M_{yx}}{\partial y} + \sum_{k=1}^n \left( z \tau_{zx} \Big|_{z_{k-1}}^{z_k} - \int_{z_{k-1}}^{z_k} \tau_{zx} dz \right) = \sum_{k=1}^n \int_{z_{k-1}}^{z_k} \rho^{[k]} \frac{\partial^2 u}{\partial t^2} z dz \quad (6.11)$$

Using the definitions of transverse shear force resultants  $Q_x$  and  $Q_y$  of equations (6.8) and (6.9), let us express them together with other force and moment resultants already defined in chapter 4 in matrix form:

$$\begin{Bmatrix} N_x \\ N_y \\ N_{xy} \\ Q_x \\ Q_y \end{Bmatrix} = \int_{-\frac{h}{2}}^{\frac{h}{2}} \begin{Bmatrix} \sigma_x \\ \sigma_y \\ \tau_{xy} \\ \tau_{xz} \\ \tau_{yz} \end{Bmatrix} dz = \sum_{k=1}^n \int_{z_{k-1}}^{z_k} \begin{Bmatrix} \sigma_x \\ \sigma_y \\ \tau_{xy} \\ \tau_{xz} \\ \tau_{yz} \end{Bmatrix}^{[k]} dz \quad (6.12)$$

$$\begin{Bmatrix} M_x \\ M_y \\ M_{xy} \end{Bmatrix} = \int_{-\frac{h}{2}}^{\frac{h}{2}} \begin{Bmatrix} \sigma_x \\ \sigma_y \\ \tau_{xy} \end{Bmatrix} z dz = \sum_{k=1}^n \int_{z_{k-1}}^{z_k} \begin{Bmatrix} \sigma_x \\ \sigma_y \\ \tau_{xy} \end{Bmatrix}^{[k]} z dz \quad (6.13)$$

The fourth term in equation (6.11) is  $-Q_x$  and the third term vanishes except for the applied external shear stresses on the top and bottom surfaces ( $\tau_{nx}$  at  $z = h/2$  and  $\tau_{1x}$  at  $z = -h/2$ ). Therefore, equation (6.11) reduces as follows:

$$\frac{\partial M_x}{\partial x} + \frac{\partial M_{yx}}{\partial y} - Q_x + \frac{h}{2} (\tau_{nx} + \tau_{1x}) = \sum_{k=1}^n \int_{z_{k-1}}^{z_k} \rho^{[k]} \frac{\partial^2 u}{\partial t^2} z dz \quad (6.14)$$

By the same method, the moment equilibrium equation in the  $y$ -direction reduces to

$$\frac{\partial M_{xy}}{\partial x} + \frac{\partial M_y}{\partial y} - Q_y + \frac{h}{2}(\tau_{ny} + \tau_{1y}) = \sum_{k=1}^n \int_{z_{k-1}}^{z_k} \rho^{[k]} \frac{\partial^2 v}{\partial t^2} z dz \quad (6.15)$$

Without surface shear stresses, equations (6.14), (6.15), and (6.7c) reduce to

$$\frac{\partial M_x}{\partial x} + \frac{\partial M_{yx}}{\partial y} - Q_x = \sum_{k=1}^n \int_{z_{k-1}}^{z_k} \rho^{[k]} \frac{\partial^2 u}{\partial t^2} z dz \quad (6.16)$$

$$\frac{\partial M_{xy}}{\partial x} + \frac{\partial M_y}{\partial y} - Q_y = \sum_{k=1}^n \int_{z_{k-1}}^{z_k} \rho^{[k]} \frac{\partial^2 v}{\partial t^2} z dz \quad (6.17)$$

$$\frac{\partial Q_x}{\partial x} + \frac{\partial Q_y}{\partial y} + p(x, y) = \rho h \frac{\partial^2 w}{\partial t^2} \quad (6.18)$$

where

$$p(x, y) = \sigma_{nz}(x, y) - \sigma_{1z}(x, y) \quad (6.19)$$

Neglecting inertia terms and solving for  $Q_x$  from equation (6.16) and  $Q_y$  from equation (6.17) and substituting into equation (6.18) yields

$$\frac{\partial^2 M_x}{\partial x^2} + 2 \frac{\partial^2 M_{xy}}{\partial x \partial y} + \frac{\partial^2 M_y}{\partial y^2} = -p(x, y) \quad (6.20)$$

All the equations derived up to now are valid only for small deformations. When the plate deformation is finite and nonlinear terms involving products of stresses and plate slopes are only retained because other terms are second order (Whitney, 1987), equation (6.3), which represents the motion of plate in the thickness direction, becomes

$$\begin{aligned} & \frac{\partial}{\partial x} \left( \tau_{zx} + \sigma_x \frac{\partial w}{\partial x} + \tau_{xy} \frac{\partial w}{\partial y} \right)^{[k]} + \frac{\partial}{\partial y} \left( \tau_{zy} + \tau_{xy} \frac{\partial w}{\partial x} + \sigma_y \frac{\partial w}{\partial y} \right)^{[k]} \\ & + \frac{\partial}{\partial z} \left( \sigma_z + \tau_{xz} \frac{\partial w}{\partial x} + \tau_{yz} \frac{\partial w}{\partial y} \right)^{[k]} + F_z^{[k]} = \rho h \frac{\partial^2 w}{\partial t^2} \end{aligned} \quad (6.21)$$

Neglecting the body force  $F_z^{[k]}$  and integrating equation (6.21) with respect to  $z$  and again interchanging the order of differentiation and integration yields

$$\begin{aligned} & N_x \frac{\partial^2 w}{\partial x^2} + 2N_{xy} \frac{\partial^2 w}{\partial x \partial y} + N_y \frac{\partial^2 w}{\partial y^2} + \frac{\partial Q_x}{\partial x} + \frac{\partial Q_y}{\partial y} + \frac{\partial w}{\partial x} \left( \frac{\partial N_x}{\partial x} + \frac{\partial N_{xy}}{\partial y} \right) \\ & + \frac{\partial w}{\partial y} \left( \frac{\partial N_{xy}}{\partial x} + \frac{\partial N_y}{\partial y} \right) + p = \rho h \frac{\partial^2 w}{\partial t^2} \end{aligned} \quad (6.22)$$

The last two terms in parentheses on the left side of equation (6.22) vanish for the static case and are second order for the dynamic case from equation (6.7) because they represent rotational inertia terms. Thus, equation (6.22) becomes

$$N_x \frac{\partial^2 w}{\partial x^2} + 2N_{xy} \frac{\partial^2 w}{\partial x \partial y} + N_y \frac{\partial^2 w}{\partial y^2} + \frac{\partial Q_x}{\partial x} + \frac{\partial Q_y}{\partial y} + p = \rho h \frac{\partial^2 w}{\partial t^2} \quad (6.23)$$

Neglecting the rotary inertia terms on the right-hand side of equations (6.16) and (6.17) and solving for  $Q_x$  from equation (6.16) and  $Q_y$  from equation (6.17) and substituting into equation (6.23) yields

$$\frac{\partial^2 M_x}{\partial x^2} + 2 \frac{\partial^2 M_{xy}}{\partial x \partial y} + \frac{\partial^2 M_y}{\partial y^2} + N_x \frac{\partial^2 w}{\partial x^2} + 2N_{xy} \frac{\partial^2 w}{\partial x \partial y} + N_y \frac{\partial^2 w}{\partial y^2} + p = \rho h \frac{\partial^2 w}{\partial t^2} \quad (6.24)$$

Relieving the assumptions of the Kirchhoff or Kirchhoff–Love hypothesis in chapter 4 that the normals to the midplane of the laminate remain straight and normal to the deformed midplane after deformation, the functional forms of the displacements for the laminated plate are

$$u(x, y, z) = u_0(x, y) + z\alpha(x, y) \quad (6.25a)$$

$$v(x, y, z) = v_0(x, y) + z\beta(x, y) \quad (6.25b)$$

$$w(x, y, z) = w_0(x, y) \quad (6.25c)$$

where  $u_0$ ,  $v_0$ , and  $w_0$  are the neutral surface displacements defined in figure 4.2, and  $\alpha(x, y)$  and  $\beta(x, y)$  represent the rotations of a linear element through the thickness. Equation (6.25) is called the first-order shear deformation theory. From the expressions of equation (6.25), the strains are expressed as follows:

$$\varepsilon_x = \varepsilon_x^0 + z\kappa_x \quad (6.26a)$$

$$\varepsilon_y = \varepsilon_y^0 + z\kappa_y \quad (6.26b)$$

$$\gamma_{xy} = \gamma_{xy}^0 + z\kappa_{xy} \quad (6.26c)$$

$$\varepsilon_z = 0 \quad (6.26d)$$

The engineering strains of the neutral surface are expressed as follows:

$$\varepsilon_x^0 = \frac{\partial u_0}{\partial x} \quad (6.27a)$$

$$\varepsilon_y^0 = \frac{\partial v_0}{\partial x} \quad (6.27b)$$

$$\gamma_{xy}^0 = \frac{\partial u_0}{\partial y} + \frac{\partial v_0}{\partial x} \quad (6.27c)$$

The engineering curvatures of the neutral surface are expressed as follows:

$$\kappa_x = \frac{\partial \alpha}{\partial x} \quad (6.28a)$$

$$\kappa_y = \frac{\partial \beta}{\partial y} \quad (6.28b)$$

$$\kappa_{xy} = \frac{\partial \alpha}{\partial y} + \frac{\partial \beta}{\partial x} \quad (6.28c)$$

### 6.3 Constitutive Equation for Classical Lamination Theory

When the displacements of an element are expressed with equation (6.25), the constitutive equations of the plate have the same forms as equations (4.22) and (4.30).

When the condition of zero transverse shear deformation is imposed, we get the relationship

$$\gamma_{xz} = \frac{\partial w}{\partial x} + \frac{\partial u}{\partial z} = \frac{\partial w}{\partial x} + \alpha = 0 \quad (6.29)$$

where  $w$  represents  $w_0$  and the subscript 0 on  $w$  will be omitted from now on.

Therefore, the rotation  $\alpha$  of a linear element with respect to the  $y$ -axis is expressed as

$$\alpha = -\frac{\partial w}{\partial x} \quad (6.30)$$

By the same method, the rotation  $\beta$  of a linear element with respect to the  $x$ -axis is expressed as

$$\beta = -\frac{\partial w}{\partial y} \quad (6.31)$$

Then, from equation (6.28), the engineering curvatures are expressed as follows:

$$\kappa_x = -\frac{\partial^2 w}{\partial x^2} \quad (6.32a)$$

$$\kappa_y = -\frac{\partial^2 w}{\partial y^2} \quad (6.32b)$$

$$\kappa_{xy} = -2 \frac{\partial^2 w}{\partial x \partial y} \quad (6.32c)$$

The results of equation (6.32) are the same as equation (4.8), which was derived based on the classical lamination theory. Therefore, the strains of the laminate plate

are expressed as:

$$\varepsilon_x = \frac{\partial u_0}{\partial x} - z \frac{\partial^2 w}{\partial x^2} \quad (6.33a)$$

$$\varepsilon_y = \frac{\partial v_0}{\partial y} - z \frac{\partial^2 w}{\partial y^2} \quad (6.33b)$$

$$\gamma_{xy} = \frac{\partial u_0}{\partial y} + \frac{\partial v_0}{\partial x} - 2z \frac{\partial^2 w}{\partial x \partial y} \quad (6.33c)$$

Using equation (6.25) in conjunction with the assumption of plane stress within each ply and the definition of force and moment resultants, equations (6.12) and (6.13), we obtain a constitutive relation of the exactly same form as that given by equation (4.39) without hygrothermal effects. For symmetric stacking sequences, the  $[B]$  matrix vanishes and the force resultants and moment resultants are uncoupled. For this case, the moment equation becomes from equation (4.39):

$$\begin{Bmatrix} M_x \\ M_y \\ M_{xy} \end{Bmatrix} = \begin{bmatrix} D_{11} & D_{12} & D_{16} \\ D_{12} & D_{22} & D_{26} \\ D_{16} & D_{26} & D_{66} \end{bmatrix} \begin{Bmatrix} \kappa_x \\ \kappa_y \\ \kappa_{xy} \end{Bmatrix} \quad (6.34)$$

If the transverse shear deformation is neglected, equation (6.34) becomes, using the results of equation (6.32):

$$M_x = -D_{11} \frac{\partial^2 w}{\partial x^2} - D_{12} \frac{\partial^2 w}{\partial y^2} - 2D_{16} \frac{\partial^2 w}{\partial x \partial y} \quad (6.35a)$$

$$M_y = -D_{12} \frac{\partial^2 w}{\partial x^2} - D_{22} \frac{\partial^2 w}{\partial y^2} - 2D_{26} \frac{\partial^2 w}{\partial x \partial y} \quad (6.35b)$$

$$M_{xy} = -D_{16} \frac{\partial^2 w}{\partial x^2} - D_{26} \frac{\partial^2 w}{\partial y^2} - 2D_{66} \frac{\partial^2 w}{\partial x \partial y} \quad (6.35c)$$

Substituting equation (6.35) into equation (6.24) results in

$$\begin{aligned} D_{11} \frac{\partial^4 w}{\partial x^4} + 4D_{16} \frac{\partial^4 w}{\partial x^3 \partial y} + 2(D_{12} + 2D_{66}) \frac{\partial^4 w}{\partial x^2 \partial y^2} + 4D_{26} \frac{\partial^4 w}{\partial x \partial y^3} \\ + D_{22} \frac{\partial^4 w}{\partial y^4} + \rho h \frac{\partial^2 w}{\partial t^2} = N_x \frac{\partial^2 w}{\partial x^2} + 2N_{xy} \frac{\partial^2 w}{\partial x \partial y} + N_y \frac{\partial^2 w}{\partial y^2} + p \end{aligned} \quad (6.36)$$

When the laminate is composed of specially orthotropic or balanced and dispersed plies, considerable simplification results (Swanson, 1997). For these cases, the values of  $D_{16}$  and  $D_{26}$  terms vanish or become small. The specially orthotropic laminate is composed of plies whose fiber angles are parallel or perpendicular to the loading direction.

If it is assumed that  $D_{16}$  and  $D_{26}$  terms vanish, then from equation (6.34)

$$M_x = D_{11}\kappa_x + D_{12}\kappa_y \quad (6.37a)$$

$$M_y = D_{12}\kappa_x + D_{22}\kappa_y \quad (6.37b)$$

$$M_{xy} = D_{66}\kappa_{xy} \quad (6.37c)$$

Then equations (6.35) are simplified as follows:

$$M_x = -D_{11} \frac{\partial^2 w}{\partial x^2} - D_{12} \frac{\partial^2 w}{\partial y^2} \quad (6.38a)$$

$$M_y = -D_{12} \frac{\partial^2 w}{\partial x^2} - D_{22} \frac{\partial^2 w}{\partial y^2} \quad (6.38b)$$

$$M_{xy} = -2D_{66} \frac{\partial^2 w}{\partial x \partial y} \quad (6.38c)$$

For this case, equation (6.36) without in-plane forces  $N_x$ ,  $N_{xy}$ , and  $N_y$  is simplified for the static case as follows:

$$D_{11} \frac{\partial^4 w}{\partial x^4} + 2(D_{12} + 2D_{66}) \frac{\partial^4 w}{\partial x^2 \partial y^2} + D_{22} \frac{\partial^4 w}{\partial y^4} = p(x, y) \quad (6.39)$$

With the definition of simplified coefficients (Vinson, 1999):

$$D_{11} \equiv D_1, \quad D_{22} \equiv D_2, \quad D_{12} + 2D_{66} \equiv D_3 \quad (6.40)$$

Then, equation (6.39) becomes

$$D_1 \frac{\partial^4 w}{\partial x^4} + 2D_3 \frac{\partial^4 w}{\partial x^2 \partial y^2} + D_2 \frac{\partial^4 w}{\partial y^4} = p(x, y) \quad (6.41)$$

This is the governing differential equation for the bending of a plate composed of a composite material, excluding transverse shear deformation, with no coupling terms ( $B_{ij}=0$ ,  $D_{16}=D_{26}=0$ ), and no hygrothermal effects ( $\Delta T=\Delta C=0$ ), subjected to a lateral distributed load  $p(x, y)$ . It can be shown that if the plate materials are isotropic, then  $D_1=D_2=D_3=D$ . Although several exact solutions of equation (6.41) are available, they should be used only for the preliminary design to size the plate initially because neglecting transverse shear deformation and hygrothermal effects can lead to significant errors.

## 6.4 Boundary Conditions for Classical Lamination Theory

In the classical plate theory (ignoring transverse shear deformation), only two boundary conditions can be satisfied at each edge of the plate. The boundary

conditions for a simply supported edge and a clamped edge are identical to those of classical beam theory.

#### 6.4.1 Simply Supported Edge

The boundary conditions for simply supported edges are that the displacement and normal moment both vanish on the boundary. If  $n$  and  $t$  represent the directions normal and parallel to the edge, the boundary conditions are expressed as follows:

$$w = 0 \quad (6.42)$$

$$M_n = 0 \quad (6.43)$$

When there is no curvature along the edge of the simply supported plate because  $w = 0$  along that edge,

$$\frac{\partial^2 w}{\partial t^2} = 0 \quad (6.44)$$

Therefore, from equation (6.38a), we get a boundary condition equivalent to that of equation (6.43):

$$\frac{\partial^2 w}{\partial n^2} = 0 \quad (6.45)$$

#### 6.4.2 Clamped Edge

For the clamped edge, the displacement  $w$  and its derivative with respect to normal coordinate should be zero:

$$w = 0 \quad (6.46)$$

$$\frac{\partial w}{\partial n} = 0 \quad (6.47)$$

#### 6.4.3 Free Edge

For a free edge of a plate,  $M_n$ ,  $Q_n$ , and  $M_{nt}$  should be zero. However, the classical plate theory only allows two boundary conditions because the classical plate theory is an approximate solution to the composite laminate. Kirchhoff devised an appropriate approximate solution to the problem. In addition to the vanishing of moment  $M_n$ , he imposed the secondary boundary condition:

$$V_n = Q_n + \frac{\partial M_{nt}}{\partial t} = 0 \quad (6.48)$$

where  $V_n$  is the shear resultant, and  $Q_n$  is the shear force resultant defined in equation (6.12).

## 6.5 Solutions of Classical Lamination Theory

### 6.5.1 Navier Solution for Rectangular Plates

When the rectangular laminated plate shown in figure 6.1 simply supported on all four edges with specially orthotropic properties is subjected to the transverse distributed load  $p(x, y)$ , a solution to equation (6.41) that satisfies the boundary conditions (6.42) and (6.45) is the form of

$$w(x, y) = \sum_{m=1}^{\infty} \sum_{n=1}^{\infty} A_{mn} \sin \frac{m\pi x}{a} \sin \frac{n\pi y}{b} \quad (6.49)$$

The distributed load  $p(x, y)$  can be expressed also by the half-range Fourier sine series

$$p(x, y) = \sum_{m=1}^{\infty} \sum_{n=1}^{\infty} q_{mn} \sin \frac{m\pi x}{a} \sin \frac{n\pi y}{b} \quad (6.50)$$

where

$$q_{mn} = \frac{4}{ab} \int_0^b \int_0^a p(x, y) \sin \frac{m\pi x}{a} \sin \frac{n\pi y}{b} dx dy \quad (6.51)$$

1. When  $p(x, y) = p_0 = \text{constant}$ ,

$$q_{mn} = \frac{16p_0}{\pi^2 mn} \quad (m, n = \text{odd number, i.e., } 1, 3, 5, \dots) \quad (6.52)$$

$$q_{mn} = 0 \quad (\text{otherwise})$$

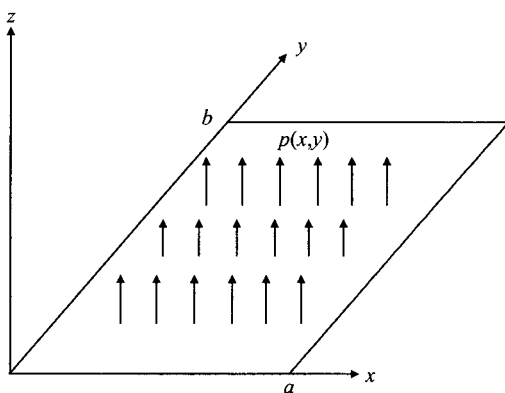


**Figure 6.1** Composite laminate plate geometry.

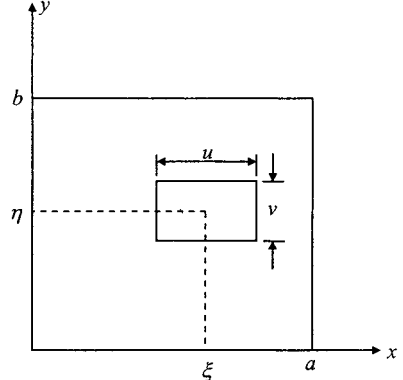


**Figure 6.2** Rectangular composite laminate with uniform load distributed over a rectangle.

2. When a uniform load  $p_0$  is distributed over a rectangle,

$$\begin{aligned} \xi - \frac{u}{2} < x < \xi + \frac{u}{2} \\ \eta - \frac{v}{2} < y < \eta + \frac{v}{2} \end{aligned} \quad (6.53)$$

as shown in figure 6.2, then

$$q_{mn} = \frac{16p_0}{mn\pi^2} \sin \frac{m\pi\xi}{a} \sin \frac{n\pi\eta}{b} \sin \frac{m\pi u}{2a} \sin \frac{n\pi v}{2b} \quad (6.54)$$

3. When a concentrated load  $P$  is applied at  $x = \xi$ ,  $y = \eta$

$$\begin{aligned} q_{mn} &= \frac{4}{ab} \lim_{\varepsilon \rightarrow 0} \frac{P}{\varepsilon^2} \frac{ab}{mn\pi^2} \left[ \cos \frac{m\pi(\xi - \varepsilon)}{a} - \cos \frac{m\pi\xi}{a} \right] \left[ \cos \frac{n\pi(\eta - \varepsilon)}{b} - \cos \frac{n\pi\eta}{b} \right] \\ &= \frac{4P}{ab} \sin \frac{m\pi\xi}{a} \sin \frac{n\pi\eta}{b} \end{aligned} \quad (6.55)$$

Therefore, the transverse deflection of the plate under the uniform load  $p_0$  is obtained by substituting equations (6.49), (6.50), and (6.52) into (6.41) as follows:

$$w(x, y) = \frac{16p_0}{\pi^6} \sum_{m=1, 3, 5, \dots}^{\infty} \sum_{n=1, 3, 5, \dots}^{\infty} \frac{\sin(m\pi x)/(a) \sin(n\pi y)/(b)}{mnD_{mn}} \quad (6.56)$$

where  $D_{mn}$  is defined as

$$D_{mn} = D_1 \left( \frac{m}{a} \right)^4 + 2D_3 \left( \frac{mn}{ab} \right)^2 + D_2 \left( \frac{n}{b} \right)^4 \quad (6.57)$$

The stresses in the plate are expressed by equation (4.15). Without hygrothermal effects, the stresses in the  $k$ th ply are expressed as

$$\begin{Bmatrix} \sigma_x \\ \sigma_y \\ \tau_{xy} \end{Bmatrix}^{[k]} = \begin{Bmatrix} \bar{Q}_{11}\varepsilon_x + \bar{Q}_{12}\varepsilon_y + \bar{Q}_{16}\gamma_{xy} \\ \bar{Q}_{12}\varepsilon_x + \bar{Q}_{22}\varepsilon_y + \bar{Q}_{26}\gamma_{xy} \\ \bar{Q}_{16}\varepsilon_x + \bar{Q}_{26}\varepsilon_y + \bar{Q}_{66}\gamma_{xy} \end{Bmatrix}^{[k]} \quad (6.58)$$

When  $\varepsilon_x^0 = \partial u_0 / \partial x = 0$ ,  $\varepsilon_y^0 = \partial v_0 / \partial x = 0$ , and  $\bar{Q}_{16} = \bar{Q}_{26} = 0$ , substituting equation (6.56) into equation (6.33), then equation (6.58) yields

$$\begin{Bmatrix} \sigma_x \\ \sigma_y \\ \tau_{xy} \end{Bmatrix}^{[k]} = \frac{16p_0}{\pi^4} \sum_{m=1,3,5,\dots}^{\infty} \sum_{n=1,3,5,\dots}^{\infty} \frac{z}{mnD_{mn}} \begin{Bmatrix} \left[ \bar{Q}_{11}\left(\frac{m}{a}\right)^2 + \bar{Q}_{12}\left(\frac{n}{b}\right)^2 \right] \sin \frac{m\pi x}{a} \sin \frac{n\pi y}{b} \\ \left[ \bar{Q}_{12}\left(\frac{m}{a}\right)^2 + \bar{Q}_{22}\left(\frac{n}{b}\right)^2 \right] \sin \frac{m\pi x}{a} \sin \frac{n\pi y}{b} \\ -2\bar{Q}_{66}\left(\frac{m}{a}\right)\left(\frac{n}{b}\right) \cos \frac{m\pi x}{a} \cos \frac{n\pi y}{b} \end{Bmatrix}^{[k]} \quad (6.59)$$

### 6.5.2 Levy Solution for Rectangular Plates

When the plate of figure 6.1 is simply supported with edges  $y=0$  and  $y=b$ , the boundary conditions for those edges are

$$w(x, 0) = w(x, b) = 0 \quad (6.60)$$

$$M_y(x, 0) = M_y(x, b) = 0 \quad (6.61)$$

The boundary conditions of equation (6.61) imply

$$\frac{\partial^2 w(x, 0)}{\partial y^2} = \frac{\partial^2 w(x, b)}{\partial y^2} = 0 \quad (6.62)$$

Levy used a solution form of a single infinite half-range Fourier sine series that satisfies the simply supported boundary conditions on both edges  $y=0$ ,  $y=b$ :

$$w(x, y) = \sum_{n=1}^{\infty} \phi_n(x) \sin \frac{n\pi y}{b} \quad (6.63)$$

The load  $p(x, y)$  was expressed in a similar form:

$$p(x, y) = \sum_{n=1}^{\infty} q_n(x) \sin \frac{n\pi y}{b} \quad (6.64)$$

where  $q_n(x)$  is expressed

$$q_n(x) = \frac{2}{b} \int_0^b p(x, y) \sin \frac{n\pi y}{b} dy \quad (6.65)$$

Substituting equations (6.63) and (6.64) into equation (6.41) yields

$$D_1 \frac{d^4 \phi_n}{dx^4} - 2D_3 \left(\frac{n\pi}{b}\right)^2 \frac{d^2 \phi_n}{dx^2} + D_2 \left(\frac{n\pi}{b}\right)^4 \phi_n = q_n \quad (6.66)$$

The homogeneous solution  $\phi_{nh}(x)$  of equation (6.66) (i.e.,  $q_n = 0$ ) can be obtained by assuming a solution type of  $e^{sxx}$ , whose characteristic equation is expressed as

$$s^4 - \frac{2D_3}{D_1} \lambda_n^2 s^2 + \frac{D_2}{D_1} \lambda_n^4 = 0 \quad (6.67)$$

where

$$\lambda_n = \frac{n\pi}{b} \quad (6.68)$$

The solutions of equation (6.67), hence the solutions of  $\phi_{nh}(x)$  have three different forms depending on the relative stiffness of the plate in various directions:

1. For the case  $\left(\frac{D_2}{D_1}\right)^{1/2} < \left(\frac{D_3}{D_1}\right)$ :

$$\begin{aligned} \phi_{nh}(x) = & C_1 \cosh(\lambda_n s_1 x) + C_2 \sinh(\lambda_n s_1 x) + C_3 \cosh(\lambda_n s_2 x) \\ & + C_4 \sinh(\lambda_n s_2 x) \end{aligned} \quad (6.69)$$

where

$$s_1 = \sqrt{\left(\frac{D_3}{D_1}\right) + \sqrt{\left(\frac{D_3}{D_1}\right)^2 - \left(\frac{D_2}{D_1}\right)}} \quad (6.70a)$$

$$s_2 = \sqrt{\left(\frac{D_3}{D_1}\right) - \sqrt{\left(\frac{D_3}{D_1}\right)^2 - \left(\frac{D_2}{D_1}\right)}} \quad (6.70b)$$

where  $C_1$ ,  $C_2$ ,  $C_3$ , and  $C_4$  are integrating constants that will be determined by boundary conditions.

2. For the case  $\left(\frac{D_2}{D_1}\right)^{1/2} = \left(\frac{D_3}{D_1}\right)$ :

$$\phi_{nh}(x) = (C_5 + C_6 x) \cosh(\lambda_n s_3 x) + (C_7 + C_8 x) \sinh(\lambda_n s_3 x) \quad (6.71)$$

where

$$s_3 = \sqrt{\left(\frac{D_3}{D_1}\right)} \quad (6.72)$$

where  $C_5$ ,  $C_6$ ,  $C_7$ , and  $C_8$  are integrating constants that will be determined by boundary conditions.

3. For the case,  $\left(\frac{D_2}{D_1}\right)^{1/2} > \left(\frac{D_3}{D_1}\right)$ :

$$\begin{aligned}\phi_{nh}(x) = & (C_9 \cos \lambda_n s_5 x + C_{10} \sin \lambda_n s_5 x) \cosh(\lambda_n s_4 x) \\ & + (C_{11} \cos \lambda_n s_5 x + C_{12} \sin \lambda_n s_5 x) \sinh(\lambda_n s_4 x)\end{aligned}\quad (6.73)$$

where

$$s_4 = \sqrt{\frac{1}{2} \left[ \left(\frac{D_2}{D_1}\right)^{1/2} + \left(\frac{D_3}{D_1}\right) \right]} \quad (6.74a)$$

$$s_5 = \sqrt{\frac{1}{2} \left[ \left(\frac{D_2}{D_1}\right)^{1/2} - \left(\frac{D_3}{D_1}\right) \right]} \quad (6.74b)$$

where  $C_9$ ,  $C_{10}$ ,  $C_{11}$ , and  $C_{12}$  are integrating constants that will be determined by boundary conditions.

The particular solution of equation (6.66) can be calculated easily if the lateral load,  $p(x, y)$ , is at most linear in  $x$ . Then,  $q_n(x)$  is at most linear in  $x$  from equation (6.65). For this case, the particular solution of equation (6.66) is

$$\phi_{np}(x) = \frac{q_n(x)}{\lambda_n^4 D_2} \quad (6.75)$$

For the constant distributed load  $p(x, y) = p_0$ ,  $q_n(x)$  can be calculated from equation (6.65) as

$$\begin{aligned}q_n(x) &= \frac{4p_0}{\pi n} \quad (n = 1, 3, 5, \dots) \\ q_n(x) &= 0 \quad (\text{other cases})\end{aligned}\quad (6.76)$$

Then,

$$\phi_{np}(x) = \frac{4p_0}{\pi n \lambda_n^4 D_2} \quad (n = 1, 3, 5, \dots) \quad (6.77)$$

The full solution of the equation (6.66) is obtained by adding the particular solution  $\phi_{np}(x)$  to the homogeneous equation  $\phi_{nh}(x)$ . Then the boundary conditions should be satisfied to determine the constants  $C_1$  to  $C_{12}$ .

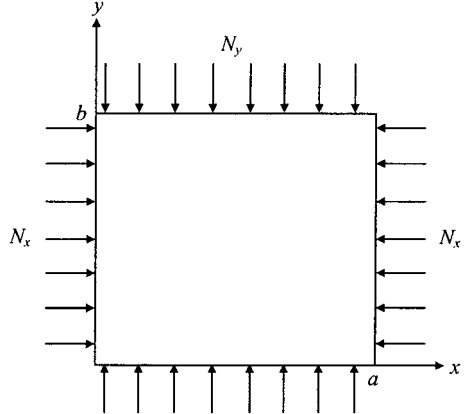


**Figure 6.3** Rectangular plate under biaxial compression ( $N_{xy}=0$ ).

### 6.6 Buckling of Simply Supported Rectangular Plates under Uniform Compression

If a simply supported symmetric rectangular plate is compressed by uniform biaxial force resultants  $N_x$  and  $N_y$  ( $N_{xy}=0$ ), as shown in figure 6.3, the plate becomes unstable when the loads  $N_x$  and  $N_y$  reach critical values. For the static case with  $p(x,y)=0$  and  $D_{16}=D_{26}=0$ , equation (6.36) reduces to

$$D_1 \frac{\partial^4 w}{\partial x^4} + 2D_3 \frac{\partial^4 w}{\partial x^2 \partial y^2} + D_2 \frac{\partial^4 w}{\partial y^4} = N_x \frac{\partial^2 w}{\partial x^2} + N_y \frac{\partial^2 w}{\partial y^2} \quad (6.78)$$

where again

$$D_1 = D_{11}$$

$$D_2 = D_{22}$$

$$D_3 = D_{12} + 2D_{66}$$

The boundary conditions for the simply supported edges are at  $x=0$  and  $a$

$$\begin{aligned} w &= 0 \\ M_x &= -D_{11} \frac{\partial^2 w}{\partial x^2} - D_{12} \frac{\partial^2 w}{\partial y^2} = 0 \end{aligned} \quad (6.79)$$

at  $y=0$  and  $b$

$$\begin{aligned} w &= 0 \\ M_y &= -D_{12} \frac{\partial^2 w}{\partial x^2} - D_{22} \frac{\partial^2 w}{\partial y^2} = 0 \end{aligned} \quad (6.80)$$

The form of deflection  $w(x, y)$  that satisfies the boundary condition may be constructed as

$$w(x, y) = \sum_{m=1}^{\infty} \sum_{n=1}^{\infty} A_{mn} \sin \frac{m\pi x}{a} \sin \frac{n\pi y}{b} \quad (6.81)$$

Substituting equation (6.81) into equation (6.78), we get for the nontrivial solution

$$\pi^2 \left[ D_1 \left( \frac{m}{a} \right)^4 + 2D_3 \left( \frac{m}{a} \right)^2 \left( \frac{n}{b} \right)^2 + D_2 \left( \frac{n}{b} \right)^4 \right] = - \left[ N_x \left( \frac{m}{a} \right)^2 + N_y \left( \frac{n}{b} \right)^2 \right] \quad (6.82)$$

For the uniform in-plane loads of the form

$$N_x = -N_0, \quad N_y = -kN_0 \quad (6.83)$$

where  $N_0 > 0$  and  $k$  denotes the ratio of  $N_y/N_x$ .

Then the value of  $N_0$  for buckling is calculated from equation (6.82) as

$$N_0 = \frac{\pi^2 [D_1(m/a)^4 + 2D_3(m/a)^2(n/b)^2 + D_2(n/b)^4]}{(m/a)^2 + k(n/b)^2} \quad (6.84)$$

An infinite number of values of  $N_0$  can be determined such that equation (6.84) is satisfied. However, the critical buckling load corresponds to the values of  $m$  and  $n$  that yield the lowest value of  $N_0$ .

## 6.7 Free Vibration of Simply Supported Rectangular Symmetric Plates

The solution procedure for the free vibration problem of a specially orthotropic simply supported rectangular symmetric plate is similar to the approach utilized for the stability analysis of the same plates. The governing equation for free vibration without in-plane or lateral loads ( $p(x, y) = N_x = N_y = N_{xy} = 0$ ) can be obtained from equation (6.36) when  $D_{16} = D_{26} = 0$ :

$$D_1 \frac{\partial^4 w}{\partial x^4} + 2D_3 \frac{\partial^4 w}{\partial x^2 \partial y^2} + D_2 \frac{\partial^4 w}{\partial y^4} + \rho h \frac{\partial^2 w}{\partial t^2} = 0 \quad (6.85)$$

The transverse deflection  $w(x, y, t)$  for the simply supported plate on all four edges may be expressed as

$$w(x, y, t) = \sum_{m=1}^{\infty} \sum_{n=1}^{\infty} A_{mn} \sin \frac{m\pi x}{a} \sin \frac{n\pi y}{b} \cos \omega_{mn} t \quad (6.86)$$

Substituting equation (6.86) into equation (6.85) yields the natural frequency  $\omega_{mn}$  as

$$\omega_{mn} = \frac{\pi^2}{\sqrt{\rho h}} \sqrt{D_1 \left( \frac{m}{a} \right)^4 + 2D_3 \left( \frac{m}{a} \right)^2 \left( \frac{n}{b} \right)^2 + D_2 \left( \frac{n}{b} \right)^4} \quad (6.87)$$

The lowest fundamental natural frequency is given for  $m=n=1$ :

$$\omega_{11} = \frac{\pi^2}{a^2\sqrt{\rho h}} \sqrt{D_1 + 2D_3\left(\frac{a}{b}\right)^2 + D_2\left(\frac{a}{b}\right)^4} \quad (6.88)$$

## 6.8 Analysis of Composite Laminates with Transverse Shear Deformation

For simplicity, let us consider a laminate plate that is midplane symmetric ( $B_{ij}=0$ ), and has no coupling terms ( $A_{16}=A_{26}=D_{16}=D_{26}=0$ ). For this case without any hygrothermal effects, the constitutive equations from equations (4.22) and (4.30) are

$$N_x = A_{11}\varepsilon_x^0 + A_{12}\varepsilon_y^0 \quad (6.89)$$

$$N_y = A_{12}\varepsilon_x^0 + A_{22}\varepsilon_y^0 \quad (6.90)$$

$$N_{xy} = A_{66}\gamma_{xy}^0 \quad (6.91)$$

$$M_x = D_{11}\kappa_x + D_{12}\kappa_y \quad (6.92)$$

$$M_y = D_{12}\kappa_x + D_{22}\kappa_y \quad (6.93)$$

$$M_{xy} = D_{66}\kappa_{xy} \quad (6.94)$$

### 6.8.1 Shear Correction Factor

The shear correction factor  $k$  is introduced to account for the fact that the transverse shear stress varies parabolically through the beam thickness of homogeneous beams, and it varies at least quadratically through the composite layer thickness. The discrepancy between the actual stress state and the constant stress state predicted by the first-order shear deformation theory of equation (6.25) is often corrected in computing the transverse shear force resultants ( $Q_x, Q_y$ ) by multiplying the integrals in equations (6.8) and (6.9) by a parameter  $k$ , called the shear correction factor:

$$\begin{Bmatrix} Q_x \\ Q_y \end{Bmatrix} = k \int_{-\frac{h}{2}}^{\frac{h}{2}} \begin{Bmatrix} \tau_{xz} \\ \tau_{yz} \end{Bmatrix} dz \quad (6.95)$$

If we use the notation similar to equation (4.19a), we have

$$A_{ij} = \int_{-\frac{h}{2}}^{\frac{h}{2}} \bar{C}_{ij} dz \quad (i, j = 4, 5) \quad (6.96)$$

Then equation (6.95) becomes from the results of equation (5.56),

$$\begin{Bmatrix} Q_y \\ Q_x \end{Bmatrix} = k \begin{bmatrix} A_{44} & A_{45} \\ A_{45} & A_{55} \end{bmatrix} \begin{Bmatrix} \gamma_{yz} \\ \gamma_{xz} \end{Bmatrix} \quad (6.97)$$

When  $A_{45}=0$ , equation (6.97) reduces as follows (Reissner, 1945; Mindlin, 1951).

$$Q_y = kA_{44}\gamma_{yz} = kA_{44}\left(\beta + \frac{\partial w}{\partial y}\right) \quad (6.98)$$

$$Q_x = kA_{55}\gamma_{xz} = kA_{55}\left(\alpha + \frac{\partial w}{\partial x}\right) \quad (6.99)$$

The introduction of the shear correction factor  $k$  has the effect of modifying the plate transverse shear stiffness. The factor  $k$  is computed such that the strain energy due to transverse shear stresses in equation (6.95) equals the strain energy due to the true transverse stresses predicted by the three-dimensional elasticity theory.

For example, consider a homogeneous beam with rectangular cross-section, with width  $b$  and height  $h$ . The actual shear stress distribution  $\tau_{xz}^a$  through the thickness of the beam is given by

$$\tau_{xz}^a = \frac{3V}{2bh} \left[ 1 - \left( \frac{2z}{h} \right)^2 \right], \quad -\frac{h}{2} \leq z \leq \frac{h}{2} \quad (6.100)$$

where  $V=bQ_x$  ( $b$ : width of beam) is the transverse shear force. While the transverse shear stress  $\tau_{xz}^f$  in the first-order shear deformation theory is a constant,

$$\tau_{xz}^f = \frac{V}{bh}, \quad -\frac{h}{2} \leq z \leq \frac{h}{2} \quad (6.101)$$

The strain energy  $U_s^a$  for the actual case and  $U_s^f$  for the first-order shear deformation theory are

$$U_s^a = \frac{b}{2G_{13}} \int_{-\frac{h}{2}}^{\frac{h}{2}} (\tau_{xz}^a)^2 dz = \frac{3V^2}{5G_{13}bh} \quad (6.102)$$

$$U_s^f = \frac{b}{2G_{13}} \int_{-h/2}^{h/2} (\tau_{xz}^f)^2 dz = \frac{V^2}{2G_{13}bh} \quad (6.103)$$

The shear correction factor  $k$  is the ratio of  $U_s^f$  to  $U_s^a$ , which gives  $k=5/6$ . The shear correction factor for a general laminate depends on lamina properties and laminate stacking sequences (Whitney, 1987).

### 6.8.2 Static Analysis of Composite Laminates with Transverse Shear Deformation

Substituting equations (6.92), (6.93), (6.94), (6.98), and (6.99) into equations (6.16) to (6.18) without inertia terms results in the following set of governing

differential equations for a laminated composite plate subjected to a static lateral load:

$$D_{11} \frac{\partial^2 \alpha}{\partial x^2} + D_{66} \frac{\partial^2 \alpha}{\partial y^2} + (D_{12} + D_{66}) \frac{\partial^2 \beta}{\partial x \partial y} - k A_{55} \left( \alpha + \frac{\partial w}{\partial x} \right) = 0 \quad (6.104)$$

$$(D_{12} + D_{66}) \frac{\partial^2 \alpha}{\partial x \partial y} + D_{66} \frac{\partial^2 \beta}{\partial x^2} + D_{22} \frac{\partial^2 \beta}{\partial y^2} - k A_{44} \left( \beta + \frac{\partial w}{\partial y} \right) = 0 \quad (6.105)$$

$$k A_{55} \left( \frac{\partial \alpha}{\partial x} + \frac{\partial^2 w}{\partial x^2} \right) + k A_{44} \left( \frac{\partial \beta}{\partial y} + \frac{\partial^2 w}{\partial y^2} \right) + p(x, y) = 0 \quad (6.106)$$

For the composite laminate simply supported on all four edges subjected to a lateral load, the following solution form can be used:

$$w(x, y) = \sum_{m=1}^{\infty} \sum_{n=1}^{\infty} C_{mn} \sin \frac{m\pi x}{a} \sin \frac{n\pi y}{b} \quad (6.107)$$

$$\alpha(x, y) = \sum_{m=1}^{\infty} \sum_{n=1}^{\infty} A_{mn} \cos \frac{m\pi x}{a} \sin \frac{n\pi y}{b} \quad (6.108)$$

$$\beta(x, y) = \sum_{m=1}^{\infty} \sum_{n=1}^{\infty} B_{mn} \sin \frac{m\pi x}{a} \cos \frac{n\pi y}{b} \quad (6.109)$$

$$p(x, y) = \sum_{m=1}^{\infty} \sum_{n=1}^{\infty} q_{mn} \sin \frac{m\pi x}{a} \sin \frac{n\pi y}{b} \quad (6.110)$$

Equations (6.107) through (6.110) satisfy the boundary condition on all edges such that

$$w = 0, \quad \frac{\partial \alpha}{\partial x} = 0 \quad \text{at } x = 0, a \quad (6.111)$$

$$w = 0, \quad \frac{\partial \beta}{\partial y} = 0 \quad \text{at } y = 0, b \quad (6.112)$$

Substituting equations (6.107) to (6.110) into the governing equations (6.104) to (6.106), we obtain the following equations:

$$\begin{bmatrix} L_{11} & L_{12} & L_{13} \\ L_{12} & L_{22} & L_{23} \\ L_{13} & L_{23} & L_{33} \end{bmatrix} \begin{Bmatrix} A_{mn} \\ B_{mn} \\ C_{mn} \end{Bmatrix} = \begin{Bmatrix} 0 \\ 0 \\ q_{mn} \end{Bmatrix} \quad (6.113)$$

where

$$\begin{aligned}
 L_{11} &= D_{11} \left( \frac{m\pi}{a} \right)^2 + D_{66} \left( \frac{n\pi}{b} \right)^2 + kA_{55} \\
 L_{12} &= (D_{12} + D_{66}) \left( \frac{m\pi}{a} \right) \left( \frac{n\pi}{b} \right) \\
 L_{13} &= kA_{55} \left( \frac{m\pi}{a} \right) \\
 L_{22} &= D_{22} \left( \frac{m\pi}{a} \right)^2 + D_{66} \left( \frac{n\pi}{b} \right)^2 + kA_{44} \\
 L_{23} &= kA_{44} \left( \frac{n\pi}{b} \right) \\
 L_{33} &= kA_{55} \left( \frac{m\pi}{a} \right)^2 + kA_{44} \left( \frac{n\pi}{b} \right)^2
 \end{aligned} \tag{6.114}$$

The solution of equation (6.113) is

$$\begin{aligned}
 A_{mn} &= \frac{L_{12}L_{23} - L_{22}L_{13}}{\Delta} q_{mn} \\
 B_{mn} &= \frac{L_{12}L_{13} - L_{11}L_{23}}{\Delta} q_{mn} \\
 C_{mn} &= \frac{L_{11}L_{22} - L_{12}^2}{\Delta} q_{mn}
 \end{aligned} \tag{6.115}$$

where  $\Delta$  is the determinant of the  $[L_{ij}]$  matrix in equation (6.113).

Having solved the problem to obtain  $\alpha$ ,  $\beta$ , and  $w$ , the curvatures  $\kappa_x = \partial\alpha/\partial x$ ,  $\kappa_y = \partial\beta/\partial y$  and  $\kappa_{xy} = (\partial\alpha/\partial y) + (\partial\beta/\partial x)$  can be determined. Then the bending stresses for a laminated composite plate can be calculated as

$$\left\{ \begin{array}{c} \sigma_x \\ \sigma_y \\ \tau_{xy} \end{array} \right\}^{[k]} = \left[ \begin{array}{ccc} \bar{Q}_{11} & \bar{Q}_{12} & 0 \\ \bar{Q}_{12} & \bar{Q}_{22} & 0 \\ 0 & 0 & \bar{Q}_{66} \end{array} \right]^{[k]} \left\{ \begin{array}{c} \kappa_x \\ \kappa_y \\ \kappa_{xy} \end{array} \right\} z \tag{6.116}$$

### 6.8.3 Dynamic Analysis of Composite Laminates with Transverse Shear Deformation

To find the natural frequencies of the composite laminate plate that has midplane symmetry ( $[B]=0$ ), without coupling terms  $D_{16}=D_{26}=A_{45}=0$ , one can rewrite equations (6.104), (6.105), and (6.106) in conjunction with equations (6.16), (6.17), and (6.18):

$$D_{11} \frac{\partial^2 \alpha}{\partial x^2} + D_{66} \frac{\partial^2 \alpha}{\partial y^2} + (D_{12} + D_{66}) \frac{\partial^2 \beta}{\partial x \partial y} - kA_{55} \left( \alpha + \frac{\partial w}{\partial x} \right) - I \frac{\partial^2 \alpha}{\partial t^2} = 0 \tag{6.117}$$

$$(D_{12} + D_{66}) \frac{\partial^2 \alpha}{\partial x \partial y} + D_{66} \frac{\partial^2 \beta}{\partial x^2} + D_{22} \frac{\partial^2 \beta}{\partial y^2} - k A_{44} \left( \beta + \frac{\partial w}{\partial y} \right) - I \frac{\partial^2 \beta}{\partial t^2} = 0 \quad (6.118)$$

$$k A_{55} \left( \frac{\partial \alpha}{\partial x} + \frac{\partial^2 w}{\partial x^2} \right) + k A_{44} \left( \frac{\partial \beta}{\partial y} + \frac{\partial^2 w}{\partial y^2} \right) - \rho h \frac{\partial^2 w}{\partial t^2} = 0 \quad (6.119)$$

where  $\rho$  was given in equation (6.6) and is rewritten here:

$$\rho = \frac{1}{h} \int_{-\frac{h}{2}}^{\frac{h}{2}} \rho^{[k]} dz = \frac{1}{h} \sum_{k=1}^n \rho^{[k]} (z_k - z_{k-1}) \quad (6.120)$$

where  $I$  is defined as

$$I = \int_{-\frac{h}{2}}^{\frac{h}{2}} \rho^{[k]} z^2 dz = \sum_{k=1}^n \rho^{[k]} \frac{z_k^3 - z_{k-1}^3}{3} \quad (6.121)$$

Similar to the static analysis in the previous sections, the following solution forms can be used for the simply supported plate:

$$w(x, y, t) = \sum_{m=1}^{\infty} \sum_{n=1}^{\infty} C'_{mn} \sin \frac{m\pi x}{a} \sin \frac{n\pi y}{b} e^{i\omega_{mn} t} \quad (6.122)$$

$$\alpha(x, y, t) = \sum_{m=1}^{\infty} \sum_{n=1}^{\infty} A'_{mn} \cos \frac{m\pi x}{a} \sin \frac{n\pi y}{b} e^{i\omega_{mn} t} \quad (6.123)$$

$$\beta(x, y, t) = \sum_{m=1}^{\infty} \sum_{n=1}^{\infty} B'_{mn} \sin \frac{m\pi x}{a} \cos \frac{n\pi y}{b} e^{i\omega_{mn} t} \quad (6.124)$$

Substituting equations (6.122) to (6.124) into equations (6.117) to (6.119), we obtain the following matrix for the eigenvalue problem:

$$\begin{bmatrix} L'_{11} & L_{12} & L_{13} \\ L_{12} & L_{22} & L_{23} \\ L_{13} & L_{23} & L'_{33} \end{bmatrix} \begin{Bmatrix} A'_{mn} \\ B'_{mn} \\ C'_{mn} \end{Bmatrix} = \begin{Bmatrix} 0 \\ 0 \\ 0 \end{Bmatrix} \quad (6.125)$$

where the unprimed quantities  $L_{ij}$  were defined in equation (6.114) and the primed quantities  $L'_{ij}$  are defined as

$$\begin{aligned} L'_{11} &= L_{11} - \frac{\rho h^3}{12} \omega_{mn}^2 \\ L'_{22} &= L_{22} - \frac{\rho h^3}{12} \omega_{mn}^2 \\ L'_{33} &= L_{33} - \rho h \omega_{mn}^2 \end{aligned} \quad (6.126)$$

Three natural frequencies result from solving equation (6.125) for each value of  $m$  and  $n$ . However, two of the frequencies are significantly higher than the third because they are associated with the rotary inertia terms, which are the last terms on the left-hand sides of equations (6.117) and (6.118) and are very seldom important in structural response (Vinson, 1999). If they are neglected, then  $L'_{11} = L_{11}$  and  $L'_{22} = L_{22}$ , and the square of the remaining natural frequency is expressed as

$$\omega_{mn}^2 = \frac{1}{\rho h} \frac{L_{11}L_{22}L_{33} + 2L_{12}L_{23}L_{13} - L_{12}^2L_{33} - L_{13}^2L_{22} - L_{23}^2L_{11}}{L_{11}L_{22} - L_{12}^2} \quad (6.127)$$

and  $A'_{mn}$ ,  $B'_{mn}$ , and  $C'_{mn}$  have the following relations:

$$A'_{mn} = \frac{L_{12}L_{23} - L_{22}L_{13}}{L_{11}L_{22} - L_{12}^2} C'_{mn} \quad (6.128)$$

$$B'_{mn} = \frac{L_{12}L_{13} - L_{11}L_{23}}{L_{11}L_{22} - L_{12}^2} C'_{mn} \quad (6.129)$$

## 6.9 Forced Vibration of a Composite Laminate Subjected to a Dynamic Lateral Load

### 6.9.1 Dynamic Response of a Mass

Let us consider an undamped SDOF (single degree of freedom) system composed of a mass  $m$  and a spring of spring constant  $k$  subjected to a force  $p(t)$  of duration  $t_d \ll T_n$  (undamped natural period) having an impulse (Craig, 1981)

$$I = \int_0^{t_d} p(t) dt \quad (6.130)$$

Let the system be at rest for  $t \leq 0$ , that is, prior to application of the excitation. If  $u(t)$  represents the displacement of mass from the equilibrium position, the equation of motion and initial conditions are

$$m\ddot{u} + ku = \begin{cases} p(t), & 0 < t \leq t_d \\ 0, & t_d < t \end{cases} \quad (6.131a)$$

$$u(0) = \dot{u}(0) = 0 \quad (6.131b)$$

where the dot ( $\cdot$ ) represents the differentiation with respect to time  $t$ . By integrating equation (6.131) with respect to time and incorporating the initial conditions of equation (6.132), we get

$$m\dot{u}(t_d) + ku_{\text{avg}} t_d = I \quad (6.133)$$

where  $u_{\text{avg}}$  is the (small) average displacement in the time interval  $0 < t \leq t_d$ .

For  $t_d \rightarrow 0$ , that is,  $t_d \ll T_n$ , the second term in equation (6.133) can be ignored, leaving

$$m\dot{u}(0^+) = I \quad (6.134)$$

Thus, an impulse consisting of a large force acting for a very short time has the effect of giving the mass an initial velocity of

$$\dot{u}(0^+) = \dot{u}_0 = \frac{I}{m} \quad (6.135)$$

with an initial displacement of

$$u(0^+) = u_0 = 0 \quad (6.136)$$

These can be used as “initial” conditions for the free vibration problem:

$$u = u_0 \cos \omega_n t + \frac{\dot{u}_0}{\omega_n} \sin \omega_n t \quad (6.137)$$

where  $\omega_n$  represents the undamped circular natural frequency expressed in radians per second. Using equations (6.135) and (6.136), we get the impulse response

$$u(t) = \left( \frac{I}{m\omega_n} \right) \sin \omega_n t \quad (6.138)$$

The Duhamel integral method for determining the response of a SDOF system subjected to general dynamic excitation can be developed from the impulse response function.

The Duhamel integral is based on the principle of superposition, which is valid only for linear systems. Figure 6.4 shows an undamped SDOF system that is initially

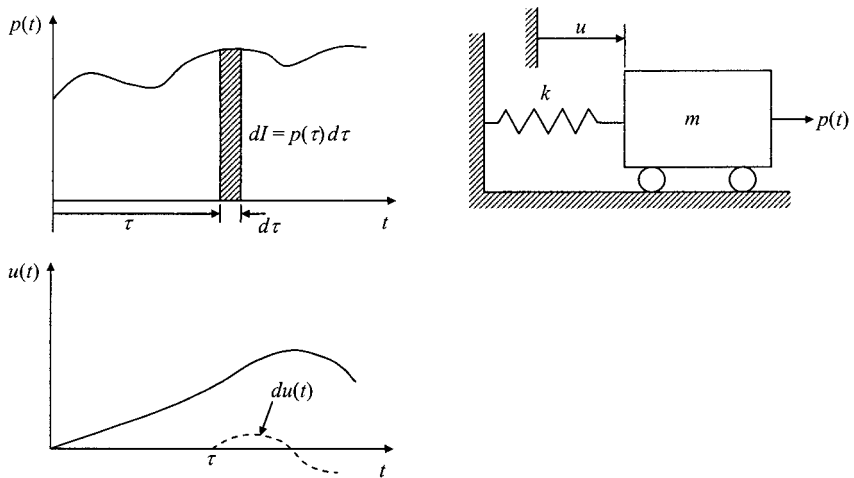


**Figure 6.4** Undamped single-degree-of-freedom vibration system.

at rest and is then subjected to an input  $p(t)$  as shown. The response of the system to an impulse  $dI = p(\tau) d\tau$  is called  $du(t)$  and is given by

$$du(t) = \left( \frac{dI}{m\omega_n} \right) \sin \omega_n(t - \tau) \quad (6.139)$$

The total response at time  $t$  will be the sum of the response due to all incremental impulses prior to time  $t$ . Therefore,

$$u(t) = \left( \frac{1}{m\omega_n} \right) \int_0^t p(\tau) \sin \omega_n(t - \tau) d\tau \quad (6.140)$$

or

$$u(t) = \int_0^t p(\tau) h(t - \tau) d\tau \quad (6.141)$$

where

$$h(t) = \left( \frac{1}{m\omega_n} \right) \sin \omega_n t \quad (6.142)$$

is the unit impulse response function ( $I=1$ ) for an undamped SDOF system.

For the damped SDOF system that is initially at rest, the same method can be used as follows:

$$u(t) = \left( \frac{1}{m\omega_d} \right) \int_0^t p(\tau) e^{-\zeta\omega_n(1-\tau)} \sin \omega_d(t - \tau) d\tau \quad (6.143)$$

where  $\zeta$  is a dimensionless quantity called the viscous damping factor and  $\omega_d = \omega_n \sqrt{1 - \zeta^2}$  is the damped circular natural frequency.

Equations (6.140) and (6.143) are referred to as the Duhamel superposition integral expressions for the response of undamped and damped SDOF systems, respectively. Equation (6.141) is frequently referred to as a convolution integral, a more general form of which is

$$u(t) = \int_{-\infty}^{\infty} f_1(\tau) f_2(t - \tau) d\tau \quad (6.144)$$

### 6.9.2 Dynamic Response of a Composite Laminate Under a Dynamic Lateral Load

For the simply supported plate with dimensions  $a$  and  $b$ , the dynamic distributed lateral load  $p(x, y, t)$  can be expressed as follows:

$$p(x, y, t) = p(x, y) F(t) = \sum_{m=1}^{\infty} \sum_{n=1}^{\infty} q_{mn} \sin \frac{m\pi x}{a} \sin \frac{n\pi y}{b} F(t) \quad (6.145)$$

where again,  $q_{mn}$  is given by

$$q_{mn} = \frac{4}{ab} \int_0^b \int_0^a p(x, y) \sin \frac{m\pi x}{a} \sin \frac{n\pi y}{b} dx dy \quad (6.146)$$

The dynamic effect  $P_{mn}(t)$  on the plate is given by

$$P_{mn}(t) = \int_0^t F(\tau) \sin \omega_{mn}(t - \tau) d\tau \quad (6.147)$$

Therefore, the solutions of the plate under a dynamic distributed lateral load  $p(x, y, t)$  neglecting the rotary inertia terms are given by

$$w(x, y, t) = \frac{1}{\rho h} \sum_{m=1}^{\infty} \sum_{n=1}^{\infty} \left( \frac{q_{mn}}{\omega_{mn}} \right) \sin \frac{m\pi x}{a} \sin \frac{n\pi y}{b} P_{mn}(t) \quad (6.148)$$

$$\alpha(x, y, t) = \frac{1}{\rho h} \sum_{m=1}^{\infty} \sum_{n=1}^{\infty} \left( \frac{q_{mn}}{\omega_{mn}} \right) \frac{L_{12}L_{23} - L_{22}L_{13}}{L_{11}L_{22} - L_{12}^2} \cos \frac{m\pi x}{a} \sin \frac{n\pi y}{b} P_{mn}(t) \quad (6.149)$$

$$\beta(x, y, t) = \frac{1}{\rho h} \sum_{m=1}^{\infty} \sum_{n=1}^{\infty} \left( \frac{q_{mn}}{\omega_{mn}} \right) \frac{L_{12}L_{13} - L_{11}L_{23}}{L_{11}L_{22} - L_{12}^2} \sin \frac{m\pi x}{a} \cos \frac{n\pi y}{b} P_{mn}(t) \quad (6.150)$$

### EXAMPLE 6.1

Find  $P(t)$  when the forcing function  $F(t)$  has the following sine pulse:

$$F(t) = F_0 \sin \frac{\pi t}{t_1}, \quad 0 \leq t \leq t_1 \quad (6.151a)$$

$$F(t) = 0, \quad t > t_1 \quad (6.151b)$$

### Solution

When  $0 \leq t \leq t_1$ ,

$$\begin{aligned} p_{mn}(t) &= \int_0^t F_0 \sin \frac{\pi \tau}{t_1} \sin \omega_{mn}(t - \tau) d\tau \\ &= -\frac{F_0}{2} \int_0^t \left\{ \cos \left[ \frac{\pi \tau}{t_1} + \omega_{mn}(t - \tau) \right] - \cos \left[ \frac{\pi \tau}{t_1} - \omega_{mn}(t - \tau) \right] \right\} d\tau \\ &= -\frac{F_0}{2} \left( \frac{1}{(\pi/t_1) - \omega_{mn}} \sin \left[ \frac{\pi \tau}{t_1} + \omega_{mn}(t - \tau) \right] \right. \\ &\quad \left. - \frac{1}{(\pi/t_1) + \omega_{mn}} \sin \left[ \frac{\pi \tau}{t_1} - \omega_{mn}(t - \tau) \right] \right)_0^t \\ &= \frac{F_0 t_1}{\pi^2 - t_1^2 \omega_{mn}^2} \left[ \pi \sin \omega_{mn} t - \omega_{mn} t_1 \sin \frac{\pi t}{t_1} \right] \end{aligned} \quad (6.152a)$$

When  $t > t_1$ ,

$$\begin{aligned}
 P_{mn}(t) &= \int_0^{t_1} F_0 \sin \frac{\pi\tau}{t_1} \sin \omega_{mn}(t-\tau) d\tau \\
 &= -\frac{F_0}{2} \left( \frac{1}{(\pi/t_1) - \omega_{mn}} \sin \left[ \frac{\pi\tau}{t_1} + \omega_{mn}(t-\tau) \right] \right. \\
 &\quad \left. - \frac{1}{(\pi/t_1) + \omega_{mn}} \sin \left[ \frac{\pi\tau}{t_1} - \omega_{mn}(t-\tau) \right] \right)_0^{t_1} \\
 &= \frac{F_0 \pi t_1}{\pi^2 - t_1^2 \omega_{mn}^2} [\sin \omega_{mn} t + \sin \omega_{mn}(t-t_1)]
 \end{aligned} \tag{6.152b}$$

## 6.10 Bending of Clamped Rectangular Laminate Plates

### 6.10.1 Ritz Method

So far, exact solutions to the governing equations and boundary conditions have been obtained. In practice, however, many cases are encountered in which exact solutions are not available and approximate methods must be utilized (Whitney, 1987). In this section, we consider the bending of a clamped rectangular plate subjected to a uniform transverse load  $p(x, y) = p_0$ . We obtain approximate solutions in conjunction with the Ritz method. The Ritz method provides a convenient method for obtaining approximate solutions to boundary value problems. This approach is equally applicable to bending, buckling, and free vibration problems. The method is based on the energy condition of plates.

The strain energy  $U$  of an elastic body in the  $x, y, z$  coordinate system is expressed as

$$U = \frac{1}{2} \iiint (\sigma_x \varepsilon_x + \sigma_y \varepsilon_y + \sigma_z \varepsilon_z + \tau_{xz} \gamma_{xz} + \tau_{yz} \gamma_{yz} + \tau_{xy} \gamma_{xy}) dx dy dz \tag{6.153}$$

where the triple integration is performed over the volume of the body. With the assumption of classical lamination plate theory ( $\varepsilon_z = \gamma_{yz} = \gamma_{zx} = 0$ ), equation (6.153) reduces to

$$U = \frac{1}{2} \iiint \left( \bar{Q}_{11}^{[k]} \varepsilon_x^2 + 2\bar{Q}_{12}^{[k]} \varepsilon_x \varepsilon_y + 2\bar{Q}_{16}^{[k]} \varepsilon_x \gamma_{xy} + 2\bar{Q}_{26}^{[k]} \varepsilon_y \gamma_{xy} + \bar{Q}_{22}^{[k]} \varepsilon_y^2 + \bar{Q}_{66}^{[k]} \gamma_{xy}^2 \right) dx dy dz \tag{6.154}$$

Using the relationships of equation (6.33), equation (6.154) can be expressed in terms of displacements  $u, v$ , and  $w$ :

$$\begin{aligned}
 U &= \frac{1}{2} \iint \left[ A_{11} \left( \frac{\partial u_0}{\partial x} \right)^2 + 2A_{12} \frac{\partial u_0}{\partial x} \frac{\partial v_0}{\partial y} + A_{22} \left( \frac{\partial v_0}{\partial y} \right)^2 \right. \\
 &\quad \left. + 2 \left( A_{16} \frac{\partial u_0}{\partial x} + A_{26} \frac{\partial v_0}{\partial y} \right) \left( \frac{\partial u_0}{\partial y} + \frac{\partial v_0}{\partial x} \right) + A_{66} \left( \frac{\partial u_0}{\partial y} + \frac{\partial v_0}{\partial x} \right)^2 \right]
 \end{aligned}$$

$$\begin{aligned}
& -2B_{11} \frac{\partial u_0}{\partial x} \frac{\partial^2 w}{\partial x^2} - 2B_{12} \left( \frac{\partial v_0}{\partial y} \frac{\partial^2 w}{\partial x^2} + \frac{\partial u_0}{\partial x} \frac{\partial^2 w}{\partial y^2} \right) \\
& - 2B_{22} \frac{\partial v_0}{\partial y} \frac{\partial^2 w}{\partial y^2} - 2B_{16} \left\{ \frac{\partial^2 w}{\partial x^2} \left( \frac{\partial u_0}{\partial y} + \frac{\partial v_0}{\partial x} \right) + 2 \frac{\partial u_0}{\partial x} \frac{\partial^2 w}{\partial x \partial y} \right\} \\
& - 2B_{26} \left\{ \frac{\partial^2 w}{\partial y^2} \left( \frac{\partial u_0}{\partial y} + \frac{\partial v_0}{\partial x} \right) + 2 \frac{\partial v_0}{\partial y} \frac{\partial^2 w}{\partial x \partial y} \right\} \\
& - 4B_{66} \frac{\partial^2 w}{\partial x \partial y} \left( \frac{\partial u_0}{\partial y} + \frac{\partial v_0}{\partial x} \right) + D_{11} \left( \frac{\partial^2 w}{\partial x^2} \right)^2 + 2D_{12} \frac{\partial^2 w}{\partial x^2} \frac{\partial^2 w}{\partial y^2} \\
& + D_{22} \left( \frac{\partial^2 w}{\partial y^2} \right)^2 + 4 \left( D_{16} \frac{\partial^2 w}{\partial x^2} + D_{26} \frac{\partial^2 w}{\partial y^2} \right) \frac{\partial^2 w}{\partial x \partial y} + 4D_{66} \left( \frac{\partial^2 w}{\partial x \partial y} \right)^2 \Big] dx dy \quad (6.155)
\end{aligned}$$

The kinetic energy  $T$  of an elastic body in the  $x, y, z$  coordinate system is

$$T = \frac{1}{2} \int \int \int \rho^{[k]} \left[ \left( \frac{\partial u}{\partial t} \right)^2 + \left( \frac{\partial v}{\partial t} \right)^2 + \left( \frac{\partial w}{\partial t} \right)^2 \right] dx dy dz \quad (6.156)$$

Using the relationships of equations (6.25), (6.30), and (6.31),

$$T = \frac{1}{2} \int \int \int \rho^{[k]} \left[ \left( \frac{\partial u_0}{\partial t} - z \frac{\partial^2 w}{\partial x \partial t} \right)^2 + \left( \frac{\partial v_0}{\partial t} - z \frac{\partial^2 w}{\partial y \partial t} \right)^2 + \left( \frac{\partial w}{\partial t} \right)^2 \right] dx dy dz \quad (6.157)$$

Integrating equation (6.157) with respect to  $z$  and neglecting time derivatives of plate slopes (rotational inertia terms), we have

$$T = \frac{1}{2} \int \int \rho h \left[ \left( \frac{\partial u_0}{\partial t} \right)^2 + \left( \frac{\partial v_0}{\partial t} \right)^2 + \left( \frac{\partial w}{\partial t} \right)^2 \right] dx dy \quad (6.158)$$

The potential energy  $W$  due to transverse load can be calculated as

$$W = - \int \int \left[ \sigma_z \left( z = \frac{h}{2} \right) - \sigma_z \left( z = -\frac{h}{2} \right) \right] w dx dy \quad (6.159)$$

Using the definition of equation (6.19), equation (6.159) reduces to

$$W = - \int \int p(x, y) w dx dy \quad (6.160)$$

The potential energy,  $V$ , of in-plane loads due to a large deflection  $w$  is expressed as (Whitney, 1987):

$$V = \frac{1}{2} \int \int \left[ N_x \left( \frac{\partial w}{\partial x} \right)^2 + N_y \left( \frac{\partial w}{\partial y} \right)^2 + 2N_{xy} \frac{\partial w}{\partial x} \frac{\partial w}{\partial y} \right] dx dy \quad (6.161)$$

The problems of bending, buckling, and free vibration are expressed as follows:

$$\Pi(u_0, v_0, w) = \text{stationary value} \quad (6.162)$$

where

$$\Pi = U + W \quad (\text{transverse bending}) \quad (6.163)$$

$$\Pi = U + W + V \quad (\text{buckling}) \quad (6.164)$$

$$\Pi = U + W + V - T \quad (\text{free vibration}) \quad (6.165)$$

For the free vibration, time can be removed from equation (6.158) by considering displacement fields of the form

$$u_0(x, y, t) = u_0(x, y)e^{i\omega t} \quad (6.166a)$$

$$v_0(x, y, t) = v_0(x, y)e^{i\omega t} \quad (6.166b)$$

$$w(x, y, t) = w(x, y)e^{i\omega t} \quad (6.166c)$$

Then, the kinetic energy can be used in the form

$$T = \frac{1}{2} \int \int \rho h \omega^2 [(u_0)^2 + (v_0)^2 + w^2] dx dy \quad (6.167)$$

This allows the free vibration problem to be solved as a static problem by considering the kinetic energy to be simply additional energy.

In the Ritz method, a solution is sought in the form

$$u_0 = \sum_{m=1}^{M_1} \sum_{n=1}^{N_1} J_{mn} U_{mn}(x, y) \quad (6.168a)$$

$$v_0 = \sum_{m=1}^{M_2} \sum_{n=1}^{N_2} K_{mn} V_{mn}(x, y) \quad (6.168b)$$

$$w_0 = \sum_{m=1}^{M_3} \sum_{n=1}^{N_3} C_{mn} W_{mn}(x, y) \quad (6.168c)$$

where  $M_i, N_i (i = 1, 2, 3)$  are integers to give sufficient accuracy to the approximation and  $J_{mn}, K_{mn}$ , and  $C_{mn}$  are undetermined coefficients. The functions  $U_{mn}, V_{mn}$ , and  $W_{mn}$  are known and usually chosen in the variables separable form  $X_m(x)Y_n(y)$ . The geometric boundary conditions must be satisfied by these functions. In addition, they should be continuous through at least the same order derivative as required in the corresponding differential equations. Substituting equation (6.168) into the energy condition (6.162) leads to a minimization problem relative to the undetermined

coefficients. Since  $\Pi$  is a function of  $J_{mn}$ ,  $K_{mn}$ , and  $C_{mn}$  only, the conditions given by equation (6.162) reduce to the equations

$$\begin{aligned}\frac{\partial \Pi}{\partial J_{mn}} &= 0 & \begin{cases} m = 1, 2, \dots, M_1 \\ n = 1, 2, \dots, N_1 \end{cases} \\ \frac{\partial \Pi}{\partial K_{mn}} &= 0 & \begin{cases} m = 1, 2, \dots, M_2 \\ n = 1, 2, \dots, N_2 \end{cases} \\ \frac{\partial \Pi}{\partial C_{mn}} &= 0 & \begin{cases} m = 1, 2, \dots, M_3 \\ n = 1, 2, \dots, N_3 \end{cases}\end{aligned}\quad (6.169)$$

For the formation presented here,  $\Pi$  is always quadratic in the undetermined coefficients. Thus, the coefficients of equation (6.169) lead to a  $\sum_{i=1}^3 M_i \times N_i$  set of linear simultaneous equations. For buckling and free vibration problems, equation (6.169) leads to a classic eigenvalue problem.

If we limit the analysis to symmetric specially orthotropic plates subjected to a uniform load  $p_0$ , the energy criterion becomes

$$U + W = \text{stationary value} \quad (6.170)$$

and

$$U = \frac{1}{2} \int_0^b \int_0^a \left[ D_{11} \left( \frac{\partial^2 w}{\partial x^2} \right)^2 + 2D_{12} \frac{\partial^2 w}{\partial x^2} \frac{\partial^2 w}{\partial y^2} + D_{22} \left( \frac{\partial^2 w}{\partial y^2} \right)^2 + 4D_{66} \left( \frac{\partial^2 w}{\partial x \partial y} \right)^2 \right] dx dy \quad (6.171)$$

$$W = - \int_0^b \int_0^a p_0 w dx dy \quad (6.172)$$

For clamped edges, we have the following boundary conditions:

*At*  $x = 0, a$

$$w = \frac{\partial w}{\partial x} = 0 \quad (6.173)$$

*At*  $y = 0, b$

$$w = \frac{\partial w}{\partial y} = 0 \quad (6.174)$$

To find an approximate solution for the plate deflection, we use the following finite series in the variables separable form:

$$w = \sum_{m=1}^M \sum_{n=1}^N C_{mn} X_m(x) Y_n(y) \quad (6.175)$$

The functions  $X_m(x)$  and  $Y_n(y)$  should satisfy the boundary conditions of (6.173) and (6.174). Using the series equation (6.175), the condition of equation (6.170) reduces to the  $M \times N$  conditions

$$\frac{\partial U}{\partial C_{mn}} = -\frac{\partial W}{\partial C_{mn}} \quad \begin{cases} m = 1, 2, \dots, M \\ n = 1, 2, \dots, N \end{cases} \quad (6.176)$$

Substituting equation (6.175) into equations (6.171) and (6.172) and differentiating with respect to  $C_{mn}$  for the relation of equation (6.176), we get

$$\begin{aligned} & \sum_{i=1}^M \sum_{j=1}^N \left[ D_{11} \int_0^a \frac{d^2 X_i}{dx^2} \frac{d^2 X_m}{dx^2} dx \int_0^b Y_j Y_n dy \right. \\ & + D_{12} \left( \int_0^a X_m \frac{d^2 X_i}{dx^2} dx \int_0^b Y_j \frac{d^2 Y_n}{dy^2} dy + \int_0^a X_i \frac{d^2 X_m}{dx^2} dx \int_0^b Y_n \frac{d^2 Y_j}{dy^2} dy \right) \\ & + D_{22} \int_0^a X_i X_m dx \int_0^b \frac{d^2 Y_j}{dy^2} \frac{d^2 Y_n}{dy^2} dy + 4D_{66} \int_0^a \frac{dX_i}{dx} \frac{dX_m}{dx} dx \int_0^b \frac{dY_j}{dy} \frac{dY_n}{dy} dy \left. \right] C_{ij} \\ & = p_0 \int_0^a X_m dx \int_0^b Y_n dy \quad \begin{cases} m = 1, 2, \dots, M \\ n = 1, 2, \dots, N \end{cases} \quad (6.177) \end{aligned}$$

As a first approximation, the functions  $X_m(x)$  and  $Y_n(y)$  may be represented as polynomials, with each term satisfying the boundary conditions (6.173) and (6.174):

$$X_m(x) = (x^2 - ax)^2 x^{m-1} \quad (6.178a)$$

$$Y_n(y) = (y^2 - by)^2 y^{n-1} \quad (6.178b)$$

Substituting equation (6.178) into equation (6.177) with  $M=N=1$  for the first approximation, we obtain

$$C_{11} = \frac{6.125p_0}{7D_{11}b^4 + 4(D_{12} + 2D_{66})a^2b^2 + 7D_{22}a^4} \quad (6.179)$$

Then the deflection function  $w$  is

$$w = \frac{6.125p_0(x^2 - ax)^2(y^2 - by)^2}{7D_{11}b^4 + 4(D_{12} + 2D_{66})a^2b^2 + 7D_{22}a^4} \quad (6.180)$$

The maximum deflection at the center is

$$w_{\max} = \frac{0.00342p_0a^4}{D_{11} + 0.571(D_{12} + 2D_{66})R^2 + D_{22}R^4} \quad (6.181)$$

where  $R$  is the plate aspect ratio  $a/b$ .

The functions  $X_m(x)$  and  $Y_n(y)$  may be selected by considering the solutions of the natural vibration of a beam with clamped ends (Craig, 1981):

$$X_m(x) = \gamma_m \cos \frac{\lambda_m x}{a} - \gamma_m \cosh \frac{\lambda_m x}{a} + \sin \frac{\lambda_m x}{a} - \sinh \frac{\lambda_m x}{b} \quad (6.182a)$$

$$Y_n(y) = \gamma_n \cos \frac{\lambda_n y}{b} - \gamma_n \cosh \frac{\lambda_n y}{b} + \sin \frac{\lambda_n y}{b} - \sinh \frac{\lambda_n y}{b} \quad (6.182b)$$

where  $\lambda_m$  and  $\lambda_n$  are the roots of the frequency equation

$$\cos \lambda_i \cosh \lambda_i = 1 \quad (6.183)$$

and

$$\gamma_i = \frac{\cos \lambda_i - \cosh \lambda_i}{\sin \lambda_i + \sinh \lambda_i} \quad (6.184)$$

where  $i = m, n$  in both equations (6.183) and (6.184).

The first five values of  $\lambda_i$  that satisfy equation (6.183) are given in table 6.1. From table 6.1, since  $\lambda_i$  is larger than 1, we may approximate

$$\cosh \lambda_i \approx \frac{1}{2} e^{\lambda_i} \quad (6.185)$$

and from equation (6.183)

$$\cos \lambda_i \approx 0 \quad (6.186)$$

or

$$\lambda_i = (2i + 1) \frac{\pi}{2} \quad (6.187)$$

In order to determine the accuracy of equation (6.187), the first five values of  $\lambda_i$  calculated from equation (6.187) are listed in table 6.2. For  $i > 2$ , equation (6.187) yields exact values for  $\lambda_i$  to five significant figures.

**Table 6.1 Values of  $\lambda_i$  Determined from Equation (6.183)**

$\lambda_1$	$\lambda_2$	$\lambda_3$	$\lambda_4$	$\lambda_5$
4.730	7.853	10.996	14.137	17.279

**Table 6.2 Values of  $\lambda_i$  Determined from Equation (6.187)**

$\lambda_1$	$\lambda_2$	$\lambda_3$	$\lambda_4$	$\lambda_5$
4.172	7.854	10.996	14.137	17.279

The functions (6.182) satisfy the boundary conditions (6.173) and (6.174). For a first approximation with  $M=N=1$ , we already have  $\lambda_1=4.730$ ,  $\gamma_1=0.9825$ . Thus,

$$X(x) = 0.9825 \cos \frac{4.73x}{a} - 0.9825 \cosh \frac{4.73x}{a} + \sin \frac{4.73x}{a} - \sinh \frac{4.73x}{a} \quad (6.188a)$$

$$Y(y) = 0.9825 \cos \frac{4.73y}{b} - 0.9825 \cosh \frac{4.73y}{b} + \sin \frac{4.73y}{b} - \sinh \frac{4.73y}{b} \quad (6.188b)$$

Substituting these relationships into equation (6.177), we obtain a single equation,

$$C_{11} = \frac{0.6903p_0a^4}{500.56[D_{11} + 0.6047(D_{12} + 2D_{66})R^2 + D_{22}R^4]} \quad (6.189)$$

Again,  $R$  represents the plate aspect ratio  $a/b$ .

The maximum deflection can be determined by evaluating  $X_1(x)$  and  $Y_1(y)$  at the center of the plate with the results

$$w_{\max} = \frac{0.00348p_0a^4}{D_{11} + 0.6047(D_{12} + 2D_{66})R^2 + D_{22}R^4} \quad (6.190)$$

The two approximate solutions (6.181) and (6.190) appear to be almost identical.

In particular, if we consider an isotropic plate with  $D_{11}=D_{22}=D_{12}+2D_{66}=D$  and  $R=1$ , equation (6.181) based on the polynomial solution yields

$$w_{\max} = 0.00133 \frac{p_0a^4}{D} \quad (6.191)$$

while equation (6.190) yields the result

$$w_{\max} = 0.00134 \frac{p_0a^4}{D} \quad (6.192)$$

Using a large number of terms in equation (6.182), we get the solution for an isotropic plate:

$$w_{\max} = 0.00126 \frac{p_0a^4}{D} \quad (6.193)$$

Therefore, the errors in the polynomial approximation (6.191) and the beam function approximation (6.192) are 5.6% and 6.3%, respectively.

The maximum moment occurs at the middle of the edge (e.g.,  $a=0$ ,  $y=b/2$ ) and can be calculated by differentiating  $w$  in conjunction with equation (6.38). For isotropic materials using the polynomial solution (6.180), we obtain

$$M_{\max} = -0.0425p_0a^2 \quad (6.194)$$

and using the beam function (6.182), we get for a one-term solution

$$M_{\max} = -0.0384p_0a^2 \quad (6.195)$$

Using a large number of terms in the series (6.182), we obtain the result

$$M_{\max} = -0.0513p_0a^2 \quad (6.196)$$

Therefore, the one-term approximation is much less acceptable for the determination of the maximum moment than for the maximum deflection.

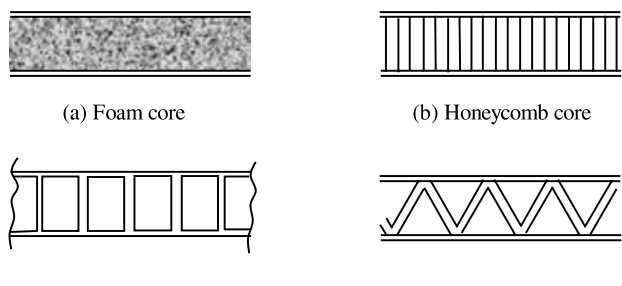
So far we have observed that the analytic solutions for the composite structure are very complicated, therefore, it is advisable to resort to finite element analysis as a better approach for complicated or large composite structures.

## 6.11 Behavior of Sandwich Structures

Structural sandwich constructions are composed of two faces, which primarily resist the in-plane and lateral (bending) loads, and a core, that resists shear and stabilizes the faces against buckling or wrinkling, as introduced briefly in figure 2.42. The faces usually consist of thin and high-performance material, while the core material is a thick, light, but relatively low-performance material. The choice of constituents depends mainly on the specific application and the design criteria set up by it (Zenkert, 1995, 1997). The core of a sandwich structure can be almost any material or architecture, but in general, cores fall into four types, as shown in figure 6.5 (Vinson, 1999): (a) foam or solid core, (b) honeycomb core, (c) web core, and (d) corrugated or truss core.

### 6.11.1 Stiffness Matrices for Sandwich Structures

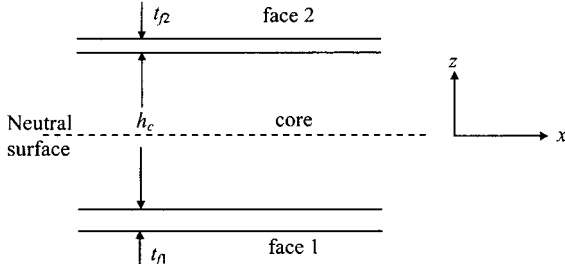
The equations for composite laminate plates so far developed can be used for a sandwich structure (figure 6.6) if the appropriate stiffness matrices are used. In figure 6.6, the lower face is face 1 and the upper face is face 2. The subscripts *f* and *c* represent face and core, respectively.



**Figure 6.5** Types of sandwich construction.

(c) Web core

(d) Corrugated or truss core

**Figure 6.6** Sandwich structure.*(a) Isotropic Symmetric Case*

If the materials used for sandwich construction are isotropic,  $\bar{Q}_{ij} = Q_{ij}$ ,  $t_{f1} = t_{f2} = t_f$ , then

$$\begin{aligned} A_{ij} &= \sum_{k=1}^3 \bar{Q}_{ij}^{[k]} (z_k - z_{k-1}) \\ &= (Q_{ij})_f \left[ -\frac{h_c}{2} - \left( -\frac{h_c}{2} - t_f \right) \right] + (Q_{ij})_c \left[ \frac{h_c}{2} - \left( -\frac{h_c}{2} \right) \right] + (Q_{ij})_f \left[ \left( \frac{h_c}{2} + t_f \right) - \frac{h_c}{2} \right] \\ &= (Q_{ij})_f t_f + (Q_{ij})_c h_c + (Q_{ij})_f t_f \\ &= (Q_{ij})_f (2t_f) + (Q_{ij})_c h_c \end{aligned} \quad (6.197)$$

Since for  $i$  and  $j = 1$  or  $2$ , to calculate the in-plane stiffness terms,

$$\begin{aligned} (Q_{ij})_f &= \frac{E_f}{1 - v_f^2} \\ (Q_{ij})_c &= \frac{E_c}{1 - v_c^2} \\ A_{11} = A_{22} &= \frac{E_f}{1 - v_f^2} (2t_f) + \frac{E_c}{1 - v_c^2} h_c \end{aligned} \quad (6.198)$$

If  $E_c$  is negligible compared with  $E_f$ , then the in-plane stiffness per unit width is

$$A_{11} = A_{22} = \frac{2E_f t_f}{1 - v_f^2} \quad (6.199)$$

The flexural rigidity  $D_{ij}$  is calculated similarly:

$$\begin{aligned} D_{ij} &= \frac{1}{3} \sum_{k=1}^3 \bar{Q}_{ij}^{[k]} (z_k^3 - z_{k-1}^3) \\ &= \frac{1}{3} (Q_{ij})_f \left[ \left( -\frac{h_c}{2} \right)^3 - \left( -\frac{h_c}{2} - t_f \right)^3 \right] + \frac{1}{3} (Q_{ij})_c \left[ \left( \frac{h_c}{2} \right)^3 - \left( -\frac{h_c}{2} \right)^3 \right] \\ &\quad + \frac{1}{3} (Q_{ij})_f \left[ \left( \frac{h_c}{2} + t_f \right)^3 - \left( \frac{h_c}{2} \right)^3 \right] \end{aligned} \quad (6.200)$$

or

$$D_{11} = D_{22} = \frac{1}{3} \left[ \frac{2E_f}{1 - v_f^2} - \left( \frac{3}{4} h^2 t_f + \frac{3}{2} h_c t_f^2 + t_f^3 \right) + \frac{E_c}{1 - v_c^2} \frac{h_c^3}{4} \right] \quad (6.201)$$

Neglecting higher powers of  $t_f$  and factoring out the first terms gives

$$D_{11} = D_{22} = \frac{1}{2} \frac{E_f h_c^2 t_f}{1 - v_f^2} \left[ 1 + \frac{1}{6} \frac{(1 - v_f^2) E_c h_c}{(1 - v_c^2) E_f t_f} \right] \quad (6.202)$$

When  $E_c h_c \ll E_f t_f$ , which is the usual case for many sandwich structures,

$$D_{11} = D_{22} = \frac{1}{2} \frac{E_f h_c^2 t_f}{1 - v_f^2} \quad (6.203)$$

### (b) Anisotropic Symmetric Case

If the materials used for sandwich construction are anisotropic such as those composed of composite laminate faces and a honeycomb core, all of the matrices  $[A]$ ,  $[B]$ , and  $[D]$  can be derived from the laminate analysis. If the resulting expressions can be simplified as shown above, the stiffnesses for symmetric case are expressed as follows:

$$A_{ij} = (\bar{Q}_{ij})_f (2t_f) \quad (i, j = 1, 2, 6) \quad (6.204a)$$

$$B_{ij} = 0 \quad (i, j = 1, 2, 6) \quad (6.204b)$$

$$D_{ij} = \frac{1}{2} (\bar{Q}_{ij})_f (h_c^2 t_f) \quad (i, j = 1, 2, 6) \quad (6.204c)$$

For this sandwich structure, the following relationship holds:

$$D_{ij} = \frac{1}{4} A_{ij} h_c^2 \quad (6.205)$$

For the transverse shear quantities  $A_{44}$  and  $A_{55}$ , following the same procedures for the isotropic sandwich structure,

$$A_{44} = A_{55} = G_c h_c + 2t_f G_f \quad (6.206)$$

Since in many cases  $G_f t_f / G_c h_c \ll 1$ ,

$$A_{44} = A_{55} = G_c h_c \quad (6.207)$$

where  $G_c$  represents the interlaminar shear modulus  $G_{23}$  or  $G_{13}$  of core in equation (3.68).

In this expression, the core acts as the web in an I-beam in that the core provides the transverse shear stiffness for the structure.

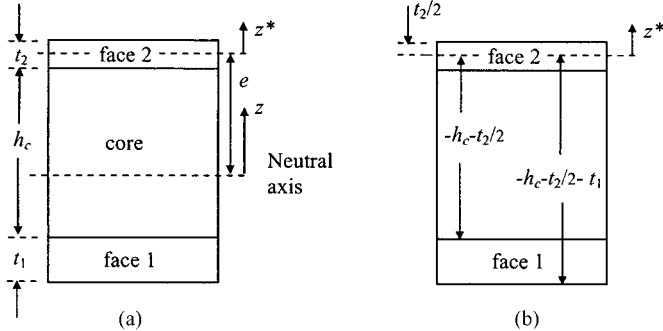


**Figure 6.7** Definition of location of the neutral axis in a sandwich construction with dissimilar faces: (a) Global coordinate system; (b) transformed coordinate system ( $z^*$ ).

(c) *Sandwich Structures with Dissimilar Faces*

For the sandwich structures of figure 6.7 with dissimilar faces (i.e., faces of different thickness and/or different materials), the position of the neutral axis must be found first. It is given by the coordinate system for which the first moment of area is zero when integrated over the entire cross-section. If we assume that only  $\kappa_x$  exists with  $\varepsilon_x^0 = \Delta T = \Delta C = 0$ , then using equation (4.15),

$$\int \sigma_x dz = \kappa_x \int \bar{Q}_{11} z dz = 0 \quad (6.208)$$

Since the location of the origin of the sought coordinate system is unknown, we make a coordinate transformation from a known point in the cross-section,  $z^* = z - e$ , as shown in figure 6.7. Then equation (6.208) becomes

$$\int (\bar{Q}_{11}) z dz = \int (\bar{Q}_{11})(z^* + e) dz^* = 0$$

or

$$-\int (\bar{Q}_{11}) z^* dz^* = e \int (\bar{Q}_{11}) dz^* \quad (6.209)$$

For a general sandwich cross-section as shown in figure 6.7, equation (6.209) reduces to

$$(\bar{Q}_{11})_1 t_1 \left( \frac{1}{2} t_1 + h_c + \frac{1}{2} t_2 \right) + (\bar{Q}_{11})_c h_c \left( \frac{1}{2} h_c + \frac{1}{2} t_2 \right) = e [(\bar{Q}_{11})_1 t_1 + (\bar{Q}_{11})_c h_c + (\bar{Q}_{11})_2 t_2] \quad (6.210)$$

For a sandwich with a weak core this reduces to

$$e = \frac{(\bar{Q}_{11})_1 t_1 d}{(\bar{Q}_{11})_1 t_1 + (\bar{Q}_{11})_2 t_2} \quad (6.211)$$

where  $d$  is defined as

$$d = \frac{1}{2}t_1 + h_c + \frac{1}{2}t_2 \quad (6.212)$$

The value  $d - e$  is expressed as

$$d - e = \frac{(\bar{Q}_{11})_2 t_2 d}{(\bar{Q}_{11})_1 t_1 + (\bar{Q}_{11})_2 t_2} \quad (6.213)$$

Then the flexural rigidity  $D$  with respect to the neutral axis is expressed as

$$\begin{aligned} D = & \frac{1}{12}(\bar{Q}_{11})_1 t_1^3 + \frac{1}{12}(\bar{Q}_{11})_2 t_2^3 + \frac{1}{12}(\bar{Q}_{11})_c h_c^3 \\ & + (\bar{Q}_{11})_1 t_1(d - e)^2 + (\bar{Q}_{11})_2 t_2 e^2 + (\bar{Q}_{11})_c h_c \left( \frac{h_c + t_2}{2} - e \right)^2 \end{aligned} \quad (6.214)$$

If the core is weak,  $E_c \ll E_f$ , equation (6.214) can be simplified using equations (6.211) and (6.213):

$$D = \frac{1}{12}(\bar{Q}_{11})_1 t_1^3 + \frac{1}{12}(\bar{Q}_{11})_2 t_2^3 + \frac{(\bar{Q}_{11})_1(\bar{Q}_{11})_2 t_1 t_2 d^2}{(\bar{Q}_{11})_1 t_1 + (\bar{Q}_{11})_2 t_2} \quad (6.215)$$

where the first two terms vanish if the faces are thin.

### 6.11.2 Sandwich Plate on an Elastic Foundation

When a sandwich plate is subjected to a local outside force, it can be treated as a plate that is supported on an elastic foundation. In most cases an elastic foundation is modeled as an elastic medium with a constant foundation modulus  $k$  of force per unit area. The force per unit area is  $-kw$ , because when  $w$  is positive the foundation modulus is acting in a negative direction, and vice versa. Then the governing equation (6.41) without considering transverse shear deformation is expressed as

$$D_1 \frac{\partial^4 w}{\partial x^4} + 2D_3 \frac{\partial^4 w}{\partial x^2 \partial y^2} + D_2 \frac{\partial^4 w}{\partial y^4} + kw = p(x, y) \quad (6.216)$$

When an isotropic plate on an elastic foundation is subjected to a uniform lateral load  $p_0$ , equation (6.216) becomes

$$D \left[ \frac{\partial^4 w}{\partial x^4} + 2 \frac{\partial^4 w}{\partial x^2 \partial y^2} + \frac{\partial^4 w}{\partial y^4} \right] + kw = p_0 \quad (6.217)$$

where  $D = D_1 = D_2 = D_3$  is the flexural stiffness.

For a plate simply supported on all four edges, we can use the following solution forms:

$$w(x, y) = \sum_{m=1}^{\infty} \sum_{n=1}^{\infty} C_{mn} \sin \frac{m\pi x}{a} \sin \frac{n\pi y}{b} \quad (6.218)$$

$$p_0 = \sum_{m=1}^{\infty} \sum_{n=1}^{\infty} q_{mn} \sin \frac{m\pi x}{a} \sin \frac{n\pi y}{b} \quad (6.219)$$

where  $q_{mn} = 16p_0/(\pi^2 mn)$  (for  $m$  and  $n$  odd only) from equation (6.52) for a uniform lateral load  $p_0$ . Substituting equations (6.218) and (6.219) into equation (6.217), we get  $C_{mn}$  for  $m$  and  $n$  odd only:

$$C_{mn} = \frac{16p_0}{mn\pi^2 D} \frac{1}{\left[\left(\frac{m\pi}{a}\right)^2 + \left(\frac{n\pi}{b}\right)^2\right] + \frac{k}{D}} \quad (6.220)$$

The amplitude of the lateral deflection is greatly reduced by the presence of the constant quantity  $k/D > 0$ . Several terms in both  $m$  and  $n$  are needed to have the maximum value converge to a constant value.

A sandwich plate may buckle locally due to in-plane loads applied to the face. In this case the plate can be considered to be supported on a uniform elastic foundation, namely the core (Vinson, 1999). For isotropic material, the buckling equation becomes, from equations (6.36) and (6.217),

$$D\nabla^4 w + kw - N_x \frac{\partial^2 w}{\partial x^2} - N_y \frac{\partial^2 w}{\partial y^2} = 0 \quad (6.221)$$

For a plate with simply supported edges on all four sides, the Navier approach is

$$w(x, y) = C_{mn} \sin \frac{m\pi x}{a} \sin \frac{n\pi y}{b} \quad (6.222)$$

Substituting equation (6.222) into equation (6.221), we get the critical buckling load  $N_{x,cr}$  as

$$N_{x,cr} = -\frac{(\pi^4 D/a^4)(m^2 + n^2 R^2)^2 + k}{(\pi^2/a^2)(m^2 + n^2 R^2 \phi)} \quad (6.223)$$

where

$$\begin{aligned} \phi &= N_y/N_x \\ R &= a/b \end{aligned}$$

Since the buckling is a localized phenomenon, we may use  $R = 1$  when  $\phi = 1$ . Then equation (6.223) reduces to

$$N_{x,cr} = -\frac{\frac{\pi^4 D}{a^2}(m^2 + n^2)^2 + ka^2}{\pi^2(m^2 + n^2)} \quad (6.224)$$

The minimum value of  $N_{x,cr}$  occurs when  $m=n=1$ , therefore

$$N_{x,cr} = -\frac{1}{2\pi^2} \left( \frac{4\pi^4 D}{a^2} + ka^2 \right) \quad (6.225)$$

The minimum value of equation (6.225) occurs when  $a$  is

$$a = \sqrt{2}\pi \left( \frac{D}{k} \right)^{1/4} \quad (6.226)$$

Then, the critical buckling load is

$$N_{x,cr} = N_{y,cr} = -2(kD)^{1/2} \quad (6.227)$$

## 6.12 One-Dimensional Structures (Beams) of Composite Materials

There are two cases of laminated plates that can be treated as one-dimensional problems: (1) laminated beams, and (2) cylindrical bending of laminated plate strips (Reddy, 1997).

When the width  $b$  in the  $y$ -direction of a laminated plate is very small compared with the length  $l$  in the  $x$ -direction, as shown in figure 6.8, it is treated as a laminated beam. The term *beam* is used when the structure is subjected to a lateral load in the  $z$ -direction. The term *rod* is used when the structure is subjected to a tensile load in the axial direction ( $x$ -direction), while the term *column* is used when the structure is subjected to a compressive load in the axial direction ( $x$ -direction) (Vinson and Sierakowski, 1987). The beam is a special laminated structure that can be treated by one-dimensional analysis.

In cylindrical bending, the laminated plate is assumed to be a plate strip that has a  $y$ -axis dimension that is very long in comparison with the dimension  $l$  along the  $x$ -axis. When this plate is subjected to a transverse load  $p(x)$  that is uniform at any section parallel to the  $x$ -axis, the deflection  $w_0$  and displacements  $(u_0, v_0)$  of the plate are functions of  $x$  only. Therefore, all derivatives with respect to  $y$  are zero, and the plate bends into a cylindrical surface. Then we can use all the governing equations so far derived with some simplification for the design and analysis of composite

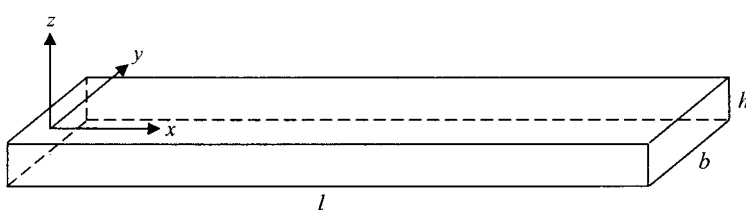


**Figure 6.8** Configuration and coordinate system of the beam.

structures. The cylindrical bending problem is also a plane strain problem ( $\varepsilon_y = 0$ ), whereas the beam problem is a plane stress problem.

Cylindrical bending is not treated in this section, but the laminated beam will be discussed. For the bending of symmetrically laminated beams ( $[B] = 0$ ) without in-plane forces, the problem is reduced to one of solving for deflection and stresses. The bending-curvature relations for this case without transverse shear deformation are expressed by equation (4.75) when there are no hygrothermal loadings:

$$\begin{Bmatrix} M_x \\ M_y \\ M_{xy} \end{Bmatrix} = - \begin{bmatrix} D_{11} & D_{12} & D_{16} \\ D_{12} & D_{22} & D_{26} \\ D_{16} & D_{26} & D_{66} \end{bmatrix} \begin{Bmatrix} \frac{\partial^2 w_0}{\partial x^2} \\ \frac{\partial^2 w_0}{\partial y^2} \\ 2 \frac{\partial^2 w_0}{\partial x \partial y} \end{Bmatrix} \quad (6.228)$$

or, in inverse form from equation (4.76) as

$$\begin{Bmatrix} \frac{\partial^2 w_0}{\partial x^2} \\ \frac{\partial^2 w_0}{\partial y^2} \\ 2 \frac{\partial^2 w_0}{\partial x \partial y} \end{Bmatrix} = - \begin{bmatrix} d_{11} & d_{12} & d_{16} \\ d_{12} & d_{22} & d_{26} \\ d_{16} & d_{26} & d_{66} \end{bmatrix} \begin{Bmatrix} M_x \\ M_y \\ M_{xy} \end{Bmatrix} \quad (6.229)$$

When only  $M_x$  is applied ( $M_y = M_{xy} = 0$ ),

$$\kappa_x = - \frac{\partial^2 w_0}{\partial x^2} = d_{11} M_x \quad (6.230)$$

$$\kappa_y = - \frac{\partial^2 w_0}{\partial y^2} = d_{12} M_x \quad (6.231)$$

$$\kappa_{xy} = -2 \frac{\partial^2 w_0}{\partial x \partial y} = d_{16} M_x \quad (6.232)$$

Equations (6.231) and (6.232) indicate that the deflection  $w_0$  cannot be independent of the coordinate  $y$  due to the Poisson effect ( $d_{12}$ ) and anisotropic shear coupling ( $d_{16}$ ). These effects can be neglected only for narrow beams when  $b/l$  is very small.

### 6.12.1 Narrow Beams

For the analysis of narrow beams, it is assumed that the transverse moment  $M_y$  and twisting moment  $M_{xy}$  are zero, and the laminated beam is narrow enough to make the effects of the Poisson's ratio and shear coupling on the deflection negligible

(Swanson, 1997). Then the deflection  $w_0$  can be treated as a function of coordinate  $x$  along the length of beam and time  $t$ :

$$w_0 = w_0(x, t) \quad (6.233)$$

and

$$\frac{\partial^2 w_0}{\partial x^2} = -d_{11} M_x \quad (6.234)$$

It should be noted that the moment resultants in equation (6.234) are on a unit-width basis, and must be multiplied by the beam width  $b$  to get the total moment used in the beam theory. In order to make equation (6.234) in the form of Euler–Bernoulli beam theory (Rao, 2004), the following quantities are introduced:

$$M_b = b M_x \quad (6.235a)$$

$$V = b Q_x \quad (6.235b)$$

$$\bar{EI} = \frac{b}{d_{11}} \quad (6.235c)$$

$$I = \frac{bh^3}{12} \quad (6.235d)$$

where  $b$  is the width and  $h$  is the thickness of the laminate. The term  $\bar{EI}$  is often called *effective bending stiffness*.

Then equation (6.234) becomes

$$M_b(x) = b M_x(x) = \bar{EI} k_x = -\bar{EI} \frac{\partial^2 w_0}{\partial x^2} = -\frac{b}{d_{11}} \frac{\partial^2 w_0}{\partial x^2} \quad (6.236)$$

The shear force and bending moments are related by

$$Q_x = \frac{\partial M_x}{\partial x} \quad \text{or} \quad V = \frac{\partial M_b}{\partial x} \quad (6.237)$$

For static bending case  $p(x, t) = p(x)$ , we have the following relation from equation (6.18):

$$\frac{dV}{dx} = b \frac{dQ_x}{dx} = -bp(x) = -\hat{p}(x) \quad (6.238)$$

where  $\hat{p}(x) = bp(x)$ . Then we have

$$\frac{d^2 M_b(x)}{dx^2} = -\bar{EI} \frac{d^4 w_0}{dx^4} = -\frac{b}{d_{11}} \frac{d^4 w_0}{dx^4} = -bp = -\hat{p} \quad (6.239)$$

**EXAMPLE 6.2**

Find the maximum deflection and stresses of a simply supported beam of length  $l$  and width  $b$  subjected to a center point load  $F$  (at  $x=l/2$ ) in the negative  $z$ -direction.

**Solution**

The bending moment is expressed as

$$M_b(x) = -\frac{F}{2}x, \quad \text{for } 0 \leq x \leq \frac{l}{2} \quad (6.240)$$

Then from equation (6.236), we have for static case

$$\bar{EI} \frac{d^2 w_0}{dx^2} = \frac{F}{2}x \quad (6.241)$$

Integrating equation (6.241) twice, we have

$$\bar{EI}w_0(x) = \frac{F}{12}x^3 + c_1x + c_2 \quad (6.242)$$

The constants  $c_1$  and  $c_2$  are evaluated using the boundary conditions of  $w_0(0) = 0$ ,  $(dw_0(l/2)/dx) = 0$ :

$$c_1 = -\frac{Fl^2}{16}, \quad c_2 = 0 \quad (6.243)$$

Then

$$w_0(x) = -\frac{Fl^3}{48\bar{EI}} \left[ 3\left(\frac{x}{l}\right)^3 - 4\left(\frac{x}{l}\right)^2 \right] \quad (6.244)$$

The deflection is maximum at  $x=l/2$ , which is given by

$$w_{\max} = -\frac{Fl^3}{48\bar{EI}} = -\frac{Fl^3}{4bh^3\bar{E}} \quad (6.245)$$

Equation (6.245) can be used to determine the modulus of the material in terms of the measured center deflection  $w_{\max}$ , applied load  $F$ , and the geometric parameters of the laminated beam in a three-point bending test:

$$\bar{E} = -\frac{Fl^3}{4bh^3w_{\max}} \quad (6.246)$$

In deriving deflection for narrow beams, it has been assumed that the laminated beam is narrow enough to make the effects of the Poisson's ratio and shear coupling on the deflection negligible. However, this condition may be relaxed somewhat to obtain the curvatures  $\kappa_y$  and  $\kappa_{xy}$  from equations (6.231) and (6.232). The maximum stress  $\sigma_x$  occurs at  $x=l/2$ , where the bending moment ( $M_b = -Fl/4$ ,  $M_x = -Fl/4b$ )

is maximum. The stresses are calculated from equation (4.15) when there is no in-plane or hygrothermal load:

$$\sigma_x^{[k]} = -\frac{Flz}{4b} (Q_{11}^{[k]} d_{11} + Q_{12}^{[k]} d_{12} + Q_{16}^{[k]} d_{16}) \quad (6.247)$$

When the beam is unsymmetric, the matrix  $[B]$  does not vanish, and the entire  $6 \times 6$  matrix must be inverted, as expressed in equation (4.44):

$$\begin{Bmatrix} \varepsilon_x^0 \\ \varepsilon_y^0 \\ \gamma_{xy}^0 \\ \kappa_x \\ \kappa_y \\ \kappa_{xy} \end{Bmatrix} = \begin{bmatrix} A'_{11} & A'_{12} & A'_{16} & B'_{11} & B'_{12} & B'_{16} \\ A'_{12} & A'_{22} & A'_{26} & B'_{12} & B'_{22} & B'_{26} \\ A'_{16} & A'_{26} & A'_{66} & B'_{16} & B'_{26} & B'_{66} \\ B'_{11} & B'_{12} & B'_{16} & D'_{11} & D'_{12} & D'_{16} \\ B'_{12} & B'_{22} & B'_{26} & D'_{12} & D'_{22} & D'_{26} \\ B'_{16} & B'_{26} & B'_{66} & D'_{16} & D'_{26} & D'_{66} \end{bmatrix} \begin{Bmatrix} N_x \\ N_y \\ N_{xy} \\ M_x \\ M_y \\ M_{xy} \end{Bmatrix} \quad (4.44)$$

When only  $M_x$  is applied, equation (4.44) reduces to

$$\begin{Bmatrix} \varepsilon_x^0 \\ \varepsilon_y^0 \\ \gamma_{xy}^0 \\ \kappa_x \\ \kappa_y \\ \kappa_{xy} \end{Bmatrix} = \begin{bmatrix} A'_{11} & A'_{12} & A'_{16} & B'_{11} & B'_{12} & B'_{16} \\ A'_{12} & A'_{22} & A'_{26} & B'_{12} & B'_{22} & B'_{26} \\ A'_{16} & A'_{26} & A'_{66} & B'_{16} & B'_{26} & B'_{66} \\ B'_{11} & B'_{12} & B'_{16} & D'_{11} & D'_{12} & D'_{16} \\ B'_{12} & B'_{22} & B'_{26} & D'_{12} & D'_{22} & D'_{26} \\ B'_{16} & B'_{26} & B'_{66} & D'_{16} & D'_{26} & D'_{66} \end{bmatrix} \begin{Bmatrix} 0 \\ 0 \\ 0 \\ M_x \\ 0 \\ 0 \end{Bmatrix} \quad (6.248)$$

or

$$\varepsilon_x^0 = B'_{11} M_x \quad (6.249a)$$

$$\varepsilon_y^0 = B'_{12} M_x \quad (6.249b)$$

$$\kappa_x = D'_{11} M_x \quad (6.249c)$$

$$\kappa_y = D'_{12} M_x \quad (6.249d)$$

From equation (6.249c), the relationship between the curvature and the moment can be expressed as

$$M_b = b M_x = \frac{b}{D'_{11}} \kappa_x = \bar{E} I \kappa_x \quad (6.250)$$

or

$$\bar{E} I = \frac{b}{D'_{11}} \quad (6.251)$$

The strain distributions are given from equation (4.6):

$$\varepsilon_x = \varepsilon_x^0 + z \kappa_x \quad (6.252a)$$

$$\varepsilon_y = \varepsilon_y^0 + z \kappa_y \quad (6.252b)$$

If a new coordinate  $\eta$  from the neutral axis is adopted rather than  $z$  from the midplane, such that

$$\eta = z - z_c \quad (6.253)$$

where  $z_c$  is the distance from the  $z$ -axis to the  $\eta$ -axis. The definition of the neutral axis is

$$\varepsilon_x = 0, \quad \text{at} \quad \eta = 0 \quad (6.254)$$

From equations (6.249a) and (6.249c), the condition of equation (6.254) reduces to

$$\varepsilon_x = \varepsilon_x^0 + z_c \kappa_x = B'_{11} M_x + z_c D'_{11} M_x = 0$$

Then

$$z_c = -\frac{B'_{11}}{D'_{11}} \quad (6.255)$$

Using the coordinate  $\eta$ , equations (6.252) are expressed as

$$\varepsilon_x = \eta \kappa_x \quad (6.256a)$$

$$\begin{aligned} \varepsilon_y &= \varepsilon_y^0 + z_c \kappa_y + \eta \kappa_y \\ &= \left( B'_{12} - \frac{B'_{11} D'_{12}}{D'_{11}} \right) M_x + \eta \kappa_y \end{aligned} \quad (6.256b)$$

When the value of  $(B'_{12} - B'_{11} D'_{12}/D'_{11})$  is negligibly small, equation (6.256b) reduces to

$$\varepsilon_y = \eta \kappa_y \quad (6.256c)$$

### 6.12.2 Wide Beams

For wide beams, the curvatures  $\kappa_y$  and  $\kappa_{xy}$  are assumed to be zero. The transverse strain  $\varepsilon_y$  is also zero when there is no midplane strain  $\varepsilon_y^0$ . Then  $w_0 = w_0(x)$  for a symmetric beam under static load. From equation (6.228), we have

$$M_x = D_{11} \kappa_x = -D_{11} \frac{d^2 w_0}{dx^2} \quad (6.257)$$

or

$$M_b(x) = b M_x = b D_{11} \kappa_x = \bar{E} I \kappa_x = -b D_{11} \frac{d^2 w_0}{dx^2} \quad (6.258)$$

Therefore,

$$\bar{E} I = b D_{11} \quad (6.259)$$

For asymmetric wide beams, the transverse curvature  $\kappa_y$  is taken to be zero. Then equation (4.44) reduces to the following equation under  $M_x$  and  $M_y$  only when  $\gamma_{xy}^0$  and  $\kappa_{xy}$  terms are neglected:

$$\begin{Bmatrix} \varepsilon_x^0 \\ \varepsilon_y^0 \\ 0 \\ \kappa_x \\ 0 \\ 0 \end{Bmatrix} = \begin{bmatrix} A'_{11} & A'_{12} & A'_{16} & B'_{11} & B'_{12} & B'_{16} \\ A'_{12} & A'_{22} & A'_{26} & B'_{12} & B'_{22} & B'_{26} \\ A'_{16} & A'_{26} & A'_{66} & B'_{16} & B'_{26} & B'_{66} \\ B'_{11} & B'_{12} & B'_{16} & D'_{11} & D'_{12} & D'_{16} \\ B'_{12} & B'_{22} & B'_{26} & D'_{12} & D'_{22} & D'_{26} \\ B'_{16} & B'_{26} & B'_{66} & D'_{16} & D'_{26} & D'_{66} \end{bmatrix} \begin{Bmatrix} 0 \\ 0 \\ 0 \\ M_x \\ M_y \\ 0 \end{Bmatrix} \quad (6.260)$$

Multiplying out equation (6.260) yields

$$\varepsilon_x^0 = B'_{11}M_x + B'_{12}M_y \quad (6.261a)$$

$$\varepsilon_y^0 = B'_{12}M_x + B'_{22}M_y \quad (6.261b)$$

$$\kappa_x = D'_{11}M_x + D'_{12}M_y \quad (6.261c)$$

$$0 = D'_{12}M_x + D'_{22}M_y \quad (6.261d)$$

From equations (6.261c) and (6.261d),

$$\kappa_x = \frac{D'_{11}D'_{22} - D'^2_{12}}{D'^2_{22}} M_x \quad (6.262)$$

Therefore, the effective bending stiffness reduces to

$$\bar{EI} = \frac{bM_x}{\kappa_x} = b \frac{D'_{22}}{D'_{11}D'_{22} - D'^2_{12}} \quad (6.263)$$

$$z_c = -\frac{B'_{11}D'_{22} - B'_{12}D'_{12}}{D'_{11}D'_{22} - D'^2_{12}} \quad (6.264)$$

### EXAMPLE 6.3

A composite laminated beam is made of 24 plies of T300/5208 carbon epoxy, with stacking sequence [0/45/ $-45$ ]<sub>4S</sub>. Find the effective bending stiffness  $\bar{EI}$  based on the narrow- and wide-beam assumptions when the ply thickness is 0.125 mm. The length  $l$  and width  $b$  of the beam are 250 mm and 12.5 mm, respectively.

#### Solution

For the stacking sequence [0/45/ $-45$ ]<sub>4S</sub> made of T300/5208 in table 2.3 with ply thickness of 0.125 mm, we have

$$D_{11} = 181.0 \text{ Nm}$$

$$d_{11} = 6.572 \times 10^{-3} \text{ 1/Nm}$$

*For the narrow-beam assumption:* From equation (6.235c),  $\bar{EI} = b/d_{11} = 1.920 \text{ Nm}^2$ .

*For the wide beam assumption:* From equation (6.259),  $\bar{EI} = bD_{11} = 2.263 \text{ Nm}^2$ .

The difference between the two estimates is about 18%. The difference in stiffness between the two cases for isotropic materials results from replacing  $E$  in the beam theory with  $E/(1 - \nu^2)$  in the plate theory.

#### Interlaminar Shear Stress in a Rectangular Beam

The interlaminar shear stress in the beam may be calculated using the same method as for isotropic beams (Gere, 2001). The interlaminar shear stress  $\tau_{xz}$  is expressed, with the assumption of  $\bar{Q}_{16}^{[k]} = 0$ , by the classical lamination theory:

$$\tau_{xz}b' = \frac{\partial}{\partial x} \int_z^{h/2} \sigma_x bdz = \frac{\partial}{\partial x} \sum_{k=k_z}^n (\bar{Q}_{11}^{[k]} \varepsilon_x + \bar{Q}_{12}^{[k]} \varepsilon_y) bt_{\text{ply}}^{[k]} \quad (6.265)$$

where  $b'$  is the width of the beam where the shear stress is to be calculated. For the rectangular beam, the width is constant ( $b' = b = \text{constant}$ ).

The above integral is performed from the value of  $z$  where the shear stress is to be calculated to the upper surface.

The strain  $\varepsilon_x$  of the symmetric laminate without any in-plane force is given by

$$\varepsilon_x = z\kappa_x = z \frac{M_b}{\bar{EI}} \quad (6.266)$$

The transverse strain  $\varepsilon_y$  is expressed as

$$\varepsilon_y = z\kappa_y = z \frac{d_{12}}{d_{11}} \kappa_x = z \frac{d_{12}}{d_{11}} \frac{M_b}{\bar{EI}}, \quad \text{for narrow beam} \quad (6.267a)$$

$$\varepsilon_y = 0, \quad \text{for wide beam} \quad (6.267b)$$

Since  $dM_b/dx = V$ , from equation (6.237), equation (6.265) reduces to

$$\tau_{xz} = \frac{V}{\bar{EI}} \sum_{k=k_z}^n (\bar{Q}_{11}^{[k]} + \bar{Q}_{12}^{[k]}\xi) \left( \frac{z_k^2 - z_{k-1}^2}{2} \right) \quad (6.268)$$

where

$$\xi = \frac{d_{12}}{d_{11}}, \quad \text{for narrow symmetric rectangular beam} \quad (6.269a)$$

$$\xi = 0, \quad \text{for wide symmetric rectangular beam} \quad (6.269b)$$

For the wide rectangular beam with angle ply stacking sequence  $[\pm\theta]_n S$ , we have  $\bar{E} = \bar{Q}_{11}^{[\theta]} = \bar{Q}_{11}^{[-\theta]}$ . Then equation (6.268) reduces to the following equation, which can also be applied to isotropic materials:

$$\tau_{xz} = \frac{V}{I} \sum_{k=k_z}^n \left( \frac{z_k^2 - z_{k-1}^2}{2} \right) \quad (6.270)$$

**EXAMPLE 6.4**

A composite laminated beam is made of 24 plies of T300/5208 carbon epoxy, with stacking sequence  $[\pm 15]_{6S}$ . The beam is simply supported at the ends and subjected to a uniformly distributed load  $\hat{p} = 1000 \text{ N/m}$ . Find the shear stress at the midplane of the beam at  $x = 0$  and  $l$ . The length  $l$  and width  $b$  of the beam are 250 mm and 50 mm, respectively, and the ply thickness is 0.125 mm.

**Solution**

The width-to-thickness ratio suggests that this is a wide beam ( $\xi = 0$ ). Then  $\bar{EI}$  is calculated by equation (6.259). For the stacking sequence  $[\pm 15]_{6S}$ , we have  $\bar{E} = \bar{Q}_{11}^{[-15]} = \bar{Q}_{11}^{[15]} = 117.2 \text{ GPa}$ ,  $I = 1.125 \times 10^{-10} \text{ m}^4$ ,  $V = 125 \text{ N}$ . Then,

$$\bar{EI} = bD_{11} = 13.19 \text{ Nm}^2$$

From equation (6.270),

$$\tau_{xz} = \frac{V}{I} \sum_{k=1}^n \left( \frac{z_k^2 - z_{k-1}^2}{2} \right) = \frac{125}{1.125 \times 10^{-10}} \left( \frac{0.0015^2 - 0}{2} \right) = 1.25 \text{ MPa}$$

For the more general stacking sequence, the shear stress in the beam does not have a smooth shape through the thickness, but changes slope at the interface of two plies with different ply angles.

### 6.12.3 Box-Type Composite Beams

Composite structures such as box-type beams and I-beams are increasingly employed in robot, machine tool, and automotive structures, due to their high specific stiffness and strength, as well as high damping (see chapters 13 to 15). The manufacturing methods for these beams are pultrusion, dry fiber preforms made from textile composites such as braids, and prepreg lay-up. In particular box-type beams are widely employed in machine tool structures and robot structures because they have both high bending and torsional stiffnesses (Koenigsberger, 1964). The general geometry of the box-type beam is shown in figure 6.9.

The analysis of the box-type beam can be performed based on the relationships of matrices of  $A$ ,  $B$ , and  $D$  calculated for the individual pieces of the cross-section taken separately, for the vertical and horizontal sections.

#### *Vertical Cross-Sections (Webs)*

The vertical cross-section is also called a web for the I-beam. The plies in the vertical cross-section lie parallel to the local vertical axis of the section. Under a vertical load on the beam, the in-plane force  $N_{x,v}$  in the vertical section varies due to the curvature  $\kappa_x$  of the beam. The in-plane strain  $\varepsilon_{x,v}$  in the infinitesimal length  $dz$  of the vertical cross-section in figure 6.9(b) is expressed as:

$$\varepsilon_{x,v} = z\kappa_x \quad (6.271)$$

The in-plane strain  $\varepsilon_{x,v}$  and  $\kappa_x$  may be obtained by solving equations (4.22) and (4.30) or alternatively, using equations (4.36) and (4.37) for the symmetric section with respect to the local axes. When the stacking sequence of the vertical section

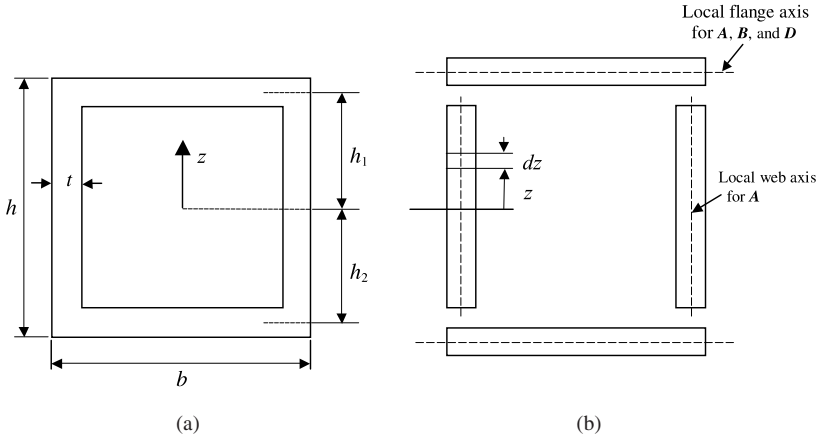


**Figure 6.9** Shape and local axes for the box-type beam: (a) Cross-sectional shape; (b) local axes attached to the web and flange.

is symmetric ( $[B]=0$ ) with respect to the local axes without any hydrothermal loads, we have the in-plane strain  $\varepsilon_{x,v}$  of the vertical section under  $N_{x,v}$  only from the simplified equation (4.72a):

$$\varepsilon_{x,v} = a_{11,v} N_{x,v} \quad (6.272)$$

The value of  $a_{11,v}$  should be calculated with respect to the local axis attached to the vertical cross-section. When the stacking sequence is not symmetric ( $[B] \neq 0$ ), equation (4.44) rather than equation (4.72a) should be used to calculate  $\varepsilon_{x,v}$ .

Using equations (6.271) and (6.272), the force distribution  $N_{x,v}$  in the vertical section can be expressed as

$$N_{x,v} = \frac{\kappa_x}{a_{11,v}} z \quad (6.273)$$

The moment  $M_{x,v}$  per one vertical section due to the stress variation in the vertical section can be calculated by integrating

$$M_{x,v} = \int_{-h/2}^{h/2} N_{x,v} z dz = \kappa_x \int_{-h/2}^{h/2} \frac{z^2}{a_{11,v}} dz = \frac{\kappa_x h^3}{12 a_{11,v}} \quad (6.274)$$

## *Horizontal Cross-Sections (Flanges)*

The horizontal section is also called a flange for the I-beam. The force  $N_{x,h}$  and moment  $M_{x,h}$  per unit width in the upper horizontal section for a symmetric beam can be expressed in terms of local strains  $\varepsilon_{x,h}$  and curvatures  $\kappa_x$  from equations (4.72a) and the results from the previous section:

$$N_{x,h} = \frac{h_1 \kappa_x}{a_{11,h}} \quad (6.275)$$

$$M_{x,h} = \frac{\kappa_x}{d_{11,h}} \quad \text{for narrow horizontal section} \quad (6.276a)$$

$$M_{x,h} = D_{11,h}\kappa_x \quad \text{for wide horizontal section} \quad (6.276b)$$

where  $h_1$  is the distance from the midplane to the center of the upper horizontal section shown in Figure 6.9.

The moment  $M_{b,hU}$  in the upper horizontal section is calculated by

$$M_{b,hU} = b(N_{x,h}h_1 + M_{x,hU}) = b\left(\frac{h_1^2}{a_{11,hU}} + \frac{1}{d_{11,hU}}\right)\kappa_x \quad \text{for narrow horizontal section} \quad (6.277a)$$

$$M_{b,hU} = b(N_{x,h}h_{1U} + M_{x,hU}) = b\left(\frac{h_1^2}{a_{11,hU}} + D_{11,hU}\right)\kappa_x \quad \text{for wide horizontal section} \quad (6.277b)$$

where  $b$  is the width of the beam.

The total moment  $M_b$  for the beam can be obtained by summing the moments for the vertical and horizontal sections:

$$M_b = 2M_{b,v} + M_{b,hU} + M_{b,hL} = \bar{E}Ik_x \quad (6.278)$$

where  $M_{b,hL}$  is the moment of the lower horizontal section.

The effective stiffness of the box-type beam with the same horizontal and vertical cross-sections is expressed as

$$\bar{EI} = \frac{h^3}{6a_{11,v}} + 2b\left(\frac{h_1^2}{a_{11,h}} + \frac{1}{d_{11,h}}\right) \quad \text{for narrow horizontal section} \quad (6.279a)$$

$$\bar{EI} = \frac{h^3}{6a_{11,v}} + 2b\left(\frac{h_1^2}{a_{11,h}} + D_{11,h}\right) \quad \text{for wide horizontal section} \quad (6.279b)$$

The stress distributions in the beam can be calculated from the strain distributions. The axial strain distribution in the entire beam is given by

$$\varepsilon_x = z\kappa_x \quad (6.280)$$

The curvature  $\kappa_y$  in the narrow horizontal section can be obtained from equations (4.76) and (6.276a)

$$\kappa_{y,h} = d_{12,h}M_{x,h} = \frac{d_{12,h}}{d_{11,h}}\kappa_x \quad (6.281)$$

The midplane strain  $\varepsilon_{y,h}^0$  in the narrow horizontal section in the  $y$ -direction can be obtained from equations (4.72b) and (6.275):

$$\varepsilon_{y,h}^0 = a_{12,h}N_{x,h} = \frac{a_{12,h}}{a_{11,h}}h_1\kappa_x \quad (6.282)$$

Then the strain in the narrow horizontal section of the box-type beam can be expressed as

$$\varepsilon_{y,h} = \varepsilon_{y,h}^0 + (z - h_1)\kappa_{y,h} = \left[\frac{a_{12,h}}{a_{11,h}}h_1 + (z - h_1)\frac{d_{12,h}}{d_{11,h}}\right]\kappa_x \quad (6.283)$$

where  $(z - h_1)$  represents a local coordinate through the thickness of the horizontal section. For the wide horizontal section of the box-type beam,  $\kappa_{y,h}$  is equal to zero. Therefore, equation (6.283) reduces to

$$\varepsilon_{y,h} = \varepsilon_{y,h}^0 = \frac{a_{12,h}}{a_{11,h}} h_1 \kappa_x \quad (6.284)$$

The *effective torsional rigidity*  $\bar{G}J$  of the box-type beam is expressed as (Gere, 2001)

$$\bar{G}J = G_{xy} \frac{2b^2 h^2}{b + h} t \quad (6.285)$$

where  $G_{xy}$  and  $t$  are the in-plane shear modulus and thickness of cross-section of the box-type beam, respectively.

The horizontal sections of the box-type beam are usually prevented from warping or deforming by the vertical sections unless the wall thickness is very small, hence the horizontal section of the box-type beam may be better predicted by the wide-beam hypothesis, while the I-beam may be better predicted by the narrow-beam hypothesis when the width of the flange is not very large.

#### *Shear Stresses in the Box-Type Beam*

The shear force in the vertical section of the symmetric box beam is calculated by the horizontal force equilibrium:

$$2t\tau_{xz,v} = 2 \frac{\partial}{\partial x} \int_z^{0.5h-t} t\sigma_{x,v} dz + \frac{\partial}{\partial x} \int_{0.5h-t}^{0.5h} b\sigma_{x,h} dz \quad (6.286)$$

where  $t$  represents the wall thickness of the vertical cross-section.

From equations (6.273) and (6.275),

$$\sigma_{x,v} = N_{x,v} = \frac{\kappa_x}{a_{11,v}} z \quad (6.287)$$

$$\sigma_{x,h} = \frac{N_{x,h}}{t} = \frac{h_1 \kappa_x}{a_{11,h} t} \quad (6.288)$$

Then equation (6.286) becomes

$$\tau_{xz,v} = \frac{1}{t} \frac{dk_x}{dx} \left[ \frac{1}{a_{11,v}} \int_z^{0.5h-t} zdz + \frac{h_1 b}{2ta_{11,h}} \int_{0.5h-t}^{0.5h} dz \right] \quad (6.289)$$

From equations (6.236) and (6.237),

$$\frac{dk_x}{dx} = \frac{1}{EI} \frac{dM}{dx} = \frac{V}{EI} \quad (6.290)$$

Therefore, equation (6.289) reduces to

$$\tau_{xz,v} = \frac{V}{EI} \left[ \frac{(0.5h-t)^2 - z^2}{2a_{11,v}} + \frac{h_1 b}{2a_{11,h}} \right] \quad (6.291)$$

When

$$a_{11,v} = a_{11,h} = \frac{1}{tE_x} = \frac{1}{t\bar{E}} \quad (6.292)$$

from the result of equation (4.54), equation (6.291) reduces to

$$\tau_{xz,v} = \frac{V}{2I} [(0.5h - t)^2 - z^2 + h_1 b] \quad (6.293)$$

If the thickness  $t$  of section is negligible compared with  $h$ , equation (6.293) reduces to

$$\tau_{xz,v} \approx \frac{V}{2I} [(0.5h)^2 + h_1 b - z^2] \quad (6.294)$$

When the stacking sequence of the box-type beam is not symmetric, the force resultants  $N_{x,v}$  and  $N_{x,h}$  should be calculated from equation (4.44) rather than equations (6.273) and (6.275).

The interlaminar shear stress in the horizontal section is usually very small compared with that of the vertical section, which is also expressed by equation (6.268).

### EXAMPLE 6.5

The first arm of the SCARA robot in section 13.3 has the shape of a composite box-type beam. The stacking sequence  $[\pm 20]_{10s}$  was used for both the vertical and horizontal sections. The height, width, and thickness of the beam are 70 mm, 120 mm, and 5 mm, respectively. Find the effective bending stiffness and effective torsional rigidity of the beam based on the wide-beam hypothesis. The composite material has the following material properties:

$$\begin{aligned} E_1 &= 207 \text{ GPa}, & E_2 &= 13.8 \text{ GPa}, & \nu_{12} &= 0.28, \\ G_{12} &= 5.9 \text{ GPa}, & t_{\text{ply}} &= 0.125 \text{ mm} \end{aligned}$$

### Solution

The dimensions of the box-type beam are

$$h = 0.07 \text{ m}, \quad b = 0.12 \text{ m}, \quad t = 0.005 \text{ m}, \quad h_1 = (h - t)/2 = 0.0325 \text{ m}$$

For the stacking sequence  $[\pm 20]_{10s}$ , we have

$$a_{11,h} = a_{11,v} = 1.506 \times 10^{-9} \text{ m/N}$$

$$D_{11,h} = 1.726 \times 10^3 \text{ Nm}$$

$$G_{xy} = 25.59 \text{ GPa}$$

From equation (6.279b),

$$\begin{aligned} \bar{EI} &= \frac{h^3}{6a_{11,v}} + 2b \left( \frac{h_1^2}{a_{11,h}} + D_{11,h} \right) \\ &= \frac{0.07^3}{6 \times 1.506 \times 10^{-9}} + 2 \times 0.12 \times \left( \frac{0.0325^2}{1.506 \times 10^{-9}} + 1.726 \times 10^3 \right) \\ &= (3.80 \times 10^4 + 16.87 \times 10^4) \text{ Nm}^2 \\ &= 2.07 \times 10^5 \text{ Nm}^2 \end{aligned}$$

The torsional rigidity is calculated from equation (6.285):

$$\begin{aligned}\overline{G}J &= G_{xy} \frac{2b^2h^2}{b+h} t \\ &= 25.59 \times 10^9 \times \frac{2 \times 0.12^2 \times 0.07^2}{0.12 + 0.07} \times 0.005 \\ &= 9.50 \times 10^4 \text{ Nm}^2\end{aligned}$$

### 6.13 Concluding Remarks

This chapter has presented the static and dynamic behaviors such as bending, buckling, and vibration of composite laminated plates and beams (solid and box type) with different boundary conditions. The behavior of sandwich structures is also considered. The laminated plate, beam, and sandwich structure are most commonly used efficient structural members.

This chapter has also presented the behavior of composites under dynamic loadings because composite structures are vulnerable to failure under dynamic loadings. More detailed cases under dynamic loadings are treated in chapter 10.

### Problems

- 6.1. Derive equation (6.54).
- 6.2. Supplement the missing steps in deriving equation (6.55).
- 6.3. Find the lowest value of  $N_0$  in equation (6.84) when  $k = 0$  and  $a = b$ .
- 6.4. Consider a square cross-ply laminate  $[0/90]_S$  of  $0.3 \text{ m} \times 0.1 \text{ m} \times 0.0005 \text{ m}$  dimensions ( $a = 0.3 \text{ m}$ ,  $b = 0.1 \text{ m}$ , and  $h = 0.0005 \text{ m}$ ), made from high-strength carbon epoxy unidirectional plies. The laminate is simply supported all around the four sides, and is subjected to a compressive resultant laminate force  $N_x$ . Find the load-bearing capability of the laminate (i.e., the maximum value of  $N_x$ ). If necessary, use the maximum stress failure criterion. The ply thickness is 0.125 mm and the material properties are as follows:

$$\begin{aligned}E_1 &= 140 \text{ GPa}, & E_2 &= 10.0 \text{ GPa}, & G_{12} &= 5.0 \text{ GPa}, \\ \nu_{12} &= 0.3, & X' &= 1500 \text{ MPa}, & X^c &= -1200 \text{ MPa}, \\ Y' &= 50.0 \text{ MPa}, & Y^c &= -250 \text{ MPa}, & S &= 70 \text{ MPa}\end{aligned}$$

- 6.5. Find the fundamental natural frequency  $\omega_{11}$  of the laminate of problem 6.4. The density of the composite material is  $1600 \text{ kg/m}^3$ .
- 6.6. The composite plate of problem 6.4 is subjected to a high-explosive bomb-blasting load. The pressure of the blast is expressed as follows:

$$p(x, y, t) = \sin \frac{\pi x}{0.3} \sin \frac{\pi y}{0.1} e^{-t} (\text{MPa})$$

where  $t$  is in seconds.

Find the transverse deflection  $w(x, y, t)$  neglecting rotary inertia.

- 6.7.** Calculate the maximum stresses in the  $0^\circ$  ply of problem 6.6 at  $t = 0.01$  s in the laminate axis.
- 6.8.** Derive equation (6.127).
- 6.9.** Explain why the both relations  $E_c h_c \ll E_f t_f$  and  $G_c h_c \gg G_f t_f$  can hold for sandwich constructions?
- 6.10.** Derive equation (6.215).
- 6.11.** Find the maximum deflection and stresses of a symmetrically laminated narrow beam of length  $l$  and width  $b$ . The beam is clamped at both ends and subjected to uniformly distributed acting downward  $p = -p_0$ .
- 6.12.** Derive the effective bending stiffness of the I-beam with narrow flanges ( $h_1 = h_2$ ) as follows:

$$\bar{EI} = \frac{h^3}{12a_{11\text{web}}} + 2b \left( \frac{h_1^2}{a_{11\text{flange}}} + \frac{1}{d_{11\text{flange}}} \right)$$

where  $b$  is the width of the flange and  $h_1$  is the distance from the midplane to the center line of the upper flange.

Also find the numerical value  $\bar{EI}$  of the composite I-beam when the stacking sequences of the flange and the web are  $[90/\pm45/0_2]_S$  and  $[90/\pm45]_S$ , respectively. The height of the web is 19.0 mm and the width of the flange is 12.5 mm. The composite material is T300/5208 with  $t_{\text{ply}} = 0.125$  mm.

- 6.13.** Verify that  $\bar{E} = \bar{Q}_{11}^{[\theta]} = \bar{Q}_{11}^{[-\theta]}$  for the wide beams composed of angle plies with a stacking sequence  $[\pm\theta]_{ns}$ .
- 6.14.** Derive equation (6.264).
- 6.15.** The second arm of the SCARA robot in section 13.3 has the shape of a composite box-type beam. The stacking sequence  $[\pm10]_{10S}$  was used for both the vertical and horizontal sections. The height, width, and thickness of the beam are 70 mm, 90 mm, and 5 mm, respectively. Find the effective bending stiffness and in-plane shear modulus  $G_{xy}$  of the beam based on the wide-beam hypothesis. The composite material has the following material properties:

$$E_1 = 207 \text{ GPa}, \quad E_2 = 13.8 \text{ GPa}, \quad \nu_{12} = 0.28,$$

$$G_{12} = 5.9 \text{ GPa}, \quad t_{\text{ply}} = 0.125 \text{ mm}$$

- 6.16.** The forearm of the anthropomorphic robot in section 13.4 has the shape of a composite box-type beam. The stacking sequence is  $[\pm15]_{10S}$ . The height, width, and thickness of the beam are 100 mm, 100 mm, and 5 mm, respectively. Find the effective bending stiffness. The composite material has the following material properties:

$$E_1 = 207 \text{ GPa}, \quad E_2 = 13.8 \text{ GPa}, \quad \nu_{12} = 0.28,$$

$$G_{12} = 5.9 \text{ GPa}, \quad t_{\text{ply}} = 0.125 \text{ mm}$$

- 6.17.** Figure 6.10 shows a typical fifth-generation double-arm-type robot system used for loading and unloading of LCD (liquid crystal display) glass panels into a storing cassette. This robot is discussed in full detail in section 13.2. The double-arm-type robot structure is composed of a base, two arms, two wrists, and two hands. The two hands are mounted on the two wrists. One wrist has a C-shape and the other has a flat plate shape to avoid interference between the upper and the lower glass panels when moving.

The glass panel size and its approximate weight are 1250 mm  $\times$  1100 mm  $\times$  0.7 mm and 27 N, respectively. The cross-section of the hand should be less

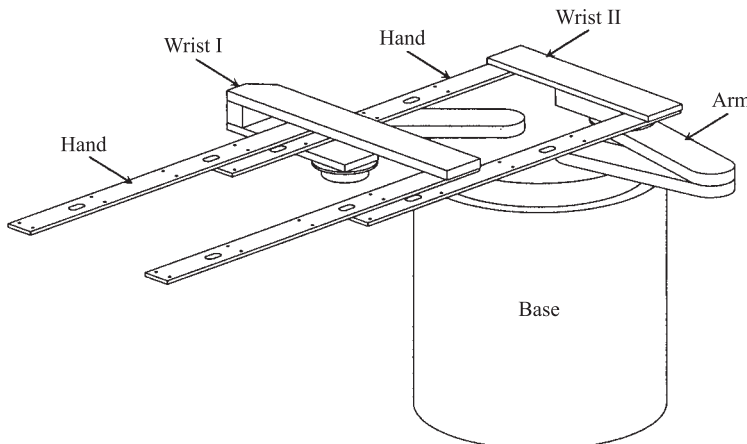


**Figure 6.10** Typical double-arm-type robot system used for loading and unloading glass panels into a cassette.

than 100 mm by 15 mm and the length of the hand is 1400 mm. The maximum deflection of the hand should be less than 2.0 mm when the side of the loaded glass panel is coincident to the end of the hand. Design the lightest composite hand as a sandwich structural form using the high-modulus pitch-based carbon-fiber epoxy composite (URN 300), whose properties are listed in table 13.3.

### References

- Craig, R. R., Jr. 1981. *Structural Dynamics*, John Wiley & Sons, New York.
- Gere, J. M. 2001. *Mechanics of Materials*, 5th edition, Brooks/Cole, Pacific Grove, Calif.
- Koenigsberger, F. 1964. *Design Principles of Metal-Cutting Machine Tools*, The Macmillan Company, New York.
- Mindlin, R. D. 1951. "Influence of Rotary Inertia and Shear on Flexural Motions of Isotropic, Elastic Plates," *Journal of Applied Mechanics*, Vol. 18, pp. 336–343.
- Rao, S. S. 2004. *Mechanical Vibrations*, 4th edition, Pearson Education, Inc., Upper Saddle River, N. J.
- Reddy, J. N. 1997. *Mechanics of Laminated Composite Plates, Theory and Analysis*, CRC Press, Boca Raton.
- Reissner, E. 1945. "The Effects of Transverse Shear Deformation on the Bending of Elastic Plates," *Journal of Applied Mechanics*, Vol. 12, pp. 67–77.
- Swanson, S. R. 1997. *Advanced Composite Materials*, Prentice-Hall, Upper Saddle River, NJ, Chapter 6.
- Vinson, J. R. 1999. *The Behavior of Sandwich Structures of Isotropic and Composite Materials*, Technomic Publishing, New York.
- Vinson, J. R. and Sierakowski, R. L. 1987. *The Behavior of Structures Composed of Composite Materials*, Martinus Nijhoff Publishers, Dordrecht.
- Whitney, J. M. 1987. *Structural Analysis of Laminated Anisotropic Plates*, Technomic Publishing, New York.
- Zenkert, D. 1995. *An Introduction to Sandwich Construction*, Emas Publishing, London.
- Zenkert, D. 1997. *The Handbook of Sandwich Construction*, Engineering Materials Advisory Services, London.

**7**

# Micromechanics for Composite Materials

## 7.1 Introduction

In previous chapters, were treated the behaviors of composite materials macroscopically, assuming that the materials are homogeneous and the effects of the constituent materials appear only as average apparent properties of composite materials. However, the behavior of composite materials is dependent on their micromechanical status in which the stresses in the fiber and matrix vary from point to point within each constituent phase.

In this chapter, composite material properties such as elastic modulus and hygrothermal expansion coefficient of unidirectional composites will be predicted from the properties and volume fraction of the constituents.

The prediction of strength is difficult, because it is a function of local defects. Therefore, the presentation of strength is limited to specific composite materials under specific failure modes. Since the strength of composite materials has to be treated statistically, the statistical approach to estimating the strength of composite materials is briefly introduced.

It may be better to start this chapter with a simple physical insight to what happens to modulus, strength, and toughness before going into these mathematical models. We have the danger of forgetting about physics. Those models that cannot predict the real behavior are not very useful.

We start out with examples as follows:

### EXAMPLE 7.1

During the development of the structure of a SCARA-type direct-drive robot for assembling PCBs (printed circuit boards) with carbon-fiber epoxy composite materials, which is treated extensively in chapter 13, a professor in robotics suggested the use of a carbon-fiber belt composed of bundle of fibers. The belt transmits the torque of a motor located on the robot base through a pulley. The direct-drive motor does not use gear transmission due to the backlash of gears, but the motors are mounted directly on the joints of arms or located on the robot base when the motor is too heavy to be mounted directly on the arms. A carbon-fiber belt was suggested because the high-modulus carbon-fiber has very high stiffness and strength, both of which are more than twice those of commercial stainless-steel belts. His idea was that the extension of the carbon-fiber belt would

be less than that of the commercial stainless-steel belt, which would increase both the accuracy and the fundamental natural frequency of robot arms. Do you think that the suggested idea was practical?

### Solution

The suggested idea cannot be implemented currently because even the best-quality carbon fibers produced have some flaws or defects along the length, for example, one flaw through a 0.1 m length. Since commercial carbon fibers normally have diameter of  $7 \mu\text{m}$ , the aspect ratio without defect may be on the order of  $10^4$ , in this situation. If the carbon-fiber belt is composed of  $10^5$  fibers, the cross-sectional area of the fiber bundle is about  $3.8 \text{ mm}^2$ . If the length of carbon-fiber belt is 0.1 m and subjected a moderate tensile load, every fiber is vulnerable to fail somewhere along the fiber length due to the brittle nature of carbon fibers. Therefore, the neat carbon-fiber belt is currently not practical.

### EXAMPLE 7.2

Although the above fact was explained, the professor in robotics was not persuaded. Therefore, the carbon-fiber bundles, of probably about  $10^5$  fibers, were broken easily by exerting a moderate tensile force before the professor. Then the professor asked why the carbon-fiber epoxy composite had such high strength, as well as high stiffness, although the neat carbon fibers were so brittle; this can be explained by the load transfer mechanism of matrix material. The matrix transmits the load from the broken fiber to the surrounding unbroken fibers, which is one of the main topics of this chapter. Since all the fibers do not break at the same distance along the fiber length, the carbon-fiber composite has high strength, although some fibers are broken somewhere along the fiber length. Then the professor suggested a belt made of carbon-fiber epoxy composite rather than the neat carbon fibers. Do you think that this new idea was practical?

### Solution

This idea was also impractical, because the bending stiffness of the composite belt becomes very high when the high-modulus carbon fibers are fixed from the neutral axis in space by an epoxy matrix because the fibers cannot change their positions from the neutral plane of the belt, which was possible for the bare fibers without a binding matrix. It might have the same low bending stiffness as stainless steel if the thickness of the composite belt was decreased, which decreases also the load transmission capability of the belt. The carbon-fiber epoxy belt might reduce some inertia, compared with the stainless-steel belt, but this is only marginal compared with other robot structures.

Examples 7.1 and 7.2 will be clear if we learn about the materials presented in this chapter.

## 7.2 Probability Distributions

Most observable phenomena in the world cannot be predicted with certainty (Haldar and Mahadevan, 2000). In general, repeated measurements of physical phenomena

generate multiple outcomes. Among these multiple outcomes, some outcomes are more frequent than others. The occurrence of multiple outcomes without any pattern is described by terms such as uncertainty, randomness, and stochasticity. For example, if several identical specimens of a steel bar were loaded until failure in a laboratory, each specimen would fail at different values of the load. The load capacity of the bar is therefore a random quantity, formally known as a random variable. In general, all the parameters of interest in engineering analysis and design have some degree of uncertainty and thus may be considered to be random variables. A random variable is usually denoted by boldface (e.g.,  $X$ ). For example, a variable exhibiting a normal distribution is expressed as  $N(\mu, \sigma)$  where  $\mu$  is a number representing the distribution mean and  $\sigma$  is the standard deviation. The coefficient of variation, abbreviated  $Cov.$  of  $X$  is  $C_x$ , which is the ratio of the standard deviation to the mean,

$$C_x = \sigma_x / \mu_x \quad (7.1)$$

Then the random variable  $X$  may be represented as

$$X = N(\mu_x, \sigma_x) = \mu_x N(1, C_x) \quad (7.2)$$

read as “ $X$  is a normally distributed variable with a mean  $\mu_x$  and a standard deviation  $\sigma_x$ ” (Shigley et al., 2004).

If data are drawn from a population with a mean  $\mu_x$ , the best estimate of  $\mu_x$  is  $\bar{x}$ , given by

$$\bar{x} = \frac{1}{N} \sum x_i \quad (7.3)$$

The sample standard deviation  $s$ , the best estimate of  $\sigma$ , is given by

$$s = \sqrt{\frac{\sum (x_i - \bar{x})^2}{N - 1}} = \sqrt{\frac{\sum x_i^2 - (\sum x_i)^2/N}{N - 1}} \quad (7.4)$$

If the data are grouped as in figure 7.1, and  $f_i$  and  $n$  are the class frequency and number of classes, respectively, then

$$\bar{x} = \frac{1}{N} \sum_{i=1}^n f_i x_i \quad (7.5)$$

where  $x_i$  is the class midpoint.

The sample standard deviation is

$$s = \sqrt{\frac{\sum_{i=1}^n f_i (x_i - \bar{x})^2}{N - 1}} = \sqrt{\frac{\sum f_i x_i^2 - (\sum f_i x_i)^2/N}{N - 1}} \quad (7.6)$$

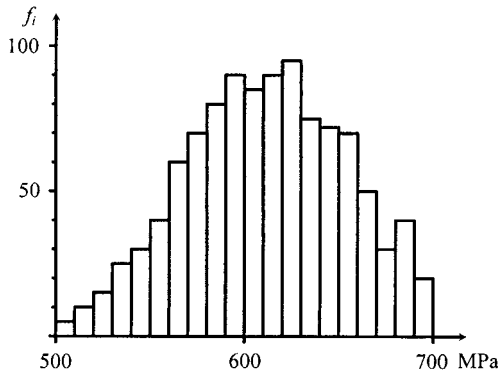


**Figure 7.1** Histogram of tensile properties of hot-rolled 1035 steel (specimen number: 1000).

The histographic display indicates the distribution's shape. A considerable amount of judgment is necessary to plot a meaningful histogram. An empirical relationship can be used for this purpose (Sturges, 1926):

$$n = 1 + 3.3 \log_{10} N \quad (7.7)$$

where  $n$  is the number of intervals and  $N$  is the number of samples. For example, with 1000 observations, equation (7.7) suggests that

$$n = 10.9 \approx 11$$

If the number of observations of a histogram increases without upper bound, and the class interval approaches zero, the limiting shape can be represented as a functional form. The probability that an observation of  $X$  lies between  $x$  and  $x + \Delta x$ , per unit of  $x$ , is given by  $f_i/(N\Delta x)$  with the number of occurrences  $f_i$ . If the limit of  $f_i/(N\Delta x)$  exists as a function  $f(x)$ , then the cumulative distribution function (CDF),  $F(x)$ , is

$$F(x) = \int_{-\infty}^x f(x) dx \quad (7.8)$$

When  $x \rightarrow \infty$ , then

$$\int_{-\infty}^{\infty} f(x) dx = 1 \quad (7.9)$$

The function  $f(x)$  is called the probability density function (PDF) of  $x$ . Differentiating the CDF of  $x$  with respect to  $x$  gives

$$\frac{dF(x)}{dx} = f(x) \quad (7.10)$$

This shows that the density function  $f(x)$  is the slope of the CDF at  $x$ . The histographic counterpart is

$$F_i = \frac{f_i w_i}{2} + \sum_{j=1}^{i-1} f_j w_j \quad (7.11)$$

where  $w_i$  is the width of the  $i$ th class.

### 7.2.1 Gaussian (Normal) Distribution

One of the most commonly used distributions in engineering problems is the normal or Gaussian distribution. The PDF of the normal distribution is

$$f(x) = \frac{1}{\sigma_x \sqrt{2\pi}} \exp\left[-\frac{1}{2}\left(\frac{x - \mu_x}{\sigma_x}\right)^2\right], \quad -\infty < x < \infty \quad (7.12)$$

The corresponding CDF is expressed as

$$F(x) = \int_{-\infty}^x \frac{1}{\sigma_x \sqrt{2\pi}} \exp\left[-\frac{1}{2}\left(\frac{x - \mu_x}{\sigma_x}\right)^2\right] dx \quad (7.13)$$

Integration of equation (7.13) requires numerical methods. Equation (7.13) can be transformed from the original random variable  $X$  into a standard normal variable with zero mean and unit standard deviation, as

$$z = \frac{x - \mu_x}{\sigma_x} \quad (7.14)$$

Then equation (7.13) is expressed as

$$F(x) = \int_{-\infty}^z \frac{1}{\sqrt{2\pi}} \exp\left(-\frac{z^2}{2}\right) dz = \Phi(z) \quad (7.15)$$

The numerical results  $\Phi(z)$  can be found in design books, such as Shigley et al. (2004), or other statistics textbooks (Devore, 2000).

### 7.2.2 Weibull Distribution

A random variable  $X$  is said to have a two-parameter Weibull distribution with parameters  $a$  and  $b$  ( $a > 0, b > 0$ ), which is expressed as  $W(x; a, b)$  if the probability density function of  $X$  is

$$f(x; a, b) = \begin{cases} \frac{a}{b^a} x^{a-1} \exp\left[-\left(\frac{x}{b}\right)^a\right], & x \geq 0 \\ 0, & x < 0 \end{cases} \quad (7.16)$$

where

$a$  = shape parameter

$b$  = scale parameter

The Weibull distribution contains within it an excellent approximation to the normal, and it displays the exponential distribution exactly when  $a=1$ . In many applications, the Weibull distribution provides a good fit to observed data for particular values of  $a$  and  $b$ . Both  $a$  and  $b$  can be varied to obtain a number of different distributional shapes, as illustrated in figure 7.2.

The CDF of a Weibull random variable having parameters  $a$  and  $b$  is expressed as

$$F(x; a, b) = \int_0^x f(x; a, b) dx = \begin{cases} 1 - \exp\left[-\left(\frac{x}{b}\right)^a\right], & x \geq 0 \\ 0, & x < 0 \end{cases} \quad (7.17)$$

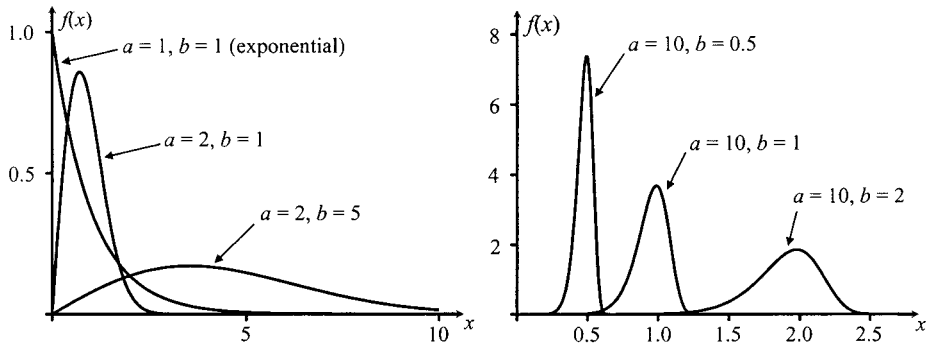


Figure 7.2 Weibull probability density function.

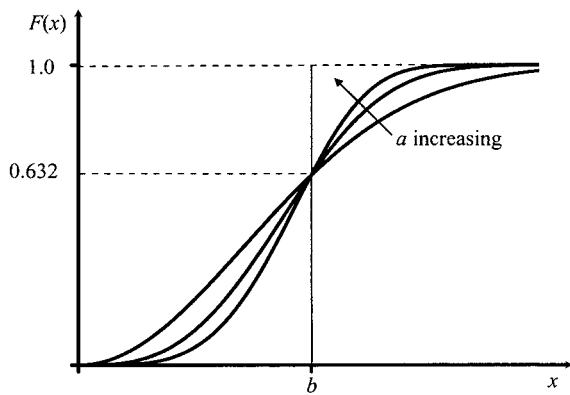


Figure 7.3 Cumulative distribution function  $F(x; a, b)$  of Weibull random variable with respect to  $a$ .

Figure 7.3 shows the shape change of  $F(x; a, b)$  with respect to the shape parameter  $a$ .

If  $F(x; a, b)$  represents the CDF of failure of some parts; there is no failure until  $x = b$  when  $a$  is very large, then all the parts fail beyond  $x = b$ . Therefore,  $a$  is called the shape parameter and  $b$  is sometimes called the location parameter. The CDF for survival is represented by

$$G(x; a, b) = 1 - F(x; a, b) = \exp\left[-\left(\frac{x}{b}\right)^a\right] \quad (7.18)$$

$G(x, a, b)$  is sometimes called the liability,  $R$ .

The mean value  $\mu_x$ , standard deviation  $\sigma_x$ , and coefficient of variation  $C_x$  of the Weibull random variable  $X$  are expressed as

$$\mu_x = b\Gamma\left(1 + \frac{1}{a}\right) \quad (7.19)$$

$$\sigma_x^2 = b^2 \left\{ \Gamma\left(1 + \frac{2}{a}\right) - \left[ \Gamma\left(1 + \frac{1}{a}\right) \right]^2 \right\} \quad (7.20)$$

$$C_x = \frac{\sigma_x}{\mu_x} \approx \frac{1.2}{a} \quad (7.21)$$

where  $\Gamma$  represents the gamma function in mathematics.

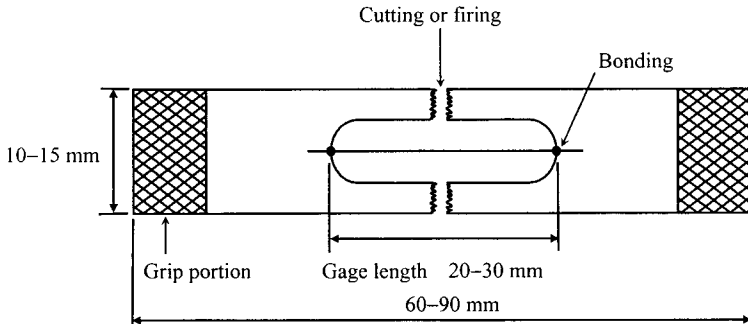


**Figure 7.4** Single filament test specimen (ASTM D3379-75).

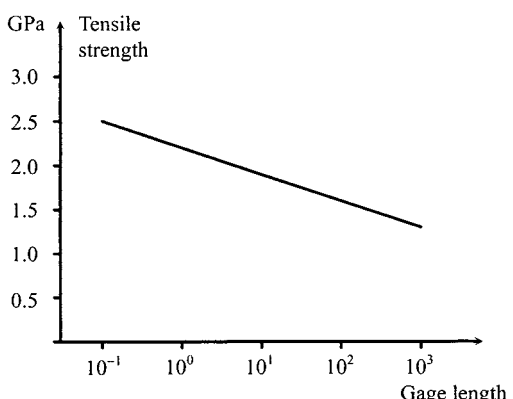


**Figure 7.5** Typical tensile strength of single carbon filament with respect to gage length.

The maximum value of  $f(x; a, b)$  occurs at  $df(x; a, b)/dx = 0$ , which is expressed as

$$x = b \left( \frac{a-1}{a} \right)^{\frac{1}{a}}, \quad a \geq 1 \quad (7.22)$$

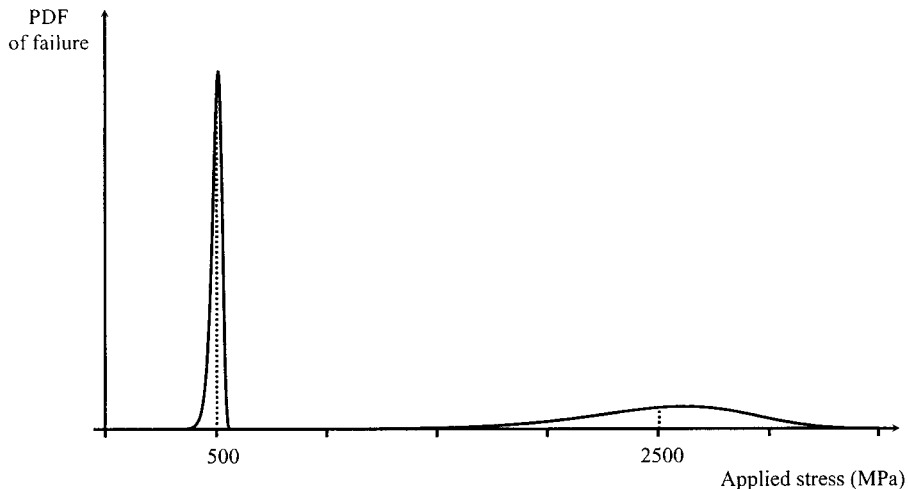
Let us consider the measurement of properties of single fibers as an application example of the Weibull distribution. The tensile strength and Young's modulus of reinforcing fibers under static longitudinal loading may be determined by the ASTM D 3379-75 standard test method for single-filament materials, as shown in figure 7.4.

The fiber specimen is adhesively bonded to a thin paper, compliant metal, or plastic backing strip, which has a central longitudinal slot of fixed gage length. Once the specimen is clamped in the grips of the tensile testing machine, the backing strip is burned or cut away, so that the filament transmits all the applied tensile load. The specimen is pulled to failure, the load and elongation are recorded, and the tensile strength and modulus are calculated. For the accurate measurement of modulus, the system compliance should be subtracted. The system compliance can be determined by testing specimens of different gage lengths, plotting the compliance versus gage length, and extrapolating the curves to zero gage length (Gibson, 1994). The measured tensile strengths of a single filament are usually dependent on the gage length, as shown in figure 7.5.

The tensile strength of the single filament decreases as the gage length of the filament increases because a longer filament will have more probability of a defect

**Table 7.1 Properties of Steel and Single Carbon Fiber**

Material	Average tensile strength (MPa)	Shape parameter <i>a</i>	COV <i>C<sub>x</sub></i> (%)
Carbon fiber	2500	6–8	15–20
Mild steel	500	25–50	3–5

**Figure 7.6** Probability density function of failure of mild steel and single carbon fiber.

along its length than short filament. It has been found that the tensile strength of figure 7.5 may be expressed as a Weibull probability distribution with the scale parameter

$$b = \left( \frac{1}{\alpha l_f} \right)^{\frac{1}{a}} \quad (7.23)$$

where  $l_f$  is the gage length of filament and  $\alpha$  is a constant determined by fiber type. If the fiber strength  $\sigma_{fu}$  is substituted for  $x$  in equation (7.16), then the probability density function of  $\sigma_{fu}$  is expressed using equation (7.23):

$$f(\sigma_{fu}) = al_f \alpha (\sigma_{fu})^{a-1} \exp(-\alpha l_f \sigma_{fu}^a) \quad (7.24)$$

The average tensile strength of the filament can be calculated from equation (7.19):

$$\bar{\sigma}_{fu} = \left( \frac{1}{\alpha l_f} \right)^{\frac{1}{a}} \Gamma \left( 1 + \frac{1}{a} \right) \quad (7.25)$$

Typical average tensile strengths and coefficients of variation (COV) of steel and single carbon-fiber are listed in table 7.1. Also the probability density functions of failure with respect to applied stress are shown in figure 7.6.

**Table 7.2 Tensile Test Result of Chopped Strand Mat Glass Fiber Polyester Composite**

<i>Class mark</i> $x$ (MPa)	<i>Number of failures</i> , $n_i$	<i>PDF</i> $f_i = n_i/Nw$	<i>CDF F</i>	$R = 1 - F$	$\ln \ln 1/R$	$\ln x$
56.5	2	0.002	0.0010	0.9990	-6.907	4.034
57.5	18	0.018	0.0110	0.9890	-4.504	4.052
58.5	23	0.023	0.0315	0.9685	-3.442	4.069
59.5	31	0.031	0.0585	0.9415	-2.809	4.086
60.5	83	0.083	0.1155	0.8845	-2.098	4.103
61.5	109	0.109	0.2115	0.7885	-1.437	4.119
62.5	138	0.138	0.3350	0.6650	-0.897	4.135
63.5	151	0.151	0.4795	0.5205	-0.426	4.151
64.5	139	0.139	0.6245	0.3755	-0.021	4.167
65.5	130	0.130	0.7590	0.2410	0.353	4.182
66.5	82	0.082	0.8650	0.1350	0.694	4.197
67.5	49	0.049	0.9305	0.0695	0.981	4.212
68.5	28	0.028	0.9690	0.0310	1.245	4.227
69.5	11	0.011	0.9885	0.0115	1.496	4.241
70.5	4	0.004	0.9960	0.0040	1.709	4.256
71.5	2	0.002	0.9990	0.0010	1.933	4.270

As shown in table 7.1, the shape parameter  $a$  of a single carbon-fiber is very low compared with that of steel. However, the shape parameter  $a$  of the single fiber becomes larger than 20 when the fibers are reinforced with a matrix. The matrix holds fibers together and transmits the applied load to other fibers if one fiber is broken. Therefore, composites of reinforcing fibers in a binding matrix are usual for load-bearing structures, rather than bare fibers.

### EXAMPLE 7.3

The results of tensile testing of 1000 chopped-strand mat polyester composites are shown in table 7.2, which was prepared from a histogram similar to figure 7.1. Assuming that the test result is of the Weibull distribution type, find two parameters of the Weibull distribution.

#### Solution

The density  $f_i$  in column 3 of table 7.2 is the number of strengths of the  $i$ th class  $n_i$  divided by the product of the sample size  $N$  and the class width  $w$ . The cumulative density function  $F$  in column 4 is the area under the histogram up to the class mark  $x$ , which is expressed as equation (7.11):

$$F_i = \frac{f_i w_i}{2} + \sum_{j=1}^{i-1} f_j w_j$$

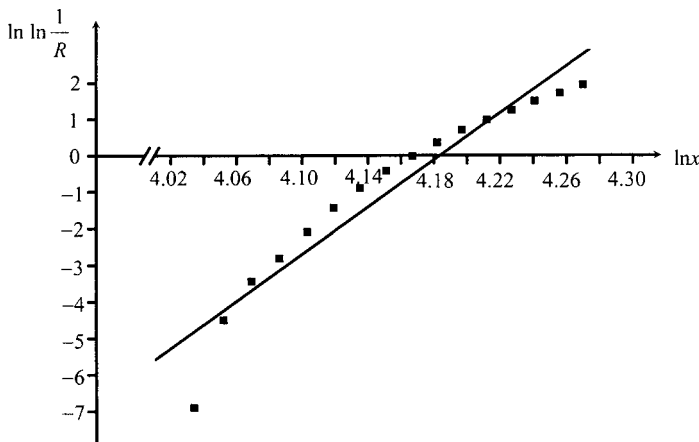


**Figure 7.7** Graph of  $\ln \ln(1/R)$  versus  $\ln x$  of example 7.3.

Columns 5, 6, and 7 are obtained next and the results are used to plot figure 7.7. From equation (7.17), we have the relationship between the values of columns of table 7.2:

$$\ln \ln \frac{1}{1-F} = \ln \ln \frac{1}{R} = a(\ln x - \ln b) \quad (7.26)$$

The value of scale parameter  $b$  in equation (7.26) can be calculated from the point of  $\ln \ln(1/R) = 0$ . When the data do not enter exactly on the line, a linear least-square method to fit a straight line to the data may be used. The value of  $\ln b = \ln x = 4.18$  from equation (7.26) when  $\ln \ln(1/R) = 0$ , from which  $b = 65.4$  MPa. The value of shape parameter  $a$  can be calculated from the slope of the fitted line. From figure 7.7, we have  $a \approx 25$ .

#### EXAMPLE 7.4

Static tensile strengths of 20 specimens made of sheet molding compound (SMC) show the following variations (in MPa):

57.54, 49.34, 68.67, 50.89, 53.20, 46.15, 71.49, 72.84, 58.10, 47.14, 67.64, 67.10, 72.95, 50.78, 63.59, 54.87, 55.96, 65.13, 47.93, 60.67

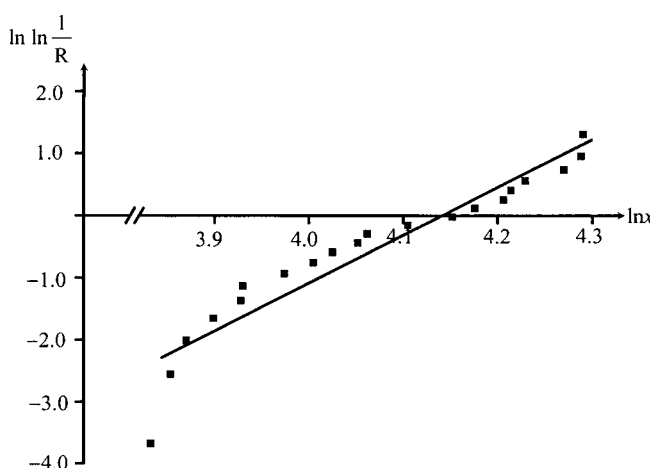
Plot the Weibull distribution curve, and determine the Weibull parameters  $a$  and  $b$  for this distribution.

#### Solution

This example is simpler than example 7.3 because the number of specimens is small and they are not classed. Starting with the smallest number, arrange the measured strength values in ascending order, as shown in table 7.3. The results of table 7.3 are plotted in figure 7.8.

**Table 7.3 Tensile Test Results of SMC of Example 7.4**

Specimen number	Strength $x$ (MPa)	PDF $f_i = n_i/N$	CDF $F$	$R = 1 - F$	$\ln \ln \frac{1}{R}$	$\ln x$
1	46.15	0.05	0.025	0.975	-3.676	3.832
2	47.14	0.05	0.075	0.925	-2.552	3.853
3	47.93	0.05	0.125	0.875	-2.013	3.870
4	49.34	0.05	0.175	0.825	-1.648	3.899
5	50.78	0.05	0.225	0.775	-1.367	3.928
6	50.89	0.05	0.275	0.725	-1.134	3.930
7	53.20	0.05	0.325	0.675	-0.934	3.974
8	54.87	0.05	0.375	0.625	-0.755	4.005
9	55.96	0.05	0.425	0.575	-0.592	4.025
10	57.54	0.05	0.475	0.525	-0.440	4.052
11	58.10	0.05	0.525	0.475	-0.295	4.062
12	60.67	0.05	0.575	0.425	-0.156	4.105
13	63.59	0.05	0.625	0.375	-0.0194	4.152
14	65.13	0.05	0.675	0.325	0.117	4.176
15	67.10	0.05	0.725	0.275	0.255	4.206
16	67.64	0.05	0.775	0.225	0.400	4.214
17	68.67	0.05	0.825	0.175	0.556	4.229
18	71.49	0.05	0.875	0.125	0.732	4.270
19	72.84	0.05	0.925	0.075	0.952	4.288
20	72.95	0.05	0.975	0.025	1.305	4.290

**Figure 7.8** Graph of  $\ln \ln(1/R)$  versus  $\ln x$  of example 7.4.

From figure 7.8, the line intercepts the  $\ln x$ -axis at the value of 4.13. Therefore,  $b = e^{4.13} = 62.18 \text{ MPa}$ . The slope of the line of figure 7.8 is 6.76, from which we obtain  $a = 6.76$ .

### EXAMPLE 7.5

A brake pad made from a new composite material is tested in cars that are driven in city traffic. The random variable  $X$ , which measures the mileage (in  $10^4 \text{ km}$  units) that the cars can be driven before the brake pads wear out, has a Weibull distribution with parameters  $a = 3.5$  and  $b = 8.33$ .

- (a) What is the median car mileage?
- (b) What is the probability that a set of brake pads lasts longer than  $10^5 \text{ km}$ ?

#### Solution

$$(a) F(x; a, b) = 1 - \exp\left[-\left(\frac{x}{8.33}\right)^{3.5}\right] = 0.5$$

Which can be solved to give  $x = 7.5$ . Consequently, it should be expected that about half the brake pads will last longer than  $7.5 \times 10^4 \text{ km}$ .

(b) The cumulative distribution function for survival that a set of brake pads lasts longer than  $10^5 \text{ km}$  is

$$G(x \geq 10) = 1 - F(10) = \exp\left[-\left(\frac{10}{8.33}\right)^{3.5}\right] = 0.15$$

## 7.3 Load Transfer between Fibers

When one fiber in a composite material is broken, the other adjacent fibers bear the load on the broken fiber. This load is transmitted through the matrix. The topic of load transfer from the matrix to the fiber has been treated by a number of researchers (Cox, 1952; Kelly and Tyson, 1965).

### 7.3.1 Cox Model

Let us concentrate on the case that a high-modulus fiber is embedded in a low-modulus matrix. Figure 7.9(a) shows the shape of a representative volume element (RVE) with a short fiber in a matrix prior to the application of an external load. We assume that the fiber and matrix are perfectly bonded and that the Poisson's ratios of the two are the same. Imaginary vertical grid lines are drawn to depict the deformation shape before and after the application of load in figure 7.9. If the load is applied axially to this RVE, the fiber and matrix experience locally different axial displacements, as shown in figure 7.9(b), because of the different elastic moduli of the components. As shown by the grid lines before and after deformation, the stiffness mismatch between fiber and matrix leads to large shear deformations near the fiber ends but no shear deformation at the middle of the fiber. The stress transfer between matrix and fiber occurs primarily through interfacial shear, which is

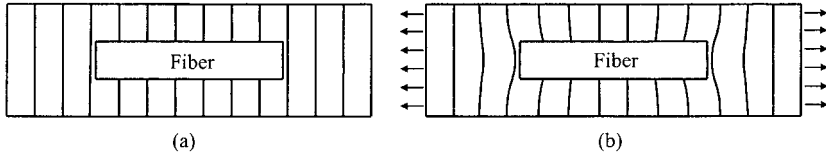


**Figure 7.9** Schematic representation of matrix shear deformation of a composite composed of high modulus fiber and low modulus matrix: (a) Before deformation; (b) after deformation.

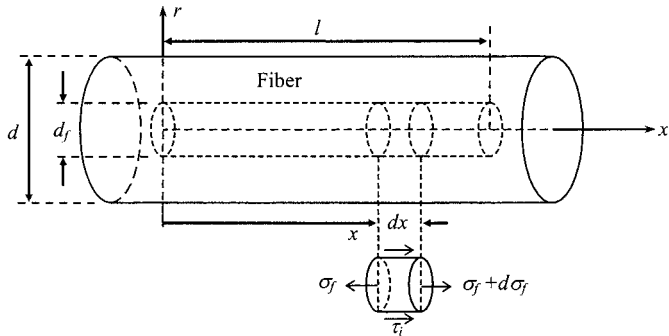


**Figure 7.10** Differential RVE of the fiber in Figure 7.9.

the greatest near the fiber ends. On the other hand, the normal stress in the fiber builds from a minimum at the ends to a maximum at the middle of the fiber (Cox, 1952).

For a differential element of the fiber from the RVE, as shown in figure 7.10, the static equilibrium of the forces along the  $x$ -direction is

$$(\sigma_f + d\sigma_f) \frac{\pi d_f^2}{4} - \sigma_f \frac{\pi d_f^2}{4} + \tau_i (\pi d_f) dx = 0 \quad (7.27)$$

where  $\sigma_f$  and  $\tau_i$  are the fiber normal stress along the  $x$ -direction and the fiber interfacial shear stress at a distance  $x$  from the end of fiber, respectively, and  $d$  and  $d_f$  are the diameters of RVE and fiber, respectively. Canceling and simplifying equation (7.27), we obtain

$$\frac{d\sigma_f}{dx} = -\frac{4\tau_i}{d_f} \quad (7.28)$$

Considering the equilibrium of forces acting on the matrix volume between  $d_f = 2r_f$  and  $d = 2r$  of figure 7.10 and neglecting normal stress in the matrix, we have

$$\pi d \tau = \pi d_f \tau_i \quad (7.29)$$

or

$$\tau = \frac{r_f}{r} \tau_i \quad (7.30)$$

The strain field around the fiber can be defined in terms of the displacement  $u_m$  of the matrix in the  $x$ -direction, relative to the position for no applied stress, as shown in figure 7.9(a). The increment of this displacement,  $du_m$ , on moving out from the fiber axis by  $dr$ , is determined by the shear strain,  $\gamma$ , and hence by the shear modulus,  $G_m$ :

$$\frac{du_m}{dr} = \gamma = \frac{\tau}{G_m} = \frac{r_f \tau_i}{r G_m} \quad (7.31)$$

where  $r$  and  $r_f$  are the radii of the RVE and the fiber, respectively. For any given value of  $x$ , the difference between the displacement of the matrix at the radius  $r$  and that of the interface at  $r_f$  is given by a simple integration:

$$u_m(r) - u(r_f) = \frac{r_f \tau_i}{G_m} \int_{r_f}^r \frac{dr}{r} = \frac{r_f \tau_i}{G_m} \ln\left(\frac{r}{r_f}\right) = \frac{d_f \tau_i}{2G_m} \ln\left(\frac{d}{d_f}\right) \quad (7.32)$$

The matrix strain is assumed to be uniform at the remote radius from the immediate vicinity of the fiber. The radius  $r$  of the RVE represents some far-field location where this condition becomes valid. The variation of  $\tau_i$  with  $x$  is unknown *a priori*, but equation (7.28) can be used to relate it to displacements and hence to axial strains. It is assumed that there is no shear strain in the fiber and the interfacial adhesion is perfect, which makes that  $u(r_f) = u_f$  = the displacement of the fiber surface. From equation (7.32)

$$\tau_i = \frac{2G_m}{d_f \ln(d/d_f)} (u_m - u_f) \quad (7.33)$$

Then equation (7.28) becomes

$$\frac{d\sigma_f}{dx} = -\frac{8G_m}{d_f^2 \ln(d/d_f)} (u_m - u_f) \quad (7.34)$$

Differentiating equation (7.34) with respect to  $x$ , we get

$$\frac{d^2\sigma_f}{dx^2} + \frac{8G_m}{d_f^2 \ln(d/d_f)} \left( \frac{du_m}{dx} - \frac{du_f}{dx} \right) = 0 \quad (7.35)$$

For the fiber, the tensile strain may be expressed as

$$\frac{du_f}{dx} = \varepsilon_f = \frac{\sigma_f}{E_f} \quad (7.36)$$

where  $E_f$  is the Young's modulus of the fiber.

The corresponding expression for the matrix is less well defined. However, the value of  $du_m/dx$  will approximate the far-field matrix strain, at least over most of the length of the fiber, and this, in turn, is close to the overall composite strain  $e$ . Thus, we assume that

$$\frac{du_m}{dx} = e = \text{strain in the matrix away from the fiber (imposed strain)} \quad (7.37)$$

Then equation (7.35) reduces to

$$\frac{d^2\sigma_f}{dx^2} - \frac{8G_m}{d_f^2 \ln(d/d_f)} \left( \frac{\sigma_f}{E_f} - e \right) = 0 \quad (7.38)$$

Equation (7.38) can be further simplified using a parameter

$$\beta = 2 \sqrt{\frac{2G_m}{d_f^2 E_f \ln(d/d_f)}} \quad (7.39)$$

such that

$$\frac{d^2\sigma_f}{dx^2} - \beta^2 \sigma_f + \beta^2 E_f e = 0 \quad (7.40)$$

The boundary conditions for equation (7.40) are

$$\sigma_f = 0 \quad \text{at } x = 0 \quad \text{and } x = l \quad (7.41)$$

The solution of equation (7.40) with the boundary conditions of equation (7.41) is

$$\sigma_f = E_f e \left( 1 - \frac{\cosh \beta(0.5l - x)}{\cosh(0.5\beta l)} \right) \quad (7.42)$$

The maximum possible value of strain in the fiber is the imposed strain  $e$ , and thus the maximum stress is  $eE_f$ . If we have a long-enough fiber, the stress in the fiber will increase from zero at the two ends to a maximum value,  $\sigma_{f\max} = eE_f$ . The average stress in the fiber,  $\bar{\sigma}_f$ , is

$$\bar{\sigma}_f = \frac{E_f e}{l} \int_0^l \left( 1 - \frac{\cosh \beta(0.5l - x)}{\cosh(0.5\beta l)} \right) dx = E_f e \left( 1 - \frac{\tanh(0.5\beta l)}{0.5\beta l} \right) \quad (7.43)$$

From equation (7.28), the interfacial shear stress  $\tau_i$  is

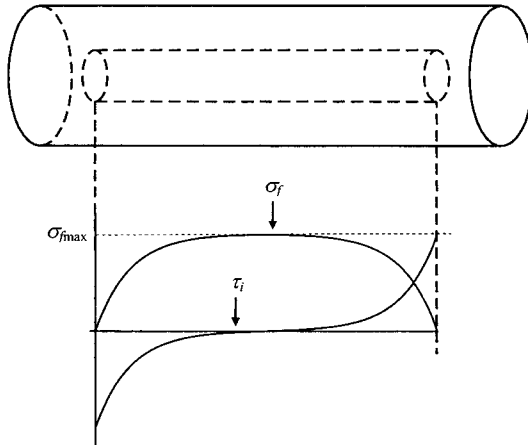
$$\tau_i = -\frac{1}{4} E_f \beta d_f e \frac{\sinh \beta(0.5l - x)}{\cosh(0.5\beta l)} \quad (7.44)$$

Figure 7.11 shows the variation of  $\tau_i$  and  $\sigma_f$  with distance  $x$ . The maximum interfacial shear stress  $\tau_i$  in equation (7.44) will be the smaller of the shear yield stress of matrix or the fiber/matrix interfacial shear strength.

The appropriate value of  $r/r_f (= d/d_f)$  in a composite containing an array of fibers is related to the proximity of neighboring fibers and hence to the fiber volume fraction  $V_f$ . The exact relationship between  $(d/d_f)$  and  $V_f$  is dependent on the way the fibers are arranged. However, because the term  $(d/d_f)$  appears in a logarithmic term, the final result is relatively insensitive to the details of the fiber arrangement.

For a hexagonal array of fibers, the volume fraction  $V_f$  is

$$V_f = \frac{\frac{\pi}{4} d_f^2}{d \left( \frac{\sqrt{3}}{2} d \right)}$$



**Figure 7.11** Schematic drawing of  $\sigma_f$  and  $\tau_i$  with respect to  $x$ .

or

$$\left(\frac{d}{d_f}\right)^2 = \frac{\pi}{2\sqrt{3}V_f} \quad (7.45)$$

Then,

$$\ln\left(\frac{d}{d_f}\right) = \frac{1}{2}\ln\left(\frac{\pi}{2\sqrt{3}V_f}\right) \quad (7.46)$$

For a *square* array of fibers, we have similarly

$$\ln\left(\frac{d}{d_f}\right) = \frac{1}{2}\ln\left(\frac{\pi}{4V_f}\right) \quad (7.47)$$

Substituting equations (7.46) and (7.47) into equation (7.39), we obtain

$$\beta = 4\left(\frac{G_m}{d_f^2 E_f \ln(\pi/2\sqrt{3}V_f)}\right)^{\frac{1}{2}} \text{ for hexagonal array} \quad (7.48)$$

$$\beta = 4\left(\frac{G_m}{d_f^2 E_f \ln(\pi/4V_f)}\right)^{\frac{1}{2}} \text{ for square array} \quad (7.49)$$

When the fiber length  $l$  without defect is larger than 0.1 mm, the stress  $\sigma_f$  in the fiber can be simplified. If the composite is carbon-fiber epoxy ( $E_f = 200$  GPa,  $G_m = 2$  GPa,  $d_f = 7$   $\mu\text{m}$ ,  $V_f = 0.6$ ), the values of  $\beta$  are

$$\beta = 8.9 \times 10^4 \text{ l/m} \quad \text{for hexagonal array}$$

$$\beta = 1.1 \times 10^5 \text{ l/m} \quad \text{for square array}$$

The approximate value of  $\beta l$  when  $l = 0.1$  mm is 10. The stress  $\sigma_f$  in the fiber from equation (7.42) is

$$\sigma_f = E_f e \left( 1 - \frac{e^{0.5\beta l} e^{-\beta x} + e^{-0.5\beta l} e^{\beta x}}{e^{0.5\beta l} + e^{-0.5\beta l}} \right) \approx E_f e (1 - e^{-\beta x} - e^{\beta(x-l)}) \quad (7.50)$$

Near the ends of fiber ( $x \ll l$ ), equation (7.50) reduces to

$$\sigma_f \approx E_f e (1 - e^{-\beta x}) \quad (7.51)$$

$$\tau_i = -\frac{d\beta e E_f}{4} e^{-\beta x} \quad (7.52)$$

The length of fiber at which the tensile stress  $\sigma_f$  reaches the value of  $0.99 e E_f$  is called the ineffective length,  $l_i$ . From equation (7.51),  $l_i$  can be expressed as

$$l_i = -\frac{1}{\beta} \ln 0.01 \approx 50 \mu\text{m} \quad (7.53)$$

When a fiber is broken, the ineffective length of both parts may be about 100  $\mu\text{m}$ , which is less than  $20d_f$ . Beyond this length, the two parts of the broken fiber sustain the full stress of the fiber. From the stress transfer mechanism of short fibers, we find that the diameter of the fiber should be small to reduce the ineffective length, hence to increase  $\beta$  in equation (7.39).

The shape parameter  $a$  of the Weibull distribution of a composite of fibers and a binding matrix is much higher than that of the naked fiber, due to the load transfer mechanism of the matrix. Table 7.4 shows typical values of shape parameter  $a$  and scale parameter  $b$  of several composite materials (Mallick, 1988).

From equilibrium of the composite for longitudinal loading, the rule of mixtures for stress for the RVE of figure 7.10 is

$$\bar{\sigma}_{c1} = \bar{\sigma}_{f1} V_f + \bar{\sigma}_{m1} V_m = \bar{\sigma}_f V_f + \bar{\sigma}_m V_m \quad (7.54)$$

Substituting equation (7.43) into equation (7.54) and dividing by  $e$ , we find the equation for the longitudinal modulus of the Cox model:

$$E_{c1} = E_f \left( 1 - \frac{\tanh(0.5\beta l)}{0.5\beta l} \right) V_f + E_m V_m \quad (7.55)$$

**Table 7.4 Weibull Parameters of Several Composite Materials**

Material	Stacking sequence	Shape parameter $a$	Scale parameter $b$ (MPa)
Boron epoxy	[0]	24.3	1300
	[90]	15.2	66.1
	[0/ $\pm 45$ /90] <sub>S</sub>	19.8	420
T300 carbon epoxy	[0 <sub>8</sub> ]	17.7	1780
	[0 <sub>16</sub> ]	18.5	1660
SMC (E-glass polyester)	SMC-R25	7.6	74.2
	SMC-R50	8.7	151

$E_f$  in equation (7.55) represents the modulus of fiber in longitudinal direction. Although the Cox model provides valuable insight into the concepts of load transfer and fiber length effects, the model does not predict accurately the stress distributions. For example, more recent results from finite element analyses and experimental photoelasticity indicate that both the magnitude and the rate of change of the interfacial shear stresses near the end of the fiber are much higher than those predicted by the Cox model (Gibson, 1994). Also, since the RVE of figure 7.10 does not include matrix material at the ends of fiber, the actual modulus values are lower than predicted by equation (7.55) (Suarez et al., 1986).

### 7.3.2 Kelly–Tyson Model

To load high-strength fibers in a ductile matrix to their maximum strength, the matrix shear strength must be large. A metallic matrix will flow plastically in response to the high shear stress developed. In metal matrix composites, assuming that the plastically deforming matrix does not work-harden, the shear stress at the fiber interface  $\tau_i$  will have an upper limit of  $\tau_y$ , the matrix shear yield strength. In polymeric matrix composites and ceramic matrix composites, frictional slip at the interface is more likely than plastic flow of the matrix. In the case of polymeric or ceramic matrix composites, the term  $\tau_i$  should replace  $\tau_y$  (Chawla, 1998).

From equation (7.28), we have

$$\int_{\sigma_0}^{\sigma_f} d\sigma_f = -\frac{4}{d} \int_0^x \tau_i dx \quad (7.56)$$

Assuming that  $\sigma_0$ , which is transferred across the ends of the fiber, is negligible, equation (7.56) becomes, when  $x \leq l/2$  (negative shear stress)

$$\sigma_f = -\frac{4}{d} \int_0^x \tau_i dx = -\frac{4}{d} \int_0^x (-\tau_y) dx = \frac{4}{d} \tau_y x \quad (7.57)$$

Equation (7.57) states that the fiber stress varies linearly with the distance from the fiber end. Since the fiber stress distribution must be symmetric at  $x = l/2$ , the fiber stress distribution  $\sigma_f$  and the corresponding shear distribution should be as shown in figure 7.12 (Kelly and Tyson, 1965).

The stress distributions in figure 7.12 are actually valid only for fibers having lengths less than “the critical length,”  $l_c$ , at which the maximum fiber stress  $\sigma_{f\max}$  reaches the fiber tensile strength,  $X'_f$ . Since the maximum fiber stress  $\sigma_{f\max}$  occurs at  $x = l/2$ , from equation (7.57),

$$\sigma_{f\max} = \frac{2\tau_y l}{d} \quad (7.58)$$

The fiber stress in a continuous fiber composite  $\sigma_{f\text{con}}$  under longitudinal composite stress  $\sigma_{c1}$  is

$$\sigma_{f\text{con}} = E_{f1} \frac{\sigma_{c1}}{E_1} \quad (7.59)$$

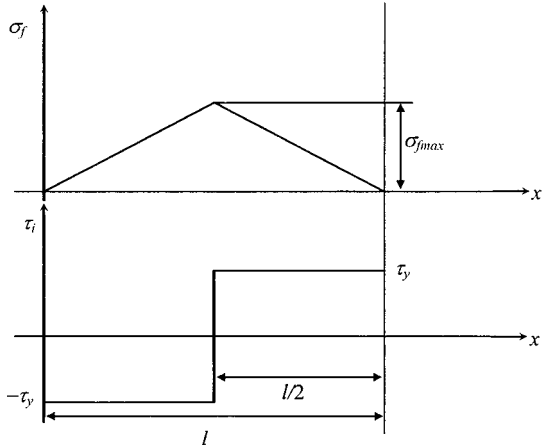


**Figure 7.12** Variation of fiber normal stress  $\sigma_f$  and interfacial shear stress  $\tau$  with distance along the fiber according to Kelly-Tyson model.

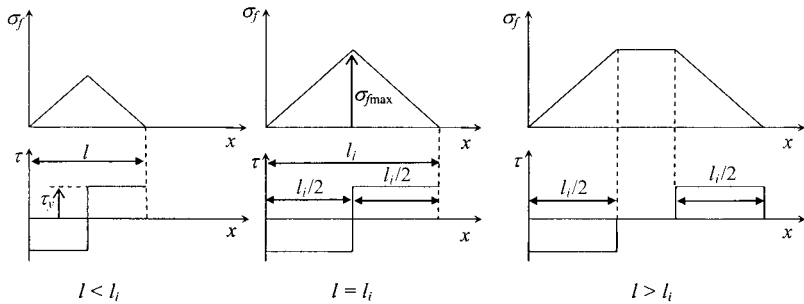


**Figure 7.13** Stress distributions versus fiber length according to Kelly-Tyson model.

The maximum fiber stress  $\sigma_{f\text{max}}$  cannot be larger than  $\sigma_{f\text{con}}$ , from which the “ineffective length”,  $l_i$ , is calculated:

$$l_i = \frac{dE_{f1}\sigma_{c1}}{2\tau_y E_1} \quad (7.60)$$

Also,  $\sigma_{f\text{con}}$  in equation (7.59) cannot be larger than the fiber tensile strength,  $X_f^t$ , from which we have the critical length  $l_c$ ,

$$l_c = \frac{dX_f^t}{2\tau_y} \quad (7.61)$$

Figure 7.13 shows the fiber stress and shear stress distributions versus fiber length.

The results of equation (7.61) were used to determine the interfacial shear strength from measurements of critical length because the interfacial shear strength  $\tau_y$  corresponding to the critical length  $l_c$  is expressed as

$$\tau_y = \frac{dX_f^t}{2l_c} \quad (7.62)$$

A specimen consisting of a single fiber embedded in a strip of translucent matrix material was mounted under a microscope and then subjected to an increasing tensile load (Drzal et al., 1982, 1983). Once the fiber stress reached  $X_f^t$ , the fiber broke up into segments that had a statistical distribution about the critical length  $l_c$  and the corresponding interfacial shear strength were calculated.

## 7.4 Strength Models

Prediction for strength of composites is more difficult than for stiffness because of the variation of strength from fiber to fiber and the random distribution of flaw sizes along each fiber. Fiber strength is not unique, but varies from one fiber to another and depends on the length over which it is measured. Therefore, the fiber strength was predicted using a statistical approach in section 7.2. Although composite materials have less statistical nature in strength than fibers due to the load transfer mechanism of the matrix, there are many limitations to the prediction of strengths of composites using micromechanics analyses due to different failure modes (fiber, matrix, or interface failure), the local nature of failure initiation, and the influence of the associated stress field, which are determined by the details of fiber packing (Matthews and Rawlings, 1994).

### 7.4.1 Longitudinal Tensile Strength

(a) When  $\varepsilon_f^t > \varepsilon_m^t$

When the tensile failure strain of a fiber,  $\varepsilon_f^t$ , is larger than the tensile failure strain of the matrix,  $\varepsilon_m^t$ , for very small fiber volume fraction  $V_f$ , the matrix cracks first under load, then complete failure of the lamina will follow if there are insufficient fibers to take the load.

Using equation (2.13), the composite longitudinal tensile strength  $X^t$  may be expressed as

$$X^t = \sigma_{fm} V_f + X_m^t (1 - V_f) \quad (7.63)$$

where  $\sigma_{fm}$  is the fiber stress at a strain corresponding to matrix failure and  $X_m^t$  is the matrix tensile strength.

At large fiber volume fraction, the fibers will take most of the load and, after matrix failure, will determine the composite strength as

$$X^t = X_f^t V_f \quad (7.64)$$

where  $X_f^t$  is the fiber tensile strength.

The crossover point between the matrix-dominated failure and the fiber-dominated failure  $V_{f\min}$  is found by equating equation (7.63) and equation (7.64):

$$V_{f\min} = \frac{X_m^t}{X_f^t - \sigma_{fm} + X_m^t} \quad (7.65)$$

For  $V_f < V_{f\min}$ , the composite strength is given by equation (7.63). For  $V_f > V_{f\min}$ , the composite strength is given by equation (7.64). For practical

composites,  $V_{f\min}$  is much smaller (typically 0.1) than the actual fiber volume fraction, so the composite longitudinal strength is given by equation (7.64).

(b) When  $\varepsilon_f^t < \varepsilon_m^t$

When the tensile failure strain of a fiber,  $\varepsilon_f^t$ , is smaller than the tensile failure strain of the matrix,  $\varepsilon_m^t$ , for very small fiber volume fraction  $V_f$ , the fibers crack first under load, then the matrix will carry the load. The composite longitudinal tensile strength  $X^t$  is given by

$$X^t = X_m^t(1 - V_f) \quad (7.66)$$

At large fiber volume fractions, once the fibers fail, the matrix cannot take the extra load and fails. For this case, the composite longitudinal tensile strength  $X^t$  is given by

$$X^t = X_f^t V_f + \sigma_{mf}(1 - V_f) \quad (7.67)$$

where  $\sigma_{mf}$  is the matrix stress at a strain corresponding to fiber failure and  $X_f^t$  is the fiber tensile strength.

The crossover point between equations (7.66) and (7.67),  $V_{f\min}$  is given by

$$V_{f\min} = \frac{X_m^t - \sigma_{mf}}{X_f^t - \sigma_{mf} + X_m^t} \quad (7.68)$$

Figure 7.14 shows the variation of composite longitudinal tensile strength  $X^t$  with respect to fiber volume fraction  $V_f$ . As shown in figure 7.14(b), if the fiber volume fraction  $V_f$  is less than the critical volume fraction  $V_{fcrit}$ , the composite longitudinal tensile strength  $X^t$  is less than the matrix tensile strength  $X_m^t$ . The critical volume fraction is expressed as

$$V_{fcrit} = \frac{X_m^t - \sigma_{mf}}{X_f^t - \sigma_{mf}} \quad (7.69)$$

Once the fibers fail in composites having  $V_f < V_{fcrit}$ , the remaining matrix can support the load up to the value

$$X^t = X_m^t(1 - V_f) \quad (7.70)$$

#### 7.4.2 Longitudinal Compressive Strength

When fiber-reinforced composites are compressed in the fiber direction, three different failure modes appear, as shown in figure 7.15 (Gibson, 1994):

- (a) Microbuckling of fibers in either shear or extensional mode
- (b) Transverse tensile rupture due to the difference of Poisson's ratio between fiber and matrix
- (c) Shear failure of fibers without buckling.

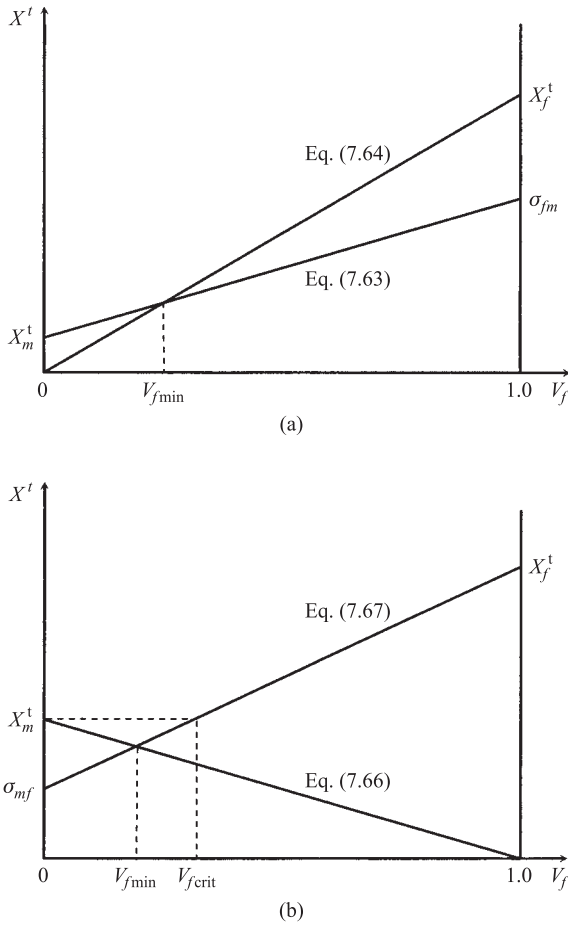


**Figure 7.14** Composite longitudinal tensile strength  $X'$  with respect to fiber volume fraction  $V_f$ :  
(a) Fiber failure strain  $\epsilon_f^t$  greater than matrix failure strain  $\epsilon_m^t$ ; (b) matrix failure strain  $\epsilon_m^t$  greater than fiber failure strain  $\epsilon_f^t$ .

### (a) Microbuckling of Fibers

Two modes of fiber buckling are possible. First, the fibers buckle out of phase relative to one another to give the “transverse” or “extensional” buckling mode in figure 7.15(a) (Jones, 1975). The mode is so named because the matrix alternatively deforms in extension and compression transverse to the fibers.

The second mode, the “shear” mode, is so named because the matrix is subjected to shearing deformation, since the fibers buckle in phase with one another antisymmetrically with respect to the line halfway between the fibers, as shown in figure 7.15(a).

In the two-dimensional models for both buckling modes, the fibers are regarded as plates of thickness  $d$  separated by a matrix of width  $2R$ , in which each fiber of length  $L$  is subjected to compressive load  $P$ . The fibers are regarded as being much stiffer than the matrix ( $G_f \gg G_m$ ) so the fiber shearing deformations are neglected.

The buckling displacement of an individual fiber in the  $y$ -direction, that is, in the transverse direction to the fibers in figure 7.15(a), may be represented by the series

$$v = \sum_{n=1}^{\infty} a_n \sin \frac{n\pi x}{L} \quad (7.71)$$

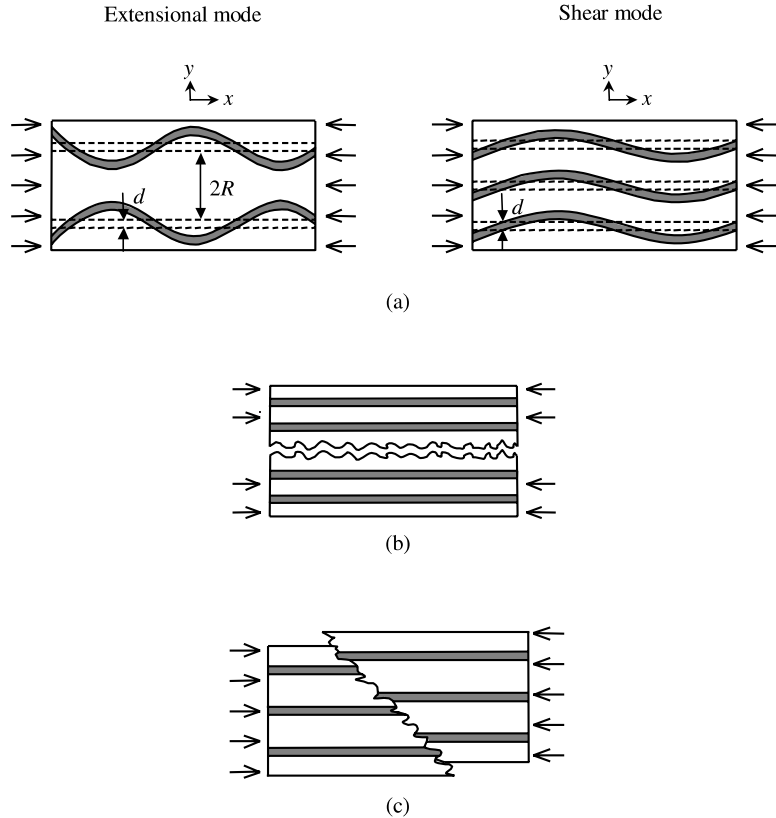


**Figure 7.15** Failure modes for longitudinal compressive loading of a unidirectional composite: (a) Fiber microbuckling; (b) transverse tensile rupture; (c) shear failure.

#### EXTENSIONAL MODE

For the transverse buckling mode in figure 7.15(a), the strain  $\varepsilon_y$  in the  $y$ -direction is

$$\varepsilon_y = \frac{2v}{2R} = \frac{1}{R} \sum_{n=1}^{\infty} a_n \sin \frac{n\pi x}{L} \quad (7.72)$$

The strain energy  $\Delta U_m$  of the matrix due to transverse strain is

$$\Delta U_m = \frac{1}{2} \int_{-R}^R \int_0^L \sigma_y \varepsilon_y dx dy \quad (7.73)$$

Assuming that the matrix behaves linearly,  $\Delta U_m$  becomes

$$\Delta U_m = \frac{E_m}{2} \int_{-R}^R \int_0^L \varepsilon_y^2 dx dy = \frac{E_m L}{2R} \sum_{n=1}^{\infty} a_n^2 \quad (7.74)$$

For the fibers, the strain energy  $\Delta U_f$  of bending (Gere, 2001) is

$$\Delta U_f = \int_0^L \frac{M^2}{2EI} dx = \frac{EI}{2} \int_0^L \left( \frac{d^2v}{dx^2} \right)^2 dx \quad (7.75)$$

$$= \frac{\pi^4 E_f d^3}{48L^3} \sum_{n=1}^{\infty} n^4 a_n^2 \quad (7.76)$$

The work done by external forces  $\Delta W$  is expressed as

$$\begin{aligned} \Delta W &= P \cdot \Delta x = P \int_0^L (ds - dx) = P \int_0^L \left( \sqrt{1 + \left( \frac{dv}{dx} \right)^2} - 1 \right) dx \\ &\approx P \int_0^L \left( \frac{dv}{dx} \right)^2 dx = \frac{P\pi^2}{4L} \sum_{n=1}^{\infty} n^2 a_n^2 \end{aligned} \quad (7.77)$$

For the two-dimensional problem, the fiber load per unit width perpendicular to the plane of figure 7.15(a) is

$$P = \sigma_f d \quad (7.78)$$

From the energy conservation law with the results of equations (7.74), (7.76), and (7.77), we have

$$\Delta U_m + \Delta U_f = \Delta W \quad (7.79)$$

The fiber buckling load  $P$  is

$$P = \left( \frac{\pi^2 E_f d^3}{12L^2} \right) \frac{\sum_{n=1}^{\infty} n^4 a_n^2 + \frac{24L^4}{\pi^4 R d^3} \frac{E_m}{E_f} \sum_{n=1}^{\infty} a_n^2}{\sum_{n=1}^{\infty} n^2 a_n^2} \quad (7.80)$$

If we assume that  $P$  has a minimum value at the  $m$ th mode, then  $\sigma_{f\text{cr}}$  is expressed as

$$\sigma_{f\text{cr}} = \frac{\pi^2 E_f d^2}{12L^2} \left( m^2 + \frac{24L^4}{\pi^4 R d^3} \frac{E_m}{E_f} \frac{1}{m^2} \right) \quad (7.81)$$

Assuming that  $\sigma_{f\text{cr}}$  is a continuous function of  $m$ , the minimum value of  $\sigma_{f\text{cr}}$  occurs at

$$m^2 = \frac{2\sqrt{6}L^2}{\pi^2 \sqrt{R d^3}} \sqrt{\frac{E_m}{E_f}} \quad (7.82)$$

The value of  $\sigma_{f\text{cr}}$  at the value of  $m$  of equation (7.82) is

$$\sigma_{f\text{cr}} = \frac{2}{\sqrt{6}} \sqrt{\frac{d}{R} E_f E_m} \quad (7.83)$$

Since the fiber volume fraction  $V_f$  in figure 7.15(a) is

$$V_f = \frac{d}{d + 2R} \quad (7.84)$$

$$\sigma_{f\text{cr}} = 2 \sqrt{\frac{V_f E_m E_f}{3(1 - V_f)}} \quad (7.85)$$

The strain of the fiber at buckling is

$$\varepsilon_{f\text{cr}} = 2 \sqrt{\frac{V_f}{3(1 - V_f)} \frac{E_m}{E_f}} \quad (7.86)$$

Assuming that the matrix has the same strain in the fiber direction as the fiber, the maximum composite stress  $X^c$  is

$$\begin{aligned} X^c &= V_f \sigma_{f\text{cr}} + (1 - V_f) \sigma_m \\ &= 2 \left[ V_f + (1 - V_f) \frac{E_m}{E_f} \right] \sqrt{\frac{V_f E_m E_f}{3(1 - V_f)}} \end{aligned} \quad (7.87)$$

For large  $E_f/E_m$ ,

$$X^c = 2V_f \sqrt{\frac{V_f E_m E_f}{3(1 - V_f)}} \quad (7.88)$$

#### SHEAR MODE

The matrix shear strain of figure 7.15(a) is expressed as

$$\gamma_{xy} = \frac{\partial v}{\partial x} + \frac{\partial u}{\partial y} \quad (7.89)$$

Since the transverse displacement of matrix is independent of the transverse coordinate  $y$ ,

$$\left. \frac{\partial v}{\partial x} \right|_{\text{matrix}} = \left. \frac{dv}{dx} \right|_{\text{matrix}} = \left. \frac{dv}{dx} \right|_{\text{fiber}} \quad (7.90)$$

the value of  $\partial u / \partial y$  can be expressed from figure 7.16:

$$\left. \frac{\partial u}{\partial y} \right|_{\text{matrix}} = \frac{1}{2R} [u(R) - u(-R)] \quad (7.91)$$

Neglecting shear deformation of the fiber,  $u(R)$  can be expressed as

$$u(R) = \left. \frac{d}{2} \frac{dv}{dx} \right|_{\text{fiber}} \quad (7.92)$$

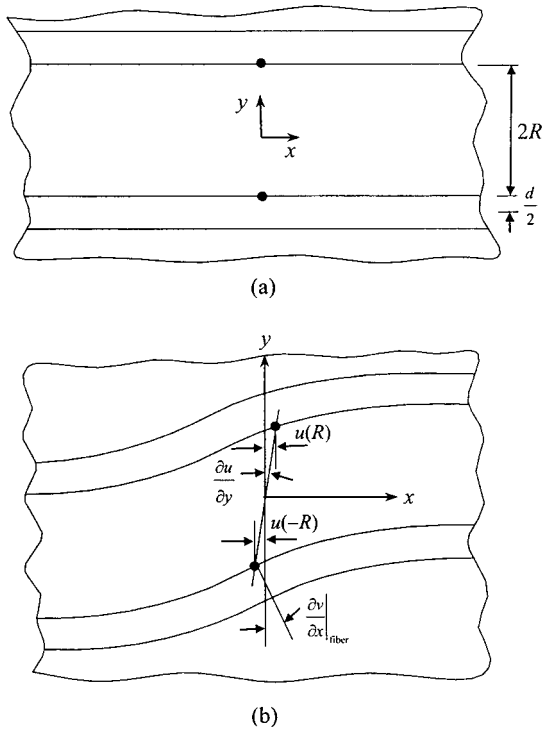


**Figure 7.16** Deformation of composite during shear buckling mode:  
(a) Before buckling; (b) after buckling.

Substituting equation (7.92) into (7.91), we obtain

$$\frac{\partial u}{\partial y} = \frac{d}{2R} \frac{dv}{dx} \Big|_{\text{fiber}} \quad (7.93)$$

Substituting equations (7.93) and (7.90) into equation (7.89), we obtain

$$\gamma_{xy} = \left( 1 + \frac{d}{2R} \right) \frac{dv}{dx} \Big|_{\text{fiber}} \quad (7.94)$$

The change in strain energy  $\Delta U_m$  of the matrix due to shear is

$$\begin{aligned} \Delta U_m &= \frac{G_m}{2} \int_{-R}^R \int_0^L \gamma_{xy}^2 dx dy \\ &= G_m R \left( 1 + \frac{d}{2R} \right)^2 \frac{\pi^2}{2L} \sum_{n=1}^{\infty} n^2 a_n^2 \end{aligned} \quad (7.95)$$

The change in strain energy of the fiber is still given by equation (7.76), and the work done is still given by equation (7.77). Therefore, using the energy conservation law,

$$\sigma_{fcr} = \frac{G_m}{V_f(1 - V_f)} + \frac{\pi^2 E_f}{12} \left( \frac{md}{L} \right)^2 \quad (7.96)$$

When the buckling wavelength  $L$  is large relative to the fiber diameter  $d$ , the second term of equation (7.96) is small. Then the fiber buckling stress is approximately

$$\sigma_{fcr} = \frac{G_m}{V_f(1 - V_f)} \quad (7.97)$$

The maximum composite stress  $X^c$  is

$$X^c = \frac{G_m}{1 - V_f} \quad (7.98)$$

and the critical strain,  $e_L^{(-)}$  of composite is

$$e_L^{(-)} = \frac{1}{V_f(1 - V_f)} \frac{G_m}{E_f} \quad (7.99)$$

When the fiber volume fraction  $V_f$  is very small, the value of  $X^c$  in equation (7.88) is smaller than that in equation (7.98). However, the shear mode whose maximum strength is expressed in equation (7.98) has the lowest strength for the composite over a wide range of practical fiber volume fractions. Therefore, for advanced composites containing a reasonably high volume fraction of fibers, the extensional mode can be neglected. These predicted values, however, are found to be considerable overestimation of compressive strength.

The shear mode of microbuckling is characterized by the formation of fiber kink bands in localized areas, as shown in figure 7.17 (Daniel and Ishai, 1994).

#### (b) Transverse Tensile Rupture

A model for transverse tensile rupture due to Poisson strains, as shown in figure 7.15(b), is based on the application of the maximum strain criterion to the tensile transverse Poisson strain under longitudinal compressive loading (Gibson, 1994).

Under the applied longitudinal stress  $\sigma_1$ , the resulting transverse Poisson strain  $\varepsilon_2$  is

$$\varepsilon_2 = -\nu_{12}\varepsilon_1 = -\nu_{12} \frac{\sigma_1}{E_1} \quad (7.100)$$

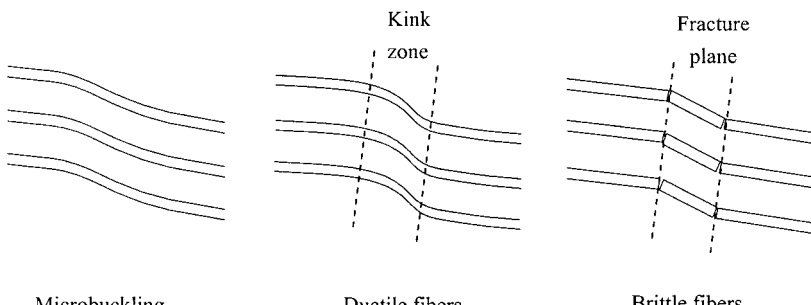


**Figure 7.17** Microbuckling leading to formation of kink zones.

When the Poisson strain  $\varepsilon_2 = e_T^{(+)}$ , the corresponding longitudinal stress is  $\sigma_1 = -X^c$ , and the compressive strength is

$$X^c = \frac{E_1 e_T^{(+)}}{\nu_{12}} \quad (7.101)$$

Equation (7.101) was reported to have better agreement with measured compressive strengths of glass-fiber epoxy composite than the microbuckling theories. A slightly higher value is predicted by a finite difference solution of the theory of elasticity model (Adams and Doner, 1967).

### (c) Shear Failure

Since the failure of fibers in direct shear due to the maximum shear stress is

$$\tau_{\max} = \frac{1}{2} X^c \quad (7.102)$$

at the angle of  $45^\circ$  to the loading axis as shown in figure 7.15(c), the compressive strength based on the assumption that the maximum shear stress is given by a rule of mixtures, is given by

$$X^c = 2(S_{f12} V_f + S_{m12} V_m) \quad (7.103)$$

where  $S_{f12}$  and  $S_{m12}$  are the shear strengths of fiber and matrix, respectively.

A number of other factors have been shown to affect longitudinal compressive strength. The fiber/matrix interfacial strength would be important in the case of transverse tensile rupture due to Poisson strains, although the fiber/matrix interfacial strength does not appear in the equations presented (Gibson, 1994). It has been reported that the compressive strength of carbon-fiber epoxy is related to the interfacial shear strength, and that fiber surface treatments, which improve the interfacial shear strength, also improve the compressive strength.

## 7.5 Halpin–Tsai Equation

Halpin and Tsai developed semiempirical equations that give satisfactory results for composite stiffnesses by adjusting curve-fitting parameters to match experimental results or elasticity results (Halpin and Tsai, 1969):

$$\frac{P}{P_m} = \frac{1 + \xi \eta V_f}{1 - \eta V_f} \quad (7.104)$$

$$\eta = \frac{P_f/P_m - 1}{P_f/P_m + \xi} \quad (7.105)$$

where  $P$  represents composite moduli ( $E_1$ ,  $E_2$ ,  $G_{12}$ ,  $G_{23}$ ), and  $P_m$  and  $P_f$  are the corresponding matrix and fiber moduli, respectively.  $V_f$  is the fiber volume fraction and  $\xi$  is an empirical factor that is used to make equation (7.104) conform to the experimental data.  $\xi$  is dependent on fiber geometry, fiber distribution, and loading conditions. When  $\xi = 0$ , equation (7.104) reduces to the inverse rule of mixtures of equations (2.20) and (2.26), whereas  $\xi = \infty$  yields the rule of mixtures of equations

(2.15) and (2.17). The difficulty in using the Halpin–Tsai equations is the determination of a suitable value of  $\xi$ . It has been suggested to use  $\xi=1$  or 2 for  $E_2$ , depending on whether a hexagonal or square array of fibers is used. At the fiber volume fraction of 0.55, it has been reported that  $\xi=1$  gives good agreement for  $G_{12}$  (Adams and Doner, 1967).

Halpin suggested a modification of the Halpin–Tsai equation for the estimation of longitudinal modulus of the aligned discontinuous fiber composite as follows:

$$\frac{E_1}{E_m} = \frac{1 + \xi \eta V_f}{1 - \eta V_f} \quad (7.106)$$

$$\eta = \frac{E_{f1}/E_m - 1}{E_{f1}/E_m + \xi} \quad (7.107)$$

with the suggested value of the curve-fitting parameter  $\xi=2l/d$ .

Halpin concluded that  $E_2$ ,  $G_{12}$ , and  $v_{12}$  are not affected much by the fiber length, hence,  $E_2$  and  $G_{12}$  can also be used for the aligned discontinuous fiber case.

## 7.6 Randomly Oriented Discontinuous Fiber Composites

When the fiber length,  $l$ , is much smaller than the thickness of the part,  $t$ , as shown in figure 7.18(a), the fiber orientation in a composite may be truly random in a three-dimensional sense, which exhibits three-dimensional isotropy.

However, parts made of short-fiber composites are usually much longer than their thickness, as shown in figure 7.18(b). In this case the material may exhibit two-dimensional or planar isotropy.

For two-dimensional isotropy, Tsai and Pagano developed the following approximate average expressions (Tsai and Pagano, 1968):

$$\tilde{E} = \frac{3}{8} E_1 + \frac{5}{8} E_2 \quad (7.108)$$

$$\tilde{G} = \frac{1}{8} E_1 + \frac{1}{4} E_2 \quad (7.109)$$

The values of  $E_1$  and  $E_2$  are estimated from the Halpin–Tsai Equations (7.106) and (7.104). Equations (7.108) and (7.109) show good agreement with experimental results (Gibson, 1994).

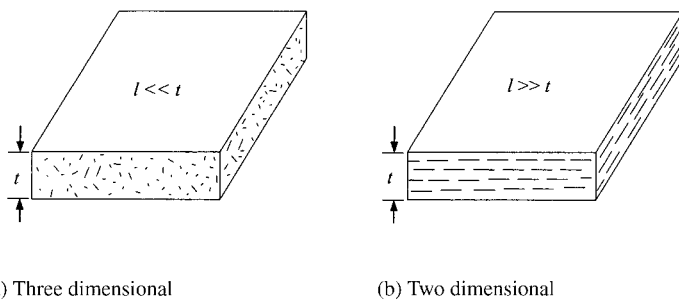


**Figure 7.18** Three dimensional and two-dimensional random orientations of fibers: (a)  $l \ll t$ , (b)  $l \gg t$ .

## 7.7 Randomly Oriented Continuous Fiber Composites

Christensen and Waals (1972) used the averaging approach to find the isotropic elastic constants for continuous fiber composites with two-dimensional and three-dimensional random fiber orientation.

They found that for the *three-dimensional* random fiber orientation:

$$\tilde{E} = \frac{[E_1 + (4v_{12}^2 + 8v_{12} + 4)K_{23}][E_1 + (4v_{12}^2 - 4v_{12} + 1)K_{23} + 6(G_{12} + G_{23})]}{3[2E_1 + (8v_{12}^2 + 12v_{12} + 7)K_{23} + 2(G_{12} + G_{23})]} \quad (7.110)$$

$$\tilde{v} = \frac{E_1 + (4v_{12}^2 + 4v_{12} + 6)K_{23} - 4(G_{12} + G_{23})}{4E_1 + (16v_{12}^2 + 24v_{12} + 14)K_{23} + 4(G_{12} + G_{23})} \quad (7.111)$$

where  $K_{23}$  is the plane strain bulk modulus for dilatation in the 2–3-plane with  $\varepsilon_{11}=0$ .

For the *two-dimensional* random fiber orientation:

$$\tilde{E} = \frac{1}{u_1} (u_1^2 - u_2^2) \quad (7.112)$$

$$\tilde{v} = \frac{u_2}{u_1} \quad (7.113)$$

where

$$u_1 = \frac{3}{8}E_1 + \frac{G_{12}}{2} + \frac{(3 + 2v_{12} + 3v_{12}^2)G_{23}K_{23}}{2(G_{23} + K_{23})} \quad (7.114)$$

$$u_2 = \frac{1}{8}E_1 - \frac{G_{12}}{2} + \frac{(1 + 6v_{12} + v_{12}^2)G_{23}K_{23}}{2(G_{23} + K_{23})} \quad (7.115)$$

## 7.8 Concluding Remarks

This chapter has presented the micromechanics of composite materials to explain the load transfer mechanism between fibers through a matrix. The load transfer mechanism between fibers has a vital role in composite properties; it governs the reliability of composite materials. This chapter has also presented several semiempirical equations for the composite stiffness to estimate it from the fiber and matrix properties, which may be used to estimate the composite stiffness when the experimental values are not available.

## Problems

- 7.1. Calculate the bending stiffness of a carbon-fiber bundle composed of  $10^5$  fibers  
 (a) without binding matrix, (b) with binding matrix filling the void between

fibers. Assume that the fibers are packed in a hexagonal close-packed array and the composite has a circular rod shape. The fiber modulus and diameter are 200 GPa and 7  $\mu\text{m}$ , respectively. Neglect the modulus of the matrix.

- 7.2. Consider the normal distributions of strength  $S \approx N(\mu_S, \sigma_S)$  and applied stress  $\sigma \approx N(\mu_\sigma, \sigma_\sigma)$ , and define a *stress margin*  $m$  such that  $m = S - \sigma$ . The margin  $m$  is normally distributed because the addition or subtraction of normals is normal. Thus,  $m \approx N(\mu_m, \sigma_m)$ . Reliability is the probability  $p$  that  $m > 0$  (Shigley 2004):

$$R = p(m > 0) = p(S - \sigma > 0) = p(m > 0)$$

To find the chance that  $m > 0$ , we form the standard normal variable  $z$  of  $m$  and substitute  $m = 0$ . Since  $\mu_m = \mu_S - \mu_\sigma$  and  $\sigma_m = (\sigma_S^2 + \sigma_\sigma^2)^{1/2}$ ,

$$z = \frac{m - \mu_m}{\sigma_m} = \frac{0 - \mu_m}{\sigma_m} = -\frac{\mu_m}{\sigma_m} = -\frac{\mu_S - \mu_\sigma}{(\sigma_S^2 + \sigma_\sigma^2)^{1/2}}$$

The reliability  $R$  associated with  $z$  is given by

$$R = \int_z^\infty \frac{1}{\sqrt{2\pi}} \exp\left(-\frac{z^2}{2}\right) dz = 1 - F = 1 - \Phi(z)$$

- (a) Find the safety factor  $\bar{n} = \mu_S/\mu_\sigma$  such that

$$\bar{n} = \frac{1 \pm \sqrt{1 - (1 - z^2 C_S^2)(1 - z^2 C_\sigma^2)}}{1 - z^2 C_S^2}$$

The plus sign is associated with  $R > 0.5$  and the minus sign with  $R < 0.5$ .

- (b) A cold-drawn 1018 steel rod has an 0.2% yield strength  $S_y \approx N(540, 40.7)$  MPa and is to be subjected to a static load of  $P \approx N(0.227, 0.0186)$  MN. What value of the design factor  $\bar{n}$  corresponds to a reliability of 0.999 against yielding ( $z = -3.09$ )? Also find the diameter of the rod.

- 7.3. The time to failure in hours of an electrical circuit subjected to a high temperature has a distribution of  $W(x; 3, 2)$  hours. Find the following:

- (a) The median failure time of a circuit.
- (b) The time that a circuit will last with 99% confidence.
- (c) Expectation and variance of the circuit failure times.
- (d) The probability that at least one circuit is working after 3 hours when a circuit has three equivalent backup circuits that have independent failure times.

- 7.4. Derive equations (7.46) and (7.47).

- 7.5. Derive equation (7.80).

- 7.6. Derive equation (7.96).

- 7.7. Prove that equation (7.104) reduces to the inverse rule of mixtures of equations (2.20) and (2.26) when  $\xi = 0$ .

- 7.8. Prove that equation (7.104) reduces to the rule of mixture equations (2.15) and (2.17) when  $\xi = \infty$ .

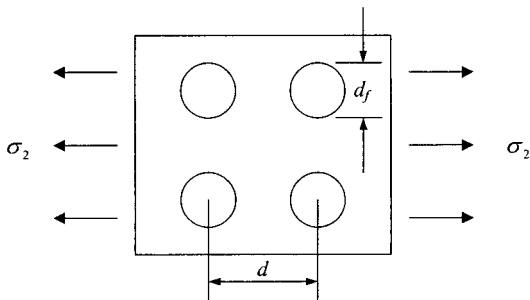


**Figure 7.19** Material model for strain concentration factor under transverse loading.

- 7.9. When the fiber volume fraction of a carbon-fiber epoxy composite is 0.6 and the tensile strengths of the fiber and the matrix are 2500 MPa and 100 MPa, respectively, estimate the longitudinal and transverse tensile strength of the composite material. The strain concentration  $K_t$  of a composite for transverse loading is

$$K_t = \frac{1}{(d_f/d)[(E_m/E_{f2}) - 1] + 1}$$

where  $d_f$  and  $d$  represent the fiber diameter and the center distance between fibers for square packing shown in figure 7.19, and  $E_m$  the modulus of matrix and  $E_{f2}$  the transverse modulus of fiber (Gibson, 1994). If linear behavior to failure can be assumed, the transverse strength is expressed as

$$Y^t = E_2 \frac{X_m^t}{E_m K_t}$$

The longitudinal modulus  $E_{f1}$  and transverse modulus  $E_{f2}$  of the fiber are 200 GPa and 15.0 GPa, respectively, and the modulus of the epoxy matrix is 3.5 GPa. Use equation (2.20) to estimate  $E_2$  of the composite.

- 7.10. A fiber has a 100  $\mu\text{m}$  diameter and its tensile strength of 2.0 GPa. When the fiber volume fraction is 0.6 and the matrix strength is 75 MPa, with a fiber/matrix interfacial strength of 50 MPa, estimate the longitudinal composite tensile strength with the assumption of a linear build-up of stress from the two ends for fibers (a) 100 mm long, and (b) 2.0 mm long.
- 7.11. Estimate the minimum interfacial shear strength  $\tau_i$ , as a percentage of the fiber tensile strength  $X_f^t$ , which is necessary to avoid interfacial failure in the composite when the fiber aspect ratio is 100.0.

## References

- Adams, D. F., and Doner, D. R. 1967. "Longitudinal Shear Loading of a Unidirectional Composites," *Journal of Composite Materials*, Vol. 1, pp. 4–17.
- Chawla, K. K. 1998. *Composite Materials*, 2nd ed. Springer, New York.
- Christensen, R. M., and Waals, F. M. 1972. "Effective Stiffness of Randomly Oriented Fiber Composites," *Journal of Composite Materials*, Vol. 6, pp. 518–532.
- Cox, H. L. 1952. "The Elasticity and Strength of Paper and Other Fibrous Materials," *British Journal of Applied Physics*, Vol. 3, pp. 72–79.
- Daniel, I. M., and Ishai, O. 1994. *Engineering Mechanics of Composite Materials*, Oxford University Press, Oxford.

- Devore, J. L. 2000. *Probability and Statistics for Engineering and Science*, Duxburg, Pacific Grove, California.
- Drzal, L. T., Rich, M. J., and Lloyd, P. F. 1982. "Adhesion of Graphite Fibers to Epoxy Matrices: I. The Role of Fiber Surface Treatment," *Journal of Adhesion*, Vol. 16, pp. 1–30.
- Drzal, L. T., Rich, M. J., Koenig, M. F., and Lloyd, P. F. 1983. "Adhesion of Graphite Fibers to Epoxy Matrices: II. The Effect of Fiber Finish," *Journal of Adhesion*, Vol. 16, pp. 133–152.
- Gere, J. M. 2001. *Mechanics of Materials*, 5th ed. Thomson Learning, Pacific Grove, California, p. 657.
- Gibson, R. F. 1994. *Principles of Composite Material Mechanics*, McGraw-Hill, New York.
- Haldar, A., and Mahadevan, S. 2000. *Probability, Reliability and Statistical Method in Engineering Design*, John Wiley & Sons, New York.
- Halpin, J. C., and Tsai, S. W. 1969. "Effect of Environmental Factors on Composite Materials," *AFML-TR-67-243*, June.
- Jones, R. M. 1975. *Mechanics of Composite Materials*, McGraw-Hill, New York.
- Kelly, A., and Tyson, W. R. 1965. "Tensile Properties of Fiber Reinforced Metals: Copper/Tungsten and Copper/Molybdenum," *Journal of the Mechanics and Physics of Solids*, Vol. 13, pp. 329–350.
- Mallick, P. K. 1988. *Fiber Reinforce Composites*, Marcel Dekker, New York.
- Matthews, F. L., and Rawlings, R. D. 1994. *Composite Materials: Engineering and Science*, Chapman & Hall, New York.
- Shigley, J. E., Mischke, C. R., and Budynas, R. G. 2004. *Mechanical Engineering Design*, 7th ed. McGraw-Hill, New York.
- Sturges, H. A. 1926. "The Choice of Class Interval," *Journal of American Statistical Association*, Vol. 21, pp. 65–66.
- Suarez, S. A., Gibson, R. F., Sun, C. T., and Chaturvedi, S. K. 1986. "The Influence of Fiber Length and Fiber Orientation on Damping and Stiffness of Polymer Composite Materials," *Experimental Mechanics*, Vol. 26, No. 2, pp. 175–184.
- Tsai, S. W., and Pagano, N. J. 1968. "Invariant Properties of Composite Materials," *Composite Materials Workshop*, Edited by Tsai, S. W., Halpin, J. C., and Pagano, N. J., Technomic Publishing, Philadelphia, pp. 233–252.

**8**

# ■ Transport Phenomena in Composite Materials

## 8.1 Introduction

The idea that materials can be *designed* to satisfy specific performance requirements is relatively new. Historically, materials were first produced by adding various alloying elements to a pool of molten materials based on phase diagrams, which were then cast and cooled at varying solidification rates to obtain desired microstructures. Next, the material was hot- and cold-worked to refine the microstructure. It was then tested to determine its properties. After the properties were determined, it was made available to customers whose need matched the properties of the material. With the accumulation of materials data and advances in materials science and engineering, the process of developing new materials has become more sophisticated. However, the old paradigm of repetitive trial-and-error is still used in the field of materials development. Therefore, it may take a long time—more than a decade—to develop a new material and have it adopted by industry.

The composites field is unique in that composites are designed to satisfy the performance requirements and then manufactured. This field has developed rapidly during the past three decades thanks to convergence of the availability materials and the need for new lightweight materials.

Among the various composite materials available, those with a polymer resin matrix are most widely used. The fabrication of polymeric matrix composites involves complex chemical and mechanical reactions. The reaction starts from monomers or oligomers and proceeds via an addition or condensation mechanism to form a three-dimensional network in the case of thermosetting resins or a high-molecular-weight thermoplastic. The reaction is relatively straightforward for the epoxy and polyester resins, but is extremely complicated for the condensation polyimide systems that evolve volatile by-products. In these reactions, heat is evolved, which governs the viscosity and flow of resin during the process. Other key parameters that must be addressed are the occurrence of voids and the characterization of fiber bed permeability and thermal conductivity.

Composites are usually subjected to changing environmental conditions during both initial fabrication and final use. Among the many environmental conditions that may influence composite mechanical behavior, changes in temperature and moisture content (or collectively hygrothermal change) are very important because they have effects on polymer materials and those properties of polymer matrix

composites that are matrix dominated, such as transverse (or off-axis) shear stiffness and strength.

From the four domains of the materials world, that is, the customer domain, the functional domain, the physical domain, and the process domain, in this chapter we concentrate on the design of processing techniques—specified by the *process variables* (PVs) in the process domain—to create the microstructure specified by design parameters (DPs) in the physical domain.

## 8.2 Resin Flow through Fiber Bed

### 8.2.1 Fiber Consolidation

Since the flow of resin in fiber bundles can be assumed to be a flow in a porous medium, it has been generally analyzed based on Darcy's law. To apply Darcy's law, the permeability and porosity of the fiber network and the viscosity of the resin must be determined. There have been several different analyses that depend on assumptions of the properties of the fiber bed and the flow field of the resin, although they are all based on Darcy's law. Among them, Dave (1990), Gutowski et al. (1987a,b), and Loos and Springer (1983) are well known. Loos and Springer (1983) assumed that the compaction of the composite was independent of pressure and it was completed sequentially from the top to the bottom surfaces of the composite material. However, the compaction in the real cure process occurs in the whole composite thickness simultaneously and the thickness of the composite is the function of the applied pressure. Dave (1990) and Gutowski et al. (1987a,b) assumed that the compaction of the fiber due to the resin outflow was the consolidation problem of the permeable material and they modeled the continuous system through the whole composite thickness. These two models had the same theoretical background and the only difference was the defined coordinate system.

Lee and Kim (1994) devised a new fiber deformation model based on the foundation model of soil mechanics. Considering an infinitely small composite representative volume element (RVE) as in figure 8.1, the resin flow in the fiber bed of the composite material may be expressed by Darcy's law:

$$u_i = -\frac{k_{ij}}{\mu} \frac{\partial p}{\partial x_j} \quad (8.1)$$

where  $u_i$  is the resin flow velocity in the  $x_i$ -direction,  $k_{ij}$  is the permeability of the fiber bed,  $p$  is the pressure in the resin, and  $\mu$  is the resin viscosity. The net resin flow

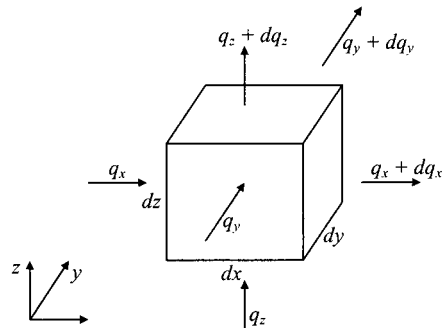


**Figure 8.1** Representative volume element (RVE) of a resin.

rate in the  $x$ -direction  $dq_x = q_x - q_{x+dx}$ , which is the difference between the resin inflow  $q_x$  and the resin outflow  $q_{x+dx}$ , is expressed by the following equation in the principal material axes:

$$dq_x = \frac{\partial}{\partial x} \left( \frac{k_{xx}}{\mu} \frac{\partial p}{\partial x} \right) dx dy dz \quad (8.2)$$

Considering the net resin flow rate in the  $x$ -,  $y$ -, and  $z$ -directions simultaneously, the total net resin flow rate  $dq = dq_x + dq_y + dq_z$  is expressed by the following equation:

$$dq = \left[ \frac{\partial}{\partial x} \left( \frac{k_{xx}}{\mu} \frac{\partial p}{\partial x} \right) + \frac{\partial}{\partial y} \left( \frac{k_{yy}}{\mu} \frac{\partial p}{\partial y} \right) + \frac{\partial}{\partial z} \left( \frac{k_{zz}}{\mu} \frac{\partial p}{\partial z} \right) \right] dx dy dz \quad (8.3)$$

If the total volume of the composite RVE is  $v$  and the fiber volume is  $v_f$ , then the void ratio  $e$ , (volume not occupied by fibers)/(volume occupied by fibers), which is widely used in soil mechanics (Bowles, 1988), is defined by the following equation:

$$e = \frac{v - v_f}{v_f} = \frac{v}{v_f} - 1 = \frac{1}{V_f} - 1 \quad (8.4)$$

where  $V_f$  is the fiber volume fraction. The void volume  $v_v = v - v_f$  from the RVE  $dxdydz$  is expressed as

$$v_v = (1 - V_f) dx dy dz = \frac{e}{1 + e} dx dy dz \quad (8.5)$$

Then the volume of resin  $v_r$  is expressed as

$$v_r = S v_v = S \frac{e}{1 + e} dx dy dz \quad (8.6)$$

where  $S$  is the degree of saturation (Bowles, 1988) defined as the percentage of the void volume that is filled with resin. The rate of change of the resin volume in the volume of the RVE is expressed by

$$\frac{\partial v_r}{\partial t} = \frac{\partial}{\partial t} \left( \frac{Se}{1 + e} dx dy dz \right) \quad (8.7)$$

Since  $dx dy dz / (1 + e)$  represents the sole fiber volume from the volume of the composite material, it can be assumed to be constant. Then, equation (8.7) reduces to

$$\frac{\partial v_r}{\partial t} = \frac{dx dy dz}{1 + e} \frac{\partial}{\partial t} (Se) \quad (8.8)$$

Combining equations (8.3) and (8.8), the following resin flow equation is obtained:

$$\frac{1}{1 + e} \frac{\partial}{\partial t} (Se) = \frac{\partial}{\partial x} \left( \frac{k_{xx}}{\mu} \frac{\partial p}{\partial x} \right) + \frac{\partial}{\partial y} \left( \frac{k_{yy}}{\mu} \frac{\partial p}{\partial y} \right) + \frac{\partial}{\partial z} \left( \frac{k_{zz}}{\mu} \frac{\partial p}{\partial z} \right) \quad (8.9)$$

Equation (8.9) can be divided into four categories based on the composite processing methods:

1. When both  $e$  and  $S$  are constant: *steady flow*.
2. When  $e$  varies, but  $S$  is constant: *consolidation* if  $e$  decreases, or *expansion* if  $e$  increases.
3. When  $e$  is constant, but  $S$  varies: *drainage* if  $S$  decreases, or *imbibition* if  $S$  increases.
4. When both  $e$  and  $S$  vary: *compression* or *expansion*.

During the processing (such as the curing operation) of the composite material, the external applied pressure  $p_{ext}(t)$  can be divided into two components;  $\sigma$ , required for the fiber deformation, and  $p(t)$ , required for the resin flow:

$$p_{ext}(t) = \sigma + p(t) \quad (8.10)$$

If we limit the processing to the consolidation of resin-impregnated fiber beds, such as vacuum bag molding of B-staged preprints, the fibers can be assumed to be thoroughly wet with resin ( $S = 1$ ). For this case, combining equations (8.9) and (8.10) results in the following equation:

$$\frac{1}{1+e} \frac{\partial e}{\partial t} = \frac{\partial}{\partial x} \left[ \frac{k_{xx}}{\mu} \frac{\partial}{\partial x} (p_{ext} - \sigma) \right] + \frac{\partial}{\partial y} \left[ \frac{k_{yy}}{\mu} \frac{\partial}{\partial y} (p_{ext} - \sigma) \right] + \frac{\partial}{\partial z} \left[ \frac{k_{zz}}{\mu} \frac{\partial}{\partial z} (p_{ext} - \sigma) \right] \quad (8.11)$$

The magnitude of stress  $\sigma$  required for the fiber deformation was modeled by Gutowski and Dillon (1997) by assuming elastic deformation of fiber bundles:

$$\sigma = \frac{3\pi E}{\beta^4} \frac{\sqrt{V_f/V_0} - 1}{(\sqrt{V_a/V_f} - 1)^4} \quad (8.12)$$

where  $V_a$  is the maximum available fiber volume fraction,  $V_0$  the initial fiber volume fraction,  $E$  the longitudinal Young's modulus of a fiber and  $\beta$  the material constant depending on the fiber bundle shape. Actually the values of  $V_a$ ,  $V_0$ , and  $\beta$  should be adjusted to fit equation (8.12) to experimental results. Using the void ratio  $e$ , equation (8.12) can be rewritten as

$$\sigma = \frac{3\pi E}{\beta^4} \frac{\sqrt{(1+e_0)/(1+e)} - 1}{\left( \sqrt{(1+e)/(1+e_{min})} - 1 \right)^4} \quad (8.13)$$

where  $e_0$  is the original (or initial) void ratio, and  $e_{min}$  is the minimum void ratio when the fiber volume fraction  $V_f$  becomes  $V_a$ . The stress  $\sigma$  in equation (8.13) becomes infinitely large as the void ratio  $e$  approaches  $e_{min}$  and becomes 0 as  $e$  approaches  $e_0$ .

Since equation (8.12) or equation (8.13) is complicated, Lee and Kim (1994) devised another fiber deformation equation based on the method of soil mechanics (Bowles, 1988) such as

$$\sigma = \sigma_0 \ln \frac{e_0 - e_{min}}{e - e_{min}} = \sigma_0 [\ln(e_0 - e_{min}) - \ln(e - e_{min})] \quad (8.14)$$

where  $\sigma_0$  is a constant determined by experiment.

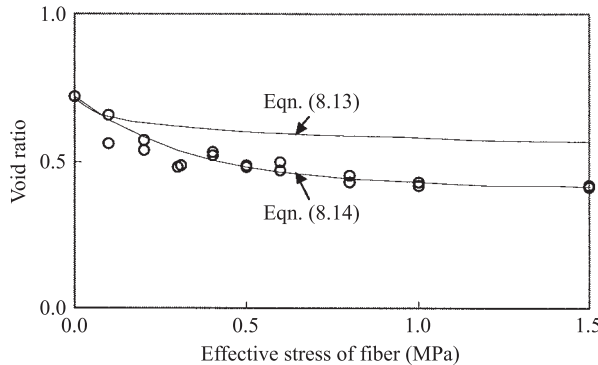


**Figure 8.2** Change of void ratio with respect to the applied fiber deformation stress.

Lee and Kim (1994) performed experiments to determine the value of  $\sigma_0$  in equation (8.14) during an autoclave vacuum bag degassing process. The prepreg used was T300/5208 with the stacking sequence [0/90]<sub>ST</sub>. The initial fiber volume fraction  $V_0$  was 0.58 ( $e_0 = 0.72$ ) and the available fiber volume fraction  $V_a$  was 0.71 ( $e_{\min} = 0.409$ ) when the applied pressure inside the autoclave was 1.5 MPa. From the experiments, the fiber volume fraction with the stacking sequence [0/90]<sub>ST</sub> was 0.6 when the fiber deformation stress was 0.06 MPa. Since the fiber volume fraction of 0.6 is the standard fiber volume fraction for aircraft industries, the two equations (8.13) and (8.14) were fitted to pass this point. The resultant equations are

$$\sigma = 2.46 \times 10^{-4} \frac{\sqrt{(1+e_0)/(1+e)} - 1}{\left(\sqrt{(1+e)/(1+e_{\min})} - 1\right)^4} \text{ (MPa)} \quad (8.13a)$$

$$\sigma = -0.34[\ln(e - 0.41) + 1.17] \text{ (MPa)} \quad (8.14a)$$

Figure 8.2 shows the experimental results for the relationship between the fiber deformation stress and the void ratio with the two fitted equations, in which Lee and Kim's model (1994) of equation (8.14) has better fitting characteristics for the experimental results.

The permeability  $k_{ij}$  in equation (8.1) has been modeled by several researchers. The simplest model is to consider the porous medium as a bundle of capillaries. In many types of fiber reinforcement, the pore geometry is very complicated on a microlevel. On the other hand, there are also simple reinforcements like unidirectional mats that can be analyzed theoretically. One of the theoretical models is the Kozeny–Carman equation (Lee, 1997), which depicts the flow along the fiber direction:

$$k_{xx} = \frac{r_f^2}{4C_x} \frac{(1 - V_f)^3}{V_f^2} \quad (8.15)$$

or, in terms of void ratio,

$$k_{xx} = \frac{r_f^2}{4C_x} \frac{e^3}{1+e} \quad (8.16)$$

where  $r_f$  is the radius of the fiber and  $C_x$  is the Kozeny–Carman constant determined by experiment. This equation is known to fit the data well, although the values of the Kozeny–Carman constant were somewhat different in various experiments.

For flow transverse to the fiber bundle, the same expression of equation (8.16) may be used by adjusting the Kozeny–Carman constant. However, the expression cannot show the stop of the flow in the transverse direction when the fiber volume fraction reaches the maximum packing efficiency. The new proposed equation (Gutowski et al., 1987b), which takes into account this effect is

$$k_{zz} = \frac{r_f^2}{4C_z} \frac{(\sqrt{V'_a/V_f} - 1)^3}{\sqrt{V'_a/V_f} + 1} \quad (8.17)$$

where  $V'_a$  is the available fiber volume fraction at which the transverse flow stops. It may not be equal to the maximum packing efficiency, since one thin layer of the aligned fibers can block the flow path, while the average fiber volume fraction may be less than the maximum packing efficiency. There are other analytical models for the calculation of permeability of aligned fabric reinforcement (Lee, 1997). If the coordinate axes chosen for the analysis are not principal material coordinates, then the permeability should be tensor-transformed according to the method in chapter 3. This method is presented in detail when treating the thermal conductivity later.

Substituting equations (8.14) and (8.16) into equation (8.11), the partial differential equation in which the void ratio is the only dependent variable when the applied pressure  $p_{ext}(t)$  is not a function of  $x_i$  is

$$\frac{1}{1+e} \frac{\partial e}{\partial t} = \frac{\partial}{\partial x_i} \left[ \frac{r_f^2 \sigma_0}{4\mu C_{xi}} \frac{e^3}{(1+e)(e-e_{min})} \frac{\partial e}{\partial x_i} \right] \quad (8.18)$$

Assuming that the composite plate is thin and wide, the flow of resin occurs only in the  $z$ -direction (vertical direction). In this case, equation (8.18) reduces to

$$\frac{1}{1+e} \frac{\partial e}{\partial t} = \frac{\partial}{\partial z} \left[ \frac{r_f^2 \sigma_0}{4\mu C_z} \frac{e^3}{(1+e)(e-e_{min})} \frac{\partial e}{\partial z} \right] \quad (8.19)$$

If the viscosity  $\mu$  is not a function of  $z$ , which is a possible assumption when the temperature is constant across the plate thickness, equation (8.19) reduces to

$$\frac{\partial e}{\partial t} = \frac{r_f^2 \sigma_0}{4\mu C_z} \left[ \frac{e^2 [e^2 + 2(1-e_{min})e - 3e_{min}]}{(1+e)(e-e_{min})^2} \left( \frac{\partial e}{\partial z} \right)^2 + \frac{e^3}{e-e_{min}} \frac{\partial^2 e}{\partial z^2} \right] \quad (8.20)$$

The initial and boundary conditions for equations (8.18), (8.19), and (8.20) are:

*When  $t=0$ ,*

$$e = e_0 = \frac{1}{V_0} - 1 \quad (8.21)$$

*At  $z=0$  (bottom surface of the composite plate),*

$$\frac{\partial e}{\partial z} = 0 \quad (8.22a)$$

*At  $z=h$  (top surface of the composite plate),*

$$p_{ext}(t) = \sigma$$

or using equation (8.14),

$$e = e_{\min} + \exp\left[-\frac{p_{ext}(t)}{\sigma_0} + \ln(e_0 - e_{\min})\right] \quad (8.22b)$$

### 8.2.2 Resin Curing Process

Since the temperature inside composite structures is not always constant, which affects the viscosity and degree of cure, the energy balance equation for the more general case should be considered in addition to the consolidation equations so far derived. The energy equation is expressed as follows when the convective heat transfer is neglected (Holman, 1997):

$$\frac{\partial(\rho c T)}{\partial t} = \frac{\partial}{\partial x}\left(K_{xx}^T \frac{\partial T}{\partial x}\right) + \frac{\partial}{\partial y}\left(K_{yy}^T \frac{\partial T}{\partial y}\right) + \frac{\partial}{\partial z}\left(K_{zz}^T \frac{\partial T}{\partial z}\right) + \rho \frac{\partial Q}{\partial t} \quad (8.23)$$

where  $T$ ,  $\rho$ , and  $c$  represent the temperature, density, and specific heat of composite material, respectively, and  $K_{xx}^T$ ,  $K_{yy}^T$ , and  $K_{zz}^T$  represent the coefficient of thermal conductivity in the  $x$ -,  $y$ -, and  $z$ -directions, respectively.  $\partial Q/\partial t$  in the last term represents the heat generated per unit mass and  $\rho(\partial Q/\partial t)$  represents the heat generated per unit volume. The heat generation term can be experimentally obtained by differential scanning calorimetry (DSC) or by solving the resin cure reaction equation (kinetic equation).

The DSC is a cure monitoring technique that measures the degree of cure by the heat generated during the cure of material. A small specimen of about 5 mg is heated either isothermally or dynamically with uniformly increasing temperature. The instrumentation in DSC monitors the rate of heat generation as a function of time. The total heat generation  $H_U$  to complete a curing reaction (100% degree of cure) is equal to the area under the curve of rate of heat generation versus time obtained in a dynamic heating experiment. It is expressed as

$$H_U = \int_0^{t_f} \left( \frac{dQ}{dt} \right)_d dt \quad (8.24)$$

where  $(dQ/dt)_d$  is the rate of heat generation in a dynamic test, and  $t_f$  is the time required to complete the reaction. Then the degree of cure  $\alpha$  is

$$\alpha = \frac{1}{H_U} \int_0^t \left( \frac{dQ}{dt} \right)_T dt \quad (8.25)$$

Equation (8.24) can be expressed differently by introducing the isothermal rate of cure  $d\beta/dt$  (Kim and Lee, 1996):

$$\frac{d\alpha}{dt} = \frac{H_T}{H_U} \frac{d\beta}{dt} \quad (8.26)$$

or, equation (8.26) can be rewritten as

$$\frac{d\beta}{dt} = \frac{1}{H_T} \left( \frac{dQ}{dt} \right)_T \quad (8.27)$$

where  $H_T$  is the heat of reaction generated during isothermal scanning (isothermal heat of reaction).

The simplest kinetic model for describing the isothermal cure of reactive resins is given by the *n*th-order rate expression (Lee, 1997):

$$\frac{d\beta}{dt} = k(1 - \beta)^n \quad (8.28)$$

where  $\beta$  is the isothermal degree of cure,  $k$  is the temperature-dependent rate constant, and  $n$  is the kinetic exponent. This model assumes a maximum initial reaction rate, and consequently, is not capable of realistically describing the curing reaction when a rate peak in the isothermal cure is observed (i.e., a bell-shaped rate profile). In many reactive processes, the following kinetic expression has been found to correlate well with isothermal differential scanning of reactive resin:

$$\frac{d\beta}{dt} = (k_1 + k_2\beta^m)(1 - \beta)^n \quad (8.29)$$

where the constants  $k_1$ ,  $k_2$ ,  $m$ , and  $n$  are determined by nonlinear least-squares curve fit to the  $d\beta/dt$  versus  $\beta$  data. Then, the constants, which were determined at each temperature, are fitted with curves as a function of temperature.

From equations (8.26) and (8.29), the rate of cure can be expressed as (Kim and Lee, 1997)

$$\frac{d\alpha}{dt} = \frac{H_T}{H_U}(k_1 + k_2\beta^m)(1 - \beta)^n \quad (8.30)$$

In general,  $k_1$  and  $k_2$  are assumed to be of the following Arrhenius form:

$$k_1 = A_1 \exp\left(-\frac{E_1}{RT}\right) \quad (8.31)$$

$$k_2 = A_2 \exp\left(-\frac{E_2}{RT}\right) \quad (8.32)$$

where the constants  $A_1$  and  $A_2$  are the Arrhenius pre-exponential factors,  $E_1$  and  $E_2$  are the activation energies,  $R$  is the universal gas constant and  $T$  is the absolute temperature. The values of  $A_1$ ,  $A_2$ ,  $E_1$ , and  $E_2$  are determined by curve fitting from the DSC data.

The value of  $m$  may be expressed as an exponential function form:

$$m = m_1 \exp(-m_2 T) \quad (8.33)$$

where  $m_1$  and  $m_2$  are constants.

The relationship between  $m$  and  $n$  is usually

$$m + n = c_0 \quad (8.34)$$

where  $c_0$  is a constant in the range between 1.0 and 2.0. For the T300/5208 carbon-fiber epoxy, it is 1.25. The isothermal heat of reaction  $H_T$  can be expressed by the following quadratic equation of temperature (Kamal, 1974):

$$H_T = C_0 + C_1 T + C_2 T^2 \quad (8.35)$$

**Table 8.1 Numerical Values of Kinetic Parameters of the Carbon Fiber Epoxy Composite (T300/5208)**

$H_U$ (kJ/kg)	100.6
$E_1$ (J/mole)	$9.710 \times 10^4$
$E_2$ (J/mole)	$6.713 \times 10^4$
$A_1$ ( $\text{min}^{-1}$ )	$1.060 \times 10^8$
$A_2$ ( $\text{min}^{-1}$ )	$1.670 \times 10^8$
$m_1$	$7.70 \times 10^2$
$m_2$	$1.896 \times 10^{-2}$
$m+n$	1.25
$C_0$ (kJ/kg)	$1.368 \times 10^{-3}$
$C_1$ [(kJ)/(kgK)]	$2.524 \times 10^{-1}$
$C_2$ [(kJ)/(kgK <sup>2</sup> )]	$-2.348 \times 10^{-5}$

Table 8.1 shows the experimentally obtained values of cure-related constants of T300/5208 (Kim and Lee, 1996).

To solve equation (8.11), the viscosity  $\mu$  should be known. The viscosity of a fluid is a measure of its resistance to flow under shear stresses. Low-molecular-weight fluids, such as water and automotive engine oil, have low viscosities and flow readily. High-molecular-weight fluids, such as polymer melts, have high viscosities and flow only under high shear stresses. Since no *in situ* chemical reaction occurs during the processing of a thermoplastic polymer, its viscosity depends only on temperature and shear rate. However, the viscosity  $\mu$  of a thermosetting resin during the curing process is a function of cure temperature  $T$ , shear rate  $\dot{\gamma}$ , and the isothermal degree of cure  $\beta$ :

$$\mu = \mu(T, \dot{\gamma}, \beta) \quad (8.36)$$

In the case of isothermal cure, the dual Arrhenius viscosity model has been recommended (Lee, 1997) as

$$\ln \mu(t, T) = \ln \mu_\infty + \frac{E_\mu}{RT} + K_0 \exp\left[-\left(\frac{E_\alpha}{RT}\right)t\right] \quad (8.37)$$

where  $\mu_\infty$  and  $K_0$  are the Arrhenius pre-exponential factors, and  $E_\mu$  and  $E_\alpha$  are the activation energies for the flow and the curing reaction, respectively.

For nonisothermal cure, where the resin temperature history is given by  $T=f(t)$ , the dual Arrhenius viscosity model is written as

$$\ln \mu(t, T) = \ln \mu_\infty + \frac{E_\mu}{Rf(t)} + K_0 \int_0^t \exp\left(-\frac{E_\alpha}{Rf(t)}\right) dt \quad (8.38)$$

Another three-parameter model is (Kardos, 1997)

$$\mu = \mu_\infty \exp\left(\frac{E_\mu}{RT} + K\beta\right) \quad (8.39)$$

where  $\mu_\infty$  is a constant,  $E_\mu$  is the activation energy for viscosity, and  $K$  is the temperature-independent constant.

### 8.2.3 Composite Thermal Conductivity

Finally, to solve the energy equation (8.23), the thermal conductivity  $K_{ij}$  of composite materials should be estimated. The composite thermal conductivities of materials composed of unidirectional fibers embedded in a matrix have been considered (Springer and Tsai, 1967). In the analysis, the following assumptions were made:

1. The composites are macroscopically homogeneous.
2. Both the matrix and the fibers are locally homogeneous and isotropic.
3. The problem is two-dimensional in the  $x$ - $y$ -plane, that is, the temperature distribution is independent of  $z$  (figure 8.3).
4. The thermal contact resistance between the fiber and the matrix is negligible.

For the rectangular packing array, as shown in figure 8.3 (other packing arrays may be possible), the composite equivalent thermal conductivity  $K_{11}$  in the fiber direction may be predicted by assuming that the fibers and the matrix are connected in parallel:

$$A_c K_{11} = A_f K_f + A_m K_m \quad (8.40)$$

where  $A_i$  and  $K_i$  represent the area occupied and the thermal conductivity; the subscripts  $c$ ,  $f$ , and  $m$  refer to the composite, fiber, and matrix, respectively.

Dividing equation (8.40) by  $A_c$ , we get

$$K_{11} = \frac{A_f}{A_c} K_f + \frac{A_m}{A_c} K_m = K_f V_f + K_m V_m \quad (8.41)$$

where  $V_f$  and  $V_m$  represent the volume fraction of fiber and matrix, respectively. Equation (8.41) gives an upper bound for the thermal conductivity.

For the thermal conductivity  $K_{22}$  in the transverse direction of fiber, the representative volume element (RVE) whose dimensions are  $(2a \times 2b \times 1)$ , can be considered. Then the equivalent thermal resistance  $1/K_{22}$  of the small element in the  $x$ -direction with thickness  $dy$  and width  $h(y)$  at any given  $y$  can be calculated first:

$$\frac{2a}{K_{22} dy} = \frac{2a - h}{K_m dy} + \frac{h}{K_f dy} \quad (8.42)$$

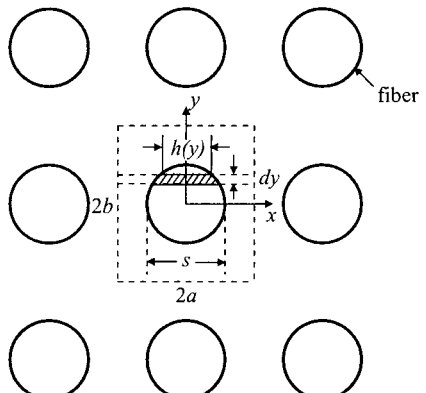


**Figure 8.3** Configuration of cylindrical fibers for the thermal conductivity model.

The above equation can be rewritten as

$$K_{22}(y) = \frac{2a}{(2a - h/K_m) + (h/K_f)} \quad (8.43)$$

The average value of  $\bar{K}_{22}$  is expressed as

$$\bar{K}_{22} = \frac{1}{2b} \int_{-b}^b K_{22}(y) dy \quad (8.44)$$

Performing integration of equation (8.44), we obtain

$$\bar{K}_{22}2b = K_m(2b - s) + \int_{-\frac{s}{2}}^{\frac{s}{2}} \frac{2a}{(2a - h/K_m) + (h/K_f)} dy \quad (8.45)$$

where  $s$  is the maximum dimension of the fiber in the  $y$ -direction. Equation (8.45) can be rewritten as

$$\frac{\bar{K}_{22}}{K_m} = \left(1 - \frac{s}{2b}\right) + \frac{a}{b} \int_{-\frac{s}{2}}^{\frac{s}{2}} \frac{dy}{(2a - h) + (K_m/K_f)h} \quad (8.46)$$

For a square fiber ( $h = s = \text{constant}$ ) and square packing array ( $a = b$ ),

$$a \int_{-\frac{d}{2}}^{\frac{d}{2}} \frac{dy}{(2a - h) + (K_m/K_f)h} = \frac{1}{\sqrt{1/V_f} + B/2} \quad (8.47)$$

where  $V_f$  (the fiber volume fraction) and  $B$  are expressed as

$$\sqrt{V_f} = \frac{s}{2a} \quad (8.48)$$

$$B = 2 \left( \frac{K_m}{K_f} - 1 \right) \quad (8.49)$$

Then equation (8.46) becomes

$$\frac{\bar{K}_{22}}{K_m} = \left(1 - \sqrt{V_f}\right) + \frac{1}{\sqrt{1/V_f} + B/2} \quad (8.50)$$

For a cylindrical fiber ( $s = d$ ) and square packing array ( $a = b$ ), equation (8.46) gives

$$\frac{\bar{K}_{22}}{K_m} = \left(1 - 2\sqrt{\frac{V_f}{\pi}}\right) + \frac{1}{B} \left( \pi - \frac{4}{\sqrt{1 - (B^2(V_f/\pi))}} \tan^{-1} \frac{\sqrt{1 - (B^2(V_f/\pi))}}{1 + B\sqrt{V_f/\pi}} \right) \quad (8.51)$$

The experimental data indicate that the assumption of cylindrical fibers is more appropriate than that of square fibers (Springer, 1981). The thermal conductivity calculated by equation (8.51) gives a value about 10% lower than that experimentally determined when the fiber volume fraction is higher than 75%; however, the values calculated using the cylindrical fiber model predict the experimental results within 5% error when the fiber volume fraction is lower than 60%.

The heat flux  $q_i^T$  per unit area per unit time in the  $x_i$ -direction is related to the temperature gradient  $\partial T/\partial x_j$  in the  $x_j$ -direction by

$$q_i^T = -K_{ij}^T \frac{\partial T}{\partial x_j} \quad (8.52)$$

In the principal axes of a unidirectional composite, the only heat flux  $q_i^T$  possible is due to the temperature gradient  $\partial T/\partial x_i$ . Therefore, equation (8.52) reduces to

$$q_1^T = -K_{11}^T \frac{\partial T}{\partial x_1} \quad (8.53a)$$

$$q_2^T = -K_{22}^T \frac{\partial T}{\partial x_2} \quad (8.53b)$$

$$q_3^T = -K_{33}^T \frac{\partial T}{\partial x_3} \quad (8.53c)$$

where  $K_{ii}$  ( $i=1, 2, 3$ ) are thermal conductivities of composite in the  $x_i$  ( $i=1, 2, 3$ ) directions, respectively.

When unidirectional composites are assumed to be isotropic in a plane normal to the fibers (i.e., transversely isotropic), the thermal conductivities  $K_{22}^T$  and  $K_{33}^T$  are equal to each other. Thus, only two independent thermal conductivities can describe the heat conduction behavior of a unidirectional composite (Tsai and Hahn, 1980).

Equation (8.53) is only valid in the principal material axes. For new transformed axes  $x, y, z$ , as shown in figure 8.4, the thermal conductivities are expressed by the tensor transformation rule in chapter 3 as follows:

$$K_{xx}^T = m^2 K_{11}^T + n^2 K_{22}^T \quad (8.54a)$$

$$K_{yy}^T = n^2 K_{11}^T + m^2 K_{22}^T \quad (8.54b)$$

$$K_{xy}^T = mn(K_{11}^T - K_{22}^T) \quad (8.54c)$$

where  $m = \cos\theta$  and  $n = \sin\theta$ .

The heat conduction equations in the transformed coordinates are expressed as

$$q_x^T = -K_{xx}^T \frac{\partial T}{\partial x} - K_{xy}^T \frac{\partial T}{\partial y} \quad (8.55a)$$

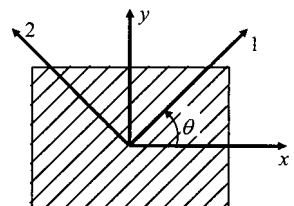


**Figure 8.4** Coordinate transformation for the calculation of thermal conductivities of unidirectional composites.

**Table 8.2 Thermal Conductivities of Various Composite Laminates and Metals**

Material	W/m °C (Btu/h ft °F)		
	Unidirectional		
	Longitudinal	Transverse	Quasi-isotropic
S-glass epoxy	3.46 (2.0)	0.35 (0.2)	0.35 (0.2)
Kevlar 49 epoxy	1.73 (1.0)	0.73 (0.1)	0.17 (0.1)
Carbon epoxy:			
High modulus	48.4–60.6 (28–35)	0.87 (0.5)	10.4–20.8 (6–12)
Ultrahigh modulus	121.1–129.8 (70–75)	1.04 (0.6)	24.2–31.1 (14–18)
Boron epoxy	1.73 (1.0)	1.04 (0.6)	1.38 (0.8)
Aluminum		138.4–216.3 (80–125)	
Steel		15.6–46.7 (9–27)	
Epoxy		0.35 (0.2)	

$$q_y^T = -K_{xy}^T \frac{\partial T}{\partial x} - K_{yy}^T \frac{\partial T}{\partial y} \quad (8.55b)$$

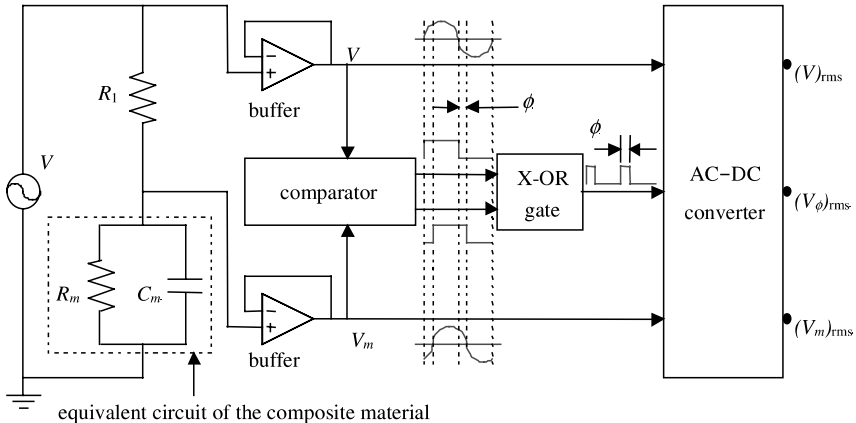
$$q_z^T = -K_{zz}^T \frac{\partial T}{\partial z} = q_3^T = -K_{33}^T \frac{\partial T}{\partial x_3} \quad (8.55c)$$

Table 8.2 lists some representative values of thermal conductivities (W/m °C) of various composite laminates and metals.

### 8.3 Cure Monitoring during Processing of Composite Materials

Cure monitoring is important for the quality control and improvement of the mechanical properties of thermosetting resin matrix composite materials. There are several cure monitoring methods, such as differential scanning calorimetry (DSC), dynamic mechanical analysis (DMA), infrared spectroscopy (IRS), optical techniques, and dielectrometry. From these methods, dielectrometry is considered the most promising *in situ* cure monitoring technique during a production molding operation because it can monitor continuously the cure chemistry of the resin throughout the process of going from monomeric liquid of varying viscosity to a cross-linked, insoluble, high-temperature solid (Kim and Lee, 1993). Since the thermosetting resins in composite materials are dielectric materials, the combination of the electrodes and the composites forms a capacitor. The charge accumulated in the capacitor depends on the mobility of dipoles and ions present in the resin to follow the alternating electric field and varies with the stage of cure.

The instrumentation includes two electrodes, which are embedded in composite materials and are connected to an alternating electric field, as shown in figure 8.5 (Kim and Lee, 1996). The amount of energy loss expended in aligning its dipoles and moving its ions in accordance with the direction of alternating field is used for measuring the state of cure.



**Figure 8.5** Electric circuit for measuring the dissipation factor of the composite material (Kim and Lee, 1996).

For an alternating field the time required for the polarization of an ideal capacitor is advanced in phase exactly  $90^\circ$  ( $\pi/2$  radians) with the applied voltage (Brown, 1988). If a capacitor composed of ideal dielectric material is subjected to a sinusoidal voltage

$$V = V_0 \exp(i\omega t) \quad (8.56)$$

the current  $I_C$  in the capacitor is (Kingley et al., 1991)

$$I_C = C \frac{dV}{dt} = i\omega C_0 \varepsilon_0 \kappa V \quad (8.57)$$

where  $\varepsilon_0$  is the permittivity of vacuum ( $= 8.85 \times 10^{-12} \text{ F/m}$ ),  $C_0$  is the value of capacitance of the plates when air only exists between the plates, and  $\kappa$  ( $= \varepsilon/\varepsilon_0$ ) is the relative dielectric constant.

However, for a real dielectric material the current  $I$  has vector components  $I_C$  and  $I_R$  for the condition of a lossy dielectric. The current  $I_C$  represents a nonlossy capacitive current proportional to the charge stored in the capacitor. It is frequency dependent and leads the voltage by  $90^\circ$ . The current  $I_R$  is the AC conduction current in phase with the applied voltage  $V$ , which represents the energy loss or power dissipated in the dielectric. This condition can be represented by a complex permittivity or dielectric constant in order to deal with the loss current as follows (Buchanan, 1986):

$$\begin{aligned} I &= i\omega C_0 \varepsilon_0 (\kappa' - i\kappa'') V \\ &= i\omega C_0 \varepsilon_0 \kappa' V + \omega C_0 \varepsilon_0 \kappa'' V \end{aligned} \quad (8.58)$$

$$= I_C + I_R \quad (8.59)$$

where  $\kappa'$  and  $\kappa''$  are the real and imaginary parts of relative dielectric constant  $\kappa$  ( $= \varepsilon/\varepsilon_0$ ), respectively.

From the magnitude of these currents, the dissipation factor  $D$  ( $= \tan\delta$ ) is defined:

$$D = \tan \delta = \left| \frac{I_R}{I_C} \right| = \frac{\kappa''}{\kappa'} \quad (8.60)$$

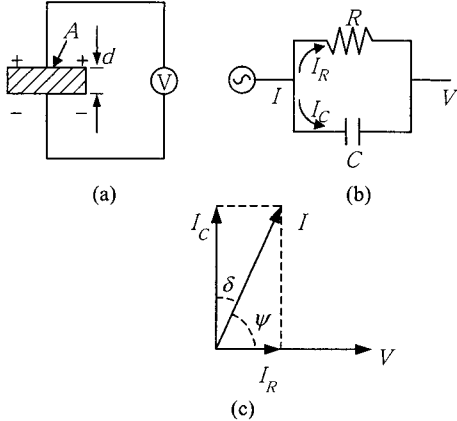


**Figure 8.6** Equivalent circuit diagrams for dielectric materials: (a) Capacitive cell; (b) charging and loss currents; (c) loss tangent for a typical dielectric (from Buchanan, 1986).

The vector relationships, illustrated in figure 8.6, show the relationship between the phase angle  $\psi$  and the loss angle  $\delta$  as follows:

$$\psi = \frac{\pi}{2} - \delta \quad (8.61)$$

The loss angle  $\delta$ , corresponding to a time lag between an applied voltage and induced current, causes loss current and energy dissipation in AC circuits.

In figure 8.5 (devised by Kim and Lee, 1996), a resistance  $R_1$  was serially connected to an equivalent circuit of the composite material and the alternating voltage  $V$  was applied to the circuit. Since the resin in the composite material has dielectric properties, the composite material was represented by the parallel arrangement of a capacitance  $C_m$  and a resistance  $R_m$ . The dissipation factor  $D$  can be calculated by the circuit theory after measuring the ratio  $|V_m/V|$  and the phase angle  $\psi$  between the applied voltage and the voltage  $V_m$  across the composite material.

The measuring part of the phase difference  $\phi$  consists of two comparators and an exclusive-or (X-OR) gate. The comparator produces a square wave of +5 V and 0 V, according to the plus and minus voltages of the input alternating signal. The square waves of  $V$  and  $V_m$  were fed into the X-OR gate via the comparators in order to obtain the square wave with duration  $\phi$  seconds. In order to make the signals stable, the square wave with duration  $\phi$  seconds was converted into a root mean square (RMS) value using a suitable converter. Then, the phase difference was calculated by the definition of RMS. The RMS value of voltage  $V(t)$  is defined as

$$V_{rms} = \sqrt{\frac{1}{T} \int_t^{t+T} V^2(t) dt} \quad (8.62)$$

where  $T$  represents the time period of the wave pattern.

Figure 8.7 shows the X-OR gate for measuring the phase difference  $\phi$  seconds ( $= [\psi/(2\pi)]T$ ) and its input and output. In figure 8.7, the value  $V_\phi$  of the square wave after the X-OR gate becomes  $V_{max}$  (= 5 V) with duration  $\phi$  seconds when the phase difference between the signals  $V$  and  $V_m$  exists, and zero in the other portion. If the square wave duration  $\phi$  seconds is substituted into equation (8.62),  $V_{rms}$  is expressed as

$$V_{rms} = \sqrt{\frac{1}{T} V_{max}^2 2\phi} = V_{max} \sqrt{\frac{2\phi}{T}} \quad (8.63)$$

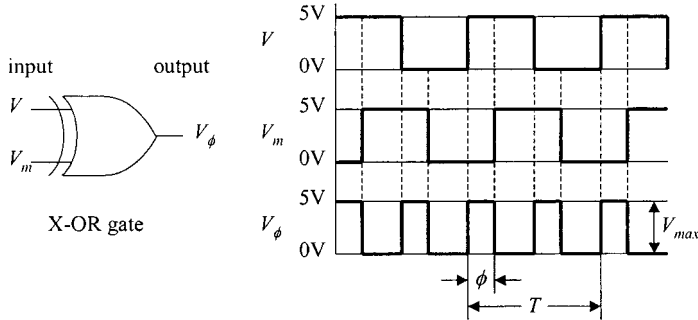


**Figure 8.7** X-OR gate (exclusive-or gate) for measuring the phase difference  $\phi$  (seconds).

Thus,  $\phi$  in equation (8.63) can be obtained as

$$\phi(\text{sec}) = \frac{T}{2} \left( \frac{V_{\text{rms}}}{5} \right)^2 \quad (8.64a)$$

where  $T$  and  $V_{\text{max}}$  were measured in seconds and volts, respectively. The above results can be transformed into the phase angle  $\psi$ :

$$\psi(\text{radians}) = \frac{2\pi}{T} \phi = \pi \left( \frac{V_{\text{rms}}}{5} \right)^2 \quad (8.64b)$$

If an alternating voltage  $V$  with angular frequency  $\omega$  is applied to the circuit of figure 8.5, the impedance  $Z_1$  across  $R_1$  and the impedance  $Z_m$  across the composite material are expressed as

$$Z_1 = R_1 \quad (8.65)$$

$$Z_m = \frac{R_m}{1 + i\omega C_m R_m} \quad (8.66)$$

The voltage  $V_m$  across the composite material of figure 8.5 is calculated as

$$V_m = \frac{Z_m}{Z_1 + Z_m} V = \frac{R_m(R_1 + R_m - i\omega C_m R_m R_1)}{(R_1 + R_m)^2 + (\omega C_m R_m R_1)^2} V \quad (8.67)$$

From equation (8.67), the ratio  $|V_m/V|$  and the phase angle  $\psi$  between  $V$  and  $V_m$  are calculated as

$$|V_m/V| = \frac{R_m}{\sqrt{(R_1 + R_m)^2 + (\omega C_m R_m R_1)^2}} \quad (8.68)$$

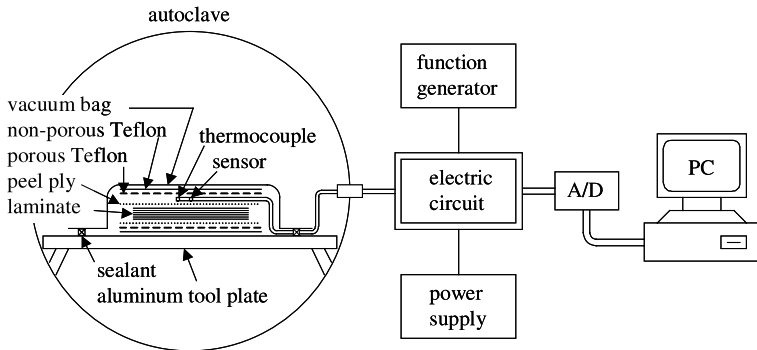


**Figure 8.8** Schematic diagram of the device for in situ monitoring of the temperature and dissipation factor of composite materials.

$$\tan \psi = -\frac{\omega C_m R_m R_1}{R_1 + R_m} \quad (8.69)$$

From equations (8.68) and (8.69),  $R_m$  and  $C_m$  can be calculated as

$$R_m = \frac{|V_m/V|}{\cos \psi - |V_m/V|} R_1 \quad (8.70)$$

$$C_m = -\frac{\sin \psi}{\omega R_1 |V_m/V|} \quad (8.71)$$

The dissipation factor  $D$  can be obtained from equation (8.60) as

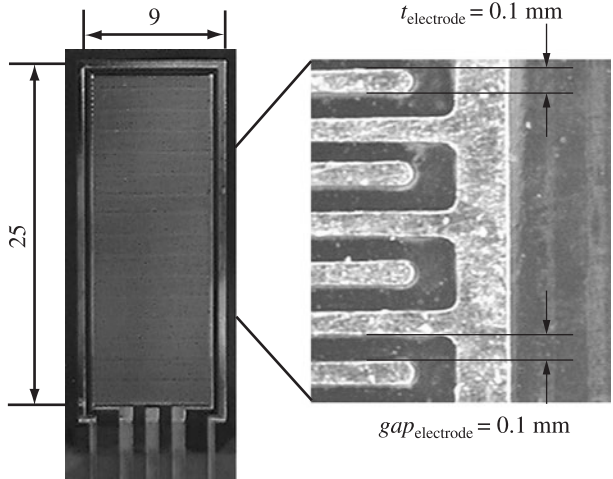
$$D = \left| \frac{I_{R_m}}{I_{C_m}} \right| = \left| \frac{|V_m/Z_{R_m}|}{|V_m/Z_{C_m}|} \right| = \frac{1}{\omega R_m C_m} \quad (8.72)$$

Substituting equations (8.70) and (8.71) into equation (8.72), the dissipation factor of the composite material of figure 8.5 is expressed as

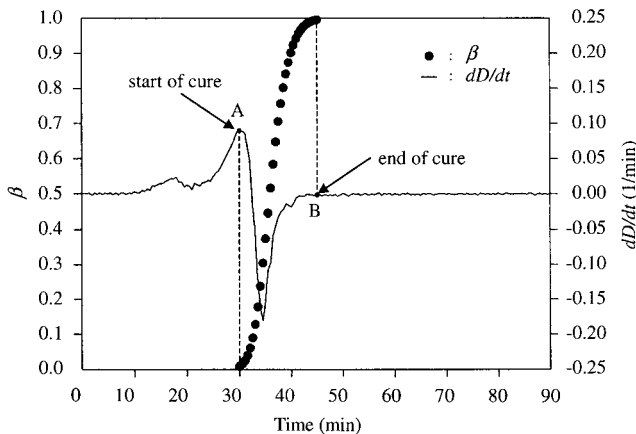
$$D = \frac{|V_m/V| - \cos \psi}{\sin \psi} \quad (8.73)$$

Figure 8.8 shows the schematic diagram of the device for in situ monitoring of the temperature and dissipation factor of composite materials. The dielectrometry device manufactured based on this method has other features such as an outside electromagnetic noise reduction mechanism and sensitivity increase device. Figure 8.9 shows an small interdigital dielectric sensor manufactured at KAIST.

Figure 8.10 shows the isothermal degree of cure  $\beta$  and the dissipation factor during cure of a carbon composite material (T300/5208). The cure started at the point of maximum value of  $dD/dt$  (point A) and ended at the point of zero value of  $dD/dt$  (point B).



**Figure 8.9** Structure of a small interdigital dielectrometry sensor (dimensions in mm).



**Figure 8.10** Isothermal degree of cure  $\beta$  and the derivative of the dissipation factor  $dD/dt$  with respect to time when the holding temperature was  $120^\circ\text{C}$ .

#### 8.4 Heat Conduction and Moisture Diffusion in Composite Materials

The composite plates are usually thin compared with the in-plane dimensions and frequently are subjected to temperature or moisture differences through the thickness direction. Therefore, the hygrothermal behavior in the thickness direction ( $z$ -direction) is sometimes important. The energy equation (8.23) becomes, without a heat generation term,

$$\frac{\partial(\rho c T)}{\partial t} = \frac{\partial}{\partial z} \left( K_{zz}^T \frac{\partial T}{\partial z} \right) \quad (8.74)$$

Equation (8.74) has been derived based on the Fourier's law of heat conduction:

$$q = -K_{zz}^T \frac{\partial T}{\partial z} \quad (8.75)$$

where  $q$  is the heat transfer rate and  $\partial T/\partial z$  is the temperature gradient in the direction of the heat flow (Holman, 1997).

If  $\rho$  and  $c$  are constant, equation (8.74) reduces to

$$\frac{\partial T}{\partial t} = \frac{K_{zz}^T}{\rho c} \frac{\partial^2 T}{\partial z^2} \quad (8.76)$$

The equation for moisture diffusion can be derived similarly from the balance of mass as

$$\frac{\partial H}{\partial t} = \frac{\partial}{\partial z} \left( K_{zz}^H \frac{\partial H}{\partial z} \right) \quad (8.77)$$

where  $H$  is the moisture concentration ( $\text{kg}/\text{m}^3$ ) and  $K_{zz}^H$  is the diffusion coefficient ( $\text{m}^2/\text{s}$ ).

Equation (8.77) has been derived based on Fick's law of diffusion:

$$\dot{m} = -K_{zz}^H \frac{\partial H}{\partial z} \quad (8.78)$$

where  $\dot{m}$  is the mass flux, which is defined as mass flow rate per unit time and area ( $\text{kg}/(\text{m}^2\text{s})$ ).

In the study of hygrothermal behavior of composite materials, the specific moisture concentration  $C$  (dimensionless) is frequently used (Tsai and Hahn, 1980):

$$C = \frac{H}{\rho} \quad (8.79)$$

where  $\rho$  is the density of the dry composite.

Physically,  $C$  represents the amount of moisture in the volume of  $\Delta V$  as a fraction of the dry mass of composite:

$$C = \lim_{\Delta V \rightarrow 0} \frac{\text{mass of moisture in } \Delta V}{\text{mass of dry composite of volume } \Delta V} \quad (8.80)$$

Then equation (8.77) becomes

$$\frac{\partial C}{\partial t} = K_{zz}^H \frac{\partial^2 C}{\partial z^2} \quad (8.81)$$

When the boundary conditions for equation (8.81) are

$$C = C_0 \quad \text{for } 0 < z < h \quad \text{at } t \leq 0 \quad (8.82a)$$

$$C = C_\infty \quad \text{for } z = 0 \text{ and } h \text{ at } t > 0 \quad (8.82b)$$

where  $h$  is the thickness of laminate. The solution of equation (8.81) with the boundary conditions of (8.82) is given by (Holman, 1997)

$$\frac{C - C_0}{C_\infty - C_0} = 1 - \frac{4}{\pi} \sum_{n=0}^{\infty} \frac{1}{2n+1} \sin \frac{(2n+1)\pi z}{h} \exp \left( -\frac{(2n+1)^2 \pi^2 K_{zz}^H t}{h^2} \right) \quad (8.83)$$

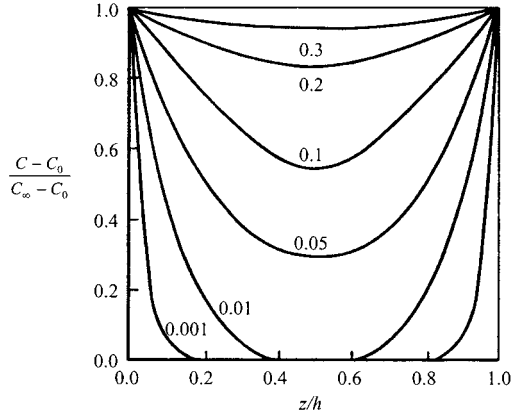


**Figure 8.11** Specific moisture concentration profile as a function of time; the numbers represent the nondimensional time  $K_{zz}^H t / h^2$  (from Tsai and Hahn, 1980).

As the time  $t$  increases, the specific moisture concentration  $C$  in equation (8.83) reaches  $C_\infty$  throughout the laminate, as shown in figure 8.11. Therefore,  $C_\infty$  is also called the equilibrium specific moisture concentration.

In actual tests of specific moisture concentration, the sample is frequently weighed to determine the average specific moisture concentration, which is the total mass of the absorbed moisture divided by the dry weight of the sample. The average specific moisture concentration  $C_{\text{avg}}$  is defined by

$$C_{\text{avg}} = \frac{1}{h} \int_0^h C dz \quad (8.84)$$

Substituting equation (8.83) into equation (8.84) yields

$$\frac{C_{\text{avg}} - C_0}{C_\infty - C_0} = 1 - \frac{8}{\pi^2} \sum_{n=0}^{\infty} \frac{1}{(2n+1)^2} \exp\left(-\frac{(2n+1)^2 \pi^2 K_{zz}^H t}{h^2}\right) \quad (8.85)$$

For a sufficiently large  $t$ , equation (8.85) can be approximated by the first term in the series

$$\frac{C_{\text{avg}} - C_0}{C_\infty - C_0} = 1 - \frac{8}{\pi^2} \exp\left(-\frac{\pi^2 K_{zz}^H t}{h^2}\right) \quad (8.86)$$

On the other hand, for short times  $t$ , an approximation can be obtained from an alternate solution (Crank, 1975):

$$\frac{C_{\text{avg}} - C_0}{C_\infty - C_0} = 4 \sqrt{\frac{K_{zz}^H t}{\pi h^2}} \quad (8.87)$$

Thus, the initial average moisture concentration increases as the square root of time.

The half sorption process is defined as

$$\frac{C_{\text{avg}} - C_0}{C_\infty - C_0} = \frac{1}{2} \quad (8.88)$$

Then the time  $t_{1/2}$  required for the half sorption process can be calculated from equation (8.86)

$$t_{1/2} = \frac{h^2}{\pi^2 K_{zz}^H} \ln \frac{16}{\pi^2} \quad (8.89)$$

**Table 8.3 Typical Hygrothermal Properties of Unidirectional Carbon-Fiber Epoxy Composite**

<i>Constant</i>	<i>Dimension</i>	<i>Value</i>
$K_0^H$	$\text{mm}^2/\text{s}$	6.51
$a$	—	0.018
$b$	—	1
$\beta_1^*$	$\text{m}/\text{m}$	0
$\beta_2 (= \beta_3)$	$\text{m}/\text{m}$	0.44
$E_d/R$	K	5722

\*Swelling coefficient in the fiber direction

The diffusion coefficient is determined from equation (8.89) as

$$K_{zz}^H = 0.04895 \frac{h^2}{t_{1/2}} \quad (8.90)$$

For two average specific moisture concentrations  $C_{\text{avg1}}$  and  $C_{\text{avg2}}$  measured at two small times  $t_1$  and  $t_2$ , respectively, the diffusion coefficient can be calculated using equation (8.87) as

$$K_{zz}^H = \frac{\pi}{16} \left( \frac{C_{\text{avg2}} - C_{\text{avg1}}}{C_\infty - C_0} \right)^2 \left( \frac{h}{\sqrt{t_2} - \sqrt{t_1}} \right)^2 \quad (8.91)$$

The equilibrium specific moisture concentration  $C_\infty$  depends on the environment. In humid air it is related to the relative humidity  $RH$  in percent by a power law:

$$C_\infty = a \left( \frac{RH}{100} \right)^b \quad (8.92)$$

where  $a$  and  $b$  are material constants listed in table 8.3 (Tsai and Hahn, 1980). The moisture diffusion coefficient strongly depends on temperature. The relationship can be described by an Arrhenius form:

$$K^H = K_0^H \exp \left( -\frac{E_d}{RT} \right) \quad (8.93)$$

where  $K_0^H$  and  $E_d$  are the pre-exponential factor and activation energy, respectively.  $R$  is the gas constant (1.987 cal/mol K). Table 8.3 shows typical hygrothermal properties of a unidirectional carbon-fiber epoxy composite.

## 8.5 Liquid Composite Molding (LCM) Processes

Liquid composite molding (LCM), briefly explained in chapter 2 (section 2.8.5), includes several composite manufacturing processes, such as resin transfer molding (RTM), vacuum-assisted RTM (VARTM), and injection compression molding

(ICM). These processes are capable of producing high-quality, complex-shaped fiber-reinforced composite products (Advani and Sozer, 2000).

From resin transfer molding, which is also a variation of the structural reaction injection molding (SRIM) process shown in figure 2.40, the VARTM and ICM have been originated.

In RTM, a dry reinforcement that has been cut or shaped into a preformed piece, generally called a preform, is placed within the mold cavity, as shown in figure 2.41. The preform must not extend beyond the desired seal or pinch-off area in the mold, to allow the mold to close and seal properly. After the mold is sealed, a polymeric resin is injected into the mold cavity, saturating the preform and expelling any air present. Any areas of the preform not saturated at the end of filling will reduce the strength of the part considerably. Therefore, injection gate and vent positions, and injection is pressure or flow rate are important design and process specifications. When the cure complete, which can take from several minutes to hours, the molded part is removed from the mold and the process can begin again to form additional parts. The molded components may require a postcure to further complete the resin reaction.

Vacuum-assisted RTM differs from RTM only in that a vacuum is drawn in the cavity before the resin is introduced. Applying a vacuum can be beneficial in reducing dry-spot formation; however, preparing molds to hold a good vacuum will add significant cost and will require the use of extra equipment. Also some systems will not be affected significantly by the application of a vacuum, while other resins will not be applicable at all, as some of their chemical components may boil.

In the process of ICM, the mold is not fully closed at the beginning of resin injection. The mold is left partially open so that the preform is under no compression at all. The initial resistance to resin flow is very low because the preform was not compressed, and the entire resin shot can be delivered quickly. After the resin is injected, the mold is closed gradually, forcing the majority of the resin to flow in the thickness direction of the part. A novel application of this process is described in Section 15.5 (“Trenchless Sewage Pipe Repair by RTM”). The benefits of this process are the reductions in injection pressure and mold filling time; however, the complicated nature of the flow may limit the complexity of parts that can be produced.

The RTM process is used today to manufacture a wide variety of articles, ranging from small armrests for buses to water treatment plant components (Johnson, 1990). Size capability is the major benefit of RTM. Large-area composite products can be produced with RTM because pressures needed to mold components can be maintained at low levels. When cycle time is not critical, pressures can be maintained at less than 0.1 MPa. For VARTM, pressures in the tool may be maintained below atmospheric pressure throughout the molding cycle. With very low pressure for injection, only minimal mold clamping pressures are required, while compression molding requires pressures up to 14.0 MPa (2000 psi) over the part surface to achieve good physical properties and appearance. In addition to large area parts, RTM is well suited to manufacture of parts that have deep draws and minimum draft on the sides of the part. Alternative fabrication technologies, such as thermoset compression molding or thermoplastic compression molding, are limited in the depth to which they can form by the pressures required for consolidation. While preplacing the reinforcement provides superior physical properties and eliminates flow-induced property variations, to make ribs and bosses in RTM is very difficult. Any small detail or molded-in feature, such as holes and grooves, may be

better achieved in other processes. Foam cores can be used in RTM for added rigidity in a structure, as well as for providing increasingly complex three-dimensional structures to be molded in one piece. The low pressures used in this process allow foams in the 50–100 kg/m<sup>3</sup> density range to be molded in place without significant deformation. Other processes allow only higher density foam to avoid crushing, which makes the structure heavier.

If the preform has smaller dimensions than the mold gap, then there will be air channels along the mold wall edges, ribs, T-joints, and stiffener inserts. Also, if the mold gap varies in thickness around the corners, it will create cavity channels. Sometimes if the edges of preform or stitched preforms cannot be held together tightly, these regions will have higher porosity than the rest of the preform. During mold filling, resin will flow faster through these air channels and higher porosity regions, since they have less resistance to resin flow. This phenomenon is known as *racetracking* in the mold filling process. Although racetracking may be undesirable or unavoidable, sometimes racetracking is created intentionally to ease the resin flow in order to reduce the injection pressure or reduce filling time.

If fabric preforms are used rather than strand mats, they are draped over a tool surface to conform the shape of the mold. The structural deformations of the preform change the porosity and permeability of preforms.

Resins for RTM have typically low viscosity, in the range 100–1000 cP. Normally, resin systems have two components and require a preinjection mixing ratio in the region of 100:1.

Structural reaction injection molding (SRIM) resins are similarly two-part, low-viscosity liquids with the viscosity range 10–100 cP at room temperature. They are highly reactive in comparison with RTM resins and require very fast, high-pressure impingement mixing to achieve thorough mixing before entering the mold. Mix ratios of typical systems are near 1:1, which is desirable for rapid impingement mixing. Preforms for RTM and SRIM systems are similar in most respects. However, due to the rapidity of the resin reaction in the SRIM system, the preforms for SRIM normally are lower in fiber content or have additional directional fibers, which act as a resin flow channel. The faster cure in the SRIM system minimizes the need to design elaborate seals and to manage the overflow of resin from the tool cavity.

These days, the two systems are approaching a single process known as high-speed resin transfer molding (HSRTM) because RTM resin systems are developed to be faster reacting and SRIM systems are slowed down to produce a longer filling time capability.

One-piece molded components can in some cases provide performance in critical applications that is unattainable using a multipiece assembly of components fabricated by other processes. Figure 8.12 shows an HSRTM process employed to manufacture a one-piece front structure of Ford passenger cars. The structure integrates 45 individual steel stampings into a single molded component (Johnson, 1990). In figure 8.12, heated flat sheets of glass reinforcement are stamped into a three-dimensional preform shell and subsequently installed over a molded foam core. After the addition of some small, high-performance attachments of preforms at certain high-stress areas, the assembled preform is transferred to a heated steel tool for resin injection with an HSRTM machine. The resultant component reduces the weight of the structure 30% over the normal steel structure with improved durability and crash performance.

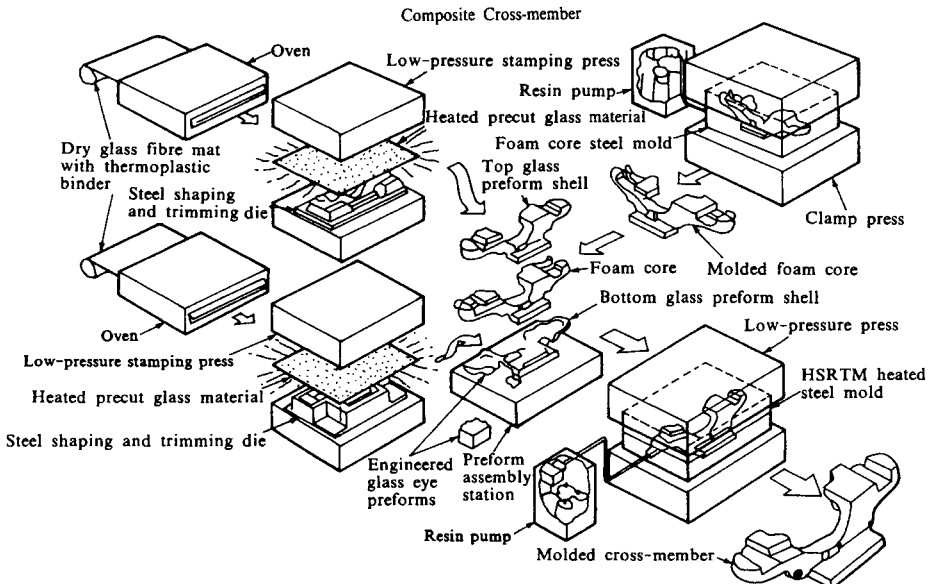


**Figure 8.12** High-speed resin transfer molding (HSRTM) process used for manufacture of automotive front structure (courtesy of Ford Motor Company).

### 8.5.1 Resin Flow and Cure Models during Liquid Composite Molding

In order to simulate the mold filling process of resin during the liquid composite molding (LCM) process, the resin front should be considered with varying degrees of saturation  $S$ , which is the imbibition case of section 8.2. Also several assumptions are usually required to simplify the problem (Lee, 1997). In general, the preplaced fabric reinforcement in the mold cavity is assumed to be rigid during mold filling. Inertia effects of resin are neglected because of the low Reynolds number of resin flow and surface tension is considered negligible compared with the dominant viscous force.

Since the mold cavity can be assumed to be much larger than the pore size of the fabric reinforcement, Darcy's law for flow through porous media is used rather than Navier–Stokes equation. However, the lubrication equation of Reynolds derived from Navier–Stokes equation is used in the fiber-free region. In a three-dimensional flow in the preform with Cartesian coordinates, the resin flow velocity components  $u_x$ ,  $u_y$ , and  $u_z$  in the  $x$ -,  $y$ -, and  $z$ -directions, respectively, are expressed from the result of equation (8.1):

$$\begin{Bmatrix} u_x \\ u_y \\ u_z \end{Bmatrix} = -\frac{1}{\mu} \begin{bmatrix} k_{xx} & k_{xy} & k_{xz} \\ k_{xy} & k_{yy} & k_{yz} \\ k_{xz} & k_{yz} & k_{zz} \end{bmatrix} \begin{Bmatrix} \frac{\partial p}{\partial x} \\ \frac{\partial p}{\partial y} \\ \frac{\partial p}{\partial z} \end{Bmatrix} \quad (8.94)$$

Since the resin can be assumed to be an incompressible fluid, the continuity equation becomes

$$\frac{\partial u_x}{\partial x} + \frac{\partial u_y}{\partial y} + \frac{\partial u_z}{\partial z} = 0 \quad (8.95)$$

Since the permeability  $k_{ij}$ , which is a second-order tensor, is usually measured in its principal directions, it is necessary to transform the permeability tensor from the principal directions of the fiber mat to the defined coordinate directions using the results of chapter 3. The transformed permeability matrix  $k_{pq}$  in the  $x,y,z$ -coordinate system is expressed using the permeability in the principal 1,2,3-coordinate system as

$$k_{pq} = l_{pi}l_{qj}k_{ij} \quad (p, q = x, y, z \text{ and } i, j = 1, 2, 3) \quad (8.96)$$

where  $l_{pi}$  is the direction cosine between the transformed  $p$ -axis and the original  $i$ -axis.

When the dimensions of thickness of the molded products is much smaller than the dimensions in the planar directions, the mold filling in a thin cavity can be modeled as a two-dimension flow in the  $x-y$ -plane. Since the pressure gradient in the thickness direction is negligibly small compared with those in other directions, the pressure in the  $z$ -direction can be assumed to be constant. Then equation (8.94) can be written in a two-dimensional form with  $p = p(x, y)$ :

$$\begin{Bmatrix} u_x(x, y, z) \\ u_y(x, y, z) \end{Bmatrix} = -\frac{1}{\mu(x, y, z)} \begin{bmatrix} k_{xx} & k_{xy} \\ k_{xy} & k_{yy} \end{bmatrix} \begin{Bmatrix} \frac{\partial p(x, y)}{\partial x} \\ \frac{\partial p(x, y)}{\partial y} \end{Bmatrix} \quad (8.97)$$

In order to eliminate the independent variable  $z$  in equation (8.97), the velocity is averaged through the  $z$ -direction:

$$\begin{Bmatrix} \bar{u}_x(x, y) \\ \bar{u}_y(x, y) \end{Bmatrix} = -\begin{bmatrix} \bar{k}_{xx} & \bar{k}_{xy} \\ \bar{k}_{xy} & \bar{k}_{yy} \end{bmatrix} \begin{Bmatrix} \frac{\partial p(x, y)}{\partial x} \\ \frac{\partial p(x, y)}{\partial y} \end{Bmatrix} \quad (8.98)$$

where

$$\begin{bmatrix} \bar{k}_{xx} & \bar{k}_{xy} \\ \bar{k}_{xy} & \bar{k}_{yy} \end{bmatrix} = \frac{1}{h} \int_{-\frac{h}{2}}^{\frac{h}{2}} \frac{1}{\mu(x, y, z)} \begin{bmatrix} k_{xx} & k_{xy} \\ k_{xy} & k_{yy} \end{bmatrix} dz \quad (8.99)$$

where  $h$  is the part thickness.

The boundary conditions for equation (8.98) are

$$\left. \frac{\partial p}{\partial n} \right|_{\text{wall}} = 0, \quad p|_{\text{front}} = 0 \quad (8.100a)$$

$$p|_{\text{gate}} = p_0 \text{ or } \bar{u}|_{\text{gate}} = \bar{u}_0 \quad (8.100b)$$

When dry spots form during mold filling, both the air pressure in the dry spots and the resin pressure in the saturated region have to be calculated.

At the beginning of the dry spot formation, the air mass  $m_a$  may be calculated by the ideal gas law:

$$m_a = \frac{p_0 V_0}{RT} \quad (8.101)$$

where  $p_0$  is the ambient pressure, which may be assumed to be one atmosphere,  $V_0$  is the initial volume of the dry spot. When the resin volume,  $\Delta V$ , flows into the dry

spot from the saturated areas around the dry spot, the volume of dry spot becomes  $V_0 - \Delta V$ . Then the air pressure  $p_a$  in the dry spot is calculated as follows:

$$p_a = R \frac{m_a T}{V_0 - \Delta V} \quad (8.102)$$

Therefore, the air pressure in a dry spot depends on the pressure in the saturated region around the dry spot that affects  $\Delta V$ . If the capillary pressure  $p_c$  is also considered, the resin pressure  $p$  in the saturated region around the dry spot is calculated as

$$p = p_a - p_c = R \frac{m_a T}{V_0 - \Delta V} - p_c \quad (8.103)$$

Equations (8.94) and (8.95) can be manipulated and integrated over a control volume:

$$\int_V \operatorname{div}(\vec{u}) dV = \oint_A \vec{u} \cdot \vec{n} dA = - \oint_A [n_x, n_y, n_z] \frac{1}{\mu} \begin{bmatrix} k_{xx} & k_{xy} & k_{xz} \\ k_{xy} & k_{yy} & k_{yz} \\ k_{xz} & k_{yz} & k_{zz} \end{bmatrix} \begin{Bmatrix} \frac{\partial p}{\partial x} \\ \frac{\partial p}{\partial y} \\ \frac{\partial p}{\partial z} \end{Bmatrix} dA = 0 \quad (8.104)$$

where  $n_x$ ,  $n_y$ , and  $n_z$  are the components of the vector normal to the surface  $A$  of the control volume  $V$ .

Equation (8.104) is the mass balance equation for solving the problems of flow through an anisotropic porous preform. The mold filling can be regarded as a quasi-steady-state process by assuming a steady-state condition at each time step during computer simulation. In other words, the problem may be solved by considering the transient solution to be a sequence of steady-state solutions separated by many small time increments.

One of the feasible methods for the liquid molding process is the control volume approach, in which the entire calculation domain is divided into a number of elements. The control volume is formed on the nodes of adjacent elements.

Boundaries of the flow domain in mold filling include the mold walls, inlets, and flow front. At the mold walls there is no flow in the direction normal to the wall, which means that the first derivative of pressure normal to the wall is zero. For the case of specified injecting flow rate, a specified flow rate (i.e., a source) is assigned to the control volumes enclosing the inlet nodes. For the case of specified injecting pressure, a specified pressure is assigned to the inlet nodes. At the flow front, a parameter  $S$ , which is the degree of saturation in equation (8.6), is used to represent the status of each control volume in the flow domain. If the control volume is empty,  $S$  is equal to zero. If the control volume is completely filled with resin,  $S$  is equal to one. If the control volume is partially filled,  $S$  is equal to the volume fraction of the resin occupying the void volume of control volume. The node pressures in

the partially filled flow front control volumes are set to zero. With the boundary conditions, then the set of linear algebraic equations can be developed.

At the beginning of mold filling, the control volumes enclosing the inlet nodes are assumed to be filled with resin. Then, the pressures of the nodes filled with resin are calculated using the given boundary conditions. For the specified flow rate, the pressures at the inlet nodes are assumed to be the same, and they are calculated to give the specified flow rate. For the specified pressure, the pressure at the inlet nodes is already known. After the pressure field is determined, the velocity field is calculated using Darcy's law in equation (8.1). For a selected time increment, the resin volume change of each flow front control volume is calculated to update the value of  $S$ . If the total resin volume in a control volume is equal to the void volume of the control volume, the control volume is considered full with  $S = 1.0$ . The new flow front in each time step can be estimated according to the velocity vector in the flow front and the time increment after the pressure is determined. After the value of  $S$  is updated, another pressure computation is performed until all the control volumes have  $S = 1.0$ .

## 8.6 Compression Molding

Compression molding has been used for molding thermosetting materials such as phenolic powders and rubber compounds (Mallick, 1990). However, it was used much, compared with the injection molding process, until the development of high-strength sheet molding compound (SMC), explained in section 2.5.2. With the greater emphasis on the mass production of composite materials, compression molding is now widely used to produce bath tubs, dishwashers, refrigerators, air conditioners and automotive components to replace porcelainized and painted steel.

In recent years, process developments such as charge preheating, vacuum-assisted molding, and in-mold coating have occurred to improve either productivity or the quality of compression-molded parts. The in-mold coating is used to mask the surface defects in a molded part, such as surface waviness, porosity due to entrapment, and sink marks that appear on the surface of a molded part directly opposite to the location of ribs and bosses, as shown in figure 8.13 (Mallick, 1988). In the in-mold coating, the mold is opened a small amount (0.2–0.5 mm) part way through the molding cycle and a flexible coating of a polyester or a polyester–urethane hybrid is injected to cover the entire surface. Then the mold is reclosed and restored to the curing operation with the normal molding pressure.

The flow of SMC in the mold is a complex phenomenon. It determines the extent of cavity filling and influences the fiber orientation, fiber distribution,

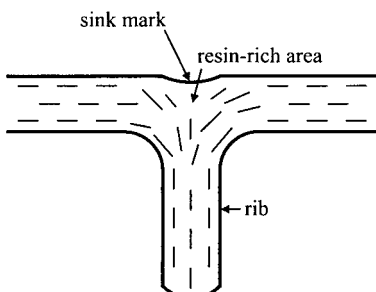


**Figure 8.13** Schematic representation of sink marks in the surface of a compression molded part.

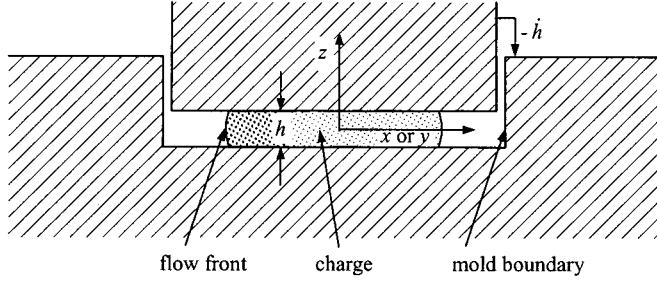


**Figure 8.14** Schematic drawing of mold flow in compression molding.

porosity, and surface defects in a molded part. The flow of SMC was investigated with the following assumptions (Lee et al., 1984):

1. SMC is an incompressible, isotropic, Newtonian fluid under the molding conditions used.
2. Nonslip conditions hold at the mold surfaces of  $z = \pm h/2$  in figure 8.14.
3. The dominant stresses are the transverse shear stresses across the narrow gap between the mold surfaces and the in-plane stresses (in  $x, y$ -plane) are negligible.

Based on these assumptions, the average velocities  $\bar{u}$ , and  $\bar{v}$  in the  $x$ - and  $y$ -directions are expressed as

$$\bar{u} = -\frac{h^2}{12\mu} \left( \frac{\partial p}{\partial x} \right) \quad (8.105)$$

$$\bar{v} = -\frac{h^2}{12\mu} \left( \frac{\partial p}{\partial y} \right) \quad (8.106)$$

where  $p$ ,  $\mu$ , and  $h(t)$  represent the pressure, viscosity, and charge thickness at time  $t$ , respectively.

The velocity  $w$  in the  $z$ -direction is expressed as

$$w = -\frac{w_0}{h(t)} z - \frac{w_0}{2} \quad (8.107)$$

where  $w_0 (= |\dot{h}(t)|)$  represents the mold closing speed (assumed to be constant) and  $z$  is the vertical coordinate measured from the midplane of the SMC.

The continuity equation in terms of the average velocity components for an incompressible fluid is expressed as

$$\frac{\partial \bar{u}}{\partial x} + \frac{\partial \bar{v}}{\partial y} + \frac{\partial \bar{w}}{\partial z} = 0 \quad (8.108)$$

Substituting equations (8.105)–(8.107) into equation (8.108), we obtain the pressure distribution in the SMC:

$$\frac{\partial^2 p}{\partial x^2} + \frac{\partial^2 p}{\partial y^2} = -\frac{12\mu w_0}{h^3} \quad (8.109)$$

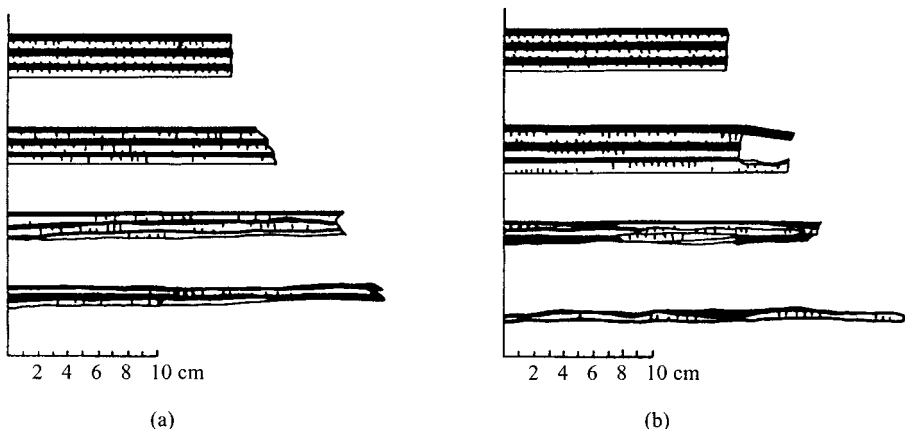


**Figure 8.15** Stages of deformation for six-layered charges: (a) Fast mold closing speed of 10 mm/s; (b) slow mold closing speed of 1.75 mm/s (from Barone and Caulk, 1985).

Equation (8.109) is the generalized Hele-Shaw model, which can be solved using either the finite difference method, finite element method, or boundary element method. If the pressure distribution is known, the velocity field can be determined from equations (8.105)–(8.107). However, the above method did not predict well the experimental results performed by Barone and Caulk (1985). Barone and Caulk used several charges of different thickness in a larger cavity with two different mold closing speeds of 1.75 and 10 mm/s. The thickness of the uncured SMC was approximately 5 mm, and it contained randomly oriented chopped fibers 25 mm long. They found two important phenomena from the experimental charge deformations, as shown in figure 8.15.

1. At the faster mold closing speed, all layers in a charge extend uniformly, with slip occurring only at the mold surface.
2. At the slower mold closing speed, the flow pattern depends on the charge thickness. For a charge five or six layers thick, the surface layers adjacent to the hot mold surfaces undergo a greater extensional deformation than the interior layers. However, as the charge thickness is reduced to three layers, the flow pattern becomes uniform, with no relative motion between the layers. For both thick and thin charges, slip occurs at the mold surface. For thick charges, slip also occurs between the surfaces of interior layers at slow molding speeds.

Barone and Caulk (1986) analyzed the experimental results of figure 8.15 for the mold flow of SMC during compression molding. With the assumption of in-plane flow, the velocity components  $u$ ,  $v$ , and  $w$  in the  $x$ -,  $y$ -, and  $z$ -directions are expressed as

$$u = u(x, y, t) \quad (8.110)$$

$$v = v(x, y, t) \quad (8.111)$$

$$w = -\frac{w_0}{h}z - \frac{w_0}{2} \quad (8.112)$$

Neglecting inertia terms, the equilibrium equations for the SMC are

$$\frac{\partial \Sigma_{ij}}{\partial x_j} = 0 \quad (8.113)$$

The stresses  $\Sigma_{ij}$  from the Newtonian incompressible fluid are

$$\Sigma_{ij} = -p\delta_{ij} + \sigma_{ij} \quad (8.114)$$

The shear stresses  $\sigma_{ij}$  are expressed as (Yih, 1977)

$$\sigma_{ij} = \mu \left( \frac{\partial u_i}{\partial x_j} + \frac{\partial u_j}{\partial x_i} \right) \quad (8.115)$$

Substituting equations (8.114) into equations (8.113) yields

$$\frac{\partial}{\partial x}(-p + \sigma_{xx}) + \frac{\partial \tau_{xy}}{\partial y} + \frac{\partial \tau_{xz}}{\partial z} = 0 \quad (8.116)$$

$$\frac{\partial \tau_{xy}}{\partial x} + \frac{\partial}{\partial y}(-p + \sigma_{yy}) + \frac{\partial \tau_{yz}}{\partial z} = 0 \quad (8.117)$$

$$\frac{\partial \tau_{xz}}{\partial x} + \frac{\partial \tau_{yz}}{\partial y} + \frac{\partial}{\partial z}(-p + \sigma_{zz}) = 0 \quad (8.118)$$

Integrating equation (8.118) through thickness yields

$$\frac{\partial}{\partial x} \left[ \int_{-\frac{h}{2}}^{\frac{h}{2}} \tau_{xz} dz \right] + \frac{\partial}{\partial y} \left[ \int_{-\frac{h}{2}}^{\frac{h}{2}} \tau_{yz} dz \right] + [-p + \sigma_{zz}]_{-\frac{h}{2}}^{\frac{h}{2}} = 0 \quad (8.119)$$

The above equation is automatically satisfied due to the symmetry of the problem. Integrating equations (8.116) and (8.117) yields

$$-\frac{\partial}{\partial x} \left[ \int_{-\frac{h}{2}}^{\frac{h}{2}} pdz \right] + \frac{\partial}{\partial x} \left[ \int_{-\frac{h}{2}}^{\frac{h}{2}} \sigma_{xx} dz \right] + \frac{\partial}{\partial y} \left[ \int_{-\frac{h}{2}}^{\frac{h}{2}} \tau_{xy} dz \right] + [\tau_{xz}]_{-\frac{h}{2}}^{\frac{h}{2}} = 0 \quad (8.120)$$

$$\frac{\partial}{\partial x} \left[ \int_{-\frac{h}{2}}^{\frac{h}{2}} \tau_{xy} dz \right] - \frac{\partial}{\partial y} \left[ \int_{-\frac{h}{2}}^{\frac{h}{2}} pdz \right] + \frac{\partial}{\partial y} \left[ \int_{-\frac{h}{2}}^{\frac{h}{2}} \sigma_{yy} dz \right] + [\tau_{yz}]_{-\frac{h}{2}}^{\frac{h}{2}} = 0 \quad (8.121)$$

In order to simplify the above equations, several notations were defined and used by Barone and Caulk (1986):

$$P = \int_{-\frac{h}{2}}^{\frac{h}{2}} pdz \quad (8.122)$$

$$\eta_{xx} = \int_{-\frac{h}{2}}^{\frac{h}{2}} \sigma_{xx} dz \quad (8.123)$$

$$\eta_{xy} = \int_{-\frac{h}{2}}^{\frac{h}{2}} \tau_{xy} dz \quad (8.124)$$

$$\eta_{yy} = \int_{-\frac{h}{2}}^{\frac{h}{2}} \sigma_{yy} dz \quad (8.125)$$

$$f_x = \tau_{xz}|_{z=\frac{h}{2}} = -\tau_{xz}|_{z=-\frac{h}{2}} \quad (8.126)$$

$$f_y = \tau_{yz}|_{z=\frac{h}{2}} = -\tau_{yz}|_{z=-\frac{h}{2}} \quad (8.127)$$

Then equations (8.120) and (8.121) become

$$-\frac{\partial P}{\partial x} + \frac{\partial \eta_{xx}}{\partial x} + \frac{\partial \eta_{xy}}{\partial y} + 2f_x = 0 \quad (8.128)$$

$$\frac{\partial \eta_{xy}}{\partial x} - \frac{\partial P}{\partial y} + \frac{\partial \eta_{yy}}{\partial y} + 2f_y = 0 \quad (8.129)$$

If the in-plane deformation does not significantly alter the random orientation of fibers, then the two-dimensional stress resultant  $\eta_{\alpha\beta}$  can be expressed as

$$\eta_{\alpha\beta} = 2\zeta h \dot{\gamma}_{\alpha\beta} \quad (8.130)$$

where the two-dimensional rate of deformation  $\dot{\gamma}_{\alpha\beta}$  of SMC is expressed as

$$\dot{\gamma}_{\alpha\beta} = \frac{1}{2} \left( \frac{\partial u_\alpha}{\partial x_\beta} + \frac{\partial u_\beta}{\partial x_\alpha} \right) (\alpha, \beta = x, y) \quad (8.131)$$

In equation (8.130),  $\zeta$  has the property of average viscosity in the  $z$ -direction.

Substituting equations (8.130) and (8.131) into equations (8.128) and (8.129) yields

$$-\frac{\partial P}{\partial x} + \zeta h \left( \frac{\partial^2 u}{\partial x^2} + \frac{\partial^2 u}{\partial y^2} \right) - 2k_H u = 0 \quad (8.132)$$

$$-\frac{\partial P}{\partial y} + \zeta h \left( \frac{\partial^2 v}{\partial x^2} + \frac{\partial^2 v}{\partial y^2} \right) - 2k_H v = 0 \quad (8.133)$$

where the coefficient of hydrodynamic friction  $k_H$  is defined as

$$f_\alpha = -k_H u_\alpha \quad (8.134)$$

For the derivation of equation (8.132), the following equality was used, assuming  $w = w_0 = \text{constant}$ ,

$$\begin{aligned}
 \frac{\partial \eta_{xx}}{\partial x} + \frac{\partial \eta_{xy}}{\partial y} &= \xi h \left( \frac{\partial^2 u}{\partial x^2} + \frac{\partial^2 u}{\partial y^2} + \frac{\partial^2 u}{\partial x^2} + \frac{\partial^2 v}{\partial x \partial y} \right) \\
 &= \xi h \left[ \frac{\partial^2 u}{\partial x^2} + \frac{\partial^2 u}{\partial y^2} + \frac{\partial}{\partial x} \left( \frac{\partial u}{\partial x} + \frac{\partial v}{\partial y} \right) \right] \\
 &= \xi h \left[ \frac{\partial^2 u}{\partial x^2} + \frac{\partial^2 u}{\partial y^2} + \frac{\partial}{\partial x} \left( \frac{w_0}{h} \right) \right] \\
 &= \xi h \left( \frac{\partial^2 u}{\partial x^2} + \frac{\partial^2 u}{\partial y^2} \right)
 \end{aligned} \tag{8.135}$$

The same equality was used to derive equation (8.133).

Differentiating equation (8.132) with respect to  $x$  and equation (8.133) with respect to  $y$ , then adding the resultant two equations results in

$$\frac{\partial^2 P}{\partial x^2} + \frac{\partial^2 P}{\partial y^2} = \xi h \left( \frac{\partial^3 u}{\partial x^3} + \frac{\partial^3 u}{\partial x \partial y^2} + \frac{\partial^3 v}{\partial x^2 \partial y} + \frac{\partial^3 v}{\partial y^3} \right) - 2k_H \left( \frac{w_0}{h} \right) \tag{8.136}$$

The first term on the right-hand side of equation (8.136) represents the resistance of the material to extensional deformation, and the second term represents the frictional resistance generated by the slip of the SMC surface layer at the mold surface.

For a thin charge with negligible resistance of material, equation (8.136) reduces to a simpler form:

$$\frac{\partial^2 P}{\partial x^2} + \frac{\partial^2 P}{\partial y^2} = -2k_H \left( \frac{w_0}{h} \right) \tag{8.137}$$

Although equations (8.109) and (8.137) are similar, the mechanism of the right-hand side is much different. In equation (8.109), the right-hand side represents the resistance to transverse shear deformations, while in equation (8.137) it represents the hydrodynamic frictional resistance at the molded surfaces. With the nonslip condition assumed in equation (8.109), the velocity profile is parabolic through the charge thickness, as shown in figure 8.16(a). Since the slip is allowed in equation (8.137), the velocity profile becomes more uniform, as shown in figure 8.16(b). Equation (8.137) predicts the experimental phenomena of figure 8.15.

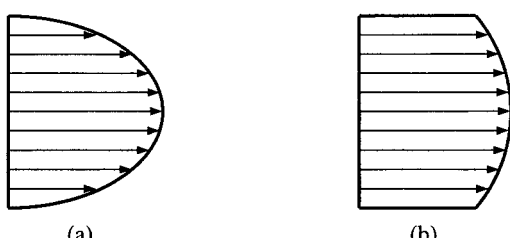


**Figure 8.16** Velocity profile through the thickness of a charge with (a) no slip at the mold wall; (b) slip allowed at the mold wall.

## 8.7 Continuous Molding Process

### 8.7.1 Filament Winding Process

In filament winding, as shown in figure 2.36, a continuous filamentary yarn, tow, or roving is first wetted with a resin and then uniformly and regularly wound about a rotating mandrel, which is termed wet winding. Alternatively, in dry winding, preimpregnated reinforcements, usually in tape form, are used. Wet winding is more flexible and cheaper but is not a clean process, unlike dry winding.

The major advantages of the filament winding process over other composite material fabrication methods are its low material and labor costs and its reproducibility due to automation using computer-controlled machines. The automated machines have the ability to rapidly change the winding patterns and to place accurately the fiber on the mandrel through eyelet manipulators. Computer-controlled machines have six degrees of freedom coupled with path smoothing options, acceleration controls, and independent yarn tension control. Also, most of the patterns and parameters can be determined in advance with off-line program development.

The major disadvantages of the filament winding process are the tooling limitation for the removable mandrel and the inability to wind on negatively curved (concave) surfaces.

Mass production for filament winding is somewhat different from mass production for other manufacturing modes. While compression or injection molding may produce thousands or more per day, the filament winding process can produce hundreds per day per machine station. Winding speeds are limited to about 61–122 m/min (200–400 ft/min), which is a practical limitation of the fiber's ability to thoroughly wet resin to all its filament surfaces (Kliger and Wilson, 1990).

The filament winding processes are used to produce pipes, pressure vessels, missile launch tubes and motor cases, automotive leaf springs and propeller shafts, and composite journal bearings.

The most commonly used resins are thermoset polyesters, vinyl esters, epoxies, and phenolics. Typical fibers are glass, carbon, and aramid. The fibers are used in several different forms:

1. *Tow*: an untwisted bundle of continuous filaments consisting of  $1.0 \times 10^3$ – $1.6 \times 10^5$  parallel filaments. A tow designated as 140 k has  $140 \times 10^3$  filaments.
2. *Yarn*: an assemblage of twisted filaments that is suitable for use in weaving into textile materials.
3. *Roving*: a number of yarns, strands, or tows, collected into a parallel bundle with little or without twist.

The filament winding process can generally be classified as helical and polar winding, as shown in figure 8.17.

In helical winding, the fiber band is fed from a translating carriage onto a rotating mandrel. The winding angle  $\phi$  is specified by the ratio of the two relative motions:

$$\tan \phi = \frac{2\pi r N}{V} \quad (8.138)$$

where  $N$  is the rotational speed (rpm),  $V$  is the speed of carriage (m/min), and  $r$  is the radius of the current winding.

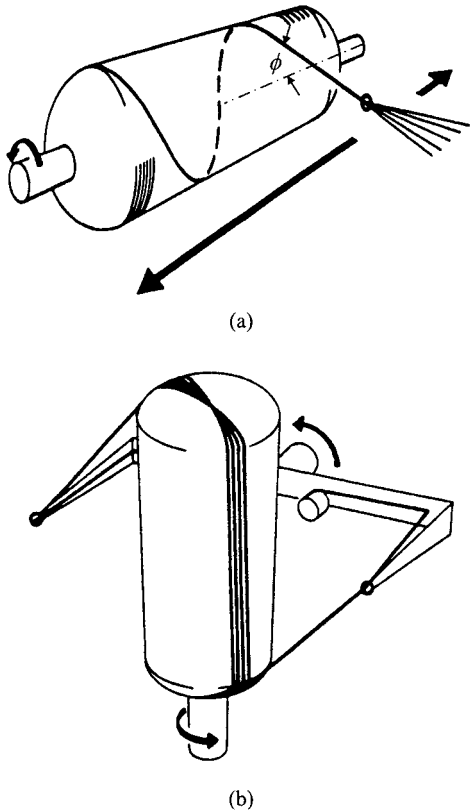


**Figure 8.17** Filament winding processes:  
(a) Helical winding; (b) polar winding.

The two motions should be precisely synchronized for uniform winding angle, because as the translating carriage reaches the end of the mandrel, it will slow down, dwell, and reverse direction, continuing to wind fiber onto the mandrel with a negative angle. If the winding mandrel is tapered or irregular, the angles and thicknesses will vary accordingly.

Although the helical winding process can produce various aspect ratios (length/diameter) of shafts, it is well suited for long slender geometries such as pressure pipe and launch tubes, where winding angles are in the range 20–90° from the shaft axis. Most pressure pipes are wound at 54.74°, which assumes a 2:1 (hoop to longitudinal) stress field in a cylindrical capped pressure vessel (see example 4.3).

In helical winding large structures, mandrel deflection and weight are critical, particularly sand and plaster units. The inertia of the mandrel often limits winding speed. Also, very low angles ranging 0–10° are usually avoided in helically wound parts with large length-to-diameter ratios.

Contrary to helical winding, polar winding favors very low winding angles. The mandrel is usually vertical and supported at the base. Since the fiber is wound in a plane intersecting the mandrel ends, the angle must be less than about 20°. Typically, polar angles are 5–15°.

In racetrack polar winding, the fiber delivery system rotates in a single plane or racetrack, as shown in figure 8.18, with either horizontal or vertical motion, while the mandrel is incrementally rotated.

During filament winding processing, the fibers may move, causing a change in fiber tension and in fiber position. Springer (1997) analyzed the fiber movement and

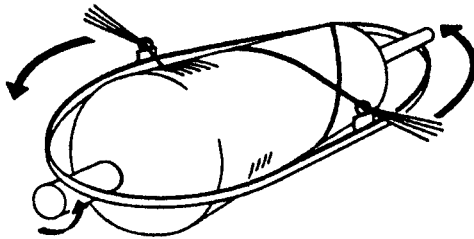


**Figure 8.18** Schematic diagram of racetrack polar winding.

fiber tension change with assumption of constant fiber winding angle. The radial position change of the fiber sheet has been considered because fiber tension in the curved fibers causes the fibers to move through the resin.

The stress  $\sigma_f$  in the direction of the fibers is

$$\sigma_f = \frac{F}{A_f} \quad (8.139)$$

where  $F$  is the instantaneous fiber tension and  $A_f$  is the cross-sectional area of the fiber sheet. The circumferential component of the fiber tension  $\sigma_\theta$  is

$$\sigma_\theta = \sigma_f \sin^2 \phi \quad (8.140)$$

where  $\phi$  is the fiber winding angle in figure 8.17(a).

The pressure difference  $\Delta p$  across a fiber sheet thickness  $\Delta\xi$  at the fiber radial position  $r_f$  is given by force equilibrium shown in figure 8.19.

$$\frac{\Delta p}{\Delta\xi} = \frac{dp}{dr} = \frac{\sigma_\theta}{r_f} \quad (8.141)$$

The radial resin flow velocity  $u_f$  through the fiber sheet thickness, which is the relative velocity between the fiber and the resin, is described by Darcy's law of equation (8.1) as

$$u_f = -\frac{k_{rr}}{\mu} \frac{dp}{dr} \quad (8.142)$$

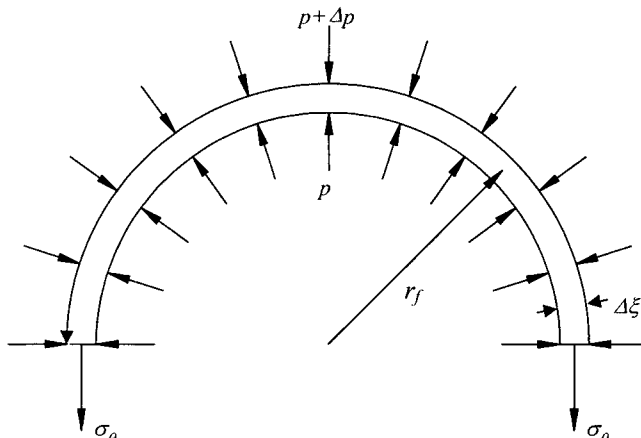


**Figure 8.19** Force equilibrium of a fiber sheet during filament winding.

Then the change of fiber position  $\Delta r_f$  during a small time step  $\Delta t$  is

$$\Delta r_f = -\frac{k_{rr}}{\mu} \frac{\sigma_f \Delta t}{r_f} \sin^2 \phi \quad (8.143)$$

The change of hoop strain in the fiber band  $\Delta \varepsilon_{f\theta}$  is

$$\Delta \varepsilon_{f\theta} = \frac{\Delta r_f}{r_f} \sin^2 \phi = \frac{\Delta L_f}{L_f} \sin^2 \phi \quad (8.144)$$

where  $\Delta L_f$  and  $L_f$  are the elongation and the original length of the fiber sheet, respectively.

The change in fiber stress corresponding to the change in strain  $\Delta \varepsilon_{f\theta}$  is

$$\Delta \sigma_f = \sigma_f^{t+\Delta t} - \sigma_f^t = E_f \Delta \varepsilon_{f\theta} \quad (8.145)$$

where  $E_f$  is the longitudinal fiber modulus. Combining equations (8.143)–(8.145) gives the fiber stress at time  $t + \Delta t$ :

$$\sigma_f^{t+\Delta t} = \sigma_f^t \left( 1 - \frac{E_f k_r \Delta t \sin^4 \phi}{\mu r_f^2} \right) \quad (8.146)$$

Solutions to equations (8.143)–(8.146) give the fiber position and fiber stress (fiber tension) at time  $t + \Delta t$ . The corresponding initial conditions at  $t = t_0$  are that the radial displacement is zero and the fiber stress is  $\sigma_f^0$ :

$$\Delta r_f = 0 \quad (8.147a)$$

$$\sigma_f = \sigma_f^0 = \frac{F_0}{A_f} \quad (8.147b)$$

where  $A_f$  is the cross-sectional area of the fiber sheet.  $A_f$  is expressed as

$$A_f = V_f A = V_f b \Delta \xi \quad (8.148)$$

where  $A$  is the cross-sectional area of the entire layer (resin + fiber sheet),  $b$  is the width of the fiber band, and  $\Delta \xi$  is the thickness of composite section.

Controlling fiber tension in filament winding has been key to optimum performance of the resulting composite structure. Yarn tension levels of between 4.5 and 18.0 N (1.0–4.0 lb) have typically been applied to helical and polar windings. Hoop windings generally use a higher tension of 27.0–36.0 N (6.0–8.0 lb) to provide a compaction layer for the structure. Servo-based tensioners are common today, but early tensioning technology relied on a spring-loaded rotary motion take-up.

### 8.7.2 Pultrusion Process

Pultrusion (pull + extrusion) is a continuous manufacturing process used to produce high-fiber-content fiber-reinforced plastic structural shapes. In the pultrusion process, fiber reinforcements that have been impregnated with resin that contains other additives are pulled through a heated die. This is to be compared with the extrusion process in which heated material is pushed through a die. The pultrusion

process is a process that combines the preforming reinforcing material, impregnating the preform with resin, and curing the wetted preform into a solid laminate, as shown in figure 2.38. Pultrusion is distinct from the hoop filament winding in that the latter places the primary reinforcement in the circumferential (hoop) direction, while pultrusion has the primary reinforcement in the longitudinal direction (Smith and Stone, 1990).

The pultrusion process can produce solid, open-sided, and hollow shapes, which can be cut to length and packaged for shipment. The pultrusion process is continuous, manufacturing from 2.0 m/h to 200 m/h depending on the part complexity, and resin viscosity. The most important factor controlling the mechanical performance of a pultruded member is the fiber wet-out. The ability to wet out fibers with resin depends on the initial resin viscosity, residence time in the bath, bath temperature, and mechanical action applied to fibers in the bath (Mallick, 1988). For a given resin viscosity, the degree of wet-out is improved as (1) the residence time is prolonged by using slower line speeds or longer baths, (2) the resin bath temperature is increased, which reduces the resin viscosity, or (3) the degree of mechanical working on fibers is increased. Since each roving pulled through the resin bath contains a large number of fiber bundles, it is extremely important that the resin penetrates inside the roving and coats each bundle uniformly. Resin penetration takes place through capillary action, as well as lateral squeezing between the bundles. Lateral pressure at the resin squeeze-out bushings located at the resin bath exit, preformers, and die entrance also improves the resin penetration.

The pultrusion machine may be utilized 24 hours a day, 7 days a week, with the only scheduled stoppage required being to perform routine cleaning, perhaps once every 2 weeks.

The curing reaction continues at an increasing rate as the fiber-resin stream moves toward the exit end of the die. Heat generated by the exothermic curing reaction raises the temperature in the fiber-resin stream. The location of the exothermic peak depends on the speed of pulling the fiber-resin stream through the die, as shown in figure 8.20 (Sumerak, 1997). As the curing reaction nears completion, the exotherm temperature decreases and a cooling period begins. The

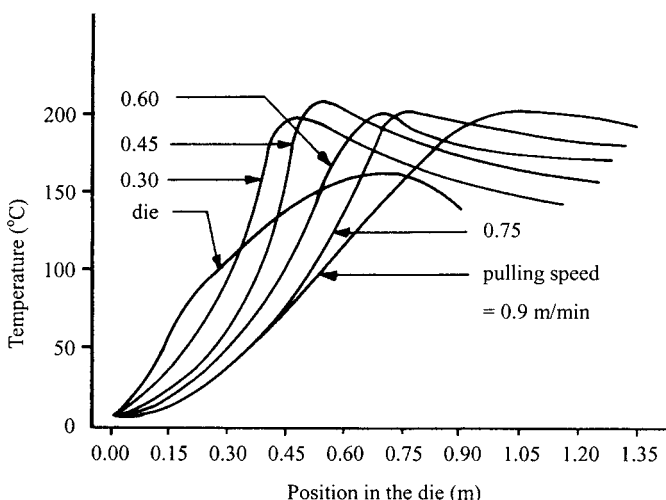


**Figure 8.20** Temperature distributions along the length of a pultrusion die (from Sumerak and Martin, 1986).

rate of heat transfer from the cured material into the die walls is increasing, owing to a lower die temperature near the exit zone. If the temperature in the interior of the cured section remains high at the time of exit from the die, interlaminar cracks may form within the pultruded member.

Although generally, no pressure is applied in a pultrusion process, the pressure in the die entrance zone is in the range 1.7–8.6 MPa (250–1250 psi) (Sumerak and Martin, 1986). The principal source for such high internal pressure is the volumetric expansion of the resin as it is heated in the die entrance zone. Hence, the pressure generated is much dependent on the preform construction and fiber packing in the die. This is particularly true in the curing of epoxies where fiber and filler volume fraction must be kept high to prevent sloughing, or resin adhesion to die surfaces, and maintain good surface finish.

As the curing reaction begins, the polymerization shrinkage reduces the pressure to near-zero values at approximately the midlength of the die. In general, the internal pressure can be increased by controlling the resin chemistry and the fiber volume fraction. Although increasing the internal pressure may also result in a higher pulling force, it will improve fiber-resin consolidation in the pultruded section.

Sumerak and Martin (1984) proposed five sources contributing to total pulling force: (1) hydraulic entrance effects, (2) thermal expansion of the liquid phase, (3) thermal expansion and contraction of the gel and solid phase, (4) volumetric packing factors, and (5) die surface and geometry factors. They divided the die into three distinct regions. The three phases contribute to the total pulling force, as expressed by the following equation:

$$F_{\text{total}} = F_{\text{liquid}} + F_{\text{gel}} + F_{\text{solid}} \quad (8.149)$$

The three components of the pulling force in equation (8.149) were estimated as

$$F_{\text{liquid}} \propto \left( \frac{\mu A_l C_s}{T u} \right) p_0 \alpha T \quad (8.150)$$

$$F_{\text{gel}} \propto f_g A_g p_0 \alpha T \quad (8.151)$$

$$F_{\text{solid}} \propto f_s p_0 \frac{T}{S} \quad (8.152)$$

where  $\mu$  = resin viscosity

$A_l$  = surface area of liquid phase

$C_s$  = consolidation (packing) fraction

$p_0$  = initial pressure due to volumetric consolidation

$u$  = line speed

$\alpha$  = coefficient of thermal expansion

$f_g$  = coefficient of friction of the gel phase

$A_g$  = surface area of gel phase

$f_s$  = coefficient of friction of solid phase

$S$  = degree of shrinkage

$T$  = temperature

Although the above equations are only qualitative, they contain insight into the effect of process variables on machine loads.

## 8.8 Autoclave Molding with Cooling and Reheating Cycles

During the cure of thick composite laminates, temperature overshoot may be considerable, which degrades the properties of cured laminates. Kim and Lee (1997) devised an autoclave cure cycle with cooling and reheating for thick thermosetting resin matrix composite materials to reduce the temperature overshoot. Figure 8.21 shows the effect of thickness on the midpoint temperature of carbon-fiber epoxy composite laminates (T300/5208), cured by the conventional cure cycle recommended by the prepreg manufacturer. Since degradation of the polymer can occur if the cure temperature is above the glass transition temperature of the fully cured resin ( $T_{g\infty}$ ), the temperature in the laminate should not exceed  $T_{g\infty}$ . The glass transition temperature  $T_{g\infty}$  of the resin in figure 8.21 was 140°C. The laminates composed of more than 50 plies (1 ply thickness = 0.15 mm) would be degraded because the maximum midpoint temperature exceeded  $T_{g\infty}$  (140°C).

Cooling and reheating steps were introduced into the conventional cure cycle to prevent the temperature overshoot of thick laminates. Two important specific variables chosen to control the thermal overshoot are the cure rate ( $d\alpha_m/dt$ ) and temperature ( $T_m$ ) of midpoint of the laminate because the state of the exothermic reaction is directly related to  $d\alpha_m/dt$  and  $T_m$  is related to the thermal overshoot. Using the variables, an autoclave cure cycle, which could maintain the midpoint temperature within the temperature limit range (120–125°C), was devised.

In this system, once the range of temperature limit, laminate thickness and material properties are set, the cure cycle with cooling and reheating steps is automatically generated by simulation method. The systematic procedure is shown below.

### 8.8.1 Cooling Step

When the exothermic reaction of resin begins, the autoclave is cooled by turning off the heater power to prevent temperature overshoot. If the autoclave is equipped

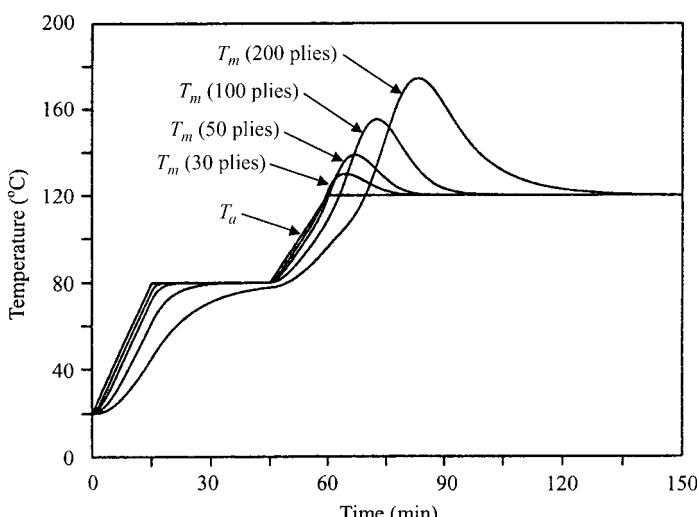


**Figure 8.21** Effect of thickness on the midpoint temperature of T300/5208 carbon epoxy composite laminate (from Kim and Lee, 1997).

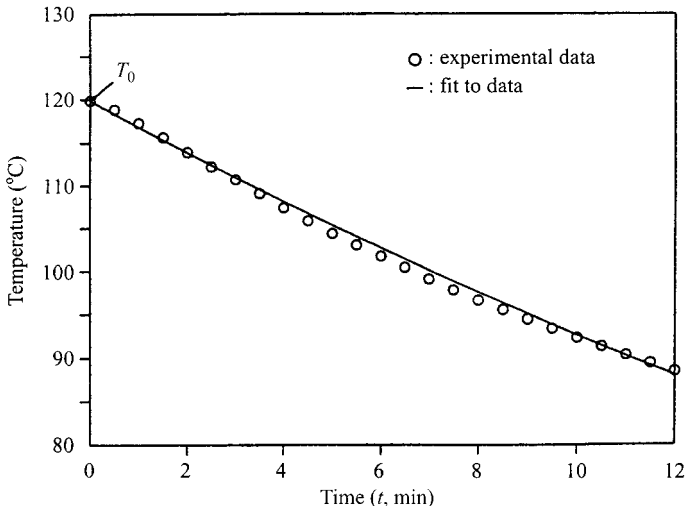


**Figure 8.22** Typical cooling curve of an autoclave when the heater power is turned off (from Kim and Lee 1997).

with a computer controlled cooler, a forced cooling method can be used. To use this method, the cooling behavior must be determined by experiment as shown in figure 8.22. For example, the cooling curve of the autoclave used for this experiment was fitted to the following exponential form:

$$T = T_0 e^{-2.57 \times 10^{-2} t} \quad (8.153)$$

where  $T_0$  is the autoclave temperature at the start of cooling and  $t$  is the elapsed time.

The start point of cooling is set by a certain value of  $d\alpha_m/dt$ , the rate of degree of cure at the midpoint of the laminate (e.g.,  $d\alpha_m/dt = 1.62 \times 10^{-4}/\text{s}$  was the starting point of cooling for the example in this section), because the rate of exothermic reaction can be estimated by the cure rate at the midpoint of the laminate where the cooling effect is smaller than that of the surfaces. Even if the autoclave is cooled at certain values of  $d\alpha_m/dt$  during the initial exothermic reaction, the midpoint temperature  $T_m$  still may increase for a while due to the heat generated from the reaction. Then it decreases due to the cooling effect after reaching a maximum value. In this case, the maximum temperature  $T_m$  is limited to 125°C and a value of  $d\alpha_m/dt$  is chosen as the start point of cooling. The value of  $d\alpha_m/dt$  can be calculated from equations (8.26)–(8.35) and equation (8.153). The cooling step ends as  $T_m$  reaches the maximum value.

### 8.8.2 Reheating Step

When the midpoint temperature  $T_m$  reaches the limit temperature (125°C) and starts to decrease, moderate reheating is necessary to maintain  $T_m$  within a given temperature range. In this case, the exothermic reaction, which is suppressed by cooling, slowly resumes the process so that the thermal overshoot can be avoided. The reheating rate of the autoclave was selected to maintain  $T_m$  between the cure temperature (120°C) and the limit temperature (125°C) in this example. When the

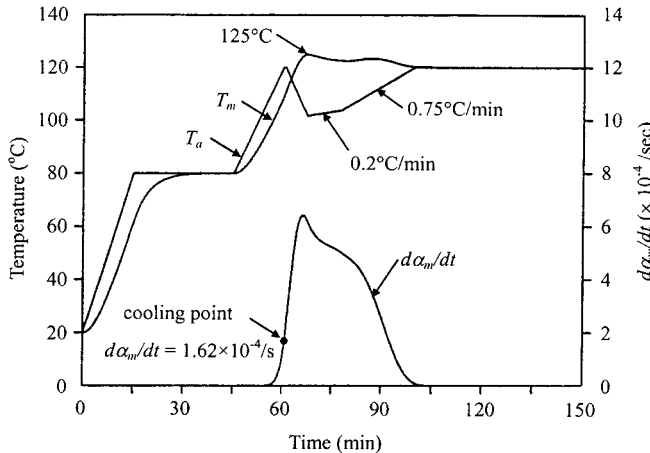


**Figure 8.23** Autoclave cure cycle for the 100-ply (15 mm) carbon epoxy laminate determined from the simulation with cooling and reheating steps (from Kim and Lee, 1997).

autoclave temperature  $T_a$  reaches the cure temperature ( $120^{\circ}\text{C}$ ) during the reheating operation, the reheating step ends and most of the cure reaction of the laminate is almost accomplished.

Figure 8.23 shows the modified autoclave cure cycle for the 100-ply (15 mm thick) laminate determined from the simulation with cooling and reheating steps. The cure rate  $d\alpha_m/dt$  that satisfies the above cooling condition was determined to be  $1.62 \times 10^{-4}/\text{s}$  by the simulation method. The two reheating steps with heating rates of  $0.2^{\circ}\text{C}/\text{min}$  and  $0.75^{\circ}\text{C}/\text{min}$ , which were also determined by the simulation method, were used for the reheating condition. Although the cure rate, reheating rates, and step length were determined with several simulations, it was found that the time required to simulate one cure cycle was only a few minutes with a personal computer. Figure 8.24 shows the experimental temperature profiles of the 100-ply laminate under the modified autoclave cure cycle of figure 8.23. In figure 8.24, there is a little

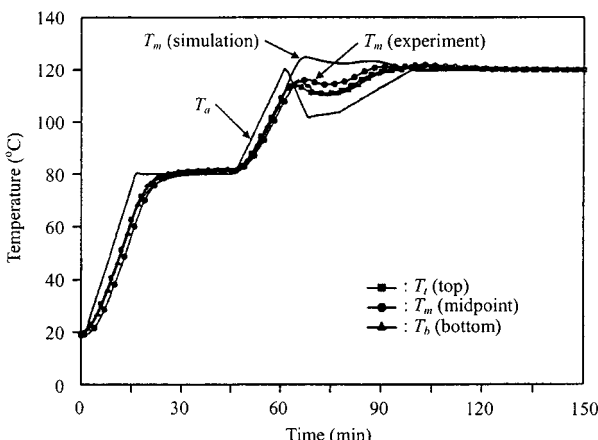


**Figure 8.24** Experimental temperature profiles of the 100-ply (15 mm) carbon epoxy laminate under the autoclave cure cycle of figure 8.23 (from Kim and Lee, 1997). ( $T_a$ : autoclave temperature.)

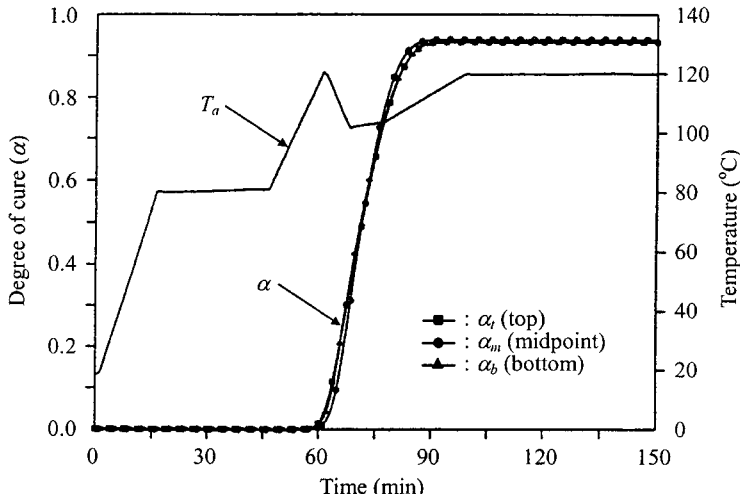
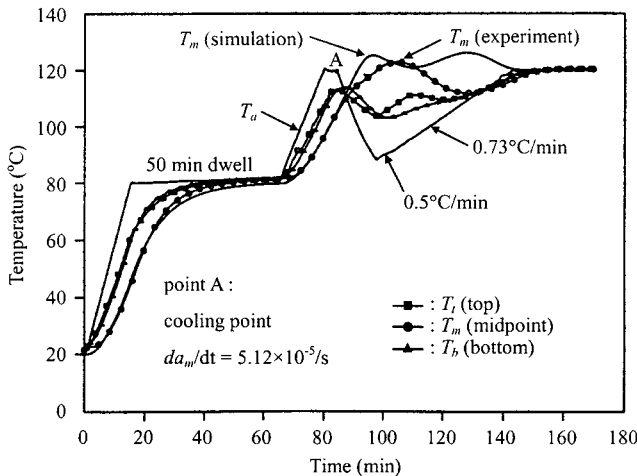


**Figure 8.25** Degree of cure ( $\alpha$ ) profiles of the 100-ply (15 mm) carbon epoxy laminate calculated from the temperature profiles of figure 8.23 (from Kim and Lee, 1997).

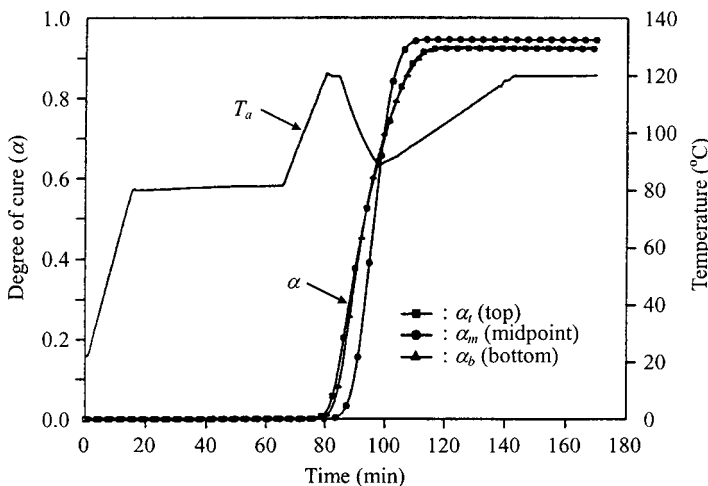
discrepancy between the experimental temperature profile at the midpoint of the laminate and the simulation result due to the error in the simulation. Also, the excess resin squeezed out of the laminate during the cure process would reduce heat generation so that the experimental temperature would be less than the simulated one. In figure 8.24, the temperature profiles at the top and bottom surfaces of the laminate were also measured to investigate the effect of surface cooling of laminate. Although the top and bottom surfaces are easier to cool than the center, it was found that they were relatively well cured by the heat generated from the exothermic reaction of the laminate. This was verified by the degree of cure profiles of the laminate calculated from the measured temperature profiles, as shown in figure 8.25. In figure 8.25,  $\alpha_t$  and  $\alpha_b$  represent the degrees of cure on the top and bottom surfaces of the laminate, respectively, and  $\alpha_m$  represents the degree of cure at the midpoint. Since there was little difference between the degree of cure profiles of the center and surfaces from figure 8.25, it was concluded that the laminate was uniformly cured.

Figure 8.26 shows the experimental temperature profiles of the 200-ply laminate under the autoclave cure cycle in which the cooling started at the cure rate of  $5.12 \times 10^{-5}/\text{s}$  and reheating started with the temperature increase rates of  $0.5^\circ\text{C}/\text{min}$  and  $0.73^\circ\text{C}/\text{min}$ . In this case, a dwell time of 50 min was given to the cure cycle for the consolidation of the laminate. Although the experimental results were different from the simulation results, the devised cure cycle prevented the laminate temperature from overshooting effectively. Figure 8.27 shows the calculated degree-of-cure profiles of the laminate with the temperature profiles of figure 8.26. Since the difference of the final degree of cure between the midpoint and the top or bottom was only about 2% ( $\alpha_m = 0.945$ ,  $\alpha_t = \alpha_b = 0.924$ ), a nearly uniform degree of cure was obtained.

By comparing the results from the conventional cure cycle and the cooling–reheating cure cycle, it was found that the developed cure cycle with the cooling and reheating steps effectively cured the thick composites without increasing the process time.



**Figure 8.26** Experimental temperature profiles of the 200-ply (30 mm) carbon-epoxy laminate under the cure cycle determined by simulation (from Kim and Lee, 1997). ( $T_a$ : autoclave temperature.)



**Figure 8.27** Degree of cure profiles of the 200-ply (30 mm) carbon epoxy laminate calculated from the temperature profiles of figure 8.26 (from Kim and Lee, 1997).

## 8.9 Concluding Remarks

Transport phenomena, such as resin flows through the fiber bed in liquid composite molding process, cure kinetics during cure of thermosetting resin matrix composites, and the temperature distributions and thermal conductivity in the composite structures, have been presented. Cure monitoring by dielectrometry was discussed in detail, because this method is the most efficient method for in-situ monitoring of the cure state of polymeric composites. Also, some current issues in the processing of composite structures such as compression molding, RTM, pultrusion, filament winding, and autoclave molding have been presented.

## Problems

- 8.1.** Derive equation (8.20).
- 8.2.** When the permeability  $k_z$  and viscosity  $\mu$  are not a function of void ratio  $e$ , derive the following equation for  $e$ :
- $$\frac{\partial e}{\partial t} = \frac{k_z \sigma_0}{\mu} \frac{1+e}{e-e_{\min}} \left[ -\frac{1}{e-e_{\min}} \left( \frac{\partial e}{\partial z} \right)^2 + \frac{\partial^2 e}{\partial z^2} \right]$$
- 8.3.** Why is equation (8.22a) valid?
- 8.4.** Derive equation (8.51).
- 8.5.** Derive equation (8.85).
- 8.6.** Derive equation (8.87).
- 8.7.** Complete the derivation of equations (8.105) to (8.109).
- 8.8.** The equilibrium specific moisture concentration in a carbon-fiber epoxy composite with stacking sequence [0/90/ $\pm 45$ ]s and 60%  $V_f$  is given by

$$C_\infty = 1.5 \times 10^{-4} (RH)^{1.8} (\%)$$

and the diffusivity in the thickness direction is  $5 \times 10^{-8} \text{ mm}^2/\text{s}$ . A panel 6.25 mm thick made of this material is exposed on both sides to air with 90% relative humidity at 25°C. The initial specific moisture concentration in the panel is 0.15%.

- (a) Estimate the time required for the specific moisture concentration to increase to 0.39%.
- (b) If the temperature is increased to 130°C on both sides, estimate the time required for the temperature at the center of the panel to increase to 115°C. The specific heat and thermal conductivity and density of the composite in the thickness direction are 0.5 kJ/(kg °C), 0.72 W/(m °C), and 1600 kg/m<sup>3</sup>, respectively. Also compare the rate of the heat conduction with the mass diffusion.
- (c) If the panel is painted on one side with a moisture-impervious material, what would be the specific moisture concentration in the panel at the end of the time period calculated in (a)?
- 8.9.** Derive equation (8.136).
- 8.10.** It has been reported that excessive sloughing occurs during pultrusion of unidirectional glass-fiber epoxy when the fiber volume fraction is less than 64% (Hunter, 1988). What should be done to prevent such sloughing? List at least three methods.

## References

- Advani, S. G., and Sozer, E. M. 2000. "Liquid Molding of Thermoset Composites," in *Comprehensive Composite Materials*, Vol. 2, Edited by Kelly, A., Elsevier, Amsterdam, pp. 807–844.
- Barone, M. R., and Caulk, D. A. 1985. "Kinematics of Flow in SMC," *Polymer Composites*, Vol. 6, pp. 105–109.
- Barone, M. R., and Caulk, D. A. 1986. "A Model for the Flow of a Chopped Fiber Reinforced Polymer Compound in Compression Molding," *Journal of Applied Mechanics*, Vol. 53, pp. 361–371.
- Bowles, J. E. 1988. *Foundation Analysis and Design*, 4th ed., McGraw-Hill, New York, Chapter 2.

- Brown, R. P. 1988. *Handbook of Plastics Test Methods*, 3rd ed., Longman Scientific & Technical, Essex.
- Buchanan, R. C. 1986. *Ceramic Materials for Electronics*, Marcel Dekker, New York.
- Crank, J. 1975. *The Mathematics of Diffusion*, 2nd ed., Oxford University Press, Oxford.
- Dave, R. 1990. "A Unified Approach to Modeling Resin Flow During Composites Processing," *Journal of Composite Materials*, Vol. 24, pp. 22–41.
- Gutowski, T. G., and Dillon, G. 1997. "The Elastic Deformation of Fiber Bundles," in *Advanced Composites Manufacturing*, Edited by Gutowski, T. G., John Wiley & Sons, New York, pp. 115–137.
- Gutowski, T. G., Morigaki, T., and Cai, Z. 1987a. "The Consolidation of Laminated Composites," *Journal of Composite Materials*, Vol. 21, pp. 172–188.
- Gutowski, T. G., Cai, Z., Bauer, S., Boucher, D., Kingery, J., and Wineman, S. 1987b. "Consolidation Experiments for Laminate Composites," *Journal of Composite Materials*, Vol. 21, pp. 650–669.
- Holman, J. P. 1997. *Heat Transfer*, 8th ed., McGraw-Hill, New York.
- Hunter, G. A. 1988. "Pultrusion of Epoxy Resin," *Proceedings of 43rd Annual Conference of Composites Institute*, SPI.
- Johnson, C. F. 1990. "Resin Transfer Molding," in *Composite Materials Technology, Processes and Properties*, Edited by Mallick, P. K., and Newman, S., Hanser Publishers, New York, pp. 393–456.
- Kamal, M. R. 1974. "Thermoset Characterization for Moldability Analysis," *Polymer Engineering and Science*, Vol. 14, pp. 231–239.
- Kardos, J. L. 1997. "The Processing Science of Reactive Polymer Composites," in *Advanced Composites Manufacturing*, Edited by Gutowski, T. G., John Wiley & Sons, New York, pp. 43–80.
- Kim, J. S., and Lee, D. G. 1993. "On-line Cure Monitoring and Viscosity Measurement of Carbon Fiber Epoxy Composite Materials," *Journal of Materials Processing Technology*, Vol. 37, pp. 406–416.
- Kim, J. S., and Lee, D. G. 1996. "Measurement of the Degree of Cure of Carbon Fiber Epoxy Composite Materials," *Journal of Composite Materials*, Vol. 30, No. 13, pp. 1436–1457.
- Kim, J. S., and Lee, D. G. 1997. "Development of an Autoclave Cure Cycle with Cooling and Reheating Steps," *Journal of Composite Materials*, Vol. 31, No. 22, pp. 2264–2282.
- Kingley, W. D., Bowen, H. K., and Uhlmann, D. R. 1991. *Introduction to Ceramics*, 2nd ed., John Wiley & Sons, New York.
- Kliger, H. S., and Wilson, B. A. 1990. "Filament Winding," in *Composite Materials Technology, Processes and Properties*, Edited by Mallick, P. K., and Newman, S., Hanser Publishers, New York.
- Lee, C. C., Folgar, F., and Tucker, C. L. 1984. "Simulation of Compression Molding for Fiber-Reinforced Thermosetting Polymers," *Journal of Engineering for Industry*, Vol. 106, pp. 114–125.
- Lee, D. G., and Kim, J. S. 1994. "Computer Simulation of the Consolidation of Fiber-Reinforced Resin Matrix Composites," *Journal of Materials Processing and Manufacturing Science*, Vol. 2, pp. 357–372.
- Lee, L. J. 1997. "Liquid Composite Molding," in *Advanced Composites Manufacturing*, Edited by Gutowski, T. G., John Wiley & Sons, New York.
- Loos, A. C., and Springer, G. S. 1983. "Curing of Epoxy Matrix Composites," *Journal of Composite Materials*, Vol. 17, pp. 135–169.
- Mallick, P. K. 1988. *Fiber-Reinforced Composites, Materials, Manufacturing, and Design*, Marcel Dekker, New York.
- Mallick, P. K. 1990. "Compression Molding," in *Composite Materials Technology, Processes and Properties*, Edited by Mallick, P. K., and Newman, S., Hanser Publishers, New York.
- Smith, C., and Stone, J. 1990. "Pultrusion," in *Composite Materials Technology, Processes and Properties*, Edited by Mallick, P. K., and Newman, S., Hanser Publishers, New York.

- Springer, G. S. 1981. "Thermal Conductivities of Unidirectional Materials," in *Environmental Effects on Composite Materials*, Edited by Springer, G. S., Technomic Publishing, Westport, Conn. pp. 7-14.
- Springer, G. S. 1997. "Filament Winding Process Model for Thermosetting Matrix Composites," in *Advanced Composites Manufacturing*, Edited by Gutowski, T. G., John Wiley & Sons, New York, pp. 373-392.
- Springer, G. S., and Tsai, S. W. 1967. "Thermal Conductivities of Unidirectional Materials," *Journal of Composite Materials*, Vol. 1, pp. 166-173.
- Sumerak, J. E., 1997. "The Pultrusion Process for Continuous Automated Manufacture of Engineered Composite Profiles" in *Composites Engineering Handbook*, Edited by Mallick, P.K., Marcel Dekker, New York, Session 1-B, p. 7.
- Sumerak, J. E., and Martin, J. D. 1984. "Pultrusion Process Variables and Their Effect upon Manufacturing Capability," *Proceedings 39th Annual Conference, Society of the Plastics Industry*.
- Tsai, S. W., and Hahn, H. T. 1980. *Introduction to Composite Materials*, Technomic Publishing, Lancaster, Penn.
- Yih, C. S. 1977. *Fluid Mechanics*, West River Press, Ann Arbor, Mich.

**9**

# Machining and Joining of Composite Materials

## 9.1 Introduction

The use of fiber-reinforced polymeric composite materials is being extended to machine components, such as robot structures and machine tools, to exploit the benefits of high specific stiffness and high damping, as well as low coefficients of thermal expansion (CTE) of these materials. For this end, several machining processes such as cutting, drilling, and grinding operations, become necessary after molding the components, using different processes to produce accurate surfaces and holes to allow precision fitting into an assembly. Although a large database of machinability for various high-speed steel and carbide cutting tool materials exists for machining metals, much of the data cannot be applied directly to fiber-reinforced composite materials due to the toughness and abrasive nature of the fibers.

Also, when composite structures are employed in a large complicated structure, joining of composite structures to other composite and metallic structures is necessary, because manufacturing the whole structure using only composites is not technically or economically feasible.

The design of joints for the assembly of separate parts has become an important research area because the structural efficiency of a structure with joints is established, with a few exceptions, by its joints, not by its basic structure, because the joints are often the weakest areas in a composite structure and composite materials do not possess the forgiving characteristics of ductile metals, namely, their capacity to redistribute local high stresses by yielding.

There are two kinds of joints, mechanical and adhesive. The mechanical joint is created by fastening the substrates with bolts or rivets, but the adhesive joint uses an adhesive interlayer between adherends (or substrates).

Mechanical joints permit quick and repeated disassembly for repairs or replacements without destroying substrates, require little or no surface preparation, and are easy to inspect for joint quality. However, they require machining of holes that interrupt the fiber continuity and may reduce the strength of the adherends, create highly localized stress concentrations around the joints that may induce failure in the adherends, add weight to the structure, and may create a potential problem such as galvanic corrosion (Mallick, 1988).

Adhesive joints distribute the load over a larger area than mechanical joints, require no holes, and add very little weight to the structure. However, they are difficult to disassemble without either destroying or damaging the substrates, may be

affected by service temperature, humidity, and other environmental conditions, are difficult to inspect for joint quality, and may create a galvanic (or potential) corrosion problem, for example, an aluminum fastener if used for joining carbon-fiber composites.

In this chapter, the machining and joining of composite materials are presented in detail because these operations not only add much value to the composite structure, but also create the weakest parts.

## 9.2 Machining of Composite Materials

Although one of the most important advantages of composite materials is that they can be manufactured in a near net shape, composite structures frequently require trimming and other machining operations, such as hole machining prior to assembly. Since composite materials are anisotropic, the machining characteristics are much dependent on the direction of reinforcing fibers, which does not allow the cutting mechanism developed for conventional isotropic materials to be applied directly to composite materials.

### 9.2.1 Trimming

Since the near net shape manufacturing of composite structures is not always possible, the most useful machining technique for composite structures is the trimming operation. Cutting tools used to trim composites are circular saws, router cutters, and abrasive tools (Boldt and Chanani, 1987).

Diamond-coated circular saw blades used in portable equipment are useful for straight-line cuts and provide long tool life. Carbide router bits with a diamond-shaped chisel cut and diamond-coated router tools are very effective in producing good finishes and may be used for any trimming operation. Abrasive tools such as sanding drums, discs, belts, and abrasive cloths are also used for trimming and in the final finishing operation.

### 9.2.2 Turning

These days, carbon-fiber epoxy composite materials are being employed in machine components, such as the structures of robots and machine tools, which require accurate machining of composite materials by turning, milling, or drilling. For example, the accurate grinding process is required to manufacture a machine tool spindle (Lee et al., 1985) and robot arm (Lee et al., 1991b, 1993).

The machining of carbon-fiber epoxy composite materials is not the same as machining of conventional metals. The wear of sintered-carbide tools and high-speed tools is very severe. Hence cutting speed and feed rate for the machining of fiber-reinforced composite materials should be selected carefully. Also, surface damage, such as cracking and delamination, in the machined composite surface is severe, and obtaining low surface roughness is not easy.

The types of chip-formation mechanisms for two-dimensional cutting observed by a high-speed camera were delamination, fiber buckling, and fiber cutting (Kim et al., 1992). When the rake angles were positive, the fiber-cutting-type chips were produced at first when the cutting tools were sharp, irrespective of fiber angles for the composites with stacking sequence  $[\pm \theta]$  when  $\theta$  is not larger than  $45^\circ$ . However, the

chip formation mechanism changed soon from the fiber-cutting to the buckling type as the cutting tool edge became dull due to the high abrasive nature of carbon fiber for both tungsten carbide tools and high-speed steel tools. Therefore, when the rake angles were negative ( $-5^\circ$ ,  $-10^\circ$ ), buckling was observed irrespective of fiber angles. In this case, the surface roughness was high. Delamination was observed when the carbon-fiber specimens were turned in the fiber transverse direction ( $90^\circ$ ) with a positive rake angle tool ( $20^\circ$ ). The chips produced were large, in splintered form.

The chips produced during turning were of two types: a shattered chip generated by fiber cutting and fiber buckling and a splintered chip generated by matrix fracture. During turning, two different wear types were observed on tools: rounding wear of the cutting edge and flank wear of the side-relief face. The rounding wear of the cutting tool arose from the abrasive action between the carbon fibers and the cutting tool edge, because the carbon fibers were bent when the sharp cutting-tool edge touched the composite surface, and abraded the sharp edge of the cutting tool as the bent fibers restored to the original position. The excessive wear of the side-relief face came from the continuous abrasion of the tool by the carbon fibers. A coated black spot was found on the peripheral area of the wear land of the tool flank face. The wear rate of tools was high at first, but decreased as the cutting time increased.

In order to present the tool wear characteristics during carbon-fiber epoxy composites, the Taylor tool-life equation was employed, which is expressed as (Degarmo et al., 1999):

$$VT^n = C \quad (9.1a)$$

or

$$\log V + n \log T = \log C \quad (9.1b)$$

where  $V$  is cutting speed (m/min),  $T$  is the tool-life (minute) associated  $V$  for a given amount of tool wear, and  $C$  is a constant that depends on all the input parameters, including feed. Since  $T$  is usually measured in minutes,  $C$  is the cutting speed that gives a 1-minute tool-life. Table 9.1 shows the values of  $n$  and  $C$  with respect to the stacking sequences of the high-strength carbon-fiber composite specimens. The tools used were throw-away-type tungsten carbide K10 (uncoated, Sandvik TNMA 331) having a  $6^\circ$  side-rake angle, and the 0.3 mm flank-wear was used for the wear criterion. From table 9.1, the values  $n$  and  $C$  are much dependent on the fiber stacking sequence. The tool wear was most sensitive to the cutting speed when the

**Table 9.1** Taylor's Tool Wear Constants when Turning Carbon Fiber Epoxy Composites with Tungsten Carbide Tool (K10), from Kim et al. (1992)

Stacking sequence	$n$	$C$
[ $\pm 0$ ]	1.125	241.5
[ $\pm 15$ ]	0.617	93.8
[ $\pm 30$ ]	0.481	72.5
[ $\pm 45$ ]	0.451	55.4

**Table 9.2 Taylor's Tool Wear Constants for Free-Machining Steels of Different Sulfur Content Machined with Tungsten Carbide Tools, from Shaw (1984)**

Steel	Sulfur content (%)	n	C
1	0.033	0.33	477
2	0.11	0.33	549
3	0.18	0.33	701
4	0.26	0.33	732
5	0.37	0.33	823

fiber stacking sequence was  $[\pm 45]$ , becoming less sensitive to the cutting speed as the angle  $\theta$  decreased from the stacking sequence pattern of  $[\pm \theta]$ . Therefore, the principal factor of tool wear in the machining of carbon-fiber epoxy composite is the fiber stacking angle. Also, the value of  $C$  was decreased quickly as the angle  $\theta$  was increased. Since the machinability becomes worse as the value of  $C$  decreases, the increases of the angle  $\theta$  decreased the machinability. The value of  $n$  for machining of ordinary steel is around 0.2 (Shaw, 1984), which is less than that for machining the carbon-fiber epoxy composite. Therefore, the tool wear of the tungsten carbide tool for machining the carbon-fiber epoxy composite was less affected by the cutting speed than for the machining of steels. Also, table 9.2 shows the values of  $n$  and  $C$  for free-machining steels with respect to sulfur content, machined with tungsten carbides for comparison (Shaw, 1984).

The value of  $C$  in the machining of the carbon-fiber epoxy composite material was about 1/8–1/4 of the value for the cutting of free-machining steels, as shown in table 9.2. Therefore, the cutting speed for the carbon-fiber epoxy composite material that reached the tool wear criterion in 1 minute was about 1/8–1/4 of the cutting speeds for the free-cutting steels under the same condition.

As explained before, the tool wear in the turning of the carbon-fiber epoxy composite material came from severe abrasive wear between the flank face of the cutting tool and the very abrasive carbon fiber when the fiber was restoring itself from the bent position at the cutting point due to the resilient soft matrix backing up the carbon fibers. Therefore, a low cutting speed (about 20–40 m/min) is recommended for turning with the tungsten carbide tool because the tool wear is so severe even at a low cutting speed.

However, the cutting speeds can be over 300 m/min for carbon-fiber composites if PCD (polycrystalline diamond) tool inserts are utilized (Kohkonen and Potdar, 1998).

Takeyama and Iijima (1988) performed the orthogonal cutting of unidirectional glass epoxy composites with fibers oriented between  $0^\circ$  and  $90^\circ$  from the cutting direction. They found that the cutting forces were relatively low when cutting parallel to the fiber direction, decreased slightly to a minimum when machining composite with  $30^\circ$  orientation, and then increased significantly as the cutting direction becomes normal to the fiber direction. Most of the energy spent in cutting was converted into heat, which caused temperature rises in the workpiece, the tool, and the chips. The heat generated in cutting due to the low thermal conductivity of the glass-fiber composite is concentrated near the tool nose, which causes tool wear in this area.

The machining of aramid fiber composites requires special tooling because aramid fibers have a tendency to recede within the matrix instead of being sheared off due to their low compressive strength (Abrate, 1997). Frayed fibers protrude from the surface, commonly known as fuzz. To turn the aramid fiber composites, large rake angles of the tools should be used.

### 9.2.3 Drilling

Hole generation is a major activity in the manufacture of assemblies of large structures, such as aircraft, because holes are not usually provided during the molding stage due to fiber orientation and shrinkage during the curing stage of composite structures. Hole characteristics, such as waviness/roughness or lack of axial straightness and roundness, can cause stress concentration at the fastener assemblies, leading to premature failure.

Drilling holes in composites can cause failures such as delamination, fracture, fiber break-out, and fiber pull-out. Delamination is a major concern during drilling composite laminates. Delamination of the top layer may be produced by high thermal stresses generated by drilling. Delamination near the exit side is produced as the tool acts like a punch, separating the thin uncut layer from the remainder of the laminate. Delaminations can be greatly reduced or eliminated by reducing feed rates near the exit and using backup plates to provide support and prevent deformations leading to exit-side delaminations.

Because glass and carbon fibers are very abrasive, drill bits made of high-speed steel (HSS) fail after drilling just a few holes in composite materials. Tungsten carbide possesses adequate life and larger number of holes can be drilled with tungsten carbide tools coated with PCD. However, PCD-coated tools are easily chipped, and cannot be resharpened.

The helix angle of the drill is not so important for machining carbon-fiber epoxy composites because the chips are in powder form and are continuously removed by suction. Positive rake angles are needed to generate the least amount of heating during cutting. However, the more positive the rake angle, the more fragile the cutting edge becomes. A small chisel angle is the second element of good tool geometry and serves to improve the penetration rate (Mackey, 1980).

### 9.2.4 Grinding

In the manufacturing of carbon-fiber epoxy composite materials, one of the popular production methods is the autoclave/vacuum degassing cure process. However, when the composite materials are to be employed in the structural elements of precision machines and robots (Lee et al., 1985, 1991b, 1993), a grinding process is indispensable after molding them in an autoclave. Also, the grinding process has been used extensively for finishing composite golf shafts and fishing rods. Silicon carbide or alumina wheels are used, and surface speeds over 1000 m/min are possible. Grinding accuracies within 10  $\mu\text{m}$  can be achieved with centerless grinding (Kohkonen and Potdar, 1998). However, the grinding of polymer matrix composites (PMC) has a number of problems. For example, melted thermoplastic matrix can load the surface of the grinder, and it is hard to get a clean ground surface on aramid fiber composites because the cutting grains of wheel cannot abrade the aramid fibers cleanly. Abrasive belts have been used on aramids with some success, but dust collection has been another problem.

The temperature rise and surface roughness during grinding process are two important issues. To estimate the temperature rise, Lee and Kim (2000) measured the temperature rise during plunge-cut grinding of carbon-fiber epoxy composites with a metal-bonded diamond-grit wheel of #140 mesh. A very thin thermocouple of 0.05 mm diameter and measuring junction of 0.05 mm, as shown in figure 9.1, was used to measure the temperature at the nearest grinding point possible because the temperature gradient might be very large near the grinding point. Figure 9.2 shows a schematic drawing of the plunge-cut grinding operation of the carbon-fiber epoxy composites.

Since the carbon fiber conducts electricity, the thermocouple should be insulated with dielectric material to measure the temperature of carbon-fiber composites. The insulation thickness should be as small as possible to measure the temperature until the grinding wheel contacts the thermocouple and the steel wires. When the metal-bonded grinding wheel contacted the thermocouple, the two steel wires near the thermocouple were short-circuited, which produced a 5 V reference signal. Figure 9.3 shows the temperature history during the cut-off grinding with respect to time. It was assumed that the grinding point temperature was equal to the temperature at the

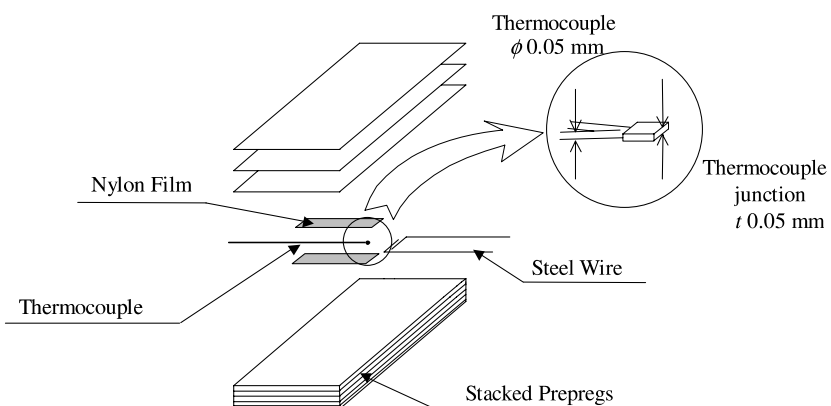


**Figure 9.1** Schematic diagram of composite specimen for measuring the temperature during grinding (from Lee and Kim, 2000).

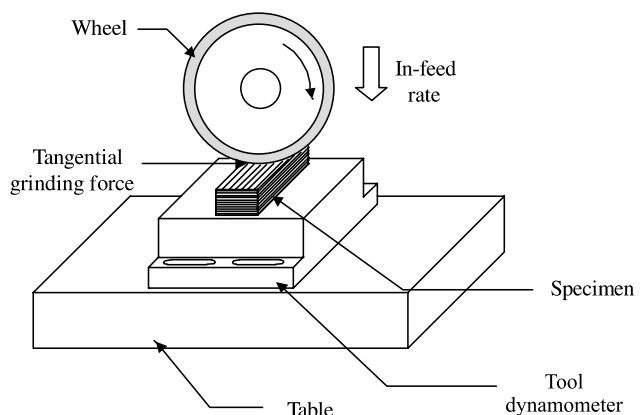


**Figure 9.2** Schematic drawing of plunge-cut grinding operation of the carbon-fiber epoxy composites (from Lee and Kim, 2000).

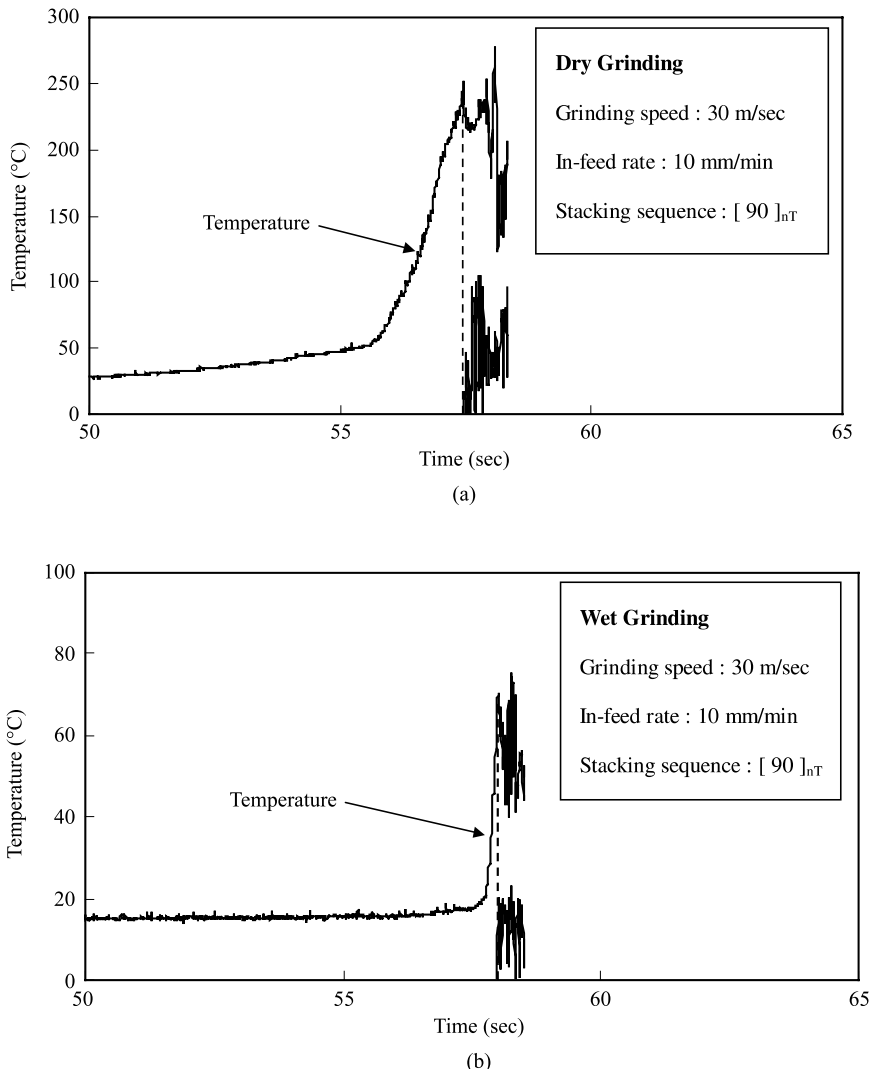


**Figure 9.3** Temperature rises during cut-off grinding with respect to time: (a) Dry grinding; (b) wet grinding (from Lee and Kim, 2000).

moment the wheel contacted the steel wires. After the wheel contacted the thermocouple, noises were generated both in the thermocouple and the steel wires.

Comparing the dry grinding and the wet grinding, as shown in figure 9.3(a) and 9.3(b), the maximum grinding temperature  $\Delta T_{\max}$  in the dry grinding was much higher than the curing temperature of 120°C, which might degrade the mechanical properties of the composites, while the cutting temperature in the wet grinding using water-based grinding fluid was far less than the curing temperature.

Since there are many situations in which grinding fluids cannot be used due to component size and machining efficiency, the temperature rise during a dry cut-off grinding operation was investigated further with respect to in-feed rate and grinding speed. As shown in figure 9.4, the maximum temperature rise  $\Delta T_{\max}$  of [90]<sub>nT</sub> was higher than that of [0]<sub>nT</sub>. The  $\Delta T_{\max}$  of [0]<sub>nT</sub> slightly decreased as the grinding speed

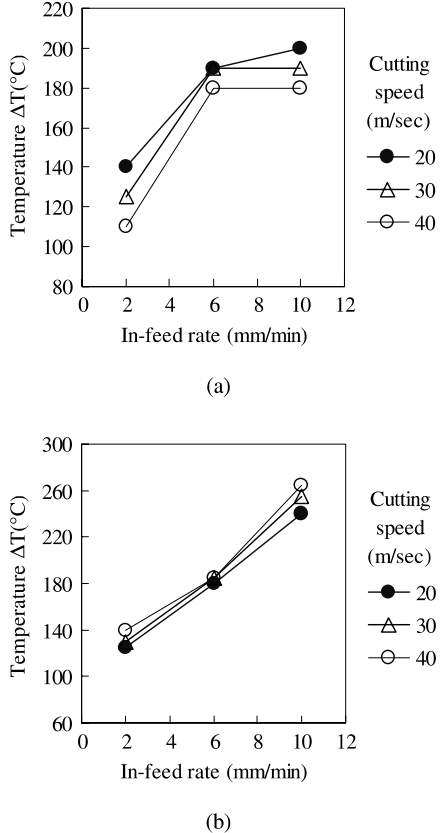


**Figure 9.4** Maximum temperature rises of the carbon epoxy composite in dry grinding with respect to grinding speed and in-feed rate: (a) Stacking sequence  $[0]_{nT}$ ; (b) stacking sequence  $[90]_{nT}$  (Lee and Kim, 2000).

increased, while that of  $[90]_{nT}$  slightly increased as the grinding speed increased. The  $\Delta T_{\max}$  of  $[0]_{nT}$  increased as the in-feed rate increased to 6 mm/min and then saturated, while that of  $[90]_{nT}$  proportionally increased as the in-feed rate increased.

From these results, it was concluded that a high cutting speed might be used for the specimen with  $[0]_{nT}$  to increase productivity, while both the grinding speed and in-feed rate must be decreased for the specimen of  $[90]_{nT}$  to reduce grinding temperature rise.

### 9.2.5 Special Machining of Composite Materials

#### *Abrasive Water Jet Machining*

A water jet that travels at velocities as great as 900 m/s (approximately Mach 3) can cut materials (McGeough, 1988). These high velocities are obtained using the equipment illustrated in figure 9.5: A hydraulic pump powered from an electric motor, typically 30 kW, supplies oil at pressures as great as 12 MPa in order to drive a reciprocating plunger pump, termed an intensifier. This device accepts water at low pressures, typically 0.4 MPa, and expels it at far higher pressures, about 380 MPa, through an accumulator, which maintains the continuous flow of the high-pressure water, and also eliminates fluctuations, or spikes, in the pressure. The accumulator relies on the compressibility of the water, which is roughly 12% at 380 MPa, in order to maintain a uniform discharge pressure and water jet velocity, when the intensifier piston changes direction.

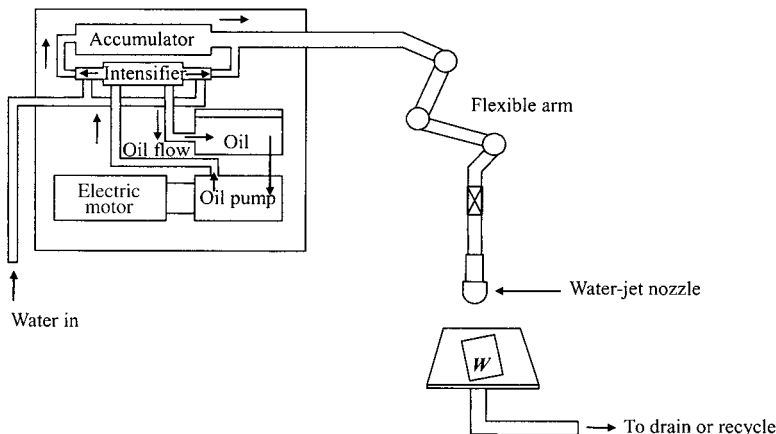


**Figure 9.5** Water jet machining system (after McGeough, 1988).

In abrasive water jet machining (AWJM), the water jet contains abrasive particles (such as silicon carbide or aluminum oxide); they increase the material removal rate above that of water jet machining. The cutting characteristics depend on water jet pressure, jet velocity, abrasive grain size, abrasive material, standoff distance, and jet impingement angle. Metallic, nonmetallic, and advanced composite materials of various thicknesses can be cut in single or multiple layers. This process is suitable particularly for heat-sensitive materials that cannot be machined by processes in which heat is produced. Cutting speeds can be as high as 7.5 m/min for fiber-reinforced plastics, but much lower for metals. The arithmetic surface roughness for cutting of carbon-fiber epoxy composites is around  $2.5 \mu\text{m}$  at the cutting speed of 1.0 mm/s. The minimum hole size that can be produced satisfactorily is about 3 mm and the maximum hole depth is on the order of 25 mm. With multiple axis and robotic control machines, complex three-dimensional parts can be machined to finish dimensions. The jet cutting nozzle, of around 0.1 mm, is normally made from synthetic sapphire or tungsten carbide.

#### *Ultrasonic Machining*

In ultrasonic machining, material is removed from a surface by microchipping and erosion with fine abrasive grains in a slurry. The tip of the tool (sonotrode) vibrates at a frequency of 20 kHz at low amplitude (0.0125–0.075 mm). This vibration, in turn, imparts a high velocity to abrasive grains between the tool and the workpiece, as shown in figure 9.6.

The stress produced by the impact of abrasive particles on the workpiece surface is high because of short contact time between the particle and the surface (10 to 100  $\mu\text{s}$ ) and the small contact area. In brittle materials, such as composites, ceramics, precious stones, and hard steels, these impact stresses are sufficiently high to cause microchipping and erosion of the workpiece surface. The process is limited to workpieces of size below 100 mm because of the limitation on the size of the tool.

#### *Laser Cutting*

Laser cutting is a noncontact, thermal process. The absence of contact allows intricate cutting of fragile workpieces, and simplifies fixturing (Migliore, 1987). Thermal

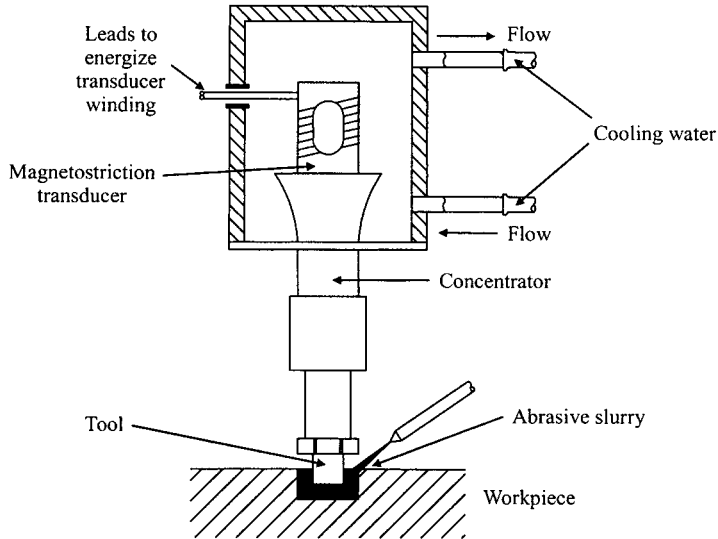


**Figure 9.6** Schematic drawing of the ultrasonic machining process.

cutting is independent of the strength or hardness of composite constituents. The thermal nature of laser cutting, however, limits its use when charring or thermal degradation is unacceptable.

There are many laser types, but only a few can be made powerful enough for use in material processing. Currently, these lasers, which are generally named for their active medium, are known as ruby, neodymium–glass, neodymium–yttrium aluminum garnet (YAG), and carbon dioxide ( $\text{CO}_2$ ) lasers. A continuous cutting process requires a continuous beam, or at least pulses rapid enough to behave as if it were continuous. This requirement reduces the suitable laser types to two: neodymium–YAG and  $\text{CO}_2$ . A  $\text{CO}_2$  laser with an output of 1500 W generally emits a beam about 20 mm in diameter. The power density in this unfocused beam varies across the diameter, and reaches a peak of about  $4.0 \times 10^7 \text{ W/m}^2$ . While this level will decompose most organics, and eventually melt some metals, it is not enough for useful cutting. Efficient cutting is accomplished by using a lens or mirror to concentrate the energy.

YAG lasers are compact and produce high peak powers that vaporize metal effectively and are thus suitable for metal matrix composites (MMCs). The low repetition rate of YAG lasers limits their maximum cutting speed to about 2 m/min. The wavelength of YAG light is absorbed well by metals, but not by organic composites, which limits the utility of YAG lasers. The  $\text{CO}_2$  lasers can produce high average power and generate both continuous and pulsed beams, hence most cutting systems use  $\text{CO}_2$  lasers because of their higher speed and greater flexibility. Continuous wave operation allows them to cut at very high speeds, such as 75 m/min on a 0.1 mm carbon-fiber epoxy composite using 1500 W unit. The  $1.06 \times 10^4 \text{ nm}$  light is strongly absorbed by all organic materials. The laser cutting of composites produces a heat-affected zone (HAZ) in which some charred matrix residues are present on the surface and fibers are protruding because the surrounding matrix has been removed (Abbate, 1997). The size of the HAZ increases as the difference between the vaporization temperatures of the fibers and that of the matrix becomes larger. The size of the HAZ is also affected by the orientation of the cutting direction relative

to the fiber direction. Heat conduction coefficients of carbon fibers are much larger than those for the epoxy matrix. Therefore, heat is conducted away from the cut surface when cutting in the direction perpendicular to the fiber reinforcement, and the HAZ will be larger than when cutting in the fiber direction. The best quality of the cut surfaces is obtained when the thermal properties of the reinforcing fibers are closest to those of the matrix. Aramid fibers and organic matrices have the closest vaporization temperatures, and the fibers have low thermal conductivities, therefore, the HAZ is small. Since carbon fibers have much higher vaporization temperatures and higher thermal conductivities, much higher temperatures are required and more heat is conducted away from the laser beam, creating a wider HAZ. With carbon fibers, a good-quality cut was obtained when the laser was operated in a pulsed mode.

When composites are machined by the laser, the fumes created by the laser-vaporized material should be ventilated because they are irritating, toxic, and carcinogenic.

#### *Electro-Discharge Machining*

Electro-discharge machining (EDM) is a versatile process for machining intricate and complex shapes in conductive materials. Two basic approaches are employed. With the die sinking method, the form of the tool is duplicated into the workpiece, while with the traveling wire electrode process, ruled surfaces corresponding to the trajectory of the wire electrode are produced.

In order to use EDM for machining of a composite, it should have an electrical resistivity of less than  $1\text{--}3 \Omega\text{m}$  (Kohkonen and Potdar, 1998). Carbon-fiber composites can be machined by EDM because carbon fibers are electrically conductive. A voltage of 100 V and peak discharge currents of 0.5–5.0 A were used with a die-sinking method. At high currents, high temperatures are produced that cause severe melting of the composite surface, thermal expansion of the carbon fibers in the lateral direction, and debonding between fibers and matrix (Abbate, 1997). Therefore, low currents must be used. Polymer matrix composites that contain a small amount of copper in the matrix, can be machined using EDM, it can also be used with conductive silicides, borides, carbides, etc. The EDM process is more accurate than abrasive water jet machining; holes of 0.25 mm diameter can be drilled in  $\text{SiC}/\text{TiB}_2$  composites. However, the EDM process is slow for many production applications.

### **9.3 Mechanical Joining**

The use of mechanically fastened joints in fiber-reinforced composite materials is a logical carry-over from the fastening technique used for structures made from isotropic materials where a wealth of experience and understanding already exists (Collings, 1987). Failure modes for advanced composite mechanical joints are similar to those for conventional metallic mechanically fastened joints. But the behavior of composite joints differs significantly from those of metallic joints because fiber-reinforced composite structures can be considerably weakened by the introduction of holes and they have little plasticity, which does not allow stress relaxation due to yielding. The tensile elastic stress concentration factors,  $K_t$  (shown in Table 5.2), due to a circular hole in a unidirectional infinite sheet, are much larger than the value

of 3 normally associated with isotropic materials. The stress concentration near discontinuities is dependent on the laminate stacking sequence, fiber volume fraction, hole quality, matrix type, washer size, when used, and fastener preload. Therefore, it is not possible to design fasteners that are universally applicable to all composites (Niu, 1992).

The efficiency of mechanical joints in unidirectional fiber-reinforced composites is very low; however, the degree of anisotropy may be reduced in the vicinity of a hole by introducing some softening or pseudo-plastic behavior, which increases the efficiency of the mechanical joint.

Joint elements tend to be subjected to loads that act primarily parallel to the joining surfaces, producing sliding or shear forces, or perpendicular to the joining surfaces, producing tensile forces. Either type of force can ultimately lead to the unacceptable separation and/or misalignment or misorientation of the joint elements. Joints are said to be shear-loaded when the applied loads are perpendicular to the fastener's axis and parallel to the joining surfaces. Joints are said to be tension-loaded when the applied loads are parallel to the fastener's axis and perpendicular to the joining surfaces (Messler, 1993).

The way in which mechanical fasteners achieve interlocking between joint elements depends on the type of applied loading. When joints are shear-loaded, the fasteners resist the load either by pinning the joint against motion using bearing forces between the fastener and the joint elements or by resisting the shear through the action of friction at the joining surfaces (between members). Since the magnitude of a frictional force depends on the product of the coefficient of friction and the applied normal force, part of the function of a fastener in a shear-loaded friction-type joint is to develop a normal force through a clamping action on the joint elements. When joints are tension-loaded, the fasteners resist the load entirely by developing a preload or clamping force.

Mechanical fasteners are broadly classified into two types: threaded fasteners and unthreaded fasteners. The former are designed to develop clamping forces or preload through the use of threads. The latter are designed primarily to resist shear through bearing with a pinning action.

Figure 9.7 shows a typical configuration and definitions of key elements of a joint. Figure 9.8 shows typical failure modes of mechanical joints; shear-out, tension, bearing, cleavage (combined shear-out and tension), bolt pull-out, and bolt shear failure.

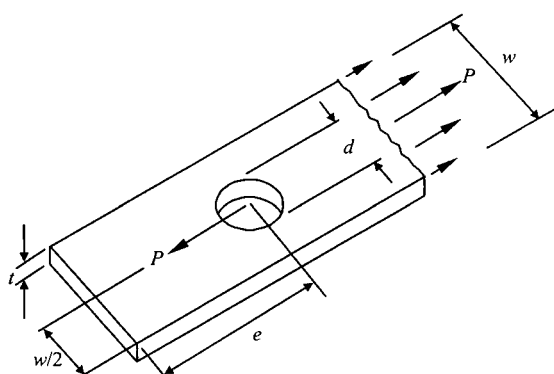


**Figure 9.7** Mechanical joint configuration.

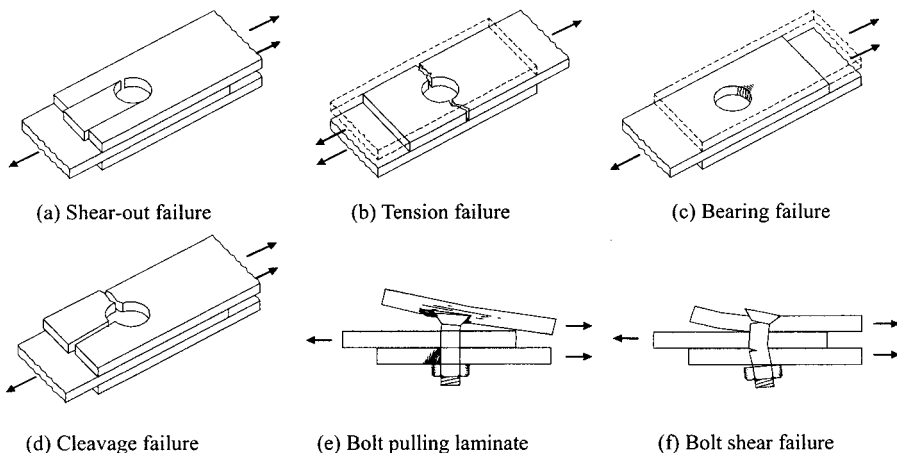


**Figure 9.8** Failure modes of fibrous composite mechanical joints.

### 9.3.1 Fastener Design

Three different types of fasteners, such as self-tapping screws, rivets, and bolts, are usually used in mechanical joints. Among these fasteners, the bolted joint was found to be most efficient for the mechanical fastening of composites. For the bolted joint, the joint is usually preloaded by the preload  $F_i$  by tightening the nut before external load  $P$  is applied. When the load  $P$  is tension, which causes the connection to elongate, the resultant bolt load  $F_b$  and the resultant load  $F_m$  on the connected members are expressed as follows when the joint is not separated by the external force  $P$  (Shigley et al., 2004):

$$F_b = \frac{k_b P}{k_b + k_m} + F_i = CP + F_i \quad (9.2)$$

$$F_m = -\frac{k_m P}{k_b + k_m} + F_i = -(1 - C)P + F_i \quad (9.3)$$

where  $C = k_b/(k_b + k_m)$  is the fraction of external load  $P$  carried by the bolt, and  $k_b$  and  $k_m$  are the bolt stiffness and member stiffness, respectively. The bolt stiffness  $k_b$  can be calculated using the concept of springs in series:

$$k_b = \frac{A_d A_t E}{A_d l_t + A_t l_d} \quad (9.4)$$

where  $A_t$  = tensile stress area of bolt

$l_t$  = length of threaded portion of grip

$A_d$  = major diameter area of fastener

$l_d$  = length of unthreaded portion in grip

These bolt parameters can be found from catalogs or by measuring dimensions.

There may be more than two members included in the grip of the fastener. All together these act like compressive springs in series, and hence the total spring rate of the members is

$$\frac{1}{k_m} = \frac{1}{k_1} + \frac{1}{k_2} + \frac{1}{k_3} + \cdots + \frac{1}{k_i} \quad (9.5)$$

If one of the members is a soft gasket, its stiffness relative to the other members is usually so small that for all practical purposes the others can be neglected and only the gasket stiffness is used. If there is no gasket, the stiffness of the members is rather difficult to obtain, except by experimentation, because the compression spreads out between the bolt head and the nut and hence the area is not uniform. The pressure distribution at the member interface has been investigated by measurement using ultrasonic techniques and analysis by the finite element method. The results show that the pressure stays out to about 1.5 bolt radii for isotropic materials. When loading is restricted to the washer-face annulus, a half-apex angle  $\alpha$  of figure 9.9 is assumed to be  $30^\circ$  for isotropic materials.

The elongation  $\delta$  of figure 9.9 can be calculated by integrating of an element of the cone of thickness  $dx$  subjected to a tensile force  $P$ :

$$\delta = \int_0^t \frac{P}{EA} dx \quad (9.6)$$

The area of the element is

$$\begin{aligned} A &= \pi(r_o^2 - r_i^2) \\ &= \pi \left[ \left( x \tan \alpha + \frac{D}{2} \right)^2 - \left( \frac{d}{2} \right)^2 \right] = \pi \left( x \tan \alpha + \frac{D+d}{2} \right) \left( x \tan \alpha + \frac{D-d}{2} \right) \end{aligned} \quad (9.7)$$

where  $D$  and  $d$  represent the washer diameter and bolt diameter, which is assumed to be the same as the hole diameter, respectively. Substituting equation (9.7) into equation (9.6) and integrating, we have

$$\delta = \frac{P}{\pi E d \tan \alpha} \ln \frac{(2t \tan \alpha + D - d)(D + d)}{(2t \tan \alpha + D + d)(D - d)} \quad (9.8)$$

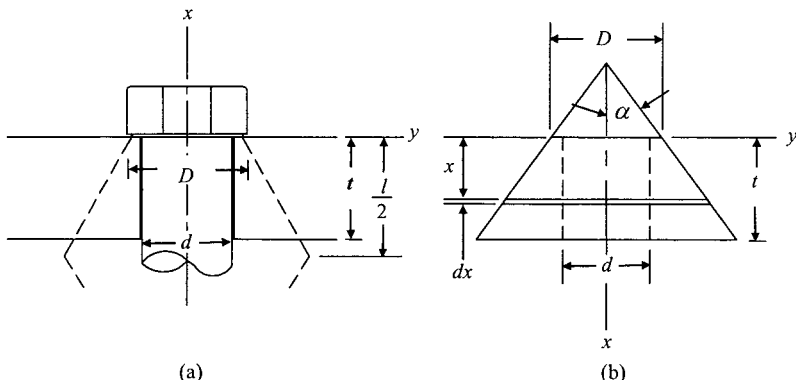


**Figure 9.9** Compression of a member with the equivalent elastic properties represented by a frustum of a hollow cone.

where  $E$  is the Young's modulus of members in the thickness direction.

With  $\alpha = 30^\circ$ , the stiffness  $k_m$  is  $0.5 P/\delta$  if the members of the joint have the same Young's modulus and same thickness because there are two members in the joint. The diameter of the washer face is about 50% greater than the fastener diameter for standard hexagon-head bolts and cap screws. Then the stiffness of the members is expressed as

$$k_m = \frac{1}{2} \frac{0.577\pi Ed}{\ln(5(0.577l + 0.5d)/(0.577l + 2.5d))} \quad (9.9)$$

For steel members joined by steel bolts, the value of  $C$  is usually less than 0.2, which means that the value of  $(1 - C)$  is larger than 0.8. Therefore, the members take over 80% of the external load. Since the Young's modulus of fiber-reinforced composite materials in the thickness direction is about one order smaller than that of steel, the fastener for fiber-reinforced composite materials should be designed carefully not to induce too much load on the fastener itself. The relative values of stiffness between the fastener and members are especially important under dynamic load. A common application of the bolted tension joint is a device such as a pressure cylinder in which the external load varies from a lower extreme of  $P = 0$  to an upper extreme of  $P$ , per bolt. The amplitude  $P_a$  and steady components  $P_m$  of the load are both  $P/2$ .

From equation (9.2), the amplitude component  $\sigma_a$  and steady component  $\sigma_m$  of the bolt stress are

$$\sigma_a = \frac{1}{2}(\sigma_{\max} - \sigma_{\min}) = \frac{1}{2} \left( \frac{CP}{A_t} + \frac{F_i}{A_t} - \frac{F_i}{A_t} \right) = \frac{CP}{2A_t} \quad (9.10)$$

$$\sigma_m = \frac{1}{2}(\sigma_{\max} + \sigma_{\min}) = \frac{1}{2} \left( \frac{CP}{A_t} + \frac{F_i}{A_t} + \frac{F_i}{A_t} \right) = \frac{CP}{2A_t} + \frac{F_i}{A_t} = \frac{CP}{2A_t} + \sigma_i \quad (9.11)$$

On the fatigue diagram the load line is

$$\sigma_a = \sigma_m - \sigma_i \quad (9.12)$$

To calculate the fatigue safety factor  $n_f$ , we may use any of the fatigue failure criteria. For example, if we apply the Goodman fatigue failure criterion:

$$\frac{\sigma_a}{S_e} + \frac{\sigma_m}{S_{ut}} = 1 \quad (9.13)$$

where  $S_e$  and  $S_{ut}$  are the fully corrected endurance strength (or limit) and ultimate tensile strength for bolts or screws, respectively (figure 9.10). If  $S_a$  and  $S_m$  are the amplitude and mean values of the applied stress, respectively, solving equations (9.12) and (9.13) simultaneously, we have when the load line of equation (9.12) crosses the Goodman failure criterion:

$$S_m = \frac{S_{ut}(S_e + \sigma_i)}{S_e + S_{ut}} \quad (9.14)$$

$$S_a = S_m - \sigma_i \quad (9.15)$$

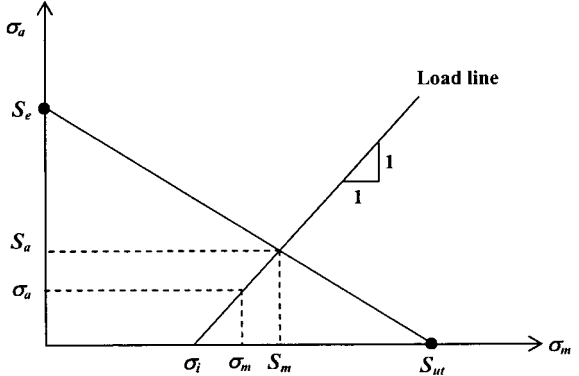


**Figure 9.10** Fatigue diagram showing the Goodman fatigue failure locus and a load line.

The factor of safety  $n_f$  for the fatigue strength of the fastener is expressed as

$$n_f = \frac{S_a}{\sigma_a} = \frac{S_m - \sigma_i}{\sigma_a} = \frac{S_{ut}A_t - F_i}{(CP/2)(1 + S_{ut}/S_e)} \quad (9.16)$$

When there is no preload, the safety factor  $n_{f0}$  is obtained with the conditions of  $F_i=0$  and  $C=1$ .

$$n_{f0} = \frac{S_{ut}A_t}{(P/2)(1 + S_{ut}/S_e)} \quad (9.17)$$

Preload is beneficial for resisting fatigue of the fastener when  $n_f/n_{f0}$  is greater than unity. For the Goodman criterion, the upper bound for  $n_f/n_{f0} \geq 1$  is

$$\sigma_i \leq (1 - C)S_{ut} \quad (9.18)$$

In order to utilize equation (9.18), the stiffness of the members should be estimated.

Mechanical joints should be loaded in shear so that the fasteners are not subjected to additional stress beyond the initial tightening. The shear loading is carried by friction between the members ensured by the clamping action of the bolts or cap screws.

For mechanical joints for carbon-fiber composites, serious corrosion problems in metals can be induced if improper coupling is used. Materials such as titanium, corrosion-resistant steels (e.g., zinc-plated), nickel, and cobalt alloys can be coupled to carbon composites without corrosive effects. Aluminum, magnesium, and steel will be adversely affected because of the electrical potential difference between these materials and carbon fibers.

### 9.3.2 Composite Member Design

Since stress concentrations exert a dominant influence on the magnitude of the allowable design stresses, mechanically fastened joints should be designed so that the critical failure mode is bearing, rather than shear-out or net tension, so that catastrophic failure should be prevented. Since stress concentrations and eccentricity effects cannot be calculated with a consistent degree of accuracy, it is advisable to verify all critical joint designs by testing a representative joint (Niu, 1992).

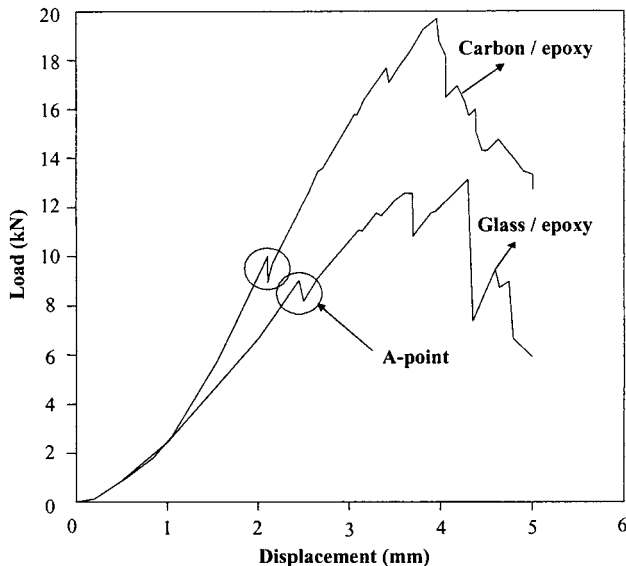


**Figure 9.11** A typical load–displacement curve for the carbon-fiber epoxy bolted joint and the glass-fiber epoxy bolted joint (clamped with finger-tightened bolt and washers) (from Oh et al., 1997).

If a laminate is dominated by  $0^\circ$  fibers with very few  $90^\circ$  fibers it is most likely to fail by shear-out. A minimum of reinforcing plies at  $90^\circ$  to the load helps prevent shear-out and cleavage failures. The edge distances should be larger than aluminum design, such as  $e/d > 3$  in figure 9.7. It is recommended to use a minimum of 40% of  $\pm 45^\circ$  plies for the dominant joint failure to be a bearing failure.

Net tension failure is influenced by the tensile strength of the fibers at fastened joints, which is maximized when the fastener spacing is approximately four times the fastener diameter. Smaller spacing results in the cutting of too many fibers, while larger spacing results in bearing failures, in which the material is compressed by excessive pressure caused by a small bearing area.

The optimum lay-up pattern for maximized member strength is realized by quasi-isotropic patterns  $[0/\pm 45/90]_S$  or  $[0/45/90/-45]_S$ . During stacking of preprints for manufacturing members, the preprints should be evenly distributed rather than blocked in the laminate to get better bearing strength.

The bearing strength of fiber-reinforced composite members is increased by giving tensile preload to fasteners because the preloaded members sustain the applied shear load by friction and the initially damaged material can still withstand compressive loads under the bolt shank, provided that there is no space for the material to be displaced. As this damage spreads, crushed composite material is displaced laterally and induces higher tensile loads in the fastener, compressing composite material even more tightly. With a pin-loaded hole with neither fastener head nor nut, on the other hand, the initially damaged material brooms out and does not continue to sustain load. The preload is beneficial for the joint under dynamic load because the amplitude of dynamic stress is reduced when the members are initially tightened as demonstrated by equation (9.10).

Figure 9.11 shows a typical example of load–displacement curves of mechanical joints fastened with finger-tightened bolts of 8 mm diameter of class 10.9 with washers. The stacking sequence of both the composites (carbon-fiber epoxy and glass-fiber epoxy) was  $[0_2/(\pm 45)_3/90_2]_S$ . The outer diameter and thickness of the washer were 20 and 2 mm, respectively. The thicknesses of glass prepreg and carbon

prepregs were 0.125 and 0.15 mm, respectively. The peak loads at A in figure 9.11 indicate the local delaminations around the holes under the washers. When the hole boundary at the peak point at A was measured by an ultrasonic C-scan, it was found that the damage developed along the loaded half of the hole circumference (Oh et al., 1997).

#### 9.4 Adhesive Joining

Four different types of stresses occur in the adhesive joint: normal, shear, cleavage, and peel stresses, as shown in figure 9.12 (Kinloch, 1987). Since the modulus and strength of the polymeric materials used as adhesives are far lower than those of metals, ceramics, or fiber-reinforced composites, the adhesive bonding technology should be employed for joining of relatively thin sheets or panels. The strain capability and toughness of adhesives are higher in compression and shear as opposed to tension, cleavage, or peel, which greatly influences the practical design of adhesive joints. When the peel or cleavage stresses exist, they place a very high stress and strain concentration on the boundary line of the crack front. The tensile strength of adhesives is somewhat lower than that in compression, hence, adhesive joints subjected to tensile stresses such as butt joints, where tensile stresses are the main stresses encountered, will fail due to cleavage stresses when there is even a small misalignment unless one of the adherends is highly compliant. Also, rubber-toughened adhesives that are very ductile should be selected, though they have lower glass transition temperature, so they cannot be used at elevated temperatures.

Therefore, the designer of adhesive joints should keep stress concentrations to a minimum and distribute the imposed loads in the adhesive layer as a combination of compressive and shear stresses, avoiding tensile, cleavage, and peel stresses as much as possible.

There are several types of adhesive joints, such as single lap, double lap, the stepped lap, and the scarf joint, as shown in figure 9.13. Among these, the single-lap joint has been studied more extensively than any other configuration through analytical, finite difference, and finite element methods, because the single-lap joint is most popular, due to its ease of manufacture and its relatively low cost.

The factors to be considered for the design of adhesively bonded joints are as follows: joint types and surface treatments of adherends, nonlinear mechanical property of the polymeric adhesive, the residual thermal stress generated by the CTE difference between the adherend and adhesive, the mechanical property and shape of the filler added to the adhesive in order to improve the mechanical and thermal properties of the adhesive, the environmental temperature at which the

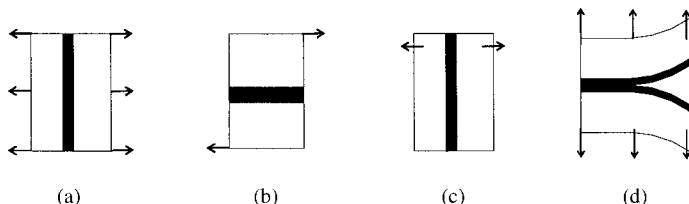


**Figure 9.12** Types of stresses in the adhesive joint: (a) Normal stress; (b) shear stress; (c) cleavage stress; (d) peel stress.

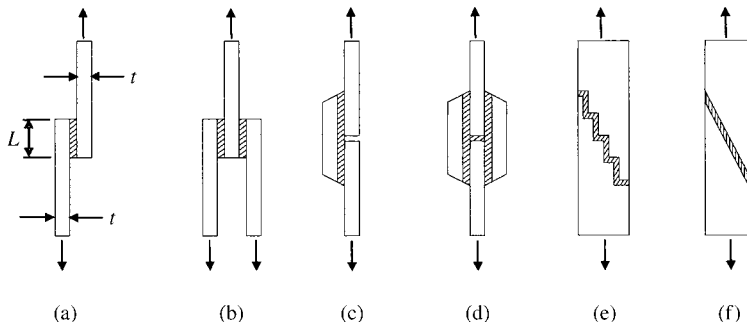


**Figure 9.13** Types of adhesive joint: (a) Single lap; (b) double lap; (c) single strap; (d) double strap; (e) stepped lap; (f) scarf (adhesive thickness exaggerated for clarity).

adhesively bonded joint is used, and the glass transition temperature of adhesive (Lee et al., 1999).

#### 9.4.1 Adhesive Properties

The following properties of adhesive are required to be compatible with adherends (or substrates) to be joined (Skeist, 1990):

1. When a liquid adhesive is involved, the adherends should allow the carrier (solvent or water) to escape as needed for proper film forming and hardening.
2. The adhesive should not significantly attack or corrode the adherends.
3. If the adhesive's hardening involves significant film shrinkage, the system (adhesive and adherend) should allow for dissipation of the shrinkage stresses rather than locking them in and prestressing the joint.
4. The adhesive should wet the adherend, that is, be able to establish extensive and intimate (molecular scale) interfacial contact with the adherend.

#### 9.4.2 Primers

Sometimes primers are used to pretreat high-surface-energy adherends prior to adhesive bonding to improve the adhesive joint quality because some adhesives (e.g., high-temperature polyimides) often possess poor wetting characteristics because their viscosity does not become low enough for suitable bonding during the bonding operation. Applying the adhesive in a solvent is undesirable since complete solvent removal from the adhesive in the joint is virtually impossible, which affects the mechanical properties of the joints. A primer is basically a solvent-diluted version of the adhesive. It will completely wet the adherend and can be cured by removing the solvent prior to the undiluted adhesive being applied. Often ingredients such as corrosion inhibiting species (chromate compounds) are added to the primer to improve environmental resistance such as moisture adsorption, which increases both initial strength and service life of the joint.

The primer establishes strong interfacial forces to both adhesive and adherend when they are difficult to bond (e.g., silane-based primer to ensure adequate adhesion between silicone-based adhesives and a variety of adherends).

The primer increases production flexibility in the bonding operation. After pre-treating a high-energy adherend with chemical or plasma surface treatments, the

active surface will readily absorb atmospheric contamination, and after a certain surface exposure time this may lead to inferior joint performance, especially with respect to durability. The allowable surface exposure time may be comparatively short, often a few hours. If a primer is applied less than few hours after surface treatment and is dried in air or oven, nontacky or only slightly tacky films are formed, so that the adherend can be handled and stored conveniently in an industrial production line. The actual adhesive bonding operation may then be delayed for up to several months.

#### 9.4.3 Adhesive Constitutive Equation

The stress-strain curves of adhesives are usually nonlinear. Figure 9.14(a) shows the uniaxial and shear stress-strain curves of a hot-cured, rubber-toughened epoxy adhesive (Osswald and Rietveld, 1990), and figure 9.14(b) shows the shear stress-strain curves of the FM-300 film adhesive at different temperatures (Baker, 1990).

The majority of the load transfer of the adhesive joint is accomplished by the nonlinear behavior of the adhesive. The contribution of the linearly elastic behavior may be as little as 10% in the case of a ductile adhesive. Therefore, the load transmission capability, especially torque transmission capability, of the adhesively bonded joint should be calculated, taking into account the nonlinear behavior of the adhesive. The difficulty is how to characterize the mechanical properties of the adhesive. Since the adhesive joint is advantageous if it is designed to be subjected to shear stresses, many researchers tried to represent the adhesive shear stress-strain

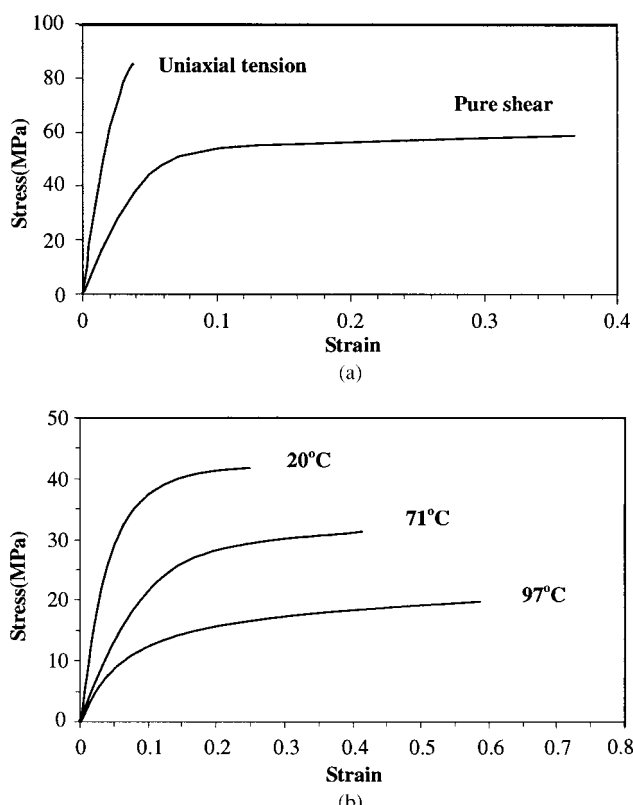


**Figure 9.14** Stress-strain curves of the adhesive:  
(a) Hot-cured rubber-toughened epoxy adhesive at 23°C; (b) shear stress-strain of FM-300 film adhesive at three different temperatures.

characteristics, from which four different methods are presented in this book: linear elastic, linear elastic–perfectly plastic, multilinear elastic strain-hardening, and two-parameter exponential approximations (Lee et al., 1995). Many other representations are also possible (Osswald and Rietveld, 1990).

*(a) Linear Elastic*

The linear elastic constitutive equation for the shear stress  $\tau_a$  versus strain  $\gamma_a$  of an adhesive is simply represented by using the initial shear modulus,  $G_a$ :

$$\tau_a = G_a \gamma_a \quad (9.19)$$

*(b) Linear Elastic–Perfectly Plastic*

The linear elastic–perfectly plastic is expressed as

$$\begin{aligned} \tau_a &= G_a \gamma_a \quad (\gamma_a \leq \gamma_y) \\ \tau_a &= \tau_m \quad (\gamma_a > \gamma_y) \end{aligned} \quad (9.20)$$

where  $\tau_m$  and  $\gamma_y$  are the ultimate shear stress and the yielding shear strain of the adhesive.

*(c) Multilinear Elastic Strain-Hardening*

The shear stress–strain curve for the multilinear elastic strain-hardening is expressed as

$$\begin{aligned} \Delta\tau_a &= G_i \cdot \Delta\gamma_i \quad (\gamma_i < \gamma_a < \gamma_{i+1}) \\ \tau_a &= \sum_{i=0}^{n-1} G_i \cdot \Delta\gamma_i \end{aligned} \quad (9.21)$$

*(d) Two-Parameter Exponential Stress–Strain*

Lee suggested to use the two-parameter exponential approximation represented by two adhesive properties: initial shear modulus,  $G_a$ , and the ultimate shear strength,  $\tau_m$  (Lee et al., 1995),

$$\tau_a = \tau_m \left[ 1 - \exp \left( -\frac{G_a}{\tau_m} \gamma_a \right) \right] \quad (9.22)$$

The two-parameter stress–strain curve is readily determined if the two material properties, initial modulus and ultimate strength, which can be easily obtained from the material suppliers, are known. The equations do not require the determination of the elastic limit of the shear strain. Figure 9.15 shows the shear stress–strain curve represented by the two-parameter exponential approximation and the experimentally determined stress–strain curve for the IPCO 9923 rubber-toughened epoxy adhesive, whose material properties are shown in table 9.3. The properties of  $G_a$  and  $\tau_m$  are functions of temperature and applied strain rate (i.e., viscoelastic).

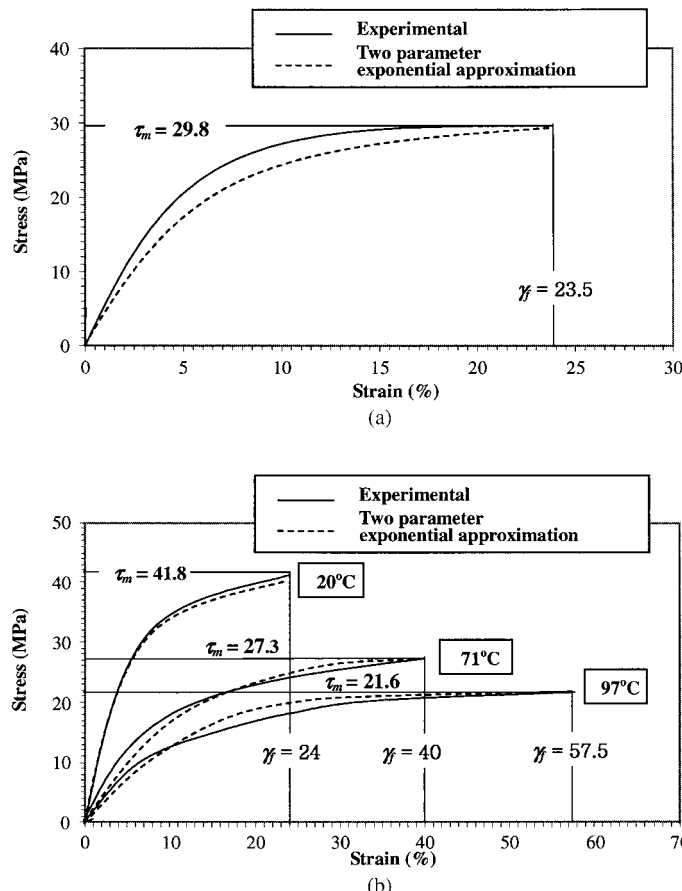


**Figure 9.15** Shear stress–strain curves represented by the two-parameter exponential approximation and the experimentally determined curve: (a) IPCO 9923 epoxy adhesive at 25°C; (b) FM-3000 film adhesive at 20°C ( $G_a = 0.74$  GPa), at 71°C ( $G_a = 0.48$  GPa), and at 91°C ( $G_a = 0.35$  GPa).

**Table 9.3 Typical Properties of Rubber Toughened Epoxy Adhesive (IPCO 9923 from National Starch Co., California)**

Tensile modulus (GPa)	1.30
Shear modulus (GPa)	0.46
Tensile strength (MPa)	39.5
Shear strength (MPa)	29.8
Lap shear strength (ASTM D1002-72) (MPa)	13.7
Shear failure strain (%)	23.5
Poisson's ratio	0.41
CTE ( $\mu$ strain/ $^{\circ}$ C)	72.0
Viscosity	Paste type
Cure temperature ( $^{\circ}$ C)	80.0
Cure time (min)	270.0

#### 9.4.4 Behavior of Tubular Single-Lap Joint under Torque

In order to derive the governing equation for the shear strain distribution, several assumptions were made: the adherends are made of elastic materials, the adhesive is under only shear stress  $\tau_{\theta\theta}$  and the adherends are under only shear stress  $\tau_{\theta z}$  (Adams and Peppiatt, 1977). The governing equations derived with these assumptions can be applied also to the joint whose adherends are made of orthotropic composite materials. Figure 9.16 shows the geometric shape and nomenclature of the tubular single-lap joint for analysis.

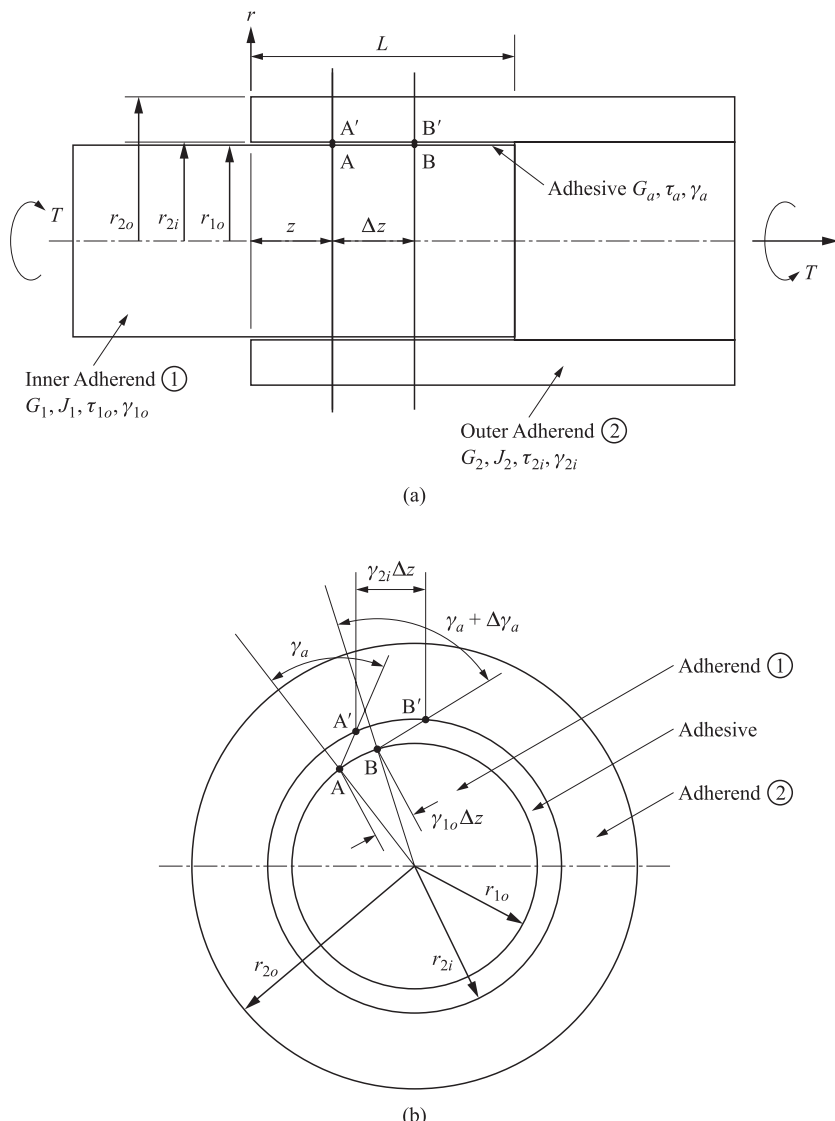


**Figure 9.16** Geometric shape of the adhesively bonded tubular single-lap joint: (a) Shape of the single-lap joint; (b) cross-section of the joint (the adhesive shear deformation  $\gamma_a$  is exaggerated for clarity).

From the torque equilibrium, the sum of torques  $T_1$  and  $T_2$  in the inner and outer adherends of figure 9.16 should be equal to the applied torque  $T$ , that is, the following equation should hold through the adhesive length:

$$T = T_1 + T_2 = \frac{\tau_{1o} J_1}{r_{1o}} + \frac{\tau_{2i} J_2}{r_{2i}} = \text{const} \quad (9.23)$$

where  $\tau_{1o}$  is the shear stress of the inner adherend at radius  $r_{1o}$ ,  $\tau_{2i}$  is the shear stress of the outer adherend at radius  $r_{2i}$ ,  $J_1$  is the sectional polar moment of inertia of the inner adherend, and  $J_2$  is the sectional polar moment of inertia of the outer adherend.

Assuming small adhesive thickness,  $\eta$ , and considering an element of the joint length,  $\Delta z$ , as shown in figure 9.16(b), geometric compatibility yields the following relationship:

$$\eta(\gamma_a + \Delta\gamma_a) - \eta\gamma_a = \gamma_{2i}\Delta z - \gamma_{1o}\Delta z \quad (9.24)$$

where  $\gamma_{1o}$  is the shear strain of the inner adherend at  $r_{1o}$ , and  $\gamma_{2i}$  is the shear strain of the outer adherend at  $r_{2i}$ . In the limit that  $\Delta z$  becomes infinitesimally small, equation (9.24) reduces to

$$\eta \frac{d\gamma_a}{dz} = \gamma_{2i} - \gamma_{1o} \quad (9.25)$$

Assuming the adhesive is an isotropic material and that the thickness of the adhesive is small, the variations of the torque in the  $z$ -direction are expressed as

$$\frac{dT_1}{dz} = -2\pi a^2 \tau_a \quad (9.26)$$

$$\frac{dT_2}{dz} = 2\pi a^2 \tau_a \quad (9.27)$$

where  $a = 1/2(r_{1o} + r_{2i})$  is the average radius of the adhesive.

Using the geometric compatibility and torque equilibrium equations so far derived, the governing equation for the adhesive can be calculated according to the three adhesive constitutive relationships.

#### (a) Linear Elastic Adhesive Properties

Assuming that the adhesive is a linear elastic material, stress and strain distributions of the tubular single-lap joint of figure 9.16 are calculated as follows. Differentiating equation (9.27) with respect to  $z$ , and using the relationships  $T_2 = \tau_{2i} J_2 / r_{2i}$ ,  $\gamma_{2i} = \tau_{2i} / G_2$  and  $\gamma_{1o} = \tau_{1o} / G_1$ , the following equation for  $\tau_{2i}$  is obtained:

$$\frac{d^2\tau_{2i}}{dz^2} = 2\pi a^2 \frac{r_{2i} G_a}{J_2 \eta} \left( \frac{\tau_{2i}}{G_2} - \frac{\tau_{1o}}{G_1} \right) \quad (9.28)$$

Since at  $z = L$ ,  $T = \tau_{2iL} J_2 / r_{2i}$ , equation (9.23) becomes

$$\tau_{1o} = \frac{r_{1o}}{J_1} \left( \frac{\tau_{2iL} J_2}{r_{2i}} - \frac{\tau_{2i} J_2}{r_{2i}} \right) \quad (9.29)$$

Substituting equation (9.29) into equation (9.28), we obtain the following second-order differential equation in  $\tau_{2i}$ :

$$\frac{d^2\tau_{2i}}{dz^2} = 2\pi a^2 \frac{G_a}{\eta} \left( \frac{r_{2i}}{G_2 J_2} + \frac{r_{1o}}{G_1 J_1} \right) \tau_{2i} - \frac{2\pi a^2 G_a \tau_{2iL} r_{1o}}{\eta G_1 J_1} \quad (9.30)$$

Equation (9.30) can be rewritten in the simplified form

$$\frac{d^2\tau_{2i}}{dz^2} = \alpha^2 \tau_{2i} - \delta \tau_{2iL} \quad (9.31)$$

where

$$\delta = \frac{2\pi a^2 r_{1o} G_a}{G_1 J_1 \eta} \quad (9.32)$$

$$\phi = \frac{G_2 J_2 r_{1o}}{G_1 J_1 r_{2i} + G_2 J_2 r_{1o}} \quad (9.33)$$

$$\alpha = \left( \frac{\delta}{\phi} \right)^{0.5} \quad (9.34)$$

The boundary conditions for equation (9.31) are:

At  $z = 0$

$$\tau_{2i} = 0 \quad (9.35)$$

At  $z = L$

$$\tau_{2i} = \frac{T r_{2i}}{J_2} \quad (9.36)$$

The solution for the adherend stress,  $\tau_{2i}$ , is

$$\tau_{2i} = \frac{T r_{2i}}{J_2} \left\{ \phi (1 - \cosh \alpha z) + \left[ \frac{1 - \phi (1 - \cosh \alpha L)}{\sinh \alpha L} \right] \sinh \alpha z \right\} \quad (9.37)$$

Then, from equation (9.27) with the relation of  $T_2 = \tau_{2i} J_2 / r_{2i}$ , the shear stress in the adhesive is expressed as

$$\tau_a = \frac{T \alpha}{2\pi a^2} \left\{ \left[ \frac{1 - \phi (1 - \cosh \alpha L)}{\sinh \alpha L} \right] \cosh \alpha z - \phi \sinh \alpha z \right\} \quad (9.38)$$

Figure 9.17 shows the stress distribution of adhesive layer from equation (9.38) under a torque of 88.5 Nm. The shear stress distribution of figure 9.17 is calculated for the adhesively bonded joint whose specifications are listed in table 9.4. According to equation (9.38), the shear stress at  $z = 0$  is larger than the shear stress at  $z = L$  when  $\phi$  is larger than 0.5. The minimum shear stress occurs at the intermediate value of  $z_{min}$ , which is expressed as (Lee et al., 1991a)

$$z_{min} = \frac{1}{2\alpha} \ln \left( \frac{1 - \phi + \phi \cosh \alpha L + \phi \sinh \alpha L}{1 - \phi + \phi \cosh \alpha L - \phi \sinh \alpha L} \right) \quad (9.39)$$

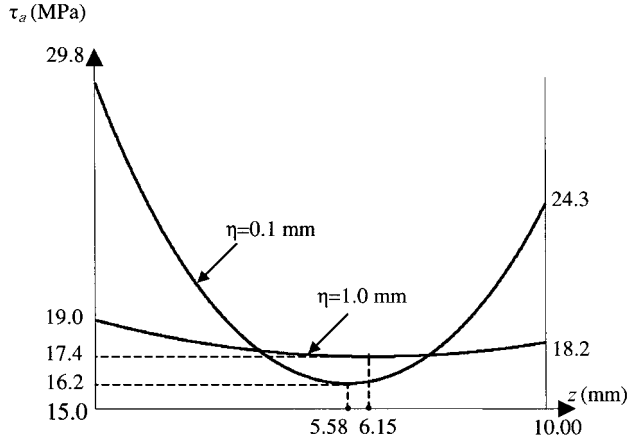


**Figure 9.17** Shear stress distributions of the adhesive layer of the joint of table 9.4 under a torque of 88.5 Nm (maximum failure torque of 0.1 mm adhesive thickness) when the bonding length is 10 mm and adhesive thicknesses are 0.1 and 1.0 mm, respectively.

**Table 9.4 Specifications of the Adhesively Bonded Tubular Single-lap Joint**

	Shear modulus (GPa)	Polar moment of inertia ( $10^{-9} \text{ m}^4$ )	Thickness (mm)	Inner radius (mm)	Outer radius (mm)	Bonding length (mm)
Adhesive (IPCO 9923)	0.46	–	0.1	8.4	8.5	10.0
Inner adherend (steel solid rod)	80.0	7.82	–	0.0	8.4	10.0
Outer adherend (steel hollow tube)	80.0	10.89	2.0	8.5	10.5	10.0

The shear stress at  $z = z_{\min}$  calculated based on the linear elastic adhesive property is usually much smaller than the shear stresses at both ends ( $z = 0$ , and  $z = L$ ), which shows a kind of stress concentration.

#### (b) Two-Parameter Exponential Approximation of Adhesive

The geometric compatibility between the shear strain of the adhesive and the shear strains of the adherends can be written as

$$\frac{d\gamma_a}{dz} = \frac{\gamma_{2i} - \gamma_{1o}}{\eta} = \frac{1}{\eta} \left( \frac{T_2 r_{2i}}{G_2 J_2} - \frac{T_1 r_{1o}}{G_1 J_1} \right) = \frac{1}{\eta} \left[ \frac{T_2 r_{2i}}{G_2 J_2} - \left( \frac{r_{1o}}{G_1 J_1} + \frac{r_{2i}}{G_2 J_2} \right) T_1 \right] \quad (9.40)$$

where  $G_1$  and  $G_2$  are the shear moduli of the inner and outer adherend, respectively. Differentiating equation (9.40) with respect to  $z$ , the following equation can be obtained:

$$\frac{d^2\gamma_a}{dz^2} = -\frac{1}{\eta} \left( \frac{r_{1o}}{G_1 J_1} + \frac{r_{2i}}{G_2 J_2} \right) \frac{dT_1}{dz} \quad (9.41)$$

Substituting equation (9.22) into equation (9.26) and then substituting the resulting equation into equation (9.41) results in the governing differential equation of the shear strain of the adhesive:

$$\begin{aligned}\frac{d^2\gamma_a}{dz^2} &= \frac{2\pi a^2}{\eta} \left( \frac{r_{1o}}{G_1 J_1} + \frac{r_{2i}}{G_2 J_2} \right) \tau_m \left[ 1 - \exp\left(-\frac{G_a}{\tau_m} \gamma_a\right) \right] \\ &= \mu \tau_m \left[ 1 - \exp\left(-\frac{G_a}{\tau_m} \gamma_a\right) \right]\end{aligned}\quad (9.42)$$

where

$$\mu = \frac{2\pi a^2}{\eta} \left( \frac{r_{1o}}{G_1 J_1} + \frac{r_{2i}}{G_2 J_2} \right)\quad (9.43)$$

Since  $T_1 = T$ ,  $T_2 = 0$  when  $z = 0$ , the following boundary conditions are obtained from equations (9.40) and (9.42):

$$\left. \frac{d\gamma_a}{dz} \right|_{z=0} = \gamma'_a(0) = -\frac{1}{\eta} \left( \frac{T r_{1o}}{G_1 J_1} \right)\quad (9.44)$$

$$\left. \frac{d^2\gamma_a}{dz^2} \right|_{z=0} = \gamma''_a(0) = \mu \tau_m \left[ 1 - \exp\left(-\frac{G_a}{\tau_m} \gamma_a(0)\right) \right]\quad (9.45)$$

Differentiating equation (9.42), the third-order derivative boundary condition is obtained:

$$\left. \frac{d^3\gamma_a}{dz^3} \right|_{z=0} = \gamma'''_a(0) = \mu G_a \gamma'_a(0) \exp\left(-\frac{G_a}{\tau_m} \gamma_a(0)\right)\quad (9.46)$$

Since  $T_1 = 0$ ,  $T_2 = T$  when  $z = L$ , another boundary condition is obtained:

$$\left. \frac{d\gamma_a}{dz} \right|_{z=L} = \gamma'_a(L) = \frac{1}{\eta} \left( \frac{T r_{2i}}{G_2 J_2} \right)\quad (9.47)$$

Equation (9.42) was solved by a numerical method using the Taylor series expansion method including the maximum third-order derivative:

$$\gamma_a(z+h) = \gamma_a(z) + \gamma'_a(z)h + \gamma''_a(z) \frac{h^2}{2} + \gamma'''_a(z) \frac{h^3}{6} + \dots\quad (9.48)$$

$$\gamma'_a(z+h) = \gamma'_a(z) + \gamma''_a(z)h + \gamma'''_a(z) \frac{h^2}{2} + \dots\quad (9.49)$$

$$\gamma''_a(z+h) = \gamma''_a(z) + \gamma'''_a(z)h + \dots\quad (9.50)$$

$$\gamma'''_a(z+h) = \gamma'''_a(z) + \dots\quad (9.51)$$

where  $\gamma_a(z)$  is the shear strain at the distance  $z$  and  $h$  is the incremental distance along the  $z$ -axis. The maximum torque transmission capability can be calculated by

assuming that either one or the other end of the adhesive reached the failure shear strain  $\gamma_f$ . Since the magnitude of the first derivative of the shear strain  $\gamma'_a(z)$  becomes smaller as the shear strain approaches the failure strain, the end that reaches the failure strain first was determined by comparing the magnitudes  $\gamma'_a(0)$  and  $\gamma'_a(L)$ . Then the other end should satisfy the condition of the first derivative of the shear strain. Since the first derivative contains the applied torque  $T$ , this condition gives the maximum torque. For the joint in table 9.4, the first adhesive failure occurred at  $z=0$ . In the numerical calculation, the first trial value of  $T$  was calculated by assuming that all of the adhesive area reaches the ultimate shear stress  $\tau_{\max}$ , and then the value of torque was decreased successively to satisfy the first derivative of the boundary conditions.

### (c) Linear Elastic–Perfectly Plastic Approximation

For the application of linear elastic–perfectly plastic approximation of adhesive to the adhesive joint of figure 9.18, it is assumed that the regions I and III reach the perfectly plastic zone, whose shear stress,  $\tau_m$ , is constant, and region II is in the elastic zone. Two sections  $z=L_{Y1}$  and  $z=L-L_{Y2}$  are the boundaries of the elastic and plastic zones. The analysis was performed in three different regions (Lee et al., 1995).

#### REGION I

Since the adhesive stress was assumed to be the constant  $\tau_m$  in region I ( $0 < z < L_{Y1}$ ) of the adhesive, the variation of torque with respect to  $z$  in region I can be expressed as

$$\frac{dT_2}{dz} = 2\pi a^2 \tau_m = -\frac{dT_1}{dz} \quad (9.52)$$

The boundary condition for equation (9.52) at  $z=0$  is

$$\text{When } z=0, \quad T_2 = \tau_{2i} = 0 \quad (9.53)$$

Integrating equation (9.52) and using the boundary condition of equation (9.53), the torques  $T_1$  and  $T_2$  can be calculated:

$$T_1 = T - 2\pi a^2 \tau_m z = \frac{\tau_{1o} J_1}{r_{1o}} \quad (9.54)$$

$$T_2 = 2\pi a^2 \tau_m z = \frac{\tau_{2i} J_2}{r_{2i}} \quad (9.55)$$

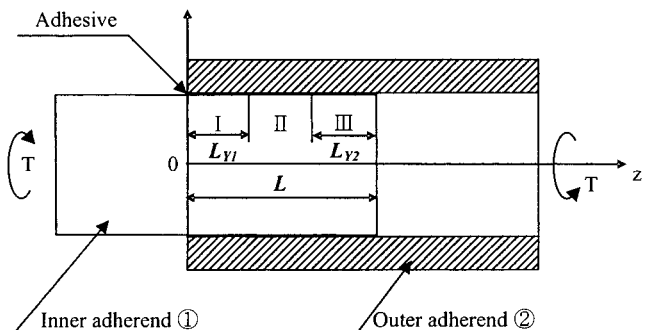


**Figure 9.18** Linear elastic and perfectly plastic zones in the bonding length.

The geometric compatibility of equation (9.40) becomes

$$\frac{d\gamma_a}{dz} = \frac{1}{\eta} (2Az - B) \quad (9.56)$$

where

$$A = \left( \frac{r_{1o}}{G_1 J_1} + \frac{r_{2i}}{G_2 J_2} \right) \pi a^2 \tau_m \quad (9.57)$$

$$B = \frac{r_{1o}}{G_1 J_1} T \quad (9.58)$$

The boundary condition for equation (9.56) is

$$\text{When } z = L_{Y1}, \quad \gamma_a = \gamma_y = \frac{\tau_m}{G_a} \quad (9.59)$$

Integrating equation (9.56) with the boundary condition of equation (9.59), the shear strain of the adhesive can be calculated:

$$\gamma_a = \frac{\tau_m}{G_a} + \frac{1}{\eta} [A(z^2 - L_{Y1}^2) - B(z - L_{Y1})] \quad (9.60)$$

## REGION II

Since region II ( $L_{Y1} < z < L - L_{Y2}$ ) of the adhesive was assumed to be an elastic zone, the variation of the torque with respect to  $z$  was expressed in equation (9.27):

$$\frac{dT_2}{dz} = 2\pi a^2 \tau_a \quad (9.27)$$

Differentiating equation (9.27) with respect to  $z$  and using the geometric compatibility of equation (9.25) and torque equilibrium equation (9.23) yields

$$\frac{d^2\tau_{2i}}{dz^2} = \alpha^2 \tau_{2i} - \delta \frac{Tr_{2i}}{J_2} \quad (9.61)$$

The boundary conditions for equation (9.61) in region II are

$$\text{When } z = L_{Y1}, \quad \tau_{2i} = \frac{2\pi a^2 r_{2i} \tau_m}{J_2} L_{Y1} = D \quad (9.62)$$

$$\text{When } z = L - L_{Y2}, \quad \tau_{2i} = \frac{Tr_{2i}}{J_2} - \frac{2\pi a^2 r_{2i} \tau_m}{J_2} L_{Y2} = E \quad (9.63)$$

Integrating equation (9.61) with the boundary conditions of equations (9.62) and (9.63),  $\tau_{2i}$  is obtained:

$$\tau_{2i} = C_1 \cosh(\alpha z) + C_2 \sinh(\alpha z) + \phi \frac{r_{2i}}{J_2} T \quad (9.64)$$

where  $C_1$  and  $C_2$  are defined as

$$C_1 = \frac{\sinh[\alpha(L - L_{Y2})](D - \phi(r_{2i}/J_2)T) - \sinh(\alpha L_{Y1})(E - \phi(r_{2i}/J_2)T)}{\cosh(\alpha L_{Y1}) \sinh[\alpha(L - L_{Y2})] - \sinh(\alpha L_{Y1}) \cosh[\alpha(L - L_{Y2})]} \quad (9.65)$$

$$C_2 = \frac{\cosh(\alpha L_{Y1})(E - \phi(r_{2i}/J_2)T) - \cosh([\alpha(L - L_{Y2})]D - \phi(r_{2i}/J_2)T)}{\cosh(\alpha L_{Y1}) \sinh[\alpha(L - L_{Y2})] - \sinh(\alpha L_{Y1}) \cosh[\alpha(L - L_{Y2})]} \quad (9.66)$$

Since  $T_2 = \tau_{2i} J_2 / r_{2i}$  can be calculated from equation (9.64), the shear stress  $\tau_a$  of the adhesive is obtained by substituting  $dT_2/dz$  into equation (9.27):

$$\tau_a = \frac{J_2}{2\pi a^2 r_{2i}} [C_1 \alpha \sinh(\alpha z) + C_2 \alpha \cosh(\alpha z)] \quad (9.67)$$

### REGION III

In region III ( $L - L_{Y2} < z < L$ ) of the adhesive, the variation of the torque with respect to  $z$  is

$$\frac{dT_2}{dz} = 2\pi a^2 \tau_m = -\frac{dT_1}{dz} \quad (9.68)$$

The boundary conditions for equation (9.68) are

$$\text{When } z = L, \tau_{2i} = \frac{T r_{2i}}{J_2} \quad (9.69)$$

$$\text{When } z = L - L_{Y2}, \gamma_y = \frac{\tau_m}{G_a} \quad (9.70)$$

The strain  $\gamma_a$  of the adhesive in region III can be calculated with the boundary conditions of equations (9.69) and (9.70) by the same method as in region I:

$$\gamma_a = \frac{\tau_m}{G_a} - \frac{1}{\eta} [A(z^2 - 2Lz + L^2 - L_{Y2}^2) + B'(z - L + L_{Y2})] \quad (9.71)$$

where  $B'$  is defined as

$$B' = \frac{r_{2o}}{G_2 J_2} T \quad (9.72)$$

Since the adhesive shear stress  $\tau_a$  in equation (9.67) is  $\tau_m$  at both  $z = L_{Y1}$  and  $z = L - L_{Y2}$ , two relationships between  $L_{Y1}$ ,  $L_{Y2}$ , and  $T$  can be obtained. If the value of  $L_{Y1}$  (or  $L_{Y2}$ ) is given, the value of  $L_{Y2}$  (or  $L_{Y1}$ ) and  $T$  can be numerically calculated from the two relationships. Then, using equations (9.60) and (9.71), the shear strains at  $z = 0$  and  $z = L$  can be calculated. If the shear strain at either end of the joint does not reach the failure strain of the adhesive, the value of  $L_{Y1}$  (or  $L_{Y2}$ ) is increased and the previous steps are repeated until the shear strain at either end of the joint reaches the failure shear strain of the adhesive. The value of  $T$  becomes the torque transmission capability of the adhesively bonded joint when the shear strain at either end reaches the failure shear strain of adhesive. The distribution of the shear stress  $\tau_a$  in region II is obtained by equation (9.67) and the distributions of the shear

strains in regions I and III are obtained by equations (9.60) and (9.71), respectively. Since the maximum shear strain of the adhesive occurs at either end of the adhesive, the two shear strains at the ends of the adhesive were calculated and compared.

*(d) Multilinear Strain-Hardening Approximation*

As we have seen the complicated procedure to obtain the stress and strain distributions of adhesive in analytical forms, the best way is to resort to the finite element method. Figure 9.19 represents the finite element meshes used for the analysis of the tubular single lap joint under torque. The finite element program used was ANSYS in which eight-node 3-D isoparametric elements were used for the analysis. The adhesive shear property was represented by many straight line segments (multilinear strain-hardening approximation). Figure 9.20 and table 9.4 show the dimensions and specifications for the adhesively bonded single-lap joint used in computations and experiments (Lee et al., 1995).

Figure 9.21 shows the shear stress and strain distributions in the adhesive of the single-lap joint when the bonding length is 10 mm under an applied torque of 120 Nm. From figure 9.21, we can see that the shear stresses calculated by the

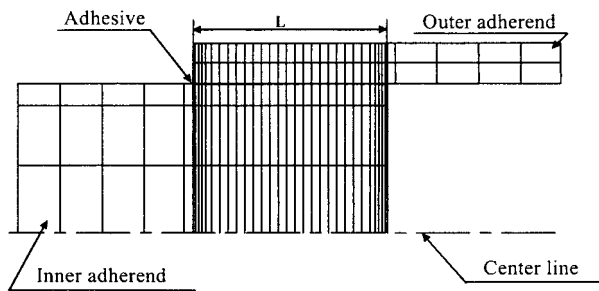


**Figure 9.19** Finite element mesh for the tubular single-lap joint.

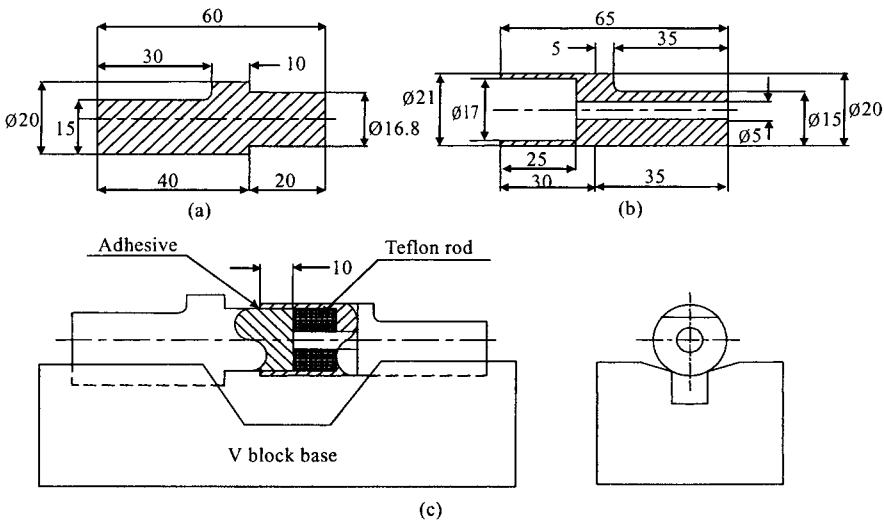


**Figure 9.20** Dimensions (mm) of the adherends of the tubular single-lap joint: (a) Inner adherend; (b) outer adherend; (c) assembled on a precision V-block.

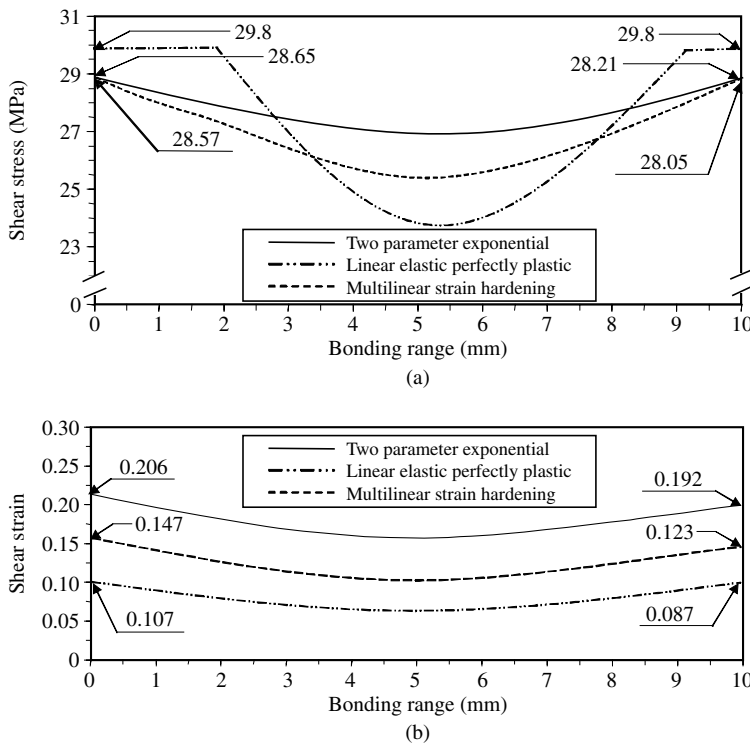


**Figure 9.21** Shear stress and strain distributions in the adhesive of the single-lap joint when the bonding length is 10 mm under an applied torque of 120 Nm (from Lee et al., 1995).

three constitutive relations are not much different, while the shear strains are much different because the majority of the adhesive is under a shear stress close to the ultimate shear strength with the shear-strain-hardening effect. The shear strains at the two ends of the joint are different because the joint is not symmetric with respect to the cross-sectional plane.

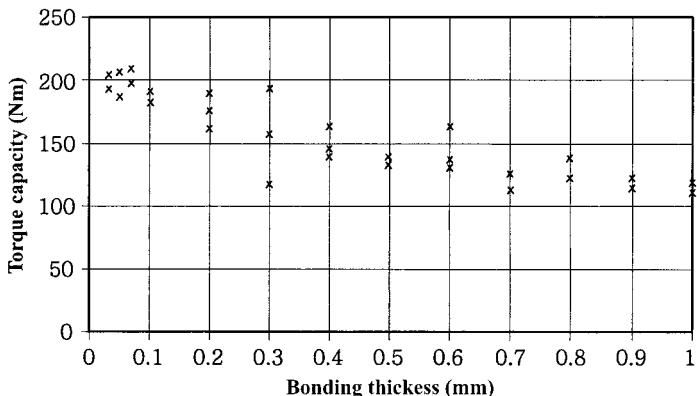
Table 9.5 shows the maximum torque transmission capabilities, experimentally measured and calculated using the four different adhesive constitutive relations, including the linear elastic adhesive properties. The adhesive model with linear elastic adhesive properties underpredicts by more than 30% of the experimental measurement, while all the other three nonlinear approximations accurately predict the torque transmission capability with errors less than 5%. The two-parameter exponential approximation method gives the best prediction with a compact form, therefore it is recommended as the constitutive equation of the adhesive for the analysis and design of adhesively bonded tubular single-lap joints.

#### 9.4.5 Adhesive Thickness Effects

The torque capacity of the adhesively bonded tubular lap joint depends heavily on the adhesive thickness. The closed-form solution, equation (9.38), and the finite element calculation (Hipol, 1984) predicted that the torque capacity of the joint increased as the adhesive thickness increased as shown in figure 9.17, which was usually contrary to the experimental test results (Lee and Lee, 1992). Figure 9.22

**Table 9.5 Maximum Torque Transmission Capabilities of the Tubular Single-Lap Joint of Table 9.4 (Bonding Length = 10 mm)**

Experiment	<i>Maximum torque (Nm)</i>	<i>Error (%)</i>
Average:	128.1	
Standard deviation:	2.6	
Analysis:		
Linear elastic	88.5	−30.9
Two-parameter	127.6	−0.4
Linear elastic–perfectly plastic	133.4	4.1
Multilinear strain hardening	131.8	2.9

**Figure 9.22** Experimentally measured static torque capacity of the adhesively bonded tubular single-lap joints (from Lee and Lee, 1992).

shows the experimental static torque transmission capability results of the single lap joint of Table 9.4 with respect to the adhesive thickness when the adhesive bonding length was 15 mm in this case. The torque transmission capabilities in this case increased about 50% compared with the results of table 9.5 because the bonding length was increased from 10 mm to 15 mm.

In figure 9.22, the static torque transmission capability of the adhesively bonded tubular single-lap joint was almost constant when the adhesive thickness was in the range 0.02–0.1 mm. The near constant torque capacity at the adhesive layer thickness of less than 0.1 mm might be explained by the fully plastic deformation of the adhesive layer without interfacial debonding between the adhesive and the adherends until one of the adhesive ends reached the failure strain.

As the adhesive thickness increased further, the torque capacity of the joint decreased rapidly, which was contrary to the calculated results. The decrease of the torque capacity beyond 0.1 mm of adhesive thickness might be explained by the interfacial debonding between the adhesive and the adherends before the adhesive reached the failure strain, because the residual thermal stresses due to fabrication increase as the adhesive thickness increases.

In order to predict the torque transmission capability of the adhesively bonded joint, both the residual thermal stresses due to fabrication and the mechanical

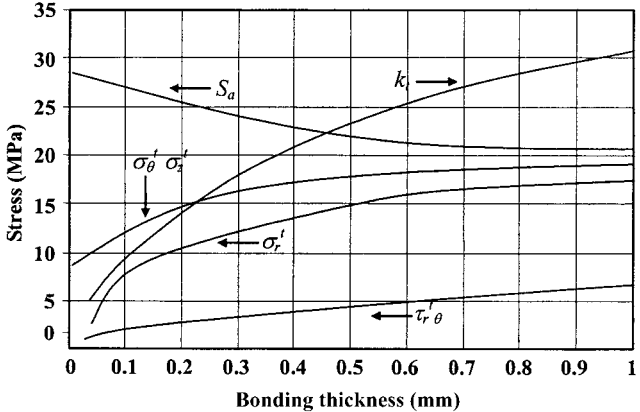


**Figure 9.23** Calculated residual thermal stresses due to fabrication ( $\sigma_r^t$ ,  $\sigma_\theta^t$ ,  $\sigma_z^t$ , and  $\tau_{r\theta}^t$ ), reduced shear strength  $S_a$ , and the nondimensional stress deviation factor  $k_t$ , w.r.t. adhesive thickness.

stresses due to applied load were calculated using the axisymmetric finite element method with the assumption of linear elastic properties of adhesive and adherends (Lee and Lee, 1992). Figure 9.23 shows the residual thermal stresses calculated by the finite element method.

Lee and Lee (1992) defined the reduced shear strength  $S_a$  by the following equation to predict the interfacial failure due to thermal residual stresses:

$$S_a = S_s \left\{ 1 - \left[ \left( \frac{\sigma_r^t}{S_t} \right)^2 + \left( \frac{\sigma_\theta^t}{S_t} \right)^2 + \left( \frac{\sigma_z^t}{S_t} \right)^2 + \left( \frac{\tau_{r\theta}^t}{S_t} \right)^2 \right] \right\}^{1/2} \quad (9.73)$$

where  $S_s$  = bulk shear strength of the adhesive

$S_t$  = bulk tensile strength of the adhesive

$\sigma_r^t$ ,  $\sigma_\theta^t$ ,  $\sigma_z^t$  = thermal residual tensile stresses in the  $r$ -,  $\theta$ -,  $z$ -directions

$\tau_{r\theta}^t$  = thermal residual shear stress in the  $r-\theta$ -plane

Here,  $S_a$  represents the reduced bulk shear strength in which the effect of the residual thermal stresses was incorporated. In figure 9.23, the reduced shear strength  $S_a$  decreased as the adhesive thickness increased. Lee and Lee (1992) defined the nondimensional stress deviation factor  $k_t$  as

$$k_t = \frac{S_s - S_a}{S_s} \quad (9.74)$$

Here,  $k_t$  represents the effect of the residual thermal stress on the adhesive failure shear strength.

The value of  $k_t$  is 0 when there is no residual thermal stress, and it increases as the residual thermal stress increases. Lee and Lee (1992) found that the adhesively bonded tubular single-lap joint of table 9.4 (bonding length = 15 mm in this case) failed with the bulk adhesive failure mode when the value of  $k_t$  was less than 0.085. They also found that the joint failure mode changed from the bulk failure of the adhesive into the interfacial failure mode via the transient failure mode in which the adhesive joint failure was caused partly by the bulk mode and partly by the interfacial mode as the value of  $k_t$  increased beyond 0.085.

In order to verify the effect of thermal residual stresses on the adhesively bonded tubular single-lap joint, Choi and Lee (1996) tested the adhesive joints cured at 20°C

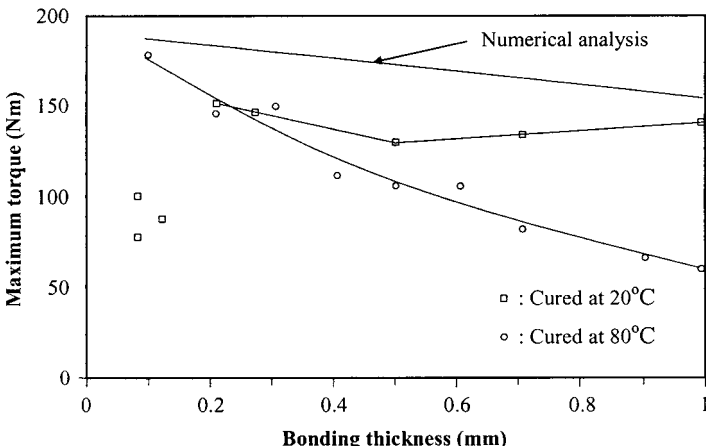


**Figure 9.24** Effect of cure temperature on the torque capacity of the adhesive joints (from Choi and Lee, 1996).

and 80°C. For the room-cured joints, the curing operation was performed for 3 days at 20°C and the specimen was postcured for 2 hours at 80°C to complete the chemical reaction. For the room-cured joints, the torque transmission capability of the joint increased, as shown in figure 9.24, when the adhesive thickness was larger than 0.3 mm. Furthermore, the torque transmission capability of the joint cured at 20°C was much larger than that of the joint cured at 80°C when the adhesive thickness was larger than 0.5 mm. Also, the trend of the torque transmission capability of the joint cured at 20°C appeared to follow the numerical solution with nonlinear adhesive properties.

However, when the adhesive thickness was smaller than 0.2 mm, the torque transmission capability of the joint cured at 20°C was much smaller than that of the joint cured at 80°C, which was caused by the interfacial failure.

In order to experimentally investigate this phenomenon, the interface between the adherend and adhesive was observed by SEM (scanning electron microscopy). In order to observe the interface between the adhesive and the adherend, a tubular adherend with a mirror surface ground flange was attached to a mirror surface ground plate, as shown in figure 9.25.

After curing the adhesive, the plate was separated from the joint and the interface of the joint was observed. Figures 9.26(a) and (b) show the interfaces between the adherend and the adhesive, which were cured at 80°C and 20°C, respectively. Both joints had the same 0.1 mm adhesive thickness. From figure 9.26, it was observed that the adhesive cured at 20°C could not penetrate into the surface of the steel adherend when the adhesive thickness was 0.1 mm. This phenomenon can be explained by the fact that the viscosity and surface tension of the adhesive were too high at the room temperature for the adhesive to penetrate into the narrow cleavage of the adherends. Actually, an ideal adhesive should possess a viscosity of no more than a few centipoises during the bonding operation to be able to spread over the solid surface and to displace air and other contaminants that may be present on the surface (Kinloch, 1987), which will be discussed in more detail in Section 9.4.8.

Figures 9.27(a) and (b) show the interfaces between the adherend and the adhesive cured at 80°C and 20°C, respectively, when the adhesive thickness is 1.0 mm. From figure 9.27, the difference in the bonding qualities cannot be easily seen, but the joint

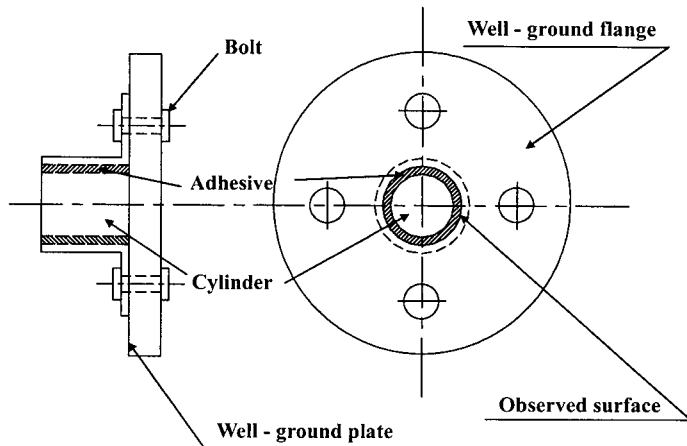


**Figure 9.25** Shape of the specimens for the SEM photograph (from Choi and Lee, 1996).

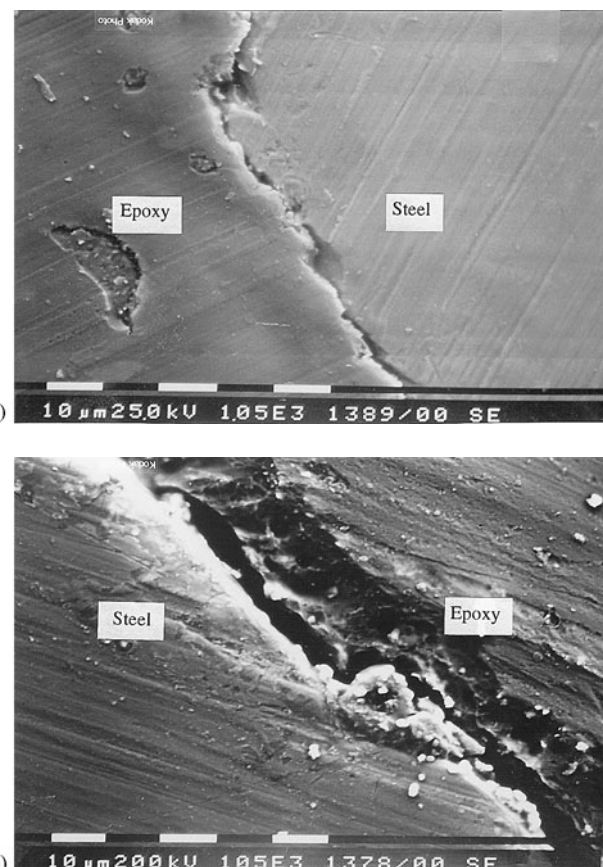


**Figure 9.26** Scanning electron micrograph (SEM) of the interface between the steel adherend and the adhesive when the adhesive thickness is 0.1 mm: (a) cured at 80°C; (b) cured at 20°C from (Choi and Lee, 1996).

cured at 80°C has a slightly larger gap due to the thermal contraction of adhesive. Therefore, it was concluded that the adhesive cured at 80°C had better wetting characteristics than the adhesive cured at 20°C when the adhesive thickness was 0.1 mm. However, the wetting characteristics of the joint cured at 20°C improved as

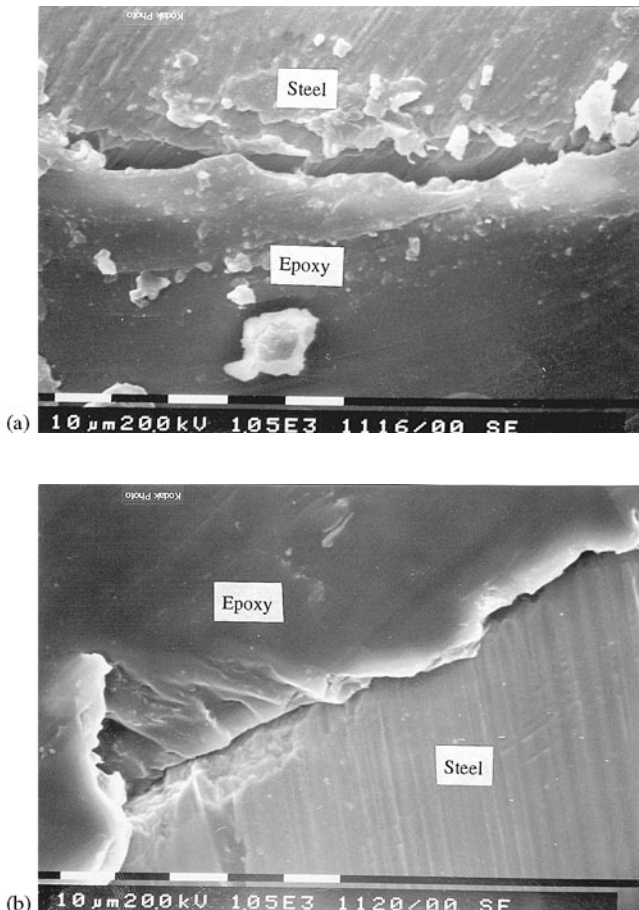


**Figure 9.27** Scanning electron micrograph of the interface between the steel and the adhesive when the adhesive thickness is 1.0 mm: (a) Cured at 80°C; (b) cured at 20°C (from Choi and Lee, 1996).

the adhesive thickness was increased. When the adhesive thickness was 1.0 mm, the torque transmission capability of the joint cured at 80°C was much lower than that of the same adhesive thickness cured at 20°C due to the fabrication thermal residual stress of the joint cured at 80°C, which might increase the nondimensional stress deviation factor  $k_t$ . From the above results, we may recommend that the adhesive joint should be cured at elevated temperature when the adhesive thickness is small, but should be cured at room temperature when the adhesive thickness is large, in order to reduce the tensile thermal residual stress. From the productivity point of view, the adhesive should be cured at elevated temperature to decrease the cure time. Therefore, the best solution might be to cure the adhesive at elevated temperature, with small adhesive thickness.

#### 9.4.6 Behavior of Tubular Double-Lap Joint under Torque

There have been several research investigations on the torque transmission capability and stress distribution of the adhesively bonded tubular double-lap joint. From the analytical solution with linear elastic adhesive properties (Lee and Lee, 1994), it was predicted that the torque transmission capabilities of the double-lap joint were about twice that of comparable-size single-lap joints. However, in the static tests, it was found that the torque transmission capability of the double-lap joint was 2.7 times

that of the single-lap joint, which was also verified by the finite element method, taking into consideration adhesive nonlinear properties (Choi and Lee, 1994). The average fatigue strength of the double-lap joint was increased 6.5 times over that of the single-lap joint. Therefore, the nonlinear adhesive properties should be used to predict accurately the behavior of adhesive joints.

#### 9.4.7 Behavior of Double-Lap Joint under Tensile Load

When a single-lap joint is under tensile load, the peel stresses perpendicular to the adhesive surface layer are generated as a result of the eccentricity of the loading of joint. To eliminate the peel stresses due to bending of adherends, let us consider the double-lap joint of figure 9.28 for simplicity of analysis (Bikerman, 1968).

If a tensile force  $F_0$  is applied to this member, the force acts on all cross-sections of the inner adherend above level  $ab$ , while tensile force acting on the inner adherend at the  $cd$  level ( $z = 0$ ) is zero. Thus, the force  $F$  along the axis of  $z$  decreases from  $F_0$  to 0 when  $z$  decreases from  $L$  to 0,  $L$  being the length of the overlap. This decrease of  $F$  occurs because  $F$  is gradually balanced by shearing forces along the adherend–adhesive interface. Considering the force balance of a horizontal slice of thickness  $dz$ , we have the relationship

$$F + \frac{\partial F}{\partial z} dz - F = 2\tau_a w dz$$

or

$$\frac{\partial F}{\partial z} = 2\tau_a w \quad (9.75)$$

where  $\tau_a$  is the adhesive shear stress and  $w$  is the thickness of the joint in the  $y$ -direction. Assuming that the tensile stress  $\sigma$  in the inner adherend is constant along the  $x$ -direction, the force  $F$  is expressed as follows:

$$F = w\delta\sigma \quad (9.76)$$

where  $\delta$  is the width of the inner adherend. Substituting equation (9.76) into equation (9.75), we obtain

$$\frac{\partial\sigma}{\partial z} = \frac{2\tau_a}{\delta} \quad (9.77)$$

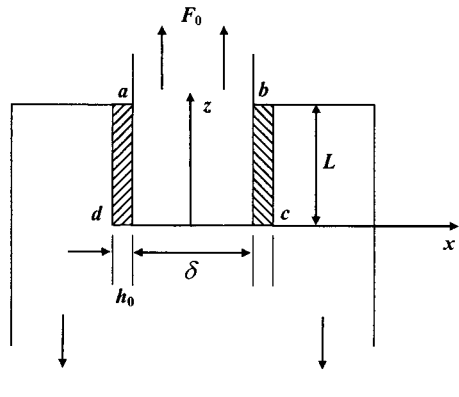


**Figure 9.28** Configuration of a double-lap joint (from Bikerman, 1968).

assuming elastic behavior of the inner adherend, that is,

$$\sigma = E \frac{\partial u}{\partial z} \quad (9.78)$$

where  $E$  and  $u$  are the Young's modulus and displacement of the inner adherend, respectively.

Substituting equation (9.78) into equation (9.77), we have

$$\frac{\partial^2 u}{\partial z^2} = \frac{2 \tau_a}{E \delta} \quad (9.79)$$

When the adhesive is assumed linear elastic, which is not a realistic assumption, however, the shear stress  $\tau_a$  of the adhesive can be expressed as

$$\tau_a = G_a \frac{u}{h_0} \quad (9.80)$$

where  $h_0$  is the adhesive thickness.

Substituting equation (9.80) into equation (9.79), we obtain

$$\frac{\partial^2 u}{\partial z^2} = \frac{2G_a}{E\delta h_0} u \quad (9.81)$$

For the boundary conditions for equation (9.81), we may give the following conditions:

$$\text{When } z = 0, \quad u = \sigma = \tau_a = 0 \quad (9.82)$$

However, there is no solution that satisfies the above three conditions simultaneously.

If we seek the solution that satisfies only two boundary conditions, such as  $u = \tau_a = 0$  at  $z = 0$ , we obtain

$$u = \frac{\sigma_0}{E\lambda} \frac{e^{\lambda z} - e^{-\lambda z}}{e^{\lambda L} + e^{-\lambda L}} \quad (9.83)$$

where

$$\lambda = \sqrt{\frac{2G_a}{E\delta h_0}} \quad (9.84)$$

In equation (9.83),  $\sigma_0$  represents the tensile stress of the inner adherend at large value of  $z$ ,  $z = L$ , which can be expressed as

$$\sigma_0 = \frac{F_0}{w\delta} \quad (9.85)$$

Equation (9.83) gives a finite value of  $\sigma$  at  $z = 0$ .

If a solution satisfying the boundary condition  $\sigma = 0$  at  $z = 0$  is sought, we obtain

$$u = \frac{\sigma_0}{E\lambda} \frac{e^{\lambda z} + e^{-\lambda z}}{e^{\lambda L} + e^{-\lambda L}} \quad (9.86)$$

When  $z = 0$ , from equations (9.80) and (9.86), we have a finite value of  $\tau_a$ .

$$\tau_{a,z=0} = \sigma_0 \sqrt{\frac{G_a \delta}{2h_0 E}} \sec h(\lambda L) \quad (9.87)$$

For the design of adhesive joints, the shear stress distribution at  $z = L$  is more important than that at  $z = 0$  because the most dangerous stress  $\tau_a$  occurs at the upper end of the overlap. If  $\lambda$  is not too small and  $L$  not too short, the two equations (9.83) and (9.86) give almost identical results for the value of  $u$  at  $z = L$ , because near this point  $e^{-\lambda z}$  is negligible compared with  $e^{\lambda z}$ . Thus, for this case,  $u$  and  $\tau_{a\max}$  are expressed as

$$u = \frac{\sigma_0}{E\lambda} = \sigma_0 \sqrt{\frac{\delta h_0}{2EG_a}} \quad (9.88)$$

$$\tau_{a\max} = \sigma_0 \sqrt{\frac{G_a \delta}{2Eh_0}} \quad (9.89)$$

The average shear stress  $\tau_{av}$  in the adhesive is

$$\tau_{av} = \frac{F_0}{2wL} = \frac{\sigma_0 \delta}{2L} \quad (9.90)$$

Hence the greatest stress concentration factor  $K_t$  is

$$K_t = \frac{\tau_{a\max}}{\tau_{av}} = L \sqrt{\frac{2G_a}{E\delta h_0}} \quad (9.91)$$

The preceding treatment and the final equation (9.91) can be used only if the adherends and the adhesive are linear elastic materials, without bending of the adherends. When the bending deformation of adherends by an external pull, as shown in figure 9.29, is induced, the joint shape will be changed, as shown in

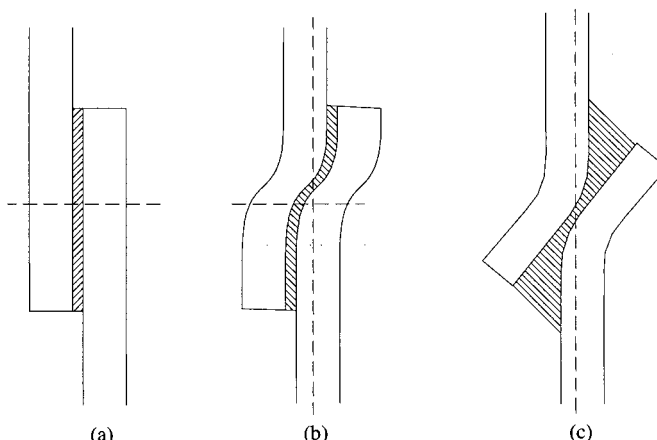


**Figure 9.29** Deformation of a flexible single-lap joint under a tensile load (from Bikerman, 1968): (a) Undeformed joint; (b) deformed joint; (c) deformed joint with little adhesive stiffness.

figure 9.29(b). If the adhesive had little stiffness, the shape would have been deformed, as indicated in figure 9.29(c).

This problem has been treated by many researchers (Adams, 1987) following the earlier analysis by Volkersen. The shear stress result in the adhesive is too complicated to be useful for design purposes. However, when the following condition is satisfied:

$$\frac{h_0}{\delta} \gg \frac{G_a}{G} \quad (9.92)$$

the maximum shear stress in the adhesive for small external force is expressed as

$$\tau_{a\max} = \frac{\sigma_0 \delta}{L} \left[ \sqrt{\frac{2G_a L^2}{E\delta h_0}} \coth \sqrt{\frac{2G_a L^2}{E\delta h_0}} \right] \quad (9.93)$$

where  $G$  is the shear modulus of the inner adherend.

#### 9.4.8 Surface Treatments for Adhesive Joining

Adhesive bonding is unique among structural fabrication methods in having surface and interface properties so dominant in controlling bond formation and bond performance properties (Skeist, 1990). A single molecular layer of contaminant can prevent proper wetting of the adhesive, or a weak adherend (substrate) boundary layer cause premature failure. For these reasons, much adhesive application effort and technical study have been focused on the adhesive–adherend interface.

##### *Mechanical Abrasion*

The adhesion characteristics of smooth surfaces can be improved by roughening with abrasives such as medium grit (#80) emery paper. Abrasion should always be followed by degreasing to remove contaminants and loose particles. Another method is sand blasting with fine grits for removing surface deposits oxide films, tarnish, rust in steel parts, mill scale, and other contaminants. The mechanical abrasion also helps intrinsic adhesion characteristics by mechanical keying, or interlocking of the adhesive into irregularities of the substrate surface. However, the attainment of good adhesion between perfectly smooth surfaces reveals that the mechanical interlocking is not the only major adhesion mechanism, but helps intrinsic adhesion (Kinloch, 1987). For intimate adhesion, the adhesive, and primer if one is employed, needs to be able to spread over the solid surface, and needs to displace air and other contaminants that may be present on the surface. To satisfy these conditions, the adhesive should exhibit a zero or near-zero contact angle (see figure 2.23). By roughening the adherend surfaces, the apparent advancing contact angle  $\theta_f$ , observed for a given liquid on a rough solid, compared with the angle  $\theta_s$ , observed on a smooth surface, can be changed. This change in the contact angle may be expressed by

$$\cos \theta_f = r_f \cos \theta_s \quad (9.94)$$

where  $r_f$  is the roughness ratio of the actual area to the projection area of the solid. If, on a smooth surface,  $\theta_s$  is less than  $90^\circ$ , then roughening the surface will result in  $\theta_f$  being even smaller. This will obviously increase the apparent surface free energy of the solid surface and consequently also increase the extent of wetting. However, if,

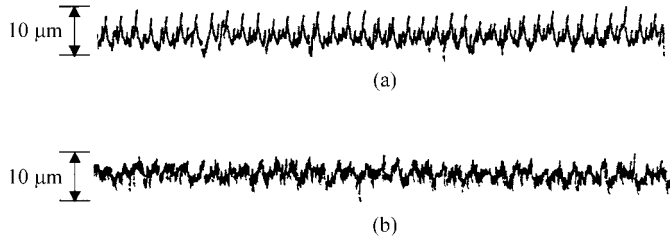


**Figure 9.30** Surface roughnesses of the adherends (from Lee et al., 1991): (a) When turned with a lathe; (b) when abraded with an abrasive paper (#180) after machining with a lathe.

for a smooth surface,  $\theta_s$  is greater than  $90^\circ$ , roughening the surface will increase the contact angle  $\theta_f$  still further and therefore decrease the degree of wetting.

There have been several investigations about the effects of adhesive thickness and adherend surface roughness on the static and dynamic characteristics of tubular single-lap joints of figure 9.20 under a torque (Lee et al., 1991a). The adhesive used was IPCO 9923, whose properties are listed in table 9.3. The adherend material was S45C steel. In order to control the surface of the adherends, the outer surface of the inner adherend was turned by a lathe and the inner surface of the outer adherend was bored out. Figure 9.30 shows the surface roughness of the adherend when machined by a lathe. The surface roughness in this figure was produced when the cutting speed, feed rate, and depth of cut of machining were 100 m/min, 0.1 mm/rev, and 0.2 mm, respectively.

The arithmetic surface roughness  $R_a$  of the machined surface may be approximated by the following equation (Boothroyd, 1981):

$$R_a = \frac{0.032f^2}{r_a} \quad (9.95)$$

where  $f$  is the feed rate (mm/rev) and  $r_a$  is the nose radius of the cutting tool. However, there are many sharp peaks in the machined surface and these sharp peaks might work as crack initiators in the adhesive under dynamic loading. Therefore, the machined surface should not be used even though average arithmetic surface roughness may be expressed by equation (9.95). Figure 9.30(b) shows the surface roughness of the same adherend when abraded with #180 abrasive paper after machining with a lathe. Then the sharp peaks in the adherend were greatly removed by abrasion.

The relationship between the surface roughness and the mesh number of the abrasive paper was measured after abrading the steel adherend with different abrasive papers ranging from 60 to 1200 mesh numbers in dry condition. From this test, it was revealed that the abraded surface roughness was dependent on the adherend material, mesh number of the abrasive paper, abrasion speed, abrasion pressure, and the surface roughness of the original adherend. Even though it was not easy to get quantitative results, it was found that the surface roughness decreased as the abrasion speed and the mesh number increased. Figure 9.31 shows the surface roughness of a S45C adherend that was 20 mm in diameter and was abraded by turning in a lathe. In this test, the abrasion speed was fixed at 4.0 m/min. The original arithmetic surface roughness was 1.0 to 1.3  $\mu\text{m}$  and the pressing force on the abrasive

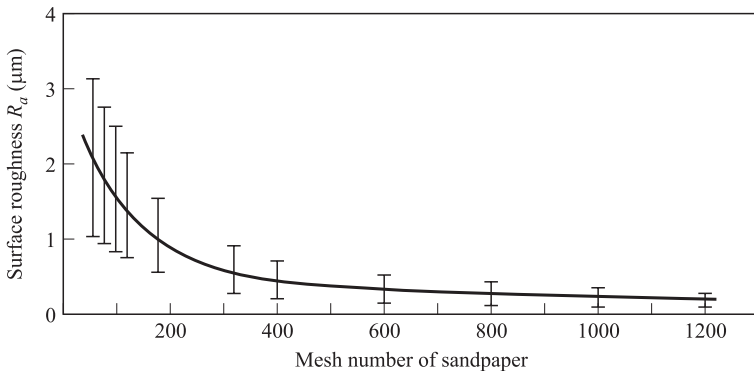


**Figure 9.31** Relationship between the surface roughness and the mesh number of the sandpaper (adherend diameter: 20 mm; abrasion speed: 4.0 m/min).

paper, which was bonded on a flat steel plate of width of 10 cm, was 300 N. The surface roughness was measured in the axial direction. The deviation of the surface roughness was rather large when the mesh number of the abrasive paper was less than 400. This may be attributed to the nonuniform abrasion pressure and the clogging of the abrasive paper. The roughness of the abraded adherend varied little when the mesh number was larger than 400.

After bonding the adherends under a pressure of 0.7 MPa at 80°C, followed by postcuring of 6 days at 30°C, fatigue tests were performed using a rotary bending and torsion type fatigue tester at a stress cycle of 2000 rpm. Although the frequency of 2000 rpm was rather high for the test of an adhesively bonded joint, the larger masses of steel adherend dissipated the heat generated by the cyclic work of the adhesive.

The torsional fatigue test results were expressed by the average fatigue strength (stress amplitude)  $S_a$ , which is defined by

$$S_a = \frac{T_a}{2\pi a^2 L} \quad (9.96)$$

where  $T_a$  is the amplitude of the cyclic torque.

All the fatigue experiments were performed under the stress ratio  $R(\sigma_{\min}/\sigma_{\max}) = -1$ . Since the dynamic characteristics of the adhesive material are dependent on the environmental temperature, the fatigue tester was enclosed in a chamber and the inside temperature was maintained at  $30 \pm 1^\circ\text{C}$  by a temperature controller. The relative humidity inside the chamber was maintained less than 60%. Figure 9.32 shows the fatigue test results (S-N curve) of the tubular single-lap joint, whose adherends were abraded with #100 mesh abrasive paper. The adhesive thickness was 1 mm. The average endurance limit of the torsional joint in this case was 3.5 MPa, which was 12% of the static shear strength and 35% of the lap shear strength.

Figure 9.33 shows the relationship between the fatigue life and the adherend surface roughness when the adhesive thickness was 1 mm and the amplitude of the cyclic stress was 4.0 MPa. From this result, it was found that the fatigue life decreased quickly when the arithmetic surface roughness was less than  $1 \mu\text{m}$ . The fatigue life changed slowly when the average surface roughness was in the range  $1.5\text{--}2.5 \mu\text{m}$ . If the average surface roughness was larger than  $2.5 \mu\text{m}$ , the fatigue life decreased quickly also. The failure of the adhesive usually occurred near the surface

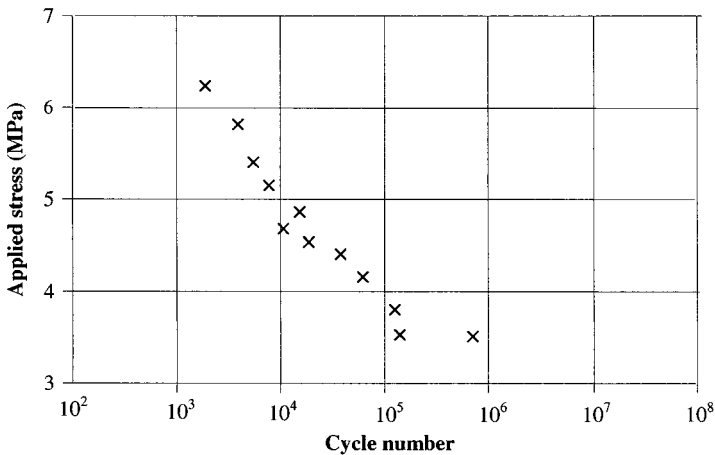


**Figure 9.32** S–N (average shear strength–number of cycles) curve of the adhesively bonded tubular single-lap joint whose adhesive thickness was 1.0 mm and whose adherends were abraded with #100 mesh sandpaper (from Lee et al., 1991a).

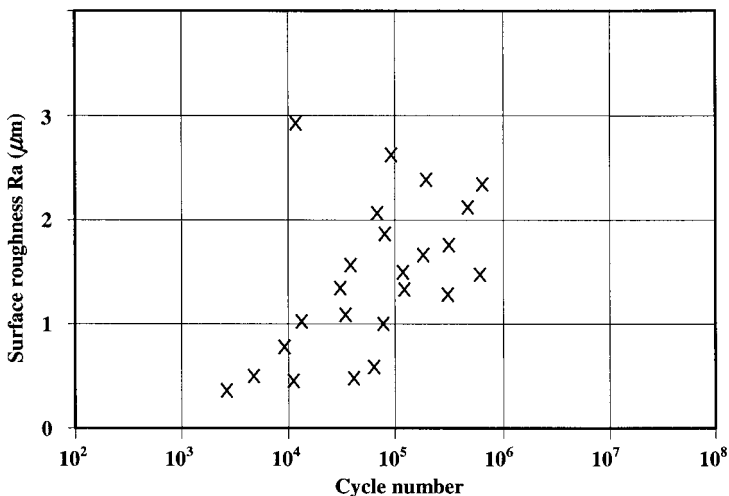


**Figure 9.33** Effect of the surface roughness on the fatigue strength of the adhesively bonded tubular single-lap joint (adhesive thickness = 1.0 mm, amplitude of average shear stress = 4.0 MPa) (from Lee et al., 1991a).

of the inner adherend. To observe the failure mechanism of the adhesive, the outer adherends of the failed adhesive joints after fatigue testing were sliced out carefully in a lathe. The surface of the failed adhesive peeled from the adherends with  $0.6 \mu\text{m}$  arithmetic surface roughness was very smooth and there was no adhesive left on the surface of the inner adherend. However, the adhesive peeled from the adherends with  $2.0 \mu\text{m}$  arithmetic surface roughness was not smooth and only part of the adhesive peeled off, while the other part was left adhering to the surface of the inner adherend. When the arithmetic surface roughness was larger than  $2.5 \mu\text{m}$ , it was found that the adhesive had usually several broken lines, which suggested that the fracture of adhesive joint initiated and propagated from the rough adherend surface when the

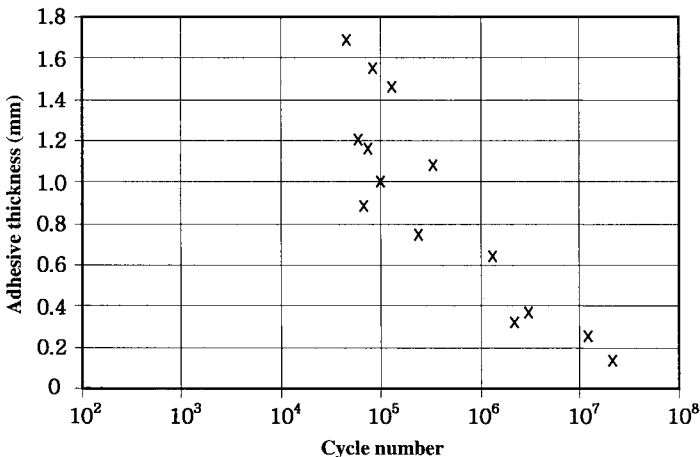


**Figure 9.34** Fatigue life–adhesive thickness behavior of the adhesively bonded tubular single-lap joint when the amplitude of average shear stress was 4.0 MPa and the average surface roughness of steel adherends was about  $2.0 \mu\text{m}$  (from Lee et al., 1991a).

surface roughness of the adherend was larger than  $2.5 \mu\text{m}$ . Therefore, the optimal surface roughness for a steel adherend may be around  $2.0 \mu\text{m}$ .

Figure 9.34 shows the relationship between the adhesive thickness and the fatigue life. In this test, the arithmetic surface roughness of the test pieces was adjusted around  $2.0 \mu\text{m}$ , and the amplitude of the average shear stress was 4.0 MPa. The endurance limit increased as the adhesive thickness decreased. This phenomenon is contrary to the theoretical prediction of shear stress distribution of equation (9.38) with linear adhesive elastic properties, which gives a smaller shear stress in the adhesive layer when the adhesive thickness becomes larger. However, it was found that the adhesive bonding operation became difficult when the adhesive thickness was smaller than 0.15 mm. Therefore, an adhesive thickness around 0.15 mm may be a practical optimal value for the tubular single-lap joint subjected to cyclic torque.

#### *Chemical Surface Treatment of Adherends*

Although solvent degreasing and abrasion, or even no pretreatment, is often sufficient to attain the required initial design joint strength, there are a few high-energy adherends that require more sophisticated treatments to attain a reasonable level of joint strength (Kinloch, 1987). Further, with nearly all high-energy adherends, such as metals, metal oxides, and ceramics, whose surface free energies are greater than  $500 \text{ mJ/m}^2$ , the maximum durability in hygrothermal environments is achieved when a chemical pretreatment, and/or a primer, is employed (Lee et al., 1998).

Two metals that usually need some form of chemical pretreatment to achieve reasonable initial joint strengths are copper and magnesium, and their alloys. These two metals have difficulty in bonding because the oxides of these materials are difficult to wet readily and are mechanically weak, they thus act as a weak boundary layer in the bonded joint (Kinloch, 1987).

Steels are frequently bonded with no (or minimum) pretreatment being employed and good, reproducible initial joint strengths are readily obtained using a combination of degreasing/mechanical abrasion techniques. Also this combination of

pretreatments may even give a reasonable service life when the joint is exposed to normal weathering conditions, especially if the applied stress levels are low and the bonded area relatively large. However, to obtain the longest service life, some form of chemical pretreatment and/or primer is inevitably necessary.

Recently, many advances have been made in developing surface treatments to alter chemical and physical properties of polymer surfaces without affecting bulk properties. For example, the effects of UV (ultraviolet) irradiation or photo-oxidation are confined to the top few microns of the surface. Common surface modification techniques include treatments by chemicals, flame, photons, corona, plasma, electron beams, ion beams, X-rays, and  $\gamma$ -rays. These treatments have been applied to achieve the following purposes (Chan et al., 1996):

1. Increase surface energy.
2. Produce special functional groups at the surface for specific interactions with other functional groups.
3. Increase hydrophobic properties or hydrophilic properties.
4. Improve chemical inertness.
5. Introduce surface cross-linking.
6. Remove weak boundary layers or contaminants.
7. Modify surface morphology (increase or decrease surface crystallinity and roughness).
8. Increase surface electrical conductivity.
9. Increase surface lubricity.
10. Improve dyeability.

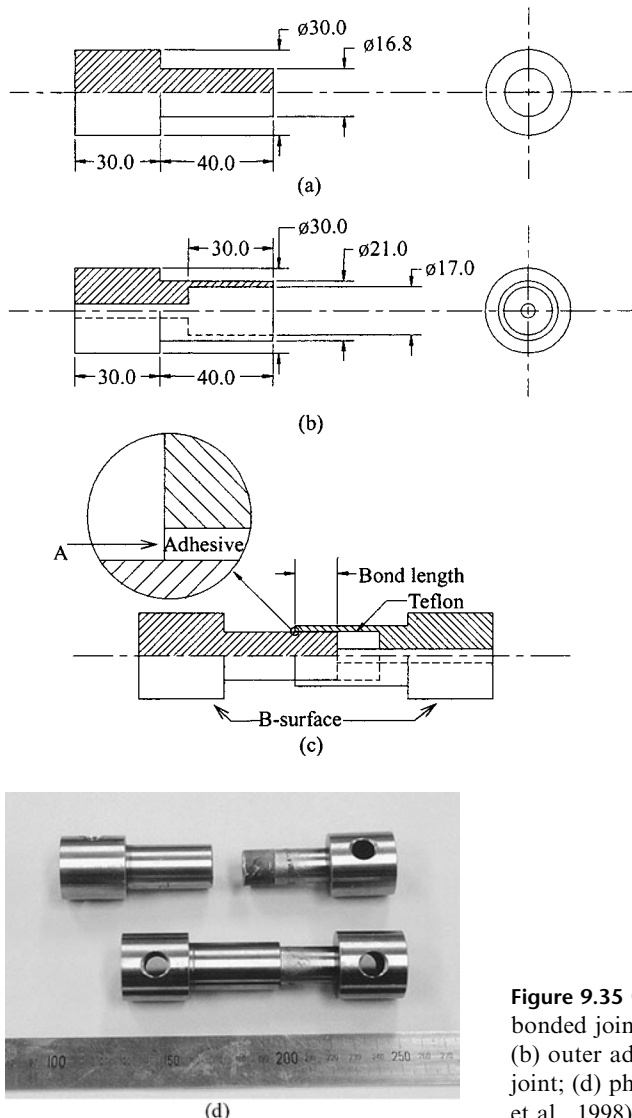
Lee et al. (1998) tested the adhesively bonded tubular single-lap joint of figure 9.35 with respect to chemical surface treatments. The steel adherends were surface-treated with either of two methods recommended by the ASTM, depicted in table 9.6 (ASTM D2651, 1990). The adhesives used were IPCO 9923, whose properties are listed in table 9.3, and HYSOL EA 9460, whose properties are listed in table 9.7.

Figure 9.36 shows SEM photographs with respect to surface treatment of the steel adherend. In the steel adherend abraded with the #80 mesh sandpaper without chemical surface treatment, a plowed valley with a smooth inside surface is seen. However, the etched steel surfaces had many small pores, which were produced by the etching operation. The pores in the steel surface may improve the joint strength, due to mechanical interlocking.

#### *Adhesive Joint Strength with Respect to Moisture Absorption*

The strength of the adhesive joint of figure 9.35 was tested with respect to moisture absorption in the adhesive. During manufacturing of the joints, the residual contaminants on the adherend surfaces which were abraded with sandpaper were removed by wiping with acetone or MEK (methyl ethyl ketone). The adhesive bond length was controlled by the length of the cylindrical Teflon bar tightly fitted to the inside of the outer adherend, as shown in figure 9.35. The adhesive bond length was fixed to be 15 mm. The adhesively bonded joints were cured in an autoclave at 80°C under 0.6 MPa pressure for 3 hours. After curing, the adhesive fillet was removed by a sharp razor to reduce the scatter in the experimental data.

The joint specimens for the torsional tests were immersed in the water chamber at 80°C with respect to the value of  $\bar{C}/C_\infty$  (average specific moisture concentration/maximum specific moisture concentration).



**Figure 9.35** Configuration of the adhesively bonded joint specimen: (a) Inner adherend; (b) outer adherend; (c) adhesively bonded joint; (d) photograph of the joint (from Lee et al., 1998).

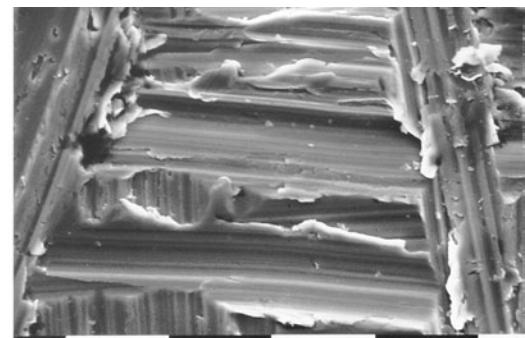
**Table 9.6** Chemical Surface Treatment Methods for Steel Adherends (ASTM D2651-90)

<i>Phosphoric acid-alcohol etching</i>	<i>Nitric-phosphoric acid etching</i>
(1) Abrade with #80 sandpaper*	(1) Abrade with #80 sandpaper
(2) Etch with 33 vol% $H_3PO_4$ (85%), 67 vol% ethanol mixture for 10–12 min at 50–60°C	(2) Etch with 30 vol% $H_3PO_4$ (85%), 5 vol% $HNO_3$ , 64.99 vol% $H_2O$ , 0.01 vol% surfactant mixture for 5–7 min at 20–25°C
(3) Rinse with deionized $H_2O$ for 3–7 min at 20–25°C.	(3) Rinse with deionized $H_2O$ for 3–7 min at 20–25°C.
(4) Dry with forced air at 60–65°C	(4) Dry with forced air at 60–65°C

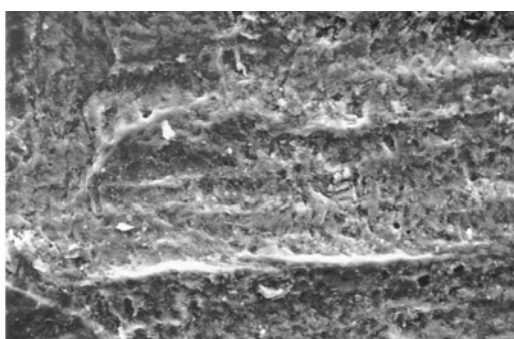
\*From the results of Lee et al. (1991a).

**Table 9.7 Material Properties of HYSOL EA 9460, an Epoxy Adhesive**

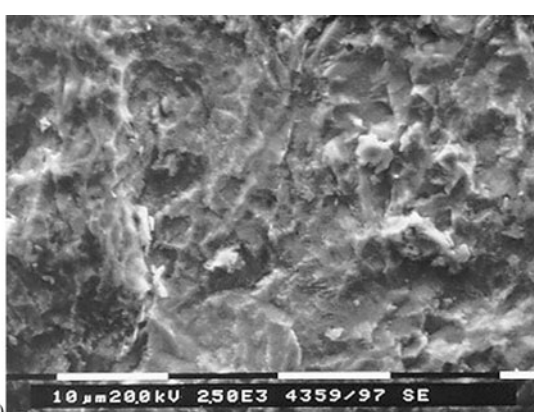
Tensile modulus (GPa)	2.80
Poisson's ratio	0.40
Tensile strength (MPa)	26.5
Shear strength (MPa)	32.0
Cure temperature (°C)	80.0
Cure time (h)	3



(a) 10 μm 20.0 kV 250E3 4356/97 SE



(b) 10 μm 20.0 kV 250E3 4355/97 SE



(c) 10 μm 20.0 kV 250E3 4359/97 SE

**Figure 9.36** SEM photographs ( $\times 2500$ ) for different surface treatments of the steel:  
 (a) Sandpaper abrasion;  
 (b) phosphoric acid–alcohol etching; (c) nitric–phosphoric acid etching (from Lee et al., 1998).

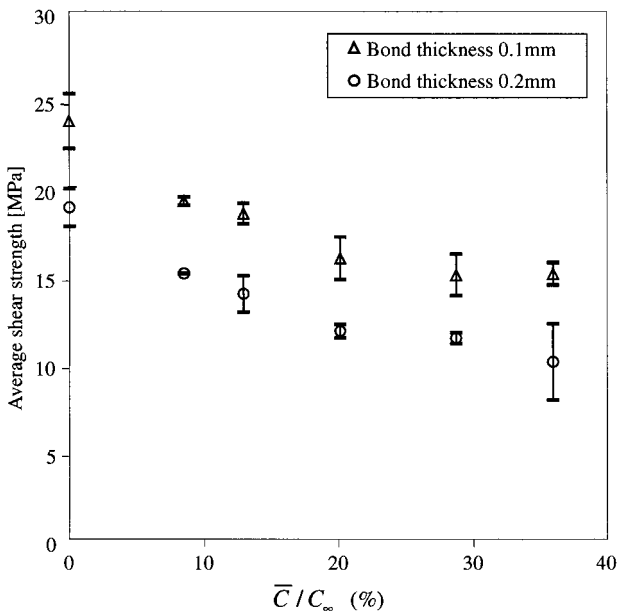


**Figure 9.37** Average shear strength of the adhesively bonded tubular single-lap joint vs.  $\bar{C}/C_{\infty}$  of the Hysol EA 9460 adhesive layer after immersion in the water chamber at 80°C (from Lee et al., 1998).

The moisture absorbed through the area A of figure 9.35(c) of the adhesively bonded joint diffused along the axial direction of the joint. The distribution of moisture inside of the adhesive was calculated by solving the moisture diffusion equation (8.81).

Figure 9.37 shows the variation of the average torsional shear strength of the joint bonded with HYSOL EA 9460 versus  $\bar{C}/C_{\infty}$  of the adhesive layer after immersion in the water chamber at 80°C.

Regardless of hygrothermal effects, the strength of joints with chemically surface-treated adherends was twice as times high as those treated using mechanical abrasion only. The joint strength was about 50% of the initial strength when  $\bar{C}/C_{\infty}$  was 20%. However, the joint strength did not decrease as the moisture ratio  $\bar{C}/C_{\infty}$  increased beyond 20%. This result was caused by the friction due to the compressive stress between the adherend surface and the swollen adhesive in the radial direction.

The adhesively bonded area of steel adherends when immersed in the water rusted as a result of moisture diffusing through the adhesive layer. However, the adherends etched with nitric-phosphoric acid rusted slowly compared with those abraded mechanically. Therefore, the chemical etching treatments for the adherends of adhesive joints under hygrothermal conditions are beneficial.

#### Plasma Surface Treatment

Since the reliability and strength of composite adhesive joints decrease at high environmental temperature or high humidity, the surface treatments of adherends are indispensable for joints in these environments. Among several adherend surface treatment methods, the plasma surface treatment of polymeric composite adherends

has proved to be very effective because the plasma surface treatment increases the surface free energy of composite adherends, which enhances the wetting between the adherend and the adhesive (Kim and Lee, 2002).

Plasma is a mixture of electrons, negatively and positively charged particles, and neutral atoms and molecules. Plasma is considered as being a state of materials, and the state is more highly activated than the solid, liquid, or gas state, therefore, it is frequently called the fourth state of materials (Inagaki, 1996).

Generally, industrial plasmas are classified into local thermodynamic equilibrium (LTE) and non-LTE plasmas. The LTE plasmas, which are called thermal plasmas, are used for plasma coating processes and for reduction or smelting of ores in extractive metallurgy. Non-LTE plasmas, which are called cold plasmas, are used for microelectronic fabrication, surface modification, surface cleaning, or surface hardening. Although the temperature of electrons in cold plasmas can reach  $10^4$ – $10^5$  K, the temperature of gas is as low as the room temperature for short-period operation (Grill, 1994). Kim and Lee (2002) devised a capacitively coupled radio-frequency plasma system composed of a gas handling system, plasma reactor, and power supply for the surface treatment of carbon epoxy composite materials, as shown in figure 9.38.

The gas handling system includes a high-purity argon gas (99.999%) supply, mass flow controller, which controls the flow rate of argon gas in the range 5–100 sccm (standard cubic centimeters per minute), four-channel mass flow controller read-out box, and vacuum system.

The four-channel mass flow controller reads the flow rate of argon gas out of the mass flow controller and controls the flow of different gases into the plasma reactor. The vacuum system is composed of a rotary-type vacuum pump and oil diffusion pump, whose pumping speeds are  $0.2 \text{ m}^3/\text{min}$  and  $0.57 \text{ m}^3/\text{s}$ , respectively.

The plasma reactor chamber, made of stainless steel, had a reactive ion etching configuration inside, which has two plane parallel-type electrodes: a grounded electrode and a powered electrode.

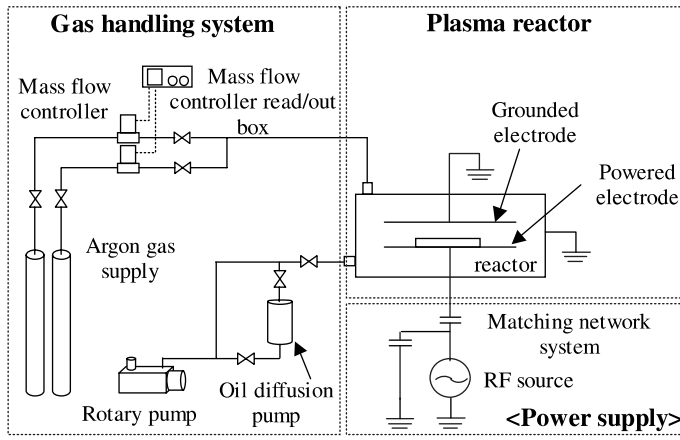
The diameter of the electrodes and distance between them were 200 and 20 mm, respectively. The power supply consisted of a 300 W radio-frequency power source, which has a frequency of 13.56 MHz and an output impedance of  $50 \Omega$ , and a matching network system for maximizing the efficiency of plasma generated in the reactor. The surface of the specimen is etched physically by energetic ions in the reactor or modified chemically by activated radicals.

When a liquid drop is on a solid surface in the equilibrium state, as shown in figure 2.23, the relationship between the surface free energies from Young's equation has been expressed in equation (2.5), which is reproduced here for convenience:

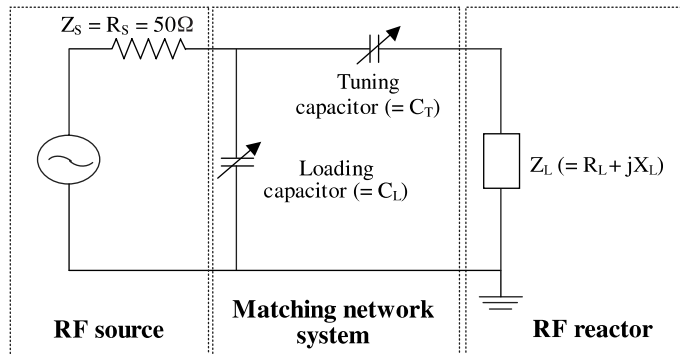
$$\gamma_{SG} = \gamma_{SL} + \gamma_{LG} \cos \theta \quad (9.97)$$

where  $\gamma_{SG}$  is the surface free energy of a solid substrate (adherend),  $\gamma_{LG}$  is the surface free energy of a liquid drop,  $\gamma_{SL}$  is the interfacial free energy between the solid substrate and the liquid drop, and  $\theta$  is the contact angle. The surface free energy  $\gamma_{SG}$  may be expressed as the sum of the polar component,  $\gamma_{SG}^p$  due to hydrogen bonding and the dispersion component,  $\gamma_{SG}^d$ :

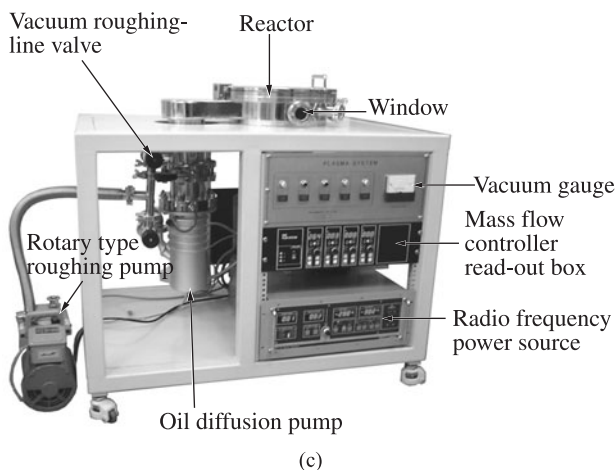
$$\gamma_{SG} = \gamma_{SG}^p + \gamma_{SG}^d \quad (9.98)$$



(a)



(b)



(c)

**Figure 9.38** Capacitively coupled radio-frequency plasma surface treatment system for carbon/epoxy composite materials:  
 (a) Schematic diagram;  
 (b) equivalent circuit diagram;  
 (c) photograph (Kim and Lee, 2002).

The interfacial free energy,  $\gamma_{SL}$ , between a liquid drop and a solid surface has been expressed by Owens and Wendt (1969):

$$\gamma_{SL} = \gamma_{SG} + \gamma_{LG} - 2\sqrt{\gamma_{SG}^p \gamma_{LG}^p} - 2\sqrt{\gamma_{SG}^d \gamma_{LG}^d} \quad (9.99)$$

**Table 9.8 Surface Free Energies of Water and Glycerol at 20°C**

Liquid	$\gamma_{LG}$ (mJ/m <sup>2</sup> )	$\gamma_{LG}^p$ (mJ/m <sup>2</sup> )	$\gamma_{LG}^d$ (mJ/m <sup>2</sup> )
Water	72.8	51.0	21.8
Glycerol	64.0	30.0	34.0

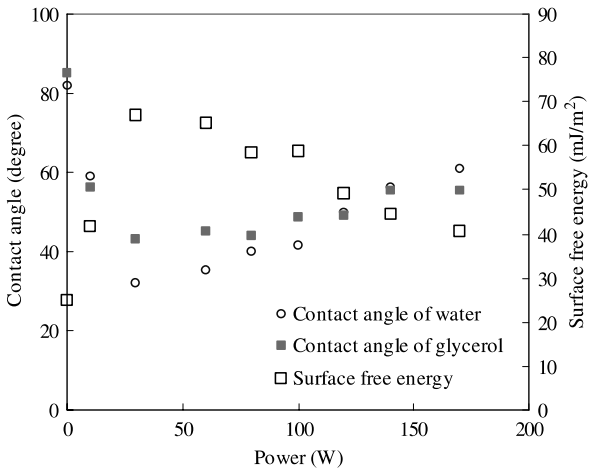


**Figure 9.39** Contact angles of water and glycerol drops and the surface free energies of the carbon-fiber epoxy composite calculated from the contact angles with respect to the plasma power applied (from Kim and Lee, 2002).

From equations (9.97) and (9.99), the relationship between the contact angle and the surface free energy can be expressed as:

$$\gamma_{LG}(1 + \cos \theta) = 2\sqrt{\gamma_{SG}^p \gamma_{LG}^p} + 2\sqrt{\gamma_{SG}^d \gamma_{LG}^d} \quad (9.100)$$

Kim and Lee (2002) measured the contact angles of water and glycerol drops. They calculated the polar component  $\gamma_{SG}^p$  and the dispersion component  $\gamma_{SG}^d$  of the surface free energy of the carbon epoxy composite from equation (9.100) using the known data of surface free energies of water and glycerol, as listed in table 9.8.

Then the surface free energy of the carbon-fiber epoxy composite was calculated from equation (9.98).

The contact angle of a liquid drop on the carbon-fiber epoxy composite with or without plasma surface treatment was measured with respect to the plasma power applied, as shown in figure 9.39. The surface free energies were decreased as the contact angles of the water and the glycerol drops were increased.

The wetting phenomena of water drops on the carbon-fiber epoxy composite surface with and without surface treatments are shown in figure 9.40. The contact angle of the liquid drop on the composite surface decreased after the plasma surface treatment because the surface free energy of the composite increased.

The effects of the plasma surface treatment of the carbon-fiber epoxy composite on the adhesive joint strength were measured by single-lap shear tests. The thickness, width, and length of the composite adherend with stacking sequence [0]<sub>10T</sub> were 1.5, 20, and 100 mm, respectively, as shown in figure 9.41. The bond length and the bond thickness of the single-lap composite adhesive joint were 10 mm and 15  $\mu$ m,

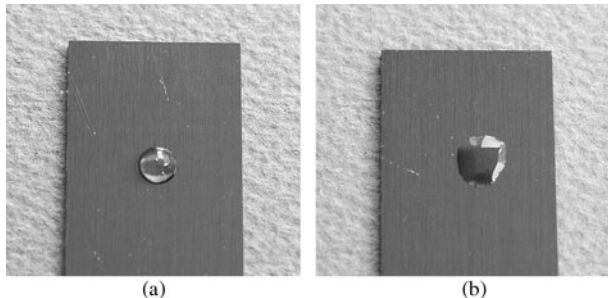


**Figure 9.40** Water drops on carbon-fiber epoxy composite  
(a) Without plasma surface treatment; (b) with plasma surface treatment (from Kim and Lee, 2002).

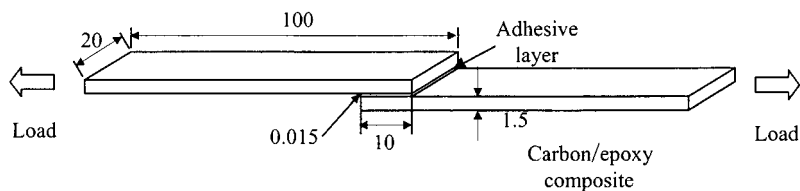


**Figure 9.41** Shape of the single-lap adhesive joint of carbon-fiber epoxy composite (units in mm) (from Kim and Lee, 2002).

**Table 9.9 Mechanical Properties of the Epoxy Adhesive (DP460, 3M, USA)**

$CTE (10^{-6}/^{\circ}C)$	59
Poisson's ratio	0.40
Density ( $\text{kg}/\text{m}^3$ )	1100
Initial elastic modulus (GPa)	2.7
Tensile strength (MPa)	45.0

respectively. The composite adherends were joined with a structural adhesive (DP460, 3M Inc., USA), whose mechanical properties are listed in table 9.9.

The average shear strength  $S_a$  of the single-lap carbon-fiber epoxy composite adhesive joint was defined in this work as

$$S_a = (\text{Load capability of the joint}) / (\text{Bond area}) \quad (9.101)$$

The surface free energy of the plasma surface-treated composites and the strength of the adhesive joints made of surface-treated composite were measured with respect to plasma surface treatment parameters, such as the flow rate of the argon gas, vacuum pressure, supply power, and the surface treatment time, as shown in figure 9.42. The test ranges for each treatment variable are listed in table 9.10.

Figure 9.42(a) shows the surface free energy  $\gamma_{SG}$  of the carbon-fiber epoxy composite and the average shear strength of the adhesive joint made of the surface-treated carbon-fiber epoxy composite with respect to the flow rate of argon gas. The surface free energies of the surface-treated specimens were about  $60 \text{ mJ}/\text{m}^2$  in the whole test range of gas flow rate of 20–60 sccm, while the surface free energy of the composite without surface treatment was about  $25 \text{ mJ}/\text{m}^2$ . The average shear strengths of the surface-treated joint were about 30 MPa in the whole test range of

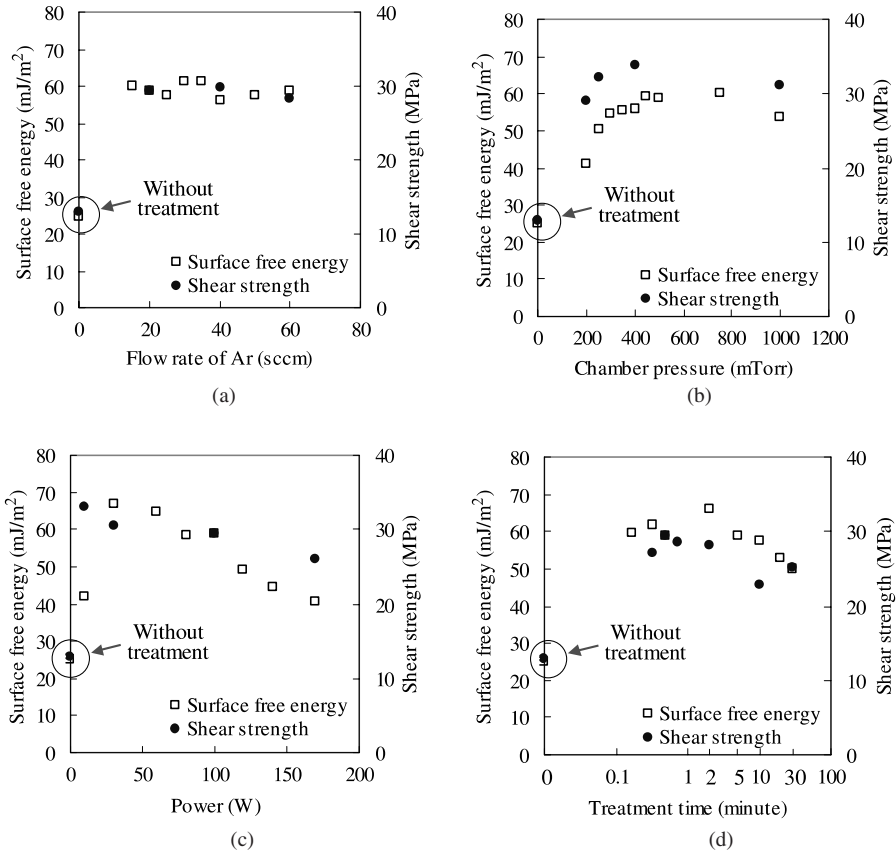


**Figure 9.42** Surface free energies of the carbon-fiber epoxy composite and the average shear strengths of the single-lap adhesive joints made of composite adherends with and without plasma surface treatment with respect to (a) flow rate of argon gas; (b) vacuum pressure in the reactor; (c) power of RF source; (d) surface treatment time (from Kim and Lee, 2002).

**Table 9.10 Surface Treatment Conditions of Carbon-Fiber Epoxy Composite**

Main variables	Fixed conditions			
	Gas flow rate (sccm)	Chamber pressure (mTorr)	Power (W)	Treatment time (min)
Gas flow rate (sccm)	15–60	500	100	0.5
Chamber pressure (mTorr)	20	200–1000	100	0.5
Power (W)	20	500	10–170	0.5
Treatment time (min)	20	500	100	0.1–30

the gas flow rate, while the average shear strength without surface treatment was 12.5 MPa. The surface free energy and the average shear strength changed little with respect to the argon gas flow rate.

Figure 9.42(b) shows the surface free energy  $\gamma_{SG}$  of the carbon-fiber epoxy composite and the average shear strength of the adhesive joint made of the surface-treated carbon-fiber epoxy composite with respect to the vacuum pressure in the

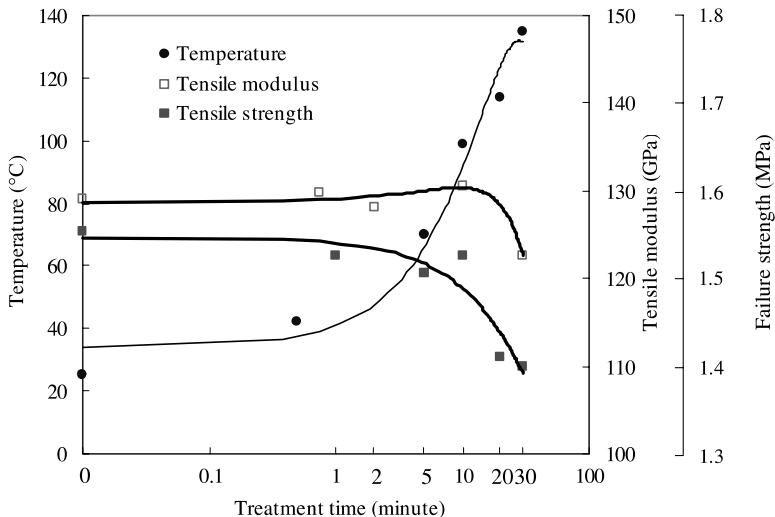


**Figure 9.43** Tensile mechanical properties and maximum surface temperatures of carbon-fiber epoxy composite with respect to plasma surface treatment time.

plasma reactor. The surface free energy and the average shear strength were about  $60\text{ mJ/m}^2$  and  $33\text{ MPa}$ , respectively, in the vacuum range of  $400\text{--}800\text{ mTorr}$  and lower than these values in other ranges. In particular, the surface free energy and average shear strength were about  $40\text{ mJ/m}^2$  and  $27\text{ MPa}$ , respectively, when the vacuum pressure was lower than  $300\text{ mTorr}$ , which resulted from the lower ion impact density on the surface of the carbon epoxy composite at the lower vacuum pressure. They were about  $54\text{ mJ/m}^2$  and  $31\text{ MPa}$ , respectively, when the vacuum pressure was higher than  $800\text{ mTorr}$  because the unstable plasmas were generated in this range.

Figure 9.42(c) shows the surface free energy  $\gamma_{SG}$  of the carbon-fiber epoxy composite and the average shear strength of the adhesive joint made of the surface-treated carbon-fiber epoxy composite with respect to the power supplied in the plasma reactor. The surface free energy increased fast up to  $65\text{ mJ/m}^2$  at  $30\text{ W}$  and decreased when the power supplied was higher than  $30\text{ W}$ . The average shear strength was highest in the range  $10\text{--}30\text{ W}$ . The surface free energy and the average shear strength had similar results with respect to the power supplied in the reactor.

Figure 9.42(d) shows the surface free energy  $\gamma_{SG}$  of the carbon-fiber epoxy composite and the average shear strength of the adhesive joint made of the surface-treated carbon-fiber epoxy composite with respect to the surface treatment time. The surface free energy was  $60\text{ mJ/m}^2$  at  $10\text{ s}$  and reached a peak value of  $66\text{ mJ/m}^2$  at  $2\text{ min}$ , then decreased slowly after  $2\text{ min}$ . The average shear strength was highest at  $1\text{ min}$  and had a similar trend to the surface free energy. However, the average shear strength of the joint at  $30\text{ min}$  did not decrease because the stress concentration on the adhesive layer of the composite adhesive joint decreased due to the decrease of tensile modulus of the composite, although the surface free energy of the composite was slightly decreased compared with other specimens.

Figure 9.43 shows the mechanical properties of the composite adherend specimens and the temperature rise with respect to plasma surface treatment time, in which the temperature of the specimen increased up to  $135^\circ\text{C}$ , which degrades the properties of the composite adherend because the curing temperature of the specimens was  $120^\circ\text{C}$ .

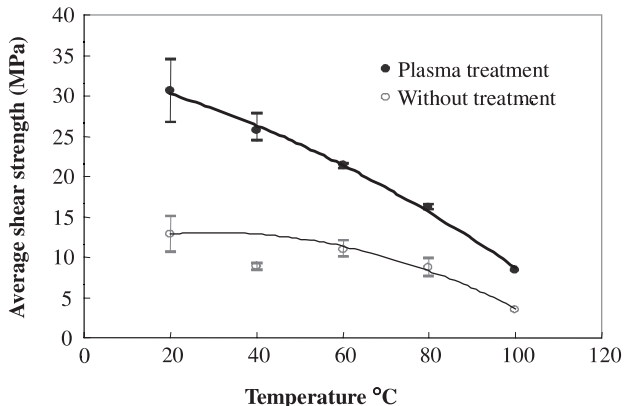


**Figure 9.44** Average shear strength of the single-lap composite adhesive joint with respect to surface treatment and environmental temperature (from Kim and Lee, 2002).

The surface of the carbon-fiber epoxy composite was scanned with an AFM (atomic force microscope) with respect to the surface treatment time. The surface of the specimen before plasma treatment had the average surface roughness of 11.6 nm, while the surface of specimen with 30 s plasma surface treatment had an average surface roughness of 17.3 nm created by ion impacts. The roughened surface with nano-size roughness increased the bond area of the adhesive joint and the effect of mechanical interlocking, which might increase the joint strength of the specimen also (Kinloch, 1987).

The lap shear tests of single-lap adhesive joints made of plasma surface-treated carbon-fiber epoxy composite were performed at elevated environmental temperatures of 20, 40, 60, 80, and 100°C with a test speed of 1 mm/min. Figure 9.44 shows the comparison of average shear strength of the composite adhesive joints with and without plasma surface treatment with respect to the environmental temperature. The plasma surface treatments of composites were performed under the conditions of gas flow rate 20 sccm, vacuum pressure 500 mTorr, power 30 W, and treatment time 30 s. The average shear strengths of the adhesive joints made of plasma surface-treated composite were higher than those without surface treatment up to 100°C. It was found that the failure mode of composite adhesive joints without surface treatment changed from the bulk failure of adhesive to the interfacial failure between the composite and the adhesive as the environmental temperature increased because the mechanical and adhesion properties of the adhesive decreased as the environmental temperature increased. The failure mode of composite adhesive joints with plasma surface treatment changed from the interlaminar failure of composite adherend to the bulk failure of adhesive as the environmental temperature increased due to the high bonding force between the carbon-fiber epoxy composite and the epoxy adhesive at the lower temperature and the decrease of mechanical strength of adhesive at the higher temperature.

#### *Ultraviolet Surface Treatment*

Among the several surface treatment methods, UV surface treatment is clean, and it is inexpensive to set up experimental equipment; the method is easily applicable to manufacturing processes, and does not require other peripheral devices like a vacuum chamber.

The ultraviolet is classified into three parts, UV-A, UV-B, and UV-C according to their bands of wavelength. The UV-C has the shortest wavelength, 100–280 nm, and

**Table 9.11 Specifications of UV-A and UV-B lamps**

	<i>Wavelength (nm)</i>	<i>Peak wavelength (nm)</i>	<i>Lamp power (W)</i>	<i>UV output (W)</i>	<i>Lamp current (A)</i>	<i>Length (mm)</i>	<i>Diameter (mm)</i>
ASTM	—	—	40	—	0.43	1220	—
UV-A	315–400	360	40	7.0	0.42	1200	38
UV-B	280–360	306	40	4.5	0.43	1200	38

almost all the UV-C contained in the solar rays incident on the atmosphere is absorbed by ozone in the stratosphere. The wavelengths of UV-B and UV-A are 280–315 nm and 315–400 nm, respectively.

Ultraviolet irradiation by UV-A and UV-B lamps can be chosen because most of the photo-degradation of polymeric materials takes place in the wavelength band 290–400 nm, which covers the region of UV-A and UV-B. For the design of the UV irradiation chamber, some standard test methods like ASTM D5208 (1997) and ASTM G53 (1997) may be consulted. The UV-A and UV-B lamps used for experiments were TL40W/05 and TL40W/12RS (Philips, the Netherlands), respectively, and the detailed specifications of UV-A and UV-B lamps in comparison with the UV lamps recommended by ASTM standards are listed in table 9.11.

The specimens for XPS (X-ray photoelectron spectroscopy) analyses and measurement of contact angles and adhesion strengths were made from 0.15 mm-thick USN 150 unidirectional carbon epoxy prepreg (SK chemicals, Korea) whose properties are shown in table 2.3. Using the vacuum bag degassing process at a temperature of 125°C and pressure of 0.6 MPa, the stacked prepreg was cured in an autoclave for 2.5 hours.

The surface analysis of specimens attempts to characterize the outermost layers of materials. Several analysis methods provide information on surface chemical composition, for instance, XPS, Auger electron spectroscopy (AES), secondary ion mass spectroscopy (SIMS), and ion scattering spectroscopy (ISS). The XPS method is one of the most versatile techniques used for analyzing surfaces chemically, so it is frequently referred to as ESCA (electron spectroscopy for chemical analysis). In various areas, including adhesion, wetting, degradation, surface modification, chemical modification, and diffusion, XPS has become increasingly important in the field of characterization of organic polymers in recent years. The XPS analysis provides information about the chemical state and concentration of elements constituting the outermost layers of a solid.

The basis of the techniques lies in Einstein's photoelectric effect, whereby photons can induce electron emission from a solid if the photon energy is greater than the work function. The energy of the emitted photoelectron is given as

$$E_k = h\nu - E_b - \phi \quad (9.102)$$

where  $h\nu$  is the photon energy of incident X-ray,  $E_k$  and  $E_b$  are the measured photoelectron kinetic and binding energy of a specific core or valence level electron, respectively, and  $\phi$  is the work function of a solid, which is defined as the minimum energy required to remove an electron from the highest occupied energy level in the solid to the vacuum level.

The XPS analysis provides the following qualitative and quantitative information (Ratner and Castner, 1997):

1. Identification of all elements (except H and He) present at concentrations  $>0.1$  atomic%.
2. Quantitative determination of the approximate elemental surface composition.
3. Information about the molecular environment (oxidation state, bonding atoms).
4. Identification of organic groups.

The XPS analyses were performed using the ESCALAB MK II spectrometer (VG Scientific, UK), employing an excitation radiation of 1253.6 eV (Mg K $\alpha$ ). All binding energies were referenced to the C<sub>1s</sub> neutral carbon peak at 284.6 eV for calibration (Moulder et al., 1995). Survey spectra were obtained in the kinetic energy range 153.6–1253.6 eV with a step of 1 eV. The X-ray source was operated at a power of 120 W (12 kV and 10 mA) and the core-level spectra were obtained at a photo-electron take-off angle of 90°. The operating pressure in the XPS chamber was maintained at  $7 \times 10^{-9}$  Torr or lower during each measurement. The XPS spectra of the surfaces of the carbon epoxy composites with respect to UV irradiation conditions are shown in figure 9.45 (Kim et al., 2003).

The spectra were composed of several peaks, major C<sub>1s</sub> and O<sub>1s</sub> peaks and minor N<sub>1s</sub> and Cl<sub>2p</sub> peaks. The atomic concentrations of the surface of carbon epoxy composite are listed in table 9.12 with respect to ultraviolet treatment conditions. Comparing the atomic concentrations listed in table 9.12, the carbon and oxygen concentrations are similar between the specimens with and without surface treatment by UV-A. However, the UV-B 12-hour-treated specimen had higher oxygen concentration than the other specimens, so it may be concluded that the chemical structures of the surface were modified by UV-B irradiation and oxygen molecules in the air (photo-oxidation).

In order to verify the effect of the UV surface treatment thermodynamically, contact angles were measured. Figure 9.46 shows the contact angles of water and

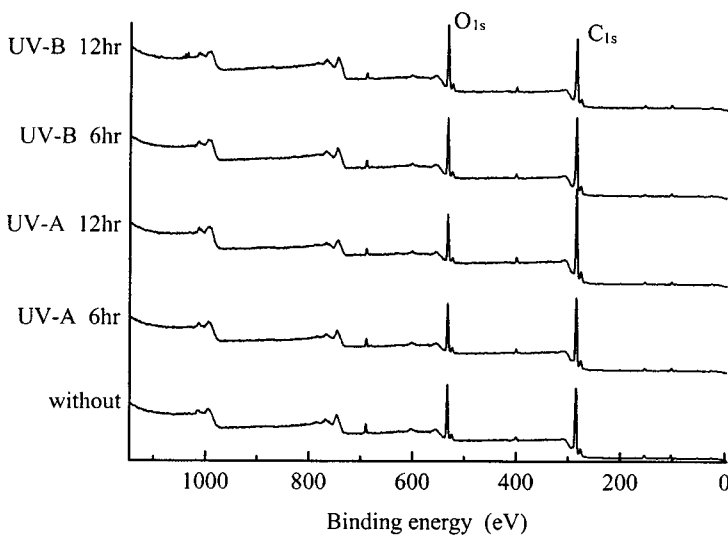


**Figure 9.45** Spectra of the surfaces of carbon epoxy composites with respect to UV irradiation conditions (from Kim et al., 2003).

glycerol droplets on the surface of the carbon epoxy composite with respect to the UV surface treatment condition.

Using the measured contact angles and equations (9.97)–(9.100), the surface free energies of the carbon epoxy composites were calculated. Figure 9.47 shows the calculated surface free energies with respect to the UV treatment conditions.

**Table 9.12 Atomic Concentrations of the Surface of Carbon Epoxy Composite with Respect to Ultraviolet Treatment Condition**

	<i>Percentage</i>			
	<i>C</i>	<i>O</i>	<i>N</i>	<i>Cl</i>
Without	73.76	23.27	2.71	0.27
UV-A 6 h	74.02	23.02	2.50	0.46
UV-A 12 h	74.75	22.32	2.44	0.49
UV-B 6 h	73.42	23.31	3.09	0.18
UV-B 12 h	69.33	27.21	3.30	0.16

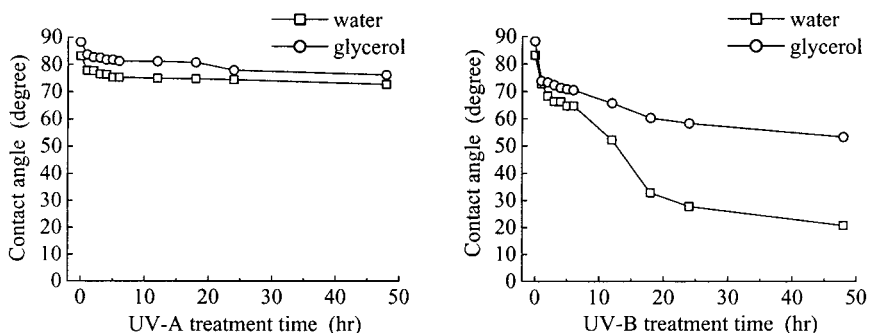


**Figure 9.46** Contact angles of water and glycerol droplets on the surface of carbon epoxy composite with respect to UV surface treatment condition (from Kim et al., 2003).

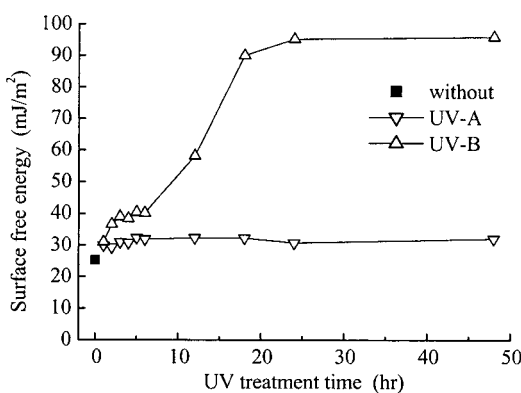


**Figure 9.47** Surface free energies on the surface of carbon epoxy composite with respect to ultraviolet treatment condition (from Kim et al., 2003).

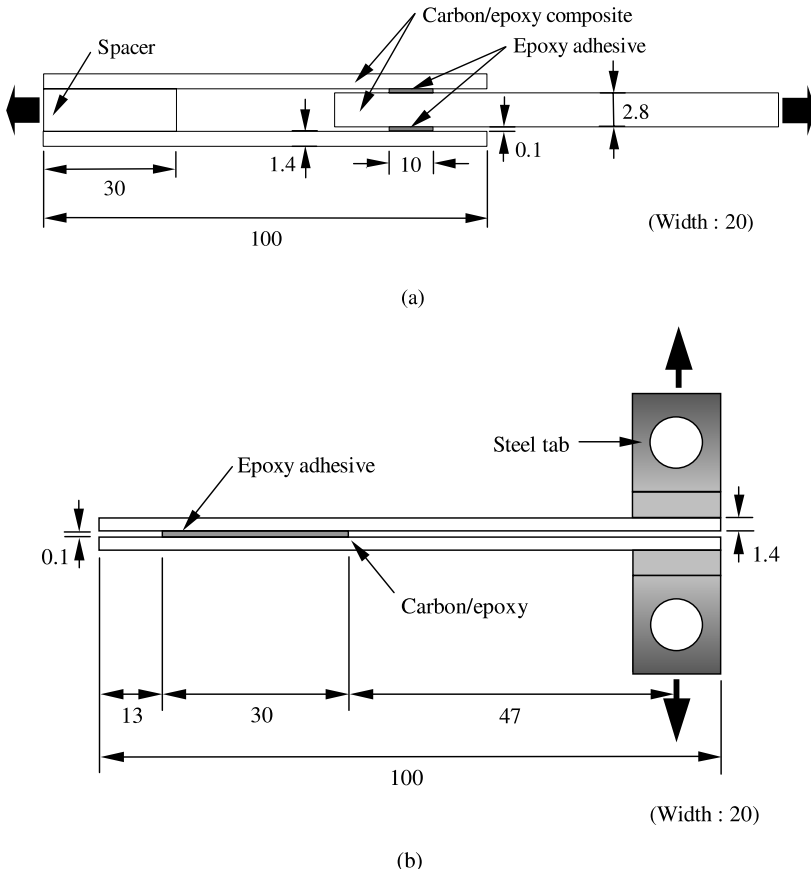
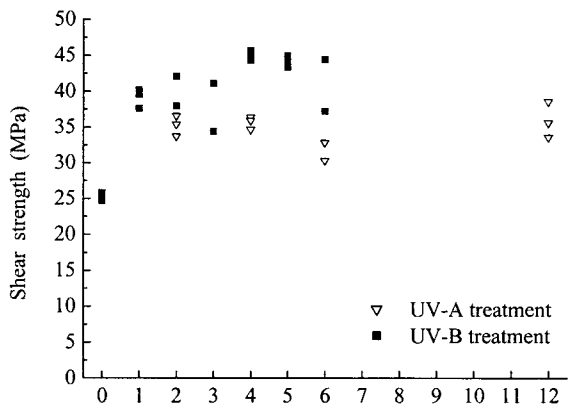


**Figure 9.48** Dimensions of specimens (units in mm): (a) Double-lap shear specimen; (b) DCB (double cantilever beam) specimen.

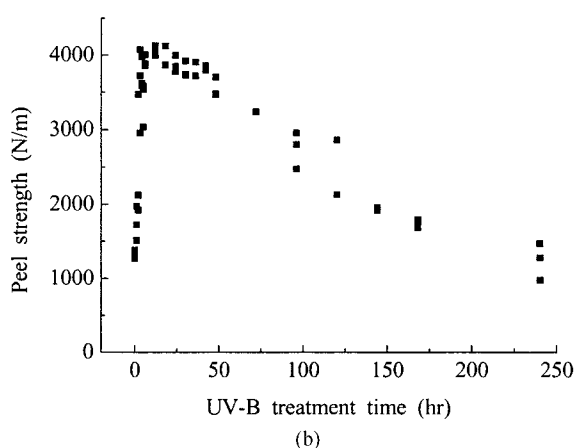
Comparing the surface free energies of the UV-treated carbon epoxy surfaces, the UV-A treatment hardly increased the surface free energy. However, the UV-B treatment caused the rapid increase of surface free energy at the early stage of UV irradiation and after 20-hour treatment the surface free energies were saturated around at  $90 \text{ mJ/m}^2$ .

Double-lap shear tests and DCB (double cantilever beam) tests were performed to verify whether the UV treatments increase the adhesion strengths. In order to adhesively bond the specimens for double-lap shear tests and DCB tests, DP460 (3M, USA), a structural epoxy adhesive was used, and its specifications are listed in table 9.9. After the epoxy adhesive was pasted on the adherend surfaces, the specimens were cured in an autoclave at a temperature of  $80^\circ\text{C}$  and pressure of 0.6 MPa for 2.5 hours.

The double-lap shear test specimens were composed of carbon epoxy composites and epoxy adhesive as shown in figure 9.48(a). The area and thickness of the epoxy adhesive layer were  $10 \text{ mm} \times 20 \text{ mm}$  and 0.1 mm. Four pieces of 0.1 mm-thick feeler gage were inserted into the end gaps of both adhesive layers when pasting the epoxy adhesive on the carbon epoxy adherends to maintain the adhesive thickness of 0.1 mm. After the epoxy adhesive was fully cured, the four pieces of feeler gage were removed from the specimen.



(a)



(b)

**Figure 9.49** Adhesion strengths of carbon epoxy composite adhesive joint with respect to UV surface treatment: (a) Shear strength; (b) peel strength (from Kim et al., 2003).

The peel test or DCB test of an adhesive joint is probably second only to the lap shear test in popularity. Although exhibiting certain disadvantages, the peel tests yield qualitative information regarding the ability of an adhesive joint to withstand the most adverse stresses that an adhesive joint may be subjected to in service (Shaw, 1993).

The DCB specimens were composed of two carbon epoxy composite plates, epoxy adhesive and two steel tabs with a pin hole, as shown in figure 9.48(b). The two steel tabs were adhesively bonded to the carbon epoxy composites using the same epoxy adhesive. The DCB specimen was connected to a load cell of a static tension tester through the tab holes. The test results of double-lap shear and DCB tests for carbon epoxy specimens are shown in figure 9.49. By UV-B irradiation on the surface of carbon epoxy composites, about 90% higher shear strength than the shear strength of specimens without any treatment was obtained.

Comparing the shear strengths of UV-A- and UV-B-treated carbon epoxy specimens, the shear strengths of UV-B-treated specimens were much higher than those of UV-A-treated specimens.

A maximum peel strength of about 4000 N/m was obtained from the 12-hour UV-B-treated specimens. After 3 hours of UV-B treatment, the peel strength reached 90% of the maximum peel strength. However, peel strengths decreased gradually

when UV-B irradiation time was longer than 12 hours because the excessive UV-B irradiation caused the degradation of carbon epoxy composites and lowered the adhesion strength.

For acceptably high adhesion strength, the low-power UV-B lamp employed in this work required a somewhat long treatment time. However, a high-power UV lamp with short wavelength or high photon energy may reduce treatment time.

### 9.5 Concluding Remarks

The machining and joining of composite materials have been presented for the manufacturing of precision composite machine components and assembling of large composite structures. The temperature rise during the grinding operation has been described in detail because the grinding process is most widely used to produce precision composite parts for the machine tools and robot structures. The cutting tool lives during turning of composite materials have also been considered.

For the mechanical joining of composite structures, the joint stiffness has been discussed because it affects greatly the fatigue strength of joints. The design and analysis of the adhesive joints have been presented in detail using the newly developed methods because the joint is usually the weakest part in composite structures, and determines the efficiency of the whole composite structure. The surface treatments such as mechanical, chemical, plasma, and UV (ultraviolet ray) treatments have been discussed in detail for the improvement of adhesive joining of composite structures.

### Problems

- 9.1. Estimate the tool life of a tungsten carbide tool (K10) for turning of high-strength carbon epoxy composite with  $[\pm 15]_s$  stacking sequence when the cutting speed is 40 m/min. How much is the tool life decreased when the cutting speed is doubled (80 m/min)?
- 9.2. When carbon-fiber composites are cut by a CO<sub>2</sub> laser in the direction perpendicular to the fiber reinforcement, the HAZ will be larger than when cutting in the fiber direction, which is a similar phenomenon to the grinding case. Explain the reason why the temperature rise and HAZ are larger for the machining in the direction perpendicular to the fiber reinforcement.
- 9.3. Derive equation (9.8).
- 9.4. Derive equation (9.16).
- 9.5. Two carbon-fiber composite plates ( $t = 10$  mm) are held together by an M10 fine-pitch series bolt with washer that are initially tightened to provide a total initial clamping force of 10,000 N. Assume that the bolt remains within its elastic range, and neglect the area reduction of the bolt due to threads. The composite modulus in the thickness direction is 10 GPa. The outside diameter and the thickness of washer are 16 mm and 2.8 mm, respectively.
  - (a) What external separating force would cause the clamping force to be reduced to 1000 N?
  - (b) If the separating force of 5000 N is repeatedly applied and removed, what are the values of the mean and alternating stresses acting on the bolt?

- 9.6.** What are the two principal roles of the primer in adhesive bonding?
- 9.7.** Derive equation (9.38).
- 9.8.** Construct figure 9.17 using equation (9.38). Assume that the thickness of outer adherend is constant (2.0 mm).
- 9.9.** The required static torque transmission capability of propeller shaft for a mid-size passenger car is 3500 Nm. The shaft maximum outside diameter and its length are 90 mm and 1.8 m, respectively. The maximum rotational speed of the shaft is 6500 rpm with the S-S (simply supported at both ends) conditions. The fundamental natural frequency  $\omega_1$  of the shaft with S-S conditions is expressed as

$$\omega_1 = \frac{9.87}{2\pi L^2} \left( \frac{EI}{m} \right)^{0.5} \text{ (Hz)}$$

where  $L$  is the shaft length,  $I$  is the sectional bending moment of inertia, and  $m$  is the mass of the shaft per unit length.

Is it possible to manufacture a one-piece propeller shaft using steel?

If it is not possible to make the shaft with steel, design the shaft with carbon-fiber epoxy composite (T300/5208 in table 2.3, ply thickness = 0.125 mm) with stacking sequence  $[\pm 15]_{4S}$ . Also design the adhesive joint that joins the steel yoke of the universal joint to the composite shaft. The plausible adhesive bonding length and adhesive thickness for mass production are 20 mm 0.2 mm, respectively. The shaft of the steel yoke has a 2 mm wall thickness and its inner diameter is 90.4 mm. Use the adhesive properties of table 9.3 and the steel properties of table 9.4.

- 9.10.** Explain why small adhesive thickness is beneficial when a hot-cured adhesive is used.

## References

- Abbate, S. 1997. "Machining of Composite Materials," in *Composites Engineering Handbook*, Edited by Mallick, P. K., Marcel Dekker, New York, pp. 777–810.
- Adams, R. D. 1987. "Theoretical Stress Analysis of Adhesively Bonded Joints," in *Joining Fiber-Reinforced Plastics*, Edited by Matthews, F. L., Elsevier, New York, pp. 185–226.
- Adams, R. D. and Peppiatt, N. A. 1977. "Stress Analysis of Adhesive Bonded Tubular Lap Joints," *Journal of Adhesion*, Vol. 9, pp. 1–18.
- ASTM D2651-90, 1990. *Standard Guide for Preparation of Metal Surfaces for Adhesive Bonding*.
- ASTM D5208-97, 1997. *Standard Practice for Operating Fluorescent Ultraviolet and Condensation Apparatus for Exposure of Photodegradable Plastics*.
- ASTM G53-97, 1997. *Standard Practice for Operating Light- and Water-Exposure Apparatus—Fluorescent and UV-Condensation Type, for Exposure of Nonmetallic Materials*.
- Baker, A. A. 1990. "Repair Techniques for Composite Structures," in *Composite Materials in Aircraft Structures*, Edited by Middleton, D. H., Longman Scientific & Technical, New York, p. 215.
- Bikerman, J. J. 1968. *The Science of Adhesive Joints*, 2nd ed., Academic Press, New York.
- Boldt, J. A., and Chanani, J. P. 1987. "Solid-Tool Machining and Drilling," in *Engineered Materials Handbook Composites*, Edited by Reinhart, T. J., ASM International, Metals Park, Ohio, pp. 669–692.
- Boothroyd, G. 1981. *Fundamentals of Metal Machining and Machine Tools*, McGraw-Hill, New York.

- Chan, C. M., Ko, T. M., and Hiraoka, H. 1996. "Polymer Surface Modification by Plasmas and Photons," *Surface Science Reports*, Vol. 24, pp. 1–54.
- Choi, J. H., and Lee, D. G. 1994. "The Torque Transmission capabilities of the Adhesively-Bonded Tubular Single Lap Joint and the Double Lap Joint," *Journal of Adhesion*, Vol. 44, pp. 197–212.
- Choi, J. H., and Lee, D. G. 1996. "An Experimental Study of the Static Torque Capacity of the Adhesively-Bonded Tubular Single Lap Joint," *Journal of Adhesion*, Vol. 55, pp. 245–260.
- Collings, T. A. 1987. "Experimentally Determined Strength of Mechanically Fastened Joints," in *Joining Fiber-reinforced Plastics*, Edited by Matthews, F. L., Elsevier, New York, pp. 105–183.
- Degarmo, E. P., Black, J., and Kohser, R. A. 1999. *Materials and Processes in Manufacturing*, 8th ed., John Wiley & Sons, New York.
- Grill, A. 1994. *Cold Plasma in Materials Fabrication from Fundamentals to Applications*, Institute of Electrical and Electronic Engineers, New York, pp. 1–23.
- Hipol, P. J. 1984. "Analysis and Optimization of a Tubular Lap Joint Subjected to Torsion," *Journal of Composite Materials*, Vol. 18, pp. 298–311.
- Inagaki, N. 1996. *Plasma Surface Modification and Plasma Polymerization*, Technomic Publishing, Lancaster, Penn.
- Kim, J. K., and Lee, D. G. 2002. "Characteristics of Plasma Surface Treated Composite Adhesive Joints at High Environmental Temperature," *Composite Structures*, Vol. 57, pp. 37–46.
- Kim, J. M., Kim, J. K., and Lee, D. G. 2003. "Ultraviolet Surface Treatment for Adhesion Strength Improvement of Carbon epoxy Composite," *Journal of Adhesion Science and Technology*, Vol. 17, No. 11, pp. 1523–1542.
- Kim, K. S., Lee, D. G., Kwak, Y. K., and Namgung, S. 1992. "Machinability of Carbon Fiber-Epoxy Composite Materials in Turning," *Journal of Materials Processing Technology*, Vol. 32, pp. 553–570.
- Kinloch, A. J. 1987. *Adhesion and Adhesives: Science and Technology*, Chapman & Hall, London.
- Kohkonen, K. E., and Potdar, N. 1998. "Composite Machining," in *Handbook of Composites*, 2nd ed., Edited by Peters, S. T., Chapman & Hall, London, pp. 596–609.
- Lee, D. G., and Kim, P. J. 2000. "Temperature Rise and Surface Roughness of Carbon Fiber Epoxy Composites During Cut-off Grinding," *Journal of Composite Materials*, Vol. 34, No. 24, pp. 2061–2080.
- Lee, D. G., Sin, H. C., and Suh, N. P. 1985. "Manufacturing of a Graphite Epoxy Composite for a Machine Tool," *Annals of the CIRP*, pp. 365–368.
- Lee, D. G., Kim, K. S., and Im, Y. T. 1991a. "An Experimental Study of Fatigue Strength for Adhesively Bonded Tubular Single Lap Joints," *Journal of Adhesion*, Vol. 35, No. 1, pp. 39–53.
- Lee, D. G., Kim, K. S., and Kwak, Y. K. 1991b. "Manufacturing of a Scara Type Direct-Drive Robot with Graphite Fiber Epoxy Composite Materials," *Robotica*, Vol. 9, pp. 219–229.
- Lee, D. G., Jeong, K. S., Kim, K. S., and Kwak, Y. K. 1993. "Development of the Anthropomorphic Robot with carbon-fiber Epoxy Composite Material," *Composite Structures*, Vol. 25, pp. 313–324.
- Lee, D. G., Jeong, K. S., and Choi, J. H. 1995. "Analysis of the Tubular Single Lap Joint with Nonlinear Adhesive Properties," *Journal of Adhesion*, Vol. 49, pp. 37–56.
- Lee, D. G., Kwon, J. W., and Cho, D. H. 1998. "Hygrothermal Effects on the Strength of Adhesively Bonded Joints," *Journal of Adhesion Science and Technology*, Vol. 12, No. 11, pp. 1253–1275.
- Lee, D. G., Kim, J. K., and Cho, D. H. 1999. "Effects of Adhesive Fillers on the Strength of Tubular Single Lap adhesive Joints," *Journal of Adhesion Science and Technology*, Vol. 13, No. 11, pp. 1343–1360.

- Lee, S. J., and Lee, D. G. 1992. "Development of Failure Model for the Adhesively Bonded Tubular Single Lap Joint," *Journal of Adhesion*, Vol. 40, pp. 1-14.
- Lee, S. J., and Lee, D. G. 1994. "A Closed-Form Solution for the Torque Transmission Capability of the Adhesively Bonded Tubular Double Lap Joint," *Journal of Adhesion*, Vol. 44, pp. 271-284.
- Mackey, B. A. 1980. "How to Drill Precision Holes in Reinforced Plastics in a Hurry," *Plastics Engineering*, Vol. 43, pp. 22-24.
- Mallick, P. K. 1988. *Fiber-Reinforced Composites*, Marcel Dekker, New York.
- McGeough, J. A. 1988. *Advanced Methods of Machining*, Chapman & Hall, London.
- Messler, R. W., Jr. 1993. *Joining of Advanced Materials*, Butterworth-Heinemann, Boston.
- Migliore, L. R. 1987. "Laser Cutting," in *Composites* Vol. 1, Edited by Reinhart, T. J., ASM International, Metals Park, Ohio, pp. 676-680.
- Moulder, J. F., Stickle, W. F., Sobol, P. E., and Bomben, K. D. 1995. *Handbook of X-ray Photoelectron Spectroscopy*, Edited by Chastain, J., and King, R. C., Jr., Physical Electronics, Eden Prairie, Minn.
- Niu, M. C. Y. 1992. *Composites Airframe Structures*, Hong Kong Conmilit Press, Hong Kong.
- Oh, J. H., Kim, Y. G., and Lee, D. G. 1997. "Optimum Bolted Joints for Hybrid Composite Materials," *Composite Structures*, Vol. 38, No. 1-4, pp. 329-341.
- Osswald, T. A., and Rietveld, J. 1990. "Measuring Constitutive Properties," in *Adhesives and Sealants*, ASM International, Metals Park, Ohio, pp. 315-316.
- Owens, D. K., and Wendt, R. C. 1969. "Estimation of the Surface Free Energy of Polymers," *Journal of Applied Polymer Science*, Vol. 13, pp. 1741-1747.
- Ratner, B. D., and Castner, D. G. 1997. "Electron Spectroscopy for Chemical Analysis" in *Surface Analysis—The Principal Techniques*, Edited by Vickerman, J. C., John Wiley & Sons, Chichester, pp. 43-92.
- Shaw, M. C. 1984. *Metal Cutting Principles*, Oxford Science Publications, Oxford.
- Shaw, S. J. 1993. "Epoxy Resin Adhesives" in *Chemistry and Technology of Epoxy Resins*, Edited by Ellis, B., Chapman & Hall, New York, pp. 397-398.
- Shigley, J. E., Mischke, C. R. and Budynas, R. G. 2004. *Mechanical Engineering Design*, 7th ed., McGraw-Hill, New York, 2004.
- Skeist, I. 1990. *Handbook of Adhesives*, 3rd ed., Van Nostrand Reinhold, New York.
- Takeyama, H., and Iijima, N. 1988. "Machinability of Glass Fiber Reinforced Plastics and Application of Ultrasonic Machining," *Annals of the CIRP*, Vol. 37, No. 1, pp. 93-96.

# 10

## Dynamic and Fatigue Performances of Composite Materials

### 10.1 Introduction

Fiber-reinforced polymer matrix composite materials are used in a wide variety of structural applications because they have high specific stiffness (stiffness/density), specific strength (strength/density), and damping characteristics. Due to these beneficial properties, they have been used for structural materials of aircraft and space vehicles. As low-cost manufacturing technologies and mass production methods for composite structures have been developed, the applications of composite materials to leisure sport goods and auto bodies are increasing.

Dynamic loadings, in particular impact type, represent a serious design concern for use of advanced aerospace composites. For example, dropping of tools during maintenance may induce damage because of the tendency toward delamination of composite materials, even when the impactor has low kinetic energy and does not appear to cause any damage. In these situations, the damage caused should be estimated. It is well known that impacts that produce little or no surface damage detectable to the eye can cause severe internal damage to composite structures.

Most failures in mechanical machinery are due to time-varying loads rather than static loads. Fatigue is the process whereby mechanical damage, caused by repetitive or fluctuating stresses, results in a material failure at lower stress levels than would be required under static loading. Fatigue damage in isotropic metals typically occurs from the initiation and growth of a single crack, and thus damage is localized. Fatigue of composite materials differs from isotropic metals in that the damage mechanisms are more complex, and may exhibit synergistic damage from several microfailure mechanisms (Jang, 1994). These multiple-damage mechanisms can blunt the stress concentration effect of a notch or crack on the load-bearing fibers for tension-tension-type loading, resulting in good fatigue behavior of composites in the fiber direction. But most structures are not loaded purely in tension, and some composites show significant fatigue weakness in compression, shear, and interlaminar shear loadings after impact.

Fatigue analysis of metallic structures involves many empirical equations derived from tests and experience. Such analysis data do not yet exist for composites because of the lack of a database (Niu, 1992). Currently, failures induced by flaws are analyzed using failure criteria rather than the classic metallic fracture toughness approach.

For the accepted design of advanced composite structures under dynamic loading such as impact and fatigue, a damage tolerance design concept has been evolved. Generally, damage tolerance is concerned with the ability of the structure to contain representative weakening defects under representative loading and environment without suffering excessive reduction in residual strength, for some stipulated period of service. The structure is required to contain the growth of the initial assumed damage for a specified period of service while maintaining a minimum level of residual strength, both during and at the end of this period (Sierakowski and Newaz, 1995).

In chapter 5, failure criteria, such as yielding, brittle failure, and crack propagation which might lead ultimate failure for composite structures, as well as stress concentration around holes were presented. Also the interlaminar stresses that lead to delamination at the edges of composite structures were discussed.

In this chapter, the dynamic behavior and damage mechanism of advanced composite structures under impact and fatigue loads are presented.

## 10.2 Impact Characteristics of Composite Structures

Impact damage of composite structures is one of the most important aspects of behavior inhibiting widespread application of composite materials in primary structures (Lee et al., 2000). For ductile materials, the incident kinetic energy is dissipated through elastic and plastic deformation. Although this may result in permanent deformation in some cases, its effect is often localized.

In composites, however, the plastic deformation is limited and the consequences of an impact can lead to a substantial amount of damage. Moreover, the influence of impact on damage tolerance properties is difficult to predict. The controlling variables during an impact include material properties, boundary conditions, deformation/failure mechanisms, environmental factors, and imposed constraints (Eckold, 1994).

### 10.2.1 Wave Propagation Due to Impact

During an impact, a stress field is established on contact. A series of stress waves is then propagated through the thickness of the material, which may or may not cause damage. For a one-dimensional model, to satisfy the zero stress condition at a free surface, an incident compressive wave of magnitude  $\sigma_m$  with pulse length  $\lambda$  and velocity  $c$ , as shown in figure 10.1, will be reflected from the free surface with a net tensile stress  $\sigma_t$  defined by (Meyers, 1994)

$$\sigma_t = \sigma_m - \sigma_i \quad (10.1)$$

where  $\sigma_i$  is the compressive incident stress at the same point as the leading edge of the reflected wave.

If the incident compressive wave magnitude  $\sigma_m$  is larger than the tensile failure stress  $\sigma_f$  of material, failure will occur at some position. At this instant the following equation holds:

$$\sigma_f = \sigma_m - \sigma_i \quad (10.2)$$

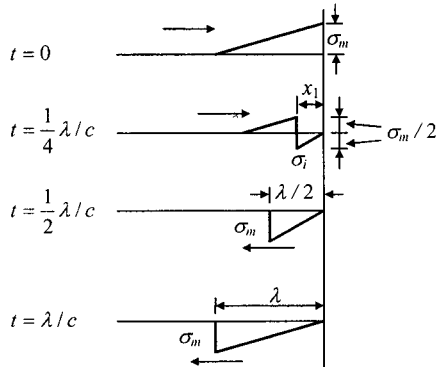
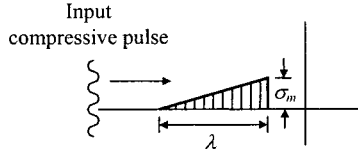


**Figure 10.1** Net stress for reflection of pulse stress with respect to time.

From the following geometric relation:

$$\frac{\sigma_i}{\lambda - 2x_1} = \frac{\sigma_m}{\lambda} \quad (10.3)$$

where  $x_1$  is the position of failure, the magnitude  $\sigma_i$  is expressed as

$$\sigma_i = \sigma_m \left( \frac{\lambda - 2x_1}{\lambda} \right) \quad (10.4)$$

The position of failure  $x_1$  measured from the free surface is given by substituting equation (10.4) into equation (10.2):

$$x_1 = \frac{\sigma_f \lambda}{\sigma_m 2} \quad (10.5)$$

From equation (10.5), the failure occurs at  $\lambda/2$  from the free surface if  $\sigma_f = \sigma_m$ . No failure will occur if  $\sigma_m < \sigma_f$ . If  $\sigma_m > \sigma_f$ , multiple fractures may occur, in which there will be a new wave and a new free surface. The failure position  $x_n$  of the  $n$ th fracture is expressed as

$$x_n = \frac{\sigma_f \lambda_n}{\sigma_{mn} 2} \quad (10.6)$$

where  $\lambda_n = \lambda_{n-1} - 2x_{n-1}$  and  $\sigma_{mn} = \sigma_i$  at the instant of the  $(n-1)$ th failure, and  $n$  denotes the number of the failures, which is expressed for a given wave as

$$n = \frac{\sigma_m}{\sigma_f} \quad (10.7)$$

Although the above analysis is only qualitative, it gives an appreciation of the phenomena involved during impact.

With the application of dynamic load, damage will be propagated at a number of sites within the thickness of the composite material because composites have low transverse tensile strength. In the case of carbon composites, which are opaque, the damage may not be apparent without the application of a sophisticated inspection method. Such barely visible damage is a major design issue.

### 10.2.2 Low-Velocity Impact in Isotropic Material

Greszczuk (1982) studied the low-velocity impact of composite materials. The three major steps of the approach in studying the response of isotropic and composite materials to low-velocity impact were:

1. Determination of impactor-induced surface pressure and its distribution.
2. Determination of internal stresses in the composite target caused by the surface pressure.
3. Determination of failure modes in the target caused by the internal stresses.

For the most general case the target was assumed to be a multilinear, generally orthotropic solid, whereas the impactor was assumed to be a body of revolution. The impactor was assumed to be linear elastic, and the impact duration was assumed to be long compared with stress-wave transit times in the impactor (or target of finite thickness) with the impact normal to the target surface. The three steps are shown in figure 10.2.

The first step for the quantitative analysis of impact is to derive relationships for the contacting force and resulting stress distribution. Ignoring vibrations and considering the contact between a stationary semi-infinite flat target and an impactor, the expressions for the rates of change of velocity during impact are given by (Timoshenko and Goodier, 1970)

$$-P = m_1 \frac{dv_1}{dt} \quad (10.8a)$$

$$-P = m_2 \frac{dv_2}{dt} \quad (10.8b)$$

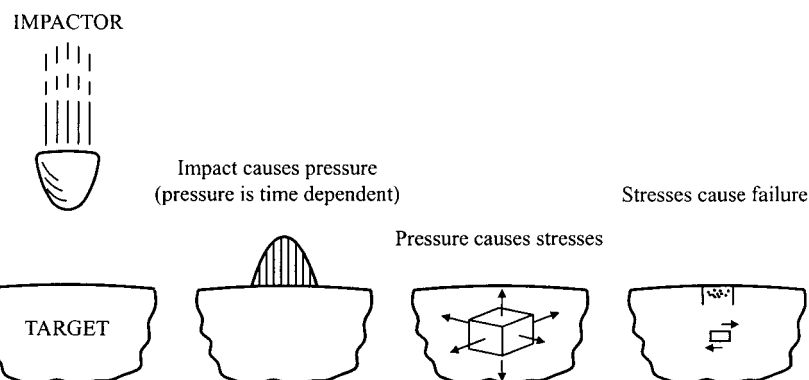


**Figure 10.2** Major steps for the analysis of low-velocity impact.

where  $P$  is the force between the impactor and the target,  $m_1$  and  $v_1$  are the mass and approaching velocity of the impactor, and  $m_2$  and  $v_2$  are the mass and approaching velocity of the target, respectively. Neglecting the vibrations provides a useful starting point, which can be justified if the contact times are long in comparison with vibration or wave propagation periods.

The velocity of approach at the point of contact is expressed as

$$\frac{d\alpha}{dt} = v_1 + v_2 \quad (10.9)$$

where  $\alpha$  is the distance that the impactor and the target approach one another because of local compression at the point of contact. Differentiating equation (10.9) with respect to time  $t$  and combining equation (10.8) yields

$$\frac{d^2\alpha}{dt^2} = -P\left(\frac{1}{m_1} + \frac{1}{m_2}\right) \quad (10.10)$$

The assumption of long contact compared with the period of vibration allows the static equation for two bodies in Hertzian contact to be used (Timoshenko and Goodier, 1970):

$$P = n\alpha^{1.5} \quad (10.11)$$

where

$$n = \frac{4\sqrt{R_1}}{3\pi(k_1 + k_2)} \quad (10.12)$$

where  $R_1$  is the radius of a spherical impactor or indenter. For isotropic materials,  $k_1$  and  $k_2$  are expressed as

$$k_1 = \frac{1 - v_1^2}{\pi E_1} \quad (10.13)$$

$$k_2 = \frac{1 - v_2^2}{\pi E_2} \quad (10.14)$$

where  $E_i$  and  $v_i$  ( $i = 1$  or  $2$ ) are the Young's modulus and Poisson's ratio, respectively, and the subscripts 1 and 2 refer to the impactor and the target. Substituting equation (10.11) into equation (10.10) yields

$$\frac{d^2\alpha}{dt^2} = -nM\alpha^{1.5} \quad (10.15)$$

where  $M$  is defined as

$$M = \frac{1}{m_1} + \frac{1}{m_2} \quad (10.16)$$

Multiplying both sides of equation (10.15) by  $\dot{\alpha}$  and integrating yields

$$\left(\frac{d\alpha}{dt}\right)^2 - v_0^2 = -\frac{4}{5}Mn\alpha^{2.5} \quad (10.17)$$

where  $v_0$  is the approach velocity of the two bodies at  $t=0$ , that is, at the beginning of impact. The maximum deformation  $\alpha_{\max}$  occurs when  $\dot{\alpha}=0$ :

$$\alpha_{\max} = \left(\frac{5v_0^2}{4Mn}\right)^{0.4} \quad (10.18)$$

Substituting equation (10.18) into equation (10.11) gives the final relationship:

$$P_{\max} = n^{0.4} \left(\frac{5v_0^2}{4M}\right)^{0.6} \quad (10.19)$$

For the case of the Hertzian contact problem involving a sphere pressed onto a flat surface by a force  $P_{\max}$ , the relationship between  $P_{\max}$  and the radius of the area of contact,  $a$ , is expressed as (Shigley et al., 2004)

$$a = \left[\frac{3\pi P_{\max}}{4}(k_1 + k_2)R_1\right]^{1/3} \quad (10.20)$$

Combining equations (10.19) and (10.20) using the result of equation (10.12), the maximum radius of the area of contact between a flat target and a spherical impactor becomes

$$a = R_1^{0.5} \left(\frac{5v_0^2}{4Mn}\right)^{0.2} \quad (10.21)$$

The pressure distribution  $p(x, y)$  over the area of contact is expressed (Timoshenko and Goodier, 1970) as

$$p(x, y) = p_0 \left(1 - \frac{x^2}{a^2} - \frac{y^2}{a^2}\right)^{0.5} \quad (10.22)$$

where  $p_0$  is the surface pressure at the center of area of contact, at  $x=y=0$ . By summing the pressures acting on the area of contact and equating the result to  $P$ , we obtain

$$p_0 = \frac{3P_{\max}}{2\pi a^2} \quad (10.23)$$

Combining equations (10.19), (10.21), (10.22), and (10.23) yields the pressure distribution in polar coordinates:

$$p(r) = \left(\frac{3n}{2\pi R_1}\right) \left(\frac{5v_0^2}{4nM}\right)^{0.2} \left[1 - \left(\frac{r}{a}\right)^2\right]^{0.5} \quad (10.24)$$

Equations (10.19), (10.21), and (10.24) are the final equations that give impact force, radius of the area of contact, and the magnitude and distribution of the surface pressure in terms of the impact velocity, geometry of the impactor, and the elastic properties and masses of the impactor and the target.

### 10.2.3 Low-Velocity Impact on Nonisotropic Material

The same approach as described in the preceding section can be used for investigation of more general cases of impact between two arbitrary bodies of revolution made of orthotropic materials. The solution of the contact problem between arbitrary bodies of revolution can be found in Timoshenko and Goodier (1970).

If an impactor at the point of contact, having principal radii of curvature  $R_{1m}$  and  $R_{1M}$ , is pressed by a force  $P$  into a target, having principal radii of curvature  $R_{2m}$  and  $R_{2M}$ , the area of contact will be elliptical, with the major and minor axes (Greszczuk, 1982)

$$a = m \left[ \frac{3\pi}{2} P(k'_1 + k'_2) C_R \right]^{1/3} \quad (10.25)$$

$$b = r \left[ \frac{3\pi}{2} P(k'_1 + k'_2) C_R \right]^{1/3} \quad (10.26)$$

where  $C_R$  is a term that takes into account the curvature effect:

$$C_R^{-1} = \frac{1}{R_{1m}} + \frac{1}{R_{2m}} + \frac{1}{R_{1M}} + \frac{1}{R_{2M}} \quad (10.27)$$

and  $k'_1$  and  $k'_2$  are parameters that are defined later.  $m$ ,  $r$ , and  $s$  are parameters that are functions of  $R_{1m}$ ,  $R_{1M}$ ,  $R_{2m}$ , and  $R_{2M}$ . Their values are listed in table 10.1 as a function of  $\theta$  that is defined as

$$\cos \theta = C_R \left[ \left( \frac{1}{R_{1m}} - \frac{1}{R_{1M}} \right)^2 + \left( \frac{1}{R_{2m}} - \frac{1}{R_{2M}} \right)^2 + 2 \left( \frac{1}{R_{1m}} - \frac{1}{R_{1M}} \right) \left( \frac{1}{R_{2m}} - \frac{1}{R_{2M}} \right) \cos(2\phi) \right]^{0.5} \quad (10.28)$$

where  $\phi$  is the angle between normal planes containing curvatures  $1/R_{1m}$  and  $1/R_{2m}$ .

**Table 10.1 Values of  $m$ ,  $r$ , and  $s$  (Greszczuk, 1982)**

$\theta$	$0^\circ$	$10^\circ$	$20^\circ$	$30^\circ$	$40^\circ$	$50^\circ$	$60^\circ$	$70^\circ$	$80^\circ$	$90^\circ$
$m$	$\infty$	6.612	3.778	2.731	2.136	1.754	1.486	1.284	1.128	1.00
$r$	0	0.319	0.408	0.493	0.567	0.641	0.717	0.802	0.893	1.00
$s$	—	0.851	1.220	1.453	1.637	1.772	1.875	1.994	1.985	2.00

The parameters  $k'_1$  and  $k'_2$  in equations (10.25) and (10.26) take into account the elastic properties of the impactor and the target. For the case of impact between isotropic solids,  $k'_1$  and  $k'_2$  have been defined already in equations (10.13) and (10.14). If the target is made of transversely isotropic material,  $k'_2$  is expressed as follows:

$$k'_2 = \frac{E_{22}^{0.5} \left[ (E_{11}^{0.5} E_{22}^{0.5} + G_{zr})^2 - (E_{12} + G_{zr})^2 \right]^{0.5}}{2\pi G_{zr}^{0.5} (E_{11} E_{22} - E_{12}^2)} \quad (10.29)$$

where

$$E_{11} = E_z \frac{1 - \nu_{r\theta}}{1 - \nu_{r\theta} - 2\nu_{zr}^2 (E_r/E_z)} \quad (10.30)$$

$$E_{22} = E_r \frac{1 - \nu_{zr}^2 (E_r/E_z)}{(1 + \nu_{r\theta}) [1 - \nu_{r\theta} - 2\nu_{zr}^2 (E_r/E_z)]} \quad (10.31)$$

$$E_{12} = E_r \frac{\nu_{zr}^2}{1 - \nu_{r\theta} - 2\nu_{zr}^2 (E_r/E_z)} \quad (10.32)$$

where  $E$ ,  $G$ , and  $\nu$  represent the Young's modulus, shear modulus, and Poisson's ratio of the target, while  $r$  and  $z$  represent the radial direction and thickness direction (in the direction of impact), respectively. For a planar isotropic material, the properties in the  $r$ - $\theta$ -plane are independent of the orientation.

The relationship between the contact force  $P$  and the combined deformation of both solids at the point of contact can be expressed similar to equations (10.11) and (10.12) as

$$P = n' \alpha^{1.5} \quad (10.33)$$

$$n' = \frac{16}{3\pi(k'_1 + k'_2)} \left( \frac{C_R}{s^3} \right)^{0.5} \quad (10.34)$$

Then equation (10.19) becomes in this case

$$P = n'^{0.4} \left( \frac{5v_0^2}{4M} \right)^{0.6} \quad (10.35)$$

Equations (10.22) and (10.23) for the pressure distribution become

$$p(xy) = p_0 \left( 1 - \frac{x^2}{a^2} - \frac{y^2}{b^2} \right)^{1/2} \quad (10.36)$$

$$p_0 = \frac{3P}{2\pi ab} \quad (10.37)$$

Combining equations (10.25), (10.26), (10.33), (10.35), and (10.37) yields the following expressions for the major axis  $a$  and minor axis  $b$  of the area of contact, the maximum deformation  $\alpha_{\max}$  at the impact site, and the maximum pressure:

$$\frac{a}{m} = \frac{b}{r} = \left[ \frac{3\pi}{2} (k'_1 + k'_2) C_R n'^{0.4} \left( \frac{5v_0^2}{4M} \right)^{0.6} \right]^{1/3} \quad (10.38)$$

$$\alpha_{\max} = \left( \frac{5v_0^2}{4Mn'} \right)^{0.4} \quad (10.39)$$

$$p_0 = \frac{1}{\pi^{4/3}} \left( \frac{3}{2\pi} \right)^{1/3} \frac{(n')^{2/15}}{mr[(k'_1 + k'_2)C_R]^{2/3}} \left( \frac{5v_0^2}{4M} \right)^{0.2} \quad (10.40)$$

There is no closed-form solution for  $k'_2$  for generally orthotropic solids, and its derivation is extremely complex. However, an approximate numerical solution for  $k'_2$  of generally orthotropic solids shows  $k'_2$  to be relatively insensitive to the in-plane fiber orientation. For a target made of orthotropic material with in-plane anisotropy ratio of  $E_x/E_y = 14.3$  and impacted by a rigid spherical impactor, the area of contact was slightly elliptical. The ratio of the major to minor axis of the ellipse was only 1.07. Since  $k'_2$  is mostly dependent on the properties associated with thickness direction  $z$ , and hardly dependent on the in-plane properties of the target, as a first approximation, average in-plane properties of  $E_r$  and  $v_r$  may be used to determine  $k'_2$ .

The parameter for a given generally orthotropic material can also be obtained experimentally from a static indentation test. For a spherical indenter ( $R_{1m} = R_{1M} = R_1$ ) made of isotropic material and a flat target ( $R_{2m} = R_{2M} = \infty$ ),  $C_R = R_1/2$ , and  $s = 2$  from equation (10.28) with  $\theta = 90^\circ$ , the value of  $k'_2$  is obtained from equations (10.13), (10.33), and (10.34) as

$$k'_2 = \frac{4}{3\pi P} (\alpha^3 R_1)^{0.5} - \frac{1 - v_1^2}{\pi E_1} \quad (10.41)$$

Thus, by conducting the static indentation test and measuring load  $P$ , versus deformation  $\alpha$ , the parameter can be determined from equation (10.41).

The maximum pressure  $p_0$  occurs at a time  $0.5t_0$  where  $t_0$  is the impact duration. From equation (10.17), the rate of deformation  $\dot{\alpha}$  is expressed, replacing  $n$  with  $n'$  for generalization, as

$$\frac{d\alpha}{dt} = \left( v_0^2 - \frac{4}{5} Mn' \alpha^{2.5} \right)^{0.5} \quad (10.42)$$

With the new notation

$$\eta = \frac{\alpha}{\alpha_{\max}} \quad (10.43)$$

equation (10.42) can be integrated using the result of equation (10.39):

$$t = \frac{2\alpha_{\max}}{v_0} \int_0^\eta \frac{d\eta}{\sqrt{1 - \eta^{2.5}}} \quad (10.44)$$

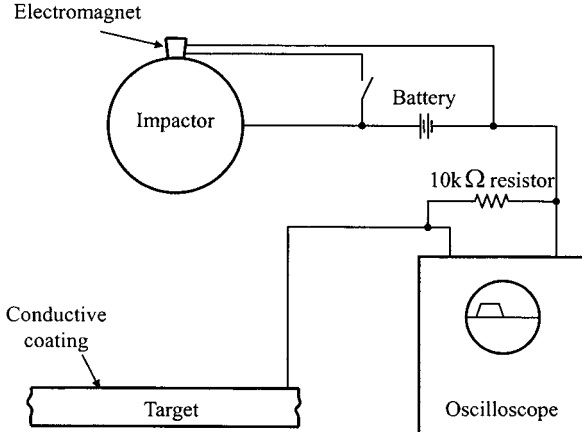


**Figure 10.3** Schematic of experimental setup for measuring contact duration during impact (Greszczuk, 1982).

The total impact duration  $t_0$  is obtained by numerically integrating equation (10.44) between the limits  $\eta=0$  and  $\eta=1$ , which is expressed as

$$t_0 = 2.94 \frac{\alpha_{\max}}{v_0} = 2.94 \left( \frac{5}{4Mn'v_0^{0.5}} \right)^{0.4} \quad (10.45)$$

To verify the accuracy of equation (10.45), the duration between aluminum and composite plates impacted by steel spheres was measured, as shown in figure 10.3 (Greszczuk, 1982). When the impactor was released the electric circuit was closed from the time the impactor first contacted the target to the time it bounced off. Equation (10.45) was proved to predict well the experimental data.

It has been shown that equation (10.44) can be approximated fairly well by the following equation (Greszczuk, 1982):

$$\alpha = \alpha_{\max} \sin \frac{\pi t}{t_0} \quad (10.46)$$

Substituting equation (10.45) into equation (10.46) yields

$$\alpha = \alpha_{\max} \sin \frac{\pi tv_0}{2.94\alpha_{\max}} \quad (10.47)$$

Substituting equation (10.33), using the result of equation (10.34), into equations (10.25), (10.26), and (10.37) and then substituting equation (10.47) into the resulting equation yields the following expressions for  $a$ ,  $b$ , and  $p_0$  as functions of time  $t$ :

$$\frac{a(t)}{m} = \frac{b(t)}{r} = \left( \frac{4C_R}{s} \alpha_{\max} \sin \frac{\pi tv_0}{2.94\alpha_{\max}} \right)^{0.5} \quad (10.48)$$

$$p_0(t) = \frac{3n's}{8\pi C_R m r} \left( \alpha_{\max} \sin \frac{\pi tv_0}{2.94\alpha_{\max}} \right)^{0.5} \quad (10.49)$$

#### 10.2.4 Effects of Target Flexibility on Impact Responses

For a flexible, plate-type target, the surface pressure, area of contact, and impact duration are functions of bending stiffness. For a given impact velocity the magnitude of dynamic force  $P$  decreases as the target flexibility increases (or target thickness decreases). An increase in target flexibility also increases contact duration and decreases the area of contact. An approximate solution for the impact response of flexible composite plates was obtained by considering the deformations shown in figure 10.4 (Greszczuk, 1982). At the point of contact, the plate undergoes the Hertzian contact deformation as well as plate bending deformation  $\delta_p$ . The Hertzian force-deformation relationship for the contact problem has already been given in equation (10.33):

$$P_c = n'\alpha^{1.5} \quad (10.50)$$

whereas the force-deflection relationship for a plate subjected to a concentrated load will be of the form

$$P_p = K_p\delta_p \quad (10.51)$$

where subscripts  $c$  and  $p$  represent the contact problem and the plate, respectively, and  $K_p$  is the stiffness constant of the plate.

With an impactor approach velocity  $v_0$ , the energy balance for the system is

$$\frac{1}{2}m_1v_0^2 = \int_0^{\delta_{\max}} P_p d\delta_p + \int_0^{\alpha_{\max}} P_c d\alpha \quad (10.52)$$

Substituting equations (10.50) and (10.51) into equation (10.52), then integrating, yields, with  $P_c = P_p = P$ :

$$\frac{1}{2}m_1v_0^2 = \frac{1}{2}\frac{P^2}{K_p} + \frac{2}{5}\frac{P^{5/3}}{n'^{2/3}} \quad (10.53)$$

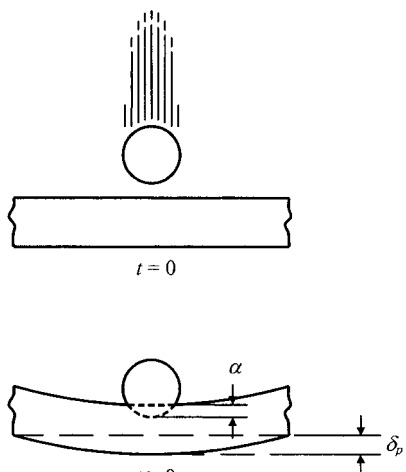


**Figure 10.4** Local and overall deformations of a flexible target.

For a circular isotropic plate of radius  $R$  and thickness  $h$  clamped along the outer boundary, the plate stiffness  $K_{pc}$  is expressed as (Young, 1989):

$$K_{pc} = \frac{P}{\delta} = \frac{4\pi E_r h^3}{3(1 - \nu_r^2)R^2} \quad (10.54)$$

For a plate with simply supported edges, the plate stiffness  $K_{ps}$  is

$$K_{ps} = \frac{P}{\delta} = \frac{4\pi E_r h^3}{3(1 - \nu_r)(3 + \nu_r)R^2} \quad (10.55)$$

For the case of simply supported boundaries, substituting equations (10.34) and (10.55) into equation (10.53) yields

$$\frac{1}{2}m_1\nu_0^2 = \frac{3}{8\pi} \frac{(1 - \nu_r)(3 + \nu_r)R^2}{E_r h^3} P^2 + \frac{2s}{5} \left[ \frac{3\pi(k'_1 + k'_2)}{16\sqrt{C_R}} \right]^{2/3} P^{5/3} \quad (10.56)$$

The first term on the right-hand side of equation (10.56) gives the plate bending effect and the second term gives the Hertzian contact effect.

#### 10.2.5 Internal Stresses Caused by Impact Pressure

In the case of a semi-infinite isotropic solid subjected to surface pressure  $p_r$  distributed according to equation (10.24), the internal triaxial stresses  $\sigma_r$ ,  $\sigma_\theta$ , and  $\sigma_z$  exist. Figure 10.5 shows the stress distributions for an isotropic material.

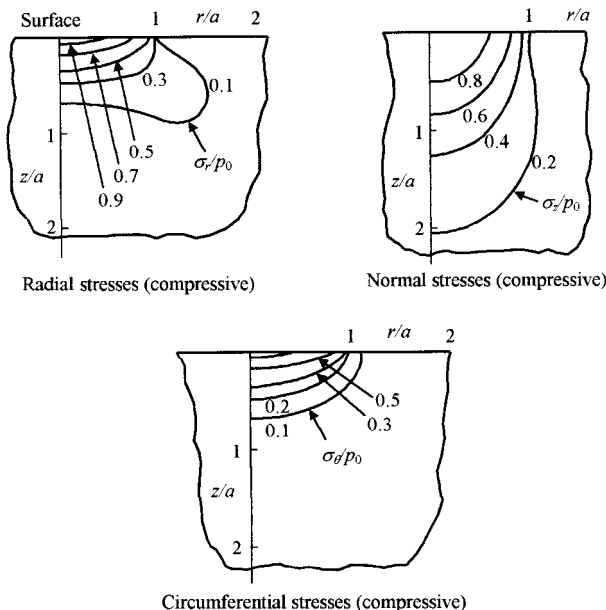


**Figure 10.5** Internal stresses for an isotropic solid subjected to a surface pressure caused by impact.

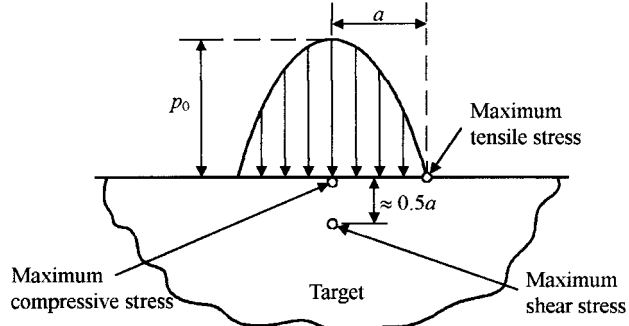


**Figure 10.6** Position of maximum stress for an isotropic solid subjected to a surface pressure caused by impact.

The maximum tensile stress  $\sigma_t$ , compressive stress  $\sigma_c$ , and shear stress  $\sigma_s$  that occur in targets made of isotropic materials are related to the surface pressure by the following equations (Timoshenko and Goodier, 1970):

$$\sigma_t = \left( \frac{1 - 2\nu}{3} \right) p_0(t) \quad (10.57)$$

$$\sigma_c = p_0(t) \quad (10.58)$$

$$\sigma_s = \left[ \frac{1 - 2\nu}{4} + \frac{\sqrt{2}}{9} (1 + \nu)^{1.5} \right] p_0(t) \quad (10.59)$$

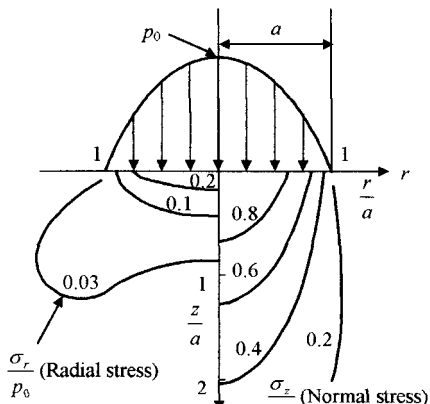
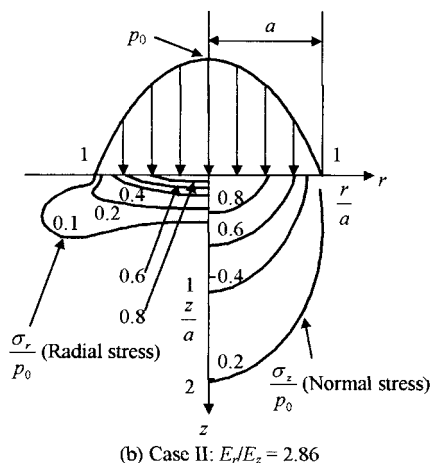
where,  $p_0(t)$  is the maximum surface pressure at time  $t$ . Figure 10.6 shows the positions of maximum stress.

For composite materials the analytic calculation is very complicated, hence finite element analysis is more feasible. Figure 10.7 shows the internal stress distributions in semi-infinite, multilayer, transversely isotropic material resulting from surface pressure caused by foreign object impact (Greszczuk, 1982). The material properties used for the numerical examples of figure 10.7 are shown in table 10.2.

#### 10.2.6 Impact Test Methods

High strain rate or impact loads may be expected in many engineering applications of composite materials, such as automotive side door composite impact beams (Cheon et al., 1997). Since an attempt to improve the tensile properties of composite usually results in a deterioration of impact properties, the suitability of a composite for impact applications is determined not only by the usual design parameters, but by its impact or energy absorbing properties. Usually, very high modulus carbon-fiber composites are more brittle than high-strength carbon-fiber composites or glass-fiber composites. Thus, it is important to have a good understanding of impact behavior of composites for both safe and efficient design of structures and to develop new composites having good impact properties, as well as good tensile properties (Agarwal and Broutman, 1990).

In terms of the energy of the impactor, current tests may be classified as either: (1) high-energy impact, in which the incident energy is sufficient enough to break the specimen, or (2) low-energy impact, in which the incident projectile damages but does not necessarily destroy the specimen (Curtis, 2000). The impact performance of a material falls into two areas: the ability to absorb energy during the impact event and the residual properties of the material after impact.

(a) Case I:  $E_r/E_z = 0.35$ (b) Case II:  $E_r/E_z = 2.86$ 

**Figure 10.7** Internal stress distributions in semi-infinite, multilayer, transversely isotropic material resulting from surface pressure caused by foreign object impact (a) When  $E_r/E_z = 0.35$ ; (b) when  $E_r/E_z = 2.86$  (Greszczuk, 1982).

**Table 10.2 Material Properties Used for the Numerical Example**

(a) Case I ( $E_r/E_z = 0.35$ )	(b) Case II ( $E_r/E_z = 2.86$ )
$E_r = 20$ GPa	$E_r = 57$ GPa
$E_z = 57$ GPa	$E_z = 20$ GPa
$G_{rz} = 5.9$ GPa	$G_{rz} = 5.9$ GPa

#### High-Energy Impact Test Methods

A very common way to evaluate high-energy impact properties is to determine material toughness by measuring the energy required to break a specimen of a particular geometry. The Charpy or Izod impact tests developed for isotropic materials are widely used in flexed beam configurations, as shown in figure 10.8 (Liaw, 2000).

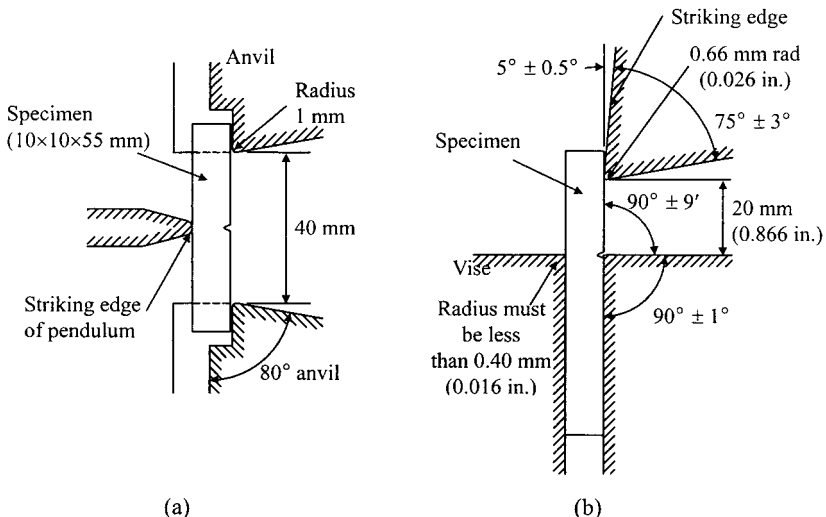


**Figure 10.8** Schematic impact test arrangements: (a) Charpy test; (b) Izod test (Liaw, 2000).

For the Charpy impact test, samples include a simple support span with or without a notch of any desired depth of cut in a narrow face. In the Izod test, the specimen is gripped at one end only, allowing the cantilevered end to be struck by the pendulum. An advantage of this method is that several notches can be made in a single specimen and the ends are broken off one at a time. The disadvantage of the Izod test is that the required time and method of clamping the specimen in an anvil preclude low-temperature testing.

The specimen in the Charpy test is supported on both ends and is broken by a single blow from a pendulum that strikes the middle of specimen on the unnotched side. The Charpy and Izod impact tests are useful for a comparative study of different materials and are adequate for studying impact behavior of isotropic metals or polymers. However, for composites in which the fracture mode and the energy absorbed are influenced by fiber orientation, specimen geometry, velocity of impact, and other test arrangements, these two tests are not always adequate.

In order to get more information during an impact test, additional instrumentation (typically an instrumented tup) is equipped with a standard Charpy impact machine to monitor the load-time response of deformation and fracture of specimen (instrumented Charpy impact test). The most commonly used approach is application of strain gages to the striker to sense the load-time behavior of the test specimen.

For the better acquisition of impact information, the drop-weight impact test, where the specimen is placed on rigid supports and a known weight is dropped on the specimen from a desired height, is generally used. The drop height can be adjusted to achieve the desired impact velocity or pneumatic power can be used to increase the impact velocity of the tup. Figure 10.9 shows the drop-weight impact test with a pneumatic cylinder to accelerate a large tup of 13 kg (Cheon et al., 1997).

The tup of the impact tester of figure 10.9 is accelerated when the electromagnet, which holds the piston in the pneumatic cylinder, is switched off. When the air pressure in the cylinder was 0.5 MPa, the velocity of the 13 kg impact tup was greater than 15 m/s (33 mph). The tup speed of 15 m/s was stipulated by

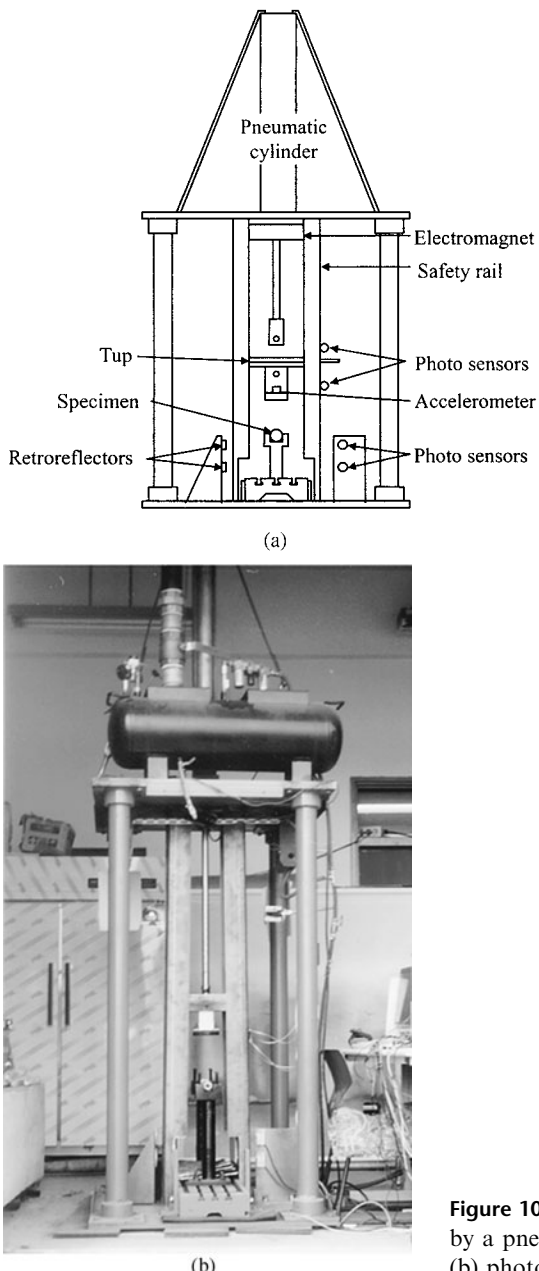


**Figure 10.9** Drop-weight impact tester accelerated by a pneumatic cylinder: (a) Schematic diagram; (b) photograph (Cheon et al., 1997).

FMVSS (Federal Motor Vehicle Safety Standards) 214 regulation. During the impact process, velocities of the impact tup before and after impact were measured with four photosensors. The upper two photosensors were used to measure the time difference through 50 mm movement, while the lower two photosensors were used to measure the time difference through 100 mm movement. Because the lower two photosensors were infrared emitted-retroreflector types, the interval between them was set to 100 mm considering the space for the retroreflective mirror mounting, whose diameter was 85 mm. On the other hand, the interval of upper two photosensors was 50 mm because the photosensors were optical-fiber types.

The acceleration of the impact tup was also measured with a piezoelectric-type accelerometer attached to the impact tup. The signals from the photosensors and the accelerometer were processed by a PC through an A/D converter. The mass of the impact tup was adjusted in the range 10–15 kg to vary the impact energy magnitude. Also, the impact velocity was adjusted in the range 1–25 m/s by varying the pressure inside the cylinder. The measured signals from the accelerometer were low-pass filtered with a 100 kHz cutoff frequency to remove noises generated during test.

#### *Low-Energy Impact Test Methods*

When the energy of the projectile is insufficient to break through or penetrate the material, it is called low-energy impact. Two-types of low-energy impact tests are used: ballistic impact test and low-velocity drop-weight impact test (Curtis, 2000). After the test, the specimen is usually visually as well as nondestructively inspected for surface and internal damage, respectively, and then tested in static tension or compression to determine its residual strength.

The ballistic impact tests use very low mass projectiles, often spherical balls, that are fired at the specimen surface at high speeds and then the specimen is inspected for damage. Above a threshold velocity, appreciable internal damage may appear in the impacted area even though the surfaces may appear undamaged. The principal internal damage is usually delamination, which is pronounced at interfaces between 0° and 90° or 0° and 45° layers. At high velocities or with thin panels, the projectile may completely pierce the material, leaving a fairly clean hole, but this usually requires higher energies.

The low-velocity drop-weight impact tests use a relatively heavy weight or ball that is dropped from a small height onto the specimen surface. The smaller the span supporting the specimen, the greater the probability of delamination failures which, in turn, can severely reduce the static compressive strength.

Low-energy impact does not necessarily cause catastrophic fracture in a laminate. The specimen may still be able to carry some mechanical load, although it has internal as well as surface damage. The load-bearing capability of an impact-damaged laminate can be measured usually by testing residual tension or compression strength. The measurement of compressive strength after impact (CAI) is performed with a specimen that has a width of 7.0 inches (177.8 mm) and a length of not less than 10.0 inches (254 mm) nor greater than 12.0 inches (304.8 mm), which is a NASA impact test specimen (Niu, 1992). After impact, the specimens are trimmed to a width of  $5.0 \pm 0.03$  inches ( $127 \pm 0.76$  mm) for compression test to failure. However, the measurement of CAI is expensive to undertake because it uses a large specimen. Therefore, the Boeing method is gaining popularity. The Boeing method uses a surface dent of 0.5 mm depth as a standard failure criterion.

A quantitative assessment of the factors important in the initiation of damage from foreign objects has been presented by Dorey (1980). He indicated that the type of damage to carbon-fiber polymeric matrix composites depended on the incident energy and momentum, material properties, and the geometry when subjected to transverse impact. He calculated the energy  $E_d$  to cause the delamination:

$$E_d = \frac{2\tau^2}{9D} \frac{wl^3}{t} \quad (10.60)$$

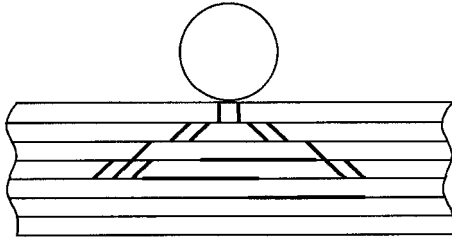


**Figure 10.10** Internal damage of brittle resin composites subjected to impact.

where  $\tau$  is the interlaminar shear strength,  $D$  the bending stiffness,  $t$  the thickness,  $l$  the length, and  $w$  the width of the specimen (Sierakowski and Newaz, 1995). For the energy  $E_f$  to cause the flexural fracture, he calculated that

$$E_f = \frac{1}{18} \frac{\sigma^2 w}{E t} \quad (10.61)$$

where  $\sigma$  is the flexural strength, and  $E$  the Young's modulus of the specimen. For the energy  $E_p$  to cause the penetration, he calculated that

$$E_p = \pi \gamma t d \quad (10.62)$$

where  $\gamma$  is the through-the-thickness fracture energy and  $d$  is the diameter of striker.

Whether delamination or flexural fracture occurs depends on the relative values of  $\tau$  and  $\sigma$  and the span-to-depth ratio  $l/t$ . Impact damage is less likely when there are low-modulus layers on the outside of the specimen such as 45° layers of Kevlar or glass fibers. Whether penetration occurs or not depends not only on the incident energy, but on the size and shape of the strikers. The penetration is more likely for small masses traveling at high velocities. The above analysis is based on linear elastic modeling and does not explain what happens when the critical values for initiation of damage are attained. If a crack is started, this crack will grow until the stored energy is dissipated. In brittle systems, this will result in crack growth, as shown in figure 10.10 (Sierakowski and Newaz, 1995).

If the composite system has the ability to yield and undergo plastic deformation, this impact energy will be dissipated without much damage growth. Since carbon fibers exhibit a linear elastic failure, improvements must be made in the matrix resins to increase impact resistance and damage tolerance. The matrix characteristic that is most critical to improving composite toughness is the ability to sustain a high stress while yielding, that is, to develop a knee in the stress-strain curve and have a large strain to failure. While equations (10.60) and (10.61) indicate that lowering the bending stiffness and Young's modulus is another means to increase resistance to delamination, a large in-plane modulus is required to control fiber microbuckling and damage growth under compressive loads, as in equation (7.88). Reductions of the composite bending stiffness should only be made by changing the laminate lay-up sequence and not through reductions in resin modulus.

#### 10.2.7 Impact Energy Absorption Mechanism

A typical load history of the impact test performed using glass-fiber polymeric matrix composites with an instrumented Charpy impact tester is shown in figure 10.11 (Lee and Cheon, 2001).

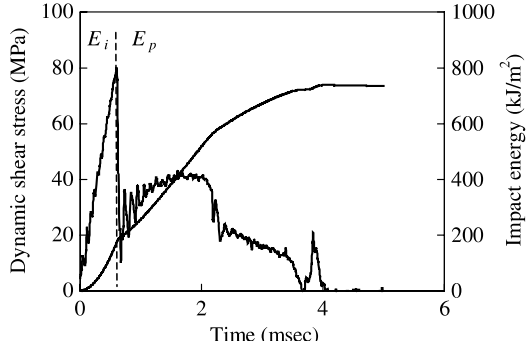


**Figure 10.11** Typical load–time history of glass-fiber polymeric matrix composite during impact test (Lee and Cheon, 2001).

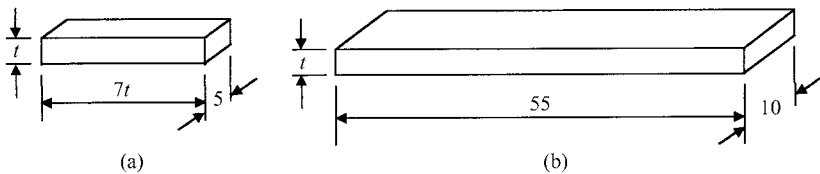


**Figure 10.12** Specimen dimensions of the short-beam shear and Charpy impact tests; the thickness of the specimen  $t$  was varied according to the fiber volume fraction. (a) Short-beam specimen; (b) Charpy specimen, dimensions in mm (Lee and Cheon, 2001).

The load–time history can be divided into two distinct regions, a region of fracture initiation and a region of fracture propagation (Agarwal and Broutman, 1990). As the load increases during the fracture initiation phase, elastic strain energy  $E_i$  is accumulated in the specimen and no gross failure takes place. However, microbuckling of the fibers on the compression side or debonding at the fiber–matrix interface is possible. When a critical load is reached at the end of the initiation phase, the composite specimen may fail either by a tensile or a shear failure, depending on the relative values of the tensile and interlaminar shear strengths. At this point the fracture propagates either in a catastrophic brittle manner or in a progressive manner, continuing to absorb energy ( $E_p$ ) at smaller loads. The total impact energy absorption  $E$ , which is the sum of  $E_i$  (fracture initiation energy) and  $E_p$  (fracture propagation energy) is obtained by integrating the fracture initiation and propagation energy components:

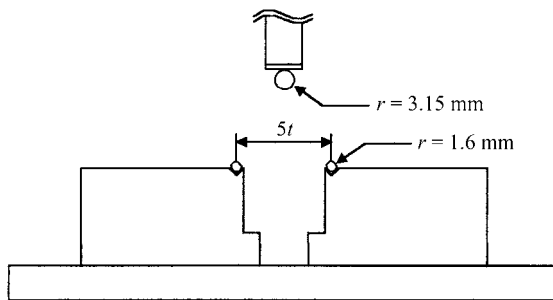
$$E = \int_0^{t_f} Pvdt \quad (10.63)$$

where  $P$  is the dynamic load acting on the specimen,  $v$  the impact speed, and  $t_f$  the time beyond which the dynamic load becomes zero.

Lee and Cheon (2001) investigated the impact energy absorption characteristics of glass epoxy composites and glass polyester composites with respect to fiber volume fraction by the instrumented Charpy impact test method. They measured also the interlaminar shear properties by the short-beam shear test to investigate the correlation between the interlaminar shear properties and the impact energy absorption characteristics. Figure 10.12 shows the specimen dimensions for the short-beam shear and Charpy impact tests. The resin content of the specimens was

**Table 10.3 Mechanical Properties of the Composite Specimens ( $V_f = 54\%$ )**

	<i>Longitudinal tensile modulus (GPa)</i>	<i>Longitudinal tensile strength (MPa)</i>	<i>Major Poisson's ratio</i>
Glass epoxy	43	1021	0.28
Glass polyester	40	611	0.25

**Figure 10.13** Jig for short-beam shear test (Lee and Cheon, 2001).**Table 10.4 Maximum Shear Strength of the Composites Obtained from the Short-Beam Shear Test ( $V_f = 54\%$ )**

<i>Composite</i>	<i>Shear strength (MPa)</i>
Glass epoxy	73
Glass polyester (with silane coupling)	57
Glass polyester (without silane coupling)	16

controlled by the amount of resin bleeder used during the autoclave vacuum bag degassing molding process. The matrix digestion method of ASTM D3171 was used to measure the fiber volume fraction of the glass-fiber epoxy composites. In this method, the composite specimens of weighed mass are immersed in 70% nitric acid solution at 80°C for 5 hours. After dissolving the epoxy resin in nitric acid, the glass fibers are filtered and weighed. The fiber volume fraction of the glass epoxy composite laminates ranged from 54.2% to 70.7%.

The fiber volume fraction of the glass polyester composite was measured by the sintering method rather than matrix digestion method because the polyester resin does not dissolve in nitric acid. The sintering method burns up the resin of composite laminates in a furnace. The fiber volume fraction of the glass polyester composite laminates in Lee and Cheon's work ranged from 53.4% to 75.7%. The thickness of the specimens was in the range 3.0–4.4 mm depending on fiber volume fraction. Table 10.3 shows the mechanical properties of the two composite materials for when the fiber volume fraction was 54%.

Short-beam shear tests were performed using a jig, as shown in figure 10.13. The ratio of span to thickness was set to 5, and the nose radii of the loading cylinder and the supporting fixtures were 3.15 mm and 1.6 mm, respectively, as recommended by ASTM D2344-84. The crosshead speed was set to 0.3 mm/min.

The interlaminar shear strengths of the composites obtained by the short-beam shear test are listed in table 10.4 for when the fiber volume fraction was 54%.

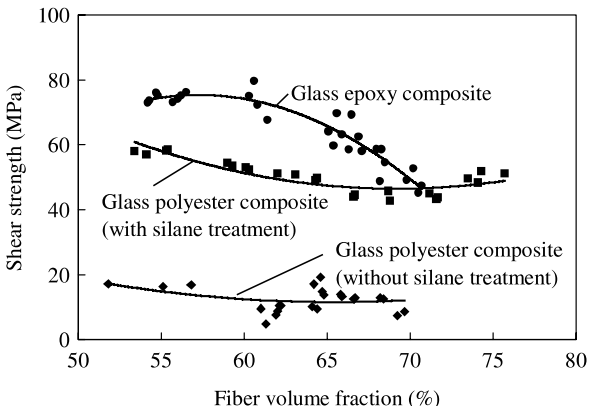


**Figure 10.14** Static interlaminar shear strengths of composite versus fiber volume fraction (Lee and Cheon, 2001).

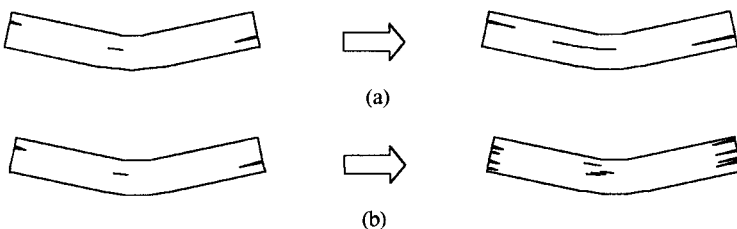


**Figure 10.15** Schematic diagrams of the static delamination modes of the composite short-beam shear specimens with respect to fiber volume fraction: (a) Propagation of delamination of fewer interfaces when the fiber volume fraction was small; (b) delamination initiation of many interfaces when the fiber volume fraction was large (Lee and Cheon, 2001).

Figure 10.14 shows the static interlaminar shear strength with respect to fiber volume fraction. For the glass epoxy composite material, the interlaminar shear strength did not change at first with respect to fiber volume fraction. However, the interlaminar shear strength decreased after the fiber volume fraction exceeded 60%. For the glass polyester composite material with silane coupling treatment, on the contrary, the interlaminar shear strength decreased at first as the fiber volume fraction increased, then the interlaminar shear strength increased slightly when the fiber volume fraction exceeded 70%, while the increase of the interlaminar shear strength of the glass-fiber polyester composites without silane coupling treatment was negligible. Moreover, the glass-fiber polyester composites without silane coupling treatment had very low interlaminar strength and failed in a ductile mode with deep indentation and compressive fiber buckling.

From the short-beam shear tests, it was found that the higher the fiber volume fraction, the more the ply interfaces delaminated. When the fiber volume fraction was larger than 75%, the interlaminar shear strength of glass-epoxy composites decreased because of poor fiber wet-out, as well as increased void contents. It was also found that the area under the load-displacement curve increased as the fiber volume fraction increased, and the failure mode changed from propagation dominant delamination to initiation dominant delamination in which the number of delaminated interfaces increased, as shown in figure 10.15.

The impact characteristics of fiber-reinforced composite beams may be overestimated when the span to thickness ratio is smaller than the critical value which is

dependent on fiber and resin types. Since the critical value exists in the range 4–6 for almost all composite beams (Bader and Ellis, 1975), the span length  $L$  was set to be 40 mm, which yielded a value of span to thickness ratio of 9–13. Notch-free Charpy specimens were used because the notch effect was known to be negligible for composite specimens. The impact speed was fixed to 5.21 m/s and the employed hammer was 12.07 kg. The force transducer was mounted on the tup section with 3 mm nose radius.

For the impact tests on the glass epoxy composites, the delamination started at the impacted site and propagated perpendicularly to the loading direction. As the fiber volume fraction was increased, the energy absorption portion by fiber breakage and fiber pull-out from the total impact energy absorption was increased until the fiber volume fraction of about 65%, then it decreased because the interlaminar crack was easily propagated through the composite specimens without fiber breakage and fiber pull-out due to the decrease of the interlaminar shear strength. Consequently, the impact energy absorption capability was decreased as the fiber volume fraction was increased beyond 65%.

For the impact tests on the silane-treated glass polyester composites, the modes of delamination failure were similar to those of glass epoxy composites. When the fiber volume fraction of these composites was lower than 60%, the specimen was divided into two parts by an interlaminar delamination crack and the fiber breakage and fiber pull-out failure was not extensive. As the fiber volume fraction approached 70%, the interlaminar delamination cracks were created at many interfaces and easily propagated through the specimen due to lack of resin between fibers. Consequently, the impact energy absorption capability had a tendency to decrease when the fiber volume fractions were high: the impact absorption capabilities of the glass-fiber epoxy specimens and the silane-treated glass-fiber polyester specimens were decreased beyond 65% and 70% of fiber volume fraction, respectively. According to these results, it may be concluded that there existed an optimum interlaminar shear strength, which gives the maximum energy absorption due to fiber breakage, fiber pull-out, and delamination.

Although the impact energy absorption capability of the glass polyester composite specimens without silane treatment decreased slightly as the fiber volume fraction increased, there was no prominent impact energy absorption characteristic for this type of composite specimen. Also, the fiber breakage and pull-out failure of these specimens did not occur in the whole tested range of fiber volume fraction, and the impact energy absorption capability was too low for practical application compared with other types of composite specimens. The results obtained in Lee and Cheon's work (2001) had a different trend from the results obtained by Yeung and Broutman (1978), in which they obtained the maximum impact energy absorption characteristics of glass fabric polyester composites when the interlaminar shear strength was 30 MPa.

From the Charpy impact test results, the maximum dynamic interlaminar shear strengths were obtained and compared with the static interlaminar shear strengths obtained from short-beam shear tests, as shown in figure 10.16 (Lee and Cheon, 2001). The maximum dynamic shear strength of the glass epoxy composites had the maximum value when the fiber volume fraction was about 62% and was 25–50% larger than the static values. The maximum dynamic shear strength of the silane treated glass polyester composites had the minimum value when the fiber volume fraction was about 67% and was 45–75% larger than the static values. The maximum dynamic shear strength of the glass polyester composites without

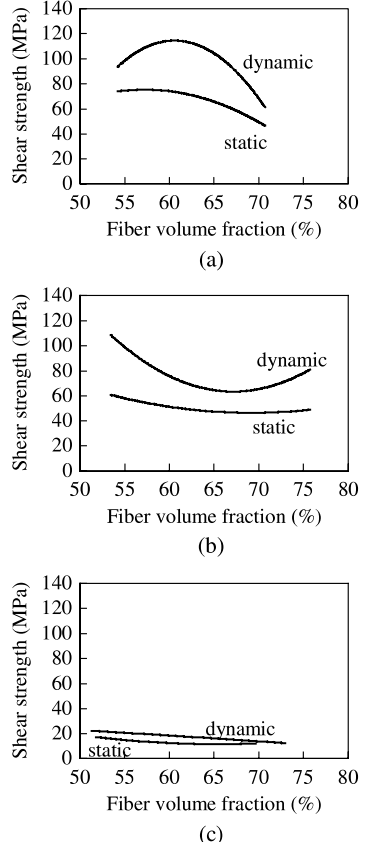


**Figure 10.16** Comparison between the static and dynamic shear strength: (a) Glass epoxy composite; (b) glass polyester composite with silane treatment; (c) glass polyester composite without silane treatment (Lee and Cheon, 2001).

silane-treatment was very low, although it was little larger than that of the static values.

#### 10.2.8 Impact Energy Absorption Characteristics of Composite Materials

During impact, the energy  $E$  absorbed by the specimen at any time was given by equation (10.63):

$$E = \int_0^{t_f} P v dt \quad (10.64)$$

As an approximation, the right-hand side of equation (10.64) may be replaced by the product of average tup velocity  $\bar{v}$  and impulse, so that

$$E = \bar{v} \int_0^{t_f} P dt \quad (10.65)$$

and

$$\bar{v} = \frac{1}{2} (v_0 + v_f) \quad (10.66)$$

where  $v_0$  is the initial velocity and  $v_f$  is the velocity at the specific instant for which  $E$  is to be calculated.

**Table 10.5 Typical Impact Energy Characteristics of Materials by Notched Charpy Impact Tests (Adams and Miller, 1975)**

Material	Impact energy (kJ/m <sup>2</sup> )
Modmor II carbon epoxy ( $V_f = 55\%$ )	114
Kevlar epoxy ( $V_f = 65\%$ )	694
S-glass epoxy ( $V_f = 72\%$ )	694
Nomex nylon epoxy ( $V_f = 70\%$ )	116
Boron epoxy ( $V_f = 60\%$ )	78
4130 Steel alloy ( $X' = 700\text{--}1120 \text{ MPa}$ )	593
4330 Steel alloy (HRC = 43–46)	214
431 Stainless steel (annealed)	509
2023 T3 Aluminum alloy	84
6061 T6 Aluminum alloy (solution treated and precipitation hardened)	153
7075 T6 Aluminum alloy (solution treated and precipitation hardened)	67

From the momentum-impulse relationship,

$$m_1(v_f - v_0) = 2m_1(\bar{v} - v_0) = \int_0^{t_f} Pdt \quad (10.67)$$

Since the impulse  $\int Pdt$  and initial impact velocity  $v_0$  are easily measured, let us define  $E_a$  as

$$E_a = v_0 \int_0^{t_f} Pdt \quad (10.68)$$

Then from equation (10.67) and (10.68), the following equation can be obtained:

$$\frac{\bar{v}}{v_0} = 1 + \frac{E_a}{4E_0} \quad (10.69)$$

where  $E_0$  is the maximum available impact energy defined by

$$E_0 = \frac{1}{2} m_1 v_0^2 \quad (10.70)$$

where  $m_1$  is the mass of the drop weight. Combining equations (10.65), (10.68), and (10.69) yields

$$E = E_a \left( 1 + \frac{E_a}{4E_0} \right) \quad (10.71)$$

Equation (10.71) represents the correction to the recorded energy absorption curves when there is a reduction in velocity of the impacting head as it fractures the specimen.

Table 10.5 represents typical impact energy absorption characteristics obtained from a standard notched Charpy impact test (Adams and Miller, 1975).

**Table 10.6 Impact Properties of Unidirectional Fiber Epoxy Composites (Broutman and Mallick, 1974)**

Fiber type	Span/depth	Dynamic flexural strength (MPa)	$E$ ( $\text{kJ}/\text{m}^2$ )	$E_i$ ( $\text{kJ}/\text{m}^2$ )	$DI$
E glass	16.1	1940	622	466	0.33
Carbon (T 300)	14.6	1580	187	86	1.2
Carbon (GY 70)	12.6	480	12	12	0.0
Kevlar 49	10.5	675	239	76	2.2

As shown in table 10.5, the carbon-fiber epoxy composite has very low impact energy absorption characteristics. An effective method of enhancing the impact properties of carbon-fiber composites is to add to them a small percentage of a low-modulus fiber, which results in higher impact performance. Glass fibers are frequently used for this purpose because glass fibers have higher impact resistance properties and are much cheaper than carbon fibers. The incorporation of two or more fibers within a single matrix is called hybridization, and the resulting material is referred to as a hybrid composite or simply hybrid (Agarwal and Broutman, 1990). In hybridization, different types of fibers may be intimately mixed throughout the resin or one type of fiber is placed in a single layer followed by dispersion of plies through the laminate. An example of a hybrid composite is discussed in section 15.3 for automotive bumper beams.

As explained earlier, the total impact energy  $E$  is the sum of the initiation energy  $E_i$  and the propagation energy  $E_p$ . Two materials having equal total impact energies may have completely different proportions of initiation and propagation energies. The ductility index  $DI$  is defined to rank the impact performance of different materials with similar geometries:

$$DI = \frac{E_p}{E_i} \quad (10.72)$$

Low values of  $DI$  mean a low value of propagation energy, which is an indication of the brittleness of the material. Table 10.6 shows some typical impact properties of several unidirectional laminates measured by Broutman and Mallick (1974). From table 10.6, E-glass epoxy composite laminates exhibit the highest energy absorbed per unit area, whereas carbon-fiber (GY 70) epoxy composite exhibits the lowest energy absorption capability. The low  $DI$  value for the E-glass epoxy composite laminate results from the very high initiation energy caused by a high strain energy absorbing capability of the E-glass fibers. Kevlar 49 epoxy composite laminates also exhibit some fiber pull-out and yielding on the compression side, and the specimens do not fracture completely.

### 10.3 Fatigue Characteristics of Composite Materials

Components of machines, vehicles, and structures are frequently subjected to repeated loads, also called cyclic or fatigue loads, and the resulting cyclic stresses can lead to microscopic physical damage to the materials involved (Dowling, 1999). Even at stresses well below a given material's ultimate strength, this microscopic

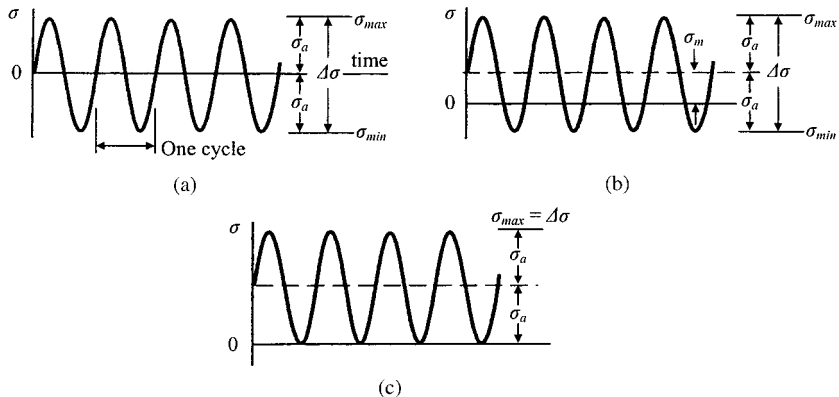


**Figure 10.17** Constant amplitude completely reversed stress cycling and the associated nomenclature: (a)  $\sigma_m = 0$ ; (b)  $\sigma_m \neq 0$ ; (c)  $\sigma_{\min} = 0$ .

damage can accumulate with continued cycling until it develops into a crack or other macroscopic damage that leads to failure of the component.

Some practical applications, and also many fatigue tests on materials, involve cycling between maximum and minimum stress levels that are constant. This is called constant-amplitude stressing, and is shown in figure 10.17.

The stress range  $\Delta\sigma$  is the difference between the maximum and the minimum values. Averaging the maximum and minimum values gives the mean stress  $\sigma_m$ . Half the range of  $\Delta\sigma$  is called the stress amplitude  $\sigma_a$ . Their relations are

$$\Delta\sigma = \sigma_{\max} - \sigma_{\min} \quad (10.73)$$

$$\sigma_m = \frac{\sigma_{\max} + \sigma_{\min}}{2} \quad (10.74)$$

$$\sigma_a = \frac{\Delta\sigma}{2} \quad (10.75)$$

$$\sigma_{\max} = \sigma_m + \sigma_a \quad (10.76)$$

$$\sigma_{\min} = \sigma_m - \sigma_a \quad (10.77)$$

Ratios of certain pairs of the above variables are sometimes used:

$$R = \frac{\sigma_{\min}}{\sigma_{\max}} \quad (10.78)$$

$$A = \frac{\sigma_a}{\sigma_m} \quad (10.79)$$

where  $R$  is called the stress ratio and  $A$  the amplitude ratio.

### 10.3.1 Fatigue Control Mode

When considering fatigue testing or fatigue data comparison, it is essential to know how the test was performed. Three methods that can be used for fatigue testing are load control, energy control, and strain control (Jang, 1994).

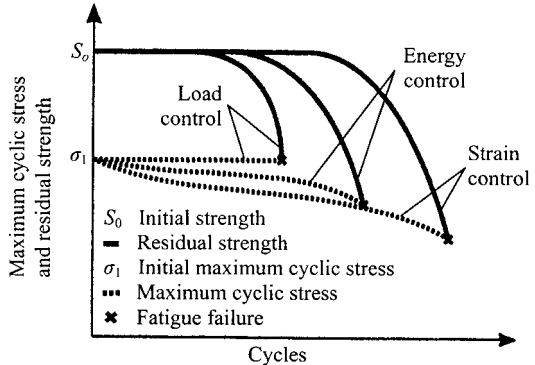


**Figure 10.18** Strength reduction and fatigue life for the three fatigue test modes (Stinchcomb and Reifsnider, 1988).

The load control maintains a constant magnitude cyclic stress on the tested specimen. As damage in the specimen occurs, the strain increases to accommodate the constant stress on the damaged laminate. This increases the strain energy per cycle. The fatigue life of load-controlled specimens is shortest among the three control methods.

The energy control maintains a constant magnitude of strain energy per cycle throughout the test by decreasing the stress applied as the specimen is damaged. This is achieved by increasing the strain to keep the area under the cyclic stress-strain curve constant. Fatigue life is greater than with load control tests but less than with strain control.

Strain control is a constant displacement fatigue test where magnitude of applied stress decreases as the laminate is damaged. The strain energy per cycle decreases as the test proceeds. This method of testing generally exhibits longer fatigue lives than load or energy control methods. Figure 10.18 shows the  $S-N$  (applied stress-number of cycles) relation for these different test controls.

Since polymer matrices are viscoelastic, a phase lag between the applied stress and resulting strain exists, which generates heat in the matrix. Because of the poor thermal conductivities in polymers, local areas of heat buildup can exist within the composites. The magnitude of local hot spots increases with increasing cyclic frequency. The cyclic frequency below 30 Hz is generally recommended where possible (Jang, 1994).

### 10.3.2 Fatigue Crack Growth

Unidirectional continuous fiber-reinforced composites possess excellent fatigue resistance in the fiber direction because the load in a unidirectional composite is primarily carried by the fibers, which generally exhibit excellent resistance to fatigue (Agarwal and Broutman, 1990). In real structures, however, composites are mostly used in the form of laminates. Because of the differences in orientation of each ply, some plies are weaker than others in the loading direction and show physical evidence of damage much before the final fracture. The evidence of damage may be in one or more forms, such as the failure of the fiber-matrix interface, matrix cracking or crazing, fiber breaking, and delamination.

The failure of the fiber-matrix interface usually initiates by the separation of fibers from the matrix (called debonding) in the fiber-rich regions of the plies in which the fibers lie perpendicular or at a large angle to the loading direction. Large stress and strain concentrations at the fiber-matrix interface are responsible for the

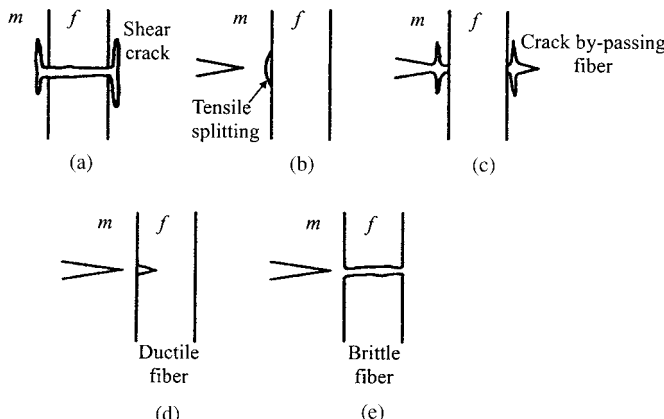


**Figure 10.19** Modes of fatigue crack growth in fiber-reinforced composites: (a) Shear crack initiation at fiber break; (b) tensile splitting of interface ahead of matrix crack; (c) matrix crack bypassing strong fiber; (d) crack initiation in ductile fiber ahead of matrix crack; (e) fracture of brittle fiber ahead of matrix crack; *m* and *f* represent matrix and fiber, respectively (Agarwal and Broutman, 1990).

initiation of these cracks. After initiation, the crack usually propagates between fibers, primarily along the fiber–matrix interface. The crack is generally perpendicular to the direction of load and extends over the entire width of the ply.

For randomly oriented fibrous composites, the initial damage occurs similarly at the strands lying perpendicular or at the largest angle to the line of load. The initiation of damage occurs in the form of debonding within a strand at any point along the length of the strand and is not particularly associated with the ends.

The crossply cracks propagate through the entire width of the ply but are unable to propagate into the adjacent ply if it is a ply having fibers aligned in the direction of load. Thus, the crossply cracks terminate at the interface of two plies. Since the crack tip produces a stress concentration ahead of itself, the high interlaminar stresses produce favorable conditions for starting a delamination crack along the ply interface.

When delamination cracks appear, the fibers in the longitudinal plies may also start fracturing, and debonding and cracks in the longitudinal plies begin to appear. The longitudinal-ply cracks do not follow any set path, unlike the crossply cracks, which are generally perpendicular to the line of load.

The composite undergoes final fracture when it is sufficiently weakened by longitudinal-ply cracks and delamination cracks. The presence of delamination cracks prevents load distribution between plies, and the composite is essentially reduced to a number of independent longitudinal plies acting in parallel to support the applied load. The weakest of these longitudinal plies fails and triggers failure of the remaining longitudinal plies. The delamination cracks, which are responsible for final fracture of the material, are manifest only at a late stage of the fatigue test, for example, after about 90% of the fatigue life.

The initiation of cracks resulting from fiber fracture and the propagation of cracks through the composite in a fiber-reinforced material is shown schematically in figure 10.19 (Agarwal and Broutman, 1990). A discontinuity produced by a fiber fracture causes high shear stress at the fiber–matrix interface and produces favorable conditions for a shear crack to grow, as shown in figure 10.19(a). Depending on the

relative values of bond strength and matrix strength, the shear crack may grow in the interface region or in the adjacent matrix material.

When a fatigue crack takes place in the matrix, as in figure 10.19(b), tensile splitting at interfaces may initiate ahead of a fatigue crack because the interface between the fiber and the matrix ahead of a crack tip is under very high tensile stress (Anderson, 1995). The crack branching with shear cracks in figure 10.19(a) and tensile splitting in figure 10.19(b) relieve some of the stress concentration in the vicinity of the crack and enhance fatigue life of the material as a consequence of a weak fiber-matrix interfacial bond. Plastic flow in a ductile matrix also blunts the crack tip and thus impedes crack growth.

When a fatigue crack in the matrix approaches a strong fiber with weak interface, the crack can bypass the fiber, as shown in figure 10.19(c). When the interface is strong, high stresses ahead of the crack tip affect the fibers, which accelerates the crack growth in the fiber, as shown in figure 10.19(d). Brittle fibers ahead of the crack fail abruptly because of the large crack tip stresses. The modes of fatigue crack growth in figures 10.19(d) and (e) generally result in poor fatigue resistance of composites. The above crack initiation and damage evolution sequence can be summarized as follows:

1. Matrix cracks are initiated early in the fatigue process. The majority of the fatigue life of a laminate is spent in the crack multiplication stage where the density of cracks increases.
2. As the crack density increases, cracks begin to grow into each other, forming larger cracks.
3. When the laminate is still further loaded, the crack density will be increased to a limiting value that could initiate other macroscopic damage mechanisms, which are usually delamination and fiber breakage.

### 10.3.3 Fatigue Performance of Composites

#### *Tension-Tension Fatigue*

The tension-tension  $S-N$  curves for unidirectional high-modulus carbon-fiber composites are almost horizontal, and fall within the scatter band of the static tensile strength, as shown in figure 10.20. The fatigue effect is slightly greater for relatively low-modulus carbon-fiber-reinforced composites (Mallick, 1988). Unidirectional boron and Kevlar 49 fiber composites also exhibit very good fatigue strength in tension-tension loading (Miner et al., 1975).

Additional fatigue data of unidirectional carbon, aramid, and glass-fiber composites indicate that the ratio of fatigue strength to static strength for long life is smallest for the glass-fiber composites and largest for the carbon-fiber composites.

Although the tensile strength of unidirectional composites is greatest in the fiber direction, in fatigue the unidirectional construction is not optimum, as shown in figure 10.21. The poor performance of unidirectional glass laminates is due to splitting in the fiber direction, which result from their relatively low transverse strength and imperfect testing or gripping conditions (Agarwal and Broutman, 1990). If the splitting problem is prevented by providing some of the plies in the  $90^\circ$  direction, the fatigue strength is improved (Boller, 1964; Davis et al., 1975).

Laminates of other stacking sequences are found to show similar  $S-N$  curves, but the actual fatigue effect depends on stacking sequence, the proportion of fibers aligned

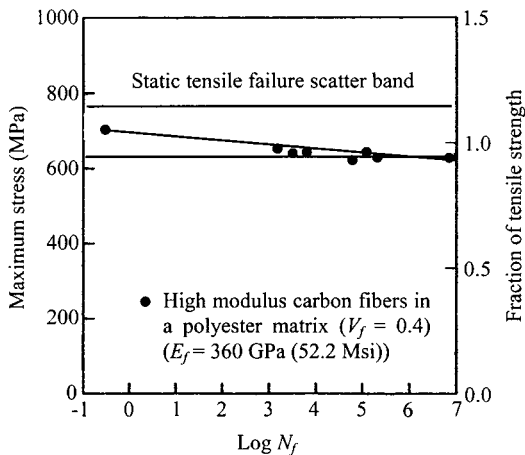


**Figure 10.20** Tension-tension  $S-N$  curves for high-modulus unidirectional carbon-fiber epoxy composites (Owen and Morris, 1971).

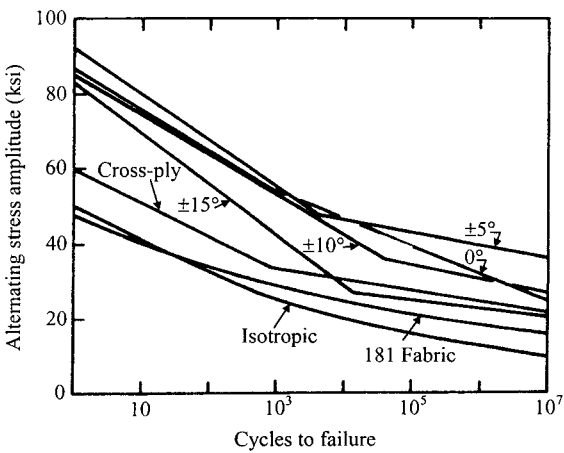


**Figure 10.21** Effect of fiber orientation on fatigue strength of the glass-fiber polymeric composites (Boller, 1964).

with the loading axis, and the mode of cycling. For example, tension-compression cycling ( $R = -0.6, -1.2$ ) produced steeper  $S-N$  curves than the tension-tension curve ( $R = +0.1$ ), as shown in figure 10.22. The same effect is shown in the case of a multidirectional carbon-fiber epoxy laminate with stacking sequence [45/0<sub>2</sub>]s for  $R = 0.0$  and  $-1.0$ , as shown in figure 10.23 (Curtis, 1988; Curtis and Dorey, 1986). This is because the plies, with and without fibers in the loading direction, develop intraply damage, and this causes local delamination at relatively short lifetimes (Mall, 1997). In tensile loading this is less serious, as the plies that contain fibers aligned along the loading direction continue to support the majority of the applied load. In compression, however, tensile-induced damage can lead to local instability and buckling, perhaps because the resin and fiber interfacial damage within the plies initiates fiber microbuckling. Thus, fatigue lives in reversed tension-compression loading are usually shorter than for tension-tension loading.

The  $S-N$  curve describes the relation between maximum stress or stress range and lifetime for a given stress ratio  $R$ . To show the effect of varying stress ratios, one presentation of fatigue data (probably the simplest one) is a modified Goodman's diagram, which presents various combinations of mean and stress amplitude for failure at a specified lifetime (Shigley et al., 2004). In Goodman's diagram, the constant values of  $R$  are represented by straight lines through the origin. Goodman's

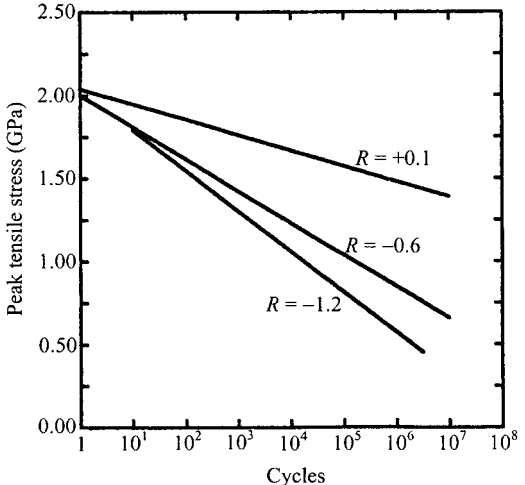


**Figure 10.22** Effect of stress ratio on fatigue strength of a unidirectional carbon-fiber epoxy composite (Curtis, 1988; Curtis and Dorey, 1986).

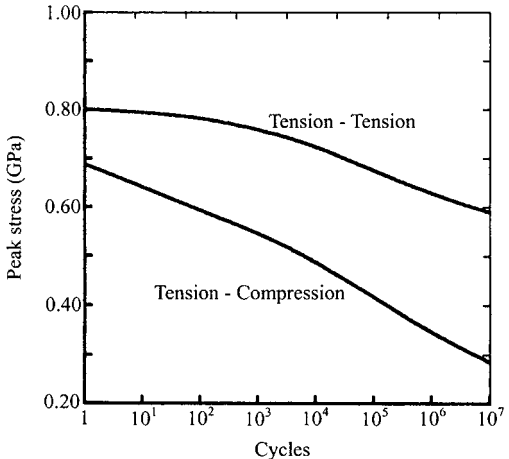


**Figure 10.23** Comparison of fatigue characteristics between tension-tension and tension-compression of multidirectional carbon-fiber epoxy laminate composites (Curtis, 1988; Curtis and Dorey, 1986).

diagram for several unidirectional composites at  $10^7$  cycles (Rosen and Hashin, 1987) is shown in figure 10.24 and for a multidirectional carbon-fiber epoxy laminate in figure 10.25 (Curtis and Dorey, 1986).

Since the modified Goodman equation is a straight line that passes through the ultimate strength and endurance limit at  $R = -1$  (Shigley et al., 2004), the modified Goodman equation may not be applicable for composite materials because the curves in figures 10.24 and 10.25 are not straight.

Fatigue tests on composites that contain some off-axis fibers (i.e., stacking angle  $\theta \neq 0^\circ$ ) show a steady deterioration in fatigue strength with increasing fiber orientation angle. As already shown in figure 10.21, a laminate that contains alternate layers of  $\pm 5^\circ$  fibers has a higher fatigue strength than a  $0^\circ$  laminate. The fatigue performance of  $0^\circ$  laminates is also improved by the addition of a small percentage of  $90^\circ$  plies, which reduces the tendency of splitting (cracks running parallel to fibers) (Mallick, 1988). However, as the percentage of  $90^\circ$  plies increases, the fatigue strength is reduced. The fatigue performance of glass-fiber laminates containing woven fabrics or randomly oriented fibers is lower than that of unidirectional or nonwoven crossply laminates, as shown in figure 10.26.

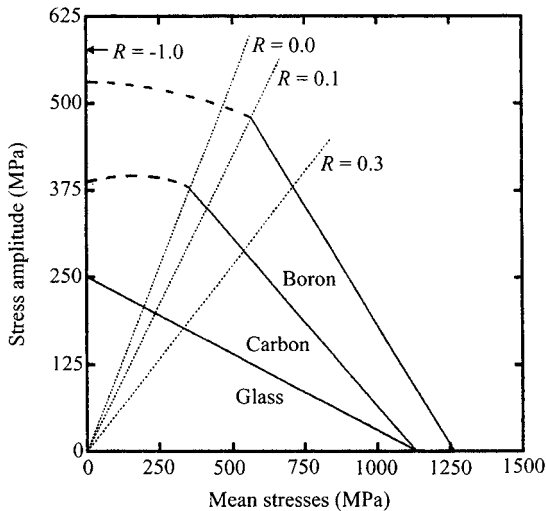


**Figure 10.24** Effect of mean stress on fatigue life at  $10^7$  cycles of several unidirectional composites (Rosen and Hashin, 1987).

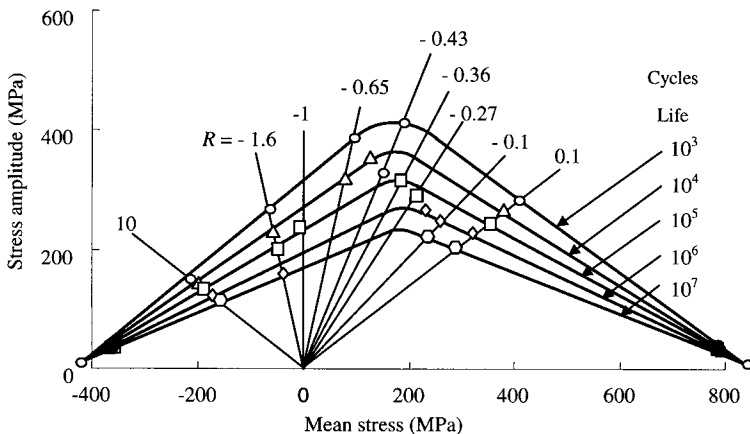


**Figure 10.25** Effect of mean stress on fatigue life of carbon-fiber epoxy composites with  $[0/\pm 30]_{2s}$  (Curtis and Dorey, 1986).

#### Flexural Fatigue

Three- or four-point bending test specimens under repeated bending have been used to characterize the flexural fatigue performance of composite materials. In general, the flexural fatigue resistance of fiber composites is inferior to the corresponding tension-tension fatigue resistance because of the weakness of laminates on the compression side (Jang, 1994). Figure 10.27 shows that the slope of the flexural S-N curve is higher than that of the tension-tension S-N curve for unidirectional carbon-fiber composites (Mallick, 1988). In a three-point bending type specimen, a short beam with small span-to-depth ratio will exhibit shear failure modes, while a longer beam will show combined compression-tension modes.

#### Interlaminar Shear Fatigue

As explained in the previous section, short-beam specimens under a flexural bending load can be used to investigate the interlaminar shear stress  $\tau_{xz}$  under fatigue

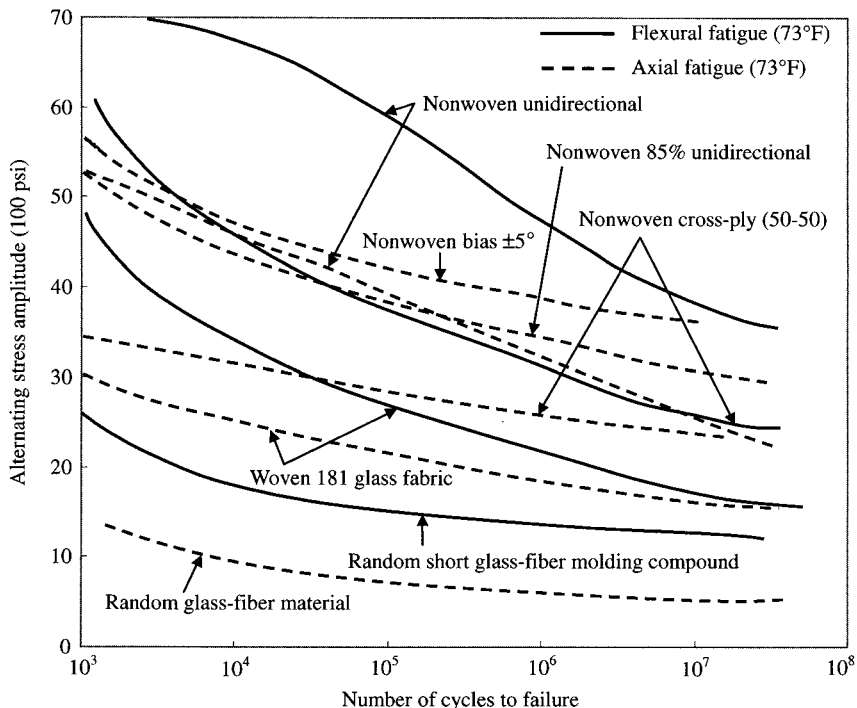


**Figure 10.26** Fatigue characteristics for different glass-fiber laminate constructions (Davis et al., 1975).

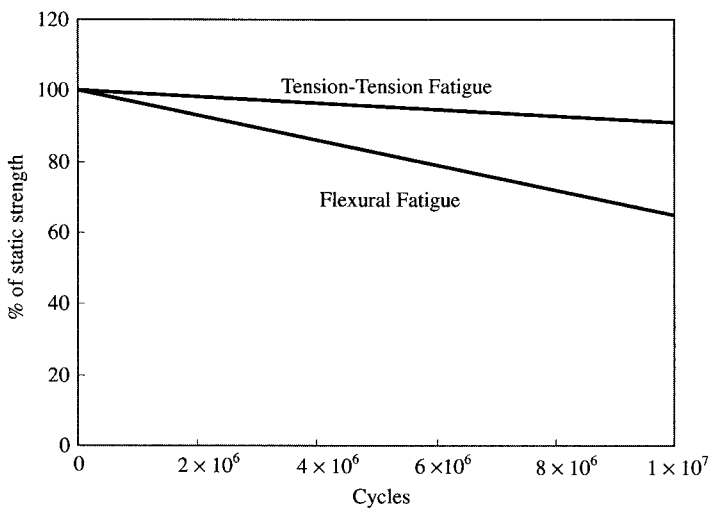


**Figure 10.27** Comparison of tension-tension and flexural fatigue lives of a unidirectional carbon-fiber epoxy composites (Mallick, 1988).

loading. The interlaminar shear fatigue strength of unidirectional carbon-fiber or boron-fiber epoxy composites was reduced to less than 55% of the static interlaminar shear strength (ILSS) after  $10^6$  cycles, whereas the corresponding tension-tension strength was nearly 80% of the static tensile strength, as shown in figure 10.28 (Romain and Williams, 1976). However, the interlaminar shear fatigue performance

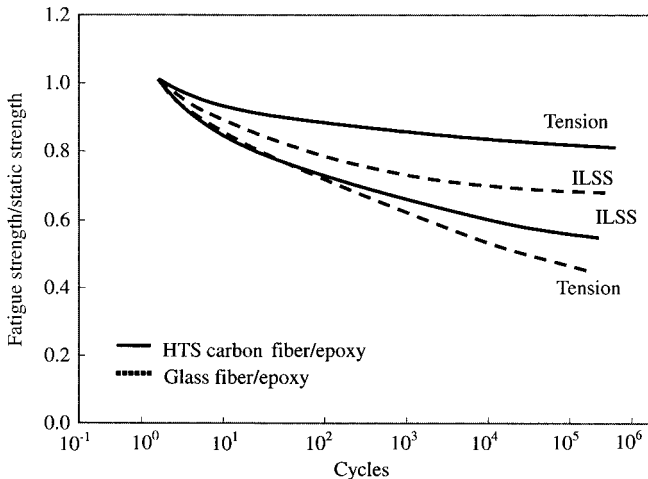


**Figure 10.28** Interlaminar shear strength (ILSS) S–N curves for unidirectional carbon and glass-fiber epoxy composite laminates.

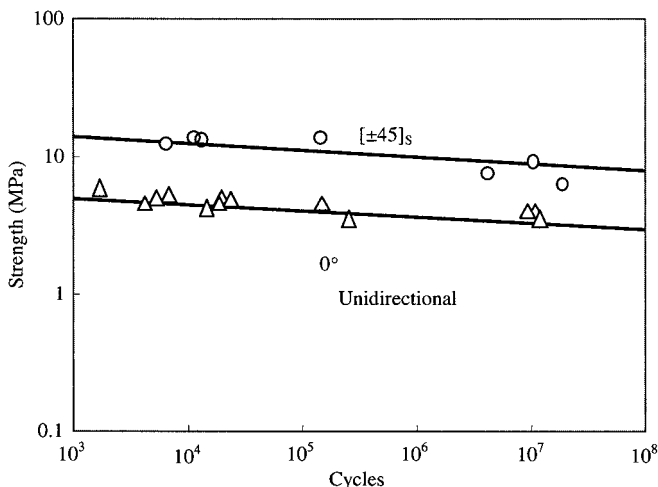


**Figure 10.29** Torsional S–N diagrams for [0] and [± 45]s high-strength carbon-fiber epoxy composites (Fujczak, 1974).

of a unidirectional S-glass reinforced epoxy composite showed the opposite trend. For this composite, the interlaminar shear fatigue strength at  $10^6$  cycles was approximately 60% of its static counterpart, but the tension-tension fatigue strength at  $10^6$  cycles was less than 40% of its static tensile strength (Pipes, 1974). This could be attributed to a better interfacial adhesion between glass fiber and epoxy, due to a good coupling agent, than that between carbon fiber and epoxy (Jang, 1994).

#### Torsional Fatigue

A tube with [0] or [± 45]s stacking sequence or a unidirectional solid rod has been used to characterize the torsional fatigue behavior of composite materials. The S–N plots in torsional fatigue with  $R = -1$  for both [0] and [± 45]s materials exhibit a linear response on a log–log scale, as shown in figure 10.29 (Fujczak, 1974), in which

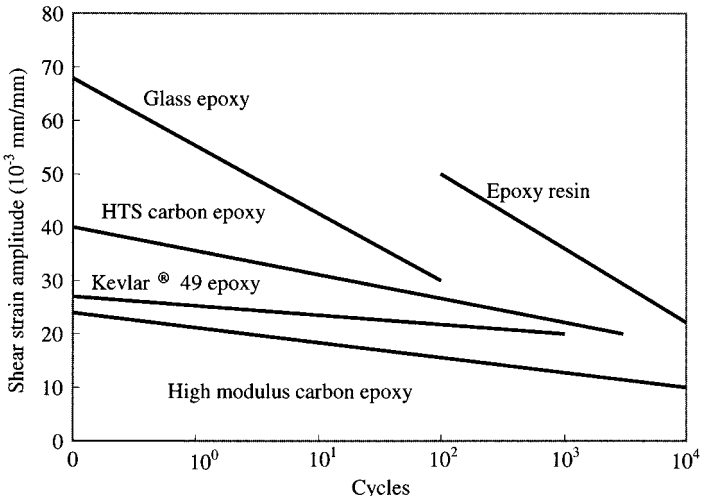


**Figure 10.30** Torsional shear strain cycle diagram for various unidirectional fiber composites (Owen and Morris, 1972).

the fatigue strength of  $[\pm 45]_S$  specimens is approximately 3.7 times higher than that of the [0] specimens at the same number of cycles. The [0] specimens failed with a few longitudinal cracks and the  $[\pm 45]_S$  specimens failed by cracking along the lines accompanied by extensive delamination.

Torsional fatigue data for a number of unidirectional fiber-reinforced composites are compared in figure 10.30. These data were obtained by shear strain cycling of solid rod specimens. All the unidirectional composites failed at approximately  $10^3$  cycles at a strain rate level of half the static shear failure strain.

#### Compressive Fatigue

Since the fibers are the principal load-bearing elements in compression, fibers should be supported by a matrix to prevent them from becoming locally unstable, undergoing buckling failure. Therefore, local resin and interfacial damage lead to fiber instability in compressive loading. The need to support the specimen to prevent macrobuckling, combined with the limitations imposed on specimen geometry by the anisotropic nature of the materials, has made it very difficult to conduct compressive tests, both static and cyclic (Jang, 1994). Therefore, little information is available on the compressive fatigue of composites.

#### 10.3.4 Fatigue Damage Mechanisms

Fatigue in composite materials exhibits both microscopic and macroscopic damage mechanisms at various stages in the fatigue process, as explained briefly in previous sections. Generally, matrix cracking occurs in the weakest ply. Crack multiplication then dominates most of the fatigue life, with cracks initiating in the progressively stronger plies. As cracks intersect each other, areas of delamination can occur. At some later stage, the fibers break in the loading direction, causing the laminate to fail (Jang, 1994). The damage mechanisms most commonly attributed to fatigue are matrix cracking, fiber–matrix debonding, delamination, and fiber breakage.

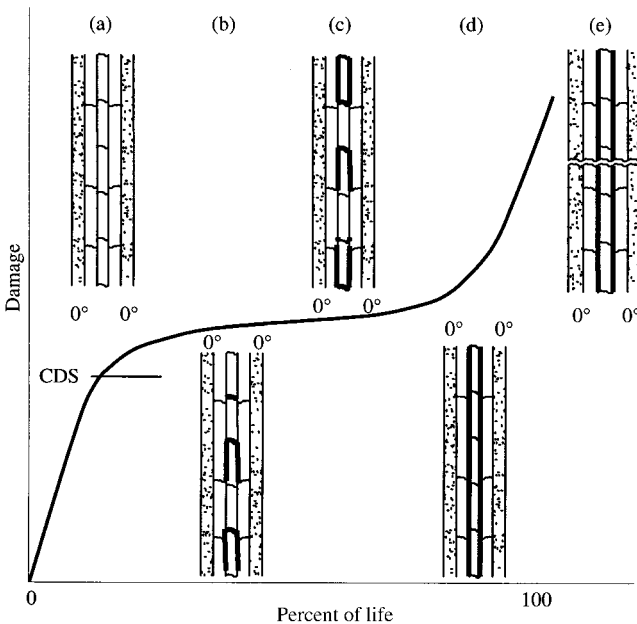


**Figure 10.31** Fatigue damage mechanisms in composite laminate; CDS represents characteristic damage state. (a) Matrix cracking, fiber breaking; (b) crack coupling, interfacial debonding, fiber breaking; (c) delamination, fiber breaking; (d) delamination growth, localized fiber breaking; (e) fracture (Reifsnider, 1990).

Figure 10.31 shows a schematic representation of fatigue damage development of unidirectional fiber composite with cycling (Reifsnider, 1990).

Transverse plies, with fibers at  $90^\circ$  to the loading direction, develop transverse cracks either upon the first tensile load cycle or with increasing number of cycles dependent on load level. This is usually referred to as first ply failure (FPF) and causes a reduction in the stiffness of the laminate (Mall, 1997). Similar intraply damage can also occur in the off-axis plies, causing a further reduction of the laminate stiffness. These types of intraply damage usually involve noninteractive matrix cracking restricted to individual plies. A well-defined crack pattern and number of cracks, in a given off-axis ply, eventually saturate during cycling, which is referred to as the characteristic damage state (CDS) of the laminate. Figure 10.32 shows the density of matrix cracks in different plies of a quasi-isotropic  $[0/90/\pm 45]_S$  carbon epoxy composite laminate with a saturation level or CDS during cycling (Kim, 1989). The CDS depends on the composite systems, as well as the stacking sequence. Therefore, the CDS will be different between  $[0/90/\pm 45]_S$  and  $[0/\pm 45/90]_S$ .

On further cycling beyond CDS, interaction and coupling of matrix cracks occur through fiber-matrix interfacial debonding and delamination with no further reduction or little reduction in modulus, as shown in figure 10.33 (Stinchcomb and Bakis, 1990).

Edge delamination may also occur in some laminates (e.g.,  $[0/\pm 45/90]_S$  laminates) because of high interlaminar stresses between various plies. As a result of delamination, local stresses in the  $0^\circ$  plies increase, since the delaminated and damaged off-axis plies cease to share load. Additional stresses in  $0^\circ$  plies in turn cause fiber failure and accelerate the fatigue failure process. The final failure mechanism is the

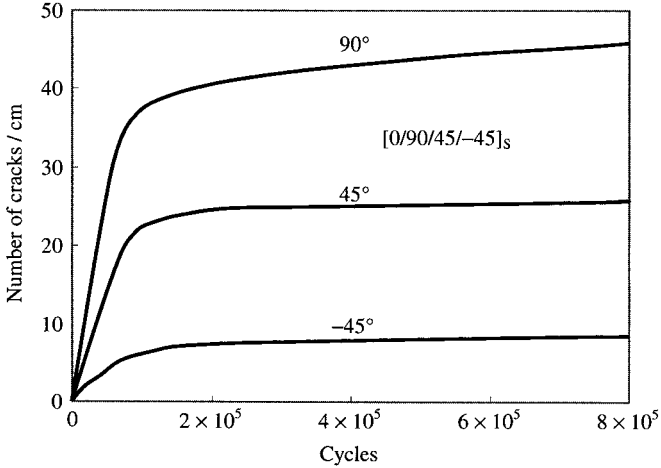


Figure 10.32 Growth of transverse matrix cracks (Kim, 1989).

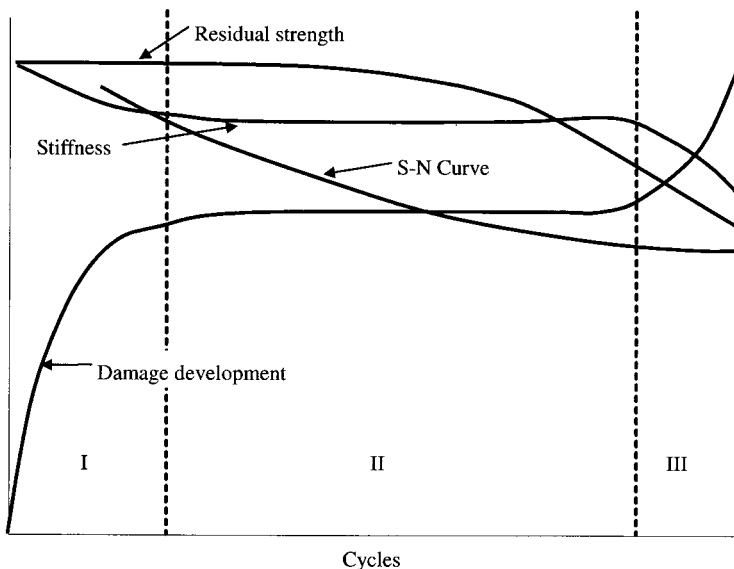


Figure 10.33 Strength and stiffness reduction during cycling (Stinchcomb and Bakis, 1990).

fiber fracture in  $0^\circ$  plies followed by debonding (longitudinal splitting) at the fiber-matrix interfaces in these plies. The fiber fracture usually develops in local areas adjacent to the matrix cracking in off-axis plies. This results in further reduction in the stiffness (Reifsnider, 1990).

As shown in figure 10.33, the damage takes place in three stages (Mall, 1997). Stage I is characterized by an initial rapid decrease in stiffness caused primarily by matrix cracking. Stage II is an intermediate but long period of small reduction in stiffness that results from additional matrix cracking in off-axis and on-axis plies, crack coupling along ply interfaces, and delaminations. The failure onset of stage III near the end of life is characterized by a rapid decrease in stiffness as a result of an increase in damage growth rates, including delamination coalescence and fiber

fracture. Therefore, one method of representing the damage  $D$  is to use the stiffness or modulus ratio:

$$D = \frac{E_i}{E_0} \quad (10.80)$$

where  $E_i$  is the instantaneous modulus at any fatigue cycle and  $E_0$  is the initial modulus before cycling.

The strength, called residual strength, of a laminate also decreases with the development of damage during cycling. Damage mechanisms such as matrix cracks and early fiber fracture that develop during the first 10–15% of the fatigue life and are widely scattered throughout the laminate have a small but measurable effect on the strength. After the characteristic damage state, the residual strength decreases at an increasing rate as the stage II damage develops. The residual strength continues to decrease throughout stage II and into stage III, where delamination and fiber fracture greatly influence the response. The actual shape of the residual strength versus cycle curve varies with material stacking sequence, loading history, and environment (Mall, 1997).

### 10.3.5 Fatigue Life Diagrams

Since the representation of fatigue behavior of  $S-N$  curves originates from the fatigue of metals, this representation is somewhat inadequate for composite materials because it does not properly reveal the roles of the constituents and the underlying mechanisms that lead to the final failure. Without a clarification of these roles numerous plots will result due to a large number of possible combinations of constituent materials and their volume fractions, fiber orientation, ply stacking sequence, and various other material and geometric factors (Talreja, 2000).

To avoid this situation and to provide a basis for a systematic assessment of fatigue of composites, a conceptual framework called the fatigue life diagram was developed by Talreja. Its horizontal axis is taken as the logarithm of the number of load cycles to failure, as in a conventional  $S-N$  diagram. The vertical axis is, however, chosen as the maximum strain reached in the first load cycle under the load control mode. The strain reached at the first application of the maximum load is the variable used for plotting. The construction of the fatigue life diagram is shown in figure 10.34 for the case of a unidirectional composite loaded in cyclic tension parallel to fibers (Talreja, 2000). Three regions are shown in the diagram. Region 1 is a scatter band (typically 5–95% failure probabilities) associated with fiber failure about the composite strain to failure,  $\varepsilon_c$ . Region 2 extends as a sloping scatter band intersecting region 1 at a certain low number of cycles and asymptotically approaching a fatigue limit,  $\varepsilon_m$ , at a large number of cycles. Region 3 is the region below the fatigue limit where no failure ensues at any number of cycles less than a number considered to be large for most applications (e.g.,  $10^6$ ).

If a specimen survives when it is subjected to a load that causes the first cycle maximum strain within the scatter band of  $\varepsilon_c$ , a certain number of fibers are likely to have failed at various sites without critically weakening any cross-section. In the second and subsequent load cycles, more fibers in the close vicinity of previous broken fibers are likely to fail. Assuming the fibers to be elastic and brittle, the progressive fiber failures will lie in the polymer matrix, which by virtue of its flow

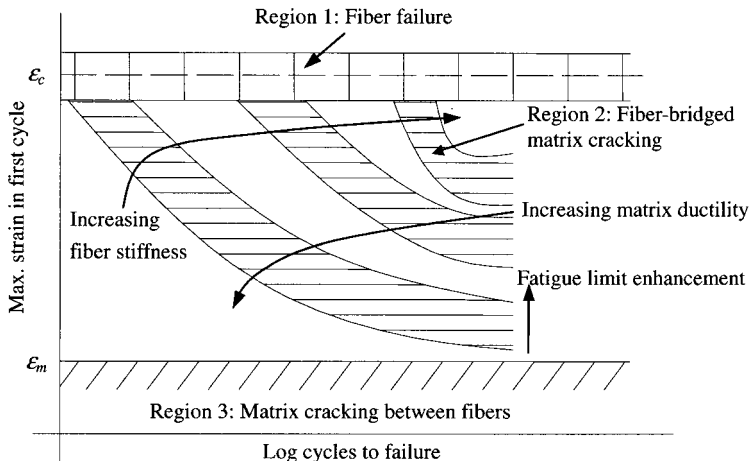


**Figure 10.34** Fatigue life diagram of a unidirectional composite loaded in cyclic tension parallel to fibers with respect to fiber stiffness and matrix ductility (Talreja, 2000).

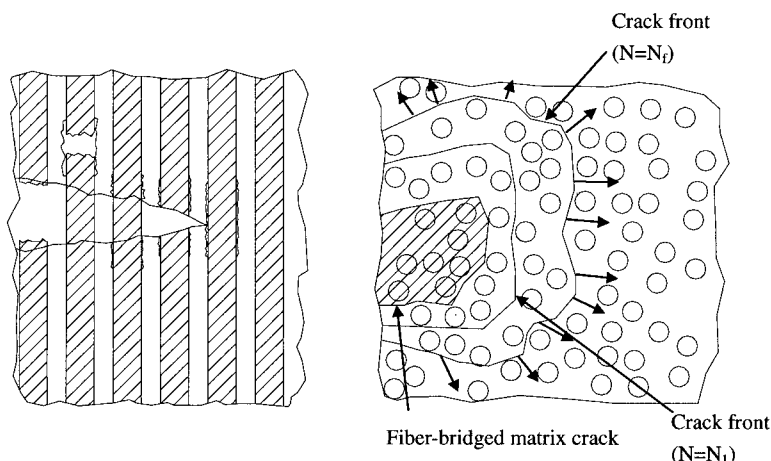


**Figure 10.35** Fiber-bridged matrix cracking mechanism in region 2 of the fatigue diagram (Talreja, 2000).

would redistribute stress on the fibers. However, the degree of this progressiveness would reduce if the matrix flow is constrained by stiff fibers.

Region 2 is characterized by the maximum first-cycle strain being too low to cause widespread fiber failure. With subsequent load cycles the matrix develops fatigue cracks that grow by either failing fibers in their way or by debonding the fibers and advancing around them. A typical matrix crack is thus bridged by fibers, as shown in figure 10.35, which manifests with a sloping scatter band, as shown in figure 10.34. The lower end of this band tends to flatten out as the fatigue limit is approached at  $\epsilon_m$ . Final failure then ensues from a crack of sufficiently large size that would grow unstably at the applied load.

Region 3, lying below the fatigue limit, is characterized by arrested, nongrowing matrix cracks, as shown in figure 10.36. The local strain in the fibers is insufficient here to cause significant numbers of fibers to fail. As a result, the opening

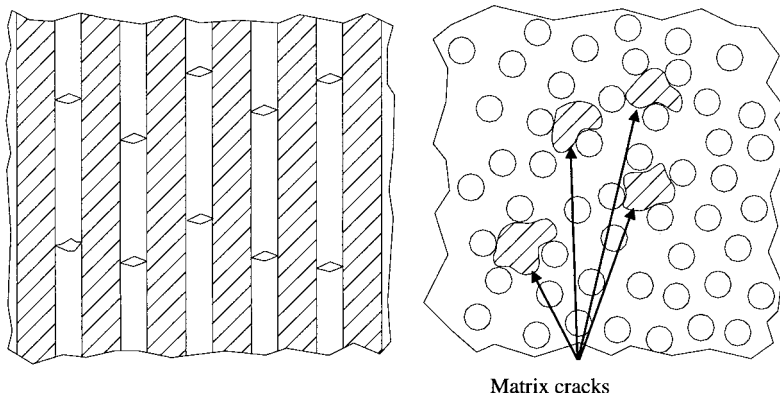


**Figure 10.36** Matrix cracking mechanism in region 3 of the fatigue life diagram (Talreja, 2000).

displacement of matrix cracks is too small to allow growth rates that would lead to failure within the design life of most components.

One advantage of the fatigue life diagram is that it facilitates assessments of the composite fatigue, such as:

1. *Effect of fiber failure strain:* The progressive fatigue damage mechanisms are possible in the range of strains between  $\varepsilon_m$  and  $\varepsilon_c$ , as seen in figure 10.34. The value of  $\varepsilon_c$  for glass fiber is greater than 2%, while it is less than 0.5% for high-modulus carbon fibers. The fatigue process can be essentially suppressed by using fibers of failure strain less than  $\varepsilon_m$ .
2. *Effect of fiber stiffness:* Since the fiber-bridged matrix cracking is the predominant damage mechanism in region 2, the crack opening displacement is restricted by the bridging fibers, more by stiff fibers than by compliant fibers. Since the fatigue life is inversely related to the crack growth rate, the effect of fiber stiffness on the scatter band of region 2 will be as shown in figure 10.34.
3. *Effect of matrix ductility:* The crack tip in an elastic matrix will be sharp, but will be rendered blunt if the matrix flows. Thus, increasing matrix ductility will increase the crack tip blunting and add to the elastic crack opening displacement, resulting in higher strain on the bridging fibers, thereby easing their failure and increasing crack growth rates. The effect of matrix ductility will therefore cause the trend illustrated in figure 10.34. This appears to contradict the conventional belief that a higher toughness matrix provides higher fatigue resistance. Although it is true for an unreinforced matrix, the advantageous effect of toughness manifested by ductility does not hold for fiber-reinforced composites.

Many fatigue data were analyzed by Talreja (2000) to verify the usefulness of the fatigue life diagram. Figure 10.37 shows the fatigue life diagram for a glass epoxy composite with three different fiber volume fractions, in which all data fall within the same scatter band. When plotted on the S-N diagram, the fatigue life data for the three volume fractions fall on separate curves. While, for an ultrahigh-modulus carbon-fiber epoxy composite, Region 2 disappeared because the fiber failure strain ( $=\varepsilon_c$ ) is less than the fatigue limit, assumed to be at  $\varepsilon_m=0.006$  (Talreja, 2000).

When the applied load is inclined to the fiber direction, the fiber-matrix interface is subjected to a normal stress and a shear stress. These two stresses combined would

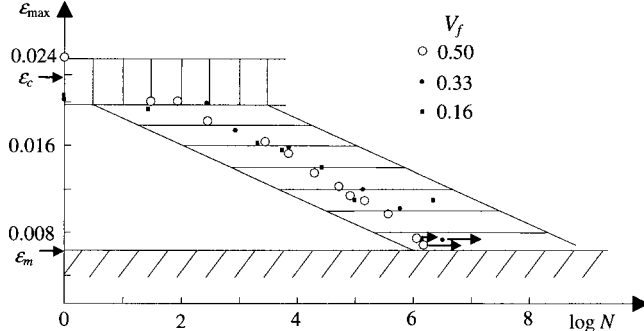


**Figure 10.37** Fatigue life diagram of unidirectional glass epoxy composites loaded in cyclic tension parallel to fibers (Talreja, 2000).

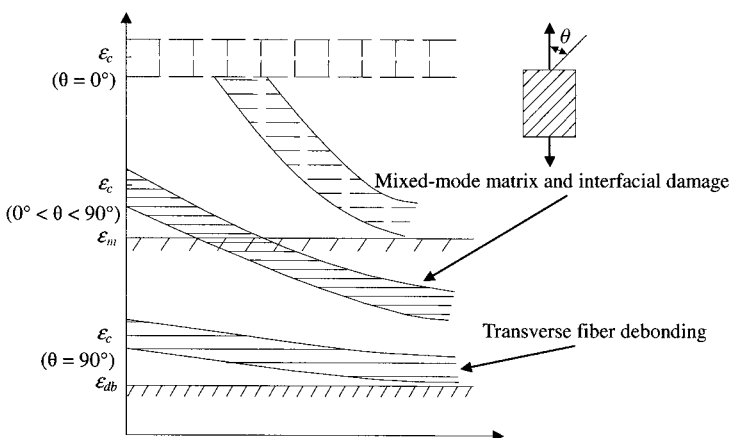


**Figure 10.38** Fatigue life diagram of unidirectional composites loaded in cyclic tension inclined at angle  $\theta$  to the fiber direction (Talreja, 2000).

likely produce interfacial cracks, which would then grow with cyclic load application. For the loading angle  $\theta$  greater than a few degrees, fiber failure is not even possible for a complete separation of specimens in two parts. Thus, region 1 of the fatigue life diagram disappears because the role of fiber failure is not present, as shown in figure 10.38. The scatter band of region 2 starts at lower strain and slopes become less as the loading angle  $\theta$  increases. The fatigue limit also decreases with increasing angle  $\theta$  due to increasing normal stress on the interface. The lowest fatigue limit  $\epsilon_{db}$  occurs at  $\theta = 90^\circ$ , in which the predominant damage mechanism is *transverse fiber debonding*.

For general laminates that are combinations of the three basic arrangements of unidirectional, angle-ply and crossply laminates, figure 10.31 shows a schematic description of the damage process. Figure 10.39 shows the fatigue life data of a glass epoxy composite laminate of  $[0/\pm 45/90]_S$  and a carbon-fiber epoxy laminate of  $[0/45/90/-45_2/90/45/0]_S$ , in which the same pattern emerges for both laminates. The scatter band of region 1 exists due to the presence of longitudinal plies and the fatigue limit corresponds to the strain for onset of the first matrix cracking. The fatigue limit in these two laminates thus depends on cracking in the transverse plies, which is affected by the constraint of the other plies of immediate neighborhood (Talreja, 2000).

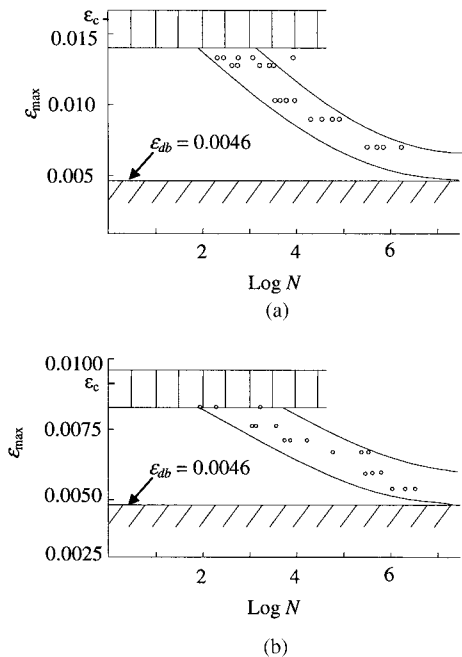


**Figure 10.39** Fatigue life diagrams of general laminates: (a) Glass-fiber epoxy composite; (b) carbon-fiber epoxy composite (Talreja, 2000).

### 10.3.6 Performance under Hot/Wet (Hygrothermal) Conditions

The material behavior under impact and cyclic loadings has been discussed in the previous sections. It is equally important to understand the material behavior under various environmental conditions, such as exposure to low and high temperatures, water, water vapor and other corrosive environments.

The polymeric matrix for composites is generally most vulnerable to hot/wet environmental conditions. Consequently, matrix-dominated properties, such as stiffness and strength under transverse, off-axis, or shear loading, as well as compressive strength, will be affected. Usually, fibers are not affected by hygrothermal changes. The swelling or contraction due to temperature and moisture change is resisted by the fibers, and therefore residual stresses develop inside the composite. A similar effect occurs at the laminate level due to mismatch of hygrothermal expansions or contractions of the laminate (Mall, 1997). Effects of temperature and moisture on the longitudinal and transverse tensile strengths of a typical carbon epoxy composite are shown in figure 10.40 (Browning, 1972). Figure 10.41 shows stress-strain curves under transverse loading for a typical carbon-fiber epoxy composite system (Browning et al., 1977). The hygrothermal conditions cause substantial reductions of both transverse strength and stiffness. Similar degradation has been observed in the case of in-plane shear loading of the composite.

## 10.4 Concluding Remarks

The impact and fatigue performance of composite materials has been presented for the design of composite structures. The low- and high-velocity impact behaviors and the methods for increasing toughness of composite structures have been discussed.

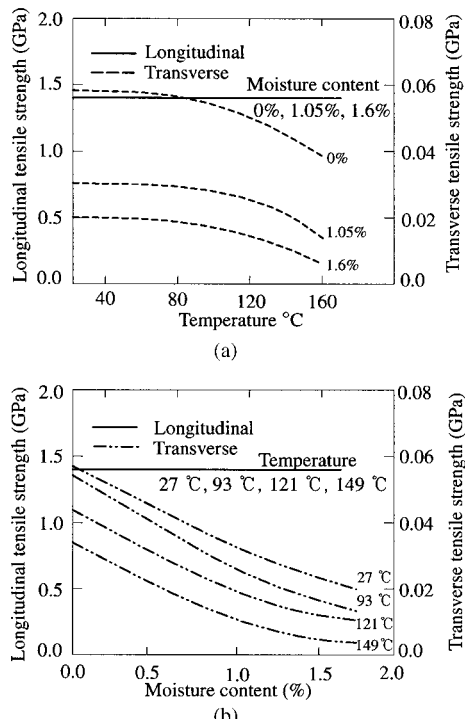


**Figure 10.40** Strength of carbon-fiber epoxy composite (AS/3501-5) with respect to (a) Temperature; (b) moisture content (Browning, 1972).

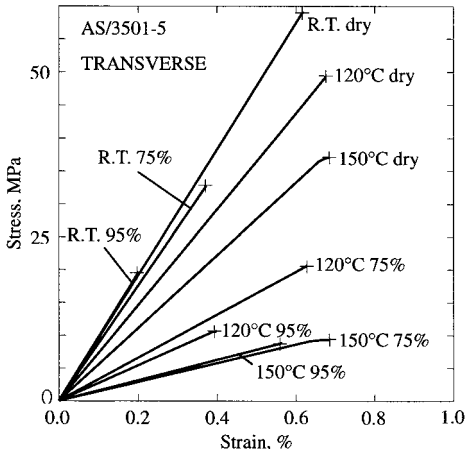


**Figure 10.41** Transverse stress-strain curves of carbon-fiber epoxy composites (AS/3501-5) at different temperatures and moisture contents (Browning et al., 1977).

The fatigue and environmental properties of composite materials in wet and hot conditions have been briefly introduced. For the fatigue life assessment of composite structures, the fatigue life diagram developed by Talreja was introduced.

## Problems

- 10.1.** Explain physically that the reflected wave at a free surface is a tensile stress wave, whose magnitude is given by equation (10.1) when the incident stress wave is a compressive wave.

- 10.2.** Derive equation (10.17).
- 10.3.** Derive equation (10.41).
- 10.4.** Derive equation (10.45).
- 10.5.** Explain the increase of probability of delamination failures in low-velocity drop-weight impact tests as the span supporting the specimen decreases.
- 10.6.** Why should the reductions of the composite bending stiffness be made by changing the laminate lay-up sequence rather than by a reduction in resin modulus in order to improve composite toughness?
- 10.7.** Some values of stress amplitude and corresponding cycles to failure are given in table 10.7 from tests on the AISI 4340 steel. The tests were done on unnotched axially loaded specimens with  $R = -1$ .

**Table 10.7 Fatigue Test Results of AISI 4340 Steel**

$\sigma_a$ (MPa)	$N_f$ (cycles)
948	222
834	992
703	6004
631	14130
579	43860
524	132150

- (a) Plot these data on log-log coordinates. If this trend seems to represent a straight line, obtain rough values for the constants for  $A$  and  $B$  in an equation form of  $\sigma_a = AN_f^B$  from two widely separated points on a line drawn through the data.
- (b) Obtain refined values for  $A$  and  $B$  using a linear least-squares fit of  $\log N_f$  versus  $\log \sigma_a$ .
- 10.8.** What error occurs if the value of  $E_a$  rather than  $E$  is used to describe the energy absorbing capability of a beam? The beam is completely fractured and the ratio of final to initial velocity is 0.8.
- 10.9.** What are the advantages using the fatigue life diagram developed by Talreja rather than using the conventional  $S-N$  fatigue diagram?
- 10.10.** Explain why a laminate that contains alternate layers of  $\pm 5^\circ$  fibers has a higher fatigue strength than a  $0^\circ$  laminate, using the fatigue life diagram developed by Talreja.

### References

- Adams, D. F., and Miller, A. K. 1975 "An Analysis of the Impact Behavior of Hybrid Composite Materials," *Material Science and Engineering*, Vol. 19, pp. 245–260.
- Agarwal, B. D., and Broutman, L. J. 1990 *Analysis and Performance of Fiber Composites*, 2nd ed., John Wiley & Sons, New York.
- Anderson, T. L. 1995 *Fracture Mechanics, Fundamentals and Applications*, 2nd ed., CRC Press, Boca Raton, Fl.
- Bader, M. G., and Ellis, R. M. 1975 "The Effect of Notches and Specimen Geometry on the Pendulum Impact Strength of Uni-axial CFRP," *Composites*, Vol. 6, pp. 253–258.

- Boller, K. H. 1964 "Fatigue Characteristics of RP Laminates Subjected to Axial Loading," *Modern Plastics*, Vol. 45, p.145.
- Broutman, L. J., and Mallick, P. K. 1974 *Impact Behavior of Hybrid Composites*, AFSOR TR-75-0472.
- Browning, C. E. 1972 *The Effects of Moisture on the Properties of High Performance Structural Resins and Composites*, Technical Report, AFML-TR-72-94, Materials Laboratory, Wright-Patterson AFB, May.
- Browning, C. E., Husman, G. E., and Whitney, J. M. 1977 "Moisture Effects in Epoxy Matrix Composites," in *Composite Materials: Testing and Design*, ASTM STP 617, Philadelphia, pp. 481-496.
- Cheon, S. S., Lee, D. G., and Jeong, K. S. 1997 "Composite Side-Door Impact Beams for Passenger Cars," *Composite Structures*, Vol. 38, pp. 229-239.
- Curtis, P. T. 1988 "Fatigue of Organic Matrix Composite," in *Advanced Composites*, Edited by Partridge, I., Elsevier, New York, pp. 331-368.
- Curtis, P. T. 2000 "Durability Testing of Polymer Composites," in *Comprehensive Composite Materials*, Vol. 5, Elsevier, Oxford, pp. 163-182.
- Curtis, P. T., and Dorey, G. 1986 "Fatigue of Composite Materials," in *Proceedings of International Conference on Fatigue of Structural Materials and Structures*, Mechanical Engineering Publications, London, p. 297.
- Davis, J. W., MacCarthy, J. A., and Schurb, J. N. 1975 "The Fatigue Resistance of Reinforced Plastics," *Materials Design Engineering*, pp. 87-91.
- Dorey, G. 1980 "Relationships Between Impact Resistance and Fracture Toughness in Advanced Composite Materials," *Proceedings of AGARD Conference, Effect of Service Environment on Composite Materials*, AGARD-CP-288, pp. 1-9.
- Dowling, N. E. 1999 *Mechanical Behavior of Materials*, 2nd ed., Prentice-Hall, Upper Saddle River, N.J.
- Eckold, G. 1994 *Design and Manufacture of Composite Structures*, Woodhead Publishing, Cambridge, England.
- Fujczak, B. R. 1974 *U. S. Army Armament Command*, Report No. WVT-TR-74006.
- Greszczuk, L. B. 1982 "Damage in Composite Materials due to Low Velocity Impact," in *Impact Dynamics*, Edited by Zukas, J. A., et al., John Wiley & Sons, New York, pp. 55-94.
- Jang, B. Z. 1994 *Advanced Polymer Composites*, ASM International, Materials Park, Ohio.
- Kim, R. Y. 1989 "Fatigue behavior," in *Composite Design*, Edited by Tsai, S. W., Technomic Publishing, Philadelphia, Chapter 19, pp. 19.1-19.34.
- Lee, D. G., and Cheon, S. S. 2001 "Impact Characteristics of Glass Fiber Composites with Respect to Fiber Volume Fraction," *Journal of Composite Materials*, Vol. 35, No. 1, pp. 27-55.
- Lee, D. G., Lim, T. S., and Cheon, S. S. 2000 "Impact Energy Absorption Characteristics of Composite Structures," *Composite Structures*, Vol. 50, pp. 381-390.
- Liaw, P. K. 2000 "Impact Toughness Testing and Fracture Mechanics," in *ASM Handbook of Mechanical Testing and Evaluation*, Vol. 8, ASM International, Materials Park, Ohio, pp. 596-611.
- Mall, S. 1997 "Laminated Polymer Matrix Composites," in *Composites Engineering Handbook*, Edited by Mallick, P. K., Marcel Dekker, New York, pp. 811-892.
- Mallick, P. K. 1988 *Fiber-Reinforced Composites*, Marcel Dekker, New York.
- Meyers, M. N. 1994 *Dynamic Behavior of Materials*, John Wiley & Sons, New York.
- Miner, L. H., Wolfe, R. A., and Zweben, C. H. 1975 "Fatigue, Creep, and Impact Resistance of Aramid Fiber Reinforced Composites," in *Composite Reliability*, ASTM STP 580, Philadelphia, pp. 549-559.
- Niu, M. C. Y. 1992 *Composite Airframe Structures*, Hong Kong Comilit Press, Hong Kong.
- Owen, M. J., and Morris, S. 1971 *Carbon Fibers: Their Composites and Applications*, Plastics Institute, London.
- Owen, M. J., and Morris, S. 1972 "Some Interlaminar-Shear Fatigue Properties of Carbon Fiber Reinforced Plastics," *Plastics and Polymers*, Vol. 4, p. 209.

- Pipes, R. B. 1974 "Interlaminar Shear Fatigue Characteristics of Fiber-Reinforced Composite Materials," in *Composite Materials: Testing and Design*, ASTM STP 546, Philadelphia, pp. 419–430.
- Ramain, S. V., and Williams, D. P. 1976 *Failure Modes in Composites III*, AIME, New York.
- Reifsneider, K. L. 1990 *Damage and Damage Mechanics in Fatigue of Composite Materials*, Elsevier, New York, pp. 11–77.
- Rosen, W. B., and Hashin, Z. 1987 "Analysis of Material Properties," in *Engineered Materials Handbook*, Vol. I, *Composites*, ASM International, Materials Park, Ohio, pp. 185–205.
- Shigley, J. E., Mischke, C. R. and Budynas R. G. 2004 *Mechanical Engineering Design*, 7th ed., McGraw-Hill, New York.
- Sierakowski, R. L., and Newaz, G. M. 1995 *Damage Tolerance in Advanced Composites*, Technomic Publishing, Philadelphia.
- Stinchcomb, W. W., and Bakis, C. E. 1990 "Fatigue Behavior of Composite Laminates," in *Fatigue of Composite Materials*, Edited by Reifsneider, K. L., Elsevier, New York, pp. 105–180.
- Stinchcomb, W. W., and Reifsneider, K. L. 1988 "The Life-Limiting Process in Composite Laminates," in *Basic Questions in Fatigue Design*, Vol. II, ASTM STP 924, Edited by Wei, R. P., and Gangloff, R. P., Philadelphia, pp. 294–303.
- Talreja, R. 2000 "Fatigue of Polymer Matrix Composites," in *Comprehensive Composite Materials*, Vol. 2, Elsevier, Amsterdam, pp. 529–552.
- Timoshenko, S. P., and Goodier, J. N. 1970 *Theory of Elasticity*, 3rd ed., McGraw-Hill, New York.
- Yeung, P., and Broutman, L. J. 1978 "The Effect of Glass-Resin Interface Strength on the Impact Strength of Fiber Reinforced Plastics," *Polymer Engineering and Science*, Vol. 18, pp. 62–72.
- Young, W. C. 1989 *Roark's Formulas for Stress and Strain*, McGraw-Hill, New York.

## Part II

# APPLICATIONS

# 11

## Fundamentals of Axiomatic Design

### 11.1 Introduction

In chapter 1, a brief introduction to axiomatic design was given. This chapter presents a more comprehensive description of axiomatic design using many examples. Axiomatic design has been used in designing a variety of different things: machines, software, organizations, systems, materials, manufacturing, complicated large systems and processes, and a variety of mechanical/electrical products. The purpose of this chapter is to provide a broad overview, which should help in understanding the materials presented in chapters 12–15.

### 11.2 Current State of Design Practice

The “project of the first decade of the 21st century” may be the development of the Orbital Space Plane (OSP) of the U.S. National Aeronautics and Space Agency (NASA). It is currently being designed to transport people and cargo from earth to the International Space Station (ISS) beginning in 2010. The OSP must be safe and robust, and satisfy all the functional requirements (FRs) of the mission. It must be developed in a relatively short period of time at a fraction of the cost that was incurred when NASA developed the Space Shuttle three decades ago. It must be able to perform its missions without extensive maintenance so as to eliminate the need to rebuild the vehicle each time it returns from its mission. (The current Space Shuttle requires 6 months of “maintenance” at a cost of over \$350 million after each mission.)

It is increasingly becoming apparent to NASA and a major aerospace company that the OSP cannot be designed and developed using the old paradigm. The old paradigm was an experience-based development process with repetitive “design-build-test” cycles repeated until the product no longer breaks down. The old paradigm of product development is not only expensive, but produces products that are unreliable and hard to maintain. An aeronautics company is now applying axiomatic design in designing the OSP to reduce the time for development, lower the cost of development, and increase reliability, safety and maintainability, and robustness of the OSP. Axiomatic design is a rational way of developing a complicated system that satisfies FRs and constraints at low cost and on time.

A more complete treatise on axiomatic design is given in Suh, *Axiomatic Design: Advances and Application* (Oxford University Press, 2001). The material presented in this chapter is adopted from chapter 1 of the book.

At MIT, four inexperienced new graduate students designed and built a complicated chemical mechanical planarization (CMP) machine that polishes the surface of silicon wafers with various circuit patterns to nanoscale flatness. They designed and built the machine, which consists of hardware and software, in 2 years, at a fraction of the cost that an industrial firm might have incurred in developing a similar machine. The CMP machine worked the way it was intended to work when they turned on the machine for the first time. The CMP machine these students built—literally with their own hands—performed better than existing commercial machines. They used axiomatic design as the general framework for design of hardware and software.

A commercial software system called Acclaro that has more than 1000 FRs was developed by one software designer in just 6 months (4 months for design and 2 months for actual coding). The Acclaro software program also worked without need for major debugging. The software designer/programmer used an axiomatic design approach to software development.

Both the CMP machine and Acclaro software were successfully developed in a short period of time at a fraction of typical development cost, because these inexperienced engineers did not make mistakes.

In most companies, design decisions are made based on experience rather than using a systematic methodology. When they design, they do so based on their experience. They initially make a “prototype” machine and then find out all the mistakes made by testing it, with the idea that they will keep improving it until it works. This old paradigm served mankind well, but we should abandon it nevertheless. It is unreliable, costly, and not safe. Many publicized failures may be traced to design mistakes due to empirical and trial-and-error processes of design. One of the biggest challenges of the design field is to change the design field as a subject in the arts into arts and sciences.

### 11.3 What Is Design?

Design has been defined in a variety of ways, depending on the specific context and/or the field of interest. Designers of composite parts design the shape of the part, considering the properties of composite materials and available fabrication techniques. Mechanical engineers often design products, and therefore when they say *design*, they typically refer to product design. Manufacturing engineers, on the other hand, think of design in terms of new manufacturing processes and systems (i.e., factories and manufacturing cells). To electrical engineers, design means developing analog or digital circuits, communication systems, and computer hardware, while system architects perceive design in terms of technical or organizational systems where many parts must work together to yield a system that achieves the intended goals. Although some software engineers think that their primary job is to write computer code, it is difficult for them to produce good software unless they first design the architecture of the software. Business managers design organizational goals.

All of these are design activities. What is common in all these activities is that the designers must:

1. Know or understand their *customers' needs*.
2. Define the problem they must solve to satisfy the needs.

3. *Conceptualize the solution through synthesis.*
4. *Perform analysis to optimize the proposed solution.*
5. *Check the resulting design solution to see if it meets the original customer needs.*

### 11.3.1 Definition of Design

Design is interplay between *what* we want to achieve and *how* we want to achieve it. This interplay (or mapping) is illustrated in figure 11.1. Therefore, a rigorous design approach must begin with an explicit statement of “*what* we want to achieve” and end with a clear description of “*how* we will achieve it.” Once we understand the customer’s needs, this understanding must be transformed into a minimum set of specifications, which will be defined later as functional requirements (FRs), that describe “*what* we want to achieve” to satisfy the customers’ needs. The descriptor of “*how* to achieve it” may be in the form of design parameters (DPs).

Often designers do not state “*what* we want to achieve” explicitly. Many designers deliberately leave their design goals implicit and then start working on design solutions even before they have clearly defined their design goals. They measure their success by comparing their design with the implicit design goals that they had in mind, which may or may not be what the customer wanted. They spend a great deal of time improving and iterating the design until the design solution and “*what* they had in mind” converge.

To be efficient and to generate the design that meets the perceived needs, the designer must specifically state the design goals in terms of “*what* we want to achieve” and begin the design process. Iterations between “*what*” and “*how*” are necessary, but each iteration loop must redefine the “*what*” clearly.

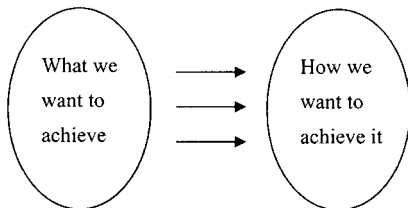


**Figure 11.1** A definition of design as a mapping between “*what* we want to achieve” and “*how* we want to achieve it.”

### EXAMPLE 11.1 REFRIGERATOR DOOR DESIGN

Consider the refrigerator door design shown in figure 11.2. Is it a good design? Each time this question is asked, we get many different kinds of answers. Some say the door is not a good design because it is inconvenient for people who are left handed. Some say it is a good design. However, the question posed cannot be answered without asking: What are the design goals (i.e., functional requirements) for the door design?

#### Solution

If the purpose of the door is to provide access to what is inside the refrigerator, then the door performs that function. Therefore, the door design is a good design. On the other hand, if the functional requirements of the door are to (1) provide access to the food in the refrigerator and (2) minimize energy

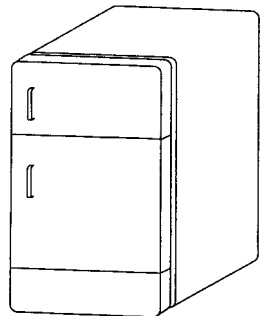


**Figure 11.2** Vertically hung refrigerator door.

consumption, then the door is a poor design because each time the door is opened, cold air inside the refrigerator is replaced by warm outside air, thus wasting energy. The door should have been designed differently to satisfy these two functional requirements. Consider some alternative designs given the two FRs stated above.

The important lesson of the above example is that you must think in terms of *functions* that the product (or software, system, process, or organization) must perform. It is necessary to learn to think *functionally* in designing products, processes, software, organizations, business plans, and policies.

In the past, many engineers have designed their products (or processes, systems, etc.) iteratively, empirically, and intuitively, based on years of experience, cleverness, or creativity, and involving much trial and error. Although experience is important because it generates knowledge and information about practical design, experiential knowledge alone is not sufficient, as it is not always reliable, especially when the context of the application changes. Experience must be augmented by systematic knowledge of design, or vice versa.

The field of design must be science based through generalizing, codifying, and systematizing so that engineers/designers can be taught to be good designers. Such codified and generalized knowledge shortens the lead time for developing good design solutions by allowing correct decisions to be made quickly and the first time around. A purpose of axiomatic design is to provide the science base to augment the designer's experience by providing the underlying principles, theories, and methodologies so that they can fully utilize their creativity.

Sometimes people equate design with "creativity" as if to imply that design cannot be done systematically. The word "creativity" has been used to describe the human activity that results in ingenious, unpredictable, or unforeseen results. In this context, creative "solutions" are discovered or derived by inspiration and/or perspiration, often without ever defining specifically what one sets out to create. This creative "spark" or "revelation" occurs because the brain is a huge information storage and processing device that can store data and synthesize solutions through the use of associative memory, pattern recognition, digestion, and recombination of diverse facts, and permutations of events. However, to think that design must rely on creativity alone is a mistake.

Sometimes the word "creativity" has been used in a mysterious sense, when we do not understand the process or the logic involved in a given intellectual endeavor (e.g., arts and music), and yet the result of the effort is intellectually, emotionally, or aesthetically appealing and acceptable. A subject is always mysterious when it relies

on an implicit thought process that cannot be stated explicitly and explained for others to understand, and that can be learned only through experience, apprenticeship, or trial and error. Design has been treated as one of these mysteries, which has delayed the development of design as a science.

Design will always benefit when inspiration, creativity, and imagination play a role, but we must augment this process by understanding the nature of the human mind and by the development of basic knowledge. Design must become a principle-based subject. The subject of design should attain the same level of intellectual understanding that fields such as thermodynamics and mechanics enjoy. Knowledge from design and other fields should converge and form a continuum of knowledge, rather than remaining as the disparate islands of knowledge that characterize the current situation. Indeed, understanding the design process is one of the most challenging of intellectual quests. The real beneficiaries of structured design knowledge will be humankind, society, industry, and the world.

Design is different from other disciplines, such as thermodynamics and mechanics, in that it deals with synthesis, whereas other disciplines often deal with analysis. Design is the opposite of reductionism of science, which reduces a natural phenomenon to a small entity that can be analyzed. Design deals with many FRs that must be satisfied at the same time.

## 11.4 Ultimate Goal of Axiomatic Design

The ultimate goal of axiomatic design is to establish a scientific basis for design and to improve design activities by providing the designer with a theoretical foundation based on logical and rational thought processes and tools. The goal of axiomatic design is manifold: to make human designers more creative, to reduce the random search process, to minimize the iterative trial-and-error process, to determine the best designs among those proposed, to be able to design and represent complex systems such as the Orbital Space Plane logically and explicitly, and to endow the computer with creative power through the creation of a scientific base for the design field.

In addition to the intellectual reasons given for developing the scientific basis for design, there are also practical reasons. The current design process is both resource intensive and ineffective. Industrial competitiveness demands that industrial firms have strong technical capability in design. These firms are under pressure to shorten the lead time for the introduction of new products, lower their manufacturing cost, improve the quality and reliability of their products, and satisfy the required functions most effectively. The greatest impact on all of these industrial needs rests on the quality and timeliness of developing design solutions. To achieve these practical goals, we must augment the essential ingredients of outstanding designers—knowledge, imagination, experience, and hard work—with science.

## 11.5 Axiomatic Design Framework

### 11.5.1 The Concept of Domains

*The design world consists of four domains.* As discussed in chapter 1, design involves interplay between “what we want to achieve” and “how we choose to satisfy the need (i.e., the what).” To systematize the thought process involved in this interplay,

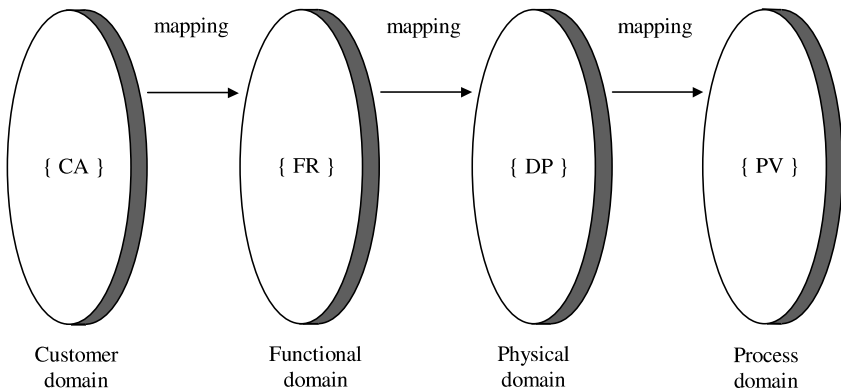


**Figure 11.3** Four domains of the design world: The {x} are the characteristic vectors of each domain. During the design process we go from the domain on the left to the domain on the right. The process is iterative in the sense that the designer can go back to the domain on the left based on the ideas generated in the right domain.

the concept of *domains* that create demarcation lines between four different kinds of design activities provides an important foundation of axiomatic design.

The world of design is made up of four domains: the *customer domain*, the *functional domain*, the *physical domain*, and the *process domain*. The domain structure is illustrated schematically in figure 11.3. The domain on the left relative to the domain on the right represents “what we want to achieve,” whereas the domain on the right represents the design solution, “how we propose to satisfy the requirements specified in the left domain.”

The *customer domain* is characterized by the needs (or attributes) that the customer is looking for in a product or process or system or materials. In the *functional domain*, the customer needs are specified in terms of *functional requirements* (FRs) and *constraints*. To satisfy the specified FRs, we conceive *design parameters* (DPs) in the *physical domain*. Finally, to produce the product specified in terms of DPs, we develop a process that is characterized by *process variables* (PVs) in the *process domain*.

Suppose that an aircraft manufacturer wishes to reduce the weight of the tail fin of a large commercial airliner. The customer wants to be sure that the tail can perform reliably under all operating conditions for the life of the airplane. All of these things are done in the customer domain. The first thing the designer (or the design team) has to do is to develop a set of FRs after careful consideration of the operating conditions, loads, and so on. They will also have to state constraints such as cost. They should establish these FRs without thinking about DPs—define FRs in a solution neutral environment. If they think about DPs first, they will simply come up with FRs that will generate the same DPs. After the FRs are defined in the functional domain, the next task is to conceive physical artifacts in the physical domain with specific DPs that can satisfy the FRs. This mapping from the FRs to DPs is the “product” design. Then, we may go to the process domain to come up with a manufacturing process in the case of product design. The PVs are selected to satisfy the DPs.

In mechanical engineering we usually think of design in terms of product design and often hardware design. In materials science and engineering, the design goal is to develop materials with certain properties (i.e., FRs). This is done through the design

of microstructures (i.e., DPs) to satisfy these FRs, and through the development of material processing methods (i.e., PVs) to create the desired microstructures. Engineers also deal with other equally important designs, such as software, manufacturing processes, systems, and even organizations. All designers go through similar thought processes regardless of the specific goal of their effort.

### 11.5.2 Definitions

In axiomatic design, the definition of key words is extremely important. Design axioms are valid only within the bounds established by the definitions of these key terms. Just as the words *heat* and *work* have unique meanings in thermodynamics, which are different from those of their daily usage, so is the case with key words used in axiomatic design.

The definitions are as follows:

*Axiom*: Self-evident truth or fundamental truth for which there are no counterexamples or exceptions. An axiom cannot be derived from other laws or principles of nature.

*Corollary*: Inference derived from axioms or from propositions that follow from axioms or from other propositions that have been proven.

*Theorem*: A proposition that is not self-evident but that can be proved from accepted premises or axioms and so is established as a law or principle.

*Functional requirements (FRs)*: A minimum set of independent requirements that completely characterizes the functional needs of the product (or software, organizations, systems, etc.) in the functional domain. By definition, each FR is independent of every other FR at the time the FRs are established.

*Constraints*: Bounds on acceptable solutions. There are two kinds of constraints: *input* constraints and *system* constraints. Input constraints are imposed as part of the design specifications. System constraints are constraints imposed by the system in which the design solution must function.

*Design parameters (DPs)*: Key physical variables (or other equivalent terms in the case of software design, etc.) in the physical domain that characterize the design that satisfies the specified FRs.

*Process variables (PVs)*: Key variables (or other equivalent term in the case of software design, etc.) in the process domain that characterize the process that can generate the specified DPs.

Most of the key words listed are associated with the independence axiom, discussed below. Additional definitions of key words associated with the information axiom will be given in a later section.

### 11.5.3 Mapping and Axioms

The customer needs or attributes (CAs) desired in a product are sometimes difficult to define or are vaguely defined. Nevertheless we have to do the best we can to understand the customer needs by working with customers to define them. It should be re-emphasized here that the FRs must be defined in a *solution-neutral environment*.

During the mapping process (e.g., going from the functional domain to the physical domain), we must make the right design decisions using the independence axiom. When several designs that satisfy the independence axiom are available, the information axiom can be used to select the best design. When only one FR is to be satisfied by having an acceptable DP, the independence axiom is always satisfied and the information axiom is the only axiom the one-FR design must satisfy.

*So what are the design axioms? How many design axioms are there?* The basic postulate of the axiomatic approach to design is that there are fundamental axioms that govern the design process. Two axioms were identified by examining the common elements that are always present in good designs. They were also identified by examining actions taken during the design stage that resulted in dramatic improvements.

The first axiom is called the *independence axiom*. It states that the independence of FRs must always be maintained, where FRs are defined as *the minimum set of independent requirements* that characterizes the design goals. In other words, since FRs are independent when they are first stated by definition, the design must be such that they remain independent of each other.

The second axiom is called the *information axiom*, and it states that among those designs that satisfy the independence axiom, the design that has the smallest information content is the best design. When the information content is greater than zero, information must be supplied to satisfy the FRs at all times. Because the information content is defined in terms of probability, the second axiom also states that the design that has the highest probability of success is the best design. Based on these design axioms, we can derive theorems and corollaries.

The axioms are formally stated as:

*Axiom 1: The independence axiom*

Maintain the independence of the FRs.

*Axiom 2: The information axiom*

Minimize the information content of the design.

The performance, robustness, reliability, and functionality of products and processes are significantly improved when these axioms are satisfied. Conversely, design axioms can be used to analyze why machines and processes are not working well and to solve the problems by coming up with alternate designs.

#### 11.5.4 The First Axiom: The Independence Axiom

As stated earlier, the FRs are defined as the minimum set of independent requirements that the design must satisfy. A set of FRs is the description of design goals. The independence axiom states that when there are two or more FRs, the design solution must be such that each one of the FRs can be satisfied without affecting the other FRs. That means we have to choose a correct set of DPs to be able to satisfy the FRs and maintain their independence.

The independence axiom is often misunderstood. Many people confuse functional independence with physical independence. The independence axiom requires that the *functions* of the design be independent of each other, not the physical parts. The second axiom suggests that physical integration is desirable to reduce the information content if the functional independence can be maintained. This is illustrated using the beverage can as an example.

**EXAMPLE 11.2 BEVERAGE CAN DESIGN**

Consider an aluminum beverage can that contains carbonated drinks. How many FRs must the can satisfy? How many physical parts does it have? What are the DPs? How many DPs are there?

**Solution**

According to an expert working at one aluminum can manufacturer, there are 12 FRs for the can. Plausible FRs: contain axial and radial pressure, withstand a moderate impact when the can is dropped from a certain height, allow stacking on top of each other, provide easy access to the liquid in the can, minimize the use of aluminum, be printable on the surface, and others. However, these 12 FRs are not satisfied by 12 physical pieces: the aluminum can consists of only three pieces: the body, the lid, and the opener tab (see figure 11.4). The independence axiom requires that the 12 FRs remain independent of one another by proper choice of DPs. The information axiom requires that the information content be a minimum, which can be done if the DPs can be integrated so that there will not be 12 physical pieces making up the can!

Where are the DPs? To satisfy the independence axiom, there must be at least 12 DPs. Most of the DPs are associated with the geometry of the can: the thickness of the can body, the curvature at the bottom of the can, the smaller diameter of the can at the top to reduce the material used to make the top lid, the corrugated geometry of the opening tab to increase the stiffness, the small extrusion on the lid to attach the tab, and so on.

The aluminum can has 12 DPs integrated in three physical pieces and satisfies the independence axiom.

After the FRs are established, the next step in the design process is the conceptualization process, which occurs during the mapping process going from the functional domain to the physical domain.

To go from “what” to “how” (from the functional domain to the physical domain) requires *mapping*, which involves creative conceptual work. After the overall design concept is generated by mapping, we must identify the DPs and complete the mapping process. During this process, we must think of all the different ways of fulfilling each of the FRs by identifying plausible DPs. Sometimes it is convenient to

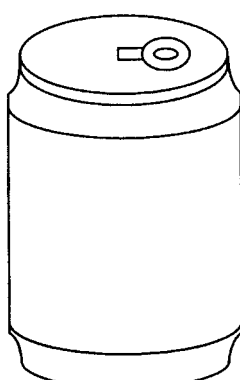


**Figure 11.4** Beverage can.

think about a specific DP to satisfy a specific FR, repeating the process until the design is completed. To conceive the design concept, databases of all kinds and all available methods may be used: brainstorming, morphological techniques, analogy from other examples, extrapolation and interpolation, laws of nature, order-of-magnitude analysis, and reverse engineering. It is relatively easy to identify a DP for a given FR but when there are many FRs that we must satisfy, the design task becomes difficult and many designers make mistakes by violating the independence axiom.

The mapping process between the domains can be expressed mathematically in terms of the characteristic vectors that define the design goals and design solutions. At a given level of the design hierarchy, the set of FRs that defines the specific design goals constitutes the FR vector in the functional domain. Similarly, the set of design parameters in the physical domain that has been chosen to satisfy the FRs constitutes the DP vector. The relationship between these two vectors can be written as

$$\{\text{FR}\} = [A]\{\text{DP}\} \quad (11.1)$$

where  $[A]$  is called the *design matrix* that characterizes the *product design*. Equation (11.1) is a design equation for the design of a product. The design matrix is of the following form for a design that has three FRs and three DPs:

$$[A] = \begin{bmatrix} A_{11} & A_{12} & A_{13} \\ A_{21} & A_{22} & A_{23} \\ A_{31} & A_{32} & A_{33} \end{bmatrix} \quad (11.2)$$

When equation (11.1) is written in a differential form as

$$\{d\text{FR}\} = [A]\{d\text{DP}\}$$

the elements of the design matrix are given by

$$A_{ij} = \partial\text{FR}_i / \partial\text{DP}_j$$

With three FRs and three DPs, equation (11.1) may be written in terms of its elements as

$$\text{FR}_i = \sum_{j=1}^3 A_{ij}\text{DP}_j$$

or

$$\begin{aligned} \text{FR}_1 &= A_{11}\text{DP}_1 + A_{12}\text{DP}_2 + A_{13}\text{DP}_3 \\ \text{FR}_2 &= A_{21}\text{DP}_1 + A_{22}\text{DP}_2 + A_{23}\text{DP}_3 \\ \text{FR}_3 &= A_{31}\text{DP}_1 + A_{32}\text{DP}_2 + A_{33}\text{DP}_3 \end{aligned} \quad (11.3)$$

In general,

$$\text{FR}_i = \sum_{j=1}^n A_{ij}\text{DP}_j$$

where  $n$  = the number of DPs.

For a linear design,  $A_{ij}$  are constants; for a nonlinear design,  $A_{ij}$  are functions of the DPs. There are two special cases of the design matrix: the diagonal matrix and the triangular matrix. In the diagonal matrix, all  $A_{ij}=0$  except those where  $i=j$ :

$$[A] = \begin{bmatrix} A_{11} & 0 & 0 \\ 0 & A_{22} & 0 \\ 0 & 0 & A_{33} \end{bmatrix} \quad (11.4)$$

In the lower triangular (LT) matrix, all upper triangular elements are equal to zero:

$$[A] = \begin{bmatrix} A_{11} & 0 & 0 \\ A_{21} & A_{22} & 0 \\ A_{31} & A_{32} & A_{33} \end{bmatrix} \quad (11.5)$$

In the upper triangular (UT) matrix, all lower triangular elements are equal to zero.

For the design of processes involving mapping from the DP vector in the physical domain to the PV vector in the process domain, the design equation may be written as

$$\{\text{DP}\} = [B]\{\text{PV}\} \quad (11.6)$$

where  $[B]$  is the design matrix that defines the characteristics of the *process design* and is similar in form to  $[A]$ .

To satisfy the independence axiom, the design matrix must be either diagonal or triangular. When the design matrix  $[A]$  is diagonal, each of the FRs can be satisfied independently by means of one DP. Such a design is called an *uncoupled* design. When the matrix is triangular, the independence of FRs can be guaranteed if and only if the DPs are determined in a proper sequence. Such a design is called a *decoupled* design. Any other form of the design matrix is called a full matrix and results in a *coupled* design. Therefore, when several FRs must be satisfied, we must develop designs that will enable us to create either a diagonal or a triangular design matrix.

### EXAMPLE 11.3 DESIGN MATRIX FOR REFRIGERATOR DOOR

Reconsider the refrigerator door design discussed in example 11.1. The FRs of the door are

$\text{FR}_1$  = Provide access to the items stored in the refrigerator

$\text{FR}_2$  = Minimize energy loss.

Determine the DPs and the design matrix. Show whether the design is uncoupled, decoupled, or coupled.

#### Solution

The DPs are chosen as

$\text{DP}_1$  = Vertically hung door

$\text{DP}_2$  = Thermal insulation material in the door.

The design matrix may be stated as

$$\begin{Bmatrix} FR_1 \\ FR_2 \end{Bmatrix} = \begin{bmatrix} X & 0 \\ X & X \end{bmatrix} \begin{Bmatrix} DP_1 \\ DP_2 \end{Bmatrix}$$

The door design is a decoupled design. Unfortunately, it is still not a good design because the thermal insulation (typically polyurethane foam with Freon) put in the door cannot compensate for the cold air that escapes the refrigerator whenever the door is opened.

One solution is to make a horizontally hung door like those found in chest freezers. In this case, the cold air stays inside when door is opened. The design matrix would then provide an uncoupled design:

$$\begin{Bmatrix} FR_1 \\ FR_2 \end{Bmatrix} = \begin{bmatrix} X & 0 \\ 0 & X \end{bmatrix} \begin{Bmatrix} DP_1 \\ DP_2 \end{Bmatrix}$$

The elements of the design matrices  $[A]$  and  $[B]$  can be either constants or functions. If the matrix elements are constants, the design is linear. If the elements are functions of DPs, the design may be nonlinear.

The design matrix is a second-order tensor, just as stress, strain, and moment of inertia are. However, there is one big difference between the design matrix and these other second-order tensors. These other tensors can be changed through coordinate transformation to convert any matrix into a diagonal matrix. The diagonal elements of the diagonal matrix are invariant, such as the principal stresses in the case of a stress tensor. However, the coordinate transformation technique cannot be applied to design equations to find the invariant (i.e., the diagonal) matrix, as the design matrix  $[A]$  typically involves physical properties that are not amenable to coordinate transformation.

Furthermore, when the matrix is a full matrix producing a coupled design, we may get a unique solution that gives the right values for FRs, but such a design generates many problems. For example, when one of the FRs is changed, all DPs must be changed. Also whenever the DPs are not exact and deviate from the desired (or set) values, the FRs may not be satisfied. Because most manufacturing processes cannot make exactly identical parts, the system or product may be individually tuned or calibrated. Also in situations in which all the elements of the design matrix cannot be precisely specified, FRs cannot be determined. Furthermore, if one of the DPs changes during the life of the product or process (say by wear), then the machine must be discarded unless all other DPs are changed accordingly.

The design goals are often subject to constraints. Constraints provide bounds on the acceptable design solutions and differ from the FRs in that they do not have to be independent.

There are two kinds of constraints: *input* constraints and *system* constraints. Input constraints are specific to the overall design goals (i.e., all designs that are proposed must satisfy these). System constraints are specific to a given design; they are the result of design decisions made.

The designer often has to specify input constraints at the beginning of the design process, because the designed product (or process or system or software or organization) must satisfy external boundary conditions, such as the voltage and the maximum current of the power supply. The environment within which the design must

function may also impose many constraints. All of these constraints must be satisfied by all proposed design embodiments regardless of the specific details of the design.

Some constraints are generated because of the design decisions made as the design proceeds. All higher level decisions act as constraints at lower levels. For example, if we have chosen to use a diesel engine in a car, all subsequent decisions related to the vehicle must be compatible with this decision. These are system constraints.

Often it is best to treat cost as a constraint. Cost is affected by all design changes, and therefore cost cannot be made independent of other FRs in an uncoupled design. If it is decided that cost must be a functional requirement, then the best we can do is to develop a *decoupled design*, which also satisfies the independence axiom. With cost as a constraint, the design is acceptable as long as the cost does not exceed a set limit. When manufacturing cost and selling price of the product are not related, price can be treated as an FR.

The FRs and DPs (as well as PVs) must be decomposed into a hierarchy until we get a complete detailed design or until the design is completed. However, contrary to conventional wisdom on decomposition, they cannot be decomposed by remaining in one domain. One must zigzag between the domains to be able to decompose the FRs, DPs, and PVs. Through this zigzagging we create hierarchies for FRs, DPs, and PVs in each design domain.

Zigzagging to decompose FRs, DPs, and PVs and to create their hierarchies is an important part of axiomatic design. For example, when we wish to design a vehicle, the highest level FRs may be four:  $FR_1 = \text{go forward}$ ,  $FR_2 = \text{go backward}$ ,  $FR_3 = \text{stop}$ , and  $FR_4 = \text{turn}$ . We cannot decompose these FRs until we decide on DPs that can satisfy the FRs by going into the physical domain (i.e., “zigging”), After we decide how we are going to satisfy  $FR_1$  by choosing a  $DP_1$ , we can go back (i.e., “zag”) to the functional domain and decompose  $FR_1$ . For example,  $FR_1$  cannot be decomposed without deciding first in the physical domain “how we propose to go forward.” If we choose a horse and buggy as a DP for moving forward, the next layer of FRs will be different from those if an automobile is chosen as the DP for moving forward.

In other words, to create FR, DP, and PV hierarchies, we must map from the domain on the left (the “what” domain) into the domain on the right (the “how” domain), and then come back to the domain on the left to generate the next level in the domain on the right, and so on. The decomposition and the design hierarchies will be discussed further in section 11.5.7.

In many cases, the customer needs or attributes cannot and need not be decomposed, as they are often expressed in terms of the highest level needs. For instance, average customers do not care about the details of automobiles as long as they satisfy their perceived need for acceleration, steering, braking, traction on slippery roads, appearance, and overall comfort. However, in the future, more products must be customized to satisfy individual tastes and preferences. This can be done by zigzagging between the customer domain and the functional domain so that customers can choose their desired functions among those FRs available at the manufacturer’s factories.

### 11.5.5 Ideal Design, Redundant Design, and Coupled Design: A Matter of Relative Numbers of DPs and FRs

So far the discussion of the independence axiom has dealt with cases in which the number of FRs and the number of DPs were the same. The coupled design was

characterized by the existence of a full design matrix, whereas a diagonal matrix and a triangular matrix characterized the designs that satisfy the independence axiom (i.e., the uncoupled design and the decoupled design). The question addressed in this section is: What happens if the number of design parameters is more than or less than the number of functional requirements?

Depending on the relative numbers of DPs and FRs, the design can be classified as coupled, redundant, or ideal.

#### *CASE 1 Number of DPs < Number of FRs: Coupled Design*

When the number of DPs is less than the number of FRs, we always have a coupled design. This is stated as theorem 1 (see the appendix of this chapter for a full list of theorems):

#### **THEOREM 1 (COUPLING DUE TO INSUFFICIENT NUMBER OF DPs)**

When the number of DPs is less than the number of FRs, either a coupled design results or the FRs cannot be satisfied.

##### **Proof**

Suppose that there are three FRs to be satisfied and the designer has proposed a design with only two DPs. Then, the design equation may be written as

$$\begin{Bmatrix} \text{FR}_1 \\ \text{FR}_2 \\ \text{FR}_3 \end{Bmatrix} = \begin{bmatrix} X & 0 \\ 0 & X \\ A_{31} & A_{32} \end{bmatrix} \begin{Bmatrix} \text{DP}_1 \\ \text{DP}_2 \end{Bmatrix}$$

If  $A_{31}$  and  $A_{32}$  are zeros,  $\text{FR}_3$  cannot be satisfied. If either  $A_{31}$  or  $A_{32}$  is not zero, the design is a coupled design.

#### *CASE 2 Number of DPs > Number of FRs: Redundant Design*

When there are more DPs than FRs, the design is called a redundant design. A redundant design may or may not violate the independence axiom, as illustrated below. Consider the following two-dimensional case:

$$\begin{Bmatrix} \text{FR}_1 \\ \text{FR}_2 \end{Bmatrix} = \begin{bmatrix} A_{11} & 0 & A_{13} & A_{14} & A_{15} \\ A_{21} & A_{22} & 0 & A_{24} & 0 \end{bmatrix} \begin{Bmatrix} \text{DP}_1 \\ \text{DP}_2 \\ \text{DP}_3 \\ \text{DP}_4 \\ \text{DP}_5 \end{Bmatrix}$$

This design takes on various characteristics, depending on which design parameters are varied and which ones are fixed. If  $\text{DP}_1$  and  $\text{DP}_4$  are varied after all other DPs are fixed to control the values of FRs, the design is a coupled design. On the other hand, if we fix the values of  $\text{DP}_1$ ,  $\text{DP}_4$ , and  $\text{DP}_5$ , the design behaves like an uncoupled design. If  $\text{DP}_3$ ,  $\text{DP}_4$ , and  $\text{DP}_5$  are fixed, then the design is a decoupled

design. If  $DP_1$  and  $DP_4$  are set first, then the design behaves like an uncoupled redundant design. Theorem 3 states this fact:

### **THEOREM 3 (REDUNDANT DESIGN)**

When there are more DPs than FRs, the design is either a redundant design or a coupled design.

#### *CASE 3 Number of DPs = Number of FRs: Ideal Design*

When the number of FRs is equal to the number of DPs, the design is an ideal design, provided that the independence axiom is satisfied. This is stated as theorem 4:

### **THEOREM 4 (IDEAL DESIGN)**

In an ideal design, the number of DPs is equal to the number of FRs, and the FRs are always maintained independent of each other.

#### **Proof**

Theorem 1 showed that if the number of FRs is larger than the number of DPs, the design is coupled. Similarly, theorem 3 states that when there are more DPs than FRs, the design is either a redundant design or a coupled design. Therefore, the only way a design can satisfy the independence axiom at all times is when the number of FRs is equal to the number of DPs and the independence axiom is satisfied. Any design with an equal number of FRs and DPs and whose design matrix is either a diagonal or a triangular matrix always satisfies the independence axiom and thus is an ideal design. In such a design, coupling cannot occur.

Many other theorems and corollaries are presented in the appendix of this chapter. They may be used as design rules for specific cases.

#### **11.5.6 Example Involving Decoupling of Coupled Designs**

This example was motivated by a case study worked out by engineers of an aircraft company as part of their exercise in learning axiomatic design. The engineers at the aircraft company solved a long-standing problem, simplifying the manufacturing process and eliminating many problems associated with the original process.

The example illustrates the importance of the theorem for ideal design (theorem 4) in addition to showing how to develop a design concept for a given set of FRs.

### **EXAMPLE 11.4 SHAPING OF HYDRAULIC TUBES**

Tubes must be bent to complex shapes in many applications (e.g., aircraft) without changing the circular cross-sectional shape of the tube. This is a particularly difficult job when the tube is made of titanium. Titanium has a hexagonal close-packed (hcp) structure so that its mechanical properties are anisotropic, and it cannot be bent repeatedly because it will fracture.

When an aircraft company tried to bend titanium tubes into complex shapes, it found that the round cross-sectional shape could not be maintained. To prevent

this distortion of the cross-sectional shape, they created a special mandrel (i.e., a flexible wire with many thin spacer disks whose diameter was equal to the inside diameter of the tube). The spacer disks were symmetrically mounted on the wire through a hole at the center of the disks. This tool was inserted through the tube to be bent. It was difficult to remove the wire with disks from the tube after the bending operation, and the engineers found that the disks scratched the inner surface of the tube. So they applied a lubricant, which made the removal of the wire easier. However, this solution to the problem created an additional operation: they had to clean the lubricant from the inside of the tube with a solvent and then dispose of the solvent.

The engineer in charge of this project happened to take the axiomatic design course specially offered at his company. As part of his term project, he solved the tube-bending problem. The solution was so successful that the company made his solution proprietary to his company. Therefore, the solution presented here to illustrate the design procedure has been obtained independently without the benefit of the engineer's design (Suh, 1995).

To design a machine and a process that can achieve the task, the functional requirements can be formally stated as:

$FR_1 = \text{Bend a titanium tube to prescribed curvatures}$

$FR_2 = \text{Maintain the circular cross-section of the bent tube.}$

Theorem 4 (see the appendix of this chapter) states that in an ideal design, the number of DPs is equal to the number of FRs. To come up with an acceptable solution according to this theorem, we must look for a design with two DPs.

The mechanical concept that can do the job is schematically shown in figure 11.5 for a two-dimensional bending case.

It consists of a set of matching rollers with semicircular grooves on their periphery. These "bending" rollers can counterrotate at different speeds and move relative to each other to control the bending, as shown in figure 11.5. A second set of "feed" rollers, which counterrotate at the same speed, feed straight tube feedstock into the bending rollers. The centers of these two bending rollers are fixed with respect to each other and the contact point of the bending rollers can rotate about a fixed point. As the tubes are bent around the rollers, the

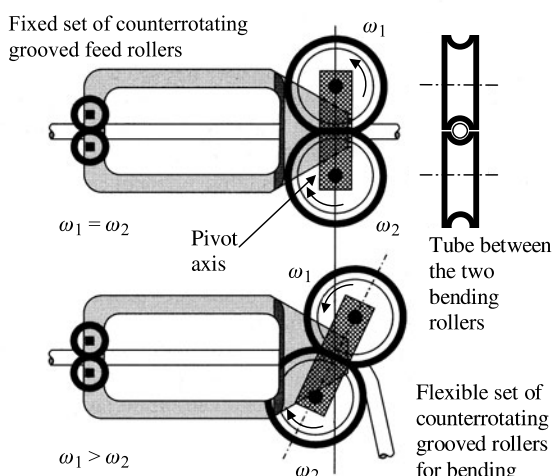


**Figure 11.5** Tube-bending apparatus.

cross-sectional shape will tend to change to a noncircular shape. The deformation of the cross section is prevented by the semicircular cam profile machined on the periphery of the bending rollers. (It may be necessary to make the groove profile slightly oval shaped at the top and bottom of the groove to prevent buckling on the compression side.)

The DPs for this design are

$DP_1$  = Differential rotation of the bending rollers to bend the tube

$DP_2$  = The profile of the grooves on the periphery of the bending rollers.

The kinematics of the roller motion needs to be determined. To bend the tube, one of the bending rollers must rotate faster than the other. In this case, the tube will be bent around the slower roller. The forward speed of the tube is determined by the average speed of the two bending rollers. The motion of these rollers can be controlled digitally using stepper motors.

The design is an uncoupled design because each of the DPs affects only one FR. Is this the best design? The only way this question can be answered is to develop alternate designs that satisfy the FRs and constraints and the independence axiom. Then we need to compute the information content of the proposed designs to select the best design among them.

If the design is acceptable so far, we need to decompose the FRs to form the next-level FRs (e.g.,  $FR_{11}$  and  $FR_{12}$  for  $FR_1$ , based on the chosen  $DP_1$ ) and then map them into the physical domain to determine the next-level DPs. This process can go on until the design is completed. However, it will not be done here. How would you decompose  $FR_1$  and  $DP_1$ ?

Another design solution that can achieve the desired goal might be to fill the tube with incompressible material, such as a low melting point metal that can be solidified in the tube before bending the tube. After bending, the metal can be molten and removed from the tube. Is this a better solution than the use of the grooved rollers?

The preceding example illustrates the power of theorem 4 (Ideal Design). From the beginning of the design process, we knew that we should seek only two DPs as there were only two FRs. This kind of discipline in the design process channeled the thought process. The redundant design originally used by the airplane company made the entire process unnecessarily complicated and probably more costly, in addition to creating secondary problems, such as the disposal of solvents.

### 11.5.7 Decomposition, Zigzagging, and Hierarchy

In the preceding example on tube bending, the design was terminated when we mapped from the functional domain to the physical domain at the highest level. The highest level conceptual design provided enough design information at the conceptual level that would bring a successful design when fully implemented. To complete the design of the tube-bending machine, however, detailed designs for the bending mechanism, groove shape, servocontrol, and so on, must be developed by decomposing the highest level FRs and DPs. This decomposition process must proceed layer by layer until the design reaches the final stage, creating a design that can be implemented. Through this decomposition process, we establish hierarchies of FRs, DPs, and PVs, which are a representation of the design architecture.

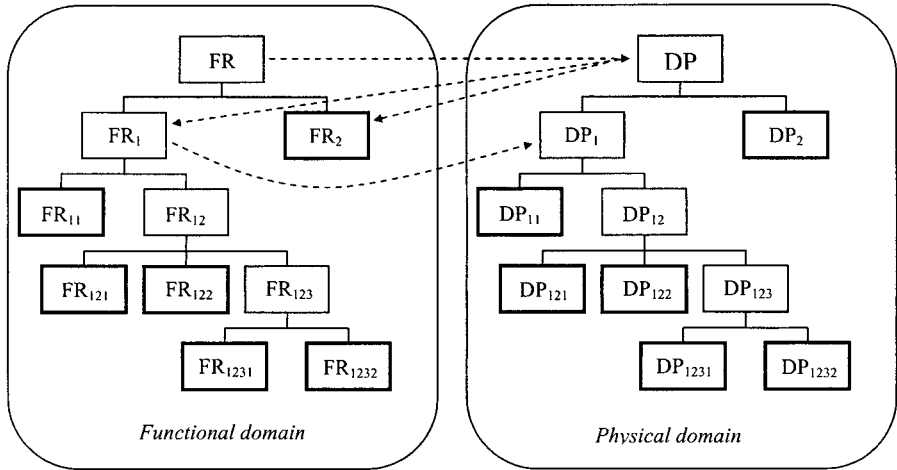


**Figure 11.6** Zigzagging to decompose FRs and DPs in the functional and the physical domains and to create the FR and DP hierarchies; Boxes with thick lines represent “leaves” that do not require further decomposition.

When the design details are missing at the highest level of design, the design equation represents the *design intent*. We must decompose the highest level design to develop design details that can be implemented. As we decompose the highest level design, the lower level design decisions must be consistent with the highest level design intent. When the independence axiom is violated by design decisions made, we should go back and redesign rather than proceed with a flawed design.

To decompose FR and DP characteristic vectors, we must zigzag between the domains. That is, we start out in the “what” domain and go to the “how” domain. This is illustrated in figure 11.6. From an FR in the functional domain, we go to the physical domain to conceptualize a design and determine its corresponding DP. Then we come back to the functional domain to create FR<sub>1</sub> and FR<sub>2</sub> at the next level that collectively satisfy the highest level FR. FR<sub>1</sub> and FR<sub>2</sub> are the FRs for the highest level DP. Then we go to the physical domain to find DP<sub>1</sub> and DP<sub>2</sub>, by conceptualizing a design at this level, which satisfy FR<sub>1</sub> and FR<sub>2</sub>, respectively. This process of decomposition is pursued until the FR can be satisfied without further decomposition when all of the branches reach their final state. The final states are indicated by thick-bordered boxes in figure 11.6, which are called “leaves.”

To be sure that we have made the right design decision, we must write down the design equation, {FRs} = [A]{DPs}, at each level of decomposition. For example, in the case shown in figure 11.6, after FR and DP are decomposed into FR<sub>1</sub>, FR<sub>2</sub>, DP<sub>1</sub>, and DP<sub>2</sub>, we must write down the design equation to indicate our design *intent* at this level. At this high level of the design process, we can only state our design intent, as we have not yet developed the lower level detailed designs. We know that the design must be either uncoupled or decoupled and, therefore, the intended design must have either a diagonal or a triangular matrix. Suppose that the designer wanted to have a decoupled design represented by the design equation

$$\begin{Bmatrix} \text{FR}_1 \\ \text{FR}_2 \end{Bmatrix} = \begin{bmatrix} X & 0 \\ X & X \end{bmatrix} \begin{Bmatrix} \text{DP}_1 \\ \text{DP}_2 \end{Bmatrix}$$

Because design details are unknown at this stage of the design process, the triangular matrix represents the *design intent*. All subsequent lower level design decisions must be consistent with this high-level design decision. The consistency of all lower level design decisions can be checked by constructing the full design matrix.

*Through the design decomposition process, the designer is transforming design intent into realizable design details.* At each level of decomposition, the design decisions made must be consistent with all higher level design decisions that were already made. That is, if the highest level design matrix is a diagonal matrix, all lower level decisions must not make—either intentionally or inadvertently—the off-diagonal elements of the highest level design matrix nonzero. To check this fidelity and consistency of design decisions, the full design matrix must be constructed by combining all lower design matrices into a single master matrix.

As a designer tries to develop detailed designs that do not violate the original design intent, the designer may find that existing technologies cannot be used. Then, the designer may develop a new technology that can achieve the original design goals. This process of recognizing the shortcomings of existing technologies and/or designs often leads to inventions and innovations. When a coupled design is replaced by an uncoupled or a decoupled design, major improvements can be made. These novel solutions often constitute inventions or innovations.

To decompose FRs and DPs, the designer must zigzag. For example, suppose you want to design a vehicle that satisfies the following four FRs: go forward, go backward, stop, and turn. We cannot decompose these FRs unless we first conceptualize DPs that can satisfy these highest level FRs. If we decide to use an electric motor as a DP to satisfy the FR of moving forward, the decomposed FRs at the next level would be quite different from those that would have resulted had we chosen gas turbines as the DP. Therefore, when we define the FRs in a solution-neutral environment, we have to “zig” to the physical domain, and after proper DPs are chosen, we have to “zag” to the functional domain for further decomposition. Organizations that have created a division for the specific task of specifying FRs at all levels without zigzagging between the domains will not get the results they are looking for and miss important opportunities for innovation.

If the design effort produces several designs that are acceptable in terms of the independence axiom, we will have to choose the best design among those proposed by invoking the information axiom. As explained extensively in a later section, the choice is made by comparing the design range with the system range. The design range is specified by the designer and the system range represents how well a given design (i.e., product or system) can meet the specified functional requirement. If there are several designs that satisfy the independence axiom, the best design is the one that has the lowest information content because it has the highest probability of success. But some may ask: What should be done if there is a coupled design that has smaller information content than an uncoupled design? Based on years of experience of creating designs or analyzing designs, we have not come across a situation in which a coupled design had lower information content than an uncoupled design. If there is such a case, one should go back and look for an uncoupled design that has a lower information content than the coupled design, as per theorem 18.

We could have come up with designs that have more DPs and FRs, thus inadvertently increasing the information content. As the number of decomposition layers and the number of DPs increase, the likelihood of increasing the information content increases. Many case studies that illustrate this point are given in Suh (1990).

To refine the design, we must model and analyze the proposed design whenever possible. In the preceding examples, the design matrix was formulated in terms of  $X$  and 0. In some cases, it may be sufficient to complete the design using simply  $X$  and 0. In many cases, we may take further steps to determine the precise values of design parameters. After the conceptual design is done in terms of  $X$  and 0, we need to model the design more precisely to replace the  $X$ s with equations or numbers. Through modeling, we can replace each  $X$  with either a constant or a function that involves the DP. We then have a set of equations that relate the FRs to the DPs. This set of equations can be solved separately for uncoupled designs or by following the sequence given by the design matrix for decoupled designs.

#### 11.5.8 Requirements for Concurrent Engineering

After or during the product design, we must be sure that the product can be manufactured. Therefore, after certain DPs are chosen, we have to map from the physical domain to the process domain (i.e., process design) by choosing the process variables (PVs). This mapping of process design must also satisfy the independence axiom. Sometimes we may simply use existing processes, and at other times we must invent new processes. When existing processes must be used to minimize capital investment in new equipment, the existing process variables must be used and thus they act as constraints in choosing DPs. In developing a product, both the product design and the process design (or selection) must be considered at the same time. This is sometimes called “concurrent engineering” or “simultaneous engineering.”

For concurrent engineering to be possible, both the product design represented by equation (11.1) and the process design represented by equation (11.6) must satisfy the independence axiom. This means that the product design matrix  $[A]$  and the process design matrix  $[B]$  both must be either diagonal or triangular so that the product of these matrices  $[C] = [A][B]$  will be diagonal or triangular.<sup>1</sup> (Each element is given by  $C_{ik} = \sum_j (A_{ij}B_{jk})$ .)

Table 11.1 shows the type of matrix  $[C]$  depending on the types of matrices  $[A]$  and  $[B]$ . For example, to get an uncoupled concurrent design, both matrices must be diagonal. If one is diagonal and the other is triangular, the resulting product of the matrices is triangular. If both  $[A]$  and  $[B]$  are triangular matrices, they must be

**Table 11.1 Type of the Concurrent Engineering Matrix  $[C]$**

Matrix type <sup>a</sup>	$[A]$	$[B]$	$[C] = [A][B]$
1. Both diagonal	[N]	[N]	[N]
2. Diagonal $\times$ full	[N]	[X]	[X]
3. Diagonal $\times$ triangular	[N]	[LT]	[LT]
4. Triangular $\times$ triangular	[LT]	[LT]	[LT]
5. Triangular $\times$ triangular	[LT]	[UT]	[X]
6. Full $\times$ full	[X]	[X]	[X]

<sup>a</sup> Note that only types 1, 3, and 4 are acceptable from the concurrent engineering point of view.

the same kind, either both [UT] or both [LT]. If one is [LT] and the other is [UT], the product is a full matrix  $[X]$ . Therefore, when  $[A]$  and  $[B]$  are triangular matrices, either both of them must be upper triangular or both of them must be lower triangular for the manufacturing process to satisfy the independence of functional requirements. This is stated as theorem 9 (Design for Manufacturability).

### 11.5.9 The Second Axiom: The Information Axiom

The information axiom provides a quantitative measure of the merits of a given design, and thus it is useful in selecting the best among those designs that are acceptable. In addition, the information axiom provides the theoretical basis for design optimization and robust design.

Among the designs that are equally acceptable from the functional point of view, one of these designs may be superior to others in terms of the probability of achieving the design goals, as expressed by the functional requirements. The information axiom states that the design with the highest probability of success is the best design. Specifically, the information axiom may be stated as follows:

*Axiom 2: The Information Axiom.*

Minimize the information content.

Information content  $I_i$  for a given  $\text{FR}_i$  is defined in terms of the probability  $P_i$  of satisfying  $\text{FR}_i$ :

$$I_i = \log_2 \frac{1}{P_i} = -\log_2 P_i \quad (11.7)$$

The information is given in units of bits. The logarithmic function is chosen so that the information content will be additive when there are many functional requirements that must be satisfied simultaneously. Either the logarithm based on 2 (with the unit of bits) or the natural logarithm (with the unit of nats) may be used.

In the general case of  $m$  FRs, the information content for the entire system  $I_{\text{sys}}$  is

$$I_{\text{sys}} = -\log_2 P_{\{m\}} \quad (11.8)$$

where  $P_{\{m\}}$  is the joint probability that all  $m$  FRs are satisfied. When all FRs are statistically independent, as is the case for an uncoupled design,

$$P_{\{m\}} = \prod_{i=1}^m P_i$$

Then  $I_{\text{sys}}$  may be expressed as

$$I_{\text{sys}} = \sum_{i=1}^m I_i = -\sum_{i=1}^m \log_2 P_i \quad (11.9)$$

When all FRs are not statistically independent, as is the case for a decoupled design,

$$P_{\{m\}} = \prod_{i=1}^m P_{i|\{j\}} \quad \text{for } \{j\} = \{1, \dots, i-1\}$$

where  $P_{i|\{j\}}$  is the conditional probability of satisfying  $FR_i$  given that all other relevant (correlated)  $\{FR_j\}_{j=1,\dots,i-1}$  are also satisfied. In this case,  $I_{sys}$  may be expressed as

$$I_{sys} = - \sum_{i=1}^m \log_2 P_{i|\{j\}} \quad \{j\} = \{1, 2, \dots, i-1\} \quad (11.10)$$

The information axiom states that the design that has the smallest  $I$  is the best design, as it requires the least amount of information to achieve the design goals. When all probabilities are equal to 1.0, the information content is zero, and, conversely, the information required is infinite when one or more probabilities are equal to zero. That is, if the probability is small, we must supply more information to satisfy the functional requirements.

#### EXAMPLE 11.5 CUTTING A ROD TO A LENGTH

Suppose we need to cut rod A to  $1 \pm 10^{-6}$  m and rod B to  $1 \pm 0.1$  m. Which has a higher probability of success?

#### Solution

The answer depends on the cutting equipment available for the job! However, most engineers with some practical experience would say that the one that has to be cut within  $1 \mu\text{m}$  would be more difficult because the probability of success associated with the smaller tolerance is lower than that associated with the larger tolerance using typical equipment. Therefore, the job with the lower probability of success is more *complex* than the one with higher probability of success.

In reality, the probability of success is governed by the intersection of the design range defined by the designer to satisfy the FRs and the ability of the system to produce the part within the specified range. For example, if the design specification for cutting a rod is  $1 \text{ m} \pm 1 \mu\text{m}$  and the available tool (i.e., system) for cutting the rod consists of only a hacksaw, the probability of success will be extremely low. In this case, the information required to achieve the goal would approach infinity. Therefore, this may be called a complex design. On the other hand, if the rod needs to be cut within an accuracy of 10 cm, the hacksaw may be more than adequate, and therefore the information required is close to zero. In this case, the design is simple.

The probability of success can be computed by specifying the *design range* (*dr*) for the FR and by determining the *system range* (*sr*) that the proposed design can provide to satisfy the FR. figure 11.7 illustrates these two ranges graphically.

The vertical axis (the ordinate) is the probability density and the horizontal axis (the abscissa) is either the FR or DP, depending on the mapping domains involved. When the mapping is between the functional domain and the physical domain as in product design, the abscissa is the FR. When the mapping is between the physical domain and the process domain as in process design, the abscissa is the DP.

In figure 11.7, the system PDF (probability density function) is plotted over the system range for the specified FR. The overlap between the design range and system range is called the *common range* (*cr*), and this is the only region where the FR is satisfied. Consequently, the area under the system PDF within the common range,

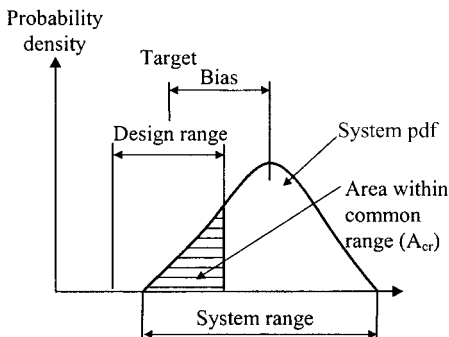


**Figure 11.7** Design range, system range, common range, and system PDF for a functional requirement.

$A_{\text{cr}}$  is the design's probability of achieving the specified goal. Then the information content may be expressed as (Suh, 1990)

$$I = \log_2 \frac{1}{A_{\text{cr}}} \quad (11.11)$$

#### EXAMPLE 11.6 CUTTING A ROD WITH A HACKSAW

Let us revisit example 11.5. We want to cut the rods as specified earlier, but now we know that the equipment available for the job is an ordinary hacksaw. The system PDF is shown in figure 11.8.

The plot of the system PDF and the design range show that in the case of cutting rod B, the system range is completely inside the design range and thus the common range and the system range are the same. Therefore, the probability of success is 1.0, and the information required to fulfill the functional requirement is zero. On the other hand, rod A has such a tight design range requirement that the common range is almost zero, making the information required approach infinity.

In normal machine shops, the information required is supplied by experienced machinists or toolmakers by carefully measuring the length and making careful cuts, even lapping the part. Because machinists' expertise or skills are limited, the information supplied may not completely compensate for the lack of system capability.

Often design decisions must be made when there are many FRs that must be satisfied at the same time. The information axiom provides a powerful criterion for making such decisions without the arbitrary weighting factors used in other decision-making theories. In equation (11.9), the information content that corresponds to each FR is simply summed up with all other terms without a weighting factor for two reasons. First, if we sum up the information terms, each of which has been modified

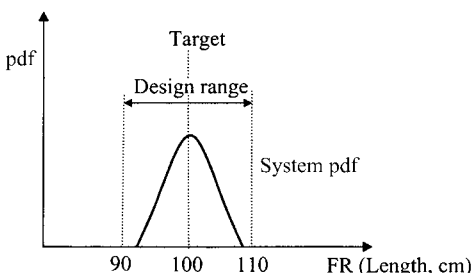


**Figure 11.8** The design range and the system PDF for cutting a rod to length.

by multiplying with a weighting factor, the total information content no longer represents the total probability. Second, the intention of the designer and the importance assigned to each FR by the designer are represented by the design range. If the design ranges for all the FRs are precisely specified and if every specified FR is satisfied within its design range, the goal of the design is fully satisfied. There is no need for rank ordering or giving weighting factors to FRs, as the design range specifies their relative importance. The following example illustrates the point.

#### EXAMPLE 11.7 BUYING A HOUSE

A family is planning to buy a new house. They decided that the following are the four important functional requirements the house must satisfy:

$FR_1$  = Commuting time must be in the range 15–30 minutes

$FR_2$  = The quality of the local high school must be good (i.e., more than 65% of the high school graduates must go to reputable colleges)

$FR_3$  = The quality of air must be good over 340 days a year

$FR_4$  = The price of the house must be reasonable (i.e., a four-bedroom house with 3000 square feet of heated space must be less than \$650,000)

They looked around towns A, B, and C and collected the following data with the help of realtors:

Town	$FR_1 = \text{Commute time (min)}$	$FR_2 = \text{Quality of schools (\%)}$	$FR_3 = \text{Quality of air (days)}$	$FR_4 = \text{Price (1000 \$)}$
A	20 to 40	50 to 70	300 to 320	450 to 550
B	20 to 30	50 to 75	340 to 350	450 to 650
C	20 to 45	50 to 80	350 and up	600 to 800

Which town meets the requirements of the family the best?

#### Solution

The FRs specify the design range. The system is given by the above table. Using these design and system ranges, the information content for each FR in each town can be computed using equation (11.7). Figures 11.9(a) and 11.9(b) illustrate the overlap (i.e., common range) between the design range and the system range for  $FR_1$  and  $FR_2$  of town A.

The information content of town A is infinite as it cannot satisfy  $FR_3$ , that is, the design range and the system range do not overlap. The information content for towns B and C is computed using equation (11.9) as follows:

Town	$I_1$ (bits)	$I_2$ (bits)	$I_3$ (bits)	$I_4$ (bits)	$\Sigma I$ (bits)
A	1.0	2.0	Infinite	0	Infinite
B	0	1.32	0	0	1.32
C	2.0	1.0	0	2.0	5.0

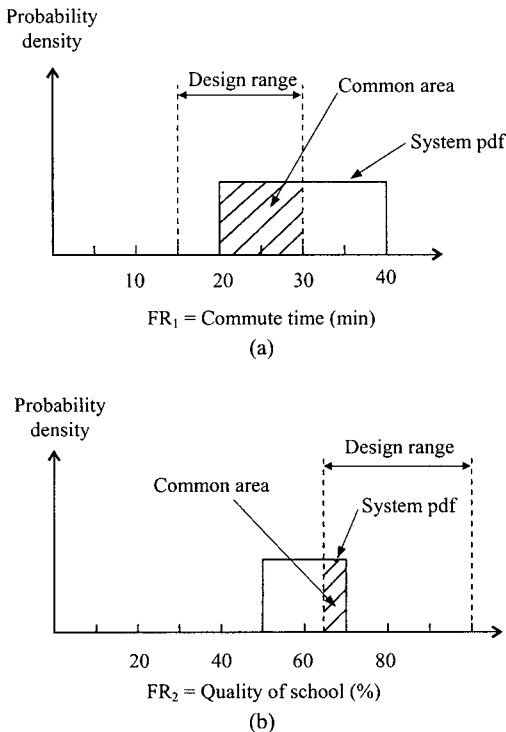


**Figure 11.9** Probability distribution of example (11.7): (a) Commuting time; (b) quality of schools.

The information associated with buying a house in town B is 1.32, whereas for town C it is 5.0. In town A, it is not likely that a house will be found unless the family is willing to change the specifications. The best town is town B. In this example, town A cannot meet the FR for clean air. In town C, it is more difficult to find houses close enough to commute in the time allowed and in the price range the family is willing to pay.

If the family thinks certain FRs are very important, they can be expressed by means of the specification of the design range without using a weighting factor.

When there is only one FR, the independence axiom is always satisfied when there is an appropriate DP that satisfies the FR. In the one-FR case, the only task left is the selection of the right values for the design matrix and the DP to come up with a robust design based on the information axiom. In the case of one-FR nonlinear design, various optimization techniques have been advanced when the task is to find a maximum or minimum of an objective function. However, when there is more than one FR, some of these optimization techniques do not work.

To develop a design with more than one FR, we must first develop a design that is either uncoupled or decoupled. If the design is uncoupled, each FR can be satisfied and the optimum points for all FRs can be found because each FR is controlled by its corresponding DP. If the design is decoupled, the FRs must be satisfied following a set sequence.

#### 11.5.10 Reduction of the Information Content: Robust Design

The ultimate goal of design is to reduce the additional information required to make the system function as designed, that is, minimize the information content as

stated by the information axiom. To achieve this goal, the design must be able to accommodate large variations in design parameters and process variables and yet still satisfy the functional requirements. Such a design is called a *robust* design.

To achieve a robust design, the variance of the system must be small and the bias must be eliminated to make the system range lie inside the design range, thus reducing the information content to zero (see figure 11.7). The bias can be eliminated if the design satisfies the independence axiom. There are four different ways of reducing the variance of a design if the design satisfies the independence axiom.

#### *Elimination of Bias*

In figure 11.7, the target value of the FR is shown at the middle of the design range. The distance between the target value and the mean of the system PDF is called *bias*. To have an acceptable design, the bias associated with each FR should be very small or zero. That is, the mean of the system PDF should be equal to the target value inside the design range.

In a one-FR design, the bias can be reduced or eliminated by changing the appropriate DP, because the DP controls this FR and we do not have to worry about its effect on other FRs. Therefore, it is easy to eliminate the bias when there is only one FR.

When there is more than one FR to be satisfied, we may not be able to eliminate the bias unless the design satisfied the independence axiom. If the design is coupled, each time a DP is changed to eliminate the bias for a given FR, the bias for the other FRs changes also, making the design uncontrollable. If the design is uncoupled, the design matrix is diagonal and the bias associated with each FR can be changed independently as if the design were a one-FR design. When the design is decoupled, the bias for all FRs can be eliminated by following the sequence dictated by the triangular matrix.

#### *Reduction of Variance*

Variance is a statistical measure of the variability of a PDF. Variability is caused by a number of factors, such as noise, coupling, environment, and random variations in design parameters. In a multi-FR design, the prerequisite for variance reduction is the satisfaction of the independence axiom. In all situations, the variance must be minimized. The variation can be reduced in a few specific situations discussed below.

##### (a) REDUCTION OF THE INFORMATION CONTENT THROUGH REDUCTION OF STIFFNESS

Suppose there is only one FR that is related to its DP as

$$\text{FR}_1 = (A_{11})\text{DP}_1 \quad (11.12)$$

In a linear design, the allowable tolerance for  $\text{DP}_1$ , given the specified design range for  $\text{FR}_1$ , depends on the magnitude of  $A_{11}$ , that is, the “stiffness.” As shown in figure 11.10, the smaller the stiffness,  $A_{11}$ , the larger the allowable tolerance of  $\text{DP}_1$ . However, there is a lower bound for stiffness.

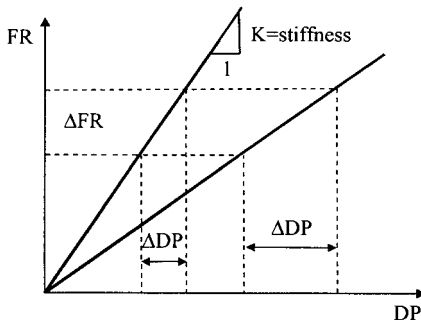


**Figure 11.10** Allowable variation of DP as a function of stiffness. For a specified  $\Delta FR$ , the allowable variation of DP increases with a decrease in the stiffness,  $A_{11}$ .

(b) REDUCTION OF THE INFORMATION CONTENT THROUGH THE DESIGN OF A SYSTEM THAT IS IMMUNE TO VARIATION

When the stiffness shown in figure 11.10 is zero, the system will be completely insensitive to variation in DP. If the goal is to vary the FR by changing the DP, the stiffness must be large enough to allow control of the FR, although from the robustness point of view, low stiffness is desired. When there are many DPs that affect a given FR, design should be done so that the FR will be “immune” to variation of all these other DPs except the one specific DP chosen to control the FR. In the case of nonlinear design, we should search for such a design window where this condition is satisfied.

The variance is the statistical measure of the spread of the distribution of the output. If a number of DPs are affecting an FR, the total variance of the FR is equal to the sum of the separate variances of the DPs when these DPs are statistically independent.

Often the variation in the system range may be due to many factors that affect the FR. Consider the one-FR design problem. The designer might have created a redundant design:

$$FR = f(DP_a, DP_b, DP_c)$$

or

$$FR = A_a DP_a + A_b DP_b + A_c DP_c \quad (11.13)$$

where  $A_a$ ,  $A_b$ , and  $A_c$  are coefficients and the DPs are design parameters that affect the FR. In this case, variation in FR can be introduced by any uncontrolled variation in all coefficients and DPs. The variance can be reduced by creating the design so that the FR is not sensitive to (or is immune to)  $DP_b$  and  $DP_c$  changes, which can be done either if  $A_b$  and  $A_c$  are small or if  $DP_b$  and  $DP_c$  are fixed so that they remain constant. In this case, because FR would be a function of only  $DP_a$ , FR can be controlled by changing  $DP_a$ . In this case, the only source of variation is the random variation of  $A_a$ .

Now consider the case of the multi-FR design given by

$$\begin{Bmatrix} FR_1 \\ FR_2 \\ FR_3 \end{Bmatrix} = \begin{bmatrix} A_{11} & 0 & 0 \\ 0 & A_{22} & 0 \\ 0 & 0 & A_{33} \end{bmatrix} \begin{Bmatrix} DP_1 \\ DP_2 \\ DP_3 \end{Bmatrix} \quad (11.14)$$

In this ideal design with a diagonal design matrix, the variance will be minimized if the random variation in  $A_{11}$ ,  $A_{22}$ , and  $A_{33}$  can be eliminated. It should be noted that any error in the DPs would contribute to the variance and the bias. Therefore, the coefficients  $A_{11}$ ,  $A_{22}$ , and  $A_{33}$  should be small, but large enough to exceed the required signal-to-noise ratio.

(c) REDUCTION OF THE INFORMATION CONTENT BY FIXING THE VALUES OF EXTRA DPs

When the design is a redundant design, the variance of the FRs can be reduced by identifying the key DPs and preventing the extra DPs from variation (i.e., fixing the values of these extra DPs).

Consider a multi-FR design given by

$$\left\{ \begin{array}{l} \text{FR}_1 \\ \text{FR}_2 \\ \text{FR}_3 \end{array} \right\} = \left[ \begin{array}{cccccc} A_{11} & 0 & 0 & A_{14} & A_{15} & 0 \\ 0 & A_{22} & 0 & 0 & A_{25} & A_{26} \\ 0 & 0 & A_{33} & A_{34} & 0 & A_{36} \end{array} \right] \left\{ \begin{array}{l} \text{DP}_1 \\ \text{DP}_2 \\ \text{DP}_3 \\ \text{DP}_4 \\ \text{DP}_5 \\ \text{DP}_6 \end{array} \right\} \quad (11.15)$$

Equation (11.15) represents a redundant design because there are more design parameters than functional requirements. The task now is to reduce the information content of this redundant design. The first thing we have to do is to find a way to make the design represented by equation (11.15) an ideal, uncoupled design as shown by equation (11.14). This can be done in two different ways: by fixing  $\text{DP}_4$ ,  $\text{DP}_5$ , and  $\text{DP}_6$  so that they do not act as design parameters or by making the coefficients associated with these DPs equal zero. Fixing  $\text{DP}_4$ ,  $\text{DP}_5$ , and  $\text{DP}_6$  also will minimize the variance in the FRs due to any variation of these three DPs. The variation can also be reduced by setting  $A_{14}$ ,  $A_{15}$ ,  $A_{25}$ ,  $A_{26}$ ,  $A_{34}$ , and  $A_{36}$  to zero so that the FRs will be immune to changes in  $\text{DP}_4$ ,  $\text{DP}_5$ , and  $\text{DP}_6$ . If the design matrix were different from the one shown above, other appropriate design elements should be made zero or other appropriate DPs should be fixed to reduce the variance of the FRs.

(d) REDUCTION OF INFORMATION CONTENT BY MINIMIZING THE RANDOM VARIATION OF DPs AND PVs

One way of reducing the variance of the FRs is to reduce the random variation of input parameters as they contribute to the total random variation of the FRs. The variance of the FRs may be expressed as

$$\sigma_{\text{FR}_i}^2 = \sum_{j=1}^n A_{ij}^2 \sigma_{\text{DP}_j}^2 + 2 \sum_{j=1}^n \sum_{k=1}^{j-1} A_{ij} A_{ik} \text{Cov}(\text{DP}_j, \text{DP}_k) \quad (11.16)$$

By reducing the variance of any of the  $\text{DP}_j$ , we can reduce the contributions to the variance of  $\text{FR}_i$ . Moreover, if some of the DPs are independent of one another, the relevant covariance terms disappear from equation (11.16), further reducing the contributions to the variance of  $\text{FR}_i$ .

(e) REDUCTION OF THE INFORMATION  
CONTENT BY COMPENSATION

The one-FR design given by equation (11.13) was a redundant design, having three DPs rather than one. For the design given by equation (11.13), we could satisfy the FR with only one DP, as per theorem 4 (Ideal Design). Therefore, the best solution for dealing with random variations (noise) for one-FR design is to eliminate the unnecessary DPs and lower the stiffness of the one DP that has been selected to satisfy the FR. However, there may be situations where a given redundant design must be made to work.

Suppose that we have to work with less than an ideal design represented by equation (11.1), and that the design cannot be made “immune” to random variations by having low stiffness, because the coefficients associated with the redundant DPs cannot be made sufficiently small. In this case, the effect of random variations of the extra DPs on FR can be eliminated by “compensating” for it through the adjustment of the selected DP.

In equation (11.13), suppose that the following is true:

$$A_a \gg A_b \text{ and } A_a \gg A_c$$

Then, we should choose  $DP_a$  as the chosen DP and try to minimize the effect of the variations of  $DP_b$  and  $DP_c$  on FR. The random variations will be represented as  $\delta DP_b$  and  $\delta DP_c$ . If we want to change FR from one state to another state, which is represented by  $\Omega FR$ , it can be done by changing  $DP_a$  by  $\Omega DP_a$ . For this change of state of FR, equation (11.13) may be written as

$$\Omega FR = A_a \Omega DP_a + \sum_{i=\text{extra terms}} A_i \delta DP_i \quad (11.17)$$

If the allowable random variation of FR (i.e., the design range of FR) is represented as  $\Delta FR$ , the random noise term represented by the second term of the RHS of equation (11.17) can be compensated by adjusting  $DP_a$ . The necessary adjustment  $\Delta DP_a$  to compensate for the random variation is given by

$$\Delta DP_a = \frac{\Delta FR - \sum_{i=\text{extra terms}} A_i \delta DP_i}{A_a} \quad (11.18)$$

In equation (11.18), if the noise term is larger than the allowable tolerance of FR, we have to look for a new design by choosing new DPs.

This means of compensating for the random error can be done with multi-FR design as well as with one-FR designs, if the independence axiom is satisfied by the multi-FR design. This kind of compensation scheme can be employed to eliminate the effect of the random variations introduced during manufacturing. It is clear from equation (11.16) that it is easier to reduce the information content for uncoupled designs because only one DP contributes to the variance of  $FR_i$  and there are no covariance terms.

(f) REDUCTION OF THE INFORMATION CONTENT BY INCREASING  
THE DESIGN RANGE

In some special cases, the design range can be increased without jeopardizing the design goals. The system range may then be inside the design range.

### 11.5.11 Reduction of the Information Content Through Integration of DPs

In the preceding section, a means of reducing the information content of a design by making the system range fit inside the design range was presented. This technique is normally called “robust design.” There is another equally significant means of reducing the information content—through integration of DPs in a single physical part without compromising the independence of FRs. In this way, the information content can be made small by reducing the likelihood of introducing errors when many physical parts are assembled or by making the manufacturing operation simple.

A good example of DP integration is the beverage can, which was illustrated in figure 11.4. There were 12 DPs, but only three physical pieces. Another example is a can and bottle opener that must open bottles and cans, but not at the same time. In this case, the DP that opens the bottle and the DP that opens the can (by punching a triangular opening on the lid of the can) may be integrated in the same steel sheet stock—the can opener at one end and the bottle opener at the other end (figure 3.3 in Suh, 1990).

When the design has been achieved by decomposing FRs and DPs to many levels, the integration of DPs can be done in the physical domain. In this case, only the leaf-level DPs of each branch need to be integrated, as higher level DPs are made up of the leaf-level DPs.

To create a system, all physical parts that contain the leaf-level DPs must be integrated into a physically functioning system. This system-level integration must be done from the viewpoint of minimizing information content. This integration process is facilitated if the system is first designed by decomposition and then the resulting leaf-level DPs are integrated to create the final system.

## 11.6 Allowable Tolerance in Multi-FR Design

When a design consists of many FRs, and if the design is a decoupled design, the off-diagonal terms of the triangular matrix represent the coupling terms. The magnitude of these coupling terms reduces robustness of the design by reducing the allowable tolerance of DPs. Therefore, even when the design is acceptable because it is a decoupled design, it is important that the magnitude of the off-diagonal element be made as small as possible relative to the magnitude of the diagonal element.

Tolerance specification is simple in the case of an uncoupled design. If the specified design range for  $FR_i$  is  $\Delta FR_i$ , then the tolerance for  $DP_i$  is simply

$$\Delta DP_i = \frac{\Delta FR_i}{A_{ii}} \quad (11.19)$$

The *design range* is defined by  $\Delta FR$ . The actual variation of FR, which is determined by the variation of the DPs as well as by the magnitude of the design matrix elements, defines the system range. If the system range determined by the random variation of FR is less than the specified design range  $\Delta FR_i$  and if the target in the design range and the peak of the system PDF coincide, then the information content is equal to zero as the system range is always inside the design range.

Consider the decoupled design shown below:

$$\begin{Bmatrix} \text{FR}_1 \\ \text{FR}_2 \\ \text{FR}_3 \end{Bmatrix} = \begin{bmatrix} A_{11} & 0 & 0 \\ A_{21} & A_{22} & 0 \\ A_{31} & A_{32} & A_{33} \end{bmatrix} \begin{Bmatrix} \text{DP}_1 \\ \text{DP}_2 \\ \text{DP}_3 \end{Bmatrix} \quad (11.20)$$

The independence axiom can be satisfied if we change the DPs in the order shown. However, to have a robust design, we must be sure that the off-diagonal elements are much smaller than the diagonal elements (i.e.,  $A_{ii} \gg A_{ij}$ ).

If the specified design ranges for FRs are  $\Delta\text{FR}_1$ ,  $\Delta\text{FR}_2$ , and  $\Delta\text{FR}_3$ , the maximum allowable tolerances for DPs may be expressed as

$$\begin{aligned} \Delta\text{DP}_1 &= \frac{\Delta\text{FR}_1}{A_{11}} \\ \Delta\text{DP}_2 &= \frac{\Delta\text{FR}_2 - |A_{21}\Delta\text{DP}_1|}{A_{22}} \\ \Delta\text{DP}_3 &= \frac{\Delta\text{FR}_3 - |A_{31}\Delta\text{DP}_1| - |A_{32}\Delta\text{DP}_2|}{A_{33}} \end{aligned} \quad (11.21)$$

For  $\Delta\text{DP}_2$  of equation (11.21), the fluctuation of  $\Delta\text{DP}_2$  due to the term  $A_{21}\Delta\text{DP}_1$  can make the term  $\Delta\text{DP}_2$  larger or smaller, depending on its sign. However, the maximum allowable  $\Delta\text{DP}_2$  corresponds to the worst possible case, that is, when  $\Delta\text{DP}_2$  is made smaller by the term  $(A_{21}\Delta\text{DP}_1)$ . A similar argument holds true for  $\Delta\text{DP}_3$ . Therefore, the absolute value represented by  $|x|$  is used to represent the worst possible case.

According to equation (11.21), the maximum tolerances for the DPs of the decoupled design are less than the corresponding tolerances for the DPs of an uncoupled design. This means that the decoupled design is inherently less robust than the uncoupled design.

Equation (11.21) was for a decoupled design with three FRs and three DPs. Extending the argument given above to the case of  $m$  FRs and  $m$  DPs, it becomes obvious that as  $m$  increases, the allowable tolerance for the last DP of the triangular matrix becomes increasingly smaller. This means that the robustness of a decoupled design diminishes as the number of FRs increases.

In the case of a coupled design, the maximum allowable tolerance is even smaller than was the case for a decoupled design.

## 11.7 Complexity and Axiomatic Design

A theory of complexity has been developed that starts from the axiomatic design theory (Suh, 1999, 2003). In this theory, complexity is defined as a measure of uncertainty in satisfying the FRs. The complexity theory provides an overall guideline in designing complicated systems to the designers. According to this theory, there are the following four kinds of complexities:

*Time-independent real complexity:* Measurement of the complexity that occurs when the system range is not inside the design range. Therefore, the real complexity is equal to the information content.

*Time-independent imaginary complexity:* A complexity that is not real complexity but arises because of the lack of knowledge on a specific design. For example, when a design is a decoupled design with a triangular matrix, we have to vary the DPs in the right order. However, if the designer does not know the design equation, the FRs may not be satisfied, giving the idea that the design is not acceptable. The probability of varying the DPs in the right order is  $1/n!$ , where  $n$  is the number of FRs. When  $n=7$ ,  $n!$  is 5040. Such a design may look very complex, although it is not.

*Time-dependent combinatorial complexity:* When the system range changes as a function of time, it can move out of the design range. This occurs when one of the FRs is subject to a combinatorial process—like the airline schedule in the United States when a snowstorm shuts down Detroit airport. The system may eventually fail when it goes into a chaotic state.

*Time-dependent periodic complexity:* Some systems have a set of FRs that repeat within a period by reinitializing themselves at the beginning of each period. The functional period can contain many different physical phenomena (temporal, geometric, chemical, processes, thermal, etc.).

When a system, which has a combinatorial process, can be changed to have a functional period and thus transform the combinatorial complexity into a periodic complexity, the complexity of the system can be reduced. This will increase the reliability and safety of the system.

## 11.8 Concluding Remarks

In this chapter, the basic concepts and methodologies of axiomatic design such as the concepts of domains, mapping, two design axioms (independent axiom and information axiom), decomposition, hierarchy, and zigzagging have been presented. Design is accomplished by first defining the FRs and constraints based on an understanding of customer needs. Then these FRs are mapped into DPs. If these DPs do not provide sufficient details, they are decomposed together with DPs until the DPs can be implemented. At each stage of mapping, the independence axiom must be checked by writing the design equation and determining the design matrix to make sure that the design is an uncoupled or a decoupled design. Similar mapping can be done between the physical domain and the process domain. When there is more than one design that satisfies the independence axiom, the information content should be determined to choose the one with the lowest information content.

The independence axiom states that the functional requirements must always be maintained independent of one another by choosing appropriate design parameters. Uncoupled and decoupled designs are shown to satisfy the independence axiom and thus acceptable. Coupled designs do not satisfy the independence axiom and thus are unacceptable.

The information axiom deals with information content, the probability of satisfying the FRs, and complexity. Information content is defined in terms of the probability of success and is the additional information required to satisfy the functional requirement. Computing the information content in a design is facilitated by the notion of the design range and the system range. The design range is specified for each FR by the designer, whereas the system range is the resulting performance of the design embodiment.

An outline of the complexity theory that is based on axiomatic design theory has been given. By applying the complexity theory in order to reduce the complexity of a system, the design can be made more reliable, robust, and safe. Complexity can be reduced by eliminating the time-independent real complexity and the time-independent imaginary complexity, and also by transforming a time-dependent combinatorial complexity into a time-dependent period complexity by identifying functional periodicity.

To make reliable and safe composites, they have to be designed right the first time by applying axiomatic design theory and complexity theory, as presented in this chapter. For further details of axiomatic design, readers should refer to Suh (2001) and Suh (2003).

## Problems

- 11.1. Prove that if each information content term of the right-hand side of equation (11.9) is multiplied by a weighting factor  $k_i$ , the total information content will not be equal to information.
- 11.2. Consider the design of a hot and cold water faucet. If we have a faucet that has one valve for hot water and another valve for cold water, the design is coupled, as the temperature and flow rate cannot be controlled independently. We can design an uncoupled faucet that has one knob for temperature control only and another knob for the flow-rate control only. Design such an uncoupled faucet by decomposing the FRs and DPs. Integrate the DPs to reduce the number of parts.
- 11.3. A surgical operating table for hospitals is to be designed. The position of the table must be adjustable along the horizontal and the vertical directions, as well as the inclination of the table. Design a mechanism that can satisfy these functional requirements. If the functional requirements of the table are modified so that the table has to change from one fixed position (i.e., fixed horizontal, vertical, and inclination) to another fixed position, how would you design the mechanism?
- 11.4. The two linear equation sets below describe two designs. Each of the design matrices can be made uncoupled or decoupled depending on whether the variable  $x$  is set to 0 or 1, respectively. Analytically compute the probability of success of each of the designs for each value of  $x$  (four cases in total). All distributions are uniform. What can you conclude about the relationship between information content and coupling?

$$\begin{Bmatrix} -1 < \text{FR}_1 < 1 \\ -1 < \text{FR}_2 < 1 \end{Bmatrix} = \begin{bmatrix} 1 & 0 \\ x & 1 \end{bmatrix} \begin{Bmatrix} 0 < \text{DP}_1 < 2 \\ 0 < \text{DP}_2 < 2 \end{Bmatrix}$$

$$\begin{Bmatrix} -1 < \text{FR}_1 < 1 \\ 1.5 < \text{FR}_2 < 3.5 \end{Bmatrix} = \begin{bmatrix} 1 & 0 \\ x & 1 \end{bmatrix} \begin{Bmatrix} 0 < \text{DP}_1 < 2 \\ 0 < \text{DP}_2 < 2 \end{Bmatrix}$$

- 11.5. The equation below describes a design with two DPs and two FRs. The first DP has a uniform distribution and the second DP has a normal distribution around its nominal value. Write a short program (in MATLAB for example) that numerically computes the probability of success of this design, and plot each

$\text{FR}(\text{DP}_1, \text{DP}_2)$ . Use the same program to recompute the results for problem 11.4, and determine the magnitude of error that was introduced by neglecting conditional probabilities.

$$\left\{ \begin{array}{l} 2 < \text{FR}_1 < 5 \\ 1.5 < \text{FR}_2 < 3.5 \end{array} \right\} = \begin{bmatrix} 0.7 & 1.6 \\ 1.1 & 0.5 \end{bmatrix} \left\{ \begin{array}{l} 1 < \text{DP}_1 < 3 \\ \text{DP}_2 = 2, \sigma = 0.8 \end{array} \right\}$$

- 11.6.** Given a system with  $m$  independent events with probability of success  $P_i$ , prove that the total information content is the sum of individual information contents of these events.

#### Note

1. It should be noted that we can always find a specific set of numbers for the elements of the full matrices  $[A]$  and  $[B]$  that yield a matrix  $[C]$  that is triangular or diagonal, but in actual design situations, it would be difficult to generate a design for such special cases that satisfy the FRs over a wide range.

#### References

- Suh, N. P. 1990. *The Principles of Design*, Oxford University Press, Oxford.  
 Suh, N. P. 1995. "Axiomatic Design of Mechanical System," *Journal of Mechanical Design* and *Journal of Vibration and Acoustics, Transactions of the ASME*, Vol. 117, pp. 1–10.  
 Suh, N. P. 1999. "A Theory of Complexity, Periodicity, and Design Axioms," *Research in Engineering Design*, Vol. 11, pp. 116–131.  
 Suh, N. P. 2001. *Axiomatic Design*, Oxford University Press, Oxford.  
 Suh, N. P. 2003. *A Theory of Complexity and Applications*, manuscript.

## Appendix: Corollaries and Theorems

Some of these theorems are derived in this book as well as in the references given. For those theorems not derived in this book, the readers may consult the original references.

### Corollaries

**Corollary 1 (Decoupling of Coupled Designs)** Decouple or separate parts or aspects of a solution if FRs are coupled or become interdependent in the designs proposed.

**Corollary 2 (Minimization of FRs)** Minimize the number of FRs and constraints.

**Corollary 3 (Integration of Physical Parts)** Integrate design features in a single physical part if the FRs can be independently satisfied in the proposed solution.

**Corollary 4 (Use of Standardization)** Use standardized or interchangeable parts if the use of these parts is consistent with the FRs and constraints.

**Corollary 5 (Use of Symmetry)** Use symmetrical shapes and/or components if they are consistent with the FRs and constraints.

**Corollary 6 (Largest Design Ranges)** Specify the largest allowable design range in stating FRs.

**Corollary 7 (Uncoupled Design with Less Information)** Seek an uncoupled design that requires less information than coupled designs in satisfying a set of FRs.

**Corollary 8 (Effective Reangularity of a Scalar)** The effective reangularity  $R$  for a scalar coupling “matrix” or element is unity. (Reangularity is defined in Suh, 1990.)

## Theorems of General Design

**Theorem 1 (Coupling Due to Insufficient Number of DPs)** When the number of DPs is less than the number of FRs, either a coupled design results or the FRs cannot be satisfied.

**Theorem 2 (Decoupling of Coupled Design)** When a design is coupled because of a larger number of FRs than DPs (i.e.,  $m > n$ ), it may be decoupled by the addition of new DPs so as to make the number of FRs and DPs equal to each other if a subset of the design matrix containing  $n \times n$  elements constitutes a triangular matrix.

**Theorem 3 (Redundant Design)** When there are more DPs than FRs, the design is either a redundant design or a coupled design.

**Theorem 4 (Ideal Design)** In an ideal design, the number of DPs is equal to the number of FRs, and the FRs are always maintained independent of each other.

**Theorem 5 (Need for New Design)** When a given set of FRs is changed by the addition of a new FR, by substitution of one of the FRs with a new one, or by selection of a completely different set of FRs, the design solution given by the original DPs cannot satisfy the new set of FRs. Consequently, a new design solution must be sought.

**Theorem 6 (Path Independence of Uncoupled Design)** The information content of an uncoupled design is independent of the sequence by which the DPs are changed to satisfy the given set of FRs.

**Theorem 7 (Path Dependency of Coupled and Decoupled Design)** The information contents of coupled and decoupled designs depend on the sequence by which the DPs are changed to satisfy the given set of FRs.

**Theorem 8 (Independence and Design Range)** A design is an uncoupled design when the designer-specified range is greater than

$$\left( \sum_{\substack{i=1 \\ i \neq j}}^n \frac{\partial \text{FR}_i}{\partial \text{DP}_j} \right) \Delta \text{DP}_j$$

in which case, the off-diagonal elements of the design matrix can be neglected from design consideration.

**Theorem 9 (Design for Manufacturability)** For a product to be manufacturable with reliability and robustness, the design matrix for the product,  $[A]$  (which relates the FR vector for the product to the DP vector of the product), times the design matrix for the manufacturing process,  $[B]$  (which relates the DP vector to the PV vector of the manufacturing process), must yield either a diagonal or a triangular matrix. Consequently, when either  $[A]$  or  $[B]$

represents a coupled design, the independence of FRs and robust design cannot be achieved. When they are triangular matrices, either both of them must be upper triangular or both must be lower triangular for the manufacturing process to satisfy independence of functional requirements.

**Theorem 10 (Modularity of Independence Measures)** Suppose that a design matrix  $[DM]$  can be partitioned into square submatrices that are nonzero only along the main diagonal. Then the reangularity and semangularity for  $[DM]$  are equal to the product of their corresponding measures for each of the nonzero submatrices. (Reangularity and semangularity are defined in Suh, 1990.)

**Theorem 11 (Invariance)** Reangularity and semangularity for a design matrix  $[DM]$  are invariant under alternative orderings of the FR and DP variables, as long as the orderings preserve the association of each FR with its corresponding DP.

**Theorem 12 (Sum of Information)** The sum of information for a set of events is also information, provided that proper conditional probabilities are used when the events are not statistically independent.

**Theorem 13 (Information Content of the Total System)** If each DP is probabilistically independent of other DPs, the information content of the total system is the sum of the information of all individual events associated with the set of FRs that must be satisfied.

**Theorem 14 (Information Content of Coupled vs. Uncoupled Designs)** When the state of FRs is changed from one state to another in the functional domain, the information required for the change is greater for a coupled design than for an uncoupled design.

**Theorem 15 (Design-Manufacturing Interface)** When the manufacturing system compromises the independence of the FRs of the product, either the design of the product must be modified or a new manufacturing process must be designed and/or used to maintain the independence of the FRs of the products.

**Theorem 16 (Equality of Information Content)** All information contents that are relevant to the design task are equally important regardless of their physical origin, and no weighting factor should be applied to them.

**Theorem 17 (Design in the Absence of Complete Information)** Design can proceed even in the absence of complete information only in the case of a decoupled design if the missing information is related to the off-diagonal elements.

**Theorem 18 (Existence of an Uncoupled or Decoupled Design)** There always exists an uncoupled or decoupled design that has less information than a coupled design.

**Theorem 19 (Robustness of Design)** An uncoupled design and a decoupled design are more robust than a coupled design in the sense that it is easier to reduce the information content of designs that satisfy the independence axiom.

**Theorem 20 (Design Range and Coupling)** If the design ranges of uncoupled or decoupled designs are tightened, they may become coupled designs. Conversely, if the design ranges of some coupled designs are relaxed, the designs may become either uncoupled or decoupled.

**Theorem 21 (Robust Design When the System Has a Nonuniform PDF)** If the probability distribution function (PDF) of the FR in the design range is nonuniform, the probability of success is equal to one when the system range is inside the design range.

**Theorem 22 (Comparative Robustness of a Decoupled Design)** Given the maximum design range for a given set of FRs, decoupled design cannot be as robust as uncoupled designs in that the allowable tolerances for DPs of a decoupled design are less than those of an uncoupled design.

**Theorem 23 (Decreasing Robustness of a Decoupled Design)** The allowable tolerance and thus the robustness of a decoupled design with a full triangular matrix diminish with an increase in the number of functional requirements.

**Theorem 24 (Optimum Scheduling)** Before a schedule for robot motion or factory scheduling can be optimized, the design of the tasks must be made to satisfy the independence axiom by adding decouplers to eliminate coupling. The decouplers may be in the form of a queue or of separate hardware or buffer.

**Theorem 25 (“Push” System vs. “Pull” System)** When identical parts are processed through a system, a “push” system can be designed with the use of decouplers to maximize productivity, whereas when irregular parts requiring different operations are processed, a “pull” system is the most effective system.

**Theorem 26 (Conversion of a System with Infinite Time-Dependent Combinatorial Complexity to a System with Periodic Complexity)** Uncertainty associated with a design (or a system) can be reduced significantly by changing the design from one of serial combinatorial complexity to one of periodic complexity.

# 12

## Axiomatic Design of Materials and Materials-Processing Techniques

### 12.1 Introduction

In the 1970s, airplane manufacturers were developing composite parts using the autoclave vacuum bag degassing method, which was discussed in chapter 2. However, the empirical approach they used encountered many problems. One of the problems was that sometimes the cured part would have a large void inside the composite structure, because the resin was depleted during the curing process. Resin depletion occurred because the viscosity of the resin initially decreased before the resin in the prepgs began to crosslink. Therefore, when a laminate consisting of prepgs and a honeycomb structure were heated in the autoclave, the resin began to flow out of the composite structure when the gelation of the resin did not occur quickly. Similarly, automotive companies spent many years developing sheet molding compound (SMC) parts that did not require hand-polishing of the surface of the cured parts. They ultimately developed the in-mold coating process that coated the rough surface with a thin layer of resin.

The purpose of this chapter is to illustrate how the axiomatic design approach—rather than the trial-and-error empirical approach—can be used to develop materials and materials-processing techniques quickly and more reliably. In chapters 1 and 11, axiomatic design theory was presented. It was shown that there are four domains in the design world: the customer domain, the functional domain, the physical domain, and the process domain. In the case of materials, the customer domain is where the desired *performance* of the materials is specified. Then, in the functional domain, the FRs are the desired *properties* of the materials that can provide the desired performance specified in the customer domain. These FRs are satisfied by choosing the *microstructure* (or morphology) as the DPs in the physical domain. Finally, the *process variables* (PVs) in the process domain specify how the desired microstructure can be created through processing. Therefore, the sequence of mapping is from the desired performance to properties to microstructure to processing variables, as shown in figure 12.1.

The mapping from the functional domain to the physical domain must be done without violating the independence axiom by creating uncoupled or decoupled designs. Similarly, the mapping from the physical domain to the process domain must be done such that the resulting design is either an uncoupled or decoupled design. The best design is the one with the minimum information content. During the

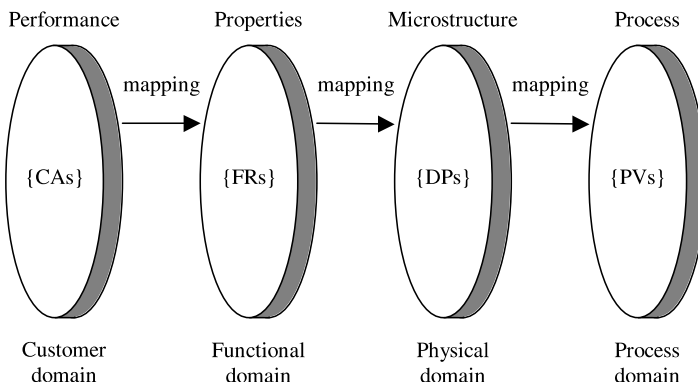


**Figure 12.1** Four domains of the materials world: *Performance* of materials characterizes the customer domain. *Properties* characterize the functional domain. *Microstructure* characterizes the physical domain. *Process variables* characterize the process domain.

design process, it is important to remember that the time-independent imaginary complexity should be eliminated and that the time-dependent combinatorial complexity should be reduced or transformed into time-dependent periodic complexity. When the information content is reduced the time-independent real complexity is also reduced.

In this chapter, four examples are given to illustrate how axiomatic design can be used to develop materials and processes: microcellular plastics, microcellular composites, layered manufacturing process, and USM high-pressure molding. Microcellular plastics were developed at MIT based on axiomatic design, which is now a commercial process. A process for manufacturing foamed SMC was also developed at MIT to improve the properties of the SMC composites. The third example is the manufacture of composites by layered manufacturing processes. The last example is that of making a sandwich structure with solid skins and foamed core, which is called USM high-pressure injection molding.

## 12.2 Microcellular Plastics

### 12.2.1 Introduction to Microcellular Plastics

Microcellular plastics (MCPs) are plastics that have a large number of uniformly sized, microscale bubbles of less than  $30\text{ }\mu\text{m}$  in a polymeric matrix (Martini, 1981; Martini et al., 1982, 1984).<sup>1</sup> A typical MCP has a myriad of small bubbles of a uniform size ( $0.1\text{--}30\text{ }\mu\text{m}$  in diameter) with a cell density of  $10^9\text{--}10^{15}$  bubbles/cm $^3$ . Figure 12.2 shows the microstructure of a typical low-density MCP. A variety of MCP parts are now commercially produced by injection molding and extrusion<sup>2</sup>.

The central idea behind MCPs was to replace plastics with a large number of very small bubbles that are smaller than the preexisting inherent flaws (Suh, 1996). Small bubbles can blunt the crack tips and act as crazing initiation sites, making the material tougher. They can be created in thermoplastics, thermosetting plastics, and elastomers. Microcellular plastics were originally designed to reduce the consumption of polymers in polymeric products and to enhance certain physical properties. However, MCP has other functional advantages such as better precision in injection

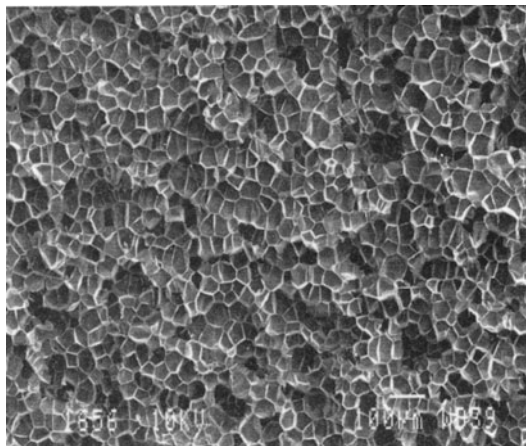


**Figure 12.2** Microstructure of microcellular plastics with average cell size of about  $30\ \mu\text{m}$ .

molded parts due to the reduced residual stress, no sink marks, and faster cycle time. Some of the MCPs are tougher than the original materials by as much as 600% and have lower dielectric constant.

The designs of both the material and the manufacturing process are based on the principles of axiomatic design. In the customer domain the need is the reduction of the manufacturing cost. This need has been mapped into the functional domain as the FR of reducing materials consumption without sacrificing the mechanical properties. The design parameter in the physical domain is the creation of MCPs. Having decided on the DP, the highest level FR is then decomposed into the next-level functional requirements as

$\text{FR}_1 = \text{Reduce the amount of plastic used}$

$\text{FR}_2 = \text{Increase the toughness of the plastic product}$

$\text{FR}_3 = \text{Make a three-dimensional geometrical shape.}$

The design parameters are

$\text{DP}_1 = \text{Number of cells}$

$\text{DP}_2 = \text{Cell size}$

$\text{DP}_3 = \text{Die design.}$

The design equation for the product may be written as

$$\begin{Bmatrix} \text{FR}_1 \\ \text{FR}_2 \\ \text{FR}_3 \end{Bmatrix} = \begin{bmatrix} X & X & 0 \\ 0 & X & 0 \\ 0 & 0 & X \end{bmatrix} \begin{Bmatrix} \text{DP}_1 \\ \text{DP}_2 \\ \text{DP}_3 \end{Bmatrix} \quad (12.1)$$

Equation (12.1) indicates that the product design is a decoupled design.

### 12.2.2 Design of a Batch Process

Having now designed microcellular plastics, our next task is to figure out how such microcellular plastics can be manufactured economically. A batch process for microcellular plastics was first developed using a thermodynamic instability phenomenon (Martini et al., 1982; Suh, 1996). The basic physics involved is as follows:

1. The plastic must be supersaturated with sufficient gas (e.g.,  $\text{CO}_2$ ) to nucleate a large number of cells simultaneously. High pressure is needed because gas solubility increases with pressure.

2. The temperature must be controlled in order to control the deformability of the plastic matrix phase during cell growth.
3. A gas with a suitable solubility and diffusivity for the given plastic must be selected.
4. Homogenous nucleation must dominate the nucleation process in order to create a large number of microcells even when heterogeneous nucleation sites are available.

The processing technique consists of forming a polymer/gas solution and then suddenly inducing a thermodynamic instability by either lowering the pressure or raising the temperature to change the solubility  $S$ . The solubility is a function of two thermodynamic properties, temperature  $T$  and pressure  $p$ :

$$S = S(p, T) \quad (12.2)$$

The change in the solubility can be expressed as

$$\Delta S = \frac{\partial S}{\partial p} \Delta p + \frac{\partial S}{\partial T} \Delta T \quad (12.3)$$

The  $\partial S / \partial p$  term of equation (12.3) is positive, whereas the  $\partial S / \partial T$  term is negative. Therefore, to decrease the solubility and induce the thermodynamic instability, either the pressure must be decreased (i.e.,  $\Delta p < 0$ ) or the temperature must be increased (i.e.,  $\Delta T > 0$ ). Furthermore, regardless of whether the process is continuous or batch type, the thermodynamic instability must be induced quickly so that cells will nucleate simultaneously. Therefore, the higher the temperature of the polymer, the quicker nucleation has to occur, which will ensure a uniform cell size distribution.

The number of cells nucleated is a function of the supersaturation levels—the higher the supersaturation level, the greater the number of cells nucleated. Furthermore, because the amount of dissolved gas that fills the nucleated cells is finite, and because all the cells are nucleated nearly at the same time, the gas distributes more or less evenly among all these cells. The final bubble size is then determined by the total gas per bubble and the flow characteristics of the polymer at the nucleation temperature.

Micrographs of several different kinds of microcellular plastics processed in batch processes, that is, extruded or injection-molded parts foamed after saturation with  $\text{CO}_2$  gas, are similar to that shown in figure 12.2. Figure 12.3 is a plot of cell density of various plastics, and figure 12.4 is a plot of the cell size of various plastics plotted in figure 12.3. It should be noted that the plastics with a large cell density have smaller cell diameters. In fact, the products of average cell volume and cell density are nearly equal when the amount of gas dissolved in the plastic is the same.

### 12.2.3 Design of Continuous Process

Although the batch process has demonstrated that microcellular plastics could be produced, the process was too slow for commercial applications. Faster production techniques that can make parts by injection molding and extrusion were needed. To create a continuous process, we must be able to design a process and associated

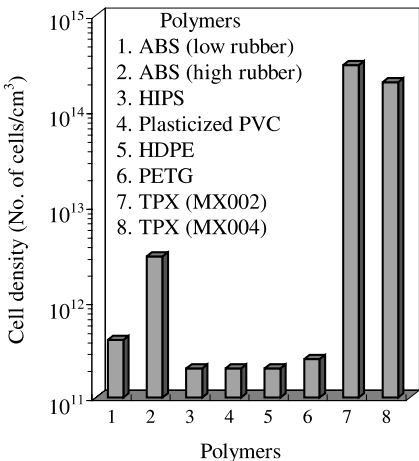


**Figure 12.3** Cell densities of microcellular foamed polymers (ambient temperature foaming).

Saturation pressure and temperature of  $\text{CO}_2$  were not the same for all polymers (Cha, 1994; Cha, et al., 1992).

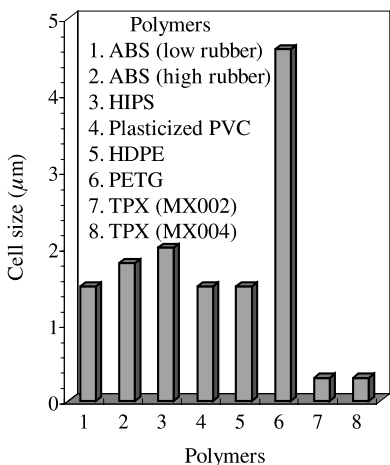


**Figure 12.4** Cell sizes of the microcellular foamed polymers (ambient temperature foaming); saturation pressure and temperature of  $\text{CO}_2$  were not the same for all polymers.

equipment to perform the following functions:

1. Rapid dissolution of gas into molten flowing polymer to form a solution.
2. Nucleation of a large number of cells.
3. Control of the cell size.
4. Control of the geometry of the final product.

The designer must fully understand each one of these processes in order to achieve the task. In this section, the physics of the continuous process is described briefly, based on several theses produced at MIT.

#### *Brief Introduction to the Physics of the Process*

##### GAS DIFFUSION AND FORMATION OF POLYMER/GAS SOLUTION

To produce the microcellular plastics at an acceptable production rate through a continuous process, we must dissolve the gas in polymers quickly despite the slow diffusion rate.

When a block of polymer is suddenly exposed to high-pressure gas at temperature  $T$ , the polymer will approach a thermodynamic equilibrium by gas diffusion into the

polymer if the polymer and gas are miscible and by thermal conduction toward an equilibrium temperature. The driving force is the free energy of the polymer/gas system. The diffusion phenomenon can be expressed with a partial differential equation as

$$\nabla(D\nabla C) = \frac{\partial C}{\partial t} \quad (12.4)$$

where  $C$  is the specific concentration of the gas,  $t$  is the time, and  $D$  is the diffusion coefficient, which may be a function of temperature and pressure. Equation (12.4) is similar to equation (8.77), where  $D$  is replaced with  $K_z^H$ . In general, the diffusivity increases with temperature by an Arrhenius relationship:

$$D = D_0 \exp\left(\frac{-\Delta G}{kT}\right) \quad (12.5)$$

where  $\Delta G$  is the activation energy of the gas,  $k$  is Boltzmann's constant, and  $T$  is the absolute temperature. The solution to equation (12.4) for the case of constant gas diffusivity has been obtained. An important implication of the solution is that the time for gas diffusion is proportional to the thickness of the plastic  $l$  as (see equation (8.89))

$$t \propto \frac{l^2}{D} \quad (12.6)$$

Table 12.1 shows the diffusivity  $D$  of  $\text{CO}_2$  and  $\text{N}_2$  in various plastics, and table 12.2 lists the diffusion times estimated by Park (1993) for various striation thicknesses of plastics as a function of diffusivity. It should be noted that it takes a long time to diffuse gas into a polymer at room temperature and that the diffusivity of  $\text{CO}_2$  and  $\text{N}_2$  are nearly the same. For example, the diffusivity of  $\text{CO}_2$  in most thermoplastics at room temperature is in the region of  $5 \times 10^{-8} \text{ cm}^2/\text{s}$  and the diffusion time estimated using equation (12.6) is approximately 14 hours when  $l$  is 0.5 mm. The diffusivity at  $200^\circ\text{C}$  is three to four orders of magnitude greater than that at room temperature. Even at high temperatures, the diffusion rate is still the rate-limiting step in continuous processes.

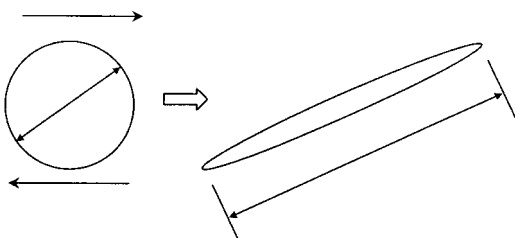
**Table 12.1 Estimated Diffusion Coefficients of Gases in Polymers at Elevated Temperatures (Durril and Griskey, 1966, 1969)**

<i>Polymer</i>	<i>D of CO<sub>2</sub> (cm<sup>2</sup>/s)</i>		<i>D of N<sub>2</sub> (cm<sup>2</sup>/s)</i>	
	<i>188°C</i>	<i>200°C</i>	<i>188°C</i>	<i>200°C</i>
PS	—	$1.3 \times 10^{-5}$	—	$1.5 \times 10^{-5}$
PP	$4.2 \times 10^{-5}$	—	$3.5 \times 10^{-5}$	—
PE	—	$2.6 \times 10^{-6}$	—	$8.8 \times 10^{-7}$
HDPE	$5.7 \times 10^{-5}$	$2.4 \times 10^{-5}$	$6.0 \times 10^{-5}$	$2.5 \times 10^{-5}$
LDPE	—	$1.1 \times 10^{-4}$	—	$1.5 \times 10^{-4}$
PTFE	—	$7.0 \times 10^{-6}$	—	$8.3 \times 10^{-6}$
PVC	—	$3.8 \times 10^{-5}$	—	$4.3 \times 10^{-5}$

**Table 12.2 Estimated Diffusion Time at Various Striation Thicknesses and Diffusion Coefficients (Park, 1993)**

Striation thickness ( <i>l</i> ) ( $\mu\text{m}$ )	Diffusion coefficient ( <i>D</i> )			
	$10^{-5} \text{ cm}^2/\text{s}$	$10^{-6} \text{ cm}^2/\text{s}$	$10^{-7} \text{ cm}^2/\text{s}$	$10^{-8} \text{ cm}^2/\text{s}$
1	$1 \times 10^{-3} \text{ s}$	0.01 s	0.1 s	1 s
10	0.1 s	1 s	10 s	100 s
50	2.5 s	25 s	4 min	42 min
100	10 s	100 s	17 min	3 h
250	63 s	10 min	2 h	17 h
500	4 min	42 min	7 h	3 days
750	9 min	94 min	16 h	7 days
1000	17 min	3 h	28 h	12 days

**Figure 12.5** Deformation of a spherical bubble in shear field to form an ellipsoid; the distance between the ellipsoids (measured perpendicular to the major axis of the ellipsoids) is the striation thickness. The dissolution rate of gas increases as the striation thickness becomes smaller and as the interfacial area of gas/polymer increases.



To accelerate the diffusion rate and shorten the time for the formation of gas/polymer solutions, we must raise the temperature and shorten the diffusion distance. Deforming the two-phase mixture of polymer and gas through shear distortion, as shown in figure 12.5, can decrease the diffusion path. This type of deformation occurs in an extruder under laminar flow conditions. The bubbles are stretched by the shear field of the two-phase mixture and eventually break up to minimize the surface energy when a critical Weber number is reached (Taylor, 1934). The Weber number *We* is defined as

$$We = \frac{\text{shear forces}}{\text{surface forces}} = \frac{(dy/dt)d_b\eta_p f(\lambda)}{2\sigma} \quad (12.7)$$

where  $\lambda$  = viscosity ratio of gas and polymer ( $\eta_g/\eta_p$ )

$$f(\lambda) = (19\lambda + 16)/(16\lambda + 16)$$

$\gamma$  = shear strain

$d_b$  = bubble diameter

$\sigma$  = surface tension

The striation thickness decreases with further shear, and the gas diffusion occurs faster as a result of the increase in the surface area and the decrease in striation thickness. The striation thickness in an extruder is estimated to decrease to about  $100 \mu\text{m}$ . At this thickness, the diffusion time is in the range of 1 minute in polyethylene terephthalate (PET), from 10 to 20 seconds in polystyrene (PS),

**Table 12.3 Estimated Gas Solubility in Polymers at 200°C and 27.6 MPa  
(Park, 1993)**

Polymer	$CO_2$ weight gain (%)	$N_2$ weight gain (%)
PE	14	3
PP	11	4
PS	11	2
PMMA	13	1

polyvinylchloride (PVC), and high-density polyethylene (HDPE), and in the region of a few seconds in low-density polyethylene (LDPE).

At thermodynamic equilibrium, the gas concentration in the polymer is related to pressure and temperature as

$$C = H(p, T) \quad (12.8)$$

where  $H$  is known as Henry's constant. At low pressures and low concentrations,  $H$  is constant. At high pressures,  $H$  depends on both pressure and temperature. The temperature dependence follows the Arrhenius-type rate equation. At higher pressure, the gas solubility is high, but the rate of the weight increase with pressure decreases with pressure.

The solubility of gas in polymers decreases with an increase in temperature. Table 12.3 lists the estimated gas solubility of  $CO_2$  and  $N_2$  in various thermoplastics. It should be noted that the solubility of  $N_2$  is considerably less than that of  $CO_2$ . Because the amount of gas that can be dissolved is a function of the saturation pressure and the gas diffusion rate is the rate-limiting process, we can use  $CO_2$  at a critical state to enhance the solubility and diffusion rate. Supercritical fluid is neither gas nor liquid in a certain temperature and pressure regime higher than the critical pressure and critical temperature of the fluid. In this state, it has both gas-like and liquid-like properties.  $CO_2$  is supercritical at pressures and temperatures greater than 7.4 MPa and 31.1°C.

With dissolution of a large number of gas molecules in polymers, the glass transition temperature and viscosity decrease with the increase in gas concentration. The change in the glass transition temperature is quite substantial at high gas concentrations. These changes affect the processibility of polymers.

### Nucleation

The key idea in the formation of microcellular plastics is the nucleation of a large number of bubbles (cells). Cells can nucleate either homogeneously or heterogeneously. Homogeneous nucleation must overcome a larger activation energy barrier than heterogeneous nucleation. Homogeneous nucleation occurs throughout the matrix. On the other hand, heterogeneous nucleation occurs at an interface between two or more different materials or phases where the interfacial energy is high. When the driving force is very high, such as when the degree of supersaturation of the gas in the polymer is large, the difference in the activation level is so much smaller than the driving force that both homogeneous and heterogeneous nucleation can occur simultaneously.

When the gas is homogeneously dissolved throughout the molten plastic by diffusion, the polymer is ready for nucleation. For nucleation to occur, a finite energy barrier has to be overcome. The energy barrier depends on two competing factors: (1) the energy available in the gas diffused into the embryo of the cell and (2) the surface energy that must be supplied to form the surface of the cell. There is a critical cell size beyond which the cell becomes stable and grows, and below which the cell embryo collapses. Typically the cell nucleation rate is expressed as

$$\frac{dN}{dt} = N_0 f e^{-\Delta G/kT} \quad (12.9)$$

where  $N$  = number of cells per unit volume

$N_0$  = number of available sites for nucleation per unit volume

$f$  = frequency of atomic or molecular lattice vibration

$\Delta G$  = activation energy barrier

$k$  = Boltzmann's constant

$T$  = absolute temperature

The activation energy term can be related to the pressure in the bubble and the surface energy (Martini, 1981; Colton, 1985) as

$$\Delta G = \frac{16\pi\gamma}{3\Delta p_0} g(\theta) \quad (12.10)$$

where  $\gamma$  is the surface energy of the polymer and  $\Delta p_0$  is the pressure difference between the cluster of gas molecules in the bubble and the surrounding pressure, which is assumed to be equal to the saturation gas pressure. The function  $g(\theta)$  depends on the wetting angle between the polymer, gas, and the second phase particle. It is equal to 1.0 in the case of homogeneous nucleation and is less than 1.0 for heterogeneous nucleation. The critical radius is given by

$$r_c = \frac{2\gamma}{\Delta p_0} \quad (12.11)$$

In homogeneous nucleation there are many possible nucleation sites, the most prominent of which are the free volume sites. Also, in the case of semicrystalline polymers, the interfaces between the amorphous region and the crystalline region could be the nucleation sites (Colton and Suh, 1987a, b, 1990, 1992). Depending on the gas supersaturation level, all or part of these nucleation sites will be activated. At this time, we cannot quantitatively delineate the importance of these various nucleation sites at a given saturation pressure. From the foregoing discussion, it can be seen that even homogeneous nucleation is not truly homogeneous in terms of the activation energy levels involved for nucleation. At high pressures, both homogeneous and heterogeneous nucleations occur because of the driving force.

### CELL GROWTH

Immediately after the cells are nucleated, the pressure in the bubble is equal to the saturation pressure. Therefore, the cells will try to expand if the polymer matrix is

soft enough to undergo viscoelastic plastic deformation. The cell expands until the final pressure inside the cell is equal to the pressure required to be in equilibrium with the surface forces and the stress in the viscoelastic cell wall.

Unlike in conventional foaming, in the case of microcellular plastics, there are so many cells nucleated and the diffusion length is so short that the diffusion of the gas to the cell growth stops relatively quickly when there is no more dissolved gas to diffuse into the nucleated cells.

In practice, the temperature of the surface of the extrudate changes as a result of heat transfer, and thus the expansion of the cell is constrained by the outer stiff layer. Also some of the gases from the cells near the surface escape, reducing the tendency to expand.

When the temperature is very high and the cell expands beyond the plastic instability point (i.e., equivalent to the ultimate tensile strength point in a uniaxial tensile test where necking begins), the cells will rupture and an open-cell microcellular structure will result.

#### CELL DENSITY AND CELL SIZE

The cell density is a function of both the concentration of dissolved gas and the pressure drop rate. When the pressure of the molten plastics is not rapidly changed, the number of cells is lower and conventional foams with large cells are produced. Microcellular plastics depend on the rapid pressure drop rate and controlled concentration of dissolved gas to nucleate a large number of cells of the desired size.

During the cell nucleation stage, there is competition for gas between cell nucleation and cell growth if the cells do not nucleate instantaneously. When some cells nucleate before others, the gas in the solution will diffuse to the nucleated cells to lower the free energy of the system. As the gas diffuses to these cells, low gas concentration regions where nucleation cannot occur are generated adjacent to the stable nuclei. As the solution pressure drops further, the system will either both nucleate additional microcells and expand the existing cells by gas diffusion or only expand the existing cells. Therefore, when the pressure drop occurs rapidly, the gas-depleted region where nucleation cannot occur will be smaller and a more uniform cell distribution will result. It has been determined experimentally that a drop rate of 2 GPa/s is the minimum pressure drop rate required for microcellular plastics processing.

The competition between cell nucleation and cell growth can be understood using two dimensionless groups (Baldwin, 1994). For nucleation to be completed in a time that is short compared with the diffusion time, the dimensionless group giving the ratio of these times must be small:

$$\frac{\text{Characteristic nucleation time}}{\text{Characteristic diffusion time}} \ll 1$$

or

$$\frac{D}{(dN/dt)d_C^5} \ll 1 \quad (12.12)$$

where  $D$  is the gas diffusivity,  $dN/dt$  is the nucleation rate per unit volume, and  $d_C$  is the cell diameter.

The second dimensionless group can be obtained by considering the length associated with the nucleation and growth of cells over finite processing times. The competition between microcell nucleation and cell growth is negligible when

$$\frac{\text{Characteristic gas diffusion distance}}{\text{Characteristic spacing between stable nuclei}} \ll 1$$

or

$$\rho_c^{1/3} (Dt_D)^{1/2} \ll 1 \quad (12.13)$$

where  $\rho_c$  is the cell density,  $D$  is gas diffusivity, and  $t_D$  is the diffusion time. For a continuous process to work, equations (12.12) and (12.13) must be satisfied.

#### *Design of a Continuous Process*

It was decided that a continuous process would be designed by modifying a conventional single-screw extruder. High-pressure CO<sub>2</sub> gas is introduced into the extruder barrel by metering the exact amount of CO<sub>2</sub> at pressures greater than 14 MPa (2000 psi). The flow rate of CO<sub>2</sub> into the extruder can be controlled using a metering pump. The gas forms a large bubble in the extruder as the flow of the gas is briefly interrupted whenever the screw flight wipes over the barrel. Then the gas in the bubble must be diffused quickly in the molten plastic by increasing the polymer/gas interfacial area and decreasing the striation thickness (i.e., the average distance between the elongated bubbles) of polymers between the gas bubbles, as the diffusion time is proportional to the thickness squared. By elongating the bubble in the barrel through the shear deformation of the two-phase mixture of the polymer and gas, the area-to-volume ratio of the gas bubble is increased and the striation thickness is reduced, promoting rapid diffusion of gas into the molten polymer.

When the striation thickness is in the range of 100 μm and the temperature is 200°C, the diffusion time of PET is 100 seconds, the diffusion time of low-density polyethylene is 1 second, and the diffusion time of polystyrene is 10 seconds. These numbers provide the approximate residency time required for diffusion and solution formation in the extruder.

The FRs and DPs were given in the preceding section as

FR<sub>1</sub> = Reduce the amount of plastic used

FR<sub>2</sub> = Increase the toughness of the plastic product

FR<sub>3</sub> = Make three-dimensional geometric shape.

DP<sub>1</sub> = Microcellular plastics (uniform cell distribution in large numbers)

DP<sub>2</sub> = Diameter of microcells

DP<sub>3</sub> = Die shape.

The PVs for the process described that can satisfy the DPs given are

PV<sub>1</sub> = Supersaturation of the plastic with a large amount of gas and sudden pressure change ( $dp/dt$ )

PV<sub>2</sub> = Temperature of the molten polymer to control the expansion of cells at the die

PV<sub>3</sub> = Cross-sectional dimensions.

The design equation for the extrusion process may be written as

$$\begin{Bmatrix} DP_1 \\ DP_2 \\ DP_3 \end{Bmatrix} = \begin{bmatrix} X & 0 & 0 \\ X & X & 0 \\ 0 & 0 & X \end{bmatrix} \begin{Bmatrix} PV_1 \\ PV_2 \\ PV_3 \end{Bmatrix} \quad (12.14)$$

Equation (12.14) shows that the process design is also a decoupled design. Therefore, each design satisfies the independence axiom. However, for concurrent engineering to be possible, the product of the process design matrices must also be diagonal or triangular. Because  $FR_i = A_{ij}DP_j$  and  $DP_j = B_{jk}PV_k$ ,  $FR_i = C_{ik}PV_k$ , where  $C_{ik} = A_{ij}B_{jk}$ . However, the process design matrix with elements given by  $C_{ik}$  is neither diagonal nor triangular. This means that the foam density and toughness of the plastic part cannot be independently controlled by means of the PVs chosen unless the tolerances on the density variation or the toughness variation are large enough to change one of the two design matrices. Experiments support this conclusion.

$DP_1$  and  $PV_1$  can be further decomposed as

$PV_{11}$  = Large number of nucleated cells

$PV_{12}$  = Uniform cell size.

$PV_{11}$  = The level of supersaturation of  $CO_2$

$PV_{12}$  = Rapid pressure drop  $dp/dt$ .

The design matrix for this design may be represented as

$$\begin{Bmatrix} DP_{11} \\ DP_{12} \end{Bmatrix} = \begin{bmatrix} X & x \\ X & X \end{bmatrix} \begin{Bmatrix} PV_{11} \\ PV_{12} \end{Bmatrix} \quad (12.15)$$

Equation (12.15) states that  $DP_{11}$  and  $DP_{12}$  are coupled slightly in that if the pressure drop rate is really slow, we cannot get a large number of cells that are of uniform size. In most cases, the effect of  $dp/dt$  on the number of cells is negligible. A typical pressure profile in a single-screw extruder is shown in figure 12.6.

The DPs were decomposed further until the designs of the process and the equipment were completed by a number of researchers (Park, 1993; Baldwin, 1994; Sanyal, 1998). Park investigated the continuous extrusion of microcellular plastics, in particular, the dissolution of gas at an acceptable production rate and the use of a

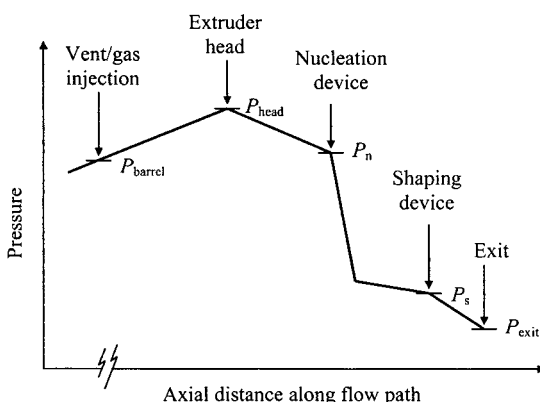
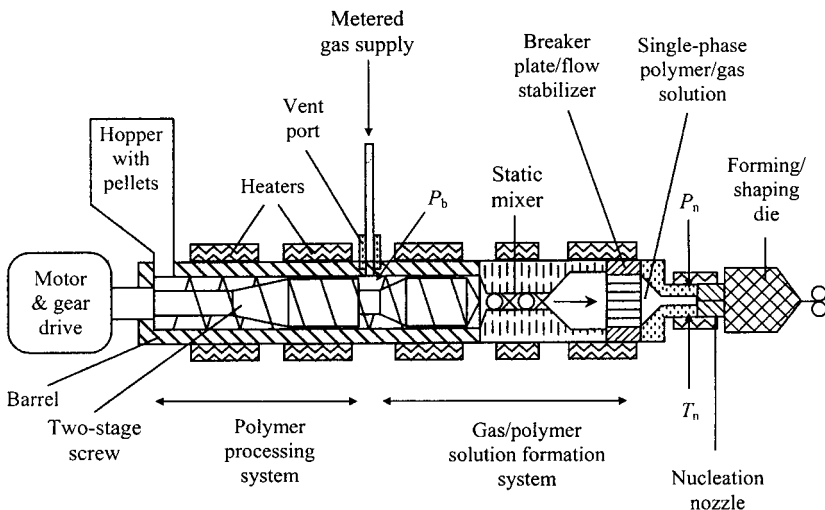


Figure 12.6 Representative pressure profile along the polymer flow field in the extruder and die (Baldwin et al., 1996).



**Figure 12.7** Schematic of the microcellular extrusion system used for the shaping and cell growth control experiments (Baldwin et al., 1996).

rapid pressure drop nozzle as a nucleation device (Park, 1993). Baldwin investigated the microcellular plastic structure in amorphous plastics and crystalline plastics using polyethylene terephthalate (PET) and polyolefin-modified polyethylene terephthalate (CPET) and also the continuous extrusion process, especially the shaping of the flat and tubular extrudates (Baldwin, 1994; Baldwin et al., 1994a, b). The work of Park and Baldwin was important as the original batch process had limited applicability because of the slow diffusion of gas into a solid plastic (Park et al., 1995, 1996). Cha investigated the use of supercritical fluids, especially  $\text{CO}_2$ , to dissolve the gas faster and to increase the amount of dissolved gas to create “super” microcellular plastics (Cha, 1994). With supercritical fluids, the bubble density was increased from  $10^9 \text{ bubbles/cm}^3$  to as high as  $10^{15} \text{ bubbles/cm}^3$ .

The final design of the equipment that can provide the PVs is shown in figure 12.7. This equipment consists of the  $\text{CO}_2$  injection system, a shearing section for the two-phase mixture, a diffusion section to ensure the homogeneity of the polymer/gas solution, and a nucleation section. The morphology of the microcellular polypropylene extruded in industry is shown in figure 12.8. Figure 12.9 shows a micrograph of the cross-section of polystyrene sheet extruded commercially (roughly 1.3 m wide and 6.35 mm thick). These cells are closed cells with an average diameter of approximately  $20 \mu\text{m}$ . Figure 12.10 shows the profile of some of the commercially extruded parts and figure 12.11 shows some of the injection-molded products by MuCell<sup>3</sup> technology.

#### EXAMPLE 12.1 EXTRUSION OF WIRE COATING WITH MICROCELLULAR PLASTICS

One-hundred-and-fifty thin coaxial cables are bundled together to transmit many electrical signals in making ultrasound imaging machines. The bundle must have a small diameter for flexibility in bending around tight corners (see equation (2.1)). Therefore, the diameter of each cable must be 1 mm. The customer is looking for a coaxial cable bundle that is highly flexible and that has certain

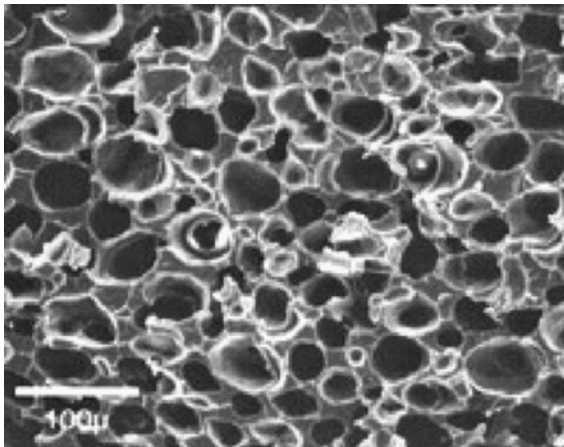


**Figure 12.8** Scanning electron microscope micrographs: extruded microcellular polypropylene.

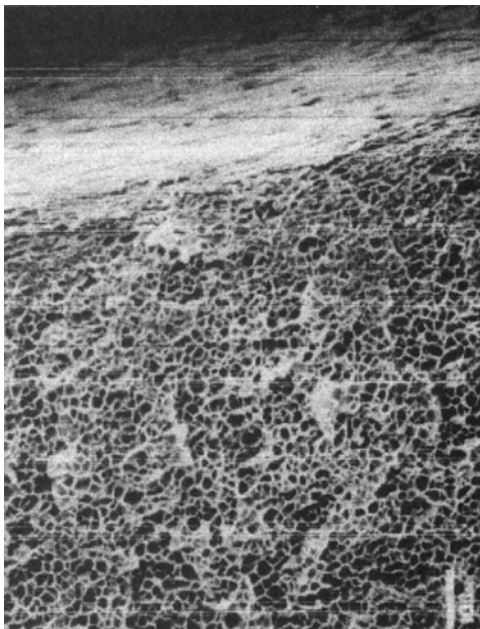


**Figure 12.9** A micrograph of commercially manufactured microcellular polystyrene.

electrical characteristics. The highest level FR that can satisfy this customer need is “produce insulation of desired size and electrical performance.” The highest level DP is “insulated wire with low dielectric constant and proper electrical performance.” The highest level PV is “the extrusion coating of microcellular plastics on a thin wire.” The design task is to develop DPs and PVs for this thin coated coaxial wire.

#### Solution

The highest level FR may be decomposed as

$$FR_1 = \text{Produce insulation of desired dielectric constant}$$

$$FR_2 = \text{Produce foam insulation of a desired electric breakdown strength.}$$

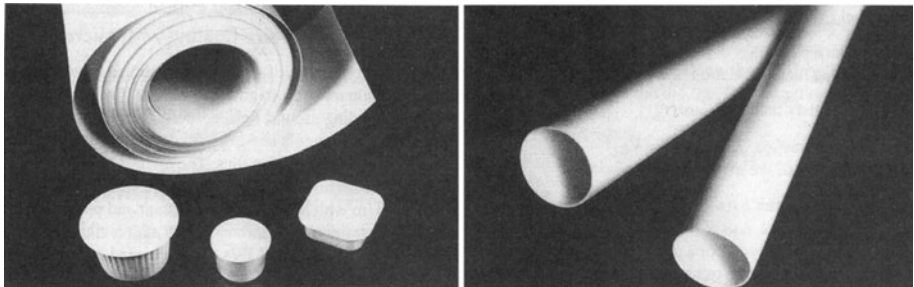


**Figure 12.10** Extruded commercial products of MuCell microcellular plastics.

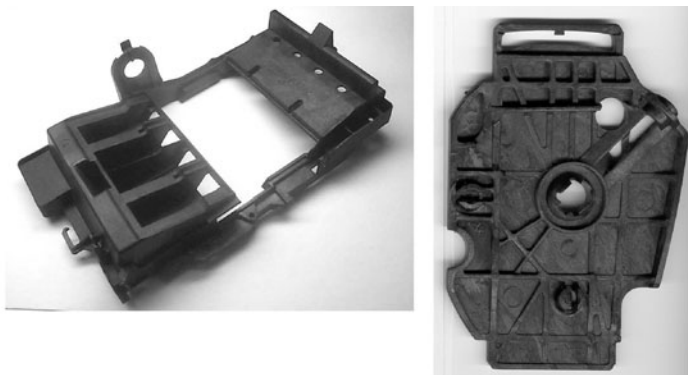


**Figure 12.11** Injection-molded MuCell microcellular plastics (courtesy of Trexel, Inc.).

The DPs that can satisfy these FRs are

$$DP_1 = \text{Volume fraction of the void} = V_F$$

$$DP_2 = \text{Thickness of the insulation} = t.$$

The constraint is that the cell size must be very small and uniformly distributed as these microcoaxial cables require a very thin layer of electric insulation. The material must be either a Teflon-family polymer or a polyethylene. Neglecting the second-order effects of voids on the electric breakdown strength, the design equation is a triangular matrix given by

$$\begin{Bmatrix} FR_1 \\ FR_2 \end{Bmatrix} = \begin{bmatrix} X & X \\ 0 & X \end{bmatrix} \begin{Bmatrix} DP_1 \\ DP_2 \end{Bmatrix} \quad (12.16)$$

Now we have to determine appropriate PVs that can satisfy the DPs. We may choose PVs as

$$PV_1 = \text{Foaming variables}$$

$$PV_2 = \text{Flow rate of the foam, } Q, \text{ relative to the speed of the wire, } v.$$

The design equation may be written as

$$\begin{Bmatrix} DP_1 \\ DP_2 \end{Bmatrix} = \begin{bmatrix} X & 0 \\ 0 & X \end{bmatrix} \begin{Bmatrix} PV_1 \\ PV_2 \end{Bmatrix} \quad (12.17)$$

The product design matrix given in equation (12.16) is triangular (i.e., a decoupled design), and the process design matrix in equation (12.17) is diagonal (i.e., an uncoupled design). Up to this stage of the design, both the product design and the process design satisfy the independence axiom, and thus concurrent engineering is shown to be possible.

It should be noted that  $PV_1$  must be decomposed further as it cannot be implemented as stated. We need to decompose  $FR_1$ ,  $DP_1$ , and  $PV_1$  by means of zigzagging. All subsequent decomposition must be such that the design intent expressed by equations (12.16) and (12.17) is satisfied.

#### **Decomposition of $FR_1$ , $DP_1$ , and $PV_1$**

$FR_{11}$  = Control the cell size

$FR_{12}$  = Control the number of cells.

$DP_{11}$  = Uniform cell size

$DP_{12}$  = Cell density.

The design matrix for the FR/DP relationship is a diagonal matrix.

$PV_{11}$  = Pressure drop rate across die =  $dp/dt$

$PV_{12}$  = Amount of the gas dissolved.

The maximum amount of the gas that can be dissolved,  $PV_{11}$ , is a function of the lowest pressure for maintaining the single-phase polymer/gas system, which is the die inlet pressure. The pressure drop is determined by the die geometry. In the case of a slit die with a constant cross-section along the die length, the pressure drop rate,  $dp/dt$ , is a function of the length of the die lip. The design matrix for the DP/PV relationship may be represented as follows:

$$\begin{Bmatrix} DP_{11} \\ DP_{12} \end{Bmatrix} = \begin{bmatrix} X & X \\ x & X \end{bmatrix} \begin{Bmatrix} PV_{11} \\ PV_{12} \end{Bmatrix} \quad (12.18)$$

The microstructure of the foam—void fraction, cell size, and cell density—determines the performance of the insulation. Using the rule of mixture, the dielectric constant  $\kappa$  of the insulation may be expressed as

$$\kappa \approx \kappa_p - (\kappa_p - 1)V_F \quad (12.19)$$

$\kappa_p$  is the dielectric constant of plastic, and the dielectric constant of gas is assumed to be equal to 1.  $V_F$  is the volume fraction of the cells.

#### **Decomposition of $FR_2$ , $DP_2$ , and $PV_2$**

The decomposition of  $FR_2$  (produce foam insulation of a desired electric breakdown strength),  $DP_2$  (thickness of the insulation), and  $PV_2$  (flow rate of foam,  $Q$ , relative to the speed of the wire,  $v$ ) will now be considered.

Assuming that microcellular plastic with desired cell size and cell density can be created, the electric breakdown of the insulation will depend on the electric field strength around the wire. Therefore, the control of the insulation thickness may be the easiest means of satisfying  $FR_2$ . The thickness can be controlled by changing the flow rate of plastics at a given wire velocity at a given diameter of the die opening.

The volume flow rate of the foam,  $Q$ , will determine the final insulation thickness at a given velocity of the wire,  $v$ . The conservation of mass yields

$$Q = \frac{\pi}{4} (D^2 - d^2) v \quad (12.20)$$

where  $D$  is the outside diameter of the insulated wire and  $d$  is the bare conductor diameter. Therefore, we can treat DP<sub>2</sub> and PV<sub>2</sub> as leaves. However, the specific choice of process variables for PV<sub>2</sub> must be determined.

The flow rate,  $Q$ , can be changed in many different ways at a fixed production rate of the insulated wire. For example, the die diameter, the rotational speed,  $\omega$ , of the extruder, and the temperature,  $T_p$ , of plastic in the die will affect the flow rate. The die diameter should be based on the ratio of the desired density of the insulation material after and before foaming. The temperature of the plastic is normally kept as low as possible to generate a stable foam structure when the gas diffuses out of the polymer/gas solution. In light of these considerations, we may choose the rotational speed of the screw as the final PV<sub>2</sub> that can control the thickness of the foam.

Since the second-order effects are ignored in this preliminary design of the production system and since our ability to model the process exactly depends on many assumptions, the final design of the system must be checked out through actual testing of the production system.

#### 12.2.4 Advantages of Microcellular Plastics

Microcellular plastics have many advantages over conventional (macrocellular) foamed plastics. First, the cells in conventional foams are so large that thin films and sheets cannot be foamed, whereas for microcellular foams, when the cell size is 0.1  $\mu\text{m}$ , 20  $\mu\text{m}$ -thick sheets can be successfully foamed with good physical integrity. Similarly, thin microcellular fibers can be also made.

Some microcellular plastics have also exhibited better physical properties (Seeler and Kumar, 1992). Many microcellular plastics are tougher and have longer fatigue life. Also the specific mechanical strength is much better than conventional large-cell foamed plastics. Microcellular plastics can have densities as low as 0.03 g/cm<sup>3</sup>, although the limit of the lowest density is not known at this time. At such low densities, thermal insulation properties of microcellular plastics are excellent because of the small cell size.

Injection molding of microcellular plastic parts has many advantages over the conventional injection molding with solid plastics. In addition to the weight reduction, which was one of the original design goals, it reduces residual stress and dimensional distortion. Since the voids under pressure expand in the mold, these voids compensate for the thermal shrinkage that occurs when the molten plastic is solidified in the mold. As a result, the residual stress in these injection molded parts is very small. Therefore, these parts do not distort after they are taken out of the mold, which allows the production of precision injection-molded parts. Other advantages of the microcellular plastic injection molding process are the faster cycle time and the low injection pressure. This is a result of the reduction in the viscosity of plastics when a large amount of gas is dissolved in the plastic, which lowers the injection pressure and temperature. Because of the low injection pressure and the elimination of the packing pressure,<sup>4</sup> the clamping tonnage of the injection molding machines can be reduced by more than 50%. Also when the gas dissolved in the plastic phase

separates from the polymer/gas solution to form the bubbles, the viscosity and the melting point of the plastic instantaneously increases, which allows a rapid removal of the molded part.

## 12.3 Lightweight SMC Composites<sup>5</sup>

Sheet molding compound (SMC) composites are used in automobiles. The details of SMC are given in chapter 2. One disadvantage of this composite is its high specific gravity, which is about 1.8, because of the large amount of mineral fillers used. The composition is given in table 12.4. For low shrinkage, nearly 50% particulate fillers by weight are used with 15–30% glass fibers by weight. The large shrinkage of the resin develops a large interfacial stress between the glass fibers and the resin, resulting in large cracks and low strength unless the shrinkage is minimized. At MIT, a lightweight SMC is made by replacing the fillers with microcellular voids. Since the fibers are fairly long in SMC compounds, the size of the void is not as critical as in microcellular plastics.

### *FRs and PVs*

In developing this process for making the lightweight SMC parts, functional requirements of the manufacturing process were defined. The FRs were

$FR_1$  = Supersaturate the resin with gas for cell nucleation

$FR_2$  = Cure the bubble walls after nucleation

$FR_3$  = Stabilize the foam before curing.

$FR_1$  is essential to induce thermodynamic instability and nucleate a large number of voids.  $FR_2$  is to control the size of the bubble after nucleation by crosslinking the resin (gelation time) by terminating bubble growth at the gelation point.  $FR_3$  is to stabilize the bubbles to prevent their collapse before gelation.

It was decided to use dielectric heating of the resin using the setup shown in figure 12.12. The process variables are

$PV_1$  = Supersaturation pressure

$PV_2$  = Electric field strength

$PV_3$  = Initial mold temperature.

**Table 12.4 Typical Composition of Commercial SMC**

Components	Weight fraction (%)	Volume fraction (%)
Polyester resin	26.0	42.2
Catalyst (Tertiary butyl perbenzoate)	0.3	0.6
Mold release (Zinc stearate)	1.0	0.4
Polyethylene	1.4	2.8
Filler (Calcium carbonate)	38.9	28.6
Pigment	2.1	1.4
Thickener (Magnesium oxide)	0.3	0.2
Glass fibers (E-glass)	30.0	23.9

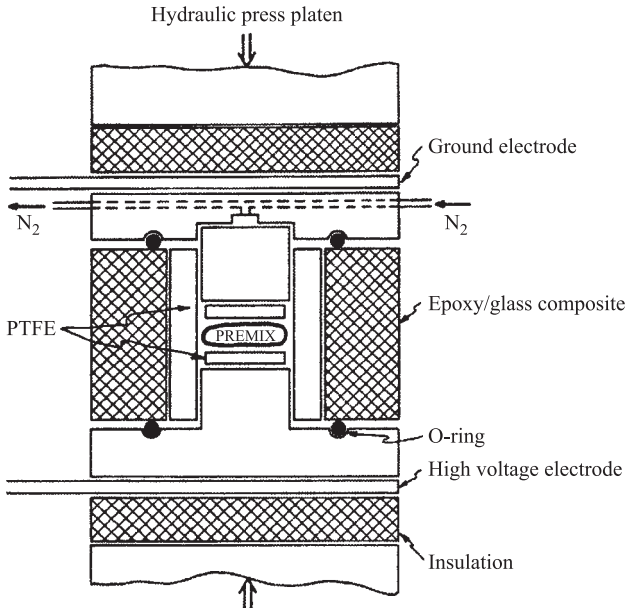


**Figure 12.12** The premix is enclosed in a pressure chamber between two heated press platens. Nitrogen gas is used to saturate the resin with gas. Dielectric power is supplied for a set duration to control the bubble size.

**Table 12.5 Physical Properties of the SMC and Foamed SMC**

	<i>SMC</i>	<i>Microcellular SMC (30% foam)</i>
Density ( $10^3 \text{ kg/m}^3$ )	1.80	1.05
Flexural strength (MPa)	112	116
Maximum strain (%)	1.9	5.7
Specific flexural strength (MPa)	62	111
Toughness ( $10^8 \text{ J/m}$ )	1.06	3.31
Specific toughness ( $10^5 \text{ J/(kg}\cdot\text{m}^2\text{)}$ )	0.59	3.15

The relationship between the FRs and PVs is given by a diagonal matrix. Therefore, the process design is an uncoupled design.

When the dielectric power was on for 10 seconds, the resulting bubble size was about  $10 \mu\text{m}$ . The physical and mechanical properties of the conventional and the foamed SMC composite are given in table 12.5.

It is interesting to note that the lightweight SMC is far superior in specific strength and toughness. Although the flexural strength is about the same for both composites, the specific strength of the lightweight SMC is much better than the conventional SMC because of its low density, which is about 60% of the conventional SMC. The foamed SMC is five times tougher than the conventional SMC.

## 12.4 Layered Manufacturing Processes for Rapid Prototyping

Another means of manufacturing composite parts is the “layered manufacturing process,” sometimes known as “rapid prototyping.” The goal of rapid prototyping is

to produce solid bodies that can be used as a prototype in product development, or as a master that can be replicated by other techniques such as casting or RTM, to make a large number of parts.

The layered manufacturing process technology can be used to make composite parts with different ingredients at different places to satisfy specific needs—a composite of composites.

There are a variety of layered manufacturing processes: 3-D printing of solid powders (Sachs et al., 1993), curing of resin layer by layer in a resin-based system, laser welding of powders, and others. Some of these techniques satisfy the independence axiom. In this section, the functional requirements of a layered manufacturing process will be stated and a rapid prototyping process will be developed. This is done to illustrate the process.

#### 12.4.1 Design of Layered Manufacturing Process

The highest functional requirement of rapid prototyping may be stated as

**FR** = Produce three-dimensional composite parts rapidly.

The design parameter is

**DP** = Rapid prototyping machine.

The process variable may be stated as

**PV** = Layered manufacturing process.

From now on, we will zigzag among the functional domain, the physical domain, and the process domain to obtain the FR, DP, and PV hierarchy. The highest level FR may be decomposed to define the FRs of the DP (rapid prototyping machine) that perform the PV (layered manufacturing process) as

**FR<sub>1</sub>** = Provide two-dimensional information for each layer of a 3-D part

**FR<sub>2</sub>** = Deposit a thin layer of selected materials

**FR<sub>3</sub>** = Bond the powders that should form a continuum

**FR<sub>4</sub>** = Remove unwanted materials

**FR<sub>5</sub>** = Build up the body layer by layer.

The design parameters are

**DP<sub>1</sub>** = Digitized two-dimensional information

**DP<sub>2</sub>** = Thin layer of selected powders

**DP<sub>3</sub>** = Adhesive ink jet

**DP<sub>4</sub>** = Vacuum suction

**DP<sub>5</sub>** = Table motion.

The process variables are

**PV<sub>1</sub>** = Computer memory for matrix table of  $n \times m$  pixels

**PV<sub>2</sub>** = Powder dispenser and horizontal table

**PV<sub>3</sub>** = Ink jet that scans in two dimensions

**PV<sub>4</sub>** = Suction tube that scans in two dimensions

**PV<sub>5</sub>** = Step motor with ball screw for motion in vertical direction.

The products and the process conceived by the above FRs, DPs, and PVs constitute a layered manufacturing process in which thin photoreactive resin

(i.e., photoresist) is deposited on a table that is scanned by a light source to cross-link the resin based on the information supplied by the computer. Unreacted resin is removed by a vacuum suction tube that also rasters the resin surface after the reaction is completed.

The product design matrix for the FR/DP relationships is

$$\begin{Bmatrix} \text{FR}_1 \\ \text{FR}_2 \\ \text{FR}_3 \\ \text{FR}_4 \\ \text{FR}_5 \end{Bmatrix} = \begin{bmatrix} X & 0 & 0 & 0 & 0 \\ 0 & X & 0 & 0 & 0 \\ 0 & 0 & X & 0 & 0 \\ 0 & 0 & 0 & X & 0 \\ 0 & 0 & 0 & 0 & X \end{bmatrix} \begin{Bmatrix} \text{DP}_1 \\ \text{DP}_2 \\ \text{DP}_3 \\ \text{DP}_4 \\ \text{DP}_5 \end{Bmatrix} \quad (12.21)$$

The product (i.e., the machine) is an uncoupled design. The design matrix for the DP/PV relationship is

$$\begin{Bmatrix} \text{DP}_1 \\ \text{DP}_2 \\ \text{DP}_3 \\ \text{DP}_4 \\ \text{DP}_5 \end{Bmatrix} = \begin{bmatrix} X & 0 & 0 & 0 & 0 \\ 0 & X & 0 & 0 & 0 \\ X & 0 & X & 0 & 0 \\ 0 & 0 & 0 & X & 0 \\ 0 & 0 & 0 & 0 & X \end{bmatrix} \begin{Bmatrix} \text{PV}_1 \\ \text{PV}_2 \\ \text{PV}_3 \\ \text{PV}_4 \\ \text{PV}_5 \end{Bmatrix} \quad (12.22)$$

The process is a decoupled design. Each one of the first-level FRs, DPs, and PVs must now be decomposed to complete design of the machine.

When a composite of composite parts is to be made, where many different kinds of powders have to be used at a given layer, the above design can be adopted to achieve the deposition of different powders. For example, after bonding the powder of a given layer, unbonded powder can be removed by vacuuming. Then a layer of the second powder should be applied to fill in the section that has just been vacuumed and the adhesive can be applied selectively. This process can be repeated until all the desired materials are placed at the right location of the layer.

The parts can be used with the adhesive bonding or they can be sintered by heating the part in a furnace at a predetermined heating and cooling rates.

#### 12.4.2 Information Content of Layered Manufacturing Process

The information content of layered manufacturing processes may be less than that of typical manufacturing processes such as casting and machining, because the information required for layered manufacturing processes is two dimensional. In the case of three-dimensional printing, regardless of the complexity of the three-dimensional part, the manufacturing process is reduced to a cyclic, two-dimensional process of depositing the powder, followed by selective bonding of particulates. The two-dimensional process repeats itself over and over again until the final part is manufactured. Thus, the information content associated with the manufacturing process is greatly reduced if the dimensional tolerance is comparable to the particle size and if the part does not have to be subjected to any additional manufacturing processes to meet other functional requirements. If the part has to be heat treated or finished to final accuracy, a layered manufacturing process may require more information.

## 12.5 USM Foam Molding Process

### 12.5.1 Statement of the Problem

USM Corporation was interested in selling machines that can make a foamed plastic shoe sole, shown in figure 12.13. The core of the sole was to be made of foamed polyvinylchloride (PVC) of uniform density  $\rho$  for light weight, comfort, and flexibility. The outer skin was to be a solid PVC layer of thickness  $b$  for good wear resistance. It was decided that the machine should be based on the injection molding process, as shown in figure 12.14, since the firm was the major supplier of injection molding machines to the shoe-making industry. A young engineer was asked to design a manufacturing process that can manufacture the shoe sole inexpensively.

### 12.5.2 Solution

In response to the problem statement, a new process was developed (Suh, 1961), which is known as the USM high-pressure foam molding process. The process is now extensively used to make furniture panels, automobile components, and television cabinets. The solution is a straightforward application of the axioms, although at the

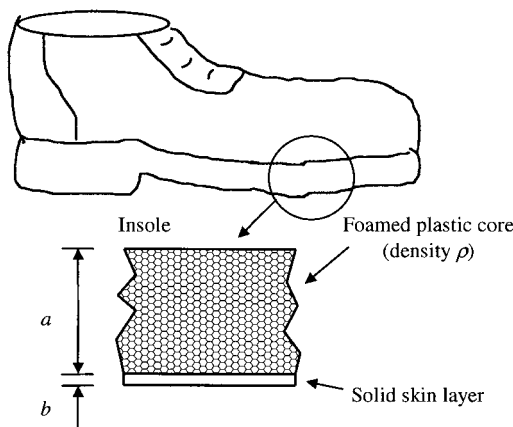


**Figure 12.13** Construction of the USM foamed plastic shoe sole; the core is to be a foamed structure and the outer layer is to be an unfoamed, solid plastic layer.

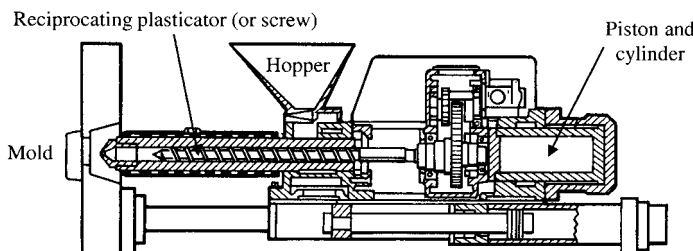


**Figure 12.14** Schematic view of a conventional injection molding machine (Tadmor and Gogos, 1979).

time of invention these principles were intuitively used, since no formal axiomatic statement was available.

Based on the perceived needs of the marketplace that the corporation was trying to satisfy, the FRs of the product may be written as

$$FR_1 = \text{Increase flexibility}$$

$$FR_2 = \text{Decrease weight}$$

$$FR_3 = \text{Increase wear resistance.}$$

The product that was designed to satisfy these FRs is shown in figure 12.13. The DPs of the product are

$$DP_1 = \text{Thickness of the foamed core, } a$$

$$DP_2 = \text{Foamed plastic core of uniform density, } \rho$$

$$DP_3 = \text{Solid plastic layer of uniform thickness, } b.$$

The design matrix may be expressed as

$$\begin{Bmatrix} FR_1 \\ FR_2 \\ FR_3 \end{Bmatrix} = \begin{bmatrix} X & 0 & 0 \\ X & X & 0 \\ 0 & 0 & X \end{bmatrix} \begin{Bmatrix} DP_1 \\ DP_2 \\ DP_3 \end{Bmatrix}$$

In order to obtain a uniform density  $\rho$  throughout the core of the shoe sole, where the thickness varies significantly, especially the heel section, it is clear that the material must be uniformly distributed in proportion to the thickness of each section of the sole. However, a compressible material such as foamed plastic cannot be uniformly distributed by injection molding unless uniform pressure can be applied to the compressible material, which is not possible in the conventional injection molding process, since the pressure is different throughout the mold. On the other hand, the incompressible material such as solid plastic can be distributed to fill a given space, even when the pressure distribution is not uniform. This reasoning leads to the solution.

However, before explaining the solution any further, the process of injection molding foamed plastic is described here briefly for those readers who are not familiar with polymer processing. Plastic granules from a hopper are fed into the reciprocating plasticator (or screw), as shown in figure 12.14, with blowing agents. The blowing agents can be in form of a chemical compound (typically a fine powder) dusted on the pellets, that decomposes into gases at the processing temperature in the reciprocating plasticator (or screw), or a physical compound that vaporizes at the processing temperature. In processing PVC, the chemical blowing agent in powder form is used. This blowing agent is thoroughly mixed in the plasticator with PVC, but the decomposed blowing agent cannot expand in the plasticator, due to the high pressure imposed on the plastic. When the plastic is extruded or injected into a low-pressure region, it expands, forming a cellular structure because of the expansion of the gas. However, if this plastic with foaming agent is injected into the mold, the density of the part will vary a great deal, due to the variation in pressure and high compressibility of the foamed plastic.

Now, returning to the specific solution sought for the problem at hand, it is clear that the molten plastic with foaming agent must be prevented from foaming until the incompressible material is uniformly distributed throughout the mold. When the incompressible, unfoamed plastic is uniformly distributed, we can let the plastic

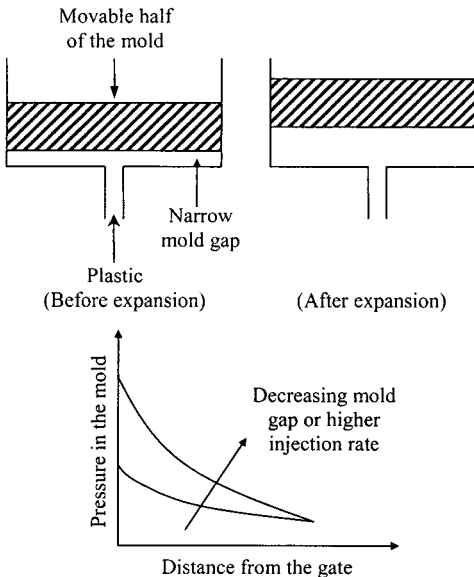


**Figure 12.15** Schematic illustration of the proposed solution; Initially the mold gap is narrowed to prevent foaming due to high pressure, and to fill the mold with unexpanded plastic. Then the mold is expanded. The thickness of the solid skin layer is determined by the temperature of the movable half of the mold and the time elapsed before expansion.

foam under uniform pressure create foamed plastic with a desired density. All of these conditions can be satisfied by using an expandable mold. The idea is as follows:

1. Make the mold such that its cavity depth can be varied by moving one side of the mold, as shown in figure 12.15.
2. Narrow the gap of the mold before injecting the plastic, and then inject the plastic at high velocity. The narrow gap and the high injection rate will increase the pressure distribution throughout the molten plastic flowing into the mold, except at the plastic flow front, which is at the ambient pressure. This is illustrated schematically in figure 12.15. Because of the high pressure, foaming will not take place until the mold is completely filled with incompressible plastic.
3. Knowing how incompressible material is distributed in the mold, the mold volume can be expanded by moving the movable half of the mold. The final density is controlled by the expansion ratio of the mold.
4. Since plastic cannot expand at low temperature even when blowing agents are present, the thickness of the skin layer at the surface can be controlled by lowering the temperature of the plastic near the mold surface. The thickness is thus controlled by cooling the mold surface, and by varying the elapsed time before the mold expansion.

We are looking for a process design that will yield  $PV_1$ ,  $PV_2$  and  $PV_3$  such that the design matrix is a diagonal matrix. If we let the expansion of the mold be  $PV_1$  (denoted by  $\varepsilon$ ), the injection velocity  $PV_2$  (denoted by  $V$ ), and the temperature of the mold surface be  $PV_3$  (denoted by  $T$ ), the design equation for the proposed manufacturing process may be written as

$$\begin{Bmatrix} a \\ \rho \\ b \end{Bmatrix} = \begin{bmatrix} X & 0 & 0 \\ X & X & 0 \\ 0 & X & X \end{bmatrix} \begin{Bmatrix} \varepsilon \\ V \\ T \end{Bmatrix} \quad (12.23)$$

The design matrix for the manufacturing process states that the proposed design is a decoupled process. Instead of using  $T$  as  $PV_3$ , the cooling time  $t$  could have been used to vary  $b$ . However, the cycle time consideration dictated that  $t$  be fixed and temperature be varied.

After the proposed design was implemented, good products were made. However, in some cases the density of the foam near the edge was lower due to larger bubbles, because the pressure at the flow front is always atmospheric. In order to solve this problem, an additional FR must be added to equation (12.23) (Suh, 1990). How would you solve this problem?

## 12.6 Concluding Remarks

In this chapter, axiomatic design theory has been applied to the design of materials and materials-processing techniques. Four case studies on microcellular plastics, microcellular composites, the layered manufacturing process for rapid prototyping of physical objects, and the USM foam molding process have been presented.

In the first example, it was shown that the materials can be designed first, and then the process for creating the designed materials can be designed logically and systematically.

In the second example, lower density SMC composites that have better mechanical properties were designed and manufactured. The lightweight SMC has much superior mechanical properties because the introduction of voids eliminates the shrinkage of the resin and thus the residual stress.

In the third example, the process of innovation was illustrated by describing how a new layered manufacturing process might be developed to make composites of composites.

In the fourth example, a new process for development of foamed plastic shoe soles was presented. The process was developed to satisfy industrial needs by developing FRs and a new manufacturing process. This process has been used commercially to make furniture panels and automotive parts rather than shoe soles.

## Problems

- 12.1. A company is interested in developing a micromirror of  $100\text{ }\mu\text{m}$  by  $100\text{ }\mu\text{m}$  (dimension of each side) that can be controlled to reflect light to different directions for illumination. The idea is to use the lithography technique of putting patterns on a silicon wafer, etching away materials, and building up desired materials by deposition. The central idea is to use the lithography technique to build piezoelectric actuators behind the mirror as an integral part. The deflection of the piezoelectric actuators will move the mirror about its pivot point to bounce off the light. Your job is to design a process that can do the job.
- 12.2. Design a process for making “solder bumps,” which are spheres of lead/tin alloy for use in bonding electrical components on a printed circuit board.
- 12.3. Design structural composites that can replace wood in constructing dwellings. They must be competitive in price and have functional advantages. The composites may use wood chips and resins.

**12.4.** Design automobile bumpers that can protect cars with a mass of 1500 kg at a collision speed of 10 km/hour. They should have mass less than 4 kg and cost less than \$5/part.

### Notes

1. This section is adopted from chapter 7 of *Axiomatic Design: Advances and Applications*, Oxford University Press, New York, 2001.
2. The microcellular plastics and the MCP process were originally invented at MIT and further developed by Trexel, Inc., Woburn, MA, USA, under the tradename MuCell as an exclusive licensee of MIT.
3. Trade name of Trexel, Inc., Woburn, MA.
4. In conventional injection molding, additional pressure (i.e., packing pressure) must be applied to the plastic after the mold is filled to pack in more plastic as the plastic shrinks so as to replicate the detailed geometry of the mold.
5. The material presented in this section is adopted from J. R. Youn, *Lightweight Polyester Composites*, Ph.D. Thesis, Department of Mechanical Engineering, MIT, 1984.

### References

- Baldwin, D. F. 1994. *Microcellular Polymer Processing and the Design of a Continuous Sheet Processing System*, Ph.D. Thesis, Department of Mechanical Engineering, MIT, Cambridge, Mass.
- Baldwin, D. F., Suh, N. P., Park, C. B., and Cha, S. W. 1994a. "Super-Microcellular Foamed Materials," *U.S. Patent 5334356*.
- Baldwin, D. F., Tate, D. E., Park, C. B., Cha, S. W., and Suh, N. P. 1994b. "Microcellular Plastics Processing Technology," *Journal of the Japan Society of Polymer Processing*, Vol. 6, pp. 187–256.
- Baldwin, D. F., Park, C. B., and Suh, N. P. 1996. "An Extrusion System for the Processing of Microcellular Polymer Sheets: Shaping and Cell Growth Control," *Polymer Engineering and Science*, Vol. 36, No. 10, pp. 1425–1435.
- Cha, S. W. 1994. *Foaming of Super-Microcellular Plastics*, Ph.D. Thesis, Department of Mechanical Engineering, MIT, Cambridge, Mass.
- Cha, S. W., Suh, N. P., Baldwin, D. F., and Park, C. B. 1992. "Microcellular Thermoplastic Foamed with Supercritical Fluid," *U.S. Patent 5158986*.
- Colton, J. S. 1985. *The Nucleation of Thermoplastic Microcellular Foam*, Ph.D. Thesis, Department of Mechanical Engineering, MIT, Cambridge, Mass.
- Colton, J. S., and Suh, N. P. 1987a. "The Nucleation of Microcellular Thermoplastic Foam with Additives: Part II: Experimental Results and Discussion," *Polymer Engineering and Science*, Vol. 27, pp. 493–499.
- Colton, J. S., and Suh, N. P. 1987b. "Nucleation of Microcellular Foam: Theory and Practice," *Polymer Engineering and Science*, Vol. 27, pp. 500–503.
- Colton, J. S., and Suh, N. P. 1990. "Microcellular Semi-Crystalline Thermoplastic Foam," *U.S. Patent 4922082*.
- Colton, J. S., and Suh, N. P. 1992. "Microcellular Foam of Semi-Crystalline Polymeric Material," *U.S. Patent 5160674*.
- Durril, P. L., and Griskey, R. G. 1966. "Diffusion and Solution of Gases in Thermally Softened or Molten Polymers: Part I. Development of Technique and Determination of Data," *AIChE Journal*, Vol. 12, pp. 1147–1151.
- Durril, P. L., and Griskey, R. G. 1969. "Diffusion and Solution of Gases into Thermally Softened or Molten Polymers: Part II. Relation of Diffusivities and Solubilities with Temperature, Pressure and Structural Characteristics," *AIChE Journal*, Vol. 15, pp. 106–110.
- Martini, J. 1981. *The Production and Analysis of Microcellular Foam*, S. M. Thesis, Department of Mechanical Engineering, MIT, Cambridge, Mass.

- Martini, J., Suh, N. P., and Waldman, F. A. 1982. "The Production and Analysis of Microcellular Thermoplastic Foam," *Society of Plastics Engineers Technical Papers*, Vol. 28, pp. 674–676.
- Martini, J., Waldman, F. A., and Suh, N. P. 1984. "Microcellular Closed Cell Foams and Their Method of Manufacture," *U.S. Patent 4473665*.
- Park, C. B. 1993. *The Role of Polymer/Gas Solutions in Continuous Processing of Microcellular Polymers*, Ph.D. Thesis, Department of Mechanical Engineering, MIT, Cambridge, Mass.
- Park, C. B., Baldwin, D. F., and Suh, N. P. 1995. "Effect of the Pressure Drop Rate on Cell Nucleation in Continuous Processing of Microcellular Polymers," *Polymer Engineering and Science*, Vol. 35, pp. 432–440.
- Park, C. B., Baldwin, D. F., and Suh, N. P. 1996. "Axiomatic Design of a Microcellular Filament Extrusion System," *Research in Engineering Design*, Vol. 8, No. 3, pp. 166–177.
- Sachs, E. M., Cima, M., Cornie, J., Brancazio, D., Bredt, J., Lee, J., and Michaels, S. 1993. "Three Dimensional Printing: the Physics and Implications of Additive Manufacturing," *Annals of CIRP*, Vol. 42, No. 1, pp. 257–260.
- Sanyal, Y. 1998. *Synthesis and Analysis of a Microcellular Plastics Extrusion System for Insulation of Fine Wires*, Ph.D. Thesis, Department of Mechanical Engineering, MIT, Cambridge, Mass.
- Seeler, K. A., and Kumar, V. 1992. "Tension-Tension Fatigue of Microcellular Polycarbonate: Initial Results," *Journal of Reinforced Plastics and Composites*, Vol. 12, pp. 359–376.
- Suh, N. P. 1961. *USM Corporation Report*, EX 18422, (unpublished).
- Suh, N. P. 1990. *The Principles of Design*, Oxford University Press, Oxford.
- Suh, N. P. 1996. "Microcellular Plastics," in *Innovation in Polymer Processing: Molding*, Edited by Stevenson, J., Hanser Publishers, New York, pp. 93–149.
- Tadmor, Z., and Gogos, C. G. 1979. *Principles of Polymer Processing*, John Wiley & Sons, New York.
- Taylor, G. I. 1934. "The Formation of Emulsion in Definable Fields of Flow," *Proceedings of the Royal Society*, London, Vol. 146A, p. 501.

# 13

## Axiomatic Design of Composite Robot Structures

### 13.1 Introduction

A robot is defined as “a machine capable carrying out a complex series of actions automatically,” by the *Oxford English Reference Dictionary*. The definition by the Robotics Institute of America is more specific: “A robot is a re-programmable multi-functional manipulator designed to move material, parts, tools, or specialized devices, through variable programmed motions for the performance of a variety of tasks.” Examples of robots include mechanical manipulators, numerical control machines, walking machines, and the humanoids of science fiction, although most people perceive robots anthropomorphically (Tsai, 1999; Koren, 1985; Craig, 1989). Most industrial robots are mechanical manipulators.

Robots can be classified according to various criteria, such as their degrees of freedom, drive technology, workspace geometry, and motion characteristics.

A manipulator with six degrees of freedom is called a general purpose robot because at least six degrees of freedom are required to manipulate an object in three-dimensional space. A redundant robot possesses more than six degrees of freedom to move around obstacles and operate in a tightly confined workspace. A deficient robot possesses less than six degrees of freedom.

If every moving link is driven by one actuator mounted on its preceding link through a gear reduction unit, this type of manipulator is called a conventional serial manipulator. On the other hand, if each joint is driven directly by an actuator without a speed reducer, the manipulator is called a direct-drive manipulator. The direct-drive technique eliminates the problems associated with gear backlash and can possibly increase the speed of manipulator (Asada and Youcef-Toumi, 1987). However, direct-drive robots use heavy and bulky DC motors. Consequently, the direct-drive technique is used to drive the first joint of a manipulator where the motor can be installed on the base. Alternatively, they can also be installed on the base to drive the second or third joint via a push-rod linkage or a metal belt.

A robot is also classified by the workspace, which is defined as the volume of space the end effector can reach. The simplest kinematic structure of a robot arm is made up three mutually perpendicular prismatic joints. This type of robot is known as a Cartesian robot. The wrist center position of a Cartesian robot can be described by three Cartesian coordinates associated with the three prismatic joints. A robot arm is called a cylindrical if either the first or second joint of a Cartesian robot is replaced by a revolute joint. A robot arm is said to be articulated or

anthropomorphic if all three joints are revolute. The workspace of an articulated robot is very complex. The SCARA (Selective Compliance Assembly Robot Arm) robot consists of two revolute joints followed by a prismatic joint. In addition, all three joint axes are parallel to each other and usually point along the direction of gravity. Thus, the first two actuators do not have to work against the gravitational forces of the links and the payload. The wrist usually has only one degree of freedom. Hence the entire robot has four degrees of freedom (Tsai, 1999). The SCARA robot is widely used for assembling parts on a plane, such as a printed circuit board (PCB).

Human beings may be thought as direct-drive robots where many muscles play a role of direct drive motors. However, contradictory to science fiction, humans are much superior to robots in the structural point of view because the densities of muscles and bones of humans are one order lower than steel or copper, which are the major structural materials for robots and electric motors.

Aluminum or titanium cannot be substitutes for steel used for precision robot structures because the specific stiffness of these two materials is almost the same, as shown in table 1.2. The typical payload of a current assembling robot weighing 2500 N is less than 100 N, which is very small compared with the capability of human weightlifters. Therefore, without overcoming this weight penalty of current robot structures, robots cannot compete with human beings except in the area of “3D” (dirty, dangerous, difficult) jobs such as welding, spray painting, and casting. In this chapter, the applications of composite materials to robot structures are presented, with examples of how to overcome the heavy weight of robot structures based on the axiomatic design principle.

## 13.2 Composite Double-Arm-Type Robot Hands and Wrists for LCD Panel Handling

Industrial robots are employed increasingly in LCD (liquid crystal display) glass panel manufacturing in clean room environments to eliminate contamination from human workers. Figure 13.1 shows a typical robot system used for loading and unloading LCD glass panels into a cassette (Oh et al., 1999). The robot has three

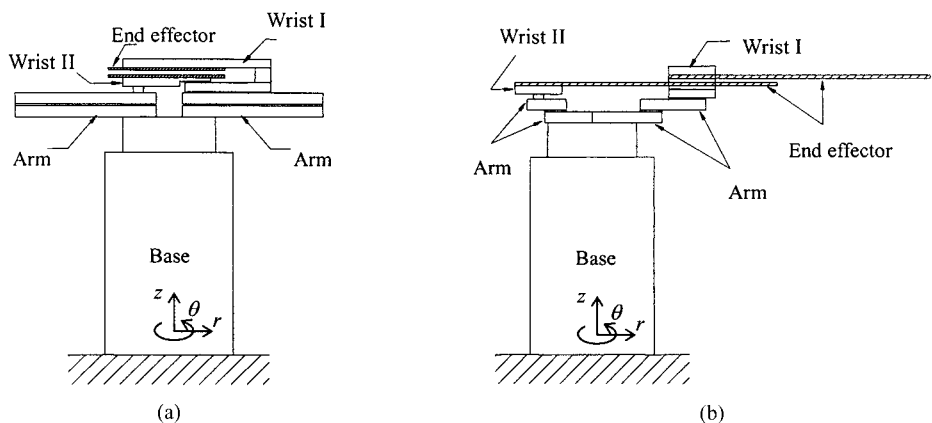


**Figure 13.1** Typical robot system used for loading and unloading glass panels: (a) Front view; (b) side view.

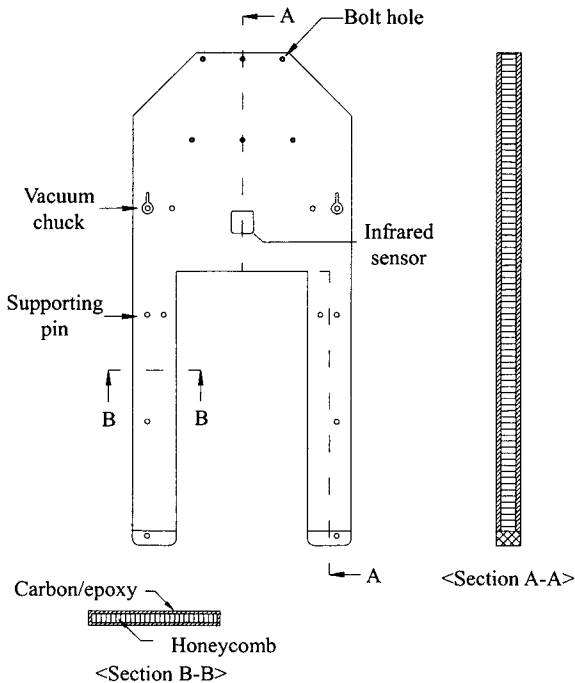


**Figure 13.2** Configuration of the fourth generation composite end effector.

degrees of freedom ( $r, \theta, z$ ), and is composed of a base, two arms, two wrists, and two end effectors (also called “hands” in this industry). The robot is shown also in figure 2.6(c).

In order to prevent particles from flowing into the clean room environment, the arm joint sections are sealed with ferrofluidic materials. A mirror surface quality of composite hands is required to prevent any dirt from adhering to the hand surface, which requires a mirror surface quality of the mold also. Figure 13.2 shows the configuration of the fourth-generation composite end effector.

The fourth-generation robot handles a glass panel of  $670\text{ mm} \times 830\text{ mm} \times 0.7\text{ mm}$ . The end effectors are mounted on the wrists located at the ends of the first and second arms using six bolts. Two vacuum chucks are located on the end effector to secure the glass panel on the end effector. The glass panel is loaded on the 10 cone-shaped pins mounted on the end effector, to prevent the end effector from scratching the surface of glass panel. An infrared sensor is used to detect the existence of the glass panel on the end effector. The central part of the end effector opposite to the wrist is eliminated to reduce weight and interference with other equipment.

The robots with double-arm-type structures are favored by glass panel manufacturers because of productivity improvement. The components of the double-arm-type robot of the fifth generation are two arms, wrists, and hands, as shown in figure 13.3 (Lee and Lee, 2004; Lee et al., 2002). The two wrists have dissimilar configurations to avoid interference when moving back and forth.

To meet the requirements of increased size of glass panel displays, the size and stiffness of the robot hands and wrists are also increased to reduce the deflection of the robot structure due to the weight of the LCD glass panel display and the dead weight of the robot structure. The size and stiffness increase of robot structure requires large working space and large motor power. The problem of increased weight of a robot for higher stiffness can be only solved if a high-specific-modulus

composite material such as carbon-fiber epoxy composite is used for robot structures because currently developed high-modulus carbon-fiber epoxy composite has a specific stiffness about ten times as high as that of conventional metals such as aluminum and steel. Moreover, carbon-fiber composite not only have high specific stiffness, but also have high specific strength, high damping (Crawley and Mohr, 1983), and low coefficient of thermal expansion.

The size of an LCD glass panel of the fifth generation has increased to 1250 mm × 1100 mm × 0.7 mm, weighing about 27 N, which requires much larger and stiffer robot structures. The difference of maximum deflections of the four hands should be less than 2.0 mm.

### 13.2.1 Problem Definition

The double-arm-type robot structure of figure 13.3 is composed of a base, two arms, two wrists, and two hands (or end effectors). The two hands are mounted on the two wrists. One wrist has a C-shape and the other has a flat plate shape to avoid interference between the upper and the lower glass panels when moving. The C-shaped wrist and its hand are defined as wrist I and hand I, and the flat-plate-shaped wrist and its hand as wrist II and hand II, respectively, for convenience.

Due to the requirement of increased speed of back-and-forth movement of the robot for productivity improvement, the large LCD glass panel is vulnerable to vibration and fracture unless robot hands and wrists have enough stiffness both in bending and twisting. Therefore, the robot wrists and hands should be designed with high bending and torsional rigidities without much increase in weight. A material with high damping will be beneficial for suppressing vibration during fast start and stop.

In addition to the high rigidities, the robot hands for glass panel handling should satisfy several other strict constraints: The cross-sectional height of the hand should be less than 15 mm because the combined height of the hand and LCD glass panel should be less than that of the cassette (about 20 mm) with the gap tolerance for inserting and removing of LCD glass panel. The cross-sectional width of the hand should be less than 100 mm to prevent the warped LCD glass panel from the contacting surface of the hand due to gravity. The deflection of the hand due

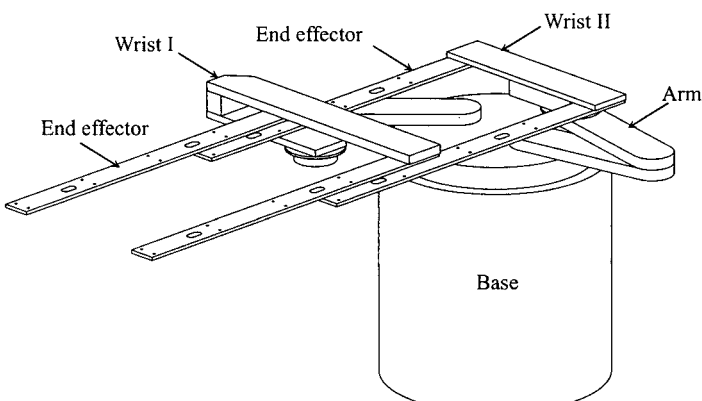


**Figure 13.3** Typical double-arm-type robot system (fifth generation) used for loading and unloading glass panels into a cassette.

to the dead weight of the robot hand and the LCD glass panel weight should be less than 2.0 mm.

Therefore, the cross-sectional shapes for the hand and wrist are determined to be sandwich structures with a foam core because the sandwich structure has the highest specific stiffness, as shown in figure 2.42 and section 6.11 of chapter 6. The width and height of the hand were determined to be 100 and 15 mm, respectively, to maximize the bending rigidity. With these constraints, the highest level functional requirements (FRs) and design parameters (DPs) of the robot hands are stated as follows:

**FR** = Enhance the specific static and dynamic bending characteristics of the robot hand

**DP** = Dimensions of the hand and structural material

**C<sub>1</sub>** = Cross-sectional area should be less than 100 mm × 15 mm

**C<sub>2</sub>** = Length of the hand should be less than 1400 mm

**C<sub>3</sub>** = Deflection of the hand should be less than 2.0 mm

**C<sub>4</sub>** = LCD glass panel should be mounted on the hand.

The specific characteristics mean the characteristics of robot divided by its density of material ( $\rho$ ) or sometimes by its specific gravity ( $\rho g$ ). The dynamic stiffness of structure is defined by the product of stiffness times damping because the amplitude of vibration at resonance is inversely proportional to the dynamic stiffness (Rivin, 1999). Since the bending deflection of the hand under a distributed load is a function of longitudinal stiffness, moment of inertia, and magnitude of distributed load, the highest level of the FRs and DPs may be decomposed as follows:

**FR<sub>1</sub>** = Increase moment of inertia,  $I$  without increasing weight

**FR<sub>2</sub>** = Increase the specific stiffness of faces of robot hand

**FR<sub>3</sub>** = Increase damping.

**DP<sub>1</sub>** = Composite face thickness of box-type sandwich cross-section

**DP<sub>2</sub>** = High-modulus carbon composite

**DP<sub>3</sub>** = Epoxy matrix and core (honeycomb and foam).

In order to increase the specific stiffness of the robot hands, very high modulus pitch-based carbon-fiber epoxy material (URN300) is selected for the robot hand because it has high specific stiffness ( $E/\rho$ ) and high damping due to the polymeric matrix (epoxy). Table 13.1 shows the FR-DP matrix for the robot hands, which is a decoupled design.

If we selected a metallic material for the hand, such as aluminum, steel, or tungsten, we would have had a coupled design matrix, or a narrow design range compared with a high-specific-stiffness carbon composite, because the metallic materials have nearly same specific longitudinal stiffness ( $E/\rho$ ) which is about one order lower than that of a high-modulus carbon-fiber epoxy composite, as shown in tables 2.2 and 2.3.

**Table 13.1 FR-DP Matrix for the Robot Hands**

	DP <sub>1</sub>	DP <sub>2</sub>	DP <sub>3</sub>
FR <sub>1</sub>	X	0	0
FR <sub>2</sub>	X	X	0
FR <sub>3</sub>	x	0	X

The damping capacity of metallic materials is very low and becomes smaller as their Young's moduli increase (Lee, 1985). Therefore, in order to increase the damping of a metallic hand, we may need some additional damping mechanism, which will increase the weight of the robot hand and degrade the surface characteristics for the clean room environment, which results in a coupled design. Another benefit of using sandwich structures composed of carbon-fiber epoxy composite faces and a foam core is the intrinsic high damping capacity due to the epoxy and foam materials. The damping capacity of polymeric material is also one order higher than those of metallic materials (Jeong et al., 1995; Lazan, 1965; Nashif et al., 1985; Sun and Lu, 1995).

For the robot wrists, the FRs and DPs are similar to those of the robot hands; however, both torsional rigidity as well as bending rigidity are important in this case. The box-type cross-sectional shape is selected for the wrist cross-sectional shape because the box-type shape gives both bending and torsional rigidities; consequently, it is recommended for machine tool structures (Koenigsberger, 1964). The highest levels of the FR and DP of the robot wrists are:

FR = Enhance the specific static and dynamic characteristics of the robot wrist  
 DP = Dimensions of the wrist and structural material

$C_1$  = Shape of the wrists

$C_2$  = Outer dimensions

$C_3$  = Maximum difference between deflections of the four hands mounted on the wrists should be less than 2.0 mm.

The highest levels of the FR and DP were decomposed as

$FR_1$  = Increase bending moment of inertia and polar moment of inertia  $J$

$FR_2$  = Increase the specific stiffness of face of the wrist

$FR_3$  = Determine the value of  $R = E/G$  to reduce the deflection of the hand due to bending and torsion

$FR_4$  = Increase damping.

$DP_1$  = Dimensions of the box-type sandwich cross-section

$DP_2$  = Carbon-fiber composite

$DP_3$  = Stacking angle of carbon fiber,  $\theta$

$DP_4$  = Epoxy matrix and core (honeycomb and foam).

Table 13.2 shows the FR-DP matrix for the robot wrists, which is a decoupled design because the FR-DP matrix is a lower triangular matrix. Since the design matrices for the hands and wrists of robot are not coupled (uncoupled and decoupled), the hands and wrists can be designed based on the axiomatic design principle.

**Table 13.2 FR-DP Matrix for the Robot Wrists**

	$DP_1$	$DP_2$	$DP_3$	$DP_4$
$FR_1$	$X$	0	0	0
$FR_2$	$X$	$X$	0	0
$FR_3$	0	0	$X$	0
$FR_4$	$x$	0	$x$	$X$

In table 13.2,  $FR_4$  (damping) is weakly dependent on the stacking angle  $DP_3(\theta)$  because the damping capacity of carbon epoxy composite material is a function of stacking sequence (Jeong et al., 1995).

### 13.2.2 Design of the Robot Hands and Wrists

#### *Design of the Robot Hands*

For the material of the hand, very high modulus pitch-based carbon-fiber epoxy composite (URN300, SK Chemicals, Korea) was selected. Table 13.3 shows its material properties. Using the materials properties of table 13.3 with the simple beam equation, the thickness of composite laminate can be calculated. Figure 13.4 shows the configuration of the robot hand.

Since the radius of gyration of the robot should not be larger than 1400 mm for this case, the length of the robot hand was determined to be 1400 mm. In order to maximize the bending rigidity of the hand, a unidirectional carbon-fiber epoxy prepreg (URN300) with the fiber direction in the beam axial direction was used. Polyurethane foam was used for the core of the sandwich structure. For the clamped boundary condition, the 150 mm end length of the hand was fixed because this length was clamped on the surface of the robot wrists with bolts. The clamped area of the composite hand was reinforced with 2.0 mm thickness aluminum plate for easy bolting. The dead weight of the composite hand and the glass panel weight were

**Table 13.3 Material Properties of the High-Modulus Composite Materials (URN300, SK Chemicals, Korea)**

Longitudinal modulus ( $E_1$ , GPa)	380
Transverse modulus ( $E_2$ , GPa)	5.1
Shear modulus ( $G_{12}$ , GPa)	5.5
Longitudinal strength ( $X'$ , MPa)	1000
Transverse strength ( $Y'$ , MPa)	65
Shear strength ( $S$ , MPa)	65
Poisson's ratio ( $\nu_{12}$ )	0.30
Density ( $\rho$ , kg/m <sup>3</sup> )	1750
Thickness ( $t$ , mm)	0.26

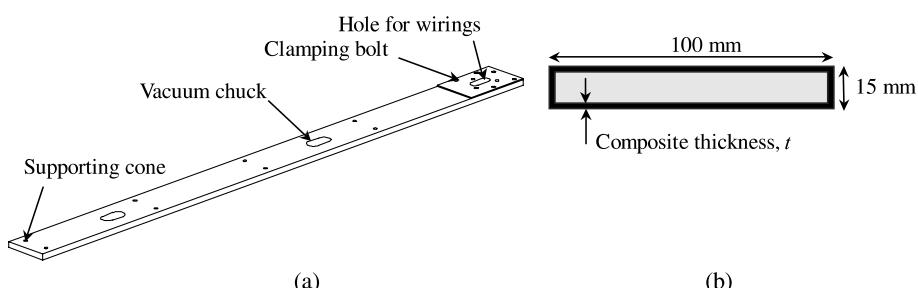


**Figure 13.4** Configuration of the robot hand: (a) Robot hand; (b) cross-sectional view.

assumed to be distributed loads. From the calculation, it was found that the thickness of the composite layer should be larger than 1.8 mm.

### *Design of the Robot Wrists*

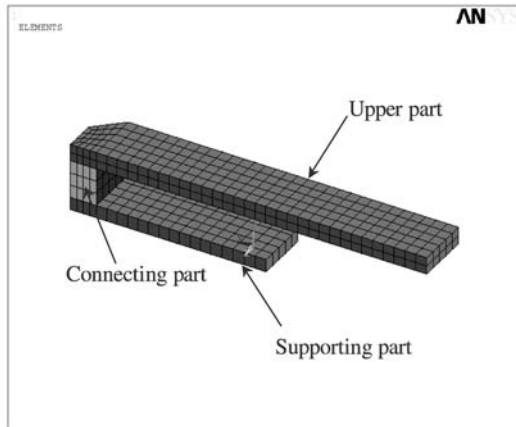
The stacking angle ( $DP_3$ ) of the composite for the robot wrists was determined by finite element analysis to find the stacking angle for the minimum deflection ( $FR_3$ ) of the hand due to torsion and bending. The thickness of the carbon-fiber composite for the minimum weight, or highest specific stiffness for the hand ( $FR_2$ ) of the robot wrists was also calculated by finite element analysis. The high-modulus carbon-fiber epoxy composite is not appropriate for the structures under shear load because the improvement in shear stiffness is only slight, and the material is expensive. Therefore, high-strength carbon-fiber epoxy prepreg (USN150, SK Chemicals, Korea) was used for the wrists. Table 13.4 shows the properties of the material. Figure 13.5 shows the finite element models of the robot wrists I and II for the determination of dimensions.

While wrist II has a light and simple shape, wrist I has a complicated C-shape to avoid interference with wrist II during movement, and consequently it is heavy. Therefore, wrist I was designed as separate components: the upper part, connecting part, and supporting part. Wrist II was also designed as separate components, the upper part and supporting part, for easy manufacturing. Since the two wrists have dissimilar shape and weight, they have different deflections at the ends of the hands, which can induce tilting of the LCD glass panel during handling. The maximum difference of deflections ( $\delta_{ij}$  of figure 13.6) of the four ends of the hands should be less than 2.0 mm, as already stated. Since wrist I has the C-shape, which is a weak shape in deflection, it should have larger a cross-section than wrist II to increase its bending and torsional rigidity, which results in a heavy wrist.

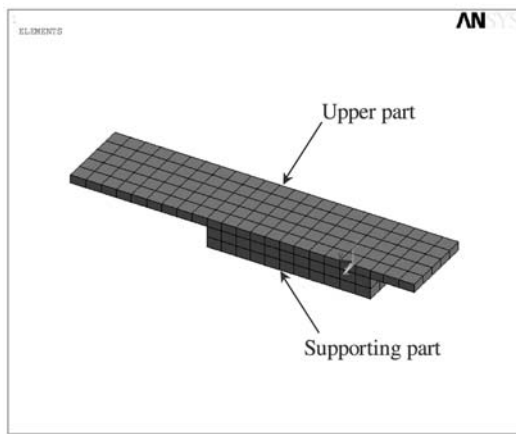
The stacking angle and thickness of the composite ply and the thickness of the foam were determined by finite element analysis using commercial software (ANSYS). The multilayered 8-node shells and 20-node quadrilateral solid elements of ANSYS were used as the modeling elements for the face and core, respectively. The multilayered 8-node shell element was adequate to model the thin structures made of composite materials because stacking angle and ply thickness of the composite structure can be input into this element. Then, the nodes around the bolt holes for

**Table 13.4 Material Properties of the High-Strength Composite Materials (USN150, SK Chemicals, Korea)**

Longitudinal modulus ( $E_1$ , GPa)	131
Transverse modulus ( $E_2$ , GPa)	10.8
Shear modulus ( $G_{12}$ , GPa)	5.65
Longitudinal strength ( $X'$ , MPa)	2000
Transverse strength ( $Y'$ , MPa)	61
Shear strength ( $S$ , MPa)	70
Poisson's ratio ( $\nu_{12}$ )	0.28
Density ( $\rho$ , kg/m <sup>3</sup> )	1540
Thickness ( $t$ , mm)	0.15



(a)



(b)

**Figure 13.5** Finite element models of the robot wrists: (a) Wrist I; (b) wrist II.

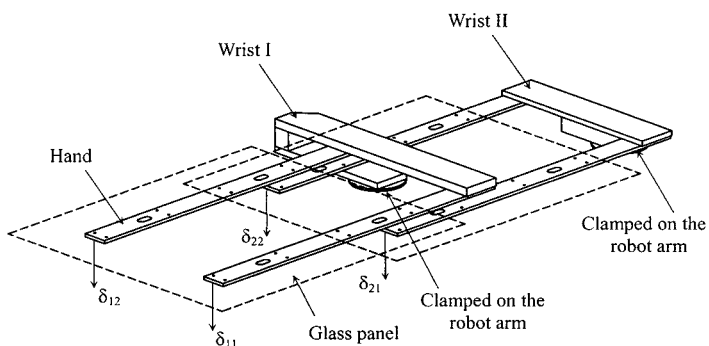


**Figure 13.6** Configuration of the hand and wrist.

clamping the wrist to the robot arm were constrained. The loads were applied in the form of nodal forces to the joining positions of the hand and glass panel for the boundary conditions. Figure 13.6 shows the configuration of the glass panel, hand, and wrist.

After the stacking sequences of the composite of the hand and wrist for the minimum deflection were determined, the outer dimensions and the composite thickness

**Table 13.5 Determined Design Variables**

<i>Wrist I</i>	<i>Wrist II</i>
$N_{IU} = 16$	$N_{IIU} = 16$
$N_{IC} = 24$	$N_{IIS} = 28$
$N_{IS} = 40$	$h_{IIU} = 25 \text{ mm}$
$h_{IU} = 40 \text{ mm}$	$h_{IIS} = 60 \text{ mm}$
$h_{IC} = 93 \text{ mm}$	$\theta_{II} = 40^\circ$
$h_{IS} = 30 \text{ mm}$	
$\theta = 30^\circ$	

**Table 13.6 Deflections of the Four Hands and Maximum Difference of Deflections (mm)**

	<i>Adjusted</i>	<i>Deflection, <math>\delta</math></i>
Wrist I:		
Hand 1	-3.8	1.9
Hand 2	-4.9	3.0
Wrist II:		
Hand 1	-2.9	1.0
Hand 2	-3.9	1.8
Maximum difference		2.0

of the faces ( $DP_1$ ) are determined by finite element analysis for the weight decrease or maximum specific stiffness ( $FR_2$ ) of the hand at constant  $R = E/G$ .

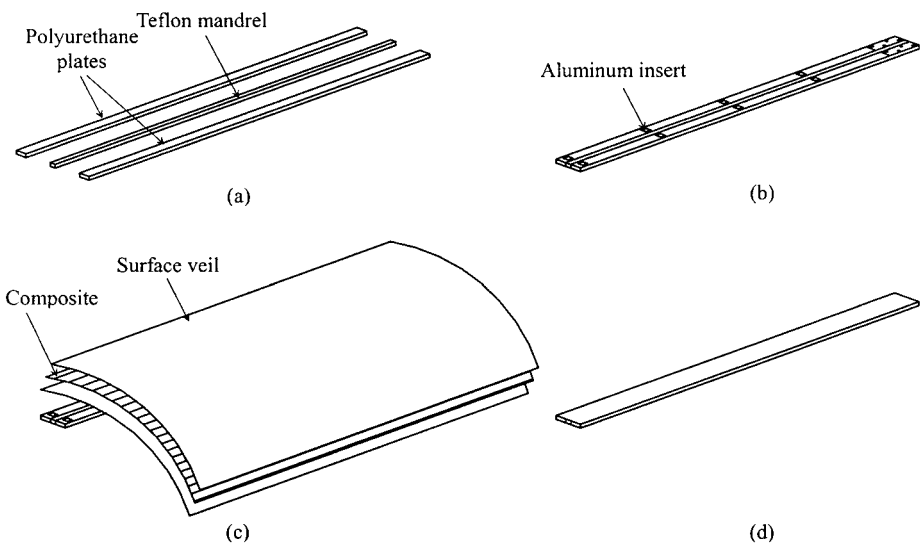
Table 13.5 shows the selected design variables and table 13.6 shows the analysis results. In table 13.5 ( $N_{IU}$ ,  $N_{IC}$ ,  $N_{IS}$ ), ( $h_{IU}$ ,  $h_{IC}$ ,  $h_{IS}$ ), and  $\theta_I$  represent the number of composite plies of the face and thicknesses of the cores of the upper part, connecting part and supporting part, and the stacking angle for wrist I, respectively. Similar notations for wrist II were used. Since the maximum difference of deflections of the four hands should be less than 2.0 mm, the initial positions of the four hands were adjusted. Then, the maximum difference of deflections of the four hands was 2.0 mm not only before, but also after loading the glass panel.

### 13.2.3 Manufacture of the Composite Robot Hands and Wrists

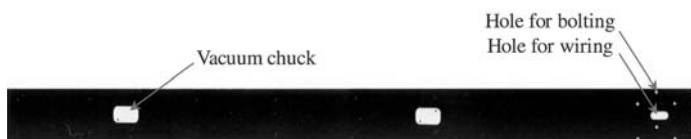
#### *Manufacture of the Robot Hands*

Figure 13.7 shows the manufacturing sequence for the composite robot hand. Eight aluminum inserts for supporting cones were adhesively bonded to the polyurethane plates. A rectangular Teflon mandrel was inserted between the two polyurethane plates to provide a passage for air tubes and electrical wiring when the Teflon mandrel was removed after curing the composite hand.

One glass surface veil was wrapped around the polyurethane foam core with aluminum blocks to eliminate galvanic corrosion between the aluminum blocks and carbon-fiber epoxy composite. Then eight-ply high-stiffness unidirectional



**Figure 13.7** Manufacturing sequence for the robot hand: (a) Polyurethane plates and Teflon mandrel before assembly; (b) assembled polyurethane plates and Teflon mandrel; (c) wrapping of composite prepreg and surface veil; (d) wrapped composite on the polyurethane plates and Teflon mandrel.



**Figure 13.8** Photograph of manufactured robot hand.

carbon-fiber epoxy prepgs were wrapped around the core. Another glass surface veil was wrapped around the stacked hand to reinforce the transverse strength of the composite hand. Then the uncured stacked composite robot hand was placed in a closed mold.

The robot hand was cured in an autoclave with a modified cure cycle, in which the dwelling time was 1 hour longer than that of the standard cure cycle. The modified cure cycle was used to give time for the excess resin in the prepg to penetrate into the polyurethane foam surface for better adhesion between the carbon epoxy composite and the polyurethane foam core. After curing the robot hand, the Teflon mandrel was removed. Then holes for vacuum chucks, bolts, and wires were machined into the composite robot surface with diamond grit drills. The end cross-sections of the robot hand were closed with nylon edge closures to prevent dust or other outside particles from being trapped. Figure 13.8 shows the manufactured robot hand. The mass of one robot hand was 0.68 kg.

#### *Manufacture of the Robot Wrists*

The manufacturing sequence for each component of the robot wrist was the same as that for the robot hands. A symmetric stacking sequence was used to prevent the wrists from warping due to the difference between the cure and room temperatures.

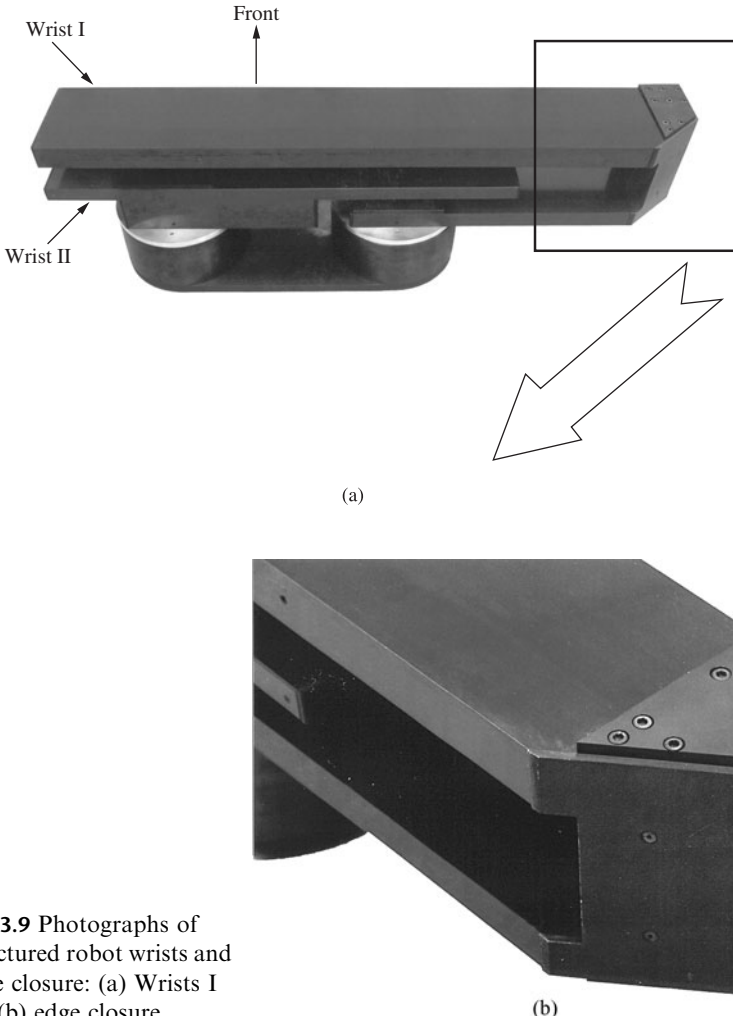


**Figure 13.9** Photographs of manufactured robot wrists and the edge closure: (a) Wrists I and II; (b) edge closure.

The separately manufactured composite components of the wrists were joined using adhesive bonding. Also the aluminum plates on which the robot hands were mounted were adhesively bonded to the surfaces of the wrists. Figure 13.9 shows photographs of the manufactured robot wrists and the edge closures. The masses of the robot wrists I and II were 7.32 and 3.43 kg, respectively.

The static deflections of the composite hands mounted on the wrists were measured under the static load of a glass panel. The constraint of the robot hand was that the deflection under the load of a glass panel should be less than 2.0 mm.

The 150 mm length of the end of the hand was clamped on the surface table. Then the glass panel was mounted on the hands and the deflection was measured. The average deflection of the hand was 1.9 mm, which satisfied the constraint. The static deflection tests of the robot wrists were performed in the same way. The hands were mounted on the wrists, and the wrists were clamped on the surface table. After adjusting initial positions of the hands, the deflections of four hands under the loading of the glass panel were measured. The maximum difference between deflections of the four hands under the loading of glass panels was 2.0 mm, which satisfied the criterion of the allowed deflection.

### 13.3 Design of Carbon Composite SCARA-Type Direct-Drive Robot

Assembly systems with industrial robots are currently mainly used for the repetitive operation of small products, such as printed circuit boards and small motors. The payload of the robot in the assembly operation need not be very large. However, fast arm acceleration and deceleration of the assembly robot are important to decrease the assembly cycle time and to increase productivity. Also, the high accuracy of the robot for the assembly operation is indispensable for correct assembly of parts.

In assembly, the traveling paths are relatively short and therefore the joints move at their maximum speed for short periods only, or they do not reach the speed limit at all. As a consequence, most paths are completed during the acceleration and deceleration periods, and increasing their permissible value shortens the assembly cycle time significantly.

The direct-drive robot has no gears for speed reduction and torque amplification, therefore, higher response and precise positioning accuracy without any backlash can be achieved. However, the heavy permanent-magnet-type direct-drive motors are mounted on the joints of the robot arm and the weight of the motors is added to the robot arm. Therefore, the size of the motor for the direct-drive robot cannot be increased indefinitely to increase the torque capacity. If we decrease the weight or the thickness of the robot arm, it will reduce the stiffness and lower the natural frequencies of the arm structures. The highly accurate operation of the robot cannot be obtained without high stiffness of the robot arm and the low natural frequencies of the robot arm structure are detrimental to the dynamic characteristics of the robot.

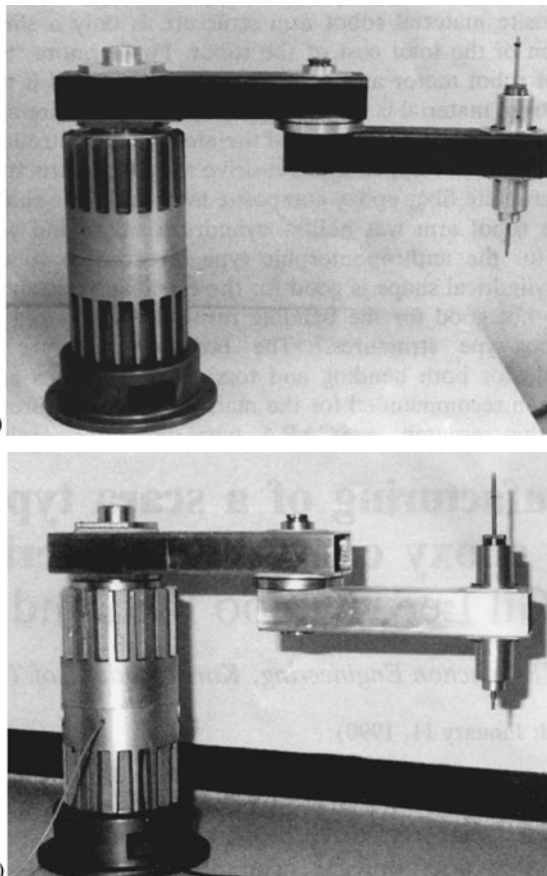
The damping of the robot arm structure is also important to dissipate the vibration which is induced in motion. The structural damping of the conventional robot arm comes largely from the transmission mechanisms, such as gears and chains. However, the direct drive has no damping from transmission and it is liable to vibrate at the resonance frequencies of the robot arm structure.

Therefore, the design problem of the direct-drive robot is exactly the same as the wrist design for the LCD glass panel handling robot in the previous section. The uncoupled or decoupled solution for the direct-drive robot arm with high specific stiffness and damping is only possible by employing high-modulus carbon-fiber composite material for the robot structure. Although the material cost is a constraint for robot marketing, in fact the cost of carbon-fiber composite material for robot arm structure is only a few percent of the total robot price.

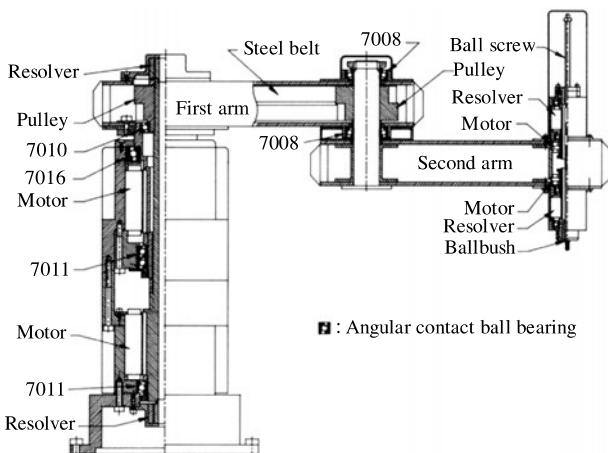
#### 13.3.1 Configuration of the SCARA-Type Direct-Drive Robot

Figure 13.10(a) shows a photograph of the direct-drive robot, whose arm is made of high-modulus carbon-fiber epoxy composite material and cast aluminum (Lee et al., 1991b). An all-aluminum robot was also manufactured to compare the performance improvement of the composite material robot arm (figure 13.10(b)). The box-type cross-sectional shape is selected because this shape gives both high bending and torsional stiffnesses. These two robots have the same dimensions. Figure 13.11 shows the configuration of the robots.

The direct-drive robots have four degrees of freedom. Two direct-drive motors, which drive the first and the second arms, were mounted on the base of the robot. The upper motor in the base drives the first arm, which is the nearer arm to the body. The lower motor drives the left pulley inside the first arm and the left pulley drives



**Figure 13.10** SCARA-type direct-drive robots: (a) Composite robot; (b) aluminum robot (Lee et al., 1991b).



**Figure 13.11** Configuration of the SCARA-type direct-drive robot (Lee et al., 1991b).

the right pulley by a steel belt. Rather than mounting the direct-drive motor on the joint of the first arm, the steel belt was used to drive the second arm because the direct-drive motor was too heavy to be mounted on the joint of the first arm. Therefore, this robot is a semi-direct-drive robot.

**Table 13.7 Specifications of the Direct-Drive Motors (Inland Co., USA)**

	<i>Rated power (W)</i>	<i>Maximum torque (Nm)</i>	<i>Maximum speed (rpm)</i>	<i>Mass (kg)</i>
Arm drive motor RBE-03006-A50	466.3	14.15	314	5.9
Wrist drive motor RBE-01200	31.9	0.10	3144	0.088

Two small direct-drive motors were mounted on the wrist of the second arm. They drive a ball screw and ball bush to produce the vertical and rotational motion of the gripper. All the direct-drive motors used were rare-earth element permanent magnet motors manufactured by Inland Co., Irving, Tex., USA. Table 13.7 shows the specifications of the motors.

Seven angular contact ball bearings were used in the joints of the first and second arms and four small angular contact ball bearings were used in the wrist. The angular contact ball bearings were employed to give high accuracy and ease of bearing mounting by adjusting the bearing preload. The stiffness of the angular contact ball bearing is lower than that of the roller bearing. However, it is easy to mount on the shaft and requires less accurate shaft machining. Two resolvers were mounted on the base to measure the position and motion of the first and the second arms, and an other two resolvers were mounted on the wrist to measure the position and motion of the gripper.

### 13.3.2 Static Deflection of the Robot Arm due to the Load at the Wrist

In order to estimate the deflection of the robot arm due to the load at the wrist, the axial and radial stiffnesses of the angular contact ball bearings must be determined using for example, bearing catalogs, such as the SNFA Bearings Catalog.

Wardle et al. (1983) give an empirical formula of the axial stiffness ( $k_a$ ) and radial stiffness ( $k_r$ ) of the preloaded angular contact ball bearings when  $P_a/P_r \geq 1.2 \tan \alpha$ :

$$k_a = 3.44 \times 10^6 P_a^{1/3} Z^{2/3} (\sin \alpha)^{5/3} D^{1/2} (\text{N/m}) \quad (13.1)$$

$$k_r = 0.64 k_a \cot \alpha \quad (13.2)$$

where  $P_a$  = axial load (or preload) (N)

$P_r$  = radial load (N)

$D$  = ball diameter (mm)

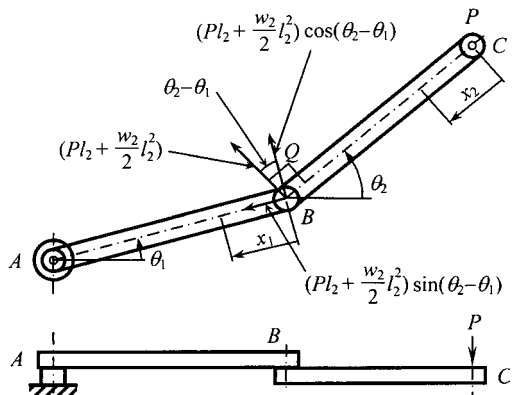
$Z$  = number of balls

$\alpha$  = contact angle

If the condition of  $P_a/P_r \geq 1.2 \tan \alpha$  is not satisfied, some of the balls of the bearing are unloaded by the radial load. Bearing stiffness increases with the one-third power of preload and the maximum practical preload range is less than 30% of the bearing's dynamic capacity. In this work, the bearing preload was selected as 30% of the bearing's static capacity because the static capacity is less than the dynamic capacity. The reason that the high value of 30% is chosen is that the rotational speed

**Table 13.8 Specification of the Angular Contact Ball Bearings**

Bearing number	Shaft diameter (mm)	Contact angle, $\alpha$ (degree)	Ball diameter, $D$ (mm)	Number of balls, $Z$	Static capacity (kN)
7008	40	25	7.93	17	11.6
7010	50	25	8.73	19	15.7
7011	55	25	10.32	18	20.7
7016	80	25	13.49	20	39.5

**Figure 13.12** Model of the SCARA-type robot arm (Lee et al., 1991b).

of the direct-drive robot is very low compared with the speed of the machine tool (Harris, 2001, Brandlein, 1999).

The axial and radial stiffnesses of the 7008 bearing of table 13.8 when the axial load  $P_a$  is equal to the one-third of the static capacity are

$$k_a = 1.67 \times 10^8 \text{ (N/m)} \quad (13.3)$$

$$k_r = 2.29 \times 10^8 \text{ (N/m)} \quad (13.4)$$

If a 10 N force acts axially to this bearing, the deflection will be 0.06  $\mu\text{m}$ . Since our aim is to design a robot that has a deflection less than 50  $\mu\text{m}$  when the load at the wrist is 10 N, the deflection due to the bearing is very small and can be neglected. Therefore, the bearing was assumed to be rigid in the derivation of the static deflection of the robot arm.

The model of the robot is shown in figure 13.12. Points  $A$  and  $B$  are the joints supported by the angular contact ball bearings.

If a static load  $P$  acts in the vertical direction, the second arm ( $BC$ ) deflects by bending moment and shear force. The deflection due to shear was included because the shear causes comparable deflections of the thick composite material beam.

The first arm ( $AB$ ) deflects due to bending moment, shear force, and torsional moment.

If the weight per unit length of the second arm is  $w_2$  and payload is  $P$ , the bending moment of the second arm is  $(-Px_2 - 0.5w_2x_2^2)$ . Therefore, the strain

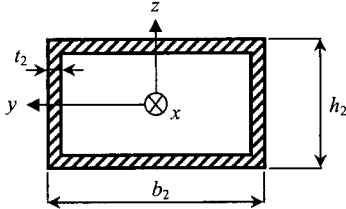


**Figure 13.13** Cross-section of the second robot arm, which has a box-type cross-section.

energy  $U_{b2}$  of the second arm due to bending moment is expressed as follows (Roark and Young, 1976)

$$U_{b2} = \int_0^{l_2} \frac{(-Px_2 - 0.5w_2x_2^2)^2}{2\bar{E}_{xy2}I_2} dx_2 = \frac{l_2^3}{\bar{E}_{xy2}I_2} \left( \frac{P^2}{6} + \frac{P}{8}w_2l_2 + \frac{w_2^2l_2^2}{40} \right) \quad (13.5)$$

where  $l_2$  = length of the second arm

$I_2$  = sectional moment of inertia of the second arm

$\bar{E}_{xy2}$  = equivalent modulus of the second arm in chapter 6

Figure 13.13 shows the model of the robot arm cross-section, which has the box-type arm cross-section and coordinates attached to it. Since the shear force at  $x_2$  is  $P + w_2x_2$ , the shear stress  $\tau_{xz2}$  of the vertical cross-section from equation (6.294) is expressed by

$$\tau_{xz2} = \frac{(P + w_2x_2)[(0.5h_2)^2 + \frac{h_2b_2}{2} - z^2]}{2I_2} \quad (13.6)$$

where  $h_2$  = height of the cross-section

$b_2$  = width of the cross-section

The strain energy  $U_{s2}$  of the second arm due to shear stress is calculated as follows:

$$U_{s2} = \int \int \int \frac{\tau_{xz2}^2}{2\bar{G}_{xy2}} dx dy dz = \frac{l_2 h_2^3}{\bar{G}_{xy2} I_2^2} \left( \frac{1}{240} h_2^2 + \frac{1}{48} h_2 b_2 + \frac{1}{32} b_2^2 \right) \left( P^2 + Pw_2 l_2 + \frac{w_2^2 l_2^2}{3} \right) \quad (13.7)$$

where  $\bar{G}_{xy2}$  is the equivalent shear modulus of the second arm material. In calculating  $U_{s2}$  in equation (13.7), the shear stresses in the upper and lower sections were neglected because of much lower values of shear stresses than the vertical sections.

The bending moment  $M_b$  and torsional moment  $M_t$  at point  $B$  due to the force  $P$  are

$$M_b = -(Pl_2 + 0.5w_2l_2^2) \cos(\theta_2 - \theta_1)$$

and

$$M_t = -(Pl_2 + 0.5w_2l_2^2) \sin(\theta_2 - \theta_1)$$

respectively, where  $\theta_1$  = angle of rotation of the first arm from a reference line, and  $\theta_2$  = angle of rotation of the second arm from a reference line.

If we assign  $Q$  as the weight of the point  $B$  due to the pulley, first arm and the angular contact ball bearings, the strain energy  $U_{b1}$  due to bending,  $U_{s1}$  due to shear and  $U_{t1}$  due to torsion are expressed as

$$\begin{aligned} U_{b1} &= \int_0^{l_1} \frac{[-(Pl_2 + 0.5w_2l_2^2) \cos(\theta_2 - \theta_1) - (P+Q)x_1 - 0.5w_1x_1^2]^2}{2\bar{E}_{x1}l_1} dx_1 \\ &= \frac{1}{2\bar{E}_{x1}I_1} \left[ (Pl_2 + 0.5w_2l_2^2)^2 l_1 \cos^2(\theta_2 - \theta_1) + \frac{1}{3}(P+Q)^2 l_1^3 + \frac{w_1^2}{20} l_1^5 + \frac{1}{4}(P+Q)w_1 l_1^4 \right. \\ &\quad \left. + (Pl_2 + 0.5w_2l_2^2)(P+Q)l_1^2 \cos(\theta_2 - \theta_1) + \frac{w_1}{3}(Pl_2 + 0.5w_2l_2^2)l_1^3 \cos(\theta_2 - \theta_1) \right] \end{aligned} \quad (13.8)$$

$$\begin{aligned} U_{s1} &= \iiint \frac{\tau_{1xz}^2}{2\bar{G}_{xy1}} dA_1 dx_1 \\ &= \frac{l_1 h_1^3}{\bar{G}_{xy1} t_1 I_1^2} \left( \frac{1}{240} h_1^2 + \frac{1}{48} h_1 b_1 + \frac{1}{32} b_1^2 \right) \left[ (P+Q+w_2l_2)^2 + (P+Q+w_2l_2)w_1l_1 + \frac{w_1^2}{3} l_1^2 \right] \end{aligned} \quad (13.9)$$

$$\begin{aligned} U_{t1} &= \int_0^{l_1} \frac{[-(Pl_2 + 0.5w_2l_2^2) \sin(\theta_2 - \theta_1)]^2}{2\bar{G}_{xy1}J_1} dx_1 \\ &= \frac{l_1 l_2^2 (P + 0.5w_2l_2)^2 \sin^2(\theta_2 - \theta_1)}{2\bar{G}_{xy1}J_1} \end{aligned} \quad (13.10)$$

where  $l_1$ ,  $\bar{E}_{x1}$ ,  $\bar{G}_{xy1}$ ,  $J_1$ , and  $t_1$  are the length, equivalent modulus, shear modulus, polar moment of inertia, and thickness of the first arm, respectively. The total energy  $U_T$  is obtained by summing all the energies calculated previously:

$$U_T = U_{b1} + U_{s1} + U_{t1} + U_{b2} + U_{s2} \quad (13.11)$$

Then, the deflection  $\delta_c$  at the load point  $C$  is obtained by Castigliano's theorem:

$$\begin{aligned} \delta_C &= \frac{\partial U_T}{\partial P} = \frac{l_2^3}{\bar{E}_{x2}I_2} \left( \frac{P}{3} + \frac{w_2l_2}{8} \right) + \frac{l_2 h_2^3}{\bar{G}_{xy2}I_2^2} \left( \frac{1}{240} h_2^2 + \frac{1}{48} h_2 b_2 + \frac{1}{32} b_2^2 \right) (2P + w_2l_2) \\ &\quad + \frac{1}{\bar{E}_{x1}I_1} \left[ l_1 l_2^2 (P + 0.5w_2l_2) \cos^2(\theta_2 - \theta_1) + \frac{1}{3}(P+Q)l_1^3 \right. \\ &\quad \left. + l_1^2 l_2 \left( P + \frac{Q}{2} + \frac{w_2l_2}{4} + \frac{w_1l_1}{6} \right) \cos(\theta_2 - \theta_1) + \frac{1}{8} w_1 l_1^4 \right] \\ &\quad + \frac{l_1 l_2^2}{\bar{G}_{xy1}J_1} (P + 0.5w_2l_2) \sin^2(\theta_2 - \theta_1) \\ &\quad + \frac{l_1 h_1^3}{\bar{G}_{xy1} t_1 I_1^2} \left( \frac{1}{240} h_1^2 + \frac{1}{48} h_1 b_1 + \frac{1}{32} b_1^2 \right) [2(P+Q+w_2l_2) + w_1l_1] \end{aligned} \quad (13.12)$$

The equivalent bending stiffnesses and torsional rigidities are calculated from equations (6.279) and (6.285). When the horizontal section area is assumed wide, we have the following relations:

$$\bar{E}_{x1}I_1 = \frac{h_1^3}{6a_{11v,1}} + 2b_1\left(\frac{(h_1 - t_1)^2}{4a_{11h,1}} + D_{11h,1}\right) \quad (13.13)$$

$$\bar{E}_{x2}I_2 = \frac{h_2^3}{6a_{11v,2}} + 2b_2\left(\frac{(h_2 - t_2)^2}{4a_{11h,2}} + D_{11h,2}\right) \quad (13.14)$$

$$\bar{G}_{xy1}J_1 = G_{xy,1} \frac{2b_1^2 h_1^2}{b_1 + h_1} t_1 \quad (13.15)$$

$$\bar{G}_{xy2}J_2 = G_{xy,2} \frac{2b_2^2 h_2^2}{b_2 + h_2} t_2 \quad (13.16)$$

where  $h_1$  and  $h_2$  represent the heights of the first and the second arms, respectively, which is a different usage from figure 6.9. In figure 6.9, they represent the distances from the midplane to the centers of the upper and lower horizontal sections, respectively.

### 13.3.3 Robot Dimensions and Optimum Stacking Sequence for the Carbon-Fiber Composite Robot Arms

The length of the robot arm is determined by considering the working envelope. The length of robot arm  $AC$  or the radius of working envelope from figure 13.12 is calculated by the cosine law:

$$r = \sqrt{l_1^2 + l_2^2 + 2l_1 l_2 \cos(\theta_2 - \theta_1)} \quad (13.17)$$

For a robot that can be used in the assembly of printed circuit boards, the difference between the maximum radius and the minimum radius of working envelope must be larger than 400 mm. If  $\theta_2 - \theta_1$ , which is the angle between the first arm and the second arm, approaches  $0^\circ$  and  $180^\circ$ , the robot arm suffers singularity. Hence,  $\theta_2 - \theta_1$  is limited to between  $30^\circ$  and  $150^\circ$ . In this case, if the length of both the first and the second arm is taken to be 320 mm, then  $r_{\max} = 618$  mm and  $r_{\min} = 166$  mm. Since the difference between the two radii is 452 mm, which is larger than 400 mm, both arm lengths were taken to be 320 mm.

The cross-section of the robot arm is determined by the transmission mechanism, such as the steel belt and the pulley, bearing mounting, and aesthetic considerations. The cross-section of the first arm was chosen 120 mm  $\times$  70 mm in order to insert 100 mm diameter pulleys, which drive the second arm through the steel belt. The cross-section of the second arm was chosen as 90 mm  $\times$  70 mm.

The thickness of the arm and the stacking sequence of the composite material can be determined by considering the static deflection equation (13.12). Then, the unit deflection  $\delta_C/P$  at the point  $C$  can be calculated using these material constants if we assign the composite arm thicknesses  $t_1$ ,  $t_2$ , and  $R = Q/P$ . Since the deflection equation (13.12) is complex, the robot arm deflection at point  $C$  was calculated by a computer program written in Turbo Pascal. The carbon-fiber epoxy composite

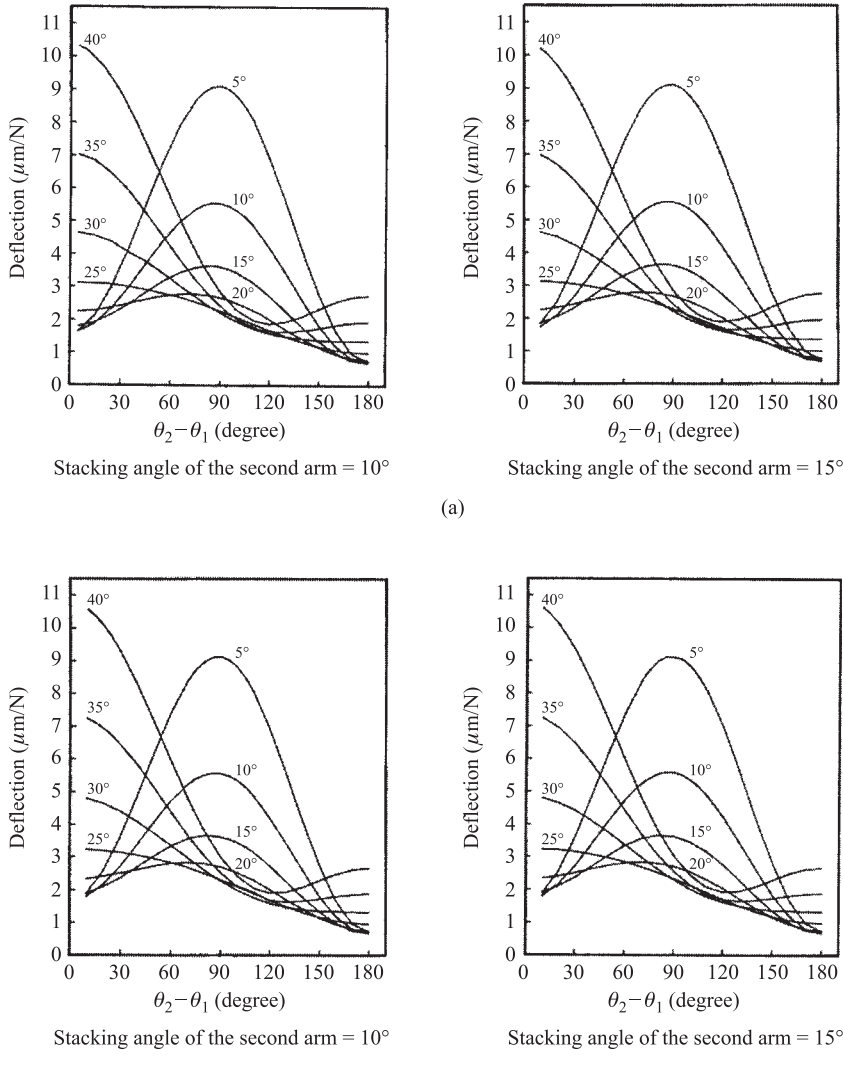


**Figure 13.14** Unit robot arm deflection  $\delta_C/P$  with respect to  $\theta_2 - \theta_1$  and the stacking angle of the second arm: (a)  $Q/P = 0.5$ ; (b)  $Q/P = 1.0$  (Lee et al., 1991b).

material used in the manufacturing of the robot arm structure has the following mechanical properties:

$$E_1 = 207 \text{ GPa}$$

$$E_2 = 7.85 \text{ GPa}$$

$$\nu_{12} = 0.28$$

$$G_{13} = G_{12} = 4.48 \text{ GPa}$$

Figure 13.14(a) shows the unit robot arm deflection at point  $C$  with respect to  $(\theta_2 - \theta_1)$  and the stacking angle of the first arm when  $t_1$  and  $t_2$  are both 5 mm, and  $R = 0.5$ . Figure 13.14(b) shows the unit robot arm deflection at point  $C$  when  $t_1$  and

$t_2$  are both 5 mm, and  $R=1.0$ . The fiber stacking angle of the second arm of the robot was limited to between  $10^\circ$  and  $15^\circ$  in the calculations of figure 13.14 because the deflection of the second arm is induced by bending moment and shear force without torsional moment.

From figure 13.14, the fiber stacking angle of the fiber for the first arm was selected as  $20^\circ$ . If the stacking angle of the fiber is less than  $10^\circ$ , the composite becomes very weak for the torsional moment, which might be induced by the load or inertia. Therefore, the fiber stacking angle for the second arm was selected as  $10^\circ$ .

The effective bending stiffness and torsional rigidity of the first arm were calculated in example 6.5 when the stacking sequence was  $[\pm 20]_{10S}$ :

$$\bar{E}_{x,1}I_1 = 2.07 \times 10^5 \text{ Nm}^2$$

$$\bar{G}_{xy,1}J_1 = 9.50 \times 10^4 \text{ Nm}^2$$

The effective bending stiffness and in-plane shear modulus of the second arm were calculated in problem 6.15 when the stacking sequence was  $[\pm 10]_{10S}$ :

$$\bar{E}_{x,2}I_2 = 2.36 \times 10^5 \text{ Nm}^2$$

$$G_{xy,2} = 11.47 \text{ GPa}$$

When the thicknesses of the composite arms are both 5 mm, the maximum deflection is less than  $30 \mu\text{m}$  per 10 N. Since the design criterion is less than  $50 \mu\text{m}$  deflection per 10 N, both composite arm thicknesses were selected as 5 mm. An aluminum robot arm that has the same dimensions and thicknesses of the composite robot arm was manufactured in order to compare the static and dynamic characteristics.

### 13.3.4 Manufacturing of the Robots

#### Base

The base of the robot has to hold the total weight of the robot and to dissipate vibration that is induced from the arm structures. Since gray cast iron has high damping capacity compared with steel or aluminum, it was selected for the robot base material. The robot base was machined by turning and drilling after casting. Figure 13.15 shows a photograph of the base. One resolver was mounted in the upper hole and there is another side hole in the base for electrical wiring.

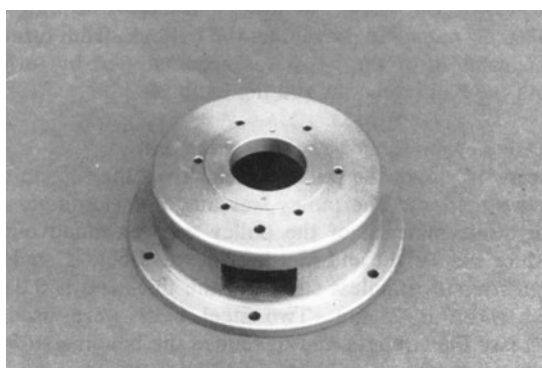


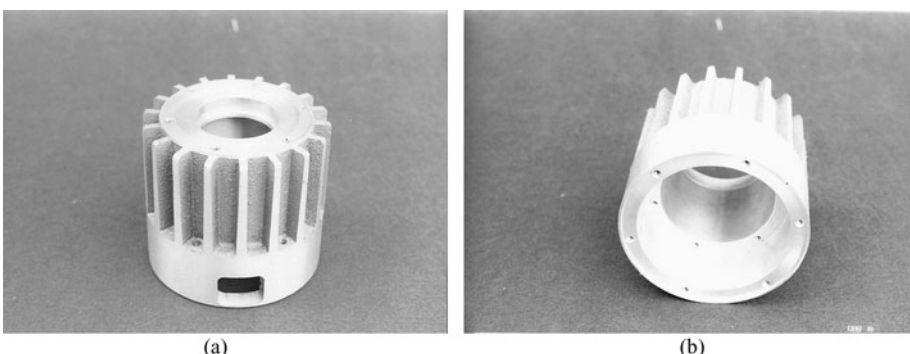
**Figure 13.15** Robot base made of cast iron (from Lee et al., 1991b).

### *Body*

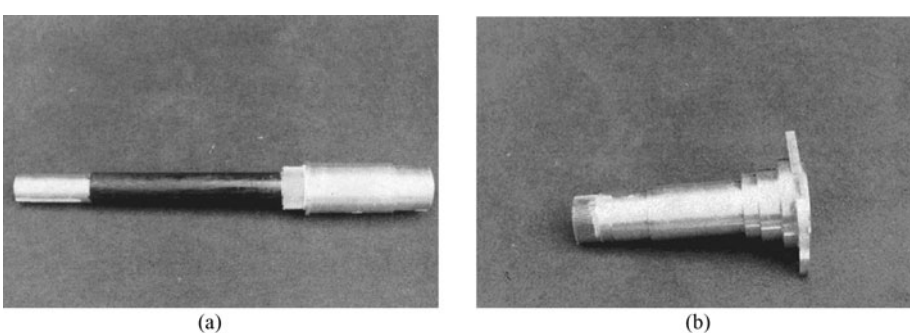
Figure 13.16(a) shows the upper part of the body of the robot and figure 13.16(b) shows the lower part. Two Inland direct-drive motors and five angular-contact ball bearings were mounted on the body of the robot. In order to increase the bearing stiffness, preload was given to the angular contact ball bearings by turning the lock nut. Since the direct-drive motors have heavy wiring and high current flows in the wiring, the body of the robot was manufactured in aluminum, and many fins were provided to dissipate heat generated from the electrical wiring.

### *Shaft*

Figure 13.17(a) is the elbow drive shaft, which drives one of the pulleys inside the first arm. Figure 13.17(b) is the shoulder drive shaft, which drives the first arm. The elbow drive shaft is mounted concentrically inside the shoulder drive shaft. Both shafts were manufactured in high-strength aluminum alloy. The elbow drive shaft was reinforced by winding the carbon-fiber epoxy composite. The winding angle was  $[\pm 15]_S$  from the shaft axis and the thickness of the composite was 1 mm. Table 13.9 shows the natural frequencies and damping of the shaft with and without fiber reinforcement. The first natural frequency and damping of the reinforced shaft by the carbon-fiber composite material were increased 11% and 39%, respectively.



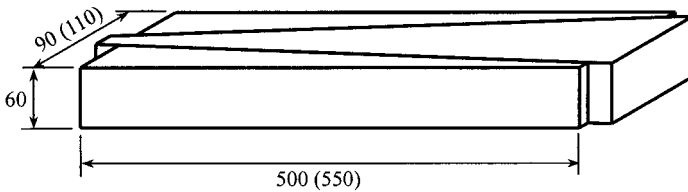
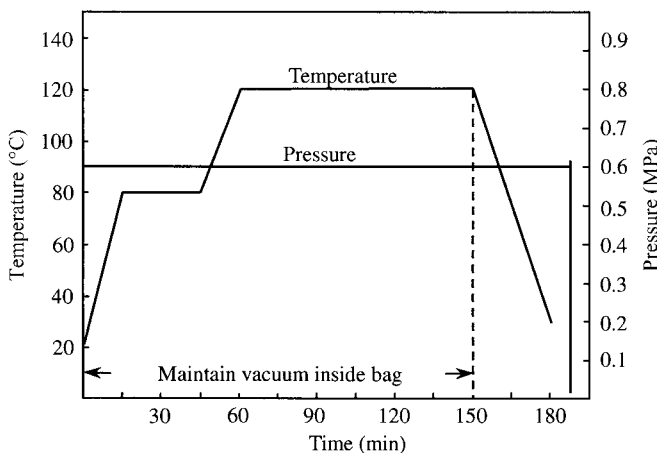
**Figure 13.16** Body of the robot: (a) Upper part; (b) lower part (from Lee et al., 1991b).



**Figure 13.17** Robot arm drive shafts: (a) Elbow drive shaft, which drives the pulley for the steel belt; (b) shoulder drive shaft, which drives the first robot arm (from Lee et al., 1991b).

**Table 13.9 Natural Frequency and Damping of the Elbow Drive Shaft with and without Reinforcement of the Carbon-Fiber Epoxy Composite Material**

	Frequency (Hz)	Damping (%)
Without composite reinforcement	778	0.35
With composite reinforcement	867	0.49

**Figure 13.18** Three-piece mold for the composite robot arm (from Lee et al., 1991b)**Figure 13.19** Cure cycle for the carbon-fiber epoxy composite robot arm.

### Arm

The carbon-fiber epoxy composite robot arm was manufactured using autoclave vacuum bag molding. In order to ease the mold separation after curing the composite arm in the autoclave, three piece molds were manufactured in aluminum, as shown in figure 13.18. Figure 13.19 shows the cure cycle of the carbon-fiber epoxy composite material. The aluminum arm was manufactured by casting and the outside surface of the arm was milled.

Two holes in the arms were bored out to mount bearings. In the boring operation of the composite arm, an aluminum plate was attached to the bottom surface to prevent fiber pull-out. Tungsten carbide tools (K10) were used in the boring operation of the arms. A bearing housing was bonded to the arm using epoxy adhesive. Figure 13.20 shows the configuration of the bearing housing bonded to the robot arm.

**Figure 13.20** Bearing housing bonded to the robot arm (from Lee et al., 1991b).

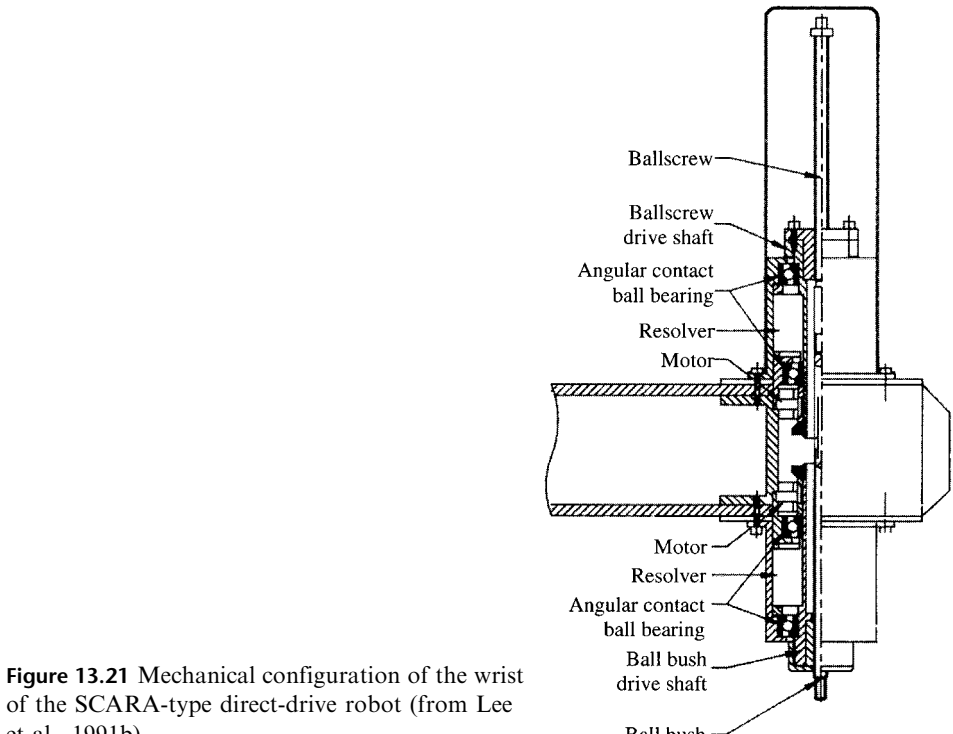
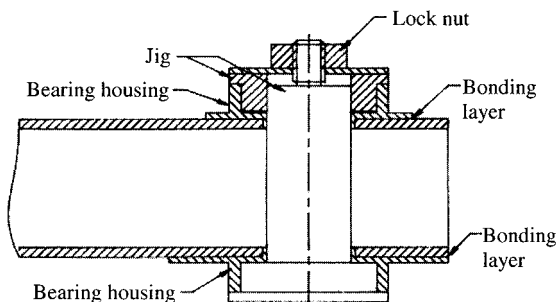


**Figure 13.21** Mechanical configuration of the wrist of the SCARA-type direct-drive robot (from Lee et al., 1991b).

### Wrist

Figure 13.21 shows the configuration of the wrist. Four angular-contact ball bearings were used for the vertical motion and rotation of the wrist. Two small Inland direct-drive motors were mounted on the wrist. The Inland motors drive a ball-screw nut and a ball bush. The vertical motion of the wrist was accomplished by turning the ball-screw nut while preventing the ball bush from turning. The rotation of the wrist was accomplished by turning both the ball-screw nut and ball bush.

### Pulley for the Drive of the Second Arm

Figure 13.22 shows the pulley that drives the second arm by a steel belt. The pulley was made of aluminum and the inside material of the pulley was machined out to reduce the weight and inertia. The steel belt is made of high-strength stainless steel

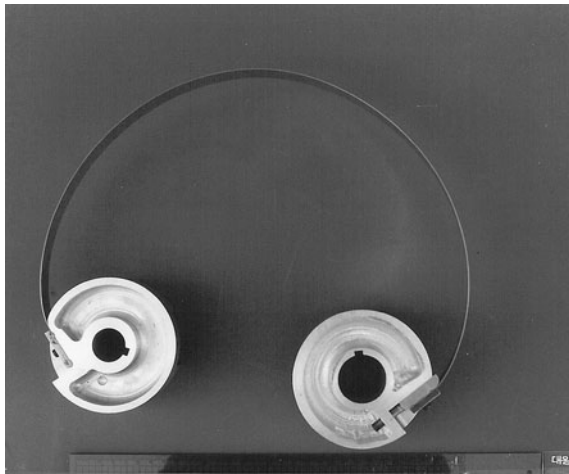


**Figure 13.22** Pulley for the steel belt (from Lee et al., 1991b).

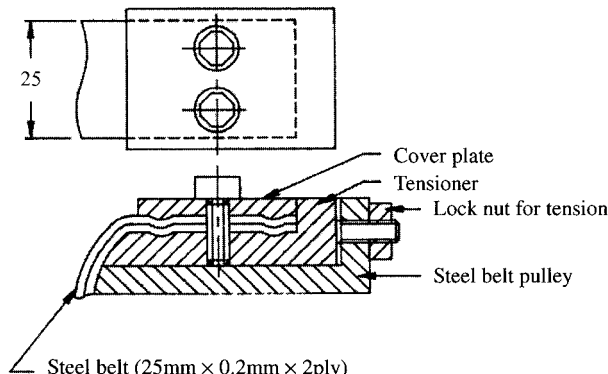


**Figure 13.23** Tensioning mechanism for the steel belt (from Lee et al., 1991b).

and its thickness and width are 0.2 mm and 25 mm, respectively. Two steel belts were used to increase the strength and to reduce the bending stiffness rather than using one thick steel belt.

A tensioning mechanism was installed between the steel belt and the pulley to give exact amount of tension to the steel belt. Figure 13.23 shows the tensioning mechanism and the tension of the steel belt was provided by turning the lock nut.

The wavy surface of the tensioning mechanism was machined to sustain more tension and epoxy adhesive was used to enhance the fixing of the steel belt to the tensioning mechanism. The surface of the tensioning mechanism was machined by electrical discharge machining (EDM) wire cutting, and 0.3 mm electrical wire proved to be satisfactory. The machined surface has high hardness and good surface roughness for epoxy bonding.

### 13.3.5 Static and Dynamic Performance of the Robot Structures

Static and dynamic tests were performed to compare the characteristics of the composite robot arm and the aluminum robot arm.

The weight of the composite robot arm was 14 N less than that of the aluminum robot arm. The static deflection at the wrist was measured by applying 10 N at the upper position of the wrist. The deflection was measured by a dial gage. The static

stiffness of the composite robot arm was 94% higher than that of the aluminum robot arm. The measured static deflection of the composite robot arm was about 30% larger than that calculated in figure 13.14. This discrepancy came from neglecting shaft and bearing deflections.

The dynamic characteristics of the robot arm were measured by applying an impulse at the top surface of the end position of the second arm. The vibration signal was measured using an accelerometer and the signal was processed using a spectrum analyzer (HP 5423A Structural Dynamics Analyzer).

The first natural frequencies of both robot arms were 18 Hz, which came from the tension vibration of the steel belt connected to the pulleys.

The second natural frequency of the robot arm came from the bending vibration of the second arm. The measured frequency of the composite robot arm was 624 Hz and the measured frequency of the aluminum robot arm was 376 Hz. The damping ratio of the composite arm at the second mode was 5.3%, whereas the damping ratio of the aluminum arm at the second mode was 2.1%. The high damping of the composite robot arm came from the material damping of the composite material and several adhesively bonded areas.

### 13.4 Composite Anthropomorphic Robot

In previous sections, it has been stated that the structure of a robot should have both high specific stiffness ( $E/\rho$ ) and high damping in order to increase positional accuracy and dynamic performance. If the thickness and the size of the robot structure are increased to stiffen the structure, the weight of the robot is also increased, which requires larger motors to give the same acceleration. Even if aluminum rather than steel is used, the stiffness cannot be increased without extra weight because the specific stiffness of aluminum is no higher than that of steel. Therefore, increasing the stiffness without increasing the weight of the robot structure is not possible with conventional metals.

The direct-drive robots in section 13.3 have small payloads because the direct-drive robots do not have any gear trains for speed reduction, whereas the conventional anthropomorphic robot uses gear trains composed of several spur gears, bevel gears, and harmonic drives (discussed in the next section) to reduce the motor speed as well as to change the direction of motion. Because of gear trains, it has more complex arm structures. Also the power transmission shafts and bearings must be mounted inside or outside of the arm of the anthropomorphic robot.

Since the anthropomorphic robot has a larger payload and working envelope as well as flexibility with the same capacity motor due to the motor speed reduction, it is widely employed as an industrial robot for loading and unloading, painting, welding, and assembly operations although it has complicated shapes, backlash of gears, and is difficult to control because of large friction and nonlinearity of the gear trains and other mechanisms.

In this section, the design and manufacture of a six-degree-of-freedom anthropomorphic robot arm with 70 N payload with high-modulus carbon-fiber epoxy composite is presented. The functional requirements (FRs) and the design parameters (DPs) are exactly the same as those for the hands of the robot handling LCD panels in section 13.2.

### 13.4.1 Robot Specifications

Figure 13.24 shows a photograph of the manufactured composite anthropomorphic robot. Its height and forearm length are about 2.0 m and 1.2 m, respectively, and its total weight is about 2000 N (Lee et al., 1993). The robot has six degrees of freedom. The roll and pitch motions of the end effector and the roll motion of the wrist are driven by the three motors (MO80) mounted on the rear of the forearm. The up-down and forward-backward motions are driven by the two motors (MO600) mounted on the back of the robot body. The whole robot structure can be rotated by the motor (MO600) mounted under the base, which is not shown in figure 13.24. The MO80 motors have 150 W power and the MO600 motors have 700 W power. All the six motors are DC servo motors manufactured by Mavilor Company (Mavilor Motor Catalog). Table 13.10 lists the specifications of the anthropomorphic robot.

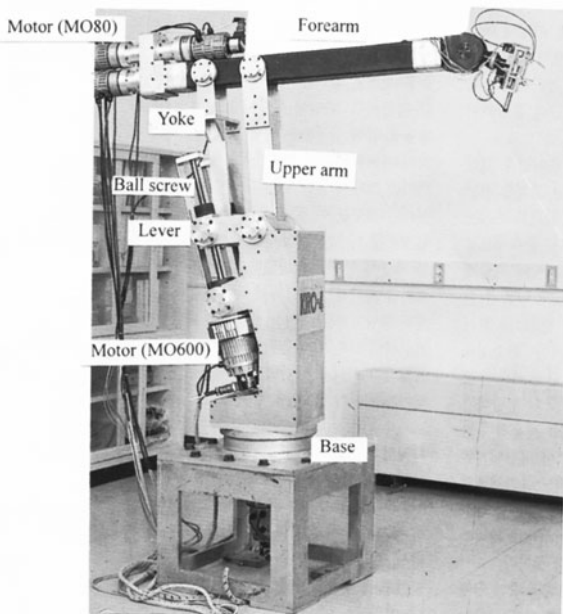


**Figure 13.24** Photograph of the manufactured composite robot (from Lee et al., 1993).

**Table 13.10 Specifications of the Anthropomorphic Robot**

Degrees of freedom	6
Payload (N)	70
Position accuracy (mm)	$\pm 0.1$
Forearm length (mm)	800
Upper arm length (mm)	600
Length of the drive shafts (mm):	Tool roll 1007 Pitch 996 Wrist roll 976
Range of rotation angles:	Forearm $\pm 50^\circ$ Upper arm $\pm 50^\circ$

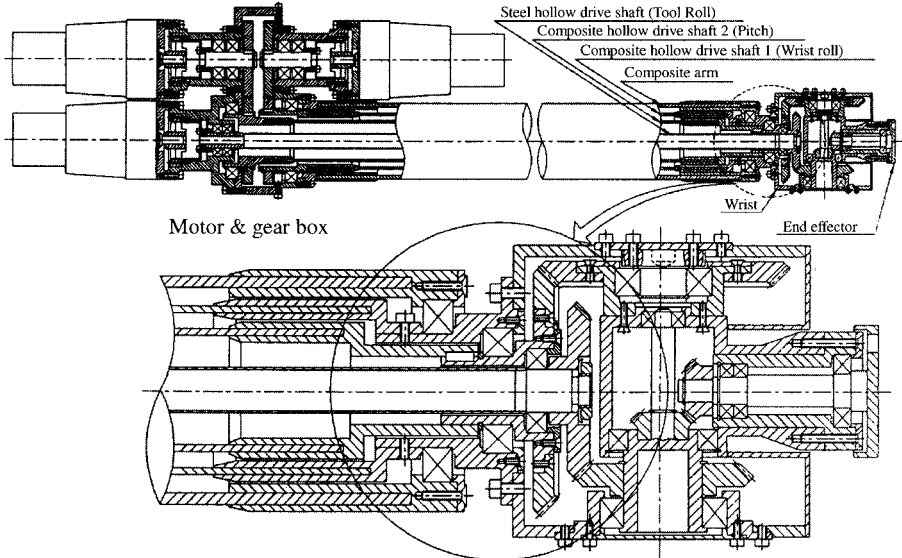


**Figure 13.25** Forearm configuration of the composite robot (from Lee et al., 1993).

Figure 13.25 shows the assembled forearm configuration. The forearm consists of the three motors, the gear box, the arm, the wrist, the end effector, and three hollow shafts for power transmission. From these components, the arm and the two outer power transmission shafts were manufactured with high-modulus carbon-fiber epoxy composite. Table 13.10 shows the specifications of the developed anthropomorphic robot.

#### 13.4.2 Deflection of the Robot Arm by Static Loads

The deflection of the end effector comes from the static weight of the robot, the payload, and the inertia force due to the acceleration of the robot. However, the inertia force was not taken into consideration in calculating the deflection because the maximum acceleration of the end effector of the robot was designed to be  $3 \text{ m/s}^2$ , which was less than the gravitational acceleration,  $9.81 \text{ m/s}^2$ .

Since the forearm's weight and the static payload affect directly the positional accuracy of the robot, the deflection of the forearm due to the forearm's own weight and the static payload were calculated using the simple moment-curvature relationship of the beam. Figure 13.26 shows the lumped mass distributions for the simple calculation of the deflection of the forearm, in which  $m_1$  represents the combined mass of the arm and the three power transmission shafts,  $m_2$  represents the combined mass of the wrist and the end effector,  $m_3$  represents the combined mass of the motors and the gear box, and  $m_t (=m_1 + m_2 + m_3)$  represents the total mass of the forearm. The points *C.M.*, *B*, and *E* in figure 13.26 represent the center of mass, the pivot point between the upper arm and the forearm, and the pivot point between the yoke and the forearm, respectively. Then  $L_8$ , the length between the point *B* and the point *C.M.*, can be calculated as follows:

$$L_8 = \frac{m_1 L_2 + m_2 L_5 - m_3 L_6}{m_t} \quad (13.18)$$

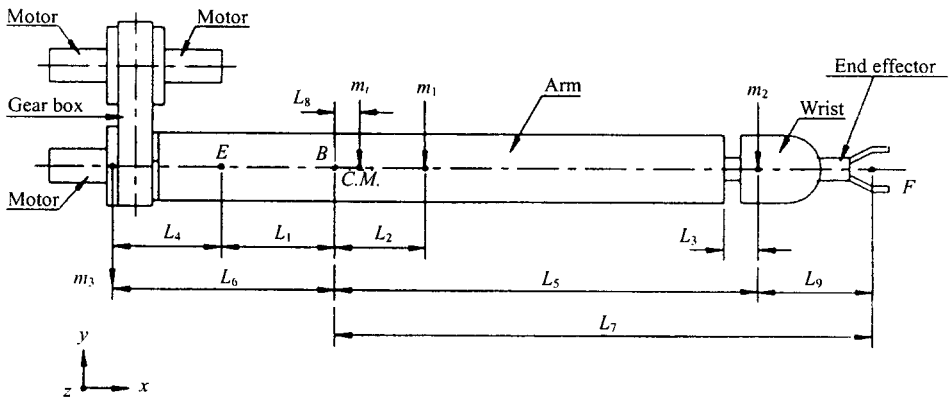


Figure 13.26 Mass distributions of the forearm (from Lee et al., 1993).

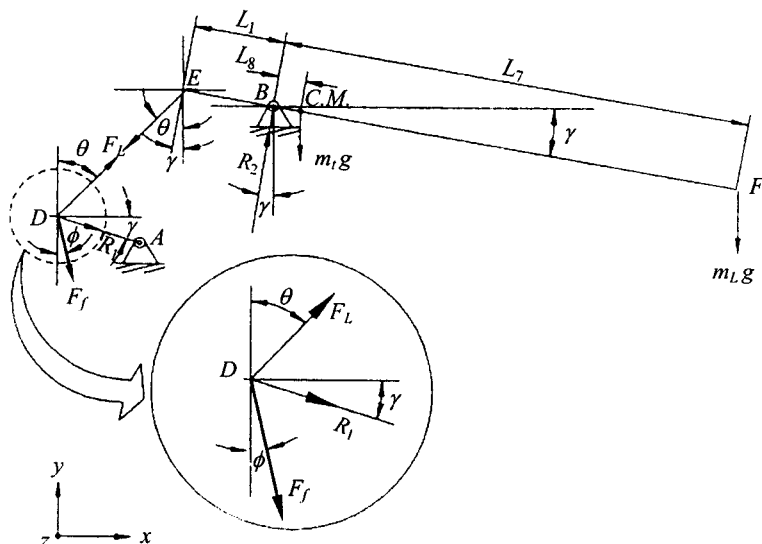


Figure 13.27 Mechanical model of the forearm (from Lee et al., 1993).

Figure 13.27 shows the free body diagram, which depicts the force relationship between the forearm ( $EF$ ), the yoke ( $DE$ ), and the lever ( $AD$ ).  $F_f$  and  $F_L$  represent the forces from the ball screw and the forearm, respectively.  $R_1$  and  $R_2$  represent the forces from the pivot points  $A$  and  $B$ , respectively.  $\gamma$  represents the angle between the horizontal and the forearm, whose range is from  $-50^\circ$  to  $50^\circ$ .  $\phi$  represents the angle between the vertical and the ball screw, whose range is from  $0^\circ$  to  $16^\circ$ .  $\theta$  represents the angle between the vertical and the yoke.  $m_L$  represents the equivalent mass of the payload.

Applying the force equilibrium equation to the point  $D$  in figure 13.27, the following relationships can be derived:

$$F_L \sin \theta + F_f \sin \phi + R_1 \cos \gamma = 0 \quad (13.19)$$

$$F_L \cos \theta - F_f \cos \phi - R_1 \sin \gamma = 0 \quad (13.20)$$

Eliminating  $R_1$  from equations (13.19) and (13.20),  $F_f$  can be derived as follows:

$$F_f = F_L \frac{\cos(\theta - \gamma)}{\cos(\gamma + \phi)} \quad (13.21)$$

From the moment equilibrium around the pivot point B, the following relationship can be derived:

$$F_L \cos(\theta - \gamma) = \left( m_t \frac{L_8}{L_1} + m_L \frac{L_7}{L_1} \right) g \cos \gamma \quad (13.22)$$

where  $g$  is the gravitational acceleration ( $9.81 \text{ m/s}^2$ ). Eliminating  $F_L$  from equations (13.21) and (13.22), the force  $F_f$ , which acts on the ball screw, can be derived in terms of  $m_t$  and  $m_L$ :

$$F_f = \left( m_t \frac{L_8}{L_1} + m_L \frac{L_7}{L_1} \right) \frac{g \cos \gamma}{\cos(\gamma + \phi)} \quad (13.23)$$

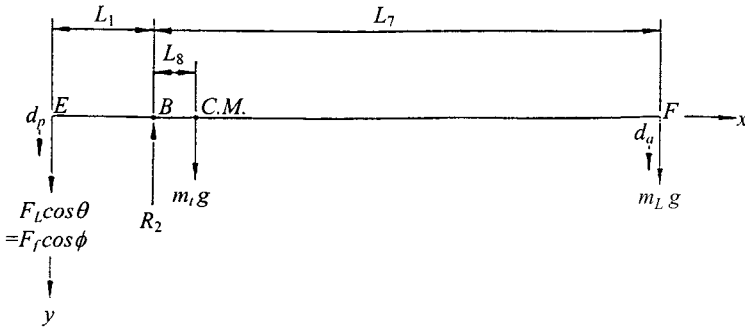
The maximum deflection of the forearm does not occur at  $\gamma = 0^\circ$  but around  $0^\circ$  because the deflection of the ball screw affects slightly the deflection of the end effector. However, the maximum deflection was calculated by assuming that it would occur when  $\gamma = 0^\circ$  because the axial deformation of the ball screw was designed to be small.

Figure 13.27 shows the kinematic mechanism of the forearm and its connected linkage. Figure 13.28 shows the deflection model of the forearm when  $\gamma = 0^\circ$ .  $d_a$  and  $d_p$  represent the deflections of the end effector and the pivot point E, respectively, and  $d_b$  represents the component of the deflection of the ball screw perpendicular to the forearm, which is caused by the compliance of the ball screw.

The deflection  $d_a$  was calculated by the moment-curvature relationship of the beam:

$$\frac{d^2y}{dx^2} = \frac{M_b}{\bar{E}_x I} \quad (13.24)$$

where  $M_b$ ,  $\bar{E}_x$ , and  $I$  represent the moment in the forearm, the longitudinal equivalent Young's modulus of the carbon-fiber epoxy composite, and the sectional



**Figure 13.28** Deflection model of the robot arm when  $\gamma = 0^\circ$  (from Lee et al., 1993).

second moment of inertia of the forearm, respectively. The moment  $M_b(x)$  can be represented using the singularity function:

$$M_b = F_f \cos \phi \langle x \rangle - R_2 \langle x - L_1 \rangle + m_l g \langle x - L_1 - L_8 \rangle \quad (13.25)$$

where the symbol  $\langle \rangle$  represents the singularity function and  $x$  represents the distance from the point  $E$ . The force  $R_2$  at the pivot point  $B$  can be calculated by the moment equilibrium about point  $F$ :

$$R_2 = F_f \cos \phi \left( 1 + \frac{L_1}{L_7} \right) + m_l g \left( 1 - \frac{L_8}{L_7} \right) \quad (13.26)$$

Two boundary conditions for equation (13.24) are:

$$\text{when } x = L_1, y = 0 \quad (13.27a)$$

$$\text{when } x = 0, y = d_p \quad (13.27b)$$

Integrating equation (13.24) with boundary conditions (13.27) using equations (13.25) and (13.26), the following deflection equation can be obtained:

$$y = \frac{F_f \cos \phi}{6E_x I} \left[ x^3 - \left( 1 + \frac{L_1}{L_7} \right) \langle x - L_1 \rangle^3 - L_1^2 x \right] + \frac{m_l g}{6E_x I} \left[ \langle x - L_1 - L_8 \rangle^3 - \left( 1 - \frac{L_8}{L_7} \right) \langle x - L_1 \rangle^3 \right] + \left( 1 - \frac{x}{L_1} \right) d_p \quad (13.28)$$

The deflection  $d_p$  at the point  $E$  can be expressed in terms of the deflection of the ball screw by assuming the yoke to be a rigid body. The deflection of the ball screw  $d_c$  due to the axial force  $F_f$  is expressed by

$$d_c = \frac{F_f}{K_N} \quad (13.29)$$

where  $K_N$  represents the axial stiffness constant of the ball screw. Then,  $d_b$ , the component of  $d_c$  perpendicular to the forearm, is expressed as

$$d_b = d_c \cos \phi = \frac{F_f}{K_N} \cos \phi \quad (13.30)$$

Since the linkage  $ABED$  was designed to be a parallelogram, the deflection at the point  $E$  has the same value as the point  $D$ . Therefore, the deflection  $d_p$  at  $x=0$  is expressed as

$$d_p = -d_b = -\frac{F_f}{K_N} \cos \phi \quad (13.31)$$

Substituting equation (13.31) into equation (13.28), the deflection  $y(x)$  can be obtained:

$$y = \frac{F_f \cos \phi}{6\bar{E}_x I} \left[ x^3 - \left( 1 + \frac{L_1}{L_7} \right) < x - L_1 >^3 - L_1^2 x \right] + \frac{m_t g}{6\bar{E}_x I} \left[ < x - L_1 - L_8 >^3 - \left( 1 - \frac{L_8}{L_7} \right) < x - L_1 >^3 \right] - \left( 1 - \frac{x}{L_1} \right) \frac{F_f}{K_N} \cos \phi \quad (13.32)$$

The deflection of the end effector  $d_a$  can be obtained by substituting  $L_1 + L_7$  for  $x$ :

$$d_a = \frac{F_f \cos \phi}{3\bar{E}_x I} (L_1^2 L_7 + L_1 L_7^2) - \frac{m_t g}{\bar{E}_x I} (2L_7^2 L_8 - 3L_7 L_8^2 + L_8^3) + \frac{F_f}{K_N} \cos \phi \left( \frac{L_7}{L_1} \right) \quad (13.33)$$

### 13.4.3 Properties of the Carbon-Fiber Epoxy Composite

The high-modulus carbon-fiber epoxy composite was chosen for both the arm and the power transmission shaft material. The unidirectional properties of the composite are

$$E_1 = 207 \text{ GPa}$$

$$E_2 = 13.8 \text{ GPa}$$

$$G_{12} = 5.9 \text{ GPa}$$

$$\nu_{12} = 0.28$$

$$t_{\text{ply}} = 0.125 \text{ mm}$$

The composite arm was manufactured by hand lay-up of preprints with stacking sequence  $[\pm\alpha]_N$ . The composite transmission shaft was manufactured by the filament winding method with the winding angle  $[\pm\alpha]_N$ .

### 13.4.4 Design and Manufacture of the Composite Arm

The design criterion of the static accuracy of the robot was that the deflection of the end effector should be less than 0.1 mm from the undeformed position when 70 N payload and gravity acted on the robot. The deflection of the end effector  $d_a$  in equation (13.33) by the payload and the robot's own weight can be calculated if the equivalent bending stiffness  $\bar{E}_x I$  of the composite arm is known. The box-type section of the arm was chosen because of its high bending and torsional rigidity. The outside sectional size of the arm was chosen as 100 mm  $\times$  100 mm and the thickness of the arm was chosen as 5 mm. Then  $I = 2.866 \times 10^{-6} \text{ m}^4$ . The stacking angle was selected by taking the torsional rigidity of the arm into consideration. If the stacking angle is chosen as 0°, the longitudinal modulus becomes maximum. However, in that case both the shear modulus and the transverse modulus become the minimum values. Since the robot arm must withstand some torsional loads, the stacking angle of the composite arm must be larger than 0°. If the stacking angle is increased

beyond  $15^\circ$ , the longitudinal Young's modulus drops quickly. Therefore the stacking sequence  $[\pm 15]_{10S}$  was chosen for the prepreg lay-up. The equivalent bending stiffness  $\bar{E}_x I$  for the forearm (calculated in problem 6.16) is  $5.15 \times 10^5 \text{ Nm}^2$ .

#### 13.4.5 Design and Manufacture of the Composite Transmission Shafts

The angular deformations of the power transmission shafts affect the accuracies of the wrist and the end effector. For the anthropomorphic robot of figure 13.24, the maximum angular deformation of the shaft was limited to  $0.033^\circ$  ( $0.58 \times 10^{-3}$  rad). The relationship between the angular deformation  $\Psi$  and the applied torque  $T$  of the composite shaft is

$$\Psi = \frac{L}{G_{xy} J} T \quad (13.34)$$

where  $L$  is length of the shaft and  $J$  is polar moment of the section.

If the inner and outer diameters of the hollow shaft are  $d_i$  and  $d_o$ , respectively, then

$$J = \frac{\pi(d_o^4 - d_i^4)}{32} \quad (13.35)$$

Since the diameter of the shaft cannot be increased beyond the size limit of the forearm, the shear modulus  $G_{xy}$  of the composite must be increased to reduce the angular deformation. The shear modulus can be increased by increasing the stacking or winding angle of the carbon fibers on condition that the fundamental bending natural frequencies of the shaft exceed the maximum rotational speed of the motor. Even though the maximum rotational speed of the motor was about  $10^4$  rpm (167 Hz), the rotational speeds of the shafts were 2 Hz because the angular speed of the motor was reduced 80 times by a harmonic drive. Therefore, the winding angle  $[\pm 45]_{nT}$  was chosen for the filament winding angle without taking the whirling of the shaft into consideration. Then the shear modulus  $G_{xy}$  of the composite was 53.5 GPa.

Figure 13.29 shows the relationship between the torque and the rotational speed of the motors (MO80) used for the end effector (pitch motion) and the wrist (roll

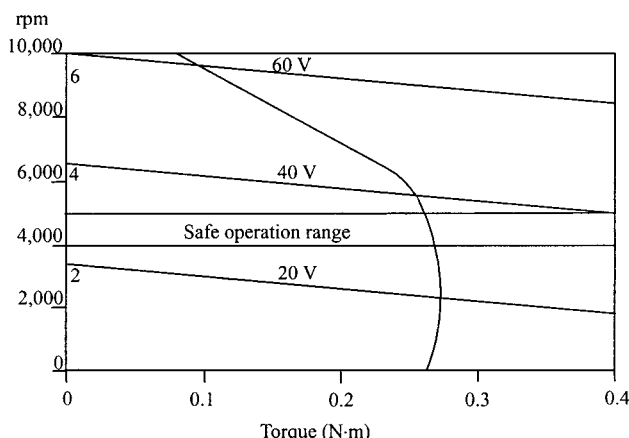


**Figure 13.29** Torque characteristics with respect to rotation speed of the MO80 motor.

**Table 13.11 Dimensions and Angular Displacements of the Steel and the Composite Hollow Drive Shafts**

		Effective length (mm)	Outer diameter (mm)	Inner diameter (mm)	Shear modulus		Angular displacement (radian)
					$G_{xy}$ (GPa)	Polar moment of section $J$ ( $m^4$ )	
<b>Pitch</b>	Steel	996	62	56	80	$48.5 \times 10^{-8}$	$0.53 \times 10^{-3}$
	Composite	996	60	50	54	$65.8 \times 10^{-8}$	$0.57 \times 10^{-3}$
<b>Wrist roll</b>	Steel	976	76	71	80	$78.0 \times 10^{-8}$	$0.32 \times 10^{-3}$
	Composite	976	74	66	54	$108.1 \times 10^{-8}$	$0.34 \times 10^{-3}$

**Table 13.12 Properties of the Hysol EA 9309.2 NA Adhesive (Data from the Hysol Aerospace and Industrial Products Division)**

Mixing ratio by weight (Part A : Part B)	100 : 22
Curing time	7 h (at 25°C)
	1 h (at 75°C)
Mixed viscosity	1500 P
Service temperature	80°C
Tensile modulus	1.20 GPa (at 25°C)
Poisson's ratio	0.4
Shear modulus	0.51 GPa (at 25°C)
Shear strength	30.0 MPa (at 25°C)
Lap shear strength	14.2 MPa (at 25°C)

motion). The motor torque at continuous 3000 rpm use was 0.27 Nm. This torque was increased to 20.5 Nm by the harmonic drive, whose efficiency was 96%. Table 13.11 shows the dimensions of the composite shafts and angular displacements when 20.5 Nm was applied to the shafts. The calculated angular displacements satisfied the limit of the angular deformation of  $0.58 \times 10^{-3}$  rad. The outside diameter of the composite shafts was 2 mm smaller than that of the steel shafts because the composite shafts required the tolerance for the fabrication of the double-lap joints.

### 13.4.6 Design and Manufacture of the Joints

Two different types of joints were designed and manufactured. In order to join the composite arm and the transmission shafts to the gear box and the bearing housings, tubular adhesively bonded double-lap joints were used. Also, the hybrid joint composed of mechanical and adhesive joints was used to join the composite arm to the upper arm and the yokes.

An epoxy adhesive (Hysol EA9309.2 NA), whose properties are shown in table 13.12, was used for bonding. The adhesive is rubber toughened and has a low viscosity before cure. The torque capacity of the adhesive joint decreases as the adhesive thickness increases because thermal residual stresses and void entrapment

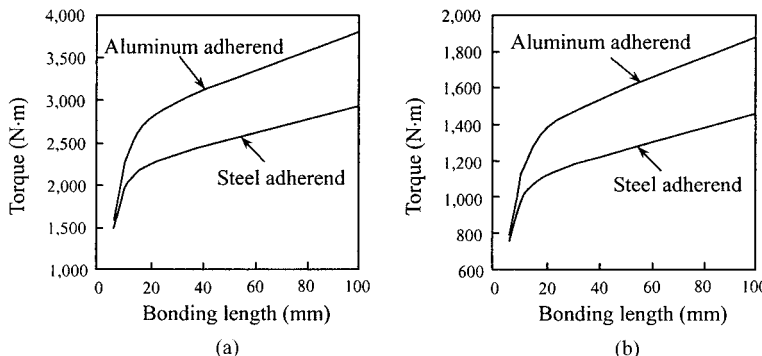


**Figure 13.30** Effects of bonding length on the maximum static torque transmission capability when the adhesive thickness was 0.1 mm: (a) Drive shaft 1; (b) drive shaft 2.

become dominant when the adhesive thickness is large. Since Lee et al. (1991a) suggested that the adhesive thickness should be smaller than 0.15 mm, an adhesive thickness of 0.10 mm was chosen.

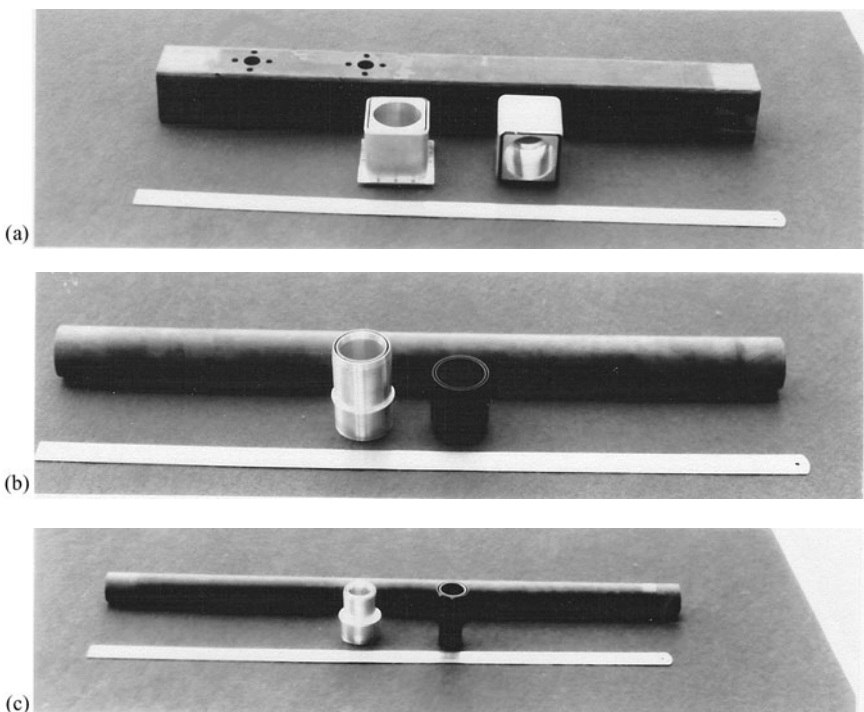
In order to estimate the torque capacity of the adhesively bonded joint, the torque capacity was calculated using the method of chapter 9 with linear elastic adhesive properties. Figure 13.30 shows the torque capacities of the joints versus joint lengths when Hysol EA 9309.2 NA was used for the adhesive. When the adhesive thickness was 0.1 mm, the rate of increase in torque capacity lessened as the adhesive length became larger than 20 mm, as shown in figure 13.30. Although the 20 mm joint length was enough, a 50 mm joint length for the transmission shafts and a 100 mm joint length for the forearm were chosen because the joining operation becomes difficult or the joint becomes weak due to the bending moment as the joint length becomes smaller. The aluminum adherends for the double-lap joints of the forearm and the transmission shafts were manufactured by electrodischarge machining.

Figure 13.31 shows the joint components of the arm and the transmission shafts. Figure 13.32 shows the adhesively bonded composite arm and transmission shafts.

The joint between the composite forearm and the yoke and the joint between the composite forearm and the upper arm must sustain tensile forces as well as shear forces. Since the adhesively bonded joint is strong for shear forces but weak for tensile forces, a hybrid-type joint that uses both mechanical and adhesive joining was designed and manufactured. The adhesively bonded part of the joint reduces the stress concentration caused by the holes fabricated for the mechanical joints. In this work the circular cup-shaped steel plate, which Nilsson (1989) suggested to reduce the stress concentration of composite materials, was chosen as the reinforcement of the hybrid joint. Figure 13.33 shows the hybrid joint configuration and figure 13.34 shows the hybrid joint after joining.

#### 13.4.7 Comparisons of the Composite Forearm and the Steel Forearm

A steel forearm of the same size as the composite forearm was manufactured in order to compare the static and dynamic performances of the two forearms. However, the size of the composite forearm was a little different from the steel forearm because the composite forearm required an adhesive joining area. Table 13.13 shows the sizes and the second moments of area of the two forearms.



**Figure 13.31** Joint components of the composite arm and the hollow drive shafts: (a) Arm and box-type metal adherends; (b) drive shaft 1 and cylindrical metal adherends; (c) drive shaft 2 and cylindrical metal adherends.

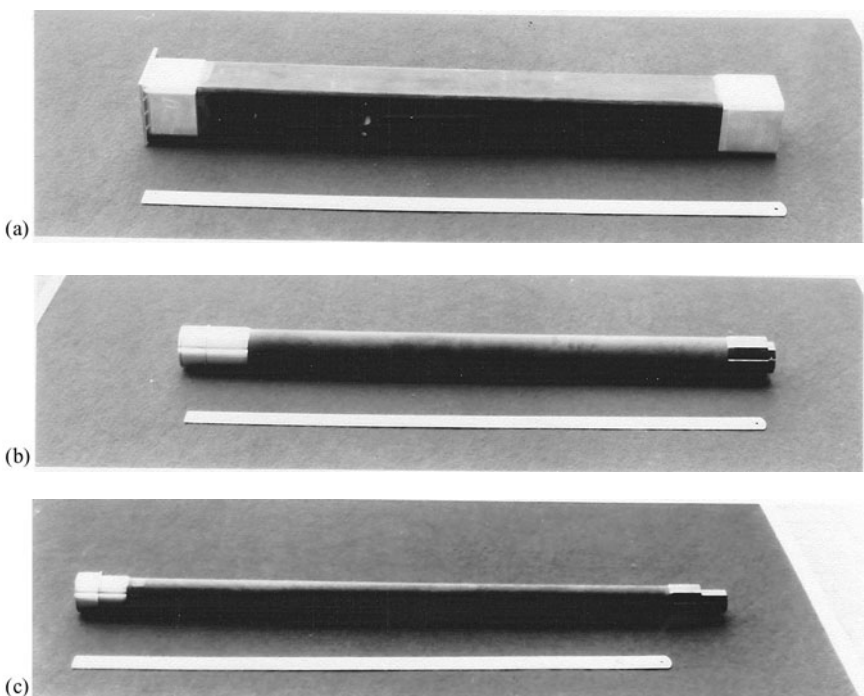


**Figure 13.32** Composite arm and hollow drive shafts after joining: (a) Arm; (b) drive shaft 1; (c) drive shaft 2.

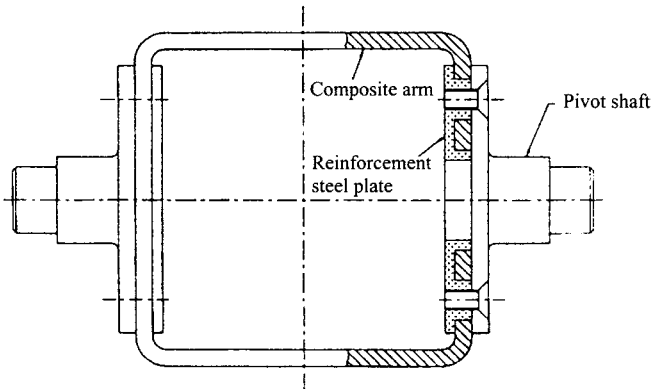


**Figure 13.33** Hybrid joint configurations of the composite forearm and the metal pivot shaft.

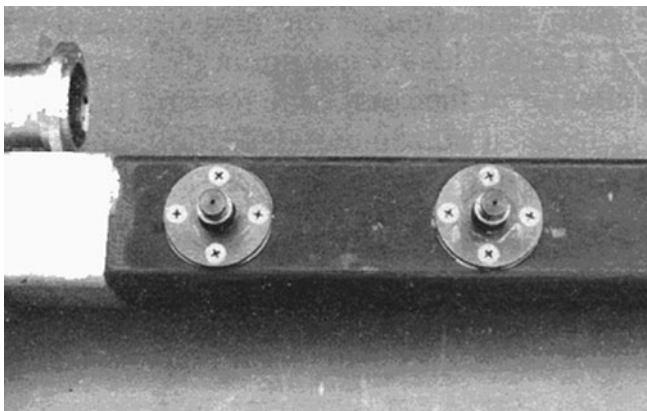


**Figure 13.34** Joint for the composite forearm and the metal pivot shafts.

**Table 13.13 Arm Dimensions of the Composite Forearm and the Steel Forearm**

	Inner area (mm <sup>2</sup> )	Outer area (mm <sup>2</sup> )	Thickness (mm)	Second moment of area (m <sup>4</sup> )
Composite	90 × 90	100 × 100	5	$2.87 \times 10^{-6}$
Steel	91 × 91	100 × 100	4	$2.36 \times 10^{-6}$

Table 13.14 shows the masses of the arms and the drive shafts. The mass of the composite arm was 3.1 kg and the composite transmission shafts for the wrist motion and the end effector pitch motion were 2.1 kg and 2.0 kg, respectively. The mass of the steel arm was 13.8 kg and the steel transmission shafts for the wrist roll motion and the end effector pitch motion were 4.8 kg and 4.5 kg, respectively. Therefore, the difference in mass between the composite forearm and the steel forearm was 15.9 kg.

Table 13.15 lists the mass distributions and lengths for the lumped model of figure 13.26.

The stiffness constant  $K_N$  of the ball-screw nut was 290 N/μm. The Young's modulus of the steel was chosen as 207 GPa. Using these data and the equivalent

**Table 13.14 Masses of the Arms and the Drive Shafts of the Forearms**

	<i>Arm</i>	<i>Drive shaft 1</i>	<i>Drive shaft 2</i>
Composite	3.1 kg	2.1 kg	2.0 kg
Steel	13.8 kg	4.8 kg	4.5 kg

**Table 13.15 Masses and Dimensions of the Composite Forearm and the Steel Forearm**

	<i>Mass (kg)</i>		<i>Dimension (mm)</i>	
Composite forearm	$m_1 = 7.27$	$m_2 = 10.44$	$L_1 = 200.0$	$L_2 = 192.0$
	$m_3 = 27.01$	$m_t = 44.72$	$L_3 = 13.0$	$L_4 = 173.4$
			$L_5 = 800.0$	$L_6 = 328.0$
			$L_7 = 1050.0$	$L_9 = 250.0$
Steel forearm	$m_1 = 24.2$	$m_2 = 8.5$	$L_1 = 200.0$	$L_2 = 192.0$
	$m_3 = 28.3$	$m_t = 61.0$	$L_3 = 13.0$	$L_4 = 173.4$
			$L_5 = 800.0$	$L_6 = 328.0$
			$L_7 = 1050.0$	$L_9 = 250.0$

mass of the payload  $m_L = 7 \text{ kg}$ , the deflection  $d_a$  of the end effector was calculated. From the numerical values, it was found that the maximum deflection of the arm occurred when  $\phi = 8^\circ$ . The calculated maximum deflection of the end effector of the composite forearm  $(d_{ac})_{\max}$  and the calculated maximum deflection of the end effector of the steel forearm  $(d_{as})_{\max}$  were

$$(d_{ac})_{\max} = 0.074 \text{ mm}$$

$$(d_{as})_{\max} = 0.077 \text{ mm}$$

These two values satisfied the 0.1 mm deflection criterion.

Figure 13.35 shows the impulse frequency responses of the composite arm and the steel arm. The two arms were suspended in the air by nylon strings and the vibrational characteristics were obtained by fast Fourier transformation (FFT) after giving an impulse to the arms. Figure 13.35(a) shows the vibrational responses in the 1.6 kHz base band and figure 13.37(b) shows the vibration responses in the 200 Hz zoom band. The fundamental natural frequencies of the steel arm and the composite arm were 650 Hz and 1340 Hz, respectively, and the damping ratios of the composite arm and the steel arm were about 0.007 and 0.001, respectively. The fundamental natural frequency and the damping ratio of the composite arm of the anthropomorphic robot were two and seven times larger, respectively, than those of the steel arm of the robot.

### 13.5 Composite Flexspline for a Harmonic Drive

The harmonic drive is a special type of speed reduction mechanism whose operation principle is based on elastic deformation rather than rigid body motion

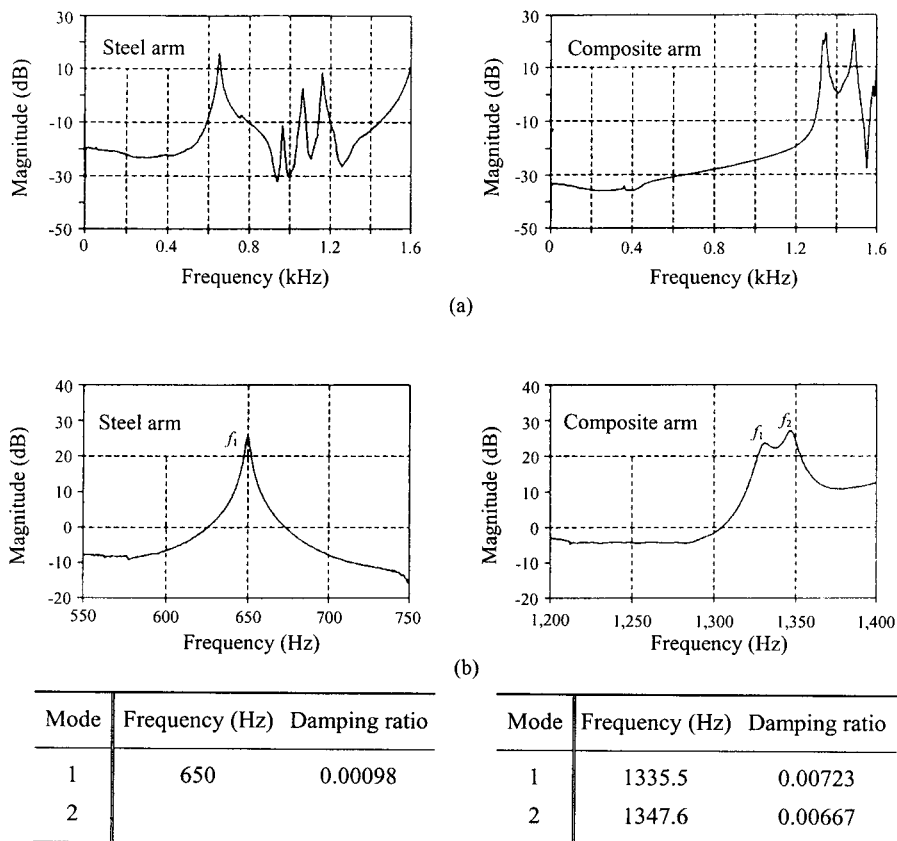


**Figure 13.35** Impulse–frequency responses of the composite and the steel arm: (a) Represented in 1.6 kHz base band; (b) represented in 200 Hz zoom band.

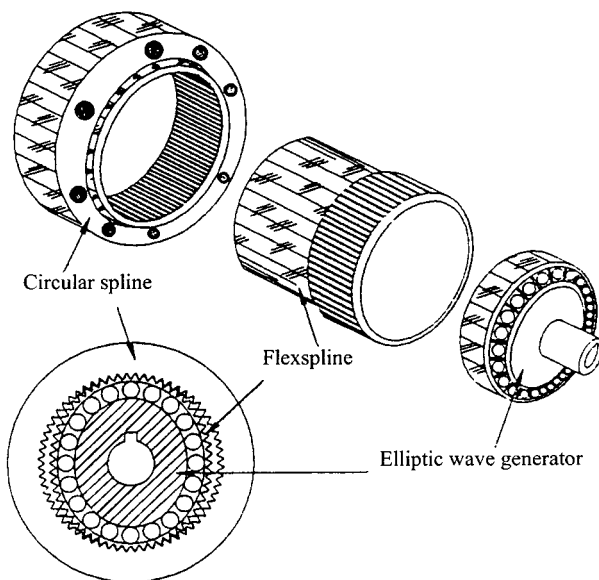


**Figure 13.36** Configuration of the cup-type harmonic drive (from Jeong et al., 1996).

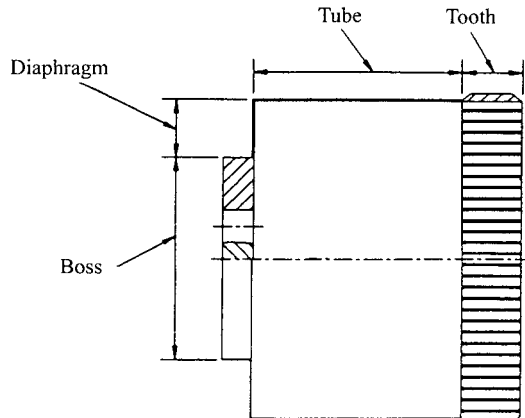


**Figure 13.37** Shape of the cup-type flexspline (from Jeong et al., 1996).

(Musser, 1959, 1960, 1961). The harmonic drive is widely used in industrial robots and precision mechanisms because of its high speed reduction ratio, high rotational accuracy, high torque transfer per unit of weight, high efficiency, and negligible backlash, compared with standard gear systems (Nicholas, 1960; Carlson, 1985; Giovanni and Rodolfo, 1992). The harmonic drive is composed of a rigid circular spline, a flexible spline (called a flexspline), and an elliptical wave generator, as shown in figure 13.36 (Jeong et al., 1996). The ball bearing mounted on the elliptical wave generator deforms the flexspline, thus engaging teeth at diametrically opposite points coincident with the major axis of the elliptical wave generator and disengaging points at the minor axis. When the circular spline is fixed, the rotation of the wave generator produces a reverse motion of the flexspline; if the rigid circular spline has 202 teeth and the flexspline has 200 teeth, then a single revolution of the wave generator rotates the flexspline backward two teeth. In this case, the rotational velocity ratio is 100:1. The number of teeth on the flexspline is usually two or four less than the number on the circular spline.

The input torque of the harmonic drive is usually applied to the shaft of the wave generator, which is pressure fitted to the open end of the flexspline, and the output torque is applied to the shaft at the closed end of the flexspline (Kiyosawa and Sasahara, 1992). Therefore, the flexspline is the most important part of the harmonic drive and determines the performance of the harmonic drive.

The flexspline of the harmonic drive usually has a one-piece cup-type shape, as shown in figure 13.37. Its manufacture usually requires a boring operation of a solid cylinder and special jigs to hob teeth, which requires much machining time and large material waste.

Even though the harmonic drive has many kinematic advantages, it has several dynamic drawbacks; the motion is not perfectly smooth, but has a ripple that has the same frequency as the wave generator (Andeen, 1988). The ripple can produce noise or vibration when the natural frequency of the flexspline becomes the same as the exciting frequency. Also, the torsional stiffness of the flexspline is small and decreases as the torque increases because it is designed as a thin cup shape to decrease the radial stiffness. For the better operation of the harmonic drive the following three functional requirements should be satisfied:

$FR_1$  = Decrease the radial stiffness for smooth operation

$FR_2$  = Increase damping

$FR_3$  = Increase torsional stiffness.

In addition to the functional requirements, the fundamental natural frequency of the flexspline in the radial direction should be larger than the operating frequency, which is a constraint. When the flexspline is made of conventional isotropic materials, such as steel and aluminum, the above functional requirements can be satisfied with a narrow margin of operating frequency. In fact, the robot employing the harmonic drive as its speed reducer is usually operated at low frequency so that the resonance vibration of the harmonic drive is not excited at its fundamental natural frequency in the radial direction. If a carbon-fiber epoxy composite is used as the material for the flexspline, the radial stiffness can be decreased about four times at the same natural frequency of the steel harmonic drive because the specific stiffness of carbon-fiber epoxy composite is more than four times higher than that of steel or aluminum, as already explained in chapter 2, or with the same radial stiffness the natural frequency of the composite harmonic drive can be increased at least twice that of the conventional drive. Also, since many high-strength adhesives have been developed, adhesive joining of separately manufactured composite parts and steel parts can be possible. The design parameters for the composite flexspline may be selected as

$DP_1$  = Stacking angle of composite

$DP_2$  = Adhesive joining

$DP_3$  = Cup length.

For the composite flexspline, the design matrix is

$$\begin{Bmatrix} FR_1 \\ FR_2 \\ FR_3 \end{Bmatrix} = \begin{bmatrix} X & 0 & x \\ x & X & 0 \\ X & 0 & X \end{bmatrix} \begin{Bmatrix} DP_1 \\ DP_2 \\ DP_3 \end{Bmatrix}$$

The above design matrix is slightly coupled. However, if we use high-strength carbon-fiber epoxy composite as the material for the flexspline, with a stacking sequence  $[\pm 45]_{nT}$ , the radial flexibility is dominated by the composite, not by the cup length, without decreasing the natural frequency much compared with that of the steel flexspline because the radial stiffness of the composite is much smaller than that of steel. Therefore, the design matrix for the flexspline with composites can be easily decoupled.

There has been an attempt to manufacture the flexspline using adhesive joining of separately manufactured parts. Figure 13.38 shows the shape of the flexspline

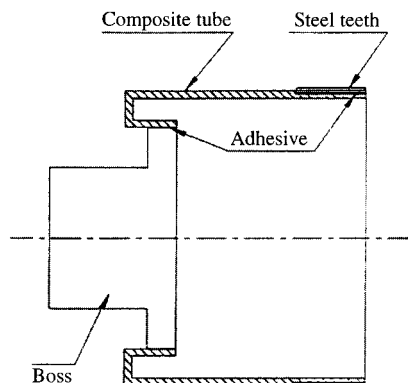


Figure 13.38 Sectional shape of the composite flexspline (from Oh et al., 1994).

manufactured by the method, in which the steel tooth section was adhesively joined to the machined surface of the composite tube. In this method, the thickness of the root tube under the steel teeth should be small to make the radial stiffness of the flexspline small. Also, the fiber breakage of the composite tube in machining was inevitable. Consequently, it was found that the tooth failed through fatigue in continuous prolonged operation.

Therefore, a new manufacturing method for the composite flexspline that can obviate the fatigue problem of the steel teeth section was developed. The one-piece, cup-type flexspline was divided into three parts, the boss, tube, and teeth sections. This method eliminated machining of the surface of the composite tube on which the steel teeth section was adhesively bonded. Since the thickness of the root tube of the teeth section can be increased without increasing the radial stiffness in this method, the possibility of failure in the teeth section was decreased. The boss and teeth sections were made of SM45C steel and the tube section was made of high-strength carbon-fiber epoxy composite material.

### 13.5.1 Design and Manufacture of the Composite Flexspline

A harmonic drive that has an average maximum torque of 100 Nm and an instant maximum torque of 150 Nm has been designed. Figure 13.39 shows the manufacturing scheme for the adhesively bonded composite flexspline. The flexspline was manufactured in three parts, as shown in figure 13.39(a), and was adhesively bonded, as shown in figure 13.39(b).

Two bonding methods may be applied in joining the three parts of the flexspline, as shown in figure 13.40. Figure 13.40(a) shows the bonding method in which the composite tube is adhesively bonded to the inside surface of the steel tooth; in figure 13.40(b), the composite tube is adhesively bonded to the outside surface of the steel tooth.

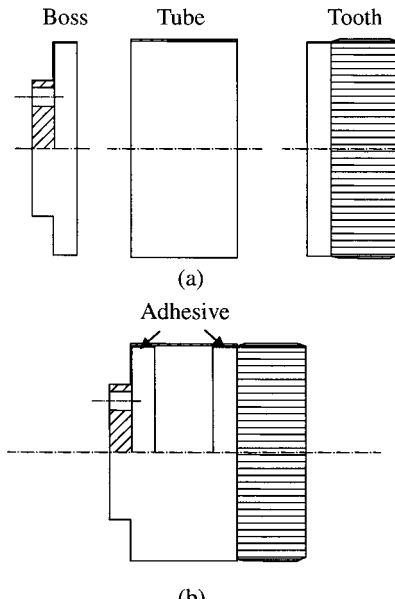


**Figure 13.39** Shapes of the developed composite flexspline: (a) Three parts; (b) assembled shape.

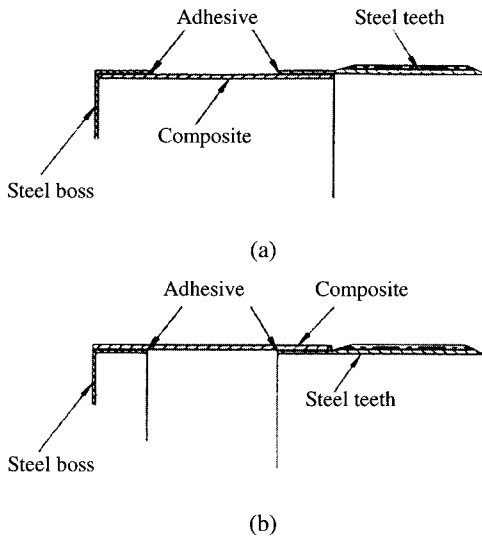


**Figure 13.40** Bonding of the composite tube to the steel tooth: (a) Inside bonding; (b) outside bonding (from Jeong et al., 1996).

Since the torsional stiffness and torque transmission capability of the adhesively bonded joint increase as the average radius of the adhesive area increases, the outside bonding, as shown in figure 13.40(b), was selected.

Since the buckling failure, as well as the shear failure, is important for the thin-walled torsional composite tube, the critical torsional buckling torque and the maximum torsional shear stress were calculated. The maximum torsional shear stress  $\tau_{\max}$  was expressed as

$$\tau_{\max} = \frac{T_{\max}}{2\pi r^2 t} \quad (13.36)$$

where  $T_{\max}$  is the applied maximum torque,  $r$  is the mean radius, and  $t$  is the thickness of the tube.

The critical buckling torque  $T_{cr}$  was expressed as (Simitses, 1967)

$$T_{cr} = 24.4 C D_{22}^{5/8} A_{11}^{3/8} r^{5/4} L^{-1/2} \quad (13.37)$$

where  $L$  is the tube length,  $A_{11}$  the extensional stiffness,  $D_{22}$  the bending stiffness, and  $C$  is the end-fixity coefficient which is 0.925 for the simply supported and 1.03 for the clamped end.

Since the torque transmission characteristics of the flexspline are most important,  $[\pm 45]_{ns}$  or  $[\pm 45]_{nT}$  stacking sequences should be employed to maximize the shear properties. If the prepreg is laid-up in the symmetric mode, there exists a seam between prepreg plies. Therefore, the stacking sequence  $[\pm 45]_{nT}$ , which does not have fiber discontinuity, was employed.

The high-strength carbon-fiber epoxy prepreg USN150 (table 13.4) was used for the flexspline material. The adhesive material used was HYSOL EA 9309.2 NA (table 13.12).

The average shear strength,  $\tau_{\max}$ , of the composite material with stacking sequence  $[\pm 45]_{nT}$  was 445 MPa, which was measured by ASTM D 4255-83. When four plies were stacked, the thickness of the composite tube was 0.6 mm and the inner radius of the composite tube was 62.4 mm. Then, the shear stress of the tube was

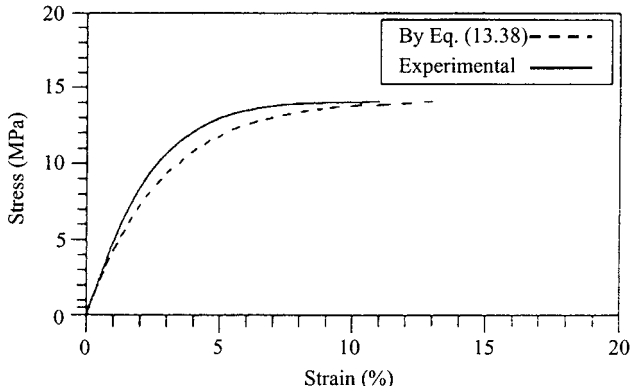


**Figure 13.41** Shear stress–strain curve of the epoxy adhesive (Hysol EA 9309.2 NA) (from Jeong et al., 1996).

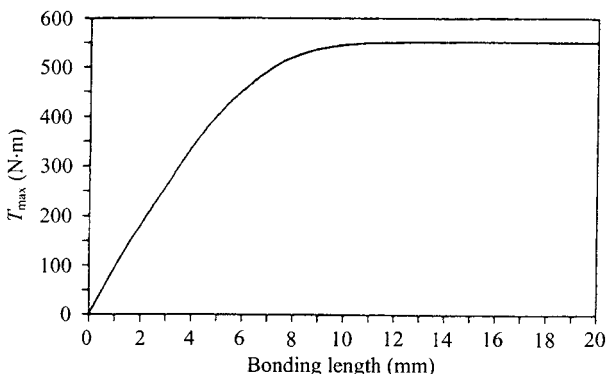


**Figure 13.42** Maximum static torque transmission capability of the flex spline with respect to bonding length.

40.1 MPa from equation (13.36) when the maximum instantaneous torque 150 Nm was applied. Since the safety factor was 11.1 in this case, this value of composite thickness was selected.

In order to determine the bonding length for the composite flex spline, the nonlinear adhesive properties must be included because the majority of the load transfer of the adhesively bonded joint is accomplished by the nonlinear elastic behavior of the adhesive, as discussed in Chapter 9. Therefore, the shear stress,  $\tau_a$ , versus shear strain,  $\gamma_a$ , curve of the adhesive was represented by the curve using two parameters, the initial shear modulus,  $G_a$ , and the ultimate shear strength,  $\tau_m$  (see Section 9.4):

$$\tau_a = \tau_m \left[ 1 - \exp\left(-\frac{G_a}{\tau_m} \gamma_a\right) \right] \quad (13.38)$$

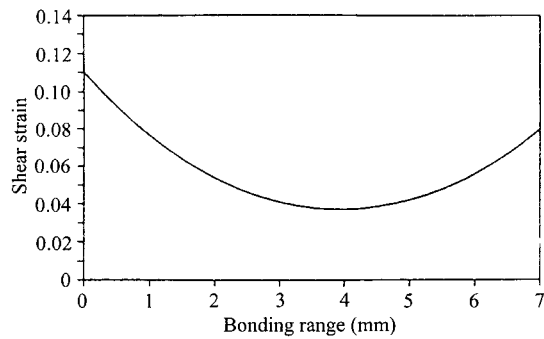
Figure 13.41 shows both the experimental shear stress–strain curve and equation (13.38) for Hysol EA 9309.2 NA adhesive in which equation (13.38) represent the experimental data with less than 7% error, which was a better representation than the linear elastic–plastic curve.

For the adhesive single-lap joint, as shown in figure 13.40(b), the torque transmission capability of the adhesively bonded joint of the flex spline was calculated following the procedure of section 9.4, with the two-parameter exponential properties of adhesive. Figure 13.42 shows the maximum torque transmission capability of the adhesive joint of figure 13.40(b) with respect to the bonding length when the data in table 13.16 were used.

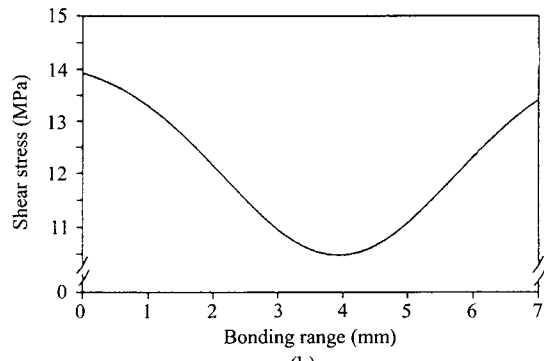
**Table 13.16 Data of the Adhesively Bonded Single-Lap Joint Used to Design the Composite Flexspline**

	<i>Shear modulus (GPa)</i>	<i>Lap shear strength (MPa)</i>	<i>Shear strain limit</i>	<i>Thickness (mm)</i>	<i>Inner radius (mm)</i>	<i>Outer radius (mm)</i>
Hysol EA 9309.2 NA	0.51	14.2	0.11	0.1	—	—
Steel tube (SM45C)	80	NR*	NR*	0.38	30.7	31.08
Composite tube [ $\pm 45$ ] <sub>2T</sub>	30.0	NR*	NR*	0.6	31.4	32.0

\*NR = not required



(a)



(b)

**Figure 13.43** Shear strain and stress distributions in the adhesive under  $T_{\max} = 490$  Nm when the bonding length is 7 mm: (a) Shear strain; (b) shear stress (from Jeong et al., 1996).

Since the maximum torque became saturated when the bonding length was larger than about 10 mm, the 7 mm bonding length was chosen. Figure 13.43 shows the shear strain and shear stress distributions in the adhesive when the bonding length is 7 mm and the maximum static torque is 490 Nm. Since the required torque of the designed harmonic drive is 150 Nm, it was found that the 7 mm bonding length is enough for the torque capacity. Then, the total length of the composite tube was determined to be 30.88 mm. Figure 13.44 shows the final dimensions of the composite flexspline.

In order to check the buckling failure of the designed composite tube using equation (13.37), the values of  $A_{11}$  and  $D_{22}$  were determined using classical lamination plate theory:

$$A_{11} = 25.7 \text{ MN/m}$$

$$D_{22} = 0.771 \text{ Nm}$$

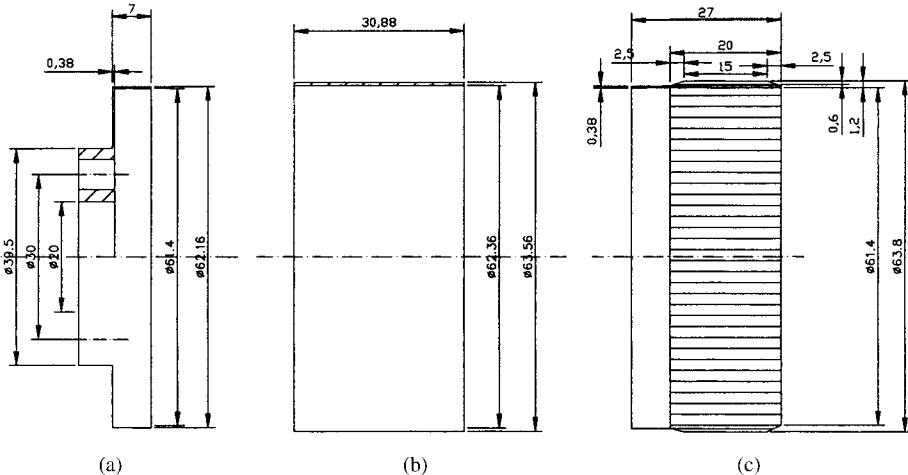


**Figure 13.44** Dimensions of the developed composite flexspline: (a) Steel boss; (b) composite tube; (c) steel teeth.

Since the input and output shafts of the flex spline are usually simply supported by ball bearings, the end fixity constant  $C$  was selected to be 0.925.

Using these values, the critical buckling torque was calculated to be 870 Nm. Since the safety factor for the buckling torque was over 4.0, the designed flexspline was satisfactory.

Figure 13.45(a) shows the separately manufactured boss, composite tube, and tooth section. Figure 13.45(b) shows the adhesively bonded composite flexspline. Figure 13.45(c) shows the conventional SM45C steel one-piece flexspline.

The static torque transmission capability of the adhesively bonded composite flexspline was compared with that of the conventional one-piece SM45C steel flexspline, as shown in figure 13.46.

In the torque transmission tests, the adhesively bonded composite flexspline failed at the adhesively bonded area between the composite tube and the tooth section, while the SM45C steel flexspline failed at the edge between the tube and the flange, as shown in figure 13.47. Since the torque transmission capability of the adhesively bonded composite flexspline was more than 475 Nm, it was concluded that the developed flexspline had enough torque transmission capability compared with the required maximum average and maximum instantaneous torque transmission capabilities, and that the developed calculation method for torque capacity using the nonlinear shear stress-strain gave a fairly accurate estimation, with an error less than 5%.

The torsional stiffness of the harmonic drive is defined as the ratio of the applied torque to the twisting angle. The initial stiffness of the harmonic drive, which is measured at a torque less than one-half of the rated capacity, is important when it is employed as a precision servo drive mechanism. Therefore, the stiffness of the harmonic drive is usually determined near the initial slope.

Figure 13.48(a) shows the method of stiffness determination. The initial stiffness,  $K_1$ , is determined in the range 0–10% of the average maximum torque, the intermediate stiffness,  $K_2$ , in the range 10–50% of the average maximum torque and the final stiffness,  $K_3$ , in the region of 50% of the maximum torque. From figure 13.48(a),  $K_1$  and  $K_2$  are important for a precise servo drive mechanism. Figure 13.48(b) shows the stiffness of the adhesively bonded composite flexspline and figure 13.48(c) shows the

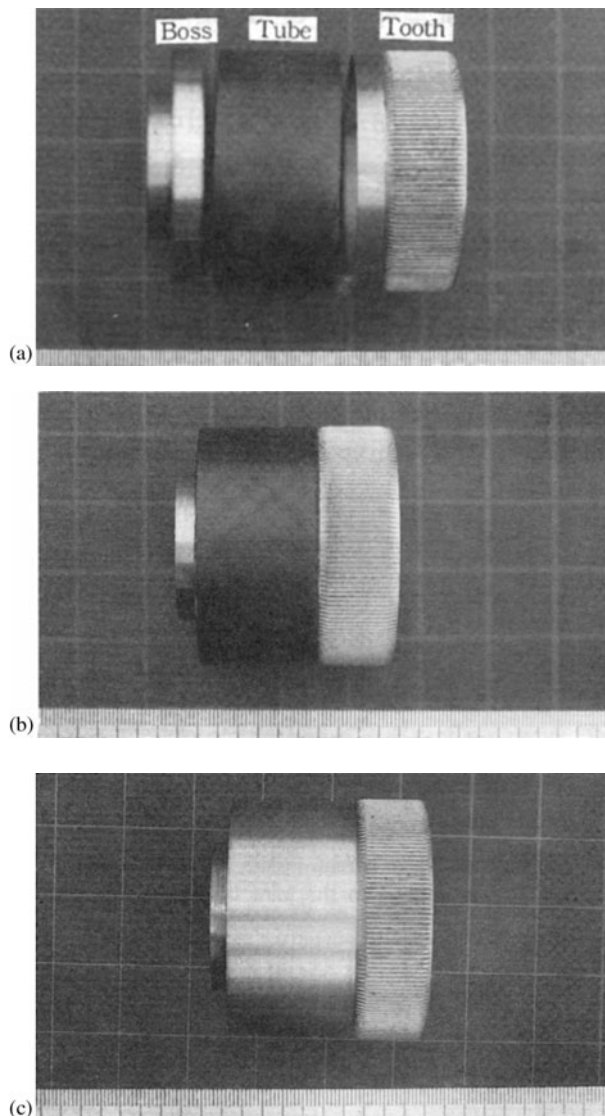


**Figure 13.45** Manufactured flexsplines: (a) Boss, tube, and tooth sections; (b) assembled composite flex spline; (c) one-piece steel flex spline (from Jeong et al., 1996).

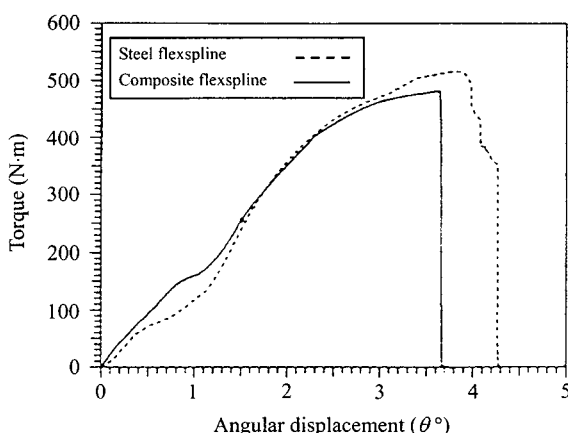


**Figure 13.46** Static torque transmission capabilities of the flexsplines.

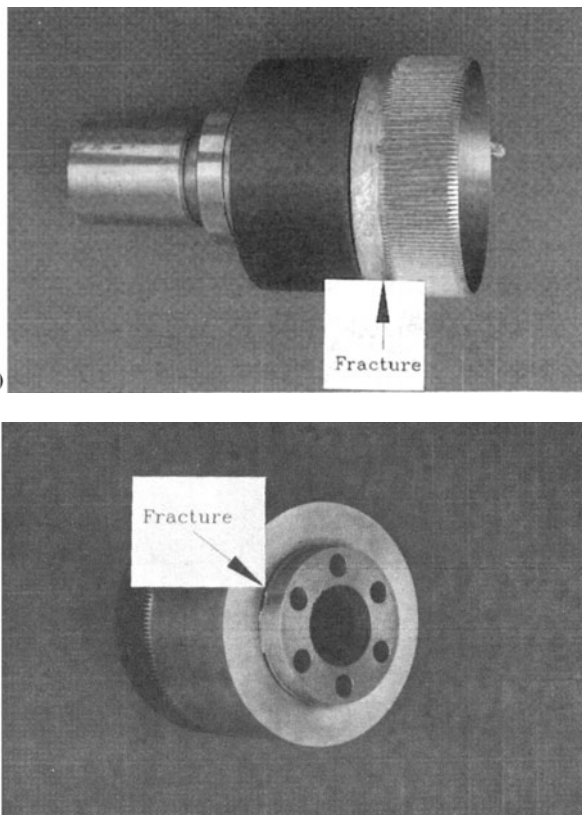


**Figure 13.47** Fracture sites of the flexsplines: (a) Composite flex spline; (b) steel flex spline (from Jeong et al., 1996).

stiffness of the conventional SM45C steel flex spline. In figure 13.48, the applied torques  $T_1$  and  $T_2$  were 10 Nm and 50 Nm, respectively.

The stiffnesses  $K_1$  and  $K_2$  were 53% and 22% greater, respectively, than those of the SM45C steel flex spline.

The radial compliances of the composite flex spline and the steel flex spline were  $17.32 \mu\text{m}/\text{N}$  and  $16.97 \mu\text{m}/\text{N}$ , respectively. Consequently, it was found that the radial stiffness of the composite flex spline was about 2% less than that of the steel flex spline.

The vibrational characteristics of the flex spline were measured by the impulse-frequency response method. In order to measure the torsional vibration characteristics of the flex spline, a small steel tip for accelerometer mounting was adhesively bonded and an impulse was applied to the opposite position of the accelerometer. Table 13.17 shows the experimental results.

From table 13.17, it was found that the fundamental natural frequency and damping of the adhesively bonded composite flex spline in the radial direction were 14% and 105% greater, respectively, and in the torsional direction, 7.5% and 190% greater, respectively, than those of the SM45C steel flex spline.

### 13.6 Concluding Remarks

In this chapter, the design and manufacture of the composite robot hands and wrists of double-arm-type robots for handling large LCD glass panels were presented in

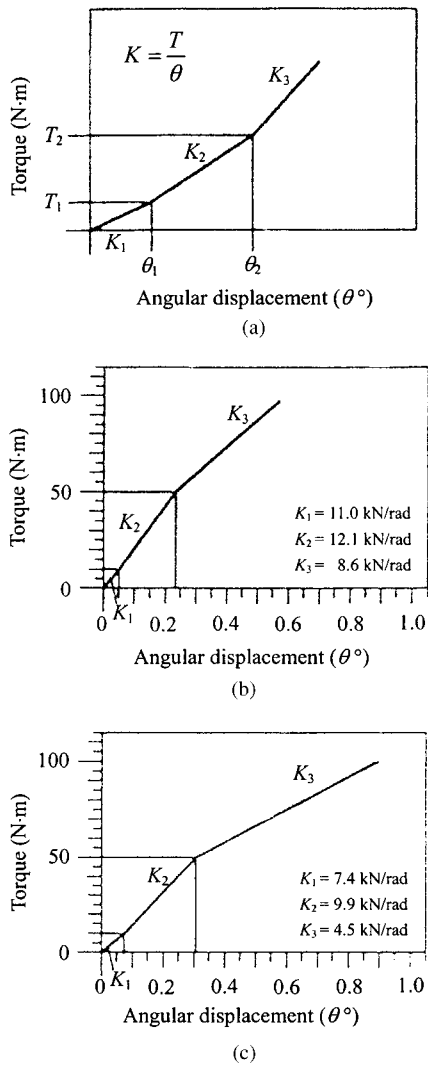


**Figure 13.48** Torque-twisting angle curves for determination of circulation direction stiffness:  
 (a) General type;  
 (b) composite flexspline;  
 (c) steel flexspline (from Jeong et al., 1996).

**Table 13.17** Fundamental Natural Frequencies and Damping Ratios of the Composite and the Steel Flexsplines

	Mode	Frequency (Hz)	Damping ratio ( $\zeta$ )
Composite flexspline	Radial	475.0	0.00351
	Torsional	396.5	0.00432
Steel flexspline	Radial	416.5	0.00171
	Torsional	368.5	0.00147

section 13.2. The hands and wrists were manufactured using sandwich structures and their weights were less than half those of the aluminum versions.

In section 13.3, the design and manufacture of arms for a SCARA-type direct-drive robot arm of 10 N payload with carbon-fiber epoxy composite material were presented. The weight saving of the composite robot arm was 14 N compared with

the aluminum robot, which is a great improvement for the robot, which assembles printed circuit boards. The fundamental natural frequency of the robot, which comes from the steel belt vibration, could not be increased; however, the second natural frequency and damping of the composite arm, which comes from the bending vibration of the arm, were 1.66 and 2.5 times larger than those of aluminum robot.

In section 13.4, the design and manufacture of the arm and transmission shafts of the anthropomorphic robot of 70 N payload with high-modulus carbon-fiber epoxy composite was presented. The mass of the composite arm was 3.1 kg and the composite transmission shafts for the wrist roll motion and the end-effector pitch motion were 2.1 kg and 2.0 kg, respectively, whereas the mass of the steel arm was 13.8 kg and the steel transmission shafts for the wrist roll motion and the end effector pitch motion were 4.8 kg and 4.5 kg, respectively. The total mass reduction of the composite forearm was 15.9 kg.

In section 13.5, a new manufacturing method for the cup-type composite flex spline for a harmonic drive was developed, using adhesive joining technology to obviate the manufacturing difficulty of the conventional one-piece, cup-type steel flex spline and to improve the dynamic characteristics of the flex spline. The boss and teeth sections of the flex spline were made of SM45C steel and the tube section was manufactured with high-strength carbon-fiber epoxy composite material. The separately manufactured parts were adhesively bonded. The torsional stiffness of the adhesively bonded composite flex spline was more than 50% and 20% greater in the initial and intermediate torque ranges, respectively, than those of the conventional one-piece SM45C steel flex spline. The damping capacities of the composite flex spline in the radial and torsional modes were more than 100% greater.

#### Note

1. Hysol Aerospace and Industrial Products Division, Dexter Co., Pittsburg, CA, USA.

#### References

- Andeen, G. B. 1988. *Robot Design Handbook*, McGraw-Hill, New York.
- Asada, H., and Youcef-Toumi, K. 1987 *Direct Drive Robots, Theory and Practice*, The MIT Press, Cambridge, Mass.
- Brändlein, J., Eschmann, P., Hasbargen, L., and Weigaud, K. 1999. *Ball and Rolling Bearings, Theory, Design and Application*, 3rd ed, John Wiley & Sons, Chichester.
- Carlson, J. H. 1985. "Harmonic Drive for Servomechanisms," *Machine Design*, January 6, pp. 102–106.
- Craig, J. J. 1989. *Introduction to Robotics, Mechanics and Control*, 2nd ed., Addison-Wesley, Reading, Mass.
- Crawley, E. F., and Mohr, D. G. 1983. "Experimental Measurements of Material Damping in Free Fall with Tunable Excitation," *AIAA/ASME/ASCE/AHS Conference Paper*, No. 83-0858-CP.
- Giovanni, L., and Rodolfo, F. 1992. "Harmonic Drive Transmissions: the Effects of Their Elasticity, Clearance and Irregularity on the Dynamic Behavior of an Actual SCARA Robot," *Robotica*, Vol. 10, pp. 369–375.
- Harris, T. A. 2001. *Rolling Bearing Analysis*, 4th ed., John Wiley & Sons, New York.

- Jeong, K. S., Lee, D. G., and Kwak, Y. K. 1995. "Experimental Investigation of the Dynamic Characteristics of Carbon Fiber Epoxy Composite Thin Beams," *Composite Structures*, Vol. 33, pp. 77-86.
- Jeong, K. S., Lee, D. G., and Kwak, Y. K. 1996. "Adhesive Joining Technology for Manufacturing of the Composite Flexspline for a Harmonic Drive," *Journal of Adhesion*, Vol. 55, pp. 329-350.
- Kiyosawa, Y., and Sasahara, M. 1992. "Development of a New Thin Harmonic Drive," *JSME, Robotics and Mechatronics Lecture Meeting Paper*, A, pp. 943-948.
- Koenigsberger, F. 1964. *Design Principles of Metal-Cutting Machine Tools*, The Macmillan Company, New York.
- Koren, Y. 1985. *Robotics for Engineers*, McGraw-Hill Book Company, New York.
- Lazan, B. J. 1965. *Multiple Band Surface Treatments for High Damping*, AFML-TR-65-269, Dayton, Ohio.
- Lee, C. S., and Lee, D. G. 2004. "Manufacturing of Composite Sandwich Robot Structures Using Co-cure Bonding Method," *Composite Structures*, Vol. 65, pp. 307-318.
- Lee, C. S., Lee, D. G., Oh, J. H., and Kim, H. S. 2002. "Composite Wrist Blocks of a Double Arm Type Robot for Handling Large LCD Glass Panels," *Composite Structures*, Vol. 57, pp. 345-355.
- Lee, D. G. 1985. *Manufacturing and Testing of Composite Machine Tool Structures*, Ph.D. Thesis, MIT, Cambridge, Mass.
- Lee, D. G., Kim, K. S., and Im, Y. T. 1991a. "An Experimental Study of Fatigue Strength for an Adhesively Bonded Tubular Single Lap Joint," *Journal of Adhesion*, Vol. 35, pp. 39-53.
- Lee, D. G., Kim, K. S., and Kwak, Y. K. 1991b. "Manufacturing of a SCARA Type Direct-drive Robot with Graphite Fiber Epoxy Composite Materials," *Robotica*, Vol. 9, pp. 219-229.
- Lee, D. G., Jeong, K. S., Kim, K. S., and Kwak, Y. K. 1993. "Development of the Anthropomorphic Robot with Carbon Fiber Epoxy Composite Materials," *Composite Structures*, Vol. 25, pp. 313-324.
- Mavilor Motor Catalog*, Mavilor Co., Ltd, Chicago, Ill.
- Musser, C. W. 1959. "Strain Wave Gearing," *United States Patent No. 2,906,143*, Sept. 29.
- Musser, C. W. 1960. "Breakthrough in Mechanical Drive Design: The Harmonic Drive," *Machine Design*, April 14, pp. 160-173.
- Musser, C. W. 1961. "A New Look at Elastic-body Mechanics," *Machine Design*, April 13, pp. 160-173.
- Nashif, A. D., Jones, D. I. G., and Henderson, J. P. 1985. *Vibration Damping*, John Wiley & Sons, Inc., New York.
- Nicholas, C. 1960. "Innovation in High-Ratio Gearing," *Product Engineering*, February 8, pp. 47-51.
- Nilsson, S. 1989. "Increasing Strength of Graphite/Epoxy Bolted Joints by Introducing an Adhesively Bonded Metallic Insert," *Journal of Composite Materials*, Vol. 23, pp. 642-650.
- Oh, H. S., Jeong, K. S., and Lee, D. G. 1994. "Design and Manufacture of the Composite Flexspline of a Harmonic Drive with Adhesive Joining," *Composite Structures*, Vol. 28, pp. 307-314.
- Oh, J. H., Lee, D. G., and Kim, H. S. 1999. "Composite Robot End Effector for Manipulating Large LCD Glass Panels," *Composite Structures*, Vol. 47, pp. 497-506.
- Rivin, E. I. 1999. *Stiffness and Damping in Mechanical Design*, Marcel Dekker, New York.
- Roark, R. J., and Young, W. C. 1976. *Formulas for Stress and Strain*, 5th ed., McGraw-Hill Book Company, New York.
- Simitses, G. J. 1967. "Instability of Orthotropic Cylindrical Shells Under Combined Torsion and Hydrostatic Pressure," *AIAA Journal*, Vol. 5, pp. 1463-1475.
- SNFA Bearings Limited, *Bearings Catalog*, 2nd ed., Section 3-2.

- Sun, C. T., and Lu, Y. P. 1995. *Vibration Damping of Structural Elements*, Prentice-Hall, Englewood Cliffs, N.J.
- Tsai, L. W. 1999. Robot Analysis, *The Mechanics of Serial and Parallel Manipulators*, John Wiley & Sons, New York.
- Wardle, F. P., Lacey, S. J., and Poon, S. Y. 1983. "Dynamic and Static Characteristics of a Wide Speed Range Machine Tool Spindle," *Precision Engineering*, Vol. 5, pp. 175-183.

## 14

# Axiomatic Design of Composite Machine Tool Structures

### 14.1 Introduction

The basic function of a machine tool is to produce a workpiece of the required geometric form with an acceptable surface finish and accuracy at as high a production rate as is economically possible (Lee, 1985; Lee et al., 1985; Choi and Lee, 1997).

Recently, in the manufacturing field, high-precision products, as well as diversified small-quantity products have been demanded, and more advanced production technologies have constantly been developed for low production cost. Therefore, there has been a growing interest in shorter machining time with increased cutting speed (Weck and Koch, 1993). However, the increase of speed in the spindle and moving parts of machine tools for productivity improvement has also increased the self-excited vibration, noise, and heat generation of spindle bearing systems.

There are two different types of vibration in machine tool structures: forced and self-excited (Tlusty, 1999). Forced vibrations are caused by an oscillating force that is produced at a distance from the cutting zone (from other machines, unbalanced shafts, gears, motors, etc.). Forced vibration occurs at the frequency of the oscillating force rather than at the natural frequency of the vibrating parts. Self-excited vibrations (chatter) occur when a surface defect produced during one revolution of the work can generate a new defect one revolution later. These vibrations occur at or near the natural frequencies of a vibrating part, and are caused by instability in the cutting process itself. Since the number of natural frequencies of a machine tool is infinite due to its continuous structural nature, chatter occurs near one of these frequencies, usually near the several lower frequencies. This type of chatter occurs when the width of cut or cutting speed exceeds the stability limit of the cut, because the interference between the cutting tool and workpiece produces a high level of energy during machining (Koenigsberger and Tlusty, 1970). The chatter, which is a vibration of the cutting tool relative to a workpiece, not only makes the surface accuracy of products worse, but also increases tool wear and deteriorates the machine tool. From the machine tool dynamics introduced briefly in appendix A of this chapter, the maximum width of cut is proportional to the static stiffness and damping ratio at the cutting tool point of the machine tool. Therefore, machine tool structures should have high static stiffness and damping without considerable

increase of temperature, because the temperature increase decreases the machining accuracy and may lead to bearing failure.

The functional requirements (FRs) of a machine tool may be expressed as

$FR_1$  = Increase the static stiffness of machine tool

$FR_2$  = Decrease the inertia of moving parts of machine tool

$FR_3$  = Increase the damping of machine tool system.

The constraints for the machine tool design are

$C_1$  = No vibration or chatter

$C_2$  = Minimize the temperature increase in the bearings, screws and other moving parts.

Many attempts have been tried to increase the dynamic stiffness, which is defined as the static stiffness times damping, without increasing the inertia of moving parts to satisfy the functional requirements of the machine tool.

The spindle bearing system from the moving parts of a machine tool is the main source of the total cutting point compliance, which is the inverse of stiffness. The spindle bearing system contributes more than 50% of the total compliance of the cutting tool point, and the other sources of compliance come from the bed, slides, and joints of the machine tool structure (Wardle et al., 1983). A simple method to increase the static stiffness and damping of the bearing of a spindle is to preload the bearing. However, excessive preloading causes bearing failure at the start of the machine tool and preloading does not always increase the damping of a machine tool spindle bearing system (Stone, 1982).

Peters (1965) developed the viscous damper in the spindle bearing structure. The viscous damper in the spindle has very good damping characteristics, but has such undesirable characteristics as power dissipation and temperature rise in the spindle bearing structure, which has adverse effects in high-speed or precision machining.

Several attempts to use high-damping materials as an additive layer in the spindle and other machine tool parts have also been conducted (Hammill and Andrew, 1973; Vandeurzen et al., 1981; Nashif et al., 1985; Jones, 1995). This method is limited by the geometric and boundary constraints and also by the lubrication and bearing mounting requirements.

One method to increase the dynamic stiffness of a machine tool is to use a material which has both high static stiffness and high damping. However, it is not possible to increase the dynamic stiffness of a conventional material because stiff conventional materials usually have low damping and vice versa, as shown in Table 14.1 (Lee, 1985).

Fiber-reinforced polymeric composite materials, on the other hand, have both high static stiffness and damping because they are composed of two materials: very high modulus fiber and high-damping polymeric matrix material. Although the principal roles of a polymeric matrix in a composite material are to transfer load between the fibers and to place fibers in space, the polymer also increases the material damping capacity of composite structures, which results in much better dynamic performance for the moving parts. Then the design parameters (DPs) can be chosen as

$DP_1$  = High-modulus carbon fiber

$DP_2$  = Box-type or hollow shaft or sandwich composite structures

$DP_3$  = Epoxy matrix.

**Table 14.1 Modulus and Damping Properties of Several Materials (from Lee, 1985a)**

Material	<i>E</i> (GPa)	Loss factor*
1018 steel	207	0.001 at 100 Hz 0.0001 at 500 Hz (Heine, 1966; Vorlichek, 1981)
Cast iron	172–193	0.003 (Adams, 1972)
Aluminum	69	0.002 at 100 Hz 0.0002 at 500 Hz (Vorlichek, 1981)
Carbon epoxy	138–500	0.01 (Crawley et al., 1983; Jeong et al., 1995)
PVC	2.1	0.2 (Reddy, 1981)
Polymer concrete	25	0.013 (Kim et al., 1995)

\*The definitions of loss factor (damping factor) are listed in Appendix B.

The design equation may be expressed as

$$\begin{Bmatrix} FR_1 \\ FR_2 \\ FR_3 \end{Bmatrix} = \begin{bmatrix} X & X & 0 \\ x & X & 0 \\ 0 & 0 & X \end{bmatrix} \begin{Bmatrix} DP_1 \\ DP_2 \\ DP_3 \end{Bmatrix}$$

There are optimum dimensions of moving structural parts when the outer dimensions of box or sandwich structures are given because section walls that are too thin may induce elastic buckling, but sections that are too thick decrease the specific stiffness of moving parts. When the high-modulus carbon-fiber epoxy composite is used for the moving parts of machine tool structures, the inertia is about one-tenth of the moving parts made of steel or aluminum because the specific stiffness of high-modulus carbon-fiber epoxy is about 10 times higher than those of conventional metals, as shown in tables 2.2 and 2.3.

Moreover, when a composite material is selected as the machine tool structure, it satisfies the high modulus and high damping requirements simultaneously. From the point of view of the information axiom, which requires the minimum content of information, the fiber-reinforced polymeric composite materials are highly beneficial because they decrease the information content for the design of moving structural parts of machine tools by integrating the high-specific-stiffness fiber and high-damping polymeric material in one structural material.

## 14.2 Composite Air Bearing Spindle System

High-speed and high-precision air spindles are widely used as components of computer hard-disk drives and dental drills, and in the machining of polygon mirrors for laser scanners because high-speed rotation with low heat generation is possible for air spindles due to the low viscosity of the air lubricant. For example, the machinability and surface roughness of wafers are improved as the speed of machining is increased, which has spurred the development and employment of higher speed air spindles in machining wafers and drilling printed circuit boards.

However, steel shafts mounted on conventional air spindles may cause either unstable operation due to whirling vibration of the shaft at relatively high rotational

speed, or rupture of the air lubricant by radial expansion of the shaft due to centrifugal force (Bang and Lee, 2002).

Until now, diverse methods for stable operation of the air spindle have been suggested and investigated by many researchers (Gross, 1962; Larson and Richardson, 1962; Taniguchi, 1967). They investigated the operating characteristics of a spindle with respect to number of supply holes, supply pressure and bearing length through experiment. The dynamic stability of an externally pressurized air bearing was modeled as a control system with feedback loop for through frequency analysis (Blondeel et al., 1980).

In order to minimize the unstable operation of air spindles, air bearings with noncircular cross-section and an active control method were suggested (Fuller, 1969; Mizumoto et al., 1996). However, the difficulty of machining precise noncircular cross-sections of the air bearing and additional devices required for active control prohibited their widespread use.

The two functional requirements of a high-speed spindle shaft are high specific stiffness ( $FR_1$ ) and high damping ( $FR_2$ ) for the improvement of stability of the air spindle. These two functional requirements can be satisfied independently by employing carbon-fiber epoxy composites for the shaft material because they have high specific stiffness ( $E/\rho$ ) and good damping property. To utilize these beneficial properties, several attempts to employ carbon-fiber composites for the shaft material of spindle have been made (Lee, 1985a; Lee et al., 1985b; Choi and Lee, 1997; Lee and Choi, 1997, Bang and Lee, 2002).

#### 14.2.1 Operational Characteristics of Air Bearing

Figure 14.1 shows a typical steel air spindle used in machining wafers and drilling printed circuit boards. The specifications of the spindle are listed in table 14.2. The carbon-fiber epoxy composite used for the air spindle shaft was USN 150, whose properties are listed in table 2.3.

Conventional air spindles are composed of air bearings, a steel shaft and an AC electric motor, as shown in figure 14.1(b), which may be modeled as a beam of bending stiffness  $EI$  supported by several springs of stiffness  $k$ , as shown in figure 14.2.

The shaft mass and stiffness of the air bearing are two major factors that influence the fundamental and second natural frequencies of the air spindle. However, the third natural frequency is determined by the bending stiffness and mass density per unit length of the shaft. The static stiffness of the air spindle at the cutting point is determined by the bending stiffness of the shaft and the radial stiffness of the air bearing.

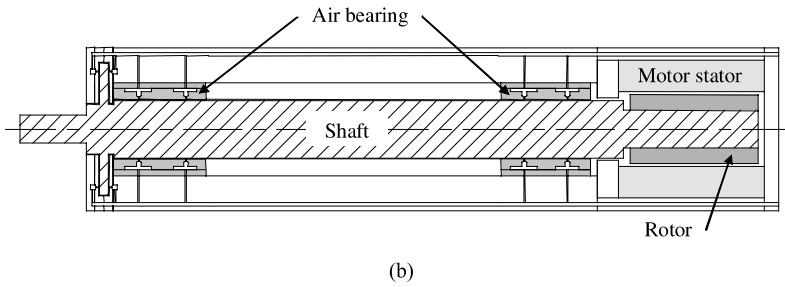
For the air bearing of figure 14.3, the outlet volume flow rate  $Q_{out}$  is expressed with the assumption of fully developed laminar flow between the parallel plates of gap  $h$  as (White, 1999)

$$Q_{out} = \frac{\pi D h^3}{12\mu} \frac{p_1 - p_0}{L} \quad (14.1)$$

where  $p_1$  and  $p_0$  represent pressures at the bearing inlet (or orifice outlet) and bearing outlet (or atmospheric pressure), respectively, and  $D$  and  $h$  represent the shaft diameter and bearing gap, respectively.



(a)



(b)

**Figure 14.1** Air spindle for machining of wafers: (a) Photograph; (b) schematic diagram.**Table 14.2 Specifications of the Air Spindle for Machining of Wafers**

Outer diameter of shaft (mm)	25
Length of shaft (mm)	210
Shaft section shape	Solid
Bearing clearance ( $\mu\text{m}$ )	15
Max. radial load capacity (N)	50
Max. radial stiffness (MN/m)	6.0
Operating speed (rpm)	$4 \times 10^4$ to $8 \times 10^4$

The mass flow rate  $\dot{M}_{\text{out}}$  may be expressed using the average air density  $\rho_{\text{avg}}$  between  $\rho_1$  at  $p_1$  and  $\rho_0$  at  $p_0$  under the assumption of constant temperature:

$$\rho_{\text{avg}} = \frac{1}{2}(\rho_0 + \rho_1) = \frac{1}{2}\left(\frac{p_1 + p_0}{p_0}\right)\rho_0 \quad (14.2)$$

$$\dot{M}_{\text{out}} = \frac{\pi D h^3}{12\mu} \frac{p_1 - p_0}{L} \rho_{\text{avg}} = \frac{\pi D h^3}{24\mu} \frac{p_1^2 - p_0^2}{L p_0} \rho_0 \quad (14.3)$$

where  $\mu$ ,  $D$ , and  $L$  represent air viscosity, diameter of the shaft, and pocket length, respectively.

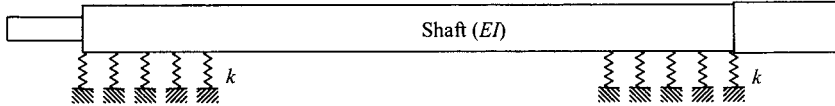


Figure 14.2 Analytic model of the air spindle.

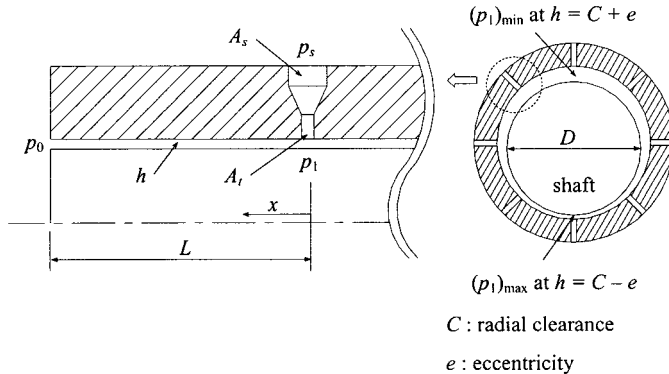


Figure 14.3 Aerostatic analysis of the air bearing.

The mass flow rate  $\dot{m}_{\text{out}}$  through one orifice is expressed under the assumption of isentropic flow (White, 1999):

$$\dot{m}_{\text{out}} = C_d A_t \sqrt{\frac{2\kappa \rho_s p_s}{\kappa - 1}} \sqrt{(p_1/p_s)^{2/\kappa} - (p_1/p_s)^{(\kappa+1)/\kappa}} \quad (14.4)$$

where  $\rho_s$  = air density at the orifice inlet

$C_d$  = orifice coefficient

$A_t$  = area of the orifice outlet

$\kappa$  = specific heat ratio

$p_s$  = pressure at the orifice inlet

When the number of orifices is  $N$ , equating equations (14.3) and (14.4) yields

$$\frac{\pi D h^3}{24\mu N} \frac{p_1^2 - p_0^2}{L p_0} \rho_0 = C_d A_t \sqrt{\frac{2\kappa \rho_s p_s}{\kappa - 1}} \sqrt{(p_1/p_s)^{2/\kappa} - (p_1/p_s)^{(\kappa+1)/\kappa}} \quad (14.5)$$

From equation (14.5), the bearing inlet pressure  $p_1$  can be calculated numerically as a function of the bearing gap  $h$ . The bearing gap  $h$  can be expressed as (Stachowiak and Batchelor, 2001)

$$h = C - e \cos \theta = C(1 - \varepsilon \cos \theta) \quad (14.6)$$

where  $C$  = bearing clearance

$e$  = eccentricity (distance between axial centers of shaft and bearing)

$\varepsilon$  = eccentricity ratio

$\theta$  = angle measured from the bottom of the shaft

The load-carrying capacity  $W$  is calculated by integrating the pressure component in the vertical direction for figure 14.3:

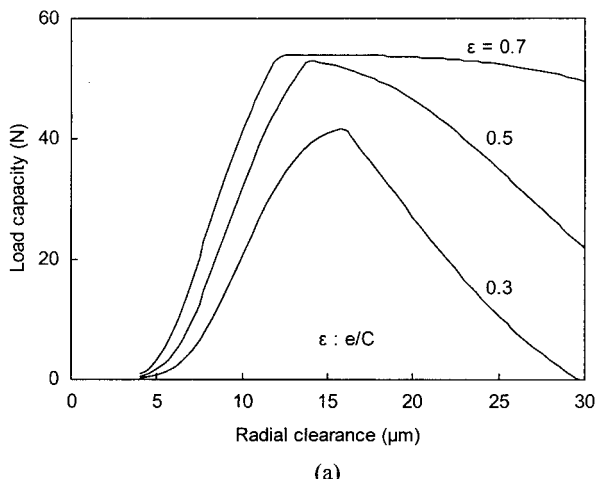
$$W = \int_0^L \int_0^{2\pi} \frac{p_1 - p_0}{L} R \cos \theta d\theta dx \quad (14.7)$$

The stiffness  $K_a$  of the air bearing is expressed as

$$K_a = \frac{W}{e} \quad (14.8)$$

However, the above derivation is only approximate because the bearing gap  $h$  was assumed constant along the circumference of the shaft in deriving equation (14.3). The better approach is to assume first the value of eccentricity ratio  $\varepsilon$  under the loading condition of  $W$ , then iterating until the correct value of  $\varepsilon$  is obtained.

Figure 14.4 shows the load capacity and stiffness of the air bearing of table 14.3. In figure 14.4, the stiffness of the air bearing increases as the radial clearance



(a)

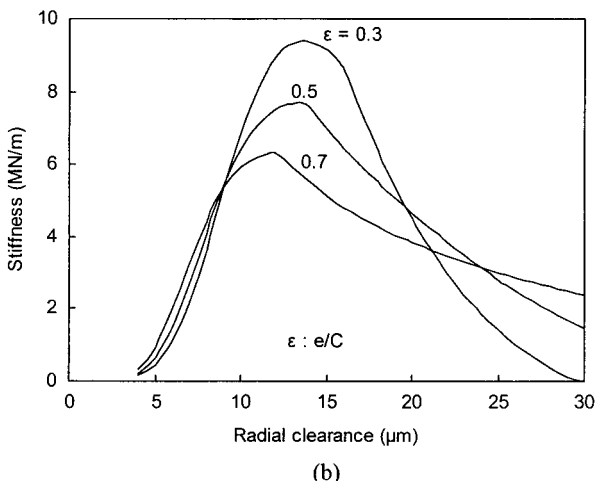


**Figure 14.4** Static characteristics of the air bearing with respect to eccentricity ratio  $\varepsilon$  and radial clearance  $h$ : (a) Load capacity; (b) stiffness.

**Table 14.3 Specifications of the Air Bearing**

Air density ( $\rho_0$ )	1.20 kg/m <sup>3</sup>
Dynamic air viscosity ( $\mu$ )	$1.8 \times 10^{-5}$ N s/m <sup>2</sup>
Specific heat ratio ( $\gamma$ )	1.4
Supply pressure ( $p_s$ )	0.5 MPa
Atmosphere pressure ( $p_0$ )	0.1 MPa
Pocket length ( $L$ )	20 mm
Bearing length	60 mm
Bearing clearance ( $C$ )	15 $\mu$ m
Orifice coefficient ( $C_d$ )	0.6
Orifice outlet diameter $d_t$	1.5 mm
Orifice outlet area $A_t$ ( $= \pi d_t^2 / 4$ )	1.766 mm <sup>2</sup>

**Table 14.4 Specifications of the Carbon Composite Shaft**

Outer diameter of shaft (mm)	25
Length of shaft (mm)	210
Shaft cross sectional shape	Hollow
Radial stiffness of air bearing (MN/m)	6
Max. operating speed (rpm)	$1.2 \times 10^5$

increases and reaches a maximum value at 15  $\mu$ m radial clearance and then decreases for the specifications of table 14.3. Since the radial clearance of the air bearing changes as the shaft expands radially due to centrifugal force and temperature rise, the stiffness of the air bearing is affected by thermomechanical characteristics of the shaft. Therefore, the shaft of the air spindle should be designed considering both dynamic and static characteristics.

The objective of the composite air spindle is to increase the operating rotational speed of the air spindle from  $8 \times 10^4$  rpm, which is the maximum operational speed of the steel spindle of figure 14.1 to  $1.2 \times 10^5$  as well as to maximize the static stiffness of the air spindle. The specifications of the carbon composite shaft in table 14.4 are the same as in table 14.2, except the maximum operating rotational speed. For the carbon-fiber composite spindle, two steel flanges were adhesively joined to the carbon-fiber shaft, as shown in figure 14.5. The two steel flanges were used for mounting a cutting tool and for the rotor of an AC electric motor.

#### 14.2.2 Vibrational Characteristics of the Carbon-Fiber Composite Spindle Shaft

To find the basic modes of vibration of the air spindle, finite element analysis of the shaft with the steel flanges was performed using the commercial FEM software, ANSYS. The shaft and the air bearings were modeled as 1-D beam elements and 1-D spring elements, respectively.

Figures 14.6 and 14.7 represent the mode shapes and natural frequencies, respectively, of the composite spindle shaft with the steel flanges. The fundamental and the second modes of figures 14.6(a) and 14.6(b) were the vibrations of the rear

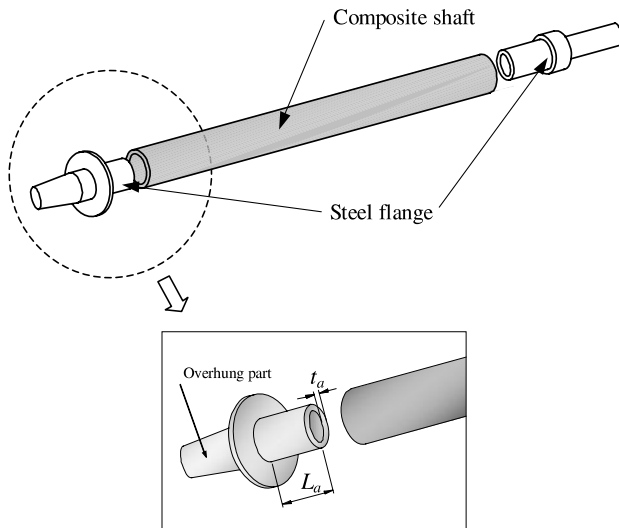


**Figure 14.5** Schematic diagram of the steel flanges and the composite shaft.

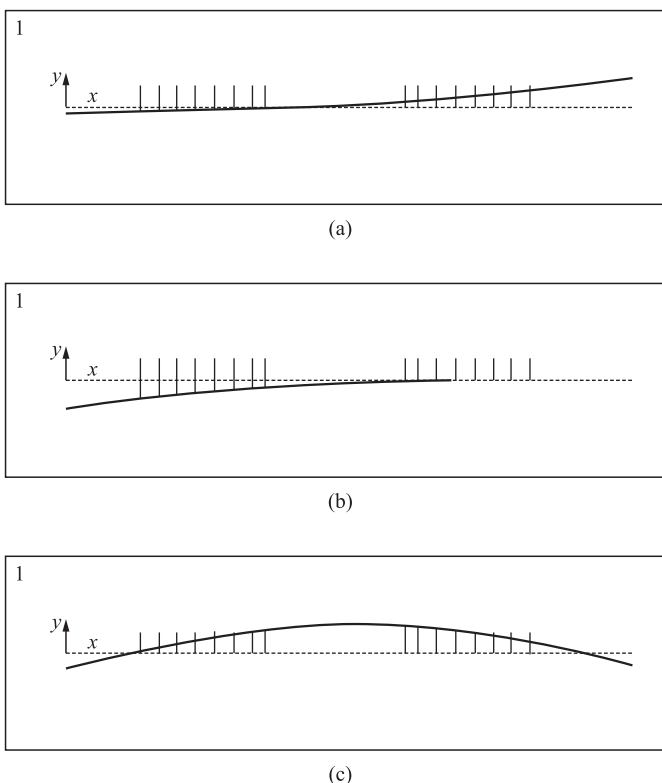


**Figure 14.6** Mode shapes of the air spindle with steel flanges: (a) Fundamental mode; (b) second mode; (c) third mode.

and front steel flanges connected to the composite shaft, respectively. The second natural frequencies of the spindle shaft with the steel flanges are a maximum when the thickness of the composite spindle shaft is around 3 mm as shown in figure 14.7(b). In figure 14.7(c), the third natural frequency of the steel shaft with

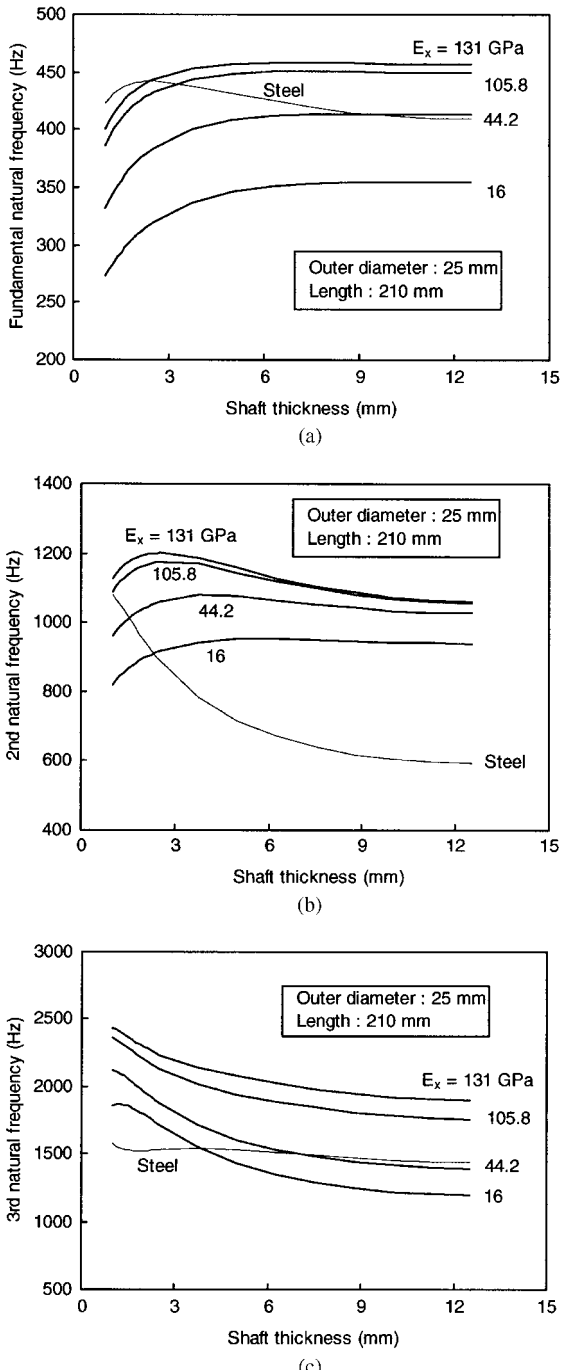


**Figure 14.7** Natural frequencies of the composite air spindles and the steel spindle with respect to thickness of the shaft: (a) Fundamental natural frequency; (b) second natural frequency; (c) third natural frequency.

solid section is about  $8.6 \times 10^4$  rpm (1430 Hz), which is below the design value of  $1.2 \times 10^5$  rpm. However, the third natural frequency of the carbon composite spindle shaft is higher than  $1.2 \times 10^5$  rpm (2000 Hz) when the shaft thickness is less than 3 mm if the axial modulus is larger than 90 GPa. Therefore, the thickness of the carbon composite spindle shaft was determined to be 3 mm, and the axial modulus of

the carbon composite spindle shaft was determined to be in the range 90–131 GPa. Also the natural frequency variation of the carbon composite spindle shaft was investigated with respect to the adherend length and adherend thickness of the steel flange when the axial modulus and thickness of the carbon composite shaft were 105.8 GPa and 3 mm, respectively.

Neglecting the stiffness and mass of the adhesive, the bending stiffness  $EI$  and mass per length  $\rho A$  of the overlapped length of the steel adherend and the carbon composite spindle shaft for the finite element model were modified as follows:

$$(EI)_{\text{eq}} = (EI)_{\text{steel}} + (EI)_{\text{composite}} \quad (14.9)$$

$$(\rho A)_{\text{eq}} = (\rho A)_{\text{steel}} + (\rho A)_{\text{composite}} \quad (14.10)$$

Figure 14.8 shows the first three natural frequencies of the carbon-fiber composite spindle shaft with respect to adherend dimensions, in which the second and third natural frequencies decrease as the adherend length and thickness increase.

#### 14.2.3 Deformations of the Carbon-Fiber Composite Spindle Shaft

The static stiffness of the air spindle is dependent on the bending stiffness of the shaft and the stiffness of the air bearing. Since the stiffness of the air bearing is much dependent on the bearing air gap, the radial expansion of the spindle shaft due to centrifugal force and the bending stiffness of the shaft should be considered during the design stage of the composite spindle shaft.

From the vibrational analysis, it was found that a stacking angle between  $0^\circ$  and  $20^\circ$  satisfies the natural frequency requirement. However, the carbon composite shaft stacked with just one angle ply is inadequate for the high-speed air spindle because the static stiffness of the air bearing may decrease by the radial expansion of the carbon composite shaft due to centrifugal force. To this end, the carbon composite shaft should have both a main stacking angle around  $0^\circ$  from the axial direction and a larger subsidiary stacking angle for the enhancement of circumferential modulus.

The static characteristics of the carbon composite shaft stacked at  $0^\circ$  at the outer part of the shaft and  $90^\circ$  at the inner part were investigated through finite element analysis using commercial FEM software, ABAQUS, under both bending load and centrifugal force, as shown in figure 14.9, which is the front part of the carbon composite spindle shaft of figure 14.5 when the thickness of the spindle shaft was 3 mm and the adherend length  $L_a$  and the adherend thickness  $t_a$  of the steel flange were 10 mm and 0.5 mm, respectively.

The static bending stiffness of the carbon composite shaft was estimated by calculating the deflection of the node 2 point in figure 14.9 when a load  $F$  of 50 N was applied at the end of the steel flange, while fixing all the axial displacements of cross-section including the node point 1. Then the effective bending stiffness  $K_{\text{eff}}$  of the carbon composite spindle shaft was defined as

$$K_{\text{eff}} = \frac{\text{Bending load}}{\delta_{\text{Node2}}} \quad (14.11)$$

Also, the maximum radial expansion of the carbon composite shaft was investigated when the rotational speed of the spindle was  $1.2 \times 10^5$  rpm.

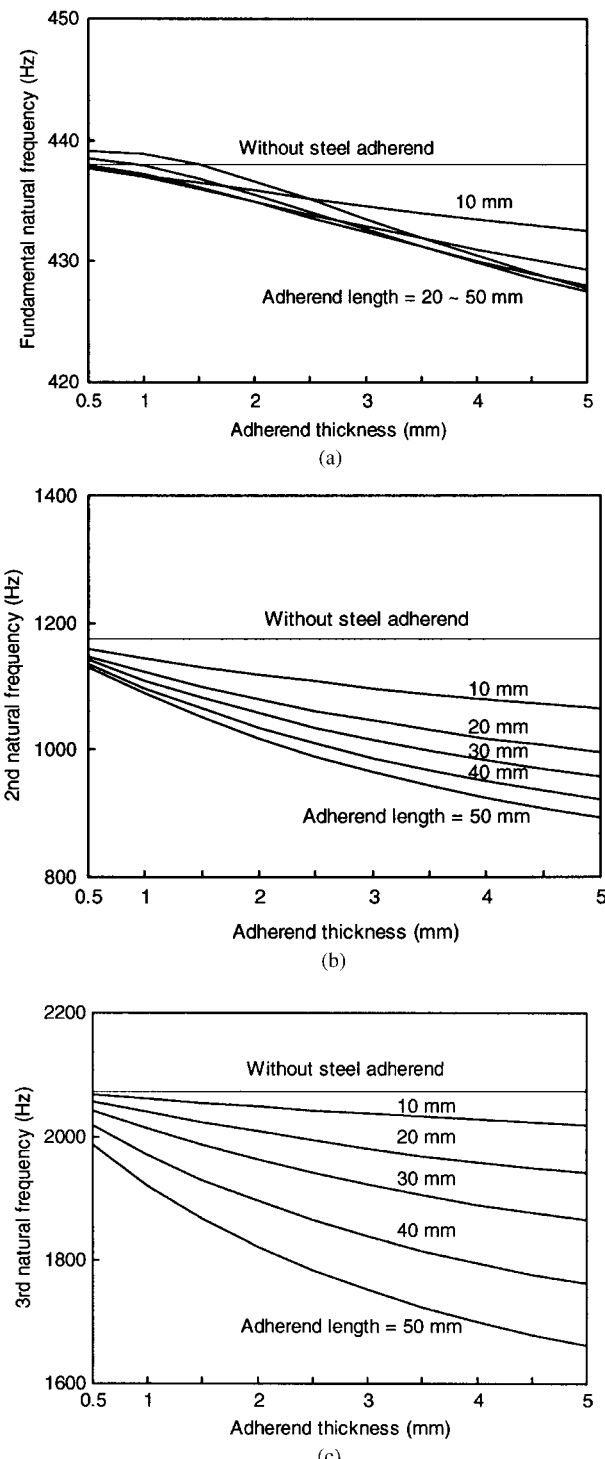


**Figure 14.8** Natural frequencies of the composite air spindle with respect to length and thickness of the steel adherend when the axial modulus is 105.8 GPa and the stacking thickness is 3 mm: (a) Fundamental natural frequency; (b) second natural frequency; (c) third natural frequency.

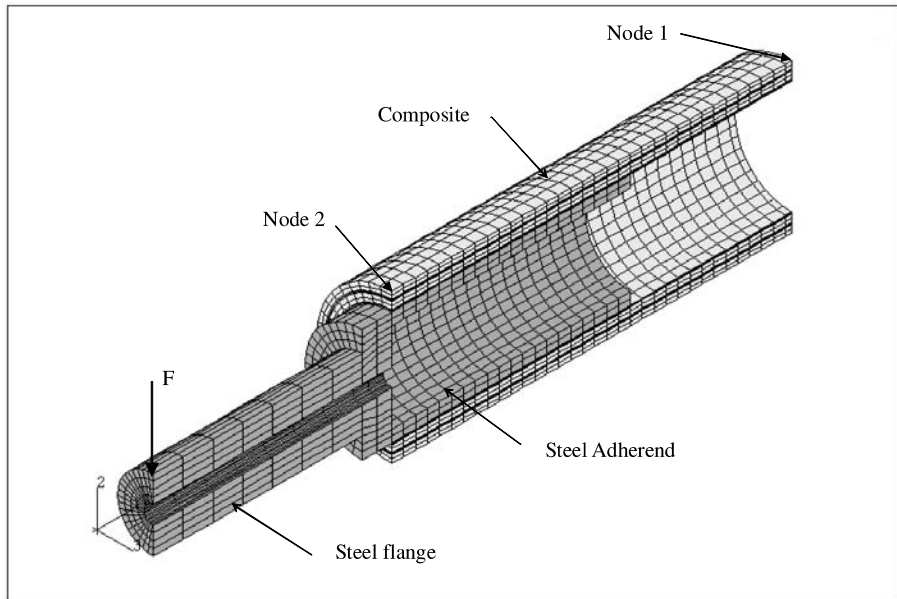


**Figure 14.9** Model of the composite shaft for finite element analysis.

Only half of the composite shaft was analyzed, owing to the symmetry of the shaft with respect to the cross-section, including the node point 1.

The effective bending stiffness and radial expansion of the carbon composite shaft with respect to stacking thickness of the subsidiary angle are shown in figure 14.10, in which the shafts without (0 mm) subsidiary plies and with 1.2 mm thickness subsidiary plies of 90° have the axial moduli of 131 GPa and 90 GPa, respectively. In figure 14.10, both the radial expansion and effective bending stiffness of the carbon composite shaft without the subsidiary plies have large values. The effective bending stiffness of the carbon composite shaft decreases and the radial expansion approaches a saturated value when the subsidiary thickness for the carbon composite shaft is larger than 0.6 mm. Therefore, the subsidiary ply thickness was determined to be 0.6 mm with stacking angle of 90°. Also, the main stacking angle was selected to be  $\pm 5^\circ$  to avoid the possibility of fracture during the grinding process of the outer surface of the composite shaft. The selected stacking angles and thickness of the carbon composite shaft are listed in table 14.5.

To investigate the static characteristics of the carbon composite shaft with respect to the stacking sequences of the main and subsidiary plies and the adherend dimensions of the steel flange, finite element analysis for the carbon composite shaft of figure 14.9 was performed with respect to the stacking patterns of figure 14.11 under bending and centrifugal forces when the adherend length of the steel flange was varied from 10 to 50 mm and the adherend thickness was varied from 0.5 mm to 5 mm. In figure 14.11, group 1 has one cluster of 90° subsidiary plies, group 2 has two clusters of 90° subsidiary plies, and group 3 has more than two clusters of 90° subsidiary plies. The stacking sequences of the nine stacking patterns, as shown in figure 14.11, are listed in table 14.6.

The effective bending stiffness and the radial expansion of the carbon composite shaft with respect to the adherend length and the adherend thickness of the steel

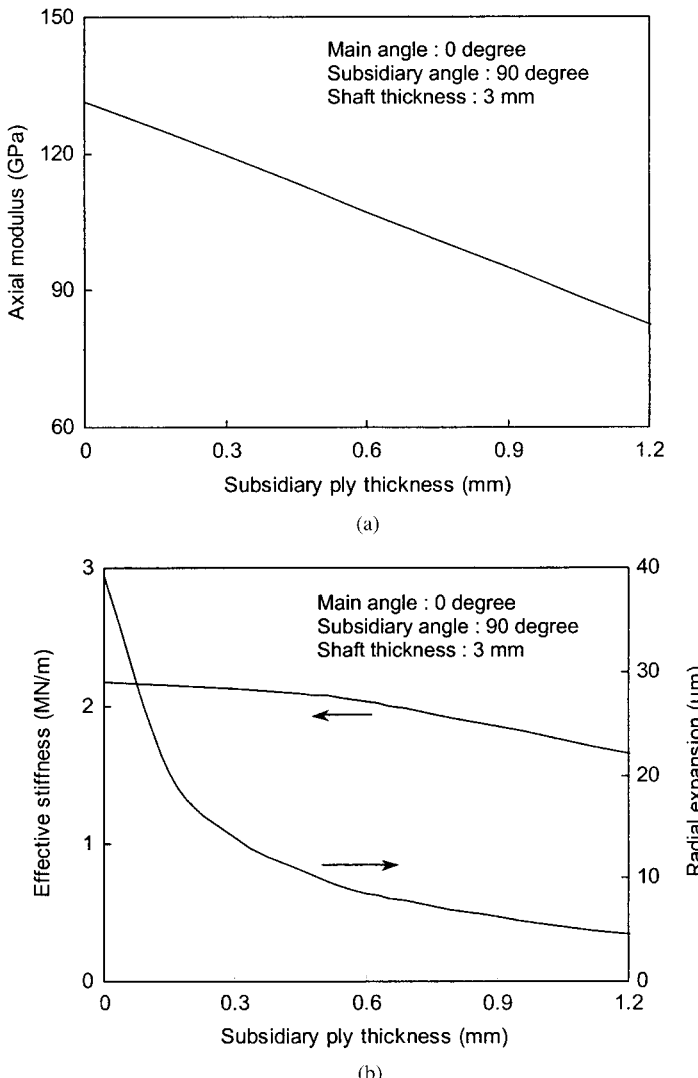


**Figure 14.10** Axial modulus, effective bending stiffness and radial expansion of the carbon composite shaft with respect to the subsidiary ply thickness when the rotational speed is  $1.2 \times 10^5$  rpm: (a) Axial modulus; (b) effective bending stiffness and radial expansion.

**Table 14.5 Stacking Angles and Thickness of the Carbon Composite Shaft**

	Stacking angle	Stacking thickness (mm)
Main	$[\pm 5]_8$	2.4
Subsidiary	$[90]_4$	0.6

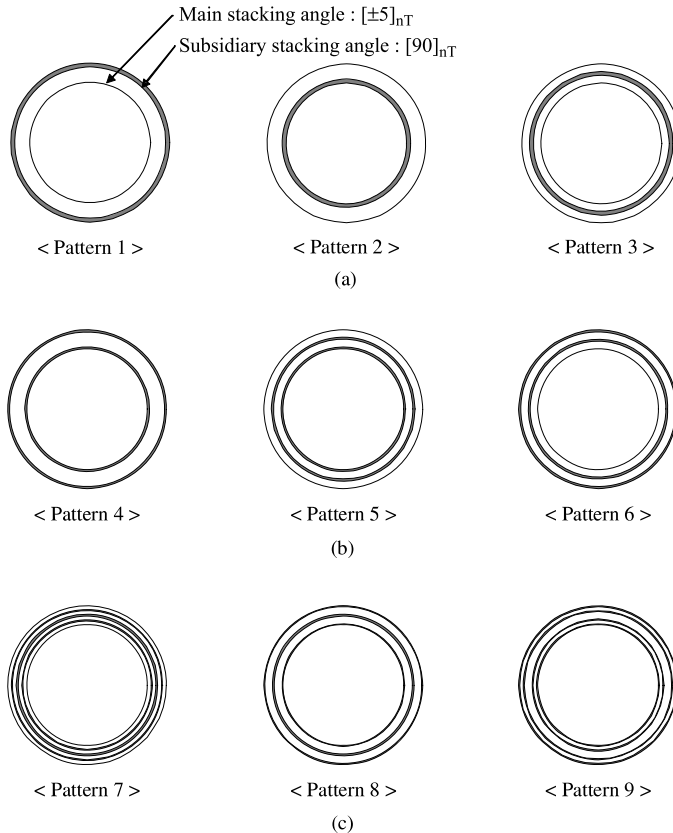


**Figure 14.11** Stacking patterns used in the evaluation of the composite shaft: (a) Group 1; (b) group 2; (c) group 3.

**Table 14.6** Stacking Sequence of Stacking Pattern for FE Analysis

Group1	Pattern 1	$[(\pm 5)_8/(90)_4]_T^*$
	Pattern 2	$[(90)_4/(\pm 5)_8]_T$
	Pattern 3	$[(\pm 5)_4/(90)_4/(\pm 5)_4]_T$
Group2	Pattern 4	$[(90)_2/(\pm 5)_8/(90)_2]_T$
	Pattern 5	$[(90)_2/(\pm 5)_4/(90)_2/(\pm 5)_4]_T$
	Pattern 6	$[(\pm 5)_4/(90)_2/(\pm 5)_4/(90)_2]_T$
Group3	Pattern 7	$[(\pm 5)_2/90/(\pm 5)_2/(90)_2/(\pm 5)_2/90/(\pm 5)_2]_T$
	Pattern 8	$[90/(\pm 5)_4/(90)_2/(\pm 5)_4/90]_T$
	Pattern 9	$[90/(\pm 5)_2/90/(\pm 5)_4/90/(\pm 5)_2/90]_T$

\*The stacking angle starts from the inner radius.

flange show similar trends regardless of the stacking patterns. The typical effective stiffness and the radial expansion curves are shown in figures 14.12(a) and 14.12(b), respectively, when the rotational speed of the spindle is  $1.2 \times 10^5$  rpm. The effective stiffness of the carbon composite shaft saturates beyond 2 mm adherend thickness of

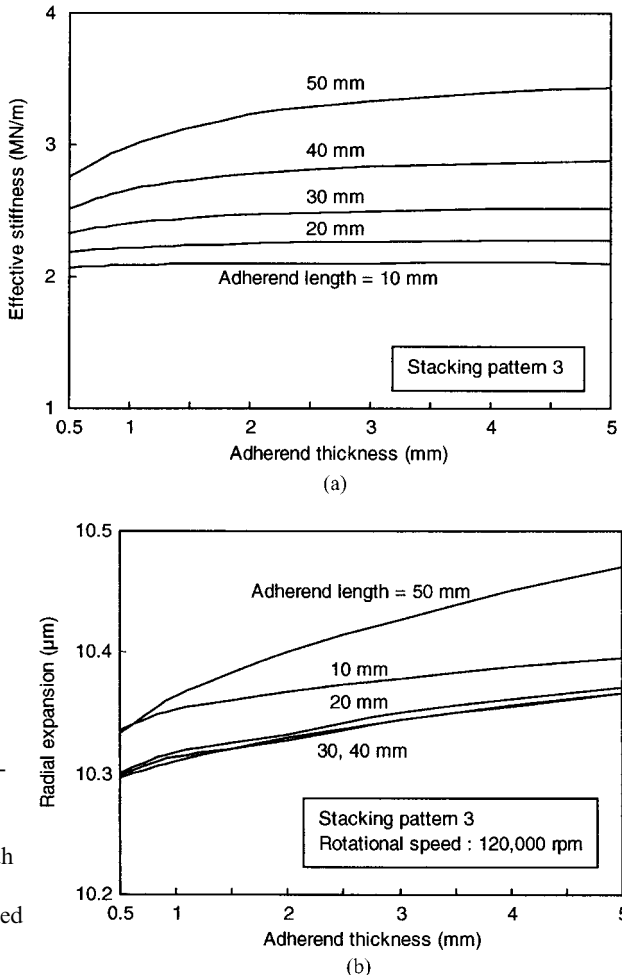


**Figure 14.12** Static characteristics of the carbon composite shaft of the stacking pattern 3 with respect to adherend length and adherend thickness of the flange when the rotational speed is  $1.2 \times 10^5$  rpm: (a) Effective stiffness; (b) radial expansion.

the steel flange and the radial expansion has a minimum value between 20 mm and 40 mm adherend length.

Figure 14.13 shows the maximum effective stiffness and figure 14.14 shows the minimum radial expansion of the carbon composite shaft with respect to stacking group. In figure 14.13, when the adherend length of the steel flange is 10 mm, the effective stiffness of the carbon composite shaft has a maximum value in the case of stacking pattern 5, in which the subsidiary plies are stacked on both the inner and middle parts. When the adherend length of the steel flange is 50 mm, the effective stiffness of the carbon composite shaft has a maximum value in the case of stacking pattern 3, in which the subsidiary plies stacked on the middle part.

Therefore, from figure 14.13, it was found that the  $90^\circ$  subsidiary plies should be stacked between the inner and middle parts to enhance the bending stiffness of the carbon composite shaft.

In figure 14.14, the radial expansion of the carbon composite shaft has a minimum value in the case of stacking pattern 2, which has the subsidiary angle in the inner part. Therefore, the  $90^\circ$  subsidiary angle should be stacked in the inner part to reduce the radial expansion of the carbon composite shaft due to centrifugal force.

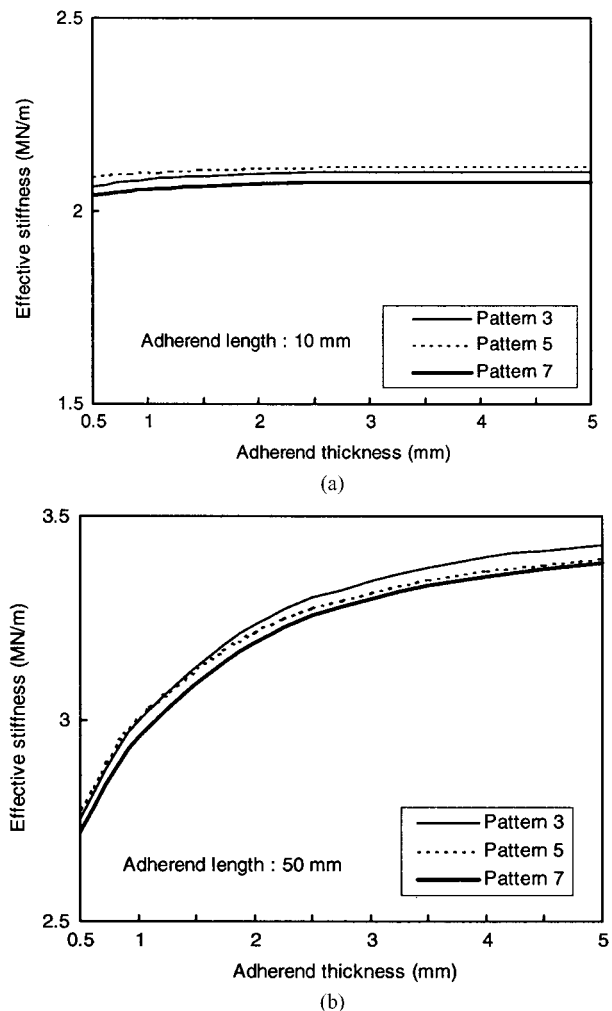


**Figure 14.13** Effective stiffness of the carbon composite shaft w.r.t. stacking patterns:  
(a) 10 mm adherend length;  
(b) 50 mm adherend length.

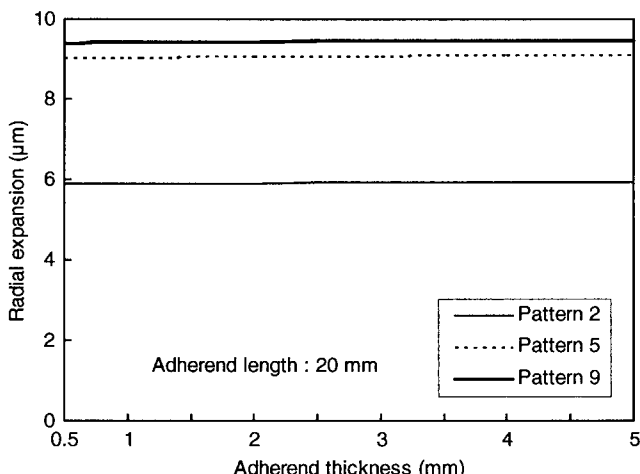


**Figure 14.14** Radial expansion of the carbon composite shaft with respect to the stacking patterns when the rotational speed is  $1.2 \times 10^5$  rpm and the adherend length is 20 mm.

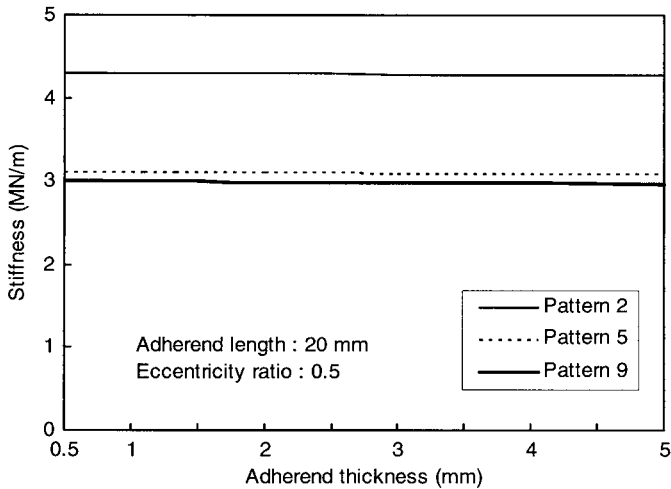


**Figure 14.15** Static stiffness of the air bearing w.r.t. the stacking patterns when the eccentricity ratio is 0.5 at  $1.2 \times 10^5$  rpm.

#### 14.2.4 Dimensions of the Carbon Composite Spindle Shaft

From the results of figures 14.13 and 14.14, the  $90^\circ$  subsidiary plies should be stacked between the inner and middle parts to increase bending stiffness, while, in order to reduce the radial expansion, the  $90^\circ$  subsidiary plies should be stacked in the inner and the outer parts.

To investigate the effect of the radial expansion of carbon composite shaft due to centrifugal force on the static stiffness of the air bearing, the static stiffness of the air bearing was calculated when the bearing rotational speed was  $1.2 \times 10^5$  rpm as shown in figure 14.15.

Although the static stiffness of the air bearing has a maximum value for the carbon composite shaft with stacking pattern 2, as shown in figure 14.15, pattern 5 of stacking group 2 was selected for the stacking sequence of the carbon composite shaft because both the bending stiffness of the shaft and the static stiffness of the air bearing were high for this case. The adherend length and thickness were determined to be 30 mm and 1 mm, respectively, considering the natural frequency of the shaft and the alignment between the shaft and the flange during adhesive bonding.

The specifications of the designed carbon composite spindle shaft are listed in table 14.7.

The composite air spindle with specifications in table 14.7 has been manufactured. The air spindle was operated successfully up to  $1.2 \times 10^5$  rpm.

### 14.3 Composite Rotor for High-Speed Induction Motors

The maximum rotating speed of high-speed spindle (or rotor) systems is usually restricted either by the maximum rotating speed of bearings,  $DN$  ( $D$ =bearing nominal diameter in mm,  $N$ =rpm), or the critical whirling vibration frequency of spindle shafts, which is proportional to  $(EI/m)^{0.5}$  ( $E$ =Young's modulus,  $I$ =flexural stiffness of shaft section, and  $m$ =mass of spindle per unit length) as discussed in chapter 6. The maximum rotating speed of bearings has been significantly increased

**Table 14.7 Specifications of the Designed Carbon Composite Shaft**

Outer diameter of shaft	25 mm
Length of shaft	210 mm
Carbon composite:	
Stacking thickness	3 mm
Stacking sequence	$[(90)_2/(\pm 5)_4/(90)_2/(\pm 5)_4]_T$
Steel flange:	
Adherend length ( $L_a$ )	30 mm
Adherend thickness ( $t_a$ )	1 mm

by employing aerostatic or magnetic bearings. For high-speed built-in motor spindle systems operating at speeds higher than 10,000 rpm, their critical whirling vibration frequencies are substantially affected by the rotor mass of the built-in motor because the rotor mass of conventional AC motors is usually larger than the shaft mass. Therefore, the rotational speed of the built-in motor spindle system can be increased if the rotor mass of motor is reduced, which increases the whirling vibration frequency and decreases the starting and stopping times of system. The rotor material should have both high magnetic permeability to increase effective magnetic flux density and low electric conductivity to decrease eddy current on the rotor surface.

The functional requirements of the rotor for a high-speed built-in motor spindle system are

$FR_1$  = Reduce the mass of motor

$FR_2$  = Increase the magnetic permeability of rotor

$FR_3$  = Increase the electrical resistivity to decrease eddy current

$FR_4$  = Guide the magnetic flux for the efficiency of the rotor.

These four functional requirements can be satisfied by employing an epoxy composite that contains magnetic powder as the rotor material with a steel ring for the guidance of magnetic flux. The electrical resistance of the magnetic-powder epoxy composite is infinite up to the volume fraction at which the direct contact of particles occurs. Therefore, the design parameters can be constructed as

$DP_1$  = Epoxy binder

$DP_2$  = Powder with high magnetic permeability

$DP_3$  = Volume fraction of magnetic powder

$DP_4$  = Steel ring.

The design equation becomes

$$\begin{Bmatrix} FR_1 \\ FR_2 \\ FR_3 \\ FR_4 \end{Bmatrix} = \begin{bmatrix} X & x & x & x \\ 0 & X & x & 0 \\ 0 & 0 & X & 0 \\ 0 & 0 & 0 & X \end{bmatrix} \begin{Bmatrix} DP_1 \\ DP_2 \\ DP_3 \\ DP_4 \end{Bmatrix}$$

High-speed motors usually require small torque at the rated power, and require less magnetic permeability at high-speed rotation. Therefore, conventional

silicon-steel rotors may be overdesigned in terms of magnetic permeability for the use at high-speed operation, which makes the dependency of the volume fraction of magnetic powder on the high-speed motor performance small.

There have been several attempts to employ magnetic-powder polymers in electric devices. The stator poles of DC motors were manufactured by injecting the mixture of Nd<sub>2</sub>Fe<sub>14</sub>B and polymer resin into the mold (Nicolaides and Antanassova, 1997). The magnetic permeability of the mixture of resin and ferromagnetic filler was measured with respect to the filler volume fraction, injection speed, temperature, and direction of filler (Fiske et al., 1997), from which it was found that a mixture of various fillers produced a synergic enhancement of relative magnetic permeability compared with that of the individual filler system. The initial permeability, resistivity and power loss of Ni-Zn ferrite bound with PVA were measured with respect to sintering conditions (Kumar et al., 1997).

#### 14.3.1 Properties of the Magnetic-Powder Epoxy

The measured mechanical and electrical properties, such as Young's modulus, coefficient of thermal expansion (CTE), and resistivity of the magnetic-powder epoxy are shown in figure 14.16 with respect to the volume fraction of powder (Chang et al., 2000). Two different high-magnetization powders (Mn-Zn ferrite and iron) and an epoxy of 2475 A/B (National Starch and Chemical, Korea) were used to manufacture the specimens.

In figure 14.16, Young's modulus increased and the CTE of the composites decreased as the powder volume fraction increased, because both powders had high Young's moduli ( $E$ ) and low coefficients of thermal expansion,  $\alpha$  compared with the epoxy resin. The experimental results were compared with the results obtained from the Halpin-Tsai equations in section 7.5 with the properties in table 14.8:

$$E = E_m \frac{1 + \xi \eta V_p}{1 - \eta V_p} \quad (14.12)$$

$$\eta = \frac{E_p/E_m - 1}{E_p/E_m - \xi}$$

Also the equation of rule of mixtures was used for the estimation of CTE:

$$\alpha = \alpha_m V_m + \alpha_p V_p \quad (14.13)$$

From the experiments, it was found that the Young's moduli of the iron powder and the ferrite powder were best fitted with  $\xi = 3$  and  $\xi = 2$ , respectively.

The ferrite epoxy composite was found to be dielectric, and the electrical resistivity of the iron-powder epoxy composite was very high when the powder volume fraction was less than 20%; it decreased rapidly when the volume fraction was higher than 30%, as shown in figure 14.16.

The magnetic permeability  $\mu$  of the materials was obtained by the magnetization curve measured by using a vibrating sample magnetometer (VSM) in which an alternating magnetic field of a certain frequency and amplitude was imposed on the specimen perpendicularly to the magnetic flux (Foner, 1996). After the relationship between the magnetic density  $B$  and the magnetic intensity  $H$  was obtained, the

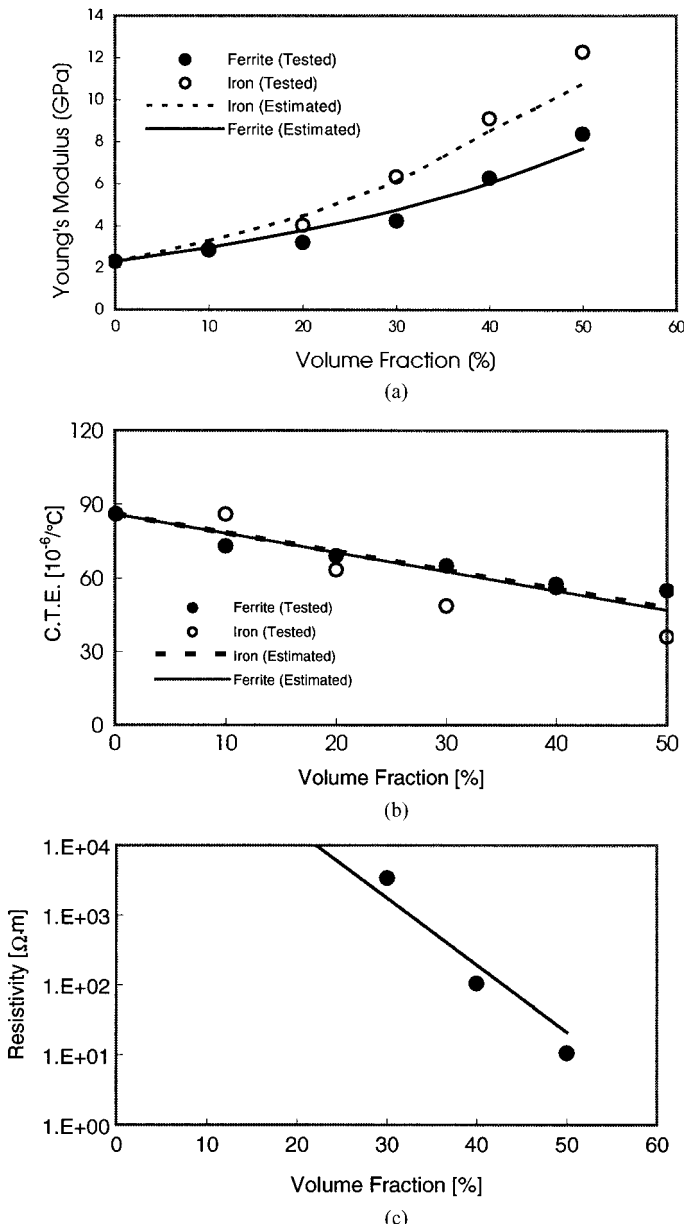


**Figure 14.16** Mechanical and electrical properties of the iron-powder epoxy with respect to volume fraction of the powder: (a) Young's modulus; (b) CTE at  $50^{\circ}\text{C}$ ; (c) electrical resistivity of the iron-powder epoxy composite.

**Table 14.8 Material Properties of the Powders**

	Young's modulus $E$ (GPa)	CTE $\alpha$ ( $\mu\text{m}/\text{m}$ )	Resistivity $\rho$ ( $\Omega\text{m}$ )
Mn-Zn ferrite	50.0	8.0	$10^6\text{--}10^{12}$
Iron powder	97.0	10.0	$10^{-7}$

magnetic permeability  $\mu$  can be calculated from the following relationship (Cullity, 1972):

$$\begin{aligned} B &= \mu_0 H + M, & B/H = \mu &= \mu_0 + M/H, & M &= \kappa H, \\ \mu &= \mu_0 + \kappa, & \mu_r &= \frac{\mu}{\mu_0} = 1 + \frac{\kappa}{\mu_0} \end{aligned} \quad (14.14)$$

where  $M$  is the magnetization ( $\text{Wb}/\text{m}^2$ ),  $\kappa$  the volume susceptibility ( $\text{Wb}/\text{Am}$ ),  $H$  the magnetic intensity ( $\text{A}/\text{m}$ ),  $B$  the magnetic density ( $\text{Wb}/\text{m}^2$ ),  $\mu_0$  the permeability of the vacuum ( $\text{Wb}/\text{Am}$ ), and  $\mu_r$ , the relative permeability.

In the case of diamagnetic or paramagnetic materials whose permeabilities are very small ( $\mu_r \approx 1$ ), the magnetic field intensity is completely proportional to the flux density. However, ferromagnetic materials, such as iron, nickel, and cobalt, and ferrimagnetic materials, such as ferrite, whose permeability are very high, show nonlinearity, owing to the magnetic hysteresis of these materials.

The relative magnetic permeabilities of the powder epoxy composites were measured with respect to a powder volume fraction of 10%, 20%, 30%, 40%, and 50%, as shown in figure 14.17. When the iron-powder volume fraction was 50%, the maximum relative permeability of the iron-powder epoxy was about one-sixth of the silicon steel; however, the relative permeability at 400 A/m, from which the saturation initiated, was about one-third.

#### 14.3.2 Design of the Composite Rotor

The rotor of an induction motor should have high magnetic permeability with little eddy current because the rotor converts electrical energy into mechanical energy through magnetic flux. The permeability of the magnetic-powder epoxy composite increases as the powder volume fraction increases, which increases the mass of the rotor also. Therefore, it is important to determine appropriate powder volume fraction. Table 14.9 shows the density of the magnetic-powder epoxy composite with respect to the powder volume fraction, and figure 14.18 shows the specific relative permeability (relative permeability/density). As shown in figure 14.18, the ferrite-powder composites have almost same specific relative permeability versus powder volume content, but the iron-powder composites show a dependency on powder volume fraction. From figure 14.18(c), for the iron-powder composite it may be recommended to use a powder volume fraction higher than 30% for light weight and good magnetic performance.

During high-speed rotation of the rotor, its radial deformation must be maintained within certain limits to prevent the rotor from contacting the stator. Therefore, the radial deformation of the high-speed rotor should be predicted in the design stage.

Figure 14.19 shows the configuration of a 1.5 kW squirrel cage rotor composed of high-permeability-powder epoxy composite material and high-conduction metal squirrel cage conductor.

The squirrel cage was manufactured by welding 11 aluminum bars of 3.4 mm diameter to two end aluminum rings. In order to guide the magnetic flux from the stator to the rotor, a hollow 2 mm-thickness tubular steel core was inserted inside the composite rotor. Also the conductor bars were exposed to the air to reduce

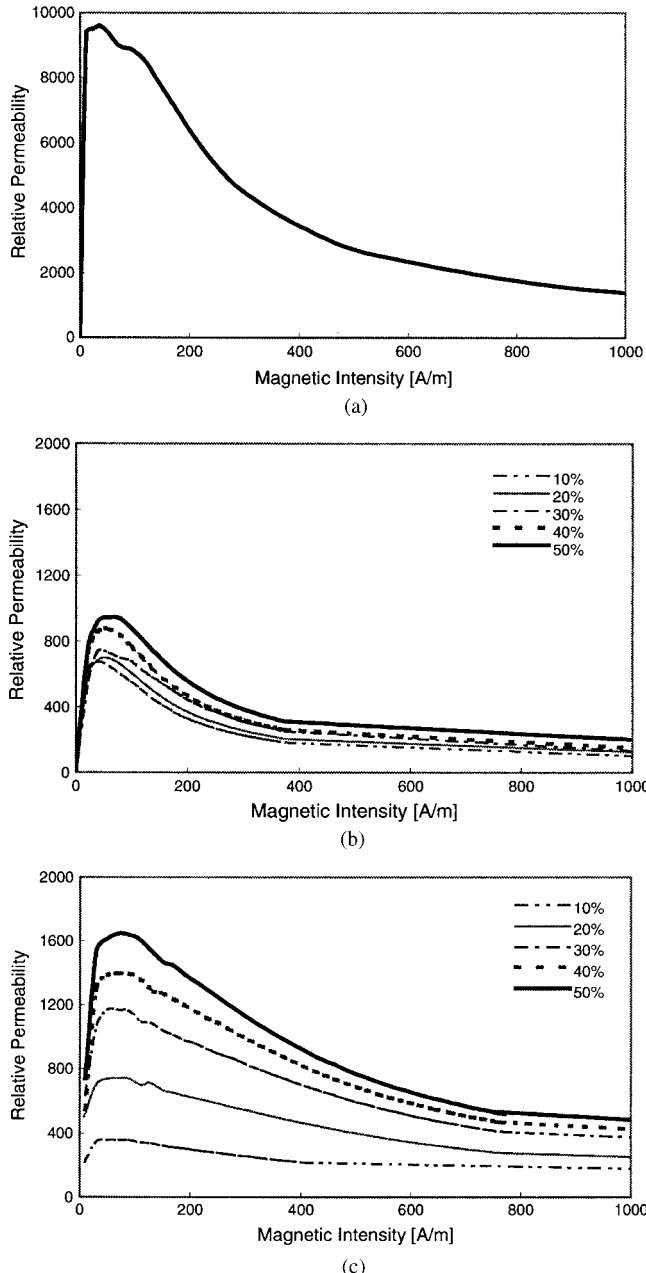


**Figure 14.17** Relative permeabilities of the various materials w.r.t. powder volume fraction:  
 (a) Silicon steel; (b) ferrite-powder epoxy composite; (c) iron-powder epoxy composite.

the rotor leakage reactance, as shown in figure 14.19(b). For the configuration of figure 14.19(c), the leakage flux  $\lambda$  is expressed as follows (Englemann and Middendorf, 1995):

$$\lambda = \mu_0 \left( 0.623 + \frac{h}{c} \right) \quad (14.15)$$

**Table 14.9 Densities of the Magnetic-powder Epoxy Composite with respect to Powder Volume Fraction**

<i>Powder volume fraction (%)</i>	<i>Density (kg/m<sup>3</sup>)</i>	
	<i>Ferrite</i>	<i>Iron powder</i>
0	1200	1200
10	1430	1800
20	1660	2400
30	1890	3000
40	2120	3600
50	2350	4200

where  $\mu_0$  represents the magnetic permeability of free space, and  $h$  and  $c$  represent dimensions of the conductor bar, as shown in figure 14.19(c). Since the value of  $h$  is zero in figure 14.19(b), the leakage flux of the composite rotor is  $0.623 \mu_0$ .

In order to compare the performance of the composite rotor with that of conventional silicon-steel rotor, a silicon-steel rotor with the same rating was manufactured. The shape and dimensions of the composite rotor and the steel rotor are shown in table 14.10.

Since the rotor may contact to the stator when the radial deformation of the rotor is excessive, the radial deformation is the most important constraint in the design of built-in high-speed motor spindle systems. For high Young's modulus and low CTE, a high powder volume fraction is important. However, the high powder fraction not only increases the density of composites but also makes the mixing operation difficult due to high viscosity of mixture. Therefore, the optimum powder volume fraction based both on the performance and manufacturability should be found.

The effect of permeability on the magnetic flux of the rotor was calculated by the equivalent circuit of figure 14.20, assuming that the permeability was independent of magnetic density  $B$ . In figure 14.20, the motor circuit was divided into the stator, the air gap, and the rotor part, which are represented by reluctances  $R_s$ ,  $R_g$ , and  $R_r$ , respectively.

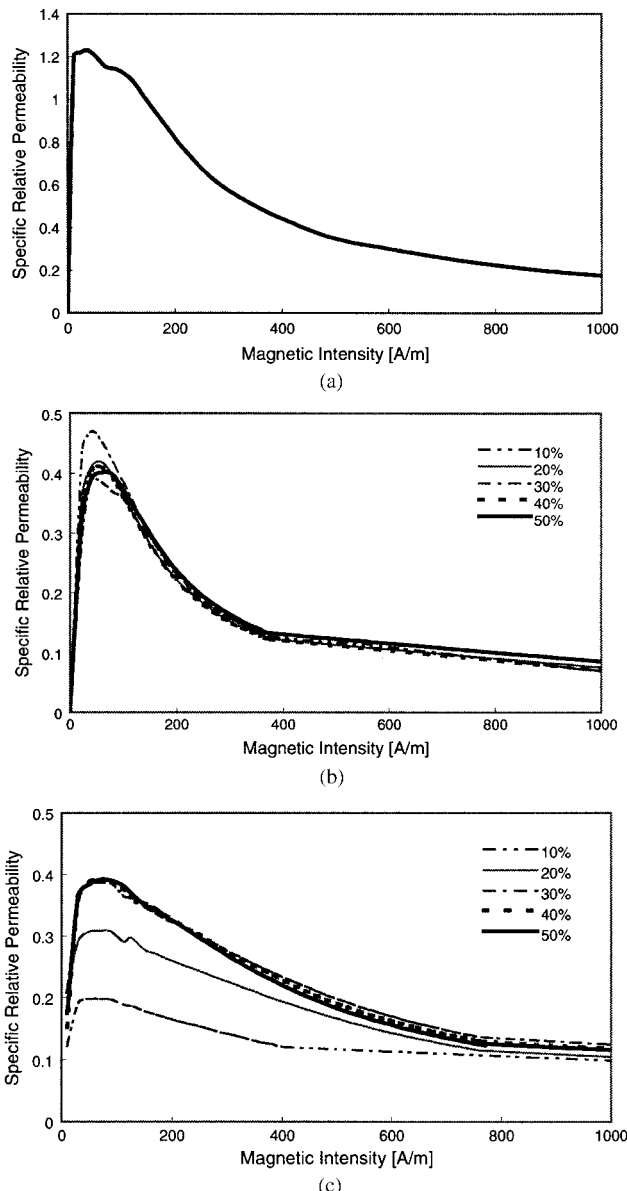
The flux  $\Phi$  flowing through the magnetic circuit in figure 14.20 can be expressed as a function of the magnetomotive force  $NI$  and reluctances  $R_s$  of the stator,  $R_g$  of air gap length  $l$ , and  $R_r$  of rotor permeability  $\mu$  (Garik and Whipple, 1961; Mishin and Mishin, 1995):

$$\Phi = \frac{NI}{R_s + R_g + R_r} \quad (14.16)$$

$$R_s = \frac{l_s}{\mu_{rs}\mu_0 S_s}, \quad R_g = \frac{l_g}{\mu_{rg}\mu_0 S_g}, \quad R_r = \frac{l_r}{\mu_{rr}\mu_0 S_r}$$

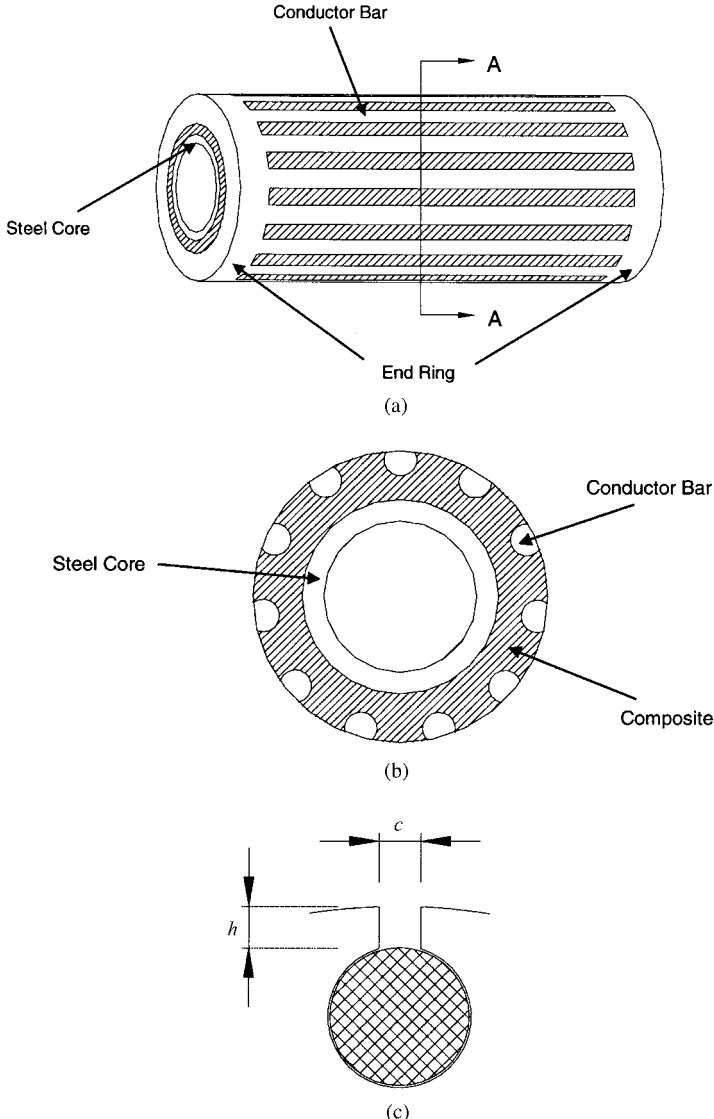
where  $\Phi$  is the flux (Wb),  $NI$  the magnetomotive force (A turns),  $l$  the magnetic path length (m),  $R$  the reluctance (A turns/Wb),  $\mu_0$  the permeability of free space (Wb/Am) ( $4\pi \times 10^{-7}$  Wb/Am),  $\mu_r$  the relative permeability, and  $S$  the cross-section of the flux path ( $m^2$ ). The subscripts  $s$ ,  $r$ , and  $g$  represent the stator, rotor, and gap.

Figure 14.21 shows the magnetic flux of the motor with respect to magnetomotive force and relative permeability of rotor material. As shown in figure 14.21,



**Figure 14.18** Specific relative permeabilities of the various materials w.r.t. powder volume fraction: (a) Silicon steel; (b) ferrite-powder epoxy composite; (c) iron-powder epoxy composite.

the magnetic flux was almost proportional to the magnetomotive force; however, it increased fast initially and then saturated as the permeability of rotor material increased. Figure 14.21(b) shows the magnetic flux with respect to the permeability of the rotor when the magnetomotive force was 210 A turns ((35 turns per slot)  $\times$  (2 slots)  $\times$  (3 A)). When the number of turns of the motor and the current are 35 and 3 A, respectively, the generated magnetic intensity is about 800 A/m. In this case the magnetic flux saturates at the value of  $1.2 \times 10^{-4}$  (Wb) ( $1.2 \times 10^4$  Maxwell). If the iron-powder volume of the epoxy is 50%, the relative permeability of the

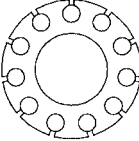
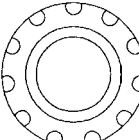


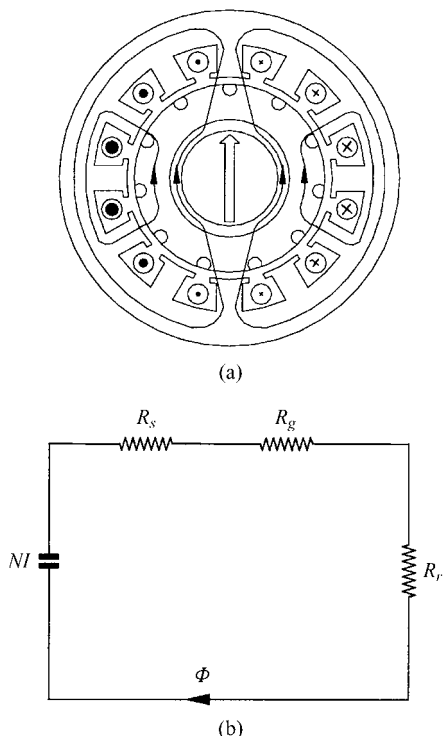
**Figure 14.19** Configuration of the composite rotor: (a) Composite rotor; (b) shape of cross-section of the composite rotor; (c) configuration of the conductor bar.

rotor material is about 600 from figure 14.17(c), while the relative permeability of silicon-steel laminate is 2000 when the magnetic intensity is 800 A/m, as shown in figure 14.17(a). When the iron-powder volume fraction was 50%, its density and CTE were  $4200 \text{ kg/m}^3$  and  $36.1 \mu\text{m/m}^\circ\text{C}$ , respectively. The mass reduction of the composite rotor including the steel core was 41%.

Since the performance of the motor is sensitive to the magnetizing reactance  $X_m$ , which is inversely proportional to the air gap size, in this study the air gap size of 0.2 mm was selected, while that of the conventional steel rotor was 0.25 mm. Currently, the machining accuracy of precision high-speed built-in motor spindle system is around  $1 \mu\text{m}$ ; consequently, the air gap of 0.2 mm between the stator and the rotor is not critical.

**Table 14.10 Configuration of the Rotors (All Dimensions in mm)**

	<i>Axial length</i>	<i>Outer diameter</i>	<i>Inner diameter</i>	<i>Steel core thickness</i>
Steel rotor				
	53.0	27.0	14.0	—
Composite rotor				
	53.0	27.1	14.0	2.0

**Figure 14.20** Magnetizing flux and magnetic circuit of the motor: (a) Magnetizing flux between the stator and the rotor; (b) equivalent magnetic circuit of the AC induction motor.

#### 14.3.3 Deformation of the Composite Rotor Due to Centrifugal Force and Temperature Rise

Since the composite rotor was composed of the aluminum squirrel cage and the magnetic-powder epoxy composite, the deformation due to thermal expansion, especially at the interface of the two materials, and the centrifugal force was numerically analyzed by commercial finite element software (ANSYS 5.3).

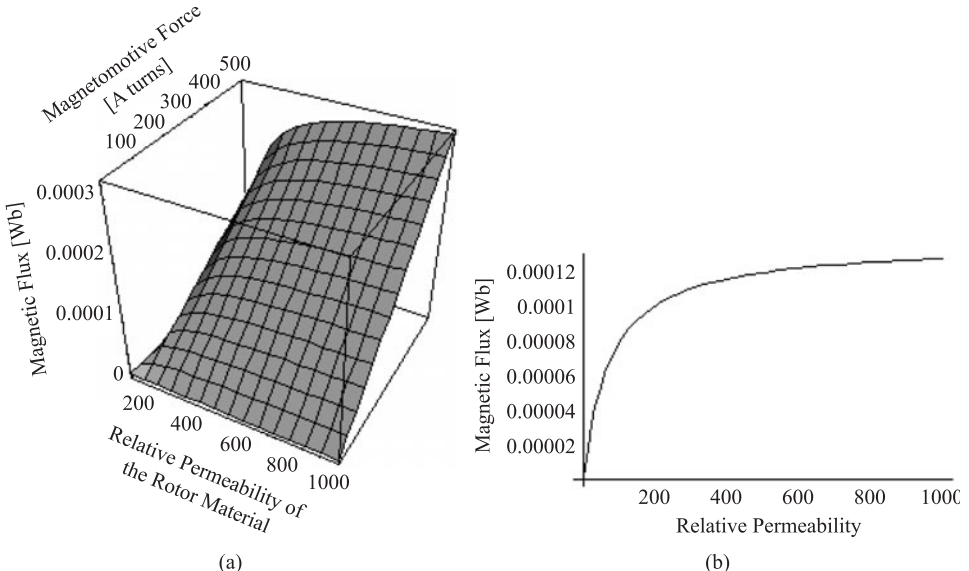


**Figure 14.21** Magnetic flux with respect to magnetomotive force and relative permeability of the rotor material: (a) 3-D view of the magnetic flux; (b) magnetic flux with respect to relative permeability of the rotor material ( $NI = 210$  A turns).

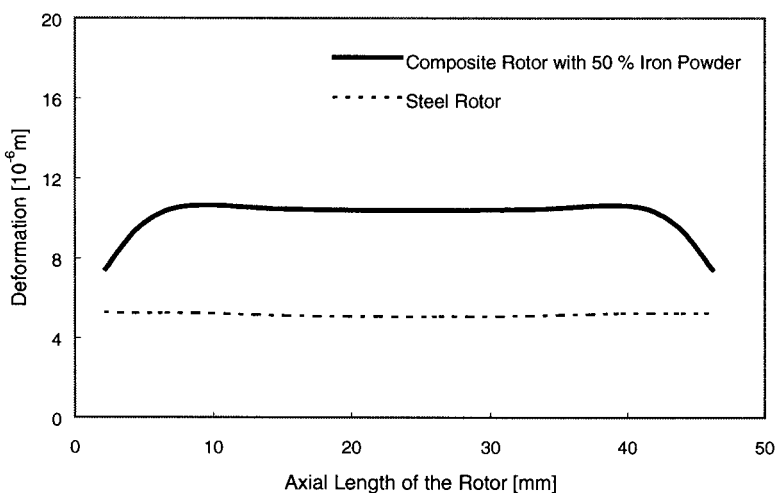


**Figure 14.22** Radial deflection due to centrifugal force and thermal stress ( $\Delta T = 25^\circ\text{C}$ ,  $\omega = 1.2 \times 10^4$  rpm).

For the modeling of the rotor, the SOLID45 elements of ANSYS (8 nodes, 3 DOF) were used.

In order to give the actual driving conditions, the centrifugal force equivalent to  $1.2 \times 10^4$  rpm (200 Hz) and temperature increments ( $\Delta T$ ) of  $25^\circ\text{C}$  from the room temperature of  $25^\circ\text{C}$  were imposed on the finite element model. Figure 14.22 represents the radial deformations of the rotors due to temperature increment and centrifugal force when the powder volume fraction was 50%. The radial deformation

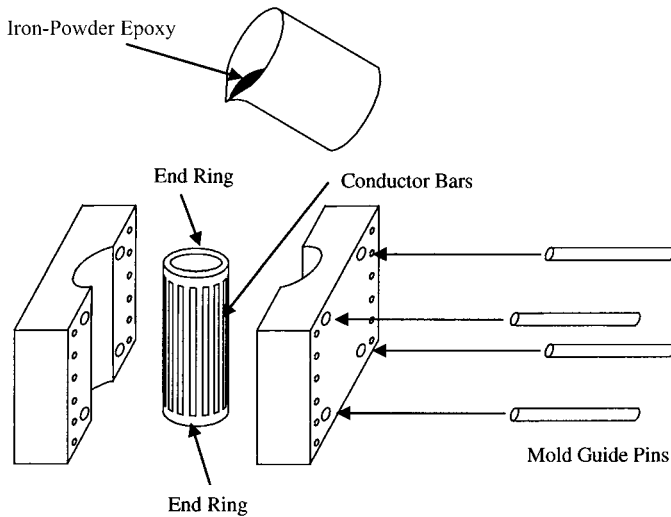


**Figure 14.23** Molding apparatus and schematic manufacturing procedures for composite rotor.

of the silicon-steel rotor showed a uniform value and that of the composite rotor had variation at the ends of the rotor. The radial deformation of the composite rotor largely came from thermal expansion because the CTE of the magnetic-powder composites ( $36.1 \times 10^{-6}/^{\circ}\text{C}$  at 50% volume fraction) is much larger than that of the silicon steel ( $13.0 \times 10^{-6}/^{\circ}\text{C}$ ). The deformation due to centrifugal force at  $1.2 \times 10^4$  rpm contributed less than 1.0% of the total deformation. Since the maximum radial deformation of the composite rotor by the temperature increase of  $25^{\circ}\text{C}$  was  $11 \mu\text{m}$ , the air gap size of  $200 \mu\text{m}$  was selected. The maximum deflection of the silicon-steel rotor was  $5.3 \mu\text{m}$ . Since the deformation was strongly affected by the temperature rise, the deformation may be reduced when the cooling apparatus is added to the motor.

Considering the magnetic permeability, CTE, and elastic modulus, the iron-powder volume fraction of the composite rotor was determined to be 50%.

#### 14.3.4 Manufacture of the Composite Rotor

The squirrel cage conductor was manufactured by inserting aluminum conductor bars into the holes of end rings and welding the conductor bars and the end rings together. Then iron-powder epoxy composite was poured inside the gap of the squirrel cage, as shown in figure 14.23. A powder size less than  $2 \mu\text{m}$  was used.

The composite rotor and mold assembly were cured in an autoclave under  $0.6 \text{ MPa}$ , at  $120^{\circ}\text{C}$  for 4 h. After curing the composite rotor, the outside of the rotor was exposed to air by grinding the conductor bars. The outer diameter of the composite rotor was 27.1 mm and the stator bore was 27.5 mm, therefore, the air gap size was 0.2 mm. Figure 14.24 shows a photograph of the composite rotor.

#### 14.3.5 Characteristics of the Composite Rotor

The slip speed, torque, and power dissipation of the composite rotor were measured using a frequency converter and wattmeter, which adjusted driving parameters.

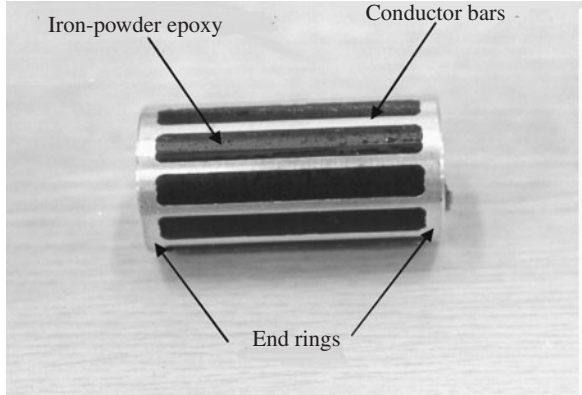


**Figure 14.24** Photograph of the composite rotor.

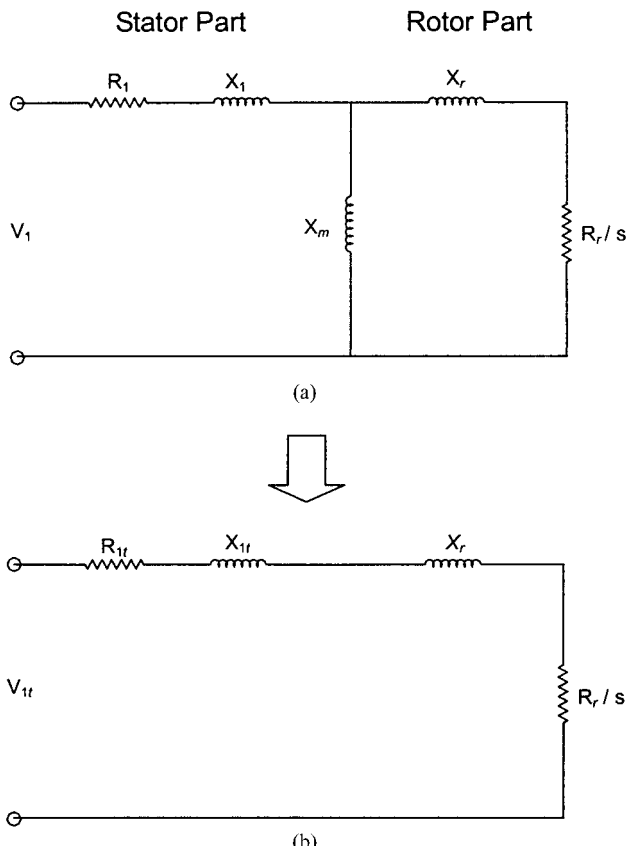


**Figure 14.25** Equivalent circuit of a three-phase AC induction motor: (a) Equivalent circuit; (b) simplified circuit.

The value of  $V/F$  (voltage/frequency) was controlled to adjust the flux of the stator and to modulate the motor speed and output power because three-phase AC motors should be driven under optimal driving condition for adequate driving performance.

Figure 14.25(a) represents the equivalent circuit of a three-phase AC induction motor, assuming that the core resistance is very high relative to the others, and figure 14.25(b) shows the manipulated equivalent circuit that includes the effect of the magnetizing reactance ( $X_m$ ) of the air gap (Englemann and Middendorf, 1995).

The torque–speed relation of figure 14.25(b) was derived as follows:

$$I_r = \frac{V_{1t}}{\sqrt{(R_{1t} + R_r/s)^2 + (X_{1t} + X_r)^2}} \quad (14.17)$$

$$T_d = \frac{P_g}{\omega_s} = \frac{3I_r^2 R_r/s}{\omega_s} = \frac{3V_{1t}^2 R_r}{s\omega_s [(R_{1t} + R_r/s)^2 + (X_{1t} + X_r)^2]}$$

where

$$R_{1t} = \frac{X_m^2 R_1}{R_1^2 + (X_1 + X_m)^2}$$

$$X_{1t} = \frac{X_m [R_1^2 + X_1(X_1 + X_m)]}{R_1^2 + (X_1 + X_m)^2}$$

$$V_{1t} = \frac{\sqrt{(V_1 X_m R_1)^2 + V_1^2 X_m^2 (X_1 + X_m)^2}}{R_1^2 + (X_1 + X_m)^2}$$

$R_r$  is the rotor resistance referred to the stator ( $\Omega$ ),  $R_1$  the stator winding resistance ( $\Omega$ ),  $X_r$  the rotor leakage reactance referred to the stator ( $\Omega$ ),  $X_1$  the stator leakage reactance ( $\Omega$ ),  $X_m$  the magnetizing reactance ( $\Omega$ ),  $V_1$  the stator induced voltage per phase (V),  $s$  the motor slip,  $\omega_s$  the synchronous speed (rad/s),  $I_r$  the rotor current (A), and  $T_d$  the developed torque (Nm).

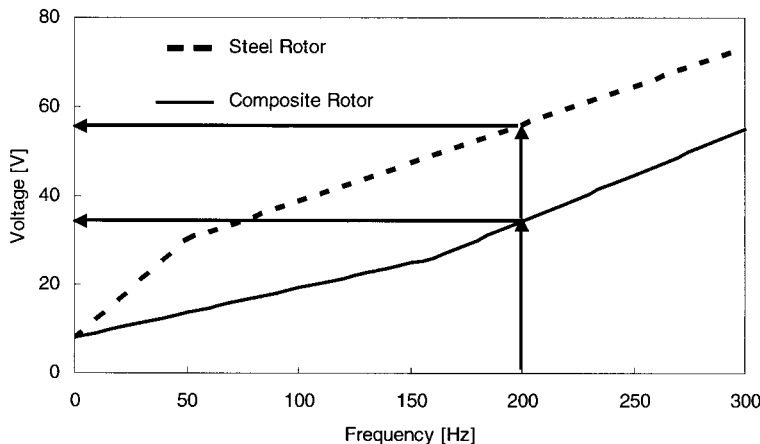
Equation (14.17) expresses the effect of the magnetizing reactance ( $X_m$ ) on the system performance. In order to obtain the exact values of the stator resistance ( $R_1$ ) and the rotor resistance ( $R_r$ ) and reactances ( $X$ 's) of the stator ( $X_1$ ), the rotor ( $X_r$ ), and the air gap ( $X_m$ ), as shown in figure 14.25, several tests, such as the no-load test, blocked rotor test, and DC test, were performed (Englemann and Middendorf, 1995). The base speed was set to  $1.2 \times 10^4$  rpm (200 Hz) and the input power, current, and voltage were measured to calculate the motor parameters.

Table 14.11 lists the parameters of the simplified circuit obtained from the tests. Figure 14.26 shows  $V/F$  control patterns for the two rotor systems. Using the parameters in table 14.11, the torque–speed curves, which are the most important characteristics of the motor, were obtained.

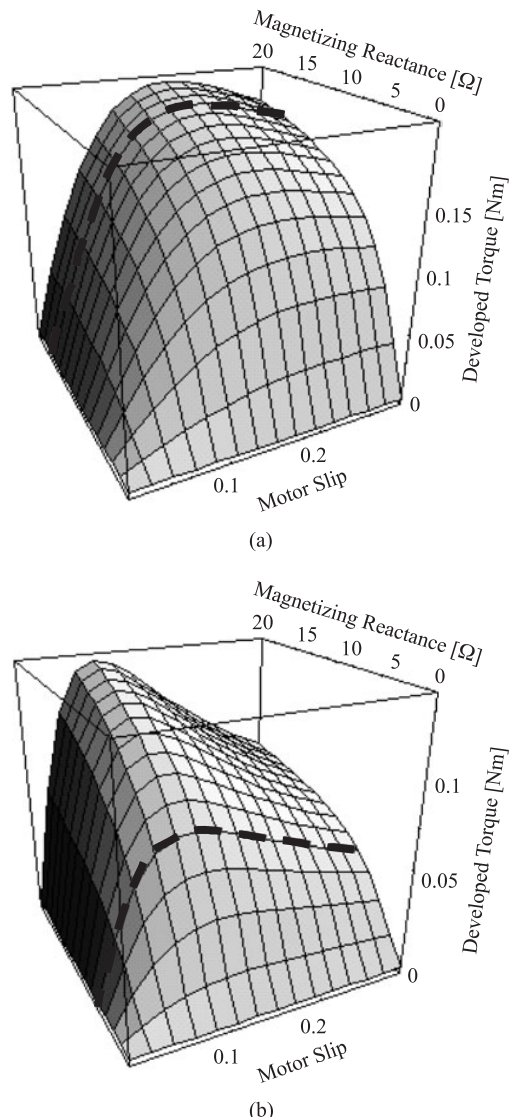
Figure 14.27 shows the torque–speed curves of the two rotor systems and table 14.12 shows the test results of the two rotor systems. As shown in figure 14.27, both the motor torques of the silicon-steel rotor and the composite rotor are strongly dependent on the magnetizing reactance up to  $5\Omega$ ; beyond  $5\Omega$ , they are almost saturated. In figure 14.27, the dashed lines represent the torque–speed curve of each rotor system.

Table 14.11 Parameters of the Three-Phase AC Induction Motor

	$R_1$ ( $\Omega$ )	$R_r$ ( $\Omega$ )	$X_r$ ( $\Omega$ )	$X_1$ ( $\Omega$ )	$X_m$ ( $\Omega$ )
Steel rotor	1.0	1.02	3.12	3.12	15.10
Composite rotor	1.0	0.70	4.43	4.43	4.34



**Figure 14.26** Control patterns of the rotor system.



**Figure 14.27** Torque–speed diagram of the two systems: (a) Silicon-steel rotor system; (b) composite rotor system.

**Table 14.12 Test Results of the Three-Phase AC Induction Motor at  $1.2 \times 10^4$  rpm (No Load)**

	<i>Power dissipated (W)</i>	<i>Input current (A)</i>	<i>Motor slip (%)</i>	<i>Rotor mass (kg)</i>
Steel rotor	50	1.6	2.2	0.155
Composite rotor	30	2.2	2.0	0.089

From the test results, it was found that both the rotor systems had almost the same slip speed of 2%. However, the maximum torque of the composite rotor system was about 33% of the silicon-steel system because the composite rotor system had a lower voltage source under operation conditions as shown in figure 14.26, and the developed torque is proportional to the square of applied voltage.

Since the applied voltage for the composite rotor was lower than that of the silicon-steel rotor, the energy consumption of the composite rotor system was lower than that of the silicon-steel rotor. Therefore, the composite rotor system is appropriate to systems that do not require high torque or power but require high speed, such as high-precision grinding machines or silicon-wafer slicing machines.

Since the slip of the composite rotor at the maximum torque is low, the composite rotor has the advantage of maintaining the driving speed with small slip at high speed. Also the mass reduction of the rotor can increase the critical speed of built-in high-speed spindle motors.

When a high voltage is used to drive the composite motor systems, there may be a temperature increase, which may degrade the strength and modulus of the epoxy material. Therefore, for a actual drive of a composite rotor at high voltage, a high-temperature epoxy material or a cooling device should be used in the composite rotor, or the epoxy may be reinforced using carbon fiber or other high-strength and high-modulus reinforcement material with high thermal conductivity.

#### 14.4 Composite Rotating Boring Bar

Boring involves the enlarging of an existing hole. The major functional requirement of boring bars is to machine holes with large ratio of the depth  $l$  to the diameter  $d$  without chatter. The machining of deep holes is often required for the improvement of productivity during manufacturing of large machine components with holes. However, high-speed boring operations of deep holes with steel or tungsten carbide boring bars are often hindered by the chatter of boring bars because steel or tungsten carbide boring bars not only have low dynamic stiffness but also low natural frequencies (Lee et al., 2003).

Chatter is a self-excited vibration that occurs in metal cutting if either the chip width is too large with respect to the dynamic stiffness of the system, or the rotating speed of a spindle or boring bar approaches one of the natural frequencies of the system (Tlusty, 1999). The dynamic stiffness of a boring bar is proportional to the damping and static stiffness of the boring bar (Cook, 1966) and the natural frequency of the boring bar is proportional to the specific stiffness  $(E/\rho g)^{0.5}$  of the boring bar material (Harris, 1998). Therefore, rotating boring bar materials should have high static stiffness and high damping as well as high specific stiffness for high rotational speed machining of deep holes.

Generally, chatter in the boring process with conventional steel boring bars usually occurs when the value of  $l/d$  of the boring bars is larger than 5 due to the low dynamic stiffness of steel. Special devices such as tuned bars, impact dampers, Lanchester dampers, and viscoelastic dampers were introduced to increase the damping of boring bars, in order to suppress the chatter. These devices increased the value of  $l/d$  of conventional steel boring bars up to 6 (Setareh, 2001; Ema and Marui, 2000; Hahn, 1951; Kim and Ha, 1987). However, the special damping devices are not suitable or reliable for solving the problems of chatter in deep hole boring operations because the geometries of boring bars and cutting tools are not only diverse, but also limited by installation difficulties (Lee and Suh, 1988).

Tungsten carbide rotating boring bars have been used for low-speed boring operations with the value of  $l/d$  larger than 6 because the Young's modulus of tungsten carbide is much larger than that of steel. Since the damping capacity of the tungsten carbide is similar to that of steel (Kinra and Wolfenden, 1992), the boring capability of the tungsten boring bar is higher than that of the steel boring bar due to the increase of static stiffness only. However, the density of tungsten carbide is about twice that of steel; consequently, its specific stiffness is similar to that of steel, which does not increase the fundamental natural frequency of the tungsten carbide. Therefore, the rotational speed of the tungsten carbide rotating boring bar that can be used during metal cutting operation is no higher than for steel boring bars (Kang, 1963). In fact, the dynamic stiffness and machining speed of boring bars made of conventional metals cannot be improved simultaneously because conventional high static stiffness metallic materials usually have low damping, and low specific stiffness (Callister, 1997).

The best way to simultaneously improve the dynamic stiffness and fundamental natural frequency of machine tool structures, including boring bars, is to employ composite materials because fiber-reinforced composite materials have high static stiffness and high damping as well as very high specific stiffness. Many researchers have investigated the applications of fiber-reinforced composite materials to various parts of rotating structures, such as composite automotive propeller shafts, high-speed spindles, and rollers (Weeton et al., 1986; Cho, 1997; Lee and Choi, 1997; Lee et al., 2000). Also there have been several studies on the design of boring bars with composite materials. Lee and Suh (1988) developed a fixed-type carbon epoxy composite boring bar whose  $l/d$  was 5.6. From metal cutting and impulse vibration tests, it was found that the allowable depth of cut of the composite boring bar was five times higher than that of the conventional steel boring bar before the onset of chatter.

There have been several studies on fixed carbon-fiber epoxy composite boring bars (Nagano et al., 1997). However, studies on rotating composite boring bars are rare, although rotating boring bars that machine fixed specimens are more widely used.

#### 14.4.1 Design of the Composite Boring Bar

The two functional requirements of rotating boring bars are high specific stiffness and high damping, which can be satisfied independently by choosing two design parameters, such as high-modulus carbon-fiber epoxy composites and adhesive joining, because the stiffness of high-modulus carbon-fiber epoxy composite material is almost same as the stiffness of tungsten carbide (about 400 GPa) and the specific modulus is about 10 times that of tungsten carbide or steel. The damping of boring

bars may be enhanced by adhesive bonding and inserting a core in the boring bar during the composite manufacturing process.

A tungsten carbide boring bar whose outside diameter is 22.5 mm is used for the boring of cam holes of aluminum automotive engine cylinder heads. Since the dynamic stiffness and natural frequency of the tungsten boring bar are limited, the boring operation is performed at 2500 rpm. Higher rotational speeds would be employed if the boring bar had a sufficiently high dynamic stiffness and fundamental natural frequency, because the aluminum workpiece allows much higher cutting speeds due to its low hardness and high thermal conductivity. Therefore, the two functional requirements of boring bars are

$$FR_1 = \text{Increase high specific bending stiffness}$$

$$FR_2 = \text{Increase damping.}$$

The two functional requirements can be satisfied by the two design parameters

$$DP_1 = \text{High-modulus carbon-fiber epoxy composite}$$

$$DP_2 = \text{Adhesive joining (thicknesses of adhesive and adherend) and damping core.}$$

The design equation becomes

$$\begin{Bmatrix} FR_1 \\ FR_2 \end{Bmatrix} = \begin{bmatrix} X & 0 \\ 0 & X \end{bmatrix} \begin{Bmatrix} DP_1 \\ DP_2 \end{Bmatrix}$$

A boring bar of 22.5 mm diameter was designed and manufactured using very high stiffness pitch-based carbon-fiber epoxy composite material. The cross-section of the developed composite boring bar is shown in figure 14.28. The outside steel cover protects the inside of the composite shank of the boring bar from being scratched by chips and cutting fluid during the machining operation.

Since the modulus of steel (207 GPa) is about half the composite stiffness (380 GPa), the outside of the steel cover was machined out, leaving only 0.25 mm thickness after adhesive joining the steel cover to the composite main shaft. A damping core was inserted into the composite shank. The damping core has two roles: one role of mandrel during composite prepreg wrapping and the other role to increase the damping capacity of the boring bar. The adhesive also has two roles: one role to join the steel cover to the composite shank and the other role to increase the damping of the boring bar through the constrained damping mechanism (Nashif et al., 1985). The composite used for the shank of the boring bar is very high stiffness pitch-based carbon-fiber epoxy prepreg, URN300 (see table 13.3), and the adhesive used to join the steel cover to the composite shank of the boring bar is rubber-toughened structural epoxy adhesive (DP 460, 3M, USA). The mechanical properties of the

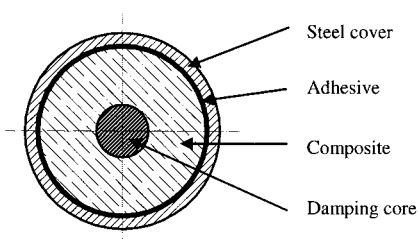


**Figure 14.28** Sectional view of the composite boring bar.

**Table 14.13 Mechanical Properties of the Tungsten Carbide, the Unidirectional Carbon-Fiber Epoxy Composite Material and Epoxy Adhesive**

	$E_1$ (GPa)	$E_2$ (GPa)	$G_{12}$ (GPa)	$\nu_{12}$	$\rho$ ( $kg/m^3$ )	$\zeta$	
Tungsten carbide		460		177	14000	$2.2 \times 10^{-3}$	
Carbon-fiber epoxy composite (URN300)	380		5.1	5.5	1750	$2.07 \times 10^{-2}$	
Epoxy adhesive (DP 460)		2.7		1.0	0.40	1100	0.1–0.2

$\zeta$  = Damping ratio.

materials used for the developed boring bar, as well as the tungsten carbide for the conventional boring bars, are listed in table 14.13.

#### 14.4.2 Dynamic Characteristics of the Composite Boring Bar

The performance of a rotating boring bar during machining is characterized by two factors, metal cutting stability and fundamental natural frequency. The maximum width of cut  $b_{\text{lim}}$  of the boring bar during a boring operation without chatter, which quantifies the metal cutting stability in appendix A is expressed as (Thusty, 1999)

$$b_{\text{lim}} \approx \frac{K_m \zeta}{k_s} \quad (14.18)$$

where  $K_m$  is the stiffness of the machine tool system including the workpiece during the cutting operation,  $\zeta$  is the damping ratio of the cutting system, and  $k_s$  is the specific cutting force (force/area) or specific cutting power (power/volume removal rate). Since  $k_s$  is determined by workpiece material, the maximum width of cut  $b_{\text{lim}}$  of the boring bar is proportional to the dynamic stiffness, defined as the product of the bending stiffness  $K_m$  and damping ratio  $\zeta$ . Therefore, the static stiffness and damping of the rotating boring bar are two important parameters for the stability of machining operation when the rotational speed of the boring bar is lower than its fundamental natural frequency.

The high fundamental natural frequency of the boring bar is another important parameter for the stable operation of the rotating boring bar without chatter because the cutting speed of the boring bar is limited by the fundamental natural frequency of the boring bar. The fundamental natural frequency  $f_1$  of the boring bar with cantilever end conditions can be obtained as follows (Harris, 1996):

$$f_1 = \frac{3.52}{l^2} \sqrt{\frac{(EI)_{\text{equiv}}}{(\rho A)_{\text{equiv}}}} \quad (\text{rad/sec}) \quad (14.19)$$

$$(\rho A)_{\text{equiv}} = (\rho A)_{\text{cover}} + (\rho A)_{\text{adhesive}} + (\rho A)_{\text{composite}} + (\rho A)_{\text{core}} \quad (14.20)$$

where  $(\rho A)_{\text{equiv}}$  and  $(EI)_{\text{equiv}}$  represent the equivalent area density (mass per unit length) and bending stiffness of the composite boring bar.

The dynamic stiffness  $D$  of a boring bar that has a cantilevered shape may be expressed as

$$D = \zeta K = \frac{3\zeta(EI)_{\text{equiv}}}{l^3} \quad (14.21)$$

Combining equations (14.19) and (14.21), the dynamic stiffness  $D$  at the fundamental natural frequency is expressed as

$$D = 0.242\zeta lf_1^2(\rho A)_{\text{equiv}} \quad (14.22)$$

In order to obtain the optimum cross-section of the boring bar to yield maximum damping capacity, the thickness of the steel cover and the adhesive, and the material type and diameter of the damping core, as shown in figure 14.28, were selected as design parameters for the composite boring bar. The performance of the boring bar can be estimated if its bending stiffness, the densities of the materials used, and the damping ratio of the composite boring bar, taking into account the clamping condition, are known. The bending stiffness can be estimated by analytical calculation; however, the damping is difficult to calculate because the damping of the boring bar comes from several sources (material damping, constrained layer damping, clamped joint damping, airborne damping, etc.), which necessitates experimental measurements rather than analyses after preparing several specimens.

The dynamic characteristics of the composite boring bar were experimentally investigated using the composite shank of a boring bar whose diameter was 22.5 mm and whose length was 240 mm, as shown in figure 14.29. The specifications of design parameters for the composite shank are listed in table 14.14, and the mechanical properties of the various core materials are listed in table 14.15. The fundamental

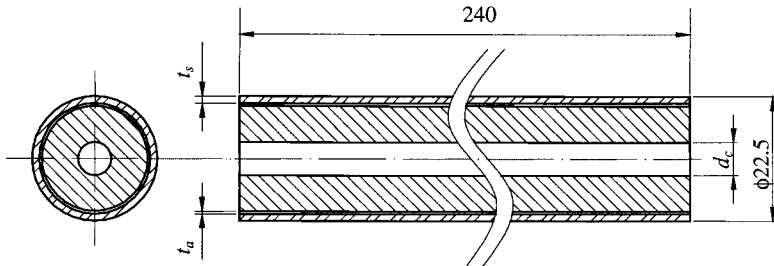


**Figure 14.29** Configuration of composite shank of the boring bar (in mm).

**Table 14.14 Design Parameters for the Composite Shank of the Boring Bar**

Design parameter	Material	Size (mm)
Steel cover ( $t_c$ )	Steel	0.25–1.25
Adhesive ( $t_a$ )	Epoxy	0.05–0.50
Core ( $d_c$ )	Steel, aluminum, tungsten carbide, polyoxymethylene (POM), teflon, lead, silicone oil (viscosity of 1 Pa·s and 100 Pa·s, alumina particles (36, 120, and 220 mesh))	2–10

**Table 14.15 Mechanical Properties of Core Materials for the Composite Boring Bar**

Core material	Young's modulus (GPa)	Density (kg/m <sup>3</sup> )
Steel	207.0	$7.85 \times 10^3$
Aluminum	69.0	$2.71 \times 10^3$
Tungsten carbide	460.0	$14.0 \times 10^3$
POM (Polyoxymethylene)	26.0	$1.42 \times 10^3$
Teflon	0.5	$2.28 \times 10^3$
Lead	0	$11.4 \times 10^3$
Silicone oil	—	$0.96 \times 10^3$
Alumina particles	—	$3.97 \times 10^3$

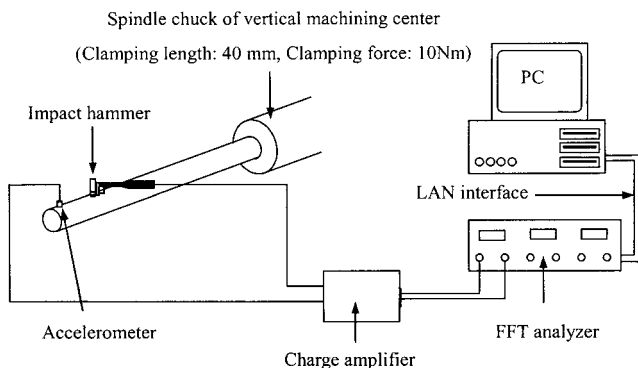
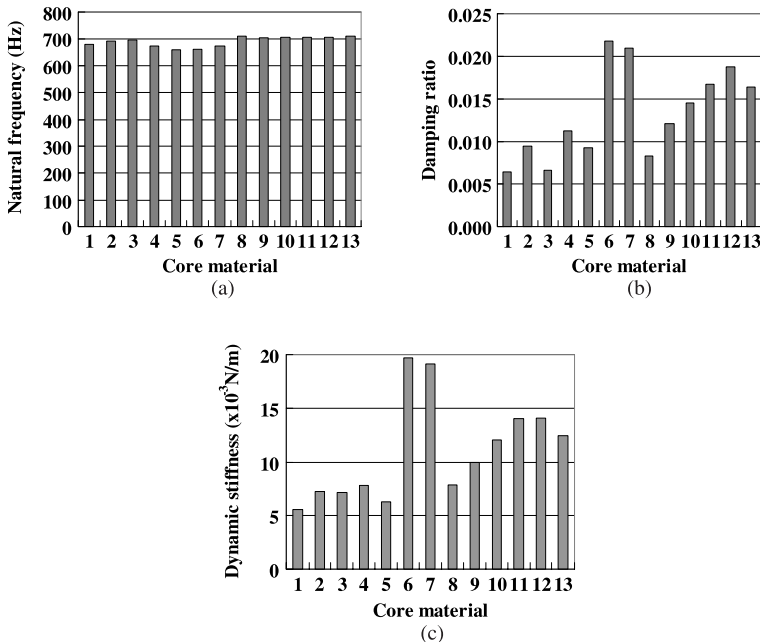


**Figure 14.30** Vibration test setup for the composite shank of the boring bar mounted on a vertical machining center.

natural frequency and damping of the specimen were obtained through impulse dynamic tests, as shown in figure 14.30. An impulse was applied to the composite shank of a boring bar clamped on a vertical machining center with the same clamping force as the actual clamping force during a boring operation, to give the same clamped joint conditions.

Various damping core materials were tested to give high damping capacity to the composite boring bar. Figure 14.31 shows the dynamic characteristics of the composite shank with respect to damping core materials when the damping core diameter, steel cover thickness, and adhesive thickness were 6 mm, 0.25 mm, and 0.10 mm, respectively. In figure 14.31, the fundamental natural frequency of the composite shank changed little with respect to the type of damping core material, while the damping ratio and consequently the dynamic stiffness of the composite shank changed much with respect to the type of material. In figure 14.31, the lead core or the lead in a stainless-steel pipe of 0.5 mm thickness yielded the largest damping ratios. Therefore, the lead core in a stainless-steel pipe of 0.5 mm was selected for the damping core of the composite boring bar. The lead core in a stainless-steel pipe rather than the bare lead was selected for the core because the bare lead was not suitable for the permanent mandrel during prepreg wrapping due to its low stiffness.



Case	Damping core material	Case	Damping core material
1	Steel	8	Stainless steel pipe
2	Aluminum	9	Alumina particle (# 36) in stainless steel pipe
3	Tungsten carbide	10	Alumina particle (# 120) in stainless steel pipe
4	Polyoxymethylene	11	Alumina particle (# 220) in stainless steel pipe
5	Teflon	12	Silicone oil (1 Pa·s) in stainless steel pipe
6	Lead	13	Silicone oil (100 Pa·s) in stainless steel pipe
7	Lead in stainless steel pipe		

**Figure 14.31** Dynamic characteristics of the composite shanks with respect to the damping core materials when the damping core diameter, steel cover thickness and adhesive thickness were 6 mm, 0.25 mm, and 0.10 mm, respectively: (a) Natural frequency; (b) damping ratio; (c) dynamic stiffness.

Figure 14.32 shows the dynamic characteristics of the composite shank of the boring bar with respect to the steel cover thickness when the outside diameter of the lead core in a stainless-steel pipe and the adhesive thickness were 6 mm and 0.10 mm, respectively. In figure 14.32, the fundamental natural frequency, damping ratio, and dynamic stiffness decreased linearly as the cover thickness increased.

In figure 14.32, the zero cover thickness represents the composite shank without the steel cover.

The damping ratio, hence the dynamic stiffness of the composite shank of the boring bar without a steel cover was much lower than that of the composite shank with a steel cover, because damping of the composite shank with the steel cover was created by the constrained damping of the epoxy adhesive between the steel cover and the inner composite shank (Nashif et al., 1985). Therefore, the steel cover

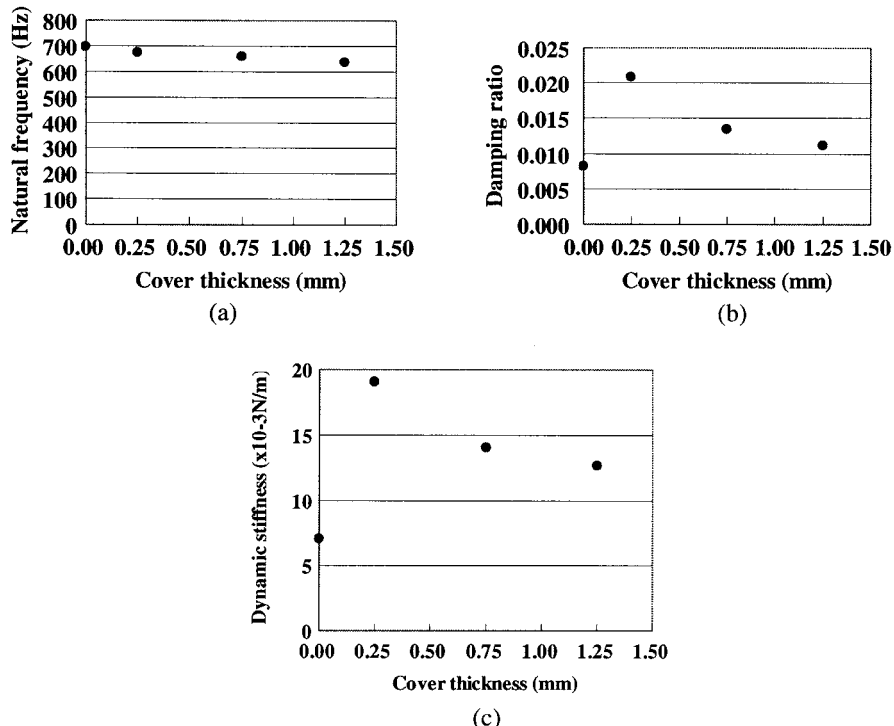


**Figure 14.32** Dynamic characteristics of the composite shanks with respect to the steel cover thickness when the diameter of the lead core in a stainless-steel pipe and the adhesive thickness were 6 mm and 0.10 mm, respectively: (a) Natural frequency; (b) damping ratio; (c) dynamic stiffness.

thickness was determined to be 0.25 mm for the composite boring bar, which was the minimum thickness that can be produced without causing machining difficulties.

Figure 14.33 shows the dynamic characteristics of the composite shank of the boring bar with respect to the adhesive thickness when the thickness of the steel cover and the outside diameter of the lead core in a stainless steel pipe were 0.25 mm and 6 mm, respectively. In figure 14.33, the fundamental natural frequency, damping ratio, and dynamic stiffness were constant when the adhesive thickness was less than 0.1 mm, while they decreased as the adhesive thickness increased over 0.1 mm. Therefore, the adhesive thickness for the composite boring bar was selected to be 0.1 mm. This thickness was reported to give the maximum fatigue strength of the adhesive joint (Lee et al., 1991). The design parameters for the composite boring bar so far determined are listed in table 14.16.

#### 14.4.3 Manufacture of the Composite Boring Bar

The composite boring bar was manufactured by wrapping preprints on the lead core in a stainless-steel pipe and curing, using an autoclave vacuum bag degassing process. The  $[\pm 5]_s$  stacking sequence was used for prepreg wrapping rather than zero-degree wrapping to avoid the matrix cracking during the grinding process of the outer surface of the composite bar (Kim et al., 2000). After curing the composite shank, its outer surface was ground precisely. Then the steel cover was bonded to

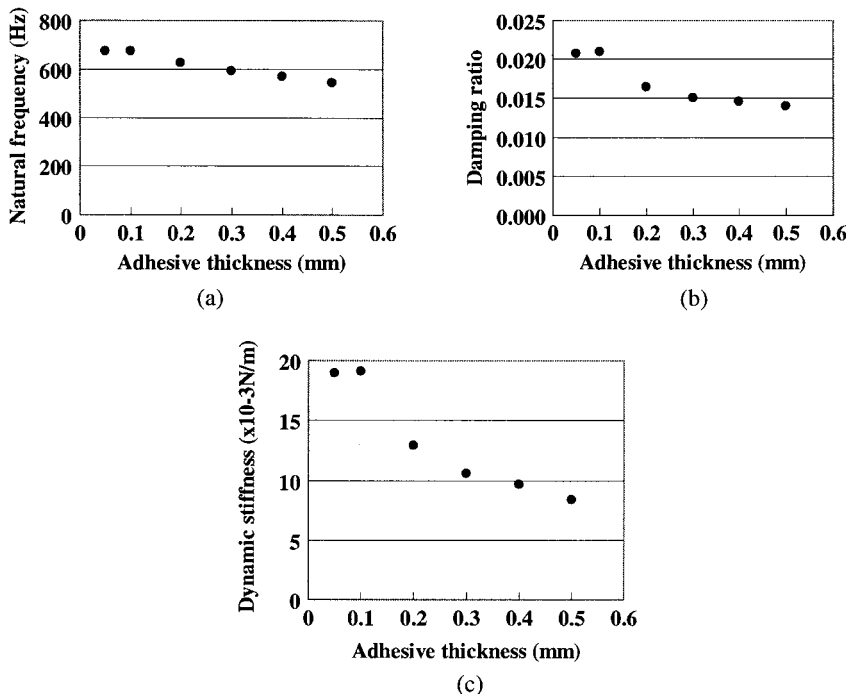


**Figure 14.33** Dynamic characteristics of the composite shanks with respect to the adhesive thickness when the thickness of the steel cover and the outside diameter of the lead core in a stainless steel pipe were 0.25 mm and 6 mm, respectively: (a) Natural frequency; (b) damping ratio; (c) dynamic stiffness.

**Table 14.16 Design Parameters for the Composite Boring Bar**

Core diameter ( $d_c$ )	Core material	Cover thickness ( $t_s$ )	Adhesive thickness ( $t_a$ )
6.00 mm	Lead in stainless-steel pipe	0.25 mm	0.10 mm

the composite shank with epoxy adhesive. Figure 14.34 shows detailed drawings of the composite boring bar. A steel insert was adhesively bonded to the tool mounting part of the composite boring bar to provide an area for installing the cutting tool tip because reliable tapping or thread cutting directly into composite material is difficult. Adjusting and fixing bolts were used for proper mounting of the cutting tool on the steel insert.

Figure 14.35 shows a photograph of the manufactured composite boring bar with a diamond cutting tool mounted.

#### 14.4.4 Performance Tests of Composite Boring Bar

In order to find the maximum value of  $l/d$  of the composite boring bar without chatter during metal cutting tests, boring tests of aluminum engine block specimens with the developed composite boring bars were performed, varying the overhang

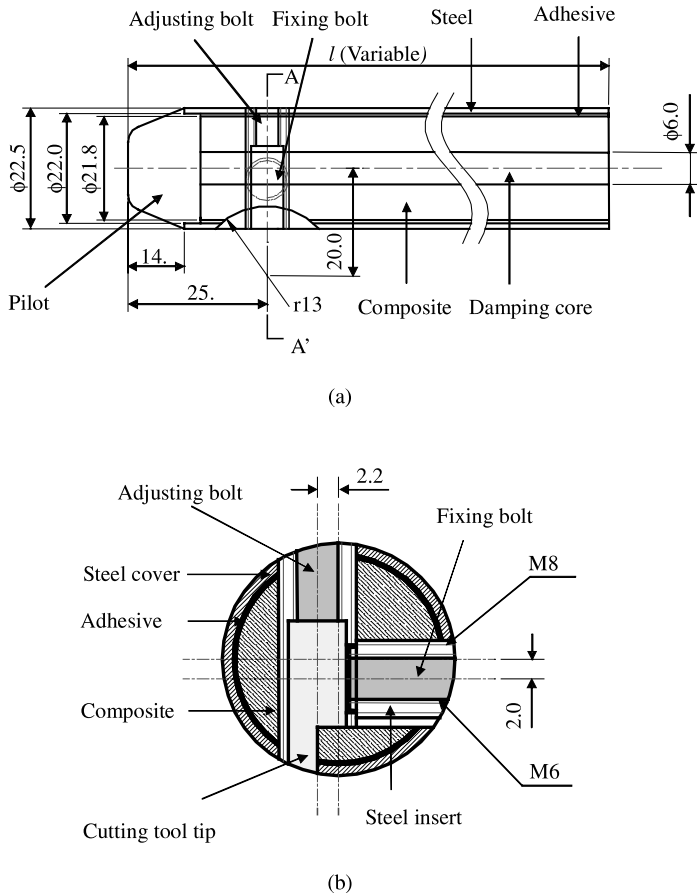


**Figure 14.34** Drawing of the composite boring bars including tool mounting part:  
(a) Composite boring bar; (b) section view of A-A' of tool mounting part (in mm).  
(Courtesy of Vision-Innotech, Seoul, Korea.)

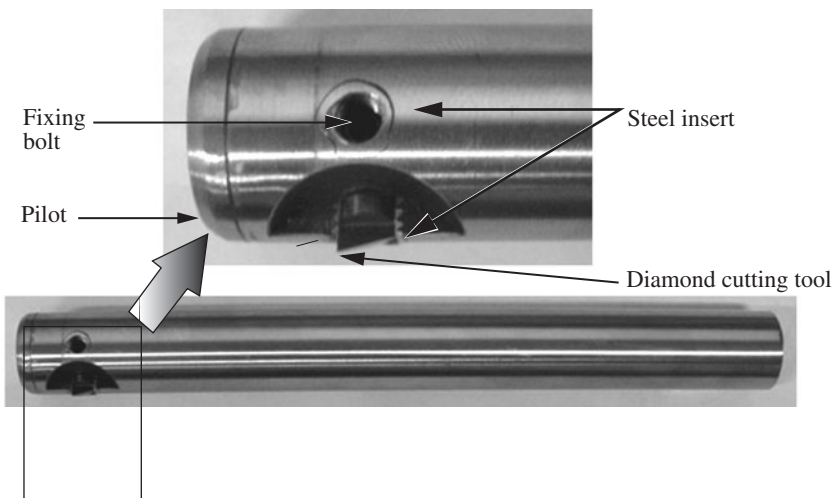


**Figure 14.35** Photograph of the developed composite boring bar. (Courtesy of Vision-Innotech, Seoul, Korea.)

**Table 14.17 Cutting Conditions for the Boring Process of Aluminum (Al 6061-T6) Workpiece**

Workpiece material	Al 6061-T6
Rotating speed (rpm)	2500
Cutting speed (m/min)	204
Feed rate (mm/rev)	0.04
Depth of cut (mm)	0.25
Cutting length (mm)	10
Cutting tool material	Diamond

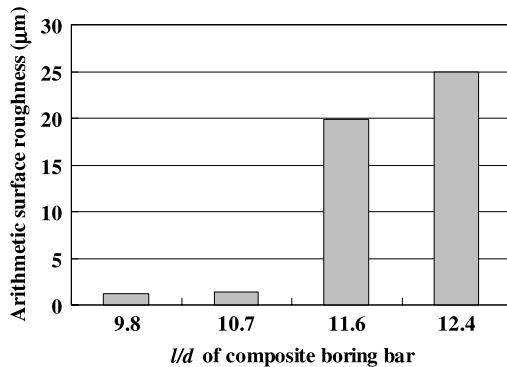


**Figure 14.36** Arithmetic surface roughness of aluminum workpieces with  $l/d$  of 9.8, 10.7, 11.6, and 12.4.

length from 160 to 420 mm, on a vertical machining center. The rotating speed of the boring bar used was 2500 rpm, which was also the speed employed for the tungsten carbide boring bar to compare the performance characteristics of the two boring bars, although the composite boring bar might allow much higher rotating speed due to its high fundamental natural frequency. The metal cutting tests for composite boring bar were performed under the same cutting conditions as for the tungsten carbide boring bar, as listed in table 14.17. The occurrence of chatter was detected by audible sharp noises during the metal cutting process and the surface roughness of the workpieces after the metal cutting tests was measured by a surface texture measurement device (Surtronic 3+, Rank Taylor Hobson Ltd., England). Figure 14.36 shows the comparisons of surface roughness of the aluminum workpieces when the value of  $l/d$  was 9.8 ( $l=220$  mm), 10.7 ( $l=240$  mm), 11.6 ( $l=260$  mm), and 12.4 ( $l=280$  mm), respectively. In figure 14.36, the arithmetic surface roughness  $R_a$  of the aluminum workpiece was less than  $1.3 \mu\text{m}$  when the value of  $l/d$  of the composite boring bar was smaller than 10.7. However, the surface of the aluminum workpieces became rough and audible sharp noises were detected during the metal cutting process when the value of  $l/d$  of the composite boring bar was larger than 11.6. From the experiments, it was found that the chatter did not initiate up to the value of  $l/d$  of 10.7 when  $l$  was 240 mm, with the cutting conditions listed in table 14.17. The maximum value of  $l/d$  of the tungsten carbide boring bar was 8. Therefore, the metal cutting ability of the composite boring bar was 33% higher than that of the tungsten carbide boring bar at the rotating speed of 2500 rpm.

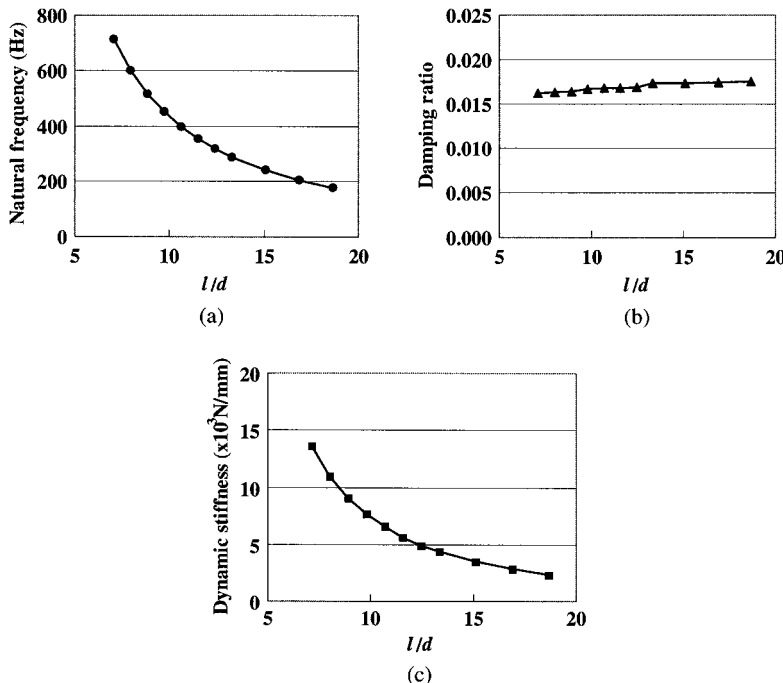


**Figure 14.37** Dynamic characteristics of the composite boring bar with respect to the value of  $l/d$  of boring bar when the thickness of the steel cover, the thickness of the adhesive and the outside diameter of the lead core were 0.25, 0.10, and 6 mm, respectively: (a) Natural frequency; (b) damping ratio; (c) dynamic stiffness.

**Table 14.18 Measured Dynamic Characteristics of the Tungsten Carbide Boring Bar and the Composite Boring Bar with the Maximum Value of  $l/d$  for Stable Boring Operation**

$l/d$	Natural frequency (Hz)	Damping ratio ( $\times 10^{-3}$ )	Dynamic stiffness (N/m)
Tungsten carbide boring bar	8.0	364	4.2
Composite boring bar	10.7	395	6600

The vibration tests depicted in figure 14.30 were performed to compare the dynamic characteristics of the tungsten carbide boring bar and the developed composite boring bar. Figure 14.37 shows the dynamic characteristics of the composite boring bar with respect to the value of  $l/d$ . From the metal cutting test, it was found that the values of  $l/d$  of the tungsten carbide boring bar and the composite boring bar were 8.0 and 10.7 for stable metal cutting, respectively. Since the values of dynamic stiffness of the two boring bars were similar at the limit of stable metal cutting, as shown in table 14.18, it was verified that the stability limit of the boring bars was dependent on the dynamic stiffness rather than the static stiffness, and consequently the composite boring bar had much advantage.

Since the material and manufacturing costs of tungsten carbide are much larger than high-stiffness pitch-based carbon-fiber epoxy composite, the carbon composite

boring bar developed may be very promising, due to its ease of manufacture and machining to provide the mounting site for cutting tools.

### 14.5 High-Speed Composite Milling Machine Tool Structures

Machine tools should have the ability to produce precise products at high machining speeds. Modern high-speed milling machines are required to have  $20 \text{ m/s}^2$  acceleration and deceleration. Unfortunately, at these speeds, the machine tool structure frequently vibrates, creating problems during manufacturing (Schmitz and Donalson, 2000; Ema and Marui, 1996; Rivin and Kang, 1989; Tobias, 1965). In this example, the design and manufacture of vertical and horizontal machine tool frames of a high-speed CNC milling machine with composite materials are presented.

For high-speed operation with high precision, machine tool structures should be designed with light moving frames without sacrificing stiffness and damping properties. Therefore, the functional requirements (FRs) of high-speed machine tool structures are

$\text{FR}_1 = \text{Increase } I \text{ of the machine tool structures}$

$\text{FR}_2 = \text{Increase the specific stiffness } (E/\rho) \text{ of the machine tool structures}$

$\text{FR}_3 = \text{Increase damping.}$

These requirements are contradictory if conventional metallic materials are employed, because conventional metals have almost the same low specific stiffness ( $E/\rho$ ) with low damping characteristics. The requirement of high specific stiffness with high damping can be satisfied by employing fiber-reinforced polymer composite materials (Lee, 1985; Lee et al., 1985). Moreover, sandwich structures with faces made of fiber-reinforced composite materials and with a honeycomb or foam core maximize their advantages when they are applied to the tool structures to resist bending moment.

The deformation of machine tool structures under cutting forces and structural inertia loads during acceleration and deceleration not only produce poor quality products but also produce noise and vibration. A simple way to reduce the deformation is to employ a larger cross-sectional structure. However, it increases the mass of machine tool structures and consequently requires larger motors, bearings, and linear motion guides. Therefore, the best way to increase the stiffness of machine tool structures without increasing mass is to employ structures that have high sectional moment of inertia, such as sandwich structures. To satisfy the above functional requirements, the design parameters (DPs) may be constructed as follows:

$\text{DP}_1 = \text{Shape of cross-section (box-type and sandwich structure)}$

$\text{DP}_2 = \text{Thickness of high-modulus carbon fiber}$

$\text{DP}_3 = \text{Epoxy matrix and core (honeycomb and foam).}$

From the FRs and DPs, we may construct the following design matrix.

	DP <sub>1</sub>	DP <sub>2</sub>	DP <sub>3</sub>
FR <sub>1</sub>	X	0	0
FR <sub>2</sub>	0	X	0
FR <sub>3</sub>	x	0	X

Following the design matrix, the vertical and horizontal moving frames of a high-speed CNC milling machine were designed and manufactured with sandwich composite structures that are adhesively bonded to welded steel structures—a hybrid machine tool structure. The natural frequency and damping capacity as well as weight savings of the composite hybrid machine tool structures were measured and compared with those of conventional steel machine tool structures (Suh and Lee, 2002).

#### 14.5.1 Design of Lightweight Composite-Reinforced Machine Tool Frames

Figure 14.38 shows a high-speed CNC milling machine of 15 kW equipped with  $3.5 \times 10^4$  rpm spindle (FH500, Daewoo Heavy Industries & Machinery Ltd., Korea) whose vertical columns and horizontal columns were reinforced with composite sandwich structures and composite plates. Both the slides are operated up to 2.0 m/s with maximum acceleration of  $14.0 \text{ m/s}^2$ . Figure 14.39 shows the horizontal slide (X-slide) composed of composite sandwich structures adhesively bonded to welded steel structures.

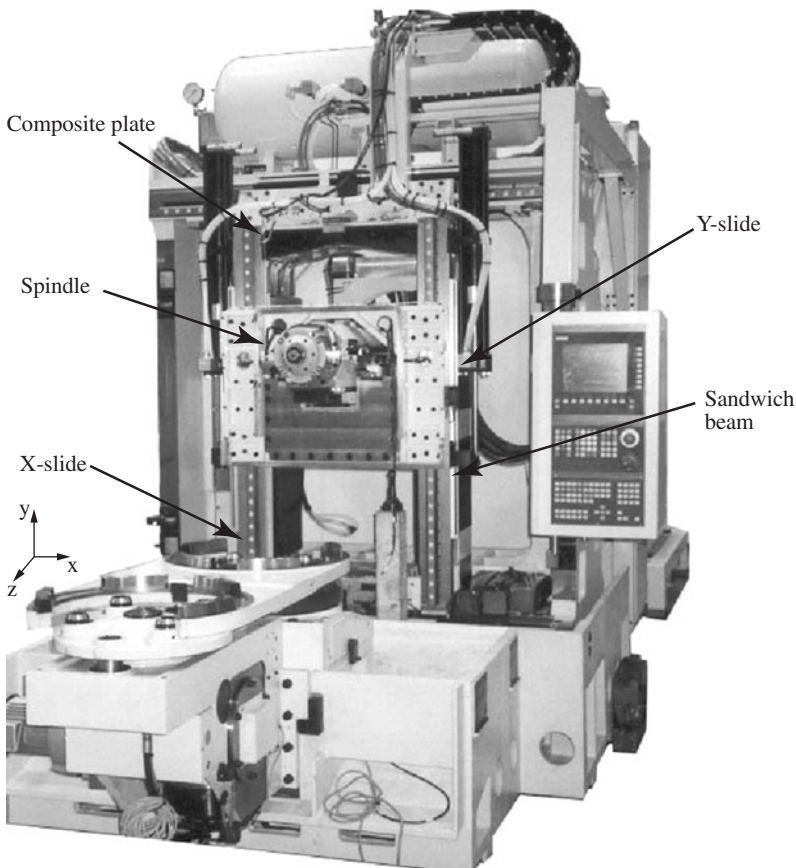


**Figure 14.38** High-speed milling machine tool structure. (Courtesy of Daewoo Heavy Industries & Machinery Ltd., Korea.)

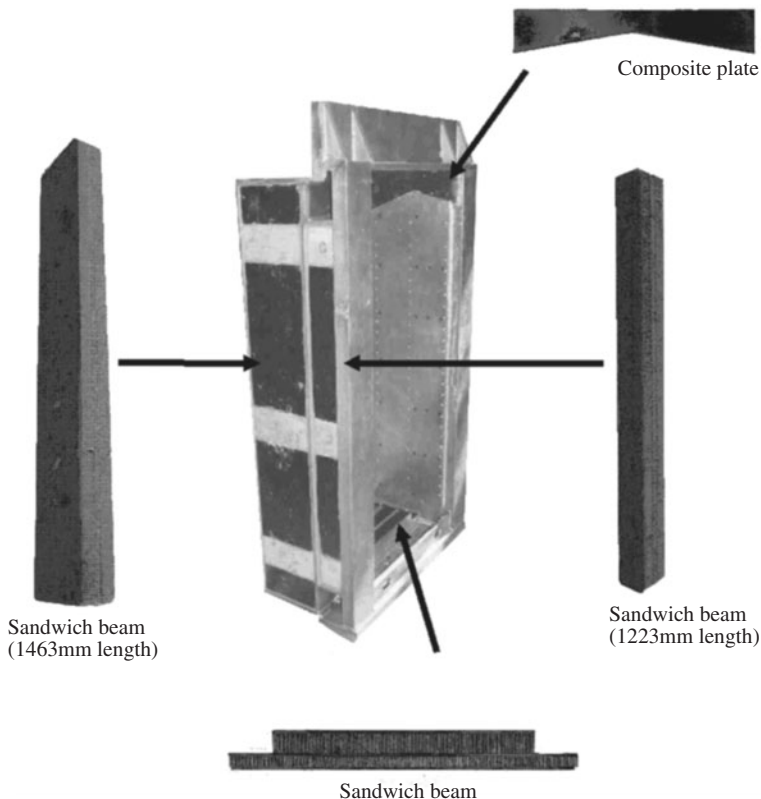


**Figure 14.39** Hybrid X-slide composite reinforcements.

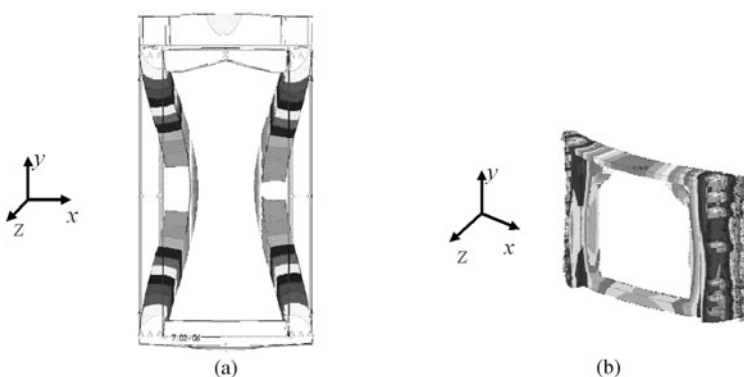


**Figure 14.40** Deformation of the moving frames of a CNC milling machine: (a) X-slide; (b) Y-slide.

In order to estimate the deflections of the milling machine during operation, the deflections of steel moving frames were calculated by FEM, as shown in figure 14.40, where the vertical columns of the X-slide were bent inward by the attraction force of 20 kN generated by the two linear motors mounted on the inner surfaces of the vertical columns of the X-slide. The horizontal columns of the Y-slide were deformed in the Z-direction by the bending moment due to the protruding spindle weight of 4000 N. In order to maximize the reinforcement effect, the vertical column of the

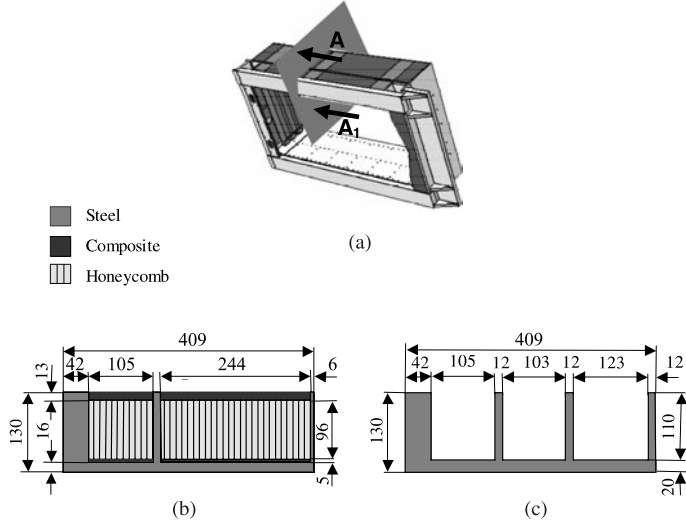


**Figure 14.41** Section views of vertical columns of the *X*-slide: (a) Reference of section view; (b) hybrid; (c) conventional.

horizontal slide (*X*-slide) and the horizontal column of the vertical slide (*Y*-slide) were selected for the main reinforcement parts because they were the weakest parts of the moving frames of the milling machine considered.

In order to develop a lighter hybrid frame, the *X*-slide steel base, made of thinner steel plate (16 mm) than conventionally employed (20 mm) was reinforced with a composite sandwich structure, as shown in figure 14.41. Since the shear deformation of a simple sandwich structure is usually large, the hybrid structure was designed as a box-type structure, as shown in figure 14.41 whose sides were reinforced with steel plates.

Since reinforcement of the outer face of the moving frames is most effective way to increase the flexural rigidity  $D$ , the inner face thickness of the sandwich was determined to be 5 mm, for joining of the inner face of the sandwich beams to the steel base with bolts.

The thickness of the outer face of the sandwich beam was tentatively determined to give  $D$  equivalent to that of the conventional one. Then more specific calculations were performed to determine suitable dimensions of the reinforcements using FEM, considering local warping or twisting. Through the above design process, the outer face thickness of sandwich beam was determined to be 13 mm.

#### 14.5.2 Manufacture of Hybrid Machine Tool Structure

High-strength carbon epoxy composite (USN150, see table 2.3) and glass-fiber fabric epoxy were used for the face of sandwich beams and reinforcing plates for the *X*- and *Y*-slides. The vertical column of the *X*-slide was reinforced with two sandwich beams 1462 mm and 1223 mm long, respectively, while the top and bottom parts were reinforced with four composite plates and six small sandwich beams. The horizontal column of the *Y*-slide that required strict dimensional tolerance to avoid interference with other parts was manufactured with very high modulus carbon-fiber epoxy composite (URN300, see table 13.3) because the spindle unit of the milling machine mounted on the *Y*-slide should resist the bending moment produced by the spindle

weight, cutting force, and the inertia force due to fast acceleration and deceleration of the slide. Also, the left and right vertical columns of the *Y*-slide were reinforced with sandwich beams. The composite reinforcements were bonded to the steel base structures with an epoxy adhesive (2216B/A, 3M, St. Paul, Minn., USA) combined with the mechanical joining with bolts to enhance the reliability and manufacturing efficiency during the joining operation.

#### 14.5.3 Dynamic Characteristics and Weight Reduction

The impulse response tests for both the conventional steel and the hybrid moving frames were performed under free-free boundary conditions. Also, the dynamic characteristics of a CNC milling machine tool structure equipped with the hybrid *X*-slide were measured. Tables 14.19 and 14.20 show comparisons of dynamic characteristics between the conventional and the hybrid slides. For the *X*-slide, the natural frequencies of the hybrid slide were 30% greater in the measuring range and the damping factors were 1.6–5.7 times greater. Furthermore, a significant increase in the damping factor was found in the third, fourth, and fifth modes corresponding to bending of the vertical column. For the *Y*-slide, the damping factors of the hybrid slide were 1.5–2.5 times greater than the conventional slides.

The accuracy of the vertical column of the *X*-slide was critical because the deflection due to the attraction force of the linear motors is an important constraint

**Table 14.19 Comparisons of Dynamic Characteristics between the Steel *X*-Slide and the Hybrid *X*-Slide under Free-Free Boundary Condition**

Mode	Steel <i>X</i> -slide			Hybrid <i>X</i> -slide		
	Natural frequency (Hz)	Mode shape	Damping factor (%)	Natural frequency (Hz)	Mode shape	Damping factor (%)
1	64	Torsion	0.90	92	Torsion	2.20
2	126	Bending	0.50	131	Tilting	0.80
3	211	Bending	0.30	281	Bending	1.20
4	261	Bending + twisting	0.20	304	Bending + twisting	0.80
5	308	Bending + twisting	0.14	357	Bending + twisting	0.80

**Table 14.20 Comparison of Dynamic Characteristics between the Steel *Y*-Slide and the Hybrid *Y*-Slide under Free-Free Boundary Condition**

Mode	Steel <i>Y</i> -slide			Hybrid <i>Y</i> -slide		
	Natural frequency (Hz)	Mode shape	Damping factor (%)	Natural frequency (Hz)	Mode shape	Damping factor (%)
1	135	Torsion	0.48	115	Torsion	0.90
2	345	Bending	0.22	341	Bending	0.35
3	365	Complex mode	0.19	589	Bending	0.30
4	572	Bending	0.22	598	Bending	0.32
5	690	Bending	0.12	620	Bending	0.28

**Table 14.21 Comparison between Masses of the X-Slide and the Y-Slide of the Conventional and the Hybrid Machine Tools**

	<i>Steel slide</i>	<i>Hybrid slide</i>	
		497 kg	
X-slide	671 kg	465 kg (steel base)	32 kg (composite)
		92 kg	
Y-slide	140 kg	84 kg (steel base)	32 kg (composite)

for proper operation of the linear motors, which operate with a 0.9 mm gap between a moving magnet and a fixed magnet face. The relative deflection of the vertical column was measured at various positions of the Y-slide, and found that the maximum relative deflection was less than 0.1 mm, which was satisfactory for operation of the linear motors.

Table 14.21 shows the mass comparison between the conventional steel slides and the hybrid slides, in which the mass reductions of the hybrid X- and Y-slides were 174 kg (26%) and 48 kg (34%), respectively, without sacrificing the stiffness of the structures.

## 14.6 Concluding Remarks

In section 14.2, the dynamic and static characteristics of the carbon composite high-speed air spindle were investigated through finite element analysis. The thickness of the carbon composite shaft was determined, considering the bending natural frequency, and the carbon composite shaft was reinforced in the circumferential direction to enhance the radial stiffness of the air spindle.

In section 14.3, the rotor of an AC induction motor was designed and manufactured with magnetic-powder epoxy composite for a high-speed built-in spindle motor system. Two high magnetic permeability powders, iron powder and ferrite powder, were evaluated to increase the magnetic permeability of the composite. The composite rotors had several advantages, such as low slip, less power consumption, and a mass 41% less than that of conventional silicon-steel rotors.

In section 14.4, a rotating composite boring bar was developed with very high stiffness pitch-based carbon-fiber epoxy composite material in order to increase the dynamic stability of the boring bar during the metal cutting operation. The dynamic characteristics of the composite shank of the boring bar were investigated by impulse dynamic tests with respect to the design parameters, such as the core diameter, core material, steel cover thickness, and adhesive thickness. The chatter of the composite boring bar did not occur up to  $l/d$  (overhang length/boring bar diameter) equal to 10.7, while the chatter of the tungsten boring bar occurred at  $l/d=8.0$ . The fundamental natural frequency, damping ratio, and dynamic stiffness of the composite boring bar were also 72%, 168% and 28% higher than those of the tungsten carbide boring bar.

In section 14.5, the horizontal slide (X-slide) and vertical slide (Y-slide) of a high-speed CNC milling machine were designed and manufactured with a hybrid machine tool structure (composite sandwich structure) that was adhesively bonded to the welded steel structure. The masses of the hybrid X-slide and the Y-slide were 26%,

34% less, respectively, than those of conventional steel slides without sacrificing bending stiffness of the structures. Also, the damping factors of the hybrid *X*-slide and *Y*-slide were 1.5–5.7 times those of the conventional slides.

## Appendix A: Chatter in Metal Cutting

Chatter is a self-excited type of vibration that occurs in metal cutting if the chip width is too large with respect to the dynamic stiffness of the system. The cutting force changes periodically, which makes the machined surface undulated. The chip thickness varies and it becomes dissected in the extreme (Tlusty, 1999). Chatter is easily recognized by the noise associated with these vibrations, by the chatter marks on the cut surface, and by the appearance of the chips. Machining with chatter is mostly unacceptable because of these effects, and because the large peak values of the variable cutting force might cause breakage of the cutting tool or some other part of the machine tool. Therefore, the chatter is often the factor limiting metal removal below a rate that would normally correspond to the available power and torque in the spindle. Although much work has been done on the chatter in machining, little attempt has been made to improve the stability of machine tools by employing composite materials in the machine tool structures (Choi and Lee, 1997).

The process of self-excitation is a closed-loop one in which the vibrations that produce undulation on the work surface cause a force variation, and the variable force in turn produces vibrations.

The tangential cutting force  $F_t$  that deflects the workpiece in turning, or the tool in boring, may be considered to be directly proportional to the chip area  $A$ , as shown in figure 14.42 for turning case:

$$F_t = k_s A = k_s b h = k_s a f_r \quad (14.23)$$

where  $b$  is chip width,  $h$  is chip thickness,  $a$  is depth of cut,  $f_r$  is feed per revolution, and  $k_s$  is specific cutting force (force/area) or specific cutting power (power/volume removal rate).

The chip thickness  $h$  consists of a steady component  $h_m$  (mean chip thickness) and the variation due to the undulation difference between the amplitude of current cut  $Y$  and the previous cut  $Y_0$ :

$$h = h_m + (Y_0 - Y) \exp(i\omega t) \quad (14.24)$$

Then the amplitude  $F$  of the variable force is expressed as

$$F = k_s b (Y_0 - Y) \quad (14.25)$$

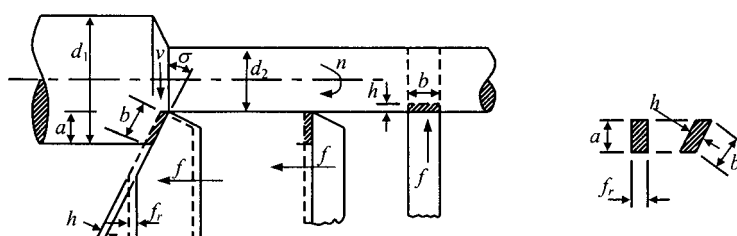


Figure 14.42 Geometry turning (from Tlusty, 1999).

The relationship between the variable force  $F$  and the amplitude of undulation  $Y$  is

$$Y = FG(\omega) \quad (14.26)$$

where  $G(\omega)$  is the frequency-dependent transfer function of the cutting system.

From equations (14.25) and (14.26), we have the following relationship:

$$\frac{Y_0}{Y} = \frac{1 + k_s b G}{k_s b G} \quad (14.27)$$

The condition for the limit of stability may be derived from the condition that the undulation amplitude does not decay:

$$\left| \frac{Y_0}{Y} \right| = \left| \frac{1 + k_s b G}{k_s b G} \right| = 1 \quad (14.28)$$

Since the imaginary part of  $(1 + k_s b G)$  is equal to  $k_s b G$ , equation (14.28) is satisfied if the real parts of the numerator and the denominator are equal because  $k_s$  and  $b$  are real numbers:

$$1 + k_s b \operatorname{Re}(G) = -k_s b \operatorname{Re}(G) \quad (14.29)$$

From equation (14.29), we have the limit of stability of the cutting operation:

$$\frac{1}{k_s b} = -2 \operatorname{Re}(G) \quad (14.30)$$

Since the chip width  $b$  is a positive number, equation (14.30) is satisfied by the negative part of the function  $\operatorname{Re}[G(\omega)]$ . Therefore, the condition for the critical limit of chatter, for which  $b < b_{\lim,cr}$ , self-excited vibration does not occur, can be expressed as follows:

$$b_{\lim,cr} = -\frac{1}{2k_s \operatorname{Re}(G)_{\min}} \quad (14.31)$$

since the minimum value of  $G$  (or maximum of  $|G|$ ) occurs close to the resonance frequency  $\omega_n$ ; to be precise, it occurs at the frequency  $\omega_d$  expressed by the following equation (Tlusty, 1999):

$$\frac{\omega_d}{\omega_n} = \sqrt{1 - \zeta^2} \quad (14.32)$$

and the minimum value is approximately

$$\operatorname{Re}(G)_{\min} \approx -\frac{1}{2K_m \zeta} \quad (14.33)$$

where  $K_m$  is the stiffness of machine tool system during the cutting operation and  $\zeta$  is the damping ratio of the cutting system. Substituting equation (14.33) into equation (14.31) yields

$$b_{\lim} \approx \frac{K_m \zeta}{k_s} \quad (14.34)$$

Equation (14.34) shows that the maximum width of cut that can be taken without expectation of chatter is approximately proportional to the static stiffness and damping of a machine tool.

## Appendix B: Definitions of Damping Parameters

Several commonly encountered damping parameters are defined in this appendix with the relationships among them.

1. The loss factor,  $\eta$  is defined as

$$\eta = \frac{\Delta U}{2\pi U_{\max}}$$

where  $\Delta U$  is the energy dissipated per cycle and  $U_{\max}$  is the maximum potential energy stored in the system.

2. Quality factor,  $Q$  (also called the dynamic amplification factor), is the inverse of the loss factor,

$$Q = \frac{1}{\eta} = \frac{2\pi U_{\max}}{\Delta U}$$

3. The specific damping capacity,  $\psi$ , is defined as

$$\psi = \frac{\Delta U}{U_{\max}}$$

4. The damping ratio,  $\zeta$  (also called the fraction of critical damping), is one-half the loss factor  $\eta$ :

$$\zeta = \frac{\Delta U}{4\pi U_{\max}}$$

5. The log decrement,  $\delta$ , is the logarithm of the ratio of two response peaks of a system undergoing free vibration:

$$\delta = \frac{1}{n} \ln \frac{y_m}{y_{m+n}}$$

where  $y_m$  and  $y_{m+n}$  are amplitudes of the  $m$ th and  $(m+n)$ th peaks, respectively, and  $n$  is the number of cycles between these peaks. For a simple spring-mass-damper system,  $\delta$  and  $\zeta$  are related as follows:

$$\delta = \frac{2\pi\zeta}{\sqrt{1 - \zeta^2}}$$

For  $\zeta \ll 1$ , the above expression reduces to

$$\delta = 2\pi\zeta$$

6. For systems with potential energy stored in the form of strain energy, the complex modulus  $E$  can be used to express both energy stored and dissipated using the viscoelastic model as (Sun and Lu, 1995)

$$E = E' + jE'' \quad (j = \sqrt{-1})$$

where  $E'$  is the real or elastic modulus and  $E''$  is the loss or dissipation modulus. Then, the loss factor  $\eta$  is related by

$$\eta = \frac{E''}{E'}$$

Finally, the relationship among the various parameters is

$$\eta = \frac{1}{Q} = \frac{\psi}{2\pi} = \frac{E'}{E''} = 2\xi \approx \frac{\delta}{\pi}$$

### References

- Adams, R. D. 1972. "The Damping Characteristics of Certain Steels, Cast Irons and Other Materials," *Journal of Sound and Vibration*, Vol. 23, pp. 199–216.
- Bang, K. K., and Lee, D. G. 2002. "Design of Carbon Fiber Composite Shafts for High Speed Air Spindles," *Composite Structures*, Vol. 55, pp. 247–259.
- Blondeel, E., Snoeys, R., and Devrieze, L. 1980. "Dynamic Stability of Externally Pressurized Gas Bearings," *Journal of Lubricant Technology, Transactions of ASME*, Vol. 102, pp. 511–519.
- Callister, W. D., Jr. 1997. *Materials Science and Engineering—An Introduction*, John Wiley & Sons, New York, Chapter 12.
- Chang, S. H., Lee, D. G., and Choi, J. K. 2000. "Composite Rotor for High-Speed Induction Motors," *Composite Structures*, Vol. 50, pp. 37–47.
- Cho, D. H., Lee, D. G., and Choi, J. H. 1997. "Manufacturing of One-Piece Automotive Drive Shaft with Aluminum and Composite Materials," *Composite Structures*, Vol. 38, pp. 309–319.
- Choi, J. K., and Lee, D. G. 1997. "Manufacture of a Carbon Fiber-Epoxy Composite Spindle-Bearing System for a Machine Tool," *Composite Structures*, Vol. 37, pp. 241–251.
- Cook, N. H. 1966. *Manufacturing Analysis*, Addison-Wesley Publishing, New York, Chapter 3.
- Crawley, E. F., and Mohr, D. G. 1983. "Experimental Measurements of Material Damping in Free Fall with Tuneable Excitation," *Proceedings of AIAA/ASME/AHS Structures, Structural Dynamics and Materials Conference*, Paper No. 83-0858-CP.
- Cullity, B. D. 1972. *Introduction to Magnetic Materials*, Addison-Wesley, Reading, Mass.
- Ema, S., and Marui, E. 1996. "Damping Characteristics of an Impact Damper and Its Application," *International Journal of Machine Tools and Manufacture*, Vol. 36, pp. 293–306.
- Ema, S., and Marui, E. 2000. "Suppression of Chatter Vibration of Boring Tools Using Impact Dampers," *International Journal of Machine Tools and Manufacture*, Vol. 40, pp. 1141–1156.
- Englemann, R. H., and Middendorf, W. H. 1995. *Handbook of Electric Motors*, Marcel Dekker, New York.
- Fiske, T. J., Gokturk, H. S., and Kalyon, D. M. 1997. "Enhancement of the Relative Magnetic Permeability of Polymeric Composites with Hybrid Particulate Fillers," *Journal of Applied Polymer Science*, Vol. 65, pp. 1371–1377.
- Foner, S. 1996. "The Vibrating Sample Magnetometer: Experiences of a Volunteer," *Journal of Applied Physics*, Vol. 79, pp. 4740–4745.
- Fuller, D. D. 1969. "A Review of the State-of-the-Art for the Design of Self Acting Gas Lubricated Bearings," *Journal of Lubricant Technology*, Vol. 91, pp. 1–16.
- Garik, M. L., and Whipple, C. C. 1961. *Alternating Current Machines*, Van Nostrand, Princeton, N.J.
- Gross, W. A. 1962. "Investigation of Whirl in Externally Pressurized Air-Lubricated Journal Bearings," *Journal of Basic Engineering, Transactions of ASME*, Vol. 84, pp. 132–138.

- Hahn, R. S. 1951. "Design of Lanchester Damper for Elimination of Metal-Cutting Chatter," *Transactions of ASME*, Vol. 73, pp. 331–336.
- Hammill, W. J., and Andrew, C. 1973. "Vibration Reduction with Continuous Damping Inserts," *Proceedings of the 14th International M.T.D.R. Conference*, pp. 495–502.
- Harris, G. M., *Shock and Vibration Handbook*, 4th ed., McGraw-Hill, New York, Chapter 1, 1988.
- Heine, J. C. 1966. *The Stress and Frequency Dependence of Material Damping in Some Engineering Alloys*, Ph.D. Thesis, Department of Mechanical Engineering, MIT, Cambridge, Mass.
- Jeong, K. S., Lee, D. G., and Kwak, Y. K. 1995. "Experimental Investigation of the Dynamic Characteristics of Carbon Fiber Epoxy Composite Thin Beams," *Composite Structures*, Vol. 33, pp. 77–86.
- Jones, D. I. 1995. "Applied Damping Treatments," in *Shock and Vibration Handbook*, 4th ed., Edited by Harris, C. M., McGraw-Hill, New York, pp. 37.1–37.23.
- Kang, C. H. 1963. "Chatter Vibration in Precision Boring," *Machine Tool Design and Production Engineering Research Conference, ASME*, pp. 171–189.
- Kim, H. S., Park, K. Y., and Lee, D. G. 1995. "A Study on the Resin Concrete for the Ultra-Precision Machine Tool Bed," *Journal of Materials Processing Technology*, Vol. 48, pp. 649–655.
- Kim, K. J., and Ha, J. Y. 1987. "Suppression of Machine Tool Chatter Using a Viscoelastic Dynamic Damper," *ASME Journal of Engineering in Industry*, Vol. 109, pp. 58–71.
- Kim, P. J., Lee, D. G., and Choi, J. K. 2000. "Grinding Characteristics of Carbon Fiber Epoxy Composite Hollow Shafts," *Journal of Composite Materials*, Vol. 34, pp. 2016–2035.
- Kinra, V. K., and Wolfenden, A. 1992. *Mechanics and Mechanism of Material Damping*, ASTM, West Conshohoken, Pa.
- Koenigsberger, F., and Tlusty, J. 1970. *Machine Tool Structures 1*, Pergamon Press, Oxford, Section 2.
- Kumar, P. S. A., Shrotri, J. J., Deshpande, C. E., and Date, S. K. 1997. "Systematic Study of Magnetic Parameters of Ni-Zn Ferrite Synthesized by Soft Chemical Approaches," *Journal of Applied Physics*, Vol. 81, pp. 4788–4790.
- Larson, R. H., and Richardson, H. H. 1962. "A Preliminary Study of Whirl Instability for Pressurized Gas Bearings," *Journal of Basic Engineering, Transactions of ASME*, Vol. 84, pp. 511–520.
- Lee, D. G. 1985. *Manufacturing and Testing of Composite Machine Tool Structures*, Ph.D. Thesis, Department of Mechanical Engineering, MIT, Cambridge, Mass.
- Lee, D. G., and Choi, J. K. 1997. "Design and Manufacture of an Aerostatic Spindle Bearing System with Carbon Fiber-Epoxy Composites," *Journal of Composite Materials*, Vol. 34, pp. 1150–1175.
- Lee, D. G., and Suh, N. P. 1988. "Manufacturing and Testing of Chatter Free Boring Bars," *Annals of the CIRP*, Vol. 37, pp. 365–368.
- Lee, D. G., Sin, H. C., and Suh, N. P. 1985. "Manufacturing of a Graphite Epoxy Composite Spindle for a Machine Tool," *Annals of the CIRP*, Vol. 34, pp. 365–369.
- Lee, D. G., Kim, K. S., and Im, Y. T. 1991. "An Experimental Study of Fatigue Strength for Adhesively Bonded Tubular Single Lap Joints," *Journal of Adhesion*, Vol. 35, No. 1, pp. 39–53.
- Lee, D. G., Bang, K. G., and Choi, J. K. 2000. "Development of Composite Pressing Rollers for Thin Film Processing," *Journal of Composite Materials*, Vol. 34, pp. 770–790.
- Lee, D. G., Hui Yun Hwang, and Kim, J. K. 2003. "Design and Manufacture of a Carbon Fiber Epoxy Rotating Boring Bar," *Composite Structures*, Vol. 60, pp. 115–124.
- Mishin, D. D., and Mishin, D. D., Jr. 1995. "The Influence of Magnetic Conductor Permeability on the Efficiency of Strong-Field Electromagnets," *Journal of Magnetism and Magnetic Materials*, Vol. 139, pp. 228–230.

- Mizumoto, H., Arii, S., Kami, Y., Goto, K., Yamamoto, T., and Kawamoto, M. 1996. "Active Inherent Restrictor for Air-Bearing Spindles," *Precision Engineering*, Vol. 19, pp. 141–147.
- Nagano, S., Koizumi, T., Fujii, T., Tsujiuchi, N., and Ueda, H. 1997. "Development of a Composite Boring Bar," *Composite Structures*, Vol. 38, pp. 531–539.
- Nashif, A. D., Jones, D. I., and Henderson, J. P. 1985. *Vibration Damping*, John Wiley & Sons, New York.
- Nicolaides G. K., and Antanassova Y. K. 1997. "Performance of a Fractional DC Electric Motor Equipped with Plastic Bonded Nd<sub>2</sub>Fe<sub>14</sub>B Stator Poles," *Journal of Applied Physics*, Vol. 81, pp. 5100–5102.
- Peters, J. 1965. "Damping in Machine Tool Construction," in *Proceedings of 6th International M.T.D.R. Conference*, pp. 191–210.
- Reddy, C. V. R. 1981. "Response of Clamped Sandwich Panels with Viscoelastic Core Under Random Acoustic Excitation," *Journal of Sound and Vibration*, Vol. 75, No. 4, pp. 481–494.
- Rivin, E. I., and Kang, H. 1989. "Improvement of Machining Conditions for Slender Parts by Tuned Dynamic Stiffness of Tool," *International Journal of Machine Tools and Manufacture*, Vol. 29, pp. 361–376.
- Schmitz, T. L., and Donalson, R. R. 2000. "Predicting High-Speed Machining Dynamics by Substructure Analysis," *Annals of the CIRP*, Vol. 49, No. 1, pp. 303–308.
- Setareh, M. 2001. "Use of Semi-Active Tuned Mass Dampers for Vibration Control of Force-Excited Structures," *Structural Engineering and Mechanics*, Vol. 4, pp. 341–356.
- Stachowiak, G. W., and Batchelor, A. W. 2001. *Engineering Tribology*, 2nd ed., Butterworth Heinemann, Boston, Mass.
- Stone, B. J. 1982. "The State of the Art in the Measurement of the Stiffness and Damping of Rolling Element Bearings," *Annals of the CIRP*, Vol. 32, pp. 529–538.
- Suh, J. D., and Lee, D. G. 2002. "Composite Machine Tool Structures for High-Speed Milling Machines," *Annals of the CIRP*, Vol. 51, pp. 285–288.
- Sun, C. T., and Lu, Y. P. 1995. *Vibration Damping of Structural Elements*, Prentice-Hall PTR, Upper Saddle River, N.J.
- Taniguchi, O. 1967. "Experimental Study on Instability of Externally Pressurized Air Journal Bearing," *JSME International Journal*, Vol. 33, pp. 997–1004.
- Thusty, J. 1999. *Manufacturing Processes and Equipment*, Prentice-Hall, Upper Saddle River, N.J.
- Tobias, S. A. 1965. *Machine Tool Vibration*, John Wiley & Sons, New York, pp. 143–146.
- Vandeurzen, V., Snoeys, R., and Peters, J. 1981. "Additive Damping Treatments for Mechanical Structures," *Annals of the CIRP*, Vol. 30, No. 1, pp. 269–274.
- Vorlichek, P. L. 1981. *Material Damping of Aluminum and Graphite/Epoxy in a Simulated Zero-Gravity Environment*, S.M. Thesis, Department of Aeronautics and Astronautics, MIT, Cambridge, Mass.
- Wardle, F. P., Lacey, S. J., and Poon, S.Y. 1983. "Dynamic and Static Characteristics of a Wide Speed Range Machine Tool Spindle," *Precision*, Vol. 5, pp. 175–183.
- Weck, M., and Koch, A. 1993. "Spindle-Bearing Systems for High-Speed Applications in Machine Tools," *Annals of the CIRP*, Vol. 42, pp. 445–448.
- Weeton, J. W., Peters, D. M., and Thomas, K. L. 1986. "Engineer's Guide to Composite Materials," *American Society for Metals*, Section 4, pp. 4.1–4.32.
- White, F. M. 1999. *Fluid Mechanics*, 4th ed., McGraw-Hill Book Company, Boston, Mass.

# 15

## Axiomatic Design of Composite Automotive Parts and Infrastructures

### 15.1 Introduction

Although continuous fiber-reinforced composite materials have about 10 times higher specific strength than low (SAE 1010) to high (SAE 4340) carbon steels, as shown in tables 2.2 and 2.3, they are not widely used in automotive or infrastructure applications due to their high cost. They are slowly becoming employed in the load-bearing structures of automotive parts and infrastructures such as bridges, guard rails, and special buildings, as the cost of composite materials becomes lower and efficient mass production methods are developed. The principal advantages of fiber-reinforced polymeric matrix composites for automotive parts are weight savings, part consolidation, and improvement in NVH (noise, vibration and harshness). The absence of corrosion problems, which lowers maintenance cost for automotive parts and infrastructures such as bridges and sewage pipes, has enabled the fiber-reinforced polymeric composites to be employed in these areas, although gradually.

The randomly oriented chopped E-glass-fiber-reinforced polymeric matrix composites, which are not load-bearing structural materials, are mainly used in the automotive industry due to their low cost. The polymers for the matrix are either thermoplastics, such as nylon, ABS, and polypropylene, or thermosets, such as unsaturated polyesters, vinyl esters, and polyurethanes. Shorter processing time is an important consideration because automotive parts are produced at a rate of one part per minute, unlike parts in the aerospace industry. Therefore, the preferred processing methods for automotive composite parts are injection molding, compression molding, reaction injection molding (RIM), structural reaction injection molding (SRIM), pultrusion, and resin transfer molding (RTM). All these methods are fast and highly automated, which compensates for the higher cost of composite materials (Mallick, 1997).

However, there have been several attempts and some successful applications of fiber-reinforced composite structural members to various parts of passenger cars, including load-bearing structural parts (Beardmore, 1986; Weeton et al., 1986). Especially, glass-fiber-reinforced polymer composites have been used for static and dynamic load-bearing structures such as bumpers and leaf springs, thanks to their high specific strength (strength/density) and impact energy absorption characteristics (Mallick and Broutman, 1977; Cheon et al., 1999; Lee et al., 2000; Lee and Cheon, 2001). Cheon et al. (1995) found that the composite bumper beam of 30%

weight of a steel bumper could be developed without sacrificing the static bending strength. Cho et al. (1997) manufactured a one-piece automotive driveshaft with aluminum and composite materials and performed static and dynamic tests. Gaudenzi et al. (1997) applied a glass-fiber sandwich panel to car body structure. Cheon et al. (1997) developed composite side-door impact beams and found that the composite impact beams allow 30–50% weight reduction based on the static and dynamic tests.

Also, many studies on joints have been performed to apply composite materials to real structures. Many researchers (Godwin and Matthews, 1980; Smith et al., 1986; Camanho and Matthews, 1997; Liu et al., 1999) have investigated the importance of width ( $w$ ), end distance ( $e$ ), hole diameter ( $d$ ), and laminate thickness ( $t$ ) on the joint strength. Ramakrishna et al. (1995) carried out tests and FE analysis for the bolted joints of pultruded sandwich composites and reported failure mode and strength with respect to  $w/d$  ratio and pultruded direction. Oh et al. (1997) evaluated bolted joint strength of the hybrid composites and developed an optimum design based on ply angle, stacking sequence, the ratio of glass epoxy to carbon epoxy, and the clamping pressure. Turvey (1998) investigated the initial stiffness, failure strength, and bolt displacement at failure of a pultrude glass-fiber reinforced plastic (GFRP) plate with respect to  $w/d$  ratio,  $e/d$  ratio, and off-axis angle. Park (2001) investigated the effects of stacking sequence and clamping force on the bearing, delamination, and ultimate strengths of mechanical joints in composite structures.

Most of the previous studies on automobile structures have been restricted only to structural designs, although the joints might be the weakest parts of the composite structures. Also, few studies on mechanical joints for composite structures that are primarily reinforced in the axial direction have been performed, although they have been widely used due to their high bending strength.

Composite materials are used in the construction industry to replace or complement conventional materials, such as steel and concrete. The main reasons for the use of composite materials are corrosion resistance, electromagnetic transparency, and weight savings (Barbero, 1998). Corrosion resistance is the most important advantage of composites compared with steel for construction applications. Unlike metals, composite materials do not interfere with electromagnetic radiation. The resin system can be selected to obtain very low loss factors, but standard resin systems are adequate for most structural applications. Buildings for electromagnetic interference (EMI) testing must be nonmagnetic to avoid attenuation and interference, and imaging equipment, such as nuclear magnetic resonance (NMR) units in hospitals must be installed in an environment free of magnetic fields. Pedestrian bridges and towers on a building made of pultruded glass-fiber polyester composites are examples of how to reduce the weight of structures without increasing construction cost.

Therefore, one of the principal functional requirements of composite structures in these areas is to lower the price of products either by reducing manufacturing cost or saving material or realizing very light structures.

In this chapter, several design examples of automotive parts, such as the composite propeller shaft, composite bumper beam, and composite impact beam are presented. Also the trenchless repairing of underground sewage pipes is presented as an application example of composites to infrastructures.

## 15.2 Automotive One-Piece Composite Propeller Shafts with Axial Preload

An automotive propeller shaft, or drive shaft, as shown in figure 15.1, transmits power from the engine to differential gears of a rear-wheel-driving vehicle. The static torque transmission capability of the propeller shaft for passenger cars, and small trucks and vans should be larger than 3500 Nm and the fundamental bending natural frequency of the propeller shaft should be higher than 8000 rpm to avoid whirling vibration. The whirling of the propeller shaft, which is a resonance vibration, occurs when the rotational speed is equal to the fundamental natural bending frequency ( $\omega_1$ ), which is inversely proportional to the square of the length ( $l$ ) of shaft and proportional to the square root of specific stiffness ( $E/\rho$ ).

Since the fundamental bending natural frequency of one-piece propeller shafts made of steel or aluminum cannot be higher than 8000 rpm when the length of the propeller shaft is longer than 1.2 m, due to the limitation of shaft diameter (normally less than 100 mm), the steel propeller shaft is usually manufactured in two pieces. However, the two-piece steel propeller shaft has a complex and heavy configuration because three universal joints and a center support bearing in addition to a spline are required, which produces noise and vibration that are transmitted to vehicles through the center support bearing.

The fundamental bending natural frequency of the carbon-fiber composite propeller shaft can be more than twice that of the steel or aluminum because the specific stiffness of carbon-fiber composite material is more than four times that of the specific stiffness of steel or aluminum (Lee et al., 1991), which makes it possible to manufacture the propeller shaft of passenger cars in one piece (Cho et al., 1997).

The composite propeller shaft has many other benefits such as light weight, and less noise and vibration. However, the composite propeller shaft requires reliable joining of the composite shaft to the steel or aluminum yoke of a universal joint (Schmelz et al., 1992; Reimpell and Stoll, 1996), which is often the most difficult task.

The first composite propeller shaft was developed by the Spicer U-Joint Division of Dana Corporation for the Ford Econoline van models in 1985. The General Motors pickup trucks adopted the Spicer product of the one-piece composite propeller shaft in 1988 (Mallick and Newman, 1990). Three different manufacturing

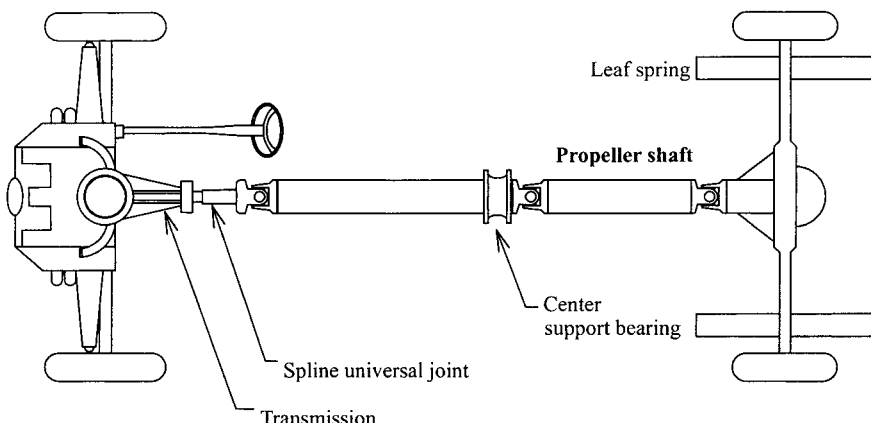


**Figure 15.1** Schematic diagram of the propeller shaft for a rear-wheel-drive vehicle.

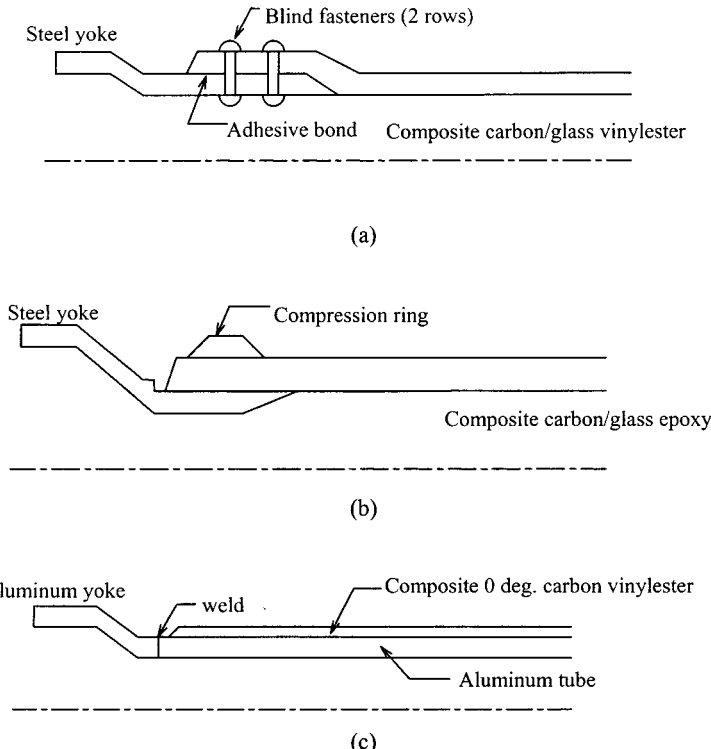


**Figure 15.2** Joining methods between the composite propeller shafts and yokes: (a) Hercules design; (b) Ciba-Geigy design; (c) Dana-MMFG design.

methods for the composite propeller shaft have been developed: Dana-MMFG, Hercules, and Ciba-Geigy methods. Figure 15.2 shows the representative manufacturing methods for the composite propeller shaft. In the Hercules and Ciba-Geigy designs, the filament-wound carbon/glass epoxy or vinylester composite tube is assembled to steel yokes with a blind fastener or a compression ring with adhesive. In the Dana-MMFG manufacturing method, glass fibers are filament-wound in the hoop direction on an aluminum tube and 0° carbon fibers are stacked by pultrusion. Forged aluminum yokes are beam welded to the aluminum tube. For the Dana-MMFG method, there is high tendency that thermal residual stresses will be produced in the aluminum tube and composites.

The co-curing of composite to metal reduces process times (Cho et al., 1997) and enhances damping, which is beneficial property for high-speed rotating machinery. For the damping enhancement of aerospace and military structures subjected to dynamic loading, co-cure joining of one or more layers of high-damping viscoelastic material to the structures has been used (Rao and He, 1993; He and Rao, 1994).

### 15.2.1 Design of the Hybrid Propeller Shaft

The functional requirements of the propeller shaft are

FR<sub>1</sub> = Transmit the required torque (> 3500 Nm)

FR<sub>2</sub> = Increase the fundamental bending natural frequency (> 8000 rpm)

FR<sub>3</sub> = Reduce the weight of the propeller shaft.

Since conventional materials, such as steel or aluminum, have low specific stiffness, as shown in table 2.2, which cannot satisfy the FR<sub>2</sub>, high-specific-modulus composite materials, such as carbon-fiber epoxy composites, should be selected for DP<sub>2</sub>.

Since the competitiveness in the automotive industry is so severe, the cost of a one-piece propeller shaft should not be higher than the conventional two-piece steel propeller shaft. Therefore, the constraint for design may be dictated as

$$C_1 = \text{Cost of the one-piece propeller shaft should not be higher than that of the two-piece propeller shaft.}$$

Although the price of the carbon-fiber epoxy composite is much higher than high-strength steel (about 40 times more expensive), the constraint can be circumvented if the propeller shaft is manufactured in one piece because two universal joints and a center support bearing are eliminated, which lowers the cost and weight of the shaft. The best way to reduce the material cost is to manufacture the hybrid shaft using both carbon-fiber epoxy composite and aluminum, in which the carbon-fiber epoxy composite increases the natural bending frequency and the aluminum satisfies the required torque transmission capability. Then the DPs for satisfying the FRs become

$$DP_1 = \text{Torsional (or shear) strength of aluminum}$$

$$DP_2 = \text{Axial (or longitudinal) specific modulus of carbon-fiber epoxy composite}$$

$$DP_3 = \text{One-piece structure to remove two universal joints and a center support bearing.}$$

Then the design equation reduces to

$$\begin{Bmatrix} FR_1 \\ FR_2 \\ FR_3 \end{Bmatrix} = \begin{bmatrix} X & 0 & 0 \\ 0 & X & X \\ x & 0 & X \end{bmatrix} \begin{Bmatrix} DP_1 \\ DP_2 \\ DP_3 \end{Bmatrix} \quad (15.1)$$

The above design equation can be decoupled if a thin aluminum tube a little larger in diameter than that of a conventional steel propeller shaft is used to transmit the required torque because the center support bearing has a larger diameter than the shaft diameter, as shown in figure 15.1. The aluminum tube with larger diameter can transmit a large torque without increasing the weight significantly because the torque transmitted is proportional to the square of the shaft diameter. This method also eliminates the joining problem between the composite and the metal yoke because the yoke of a universal joint can be welded to the aluminum shaft or joined using a serration or interference fit. Also, a preload can be given to the aluminum shaft before co-curing the composite to the aluminum shaft to reduce the thermal residual stresses between the aluminum tube and the composite shaft.

For the propeller shafts of passenger cars, and small vans and trucks, the minimum values of the torque transmission capability and natural bending frequency are 3500 Nm and 8000 rpm, respectively. Taking into account these requirements, the dimensions of the aluminum tube and the number of stacking plies of the composite were calculated. Since the outer diameter of the propeller shaft is usually less than 100 mm for passenger cars, the outer and inner diameters of the aluminum shaft were

determined to be 74 and 70 mm, respectively. One ply of glass-fiber epoxy fabric was laid-up first on the aluminum tube to eliminate galvanic corrosion between aluminum and carbon fiber, then eight plies of carbon-fiber epoxy preprints with stacking sequence  $[\pm 5]_{4T}$  from the shaft axis were laid-up on the glass epoxy fabric. The carbon-fiber epoxy prepreg was USN150 (see table 2.3). Table 15.1 shows the specification of the composite propeller shaft and table 15.2 shows the mechanical properties of the aluminum tube (6061-T6).

For the high natural bending frequency of the shaft, the stacking angle of the fiber from the shaft axis should be small. The stacking sequence  $[\pm 5]_{4T}$  was employed because the transverse tensile strength of the composite with the stacking sequence  $[0]_{8T}$  was too low. Table 15.3 shows the laminate properties calculated by the classical lamination theory in chapter 4.

**Table 15.1 Specifications of the Composite Propeller Shaft**

Shaft length	1.35 m
Thickness of composite	1.2 mm
Ply thickness	0.15 mm
Stacking sequence	$[\pm 5]_{4T}$
Inner diameter of aluminum	70.0 mm
Outer diameter of aluminum	74.0 mm

**Table 15.2 Properties of the Aluminum Tube (6061-T6)**

$E$	72 GPa
$G$	27 GPa
$\alpha_T$	$23.0 \times 10^{-6}/^\circ\text{C}$
$\rho$	2695 kg/m <sup>3</sup>
Tensile strength	350 MPa
Yield strength	325 MPa
Shear strength	210 MPa

**Table 15.3 Laminate Properties of the Carbon-fiber Epoxy Prepreg**

Stacking sequence	$[\pm 5]_{4T}$
$E_x$	128.7 GPa
$E_y$	10.8 GPa
$G_{xy}$	6.51 GPa
$\alpha_x$	$-1.06 \times 10^{-6}/^\circ\text{C}$
$\alpha_y$	$26.7 \times 10^{-6}/^\circ\text{C}$
$\alpha_{xy}$	0

The torque transmission capability of the hybrid propeller shaft was calculated using the following equations:

$$T = T_{al} + T_{co} \quad (15.2)$$

$$T_{al} = \frac{G_{al}J_{al}}{G_{al}J_{al} + G_{co}J_{co}} T = \frac{\tau_y J_{al}}{r_o} \quad (15.3)$$

where  $T$ ,  $T_{al}$ , and  $T_{co}$  are the torque transmitted by the hybrid shaft, the aluminum shaft, and the composite shaft, respectively, and  $G$  represents shear modulus,  $J$  second moment of inertia,  $\tau_y$  the shear strength of aluminum, and  $r_o$  the outer radius of the aluminum shaft. When the thickness of the carbon-fiber epoxy composite was 1.2 mm and the outer and inner diameters of the aluminum shaft were 74 and 70 mm, respectively, the calculated torque capability was 3770 Nm, which was larger than 3500 Nm.

The first bending natural frequency  $\omega_1$  of the hybrid propeller shaft was calculated using the following equation with simply supported boundary conditions (see problem 9.9):

$$\omega_1 = \frac{9.87}{2\pi l^2} \sqrt{\frac{E_{al}I_{al} + E_{co}I_{co}}{m_{al} + m_{co}}} \text{ (Hz)} \quad (15.4)$$

where  $l$  is the length of the shaft,  $E$  the Young's modulus,  $I$  the mass moment of inertia, and  $m$  the mass per unit length. When the length of the shaft was 1.35 m, the calculated fundamental bending natural frequency of the shaft was 9055 rpm.

### 15.2.2 Method of Eliminating the Fabricational Thermal Residual Stresses

The thermal residual stresses are induced at the interface between the composites and the aluminum of the hybrid propeller shaft during the co-curing operation due to the large difference in the coefficient of thermal expansion (CTE). The aluminum tube expands as the temperature rises to the curing temperature of 120°C without constraint by the composites. After co-curing composites to the aluminum tube, the hybrid propeller shaft was cooled down to the room temperature of 20°C. Since the CTE of the composite shaft in the axial direction is near zero when the stacking angle of the composite is less than 15° from the axis of the shaft, the tensile stress in the axial direction occurs in the aluminum shaft and the axial compressive stress occurs in the carbon-fiber composite when the shaft is cooled down.

When the stacking angle of composites was  $[\pm 5]_{4T}$ , the calculated thermal residual stresses, using the method of solid mechanics, were 62.46 MPa and -79.42 MPa in the aluminum tube and the composite, respectively. The residual thermal stresses were calculated on the assumption that the hoop stress components in the co-cured shaft were not produced because the difference of the CTEs of the two materials in the hoop direction was small. However, a large shear stress in the axial direction occurs at the interface of the two materials due to the large difference of the CTEs of the two materials. This large shear stress at the interface of the hybrid shaft lowers the torque transmission capability of the shaft.

To reduce the thermal residual stresses produced at the interface of the two materials of the hybrid shaft during the co-curing operation, a compressive preload

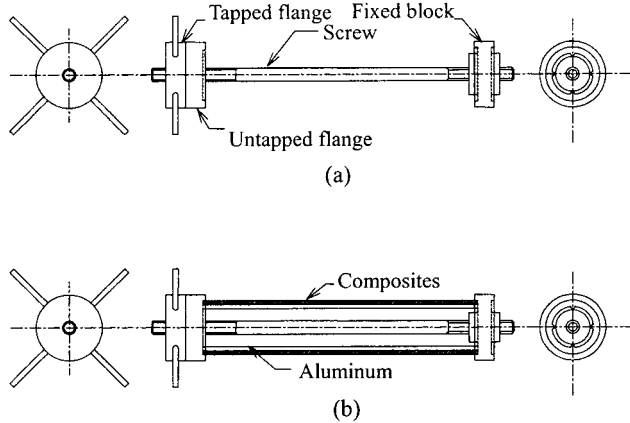


**Figure 15.3** Compressive jig:  
(a) Schematic diagram;  
(b) hybrid propeller shaft compressed by the jig (from Cho et al., 1997).

was applied to the aluminum tube before the co-curing operation. To apply a compressive preload to the aluminum tube, a compressive jig similar to a vise was used. Figure 15.3 shows the compressive jig, which is composed of a steel screw of 1 mm pitch thread, a fixed block, an untapped flange, and a tapped flange with a thrust bearing.

The method for eliminating the thermal residual stresses in the hybrid propeller shaft by applying a preload is described by the following four steps. In the first step, the carbon-fiber epoxy prepreg was laid-up on the surface of the preloaded aluminum tube. In the second step, the composite was co-cured on the surface of the preloaded aluminum tube. In the third step, the co-cured shaft was cooled down to the room temperature of 20°C without removing the preload in the aluminum tube. In the fourth step, the preload by the compressive jig was removed, then the thermal residual stresses in the composite and the aluminum tube were eliminated.

The applied compressive displacement was calculated by the following method, considering the axial stress component ( $\sigma_z$ ). If the displacements of the aluminum tube and the jig, both of length  $l$ , are  $\delta_a$  and  $\delta_j$ , respectively, then the total displacement  $\delta$  produced by the rotation of the tapped flange in the compressive jig is  $\delta = \delta_a + \delta_j$ , as shown in figure 15.4. Therefore, the total displacement  $\delta$  can be expressed as

$$\frac{\delta}{l} = \frac{\delta_j}{l} + \frac{\delta_a}{l} = \varepsilon_j - \varepsilon_a = \frac{\sigma_j}{E_j} - \frac{\sigma_a}{E_a} \quad (15.5)$$

where  $\varepsilon_j$  and  $\varepsilon_a$  are the axial strains of the jig and the aluminum tube, respectively,  $\sigma_j$  and  $\sigma_a$  the axial stresses of the jig and the aluminum tube, respectively, and  $E_j$  and  $E_a$  the Young's moduli of the jig and the aluminum tube, respectively.

From the force equilibrium between the aluminum tube and the jig, the following equation holds:

$$A_a \sigma_a + A_j \sigma_j = 0 \quad (15.6)$$

where  $A_a$  and  $A_j$  are the cross-sectional areas of the aluminum tube and the jig, respectively.

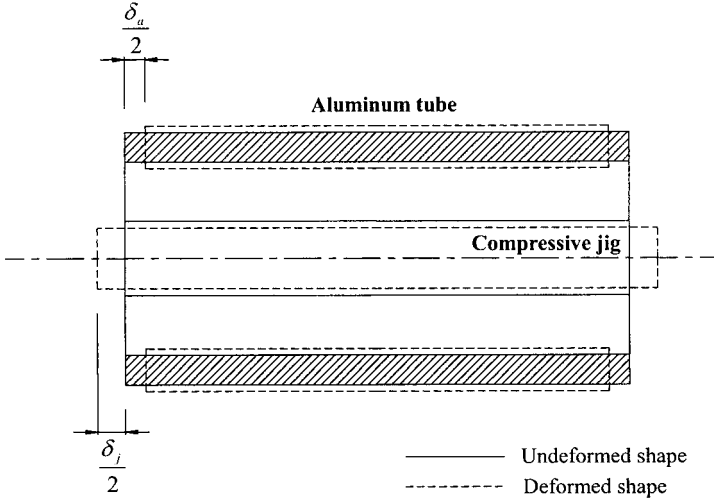


**Figure 15.4** Total compressive displacement ( $\delta$ ) of jig composed of  $\delta_a$  and  $\delta_j$  (from Cho et al., 1997).

Using equations (15.5) and (15.6), the tensile stress in the jig and the compressive stress in the aluminum tube in the first step can be calculated in terms of  $\delta$ :

$$\sigma_j|_1 = \frac{E_j E_a A_a}{E_j A_j + E_a A_a} \frac{\delta}{l} \quad (15.7)$$

$$\sigma_a|_1 = -\frac{E_j E_a A_j}{E_j A_j + E_a A_a} \frac{\delta}{l} \quad (15.8)$$

In the second step, the jig and the aluminum tube expand the same amount due to the temperature increase  $\Delta T$ . Then, the strain–temperature relationship can be written as

$$\frac{\sigma_a}{E_a} + \alpha_a \Delta T = \frac{\sigma_j}{E_j} + \alpha_j \Delta T \quad (15.9)$$

Using equations (15.6) and (15.9), the axial stresses in the jig and the aluminum tube in the second step can be calculated:

$$\sigma_j|_2 = (\alpha_a - \alpha_j) \Delta T \frac{E_j E_a A_a}{E_j A_j + E_a A_a} \quad (15.10)$$

$$\sigma_a|_2 = -(\alpha_a - \alpha_j) \Delta T \frac{E_j E_a A_j}{E_j A_j + E_a A_a} \quad (15.11)$$

In the third step, the jig, the aluminum tube, and the composite are cooled down to the room temperature ( $-\Delta T$ ). Therefore, the force equilibrium among the three materials is

$$\sigma_a A_a + \sigma_j A_j + \sigma_c A_c = 0 \quad (15.12)$$

where  $\sigma_c$  and  $A_c$  are the axial stress and the area of the composite, respectively.

In the third step, the length changes or strains of the three materials are same:

$$\frac{\sigma_a}{E_a} - \alpha_a \Delta T = \frac{\sigma_j}{E_j} - \alpha_j \Delta T = \frac{\sigma_c}{E_c} - \alpha_c \Delta T \quad (15.13)$$

From equations (15.12) and (15.13), the axial stresses in the three materials were calculated:

$$\sigma_a|_3 = \left( \alpha_a - \frac{E_a A_a \alpha_a + E_j A_j \alpha_j + E_c A_c \alpha_c}{E_a A_a + E_j A_j + E_c A_c} \right) E_a \Delta T \quad (15.14)$$

$$\sigma_j|_3 = \left( \alpha_j - \frac{E_a A_a \alpha_a + E_j A_j \alpha_j + E_c A_c \alpha_c}{E_a A_a + E_j A_j + E_c A_c} \right) E_j \Delta T \quad (15.15)$$

$$\sigma_c|_3 = \left( \alpha_c - \frac{E_a A_a \alpha_a + E_j A_j \alpha_j + E_c A_c \alpha_c}{E_a A_a + E_j A_j + E_c A_c} \right) E_c \Delta T \quad (15.16)$$

Finally, in the fourth step, the preload by the compressive jig is released. When the jig is removed, it is assumed that the preload of the compressive jig is transferred to the composites and the aluminum tube. Therefore, in the fourth step the following equations hold:

$$\sigma_j A_j = \sigma_a A_a + \sigma_c A_c \quad (15.17)$$

$$\frac{\sigma_a}{E_a} = \frac{\sigma_c}{E_c} \quad (15.18)$$

From equations (15.17) and (15.18), the axial stresses were calculated:

$$\sigma_a|_4 = \frac{E_a}{E_a A_a + E_c A_c} A_j \sigma_j|_4 \quad (15.19)$$

$$\sigma_c|_4 = \frac{E_c}{E_a A_a + E_c A_c} A_j \sigma_j|_4 \quad (15.20)$$

where

$$\sigma_j|_4 = \sigma_j|_1 + \sigma_j|_2 + \sigma_j|_3 \quad (15.21)$$

Then the final stresses in the aluminum tube and composites are the sums of the stresses calculated in the previous steps:

$$\sigma_a|_{\text{final}} = \sigma_a|_1 + \sigma_a|_2 + \sigma_a|_3 + \sigma_a|_4 \quad (15.22)$$

$$\sigma_c|_{\text{final}} = \sigma_c|_3 + \sigma_c|_4 \quad (15.23)$$

Using the above equations, the thermal residual stress distributions when the stacking angle of composites was  $[\pm 5]_{4T}$  were calculated with respect to the compressive displacement ( $\delta$ ), as shown in figure 15.5. The thermal residual stresses in the aluminum and the composite were almost zero when the compressive

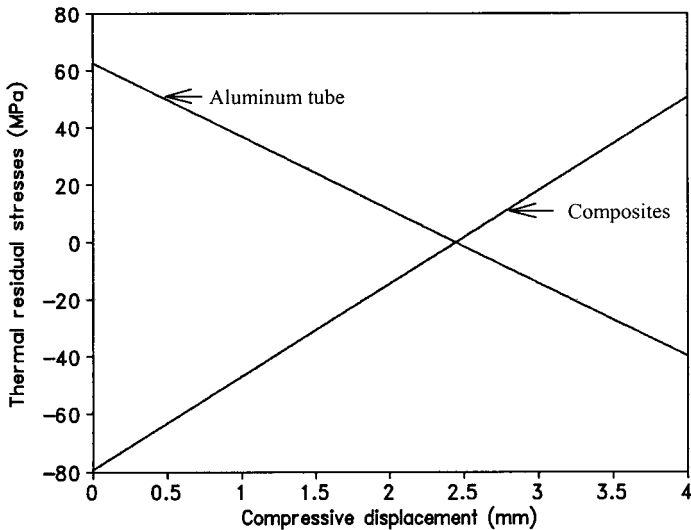


**Figure 15.5** Compressive displacement vs. thermal residual stresses in the co-cured propeller shaft, from Cho et al. (1997).

**Table 15.4 Stresses in the Four Steps of Co-curing with the Stacking Angle  $[\pm 5]_{4T}$  of the Composite**

Step	Temperature ( $^{\circ}\text{C}$ )	$\sigma_a$ (MPa)	$\sigma_c$ (MPa)	$\sigma_j$ (MPa)
1	20	-106.66	—	68.26
2	120	-173.21	—	130.38
3	20	-84.84	-152.39	112.95
Final	20	0.01	-0.02	—

displacement  $\delta$  of the jig was 2.445 mm, in which the compressive displacement  $\delta_a$  of the aluminum tube was 2.0 mm and the tensile displacement  $\delta_j$  of the jig was 0.445 mm. Table 15.4 shows the stresses and temperatures of each loading step in the hybrid shaft when the compressive displacement of the aluminum tube was 2.0 mm. In table 15.4, a very small tensile stress of 0.01 MPa in the aluminum tube and very small compressive stress of -0.02 MPa in the composite were produced in the final stage.

### 15.2.3 Manufacture of the Hybrid Joint

The hybrid propeller shaft consists of the co-cured shaft and the two yokes. The inner-serrated aluminum bushes were welded at both ends of the aluminum tube, as shown in figure 15.6. The steel yoke consists of the outer-serrated part, a universal joint, and a spline universal joint. Figure 15.7 shows a photograph of the inner and outer serrations with 90 teeth. The inner serration was formed with a slotting machine and the outer serration was machined with a hobbing machine.

The hybrid propeller shaft was manufactured by co-curing after wrapping one glass-fabric prepreg and eight carbon-fiber epoxy preps on the surface-treated aluminum tube with a predetermined preload. The outer-serrated part of the universal

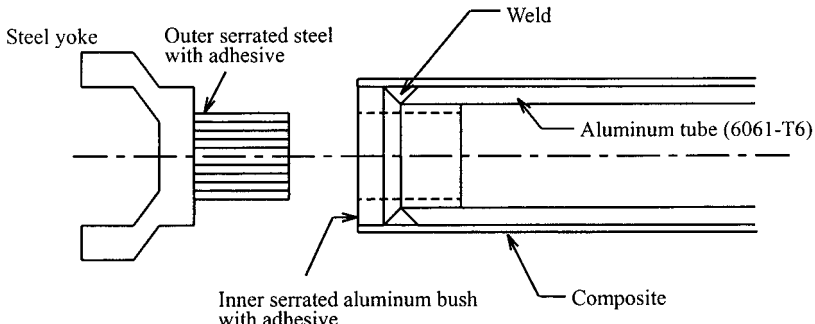


**Figure 15.6** Joining method of the steel yoke to the hybrid shaft using serrations.



**Figure 15.7** Photograph of the inner serratation and the outer serratation.

joint was assembled with an interference fit into the inner-serrated part of the hybrid propeller shaft. Figure 15.8 shows a photograph of the manufactured conventional two-piece steel propeller shaft and the one-piece hybrid propeller shaft. The hybrid propeller shaft was 50% lighter than the steel propeller shaft.

#### 15.2.4 Experimental Results

The vibration characteristics of the hybrid propeller shaft were measured by an impulse-frequency response test using a fast Fourier transform analyzer. The fundamental natural bending frequency was 9100 rpm and the error between the measured value and the calculated value (9055 rpm) was about 0.5%. The damping ratio was 0.01, which was about seven times larger than that of the steel propeller shaft.

From the static torque test, the average torque transmission capability of the four test specimens was 3600 Nm with a maximum and minimum torque transmission capability of 3650 and 3550 Nm, respectively. All the fractures of the hybrid propeller shafts occurred at the circumferential weld line between the aluminum tube and the inner-serrated bush, rather than the composite shaft.

A dynamic torque test of the prototype hybrid propeller shaft was performed and it was found that the hybrid propeller shaft did not fail until  $10^7$  cycles under a dynamic torque of  $\pm 500$  Nm.

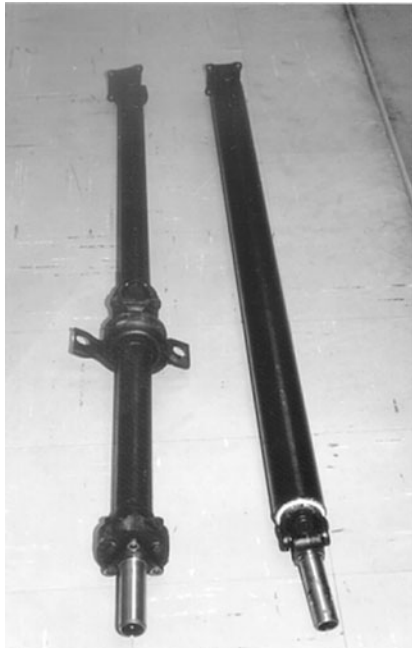


**Figure 15.8** Photograph of the two-piece steel propeller shaft and the one-piece hybrid propeller shaft manufactured (from Cho et al., 1997).

### 15.3 Design of Composite Bumper Beams for Passenger Cars

Since a head-on crash in a passenger car is the cause of most fatalities among traffic accidents, much effort has been made to reduce injury from such crashes using air bags and energy-absorbing bumpers (Cheon et al., 1995). Recently, in order to reduce the weight of cars and increase energy absorption capacity, most passenger cars employ engineering plastics bumpers that are usually made of polypropylene or polycarbonate/PBT alloy. Also reinforced plastics bumper beams made by compression molding with sheet molding compound (SMC), resin transfer molding (RTM), and reaction injection molding (RIM) have been successfully applied (Margolis, 1986).

Although the role of the bumper is to absorb the collision energy, it usually only satisfies the 5 miles/h collision regulation and the impact energy is not absorbed sufficiently at higher speeds. If the car collides with a speed higher than 5 miles/h, the bumper bracket, engine, and other parts of the car absorb the impact energy of the car through collapsing. In this case, deceleration of passengers usually becomes large because the bumper brackets and other parts of the car cannot absorb effectively the large impact energy of car compared with that of bumper beam. Therefore, bumper beams when installed inside bumper fascias absorb more impact energy (Schmueser and Wickliffe, 1987).

The weight of cars can be reduced significantly and also impact characteristics can be improved if car structures are manufactured using polymeric matrix fiber-reinforced composite materials, since they have high specific stiffness ( $E/\rho$ ), specific strength ( $S/\rho$ ), and damping characteristics, as discussed in chapter 2. Therefore, a hybrid composite bumper beam made of glass-fiber epoxy composite and carbon-fiber epoxy composite may increase the energy absorption capability of the bumper beam during a head-on crash (see discussion in section 10.2.8).

Also, steel pads attached to the ends of the bumper beam were tried in order to increase energy absorption capacity through collapsing the front two tires of cars, and two tapered beams attached to the ends of the bumper beam were also tried in order to increase the energy absorption capacity by the progressive failure of the tapered beams during collision.

### 15.3.1 Design of Hybrid Composite Bumper Beams

The two functional requirements of the bumper beam may be

$FR_1$  = Endure up to a speed of 5 miles/h without damage to the bumper.

$FR_2$  = Increase the impact energy absorption during collision of automobile.

Two DPs for satisfying these FRs may be stated as

$DP_1$  = Static strength of the bumper

$DP_2$  = Impact energy absorption mechanism (steel pads and tapered-end beams of bumper).

Since the competitiveness in the automotive industry is so severe, the cost of the composite bumper beam with extra impact energy absorption mechanism should not be much higher than the conventional plastics bumper beam. Also, the weight of the bumper should not be increased much due to the strict regulation of fuel efficiency in future. Therefore, the constraints for design may be expressed as

$C_1$  = Cost of the bumper beam

$C_2$  = Weight of the bumper.

Since the configuration of a bumper is limited by the size of a car, we have little freedom to change the shape of the bumper to increase its static strength. The only way to fulfill the  $FR_1$  through  $DP_1$  is to use fiber-reinforced composite materials without violating the constraint  $C_2$  because conventional materials, such as steel or aluminum, have low specific strength, as shown in tables 2.2 and 2.3. Then the following design equation may represent the bumper beam made of composite materials:

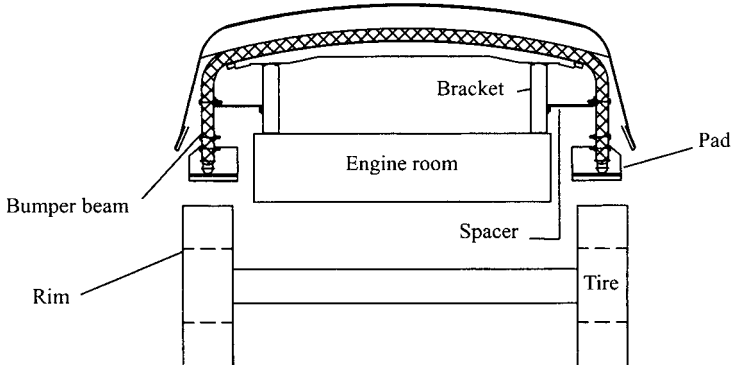
$$\left\{ \begin{array}{l} \text{Static strength} \\ \text{Impact energy} \end{array} \right\} = \begin{bmatrix} X & 0 \\ x & X \end{bmatrix} \left\{ \begin{array}{l} \text{Composite material} \\ \text{Absorption mechanism} \end{array} \right\}$$

The above design equation is decoupled by employing composite materials with high specific strength and high-impact energy absorption mechanism of the bumper.

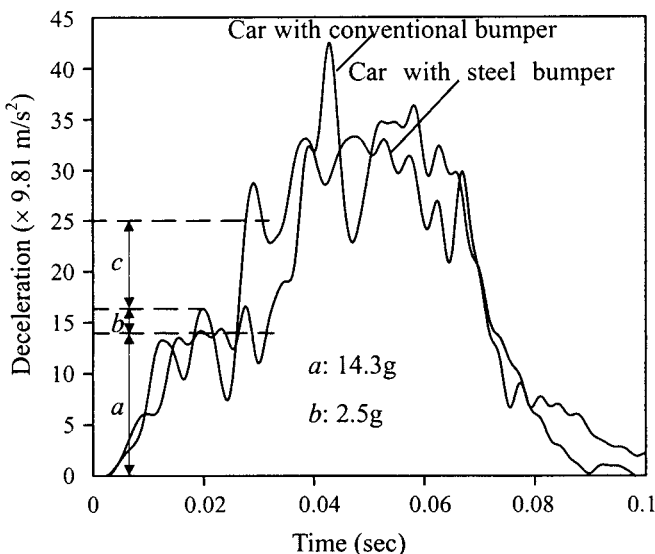
### 15.3.2 Head-On Crash Test of Steel Bumper Beams

Figure 15.9 shows the configuration of a bumper beam that has two pads at the ends of the beam (Cheon et al., 1995). The two pads ( $DP_2$ ) were employed in order to absorb energy through collapsing the front tires and tire rims during collision.

To investigate the effect of bumper bending stiffness on the deceleration characteristics of a car during collision, three circular steel tubes whose ultimate tensile strength and strain are 240 MPa and 0.23, respectively, were bent into the bumper shape and connected in parallel by welding. The welded tubular steel bumper beam composed of three tubes was installed inside the bumper fascia made of



**Figure 15.9** Configuration of the bumper beam with the two pads (from Cheon et al., 1995).



**Figure 15.10** Deceleration curves of the cars during collision (from Cheon et al., 1995).

polypropylene. The gap between the steel bumper beam and the bumper fascia was filled with polyurethane foam. The mass of the manufactured steel bumper beam was 20 kg. The collision test was performed using a subcompact passenger car of 9500 kg mass. In order to compare the energy absorption characteristics of the steel bumper beam, a car of the same model with the conventional bumper without the steel bumper beam was also tested. In order to make the weights of the two cars the same, a sandbag weighing 200 N was added to the car with the conventional bumper.

The deceleration signals from the left and right sides of the lower part of the B-pillar and the left and right sides of the engine room were obtained using accelerometers during collision. Figure 15.10 shows the magnitude of the deceleration of the cars with the conventional and the steel bumper beam during a head-on collision at 30 miles/h.

In figure 15.10, the magnitude of the deceleration of the car with the steel bumper was larger than that of the car with the conventional bumper during the initial

collision period because the front tires imposed force on the pads of the steel bumper beam (deflection  $b$ ). However, the energy absorption due to tire collapsing was not large. After the collapsing the steel pads, the magnitude of the maximum deceleration of the car with the steel bumper beam was smaller than that of the car with the conventional bumper: the magnitude of the maximum deceleration of the car with the steel bumper beam was  $33g$  ( $g$ =gravitational acceleration), while that of the car with the conventional bumper was  $43g$ . Furthermore, the steel bumper beam absorbed 23% more impact energy than the conventional bumper. Therefore, it was concluded that the steel bumper beam had better energy absorption characteristics, based on the head injury criteria. Although the energy absorption characteristics of the steel bumper beam were good, the 200 N weight increase was not desirable. Therefore, it was determined to design and manufacture the composite bumper beam using glass-fiber epoxy composite for the section that requires strength and carbon-fiber epoxy composite for the section that requires stiffness.

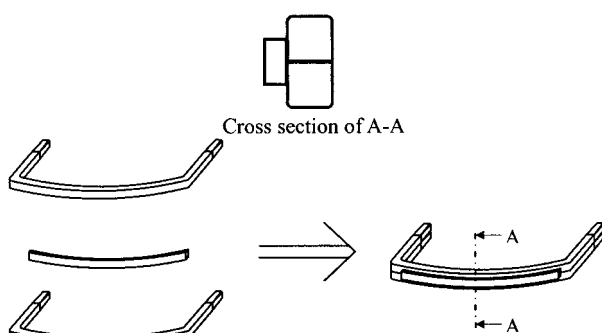
### 15.3.3 Design of the Composite Bumper Beam

Table 15.5 shows the properties of the two composites used in the composite beams.

The box-type cross-section of the composite bumper beam was employed because it gives high bending stiffness compared with the tubular shape. Since there was space limitation in the bumper fascia, the outside dimension of the beam was fixed to be  $40\text{ mm} \times 40\text{ mm}$ . The two main bumper beams and another small beam whose cross-section was  $20\text{ mm} \times 40\text{ mm}$  were adhesively bonded, as shown in figure 15.11. The small bumper beam was employed for the initial energy absorption during collision. Based on the force boundary conditions calculated from the

**Table 15.5 Properties of Composites**

Prepreg	Tensile modulus $E_l$ (GPa)	Tensile strength $X^t$ (GPa)	Ply thickness (mm)
Fabric glass fiber epoxy	36	0.680	0.18
Unidirectional carbon fiber epoxy	131	2.0	0.15



**Figure 15.11** Configuration of the composite bumper beam.

deceleration curves of figure 15.10, the thicknesses of the cross-section of the composite bumper beam were determined by the finite element method.

#### *Load Analysis During Collision*

The collision analysis (Lal, 1983) for the composite bumper beam is only possible if the impact characteristics of all the structures of cars are known and the mechanical properties and impact characteristics (Sun and Chattopadhyay, 1975) of the composites are previously determined, which is a difficult task. Therefore, the force boundary conditions obtained using deceleration graphs of the car with the steel bumper beam during the head-on crash test were used in the design of the composite bumper. The strength and stiffness analyses were performed using commercial finite element method (FEM) software, ANSYS. In the analysis, 225 elastic beam elements were used and only half of the bumper beam was analyzed due to the symmetry.

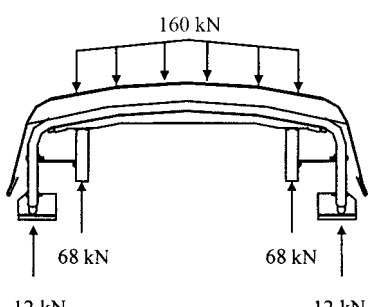
The analysis was performed in two steps whose boundaries were determined by the time at which the pads of the bumper touched the rims of the front two wheels, and after collapse of the two tires.

#### (a) FIRST STEP

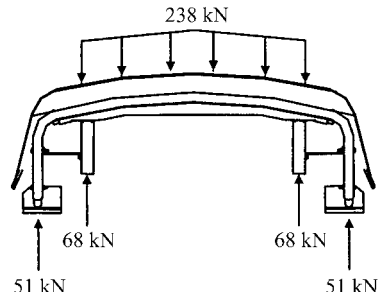
The deceleration  $a$  in figure 15.10 was originated from the load of 136 kN acting on the brackets (68 kN per bracket), and  $b$  from the load acting on the front two tires (24 kN) before collapse of the tires.

Figure 15.12 shows the force boundary conditions of the bumper beam at the first step. From FEM analysis, the maximum stress of the bumper was found to be 560 MPa at the center of the bumper beam when the thicknesses of the main bumper beam and the small bumper beam were 5.4 mm and 1.44 mm, respectively, which was obtained in the second step.

During the first step, the transverse displacement should be small because the pads would miss the front tires if the displacement were large. Since the width of the tire employed was 175 mm, it was determined that the maximum displacement should be smaller than the half of the width (87.5 mm). The analysis performed by FEM showed that the side displacement of the end of the bumper was 84 mm when the 160 kN load was applied to the bumper beam. Since the total transverse displacement was less than 87.5 mm, the dimensions of the bumper determined were used in the manufacture of the composite bumper beam. Since the steel spacer was neglected in the analysis, the actual displacement will be smaller than the calculated value.



**Figure 15.12** External loads and reaction forces at the first step (from Cheon et al., 1995).



**Figure 15.13** External loads and reaction forces at the second step (from Cheon et al., 1995).

#### (b) SECOND STEP

During the second step, the pads located at the ends of the bumper beam were resisted by the rims of the wheels after collapse of the tires. The total load on the bumper beam was 238 kN because the load resisted by the brackets was 136 kN ( $a$  in figure 15.10) and the load resisted by the rims of the wheels was 102 kN ( $c$  in figure 15.10; the upper value of  $c$  was selected to be 25g in order to decrease the magnitude of maximum deceleration for the composite bumper beam). Figure 15.13 shows the force boundary conditions on the bumper beam at the second step.

When the thickness of the glass-fabric epoxy composite was 5.4 mm (30 plies), the analysis by FEM showed that the maximum stress at the center of the bumper beam was 675 MPa. Since the tensile strength of the glass-fabric epoxy materials was 680 MPa, the thickness of the cross-section of the composite bumper beam was determined to be 5.4 mm. Then, the thickness of the smaller composite beam located at the front side of the two main bumper beams for the initial energy absorption was determined to be 1.44 mm (8 plies), which is much weaker than the two main bumper beams.

#### *Buckling Test of the Tapered Ends of the Bumper Beam*

If the tapered ends of the bumper beam ( $DP_2$ ) collapse progressively during collision, the energy absorption capability of the bumper beam can be improved (Thornton and Jeryan, 1988). For the design of the tapered end of the bumper beam, the starting and end thicknesses and slope of the taper must be determined. The buckling analysis of isotropic materials, such as steel, can be performed by FEM analysis; however, the buckling analysis of anisotropic materials, such as composite materials, is not easy (Chen and Sun, 1985). Therefore, FEM analysis with three-dimensional eight node isoparametric elements was used only for the determination of the starting thickness and end thickness of the taper. The slopes of the taper were determined by compression tests. From the analytical and experimental results, the starting and end thicknesses of the taper for progressive buckling of the ends during collision were determined to be 1.44 mm (eight plies) and 0.9 mm (five plies), respectively. Figure 15.14 shows the configuration of the tapered end of the composite bumper.

When the slope of the taper was small, cracking rather than buckling would initiate (Williams, 1988). However, the energy absorption would be small if the slope was large. Therefore, the slope of the taper was determined by the compression tests of the specimens representing the end of the composite bumper beam.

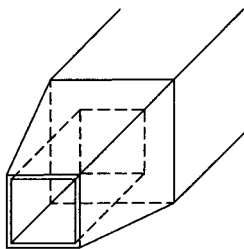


**Figure 15.14** Configuration of the tapered end of the composite bumper (from Cheon et al., 1995).

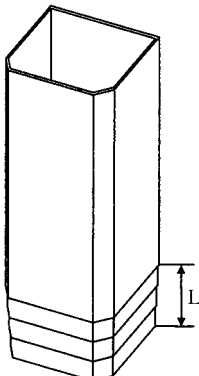


**Figure 15.15** Tapered end specimen for the composite bumper beam (from Cheon et al., 1995).

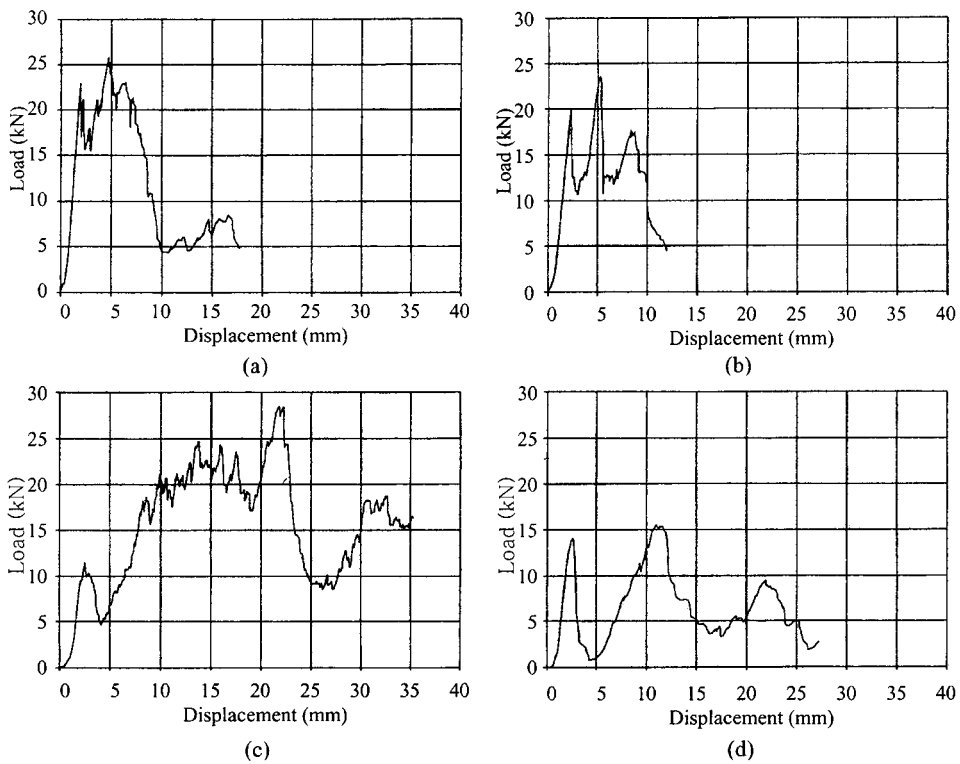
The specimens, which had four different tapered lengths ( $L = 5, 10, 20$ , and  $30\text{ mm}$ ) were tested. Figure 15.15 shows the tapered end specimen for the composite bumper beam. Tests were performed by an Instron machine with the test speed of  $2\text{ mm/min}$ .

Figure 15.16 shows the compression test results of the specimens of figure 15.15. From the tests, it was found that when  $L$  was  $30\text{ mm}$ , cracking initiated through the lengthwise direction rather than progressive buckling. When  $L$  was  $5, 10$ , and  $20\text{ mm}$ , it was found that progressive buckling of the specimens occurred. Since the energy absorption capacity of the specimen with  $L = 20\text{ mm}$  was largest, this value, which gives the slope  $20\text{ mm}/3\text{ plies}$  was employed in the design of the composite bumper beam.

#### 15.3.4 Manufacture of the Composite Bumper Beam

The composite beam may be manufactured using a pull-forming process, which is a variation of the pultrusion process in which both curved and straight product sections are fabricated with the ability to change cross-sectional dimensions of the product (Wilson, 1998). The pull-forming process can be thought of as a combination of pultrusion and compression molding. Since this development is only for the prototype, the composite bumper beams were manufactured using an internal separable mold made of stainless-steel plates. Figure 15.17 shows a schematic diagram of the mold.

Figure 15.17(a) represents the main frame of the mold, composed of four plates. The four plates were assembled with high-strength bolts and nuts, whose strength could resist  $0.7\text{ MPa}$  internal air pressure during the manufacturing process. Figure 15.17(b) and figure 15.17(c) represent the end cap and the air seal with an



**Figure 15.16** Compression test results of the tapered specimens of figure 15.15: (a)  $L = 5\text{ mm}$ ; (b)  $L = 10\text{ mm}$ ; (c)  $L = 20\text{ mm}$ ; (d)  $L = 30\text{ mm}$  (from Cheon et al., 1995).

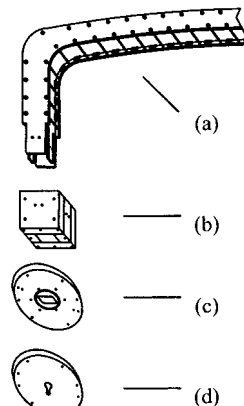
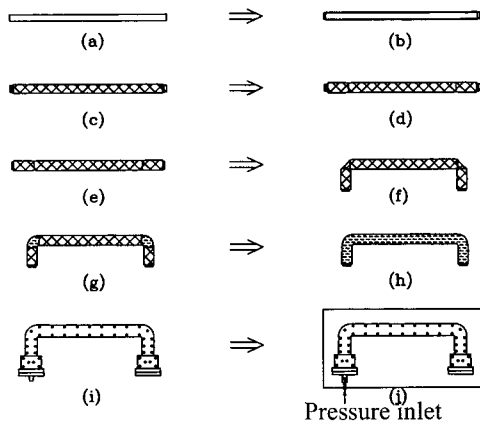


**Figure 15.17** Schematic diagram of the mold (from Cheon et al., 1995).

o-ring, respectively. Figure 15.17(d) is the plate with a small tube for a quick coupler for the air supply.

Glass-fabric epoxy prepreg and unidirectional carbon-fiber prepreg were used in the manufacture of the composite bumper beam. Figure 15.18 shows the manufacturing sequence of the composite bumper beam.

The stainless-steel mandrel shown in figure 15.18(a) was wrapped with a vacuum bag and a nonporous Teflon sheet, as shown in figure 15.18(b). During the manufacturing process, fiber folding occurred at the elbow section of the composite



☒ Glass fiber fabric epoxy prepreg  
 ☐ Uni-directional carbon fiber epoxy prepreg

**Figure 15.18** Manufacturing sequence of the composite bumper beam (from Cheon et al., 1995).

bumper beam when the entire part of the bumper beam was manufactured with glass-fabric epoxy prepreg. Therefore, after stacking eight-ply glass fabric on the whole length of the mandrel as shown in figure 15.18(c), 22-ply glass-fabric epoxy prepreg was stacked, except the elbow section, as shown in figure 15.18(d). After removing the stainless-steel mandrel, as shown in figure 15.18(e), the elbow section was bent, as shown in figure 15.18(f). At the elbow section, 20-ply unidirectional carbon-fiber epoxy prepreg was stacked as shown in figure 15.18(g). Then three-ply unidirectional carbon-fiber epoxy prepreg was stacked on the whole length of the bumper beam in order to increase the bending strength of the bumper beam, as shown in figure 15.18(h). The prepreg covered with nonporous Teflon tape was put into the mold, which was treated with mold release. Then the mold was assembled using the end caps and the sealing plates, as shown in figure 15.18(i). After placing the charged mold inside the heating chamber of Figure 15.18(j), 0.7 MPa air pressure was supplied inside the mold. The temperature of the heating chamber was monitored by thermocouples and controlled by a temperature controller. Figure 15.19 shows the prototype composite bumper beam manufactured with this method.

The composite bumper beam was composed of three parts, as shown in figure 15.19. The three parts were adhesively bonded using structural adhesives. The total mass of the composite bumper beam was 5.5 kg, which was only 27.5% of the steel bumper beam, whose mass was 20 kg.

The tapered section of the end of the composite bumper beam was made by a grinding process and the two pads were attached to the end of the beams using structural adhesive. Figure 15.20 shows a photograph of the composite bumper beam with pads and the bumper fascia.

Polyurethane foam was inserted between the bumper beam and the bumper fascia to distribute the impact load and increase the energy absorption during collision.

When the composite bumper was tested in a head-on collision test, the value of  $c$  in figure 15.10 was about 25g ( $g = 9.8 \text{ m/s}^2$ ), and other regions were almost same as the steel bumper beam. Since the composite bumper beam eliminated the peak in the deceleration curve and had only 27.5% of the mass of the steel bumper beam, it may be useful in future automotive applications.



**Figure 15.19** Photograph of the prototype composite bumper beam (from Cheon et al., 1995).

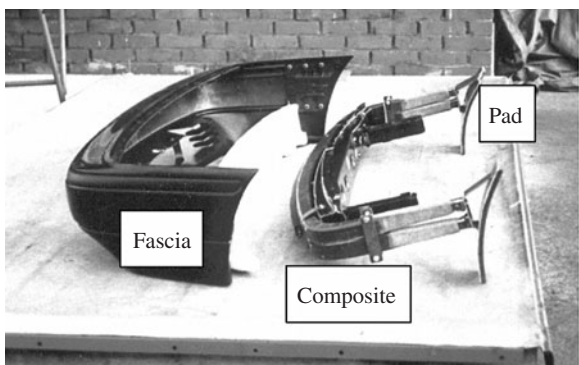


**Figure 15.20** Photograph of the composite bumper with pads and the bumper fascia (from Cheon et al., 1995).

#### 15.4 Composite Side-Door Impact Beams for Passenger Cars

While the composite bumper in the previous section is used to absorb the energy during a head-on collision, side-door impact beams are mounted on the door panels of passenger cars to guarantee passengers' safety from side-impact damage. The two functional requirements of impact beams are to have large static strength without increasing the weight of beam (i.e., high specific strength) and high-impact energy absorption capability. These two properties are seldom possessed simultaneously by conventional metals because metals with high strength usually have low toughness and vice versa. To meet the high strength and high toughness properties of the impact beams of passenger cars, conventional impact beams are made of high-strength alloy steel with several heat-treatment processes. However, the steel impact beams increase the weight of the car and the heat-treated steel impact beam usually has a low nil-ductility temperature.

These days, the weight reduction of cars is of great concern due to the international movement to regulate fuel efficiency and emission gases of passenger cars. The best way to increase both the static strength and impact absorption characteristics without increasing the structural weight of the impact beam is to

employ composite materials because fiber-reinforced composite materials have very high specific strength and can possess energy-absorbing capability through the design of an energy absorption mechanism. Also, they can be mass-produced by employing an automated manufacturing process, such as pultrusion, to meet the production rate of one part per minute for passenger cars.

#### 15.4.1 Design of Composite Impact Beams

The two functional requirements of the side-door impact beam may be

$FR_1$  = Increase the specific strength of impact beam

$FR_2$  = Increase the bending impact energy absorption during the side collision of passenger cars.

Two DPs for satisfying these FRs may be stated as

$DP_1$  = Fiber stacking sequences

$DP_2$  = Impact energy absorption joints.

Since the competitiveness in the automotive industry is so severe, the cost of the composite impact beam with joints for energy absorption mechanism should not be much higher than the conventional high-strength steel impact beam. Therefore the constraint for design may be dictated as

$C_1$  = Minimize the cost of the bumper beam.

The design equation for the impact beam may be written as

$$\begin{Bmatrix} FR_1 \\ FR_2 \end{Bmatrix} = \begin{bmatrix} X & 0 \\ x & 0 \end{bmatrix} \begin{Bmatrix} DP_1 \\ DP_2 \end{Bmatrix} \quad (15.24)$$

If the joint is designed to absorb the major part of the impact energy during collision, the above design matrix becomes uncoupled. Figure 15.21 shows the shape and mounting configuration of the side-door impact beams. The unidirectional glass-fiber epoxy prepreg (UGN 150, SK Chemicals, Korea) and crowfoot satin woven glass-fiber epoxy prepreg (GEP 215, SK Chemicals, Korea) whose warp and weft ratio is 70 to 30 were used for the materials of the composite impact beams. The tensile and shear properties of these materials were measured by ASTM D 3039

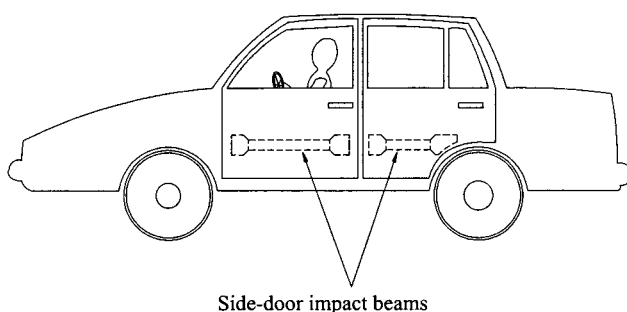


**Figure 15.21** Shape and mounting configuration of the side-door impact beams (from Cheon et al., 1997).

**Table 15.6 Mechanical Properties of the Glass Epoxy Composites and the High-strength Steel**

	$\rho$ (kg/m <sup>3</sup> )	$E_1$ (GPa)	$E_2$ (GPa)	$G_{12}$ (GPa)	$\nu_{12}$	$X^t$ (MPa)	$Y^t$ (MPa)	$S$ (MPa)
High strength steel (AISI 4340)	7870	210	210	81	0.3	1500	—	—
Glass epoxy (Unidirectional, UGN 150)	1980	43.3	14.7	4.4	0.3	1050	65	75
Glass epoxy	1950	35.5	17.2	3.7	0.22	600	100	60

and ASTM D 3518, respectively, using a static universal testing machine (Instron 4206). Table 15.6 shows the mechanical properties of the composites made of the two preprints as well as the high-strength steel (AISI 4340) used for conventional impact beams.

#### *Static Characteristics*

Since a box-type beam has better bending strength than a circular one, the composite impact beams were designed with a regular square box whose outer dimension was 31.8 mm, which was limited by the size of the steel brackets used for mounting the impact beams on the car body. The thickness of the composite beam was determined to be 5.4 mm because the composite impact beam was designed to have 70% of the weight of the high-strength steel impact beam (Cheon et al., 1997). The outer and inner diameters of the steel impact beam were 31.8 and 26.6 mm, respectively.

Five different stacking sequences,  $[0]_{nT}$ ,  $[0_5/90]_{nT}$ ,  $[0_3/90]_{nT}$ ,  $[#_2/0_n]_T$ , and  $[#_2/0_n/#_2]_T$ , were selected for the glass-fiber epoxy composite impact beams, in which # means the satin weave glass-fiber epoxy prepreg whose thickness was 0.15 mm. The stacking sequence starts from the outer to the inner plies, for example,  $[#_2/0_n]_T$  means a beam with 0° stacking angle surrounded by outer two plies of the satin weave glass-fiber epoxy prepreg. To manufacture the prototype composite beams in a laboratory by the autoclave vacuum bag degassing process rather than the pultrusion process, the inner vacuum bag molding method was used (Cheon et al., 1997). The length of the composite impact beams was 540 mm, which was the length of an actual rear-door impact beam of a compact passenger car, and the mass of the beams was 0.614–0.623 kg, about 70% of the high-strength steel impact beam.

The jig and the loading cylinder were prepared based on the FMVSS 214 (Federal Motor Vehicle Safety Standard 214) regulation, which regulates the static properties of the side doors of passenger cars. Figure 15.22 shows the jig for the three point bending test of the impact beams (Lim and Lee, 2002).

As shown in figure 15.22, the jig span was 470 mm and two 25.4 mm-diameter cylinders were used to support the impact beam. The load was applied by a static universal testing machine (Instron 4206) with a 305 mm-diameter half-cylinder at the midpoint of the impact beam.

From the experiments, it was found that the maximum bending load-carrying capacity of the composite impact beams was 32.6 kN, while the bending load-carrying capacity of the high-strength steel beam was 27.3 kN. Table 15.7 and

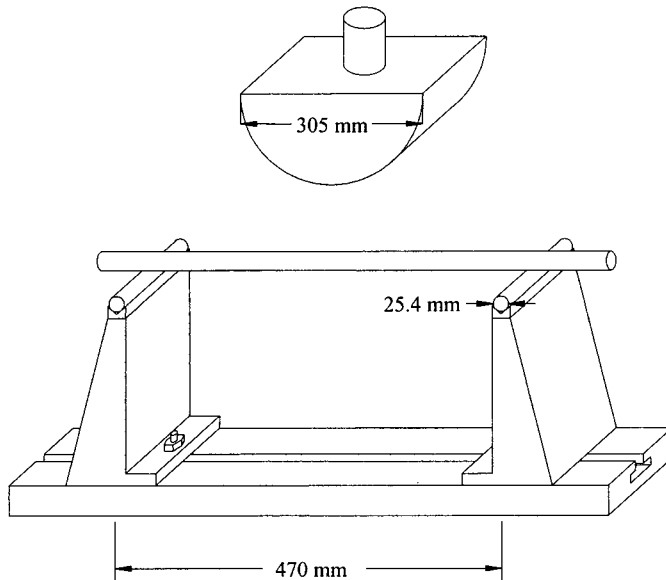


**Figure 15.22** Jig for the three point static bending test (from Lim and Lee, 2002).

**Table 15.7 Static Bending Load Capabilities of the Hollow Rectangular Composite Beams w.r.t. Stacking Angle**

Stacking sequence	Maximum load (kN)	Deflection (mm)
$[0]_{nT}$	24.26	23.44
$[0_5/90]_{nT}$	27.86	29.99
$[0_3/90]_{nT}$	26.19	30.37
$[\#_2/0_n]_T^*$	23.66	25.35
$[\#_2/0_n/\#_2]_T^*$	32.58	34.41

\* # means crowfoot satin weave.

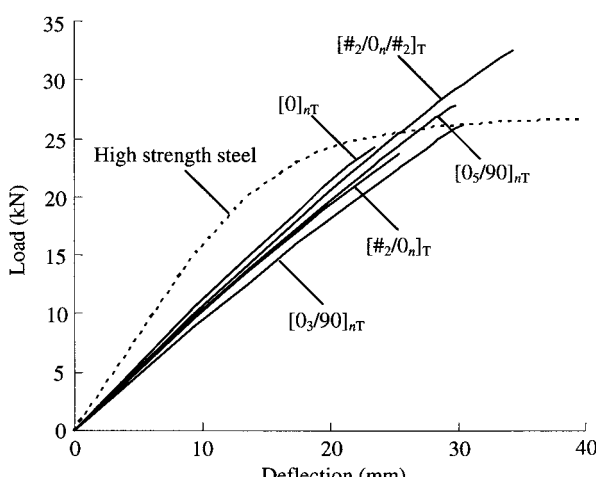


**Figure 15.23** Load-deflection curves from the static bending test of impact beams (470 mm span) (from Lim and Lee, 2002).

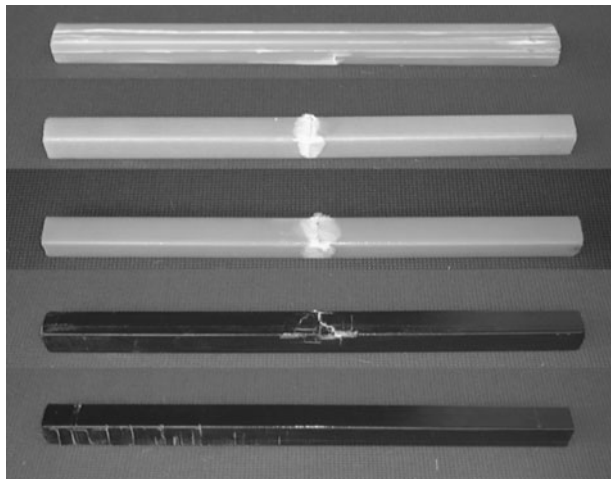


**Figure 15.24** Fracture modes of the box type composite beams, from top to bottom,  $[0]_{nT}$ ,  $[0_5/90]_{nT}$ ,  $[0_3/90]_{nT}$ ,  $[#_2/0_n]_T$ , and  $[#_2/0_n/#_2]_T$  (# represents crowfoot satin weave) (from Lim and Lee, 2002).

figure 15.23 show the test results of the three-point bending test and figure 15.24 shows the fracture modes of the composite impact beams.

Although the composite impact beam with the stacking sequence  $[0]_{nT}$  had the highest axial stiffness, it could not effectively resist the external bending load because of its low hoop strength. Also, it was found that the outer satin weave prepreg of  $[#_2/0_n]_T$  was ineffective at preventing this catastrophic shear fracture. The composite beams with stacking sequences  $[0_5/90]_{nT}$  or  $[0_3/90]_{nT}$  have higher bending strength but these composite beams are not easy to mass-produce due to the hoop winding. Therefore, the composite beams with stacking sequence  $[#_2/0_n/#_2]_T$  were tested, and it was found that they had the highest bending strength thanks to the outer- and inner-reinforced satin weave prepgres and that the strength of these beams was 20% higher than that of the conventional high-strength steel impact beam.

To increase further the bending strength of the longer composite beam for front-door application, whose beam length was 850 mm, the central part of the composite beam was reinforced with prepreg. The stacking sequence of the impact beam was  $[#_2/0_n/#_2]_T$ , and the mass of the beams was 1.15 kg, 70% of the high-strength steel beam. The manufacturing method of the center-part enhanced beams is shown in figure 15.25. A Teflon film, satin weave prepreg, unidirectional prepreg, and another satin weave prepreg were wound on the base composite beam. The Teflon film was

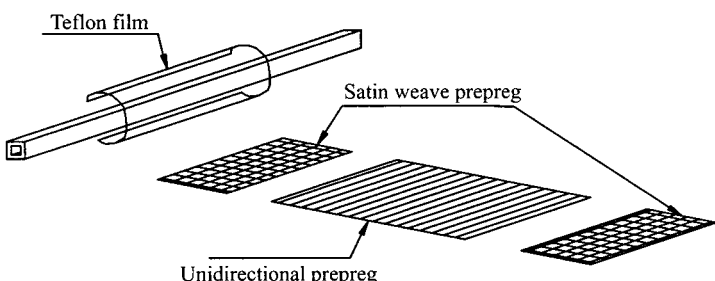


**Figure 15.25** Manufacturing method of a center-part enhanced beam (from Lim and Lee, 2002).

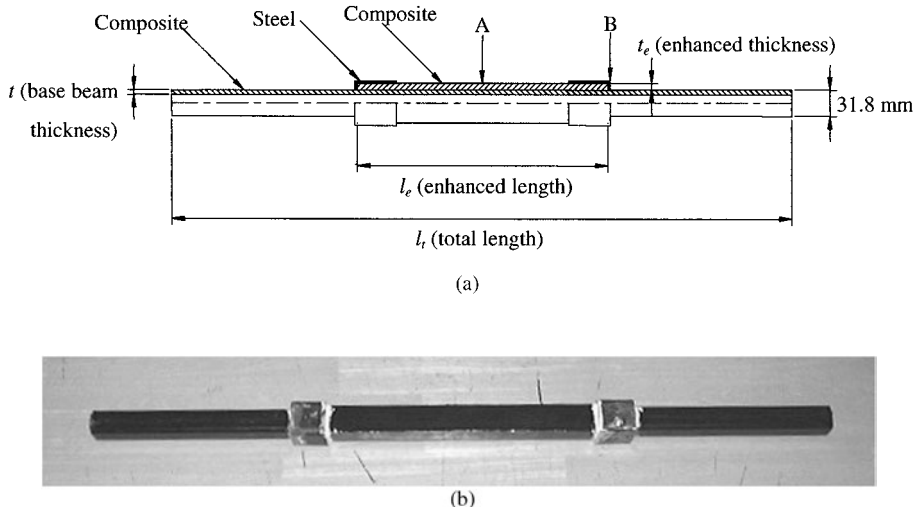


**Figure 15.26** Center-enhanced box-type beam with steel caps: (a) Configuration; (b) photograph (from Lim and Lee, 2002).

used to separate the reinforced prepreg from the base composite impact beam, which simulates the impact beam manufactured by inserting the base composite impact beam into the separately manufactured composite hollow shaft, both manufactured by pultrusion. The thickness of the base composite beam was 4.3 mm, while the thickness and length of the enhanced part were 3 mm and 405 mm, respectively, which were selected to make the induced stresses at the areas of A and B of figure 15.26(a) the same value. The outer-reinforced composite shafts were further reinforced with two steel caps to prevent splitting by hoop stress, as shown in figure 15.26(b).

The three-point bending tests were carried out using a static universal testing machine (Instron 4206) with a span length of 800 mm. From the experiments, it was found that the maximum load-carrying capacity of the composite impact beams was 19.6 kN, while the load-carrying capacity of the high-strength steel beam was 17.5 kN, as shown in figure 15.27.

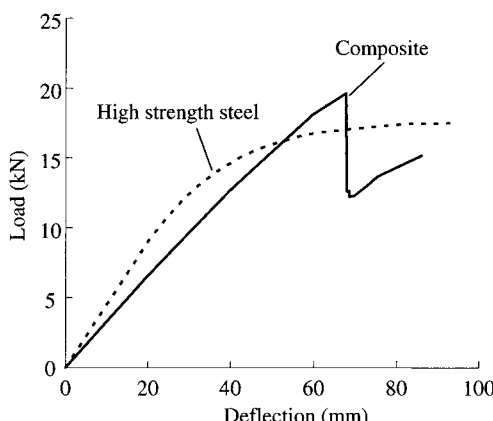


**Figure 15.27** Load-deflection curves from the static bending test of the impact beams (800 mm span) (from Lim and Lee, 2002).

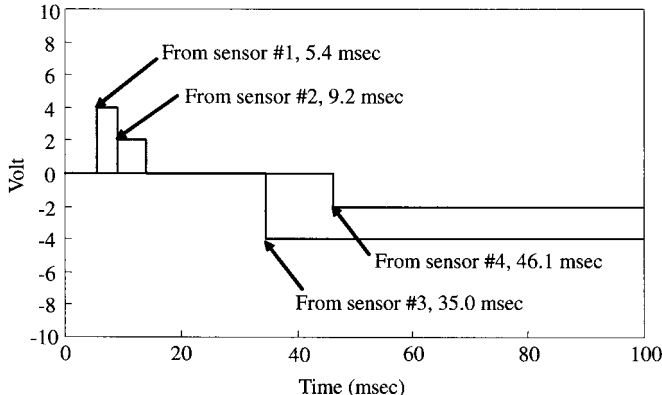


**Figure 15.28** Signal from the photo-interrupt sensor (from Cheon et al., 1997).

#### *Impact Characteristics*

A high-strength steel circular impact beam whose outer diameter and inner diameter were 30 and 27.4 mm, respectively, was tested with the pneumatic impact tester shown in figure 10.9. The outer diameter of the steel impact beam was decreased a little to meet the capacity of the impact tester. The high-strength steel, which was heat-treated through its thickness, had an ultimate tensile strength of 1.5 GPa. The mass and length of the high-strength steel circular impact beam were 0.50 kg and 507 mm, respectively. A simply supported jig span of 360 mm was used during impact tests. When the tup mass and the cylinder pressure were 13 kg and 0.5 MPa, respectively, the velocity of the tup was 13.0 m/s (29 m.p.h. = 47 km/h), which was close to the standard velocity of 30 m.p.h. for the side-crash test of FMVSS 214. In the tests, about 1100 J of dynamic energy was given to each specimen.

In dynamic tests, because the composite impact beams of 0.25 kg (50% weight ratio) showed a sufficient dynamic energy absorption capability, only the composite impact beams of 0.25 kg were tested. Figure 15.28 shows the time difference checked by the four photo-interrupt sensors during dynamic testing of the high-strength steel impact beams at 25°C.

From figure 15.28, the measured initial velocity of the impact tup was 13.2 m/s ( $V_i = 50 \text{ mm}/3.8 \text{ ms}$ ), and the measured velocity after impact of the high-strength steel impact beam was 9.0 m/s ( $V_f = 100 \text{ mm}/11.1 \text{ ms}$ ). Therefore, the energy absorption ratio, which is defined as  $1 - V_f^2/V_i^2$ , was 53.5%. The glass fiber epoxy composite impact beam, which had a mass of 0.25 kg was found to absorb 53% of the given impact energy at a room temperature of 25°C. Therefore, it was found that a 50% weight saving could be obtained when the composite impact beams were used instead of steel ones, based on the dynamic energy absorption capability. Moreover, the composite impact beams showed almost the same dynamic energy absorption capabilities regardless of their cross-sectional shapes, as shown in table 15.8, although the static strengths were much dependent on the cross-sectional shapes on the composite impact beams. Therefore, it was decided that in this study only circular composite impact beams were to be investigated.

In order to investigate the temperature dependence of the impact beams, the impact tests were performed at several low temperatures. Figure 15.29 shows the impact energy absorption of the impact beams with respect to environmental temperatures. The low environmental temperature was established by placing the impact

**Table 15.8 Dynamic Energy Absorption Ratio of Four Different Sections of Composite Impact Beams**

Cross-sectional shape	Energy absorption rate (%)
Circular type (0.25 kg)	53.2
Regular square (0.25 kg)	52.9
Regular square + rib (0.25 kg)	52.5
I-beam type (0.25 kg)	53.3

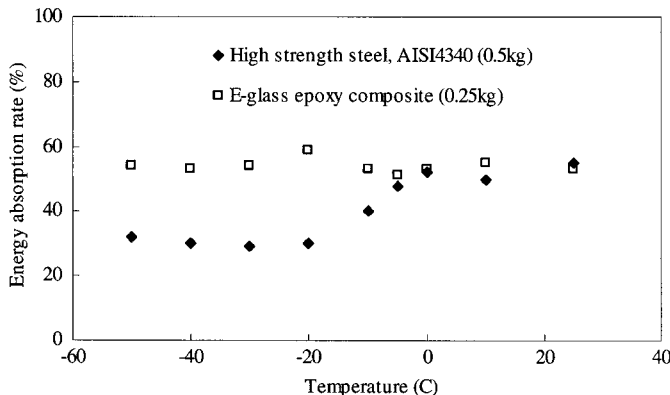


**Figure 15.29** Dynamic energy absorption results with respect to temperature (from Cheon et al., 1997).

beams inside a box containing dry ice, and the outside temperature of the impact beam was measured by a touch-probe-type thermometer.

From figure 15.29, it was revealed that the energy absorption of the steel impact beams decreased as the environmental temperature was lowered; however, the composite impact beam had an almost constant energy absorption capacity. As it was expected that the slope of energy absorption ratio was steep between 0 and  $-10^{\circ}\text{C}$ , an impact test was performed at  $-5^{\circ}\text{C}$ . From the test it was estimated that the nil ductility temperature (Hertzberg, 1996) of the steel impact beam might exist between  $-5$  and  $-10^{\circ}\text{C}$ .

#### 15.4.2 Design of the Composite Joint

Conventional steel side-door impact beams are mounted on the car body by welding the impact beams to the mounting brackets, and then by welding the mounting brackets to the car body chassis. However, the composite impact beam should be adhesively or mechanically joined to mounting brackets. The mechanical joining method using bolts or rivets might have high-impact energy absorption during progressive failure if the joint was designed to have the composite shear-out failure mode ( $\text{DP}_2$ ). Figure 15.30(a) shows the schematic diagram of the joint between the composite beam and the brackets and figure 15.30(b) shows a failure mode of composite shear-out. Since the major force in the impact beam during bending impact is a tensile force due to the flexible nature of the mounting brackets and car

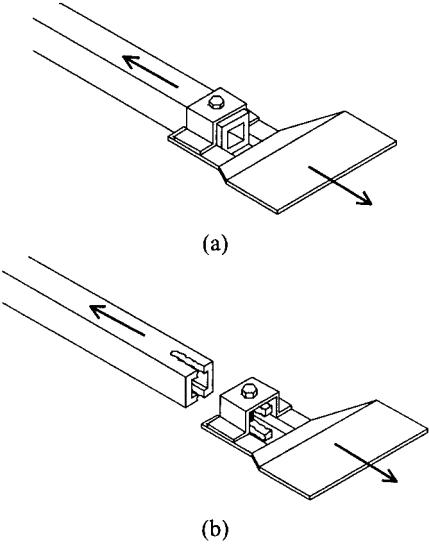


**Figure 15.30** Mechanical joint between the impact beam and the steel bracket: (a) Schematic diagram; (b) composite shear-out failure mode (from Lim and Lee, 2002).

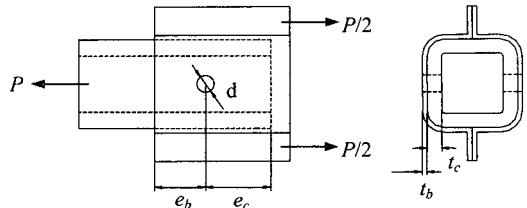


**Figure 15.31** Geometric design parameters of a joint (from Lim and Lee, 2002).

body chassis, the design of the joint was focused on the maximizing tensile load capabilities by employing experiments and FE analysis.

For the design of the mechanical joints of the composite impact beams, the dimensions of the pin diameter ( $d$ ), thicknesses of the composite and the bracket ( $t_c$ ,  $t_b$ ), and the end distances ( $e_c$ ,  $e_b$ ) of the composite and the bracket, as shown in figure 15.31, should be determined. The tensile load capacities  $P$  with respect to the different failure modes are

$$P = 4t_c e_c S_c \quad (\text{composite shear-out}) \quad (15.25a)$$

$$P = 2t_c d X_c \quad (\text{composite bearing}) \quad (15.25b)$$

$$P = 2 \frac{\pi}{4} d^2 S_p \quad (\text{pin shear}) \quad (15.25c)$$

$$P = 4t_b e_b S_b \quad (\text{bracket shear-out}) \quad (15.25d)$$

$$P = 2t_b d X_b \quad (\text{bracket bearing}) \quad (15.25e)$$

where  $S$  and  $X$  represent the ultimate shear and compressive strengths, respectively, and the subscripts  $b$ ,  $c$ , and  $p$  represent the bracket, the composite, and the pin, respectively.

Since the compressive strength of a unidirectional glass composite is much higher than its shear strength, only the shear-out failure mode of the composite beam was

considered. For the bracket, the shear-out failure mode was only considered to dissipate large impact energy.

The sum of end distances  $l$  of the composite and the bracket from their holes is limited by the geometry of the bracket:

$$e_b + e_c = l \quad (15.26)$$

For the efficiency of the composite impact beam, the tensile load capabilities of the composite beam and the bracket should be same:

$$P = 4t_c e_c S_c = 4t_b e_b S_b \quad (15.27)$$

Generally, the stress concentration factor need not be considered in the case of plastic failure of steel; however, the stress concentration factor of composite structures must be considered because they have little plastic deformation up to failure. Therefore, equations (15.25) and (15.27) were modified:

$$P = 4t_c e_c \frac{S_c}{K} \quad (15.28)$$

$$P = 4t_c e_c \frac{S_c}{K} = 4t_b e_b S_b \quad (15.29)$$

Since the shear failure mode of the pin is not beneficial, which may absorb little impact energy during failure, the following relationship was used during the design stage:

$$d^2 \pi \frac{S_p}{S.F.} \geq 8t_b e_b S_b \quad (15.30)$$

where  $S.F.$  represents the safety factor of the pin and  $S_p$  represents the shear strength of the pin.

Since the stress concentration factor in equation (15.28) depends on the geometry of the joint, in this study, the stress concentration factors were calculated by FE analysis and compared with the experimental results. For the FE analysis, ABAQUS standard (H.K.S. Inc., Rhode Island, USA), a commercial FE analysis package, was used, as shown in figure 15.32, in which a quarter part of the joint was modeled using symmetric boundary conditions when the thicknesses of the composite beam and the steel bracket were 6.5 mm and 1.5 mm, respectively. A distributed load was applied at the end of the bracket and a fixed boundary condition at the end of the composite beam was used. The contact phenomenon between the pin and the composite beam was considered with the assumption of a rigid pin. The material properties used in the analysis are shown in table 15.9.

Figure 15.33 shows the stress distribution of the pin-jointed composite beam under a 15 kN load. The stress concentration factor  $K$  was calculated from the maximum shear stress  $\tau_{\max}$  obtained from FE analysis and the average applied shear stress  $\tau_{\text{avg}}$ , which is the applied load of 15 kN divided by the shear loading area:

$$K = \frac{\tau_{\max}}{\tau_{\text{avg}}} \quad (15.31)$$

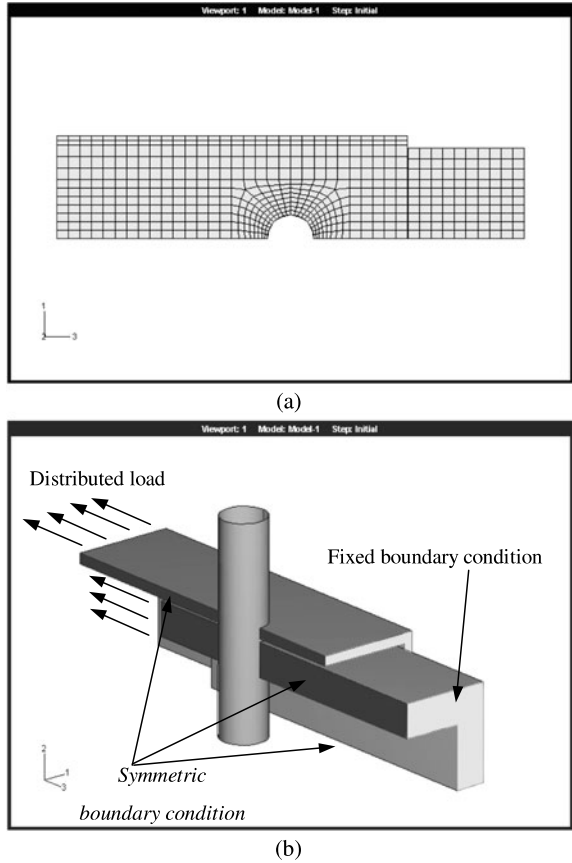


**Figure 15.32** Finite element mesh for the pin jointed composite impact beam: (a) Finite element mesh; (b) boundary conditions (from Lim and Lee, 2002).

**Table 15.9 Properties of the Steel Bracket and the Glass Epoxy Composite for the Mechanical Joint**

	$E_1$ (GPa)	$E_2$ (GPa)	$G_{12}$ (GPa)	$\nu_{12}$	$S$ (MPa)
Bracket	210	210	81	0.3	165
Composite	43	14.7	4.4	0.3	75

The stress concentration factors were calculated with respect to the end distance of composite beam  $e_c$ , pin diameter  $d$ , and  $e_c/d$ , as shown in figure 15.34.

To assess the validity of the calculated stress concentration factor of the composite beams, tensile tests of the composite beams mechanically joined to the bracket were performed with the static universal testing machine (Instron 4206) and the loading fixture shown in figure 15.35. The bracket and the steel fixture were joined with four M6 bolts and the composite beam was connected to the bracket using a pin. The thicknesses of the composite beam and the steel bracket were 6.5 mm and 1.5 mm, respectively, and the pin diameter and end distances were adjusted for the verification of the above analysis results.

Figure 15.36(a) shows the failure mode of the composite beam shear-out and figure 15.36(b) shows the bracket shear-out failure mode. The comparisons between the calculated and the experimentally obtained load capacities and failure modes

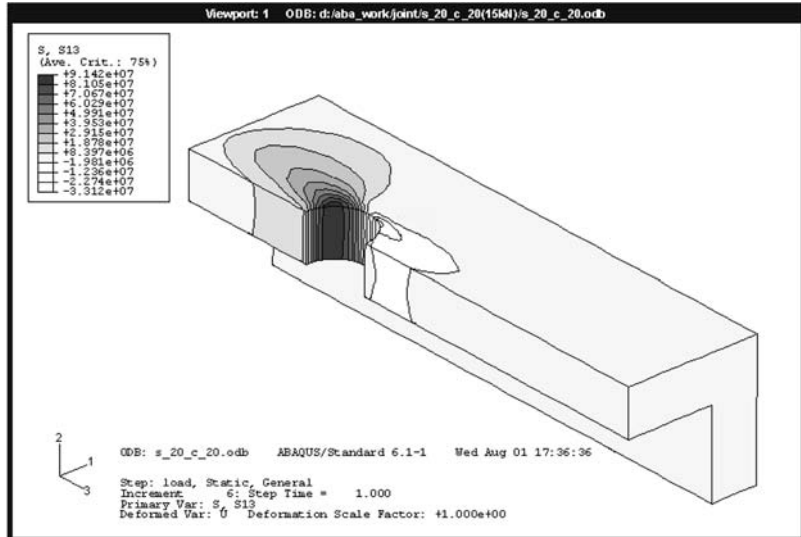
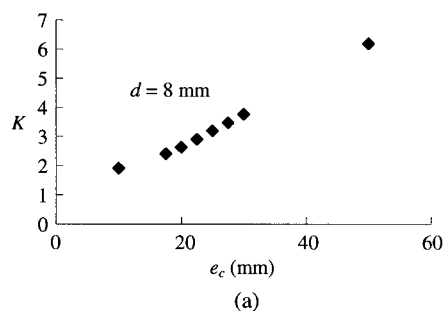
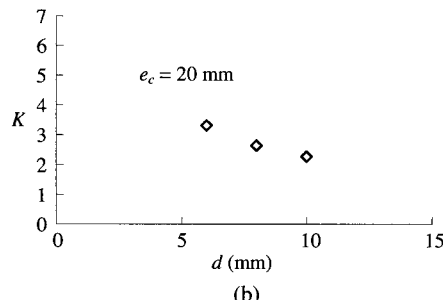


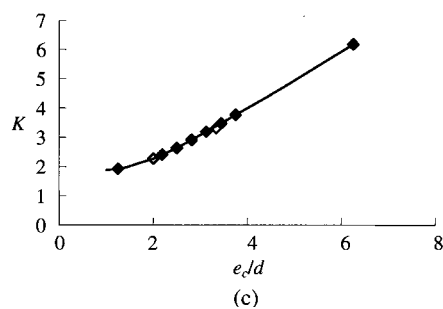
**Figure 15.33** Stress distribution of the composite beam under 15kN load (from Lim and Lee, 2002).



(a)



(b)



(c)

**Figure 15.34** Stress concentration factor  $K$  of the pin-jointed composite impact beam: (a) With respect to shear-out length  $e_c$  when  $d=8$  mm; (b) with respect to pin diameter  $d$  when  $e_c=20$  mm; (c) with respect to  $e_c/d$  (from Lim and Lee, 2002).

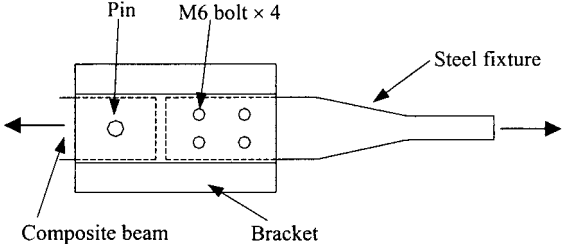


**Figure 15.35** Schematic diagram of the loading fixture for the tensile test of the joint (from Lim and Lee, 2002).

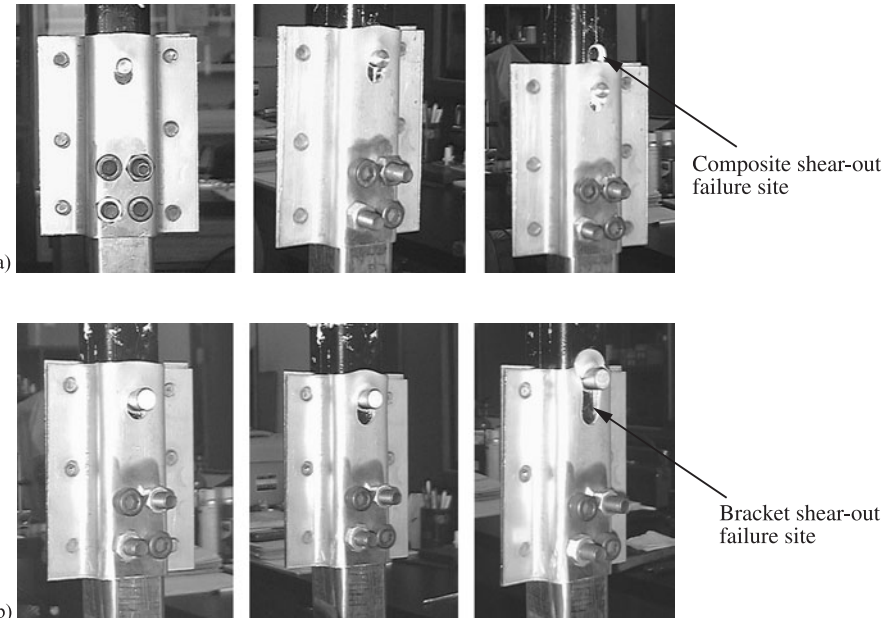


**Figure 15.36** Failure modes: (a) Composite shear-out failure; (b) bracket shear-out failure (from Lim and Lee, 2002).

from the tensile tests are shown in table 15.10. The data were calculated using equations (15.25d) and (15.28), and show a relatively good agreement with the experimental results.

To determine the design variables,  $e_c$  and  $d$ , the relationships were obtained from equations (15.26), (15.29), and (15.30):

$$e_c = \frac{l}{[(t_c S_c)/(t_b S_b) \cdot (1/K) + 1]} \quad (15.32)$$

$$d \geq 2 \sqrt{\frac{2(l - e_c)t_b S_b \cdot S.F.}{\pi S_p}} \quad (15.33)$$

Since the value of  $K$  depends on the values of  $e_c$  and  $d$ , the design variables  $e_c$  and  $d$  should be calculated by the iteration method. At first, the values of  $e_{c0}$  and  $d_0$  that satisfy equation (15.33) were assumed, then  $K$  at the assumed values of  $e_{c(i)}$  and  $d_{(i)}$  were determined from figure 15.34(c), from which the next value of  $e_{c(i+1)}$  was calculated from equation (15.32).

**Table 15.10 Static Tensile Loads and Failure Modes w.r.t. Design Variables**

Design variables			Tested		Calculated		Error (%)
<i>d</i> (mm)	<i>e<sub>c</sub></i> (mm)	<i>e<sub>b</sub></i> (mm)	Load <i>P</i> (kN)	Failure mode*	Load <i>P</i> (kN)	Failure mode*	
8	20	20	16.05	C	14.81	C	-7.7
8	20	20	15.90	C	14.81	C	-6.8
8	20	25	16.58	C	14.81	C	-10.7
8	30	15	13.74	B	14.85	B	8.1
10	30	15	15.62	B	14.85	B	-4.9
8	25	20	18.74	C	15.29	C	-18.4

\*C: composite shear-out failure mode; B: bracket shear-out failure mode.

### 15.4.3 Door Static Bending Test

The center-reinforced impact beam was also manufactured and mounted on the side door of a compact passenger car. The method of the previous section was used to design the joint of the impact beam with the following geometric parameters:

$$e_c + e_b = 40 \text{ mm} \quad (15.34a)$$

$$t_c = 5.4 \text{ mm} \quad (15.34b)$$

$$t_b = 1.5 \text{ mm} \quad (15.34c)$$

Using the iteration method, the values of *d*, *e<sub>c</sub>*, and *e<sub>b</sub>* were determined to be 8 mm, 25 mm, and 15 mm, respectively.

The jigs and loading cylinder for the three-point bending test were prepared based on the FMVSS 214 regulation. The load was applied at the midpoint of the door by a 305 mm-diameter half-cylinder mounted on the static universal testing machine (Instron 4206), as shown in figure 15.37. Since this test might be different from the real collision test, the test results were used in comparing the static bending load capabilities between the composite impact beam and the conventional high-strength steel impact beam. Figure 15.38 shows the load characteristics of the side-doors reinforced with the composite and the high-strength steel impact beams. The bends and kinks in the load-displacement curves of the door reinforced with the steel impact beam may come from the loosening and failure of the mounting area of the car body, while those of the door reinforced with the composite impact beam may come from the failure of steel caps or shear-out failure of the joints, or different failure loads between the inner base beam and the outer-reinforced beam.

Although the primary load on the side-door impact beam during collision is a dynamic load rather than a static load, the actual dynamic collision test could not be performed, as it required many large facilities. However, it has been reported that the dynamic strength of glass-fiber composites is much higher than the static strength, sometimes 180% (Lee et al., 2000; Lee and Cheon, 2001), while the dynamic strength of the steel impact beam is similar to its static strength at room

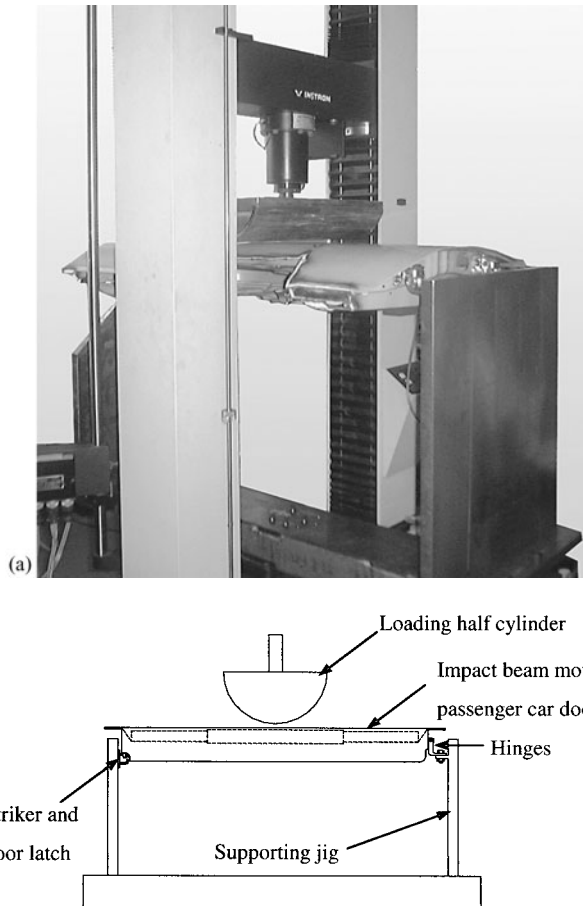


**Figure 15.37** Static bending test of an impact beam mounted on the side door of a compact passenger car: (a) Photograph; (b) schematic diagram.

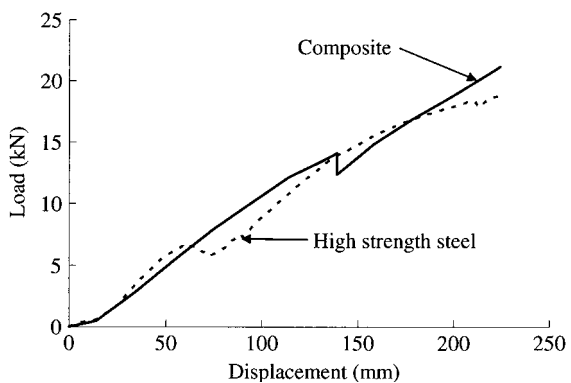


**Figure 15.38** Load-displacement curves from the static bending test of the real front side-door reinforced with the composite and the high-strength steel impact beams.

temperature, and much lower at the temperature below its nil-ductility temperature. Therefore, it may be concluded that the composite impact beam with static strength comparable to a high-strength steel impact beam will have higher dynamic performance than the steel beam.

## 15.5 Trenchless Sewage Pipe Repair by Resin Transfer Molding

The excavation technology that has been mainly used in the repair of retired or damaged underground pipes induces traffic congestion and a large amount of waste. To overcome these disadvantages, the repair of worn-out underground pipes has been tried using trenchless techniques without any excavation of the ground (Kurz et al., 1997; Trent, 1998). The various trenchless repair technologies may be classified into four kinds: slip-lining process, cured-in-place-pipe (CIPP) lining process, close-fit lining process, and spirally wound pipe lining process. Among them the in situ reverse lining process (or in situ form process), a sort of cured-in-place-pipe lining process, is most practiced. However, this technology requires high construction cost, is an inconvenient operation, and has size limitation (Lee et al., 2002; Chin et al., 2003). From the viewpoint of axiomatic design methodology, these problems are induced by the coupling between functional requirements (what the process wants to achieve) and design parameters (how the process wants to achieve those functional requirements) of the processes (Suh, 2001). This means that a better repair process could be developed through the right decompositions of functional requirements and design parameters to remove those couplings.

Therefore, in this section a new trenchless repair process for underground pipes through the axiomatic design approach is presented in order to overcome such problems of conventional technologies. For repairing underground large composite structures, modified RTM (resin transfer molding), which is a kind of liquid composite molding process (discussed in section 8.5.1) was used with the reinforcement of E-glass/polyester composites, which has been proved to save time and cost.

### 15.5.1 Development of Trenchless Repair Process Through Design Axioms

The new repair process should be adequate for implementation along high-traffic roads and must ensure high durability, reinforcing strength, longer life span, and a safe construction environment. This process also requires shorter operation time and lower cost than other trenchless technologies. In this case, the purpose of the process can be stated in terms of two functional requirements (FRs):

$FR_1$  = Prepare the reinforcing element

$FR_2$  = Repair the target pipes using the reinforcing element.

Two DPs for satisfying these FRs are stated as

$DP_1$  = Reinforcing element

$DP_2$  = Detailed repair process of sequential order.

The following design equation may represent this repair system:

$$\begin{Bmatrix} FR_1 \\ FR_2 \end{Bmatrix} = \begin{bmatrix} X & 0 \\ X & X \end{bmatrix} \begin{Bmatrix} DP_1 \\ DP_2 \end{Bmatrix} \quad (15.35)$$

Since this system is closely related to economic benefit, the constraints for design may be dictated as

$C_1$  = Minimize the material cost

$C_2$  = Minimize the total operation time and cost.

*Decomposition of the FR<sub>1</sub> and DP<sub>1</sub> Branch*

In order to embody this repair system, the reinforcing element for repairing damaged underground pipes should be prepared in the first place. For this, decomposition of the FR<sub>1</sub> and DP<sub>1</sub> branch was performed, considering the problems and requirements of actual situations.

Since the fiber-reinforced polymeric composite material has high specific strength and corrosion-resistant characteristics (as discussed in chapter 2), it was selected for the reinforcement of the underground pipes in order to increase the reinforcing strength and enhance the environmental resistance. Thus, the reinforcing element should contain the reinforcing fibers and be mixed with polymeric resin. To decrease the operation cost and time, E-glass fiber and unsaturated polyester were selected and the RTM technology for fabricating and repairing underground large composite structures has been adopted because the RTM process has the capability to fabricate large and complex three-dimensional structures at low production cost (Mallick, 1988). Although there are many studies related to RTM (Pillai and Advani, 1998; Golestanian and El-Gizawy, 1998; Skordos et al., 2000; Diallo et al., 1998; Minaie et al., 2002; Kim and Daniel, 2002), the RTM process has hardly been attempted for the repair of underground pipes.

The reinforcing element should be manufactured with the consideration of the above-mentioned information, and should be adequate for RTM. The detailed repair process may be a modification of the general RTM process.

Having chosen DP<sub>1</sub>, we can decompose FR<sub>1</sub>.

As mentioned above, the reinforcing element should contain an E-glass-fiber preform, the reinforcing material, to sustain the load induced by both the ground and traffic. This preform material has to be protected so as not to be damaged by the internal surface of any conduits, and the dirty water within, during the placement of the reinforcing element, and should also be encapsulated in order to act as the mold for the RTM process.

Decomposition of FR<sub>1</sub> and DPs for satisfying decomposed FRs are stated as

FR<sub>11</sub>=Sustain the external load induced by ground and traffics

FR<sub>12</sub>=Protect the fiber preform from dirty water, subterranean water, or protrusions

FR<sub>13</sub>=Encapsulate the fiber preform and play the role of the mold for RTM process.

DP<sub>11</sub>=E-glass-fiber preform as the reinforcement

DP<sub>12</sub>=Protection film placed on the outside of the fiber preform

DP<sub>13</sub>=Protection film placed on the inside of the fiber preform.

The design equation for the reinforcing element may be written as

$$\left\{ \begin{array}{l} \text{FR}_{11} \\ \text{FR}_{12} \\ \text{FR}_{13} \end{array} \right\} = \left[ \begin{array}{ccc} X & 0 & 0 \\ 0 & X & 0 \\ 0 & X & X \end{array} \right] \left\{ \begin{array}{l} \text{DP}_{11} \\ \text{DP}_{12} \\ \text{DP}_{13} \end{array} \right\} \quad (15.36)$$

The shape of the reinforcing element, as shown in figure 15.39, satisfies the functional requirements, FR<sub>11</sub>, FR<sub>12</sub>, and FR<sub>13</sub> by the design parameters, DP<sub>11</sub>, DP<sub>12</sub>, and DP<sub>13</sub>.

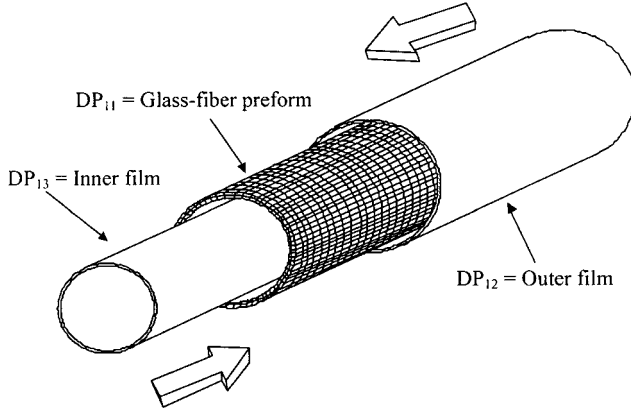


**Figure 15.39** Shape and preparation of the reinforcing element for the repairing underground.

#### Decomposition of the $FR_{11}$ and $DP_{11}$ Branch

Considering the functional requirements of chosen DPs, further decomposition of  $FR_{11}$ ,  $FR_{12}$ , and  $FR_{13}$  was performed based on the target value that the reinforcement strength should assure 150% of the maximum compressive load of concrete pipes with the same diameter. Among the three stages of the general RTM process, preforming, resin wetting, and curing, the resin wetting stage is the core process of RTM because the product quality is largely dependent on the degree of wetting (Advani, 1994). Since the resin flow during the repair process is a viscous flow through porous media, the degree of wetting and resin wetting time are closely related to the permeability of the fiber preform. The average resin velocity  $\bar{u}_i$  has been defined by Darcy's law from equation (8.1), which is repeated here:

$$\bar{u}_i = -\frac{k_{ij}}{\mu} \frac{\partial p}{\partial x_j} \quad (15.37)$$

where  $k_{ij}$  is the permeability of fiber preform,  $\mu$  the viscosity of resin, and  $\partial p / \partial x_j$  the pressure gradient. The permeability of fiber preform,  $k_{ij}$ , should be maximized to reduce the overall process time and enhance the degree of wetting.

From the chosen  $DP_{11}$ ,  $FR_{11}$  can be decomposed as

$FR_{111}$  = Assure 150% of the maximum compressive load of concrete pipes of the same diameter for underground applications

$FR_{112}$  = Wet the reinforcement with polyester resin completely in a short time.

$DP_{111}$  = Strength of the fiber preform

$DP_{112}$  = Large permeability of the fiber preform.

$C_{11}$  = Minimize the thickness of the fiber preform to reduce the material cost.

The design equation for this branch may be written as

$$\begin{Bmatrix} FR_{111} \\ FR_{112} \end{Bmatrix} = \begin{bmatrix} X & x \\ x & X \end{bmatrix} \begin{Bmatrix} DP_{111} \\ DP_{112} \end{Bmatrix} \quad (15.38)$$

Actually, the strength and permeability of the fiber preform are closely coupled with each other, so the design matrix may be the full matrix. But these two DPs

**Table 15.11 Permeabilities of the Various E-glass-fiber Mats**

Type of mat	Volume fraction (%)	$K_{xx} (m^2) \times 10^{-10}$	$K_{yy} (m^2) \times 10^{-10}$
Unidirectional	42.1	45.5	39.2
	47.0	7.52	5.32
Continuous strand	9.1	17.8	17.6
	13.5	9.96	9.99
Stacked [UD/CSM/CSM/UD] <sub>T</sub>	25.8	41.1	40.0
Satin woven	45.5	0.713	0.588
	50.0	0.447	0.324
	54.5	0.255	0.190
Plain woven	45.5	0.639	0.537
	50.0	0.429	0.326
	54.5	0.213	0.182

UD: unidirectional; CSM: continuous strand mat.

**Table 15.12 Tensile Test Results of Glass/Polyester Composite Materials**

Type of mat	Fiber volume fraction (%)	Tensile strength (MPa)	Young's modulus (GPa)
Unidirectional	47	630	33.9
Continuous strand	10	55	6.87
	14.5	77.2	7.4
Stacked [UD/CSM/CSM/UD] <sub>T</sub>	29.5	340	18.2
	26.6	288	16.6
Satin woven	42.4	471	28.2
Plain woven	28.5	259	13.5

UD: unidirectional; CSM: continuous strand mat.

can be decoupled by making some artificial flow channels in the preform, which makes off-diagonal terms small.

In order to select proper materials for the fiber preform, the permeability and tensile strength of various E-glass fiber mats, unidirectional mats, continuous strand mats, crowfoot satin woven mats, and plain woven mats were measured by Adams et al. (1988). Table 15.11 shows the measured permeabilities of various fiber mats, with ASTM D 3039/D 3039M-95a method, and table 15.12 shows their tensile strengths when cured. From the test results, the stacked mat of high permeability and moderate tensile strength was selected for the preform material.

For the improvements of hoop strength as well as some axial strength of the composite pipe, two continuous strand mats, which have low fiber volume fraction and tensile strength, were inserted between the two layers of unidirectional mats. The stacking sequence of the composite reinforcement is [unidirectional mat 1 ply/continuous strand mat 2 plies/unidirectional mat 1 ply]<sub>T</sub>.

After resin injection into the reinforcement, the internal cavity of the reinforcement should be inflated for the reinforcement to adhere to the concrete pipe and

to squeeze out the excess polyester resin. From several previous experiments, it has been found that the air pressure of 0.1 MPa is sufficient for these purposes. Therefore, the outer protection film ( $DP_{12}$ ) should sustain the tensile load up to 78.5 kN induced by air pressure when the pipe diameter is 1000 mm. When the safety factor of the film is 2, the outer protection film should sustain about 160 kN. It should also protect the fiber preform from protrusions and dirty water, and sustain traction force during the process. In order to play the role of the mold for RTM, it should have no pores and be chemically stable with styrene monomer hardener for the polyester resin.

*Decomposition of the  $FR_{12}$ - $DP_{12}$  Branch and  
 $FR_{13}$ - $DP_{13}$  Branch*

Considering these requirements,  $FR_{12}$  and  $DP_{12}$  were decomposed as follows:

$FR_{121}$  = Have stability when contacted with unsaturated polyester resin and styrene monomer without any porosity

$FR_{122}$  = Endure the friction force between the film and the inner surface of underground pipes during pulling of the reinforcement

$FR_{123}$  = Sustain the tensile load of 160 kN in order to endure the internal air pressure and traction force during the process.

$DP_{121}$  = Composition of film

$DP_{122}$  = Durability of film

$DP_{123}$  = Tensile strength of film.

The design equation can be expressed as

$$\begin{Bmatrix} FR_{121} \\ FR_{122} \\ FR_{123} \end{Bmatrix} = \begin{bmatrix} X & 0 & 0 \\ x & X & 0 \\ x & 0 & X \end{bmatrix} \begin{Bmatrix} DP_{121} \\ DP_{122} \\ DP_{123} \end{Bmatrix} \quad (15.39)$$

The inner protection film ( $DP_{13}$ ) also sustains the tensile load up to 160 kN induced by air pressure and traction force during the pulling process of reinforcement with outer protection film. It also plays the role of the mold for RTM. The decomposition of  $FR_{13}$  and  $DP_{13}$  gives

$FR_{131}$  = Have stability when contacted with unsaturated polyester resin and styrene monomer without any porosity

$FR_{132}$  = Sustain the tensile load up to 160 kN in order to endure the internal air pressure and drag force during the pulling process of reinforcement.

$DP_{131}$  = Composition of film

$DP_{132}$  = Tensile strength of film.

Similarly the design matrix is a diagonal matrix:

$$\begin{Bmatrix} FR_{131} \\ FR_{132} \end{Bmatrix} = \begin{bmatrix} X & 0 \\ x & X \end{bmatrix} \begin{Bmatrix} DP_{131} \\ DP_{132} \end{Bmatrix} \quad (15.40)$$

To select a suitable material for these protection films for the reinforcing element, static tensile tests and chemical stability tests with the unsaturated polyester resin were performed. Several film materials such as PVC (polyvinylchloride), PE

**Table 15.13 Tensile Properties of Various Film Materials**

Material	Strength (MPa)		Failure strain (m/m)		Required thickness (mm)		Available thickness (mm)
	A	B	A	B	A	B	
PVC	12.0	7.2	2.7	3.3	2.1	3.5	0.1–1.0
PU	28.4	12.2	3.1	6.1	0.9	2.0	0.1–0.5
PE	12.4	12.4	4.8	4.8	2.0	2.0	0.1–0.17
Aqua-Tex	78.8	63.2	0.33	0.30	0.32	0.4	0.45–1.0
Pro-Top	38.4	36.4	0.29	0.28	0.65	0.69	0.35–0.6
Pro-Sol	94.5	80.3	0.30	0.35	0.26	0.31	0.55–1.0

A: Without soaking.

B: Soaking in unsaturated polyester resin (PC670) for 12 hours.

**Table 15.14 Master Design Matrix of FR<sub>1</sub> and DP<sub>1</sub> Branch**

		DP <sub>1</sub>						
		DP <sub>11</sub>		DP <sub>12</sub>			DP <sub>13</sub>	
		DP <sub>111</sub>	DP <sub>112</sub>	DP <sub>121</sub>	DP <sub>122</sub>	DP <sub>123</sub>	DP <sub>131</sub>	DP <sub>132</sub>
FR <sub>1</sub>	FR <sub>11</sub>	FR <sub>111</sub>	X	x	0	0	0	0
		FR <sub>112</sub>	X	X	0	0	0	0
	FR <sub>12</sub>	FR <sub>121</sub>	0	0	X	0	0	0
		FR <sub>122</sub>	0	0	x	X	0	0
	FR <sub>13</sub>	FR <sub>123</sub>	0	0	x	0	X	0
		FR <sub>131</sub>	0	0	0	0	0	X
	FR <sub>132</sub>	FR <sub>132</sub>	0	0	0	0	0	x

(polyethylene), PU (polyurethane), and tarpaulin films that are composed of polyester fabric and PVC resin were tested according to ASTM D882. For the tarpaulin films, Pro-top, Pro-sol, and Aqua-tex (LG Chem., Seoul, Korea) were tested.

The specimens were prepared with and without being soaked in the unsaturated polyester resin for 12 hours. In case of the PVC, PU, and tarpaulin films, the tensile properties were degraded due to the infiltration of styrene monomer into the materials, which accompanied the change of dimensions, and PVC and PU films with the required thickness were not commercially available. Although there were no changes in strength and strain for the PE film, commercial films with the required thickness were not available either. Since the Pro-Sol film had superior tensile properties, chemical stability with styrene monomer in polyester resin, and availability compared with other materials, as shown in table 15.13, it was selected for the protection films for the reinforcing element. Also, since it can be manufactured according to customer requirements, off-diagonal terms of previous design matrices of equations (15.39) and (15.40) can be negligible.

In this way the decomposition of FR<sub>1</sub> and DP<sub>1</sub> branch can be completed. The master design matrix of the FR<sub>1</sub> and DP<sub>1</sub> branch, which indicates three levels of decomposition, is shown in table 15.14.

*Decomposition of the FR<sub>2</sub> and DP<sub>2</sub> Branch*

From the previous decomposition of the FR<sub>1</sub> and DP<sub>1</sub> branch, the manufacturing criteria for the reinforcing element have been established. In order to fully develop the trenchless repair process of underground pipes, decompositions of the FR<sub>2</sub> and DP<sub>2</sub> branch should be followed. Since the process has a certain sequential order, decomposition of the FR<sub>2</sub> and DP<sub>2</sub> branch has to be done according to that order.

The whole repair process may be divided into several subprocesses, and these will represent the low levels of the FR<sub>2</sub> and DP<sub>2</sub> branch.

Using chosen DP<sub>2</sub>, decomposition of FR<sub>2</sub> was carried out following the process sequences:

FR<sub>21</sub> = Preprocess the underground pipes

FR<sub>22</sub> = Place the reinforcing element through the target pipes

FR<sub>23</sub> = Seal both ends of reinforcing element

FR<sub>24</sub> = Remove the wrinkles and twists of reinforcing element

FR<sub>25</sub> = Inject the unsaturated polyester resin into the reinforcing element

FR<sub>26</sub> = Wet the reinforcing element with the injected resin

FR<sub>27</sub> = Cure the wetted resin and finish the whole process.

Cleaning and the removal of protrusions were performed using a commercial mobile robot, which is also available for inspecting the surface damage of underground pipes. A winding machine can easily do the placement of the reinforcing elements. Since the whole process is done using RTM, the reinforcing element should be encapsulated to prevent the undesirable leakage of resin. Therefore, both ends of the reinforcing element must be sealed. For the smooth surface, the wrinkles and twists of the reinforcing element that might be generated during the placing process should be removed. Also, the resin injection method and curing method should be devised. The DPs for satisfying these FRs can be stated as

DP<sub>21</sub> = Preprocessing equipment (mobile robot and water cleaner)

DP<sub>22</sub> = Placing equipment (winding or pulling machine and lubricant supplier)

DP<sub>23</sub> = Sealing devices

DP<sub>24</sub> = Equipment for removing wrinkles and twists

DP<sub>25</sub> = Resin injection equipment

DP<sub>26</sub> = Wetting equipment

DP<sub>27</sub> = Curing equipment.

Then the design equation may be written as

$$\left\{ \begin{array}{l} \text{FR}_{21} \\ \text{FR}_{22} \\ \text{FR}_{23} \\ \text{FR}_{24} \\ \text{FR}_{25} \\ \text{FR}_{26} \\ \text{FR}_{27} \end{array} \right\} = \left[ \begin{array}{ccccccc} X & 0 & 0 & 0 & 0 & 0 & 0 \\ 0 & X & 0 & 0 & 0 & 0 & 0 \\ 0 & 0 & X & 0 & 0 & 0 & 0 \\ 0 & 0 & 0 & X & 0 & 0 & 0 \\ 0 & 0 & 0 & 0 & X & 0 & 0 \\ 0 & 0 & 0 & 0 & 0 & X & 0 \\ 0 & 0 & 0 & 0 & 0 & 0 & X \end{array} \right] \left\{ \begin{array}{l} \text{DP}_{21} \\ \text{DP}_{22} \\ \text{DP}_{23} \\ \text{DP}_{24} \\ \text{DP}_{25} \\ \text{DP}_{26} \\ \text{DP}_{27} \end{array} \right\} \quad (15.41)$$

*Decomposition of the FR<sub>21</sub> and DP<sub>21</sub> Branch*

Prior to repairing the underground pipes, inspection of the internal surface of the conduits should be performed in order to know where and how much the pipes are damaged. Then, the deposits and protrusions within the conduits must be removed for easy and reliable installation of the reinforcing element. These preprocesses are matched to the FR<sub>21</sub> and DP<sub>21</sub> branch. From the chosen DP<sub>21</sub>, decomposition of FR<sub>21</sub> gives

FR<sub>211</sub>=Inspect the internal surface of underground pipes

FR<sub>212</sub>=Remove the protrusions from internal surface of underground pipes

FR<sub>213</sub>=Clean the inside of the target underground pipes

FR<sub>214</sub>=Place the wire along the target conduits.

Design parameters that satisfy the decomposed FRs can be stated as

DP<sub>211</sub>=CCD camera of mobile robot

DP<sub>212</sub>=Grinder of mobile robot

DP<sub>213</sub>=Water cleaner of mobile robot

DP<sub>214</sub>=Mobile robot.

In this case the design matrix is a diagonal matrix, and figure 15.40(a) may represent brief explanations of this branch.

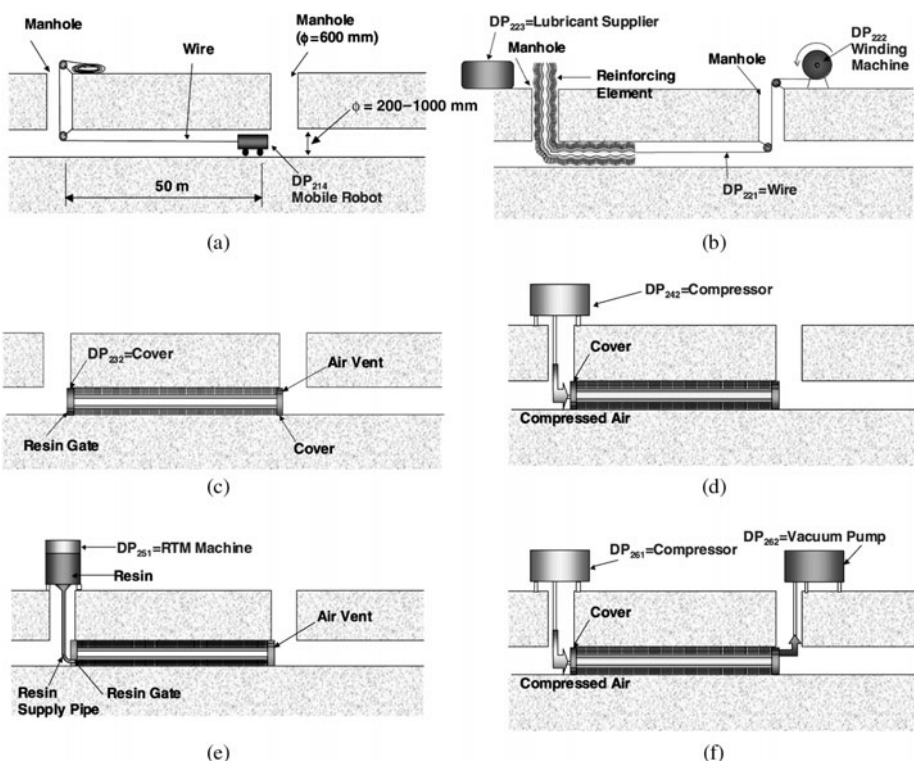


**Figure 15.40** Repair processes for underground pipes with RTM: (a) Preprocessing; (b) placing of the reinforcing element; (c) attaching of the covers and sealing; (d) removal of wrinkles and twists of the reinforcing element; (e) injection of polyester resin; (f) wetting of resin into the fiber preform and removing voids and excessive resin within the preform.

### *Decomposition of the FR<sub>22</sub> and DP<sub>22</sub> Branch*

After preprocessing the target conduits, the reinforcing element for repairing damaged pipes should be placed along the conduits. As shown in figure 15.40(b), one end of reinforcing element is connected to the wire and pulled by a winding machine, while lubricant (adhesive of suitable viscosity) is applied to the outer protection film of the reinforcing element to reduce the friction force.

Actually, the FR<sub>22</sub> and DP<sub>22</sub> branch is closely related to the installation of reinforcing element, and the decomposition of FR<sub>22</sub> can be stated as

FR<sub>221</sub>=Connect one end of the wire to the reinforcing element and the other end to the winding machine

FR<sub>222</sub>=Pull the reinforcing element into the conduits

FR<sub>223</sub>=Supply the lubricant to the outer protection film of the reinforcing element.

The DPs for satisfying the chosen FRs are

DP<sub>221</sub>=Wire

DP<sub>222</sub>=Winding machine

DP<sub>223</sub>=Lubricant supplier.

The design equation may then be expressed as the following matrix:

$$\begin{Bmatrix} \text{FR}_{221} \\ \text{FR}_{222} \\ \text{FR}_{223} \end{Bmatrix} = \begin{bmatrix} X & 0 & 0 \\ X & X & 0 \\ 0 & 0 & X \end{bmatrix} \begin{Bmatrix} \text{DP}_{221} \\ \text{DP}_{222} \\ \text{DP}_{223} \end{Bmatrix} \quad (15.42)$$

### *Decomposition of the FR<sub>23</sub> and DP<sub>23</sub> Branch*

After installation of the reinforcing element, both ends are closed, as shown in figure 15.40(c) using specially designed covers that are composed of a steel ring and an acryl disk, as shown in figure 15.41, in which the assembly method is also

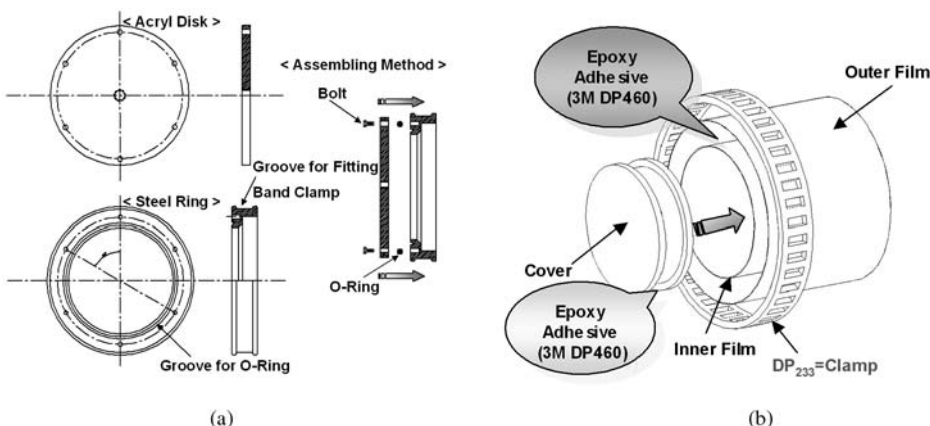


**Figure 15.41** Cover design and assembling method: (a) Detailed design of the cover (steel ring + acryl disk) and its assembling method; (b) sealing-clamping method of the covers and positions for pasting adhesive.

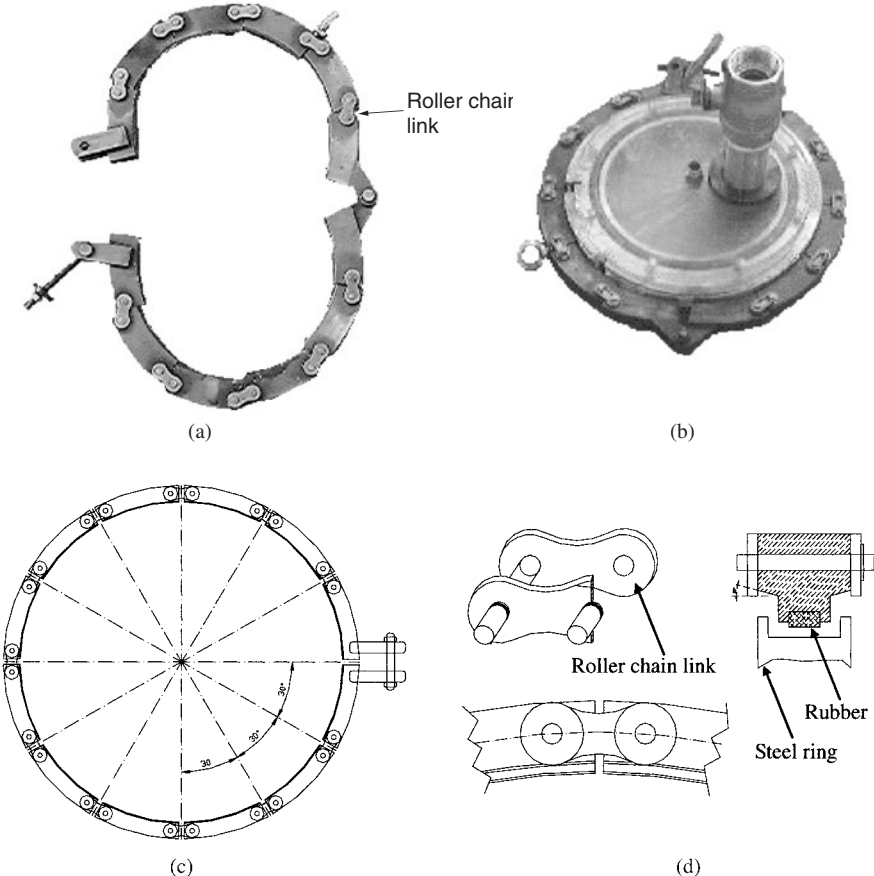


**Figure 15.42** Multijoint clamp: (a) Multijoint clamp with roller chain links; (b) assembly of cover and clamp; (c) detailed design of the multijoint clamp; (d) roller chain link and detailed design of joining part.

depicted. In order to seal the gap between the inner and outer protection film and to seal the internal cavity of reinforcing element, thermosetting adhesive (DP460, 3M) is pasted on the interfaces of two films, and a steel ring with a circumferential groove, which is abraded with 80-mesh sandpaper to increase the adhesion strength, is placed inside the inner protection film (Kwon and Lee, 2000). Then the multijoint clamp made of chain-links shown in figure 15.42 tightens the steel ring with inner and outer protection films that are fitted into the groove of the ring. From the chosen DP<sub>23</sub>, the decomposition of FR<sub>23</sub> can be performed as follows. The DPs for satisfying those FRs also are specified:

FR<sub>231</sub> = Seal the gap between the inner and outer protection films at the both ends of reinforcing element

FR<sub>232</sub> = Seal the internal cavity of reinforcing element

FR<sub>233</sub> = Clamp both ends in order to maintain the seal.

DP<sub>231</sub> = Thermosetting adhesive

DP<sub>232</sub> = Covers with circumferential groove

DP<sub>233</sub> = Multijoint clamp with chain-link.

The design equation of this branch may be expressed as

$$\left\{ \begin{array}{l} \text{FR}_{231} \\ \text{FR}_{232} \\ \text{FR}_{233} \end{array} \right\} = \begin{bmatrix} X & 0 & 0 \\ X & X & 0 \\ X & X & X \end{bmatrix} \left\{ \begin{array}{l} \text{DP}_{231} \\ \text{DP}_{232} \\ \text{DP}_{233} \end{array} \right\} \quad (15.43)$$

#### *Decomposition of the FR<sub>24</sub> and DP<sub>24</sub> Branch*

After sealing both ends of the reinforcing element, compressed air is supplied to the internal cavity through the air inlet of covers, which expands the inner protection film. This makes the outer protection film and fiber preform contact closely to the internal surface of the conduits, and removes wrinkles and twists in the reinforcing element that might occur during the placing operation, as shown in figure 15.40(d). Then the air pressure in the cavity is reduced to help the resin transfer by increasing the porosity of fiber reinforcement. The decomposition of the FR<sub>24</sub> and DP<sub>24</sub> branch gives

FP<sub>241</sub> = Connect the compressor to the cavity of reinforcing element

FR<sub>242</sub> = Apply the pressurized air to the cavity of reinforcing element

FR<sub>243</sub> = Reduce the air pressure in the cavity of reinforcing element.

DP<sub>241</sub> = Air inlet of cover

DP<sub>242</sub> = Compressor

DP<sub>243</sub> = Air vent of cover.

The design matrix of this branch is also a diagonal matrix.

#### *Decompositions of the FR<sub>25</sub> and DP<sub>25</sub> Branch*

After the air pressure in the cavity is reduced, a predetermined amount of unsaturated polyester resin is injected into the fiber preform with an RTM machine, which mixes the resin with a cure catalyst (MEKPO; methyl-ethyl-ketone-peroxide) at the predetermined rate. Since this RTM machine is actuated by high pneumatic pressure, equipment for supplying pressurized gas to the RTM machine is needed. In this study, high-pressure nitrogen gas was used. In order to supply the resin uniformly along the reinforcing element, a resin injection pipe with small pinholes is installed along the lower surface of reinforcing element, as shown in figure 15.43. This resin injection pipe can be easily removed by pulling out one end of the

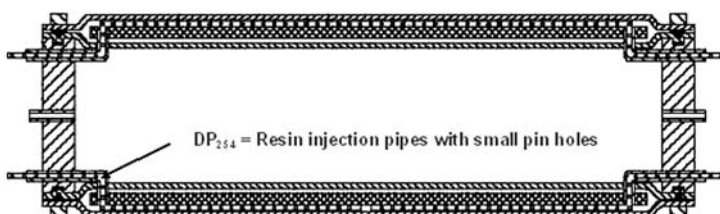


Figure 15.43 Resin injection pipes for uniform resin supply along the reinforcing element.

pipe before curing of resin. Decomposition of  $DP_{25}$  produces the following sub-FRs and DPs:

$FR_{251}$  = Mix the unsaturated polyester resin with the cure catalyst

$FR_{252}$  = Supply the unsaturated polyester resin

$FR_{253}$  = Actuate the RTM machine

$FR_{254}$  = Supply the resin uniformly along the reinforcing element.

$DP_{251}$  = RTM machine

$DP_{252}$  = Resin tank containing a predetermined amount of unsaturated polyester resin

$DP_{253}$  = Liquefied nitrogen vessel equipped with a vaporizer

$DP_{254}$  = Resin injection pipe with small pinholes, which is installed along the reinforcing element.

Then the design equation of this branch may be expressed as

$$\begin{Bmatrix} FR_{251} \\ FR_{252} \\ FR_{253} \\ FR_{254} \end{Bmatrix} = \begin{bmatrix} X & 0 & 0 & 0 \\ X & X & 0 & 0 \\ 0 & 0 & X & 0 \\ X & 0 & X & X \end{bmatrix} \begin{Bmatrix} DP_{251} \\ DP_{252} \\ DP_{253} \\ DP_{254} \end{Bmatrix} \quad (15.44)$$

This stage is shown in figure 15.40(e).

#### *Decomposition of the $FR_{26}$ and $DP_{26}$ Branch*

After injecting the unsaturated polyester resin, the RTM machine is separated from the reinforcing element. Then, compressed air is fed into the cavity to make the injected resin wet the glass-fiber preform uniformly, as well as making the reinforcing element contact closely the internal surface of the conduits, as shown in figure 15.40(f). This occurs while a vacuum is applied to the reinforcing element to help wet the resin and to remove the microvoids and excess resin within the fiber preform. For this, a porous breathing tube with small holes is inserted into the upper position of the reinforcing element, as shown in figure 15.44. This porous breathing tube can be removed easily in the same way that the resin injection pipe is removed. The resin reservoir, shown in figure 15.45, which is placed between the reinforcing element and a vacuum pump, prevents the excess resin from going into the vacuum pump directly and separates voids from the resin extracted through

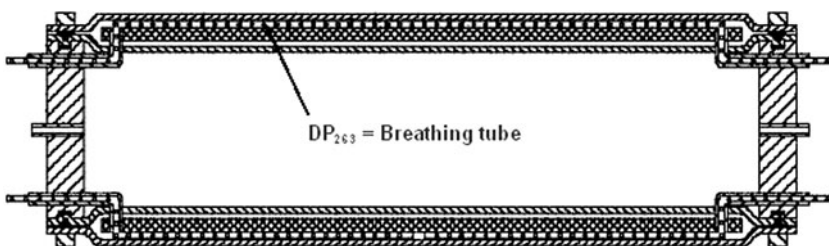
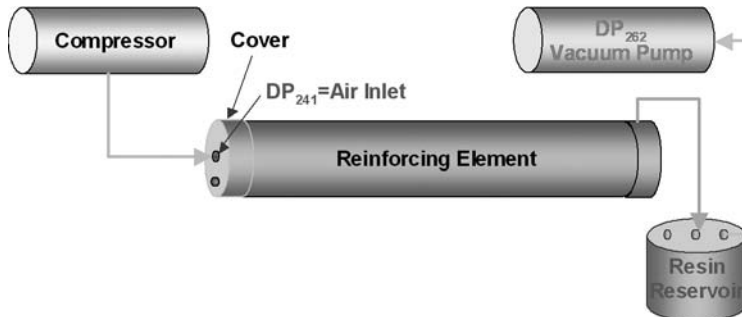


Figure 15.44 Porous breathing tube for removing microvoids and excess resin in the preform.



**Figure 15.45** Schematic diagram of resin wetting and void removal process.

the breathing tube. The decomposed FRs and DPs are

$FR_{261}$  = Pressurize the injected resin

$FR_{262}$  = Apply vacuum pressure to the reinforcing element

$FR_{263}$  = Remove the microvoids and excess resin within the fiber preform

$FR_{264}$  = Separate the voids from the extracted resin.

$DP_{261}$  = Compressor

$DP_{262}$  = Vacuum pump

$DP_{263}$  = Breathing tube

$DP_{264}$  = Resin reservoir.

The design equation of this branch is expressed as

$$\left\{ \begin{array}{c} FR_{261} \\ FR_{262} \\ FR_{263} \\ FR_{264} \end{array} \right\} = \begin{bmatrix} X & 0 & 0 & 0 \\ 0 & X & 0 & 0 \\ 0 & X & X & 0 \\ 0 & 0 & 0 & X \end{bmatrix} \left\{ \begin{array}{c} DP_{261} \\ DP_{262} \\ DP_{263} \\ DP_{264} \end{array} \right\} \quad (15.45)$$

#### *Decomposition of the $FR_{27}$ and $DP_{27}$ Branch*

When the excess resin and voids within the fiber preform are completely removed, the wetting of the fiber preform and the flow of resin through the breathing tube are ceased. Then, the curing of the resin should follow. In order to prevent the resin within the fiber preform from flowing down due to gravity, the air pressure of the cavity must be maintained, while increasing the temperature up to  $60^{\circ}\text{C}$ . The following statements show the decomposition of this branch, and the design matrix may be expressed as a diagonal matrix:

$FR_{271}$  = Maintain the air pressure in the cavity of reinforcing element

$FR_{272}$  = Increase the temperature of cavity up to  $60^{\circ}\text{C}$

$DP_{271}$  = Compressor with hot-air blower fan

$DP_{272}$  = Heater with hot-air blower fan.

#### 15.5.2 Application of the Developed Process

Using the developed repair process, several real construction experiments were performed in the concrete pipes that are used for underground applications, as



**Figure 15.46** Real construction experiment using concrete pipes and internal surface of repaired pipes: (a) The repaired concrete pipes; (b) internal surface of repaired concrete pipes.

**Table 15.15 Comparison of Repair Cost with Reverse-lining Process**

	Cost (US\$/m)				
	Material	Process	Extra	Total	Margin
RTM method	38	95	$\alpha$	$133 + \alpha$	85
In situ reverse-lining process	72	146	$\alpha$	$218 + \alpha$	

\*Material cost: reinforcing element, resin, adhesive, tubes, etc.

Extra cost: inspection, cleaning, perforation of junction, etc.

Repair cost of excavation technology: 380 US\$/m.

shown in figure 15.46. The diameters and the lengths of the three concrete pipes were 300 mm and 10 m, 600 mm and 10 m, and 600 mm and 30 m, respectively. From the experiments, it was possible to apply large three-dimensional composite reinforcement structures on the inner surfaces of these concrete pipes. Then, the comparison of repair cost and time with the in situ reverse lining process, the most representative trenchless technology, was carried out on the assumption that the extra cost such as inspection, cleaning, and perforation of junctions is same. The results of repairing the conduits of 300 mm diameter are shown in table 15.15.

From the results, it was found that the margin of repairing cost of the developed process is about US\$ 85, and the margin of repair time is about 16 hours. When compared with the excavation technology, this newly developed process could cut cost of excavation technology by more than 40%. If the diameter of the conduits is increased, the effect of cost saving will be further increased.

## 15.6 Concluding Remarks

In this chapter, three design examples of composite automotive components and an application of composite processing to trenchless repair of sewage pipes have been presented. In section 15.2, the design and fabrication example of a one-piece

hybrid propeller shaft composed of a carbon-fiber epoxy composite and an aluminum tube was presented. The hybrid shaft was manufactured by co-curing the composite to the aluminum shaft with an axial preload to the aluminum before co-curing to reduce thermal residual stresses. The hybrid propeller shaft was 50% lighter than the existing steel propeller shafts and the fundamental bending natural frequency of the hybrid propeller shaft was 9100 rpm, which was much higher than the required whirling vibration frequency of 8000 rpm. The average static torque transmission capability of the hybrid propeller shaft was 3600 Nm, which also satisfied the required torque capability of 3500 Nm, and the hybrid propeller shaft did not fail until  $10^7$  cycles under a dynamic torque of  $\pm 500$  Nm.

In section 15.3, the composite bumper beam for a subcompact passenger car was designed and manufactured based on the magnitude of the deceleration curves obtained during the front collision test of the car. From the force boundary conditions, the optimal cross-sectional dimensions and thickness of the composite bumper beam were determined to be 40 mm  $\times$  40 mm and 5.4 mm, respectively. The end of the bumper beam was designed to be tapered for the improvement of energy absorption characteristics by inducing progressive buckling during collision.

In section 15.4, a fiber-reinforced side-door impact beam for passenger cars was designed in order to reduce the weight compared with the conventional steel equivalent. Also the mechanical joint for the impact beam was designed to fail in a fiber shear-out mode in order to dissipate energy during collision. The static strength of the composite impact beam manufactured with this method was increased about 20% when the weight of the composite beam was 70% of the steel impact beam.

In section 15.5, a new trenchless repair process for retired or damaged underground pipes using RTM (resin transfer molding) and fiber-reinforced composite materials has been developed through the axiomatic design methodology. From the highest level of the FR and DP branch, decompositions were performed in consideration of many process variables and constraints. For a reliable repair process, the glass-fiber preform was covered with tarpaulin films that worked as a flexible mold and protection skin. A porous breathing tube was used to remove microvoids in the fiber preform, and a resin injection pipe with small pinholes was used to supply the resin to the fiber preform uniformly along the reinforcing element. The developed process was applied to real construction experiments, in which concrete pipes of large diameter and length were used. From the comparison of processing cost and processing time with the conventional trenchless rehabilitation technology, it was found that the developed process was very effective both in time and cost saving.

## References

- Adams, K. L., Russel, W. B., and Rebenfeld, L. 1988. "Radial Penetration of a Viscous Liquid into a Planar Anisotropic Porous Medium," *International Journal of Multiphase Flow*, Vol. 14, pp. 203–215.
- Advani, S. G. 1994. *Flow and Rheology in Polymer Composites Manufacturing*, Elsevier, New York, pp. 466–468.
- Barbero, E. J. 1998. "Construction," in *Handbook of Composites*, Edited by Peters, S. T., Chapman & Hall, London, pp. 982–1003.
- Beardmore, P. 1986. "Composite Structures for Automobiles," *Composite Structures*, Vol. 5, pp. 163–176.

- Camanho, R. P., and Matthews, F. L. 1997. "Stress Analysis and Strength Prediction of Mechanically Fastened Joints in FRP: a Review," *Composites Part A*, Vol. 28A, pp. 529–547.
- Chen, J. K., and Sun, C. T. 1985. "Analysis of Impact Response of Buckled Composite Laminates," *Composite Structures*, Vol. 3, pp. 97–118.
- Cheon, S. S., Choi, J. H., and Lee, D. G. 1995. "Development of the Composite Bumper Beam for Passenger Cars," *Composite Structures*, Vol. 32, pp. 491–499.
- Cheon, S. S., Lee, D. G., and Jeong, K. S. 1997. "Composite Side-Door Impact Beams for Passenger Cars," *Composite Structures*, Vol. 38, pp. 229–239.
- Cheon, S. S., Lim, T. S., and Lee, D.G. 1999. "Impact Energy Absorption Characteristics of Glass Fiber Hybrid Composites," *Composite Structures*, Vol. 46, pp. 267–278.
- Chin W. S., Kwon J. W., and Lee, D. G. 2003. "Trenchless Repairing of Underground Pipes Using RTM Based on the Axiomatic Design Method," *Journal of Composite Materials*, Vol. 37, No. 22, pp. 1109–1126.
- Cho, D. H., Lee, D. G., and Choi, J. H. 1997. "Manufacture of One-piece Automotive Drive Shafts with Aluinum and Composite Materials," *Composite Structures*, Vol. 38, pp. 309–319.
- Diallo, M. L., Gauvin, R., and Trochu, F. 1998. "Experimental Analysis and Simulation of Flow Through Multi-layer Fiber Reinforcements in Liquid Composite Molding," *Polymer Composites*, Vol. 19, pp. 246–256.
- Gaudenzi, P., Pascucci, A., Barboni, R., and Horoschenkoff, A. 1997. "Analysis of a Glass-Fibre Sandwich Panel for Car Body Constructions," *Composite Structures*, Vol. 38, pp. 421–433.
- Godwin, E. W., and Matthews, F. L. 1980. "A Review of Strength of Joints in Fibre-Reinforced Plastics," *Composites*, Vol. 11, pp. 155–160.
- Golestanian, H., and El-Gizawy, A. S. 1998. "Physical and Numerical Modeling of Mold Filling in Resin Transfer Molding," *Polymer Composites*, Vol. 19, pp. 395–407.
- He, S., and Rao, M. D. 1994. "Residual Stresses and Delamination Problems Induced by Co-curing of Damped Composite Laminates," *Journal of Composite Materials*, Vol. 28, No. 2, pp. 112–129.
- Hertzberg, R.W. 1996. *Deformation and Fracture Mechanism of Engineering Materials*, 4th ed., John Wiley & Sons, Chichester.
- Kim, Y. K., and Daniel, I. M., "Cure Cycle Effect on Composite Structures Manufactured by Resin Transfer Molding," *Journal of Composite Materials*, Vol. 36, pp. 1725–1743, 2002.
- Kurz, G. E., Anderson, D. J., and Burgett, M. A. 1997. "SSO and I/I Reduction Using Sewer Rehabilitation," *Proceedings of the Construction Congress V—Managing Engineered Construction in Expanding Global Markets*, Vol. 1, ASCE, Minneapolis, Minn., October 5–9.
- Kwon, J. W., and Lee, D. G. 2000. "The Effects of Surface Roughness and Bond Thickness on the Fatigue Life of Adhesively Bonded Tubular Single Lap Joints," *Journal of Adhesion Science and Technology*, Vol. 14, No. 8, pp. 1085–1102.
- Lal, K. M. 1983. "Low Velocity Transverse Impact Behavior of 8-ply Graphite-Epoxy Laminates," *Journal of Reinforced Plastics and Composites*, Vol. 2, pp. 216–225.
- Lee, D. G., and Cheon, S. S. 2001. "Impact Characteristics of Glass Fiber Composites with respect to Fiber Volume Fraction," *Journal of Composite Materials*, Vol. 35, pp. 27–56.
- Lee, D. G., Kim, K. S., and Kwak, Y. K. 1991. "Manufacturing of a SCARA-Type Direct-Drive Robot with Graphite/Epoxy Composite Materials," *Robotica*, Vol. 9, pp. 219–229.
- Lee, D. G., Lim, T. S., and Cheon, S.S. 2000. "Impact Energy Absorption Characteristics of Composite Structures," *Composite Structures*, Vol. 50, pp. 381–390.
- Lee, D. G., Chin, W. S., Kwon, J. W., and Yoo, A. K. 2002. "Repair of Underground Buried Pipes with RTM," *Composite Structures*, Vol. 57, pp. 67–77.

- Lim, T. S., and Lee, D. G. 2002. "Mechanically Fastened Composite Side-Door Impact Beams for Passenger Cars Designed for Shear-Out Failure Modes," *Composite Structures*, Vol. 56, pp. 211–221.
- Liu, D., Raju, B. B., You, J. 1999. "Thickness Effects on Pinned Joint for Composites," *Journal of Composite Materials*, Vol. 33, pp. 2–21.
- Mallick, P. K. 1988. *Fiber-Reinforced Composites*, Marcel Dekker, New York.
- Mallick, P. K. 1997. "Introduction: Definitions, Classifications, and Applications," in *Composites Engineering Handbook*, Edited by Mallick, P. K., Marcel Dekker, New York, pp. 1–50.
- Mallick, P. K., and Broutman, L. J. 1977. "Static and Impact Properties of Laminated Hybrid Composites," *Journal of Testing and Evaluation*, Vol. 5, pp. 190–200.
- Mallick, P. K., and Newman, S. 1990. *Composite Materials Technology*, Hanser Publishers, New York, Chapter 6.
- Margolis, J. M. 1986. *Advanced Thermoset Composites*, Van Nostrand Reinhold Company, New York.
- Minaie, B., Chen, Y. F., and Mescher, A. M. 2002. "A Methodology to Obtain a Desired Filling Pattern during Resin Transfer Molding," *Journal of Composite Materials*, Vol. 36, pp. 1677–1692.
- Oh, J. H., Kim, Y. G., and Lee, D. G. 1997. "Optimum Bolted Joints for Hybrid Composite Materials," *Composite Structures*, Vol. 38, pp. 321–328.
- Park, H. J. 2001. "Effects of Stacking Sequence and Clamping Force on the Bearing Strength of Mechanically Fastened Joints in Composite Laminates," *Composite Structures*, Vol. 53, pp. 213–221.
- Pillai, K. M., and Advani, S. G. 1998. "Numerical Simulation of Unsaturated Flow in Woven Fiber Preform During the Resin Transfer Molding Process," *Polymer Composites*, Vol. 19, No. 1, pp. 71–80.
- Ramakrishna, S., Hamada, H., and Nishiwaki, M. 1995. "Bolted Joints of Pultruded Sandwich Composite Laminates," *Composite Structures*, Vol. 32, pp. 227–235.
- Rao, M. D., and He, S. 1993. "Dynamic Analysis and Design of Laminated Composite Beams with Multiple Damping Layers," *AIAA Journal*, Vol. 31, No. 4, pp. 736–745, 1993; *AIAA Journal of Composite Materials*, Vol. 24, No. 4, pp. 92–102.
- Reimpell, J., and Stoll, H. 1996. *The Automotive Chassis*, Society of Automotive Engineers, Chapter 1.
- Schmelz, F., Seherr-Thoss, C., and Aucktor, E. 1992. *Universal Joints and Driveshafts*, Springer-Verlag, Berlin, Chapter 4.
- Schmueser, D. W., and Wickliffe, L. E. 1987. "Impact Energy Absorption of Continuous Fiber Composite Tubes," *Journal of Engineering Materials and Technology*, Vol. 109, pp. 72–77.
- Skordos, A. A., Karkanas, P. I., and Partridge, I. K. 2000. "A Dielectric Sensor for Measuring Flow in Resin Transfer Moulding," *Measurement Science and Technology*, Vol. 11, pp. 25–31.
- Smith, P. A., Pascoe, K. J., Polak, C., and Stroud, D. O. 1986. "The Behavior of Single-Lap Bolted Joint in CFRP Laminates," *Composite Structures*, Vol. 6, pp. 42–55.
- Suh, N. P. 2001. *Axiomatic Design*, Oxford University Press, New York.
- Sun, C. T., and Chattopadhyay, S. 1975. "Dynamic Response of Anisotropic Plates Under Initial Stress due to Impact Mass," *Journal of Applied Mechanics*, Vol. 42, pp. 693–698.
- Thornton, P. H., and Jeryan, R. A. 1988. "Crash Energy Management in Composite Automotive Structures," *International Journal of Impact Engineering*, Vol. 7, 167–180.
- Trent, J. S. 1998. "Rehabilitation of Existing Sewers and Conduits Using Folded/Formed Poly Vinyl Chloride (PVC) Pipe," *Proceedings of the Vinyl Technical Conference*, SPE, pp. 65–69.
- Turvey, G. L. 1998. "Single-Bolt Tension Joint Tests on Pultruded GRP Plate—Effects of Tension Direction Relative to Pultrusion Direction," *Composite Structures*, Vol. 42, pp. 341–351.

- Weeton, J. W., Peters, D. M., and Thomas, K. L. 1986. "Engineer's Guide to Composite Materials," *American Society for Metals*, Section 4.
- Williams, J. G. 1988. "On the Calculations of Energy Release Rates for Cracked Laminates," *International Journal of Fracture*, Vol. 36, pp. 101–119.
- Wilson, B. A. 1998. "Pultrusion," in *Handbook of Composites*, Edited by Peters, S. T., Chapman & Hall, London.

## Glossary

### A

**Abrasion** A process where hard particles are forced against and moved along a solid surface.

**Abrasive** A hard and wear-resistant material (commonly a ceramic) that is used to wear, grind, or cut away other material.

**Abrasive belt** A grinding belt composed of an abrasive grit and binding agent.

**Abrasive particle** The abrasive particles commonly used are emery, corundum, quartz, garnet, aluminum oxide, silicon carbide, cubic boron nitride, and diamond.

**Abrasive water jet machining** A machining process that uses a water jet with fine abrasives added. The abrasives are added after the stream has left the jet orifice.

**Absorption** The penetration into the mass of one substance by another. The process whereby energy is dissipated within a specimen placed in a field of radiant energy. The capillary or cellular attraction of adherend surfaces to draw off the liquid adhesive film into the substrate.

**Acrylic** Polymers of acrylic or methacrylic esters, sometimes modified with non-acrylic monomers, such as the ABS groups. The acrylates may be methyl, ethyl, butyl, or 2-ethylhexyl. Usual methacrylates are methyl, ethyl, butyl, lauryl, and stearyl. The resins may be in the form of molding powders or casting syrups, and are noted for their exceptional clarity and optical properties. Acrylics are widely used in lighting fixtures because they are either slow burning or self-extinguishing, and do not produce harmful smoke or gases in the presence of flame.

**Addition polymerization** A chemical reaction in which simple molecules (monomers) are added to each other to form long-chain molecules (polymers) without forming by-products.

**Additives** Any substance added to another substance, usually to improve properties of plastics, such as plasticizers, initiators, light stabilizers, and flame retardants.

**Adherend** A body that is held to another body, usually by an adhesive. A detail or part prepared for bonding (also called substrate).

**Adhesion** The state in which two surfaces are held together at an interface by mechanical or chemical forces or interlocking action or both.

**Adhesive** A substance capable of holding two materials together by surface attachment. Adhesive can be in film, liquid, or paste form.

**Adhesive joint** The location at which two adherends or substrates are held together with a layer of adhesive. The general area of contact for a bonded structure.

**Air bearings** Bearings that utilize a thin film of high pressure to support a load.

**Air spindle** A spindle that employs air bearings to resist the applied load.

**Alumina** Any of various forms of aluminum oxide occurring naturally, such as corundum.

**Alumina trihydrate** A white powder insoluble in water, soluble in hydrochloric or sulfuric acid or sodium hydroxide, which is used in the manufacture of ceramic glasses and in paper coating. ( $\text{Al}_2\text{O}_3 \cdot 3\text{H}_2\text{O}$  or  $\text{Al}(\text{OH})_3$ .)

**Aluminum oxide fiber** Short, linear crystals of alumina, which have strength of up to 1.5 GPa.

**Angular-contact ball bearings** Bearings designed to support combined radial and thrust loads, or heavy thrust loads, depending on the contact angle magnitude.

**Anisotropic** Not isotropic. Exhibiting different properties when tested along axes in different directions.

**Anthropomorphic** Used to describe artifacts, art work, or a robot decorated with human features or with a human-like appearance.

**Aramid fiber** Artificial fiber in which the fiber-forming substance is a long-chain synthetic aromatic polyamide in which at least 85% of the amide linkages are directly attached to two aromatic rings. Commercial name "Kevlar" (DuPont).

**Articulated robot** A robot that has all three revolute joints.

**Arithmetic surface roughness** The average deviation of an individual point, measuring heights and depths from the arithmetic mean elevation of the surface profile ( $R_a$ ).

**Aromatic** Unsaturated hydrocarbon with one or more benzene ring structures in the molecule.

**Arrhenius dependence** The relationship whereby the specific reaction rate constant is proportional to  $\exp(-\Delta E_{\text{act}}/RT)$ , where  $\Delta E_{\text{act}}$  is the activation energy,  $R$  the gas constant, and  $T$  absolute temperature.

**Aspect ratio** The ratio of length to diameter (of a fiber).

**Auger electron spectroscopy (AES)** Method to examine the chemistry of a surface by measuring the energy of electrons emitted from that surface when it is irradiated with electrons of energy in the range 2–50 keV. Some of the electrons emitted from the surface have energies characteristic of the element from which they were emitted, and in some cases, the bonding state of those atoms.

**Autoclave** A closed vessel for conducting and completing a chemical reaction or other operation under pressure, vacuum, and heat.

**Autoclave molding** A composite manufacturing process in which, after lay-up, winding, or wrapping of composite preprints or polymer charges, an entire assembly is placed in a heated autoclave, usually at 0.34 to 1.38 MPa (50–200 psi) to complete the cure or consolidation of composites or polymers. Additional pressure permits higher density and improved removal of volatiles from the resin. The lay-up is usually vacuum bagged with a bleeder and release cloth (vacuum bag degassing process).

**Automotive composite propeller shaft** A composite shaft that connects the transmission output shaft to the differential pinion shaft (usually one piece rather than the two pieces in steel propeller shafts).

**B**

**Balanced laminate** A composite laminate in which all laminate at angles other than 0° and 90° occur only in opposing pairs (not necessarily adjacent) that are symmetrical around the centerline.

**Batch process** A quantity of materials formed during the same process or in one continuous process and having identical characteristics throughout. Also called a “lot”.

**Benzene rings** The basic structure of benzene, which is the most important aromatic chemical. It is an unsaturated, resonant carbon ring having three double bonds. One or more of the six hydrogen atoms of benzene may be replaced by other atoms or groups.

**Benzoquinone** Any of a class of aromatic yellow compounds that are biologically important as coenzymes or acceptors or vitamins used in making dyes.

**Benzoyl peroxide** A white crystalline peroxide used in bleaching (flour, oils, or fats) and as a catalyst for free-radical reactions.

**Bias** Partiality that prevents objective consideration of an issue or situation.

**Bismaleimide (BMI)** A type of polyimide that cures by addition rather than condensation reaction, thus avoiding problems with volatile formation, and which is produced by a vinyl-type polymerization of a prepolymer terminated with two maleimide groups. Intermediate in temperature capability between epoxy and polyimide.

**Bleeder papers** A woven or nonwoven layer of material used in the manufacture of composite parts to allow the escape of excess gas and resin during cure. The bleeder cloth is removed after the curing process and is not part of the final composite.

**Blowing agents** A compounding ingredient used to produce gas by chemical or thermal action, or both, in the manufacture of hollow or cellular articles.

**Break-out** Fiber separation or break on surface plies at drilled or machined edges.

**B-stage** A secondary stage in the reaction of some thermosetting resins, characterized by softening of the resin when heated, without being completely fused or dissolved. The B-stage is also characterized by a progressive increase in viscosity. The resin portion of an uncured thermosetting adhesive or prepreg is usually in this stage. (Also called resitol.)

**Buckling** A mode of failure generally characterized by an unstable lateral material deflection due to compressive action on the structural element involved.

**Buckminster fullerene** A type of carbon nanotube.

**Bulk modulus** The ratio of the hydrostatic pressure to the volume strain.

**Butt joint** A type of edge joint in which the edge faces of the two adherends are at right angles to the other faces of the adherends.

**C**

**Calcium carbonate** A salt found in nature as chalk, calcite, or limestone.

**Cantilever beam** Beam supported at one end only.

**Capacitance** The property of a system of conductors and dielectrics that permits the storage of electricity when a potential difference exists between the conductors. Its value is expressed as the ratio of the quantity of electricity to the potential difference.

**Compressive strength after impact (CAI)** A test method for the impact damage of a composite structure by measuring the decrease of compressive strength of the impacted structure.

**Carbon** The element that provides the backbone for all organic polymers. Graphite is a more ordered form of carbon. Diamond is the densest crystalline form of carbon.

**Carbon black** A black pigment produced by the incomplete burning of natural gas or oil. It is widely used as filler, particularly in the rubber industry. Because it possesses useful ultraviolet protective properties, it is also much used in molding compounds intended for outside weathering applications.

**Carbon fiber** Fiber produced by the pyrolysis of organic precursor fibers, such as rayon, polyacrylonitrile (PAN), and pitch, in an inert environment. The term is often used interchangeably with the term graphite fiber. See **pyrolysis**.

**Catalyst** A substance that changes the rate of a chemical reaction without itself undergoing permanent change in composition or becoming a part of the molecular structure of the product.

**Catastrophic failure** Totally unpredictable failure of a mechanical, thermal, or electrical nature.

**Cavity channel** Passage of resin or cooling water in a mold.

**Centrifugal force** The outward force on a body moving in a curved path around another body.

**Ceramic** A rigid, frequently brittle material made from clay and other inorganic, nonmetallic substances and fabricated into articles by sintering, that is, cold molding followed by fusion of the part at high temperature.

**Charge** The raw material placed in the mold in compression molding. The quantity of unbalanced electricity in a body (either positive or negative) and construed as an excess or deficiency of electrons.

**Charpy test** A test for shock loading in which a centrally notched sample bar is held at both ends and broken by striking the back face in the same plane as the notch.

**Chatter** The rapid series of noises made by the parts of a machine.

**Chemical vapor deposition** Process used in manufacture of several composite reinforcements, especially boron and silicon carbide, in which the desired reinforcement material is deposited from the vapor phase onto a continuous core, for example, boron on tungsten wire (core).

**Coal tar pitch** A by-product of the distillation of coal tar, used especially in making road surfaces, and in carbon electrodes.

**Coefficient of friction** A measure of the resistance to sliding of one surface in contact with another surface.

**Coefficient of hygroscopic expansion (CHE)** The change in length per unit length produced by unit concentration increase in moisture.

**Coefficient of thermal expansion (CTE)** The change in length per unit length produced by unit rise in temperature.

**Column** A structure subjected to a compressive load in the axial direction.

**Compaction** The application of pressure and vacuum to the vacuum bag to remove trapped air and compact the composite lay-up.

**Compensation** An addition of specific materials or devices to counteract a known error.

**Complex modulus** The ratio of stress to strain in which each is a vector that may be represented by a complex number.

**Compliance** Tensile compliance is the reciprocal of Young's modulus. Shear compliance is the reciprocal of shear modulus. The term is also used in the evaluation of stiffness and deflection.

**Composite boring bar** A machine tool structure with a stiff bar made of composite materials that has multiple cutting bits and is used to make holes, such as in engine cylinders.

**Composite materials** A combination of two or more materials (reinforcing elements, fillers, and matrix binder), differing in form or composition on a macroscale. The constituents retain their identities; that is, they do not dissolve or merge completely into one another, although they act in concert. Normally, the components can be physically identified and exhibit an interface between one another.

**Composite propeller shaft** A propeller shaft made of fiber-reinforced composite in which the fibers are usually glass and/or carbon and made possibly in a single piece.

**Composite rotor** The rotating armature of a motor or generator made of composite material.

**Compressive strength** The ability of a material to resist a force that tends to crush or buckle. The maximum compressive load sustained by a specimen divided by the original cross-sectional area of the specimen.

**Concurrent engineering** Product design that considers all stages of a product from its conception to its eventual withdrawal from the market.

**Condensation polymerization** A chemical reaction in which two or more molecules combine, with the separation of water or some other simple substance. If a polymer is formed, the process is called polycondensation.

**Conductivity** Reciprocal of volume resistivity. The electrical or thermal conductance of a unit cube of any material (conductivity per unit volume).

**Consolidation** In metal matrix or thermoplastic composites, a processing step in which fiber and matrix are compressed by one of several methods to reduce voids and achieve desired density.

**Core** Foam or honeycomb of a sandwich construction to which the faces of the sandwich structure are attached or bonded. A channel in a mold for circulation of heat transfer media. A device on which prepreg is wound.

**Corollary** An inference that follows directly from the proof of another proposition.

**Creep property** The change in dimension of a plastic or metal under a given load and temperature over a period of time, not including the initial instantaneous elastic deformation.

**Cross-ply** A laminate composed of  $0^\circ$  and  $90^\circ$  plies only.

**Crystal** A solid formed by the solidification of a chemical and having a highly regular atomic structure.

**Cumulative distribution function for survival** See **reliability**.

**Cure** Irreversible change in the properties of a thermosetting resin by chemical reaction, that is, condensation, ring closure, or addition. Cure may be accomplished by addition of curing (cross-linking) agents, with or without heat and pressure.

**Cure monitoring** Techniques to detect changes in the properties of the resin molecules during cure.

**Curing agent** A catalytic or reactive agent that, when added to a resin, causes polymerization. Also called hardener.

**Curvature** The amount by which a curve, surface, or other manifold deviates from a straight line or (hyper) plane.

**Customer attributes** Anything that customers want to have in the product.

## D

**Damage tolerance design** Cracks in damage-tolerant-designed structures are not permitted to grow to critical size during expected service life.

**Damping** The decay of the amplitude of free vibrations of a specimen with time or energy consumption ratio of structure to its potential energy. Damping terms can be calculated using many methods. (See appendix B in chapter 14.)

**Darcy's law** Flow equation for porous medium.

**Degradation** A deleterious change in the chemical structure, physical properties, or appearance of a plastic or composite.

**Delamination** Separation of the layers of material in a laminate, either local or covering a wide area.

**Diagonal matrix** Square matrix with all off-diagonal elements equal to zero.

**Die sinking method** Process used in EDM or ECM.

**Dielectric constant** A relative measurement of the degree of polarization (shift of positive charge toward the negative electrode and negative charge toward the positive electrode) that occurs when a material is placed in an electric field.

**Dielectric material** A nonconducting material of electricity.

**Dielectric strength** The ability of a material to resist the flow of an electrical current.

**Dielectrometry** Use of electrical techniques to measure the changes in loss factor (dissipation) and in capacitance during cure of the resin in a laminate.

**Dielectrometry interdigital sensor** A dielectric sensor with many small electric lines.

**Diethylene triamine (DETA)** A yellow, hygroscopic liquid with a boiling point of 206.7°C.  $(\text{NH}_2\text{C}_2\text{H}_4)_2\text{NH}$ .

**Differential scanning calorimetry (DSC)** Device to measure the heat evolved in a curing reaction and relate it to the degree of cure achieved at any time during the curing process. Measuring is performed using a small sample of few milligrams, heating either isothermally (at constant temperature) or dynamically (with uniformly increasing temperature).

**Diluent** In an organosol, a liquid component that has little or no solvating action on the resin. The term diluent is commonly used in place of the term plasticizer.

**Direct-drive manipulator** Manipulator whose joints are driven directly by actuators without speed reducers.

**Dissipation factor** The ratio of the power loss in a dielectric material to the total power transmitted through the dielectric. Also called electrical dissipation factor.

**Double cantilever beam (DCB) test** Specimen type frequently employed for test of delamination.

**Drainage** Removal of liquid due to the reduced pressure.

**Drop-weight impact tester** Impact tester using a falling weight accelerated by either gravity, or a pneumatic or hydraulic cylinder.

**Dry grinding** A grinding process without using cutting fluid.

**Dry spot** An area without resin or deficiency of resin in the composite.

**Dry winding** A term used to describe filament winding using preimpregnated roving. To be differentiated from **wet winding**, where unimpregnated roving is pulled through a resin bath just before being wound onto a mandrel.

**Ductility index** Measuring index for the ductility of material.

**Duhamel integral method** Method for the integration of continuously varying function.

**Dwelling time** The time required to maintain a constant temperature to squeeze out the excess resin in the composite laminate.

**Dynamic amplification factor** See **quality factor**.

**Dyneema** Polyethylene fiber produced by DSM (Dutch State Miners).

## E

**Eccentricity** Circularity around a noncentral point or deviation from a circular path.

**Eddy current** An induced electric current circulating wholly within a mass of metal.

**E-Glass** A family of glasses with a calcium alumino borosilicate composition and a maximum alkali content of 2.0%. A general purpose fiber that is most often used in reinforced plastics, and is suitable for electrical laminates because of its high resistivity. Also called electric glass.

**Electro-discharge machining (EDM)** Machining technique by electric discharge for extremely hard materials or materials that are difficult to machine cleanly using conventional methods.

**Electron spectroscopy for chemical analysis (ESCA)** See **X-ray photoelectron spectroscopy (XPS)**.

**End** A strand of roving consisting of a given number of filaments gathered together. The group of filaments is considered an “end” or strand before twisting, a “yarn” after twist has been applied.

**End effector of a robot** Device attached at the output link of a mechanical manipulator to grasp, lift, and manipulate workpieces.

**Epoxy resin** A thermosetting resin used chiefly in strong adhesives and coatings and laminates.

**Ethylene** A flammable colorless gaseous alkene that is obtained from petroleum and natural gas and used in manufacturing many other chemicals.

**Eutectic** A mixture of substances having a minimum melting point.

**Exothermic reaction** A chemical reaction accompanied by the evolution of heat.

## F

**Fastener** Component used for joining several structures such as screws, bolts and nuts, and rivets.

**Fatigue** The failure or decay of mechanical properties after repeated applications of stress. Fatigue tests give information on the ability of a material to resist the development of cracks, which eventually bring about failure as a result of a large number of cycles.

**Fiber** A general term used to refer to filamentary materials. Often, fiber is used synonymously with filament. It is a general term for a filament with a finite length that is at least 100 times its diameter, which is typically 0.10–0.13 mm

(0.004–0.005 in.). In most cases it is prepared by drawing from a molten bath, spinning, or deposition on a substrate. A whisker, on the other hand, is a short single-crystal fiber or filament made from a wide variety of materials, with diameters ranging from 1 to 25  $\mu\text{m}$  (40 to 980  $\mu\text{in.}$ ) and aspect ratio (length/diameter) between 100 and 15,000. Fibers can be continuous or short lengths (discontinuous), normally no less than 3.2 mm (1/8 in.).

**Filament winding** A process for fabricating a reinforced plastic or composite structure in which continuous reinforcements (filament, wire, yarn, or tape) either previously impregnated (dry winding) with a matrix material or impregnated (wet winding), are placed over a rotating mandrel in a prescribed way to meet certain stress conditions.

**Filler** A relatively inert substance added to a material to alter its physical, mechanical, thermal, electrical, and other properties or to lower cost or density. Sometimes the term is used specifically to mean particulate additives.

**Flame retardants** Certain chemicals that are used to reduce or eliminate the tendency of a resin to burn.

**Flange** Horizontal member of an I-beam or box-type beam.

**Flank wear** Wear on the relief face of the tool due to rubbing of the tool along the machined surface, which causes adhesive and abrasive wear.

**Flexibilizer** An additive that makes a finished plastic more flexible or tough. Also called **plasticizer**.

**Flex spline** A thin circular member with many small teeth in a harmonic drive.

**Flexural stiffness** The ratio, within the elastic limit, of the applied stress on a test specimen in flexure to the corresponding strain in the outermost fibers of the specimen. Also called flexural modulus.

**Flow** The movement of resin under pressure, allowing it to fill all parts of a mold. The gradual but continuous distortion of a material under continued load, usually at high temperatures, also called creep.

**Formaldehyde** A gas at room temperature, and a poisonous, clear, colorless liquid solution with pungent odor used to make synthetic resins by reaction with phenols, urea, and melamine. HCHO.

**Fracture** The separation of a body. Defined both as rupture of the surface without complete separation of laminate and as complete separation of a body because of external or internal forces.

**Fracture toughness** A measure of the damage tolerance of a material containing initial flaws or cracks.

**Free-machining steels** Steels with added lead and sulfur to improve their machinability.

**Friction** See **coefficient of friction**.

**Fundamental natural bending frequency** The lowest natural frequency of a structure.

## G

**Galvanic corrosion** Electrochemical corrosion associated with the current in a galvanic cell, caused by dissimilar metals in an electrolyte because of the difference in potential (EMF) of two metals.

**Gamma irradiation** Exposure of a material to gamma rays.

**Gaussian distribution** Normal distribution.

**Glass fiber** A fiber melt, spun from various types of glasses, that is cooled to a rigid condition without crystallizing.

**Glass transition temperature ( $T_g$ )** The approximate midpoint of the temperature range over which the glass transition takes place. Glass and silica fiber exhibit a phase change at approximately 955°C (1750°F) and carbon or graphite fibers at 2205–2760°C (4000–5000°F). The temperature at which increased molecular mobility results in significant changes in the properties of a cured resin system. Also, the inflection point on a plot of modulus versus temperature. The measured value of  $T_g$  depends to some extent on the test method.

**Graphite fiber** A fiber made from a precursor by oxidation, carbonization, and graphitization process (which provides a graphitic structure). See also **carbon fiber**.

**Graphitization** The process of pyrolyzation in an inert atmosphere at temperatures in excess of 1925°C (3500°F), usually as high as 2480°C (4500°F), and sometimes as high as 5400°C (9750°F), converting carbon to its crystalline allotropic form. Temperature depends on precursor and properties desired.

## H

**Hand of the robot** End effector of the robot handling LCD panels.

**Harmonic drive** A drive system that uses inner and outer gear bands to provide smooth motion with a very high speed reduction ratio, usually higher than 100.

**Heat-affected zone (HAZ)** Area of a material in which the microstructure or property is different from that of rest material due to elevated temperature during welding, laser cutting, and grinding.

**Heat deflection temperature (HDT)** The temperature at which a standard test bar deflects a specified amount under a stated load.

**Helical winding** In filament wound items, a winding in which a filament band advances along a helical path, not necessarily at a constant angle except in the case of a cylinder.

**Hexamethylene tetramine** A white, crystalline powder, melting at 280°C used to make synthetic resins. It is also called cystamine.  $(\text{CH}_2)_6\text{N}_4$ .

**Homogeneous** Descriptive term for a material of uniform composition throughout. A medium that has no internal physical boundaries. A material whose properties are constant at every point, that is, constant with respect to spatial coordinates (but not necessarily with respect to directional coordinates).

**Honeycomb** Manufactured product of resin-impregnated sheet material (paper, glass fabric, etc.) or metal foil, formed into hexagonal cells. Used as a core material in composite sandwich construction.

**Hybrid composite** A composite made of two different fibers or matrices, such as glass fiber and carbon fiber in an epoxy matrix.

**Hydroquinone** White crystals that melt at 170°C and boil at 285°C, soluble in alcohol, ether, and water. It is used in photographic dye chemicals, in medicine as an antioxidant and inhibitor, and in paints, varnishes, and motor fuels and oils.

**Hygroscopic** Property related to expansion due to water absorption.

**Hygrothermal** Property related to expansion due to water absorption and temperature rise.

**I**

**Ignition loss method** Measuring method of fiber or filler content by burning off matrix, binder, or size.

**Impulse dynamic test (impulse response test)** Measuring method of dynamic characteristics (frequency, damping, and transfer function) of structure by giving an impulse to the structure and measuring its response.

**Information axiom** Design axiom that states that the design with the highest probability of success has the lowest information content.

**Inhibitor** A substance that retards a chemical reaction. It is used in certain types of monomers and resins to prolong storage life.

**Initiator** Peroxides used as sources of free radicals. They are used in free-radical polymerizations for curing thermosetting resins. Cross-linking agents for elastomers and polyethylene, and for polymer modification.

**Injection molding** Method of forming a plastic to the desired shape by forcing the melted plastic into a relatively cool cavity under high pressure.

**Insulator** A material of such low electrical conductivity that the flow of current through it can usually be neglected. Similarly, a material of low thermal conductivity, such as that used to insulate structural shells.

**Interlaminar** Descriptive term pertaining to an object (e.g., voids), event (e.g., fracture), or potential field (e.g., shear stress) referenced as existing or occurring between two or more adjacent laminas.

**Internal mold release agent** Substance of low melting temperature mixed with the material before molding. It melts at the mold temperature and works as a lubricant during demolding of product.

**Ion-scattering spectroscopy (ISS)** A spectroscopic technique in which a low-energy (about 1000 eV) beam of inert gas ions is directed at a surface, and the energies and scattering angles of the scattered ions are used to identify surface atoms.

**Isophthalic acid** Colorless crystals that sublime at 345°C, slightly soluble in water, soluble in alcohol and acetic acid, and insoluble in benzene. It is used as an intermediate for polyester and polyurethane resins, and as a plasticizer.  $C_6H_4(COOH)_2$ .

**Isotropic** Having uniform properties in all directions. The measured properties of isotropic material are independent of the axis of testing.

**Izod impact test** A test to determine the resistance of a material to a shock loading, in which a notched specimen bar is held at one end and broken by striking, and the energy absorbed is measured.

**K**

**Kevlar** See aramid fiber.

**L**

**LCD** Liquid crystal display.

**Loss factor  $\eta$**   $\eta = \Delta W/(2\pi)/W = (\text{Energy dissipated during one cycle of harmonic displacement/radian})/(\text{Maximum strain energy in cycle})$ .

**Low-profile resins** Special polyester resin systems for reinforced plastics that are combinations of thermoset and thermoplastic resins. Although the terms low-profile and low-shrink are sometimes used interchangeably, there is a difference. Low-shrink resins contain up to 30 wt% thermoplastic polymer, while low-profile resins contain from 30 to 50 wt%. Low-shrink offers surface waviness in the molded part as low as 25  $\mu\text{m}$ , while low profile offers surface waviness less than 12.7  $\mu\text{m}$ .

## M

**Macromechanics** Mechanics that treat the material behavior at the lamina level.

**Maleic anhydride** A caustic crystalline cyclic anhydride used especially in making resins.  $\text{C}_4\text{H}_2\text{O}_3$ .

**Mandrel** Any of various rotating shafts that serve as axes for larger rotating parts.

**Material removal rate** Material that is cut away per unit time in the machining process.

**Matrix** The essentially homogeneous resin or polymer material in which the fiber system of the composite is embedded. Both thermoplastic and thermoset resins may be used, as well as metals, ceramics, and glasses.

**MEKPO** See **Methyl ethyl ketone peroxide**.

**Mesophase** An intermediate phase in the formation of carbon from a pitch precursor. This is a liquid crystal phase in the form of microspheres, which upon prolonged heating above 400°C (750°F) coalesce, solidify, and form regions of extended order. Heating to above 2000°C (3630°F) leads to the formation of a graphite structure.

**Methyl ethyl ketone peroxide (MEKPO)** The most common ambient-temperature cure system, known as a catalyst.

**Methylene chloride** A nonflammable liquid used as a solvent and paint remover and refrigerant.

**Microcellular plastics** Plastics that have a large number of uniformly sized, microscale bubbles of less than 30  $\mu\text{m}$  in a polymeric matrix.

**Micromechanics** Mechanics that treat the material behavior at the level of fiber and matrix.

**Moisture absorption** The pickup of water vapor by a material.

## N

**Nanomechanics** Mechanics that treat the material behavior at the atomic and molecular level.

**Netting analysis** The analysis of composite structure that assumes that the stresses induced in the structure are carried entirely by the reinforcements, and the strength of the resin is neglected, and that also assumes that the reinforcements possess no bending or shearing stiffness, and carry only the axial tensile loads.

**Novolac** Condensation polymerization product of phenol and formaldehyde in an acid solution with insufficient formaldehyde. It is a linear thermoplastic B-staged phenolic resin, which, in the presence of methylene or other cross-linking groups, reacts to form a thermoset phenolic.

**Nylon** The generic name for all synthetic polyamides.

**O**

**Organic peroxide** An organic compound containing the divalent ion  $-O-O-$ .

**Orthotropic material** Material with three perpendicular planes of symmetry characteristics.

**P**

**PAN-based carbon fiber** See **Carbon fiber**, and **Pyrolysis**.

**Peel strength** Adhesive bond strength, in newtons per meter of width, obtained by a stress applied in a peeling mode.

**Permeability** The passage or diffusion of a gas, vapor, liquid, or solid through a barrier without physically or chemically affecting it.

**Phenolic resin** A thermosetting resin produced by the condensation of an aromatic alcohol with an aldehyde, particularly of phenol with formaldehyde. Used in high-temperature applications with various fillers and reinforcements. See **resole resins**, and **Novolac**.

**Plasticizer** An additive that makes a finished plastic more flexible or tough. See also **flexibilizer**.

**Plunge grinding** Grinding process in which the grinding wheel is moved radially into the workpiece.

**Ply** In general, fabrics of felts that consist of one or more layers (laminates, etc.). The layers that make up a stack. Yarn that results from twisting operations (three-ply yarn, etc.). A single layer of prepreg. A single pass in filament winding.

**Poisson's ratio** The ratio of the change in lateral width per unit width to change in axial length per unit length caused by the axial stretching or stressing of a material. The ratio of transverse strain to the corresponding axial strain below the proportional limit.

**Polar winding** A winding in which the filament path passes tangentially to the polar opening at one end of the chamber and tangentially to the opposite side of the polar opening at the other end. A one-circuit pattern is inherent in the system.

**Polyacrylonitrile (PAN)** Used as a base material or precursor in the manufacture of certain carbon fibers. See also **pyrolysis**.

**Polyamideimide** A polymer containing both amide (nylon) and imide (as in polyimide) groups with properties that combine the benefits and disadvantages of both.

**Polyarylsulfone (PAS)** A high-temperature-resistant thermoplastic with the glass transition temperature  $T_g$  of 275°C.

**Polybutylene terephthalate (PBT)** A member of the polyalkylene terephthalate family, similar to polyethylene terephthalate in that it is derived from a polycondensate, which in turn is derived from terephthalic acid, the diol component of which is butanediol rather than glycol, as in the case of polyethylene terephthalate. Properties include high strength, dimensional stability, low moisture absorption, good electrical characteristics, and resistance to heat and chemicals when suitably modified.

**Polycaprolactone** A biodegradable thermoplastic polymer derived from the chemical synthesis of crude oil. Although not produced from renewable raw materials, it is fully biodegradable. Polycaprolactone has good water, oil, solvent, and chlorine resistance.

**Polycarbonate** A thermoplastic polymer derived from the direct reaction between aromatic and aliphatic dihydroxy compounds with phosgene or by the ester exchange reaction with appropriate phosgene-derived precursors. Highest impact resistance of any transparent plastics.

**Polyetherether ketone (PEEK)** A linear aromatic crystalline thermoplastic. A composite with a PEEK matrix may have a continuous-use temperature as high as 250°C (480°F).

**Polyethylene** Thermoplastic materials composed of polymers of ethylene. They are normally translucent, tough, waxy solids that are unaffected by water and by a large range of chemicals. In common usage, these plastics have no less than 85% ethylene and no less than 95% total olefins.

**Polyethylene terephthalate (PET)** A saturated, thermoplastic polyester resin made by condensing ethylene glycol and terephthalic acid and used for fibers, films, and injection-molded parts. It is extremely hard, wear resistant, dimensionally stable, and resistant to chemicals, and it has good dielectric properties. Also known as polyethylene glycol terephthalate.

**Polyimide** A polymer produced by reacting an aromatic dianhydride with an aromatic diamine. It is a highly heat-resistant resin (usable at >315°C, 600°F). Similar to a polyamide, differing only in the number of hydrogen molecules contained in the grouping. Suitable for use as a binder or adhesive. May be either thermoplastic or thermoset.

**Polymer** A high-molecular-weight organic compound, natural or synthetic, whose structure can be represented by a repeated small unit, the mer, for example, polyethylene, rubber, and cellulose. Synthetic polymers are formed by addition or condensation polymerization of monomers. Some polymers are elastomers, some are plastics, and some are fibers. When two or more dissimilar monomers are involved, the product is called a copolymer. The chain lengths of commercial thermoplastics vary from near a thousand to over one hundred thousand repeating units. Thermosetting polymers approach infinite chain length after curing, but their resin precursors often have a few hundred or fewer repeating units.

**Polymerization** A chemical reaction in which the molecules of a monomer are linked together to form large molecules whose molecular weight is a multiple of that of the original substance. When two or more monomers are involved, the process is called copolymerization.

**Polyphenylene sulfide (PPS)** Crystalline polymer having a symmetrical, rigid backbone chain consisting of recurring *para*-substituted benzene rings and sulfur atoms. Known for excellent chemical resistance, thermal stability, and fire resistance. Its inertness to organic solvents, inorganic salts, and bases makes it corrosion resistant. Commercial engineering grades are always fiber reinforced.

**Polypropylene** A tough, lightweight, thermoplastic made by the polymerization of high-purity propylene gas in the presence of an organometallic catalyst at relatively low pressures and temperatures.

**Polystyrene** White homopolymer thermoplastic produced by the polymerization of styrene (vinyl benzene). It has outstanding electrical properties, good thermal and dimensional stability, and straining resistance. Because it is somewhat brittle, it is often copolymerized or blended with other materials to obtain the desired properties.

**Polyurethanes** A thermosetting resin prepared by the reaction of diisocyanates with polyolephin, polyamides, alkyd polymers, and polyether polymers.

**Polyvinyl acetate** A thermoplastic material composed of polymers of vinyl acetate in the form of a colorless solid. It is obtainable in the form of granules, solutions, lattices, and pastes, and is used extensively in adhesives, for paper and fabric coatings, and in bases for inks and lacquers.

**Porous release cloth** A porous cloth, serving as a protectant and/or carrier for an adhesive film or mass, which is easily removed from the film or mass prior to use.

**Preform** A preshaped fibrous reinforcement formed by distribution of chopped fibers or cloth by air, water flotation, or vacuum over the surface of a perforated screen to the approximate contour and thickness desired in the finished part. Also, a preshaped fibrous reinforcement of mat or cloth formed to the desired shape on a mandrel or mock-up before being placed in a mold press.

**Preheating** The heating of a compound before molding or casting, to facilitate the operation or reduce the molding cycle.

**Prepreg** Either ready-to-mold material in sheet form or ready-to-wind material in roving form, which may be cloth, mat, unidirectional fiber, or paper impregnated with resin and stored for use. The resin is partially cured to a B-stage and supplied to the fabricator, who lays up the finished shape and completes the cure with heat and pressure.

**Primer** A coating applied to a surface, before the application of an adhesive, lacquer, enamel, and so forth, to improve the adhesion performance or load-carrying ability of the bond.

**Probability density function (PDF)** A real-valued function whose integral over any set gives the probability that a random variable has values in this set.

**Propylene glycol** A viscous colorless liquid, miscible with water, alcohol and many solvents. It boils at 188°C and used as a chemical intermediate, antifreeze, solvent, lubricant, plasticizer, and bactericide.  $\text{CH}_3\text{CHOHCH}_2\text{OH}$ .

**Pultrusion** A continuous process for manufacturing composites that have a constant cross-sectional shape. The process consists of pulling a fiber-reinforcing material through a resin impregnation bath and through a shaping die, where the resin is subsequently cured.

**Pyrolysis** With respect to fibers, the thermal process by which organic precursor fiber materials, such as rayon, polyacrylonitrile (PAN), and pitch, are chemically changed into carbon fiber by the action of heat in an inert atmosphere. Pyrolysis temperatures can range from 800 to 2800°C (1470 to 5070°F), depending on the precursor. Higher processing graphitization temperatures of 1900–3000°C (3450–5430°F) generally lead to higher modulus carbon fibers, usually referred to as graphite fibers. During the pyrolysis process, molecules containing oxygen, hydrogen, and nitrogen are driven from the precursor fiber, leaving continuous chains of carbon.

## Q

**Quality factor** The inverse of the loss factor. Also called the dynamic amplification factor.

**Quasi-Isotropic laminate** A laminate approximating isotropy by orientation of plies in several or more directions.

**R**

**Rayon** A fiber made from regenerated cellulose, using the viscose or cuprammonium process.

**Reaction injection molding (RIM)** A process for molding polyurethane, epoxy, and other liquid chemical systems. Mixing of two to four components in the proper chemical ratio is accomplished by a high-pressure impingement-type mixing head, from which the mixed material is delivered into the mold at low pressure, where it reacts (cures).

**Reinforcement** A strong material bonded into a matrix to improve its mechanical properties. Reinforcements are usually long fibers, chopped fibers, whiskers, particulates, and so forth. The term should not be used synonymously with **filler**.

**Reliability** The probability that a component part, equipment, or system will satisfactorily perform its intended function under given circumstances, such as environmental conditions, limitations as to operating time, and frequency and thoroughness of maintenance for a specified of time.

**Residual stress** The stress existing in a body at rest, in equilibrium, at uniform temperature, and not subjected to external forces. Often caused by the forming and curing process.

**Resin** A solid or pseudo-solid organic material, usually of high molecular weight, that exhibits a tendency to flow when subjected to stress. In reinforced plastics, the material used to bind together the reinforcement material (i.e., matrix).

**Resin transfer molding** A process whereby catalyzed resin is transferred or injected into an enclosed mold in which the fiber reinforcement has been placed.

**Resole resins** Condensation polymerization product of phenol and formaldehyde in an alkali solution with excess formaldehyde.

**RIM** See **reaction injection molding**.

**Roving** A number of yarns, strands, tows, or ends collected into a parallel bundle with little or no twist.

**RTM** See **resin transfer molding**.

**S**

**Sandwich structure** Panels composed of a lightweight core material, such as honeycomb, foamed plastic, and so forth, to which two relatively thin, dense, high-strength or high-stiffness faces or skins are bonded.

**Scanning electron microscope** A type of electron microscope in which a beam of electrons, a few hundred angstroms in diameter, systematically sweeps over the specimen. The intensity of secondary electrons generated at the point of impact of the beam on the specimen is measured and the resulting signal is fed into a cathode ray tube display, which is scanned in synchronism with the scanning of the specimen.

**SCARA robot** A robot that consists of two revolute joints followed by a prismatic joint in which all three joints are parallel to each other and usually point along the direction of gravity (selective compliance assembly robot arm).

**Scarf adhesive joint** A joint made by cutting away similar angular segments on two adherends and bonding the adherends with the cut areas fitted together.

**Self-excitation vibration** See **chatter**.

**SEM** See **scanning electron microscope**.

**S-glass** A magnesium aluminosilicate composition that is especially designed to provide very high tensile strength glass filaments. S-glass and S-2 glass fibers have the same glass composition but different finishes (coatings). S-glass is made to more demanding specifications, and S-2 is considered the commercial grade.

**Shear** An action or stress resulting from applied forces that causes or tends to cause two contiguous parts of a body to slide relative to each other in a direction parallel to their plane of contact. In interlaminar shear, the plane of contact is composed primarily of resin.

**Shear strain** The tangent of the angular change, caused by a force between two lines originally perpendicular to each other through a point in a body.

**Shear strength** The maximum shear stress that a material is capable of sustaining. Shear strength is calculated from the maximum load during a shear or torsion test and is based on the original cross-sectional area of the specimen.

**Sheet molding compound (SMC)** A composite of fibers, usually a polyester resin, and pigments, fillers, and other additives that have been compounded and processed into sheet form to facilitate handling in the molding operation.

**Shelf life** The length of time a material, substance, or product can be stored under specified environmental conditions and continue to meet all applicable specification requirements and/or remain suitable for its intended function.

**Shrinkage** The relative change in dimension from the length measured on the mold when it is cold to the length of the molded object 24 hours after it has been taken out of the mold.

**Silicon carbide** Reinforcement, in whisker, particulate, and fine or large fibers, that has application as metal matrix reinforcement because of its high strength and modulus, density equal to that of aluminum, and comparatively low cost. As a whisker or particulate, it gives the composite isotropic properties and is easily machined.

**Sink mark** A shallow depression or dimple on the surface of an injection or compression molded part due to collapsing of the surface following local internal shrinkage. An incipient short shot for an injection molded part.

**Sonotrode** See **ultrasonic machining**.

**Specific cutting force (specific cutting power)** Energy required to cut away a unit volume of material.

**Specific properties** Material properties divided by the material density.

**Spectra Allied Signal** Polyethylene fiber produced by AlliedSignal (now Honeywell) Colonial Heights, Va., USA.

**Squirrel cage** The shape of a rotor of an electrical AC motor.

**Stacking sequence** A description of a laminate that details the ply orientations and their sequence in the laminate.

**Standard deviation** Square root of variance used for the behavior of samples.

**Static stiffness** The ratio of stress to strain under static conditions. It is calculated from static stress-strain tests, in shear, compression, or tension. Expressed in force per unit area.

**Stiffness** A measure of modulus. The relationship of load and deformation. The ratio between the applied stress and resulting strain.

**Strain** Elastic deformation due to stress. Measured as the change in length per unit of length in a given direction, and expressed in m/m (in./in.).

**Strand** Normally an untwisted bundle or assembly of continuous filaments used as a unit, including slivers, tows, ends, yarn, and so forth. Sometimes a single fiber or filament is called a strand.

**Stress** The internal force per unit area that resists a change in size or shape of a body. Expressed in force per unit area.

**Stress concentration** On a macromechanical level, the magnification of the level of an applied stress in the region of a notch, void, hole, or inclusion.

**Stress concentration factor** The ratio of the maximum stress in the region of a stress concentrator, such as a hole, to the stress in a similar strained area without a stress concentrator.

**Structural reaction injection molding (SRIM)** Reaction injection molding employed to make reinforced RIM products.

**Styrene** A monomer for polystyrene; a colorless oily liquid.

**Styrene–butadiene copolymer** Rubbery substance added to polystyrene to improve its impact toughness.

**Surface active agent (coupling agent)** Any chemical substance designed to react with both the reinforcement and matrix phases of a composite material to form or promote a stronger bond at the interface.

**Surface roughness** See **arithmetic surface roughness**.

**Surface treatment** A physical or chemical process to increase the bonding or wetting characteristics of the surface to be wetted or bonded.

**Swelling coefficient** The coefficient that represents the linear or volumetric increase of composite due to moisture absorption.

**Symmetric laminate** A composite laminate in which the sequence of plies below the laminate midplane is a mirror image of the stacking sequence above the midplane.

## T

**Talc** A fine-grained mineral having a soft soapy feel and consisting of hydrated magnesium silicate; used in a variety of products, including talcum powder.

**Tarpaulin film** A sheet of waterproof canvas or other material used to cover and protect construction materials and equipment, athletic fields, vehicles, or other exposed objects.

**Teflon** A material used to coat cooking utensils and in industrial applications where sticking is to be avoided or low friction is required.

**Tensile strength** The maximum load or force per unit cross-sectional area, within the gage length of the specimen. The pulling stress required to break a given specimen.

**Tension failure of mechanical joint** A failure mechanism of mechanical joint in which the adherend fails by tensile rupture.

**Thermal conductivity** Ability of a material to conduct heat. The physical constant for the quantity of heat that passes through a unit cube of substance in unit time when the difference in temperature of two faces is 1°.

**Thermoplastic polymers** Capable of being repeatedly softened by an increase of temperature and hardened by a decrease in temperature. Applicable to those materials whose change upon heating is substantially physical rather than chemical and that in the softened stage can be shaped by flow into articles by molding or extrusion.

**Thermoset plastic** A plastic that, when cured by application of heat or chemical means, changes into a substantially infusible and insoluble material by cross-linking.

**Thickener** Components that increase the viscosity of polyester or vinyester SMCs, such as MgO, CaO, and Mg(OH)<sub>2</sub>.

**Through-thickness strain** Strain in the thickness direction of a plate.

**Tolerance** The guaranteed maximum deviation from the specified nominal value of a component characteristic at standard or stated environmental conditions.

**Toluene diisocyanate** A liquid at room temperature with sharp, pungent odor, miscible with ether, acetone, and benzene, used to make polyurethane foams and other elastomers. CH<sub>3</sub>C<sub>6</sub>H<sub>3</sub>(NCO)<sub>2</sub>.

**Toughness** A property of a material for absorbing work or energy. The actual work per unit volume or unit mass of material that is required to rupture it. Toughness is proportional to the area under the load–elongation curve from the origin to the breaking point.

**Tow** An untwisted bundle of continuous filaments. Commonly used in referring to artificial fibers, particularly carbon and graphite, but also glass and aramid. A tow designated as 140 k has 140,000 filaments.

**Transverse strain** The linear strain in a plane perpendicular to the loading axis of a specimen.

**Transverse stress** The linear stress in a plane perpendicular to the loading axis of a specimen.

**Transversely isotropic** Term describing a material exhibiting a special case of orthotropy in which properties are isotropic in one plane.

**Trenchless sewage pipe repair by RTM** Method of repairing underground sewage pipes by RTM.

**Tresca theory** Maximum shear stress theory. It predicts that yielding begins whenever the maximum shear stress in any element equals or exceeds the maximum shear stress in a tension-test specimen of the same material when that specimen begins to yield.

**Trichloride** Any compound containing three chlorine atoms in each molecule.

**Triclinic material** Fully anisotropic material without any symmetric plane or property.

## U

**Ultrasonic machining** Material removal process by microchipping and erosion with fine abrasive grains in a slurry. The tip of the tool (sonotrode) vibrates at a frequency of 20 kHz and low amplitude (12.5–75 µm).

**Ultraviolet** Zone of invisible radiation beyond the violet end of the spectrum of visible radiation. Since UV wavelengths are shorter than visible wavelengths, their photons have more energy, enough to initiate some chemical reactions and to degrade most plastics, particularly aramids.

**Unidirectional (UD) lamina** A reinforced laminate in which substantially all of the fibers are oriented in the same direction.

**Unsaturated polyester resin** Thermosetting polyester resin.

## V

**Vacuum-assisted RTM (VARTM)** Resin transfer molding during which a vacuum is applied to remove air bubbles or volatiles generated.

**Vacuum bagging process (molding)** A process in which a sheet of flexible transparent material plus bleeder cloth and release film are placed over the lay-up on the mold and sealed at the edges. A vacuum is applied between the sheet and the lay-up. The entrapped air is mechanically worked out of the lay-up and removed by the vacuum, and the part is cured with temperature, pressure, and time. Also called bag molding.

**Van der Waals bond** A bond produced between the adherend and the adhesive by a weak secondary force.

**Variance** Coefficient of variation that is the ratio of the standard deviation to the average.

**Vibrating sample magnetometer (VSM)** A device that measures the magnetic permeability of a material.

**Vinyl esters** A class of thermosetting resins containing esters of acrylic and/or methacrylic acids, many of which have been made from epoxy resin.

**Viscoelastic** A property involving a combination of elastic and viscous behavior in the application of which a material is considered to combine the features of a perfectly elastic solid and a perfect fluid. Phenomenon of time-dependent, in addition to elastic, deformation (or recovery) in response to load.

**Viscosity** The property of resistance to flow exhibited within the body of a material, expressed in terms of the relationship between applied shearing stress and resulting rate of strain in shear.

**Void** Air or gas that has been trapped and cured into a laminate. Porosity is an aggregation of microvoids.

**Voigt model** Property equation of a mixture in terms of its constituent properties derived based on the equal strain hypothesis.

**Volatiles** Materials, such as water and alcohol, in a sizing or a resin formulation, that are capable of being driven off as a vapor at room temperature or at a slightly elevated temperature.

**Volume fraction** Fraction of a constituent material based on its volume.

**Von Mises theory** Distortion energy theory for ductile materials. It predicts that yielding occurs when the distortion strain energy per unit volume reaches or exceeds the distortion strain energy per unit volume for yield in simple tension or compression of the same material.

## W

**Warp** Yarn arranged lengthwise on a loom and crossed by the weft.

**Water jet machining** Machining or cutting operation using a water jet that travels at velocities as great as 900 m/s (approximately Mach 3).

**Web** A vertical member of an I-beam or box-type beam.

**Weft** Transverse threads or fibers in a woven fabric running perpendicular to the warp. Also called filler, filler yarn, and woof.

**Weibull distribution** A distribution used for expressing reliability. It contains a good approximation of the normal distribution as well as an exact representation of the exponential distribution.

**Weight fraction** Ratio of fiber or matrix weight (or mass) to the composite weight (or mass).

**Wet grinding** Grinding process performed with cutting fluid.

**Wet winding** In filament winding, the process of winding glass on a mandrel in which the strand is impregnated with resin just before contact with the mandrel.

**Wet-out** The condition of an impregnated roving or yarn in which substantially all voids between the sized strands and filaments are filled with resin.

**Wettability** The state or condition of being wettable, or the relative affinity of liquid for the surface of a solid, such as the affinity of water for paper or leather.

**Wetting of matrix into fiber** The spreading, and sometimes absorption, of a matrix on the surface of fiber.

**Whirling vibration** Vibration induced when the rotating speed of a shaft is equal to one of the bending natural frequencies of the shaft.

**Whisker** A short single-crystal fiber or filament used as reinforcement in a matrix.

Whisker diameters range from 1 to 25  $\mu\text{m}$  (40 to 980  $\mu\text{in}.$ ), with aspect ratios between 100 and 15,000.

**Winding angle** The angular measure in degrees between the direction parallel to the filaments and an established reference. In filament-wound structures it is the convention to measure the winding angle with reference to the centerline through the polar bosses, that is, the axis of rotation.

**Woven fabric continuous fiber composite** A material (usually a planar structure) constructed by interlacing yarns, fibers, or filaments, to form such fabric patterns as plain, twill, or harness satin weaves.

**Wrist of the robot** The subassembly associated with the last moving (usually three) links.

## X

**X-Ray photoelectron spectroscopy (XPS)** A technique used for analyzing surfaces chemically (also called electron spectroscopy for chemical analysis).

## Y

**Yarn** An assemblage of twisted filaments, fibers, or strands, either natural or manufactured, that form a continuous length that is suitable for use in weaving or interweaving into materials.

**Young's equation** An equation that relates the surface forces (or surface free energy) at equilibrium of the spreading (or wetting) film.

## Z

**Zigzagging** An operation to decompose FRs and DPs in the functional and physical domains and to create the FR and DP hierarchies.

# INDEX

---

## Index Terms

## Links

### A

Abrasion	357				
Abrasive					
belt	329				
particle	343				
water jet machining	342	343			
Absorbers	41				
Absorption	34	41			
Acid-catalyzed reaction	32				
Acrylic	33	296			
Acrylonitrile–Butadiene copolymer	41				
Activation energy	28				
Active agents (coupling agent)	36				
Advanced composites	15				
Addition					
mechanism	289				
polymerization	27				
Additives	37				
Adherend					
length	573	575	580	582	
thickness	573	575	580	582	
Adhesion	35				
Adhesive					
bonding	352	375			
constitutive equation	354				
joining	352				
joint	352				
thickness	366	601			

## Index Terms

## Links

Adhesively bonded joint				
applications in the harmonic drive	553	554		
applications in the robot	546	547		
Advantage of fatigue life diagram	437			
Air bearing	568			
Air spindle	568			
Alkaline catalyst	32			
Allowable flaw size	185			
Allowable tolerance	478			
Alumina	54			
Alumina trihydrate	38			
Aluminum oxide fiber	25			
Aminosilane	36			
Angular contact ball bearing (applications				
in the robot)	527	528		
Anisotropic	23			
strength property	131			
symmetric (sandwich structure)	236			
Anthropomorphic robot	18	513	526	538
	539			
Applications				
in the hand of the handling robot	514			
in the hand of the LCD robot	514			
in the harmonic drive	550			
in the robot	514			
in the wrist of the handling robot	525			
in the wrist of the LCD robot	520			
Aramid fiber	25	26		
Aramid–phenolic composites	31			
Arithmetic surface roughness	376	607	608	
Arm in the robot	514	515		
Arm-type robot for LCD panel handling	516			

## Index Terms

## Links

Aromatic		
hydrocarbons	23	
ring structures	33	
Arrhenius dependence	28	
Articulated robot	513	
Aspect ratio	14	233
Auger electron spectroscopy (AES)	391	
Autoclave		
cure cycle with cooling and reheating	327	
molding	37	327
vacuum bag degassing process	604	
Automotive one-piece composite propeller		
shaft	623	
Average		
engineering CTE	140	
shear strain	45	
stress	123	
stress criteria	191	
through-thickness strain	146	
Axial		
modulus	42	
modulus of the laminate	124	125
Poisson s ratio	43	
shear modulus	45	
stiffness of the preloaded angular		
contact ball	527	528
strain of the box-type beam	248	250
Axiom	18	455
Axiomatic design	449	
<b>B</b>		
Balance equation	125	179
Balanced laminate	125	

<u>Index Terms</u>	<u>Links</u>
Basal planes	24
Batch process	488
Beam	240
Bearing	209
material	33
stiffness of the preloaded angular contact ball	527
528	577
592	
Bearing failure (of mechanical joint)	346
Bed	566
Belt	536
Bending	537
of a plate	209
of clamped laminate plate	227
of symmetrically laminated beam	241
moment of narrow beam	242
response	121
stiffness	68
stiffness matrix	119
Bending stiffness	119
of wide beam	245
Bending–stretching coupling	116
Benzene rings	26
Benzoquinone	28
Benzoyl peroxide	28
Bias	471
474	
Biaxial ratio	170
Bismaleimide (BMI)	73
Bleeder papers	52
Blowing agents	508
509	
Bolt	
pull-out (of mechanical joint)	346
shear failure (of mechanical joint)	346
stiffness	347

## Index Terms

## Links

Boron				
epoxy composite	104			
fiber	24			
trichloride	24			
Box-type				
beam for side-door impact beam	644			
beam fracture mode	646			
composite beam	248			
cross-sectional shape in the robot	518	529		
B-stage	30	37		
Buckling	229	239	240	
load	217	239		
of simply supported rectangular plates	216			
torque	555			
Buckminster fullerene	23			
Bulk				
modulus	86			
polymers	19			
Bumper beams	633	634		
Butt joint	352			
<b>C</b>				
Calcium carbonate	38			
Cantilever beam	195			
Capacitance	302			
Carbon	22			
black	39			
epoxy composite robot structures	18			
epoxy composite spindle shaft	17			
fiber	15	23		
fiber epoxy composite	60	107	177	181
	187	255	256	287
	297	309	327	337

## Index Terms

## Links

Carbon ( <i>Cont.</i> )				
	340	386	424	516
	535	567	598	612
	625	633	636	671
Cartesian robot	513			
Cartesian tensors	68			
Castigliano's theorem in calculating the deflection of robot	195	530		
Catalysts	27			
Catastrophic failure	350			
Cavity channel	310			
Center-part				
enhanced beam	647			
enhanced beam manufacturing method	646			
enhanced beam three point bending test	647			
Centrifugal force	568	572	575	
Ceramic				
fibers	25			
matrix	34			
matrix composite (CMC)	34			
Chain-like molecules	26			
Change	316			
Characteristic damage state (CDC)	435	437		
Charge	50			
preheating	315			
Charpy test	414			
Chemical mechanical planarization (CMP)	450			
Chemical surface treatment	379	380		
Chemical vapor deposition	24			
Chentsov coefficients	105			
Chisel angle	339			
Chopped strand mat (CSM)	22			
Clamped edge (boundary condition of a plate)	210			

<u>Index Terms</u>	<u>Links</u>			
Clamped laminate plate	227			
Classical laminated plate theory (CLPT)	111	138	148	
Classical lamination theory (CLT)	111	148		
Cleavage failure (of mechanical joint)	346	347	351	
Coal tar pitch	23			
Coefficient				
of friction	346			
of hygroscopic expansion (CHE)	113			
of mutual influence	104			
of mutual influence of the laminate	124			
of thermal expansion (CTE)	49	113	139	148
of variation	258			
Collision analysis for composite bumper				
beam	639			
Column (definition)	240			
Combinational complexity	479	480		
Common range (CR)	470			
Compaction	280			
Comparative robustness of a decoupled				
design	485			
Compatibility equation	71			
Compensation	477			
Complex modulus	617			
Complexity	479	487		
Compliance matrix	75	94	146	
Complicated chemical mechanical				
planarization (CMP)	450			
Composite boring bar	597			
Composite bumper beam design	636			
Composite finite element (FE) analysis	520	572	575	577
	579	614		
Composite joint design	649			
composite shear-out failure mode	649			

<u>Index Terms</u>	<u>Links</u>
Composite laminate plate	202
Composite materials	14
Composite propeller shaft	623
joining	625
manufacturing method	624      625
Composite rotor	582
Composite shear-out failure mode	649
Composite side-door impact beam	642
dynamic energy absorption	649
energy absorption ratio	648
impact characteristics	648
impact energy absorption	649
three-point bending	644
Composite stress concentration factor	651
Composite structure	110
Compression	292
fatigue	434
incident stress	401
molding	50      311      315
preload for propeller shaft	628
strength after impact (CAI)	416
Compressive strength	
of composite extensional mode	
microbuckling	278
of composite shear failure	283
of composite shear mode microbuckling	280
of composite transverse tensile rupture	282
Concurrent engineering	468
Condensation mechanism	289
Condensation polymerization	27
Condition of symmetry of the compliances	87
Conductivity	583      597      599
Consolidation	290

<u>Index Terms</u>	<u>Links</u>
Constant of randomly oriented continuous fiber composite	285
discontinuous fiber composite	284
Constituents	14
Constitutive equation	96
Constrained damping mechanism	599
Constraint	454      455      460
applications in the hand of the LCD robot	516
applications in the harmonic drive	552      553
applications in the wrist of the LCD robot	517      518
for bumper beams	624
for propeller shaft	625
for side-door impact beam	643
for trenchless sewage pipe repair	657      658
Contact angle	35      375      384      386
	391      393
Control volume approach	314
Conventional serial manipulator	513
Core	
corrugated core	234
foam core	234
honeycomb core	234
materials	15
truss core	234
weak core	239
web core	234
Corollary	455
Correction factor	218
Corrugated core	234

<u>Index Terms</u>		<u>Links</u>			
Coupled design	459	461			
applications in the hand of the handling					
robot	518	519			
Coupling	117	122	131	132	
	137				
Coupling coefficient of the quasi-isotropic					
laminate	131				
Covalent					
diamond structure	23				
interaction	25				
Cox					
model ineffective length	272				
model longitudinal modulus	272				
model representative volume element					
(RVE)	269				
Cracking	4	34	336		
Crash test of bumper beams	634	637	648		
Creativity	452				
Creep property	27				
Criterion	115	153	160	180	
Critical					
buckling load	219	239			
damping (damping ratio)	617				
energy release rate	193				
failure mode	350				
stress intensity factor	185	193			
Crossply	14				
Crystal	18	21	33		
Crystalline	22				
Crystallinity	33				
Crystallites	33				
Cumulative distribution function	259				
Cure cycle with cooling and reheating	327				

<u>Index Terms</u>	<u>Links</u>			
Cure monitoring	301			
Curing agent	27			
Curvature	113	121	123	
in classical lamination theory	207			
in flange of the box-type beam	248			
of a plate	113	121	122	
of narrow beam	243			
of symmetrically laminated beam	241			
of wide beam	245			
Customer				
attributes	455			
Customer domain	454			
Customer's needs	451			
Cut-off grinding	340			
Cutting force	341			
Cycloaliphatics	30			
Cylindrical bending (of laminated plate strips)	241			
<b>D</b>				
Damage				
tolerance	401			
tolerant design	183	401		
Damping				
characteristics	566			
core	599	603		
core material	599	603		
ratio (critical damping)	565	598	608	616
	617			
ratio, experimental data	538	550	551	
Damping capacity	617			
Drainage	292			
Darcy's law	290	323	659	
Double cantilever beam (DCB) test	394			

<u>Index Terms</u>		<u>Links</u>
Debonding	64	440
Decomposition	461	465
of FR and DP for trenchless sewage repair	657	
Decomposition process	465	
Decoupled design	459	
applications in the hand of the handling robot	518	
applications in the wrist of the handling robot	518	519
Decoupling of decoupled design	482	483
Deflection of narrow beam	242	
Degradation of polymer	327	389
Degree		
of cure	295	
of saturation	291	
of wet-out	325	
Delamination	340	
energy	416	
failure	173	
Delivery system	322	
Deposit-oxide film	375	
Design	450	451
in the absence of complete inform	484	
axioms	456	
decomposition process	467	
equation for bumper beams	634	
equation for propeller shaft	625	
equation for side-door impact beam	643	
equation for trenchless sewage pipe repair	657	

## Index Terms

## Links

Design ( <i>Cont.</i> )		
hierarchy	458	
intent	466	467
for manufacturability	483	
manufacturing interface	484	
matrix	458	459
parameter	18	451
parameter for bumper beams	634	
parameter for propeller shaft	625	
parameter for side-door impact beam	643	
parameter for trenchless sewage pipe		
repair	657	
parameter, in the hand of the handling		
robot	516	517
parameter, in the harmonic drive	552	
parameter, in the wrist of the handling		
robot	517	518
parameters	455	
range	470	478
range and coupling	484	
Design-build-test	499	
Diagonal matrix	459	462
Diamine	33	
Diamond structure	23	
Die sinking method	345	
Dielectric		
constant	302	
materials	301	
Dielectrometry	301	
interdigital sensor	306	
Diethylene triamine (DETA)	29	

<u>Index Terms</u>		<u>Links</u>
Differential scanning calorimetry (DSC)	295	301
Diffusion coefficient	307	
Diglycidyl ether of bisphenol A (DGEBA)	28	
Diluent	28	
Dimensional stability	36	
Direct-drive manipulator	513	525
Discontinuous fiber	14	
Dissipation factor	258	302
Domain		
customer domain	486	
functional domain	486	
physical domain	486	
process domain	486	
Double		
arm-type robot for LCD panel handling	514	
cantilever beam	195	394
lap adhesive joint	352	353
strap adhesive joint	353	372
Drilling	339	
Drive shaft (transmission shaft) in the robot	540	545
Drop-weight impact test	415	416
Dry		
grinding	340	
spot	314	
winding	321	
Ductility index	424	
Duhamel integral method	224	
Duration measuring	409	
Dwelling	52	
Dynamic amplification factor (quality factor)	617	
Dynamic energy absorption	648	
Dynamic response (of composite laminate)	225	

<u>Index Terms</u>	<u>Links</u>
Dynamic stiffness in the robot	517
Dyneema® (DSM)	25
<b>E</b>	
Eccentricity	
effect	350
ratio	570      582
Eddy current	583      586
Edge (boundary condition of a plate)	209      219
Edge distance	351
Effect	
of fiber orientation on fatigue strength	429
of mean stress on fatigue life	431
of stress ratio on fatigue strength	430
of target flexibility	410
of temperature and moisture	442
Effective	
bending stiffness (definition)	242
bending stiffness (of wide beam)	246
stiffness (of the box-type beam)	250
torsional rigidity (of the box-type beam)	251
Effector (hand) in the robot	515      516
E-glass	21
Einstein's photoelectric effect	371
Elastic constant of	
foundation	238
quasi-isotropic composite	133
randomly oriented continuous fiber	
composite	285
randomly oriented discontinuous fiber	
composite	284
Elastic shear stress-strain characteristics	355

## Index Terms

## Links

Elastic–perfectly plastic shear stress–strain characteristics	355	
Electric conductivity	582	
Electrical		
insulator	22	
resistivity	345	
Electro-discharge machining (EDM)	345	
Electron spectroscopy for chemical analysis (ESCA)	391	
Electrostatic bonding	36	
End		
effector (hand) in the robot	514	515
notched flexure	195	
End beam buckling test	638	
End beam compression test	638	
End beam of bumper beams	634	638
Energy		
balance equation	295	
control	426	
criterion	230	
criterion approach	183	192
release rate	192	
Energy absorption characteristics	417	
Energy absorption ratio	417	
Energy method	195	
Energy release rate	192	
Engineering		
constants	82	102
shear strains	68	
Epoxy resin	28	
Equality of information content	484	
Equation for moisture diffusion	307	
Equilibrium	69	

## Index Terms

## Links

Equivalent	
hygroscopic bending moment	120
hygroscopic force	118
thermal bending moment	120
thermal force	118
Ethylene	28
Euler–Bernoulli beam theory	242
Eutectic	22
Existence of uncoupled or decoupled	
design	404
Exothermic reaction	327
Expansion	292
<b>F</b>	
Failure (of mechanical joint)	347
Failure criterion	160
Failure-inducing surface crack	19
Failure index	169
Fastener	349
Fatigue	
characteristics	424
control mode	425
damage mechanisms	426
diagram	349
failure criterion	349
life diagram	437
safety factor	349
FEM (finite element method)	
of bumper beams	637
in the wrist of the handling	
robot	521

## Index Terms

## Links

Fiber			
bed	290		
break-out	339		
buckling	336		
cutting	336		
deformation	292		
delivery system	322		
impregnation	27		
kink	282		
preform for trenchless sewage pipe			
repair	658		
pull-out	339		
reinforced polymeric matrix composite			
for automotive parts	621		
tension	323		
volume	291		
volume fraction	41	46	291
weight fraction	41		
wet-out	325		
Fiber–resin stream	325		
Fick's law of diffusion	307		
Filament winding	37	53	321
patterns	53		
Filler	37	38	352
Filler-to-resin ratio	39		
Finite difference method	317		
First-order shear deformation theory	206	219	
First-ply failure (FPF)	171		
Flake	18		
Flame retardants	41		
Flange definition of box-type beam	249		
Flank wear	337		

<u>Index Terms</u>	<u>Links</u>
Flexibility	21
Flexibilizers	28
Flex spline	550
Flexural	
fatigue	431
rigidity	612
rigidity (of isotropic symmetric sandwich structure)	235
rigidity (of sandwich structure with dissimilar faces)	238
stiffness	238
stiffness-to-weight ratios	15
Flux density	586
Foam core	
applications in the robot	518
Forced	522
vibration	565
vibration (of a composite laminate subjected to dynamic lateral load)	223
Forces per unit length	120
Formaldehyde	32
Fourier's law of heat conduction	306
Four-point bending test of the quasi-isotropic laminates	132
Fracture	182
energy	34
initiation energy	36
toughness	27
	41
	186
Free	
body diagram	174
edge (boundary condition of a plate)	210
vibration	229

## Index Terms

## Links

Free ( <i>Cont.</i> )					
vibration (of simply supported					
symmetric plate)	217				
Friction resistance	31				
Functional domain	454	461	465		
Functional requirement	18	449	451	455	
applications in the hand of the handling					
robot	516				
applications in the wrist of the handling					
robot	517	518			
applications in the harmonic drive	552				
bumper beams	634				
propeller shaft	624				
side-door impact beam	643				
trenchless sewage pipe repair	657				
Fundamental natural bending frequency					
of propeller shaft	623	625			

## **G**

Galvanic corrosion	335	626			
Gamma irradiation	28				
Gas diffusion	490				
Gaussian (normal) distribution	260				
Geometric compatibility	358	360	363		
Glass epoxy composite	104				
Glass-fiber composites	16				
Glass fibers	15	21			
Glass sphere	38				
Glass transition temperature	40	327	352	353	
	493				
Global laminate coordinate	111	115			
Global system of coordinates	66	153			
Goodman fatigue failure criterion	349	350			

<u>Index Terms</u>	<u>Links</u>			
Graphite fiber	23			
Graphite structure	22	23		
Graphitization	24			
Griffith	192			
Grinding	339			
<b>H</b>				
Half sorption process	308			
Half-apex angle	348			
Halpin–Tsai equations	283	284		
Hand (end effector) in the robot	519			
Hand of the handling robot	519			
Harmonic drive	550			
Heat-affected zone (HAZ)	344			
Heat conduction equations in the transformed coordinate	300			
Heat deflection temperature (HDT)	31			
Heat flux	300			
Heat generation	295			
Heat transfer rate	307			
Hele–Shaw model, generalized	317			
Helical winding	322			
Helix angle	339			
Henry s constant	493			
Hexagonal layers	23			
Hexamethylenetetramine	32			
Hierarchy	461	465		
High-speed aerostatic spindle	567	575	582	588
	590	597		
High-speed resin transfer molding (HSRTM)	311			
Histogram	259			
Homogeneous	72			

<u>Index Terms</u>	<u>Links</u>
Honeycomb core	609
Hooke's law	146
Hybrid composite	15
Hybrid joint, applications in the robot	547
Hybrid joint for propeller shaft	631
Hybrid machine tool structure	612
Hybrid propeller shaft	623
Hybrid propeller shaft design	623
Hydrocarbons	23
Hydrodynamic friction coefficient	319
Hydroquinone	28      39
Hydrostatic state	168
Hygroscopic	
bending moment	120
expansion	113
force	118
influence coefficient	117
in-plane influence coefficient	117
strain	113
Hygrothermal	
change	289
effect	208
properties of unidirectional carbon epoxy	
composite	309
residual stress	141
<b>I</b>	
Ideal design	461      463      483
Ignition loss method	42
Imbibition	292
Immunity of FR	475

## Index Terms

## Links

Impact		
damage	401	
energy absorption characteristics	417	
isotropic materials	403	
modifiers	41	
nonisotropic materials	406	
resistance	423	
Impact energy absorption	417	
Impingement mixing	55	311
Impregnation	29	
Impulse	223	
Impulse dynamic test		
(impulse response test)	602	614
In-plane shear loading	183	
In situ monitoring of the temperature and		
dissipation	305	
Incident stress	401	
Independence and design range	483	
Independence axiom	456	486
Inertia effects of resin	312	
Information axiom	456	469
Information content	456	469
Infrastructure constructions	17	
Inhibitor	28	39
Inhomogeneous	14	
Initiation energy	418	424
Initiator	28	
Injection		
compression molding (ICM)	309	310
molding	508	
In-plane		
force	121	122
forces per unit length	121	

## Index Terms

## Links

In-plane ( <i>Cont.</i> )		
shear modulus	251	
shear strength	26	
stiffness	116	235
strain	147	
strain (in web of the box type)	248	
Insulator	22	31
Integration of physical parts	482	
Interdiffusion	36	
Interdigital sensor	305	306
Interfacial bonding	35	
Interfacial free energy	384	
Interlaminar		
fracture	195	
shear fatigue	431	
shear strain	146	
shear strength	26	
shear stress (in the box-type beam)	251	
shear stress (of a rectangular beam)	247	
strength	112	
stress	112	173
tensile strength	180	195
Interlocking	375	
Internal mold release agent	39	
International space station (ISS)	449	
Invariance	484	
Invariant	460	
Ion-scattering spectroscopy (ISS)	391	449
Ionic bond	34	
Isophthalic	28	
Isothermal degree of cure	296	
Isothermal rate of cure	295	
Isothermal scanning	295	

## Index Terms

## Links

Isotropic	209
plate	233
symmetric (sandwich structure)	235
Isotropic materials	80
Izod test	117
	118

## **J**

Jet impingement angle	343
Joint	346
for composite materials	671

## **K**

Kaolin clay	38
Kelly–Tyson model	
critical length	274
ineffective length	274
interfacial shear strength	274
Kevlar	25
Keying	25
Kinetic energy (of an elastic body)	228
Kink	282
Kirchhoff	206
Kirchhoff–Love hypothesis	111
Kirchhoff's hypothesis	111
Kozeny–Carman constant	146
	294

## **L**

Lamellae	33
Lamina	66
average stress	113
beam	240
coordinate	66
hygroscopic in-plane influence	111

## Index Terms

## Links

Lamina ( <i>Cont.</i> )			
coefficient	117		
strain	112	123	146
thermal bending influence coefficient			
matrix	119		
thermal influence coefficient	117		
thermal in-plane influence coefficient	116		
Laser cutting	343		
Last-ply failure (LPF)	172		
Layered manufacturing process (rapid prototyping)	504		
LCD (liquid crystal display) glass panel			
handling robot	18	514	
Leakage flux	587		
Leakage reactance	587		
Leaves	466		
Levy solution (for rectangular plates)	213		
Life diagrams	437		
Linear			
elastic adhesive property	358		
elastic–perfectly plastic approximation	362		
elastic–perfectly plastic shear			
stress–strain	355		
elastic shear stress–strain characteristics	355		
Liquid			
composite molding (LCM)	309		
crystal	23		
temperature	22		
Load transmission capability	354		
Local			
plastic deformation	183		

## Index Terms

## Links

Local (*Cont.*)

ply coordinate (principal material coordinate)	111
thermodynamic equilibrium	384
Log decrement	617
Long fiber	14
Longitudinal compressive strength of composite	276
extensional mode microbuckling	278
shear failure	283
shear mode microbuckling	280
transverse tensile rupture direction	282      283
Longitudinal tensile strength of composite	
critical volume fraction	276
fiber dominated failure	275      276
loss angle	303
matrix dominated failure	275      276
Loss factor	567      617
Low-energy impact	416
Low-profile additives	40
Low-velocity impact	416
Lower triangular matrix	459

## **M**

Machinability	358
Machine tool	565
Machine tool dynamics	565
Machining	336
Macromechanics	64
Macromolecular chains	25
Magnetic density	584      585      588
flux density	588

<u>Index Terms</u>	<u>Links</u>			
Magnetic ( <i>Cont.</i> )				
intensity	584	586	589	590
permeability	583	586		
powder epoxy composite	583	586		
Magnetization	583	586		
Magnetizing reactance	590	594	595	
Magnetomotive force	591			
Major Poisson's ratio of the laminate	124	126		
Maleic anhydride	28	33		
Mandrel	32	53		
Manufacturing of composite bumper beam	639			
Mapping	458			
Mass balance equation	314			
Mass flow rate	569	570		
Master design matrix for trenchless sewage				
pipe repair	662			
Material removal rate	3	43		
Matrix	14	26		
cracking	159	434		
digestion method	42	419		
weight fraction	42			
Maturation	39			
Maximum allowable tolerance	479			
Maximum				
strain criterion	165			
stress criterion	160			
stress failure criterion	160			
Mean stress, effect on fatigue life	431			
Mechanical				
abrasion	375			
bonding	36			
fastener	346			
interlocking	35			

## Index Terms

## Links

Mechanical ( <i>Cont.</i> )		
joining	345	
joint	345	
Melt spinning	23	
Melt-crystallized polyethylene	25	
Mercury seal	25	
Mesophase	23	
Metal cutting stability	600	
Methyl ethyl ketone peroxide (MEKPO)	28	669
Methylene chloride	36	
Microcellular	487	
plastics advantages	502	
plastics batch process	488	
Microchipping	343	
Micromechanics	64	
Midplane strain	113	123
Minimization of FRs	482	
Minimum set of independent requirement	456	
Minor Poisson's ratio of the laminate	124	126
Mixed chopped and continuous fibers		
(mixed fiber)	15	
Mode of fatigue crack growth	427	
Moisture	442	
absorption	113	380
concentration	113	307
diffusion	309	383
Mold closing speed	316	
Moldability	38	
Molten glass	22	
Moment of inertia	21	
Moments per unit length	118	
Monoclinic	76	
Monocrystalline fibers	18	

## Index Terms

## Links

Multidirectional continuous fiber composite	14
Multilayered composites or laminates	14
Multilinear elastic strain-hardening characteristics	335
Multilinear strain-hardening approximation	365
Mutual influence of the laminate	124
	126

## **N**

Nanomechanics	64
Narrow beam	241
National aeronautics and space agency (NASA)	449
Natural frequency damped	225
experimental data	538
of simply supported symmetric plate	219
of the composite laminate plate	223
Natural generalization of Hooke's law	72
Natural vibration (of a beam)	232
Navier approach	239
solution (for rectangular plates)	211
Navier–Stokes equation	312
Netting analysis	131
Neutral axis	237
Neutral axis (of narrow beam)	245
Neutral surface (of laminated plate)	206
Nomex	31
Non-cross-linked resins	32
Noncrystalline material	21
Nondimensional stress deviation factor	368
Nonlinear behavior of adhesive	354

## Index Terms

## Links

Normal shelf life	37		
Novolac	32		
Nucleation	56	493	494
Number of classes	258		
Nylon	26	33	

## **O**

Optimum scheduling	485	
Orbital space plane (OSP)	449	
Organic fibers	25	
Organic peroxide	28	
Organosilanes	22	
Oriented polyethylene fibers	25	
Orowan–Irwin fracture criterion	193	
Orthophthalic	28	
Orthotropic	64	
Orthotropic material	113	140
Out-of-plane shear	184	

## **P**

Packing		
array	298	
efficiency	294	
pressure	502	
Pad of bumper beams	634	
PAN-based carbon fiber	24	
Parabenoquinone	39	
Particulate reinforcement	14	
Path dependence of uncoupled and decoupled design	483	
Path independence of uncoupled design	483	
Peel stress	36	352
Penetration rate	339	

<u>Index Terms</u>	<u>Links</u>
Permeability	290      313
for trenchless sewage pipe repair	659
matrix	313
of vacuum	302
Periodic complexity	480      485
Petroleum	23
Phase	
angle	303
difference	303
Phenolic resin	31
Photoreactive resin	505
Physical domain	461      465      484
Pigments	37      41
Planar	
moment	118
stress	115
strain	240
Plasma surface treatment	383
Plastic work per unit area	193
Plate, simply supported	239
Platinum orifice	21
Plunge cut grinding	340
Ply	64
angle	111      115      125
stress	153
thermal influence coefficient	141
thickness	115
Ply coordinate (principal material	
coordinate)	111
Point-stress criterion	188
Poisson's effect	241
Poisson's ratio	147      167
Polar winding	322

<u>Index Terms</u>	<u>Links</u>
Polyacrylate copolymers	40
Polyacrylonitrile (PAN)	23
Polyamideimide (PAI)	33
Polyarylsulfone	33
Polybutylene terephthalate (PBT)	33
Polycaprolactone	40
Polycarbonate	33
Polyetherether ketone (PEEK)	33
Polyethylene	25
Polyethylene terephthalate (PET)	33
Polyimides	32      33      353
Polymer matrix composite (PMC)	27
Polymer pyrolysis	25
Polymeric chains	25
Polymeric composite structure	113
Polymeric fibers	19
Polymeric matrix	113
Polymerization	27
Polymerize	23
Polyphenylene sulfide (PPS)	33
Polypropylene	33
Polystyrene	33
Polyurethanes	31
Polyvinylacetate	40
Porous release cloth	52
Potential energy due to a deflection	228
Power dissipation	566      593
Preform for trenchless sewage pipe repair	31
Preinjection mixing ratio	311
Preload for propeller shaft	623      671
Prepreg	30      37      51
Primer	36      353
Principal material coordinate	89      111      153

<u>Index Terms</u>		<u>Links</u>	
Probability density function (PDF)	256	260	
Probability of success	471		
Process design	459		
Process domain	454		
Process variables	454	455	
Product design	458		
Propagation energy	418		
Propeller shaft (or drive shaft)	15	623	
Propylene glycol	28		
Pseudoplastic behavior	346		
Pulling force	326		
Pull-out	343	346	
Pull system	485		
Pull winding	55		
Pultrusion	37	53	324
Push system	485		
Pyrolysis	23		
Pyrolytic graphite-coated carbon-fiber core	25		
<b>Q</b>			
Quadratic delamination criterion	180		
Quality factor (dynamic amplification factor)	617		
Quasi-isotropic laminate	131		
<b>R</b>			
Racetracking in mold filling process	311		
Racetrack polar winding	322		
Radial clearance	590	591	
Radial resin flow velocity	323		
Radial stiffness of the angular contact ball bearing	527	528	
Rake angle	336		

<u>Index Terms</u>	<u>Links</u>
Random coil configuration	25
Random variable	258
Random variation	476
Rate	
of cure	295      296
of deformation of SMC	319
of degree of cure	328
Rayon	23
Reaction heat	295
Reaction injection molding (RIM)	55
Ready-to-mold fiber-reinforced	
polymer sheets	37
Reduced stiffness	96
Redundant design	461      463      483
Reheating stop	328
Reinforcement	14      18
Reinforcement–matrix interaction	34
Relative permeability	659
Release rate	344
Reliability (cumulative distribution function	
for survival)	261      290      291      298
Representative volume element (RVE)	267
Residual strength	436
Residual stress	624      627
Residual stress in hybrid propeller shaft	627
Residual thermal stress	352      624
Resin	
curing process	295
flow	290      291      312
flow during trenchless	
sewage pipe repair	659
penetration	325

## Index Terms

## Links

Resin ( <i>Cont.</i> )			
transfer molding (RTM)	55	310	659
volume	291		
Resistance of			
the material to extension deformation	320		
the material to transverse shear	320		
Resistivity	584	585	
Resole resins	32		
Rigidity of			
isotropic symmetric			
sandwich structure	235	236	
sandwich structure with			
dissimilar faces	237	238	
Ring structures	32	33	
Ritz method	227		
Rivet	347		
Robot (definitions and classifications)	513	514	
Robust design	473	474	477
Robustness of design	484		
Rod (definition)	240		
Rounding wear	337		
Roving	53	321	
RTM	19	310	
for underground large composite			
structures	659		
Rubber-toughened adhesive	352	354	355
Rule of mixtures (ROM)	43	182	272
<b>S</b>			
Sample standard deviation	258		
Sandwich			
plate (on an elastic foundation)	238		

## Index Terms

## Links

Sandwich ( <i>Cont.</i> )					
structure	15	234	566	609	
	612				
structure, applications in the robot	518				
structures (with dissimilar faces)	237				
SCARA					
robot	18	525			
type robot	514	525			
Scarf adhesive joint	352	353			
SDOF (single-degree-of-freedom system)	223	224			
Secondary ion mass spectroscopy (SIMS)	391				
Self-excitation vibration (chatter)	565	605	606	615	
Self-tapping screw	347				
SEM	370	371			
S-glass	22				
Shattered chip	337				
Shear					
correction factor	213				
coupling	241				
coupling coefficient of the					
quasi-isotropic laminate	131				
failure (of mechanical joint)	347				
force (of narrow beam)	242				
rate	297				
strength versus fiber volume fraction	420				
stress	352				
stress (in the box-type beam)	251				
Sheet molding compound (SMC)	19	37	50	315	
	503	504			
Short fiber	14				
Short-range network structure	21				
Shrinkage	28				
stress	353				

<u>Index Terms</u>	<u>Links</u>
Side-door impact beam	642
Side-relief face	337
Silane coupling	36
Silica	21
Silicon	
carbide fiber	25
simultaneous engineering	468
steel rotor	583
	584
	591
	593
Simple bending theory	21
Simply supported edge (boundary condition of a plate)	210
Simply supported symmetric plate	216
Single crystalline region	33
Single edge-notched tension	187
Single-lap adhesive joint	352
Single-strap adhesive joint	353
Single-stage resin	32
Singularity	178
Sink mark	29
Sinking method	345
Slip speed	593
Slip speed	596
Slip speed	597
Sol-gel technique	25
Solution-neutral environment	455
Solvent	37
Sonotrode	343
Specially orthotropic laminate	208
Specific	
cutting force (specific cutting power)	600
damping capacity	617
moisture asorption	121
moisture concentration	131
	307

## Index Terms

## Links

Specific ( <i>Cont.</i> )					
relative permeability	586				
stiffness	16	46	567	597	
	598	609			
strength	16	46			
surface energy	192				
<i>Spectra</i> ® (AlliedSignal)	25				
Splintered chip	337				
Squirrel cage	587	591			
Stability (of simply supported					
symmetric plate)	217				
Stability limit	565	607	608		
Stacking sequence	66	579			
Standard deviation	258				
Starch–oil emulsion	22				
Static characteristics of side-door					
impact beam	644				
Static stiffness	565	568	574	575	
	607				
Steady flow	292				
Steel					
belt in the SCARA-type robot	536	537			
cover	601	602	604		
cover thickness	601	602	604		
Stepped-lap adhesive joint	352	353			
Stiffness	474				
Stiffness design	565				
Stiffness matrix	75	117	125	152	
for sandwich structure	234				
Stiffness of the preloaded angular contact					
ball	527				
Stiffness transformation equation	93				

## Index Terms

## Links

### Strain

axial strain of the box-type beam	250
capability	352
control	426
distribution of narrow beam	244
energy (of an elastic body)	227
energy release rate	192
in flange of the box-type beam	249
in web of the box-type beam	249
of symmetric laminate without in-plane force	247
of the laminate plate	112      208
transformation matrix	92
variation	115

### Strand

Strap adhesive joint	353
Strength design	152      196

### Strength properties of the quasi-isotropic

composite	186
-----------	-----

### Strength tensors

### Strength versus fiber volume

fraction	420
----------	-----

### Stress

concentration	352	360	374
concentration factor	189		
distribution	130	138	
failure criterion	161		
gradient	114		
intensity factor	190		
ratio on fatigue strength	430		
transformation matrix	90		
variation	114		

### Stretching response

<u>Index Terms</u>	<u>Links</u>		
Structural flexibility	23		
Structural reaction injection molding (SRIM)	57	310	311
Styrene monomer	32	661	662
Styrene–butadiene copolymer	41		
Supercritical fluid	493		
Sum of information	484		
Surface			
active agents (coupling agent)	36		
deposit-oxide film	375		
energy	192		
free energy	35	384	
modification	26		
roughness	36	375	
treatment	26	375	
Swelling coefficient	309		
Symmetric sandwich structure	235		
Symmetric laminate	66	175	
Symmetrically laminated beam	240	241	
Synthetic composites	15		
System			
constraint	460	461	
probability density function (PDF)	470		
range	470		
<b>T</b>			
Talc	38		
Tapered			
end beam of bumper beams	639	640	
end beam buckling test	639	640	
end beam compression test	639	640	
Target flexibility	410		

## Index Terms

## Links

Tarpaulin film for trenchless sewage pipe repair	662	
Teflon	51	522
Temperature gradient	300	307
Tension failure (of mechanical joint)	346	351
Tensioning mechanism in the SCARA-type robot	537	
Tension–tension fatigue	428	
Tension–tension $S$ – $N$ curve	428	
Tensor		
notation	114	
transformation relation	140	
Theorem	455	
Theoretical cohesive strength	19	
Theoretical stress concentration factor	189	
Thermal		
bending influence coefficient matrix	119	
bending moment	120	
conductivity	298	338
contraction ratio	40	
force	118	
influence coefficient	117	
in-plane influence coefficient	114	119
residual stress	141	
residual stress in hybrid propeller shaft	627	
resistance	298	
shrinkage	40	
Thermodynamic equilibrium	490	493
Thermoplastic injection molding (TIM)	55	
Thermoplastic polymers	27	33
Thermosets	27	
Thermosetting polymers	27	

<u>Index Terms</u>	<u>Links</u>		
Thick composite laminate	327		
Thickener	39		
Thickening agents	37		
Thickness integral	115	118	
Three-piece molds	534	535	
Three-point bending	645		
Through-thickness strain	146		
Time-dependent			
combinational complexity	480		
periodic complexity	480		
Time-independent			
real complexity	479		
imaginary complexity	480		
Tolerance	474		
Toluene diisocyanate	36		
Tool wear	565		
Torque transmission capability			
of hybrid propeller shaft	361	623	627
Torsional fatigue	433		
Torsional rigidity (of the box-type beam)	251		
Torsional shear strain-cycle diagram	434		
Torsional S–N diagram	433		
Toughness	15		
Tow	53	321	
Traction-free condition	177		
Transformation matrix	89		
Transformed constitute equation	102		
Transmission shaft (drive shaft) in the			
robot	540	545	
Transport phenomena	328		
Transverse			
direction	46		
modulus	44		

## Index Terms

## Links

Transverse ( <i>Cont.</i> )		
modulus of the laminate	124	125
moment (of narrow beam)	241	
shear deformation	207	217
shear deformation (in dynamic analysis of composite)	221	
shear deformation (in static analysis of composite)	219	
shear force	204	
shear stress	219	
Transversely isotropic	79	
Traveling wire electrode process	345	
Trenchless sewage pipe repair		
by RTM	657	
development through design axioms	657	
Tresca theory	160	
Triangular matrix	459	462
Triclinic material	76	
Trimming	336	
Truss core	234	
Tsai–Hill criterion	167	
Tsai–Wu tensor failure criterion	169	
Tubular double-lap joint	371	
Tubular single-lap joint	357	
Tungsten carbide boring bar	597	598
Twisting moment (of narrow beam)	241	
Two-parameter exponential approximation		
of adhesive	335	
Two-parameter shear stress–strain		
characteristics	360	
Two-stage resins	32	

## Index Terms

## Links

### **U**

Ultrasonic machining	343
Ultraviolet	28
absorbers	41
surface treatment	390
Uncoupled design	459
with less information	483
Unidirectional continuous fiber composite	14
Unidirectional (UD) lamina	64
Unsaturated points	32
Unsaturated polyester resin	28
Upper triangular matrix	459
Use of standardization	482
Use of symmetry	482
USM foam molding process	507

### **V**

Vacuum-assisted molding	315
Vacuum-assisted RTM (VARTM)	310
Vacuum bag degassing process	52
Vacuum bagging process	51
Van der Waals type bond	23
Variance	474
Velocity profile	320
Vibrating sample magnetometer (VSM)	584
Vibration	
of simply supported symmetric plate	217
of a composite laminate subjected to	
dynamic lateral load	223
Vinyl esters	32
Vinylsilane	36
Viscoelastic	27
Viscosity of a thermosetting resin	297

<u>Index Terms</u>	<u>Links</u>	
Viscous damping factor	225	
Void ratio	291	
Void volume	291	
Volatile	32	
Volume		
flow rate	568	569
susceptibility	584	
Von Mises theory	160	
<b>W</b>		
Warpage	148	
Water jet machining	342	343
Water-resistant polyester glass-fiber		
composite	20	
Waviness	339	
Weak core	237	
Web (definition)	248	
Web core	234	
Weber number	492	
Weibull		
distribution	260	
distribution scale (location) parameter	260	
distribution shape parameter	260	
parameters of composite materials	272	
Weight fraction	42	
Wet		
grinding	340	
winding	53	321
Wettability	35	
Wetting of matrix into fiber	35	659
Whirling of propeller shaft	623	
Whirling vibration	567	568
Whisker	18	582

<u>Index Terms</u>	<u>Links</u>
Whitney–Nuismer failure criterion	188
Wide beam	245
Winding angle	322
Woven fabric continuous fiber	
composite	14
Wrist of the robot	520
Wrist of the handling robot	513
	520
	539
<b>X</b>	
X-Ray photoelectron spectroscopy (XPS)	3
	91
<b>Y</b>	
Yarn	53
tension	325
Young's equation	35
<b>Z</b>	
Zigzagging	461
	465
	466